REPORT DOCUMENTATION PAGE

AFRL-SR-AR-TR-02-

Public reporting burden for this collection of information is estimated to average 1 hour per response, including the time for reviewing instructions, searching existing the collection of information. Send comments regarding this burden estimate or any other aspect of this collection of information, including suggestions for re Operations and Reports, 1215 Jefferson Davis Highway, Suite 1204, Arlington, VA 22202-4302, and to the Office of Management and Budget, Paperwork Reductic

0416

1. AGENCY USE ONLY *(Leave blank)*

2. REPORT DATE
DEC-15-2001

3. REPORT TYPE AND DATES COVERED
FINAL (01-DEC-2000 TO 30-NOV-2001)

4. TITLE AND SUBTITLE
THIRD AFOSR INTERNATIONAL CONFERENCE ON DNS/LES

5. FUNDING NUMBERS
F49620-01-1-0065

6. AUTHOR(S)
DR. CHAOQUN LIU

7. PERFORMING ORGANIZATION NAME(S) AND ADDRESS(ES)
UNIVERSITY OF TEXAS AT ARLINGTON
DEPARTMENT OF MATHEMATICS
BOX 19408
ARLINGTON, TX 76019-0408

8. PERFORMING ORGANIZATION REPORT NUMBER

9. SPONSORING/MONITORING AGENCY NAME(S) AND ADDRESS(ES)

AFOSR/NA
4015 WILSON BLVD, RM 713
ARLINGTON, VA 22203

10. SPONSORING/MONITORING AGENCY REPORT NUMBER

11. SUPPLEMENTARY NOTES

12a. DISTRIBUTION AVAILABILITY STATEMENT

Approved for public release;
distribution unlimited.

12b. DISTRIBUTION CODE

Copyright 2001 by Chaoqun Liu, University of Texas at Arlington.
This work relates to Department of the Air Force Grant F49620-01-1-0065 issued by Air Force Office of Scientific Research. The United States Government has a royalty-free license throughout the world in all copyrightable material contained herein.

13. ABSTRACT *(Maximum 200 words)*

This is the third time for worldwide DNS/LES experts to get together to introduce research progress, exchange ideas, and discuss future research directions since the US Air Force Office of Scientific Research (A.FOSR) sponsored the First AFOSF. International Conference on DNSILES (FAICDL) at Louisiana Tech University in 1997. The second conference was held at Rutgers - The State University of New Jersey in 1999. I am very pleased that many scientists and engineers are interested in this conference. I have received over 90 regular papers, in addition to 19 invited papers. It clearly shows that the DNS/LES community is much larger than ever before.

Significant progress has been achieved during the past decade. It is difficult to give a complete review in this area. People may take a reference from reviews by Moin & Mehesh (1998) for DNS and Leseiur & Metais (1996) and Piomelli (1999) for LES. Sagaut (2000) just published a LES book, which gives discussions on many issues related to LES. It is also very difficult to invite all of the important contributors to give invited lectures for the conference. During this conference, Germano will give a review on LES; Visbal and Gatski will talk about Air Force and NASA needs on DNSILES and their applications; Sagaut, Kato, and Shan will talk about complicated configurations and industrial application; Jolsin will talk about DNS for flow control; Adams and Thong about high speed flow transitions; Givi about LES for reacting flow, Shu and Jiang about high order discretization, Karniadakis about DNS for unstructured grids; Vasilyev about some important LES constrains. In addition, Knight, Piomelli, Satofuka, Verstappen will also give lectures about their own distinguished work.

14. SUBJECT TERMS

15. NUMBER OF PAGES
16

16. PRICE CODE

17. SECURITY CLASSIFICATION OF REPORT	18. SECURITY CLASSIFICATION OF THIS PAGE	19. SECURITY CLASSIFICATION OF ABSTRACT	20. LIMITATION OF ABSTRACT
UNCLASSIFIED	UNCLASSIFIED	UNCLASSIFIED	

Final Report for

Third AFOSR International Conference on DNS/LES

(Grant No. F49620-01-1-0065)

From
Dr. Chaoqun Liu, Professor
Department of mathematics
Box 19408
University of Texas at Arlington
Arlington, TX 76019-0408
Tel: (817) 272-5151
Fax (817) 272-5802
Email: cliu@omega.uta.edu



To
Dr. Tom Beutner
Program Manager
AFOSR/NA
801 North Randolph Street
Arlington, VA 22203-1977
Phone : (703) 696-6961
Fax: (703) 696-8451
Email tom.beutner@afosr.af.mil

Dec. 15, 2001

20021227 001

Third AFOSR International Conference on
Direct Numerical Simulation and Large Eddy Simulation
(TAICDL)
University of Texas at Arlington
August 5-9, 2001

1. Conference Location and Date:

The conference was held at Nedderman Hall, University of Texas at Arlington on August 5-9, 2001. The conference chairperson is Chaoqun Liu, Professor of UTA and PI of this grant.

2. Conference Participants:

The conference attracted 104 participants from 15 countries and regions all over the world. Dr. Tom Beutner from AFOSR attended the conference and gave a welcome speech at the opening ceremony. A full list of all participants is attached as appendix A.

3. Conference Presentations and Proceedings:

We have 18 invited papers (appendix B) and 70 regular contributions. Most of invited speakers are worldwide recognized experts. A conference schedule can be found from the attached abstracts book. All papers presented in the conference have been collected as a book titled as 'DNS/LES – Progress and Challenges' and edited by Liu, Sakell, and Beutner, which is published by Greyden Press, a scientific publisher at Columbus, Ohio.

4. Scientific advisory committee:

The committee consists of 30 people form 14 countries including Dr. Sakell and Dr. Herklotz from AFOSR. Most of committee members are worldwide well-known experts on DNS/LES. A committee member list is attached as appendix C.

5. Local organizing committee:

The local committee was formed by 9 personnel from UTA. Most of them are UTA students. A committee member list is attached as appendix D.

6. Sponsorship:

AFOSR International Conference on Direct Numerical Simulation (DNS) and Large Eddy Simulation (LES) is a major international conference focused solely on the development and application of DNS and LES, and sponsored by the US Air Force Office of Scientific Research (AFOSR). AFOSR provided a grant of $15,000, Lockheed-Martine Aeronautics gave a support of $5,000 in cash, and UTA provided space, equipment, and secretary support for the conference.

7. Conference History:

The first conference was held in August 1997 at Louisiana Tech University, Ruston, LA. The written papers were published in 'Advances in DNS/LES,' Greyden Press, 1997. The second conference was held on June 7-9, 1999 in Rutgers - The State University of New Jersey, New Brunswick, New Jersey. Contributions were published in 'Recent Advances in DNS and LES', Kluwer Academic Publishers, 1999.

Appendix A. CONFERENCE PARTICIPANTS

Adams, Nikolaus
Swiss Federal Institute of Technology
Institute of Fluid Dynamics
ETH Zentrum, CH-8092 Zurich
Switzerland
Tel: +4116325271
Fax: +4116321147
Email: Nikolaus.Adams@ethz.ch

Amati, Giorgio
CASPUR
P.le Aldo Moro 5
Roma 1-00-185
Italy
Tel: 0039-06-4991-13095
Fax: 0039-06-4957083
Email: g.amati@caspur.it

Arunajatesan, Srinivasan
Combustion Research and
Flow Technology, Inc
174 N. Main St, P O Box 1150
Dublin, PA 18917, USA
Tel: 215-249-9780
Fax: 215-249-9796
Email: ajs@craft-tech.com

Avancha, Ravikanth
2025 H.M. Black Eng. Building
Iowa State University
Ames, IA 50011
USA
Tel: 515-292-6954
Fax: 515-294-3261
Email: ark@iastate.edu

Bernfeld, Stephen R.
Department of Mathematics
Box 19408
University of Texas at Arlington
Arlington, TX 76019, USA
Tel: 817-272-5682
Fax: 817-272-5802
Email: bernfeld@uta.edu

Beutner, Thomas
AFOSR/NA
801 N. Randolph St
Arlington, VA 22203-1977
USA
Tel: 703-696-6961
Fax: 703-696-8451
Email: tom.beutner@afosr.af.mil

Boersma, Bendiks Jan
Delft University of Technology
Mekelweg 2, 2628 CD Delft
The Netherlands
Tel: +31 15 2787979
Fax: +31 15 2782947
Email: b.j.boersma@wbmt.tudelft.nl

Blaisdell, Gregory A.
Purdue University
West Lafayette, IN 47907-1282
USA
Tel: 765- 494-1490
Fax: 765- 494-0307
Email: blaisdel@ecn.purdue.edu

Braun, Carsten
Mechanics Department
RWTH Aachen, Templegraben 64
Aachen 52062, Germany
Tel: 49 (0)241 80-4637
Fax: 49 (0)241 8888126
Email: carsten@lufmech.rwth-aachen.de

Broglia, Riccardp
INSEAN
Via di Vallerano 139
Rome 00128
Italy
Tel: +39-06-50299297
Fax: +39-06-5070619
Email: r.broglia@insean.it

Calhoon, Jr., William
Combustion Research and Flow Technology, Inc.
174 N. Main St., P O Box 1150
Dublin, PA 18917, USA
Tel: 215-249-9780
Fax: 215-249-9796, Email: calhoon@cfd.rdec.redstone.army.mil

Chelyshkov, Vladimir S.
Deparment of Mathematics
University of New Orleans
New Orleans, LA 40148
USA
Tel: 504-280-7498
Fax: 504-280-5516
Email: vchelysh@uno.edu

Chern, Shuhyi
Lockheed Martin
P O Box 179
Mail Stop TSB5009
Denver, CO. 80201
USA
Tel: 303-971-4279
Email: shuhyi.y.chern@lmco.com

Choi, Haecheon
School of Mechanical and Aerospace Engineering
Seoul National University
Seoul 151-742, Korea
Tel: 82-2-880-8361
Fax: 82-2-878-3662
Email: choi@socrates.snu.ac.kr

Chyczewski, Thomas
Applied Research Laboratory
Penn State Univ.
P O Box 30
State College, PA 16804
USA
Tel: 814-865-2251
Fax: 814-865-8896
Email: tsc@wt.arl.psu.edu

Das, A.
Department of Theoretical and Applied Mechanics
Univ. of Illinois
at Urbana-Champaign
104 S. Wright St.
Urbana, IL 61081, USA
Tel: 217-333-3578
Email: arupdas@uiuc.edu

De Lange, H.C.
Section Engergy Technology
Dept. of Mechanical Engineering
Eindhoven University of Technology
P O Box 513 (wh 3.128)
Eindhoven, The Netherlands
Tel: +31-247-2129
Fax: +31-2433445
Email: h.c.d.lange@tue.nl

Debliquy, Olivier
Universite Libre de Bruxelles
Physique Statistique et Plasmas
Boulevard du Triomphe
Campus Plaine-CP.231
B-1050 Bruxelles, Belgium
Tel: 32-2-650.59.08
Fax: 32-2-650.58.24
Email: odebliqu@ulb.ac.be

Deng, Shutian
Department of Mathematics
Box 19408
University of Texas at Arlington
Arlington, TX 76019
USA
Tel: 817-272-3261
Fax: 817-272-5802
Email: deng_shutian@yahoo.com

De Stefano, Giuliano
Dipartimento di Ingegneria Aerospaziale
Seconda Universita' di Napoli
via Roma 29, 81031 Aversa
Italy
Tel: 0039 081 5010265
Fax: 0039 081 5010264
Email: giuliano.destefano@unina2.it

Dyer, Danny
Mathematics Department
University of Texas at Arlington
Box 19408
Arlington, TX 76019
USA
Tel: 817-272-3246
Fax: 817-272-5802
Email: dyer@uta.edu

Ertem-Müller, Senem
Darmstadt University of Technology,
Department of Numerical Methods in
Mechanical Engineering,
Petersenstr. 30, 64287 Darmstadt
Germany
Tel: 0049-6151-162879
Fax: 0049-6151-164479
Email: ertem@fnb.tu-darmstadt.de

Eshpuniyani, Brijesh
School of Aeronautics
and Astronautics
Purdue University
West Lafayette, IN 47907-1282
USA
Tel: (765) 494-7864
Fax: : 765-494-0307
Email: eshpuniy@ecn.purdue.edu

Felten, Frederic N.
Department of Mechanical
Engineering
Box 19019
University of Texas at Arlington
Arlington, TX 76010-0019
USA
Tel: 817-272-2860
Email: felten@surya.uta.edu

Garnier, Eric
ONERA D.A.A.P/M.H.L.
29, Avenue de la Division Leclerc
BP72
92322 Chatillon cedex
France
Tel: 01.46.73.42.65
Email: Eric.Garnier@onera.fr

Garrick, Sean C.
Dept. of Mechanical Engineering
111 Church Street S. E.
University of Minnesota-Twin Cities
Minneapolis, MN 55455-0111, USA
Tel: 612-624-5741
Fax: 612-624-5230
Email: garrick@me.umn.edu

Gatski, Thomas B.
M/S 128, Computational Modeling &
Simulation Branch
NASA Langley Research Center
Hampton, VA 23681-2199
USA
Tel: 757-864-5552
Fax: 757-864-8816
Email: t.b.gatski@larc.nasa.gov

Germano, Massimo
Politecnico di Torino
Dip. Ing. Aeronautica e Spaziale –
DIASP -
C.so Duca degli Abruzzi, 24
10129 Torino, Italy
Tel: +39 011 564.6814
Fax: +39 011 564.6899
Email: germano@polito.it

Givi, Peyman
Mech. and Aero. Engineering
State University of New York at
Buffalo, Buffalo, NY 14260-4400
USA
Tel: 716-645-2593 ex2320
Fax: 716-645-3875
Email: givi@eng.buffalo.edu

Goldstein, David
Dept. of Aerospace Engineering and
Engineering Mechanics
The University of Texas at Austin
Austin, TX 78712
USA
Tel: 512-471-4187
Email: david@cfdlab.ae.utexas.edu

Hamed, Awatef
Dept. of Aerospace Engineering and Engineering Mechanics
University of Cincinnati
Cincinnati, OH 45221-0070
USA
Tel: 513-556-3553
Fax: 513-556-5038
Email: a.hamed@uc.edu

Haselbacher, Andreas
Center for Simulation of Advanced Rockets
Univ. of Illinois at Urbana-Champaign
Urbana, IL 61801, USA
Tel: 217-333-8683
Fax: 217-333-8497
Email: haselbac@uiuc.edu

Higbee, Beverly
Mathematics Department
University of Texas at Arlington
Box 19408
Arlington, TX 76019
USA
Tel: 817-272-5259
Fax: 817-272-5802
Email: bjhigbee@uta.edu

Hoang, Ngocle
Math Department
Box 19408
University of Texas at Arlington
Arlington, TX 76019
USA
Tel: 817-272-7526
Fax: 817-272-5802
Email: hoangle@uta.edu

Huckaby, E. David
U.S. Department of Energy
National Energy Technology Laboratory, PO Box 880
Morgantown, WV 26507-0880
USA
Tel: 304-285-5457
Fax: 304-285-4403
Email: huckaby@netl.doe.gov

Iannelli, Pierluigi
Dipartimento di Ingegneria Aerospaziale
Seconda Universita di Napoli
81031 Aversa
Italy
Tel: +39 081 5010265
Fax: +39 081 5010264
Email: pierluigi.iannelli@unina2.it

Iliescu, Traian
Argonne National Laboratory
Bldg. 221, C-219, 9700 S. Cass Ave
Argonne, IL 60439
USA
Tel: 630-252-0926
Fax: 630-252-5986
Email: iliescu@mcs.anl.gov

Jenkins, Karl. W.
Cambridge University
Trumpington Street
Cambridge CB2 1PZ
UK
Tel: +44-0-1223-332748
Fax: +44-0-1223-332662
Email: kwj20@eng.cam.ac.uk

Jiang, Li
Department of Mathematics
Box 19408
University of Texas at Arlington
Arlington, TX 76019
USA
Tel: 817-272-7119
Fax: 817-272-5802
Email: ljiang@omega.uta.edu

Joslin, Ronald D.
Applied Research Laboratory
Penn State University
P.O. Box 30
State College, PA 16804
USA
Tel: 814-863-6128
Fax: 814-865-889
Email: RDJoslin@psu.edu

Kadjo, Hilaire
Department of Mathematics
Box 19408
University of Texas at Arlington
Arlington, TX 76019
USA
Tel: 817-801-7172
Fax: 817-272-5802
Email: hilaire@uta.edu

Kaltenbach, Hans-J.
Hermann-F"ottinger-Institut
Technische Universit"at Berlin
Sekretariat HF-1
Strasse des 17. Juni 135
D-10623 Berlin, Germany
Tel: +49-30-314 23463
Fax: +49-30-314-21101
Email: kaltenbach@pi.tu-berlin.de

Kannepalli, Chandrasekhar
Craft-Tech
1 Coliseum Dr
Room 1150
University, MS 38655
USA
Tel: 662-915-6748
Fax: 662-915-6745
Email: kchandra@olemiss.edu

Karniadakis, George
Division of Applied Mathematics
Box F
Brown University
Providence, RI 02912
USA
Tel: 401-863-1217
Fax: 401-863-3369
Email: gk@cfm.brown.edu

Kato, Chisachi
Institute of Industrial Science
University of Tokyo
4-6-1 Komaba Meguro-ku
Tokyo, 153-8505
Japan
Tel: +81-3-5452-6190
Fax: +81-3-5452-6191
Email: ckato@iis.u-tokyo.ac.jp

Kimmel, Shari J.
Department of Mechanical
Engineering and Mechanics
Lehigh University
Bethlehem, PA 18015-3085
USA
Tel: 610-758-4017
Fax: 610-758-6224
Email: sjk4@lehigh.edu

Klioutchnikov, Igor
Mechanics Department
RWTH Aachen
University of Technology
Templegraben 64, Aachen 52062
Germany
Tel: +49-0-241-80-4637
Email: klutchnikov@lufmech.rwth-aachen.de

Knaepen, Bernard
Université Libre de Bruxelles
Service de Physique Théorique
et Mathématique
Campus Plaine - CP 231
Boulevard du Triomphe
B-1050 Bruxelles, Belgium
Tel: 32-2-650.59.18
Email: bknaepen@ulb.ac.be

Knight, Doyle
Dept of Mech. and Aero. Engineering
Rutgers-The State University of New Jersey, 98 Brett Road
Piscataway, N.J. 08854-0858
USA
Tel: 732-445-4464
Fax: 732-445-3124
Email: ddknight@rci.rutgers.edu

Krajnovic, Sinisa
Department of Thermo and Fluid Dynamics
Chalmers University of Technology
SE-412 96 Goteborg
Sweden
Tel: +46-31-772-1400
Fax: +46-31-180-976
Email: sinisa@tfd.chalmers.se

Lacor, Chris
Department of Fluid Mechanics
Vrije Universiteit Brussel
Pleinlaan 2
1050 Brussel
Belgium
Tel: ++ 32.(0)2.629.23.79
Fax: ++ 32.(0)2.629.28.80
Email: chris.lacor@vub.ac.be

Ladeinde, Foluso
Director of Research
Aerospace Research Corp., LI
25 East Loop Road, Suite 202
P. O. Box 1527
Stony Brook, NY 11790
USA
Tel: 631-632-9293
Email: ladeinde@thaerocomp.com

Larcheveque, Lionel
ONERA-DSNA/ETRI
BP72-29 Avenue
de la division Leclerc
92322 Chatillon cedex
France
Tel: 33 (0)1 46 73 42 07
Email: lionel.larcheveque@onera.fr

Layton, William
Department of Mathematics
University of Pittsburgh
Pittsburgh, PA 15260
USA
Tel: 412-624-8312
Fax: 412-624-8397
Email: wjl@pitt.edu

Lei, Kangbin
Computer and Information Division
Advanced Computing Center, (RIKEN)
The Institute of Physical and Chemical Research, 2-1 Hirosawa
Wako-shi, Saitama 351-0198, Japan
Tel: +81-(0)48-462-1111 Ext. 3848
Fax: +81-(0)48-462-4634
Email: lei@riken.go.jp

Lessani, Bamdad
Department of Fluid Mechanics
Vrije Universiteit Brussel
Pleinlaan 2
1050 Brussel
Belgium
Tel: ++ 32.(0)2.629.29.94
Fax: ++ 32.(0)2.629.28.80
Email: bamdad@stro.vub.ac.be

Liao, Guojun
Department of Mathematics
Box 19408
University of Texas at Arlington
Arlington, TX 76019
USA
Tel: 817-272-2647
Fax: 817-272-5802
Email: liao@uta.edu

Liu, Yue
Department of Mathematics
Box 19408
University of Texas at Arlington
Arlington, TX 76019
USA
Tel: 817-272-5680
Fax: 817-272-5802
Email: yliu@uta.edu

Liu, Chaoqun
Department of Mathematics
Box 19408
University of Texas at Arlington
Arlington, TX 76019
USA
Tel: 817-272-7527
Fax: 817-272-5802
Email: cliu@uta.edu

Lund, Thomas S.
Dept of Mech. and Aero. Engineering
Box 19018
University of Texas at Arlington
Arlington, TX 76019-0018
USA
Tel: 817-272-7053
Fax: 817-272-5010
Email: lund@uta.edu

Luo, Sheng
Department of Mathematics
University of Texas at Arlington
Box 19408
Arlington, TX 76019
USA
Tel: 817-272-7527
Fax: 817-272-5802
Email: sluo@uta.edu

Madnia, Cyrus K.
Dept of Mech. and Aero. Engineering
State University of New York at
Buffalo
Buffalo, NY 14260
USA
Tel: 716-645-2593 ext. 2315
Fax: 716-645-3875
Email: madnia@eng.buffalo.edu

Mallier, Roland
Department of Applied Mathematics
University of Western Ontario
London, ON N6A 5B7
Canada
Tel: 519-473-6133
Fax: 519-661-3523
Email: mallier@uwo.ca

Martin, M. Pino
Princeton University
Mech. and Aero. Engineering
D_307 Engineering Quadrangle
Olden Street, Princeton, NJ 08544
Tel: 609 258-7318
Fax: 609 258-6109
Email: pmartin@princeton.edu

Mavriplis, Dimitri
ICASE MS 132C
NASA Langley Research Center
Hampton, VA 23681
USA
Tel: 757-864-2213
Fax: 757-864-6134
Email: dimitri@icase.edu

Meinke, Matthias
Aerodynaisches Institut
RWTH Aachen, 52062 Aachen
Wullnerstr.zw 5 u. 7
Germany
Tel: +49-241-805417
Fax: +49-241-8888257
Email: matthias@aia.rwth-aachen.de

Meng, Ning
2200 Waterview Pkwy. #1826
Richardson, TX 75080
USA
Email: nmeng@iastate.edu

Mitchell, Brian
GE Corporate Research
and Development
P O Box 8, Bldg. K1-ES203
Schenectady, NY 12301
USA
Tel: 518-387-7845
Fax: 518-387-7104
Email: mitchellb@crd.ge.com

Mitran, Sorin M.
Department of Applied Mathematics
University of Washington
Box 352420
Office 408C
Seattle, WA 98195-2420
USA
Tel: 206-685-9298
Fax: 206-685-1440
Email: mitran@amath.washington.edu

Miyake, Yutaka
Department of Mechano-physics
Graduate School of Osaka University
2-1 Yamada-oka
Suita 565-0871
Japan
Tel: +81-6-6879-7248
Fax: +81-6-6879-7250
Email: miyake@mech.eng.osaka-u.ac.jp

Nakamori, Ichiro
Complex Flow Systems Laboratory
Complex Flow Division
Institute of Fluid Science
Tohoku University, Sendai
Japan
Tel: +81-22-217-5229
Fax: +81-22-217-5311
Email: nakamori@cfs.ifs.tohoku.ac.jp

Nakayama, Akihiko
Graduate School of Science and Technology
Kobe University
1-1 Rokkodai, Nada-ku
Kobe 657-8501
Japan
Fax: +81-78-803-6011
Email: nakayama@kobe-u.ac.jp

Pantelis, Garry
School of Aerospace
Mechanical and Mechatronic Eng.
University of Sydney
Sydney NSW 2006
Australia
Tel: +61-2-9351-2591
Fax: +61-2-9351-7060
Email: gpa@mech.eng.usyd.edu.au

Peltier, Leonard Joel
The Applied Research Laboratory
The Pennsylvania State University
P O Box 30
State College, PA 16804
USA
Tel: 814-863-3014
Fax: 814-865-8896
Email: ljp@wt.arl.psu.edu

Piller, Marzio
Dipartimento di Ingegneria Navale
del Mare e per l'Ambiente-Sezione
di Fisica Tecnica
University of Trieste, 34127 Trieste
Italy
Tel: +38-040-676-3502
Fax: +39-040-572033
Email: piller@univ.trieste.it

Piomelli, Ugo
Department Of Mechanical Engineering
University of Maryland
College Park, MD 20742
USA
Tel: 301-405-5254
Fax: 301-314-9477
Email: ugo@eng.umd.edu

Pletcher, Richard
Department of Mechanical Engineering
Iowa State University
Ames, IA 50011
USA
Tel: 515-294-2656
Fax: 515-294-3261
Email: pletcher@iastate.edu

Pruett, C. David
Dept. of Mathematics & Statistics
MSC 7803,
James Madison University
Harrisonburg, VA 22807, USA
Tel: 540-568-6227
Fax: 540-568-6857
Email: dpruett@math.jmu.edu

Rizzetta, Donald P.
AFRL/VAAC
Bldg. 146 Room 225
2210 Eight Street
WPAFB, OH 45433-7521
USA
Tel: 937-904-4077
Fax: 937-656-7867
Email: rizzetta@vaa.wpafb.af.mil

Sagaut, Pierre
ONERA
DSNA/ETRI
29, Avenue de la Division Leclerc
92320 Chatillon
France
Tel: (33) 01 46 73 42 71
Fax: (33) 01 46 73 41 66
Email: sagaut@onera.fr

Satofuka, Nobuyuki
Department of Mechanical Engineering
Kyoto Institute of Technology
Matsuzaki Gosho Kaidou-cho
Sakyou-ku,Kyoto 606-0962
Japan
Tel: +81-75-724-7312
Fax: +81-75-724-7390
Email: satofuka@ipc.kit.ac.jp

Shan, Hua
Department of Mathematics
Box 19408
University of Texas at Arlington
Arlington, TX 76019
USA
Tel: 817-272-7119
Fax: 817-272-5802
Email: hshan@omega.uta.edu

Shu, Chi-Wang
Division of Applied Mathematics
Brown University
Providence, RI 02912
USA
Tel: 401-863-2549
Fax: 401-863-1355
Email: shu@cfm.brown.edu

Smith, Brian R.
Lockheed Martin Aeronautics
P. O. Box 748, MZ 9333
Fort Worth, TX 76101
USA
Tel: 817-935-1127
Fax: 817-935-1212
Email: Brian.R.Smith@lmco.com

Sudduth, R.D.
Chemical Engineering
University of Louisiana at Lafayette
Lafayette, LA 70504
USA
Tel: 337-482-6837
Email: richsudduth@earthlink.net

Taniguchi, Nobuyuki
Institute of Industrial Science
University of Tokyo
4-6-1, Komaba, Meguro-Ku
Tokyo,153-8505, Japan
Tel: 81-3-5841-2741
Fax: 81-3-5452-6196
Email: ntani@iis.u-tokyo.ac.jp

Tokunaga, Hiroshi
Department of Mechanical & System Engineering
Kyoto Institute of Technology
Matsugasaki
Sakyo-ku, Kyoto 606-8585
Japan
Tel: 81+75-724-7314
Fax: 81+75-724-7300
Email: tokunaga@ipc.kit.ac.jp

Tsujimoto, Koichi
Department of Mechanical Engineering
Osaka University
2-1 Yamada-oka, Suita 565-0871
Japan
Fax: +81-6-6879-7250
Tel : +81-6-6879-7250
Email: tujimoto@mech.eng.osaka-u.ac.jp

Tyagi, Mayank
Mechanical Engineering Department
Louisiana State University
Baton Rouge, LA 70803
USA
Tel: 225-578-5217
Fax: 225-578-9195
Email: tyagi_mayank@hotmail.com

Uittenbogaard, Rob
Delft Hydraulics
P O Box 177
2600 M H Delft
The Netherlands
Tel: +31 15 285 87 81
Fax: +31 15 285 85 82
Email: rob.uittenbogaard@wldelft.nl

Vasilyev, Oleg V.
E2411 Engr. Bldg. East
Mechanical & Aerospace Engineering
University of Missouri-Columbia
Columbia, MO 65211, USA
Tel: 573-882-3755
Fax: 573-884-5090
Email: VasilyevO@missouri.edu

Veenman, M. P. B.
Section of Process Technology
Dept. of Mechanical Engineering
Eindhoven University of Technology
P.O. Box 513, 5600 MB Eindhoven
The Netherlands
Tel: +31-0-40-2472135
Email: M.P.B.Veenman@tue.nl

Verstappen, Roel
Dept. of Math
University of Groningen
P O Box800
Groningen NL-9700AV
The Netherlands
Tel: +31-503633958
Fax: +31-503633800
Email: verstappen@math.rug.nl

Visbal, Miguel R
AFRL/VAAC
Bldg. 146 Room 225
2210 Eight Street
WPAFB, OH 45433-7521
USA
Tel: 937-255-2551
Fax: 937-656-7867
Email: visbal@vaa.wpafb.af.mil

Wang, Liqiu
Department of Mechanical Engineering
The University of Hong Kong
Pokfulam Road
Hong Kong
Tel: 852-2859-7908
Email: lqwang@hku.hk

Xia, Jian
Department of Mathematics
University of Texas at Arlington
Arlington, TX 76019, USA
Tel: 817-272-7527
Fax: 817-272-5802
Email: jxia@uta.edu

Yan, Hong
Dept. Of Mech. and Aero. Engineering
Rutgers University-The State University
of New Jersey, 98 Brett Road
Piscataway, NJ 08854-8058
USA
Tel: 732-445-4351
Email: honyan@jove.rutgers.edu

Yarala, Pavan
Dept. of Chemical Engineering
University of Louisiana at Lafayette
Lafayette, LA 70504
USA
Tel: 337-482-6837
Email:
richard.d.sudduth@louisiana.edu

Yee, H. C.
NASA Ames Research Center
Mail Stop T27B-1
Moffett Field, CA 94035
USA
Tel: 650-604-4769
Fax: 650-604-1095
Email: yee@nas.nasa.gov

Yokojima, Satoshi
Division of Grobal Development Sci.
Graduate School of Sci. and Tech.
Kobe University, 1-1, Rokkodai,
Nada, Kobe 657-8501, Japan
Tel: +81-78-881-1212 Ext6280
Fax: +81-78-803-6011
Email: 970d925n@yku.kobe-u.ac.jp

Zajaczkowski, Frank J.
The Applied Research Laboratory
The Pennsylvania State University
P O Box 30
State College, PA 16804
USA
Tel: 814-863-5477
Fax: 814-865-8896
Email: fjz@wt.arl.psu.edu

Zhong, Xiaoling
Dept of Mech. and Aero. Engineering
Univ. of California at Los Angeles
46-147C, Engineering IV Building
405 Hilgard Avenue
Los Angeles, CA 90095-1597, USA
Tel: 310-825-2905
Fax: 310-206-4830
Email: xiaolin@seas.ucla.edu

Zhou, Xu
Dept. of Mech. and Aero. Engineering
Rutgers University-The State University
of New Jersey, 98 Brett Road
Piscataway, N.J. 08854-0858
USA
Tel: 732-445-4464
Fax: 732-445-3124
Email: zhou@pinky.rutgers.edu

Appendix B. INVITED SPEAKERS

Adams, Nikolaus	Swiss Federal Institute of Technology (Switzerland)
Beutner, Thomas	Air Force Office of Scientific Research
Gatski, Thomas B.	NASA Langley Research Center
Germano, Massimo	Politecnico di Torino (Italy)
Givi, Peyman	State University of New York at Buffalo
Jiang, Li	University of Texas at Arlington
Joslin, Ronald D.	Penn State University
Liu, Chaoqun	University of Texas at Arlington
Karniadakis, George	Brown University
Kato, Chisachi	University of Tokyo (Japan)
Knight, Doyle	Rutgers – The State University of New Jersey
Piomelli, Ugo	University of Maryland
Sagaut, Pierre	ONERA (France)
Satofuka, Nobuyuki	Kyoto Institute of Technology (Japan)
Shan, Hua	University of Texas at Arlington
Shu, Chi-Wang	Brown University
Vasilyev, Oleg V.	University of Missouri-Columbia
Verstappen, Roel	University of Groningen (the Netherlands)
Visbal, Miguel R.	WPAFB, AFRL/VAAC
Zhong, Xiaoling	University of California, Los Angeles

Appendic C. SCIENTIFIC ORGNIZING COMMITTEE

Liu, Chaoqun, Chair	University of Texas at Arlington
Sakell, Len, Co-Chair	Air Force Office of Scientific Research
Herklotz, Robert, Co-Chair	Air Force Office of Scientific Research
Adams, Nikolaus	Swiss Federal Institute of Technology (Switzerland)
Blaisdell, Gregory A.	Purdue University
Carati, Daniele	Universit Libre de Bruxelles (Belgium)
Chelyshkov, Vladimir	University of New Orleans
Chern, Shuhyi	Lockheed Martin
Dalton, Charles	University of Houston
Friedrich, Rainer	Technische University Muenchen (Germany)
Germano, Massimo	Politecnico di Torino (Italy)
Hadid, Ali	Boeing/Rocketdyne
Jimenez, Javier	U. Politecnica (Spain)
Johansson, Arnea	Royal Institute of Technology (Sweden)
Joslin, Ronald D.	Penn State University
Karniadakis, George	Brown University
Knight, Doyle	Rutgers – The State University of New Jersey
Kwak, Dochan	NASA Ames Research Center
Ladeinde, Foluso	Aerospace Research Corp., LI
Lee, Moon Joo	Pohang Univ. of Science and Technology (South Korea)
Lele, Sanjiva K.	Stanford University
Miyake, Yutaka	Osaka University (Japan)
Nieuwstadt, F.T.M.	Delft University of Technology (the Netherlands)
Pantelis, Garry	University of Sydney (Australia)
Piomelli, Ugo	University of Maryland
Sagaut, Pierre	ONERA (France)
Tam, Christopher	Florida State University
Visbal, Miguel R.	WPAFB, AFRL/VAAC
Voke, Peter	The University of Surrey (UK)
Zhang, Zhaoshun	Tsinghua University (China)

Appendix D. LOCAL ORGANIZING COMMITTEE

Deng, Shutian, PhD Student, Math, UTA
Higbee, Beverly, Coordinator, Administrative Assistant II, Math, UTA
Hoang, Ngocle, MS Student, Math, UTA
Jiang, Li, Research Associate, Math, UTA
Liu, Chaoqun, Professor, Math, UTA
Kadjo, Hilaire, PhD Student, Math, UTA
Luo, Sheng, PhD Student, Math, UTA
Shan, Hua, Research Associate, Math, UTA
Xia, Jian, Research Associate, Math, UTA

DNS/LES – Progress and Challenges

Proceedings of the Third AFOSR International Conference on DNS/LES

University of Texas at Arlington
Arlington, Texas, USA
August 5-9 2001

Edited by

Chaoqun Liu
Department of Mathematics
University of Texas at Arlington (UTA)
Arlington, TX 76019-0408, USA

Leonidas Sakell
US Air Force Office of Scientific Research (AFOSR)
Arlington, VA, USA

Thomas Beutner
US Air Force Office of Scientific Research (AFOSR)
Arlington, VA, USA

Conference Chair:	**Chaoqun Liu**
Conference Co-Chairs:	**Leonidas Sakell**
	Robert Herklotz

Greyden Press
Columbus

A C.I.P. Catalogue record for this book is available from the library of Congress

DNS/LES – Progress and Challenges

Proceedings of the Third AFOSR International Conference on DNS/LES

Editors:

Chaoqun Liu, UTA
Leonidas Sakell, AFOSR
Thomas Beutner, AFOSR

Publisher:

Greyden Press
2020 Builders Place
Columbus, Ohio 43204, USA

October 2001

ISBN 1-57074-488-2

Copy right @ 2001 by Chaoqun Liu, University of Texas at Arlington. All rights reserved. Printed and bound in the United States of America. Except as permitted under the United States Copyright Act of 1976, no part of this publication may be reproduced or distributed in any form or by any means, or stored in a data base retrieval system, without prior written permission of the copyright owner, except for brief excerpts in connection with reviews or scholarly analysis.

DNS/LES PERSPECTIVE

(Preface for TAICDL Proceedings)

CHAOQUN LIU, PhD
Professor and TAICDL Chairman
Department of Mathematics, University of Texas at Arlington
Arlington, TX 76019-0408, USA
September 15, 2001

For the third time in the last four years, DNS/LES experts from all over the world gathered at the University of Texas at Arlington for the Third AFOSR International Conference on DNS/LES (TAICDL) to introduce research progress, exchange ideas, and discuss future research directions. The US Air Force Office of Scientific Research (AFOSR) sponsored the First AFOSR International Conference on DNS/LES (FAICDL) at Louisiana Tech University in 1997. The second conference was held at Rutgers - The State University of New Jersey in 1999. The number of papers I received this time, In fact more than 90 regular papers and 18 invited papers were received, clearly demonstrates the tremendous growth in the research on DNS and LES.

Not so long ago, catching the shocks and small vortices by a single high order scheme was considered the Holy Grail. Now it has become reality (Joslin, Pruett, TAICDL; Adams, Shu, Jiang, TAICDL). Real engineering applications using LES was another overriding concern in the eyes of scientists and engineers, but has been reported by a number of authors at TAICDL (e.g. Kato, Sagaut, TAICDL). Significant progress has been achieved during the past decade. For a more complete review, people may read review papers by Moin & Mehesh (1998) for DNS and Leseiur & Metais (1996) and Piomelli (1999) for LES. Sagaut (2000) just published a LES book which gives discussions on many issues related to LES. However, it was not possible to invite all of the important contributors in this field to give invited lectures for the conference. Some of the highlights in invited talks presented during this conference included: Germano, review on LES; Visbal and Gatski, Air Force and NASA needs on DNS/LES and their applications; Sagaut, Kato, and Shan, complicated configurations and industrial applications; Jolsin, DNS for flow control; Adams and Zhong, high speed flow transitions; Givi, LES for reacting flow; Vasilyev, some important LES constraints; Shu and Jiang, high order discretization; Karniadakis, DNS for unstructured grids; Knight, unstructured LES for supersonic turbulent flow; Piomelli, immersed boundary technique; Satofuka, Lattice Boltzmann method; and Verstappen, symmetry-preserving discretization.

Besides the outstanding invited talks, many excellent papers on a wide variety of topics are included in this volume. These papers address numerical

methods, new filters and subgrid models, applications in flow transition, chemical reaction, aero-acoustics, geophysical flow, flow around automobiles and constructions, and other engineering applications. I particularly note important work done by Pruett, Pantelis, Layton, and De Stefano who gave important comments on LES from a mathematical point of view. Moser, Wang, and Yee also introduced their new ideas and methods. There is no doubt that we are now understanding the mathematical foundation for LES and DNS much better than ever before. While many authors are focusing on the consistency between the filter and subgrid models, we also need to observe the consistency between the LES method and numerical discretization.

The feasibility of numerical simulation for fluid flow using Navier-Stokes system is based on the following two assumptions:

1. The time dependent Navier-Stokes equations are the governing system for both laminar and turbulent flow.
2. The time dependent Navier Stokes equations have a unique solution.

After more than one hundred years of effort in developing effective flow prediction methods for transitional and turbulent flow, we are still far away from the end and still face serious obstacles. The Reynolds averaged Navier-Stokes (RANS) (see Speziale, 1991) approach, which is widely used by the industry, can only predict the mean value, but does not provide useful information for instantaneous quantities, which is important for many time dependent processes like flow transition, aero-acoustics, wakes, separations, shock-boundary layer interaction, active flow control, interaction between fluid flow and structures, etc. Even for the mean value, RANS has closure problems and the RANS model is in general empirical and case related. Most popular eddy viscosity models assume $\overline{u'v'} = \nu_t(\frac{\partial \bar{u}}{\partial y} + \frac{\partial \bar{v}}{\partial x})$, here $\bar{u}$ *and* $\bar{v}$ are mean values and u' *and* v' are fluctuations, but modern fluid mechanics has found that there is no such a correlation even for very basic flows, which means RANS eddy viscosity models do not have any solid scientific foundation. People realize that we have to use direct numerical simulation (DNS) (Orszag, S. A. & Patterson, G. S., 1972; Moin and Mahesh, 1998) to resolve all important time dependent scales. However, it will lead to extremely high computational cost. Then the large eddy simulation (LES) (Lilly, 1966; Leseiur & Metais, 1996; Sagaut, 2000) is the most promising choice for the near future. However, LES is not very matured yet. First, LES still needs very fine grids and very small time steps for engineering applications, otherwise LES will meet the same problem as RANS, and, second, the subgrid model is still not very reliable.

Let us first take a look at a typical LES (RANS is similar) process. The original incompressible N-S equation can be written as:

$$\frac{\partial u_i}{\partial t}+\frac{\partial u_i u_j}{\partial x_j}-\mu\frac{\partial^2 u_i}{\partial x_j^2}+\frac{\partial p}{\partial x_i}=0 \tag{1}$$

A LES low-pass filter can be defined as a convolution product:

$$\bar{\phi}(x,t)=\int_{-\infty}^{+\infty}\int_{-\infty}^{+\infty}\phi(\zeta,t')G(x-\zeta,t-t')dt'd^3\zeta \tag{2}$$

Assume the filter is commutable, we can obtain the following filtered N-S system:

$$\frac{\partial \overline{u_i}}{\partial t}+\frac{\partial \overline{u_i u_j}}{\partial x_j}-\mu\frac{\partial^2 \overline{u_i}}{\partial x_j^2}+\frac{\partial \overline{p}}{\partial x_i}=0 \qquad \text{or} \tag{3}$$

$$\frac{\partial \overline{u_i}}{\partial t}+\frac{\partial \overline{u_i}\,\overline{u_j}}{\partial x_j}-\mu\frac{\partial^2 \overline{u_i}}{\partial x_j^2}+\frac{\partial \overline{p}}{\partial x_i}+\tau_U=0 \tag{4}$$

There is a unknown term representing the unresolved scales:

$$\tau_U=\frac{\partial \overline{u_i u_j}}{\partial x_j}-\frac{\partial \overline{u_i}\,\overline{u_j}}{\partial x_j} \tag{5}$$

Let us use a term, τ_M, to represent the subgrid scale (SGS) model we use, we have

$$\frac{\partial \overline{u_i}}{\partial t}+\frac{\partial \overline{u_i}\,\overline{u_j}}{\partial x_j}-\mu\frac{\partial^2 \overline{u_i}}{\partial x_j^2}+\frac{\partial \overline{p}}{\partial x_i}+\tau_M+(\tau_U-\tau_M)=0 \tag{6}$$

We then use the finite difference method to discretize the filtered N-S system:

$$\frac{\Delta \overline{u_i}}{\Delta t}+\frac{\Delta \overline{u_i}\,\overline{u_j}}{\Delta x_j}-\mu\frac{\Delta^2 \overline{u_i}}{\Delta x_j^2}+\frac{\Delta \overline{p}}{\Delta x_i}+\tau_{M,h}+(\tau_{U,h}-\tau_{M,h}+\tau_{i,h})=0 \tag{7}$$

where $\tau_{i,h}$ is the truncation error and Δ represents the finite difference operator. The discretized system for an approximation is given by

$$\frac{\Delta \overline{v_i}}{\Delta t}+\frac{\Delta \overline{v_i}\,\overline{v_j}}{\Delta x_j}-\mu\frac{\Delta^2 \overline{v_i}}{\Delta x_j^2}+\frac{\Delta \overline{P}}{\Delta x_i}+\tau_{M,h}=0 \tag{8}$$

where $\overline{v}\neq\overline{u}$, in general.

The idea case is that $\tau_{U,h}-\tau_{M,h}+\tau_{i,h}=0$ and we can then obtain the exact solution for the filtered large scales. However, it is very difficult to get $\tau_{U,h}-\tau_{M,h}+\tau_{i,h}=0$ because $\tau_{U,h}$ and $\tau_{i,h}$ are not predictable while $\tau_{M,h}$ is specified by the resolved scales. The requirement to avoid a case-related

and grid-related solution should include that, first, $\tau_{U,h}$ is very small and, second, the first two terms have higher orders than the last term, which obviously requires the use of very fine grids to resolve most of the important scales and very accurate subgrid models. For flow instability and transition problems, the dominant scales are comparable with the grid size, which means $\tau_{U,h}$ is trivial, and the perturbation is very small in magnitude. The high-order accuracy of the schemes is then essential in catching physics. However, for turbulent flow especially for high Reynolds number flows with complex geometry, the unresolved scales are important and large in magnitude, in other words, $\tau_{U,h}$ is large. We cannot achieve fourth or higher order accuracy if the SGS model is not very accurate although a fourth or higher order scheme is used. Numerical experiment (Visbal et al, 2001) has shown a fourth or higher order is necessary for even a simple vortex development case. Unless we use an extremely fine grid, we need to use at least fourth-order schemes for large eddy simulation if we really want to resolve large scale modes accurately.

We must also consider what experimental data is needed to validate or advance the LES simulations. In this regard, some of the data available for RANS validation is not suitable for LES validation. In particular, it is important to compare LES simulations with instantaneous experimental data before the LES can be a useful tool for flow prediction and design. Most people believe we should select some fundamental flow with simple geometry but some complex physics (Piomelli, Sagaut, TAICDL), channel flow or cavity flow for example. There is a serious question of how to document the inflow condition for LES? There will not be any significant validation if LES uses a different inflow condition from the measured one. We also have serious problems in the near wall region where we cannot resolve the extremely small but very important scales for the wall bounded flow with high Reynolds numbers and complex geometries. We need 'wall modeling'. Some methods have been proposed which use RANS for the near wall region and LES for others, but some people argued we will meet the same problem with RANS again and it is difficult to match RANS results with LES simulations. The problem is particularly important for industrial applications and cannot be bypassed (Piomelli, TAICDL).

There are still a number of other questions regarding current LES approaches:

1. What kind of filter we should use based on the low-pass property and computation cost?
2. Can we use the same SGS model (e.g. Smagorinsky) for all different filters when the filtered subgrid scales are quite different?

3. Should the unresolved term, $\tau_{U,h}$, and the SGS model term, $\tau_{M,h}$, have the same or higher order than the truncation error, $\tau_{i,h}$, when a fourth or higher order is preferable for LES?
4. How to use the filter and subgrid model set for non-uniform grid and complex configurations?

Frankly, it is very difficult to find industrial interest if we cannot reduce the DNS/LES cost. A coarse grid DNS (CGDNS) or coarse grid LES without explicit filter and subgrid model were tried by a number of authors. For DNS, $\tau_{U,h}=0$ and $\tau_{M,h}=0$; In CGDNS, $\tau_{U,h}\neq 0$ but $\tau_{M,h}=0$; In any case, $\tau_{i,h}\neq 0$. CGDNS has been successful in many applications such as low Reynolds number channel or flat plate flow, receptivity, flow instability, flow transition, noise prediction, etc. because $\tau_{U,h}$ is small. Here CGDNS means using a grid acceptable by currently available computers. The high-order schemes and adaptive grids then become critical for CGDNS in achieving a maximum resolution and accuracy with limited computational resources. Sagaut (TAICDL) points out we need CGDNS and Germano (TAICDL) emphasizes we should study why it works without SGS model. One possible answer is 'no model is better than bad models for complex geometry but rather coarse grids'. Therefore, we should improve SGS models which will lead to better results than CGDNS. In order to do it, we need cooperation among researchers (Germano, TAICDL).

My prediction on future flow simulation is as follows:

1. RANS will continue to be used heavily by industry due to its low cost while RANS models have no solid theoretical foundation and are grid related and case related.
2. LES will be more and more applied not only for basic research, but also for some engineering applications. However, consistency between filter, subgrid model, and numerical disretization should be studied and more reliable sets should be developed. Critical experiments for some fundamental time-dependent flows should be conducted and documented for validating the LES simulations.
3. DNS will continue to play roles in prediction for flow instability, flow transition, flow separation, flow control, fluid flow and structure interaction, and low Reynolds number turbulent flow as the computer capability increases and numerical methods advance.
4. Coarse grid DNS or coarse grid LES without explicit filter and subgrid model for acceptable DNS or LES results will be sought for engineering applications.

5. Large scale DNS and LES will be continued for basic research and as a database for turbulence modeling.

6. More advanced numerical algorithms and computing technologies will be developed which will allow us to use more grid points and get more accurate results especially for shocks and other discontinuities.

In closing, I would like to express my appreciations to all of the TAICDL Scientific Committee and Paper Review Committee members for their faithful services and all of the invited speakers for their outstanding work and lectures. I am grateful to Beverly Higbee and all of the local committee members for their hard work. I also like to thank all of the participants for their contributions. I appreciate the financial support and sponsorship of the Lockheed-Martin tour from Lockheed Martin Aeronautics. In particular, I would like to thank Dr. Sakell, Dr. Herklotz, Dr. Beutner and the Air Force Office of Scientific Research for their sponsorship which makes this international conference possible.

References:

[1] Lesieur, M. & Metais, O., "New trends in large-eddy simulations of turbulence", Ann. Rev. Fluid Mech. Vol 28, pp45-82, 1996.

[2] Lilly, D. K., NCAR Manuscript 123, National Center for Atmospheric Res. Boulder, Co. 1966.

[3] Moin, P. & Mahesh, K., "Direct numerical simulation: a tool in turbulent research", Annu. Rev. Fluid Mech., Vol 30, pp539-578, 1998.

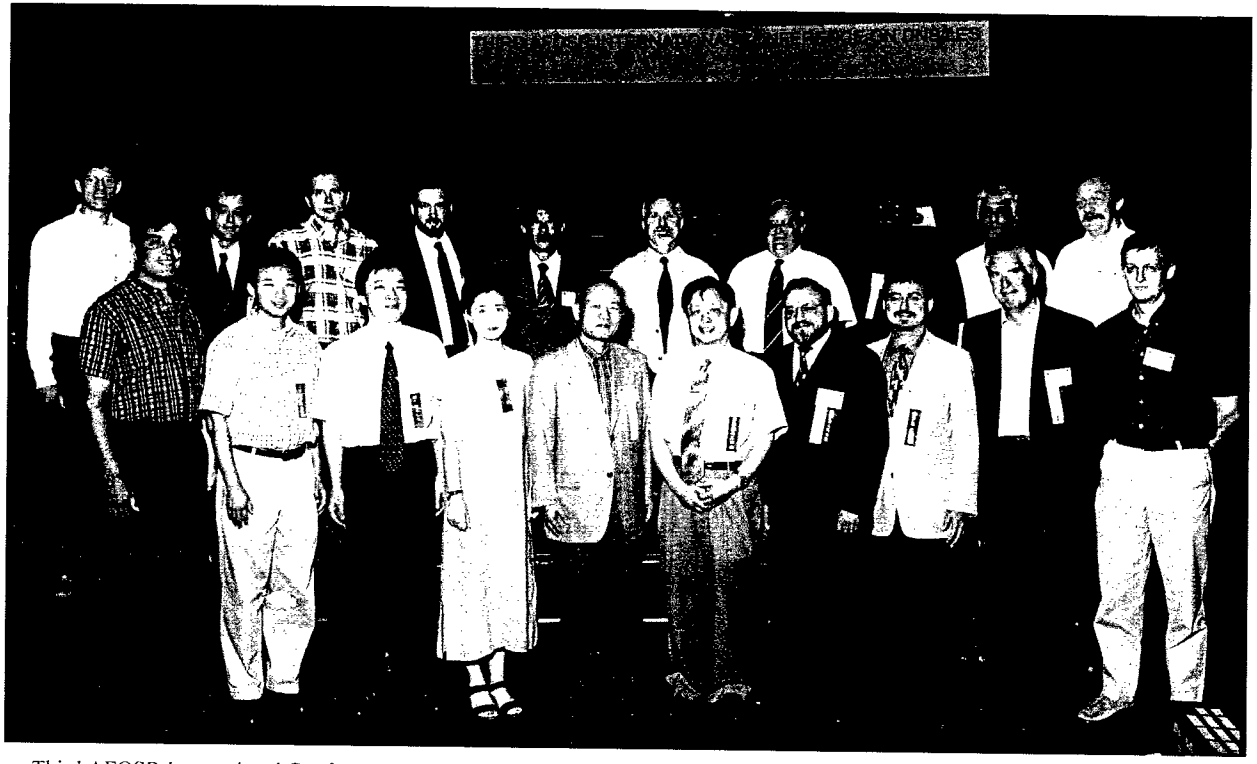
[4] Orszag, S. A. & Patterson, G. S., "Numerical simulation of three-dimensional homogeneous isotropic turbulence", Phys. Rev. Lett. Vol 2, pp76-79, 1972.

[5] Piomelli, U., "Large-eddy simulation: achievements and challenges", Progress in Aerospace Sciences, 35, pp. 335-362, 1999.

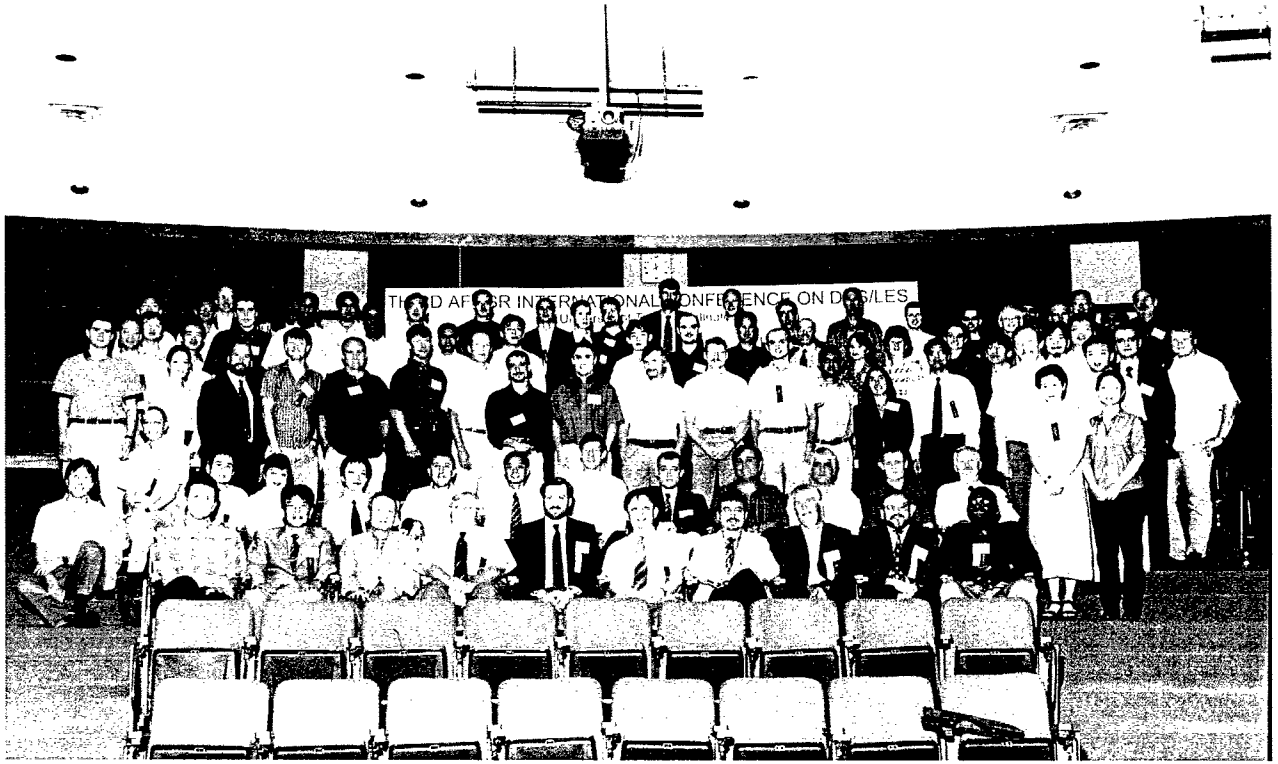
[6] Sagaut, P., "Large eddy simulation for incompressible flows", Springer, 2000

[7] Speziale, C. G., "Analytical methods for the development of Reynolds stress closures in turbulence", Annu. Rev. Fluid Mech. Vol 23, pp107-157, 1991.

[8] Visbal, M., Gaitonde, D., and Rizzetta, D., "High order schemes for DNS/LES and CAA on curvilinear dynamic meshes", Third AFOSR International Conference on DNS/LES, University of Texas at Arlington, August 5-9, 2001.



Third AFOSR International Conference on DNS/LES, University of Texas at Arlingtion, Arlington, Texas, USA, August 5-9, 2001
Part of Committee Members and Invited Speakers (from left to right):
First row: Givi, Shan, Kato, Jiang, Miyake, Liu, Visbal, Piomelli, Germano, Adams
Second row: Blaisdell, Sagaut, Vasilyev, Beutner, Satofuka, Knight, Gatski, Ladeinde, Pantelis, Chelyshkov



Third AFOSR International Conference on DNS/LES, University of Texas ar Arlington, Arlingtion, Texas, USA, August 5-9, 2001
Part of Participants

TABLE OF CONTENTS

DNS/LES Perspective
Chaoqun Liu i

Invited Papers

LES Overview
M. Germano 1

High-Order Schemes for DNS/LES and CAA on Curvilinear Dynamic Meshes
M. Visbal, D.Gaitonde and D.Rizzetta 13

DNS/LES for NASA Aerodynamic Needs and Engineering Applications
T. B. Gatski 25

DNS/LES for Complex Flows and Industrial Interest
P. Sagaut 35

Industrial Applications of LES in Mechanical Engineering
Chisachi Kato, Masayuki Kaiho and Akira Manabe 47

Numerical Simulation of Complex Flow around a 85 Delta Wing
H. Shan, L. Jiang and C. Liu 59

A Review of Modern Developments in Large Eddy Simulation of Turbulent Reactive Flows
Peyman Givi 81

Computational Constrains on LES of Inhomogeneous Turbulent Complex Geometry Flows
Oleg V. Vasilyev 93

Numerical Simulations Using the Immersed Boundary Technique
Ugo Piomelli and Elias Balaras 105

Recent Development and Applications of WENO Schemes
Chi-Wang Shu 117

Weighted Compact Scheme
Li Jiang, Hua Shan and Chaoqun Liu 129

High-order Discontinuous Galerkin Method: Simulation of Coil Flows
I. Pivkin, R. M. Kirby and G. E. Karniadakis 145

Coupling DNS with Polymer Models for Flow Control
Ronald D. Joslin 157

Direct Numerical Simulation of Transition in Compressible Flows
N. A. Adams 171

Large Eddy Simulation of Supersonic Turbulent Flows In Expansion-compression Corner
Doyle Knight, Hong Yan and Alexander Zheltovodov 183

DNS of Hypersonic Boundary Layer Stability and Transition Using High-order Nonuniform-grid Schemes
Xiaolin Zhong 195

Direct Numerical Simulation of Turbulence Using Symmetry-preserving Discretization
R.W.C.P. Verstappen and A.E.P. Veldman 207

DNS of Incompressible Flows Using Lattice Boltzmann Method
Nobuyuki Satofuka 219

LES Method

Toward the De-mystification of LES
C. D. Pruett 231

Residual Scale Dependence and PDE Filters
G. Pantelis 239

A Study of the Effect of Smooth Filtering in LES
Giuliano De Stefano and Oleg V. Vasilyev 247

Characterization of Optimal LES in Turbulent Channel Flow
R. D. Moser, S. Volker and P. Venugopal 255

Physics-preserving Turbulent Closure Models: SGS Flux Vectors of Mass and Energy
Liqiu Wang 263

Large Eddy Simulation Using Complete Fourth Order Difference Method and Vorticity-Vector Potential Formulation in Generalized Coordinate
Hiroshi Tokunaga and Kazunari Okuda 275

A 3D Channel Flow Simulation at Re = 180 Using a Rational LES Model
P. Fischer and T. Iliescu 283

Discrete Filtering on Unstructured Grids Based on Least-Squares Gradient Reconstruction
A. Haselbacher 291

Performance of Subgrid Flamelet Model in LES of Reacting, Turbulent Flows
Xiaodan Cai and Foluso Ladeinde 299

A Dynamic Procedure for Calculating the Turbulent Kinetic Energy
B. Knaepen O. Debliquy and D. Carati 311

Generation of Turbulent Inflow Data with a Prescribed Shear-stress Profile
A. Spille-Kohoff and H.-J. Kaltenbach 319

Velocity Filtered Density Function for Large Eddy Simulation of a Turbulent Mixing Layer
L.Y.M. Gicquel, P.Givi, F. A. Jaberi and S.B.Pope 327

A New Dynamic Model for Large Eddy Simulation of Particle-Laden Turbulent Flow
Kangbin Lei, Nobuguki Taniguchi and Toshio Kobayashi 335

Evaluation of Time and Space Scales in a Spatially Developing 3D Turbulent Incompressible Mixing Layer by Using LES
S. Pellerin, A. Dulieu, C.Tenaud and L. Ta Phuoc. 343

Large Eddy Simulation of Rotating Turbulent Convection Using the Subgrid Scale Estimation Model
Shari J. Kimmel and J. Andrzej Domaradzki 351

Numerical Method

Numerical Analysis of Large Eddy Simulation
A. Dunca, V. John, W. J. Layton and N. Sahin 359

Adaptive Numerical Dissipation/Filter Controls for High Order Numerical Methods
H.C.Yee and B. Sjögreen 365

Large Eddy Simulation of Supersonic Compression Corner Using ENO Scheme
Hong Yan, Doyle Knight and Alexander A. Zheltovodov 381

Filtering Boundary Conditions for LES and Embedded Boundary Simulations
A. Das and R. D. Moser 389

A Comparison of Adaptive Mesh Refinement Approaches for Large Eddy Simulation
Sorin M. Mitran 397

An Effective Fourth Order Finite Volume Method for DNS/LES on Non-uniform Grid
P. Iannelli, F.M. Denaro and G. De Stefano 409

Large Eddy Simulations of Complex Turbulent Flows Using Immersed Boundary Method
Mayank Tyagi and Sumanta Acharya 417

Numerical Efficiency of Explicit and Implicit Methods with Multigrid for Large Eddy Simulation
Senem Ertem-Müller and Michael Schäfer. 425

Large Eddy Simulation of Square Jet
X. Zhou and D. D. Knight 433

Efficient Large Eddy Simulation of Low Mach Number Flows Using Preconditioning and Multigrid
Bamdad Lessani, Jan Ramboer and Chris Lacor 441

Critical Comparison of the Collocated and Staggered Grid Arrangements for Incompressible Turbulent Flows
Frederic N. Felten and Thomas S. Lund 449

Large Eddy and Detached Eddy Simulations Using an Unstructured Multigrid Solver
Dimitri J. Mavriplis, Juan Pelaez and Osama Kandil 461

Truncation Error Reduction Method for Poisson Equation
Chaoqun Liu and Jian Xia 471

Direct Numerical Simulation of Supersonic Turbulent Ramp and Step Flow
I. Klutchnikov and J.Ballmann 479

A Multigrid Method for Elliptic Grid Generation Using Finite Volume Method
Sheng Luo, Chaoqun Liu and Hua Shan 487

Application of High-order Compact Scheme in a Computer Flow Solver for Incompressible Turbulent Flow
Chao-Ho Sung, Li Jiang and Chaoqun Liu 495

DNS Applications

Hairpin Vortex Formation in Poiseuille Flow Due to Two-hole Suction
D. B. Goldstein, J. Cohen and V. Levinski 501

DNS of Boundary Layer Transition Induced by a Coherent Perturbation
H.C. De Lange and R. J. M. Bastiaans 509

Modal Interaction in a Bickley Jet by Direct Numerical Simulation
Roland Mallier and Michael Haslam 517

Direct Numerical Simulation of Turbulent Flow and Heat Transfer in a Square Duct at Low Reynolds Number
M. Piller and E. Nobile 525

Direct Numerical Simulation of Fully Developed Flow Near a Flat Plate
V. S. Chelyshkov and Chaoqun Liu 533

Direct Numerical Simulation of the Turbulent Mixing in a Rough-Wall Flow
K. Tsujimoto, Y. Miyake and N. Nagai 541

Particle Dispersion in Homogeneous Turbulent Flow
M.P.B. Veenman, J.G.M. Kuerten and J.J.H. Brouwers 549

DNS of Multiplicity and Stability of Mixed Convection in Rotating Coolant/Separation Ducts
Liqiu Wang and Tianliang Yang 557

Direct Numerical Simulation of the Fully Developed Open-channel Flow at Subcritical Froude Numbers
A. Nakayama and S. Yokojima 569

2D DNS of Quasi-2D Turbulence in Shallow Water
Rob Uittenbogaard and Bas Van Vossen 577

Direct Numerical Simulation of Jet Noise
Bendiks Jan Boersma 589

Direct Numerical Simulation of High Speed Flow Over Cavity
A. Hamed, D. Basu, A.Mohamed and K.Das 597

Flame Kernel Interactions in a Turbulent Environment
K. W. Jenkins and R. S. Cant 605

Anisotropy in Reacting Compressible Turbulent Shear Flow
D. Livescu and C. K. Madnia 613

Simulation of Particle Coagulation in Temporally Developing Mixing Layer
S. C. Garrick, S. Modem, M. R Zachariah, K. E. J. Lehtinen 621

Numerical Simulation for Flow Separation around a 2-D Airfoil
Shutian Deng and Chaoqun Liu 629

Measurement and 3D Computer Simulation of the Crystallinity Distribution in Injection Molded Syndiotactic Polystyrene
Richard D. Sudduth , Pavan K. Yarala, Qin Sheng and Kevin Nichols 637

Numerical Investigation of Boundary Layer Transition over Flat-plate
Kunlun Liu, Khoon Seng Yeo, Chang Shu and Zhengyi Wang 647

DNS of a Strained Turbulent Axial Vortex
B. Eshpuniyani and G. A. Blaisdell 657

LES Applications

Large-Eddy Simulation of Mach 3.0 Flow Past A 24-Degree Compression Ramp
Donald P. Rizzetta and Miguel R. Visbal 665

On the Operation of Hybrid RANS-LES and Proper Orthogonal Decomposition Techniques to Control of Cavity Flow
Srinivasan Arunajatesan, Neeraj Sinha and Lawrence Ukeiley 673

LES Based Trailing-edge Noise Prediction
W. Schröder, M. Meinke, R.Ewert and W. A. El-Askary 689

Large Eddy Simulation for a Rib-roughened Turbulent Channel Flow with Heat Transfer and Property Variations
Ning Meng and Richard H. Pletcher 699

Large Eddy Simulation of the Turbulent Flow Past a Backward Facing Step: Isothermal Flow and Flows with Heat Transfer and Property Variation
Ravikanth Avancha and Richard H. Pletcher 707

LES Studies of Scalar Fluctuations at High Convective Mach Numbers
William H. Calhoon, Jr. Chandrasekhar Kannepalli and Sanford M. Dash . 715

Instability of the Shear Layer Separating from a Circular Cylinder
Jinsung Kim and Haecheon Choi 727

Large Eddy Simulation of Turbulent Flow over a Sphere Using an Immersed Boundary Method
Dongjoo Kim and Haecheon Choi 735

Large Eddy Simulation of Transonic Turbulent Flow over an Airfoil Using a Shock Capturing Scheme with Zonal Embedded Mesh
Ichiro Nakamori and Toshiaki Ikohagi 743

Numerical Study on Pollutant Dispersion in Urban Street Canyon
Guixiang Cui, Yi Liu, Xueling Cheng and Zhaoshun Zhang 751

Large Eddy Simulation of a Subsonic Flow over a Deep, Open Cavity
L. Larchevêque, O. Labbé, I. Mary and P. Sagaut 759

Large Eddy Simulation of Shock/Boundary Layer Interaction
E. Garnier, P. Sagaut, and M. Deville 767

Large Eddy Simulation of the Flow around a Simplified Bus
Sinisa Krajnovic and Lars Davidson 775

Large Eddy Simulation of a Supersonic Cavity Flow with an Unstructured Grid Flow Solver
Brain R. Smith 783

Preliminary LES over a Hypersonic Elliptical Cross-section Cone
M. P. Martin, W. Wright, G. V. Candler, U. Piomelli, G. Weirs and H. Johnson 791

Flow and Heat Transfer Predictions for the Film-cooling Flow Using Large Eddy Simulations
Mayank Tyagi and Sumanta Acharya 799

Large Eddy Simulations of Rotating Square Duct with Normal Rib Turbulators
Mayank Tyagi , Arun K. Saha and Sumanta Acharya 807

Large Eddy Simulation of a Shear-free Magnetohydrodynamic Mixing Layer
O. Debliquy, B. Knaepen and D. Carati 815

Energy-containing-range Modeling of Fully Developed Channel Flow Using Hybrid RANS/LES Technique
Frank J. Zajaczkowski and Leonard J. Peltier 823

Maintenance of the Near-wall Cycle of Turbulence for Hybrid RANS/LES of Fully Developed Channel Flow
Leonard J. Peltier and Frank J. Zajaczkowski 829

Appendices

A. Panel Discussion 837
B. List of Scientific Organizing Committee. 850
C. List of Invited Speakers. 851
D. List of Local Organizing Committee 852
E. List of Participants 853

LES OVERVIEW

M. GERMANO
Dip. di Ing. Aeronautica e Spaziale
Politecnico di Torino, Italy

Abstract. In the paper the different current approaches to the Large Eddy Simulations of turbulent flows are examined and critically discussed. A LES is usually defined as a numerical computation in which some scales are captured and others are modelled, but different procedures are used for such decomposition. As regards the modeling of the unresolved scales they are in the paper tentatively classified as *exact modeling* and *statistical modeling*. A third procedure, the *dynamic modeling* is examined as a technique based on the use of general relations that connect the subgrid scale turbulent stresses at different levels. Their implementation to standard models, like the Smagorinsky eddy viscosity one, can improve the results and can efficiently extend the range of their application. The connections between LES and RANS, the simulations based on the Reynolds Averaged Navier-Stokes equations, are finally examined and some critical issues related to the extraction of the statistical averages from LES databases are discussed.

1. Introduction

An overview of the many approaches that can be classified as Large Eddy Simulations, (LES), of turbulent flows, cannot be done without considering the limiting procedures of the Direct Numerical Simulation, (DNS), and the Reynolds Averaged Navier-Stokes Simulation, (RANS). If compared with the complex scenario of different definitions, filtering operators, truncations and models adopted by the current different LES techniques, these two asymptotic approaches to the simulation of turbulent flows should appear well defined, consolidated basic points, but that is far from true. As regards the Reynolds averages the only thing that we can say, following Frisch (1995), is that *for the moment the partial understanding of chaos in deterministic systems gives us the confidence that a probabilistic descrip-*

tion of turbulence is justified, and as regards the DNS it is important to remark with Lee (1995) that *an instantaneous flowfield of direct numerical simulation must be viewed not as the true solution of the Navier Stokes equations, but only as a snapshot of the evolving flowfield at some fictitious time*. Uncomfortable as it can be, anyway we can only conclude with Lee (1995) that, due to the chaotic nature of the turbulent field, the *only viable outcome of both approaches*, DNS and RANS, *is prediction of the averaged flow quantities*, and that is only the beginning of a lot of problems. A statistical description needs the definition of a statistical ensemble of flow realizations, and following with the citations let us notice now with Aubry (1991) that this definition in the applications *has been quite flexible*. As a matter of fact the *statistical* ensemble usually consists of a temporal domain under the ergodicity assumption, or of a symmetry group under which the equations for that particular flow are invariant, or of an ensemble of discrete times conditionally determined. The basic ensemble, a set of initial conditions, is usually never considered, for obvious practical considerations.

Let us now examine the LES. From the basic point of view a Large Eddy Simulation should produce a filtered representation $\langle a \rangle_f$

$$\langle a \rangle_f \equiv \mathcal{F}(a) \tag{1}$$

of the original quantity a, where $\mathcal{F}$ is a general filtering operator provided with some particular smoothing properties. One particular aim of this approach is to derive, given the evolutionary equation of a, the evolutionary equation for the filtered quantity $\langle a \rangle_f$. That is not so easy, and different approaches can be imagined. Let us define as usual, Leonard (1974), the filtered quantity $\langle a \rangle_f$ as given by

$$\langle a \rangle_f = \int a(t') F(t - t') dt' \tag{2}$$

where $F(z)$ is a frequency function, see Hirschman & Widder (1955). If

$$\frac{da}{dt} = A(a) \tag{3}$$

is the evolutionary equation for a, the evolutionary equation for $\langle a \rangle_f$

$$\frac{d\langle a \rangle_f}{dt} = \cdots \tag{4}$$

will usually contain, if non linear, unresolved moments. Three basic approaches can be conceived, one strictly deterministic and the others statistical in order to *close* this filtered equation. The first one, that we will call *exact modeling*, is based on the analytic properties of the convolution

kernel, the frequency function $F(z)$, and it is clear that for very high resolutions a LES is similar to a DNS, so that statistical ingredients seem unadapted. We remark that the statistical approaches are based on a probabilistic interpretation of the definition (2), and that seems a little difficult to understand. It is however easy to see that we can read this physical deterministic average in terms of a filtered density function $p_f(a,t)$. We can write

$$\langle a \rangle_f = \int p_f(a,t) a da \tag{5}$$

where

$$p_f(a,t) = \int \delta[a - a(t)] F(t - t') dt' \tag{6}$$

and two statistical procedures can be conceived, the first one based on the derivation of the evolutionary equations for the different moments that appear in the evolutionary equation of $\langle a \rangle_f$ and the second one based on the evolutionary equation for the filtered density function $p_f(a,t)$. That is similar to RANS. Also in this case the usual definition of the mean, easy to compare with the experiments, is based on an infinite time average, but from the fundamental point of view it is more correct to think in terms of an ensemble operator $\mathcal{E}$ based on a set of initial conditions

$$\langle a \rangle_e = \int P_e(\alpha) a(\alpha, t) d\alpha \tag{7}$$

where $P_e(\alpha)$ is a probability density function on the initial states at the time $t = 0$

$$\alpha = a(0) \tag{8}$$

If

$$\frac{da}{dt} = A(a) \tag{9}$$

is the evolutionary equation for a, also in this case the basic problem is to derive the evolutionary equation for $\langle a \rangle_e$

$$\frac{d\langle a \rangle_e}{dt} = \cdots \tag{10}$$

and we remark that if we write

$$\langle a \rangle_e = \int p_e(a,t) a da \tag{11}$$

where now $p_e(a,t)$ is a probability density function on a, given by

$$p_e(a,t) = \int \delta[a - a(\alpha, t)] P_e(\alpha) d\alpha \tag{12}$$

another challenging problem is to derive the evolutionary equation for $p_e(a,t)$

$$\frac{\partial p_e}{\partial t} = \cdots \tag{13}$$

In the following we will examine these two approaches, the *exact modeling* and the *statistical modeling*, in some detail and we will finally make some comments on a third modeling technique that is of some usefulness in improving dynamically the previous procedures. We will call it *dynamic modeling* and we remark that it is based on general operational relations that any modeling procedure, deterministic or not, must verify, like the tensorial or the Galilean invariance.

2. Exact modeling

We tentatively classify as exact modeling the procedures based on the analytical properties of an explicit convolutional filtering operator $\mathcal{F}$

$$\mathcal{F}(a) \equiv \langle a \rangle_f = \int_{-\infty}^{\infty} a(t')F(t-t')dt' \tag{14}$$

where, as remarked in the introduction, the kernel $F(z)$ is a frequency function. It is interesting to notice, Hirschman & Widder (1955), that if $L(s)$ is the inverse of the bilateral Laplace transform of $F(z)$

$$\frac{1}{L(s)} = \int_{-\infty}^{\infty} F(z)e^{-zs}dz \tag{15}$$

a useful inversion formula is the following

$$L(\mathcal{D})\langle a \rangle_f = a \tag{16}$$

where $\mathcal{D}$ stands for the derivative operator

$$\mathcal{D} \equiv \frac{d}{dt} \tag{17}$$

From the operational point of view the differential operator $L(\mathcal{D})$ is the inverse of the integral operator $\mathcal{F}$

$$L(\mathcal{D}) \equiv \mathcal{F}^{-1} \tag{18}$$

and an interesting class of filters is the following

$$\mathcal{F}^{-1} = (1-\alpha_1\mathcal{D})((1-\alpha_2\mathcal{D})\cdots(1-\alpha_n\mathcal{D}) \tag{19}$$

It can be shown that these filters are *variation diminishing* in the sense that the number of changes of sign of the filtered function $\langle a \rangle_f$ never exceeds the

number of changes of sign of the original function a, and other interesting properties are related to the mean m_f and the variance v_f of the kernel of the inverse convolutional filter, the frequency function $F(z)$, given by

$$m_f = -\sum_1^n \frac{1}{\alpha_k} \qquad v_f = \sum_1^n \frac{1}{\alpha_k^2} \tag{20}$$

We remark that the smoothing properties of the variation diminishing transform are particularly interesting for LES, and till now unexplored. Historically they were first introduced by Schoenberg, and are connected to the *zero crossing* rate of a turbulent fluctuation that, as remarked in the past by Liepmann, is directly related to the dissipation.

Many other different filters have been proposed for LES, and a complete review of all them should require many pages. We refer for that to the recent book of Sagaut (2001) where definitions and properties of classical filters for LES are discussed both for the homogeneous and the inhomogeneuos case. This last issue is very important for the applications, and we remark that a general class of *differential filters*, Germano (1986), is particularly interesting in order to explore what happens when nonhomogeneous filtering operators do not commute with differentiation, Germano (2000). As an example let us consider a linear differential form of the second order

$$\mathcal{D} = \mathcal{I} + \vartheta \mathcal{D}_t + \Delta_k \mathcal{D}_k + \Delta_{kl} \mathcal{D}_k \mathcal{D}_l \tag{21}$$

where

$$\mathcal{D}_t \equiv \frac{\partial}{\partial t} \qquad \mathcal{D}_k \equiv \frac{\partial}{\partial x_k} \tag{22}$$

and let us associate to this differential operator a filtering operator $\mathcal{F}$ defined as

$$\mathcal{I} = \mathcal{D}\mathcal{F} \tag{23}$$

where $\mathcal{I}$ is the identity. It is interesting to remark that the differential operator $\mathcal{D}$ is by definition the inverse of the filtering operator $\mathcal{F}$

$$\mathcal{D} = \mathcal{F}^{-1} \tag{24}$$

and formally $\mathcal{F}$ can be expressed by an integral convolution with a kernel given by the Green's function associated to $\mathcal{D}$. We notice that if the parameters $\vartheta, \Delta_k, \Delta_{kl}$ are not constant the operator $\mathcal{F}$ does not commute with the derivatives $\mathcal{D}_t$ and $\mathcal{D}_k$, and what is interesting with these filters is that provided with the exact inverse of $\mathcal{F}$ we can easily write the exact expressions for the commutative terms

$$\mathcal{F}\mathcal{D}_t - \mathcal{D}_t\mathcal{F} \qquad \mathcal{F}\mathcal{D}_k - \mathcal{D}_k\mathcal{F} \tag{25}$$

In fact if $\mathcal{G}$ is a generic operator we obtain by applying the relation (23)

$$\mathcal{G}\mathcal{D}\mathcal{F} = \mathcal{D}\mathcal{F}\mathcal{G} \tag{26}$$

and we can write

$$(\mathcal{G}\mathcal{D} - \mathcal{D}\mathcal{G})\mathcal{F} = \mathcal{D}(\mathcal{F}\mathcal{G} - \mathcal{G}\mathcal{F}) \tag{27}$$

If we now compare this relation with the relation (23) we obtain

$$\mathcal{F}\mathcal{G} - \mathcal{G}\mathcal{F} = \mathcal{F}(\mathcal{G}\mathcal{D} - \mathcal{D}\mathcal{G})\mathcal{F} \tag{28}$$

that provides the exact form for the commutative *errors* in terms of the filtered quantities.

3. Statistical modeling

As remarked before statistical modeling reads the filtering length as an interval of indeterminacy that separates what can be calculated analytically from what has to be guessed statistically. This point of view can be similarly applied to a projection. If we express the generic turbulent velocity field u_i in terms of a generalized Fourier expansion

$$u_i = \sum_1^\infty u_{ik}\varphi_k \tag{29}$$

where φ_k is a particular set of basis functions and u_{ik} are random Fourier coefficients, following Yoshizawa (1982) we can define a *partial* statistical operator $\mathcal{E}_f$ that applied to u_i gives the $\mathcal{F}$-level statistical representation

$$\mathcal{E}_f(u_i) = \sum_1^f u_{ik}\varphi_k + \sum_{f+1}^\infty \langle u_{ik}\rangle_e \varphi_k \tag{30}$$

The *partial* statistical theory of turbulence is at the beginning, and in the opinion of the author the Large Eddy Simulation has stimulated the research in the field. We recall that the probability density function approach has been pioneered in turbulence by Lundgren (1967). His method derives directly the evolutionary equation for the ensemble pdf from the differential equations which define the conservation laws, and the principal fields of application are the reacting turbulent flows, but recently this approach has been extended to LES, see Pope (1990) and Gao & O'Brien (1993). This concept of a *pdf within the subgrid*, Madnia & Givi (1993), is very promising for LES and some first simulations based on a velocity filtered density function computed by a Lagrangian Monte Carlo procedure have been recently performed by Gicquel *et al.* (2001).

As remarked in the introduction the *exact* and the *partial statistical* modeling based on filtered pdf could seem incompatible. If the filtering operation is defined as a convolution in the physical space

$$\langle a \rangle_f = \int_X a(x')F(x-x')dx' \tag{31}$$

we have

$$\tau_f(a,b) = \tau_f(-a,-b) \tag{32}$$

where by definition the generalized central moment associated to the quantities a and b is given by

$$\tau_f(a,b) = \langle ab \rangle_f - \langle a \rangle_f \langle b \rangle_f \tag{33}$$

and this condition of *reversibility* should be respected by modeling. It is however important to recall that the Smagorinsky model, based on statistical considerations and applied to the anisotropic part of the subgrid turbulent stress,

$$\tau_f^a(u_i,u_j) \sim M_f(u_i,u_j) = -2\nu_f \langle s_{ij} \rangle_f \tag{34}$$

is such that

$$M_f(u_i,u_j) = -M_f(-u_i,-u_j) \tag{35}$$

and this condition is violated. This situation is reminiscent of the *reversibility paradox* related to the connections between the statistical kinetic theory and the microscopic laws of mechanics that are invariant under time reversal. We remark, Germano (2001), that if we rewrite the integral (31) in its Lebesgue version

$$\langle a \rangle_f = \int_X a(x')F(x-x')dx' = \int_A ap(x,a)da \tag{36}$$

where

$$p(x,a) = \int_X F(x-x')\delta[a-a(x')]dx' \tag{37}$$

the Smagorinsky model could be recovered by an assumed probability distribution $p(x,C_i)$ given by

$$\begin{aligned} p(x,C_i) &= (2\pi U^2)^{-3/2} \exp[-C^2/2U^2] \cdot \\ &\cdot \left\{ 1 - \frac{\nu_f}{U^2} \left[\left(\frac{C^2}{2U^2} - \frac{5}{2} \right) \frac{C_i}{U^2} \frac{\partial U^2}{\partial x_i} + \frac{C_i \langle s_{ij} \rangle_f C_j}{U^2} \right] \right\} \end{aligned} \tag{38}$$

where $C_i = u_i - \langle u_i \rangle_f$, $C^2 = C_i C_i$ and

$$3U^2 = \tau_f(u_i,u_i) \tag{39}$$

It seems in conclusion that the eddy viscosity model could only be justified on the basis of probabilistic arguments, and that the irreversible LES could only find its formulation in the large eddy probabilistic density function.

4. Dynamic modeling

The dynamic modeling procedures are based on identities that relate the subgrid scale stresses at different resolution levels. The simplest one is the following

$$\tau_{fg}(u_i,u_j) = \langle \tau_f(u_i,u_j)\rangle_g + \tau_g(\langle u_i\rangle_f,\langle u_j\rangle_f) \tag{40}$$

where the various terms are given by definition by the expressions

$$\begin{aligned}
\tau_f(u_i,u_j) &= \mathcal{F}(u_iu_j) - \mathcal{F}(u_i)\mathcal{F}(u_j)\\
\tau_{fg}(u_i,u_j) &= \mathcal{GF}(u_iu_j) - \mathcal{GF}(u_i)\mathcal{GF}(u_j)\\
\langle \tau_f(u_i,u_j)\rangle_g &= \mathcal{GF}(u_iu_j) - \mathcal{G}(\mathcal{F}(u_i)\mathcal{F}(u_j))\\
\tau_g(\langle u_i\rangle_f,\langle u_j\rangle_f) &= \mathcal{G}(\mathcal{F}(u_i)\mathcal{F}(u_j)) - \mathcal{GF}(u_i)\mathcal{GF}(u_j)
\end{aligned} \tag{41}$$

and where $\mathcal{F}$ and $\mathcal{G}$ are respectively the LES filter and the test filter. Also in this case to discuss the many applications and variants adopted since the first dynamic model, Germano *et al.* (1991), should require a lot of space, and we refer to a recent paper of Piomelli (1999) for a critical analysis. It is perhaps more interesting for this brief review to remark that this procedure is based on purely formal properties and can only improve an existing model, like the Smagorinsky eddy viscosity model, or the structure function model. That is good from one side, because as such its range of application is very large, and we recall a recent interesting extension, Im *et al.* (1997), of the dynamic procedure applied to the so called G-equation that predicts the evolution of the propagating front of laminar flamelets corrugated by turbulent eddies. From the other side however that is a limit, because in some sense there is nothing new that is added *physically* by this procedure, and the improvement is due to a better consistency with the formal properties of the real subgrid stresses. This point seems to the author very important and has been the matter of an interesting criticism by Pruett (1997). With reference to the relation (40) he states that this identity is *mathematically tautological,* and *unnecessary* as a *basis for dynamic SGS models*, and in our opinion this criticism is applicable or not according to the situation. Let us examine the identity (40) from the point of view of the *exact modeling.* In this case we assume that *both* the test filter $\mathcal{G}$ and the LES *filter* $\mathcal{F}$ are explicitly known, and as in Brun & Friedrich (2000) we can expand them in one dimension as follows

$$\mathcal{F} = \mathcal{I} + a_f\mathcal{D} + b_f\mathcal{D}^2 + c_f\mathcal{D}^3\cdots$$

$$\mathcal{G} = \mathcal{I} + a_g\mathcal{D} + b_g\mathcal{D}^2 + c_g\mathcal{D}^3\cdots \tag{42}$$

where $\mathcal{D}$ stands for the derivative. If the problem is to find an expression for the turbulent stress at the $\mathcal{FG}$

$$\tau_{fg}(u_i,u_j) = \mathcal{GF}(u_iu_j) - \mathcal{GF}(u_i)\mathcal{GF}(u_j) \tag{43}$$

we can in this case derive an explicit expression for $\mathcal{FG}$

$$\mathcal{GF} = \mathcal{I} + a_{fg}\mathcal{D} + b_{fg}\mathcal{D}^2 + c_{fg}\mathcal{D}^3\cdots \tag{44}$$

where

$$\begin{aligned} &a_f + a_g = a_{fg}\\ &b_f + a_fa_g + b_g = b_{fg}\\ &c_f + b_fa_g + a_fb_g + c_g = c_{fg}\\ &\cdots \end{aligned} \tag{45}$$

and it is clear that in this case Pruett is right. In fact we can easily derive directly that

$$\tau_{fg}(u_i,u_j) = (2b_{fg} - a_{fg}^2)\mathcal{D}(u_i)\mathcal{D}(u_j) + \cdots \tag{46}$$

and the identity (40) is unessential. On the contrary if we are provided only with an explicit LES *model*, and we do not exactly know the explicit originating LES *filter*, we can only write that

$$\begin{aligned} \langle\tau_f(u_i,u_j)\rangle_g &= \tau_f(u_i,u_j) + a_g\frac{\partial\tau_f(u_i,u_j)}{\partial x} + b_g\frac{\partial^2\tau_f(u_i,u_j)}{\partial x^2} + \cdots\\ \tau_g(\langle u_i\rangle_f,\langle u_j\rangle_f) &= (2b_g - a_g^2)\mathcal{D}(\langle u_i\rangle_f)\mathcal{D}(\langle u_j\rangle_f) + \cdots \end{aligned} \tag{47}$$

and the only way to derive the turbulent stress at the $\mathcal{FG}$ level remains to apply the identity (40).

5. Connections between LES and RANS

The comparisons among DNS, LES and RANS databases pose a lot of problems that in some cases can be neglected, but that conceptually remain. The first concerns the recovery of the statistical data from a LES database. We remark that what we produce by LES are filtered quantities, for example the filtered values of the velocity field, $\langle u_i\rangle_f$. When we apply an explicit *model* we have no idea of its explicit generating filter, if ever exist. If we define the LES fluctuations u_i' to the statistical mean as

$$u_i' = \langle u_i\rangle_e - \langle u_i\rangle_f \tag{48}$$

we notice that only in the case $\langle u_i' \rangle_e = 0$ the simple usual relations

$$\begin{aligned} \tau_e(u_i,u_j) &= \langle u_i'u_j' \rangle_e + \langle \tau_f(u_i,u_j) \rangle_e \\ \tau_e(u_i,u_j,u_k) &= \langle u_i'u_j'u_k' \rangle_e + \langle \tau_f(u_i,u_j,u_k) \rangle_e + \langle u_i' \tau_f(u_j,u_k) \rangle_e + \\ &+ \langle u_j' \tau_f(u_k,u_i) \rangle_e + \langle u_k' \tau_f(u_i,u_j) \rangle_e \end{aligned} \tag{49}$$

are valid, and that is not so good. As remarked in Hussaini *et al.* (1989) *if higher order turbulence statistics are needed beyond the mean velocity, the problem of defiltering arises*, and *this problem becomes most critical when more than* $10-20\%$ *of the turbulent kinetic energy is in the subgrid scale motions.* The literature on the estimation of the second and the third order statistical moments based on LES databases is relatively poor, and in some cases we are obliged to think that probably the subgrid models are considered very important dynamically, in order to compute the mean values, but not so reliable in order to be implemented in the relations (49). We remark, Germano (2001), that only in the case that the following chain of relations is satisfied

$$\begin{aligned} \langle u_i' \rangle_e &= 0 \\ \langle \tau_f(u_i,u_j) \rangle_e &= 0 \\ \langle u_i' \tau_f(u_j,u_k) \rangle_e &= 0 \\ \langle \tau_f(u_i,u_j,u_k) \rangle_e &= 0 \\ \cdots &= \cdots \end{aligned} \tag{50}$$

the filtering procedure produces statistical moments simply given by

$$\begin{aligned} \tau_e(u_i,u_j) &= \langle u_i'u_j' \rangle_e \\ \tau_e(u_i,u_j,u_k) &= \langle u_i'u_j'u_k' \rangle_e \\ \tau_e(u_i,u_j,u_k,u_l) &= \langle u_i'u_j'u_k'u_l' \rangle_e \\ \cdots &= \cdots \end{aligned} \tag{51}$$

and the study of explicit filters or explicit models that implement these statistical constraints are currently under way.

6. Conclusions

The various modeling approaches and numerical procedures that since the first applications in meteorology have been applied to simulate the large scales of turbulence, have stimulated during the time a lot of different interests and have raised a lot of different questions. A general overview of all

that is nearly impossible, and inevitably is a little biased by the particular attitudes or tendencies of the reviewer. If we look at the agenda of this meeting we can see that the applications of LES are very promising and wide-spread on a lot of different fields of application, from the aeronautical engineering to the estimate of the pollution dispersion, in reactive flows as in heat transfer. Industrial needs and interests motivate obviously the future of LES, that will probably still remain for a long time the only viable way for accurate calculations of turbulent flows. Hybrid RANS-LES strategies like the Detached Eddy Simulation or time dependent RANS are presently developed in order to simulate complex turbulent flows and to combine LES with standard and well developed computational and modeling procedures. In this particular case, as in many others, practical and theoretical issues are strongly intermixed. From one side the motivation of these hybrid procedures is mainly practical : LES remains after all very expensive, and simplest computational strategies remain very attractive. From another side however the final goal is very ambitious and aims to construct a unified turbulence model useful for all purposes, from wall modeling to the wake. This point, as many others, is a real challenge and imposes a big effort in a lot of different fields, from the exploration of higher order computational schemes to the basic research on turbulence, from the study of unstructured grids to the speculations about statistical and deterministic issues in chaotic systems. The fundamentals of turbulence remain one of the most fascinating unresolved problem and the hopes placed in a more rational design of aircraft, automobiles, turbines and many others industrial processes based on an improved computational ability of fluid flows are more and more increasing. In order to cope with all these problems we need the effort of everybody and a strong cooperation among different partners.

References

AUBRY N. 1991 On the hidden beauty of the Proper Orthogonal Decomposition. *Theoret. Comput. Fluid Dynamics*, **2**, page 341

BRUN, C. & FRIEDRICH, R. 2000 Modelling the Germano identity. An alternative dynamic approach. (*Submitted for the publication*)

FRISCH U. 1995 Turbulence. The legacy of A. N. Kolmogorov. *Cambridge University Press*, page 39

GAO F., & O'BRIEN E. E. 1993 A large eddy simulation scheme for turbulent reacting flows. *Phys. Fluids*, **A5**, 1282–1284

GERMANO M. 1986 Differential filters for the large eddy numerical simulation of turbulent flows. *Phys. Fluids* **29**, 1755–1757

GERMANO, M., PIOMELLI, U., MOIN, P. & CABOT, W. H. 1991 A dynamic subgrid-scale eddy viscosity model. *Phys. Fluids* **A3**, 1760–1765

GERMANO M. 2000 On the physical effects of variable filtering lengths and times in LES. *Proceedings of the EUROMECH Colloquium 412*, (submitted)

GERMANO, M. 2001 Ten years of the dynamic model. *Modern simulation strategies for turbulent flows*, Geurts B. J. ed., Edwards, 173–190

GICQUEL L. Y. M., GIVI P., JABERI F.A., & POPE 2001 Velocity filtered density function for large eddy simulation of turbulent flows. (private communication)

HIRSCHMAN I. I. & WIDDER D. V. 1955 The convolution transform. *Princeton University Press*, Princeton, NJ

HUSSAINI M. Y., SPEZIALE C. G., & ZANG T. A. 1989 The potential and limitations of direct and large eddy simulations. *Whither turbulence? Turbulence at the crossroads*, Lecture Notes in Physics 357, J.L.Lumley ed., Springer, 354-368

IM, H. G., LUND, T. S. & FERZIGER, J. H. 1997 Large eddy simulation of turbulent front propagation with dynamic subgrid models. *Phys. Fluids* **9**, 3826–3833

LEE J. 1995 Chaos and direct numerical simulation in turbulence. *Theoret. Comput. Fluid Dynamics*, **7**, page 391

LEONARD A. 1974 Energy cascade in Large-Eddy Simulations of turbulent fluid flows. *Adv. in Geophysics*, **18A**, 237–248

LUNDGREN T. S. 1967 Distribution functions in the statistical theory of turbulence. *Phys. Fluids* **10**, 969–975

MADNIA C. K. & GIVI P. 1993 Direct numerical simulation and large eddy simulation of reacting homogeneous turbulence. *Large eddy simulation of complex engineering and geophysical flows*, Galperin B. and Orszag S. A. eds., Cambridge University Press, 315–346

PIOMELLI, U. 1999 Large-eddy simulation : achievements and challenges. *Progress in Aerospace Sciences* **35**, 335–362

POPE S. B. 1990 Computations of turbulent combustion: progress and challenges. *Twenty Third Symposium (International) on Combustion, Plenary Lecture*, Orléans, France, July 22-27, 1990

PRUETT, C. D. 1997 Toward simplification of dynamic subgrid scale models. *Advances in DNS/LES*, eds. Liu C. and Liu Z., Greyden Press, 291–298

SAGAUT P. 2001 Large Eddy Simulation for incompressible flows. *Springer*

YOSHIZAWA A. 1982 A statistically derived subgrid model for the large-eddy simulation of turbulence. *Phys. Fluids* **25**, 1532–1538

HIGH-ORDER SCHEMES FOR DNS/LES AND CAA ON CURVILINEAR DYNAMIC MESHES

M. VISBAL, D. GAITONDE AND D. RIZZETTA
Air Force Research Laboratory
Wright-Patterson Air Force Base, Ohio 45433-7521

1. Introduction

Despite significant progress in computational sciences, challenges persist in the accurate numerical simulation of a broad spectrum of dynamic, multi-physics phenomena relevant to aerospace systems. These challenging areas include the direct and large-eddy simulation of turbulence, aeroacoustics, fluid/structure interactions, electromagnetics, and magneto-gasdynamics. In order to reduce the severe computational requirements of standard low-order schemes, higher-order formulations, as well as massively parallel approaches are being actively pursued. Due to their spectral-like resolution and ease of extension to multiple disciplines, high-order compact schemes[1] represent an attractive choice for reducing dispersion, anisotropy and dissipation errors associated with spatial discretizations. Until recently, these schemes have mostly been used in conjunction with explicit time-integration methods to address complex flow physics on simple Cartesian geometries.

Recent work performed at the Air Force Research Laboratory [2, 3, 4, 5, 6, 7] has extended the use of compact algorithms to more practical applications. This has been achieved through the development and improved treatment of the various critical elements comprising the overall numerical approach. Particular attention has been focused on enhanced high-order (up to 10th-order) low-pass filtering techniques, accurate and robust near-boundary formulations, proper metric evaluation, multi-domain implementation strategies, and sub-iterative implicit time-advancement methods. As an outcome of this sustained effort, the highly accurate compact algorithm has been successfully applied to efficiently solve a range of multi-physics phenomena described by the Euler, Navier-Stokes and MHD equations on 3-D curvilinear and dynamic grids using either explicit or implicit time integration approaches.

These high-fidelity computational tools are currently being transitioned to the multidisciplinary simulation of complex phenomena relevant to Air Force systems, including: weapon-bay cavity acoustics, hypersonic flow control, high- angle-of-attack aerodynamics, and non-linear aeroelastic response. A brief description of the governing equations, the various elements of the numerical approach, as well as a few representative applications are included in this paper.

2. Governing Equations

In order to develop a procedure suitable for nonlinear fluid dynamic, aeroacoustic and aeroelastic applications over complex configurations, the full Navier-Stokes equations are selected and are cast in strong conservative form introducing a general time-dependent curvilinear coordinate transformation $(x, y, z, t) \rightarrow (\xi, \eta, \zeta, \tau)$. In vector notation, and employing non-dimensional variables, these equations are:

$$\frac{\partial}{\partial \tau}\left(\frac{\vec{U}}{J}\right) + \frac{\partial \hat{F}}{\partial \xi} + \frac{\partial \hat{G}}{\partial \eta} + \frac{\partial \hat{H}}{\partial \zeta} = \frac{1}{Re}[\frac{\partial \hat{F}_v}{\partial \xi} + \frac{\partial \hat{G}_v}{\partial \eta} + \frac{\partial \hat{H}_v}{\partial \zeta}] + \vec{S}/J \qquad (1)$$

where $\vec{U} = \{\rho, \rho u, \rho v, \rho w, \rho E\}$ denotes the solution vector, $\hat{F}$, $\hat{G}$, $\hat{H}$, $\hat{F}_v$, $\hat{G}_v$, $\hat{H}_v$ are the fluxes, S denotes a source term, and $J = \partial(\xi, \eta, \zeta, \tau)/\partial(x, y, z, t)$ is the transformation Jacobian which for dynamic meshes is a function of time.

3. Numerical Method

3.1. SPATIAL DISCRETIZATION

A finite-difference approach is employed to discretize the governing equations. This choice is motivated by the relative ease of formal extension to higher-order accuracy. For any scalar quantity, ϕ, such as a metric, flux component or flow variable, the spatial derivative ϕ' is obtained in the transformed plane by solving the tridiagonal system:

$$\Gamma\phi'_{i-1} + \phi'_i + \Gamma\phi'_{i+1} = b\frac{\phi_{i+2} - \phi_{i-2}}{4} + a\frac{\phi_{i+1} - \phi_{i-1}}{2} \qquad (2)$$

where Γ, a and b determine the spatial properties of the algorithm. The formula yields the compact five-point, sixth-order *C6*, and three-point fourth-order *C4* schemes [1] with $\Gamma = 1/3$, $a = 14/9$, $b = 1/9$ and $\Gamma = 1/4$, $a = 3/2$, $b = 0$ respectively. Equation (2) also incorporates the standard explicit fourth-order (*E4*) and second-order (*E2*) approaches for which the coefficients are ($\Gamma = 0$, $a = 4/3$, $b = -1/3$) and ($\Gamma = 0$, $a = 1$, $b = 0$) respectively. The dispersion characteristics and truncation error of the above

schemes can be found in Refs. [1, 5]. It should be noted that for a given order of accuracy, the compact schemes are significantly superior to their explicit (non-compact) counterparts. The scheme of Eqn. (2) cannot be applied at a few points near each boundary where the stencil protrudes the domain. Here, special one-sided boundary schemes, such as those described in Refs. [5, 8] are employed.

In order to compute the residual, the derivatives of the inviscid fluxes are obtained by first forming the fluxes at the nodes and subsequently differentiating each component with the above formulas. Viscous terms are obtained by first computing derivatives of the primitive variables. The components of the viscous flux are then constructed at each node and differentiated by a second application of the same scheme. Although this approach is not as accurate as that in which a Pade-type scheme is employed directly for the second-derivative, it is significantly cheaper to implement in curvilinear coordinates. As previously demonstrated in Ref. [2], successive differentiation yields an accurate and stable method in conjunction with the added filtering component which is described next.

3.2. HIGH-ORDER FILTERING SCHEME

Compact-difference discretizations, like other centered schemes, are non-dissipative and are therefore susceptible to numerical instabilities due to the unrestricted growth of high-frequency modes. These difficulties originate from several sources including mesh non-uniformity, approximate boundary conditions and nonlinear flow features. In order to extend the present solver to practical simulations, while retaining the improved accuracy of the spatial compact discretization, a high-order implicit filtering technique [2, 4] is incorporated. If a typical component of the solution vector is denoted by ϕ, filtered values $\hat{\phi}$ satisfy,

$$\alpha_f \hat{\phi}_{i-1} + \hat{\phi}_i + \alpha_f \hat{\phi}_{i+1} = \Sigma_{n=0}^{N} \frac{a_n}{2} (\phi_{i+n} + \phi_{i-n}) \tag{3}$$

Equation (3), with the proper choice of coefficients, provides an $2N$th-order formula on a $2N+1$ point stencil. The $N+1$ coefficients, $a_o, a_1, ..., a_N$, are derived in terms of α_f with Taylor- and Fourier-series analyses and are found in Refs. [2, 3] along with some spectral filter responses. The adjustable parameter α_f satisfies the inequality $-0.5 < \alpha_f < 0.5$, with higher values of α_f corresponding to a less dissipative filter. In multi-dimensional problems the filter operator is applied sequentially in each coordinate direction. For the near-boundary points, the filtering strategies described in Refs. [2, 3] are employed. Up to tenth-order filter formulas have been successfully applied to solve the Maxwell [4], Navier-Stokes [2, 9, 10, 11], and MHD [12] equations in curvilinear geometries.

3.3. METRIC EVALUATION FOR CURVILINEAR DYNAMIC MESHES

The extension of high-order schemes to 3-D curvilinear meshes demands that issues of freestream preservation and metric cancellation be carefully addressed. These errors, which arise in finite-difference discretizations of governing equations written in strong-conservation form, can catastrophically degrade the fidelity of standard second-order as well as higher-order approaches [3]. In deriving the flow equations in strong-conservation form, the following metric identities have been implicitly invoked,

$$I_1 = (\xi_x/J)_\xi + (\eta_x/J)_\eta + (\zeta_x/J)_\zeta = 0 \tag{4}$$

$$I_2 = (\xi_y/J)_\xi + (\eta_y/J)_\eta + (\zeta_y/J)_\zeta = 0 \tag{5}$$

$$I_3 = (\xi_z/J)_\xi + (\eta_z/J)_\eta + (\zeta_z/J)_\zeta = 0 \tag{6}$$

$$I_4 = (1/J)_\tau + (\xi_t/J)_\xi + (\eta_t/J)_\eta + (\zeta_t/J)_\zeta = 0 \tag{7}$$

In Ref. [2] it was shown that on stretched curvilinear 2-D meshes, the compact scheme exhibits freestream preservation when the metrics are evaluated with the same finite-difference expressions as those employed for the fluxes. It was also demonstrated that the practice of prescribing *analytic* metrics on stretched curvilinear grids can lead to unacceptable errors and therefore should in general be avoided. The previous straightforward approach of calculating the metrics, although effective in 2-D, fails to provide metric cancellation for general 3-D curvilinear configurations. To illustrate this point, consider the standard metric relations:

$$\begin{aligned} \xi_x/J &= y_\eta z_\zeta - y_\zeta z_\eta \\ \eta_x/J &= y_\zeta z_\xi - y_\xi z_\zeta \\ \zeta_x/J &= y_\xi z_\eta - y_\eta z_\xi \end{aligned} \tag{8}$$

associated with the identity I_1. Evaluation of the y and z derivatives in the previous expressions using explicit or compact centered schemes does not satisfy I_1, and as a result, significant grid-induced errors may appear. To extend the high-order compact scheme to general geometries, the metric terms are rewritten prior to discretization in the equivalent ('conservative') form [13]:

$$\begin{aligned} \xi_x/J &= (y_\eta z)_\zeta - (y_\zeta z)_\eta \\ \eta_x/J &= (y_\zeta z)_\xi - (y_\xi z)_\zeta \\ \zeta_x/J &= (y_\xi z)_\eta - (y_\eta z)_\xi \end{aligned} \tag{9}$$

Similar expressions are employed for the remaining metric terms in order to satisfy the identities I_2 and I_3 above. When the transformation metrics are

recast in this manner, and the derivatives are evaluated with the same high-order formulas employed for the fluxes, freestream preservation is again recovered in general time-invariant 3-D curvilinear geometries [3].

For deforming and moving meshes, the identity I_4 must be also satisfied to eliminate metric cancellation errors and to ensure freestream preservation [6]. This metric identity is referred to in the literature [13] as the Geometric Conservation Law (*GCL*). For the time-integration methods employed in this work, the time-derivative term in Eqn. (1) is split using chain-rule differentiation as follows:

$$(\vec{U}/J)_\tau = (1/J)\vec{U}_\tau + \vec{U}(1/J)_\tau \tag{10}$$

Rather than attempting to compute the time derivative of the inverse Jacobian directly from the grid coordinates at various time levels (either analytically or numerically), we simply invoke the *GCL* identity I_4 to evaluate $(1/J)_\tau$, i.e.

$$(1/J)_\tau = -[(\xi_t/J)_\xi + (\eta_t/J)_\eta + (\zeta_t/J)_\zeta] \tag{11}$$

where

$$\begin{aligned} \xi_t/J &= -[x_\tau(\xi_x/J) + y_\tau(\xi_y/J) + z_\tau(\xi_z/J)] \\ \eta_t/J &= -[x_\tau(\eta_x/J) + y_\tau(\eta_y/J) + z_\tau(\eta_z/J)] \\ \zeta_t/J &= -[x_\tau(\zeta_x/J) + y_\tau(\zeta_y/J) + z_\tau(\zeta_z/J)] \end{aligned} \tag{12}$$

For the case of an analytically prescribed dynamic mesh transformation, the grid speeds (x_τ, y_τ, z_τ) are obtained from the corresponding analytic expressions. An example in which the grid speeds are known analytically corresponds to the case of a maneuvering wing when the entire mesh moves in a rigid fashion. In many practical applications involving deforming meshes (e.g. dynamic aeroelastic simulations), the grid speeds are not known a priori, and must therefore be approximated to the desired degree of accuracy employing the evolving grid coordinates at several time levels. As demonstrated in Ref. [6], the high-order method retains its superior accuracy on rapidly distorting meshes when the procedure outlined above is incorporated for the time metrics.

3.4. TIME-INTEGRATION SCHEME

Two different time-integration approaches are incorporated in the present family of solvers. For wave propagation applications, the equations are integrated in time with the classical fourth-order four-stage Runge-Kutta method (*RK4*). The scheme is implemented in low storage form requiring three levels of storage. For wall-bounded viscous flows, the stability constraint of the explicit time-marching scheme is found to render the approach

too restrictive and inefficient. Therefore, the implicit, approximately-factored method of Beam and Warming [14] is also incorporated and augmented through the use of Newton-like subiterations in order to achieve second-order time accuracy. In delta form, the scheme may be written as

$$\begin{aligned}
&\left[J^{-1^{p+1}} + \phi^i \Delta\tau \delta_\xi^{(2)} \left(\frac{\partial \hat{F}^p}{\partial U}\right)\right] J^{p+1} \times \\
&\left[J^{-1^{p+1}} + \phi^i \Delta\tau \delta_\eta^{(2)} \left(\frac{\partial \hat{G}^p}{\partial U}\right)\right] J^{p+1} \times \\
&\left[J^{-1^{p+1}} + \phi^i \Delta\tau \delta_\zeta^{(2)} \left(\frac{\partial \hat{H}^p}{\partial U}\right)\right] \Delta U \\
&= -\phi^i \Delta\tau \left[J^{-1^{p+1}} \frac{(1+\phi)U^p - (1+2\phi)U^n + \phi U^{n-1}}{\Delta\tau}\right. \\
&+ U^p (1/J)_\tau{}^p + \delta_\xi \left(\hat{F}^p\right) + \\
&\left.\delta_\eta \left(\hat{G}^p\right) + \delta_\zeta \left(\hat{H}^p\right)\right]
\end{aligned} \tag{13}$$

where $\partial \hat{F}/\partial U$ etc are flux Jacobians, δ represents the spatial difference operator and $\Delta U = U^{p+1} - U^p$. For improved efficieny, the method incorporates the diagonalization procedure of Ref. [15]. In addition, nonlinear artificial dissipation terms [16]are appended to the implicit operator to enhance stability. Note that while the derivatives of the flux Jacobians have been obtained to second-order accuracy (denoted with the superscript (2) in Eqn. (13)), those on the right hand side, *i.e.*, in the residual, are evaluated with the compact-difference higher-order method. In order to reduce errors associated with these simplifications, a sub-iteration strategy is employed. Thus, for the first subiteration, $p = 1$, $U^p = U^n$ and as $p \to \infty$, $U^p \to U^{n+1}$. Typically, three subiterations are applied per time step. A range of numerical experiments suggests that second-order accuracy in time is adequate for the problems considered [6].

3.5. MULTI-DOMAIN STRATEGY

Domain-decomposition techniques constitute an important component of modern computational strategy. Due to their spatially implicit nature, Pade-type schemes are more difficult to utilize in a multi-domain environment than explicit methods. However, a finite-size overlap can be employed with the present compact/filtering methodology to generate a powerful approach applicable to complicated curvilinear meshes [3]. Figure 1 depicts schematically the problem of a vortex traveling to the right in a rectilinear path. The domain of computation is divided into two parts to be distributed to different processors. Each sub-domain is supplemented with several points from the adjacent sub-domain to form an overlap region, whose details for a five-point vertical overlap are also shown in Fig. 1. Although the overlap points are collocated they have been shown slightly staggered for clarity. Each vertical line is denoted by its i-index. Data is

exchanged between adjacent subdomains at the end of each sub-iteration of the implicit scheme (or each stage of *RK4*), as well as after each application of the filter. The values at points 1 and 2 of Mesh 2 are set to be identically equal to the corresponding updated values at points $IL-4$ and $IL-3$ of Mesh 1. Similarly, reciprocal information is transferred through points 4 and 5 of Mesh 2 which "donate" values to points $IL-1$ and IL of Mesh 1. More details on the accuracy and robustness of the present multi-domain approach can be found in Ref. [3].

4. Results

The previous computational methodology has been successfully demonstrated for a number of applications, including: unsteady vortical flows [2], DNS of pulsed walljet [9] and synthetic jet actuators [17], LES of subsonic and supersonic flows [10, 11], non-linear fluid structure interaction [18], and benchmark problems for acoustic scattering [7] and MHD [12]. In the interest of brevity, only a subset of these results is presented here.

4.1. MULTI-DOMAIN ACOUSTIC SCATTERING SIMULATION

The low dispersion error characteristic of compact-difference schemes is an attractive property in the simulation of wave propagation phenomena associated with acoustic and electromagnetic scattering. In order to demonstrate the capability of the present numerical approach to treat acoustic phenomena in a multiple-domain situation, consider the scattering of a periodic acoustic source with the two-zone overlap configuration shown schematically in Fig. 2a.

The single-domain grid, consisting of 361×321 points, is split along $\theta = 90^o$, where extra ξ-lines are added to form a five-point overlap as in Fig. 1. Solutions are advanced separately on each subdomain, and information is exchanged at the overlap points in the manner previously discussed in Section 3.5. The *C6* scheme is employed for interior points along with fourth- and fifth-order compact operators at the boundary and next-to-boundary points respectively whereas *RK4* is utilized for time-integration. In the interior of each domain, a 10th-order filter is utilized while high-order one-sided techniques, described in Refs. [3, 7], are invoked near boundaries. For all filter operators, the coefficient $\alpha_f = 0.45$ is specified.

Figure 2b displays instantaneous pressure contours in the vicinity of the cylinder. It is apparent that the pressure waves cross the grid interface without producing any noticeable disruptions of the interference pattern even though pressure waves generated by the source propagate through the overlap region in an oblique direction to the zonal interface. A quantitative comparison of the single-domain, multiple-domain and analytic solutions

is given in Fig. 2c in terms of the directivity of the radiated sound at $r/D = 5$. The directivity obtained with a 6th-order near-boundary filter in the overlap region is essentially the same as the corresponding single-domain baseline solution, and both results are in excellent agreement with the theoretical solution. These results highlight the potential of the present high-order methodology for domain-decomposition applications on parallel computers. Additional details on the manner in which the high-order filter may be applied to yield a robust farfield radiation treatment for acoustic simulations may be found in Ref. [19].

4.2. DNS OF A PULSED WALLJET

As another example, the method has been employed to simulate the three-dimensional transition of a forced, finite aspect-ratio, plane wall jet [9]. The wall jet configuration considered is shown in Fig. 3a. The main parameters governing the flow are the Reynolds number, the disturbance characteristics at the jet nozzle, the aspect ratio of the channel, and the length of the wall. In the present study, the Reynolds number, based on jet maximum velocity (U_{max}) and nozzle height (h), is 2150. The aspect ratio of the channel is $2b/h = 20$. The mean velocity profile in the normal direction at the nozzle exit is parabolic and corresponds to a fully-developed laminar channel flow in that direction. The flow is forced at the nozzle exit with a frequency of $200Hz$ and amplitude corresponding to 6% of the jet centerline velocity.

The overall flow structure is shown in Fig. 3b in terms of an iso-surface of vorticity magnitude. The transition process begins with the formation of shear-layer and wall vortex pairs which, due to the energetic forcing, appear close to the nozzle exit and are phased-locked for a short distance downstream. In the process of their spanwise evolution, the rollers are first split into a double-helical structure, which is clearly discernable near the sidewalls. This feature propagates toward the center while also expanding in the radial direction. The spiral vortex branches are wound in a sense opposite to that of the swirl direction of the vortex, but consistent with the direction of the induced axial flow which exists within the vortex core. This vortex branching and helical twisting spreads rapidly through self-induction effects, and eventually reaches the symmetry plane where the vorticity magnitude within the vortex core is drastically diminished (hence the apparent break in the iso-surface, region 'γ' in Fig. 3b). The ability of of the present high-order solver to discern the fine-scale breakdown to turbulence is shown in Fig. 3c which displays contours of vorticity magnitude on a horizontal plane ($y/h = 0.5$). Additional details of the simulation, as well as comparison with high-resolution experimental measurements may be found in Ref. [9].

4.3. LES OF A SPATIALLY-EVOLVING SUPERSONIC BOUNDARY LAYER

This simulation considers a zero-pressure-gradient, flat-plate boundary layer at a Mach number of 2.25 and $Re_\theta \approx 6000$, which corresponds to the computational studies of Refs. [20, 21] Details of the stretched Cartesian grids and the initial/boundary conditions employed are given in Ref. [11]. In this section, only results (denoted as 'no-model') obtained using the 10th-order low-pass filter without the inclusion of an SGS model are considered. Solutions for both the Smagorinsky and dynamic subgrid-scale stress models can be found in Ref. [11].

Figure 4a shows the spanwised-averaged, mean skin-friction coefficient. Downstream of the transition location (which is sensitive to the numerical scheme and forcing employed), the present results compare favorably with those of Ref. [20]. This fact is encouraging since a coarser mesh ($371 \times 61 \times 151$) is used in the present computations with the sixth-order compact approach. The calculations of Ref. [20] were performed on a much finer grid ($971 \times 55 \times 321$) utilizing a fifth-order upwind-bias algorithm for the convective terms. Reasonable agreement in terms of the mean streamwise velocity profile is also shown in Fig. 4b. Finally, contours of the instantaneous spanwise vorticity component at a height of $y^+ \approx 1.0$ are shown in Fig. 4c and display the longitudinal structures characteristic of turbulent wall-bounded flows.

4.4. BOUNDARY-LAYER TRANSITION OVER A FLEXIBLE PANEL

As a final example of a simulation of multi-disciplinary physics with the present methodology, consider a transitional boundary-layer flow over a flexible finite panel embedded in a rigid surface as shown schematically in Fig. 5a. This problem is closely related to classic panel flutter phenomena, as well as to viscous flow over compliant surfaces. The panel of length a and thickness h extends over the region $0.5 \leq x/a \leq 1.5$. The leading-edge region of the plate ($-0.5 \leq x/a \leq 0.0$) is formed by an ellipse of half-thickness $0.05h$ (*i.e.* aspect ratio 10). An additional challenge posed by this aeroelastic simulation is the need to accomodate the surface deflection with a dynamically deforming mesh. The problem has been examined in great detail in Ref. [18] which should be consulted for details regarding boundary condition implementation and mesh resolution studies.

For brevity, only select results obtained at $M_\infty = 0.8$ and $Re_a = 10^5$ are summarized here to highlight the ability of the method to capture the complicated unsteady phenomena under the influence of flow-induced surface deformation. At low values of the dynamic pressure, a steady flow is obtained despite the adverse pressure gradient induced by the downward deflection of the panel. At higher dynamic pressures, however, a travelling-

wave-flutter phenomenon is observed as summarized in Fig. 5b, c. The instantaneous panel shapes (not shown) display a seventh-mode oscillation with a dominant nondimensional frequency $St = fa/U_\infty = 1.52$ which is substantially higher than the fundamental frequency of the elastic plate. The high-mode flexural deflections are observed to travel along the panel and to reflect at the panel edges. These high-frequency fluctuations result in a pronounced acoustic radiation pattern above the vibrating plate, shown in Fig. 5b in terms of the instantaneous pressure field. Downstream of the flexible surface, a regular train of vortical disturbances is observed (Fig. 5c) with characteristic wavelength and frequency compatible with those of Tollmien-Schlichting (T-S) instability. The travelling wave flutter appeared to originate from the coupling of the T-S waves with the panel high-mode transverse fluctuations, and this convective instability ceases below a critical value of Reynolds number.

5. Acknowledgments

The work presented here was sponsored by the U. S. Air Force Office of Scientific Research under Task 2304N402 and was monitored by W. Hilbun and T. Beutner.

References

1. S.K. Lele. Compact Finite Difference Schemes with Spectral-like Resolution. *Journal of Computational Physics*, 103:16–42, 1992.
2. M.R. Visbal and D.V. Gaitonde. High-Order Accurate Methods for Complex Unsteady Subsonic Flows. *AIAA Journal*, 37(10):1231–1239, 1999.
3. D.V. Gaitonde and M.R. Visbal. Further Development of a Navier-Stokes Solution Procedure Based on Higher-Order Formulas. *AIAA Paper 99-0557*, January 1999.
4. D.V. Gaitonde, J.S. Shang, and J.L. Young. Practical Aspects of Higher-Order Numerical Schemes for Wave Propagation Phenomena. *Int. Jnl. for Num. Methods in Eng.*, 45:1849–1869, 1999.
5. D.V. Gaitonde and M.R. Visbal. High-Order Schemes for Navier-Stokes Equations: Algorithm and Implementation into FDL3DI. Technical Report AFRL-VA-WP-TR-1998-3060, Air Force Research Laboratory, Wright-Patterson AFB, 1998.
6. M.R. Visbal and R.E. Gordnier. A High-Order Flow Solver for Deforming and Moving Meshes . *AIAA Paper 2000-2619*, June 2000.
7. M.R. Visbal and D.V. Gaitonde. Computation of Aeroacoustic Fields on General Geometries using Compact-Differencing and Filtering Schemes. *AIAA Paper 99-3706*, June 1999.
8. M.H. Carpenter, D. Gottlieb, and S. Abarbanel. The Stability of Numerical Boundary Treatments for Compact High-Order Finite-Difference Schemes. *Journal of Computational Physics*, 108:272–295, 1993.
9. M.R. Visbal, D.V. Gaitonde, and S.P. Gogineni. Direct Numerical Simulation of a Forced Transitional Plane Wall Jet. *AIAA Paper 98-2643*, June 1998.
10. D. P. Rizzetta, M. R. Visbal, and G. A. Blaisdell. Application of a High-Order Compact Difference Scheme to Large-Eddy and Direct Numerical Simulation. *AIAA Paper 99-3714*, June 1999.
11. D.P. Rizzetta, M.R. Visbal, and D.V. Gaitonde. Direct Numerical and Large-Eddy

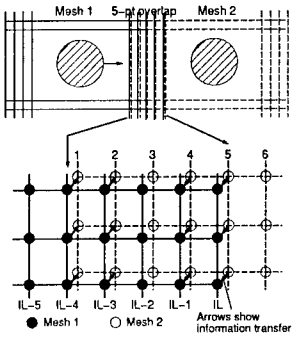


Figure 1. Schematic of mesh overlap for multi-domain strategy

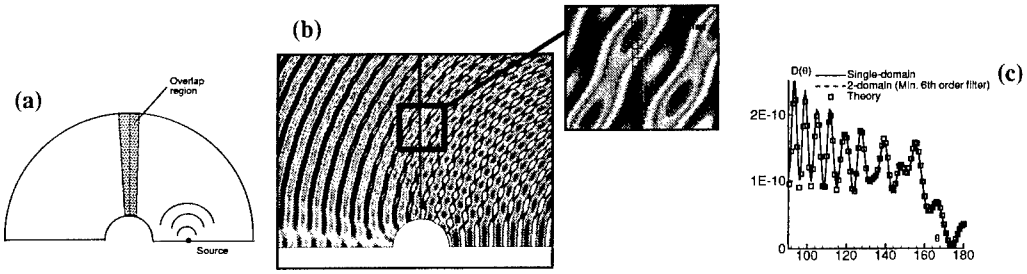


Figure 2. Multi-Domain Acoustic Scattering Simulation

Simulation of Supersonic Flows by a High-Order Method. *AIAA Paper 2000-2408*, 2000.

12. D.V. Gaitonde. Development of a Solver for 3-D Non-ideal Magnetogasdynamics. *AIAA Paper 99-3610*, June 1999.
13. P.D. Thomas and C.K. Lombard. Geometric conservation law and its application to flow computations on moving grids. *AIAA Journal*, 17(10):1030–1037, 1979.
14. R. Beam and R. Warming. An Implicit Factored Scheme for the Compressible Navier-Stokes Equations. *AIAA Journal*, 16(4):393–402, 1978.
15. T.H. Pulliam and D.S. Chaussee. A Diagonal Form of an Implicit Approximate-Factorization Algorithm. *Journal of Computational Physics*, 39(2):347–363, 1981.
16. T. Pulliam. Artificial Dissipation models for the Euler Equations. *AIAA*, 24(12):1931–1940, 1986.
17. D. P. Rizzetta, M. R. Visbal, and M. J. Stanek. Numerical Investigation of Synthetic-Jet Flow Fields. *AIAA Journal*, 37(8), 1999.
18. M.R. Visbal and R.E. Gordnier. Direct Numerical Simulation of the Interaction of a Boundary Layer with a Flexible Panel. *AIAA Paper 2001-2721*, June 2001.
19. M. Visbal and D. Gaitonde. Very high-order spatially implicit schemes for computational acoustics on curvilinear meshes. *J. Comp. Acoustics*, 2001 (In press).
20. M.M. Rai, T.B. Gatski, and G. Erlebacher. Direct simulation of spatially evolving compressible turbulent boundary layer. *AIAA Paper 95-0583*, Jan. 1995.
21. E.T. Spyropoulus. On dynamic subgrid-scale modeling for large-eddy simulation of compressible turbulent flows. *PhD Thesis, Purdue University*, 1996.

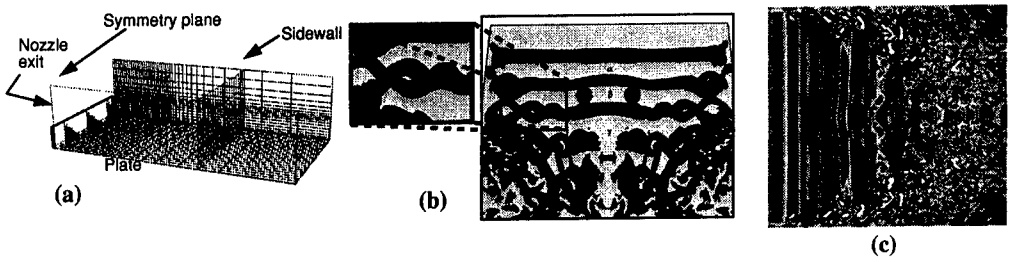


Figure 3. DNS of Forced Transitional Walljet

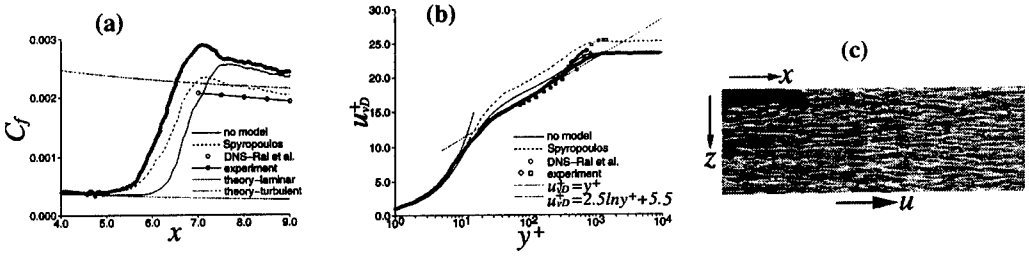


Figure 4. LES of Supersonic Flat-Plate Boundary Layer

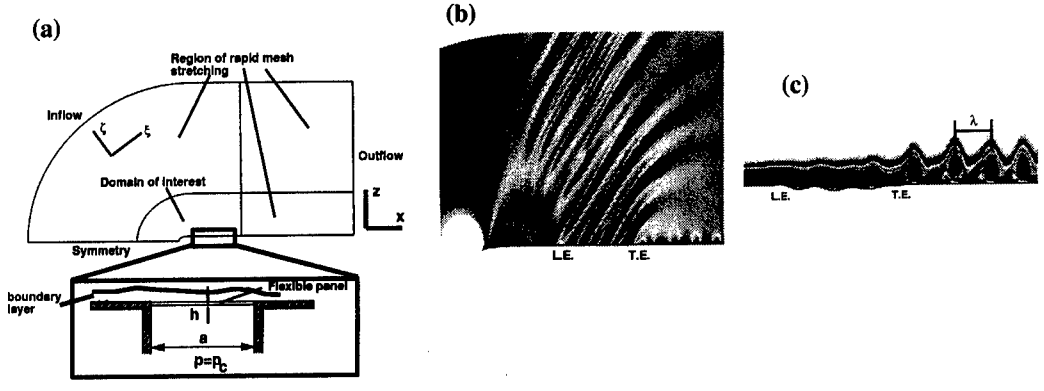


Figure 5. Transitional Boundary-Layer Flow Over a Fluttering Elastic Panel

DNS/LES FOR NASA AERODYNAMIC NEEDS AND ENGINEERING APPLICATIONS

T. B. GATSKI
Computational Modeling & Simulation Branch
NASA Langley Research Center
Hampton, VA 23681, USA

1. Introduction

While both direct numerical simulation (DNS) and large eddy simulation (LES) are at or near the top of a hierarchy of solution methods for turbulent flow fields, the Reynolds number constraints and extensive computational requirements preclude their widespread use as a practical tool in aerodynamic applications. Nevertheless, these methodologies can be used in support of more practical engineering tools such as Reynolds-averaged Navier-Stokes (RANS) formulations.

Aerodynamic flow fields present several challenges even for the most robust RANS approaches. Geometric complexity, Mach number effects, and Reynolds numbers of $\mathcal{O}(10^7)$ contribute significantly to the stringent requirements needed for successful flow field computations. Nevertheless, even with this apparent disparity between the capabilities of DNS and LES and the requirements for accurate prediction of relevant aerodynamic flow fields, both types of simulations can provide useful information if properly chosen "unit problems" are studied. Two examples of practical aerodynamic flow fields will serve to highlight some of the critical dynamical problems as well as the need for well chosen simulations that can help improve the predictive capability of RANS calculations or composite solution approaches.

The inability of RANS formulations to correctly predict critical dynamic features of complex flow fields lies with inadequacy of the closure models for the higher-order correlations that appear in the RANS formulation. A detailed discussion of such closures is outside the scope of the current topic; however, correlations involving the pressure-strain rate or pressure velocity, triple-velocity and (tensor) dissipation rate all can contribute significantly to the predictive accuracy of a RANS formulation. Since experimental stud-

ies are unable, in general, to accurately measure these higher-order correlations, numerical simulations that can help delineate the role of such terms in complex flows is extremely useful.

Ever increasing computational power as well as improved understanding of the effect of filter cut-off on subgrid scale models will continue to move LES (and DNS) towards the realm of an engineering tool. In addition, extensions of RANS formulations to unsteady RANS and related methodologies will continue to move these type of formulations closer toward the realm of a large-eddy solution technique. The future of obtaining such composite formulations will depend on the inherent consistency between the (velocity) fields computed. An example of such a consistency requirement will be discussed here and its effect on model development.

2. Airframe Dynamics

High-lift devices composed of multi-element airfoils (Fig. 1) generate complex aerodynamic flow fields. At cruise conditions, these flows are generally at the high subsonic speed range although conditions can exist in some regions for shocks to develop. Each element of the multi-element system has characteristic features which are of interest in their own right (Rumsey *et al.*, 1998).

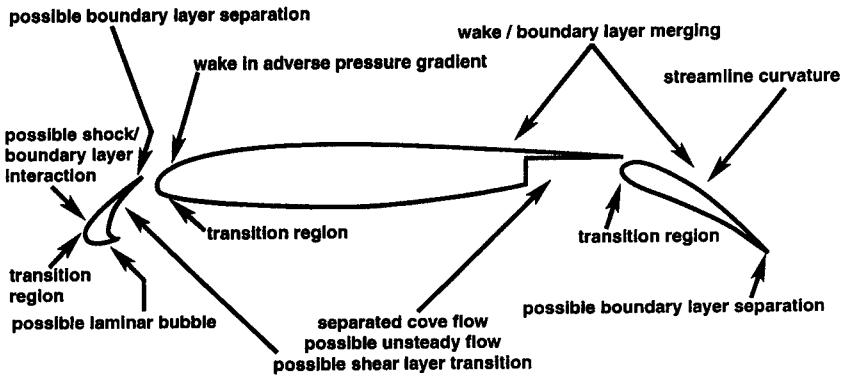


Figure 1. Sketch of multi-element airfoil configuration and important dynamic characteristics (C. L. Rumsey, private communication)

Common to all elements is the need for accurate (natural) transition prediction. Within a RANS formulation, the turbulence closure models need to be properly sensitized to the transition process. Corresponding to the usual practice of turbulence model calibration using both DNS and LES results, can such simulations be performed on (natural) transitioning flows with the goal of providing the information needed for calibration of RANS

closure models? Simulations of transitional flows have been undertaken previously; however, the motivation was not to develop a data base for model development but was to obtain a detailed description of the (nonlinear) stability process leading to a turbulent flow. As such, parameter ranges and dynamics studied did not focus on the data needed to help refine models for disturbance stress fields which would be suitable for RANS-type closures.

Another feature of this multi-element system is that all the elements are dynamically coupled through the interaction of a wake(s) generated by an upstream element and the boundary layer of a downstream element. It has not been possible to accurately predict the downstream evolution of these generated wakes and as such, the downstream predictions have not been accurate as well (Rumsey and Gatski, 2002). It is not clear whether the closure model deficiencies are due to the strong pressure gradients imposed on these wakes (such as the slot generated wake), or the sequence of pressure-gradients the developing wakes experience as they evolve downstream. In isolation, prediction of the near-wake flow field has been successful, at least over a limited range of pressure gradients (Carlson *et al.*, 2000). While DNS of a wake flow has been performed previously (Moser *et al.*, 1998), it did not focus on effects of pressure gradient or other issues related to the multi-element dynamics of interest here. Nevertheless, a well-posed and accurate DNS (or LES) could be used to validate the predictive capability of a RANS model for such wakes in relative isolation to other complicating dynamic features associated with the full configuration.

In addition to transition location and wake evolution which affect the global behavior of the multi-element flow field, each element of the system also has some characterizing dynamic features. The slat, for example, is composed of a curved, transitional flow which can sustain shocks depending on configuration, and a possible unsteady, transitioning shear flow in the lower surface cove region. Thus, shock boundary-layer interaction prediction on the curved upper surface can be an important feature of any overall prediction scheme of high-lift dynamics. Unfortunately, the ability to accurately predict such shock-boundary layer interactions are strongly problem dependent. On the lower surface of the slat experiments have shown an inherent unsteadiness in the flow. Unfortunately, such measurements are difficult and detailed mappings are unavailable. In any case, such unsteady effects produce a significant challenge to any prediction scheme. Well-focused simulations of model flows which can partially capture some of these key features of the practical configuration can be critical to identifying specific deficiencies of a particular RANS closure scheme.

The main element has been less problematic once the transition location is properly predicted or fixed. Errors in the slat wake predictions inherently persist downstream; however, the slat wake velocity deficit only begins to

interact with the main element boundary layer near the aft portion of the element. In addition, the flow over the flap is moderately curved which further complicates the dynamics. Turbulence models currently available are only moderately successful in capturing all these dynamics, even in well-posed comparative studies with experiments. Clearly, a significant challenge is to identify suitable test flow fields that can be accurately computed with DNS or LES approaches, and still provide a database that can be used to validate turbulent closure models that could lead to improved closures.

The mean velocity field over the flap is characterized by a velocity deficit produced by the merging of the slat wake with the main element boundary-layer flow and an altered inner layer velocity field due to the gap between the main element and flap. As the angle-of-attack increases, flow separation over the high-lift device may be initiated over the flap adding to the complexity of the flow. Obviously, prediction schemes are not successful over a wide parameter range and could benefit from simulations which isolate key features. One area of particular interest would be the flow field dynamics in the region downstream of the separation point. A detailed mapping of this flow would hopefully allow for improved model development.

3. Engine Flow Fields

A second example of a complex aerodynamic flow field is that associated with scramjet/ramjet engines (Fig. 2). The inlet flow field is composed of complex shock boundary-layer interactions and the detailed dynamics of such flows is not well understood. Downstream in the combustor, high speed fuel injection occurs resulting in a complex mixing process with shocks present.

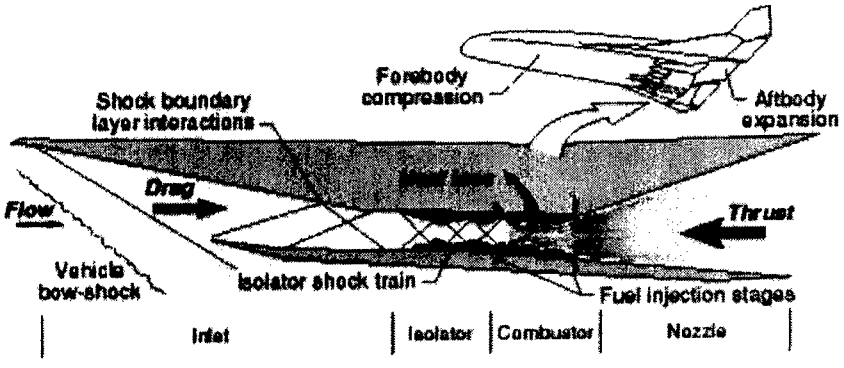


Figure 2. Sketch of inlet flow field of scramjet/ramjet engine and important dynamic characteristics (J. A. White, private communication)

Once again, such flow field predictions are beyond the capabilities of ei-

ther direct or large-eddy simulations. Thus, at this time a RANS approach is the only practical means of obtaining predictions of the flow field. The challenge, then, is to identify important dynamical features which characterize different regions of the flow field and formulate suitable DNS and LES unit problems that can be studied to improve the RANS closure models. Compressible RANS approaches using Favre-averaged variables have been the methodology most commonly used in such flows. Such approaches yield additional correlations in the governing equations which are due to compressibility and for which closure models need to be developed. These may include heat and mass flux models as well as dilatation models. Depending on the degree of compressibility, the turbulence can be significantly altered from its incompressible behavior. If so, several modeling issues arise which, unlike the incompressible case, need to be resolved. While numerical simulations have been performed in the last decade on compressible flow fields (e.g. Freund *et al.* 2000, Sarkar and Pantano 1999), the results have not been extensively utilized in model development. Thus, at the outset it would be beneficial to examine simulations already performed and evaluate their usefulness on improving existing currently available models.

As Fig. 2 shows, the inlet region is dominated by a complex shock pattern which has a significant impact on the flow field. Useful information could be obtained from a simple boundary-layer computation with an impinging shock (e.g. Adams 2000). Such a calculation would give some insight into the dominant dynamic features that would need to be considered in the full problem. Another important feature of such flows is the high-speed fuel injection process. The injection produces a very complex flow field which is very challenging to predict. Can a representative DNS or LES unit problem be devised that would successfully replicate some of the important physics? Such a database could be used to validate existing models or lead to the development of improved closure models.

Certainly complex flow field dynamics are not limited to the scramjet/ramjet engines. Unlike the scramjet/ramjet engines, turbofan engines contain a rotor/stator assembly which introduces extra strain effects into the turbulent flow field. Flow curvature and non-inertial effects adds to an already complex flow that includes leading-edge shocks ahead of the rotor blades, shedding vortices, and unsteady wakes.

4. Future Challenges

Many new challenging problems continue to arise predicated on the need to better control the flow field dynamics in complex configurations. Adaptive flow and noise control are but two examples along with the continuing need to improve the predictions of the type of flow fields discussed in the previous

sections.

Adaptive or active flow control comprise a closed system where a continuous feedback loop exists to optimize some flow field characteristic. Active cavity, fluid/structural shaping and separation are examples of control mechanisms that can be used. Each of these control mechanisms when embedded in complex aerodynamic configurations would require highly resolved simulations in order to adequately describe the complex flow field dynamics. The same holds true for improved airframe, fan and jet noise control. Detailed simulations of full configuration slat leading edge, flap trailing and side-edge, and/or landing gear geometries are prohibitive.

As in the previous sections, DNS and LES methodologies may be best suited to problems that describe the complex flow field structure in simplified geometries but which still capture the key dynamic features of the full flow field. Another approach would be to develop composite methodologies capable of achieving the accuracy of the DNS and LES methodologies, but in full configurations. Such composite or hybrid approaches have begun to be formulated and these include the Detached Eddy Simulation (DES) (e.g. Spalart 1999) and the Flow Simulation Methodology (FSM) (e.g. Zhang *et al.* 2000).

Such composite approaches can be constructed from modified Reynolds averaged Navier-Stokes (RANS) and LES formulations, for example. The usual RANS-type formulations are probably unacceptable since they do not in general handle non-equilibrium effects properly and are not properly sensitized to the broad spectrum of scales present. Extensions to the usual RANS-type formulations include, for example, the triple-decomposition approach originally proposed by Reynolds and Hussain (1972) and the Semi-Deterministic Method (SDM) (Ha Minh and Kourta 1993). Such extensions inherently solve time-dependent RANS-type formulations and as such have been referred to as unsteady RANS (URANS), time-dependent RANS (T-RANS) and VLES. The label VLES (Very Large Eddy Simulation) of course being put forward to establish a formal link with the LES approach. Some new alternatives to LES are now also appearing such as the Navier-Stokes-α model which includes nonlinear dispersive effects (Chen *et al.* 2000), and the Coherent Vortex Simulation (CVS) approach (Farge *et al.* 2000, see also Goldstein *et al.* 2000). It remains to be seen whether such approaches provide better modeling insight for RANS-type closures or a more conducive basis for composite formulations.

It should be recognized that while the RANS and LES equations are formally equivalent, the flow field is being described differently due to the disparity of scales being resolved. Thus, one might naturally ask whether there is some way in which both methods would produce the same flow field as described by the velocity field, for example.

It is worthwhile to look at a strategy proposed by Germano (1999). Consider the ensemble mean of both the velocity and pressure fields and assume that for $f(\mathbf{x},t)$ ($u_i(\mathbf{x},t)$ or $p(\mathbf{x},t)$)

$$E\{\underbrace{f(\mathbf{x},t)}_{\text{DNS}}\} = E\{\underbrace{\overline{f}(\mathbf{x},t)}_{\text{LES}}\} = \underbrace{F(\mathbf{x},t)}_{\text{ANS}} \tag{1}$$

The ambiguity associated with averaged Navier-Stokes variable is intentional. In both DNS and LES, the statistical average of the variable (DNS) or the filtered variable (LES) is performed simultaneously with (or post-processed after) the numerical solution of the Navier-Stokes equations. In RANS-type formulations (which are labeled here as ANS for Averaged Navier-Stokes), it is the averaged variable which is solved for directly. For this reason, the ANS mean velocity and pressure will simply be represented by U_i and P, respectively.

Now, in addition to Eq. (1) which assumes the equivalence of the ensemble mean of the filtered quantity with the ensemble mean, it is also required that the corresponding mean momentum equations be equivalent, then

$$\left(\frac{D}{Dt} - \nu\frac{\partial^2}{\partial x_j \partial x_j}\right) E\{u_i\} + \frac{\partial}{\partial x_i}E\{p\} = \mathcal{S}_{\text{DNS}} \tag{2}$$

$$\left(\frac{D}{Dt} - \nu\frac{\partial^2}{\partial x_j \partial x_j}\right) E\{\overline{u}_i\} + \frac{\partial}{\partial x_i}E\{\overline{p}\} = \mathcal{S}_{\text{LES}} \tag{3}$$

$$\left(\frac{D}{Dt} - \nu\frac{\partial^2}{\partial x_j \partial x_j}\right) U_i + \frac{\partial}{\partial x_i}P = \mathcal{S}_{\text{ANS}} \tag{4}$$

where

$$\frac{D}{Dt} = \frac{\partial}{\partial t} + E\{u_j\}\frac{\partial}{\partial x_j} = \frac{\partial}{\partial t} + E\{\overline{u}_j\}\frac{\partial}{\partial x_j} = \frac{\partial}{\partial t} + U_j\frac{\partial}{\partial x_j}, \tag{5}$$

and

$$\mathcal{S}_{\text{DNS}} = -\frac{\partial}{\partial x_j}E\{(u_i - E\{u_i\})(u_j - E\{u_j\})\} \tag{6}$$

$$\begin{aligned}\mathcal{S}_{\text{LES}} &= -\frac{\partial}{\partial x_j}\left(E\{\overline{u_i u_j}\} - E\{\overline{u}_i\}E\{\overline{u}_j\}\right) \\ &= -\frac{\partial}{\partial x_j}\left[E\{\left(\overline{u}_i - E\{\overline{u}_i\}\right)\left(\overline{u}_j - E\{\overline{u}_j\}\right)\} + E\{\tau_{ij}^{\text{SGS}}\}\right]\end{aligned} \tag{7}$$

$$\mathcal{S}_{\text{ANS}} = -\frac{\partial}{\partial x_j}\tau_{ij} \tag{8}$$

Note that here the second-moment of the fluctuating velocity τ_{ij} is given by some statistical average of $(u_i - U_i)\,(u_j - U_j)$.

The partitioning suggested by $\mathcal{S}_{\rm LES}$ can also be clearly shown in spectral space. For a statistically homogeneous field using a sharp cut-off filter $(\hat{G}(\mathbf{k}) = \mathcal{H}(k_c - |k|))$

$$E\{\left(\overline{u}_i - E\{\overline{u}_i\}\right)\left(\overline{u}_j - E\{\overline{u}_j\}\right)\} = \int_{\forall k} d^3\mathbf{k}\ \hat{G}^2(\mathbf{k})\Phi_{ij}(\mathbf{k},t) = \int_{|k|\le k_c} d^3\mathbf{k}\ \Phi_{ij}(\mathbf{k},t) \tag{9}$$

and

$$E\{\overline{u_i u_j} - \overline{u}_i\overline{u}_j\} = E\{\tau_{ij}^{\rm SGS}\} = \int_{\forall k} d^3\mathbf{k}\ (1 - \hat{G}(\mathbf{k}))^2\Phi_{ij}(\mathbf{k},t) = \int_{|k|\ge k_c} d^3\mathbf{k}\ \Phi_{ij}(\mathbf{k},t) \tag{10}$$

where the energy spectrum tensor $\Phi_{ij}(\mathbf{k},t)$ is related to the Fourier transformed instantaneous velocity $\hat{u}_i$ by

$$E\{(\hat{u}_i - E\{\hat{u}_i\})\,(\hat{u}_j - E\{\hat{u}_j\})\} = \delta^3(\mathbf{k} + \mathbf{k}')\Phi_{ij}(\mathbf{k},t) \tag{11}$$

Equations (9) and (10) show that as the cut-off wavenumber increases, the contribution from $\tau_{ij}^{\rm SGS}$ diminishes and the LES formulation evolves toward a full DNS; whereas, as the cut-off wavenumber decreases, the contribution from $\tau_{ij}^{\rm SGS}$ increases and more of spectrum needs to be modeled.

In order that the velocity fields $E\{\overline{u}_i\}$ and U_i computed from either an LES Eq. (3) or a RANS-type Eq. (4) formulation be the same, a formal requirement for consistency between the two methodologies would be

$$\tau_{ij} = E\{\left(\overline{u}_i - E\{\overline{u}_i\}\right)\left(\overline{u}_j - E\{\overline{u}_j\}\right)\} + E\{\tau_{ij}^{\rm SGS}\}, \tag{12}$$

or using Eqs. (9) and (10),

$$\int_{\forall k} d^3\mathbf{k}\ \Phi_{ij}(\mathbf{k},t) = \int_{|k|\le k_c} d^3\mathbf{k}\Phi_{ij}(\mathbf{k},t) + \int_{|k|\ge k_c} d^3\mathbf{k}\Phi_{ij}(\mathbf{k},t). \tag{13}$$

The relation in (12) can also be shown to be a direct consequence (Germano 1999) of the initial assumption about the mean fields in Eq. (1). Germano (1999) used the result in Eq. (12) to derive a simple relation for the subgrid scale eddy viscosity. An alternative view would be to use (12) as a guide to improved modeling of τ_{ij}.

In a statistically steady flow, where the ANS is simply the usual RANS (e.g. long time average) formulation, τ_{ij} contains the entire effect of the

turbulence on the mean flow, and in a sense corresponds to the limiting value for a decreasing cut-off wavenumber k_c. However, in statistically unsteady flows where methods such as unsteady RANS (URANS or T-RANS, VLES) may be needed, contributions from both Eqs. (9) and (10) need to be properly represented by τ_{ij} in order for consistency with an LES formulation. In practice, for inhomogeneous flows the mean (velocity) fields obtained from a RANS-type formulation are associated with temporal averages. This further complicates any consistency arguments due to the fact that any coupling between such a temporal average and the spatial filtering associated with an LES would necessarily involve a complicated (and probably unknown) dispersion relation (Pruett, 2000) that needs to be taken into account.

5. Summary

While direct and/or large eddy simulations are probably not going to be capable of predicting complex aerodynamic flow field themselves, the methodologies can and should be utilized to solve flow problems that replicate the essential dynamic features of the full problem. In the near term, this may be the most useful role of such methodologies rather than as a substitute to the currently available RANS-type models. These simulation results can then be used to develop improved closure models for higher-order correlations that appear in the models for the Reynolds stress tensor.

Within this framework, examples of complex aerodynamic flow fields including a high-lift system composed of a multi-element airfoil configuration and a scramjet/ramjet engine configuration were used to highlight the need for well chosen unit problems that would isolate the key dynamics associated with such flows.

Currently, composite methodologies are appearing which attempt to utilize both the LES and RANS-type formulations. Formal and complete methods which correctly utilize these two formulations may need to satisfy some consistency requirements in order to insure that both the LES and RANS-type formulation will yield the same mean flow fields.

References

Adams, N. (2000) Direct simulation of the turbulent boundary layer along a compression ramp at $M = 3$ and $Re_\theta = 1685$, *J Fluid Mech.***Vol. 420**, pp. 47–83.

Carlson, J. R., Duquesne, N., Rumsey, C.L., and Gatski, T.B. (2001) Computation of turbulent wake flows in variable pressure gradient, *Comput. Fluids***Vol. 30**, pp. 161–187.

Chen, S., Foias, C., Holm, D. D., Olson, E., Titi, E. S., and Wynne, S. (1999) The Camassa-Holm equations and turbulence in pipes and channels, *Physica D***Vol. 133**, pp. 49–65.

Farge, M., Schneider, K., and Kevlahan, N. (1999) Non-Gaussianity and coherent vortex simulation for two-dimensional turbulence using an adaptive orthogonal wavelet basis, *Phys. Fluids***Vol. 11**, pp. 2187–2201.

Freund, J. B., Lele, S. K., and Moin, P. (2000) Compressibility effects in a turbulent annular mixing layer. Part 1. Turbulence and growth rate, *J Fluid Mech.***Vol. 421**, pp. 229–267.

Germano, M. From RANS to DNS: Towards a bridging model *Direct and Large-Eddy Simulation-III*, P. R. Voke, N. D. Sandham and L. Kleiser (eds.), Kluwer, pp. 225–236.

Goldstein, D. E., Vasilyev, O. V., Wray, A. A., and Rogallo, R. S. Evaluation of the use of second generation wavelets in the coherent vortex simulation approach, *Proceedings of the 2000 Summer Program*, Center for Turbulence Research, pp. 293–304.

Ha Minh, H., and Kourta, A. (1993) Semi-deterministic turbulence modelling for flows dominated by strong organized structures, *Proc. 9th Symp. on Turbulent Shear Flows*, Kyoto, Japan, pp. 10.5.1–10.5.6.

Moser, R. D., Rogers, M. M., Ewing, D. W. (1998) Self-similarity of time-evolution plane wakes, *J Fluid Mech.***Vol. 367**, pp. 255–289.

Pruett, C.D. (2000) Eulerian Time-Domain Filtering for Spatial LES, *AIAA J.***Vol. 38**, pp. 1634–1642.

Reynolds, W. C., and Hussain A. K. M. F. (1972) The mechanics of an organized wave in turbulent shear flow. Part 3. Theoretical models and comparisons with experiments, *J Fluid Mech.***Vol. 54**, pp. 263–288.

Rumsey, C.L., and Gatski, T.B. (2002) Recent turbulence model advances applied to multielement airfoil computations, J. Aircraft, To Appear.

Rumsey, C.L., Gatski, T.B., Ying, S. X., and Bertelrud, A. (1998) Prediction of high-lift flows using turbulent closure models, *AIAA J.***Vol. 36**, pp. 765–774.

Sarkar, S., and Pantano, C. (1999) Contributions of DNS to the investigation of compressible, turbulent shear flows, *Direct and Large-Eddy Simulation-III*, P. R. Voke, N. D. Sandham and L. Kleiser (eds.), Kluwer, pp. 371–382.

Spalart, P. R. (1999) Strategies for turbulence modelling and simulations, In *Engineering Turbulence Modelling and Experiments 4* W. Rodi and D.Laurence (eds.), Elsevier, pp. 3–17.

Zhang, H. L., Bachman, C. R., and Fasel, H. F. (2000) Application of a new methodology for simulations of complex turbulent flows, *Fluids 2000*, AIAA Paper No. 2000-2535.

DNS/LES FOR COMPLEX FLOWS AND INDUSTRIAL INTEREST

P. SAGAUT
ONERA
29 av. de la division Leclerc, 92322 Châtillon cedex, France
Tel : 33 (0)1 46 73 42 71
email : sagaut@onera.fr

Abstract.

This paper presents a general overview of the recent works dealing with LES/DNS carried out at ONERA. The emphasis is put on developments aiming at extending or using these techniques for complex flows directly connected with practical applications.

1. Introduction

Unsteady numerical simulation of flows of theoretical and practical interest is more and more popular. It allows us to gain a deeper insight in involved physical mechanisms, and practical experience shows that it reduces the constraint on the turbulence modeling (when compared to steady RANS computations), since a significant part of the turbulent motion is directly captured. Main drawbacks are that the solution is often much more sensitive to numerical errors than steady RANS computations and that huge amounts of grid points is needed to obtain a satisfactory solution.

The rapid increase of the computing power makes it now possible to perform DNS and/or LES of complex flows, which cannot be considered as "academic test cases".

In this paper, we will discuss some applications of DNS and/or LES to flows of practical interest performed at ONERA :

- Subsonic flow around a two-dimensional wing near stall.
- Flow around a Delta wing with vortex breakdown.
- Flow around a low-pressure turbine blade.

For all these applications, the parameters of the wind-tunnel experiments (geometry, Reynolds number) are strictly reproduced in the simulations. All these flows involve a wide range of physical phenomena, such as transition, separation, boundary layer, wake, etc. As a consequence, they are challenging cases for LES and DNS, since they cannot be treated with one of these approaches only. Because of the high value of the Reynolds number (up to several millions in some cases), a full DNS cannot be employed over the whole computational domain, and LES must be used. But transitional region must be treated with DNS or quasi-DNS resolution. This kind of complex applications thus requires the development of hybrid approaches, based on self-adaptive subgrid models and *ad hoc* numerical techniques, which must be able to provide some numerical stabilization without polluting the solution.

New developments dealing with zonal multiresolution DNS/LES techniques are presented in Sec. 2. Problems dealing with the control of numerical dissipation are discussed in Sec. 3. Results dealing with the previously mentioned applications and obtained making use of the zonal techniques are presented in Sec. 4. Then, new ways to reduce the computational cost of DNS/LES are discussed in Sec. 5.

2. Development of zonal multiresolution DNS/LES techniques

Most of the known works dealing with LES (see [1] for a recent review) and DNS on structured meshes make use of monodomain numerical algorithm, or conformal multidomain approach. This results in a severe limitation in the capability to concentrate the computational nodes in areas where important physical mechanisms occur while keeping the total number of grid points as low as possible. This limitation renders the use of classical DNS/LES approaches very expensive for complex geometries, where these "important areas" are very small when compared to the full geometry. This is well known for the classical example of the turbulent boundary layer.

In order to alleviate this problem, a zonal multiresolution approach has been developped [18], which in practice appears as a non-conformal subdomain technique. From the theoretical point of view, this approach leads to the problem of the coupling of two solutions with different filter lengths at the subdomain interface. It can be shown that, in the most general case, neither the instantaneous field nor the mean or rms fields are continuous at the interface, because of the difference in the filters. As a consequence, classical conservative treatments of the interface are no longer valid.

The proposed method rely on the definition of two operators at the interface: a restriction operator (from fine to coarse subdomains), and an

enrichment operator (from coarse to fine subdomains) to reconstruct the high frequencies on the interface. The restriction operator is defined as a filter applied to the high frequency solution. The enrichment algorithm is based on the extrapolation of the difference between the solution in the two subdomain near the interface. This algorithm was demonstrated to be efficient for filter length ratio as high as 4 for wall bounded turbulent flows (plane channel, 2D wings or delta wing).

The use of this technique has been extended to the definition of coupling between 2D and 3D subdomains [15]. This extension makes it possible to reduce the number of grid points for flows around 2D profiles by using 3D subdomains in turbulent zones only (boundary layer, wake), while 2D domains are defined everywhere else.

3. About the control of numerical dissipation

Another important problem which occurs for high Reynolds number complex flows is the stabilization of the simulation. Daily experience shows that subgrid models (even the most dissipative ones) do not prevent the occurance of spurious wiggles. This is even more obvious when transonic flows are aimed [7, 8, 9].

For schock-free flows, a modified version of the AUSM+(P) scheme has been developped [15]. This modification is based on the introduction of a wiggle detector, the dissipative part of the AUSM scheme being set to zero at locations where no wiggles are detected. This wiggle detector Φ is computed as follows in cell number i :

$$\Delta_\phi^i = \begin{cases} -1 & \text{if } (\phi_{i+2} - \phi_{i+1})(\phi_{i+1} - \phi_i) < 0 \\ 1 & \text{otherwise} \end{cases} \tag{1}$$

$$W_{\psi_k} = \begin{cases} 1 & \text{if } \Delta_{\psi_k}^i + \Delta_{\psi_k}^{i+1} < 0 \quad \text{or} \quad \Delta_{\psi_k}^i + \Delta_{\psi_k}^{i-1} < 0 \\ 0 & \text{otherwise} \end{cases} \tag{2}$$

The sensor is then defined as $\Phi = Max(W_{\psi_k}), k = 1, .., 5$, where ψ is the primitive variable vector. This sensor was shown to yield a very large reduction of the amount of numerical dissipation, preventing a possible conflict with the true subgrid dissipation induced by the models, as observed for classical upwind schemes [6, 17]. When MILES [2, 5] computations are wanted, the sensor is set to 1 everywhere.

When shocks are present, it is necessary to use some numerical stabilization. High-order ENO filters have been developped [8], which lead to an important cost reduction (up to a factor 15) when compared to classical ENO schemes. These filters are localized near discontinuities thanks to the use of a shock detector based on the proposal of Ducros *et al.* [4].

4. Examples of application

We now present three applications, which are good examples of recent achievements of LES/DNS at ONERA. All these simulations have been carried out using the multidomain/multiresolution technique and the wiggle detector describe above.

4.1. FLOW AROUND A TWO-DIMENSIONAL WING NEAR STALL

The first computational case is related to the flow around the Aerospatiale A-airfoil near stall (the angle of attack is equal to 13.3^o). The chord Reynolds number is equal to 2.1 10^6. This case was selected during the LESFOIL project, and details of ONERA's results can be found in Ref. [15]. This configuration represents a challenging test case for both RANS and LES computations because of the complexity of the suction side boundary layer: the adverse pressure gradient induces a laminar separation with turbulent reattachment near the leading edge, and a massive separation occurs at the trailing edge.

The best results have been obtained when the transition process was directly captured by the simulation, i.e. when the grid in the boundary layer region was fine enough to represent the small scale physics. The corresponding grid contains 2048 points on the suction side, yielding $\Delta x^+ \approx 100$ everywhere. In the two other direction, the following criteria were fulfilled: $\Delta y^+ \leq 20$ and $\Delta z^+ \leq 2$. The total number of grid points is 7.2 millions. The corresponding number of grid points required to get the same grid resolution with a monodomain C mesh is 21 millions.

Good results have been obtained using the Mixed Scale Model [20, 11, 12, 1]. Pressure and friction coefficients are compared with experimental data in Fig. 1. Computed lift and drag are 1.539 and 0.0250, respectively. These values compare favourably with experimental results: 1.548-1.515 and 0.0206-0.0308, respectively.

With the same resolution, MILES results are less accurate but still reliable, mainly because the transition is affected. This is in agreement with the results of Mossi and Sagaut [17] for the plane channel case.

4.2. FLOW AROUND A DELTA WING WITH VORTEX BREAKDOWN

The flow around a Delta wing at high angle of attack with vortex breakdown is an example of 3D geometry. The Reynolds number based on the chord and the angle of attack are equal to 1.5 10^6 and 27^0, respectively. We present here the results obtained using the MILES approach, which is a good candidate for this kind of application involving massive separation and nearly-free shear layer dynamics.

The total number of subdomains is equal to 21, corresponding to 4 millions grid points. The equivalent number of grid points with a conformal subdomain technique is 200 millions. In order to reduce the number of grid points, a coarse grid was used in the near-wall region and a wall-model was employed to provide boundary conditions on solid walls.

A general view of the instantaneous flow is shown in Fig. 2, where the vortex breakdown is clearly observed. Mean velocity profile is compared with experimental data in Figs. 3 and 4, showing a satisfactory agreement.

4.3. FLOW AROUND THE T106 LOW-PRESSURE TURBINE BLADE

The last example deals with the transitional flow around the T106 low-pressure turbine blade, at a chord Reynolds number equal to 1.6 10^5. The inlet flow angle and the exit flow angle are equal to 37.7 and -63.2 degrees, respectively. The pitch to chord ratio is taken equal to 0.799. The computational setup corresponds exactly to the experimental configuration. This example is characterictic of applications which can be treated using both DNS and LES. Extensive DNS simulations have been performed by Durbin and his coworkers [3] on the same geometry, and the idea was here to reduce the number of grid points while preserving the quality of the results.

Once again, the grid was fine enough to capture durectly the transition process: $\Delta x^+ < 40$, $\Delta y^+ < 20$ and $\Delta z^+ < 1$, corresponding to the use of 920 grid points on the profile. The total number of grid points is reduced to 1 million, thanks to the use of 2D subdomain and progressive mesh refinement in the 3D zone along the profile based on the zonal multiresolution technique. The total number of subdomains is five 2D domains and six 3D domains. This is to be compared to the 25.10^6 points grid used for DNS at CITS.

A general view of the instantaneous flow is presented in Fig. 5. The transition process and the topology of the wake are clearly identified. Results of both MILES and classical LES (using the Mixed Scake Model) are compared with experimental results in Fig. 6. It is observed that a general very good agreement is recovered. An interesting point is that the two approaches yield the same results. This can be explained by the fact that the grid resolution is very good (meshes are at most twice larger as in the DNS grid), leading to very small subgrid effects. The discrepancy with the conclusion drawn from the A-profile simulations could be explained by the fact that the size of the mesh in streamwise direction is twice smaller in the blade case than in the wing computation, and the Reynolds number in smaller.

5. Further reduction of the computational cost

The applications presented above make use of the zonal multiresolution technique, but they all rely on the usual LES/DNS approaches. Further reduction of the CPU cost can be obtained thanks to the coupling of DNS/LES with new methods. We discuss here some approaches dealing with the coupling of LES with multilevel algorithms and two ways of performing RANS/LES coupling, which have not yet been applied to complex configurations.

5.1. MULTILEVEL ALGORITHMS

A possible way to reduce CPU cost of the LES approach is to define a multilevel algorithm [13], than can be interpreted as a time-consistant extension of the usual multigrid algorithm. The resulting method can be considered both as an acceleration technique and a new way to close the filtered Navier-Stokes equations without making use of the subgrid viscosity approach. In practice, N levels of embedded grids are defined, each one corresponding to a different filtering level. The key points of the method are: (i) the definition of a cycling strategy and (ii) the closure at each level.

Terracol *et al.* have proposed a V-cycle algorithm [21, 22, 23], based on a fixed or self-adaptive evaluation of the integration time on each grid, together with an extension of dynamic mixed model or a hierarchical closure. The tests show a reduction of the CPU time by a factor up to 5 (compared to monolevel LES on the same grid) without noticeable loss on the accuracy of the results for the plane channel flow and the plane mixing layer.

5.2. ZONAL RANS/LES COUPLING

A first way to couple RANS and LES is to define a zonal approach, as it is implicitely done in the Detached Eddy Simulation approach. From a theoretical point of view, this way of coupling RANS and LES appears as an extension of the zonal multiresolution LES algorithm discussed above in the paper. This analysis is conducted by Quéméré *et al.* [21, 19]. The main new points are: (i) RANS and LES solutions do not correspond to the same effective filter (that can be analyzed in the same way as LES effective filters [14]); (ii) RANS and LES solutions do not necessarily have the same dimension and (iii) the number of unknown is not the same if turbulence models based on transport equations are used.

An interface treatment for zero-equation SGS model and two-equations turbulence model has been assessed on the plane channel configuration, with reliable results on the mean velocity and the resolved Reynolds stresses. Examples of computed resolved Reynolds stresses for the plane channel con-

figurations are shown in Fig. 7. Two configurations have been investigated: near-wall RANS subdomain with LES domain at the center of the channel, and near-wall LES computation with RANS domain at the center of the channel.

5.3. ANOTHER RANS/LES COUPLING: THE NLDE APPROACH

The last point discussed in this paper deals with the reconstruction of turbulent fluctuations around a mean profile obtained using the RANS approach. An approach has recently been developped by Labourasse *et al.* [21, 10], which belongs to the Non-Linear Disturbance Equations family, as defined by Morris and his co-workers [16].

The idea is here to reconstruct locally the turbulent fluctuations for particular purposes (aeroacoustics, aero-optics) using a LES-like equations for the fluctuations, with source terms corresponding to the coupling with the mean flow. Assessment in the fully general compressible case, including unsteady mean flow, on the channel flow configuration is given in Ref. [10]. These results also show that the NLDE approach is more robust than classical LES. Examples of reconstructed resolved Reynolds stresses are compared to classical LES solutions in Fig. 8.

Acknowledgements

The author would like to emphasize the contribution of all his co-workers during the five past years: I. Mary, E. Garnier, P. Quéméré, M. Terracol, E. Lernormand, B. Raverdy, E. Labourasse, Ph. Guillen.

References

1. Sagaut, P., (2001) *Large-eddy simulation for incompressible flows.* Springer-Verlag, Berlin.
2. Boris, J.P., Grinstein, F.F., Oran, E.S., Kolbe, R.L., (1992) New insights into large-eddy simulation. *Fluid Dyn. Res.* 10, pp.199–228
3. CITS annual technical report (chapter 2.4), (2000), Stanford University
4. Ducros, F., Ferrand, V., Nicoud, F., Weber, C., Darracq, D., Gacherieu, C., Poinsot, T., (1999) Large-eddy simulation of shock/turbulence interaction. *J. Comput. Phys.* 152, pp. 517–549
5. Fureby, C., Grinstein, F.F., (1999) Monotonically integrated large-eddy simulation of free shear flows. *AIAA Journal* 37(5), pp.544–556
6. Garnier, E., Mossi, M., Sagaut, P., Deville, M., Comte, P. (1999) On the use of shock-capturing schemes for large-eddy simulation. *J. Comput. Phys.* 153, pp. 273–311
7. Garnier, E., Sagaut, P., Deville, M., (1999) Large-eddy simulation of shock/turbulence interaction. *Computers & Fluids, to appear*
8. Garnier, E., Sagaut, P., Deville, M., (2001) A class of explicit ENO filters with application to unsteady flows. *J. Comput. Phys.* 170, pp. 184–204

9. Garnier, E., Sagaut, P., Deville, M., (2000) Large-eddy simulation of the shock/boundary layer interaction. *submitted to AIAA Journal*
10. Labourasse, E., Sagaut, P., (2001) Reconstruction of turbulent fluctuations using a hybrid RANS/LES approach. *submitted to J. Comput. Phys.*
11. Lenormand, E., Sagaut, P., Ta Phuoc, L. (2000) Large eddy simulation of subsonic and supersonic channel at moderate Reynolds number. *Int. J. Numer. Methods Fluids* 32, pp. 369–406
12. Lenormand, E., Sagaut, P., Ta Phuoc, L., Comte, P. (2000) Subgrid-scale models for large-eddy simulation of compressible wall bounded flows. *AIAA Journal* 38(8), pp. 1340–1350
13. Liu, C., Liu, Z., (1995) Multigrid mapping in box relaxation for simulation of the whole proces of flow transition in 3D boundary layers. *J. Comput. Phys* 119, pp. 325–341
14. Magnient, J.C., Sagaut, P., Deville, M., (2001) A study of build-in filter for some eddy-viscosity models in Large-Eddy Simulation, *Phys. Fluids* 13(5), pp. 1440–1449
15. Mary, I., Sagaut, P., (2001) Large-eddy simulation of flow around an airfoil near stall. *submitted to AIAA Journal*; also AIAA Paper 2001-2559
16. Morris, P.J., Long, L.N., Bangalore, A., Wang, Q., (1997) A parallel three-dimensional computational aeroacoustics method using nonlinear disturbance equations. *J. Comput. Phys.* 133, pp. 56
17. Mossi, M., Sagaut, P., (2001) Numerical investigation of fully developped channel flow using shock-capturing scheme. *Computers and Fluids, to appear*
18. Quéméré, P., Sagaut, P., Couaillier, V., (2001) A new multidomain/multiresolution method for large-eddy simulation. *Int. J. Numer. Methods Fluids* 36, pp. 391–416
19. Quéméré, P., Sagaut, P., (2001) Zonal multi-domain RANS/LES simulations of turbulent flows. *submitted to Int. J. Numer. Methods Fluids*
20. Sagaut, P., Montreuil, E., Labbé, O., (1999) Assessment of some self-adaptive SGS models for wall bounded flows. *AST* 3(6), pp. 335-344
21. Sagaut, P., Labourasse, E., Quéméré, P., Terracol, M. (2000) Multiscale approaches for unsteady simulation of turbulent flows. *Int. J. Nonlinear Sciences and Numerical Simulation* 1(4), pp. 285–298
22. Terracol, M., Sagaut, P., Basdevant, C., (2001) A multilevel algorithm for large-eddy simulation of turbulent compressible flows. *J. Comput. Phys.* 167, pp. 439–474
23. Terracol, M., Sagaut, P., Basdevant, C., (2000) A time self-adaptive multilevel algorithm for large-eddy simulation with application to the compressible mixing layer. *submitted to Phys. Fluids*

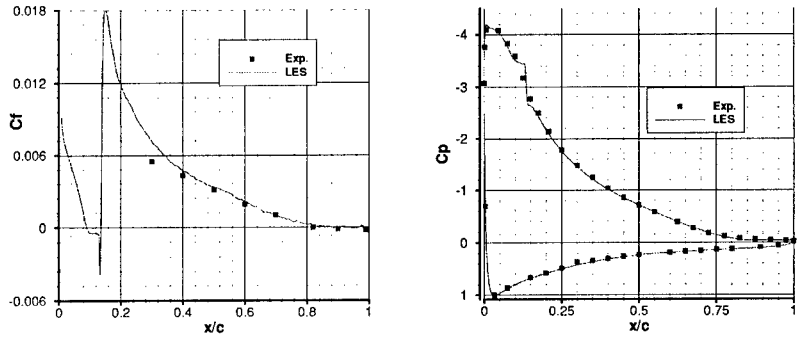


Figure 1. Flow around a 2D airfoil near stall - Skin friction (Left) and Pressure (Right) coefficients. Line: LES, Symbols: experiments

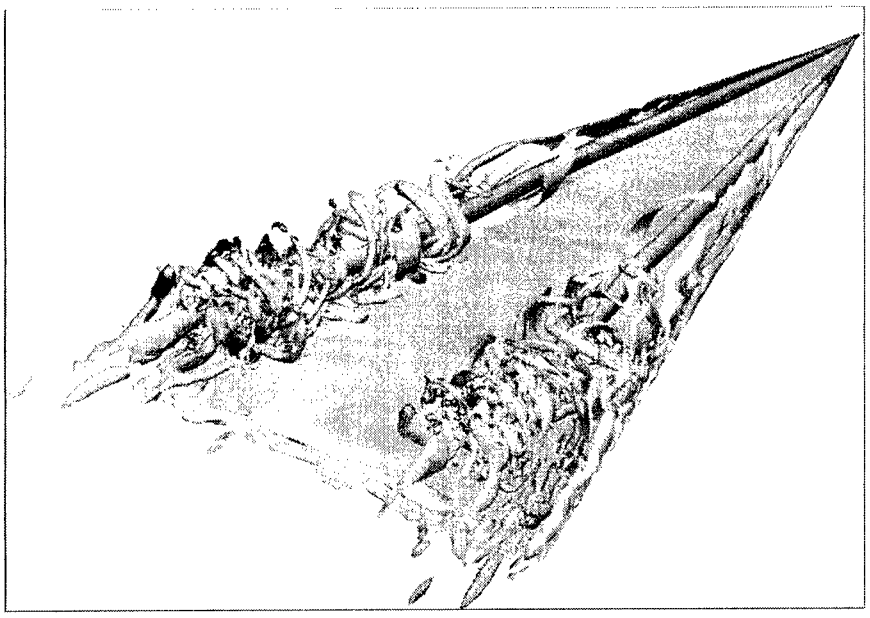


Figure 2. Flow around a Delta wing with vortex breakdown (instantaneous vorticity and pressure iso-surfaces)

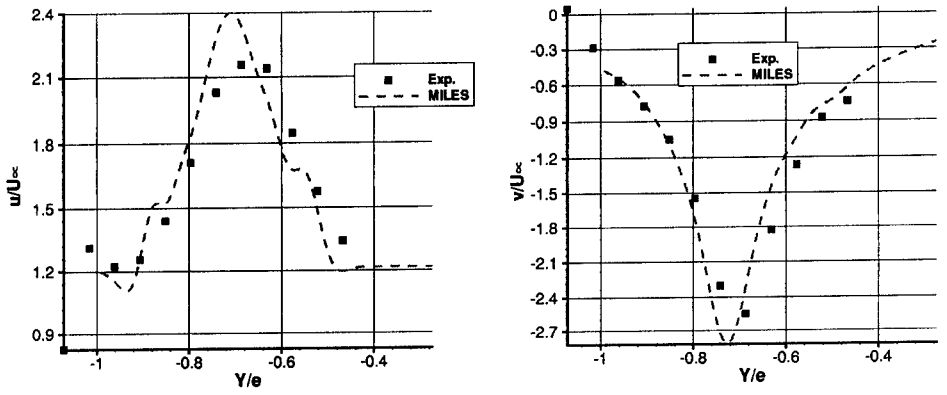


Figure 3. Flow around a Delta wing with vortex breakdown - Mean streamwise velocity (Left) and mean spanwise velocity (Right) profiles downstream the breakdown. Line: LES, Symbol: experiments

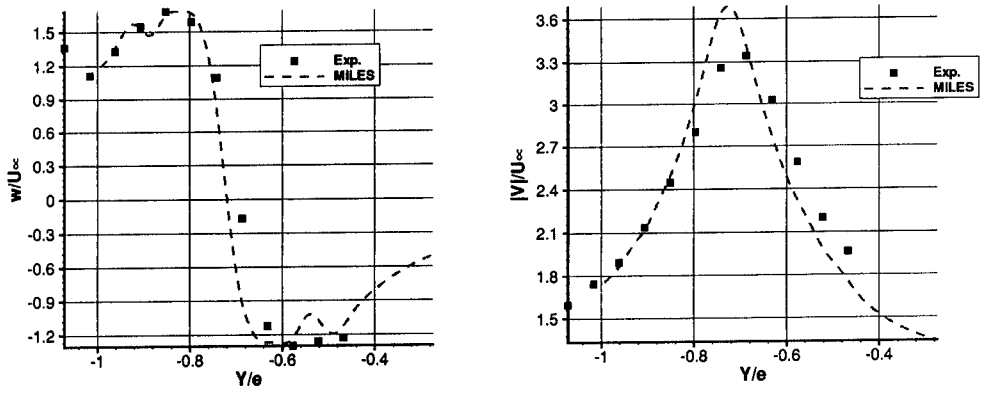


Figure 4. Flow around a Delta wing with vortex breakdown - Mean wall-normal velocity (Left) and mean velocity modulus (Right) profiles downstream the breakdown. Line: LES, Symbol: experiments

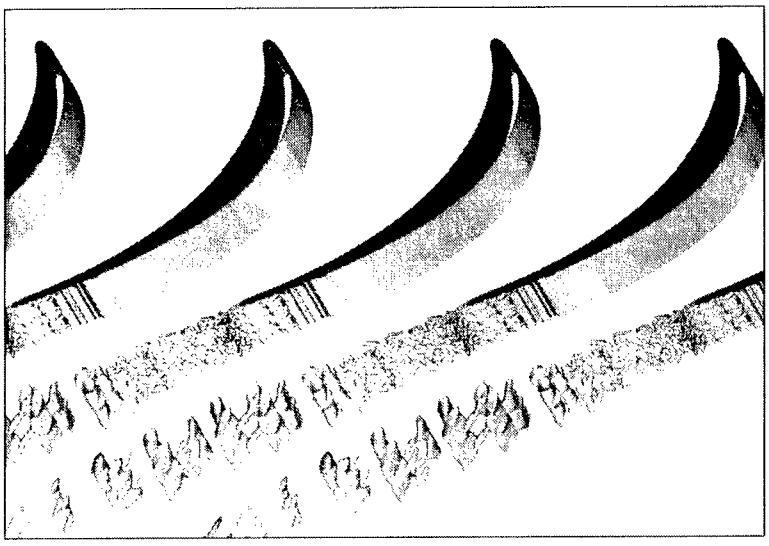


Figure 5. Flow around a low-pressure turbine blade (instantaneous vorticity iso-values)

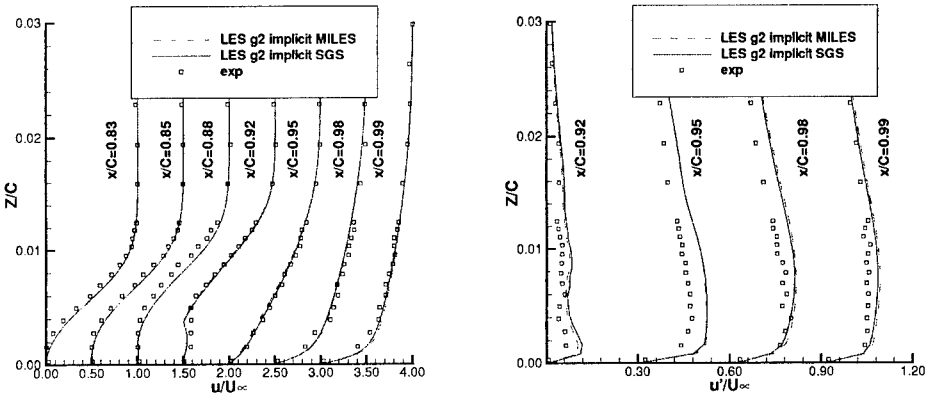


Figure 6. Flow around a low-pressure turbine blade. Mean velocity profile (Left) and RMS velocity profile (Right). Line: LES, Symbols: experiments

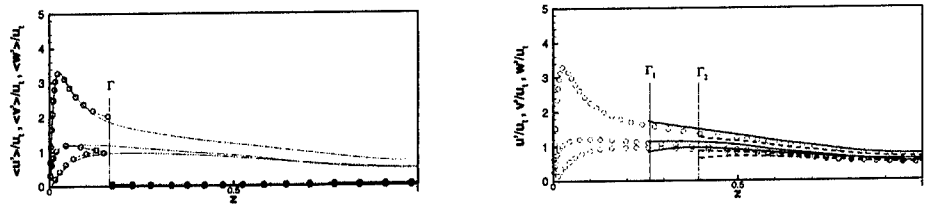


Figure 7. Zonal RANS/LES coupling - Channel flow, $Re_\tau = 590$ - Streamwise, spanwise and wall-normal *rms* velocity fluctuations. Near-wall LES treatment with RANS subdomain at the center of the channel; line: classical LES, symbols: coupled simulation (Left) and near-wall RANS simulation with LES domain at the center of the channel; symbols: classical LES, lines: coupled simulation (Right). Vertical lines note the position of the interface.

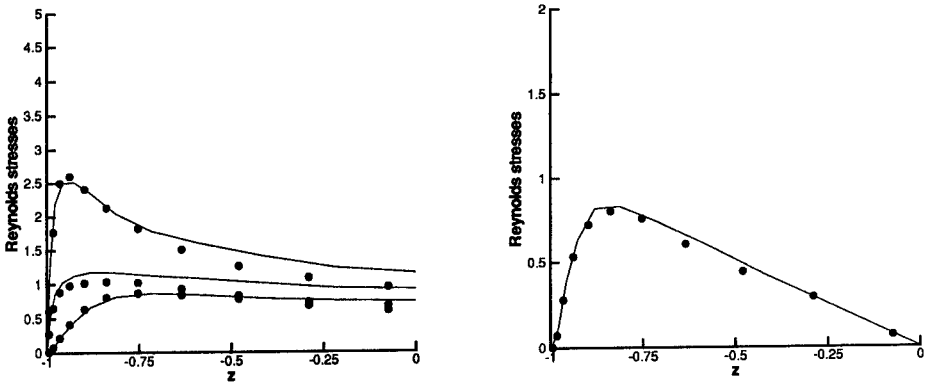


Figure 8. RANS/LES coupling - NLDE Approach - Channel flow, $Re_\tau = 395$ - Streamwise, spanwise and wall-normal *rms* velocity fluctuations (Left) and shear stress (Right). Line: NLDE, Symbol: classical LES

INDUSTRIAL APPLICATIONS OF LES IN MECHANICAL ENGINEERING

CHISACHI KATO
Institute of Industrial Science
University of Tokyo, Tokyo, Japan

MASAYUKI KAIHO, AKIRA MANABE
Mechanical Engineering Research Laboratory
Hitachi LTD., Ibaraki, Japan

Abstract

This paper describes industrial applications of LES with a particular emphasis on internal-flow simulations of turbomachinery and simulations of aeroacoustics. The aerodynamic sound is assumed to be generated by flows, at relatively low Mach numbers, around an object, and it is therefore calculated from fluctuating surface-pressure as obtained by the LES. In order to deal with a moving boundary interface in the flow field, a form of the finite-element method in which overset grids are applied from multiple dynamic frames of reference has been developed. The overset-grid approach is also applied to increase the grid resolution around the body of interest for computations in the field of aeroacoustics. The method is implemented as a parallel program by applying a domain-decomposition programming model. The validity of the proposed method is shown through two numerical examples: prediction of the internal flows of a hydraulic pump stage and prediction of the far-field sound that results from unsteady flow around an insulator mounted on a high-speed train.

1. Introduction

At present, the Reynolds-averaged Navier-Stokes (RANS) equations are used as the governing equations in most computations of flow field for engineering applications. Since the RANS equations are in terms of time averages, computation with RANS has inherent limitations in predicting the unsteady nature of a flow field. Solutions from the RANS equations usually deteriorate when the flow field of interest involves the large-scale separations that are often encountered in engineering applications. On the other hand, the large eddy simulation (LES), in which turbulent eddies of a scale larger than the

computational grid are directly computed, has the potential to predict unsteady flows and/or flow fields that include regions of large-scale separation much more accurately than RANS-based computation does in general. The goal of the present study is to develop a practical engineering tool that is based on LES, with a particular emphasis on internal-flow simulations of turbomachinery and simulations of aeroacoustics.

2. Governing Equations

2. 1 Flow-Field Computation

The governing equations on which the present study is based are the spatially filtered continuity equation and Navier-Stokes equations for the flow of an incompressible fluid, as represented in Cartesian coordinates. The inertial forces associated with the motion of the frames of reference are added to Navier-Stokes equations. The standard Smagorinsky model[1], incorporated with the Van-Driest wall-damping function that represents the near-wall effects, is adopted as the subgrid-scale model of turbulence. The Smagorinsky coefficient is fixed to 0.15, which is a standard value for flows with large separation, and the grid-filter size is computed as the cube-root of the volume of each finite element.

2. 2 Computation of the Acoustic Field

In the present study, the aerodynamic sound is assumed to be generated by flows, at relatively low Mach numbers, around an object whose dimension is much smaller than the wavelength of sound. In this case, the far-field sound radiated from the unsteady flow can be calculated from Curle's equation[2]:

$$p_a = \frac{1}{4\pi a}\frac{x_i}{r^2}\frac{\partial}{\partial t}\int_S n_i p(y, t - r/a)dS \tag{1}$$

where a denotes the speed of sound in the ambient fluid, p the static pressure in the flow field, p_a the far-field sound pressure, x_i the location of the sound-observation point, y the coordinates at the noise source, r the distance between the noise source and the sound-observation point, and n_j the outward unit vector normal to the solid boundaries. In the above expression, the assumption that the flow has a high Reynolds number makes the contribution of viscous stresses to the surface integral negligible. It is thus possible to calculate the far-field sound from the fluctuating surface pressure as obtained by the LES.

3. Numerical Method

3. 1 Overset Grids from Multiple Dynamic Frames of Reference

In the present study, a moving boundary interface in the flow field is treated with overset grids from multiple dynamic frames of reference[3]. The application of this method to the interaction between a rotating impeller and a stationary casing in a pump is schematically depicted in **figure 1**. A computational mesh that rotates along with the impeller is used to compute the flow within the impeller. On the other hand, a dedicated stationary computational mesh for each part computes the flow in stationary parts of the pump. Each mesh includes appropriate margins of overlap with its neighboring meshes upstream and downstream. At every time step, the velocity components and static pressure within each such margin are the values interpolated in the computational mesh of the corresponding neighbor. Element-wise tri-linear functions are used to interpolate both the velocity components and the static pressure[4,5]. When velocity components are overset, an appropriate coordinate transformation must be applied to take the differences between the frames of reference into account.

3. 2 Finite-Element Formulation

A streamline-upwind finite-element formulation[6] is used to discretize the governing equations of the flow field. This formulation is based on the explicit Euler's method, but shifts the spatial residuals of the governing equations in the upstream direction of the local flow. The magnitude of this shift is one half of the time increment multiplied by the magnitude of the local flow velocity. This shift exactly cancels out the negative numerical dissipation that is otherwise the result of applying Euler's method and guarantees stability and the accuracy of solutions. The proposed formulation essentially possesses second-order accuracy in terms of both time and space, and has been successfully applied to the LES of external as well as internal flows[3,6,7].

3.3 Parallel Implementation

We have implemented the formulation described in the previous sections as a parallel program by using the domain-decomposition programming model. In this programming model, the global computational domain is partitioned into a prescribed number of subdomains (see **figure 2** for an example of mesh partitioning), and each of the subdomains is assigned to a dedicated processing node. The communicating pairs and/or local coordinates where given interpolations are taking place change at the moving-boundary interfaces on every time step. The usual (unsophisticated) parallel implementation therefore includes broadcast communications on every time step as the processing node searches for its new communication pairs. This communication overhead seriously deteriorates the overall parallel computing performance. In the present

study, the communication pairs are searched in advance by a serial computation and they are fed to the parallel flow solver as input data on every time step. This procedure not only avoids the otherwise inevitable communications overhead but also brings in greater flexibility with the flow solver. By preparing appropriate input data for the moving-boundary interfaces, the flow solver is capable of computing flow fields with an arbitrary number of moving-boundary interfaces that move in an arbitrary (but defined) manner. The performance of the proposed method in terms of parallel computing was evaluated on various hardware platforms. **Table 1** shows one such example, where the method was tested on Hitachi's SR8000 super-computer. The sustained performance ranges from 12% to 14% of the peak performance. **Figure 3** is a plot of the overall sustained performance against the number of the processing nodes for the same benchmark test. A parallel computing efficiency of over 85% is achieved on this platform and this confirms that it is possible to complete a large-scale computation of flow with a grid that has more than 10 million divisions within a practical period of time on a high-end computer of the current generation.

4. Simulation Examples

After ensuring the validity of the LES code we developed by applying it to the calculation of basic flows of various types[6,7], the code is now being tested on real-world problems. Two examples will be described below: one from the simulation of turbomachinery and the other from aeroacoustical simulations.

4. 1 Simulation of Unsteady Flow in a Mixed-Flow Pump

The code was applied to the computation of the internal flow in a mixed-flow pump stage with a high designed specific-speed. The measured total heads of this pump exhibited slightly unstable characteristics at a flow-rate ratio of around 60%. In order to obtain comparative data for use in validation, the mean-velocity profiles at the impeller's inlet and exit cross-sections were measured by a two-dimensional LDV.

The computational mesh used in this study is shown in **figure 4**. At the upstream of the regulation-plate mesh, a driving section (not shown in this figure) is overset, and therefore, on every time step, the inlet velocities of the regulation-plate mesh were the values interpolated from instantaneous velocities of the driving section (see **figures 5** and **6**, respectively for typical instantaneous secondary-flow velocity and fluctuations in centerline velocities in this section). The flow rate of the pump was set by adjusting the magnitude of uniform acceleration that was applied to the driving section in the axial direction (see **figure 7** for a comparison of the measured and predicted mean-velocity profiles in the driving section). The Reynolds number based on the impeller's exit

diameter D_2 and the circumferential velocity u_2 at this point is 5.7×10^6. In order to investigate effects of grid resolution on the accuracy of the solution, two sets of meshes with different grid resolution were used. The numbers of elements are approximately 1.7 million for the coarse mesh and 5 million for the fine mesh. The time increment was set so that 8,000 time steps corresponded to a single revolution of the impeller and the total pump head and mean-velocity distributions were evaluated by averaging the flow field during 10 impeller's revolutions. The computations were carried out by using 16 processing nodes on the Hitachi SR8000 super-computer. The required CPU time was about 1.6 seconds per time step for the fine-mesh LES. The total CPU time for a single flow-rate ratio was thus about 35 hours for this case.

The computed total pump-heads, together with their measured equivalents, are plotted in **figure 8**. The total pump-heads predicted by the fine-mesh LES agree fairly well with the measured values down to a flow-rate ratio of 60%, where the measured head-flow characteristics indicate an onset of the total stall. The fine-mesh LES predicted an onset of the total stall at a flow-rate ratio of 54%, which is 6% lower than the measured value. In the following, we are presenting flow fields at flow-rate ratios of 60% and 43% as they respectively represent the pre-stall and post-stall flow fields. **Figure** 9 shows instantaneous distributions of axial velocity in the centerline plane of the pump. **Figure 10** shows the computed and measured mean-velocity profiles at the impeller's inlet cross-section (see figure 9 for its location) where *C*m and *C*u respectively denote the meridional and circumferential velocities. The fine mesh LES accurately predicts, for the post-stall case, the large region of reverse flow near the impeller's tip and intense pre-rotation that results from this reverse flow and results in the decrease in the total pump head. Finally, **figure 11** shows mean-velocity profiles at the impeller's exit section. The velocity profiles predicted by the fine-mesh LES are in reasonably good agreement with the measured profiles and the changes in the flow pattern to the centrifugal type at the post-stall condition are clearly captured by the fine-mesh LES. The hydrodynamic mechanism in which characteristics instability occurs is now being investigated by using the simulated flow-field data, which will hopefully lead us to the establishment of a general design rule for avoiding this occurrence.

4. 2 Aeroacoustical Simulation of a Pantograph Insulator

To achieve further increases in the speeds of high-speed trains, which is presently running at 300 km/h in Japan, a reduction in the generation of aerodynamic noise by the pantograph (the electric-current collector on the train's roof) has become a matter of great concerns in terms of the aerodynamic design of the vehicle. Past research has indicated that, among the various noise sources of a pantograph, the insulator provides the dominant contribution to the overall level of noise. We have therefore simulated the near-wake of flow around an

insulator and the resulting far-field sound, with the particular aim of identifying the primary source of noise[8].

Figures 12 and **13** show an overset mesh for the near-wake LES of the insulator that was simulated in the present study. Two sets of overset grids with different resolution were used in the LES and the effects of grid resolution on the fluctuations in the near wake as well as on the resulting far-field sound were investigated. The numbers of elements are approximately 2 million for the coarse mesh and 6 million for the fine mesh. In the following, we are presenting results from the fine-mesh LES unless we state otherwise.

To illustrate the temporal wake structure, regions of instantaneous reverse flow are shown in **figure 14**. The boundary layer that develops on the surface of the insulator separates from the surface while the flow is still laminar, but a transition to turbulence takes place soon after that. **Figure 15** shows an instantaneous distribution of streamwise velocity in the insulator's mid-height plane. The wake still possesses a large vortical structure, similar to the well-known Karman vortex, but this large structure is rather weak due to the enhancement of spanwise mixing effects by the circular disks. **Figure 16** shows the instantaneous distribution of static-pressure on the insulator's surface and base plate.

Typical fluctuations in streamwise velocity in the near wake and their power spectra, for both the coarse- and fine-mesh cases, are shown in **figure 17**. The frequency range that is resolvable by the coarse-mesh LES has its upper bound at a Strouhal number of approximately 1.0 (five times the usual Karman vortex frequency). The upper bound is extended to a Strouhal number of about 6 by the fine-mesh LES.

The fluctuations in far-field sound pressure and the power spectra of these fluctuations are shown in **figure 18**, for both the coarse-mesh and fine-mesh cases, together with the experimental value as measured in a wind tunnel. For convenience, the sound pressure are converted to actual values that correspond to a vehicle speed of 350 km/h (97.2 m/s) by assuming the Reynolds number similarility of the flow fields for the model and for the actual structure. The sound-pressure levels predicted by the coarse-mesh LES and the fine-mesh LES are surprisingly different. The fine-mesh LES provides a reasonably good prediction of the sound-pressure level at frequencies up to around 2.5 kHz, which corresponds to the Strouhal number of 6.4. This is approximately identical to the resolved frequency range for the near-wake velocity fluctuations.

Finally, the instantaneous sound-source distributions are investigated according to Powell's equation[9]. **Figure 19** shows the instantaneous distributions of the sound source term, which are obtained from the LES. By examining these sound-source distributions, the longitudinal vortices generated by the circular

disks are identified as being primarily responsible for the generation of sound by this flow.

The two examples mentioned above (and many others not given here) have clearly indicated that LES is now beginning to serve as a vital design tool in at least some cases of mechanical engineering.

5. Conclusions

Large eddy simulation has been applied to the prediction of internal flows in turbomachinery and aerodynamic sound that results from unsteady flow around a complex object. The standard Smagorinsky model, incorporated with the Van-Driest damping function, is adopted as the subgrid-scale model. The numerical method is based on a streamline-upwind finite-element formulation with accuracy of the second-order in both time and space, and incorporates the application of overset grids from multiple and dynamic frames of reference. The method is implemented as a parallel program by a domain-decomposition programming model.

Initially, the internal flow of a high-specific-speed mixed-flow pump stage was simulated, as a way of evaluating the validity of the proposed method. The predicted total pump-head and mean-velocity distributions at the impeller's inlet and exit cross-sections were in good agreement with the measured values. The near wake and the resulting far-field sound were then computed for flow around an insulator mounted on a high-speed train. The predicted sound-pressure level was also in reasonably good agreement with the wind-tunnel measurement.

The proposed method thus seems to be a promising candidate for use as an aerodynamic/aeroacoustic design tool in the next decade.

References

1. Smagorinsky, J., 1963, *Mon. Weath. Rev.*, **Vol. 91**, No. 3, pp. 99-164.
2. Curle, N., 1955, *Proc. Roy. Soc.*, **A231**.
3. Kato, C., et al., 1999, *ASME-FEDSM99-7802.*
4. Ikegawa, M., et al., 1994, *Comput. Methods Appl. Mech. Engrg*, **Vol. 112**, pp. 149-163.
5. Kaiho, M., et al., 1997, *Int. J. Numer. Meth. Fluids*, **Vol. 24**, pp. 1341-1352.
6. Kato, C., and Ikegawa, M., 1991, *ASME FED-Vol. 117*, pp. 49-56.
7. Kato, C., et al., 1993, *AIAA Paper 93-0145.*
8. Kato, C., et al., 2000, *AIAA Paper 2000-1942.*
9. Powell, A., 1964, *J. of Acoust. Soc. Am.*, **Vol. 33**, pp. 177-195.

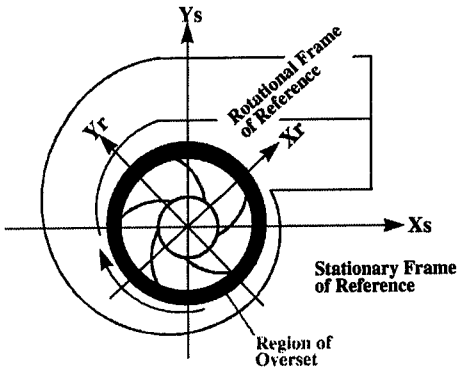


Figure 1. Schematic view of an example of overset grids from dual frames of reference.

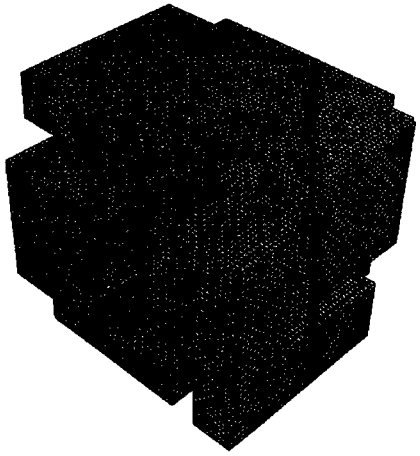


Figure 2. Example of a sub-domain mesh partitioned by the recursive graph-bisection method (computational mesh for flow in a cubic cavity partitioned into 8 sub-domains).

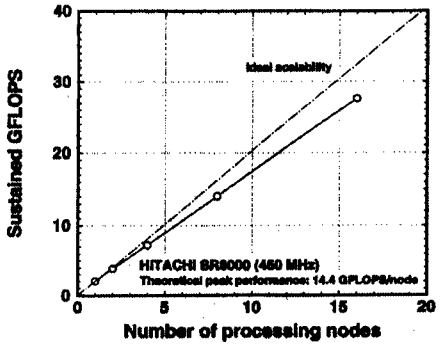


Figure 3. Sustained parallel computing performance

Table 1. Results of benchmark tests (CPU time needed to advance by a single time step in a cubic-cavity flow simulation on Hitachi's SR8000).

Number of processing nodes	1	2	4	8	16
Number of elements in millions	1.0	2.0	4.0	8.0	16.0
Seconds taken by CPU per time step	3. 45	3. 62	3. 89	3. 99	4. 06
Sustained GFLOPS	2. 03	3. 87	7. 23	14. 04	27. 60
Ratio of sustained to peak performance (%)	14. 1	13. 4	12. 6	12. 2	12. 0

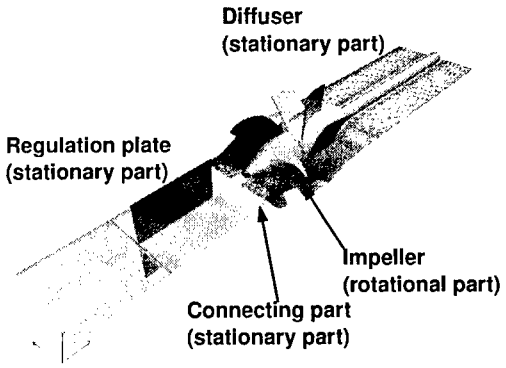


Figure 4. Computational mesh for a mixed-flow pump stage, composed of meshes for 5 parts (note: the mesh for the inlet driving-section is not shown here).

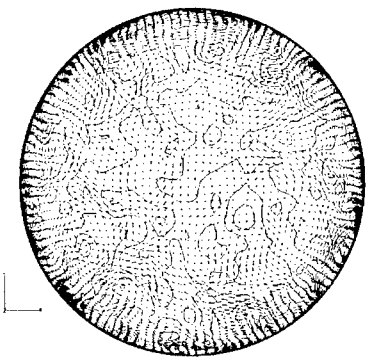


Figure 5. Instantaneous distribution of secondary flow in the driving section.

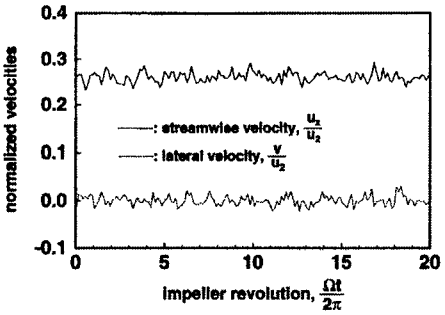


Figure 6. Fluctuations in centerline velocities in the driving section.

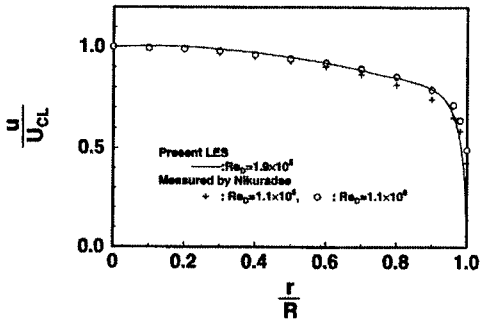


Figure 7. Time-averaged distribution of streamwise velocity in the driving section.

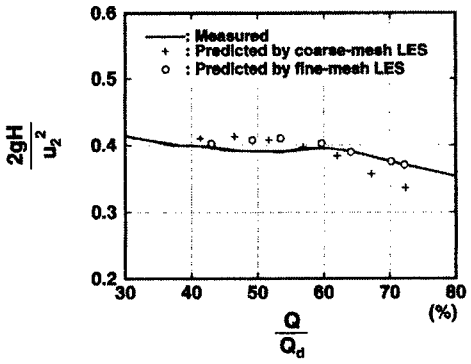


Figure 8. Comparison of measured and predicted head-flow characteristics.

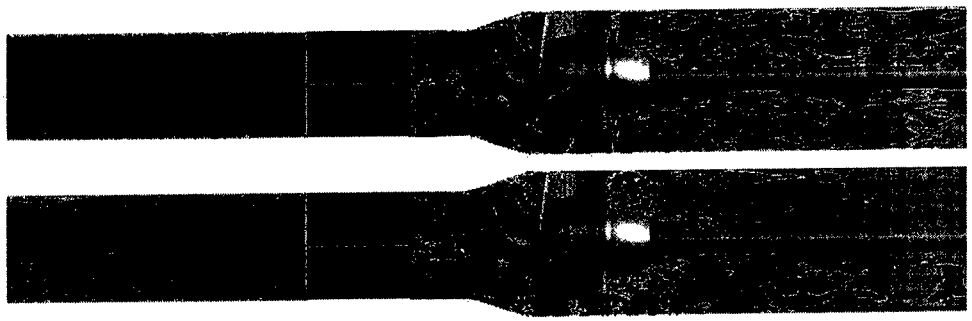


Figure 9. Instantaneous distributions of axial velocity component for Q=60% (upper) and Q=43% (lower) [fine-mesh LES]. Black lines in the upper figure indicate the approximate locations where velocity profiles were measured by a two-dimensional LDV for the impeller's inlet and exit cross-section.

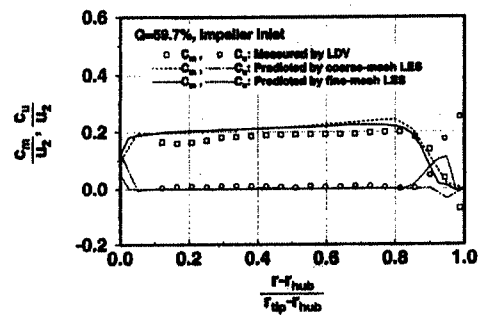


Figure 10. Predicted and measured distributions of phase-averaged velocities at the impeller's inlet cross-section for Q=60% (upper) and 43% (lower).

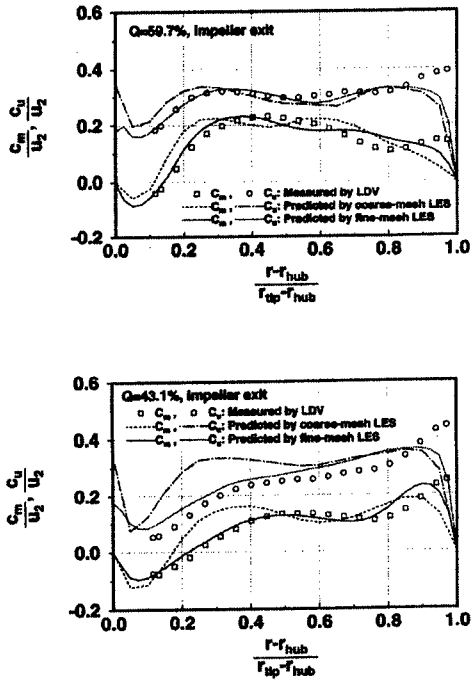


Figure 11. Predicted and measured distributions of phase-averaged velocities at the impeller's exit cross-section for Q=60% (upper) and 43% (lower).

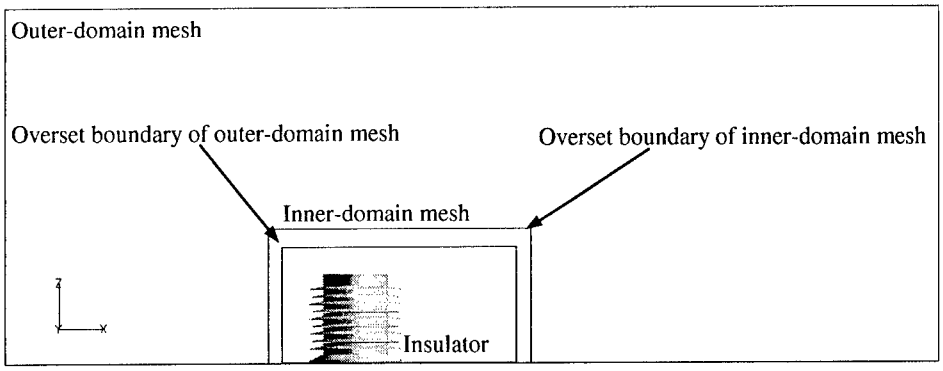


Figure12. Computational region for an overset LES of unsteady flow around an insulator

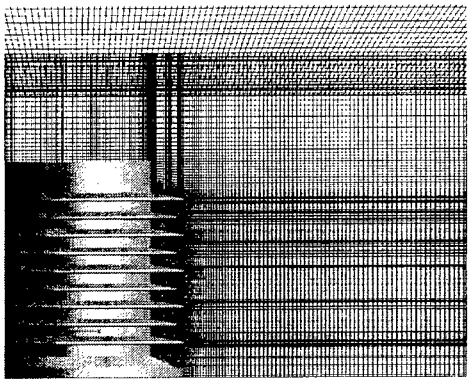


Figure 13. Overset meshes for flow around an insulator (fine-mesh case).

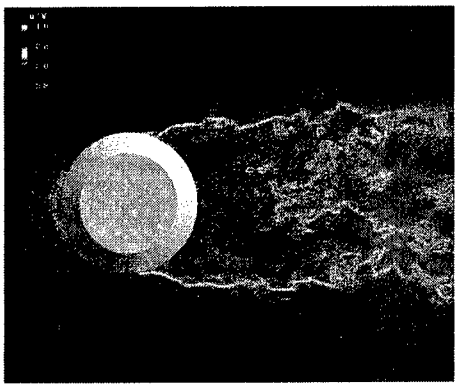


Figure 15. Instantaneous distribution of streamwise-velocity



Figure 14. Reqions of instantaneous reverse flow.

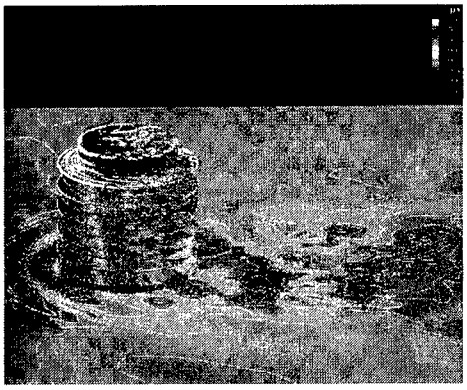


Figure 16. Instantaneous distribution of surface pressure.

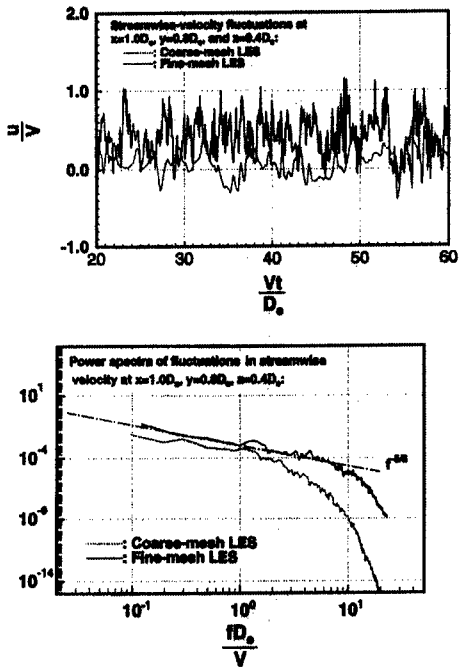


Figure 17. Fluctuations in streamwise velocity in the near wake (upper) and the power spectra of these fluctuations (lower).

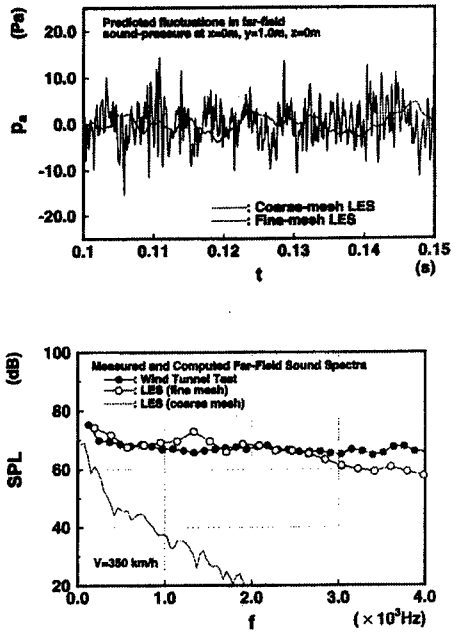


Figure 18. Computed far-field sound-pressure fluctuations (upper) and their power spectra (lower).

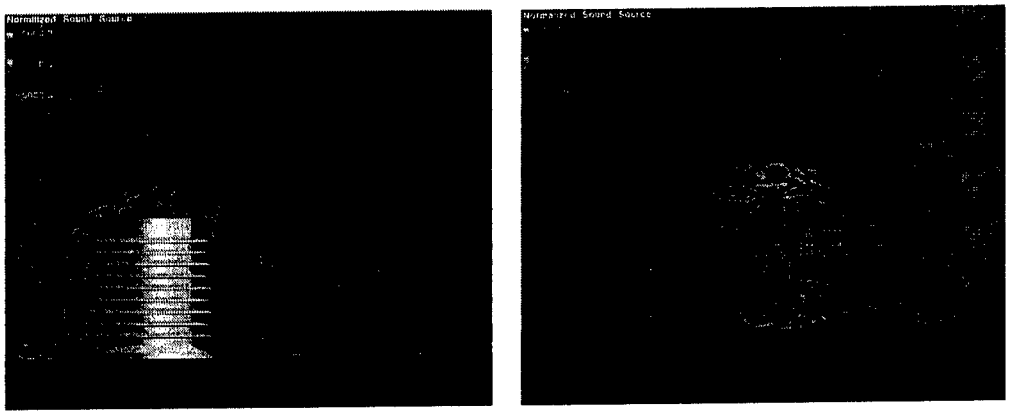


Figure 19. Instantaneous sound-source distributions in the near wake: center-line plane (left), and a plane one diameter downstream from the insulator (right).

NUMERICAL SIMULATION OF COMPLEX FLOW AROUND A 85° DELTA WING

H. SHAN, L. JIANG, C. LIU

Department of Mathematics
University of Texas at Arlington, Arlington, Texas, U.S.A.

Abstract.

The three-dimensional separated flow around a slender flat-plate delta wing with sharp leading-edge at a 12.5° angle of attack has been studied by solving the full compressible Navier-Stokes equations in the generalized curvilinear coordinates. The time integration is carried out by using the second-order LU-SGS implicit scheme. A fourth-order centered compact difference scheme is used for spatial derivatives. A sixth-order implicit filter is employed to reduce numerical oscillation. Non-reflecting boundary conditions are imposed at the far-field and outlet boundaries to avoid possible non-physical wave reflection. Parallel computing based on Message Passing Interface (MPI) has been utilized to improve the performance of the code.

Two Reynolds numbers have been selected. At a lower Reynolds number of 5×10^4 based on the chord length and the freestream velocity, the flow is stable and dominated by a pair of leading-edge primary vortices. At a higher Reynolds number of 1.96×10^5, the small-scale vortex shedding is observed near the leading-edge of the delta wing. The computational results are compared with the experimental work of Riley & Lowson (1998). The periodic shedding of small-scale vortical structures near the leading-edge has been studied in detail, and the vortex shedding is found to be associated with the Kelvin-Helmholtz-type instability and the secondary vortex. The period of vortex shedding is obtained from the time series of the three velocity components recorded near the leading-edge. The time-averaged features of the vortical structures are also discussed.

1. Introduction

Recent developments in aerospace technology have revived the interest to the study of flow separations around an aircraft maneuvering dynamic operations. Understanding of the complex separated vortical flow is crucial to the aerodynamic design of modern aircraft. Vortical structures, which develop over the leading-edge extension, slender fore-body, and main wing, may have severe effect on the aerodynamic characteristics and performance of modern fighter aircraft.

A flat-plate delta wing with sharp leading-edge provides a simple configuration to investigate the development of the vortical structures. The experimental study of delta wing started in the early 1950's. The experimental results have shown that the flow over the suction side of a delta wing at a high angle of attack is dominated by a pair of counter-rotating vortices, i.e. the leading-edge primary vortices. These vortices are formed as a result of the rolling-up of the vortex sheet shedding from the leading-edge. The flow induced by the leading-edge vortices separates near the wing surface and forms a pair of oppositely rotating secondary vortices. At large sweep angle, the size and strength of the leading-edge vortices increase with the angle of incidence, resulting in a substantial nonlinear lift increment, sometimes called vortical lift. But the maximum lift of a delta wing is limited by a phenomenon known as vortex breakdown(Visser & Nelson 1993).

The breakdown of the primary vortex has drawn considerable attentions. Payne *et al.* (1988) used smoke flow visualization and laser sheet technique to study the vortical flow field above the delta wing at high angles of attack. Two types of vortex breakdown were testified, i.e. the bubble mode and the spiral mode. However, as it was pointed by Rieley & Lowson (1998), most studies have been concentrated on the nature and breakdown of the primary vortex instead of the leading-edge shear layer itself. Actually, there are several mechanisms associated with the leading-edge shear layer. The most obvious one is the Kelvin-Helmholtz instability of two-dimensional free shear layer. Two types of instabilities are observed in experiments, i.e. the unsteady, and steady instability. The experimental study carried out by Gad-el-Hak and Blackwelder (1985) using dye visualization has shown the unsteady instability, where small-scale vortices are shed from the leading-edge, travel up and around the shear layer, and finally feed into the core of large-scale leading-edge vortex. The pairing of the small-scale vortices were observed in the same experiment. The experiential observation of the pairing of Kelvin-Helmholtz type vortex during flow separation around a delta wing was confirmed by Lowson (1988). Similar phenomenon has been reported in a simple tow-dimensional shear layer (Winant & Browand, 1974). It is generally found that the phenomena as-

sociated with the traveling Kelvin-Helmholtz instability in strongly curved shear layer are parallel to the effects observed in a two-dimensional free shear layer. The experiments also indicate that the unsteady instability is exceptionally sensitive to external disturbance. The steady instability was observed in the experiment of Payne *et al.* (1988). The static small-scale vortical-like structures were found in the shear layer of a delta wing with a 85° sweep angle and at 40° angle of attack. The growth of these structures was found to be similar to the evolution of the classic Kelvin-Helmholtz instability. In this experiment, the pairing of the small-scale vortices was not observed. The stationary cellular substructures that do not rotate around the primary vortex were also observed by Honkan & Andreopoulos (1997) in their experiment. The recent experimental work of Rieley & Lowson (1998) revealed, using flow visualization and laser Doppler anemometer measurement, the existence of static small vortical structures in the free shear layer shedding from the sharp leading-edge of a delta wing. A local three-dimensional Kelvin-Helmholtz-type instability was suggested by the authors for the formation of these vortical structures in the free shear layer. Similar vortical structures were also observed in the investigations of Cipolla & Rockwell (1998), where small-scale concentrations of vorticity form near the leading-edge of a rolling delta wing. These vortices appear to evolve in a coupled fashion, which has been considered as the wake-like instability.

Numerical simulations of vortex breakdown above a stationary sharp edged delta wing over a range of angles of attack were carried out by Modiano & Murman (1994). Their computation was based on an Euler solver with adaptive mesh system. The spiral form of vortex breakdown was observed without the emergence of the small-scale vortical structures inside the shear layer. In the numerical investigation by Argwal *et al.* (1992), the well-known Euler/Navier-Stokes code CFL3D was used to simulate the leading-edge vortex breakdown of a low-speed flow on a flat-plate delta wing with sharp leading-edges. Although the vortex breakdown positions obtained from the computation were reported in good agreement with experimental data, the small-scale vortices were not observed, which could be attributed to the lack of numerical resolution/accuracy. A numerical investigation of the unsteady vortex structure over a 76° sweep wing at 20.5° angle of attack was carried out by Gordnier & Visbal (1994). Their numerical calculation indicated that the small-scale vortical structures emanated from the leading-edge was brought on by the Kelvin-Helmholtz-type instability. Pairing of the small vortices was not observed in the computational results. No computational result has indicated the existence of the steady instability.

The intend of present work is to study the mechanism of the shear layer

instability of a slender flat-plate delta wing with sharp leading-edges at a fixed angle of attack. High-resolution numerical simulation is employed to give a detailed description of flow instability and vortex shedding near the leading-edge of the delta wing. The interactions between the small-scale vortical structures and the primary vortex is also studied.

2. Governing Equations

The three-dimensional compressible Navier-Stokes equations in generalized curvilinear coordinates (ξ, η, ζ) are written in conservative forms:

$$\frac{1}{J}\frac{\partial Q}{\partial t} + \frac{\partial (E - E_v)}{\partial \xi} + \frac{\partial (F - F_v)}{\partial \eta} + \frac{\partial (G - G_v)}{\partial \zeta} = 0 \tag{1}$$

The flux vectors are

$$Q = \begin{pmatrix} \rho \\ \rho u \\ \rho v \\ \rho w \\ e \end{pmatrix} \quad E = \frac{1}{J}\begin{pmatrix} \rho U \\ \rho U u + p\xi_x \\ \rho U v + p\xi_y \\ \rho U w + p\xi_z \\ U(e+p) \end{pmatrix} \quad F = \frac{1}{J}\begin{pmatrix} \rho V \\ \rho V u + p\eta_x \\ \rho V v + p\eta_y \\ \rho V w + p\eta_z \\ V(e+p) \end{pmatrix}$$

$$G = \frac{1}{J}\begin{pmatrix} \rho W \\ \rho W u + p\zeta_x \\ \rho W v + p\zeta_y \\ \rho W w + p\zeta_z \\ W(e+p) \end{pmatrix} \qquad E_v = \frac{1}{J}\begin{pmatrix} 0 \\ \tau_{xx}\xi_x + \tau_{yx}\xi_y + \tau_{zx}\xi_z \\ \tau_{xy}\xi_x + \tau_{yy}\xi_y + \tau_{zy}\xi_z \\ \tau_{xz}\xi_x + \tau_{yz}\xi_y + \tau_{zz}\xi_z \\ q_x\xi_x + q_y\xi_y + q_z\xi_z \end{pmatrix}$$

$$F_v = \frac{1}{J}\begin{pmatrix} 0 \\ \tau_{xx}\eta_x + \tau_{yx}\eta_y + \tau_{zx}\eta_z \\ \tau_{xy}\eta_x + \tau_{yy}\eta_y + \tau_{zy}\eta_z \\ \tau_{xz}\eta_x + \tau_{yz}\eta_y + \tau_{zz}\eta_z \\ q_x\eta_x + q_y\eta_y + q_z\eta_z \end{pmatrix} \quad G_v = \frac{1}{J}\begin{pmatrix} 0 \\ \tau_{xx}\zeta_x + \tau_{yx}\zeta_y + \tau_{zx}\zeta_z \\ \tau_{xy}\zeta_x + \tau_{yy}\zeta_y + \tau_{zy}\zeta_z \\ \tau_{xz}\zeta_x + \tau_{yz}\zeta_y + \tau_{zz}\zeta_z \\ q_x\zeta_x + q_y\zeta_y + q_z\zeta_z \end{pmatrix}$$

where J is Jacobian of the coordinate transformation, and ξ_x, ξ_y, ξ_z,η_x,η_y,η_z,ζ_x, ζ_y,ζ_z are coordinate transformation metrics. τ_{kl}'s and q_k's are the viscous stress and the heat flux, respectively.

In Eq. (1), a second order Euler Backward scheme is used for time derivatives, and the fully implicit form of the discretized equations is given by

$$\frac{3Q^{n+1} - 4Q^n + Q^{n-1}}{2J\Delta t} + \frac{\partial (E^{n+1} - E_v^{n+1})}{\partial \xi} + \frac{\partial (F^{n+1} - F_v^{n+1})}{\partial \eta} + \frac{\partial (G^{n+1} - G_v^{n+1})}{\partial \zeta} = 0$$

(2)

Q^{n+1} is estimated iteratively as:

$$Q^{n+1} = Q^p + \delta Q^p \tag{3}$$

where,

$$\delta Q^p = Q^{p+1} - Q^p \tag{4}$$

At step $p = 0$, $Q^p = Q^n$; as δQ^p is driven to zero, Q^p approaches Q^{n+1}. The flux vectors are linearized as follows:

$$\begin{aligned} E^{n+1} &\approx E^p + A^p \delta Q^p \\ F^{n+1} &\approx F^p + B^p \delta Q^p \\ G^{n+1} &\approx G^p + C^p \delta Q^p \end{aligned} \tag{5}$$

So that Eq. (2) can be written as:

$$[\frac{3}{2}I + \Delta t J(D_\xi A + D_\eta B + D_\zeta C)]\delta Q^p = R \tag{6}$$

where R is the residual:

$$R = -(\frac{3}{2}Q^p - 2Q^n + \frac{1}{2}Q^{n-1}) - \Delta t J[(D_\xi(E-E_v) + D_\eta(F-F_v) + D_\zeta(G-G_v)]^p \tag{7}$$

D_ξ, D_η, D_ζ represent partial differential operators, and A, B, C are the Jacobian matrices of flux vectors:

$$A = \frac{\partial E}{\partial Q}, \qquad B = \frac{\partial F}{\partial Q}, \qquad C = \frac{\partial G}{\partial Q} \tag{8}$$

The right hand side of Eq. (6) is discretized using fourth-order compact scheme (Lele, 1992) for spatial derivatives, and the left hand side of the equation is discretized following LU-SGS method (Yoon & Kwak, 1992). In this method, the Jacobian matrices of flux vectors are split as:

$$A = A^+ + A^-, \quad B = B^+ + B^-, \quad C = C^+ + C^-$$

where,

$$A^\pm = \frac{1}{2}[A \pm r_A I], \quad B^\pm = \frac{1}{2}[B \pm r_B I], \quad C^\pm = \frac{1}{2}[C \pm r_C I] \tag{9}$$

and,

$$r_A = \kappa max[|\lambda(A)|] + \tilde{\nu}, \quad r_B = \kappa max[|\lambda(B)|] + \tilde{\nu}, \quad r_C = \kappa max[|\lambda(C)|] + \tilde{\nu}$$

where $\lambda(A), \lambda(B), \lambda(C)$ are eigenvalues of A, B, C respectively, κ is a constant greater than 1. $\tilde{\nu}$ is taken into account for the effects of viscous terms, and the following expression is used:

$$\tilde{\nu} = max[\frac{\mu}{(\gamma-1)M_r^2 R_e P_r}, \frac{4}{3}\frac{\mu}{R_e}]$$

The first-order upwind finite difference scheme is used for the split flux terms in the left hand side of Eq. (6). This does not effect the accuracy of the scheme. As the left hand side is driven to zero, the discretization error will also be driven to zero. The finite difference representation of Eq. (6) can be written as:

$$\begin{aligned} [\frac{3}{2}I &+ \Delta tJ(r_A + r_B + r_C)I]\delta Q^p_{i,j,k} = R^p_{i,j,k} \\ -\Delta tJ &[A^-\delta Q^p_{i+1,j,k} - A^+\delta Q^p_{i-1,j,k} \\ &+ B^-\delta Q^p_{i,j+1,k} - B^+\delta Q^p_{i,j-1,k} \\ &+ C^-\delta Q^p_{i,j,k+1} - C^+\delta Q^p_{i,j,k-1} \ ] \end{aligned} \tag{10}$$

In LU-SGS scheme, Eq. (10) is solved by three steps. First initialize δQ^0 using

$$\delta Q^0_{i,j,k} = [\frac{3}{2}I + \Delta tJ(r_A + r_B + r_C)I]^{-1} R^p_{i,j,k}$$

In the second step, the following relation is used:

$$\begin{aligned} \delta Q^*_{i,j,k} &= \delta Q^0_{i,j,k} + [\frac{3}{2}I + \Delta tJ(r_A + r_B + r_C)I]^{-1} \\ &\times[\Delta tJ(A^+\delta Q^*_{i-1,j,k} + B^+\delta Q^*_{i,j-1,k} + C^+\delta Q^*_{i,j,k-1})] \end{aligned}$$

For the last step, δQ^p is obtained by

$$\begin{aligned} \delta Q^p_{i,j,k} &= \delta Q^*_{i,j,k} - [\frac{3}{2}I + \Delta tJ(r_A + r_B + r_C)]^{-1} \\ &\times[\Delta tJ(A^-\delta Q^p_{i+1,j,k} + B^-\delta Q^p_{i,j+1,k} + C^-\delta Q^p_{i,j,k+1})] \end{aligned}$$

The sweeping of the computational domain is performed along the planes of $i + j + k = const$, i.e. in the second step, sweeping is from the low-left corner of the grid to the high-right corner, and then vice versa in the third step.

In order to depress numerical oscillation caused by central difference scheme, a spatial filtering is used instead of artificial dissipation. Implicit sixth-order compact scheme for space filtering (Lele, 1992) is applied for primitive variables u, v, w, ρ, p after each time step.

For subsonic flow, u, v, w, T are prescribed at the inflow boundary, ρ is obtained by solving modified N-S equation based on the characteristic analysis. On the far field and out flow boundary, non-reflecting boundary conditions are applied. Adiabatic, non-slipping conditions are used for the wall boundary. All equations of boundary conditions are solved implicitly with internal points. Specific details of boundary treatment can be found in Jiang *et al* (1999).

3. Computational Details

Numerical simulation has been implemented to investigate the compressible flow separation around a slender delta wing. The geometry of the delta wing, taken from the experimental work of Rieley & Lowson (1998), is shown in Figure 1. The sweep angle denoted by Λ is 85° and the leading-edge angle denoted by σ is 30°. The chord length is taken as the characteristic length L, such that the non-dimensional chord length is $c = 1.0L$. The non-dimensional thickness of the delta wing is $h = 0.024L$. The freestream velocity U_∞ is the characteristic velocity.

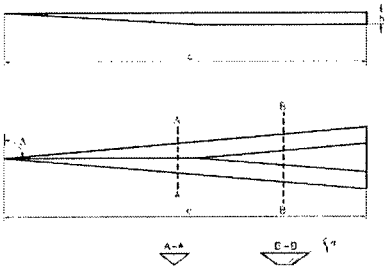


Figure 1. Schematic of the delta wing

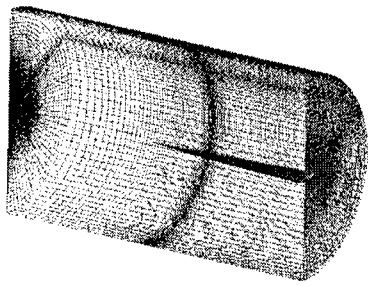


Figure 2. H-C type grid around a 85° sweep delta wing

3.1. GRID GENERATION

An H-C type mesh system for a half-plane model of the delta wing is used based on the assumption that the flow is symmetrical to the the half-plane. The mesh is H-type in the meridian section and C-type in the cross section. An elliptic grid generation method, first proposed by Spekreijse (1995), is used to generate the three-dimensional grids. This method is based on a composite mapping, which is consisted of a nonlinear transfinite algebraic transformation and an elliptic transformation. The grids are orthogonal on the delta wing surface. The sharp leading-edge is approximated by a round

edge with a small radius of $1.0 \times 10^{-3}L$, while in the experiment of Rieley & Lowson (1998), the average thickness of the leading-edge was 0.12 mm, which was approximately $2.55 \times 10^{-4}L$. Computations are carried out on three meshes, i.e. one lower resolution mesh with $140 \times 70 \times 70$ grid nodes and two higher resolution meshes with $180 \times 150 \times 70$, and $180 \times 250 \times 120$ grid nodes, where the three numbers N_ξ, N_η, N_ζ in the sequence $N_\xi \times N_\eta \times N_\zeta$ are corresponding to grid numbers in ξ, η, and ζ directions of the computational domain. In the physical domain, the ξ, η, and ζ directions are approximately corresponding to the axial, azimuthal, and wall-normal directions, respectively. An example of the three-dimensional grid is displayed in Figure 2, where only the grids of inflow- and outflow boundaries, and the far field are displayed.

3.2. PARALLEL COMPUTING

The parallel version of the numerical simulation code based on the Message Passing Interface (MPI) has been developed to improve the performance. The parallel computing is combined with domain decomposition method. The computational domain is divided into n equal-sized subdomains along the ξ direction as shown in Figure 3, where n is the number of processors. This is a simple partition with a balanced load for each processor. During computation, a processor communicates with it neighbors through exchanging the data at left and right boundary of each subdomain. But this type of communication is not suitable for calculating derivative in the ξ direction while using the compact finite difference scheme. If each grid node along a ξ grid line locates in the same processor, it will be straightforward to use the compact scheme. In Figure 4, a data structure with four processors is used as an example to illustrate a special type of data exchange which has been utilized to accomplish the data structure transformation. The top figure shows the original partition where the computational domain is divided along the ξ direction. This data structure can be transformed to a new structure shown in the bottom figure where the domain is divided along the ζ direction. The transformation is accomplished by first defining two new data types and then calling a MPI routine "MPI_ALLTOALL" from the MPI library. In the new data structure, all the grid nodes along a ξ grid line are stored in one processor. After the calculation of derivative is completed, an inverse transformation is used to the transfer the data structure back to original partition.

A test case has been used to evaluate the performance of the MPI code to calculate the derivatives in the ξ, η, and ζ directions on a $480 \times 160 \times 80$ grid. The performance of a parallel computing is measured by the speedup $S(n,p)$ which is defined as the ratio of the runtime of a serial program to the

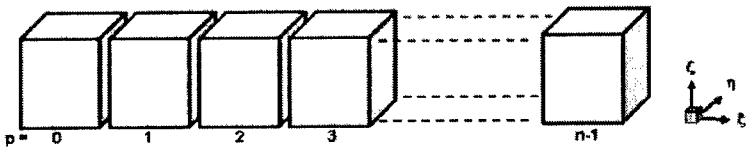


Figure 3. The domain decomposition along ξ direction in the computational space

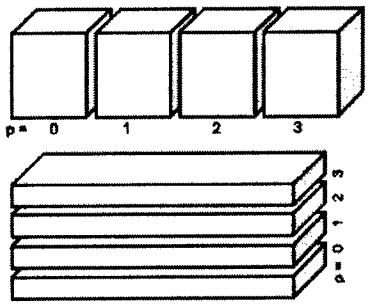


Figure 4. The change of data structure for calculating derivative in ξ direction using the compact scheme.

runtime of the parallel program. In Figure 5, the speedups on a SGI Origin 2000 computer are displayed as a function of the number of processors. The dashed line represents the linear speedup. Super-linear performance has been achieved to calculate derivatives in the η, and ζ directions where no data exchange is required. In the ξ direction, the speedup is much lower because of the massive data exchange in the data structure transformation introduced above.

Next, the total performance of the MPI code to simulate the flow around the delta wing has been tested and compared with the serial code compiled using the automatic parallelization option provided by SGI MIPSpro 7 Fortran 90 compiler. The comparison is displayed in Figure 6, where the performance of the parallel code running on 4, 6, and 15 processors is much better than the serial code. For the parallel simulation of flows around the delta wing, 10 processors have been used on a grid of $180 \times 150 \times 70$ and 12 processors have been used on a $180 \times 250 \times 120$ grid.

4. Results and Discussions

4.1. GENERAL FEATURES

All results presented here are obtained from numerical simulation of flow around a 85° sweep delta wing with a flat-plate suction surface, which has

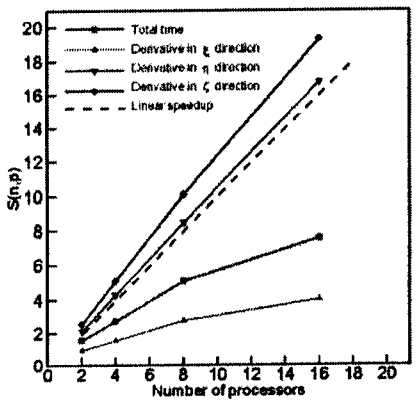


Figure 5. Speedup $S(n,p)$ of calculation of derivatives in ξ, η, and ζ directions.

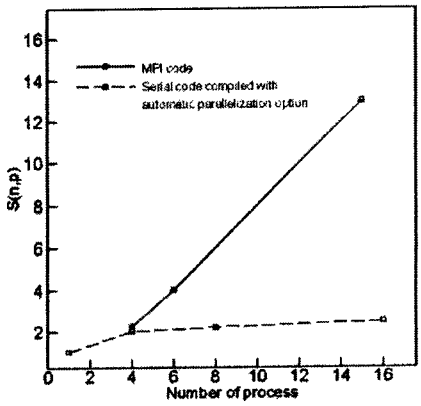


Figure 6. Speedup $S(n,p)$ of parallel computing using MPI compared with using automatic parallelization

been introduced in Section 3. The angle of attack is fixed at 12.5°. The free-stream Mach number is $Ma = 0.1$.

The numerical simulation of three cases has been carried out. In case 1, the Reynolds number based on the chord length and the free-stream velocity is $Re_c = 5 \times 10^4$. The number of grid is $140 \times 70 \times 70$. In case 2 and 3, the Reynolds number is $Re_c = 1.96 \times 10^5$. The grid numbers are $180 \times 150 \times 70$ for case 2 and $180 \times 250 \times 120$ for case 3. No initial or boundary disturbance are imposed for all three cases. Therefore, the dependence of the instability to the external disturbance has not been covered in the current work.

4.1.1. *Case 1*

The flow is stable at $Re_c = 5 \times 10^4$. The contours of the axial vorticity on selected cross sections are displayed in Figure 7. It is quite clear that a pair of counter-rotating vortices, so called the leading-edge primary vortices, appears over the suction side of the delta wing. These vortices form as a result of flow separation and the rolling-up of the vortex sheet shedding from the leading-edge. The primary vortices are steady and stable at this Reynolds number. The primary vortices are composed of a pair of counter-rotating oblique vortex tubes starting from the apex of delta wing, from a three-dimensional point of view. Beneath the primary vortices, near the suction surface of the delta wing, the secondary vortices, which have an opposite rotating direction to the primary vortices, are formed as a result of the spanwise outflow induced by the primary vortex. Figure 8 shows the iso-surface of the instantaneous axial vorticity above the suction surface the delta wing. The computational results are in good agreement with the experimental results of Riley & Lowson (1998). During the computa-

tion for the high Reynolds number case, the flow becomes unsteady and small-scale vortical structures keep shedding from the leading-edge. In the experiment of Riley & Lowson (1998), flow instability was observed when the Reynolds number was raised above $Re_c = 100,000$. In order to study the flow instability near the leading edge, the numerical simulations with higher resolutions and a higher Reynolds number have been conducted, the results are discussed in next sections.

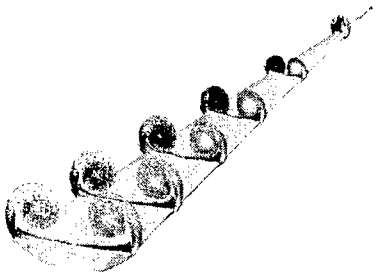


Figure 7. Contours of the axial vorticity on selected cross sections, angle of attack $\alpha = 12.5°$, $Re = 5 \times 10^4$, $Ma = 0.1$

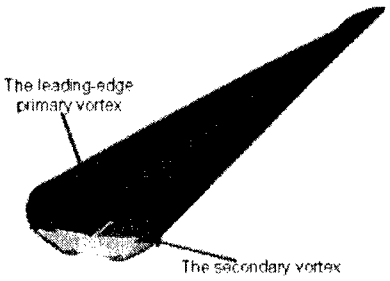


Figure 8. Iso-surface of axial vorticity above the suction surface of a 85° sweep delta wing at an angle of attack $\alpha = 12.5°$, $Re = 5 \times 10^4$, $Ma = 0.1$

4.1.2. *Case 2*

At a higher Reynolds number, i.e. $Re_c = 1.96 \times 10^5$, flow instability occurs near the leading edge of the delta wing. In order to capture the small vortical structures observed in the experiment, the numerical simulation is accomplished on a $180 \times 150 \times 70$ grid which has a higher resolution. During the simulation, flow instability and periodic shedding of small vortical structures from the leading edge are observed. Since there is no disturbance imposed as the initial or boundary condition for the computation, the unstable behavior presented by the flow in the computational results are rather intrinsic.

The distributions of the instantaneous axial vorticity on various cross section are shown in Figure 9. Compared with the low Reynolds number results of Figure 7, the flow is still dominated by a pair of primary vortices. But instability appears at the leading-edge of delta wing, where vortex shedding is observed. On the suction surface near the leading-edge, the secondary vortices are still visible in this figure.

In Figure 10 the contours of axial vorticity at different time on a cross section at $x = 0.88L$ are displayed through (a) to (h), each frame is corresponding to a snapshot of a two-dimensional flow field at a certain time.

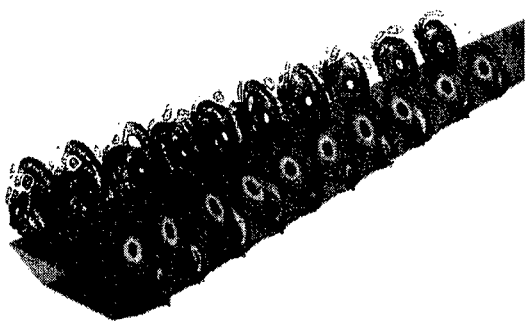


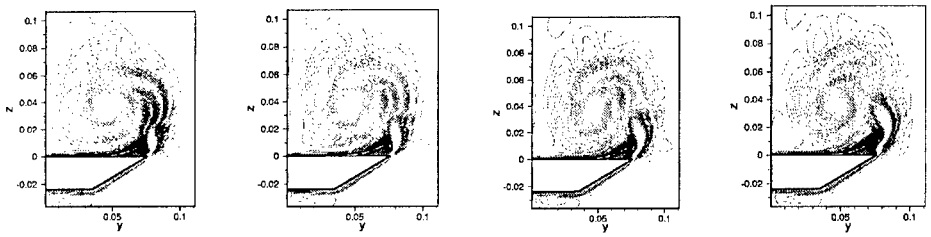
Figure 9. The instantaneous distributions of the axial vorticity on various cross sections. Angle of attack $\alpha = 12.5°$, $Re = 1.96 \times 10^5$, $Ma = 0.1$

Flow instability is quite obvious in these figures. The primary vortex deforms compared to the low Reynolds number case. The flow pattern inside the primary vortex resembles that of the spiral instability mode, which presented occasionally in the experiment of Rieley & Lowson(1998). Two strong shear layers are visible in Figure 10 through the concentration of axial vorticity contours. The first one is the leading-edge shear layer whose axial vorticity is positive (shown in light color in Figure 10), which wraps the leading-edge corner from below and feeds into the primary vortex. The other one lies between the primary vortex and the suction surface of the delta wing and has a negative axial vorticity (shown in dark color in Figure 10), which is associated with the secondary vortex. Therefore, the shear layer below the primary vortex is also called the secondary shear layer. As it will be discussed later, both the leading-edge shear layer and the secondary shear layers are related to the instability and vortex shedding process near the leading-edge.

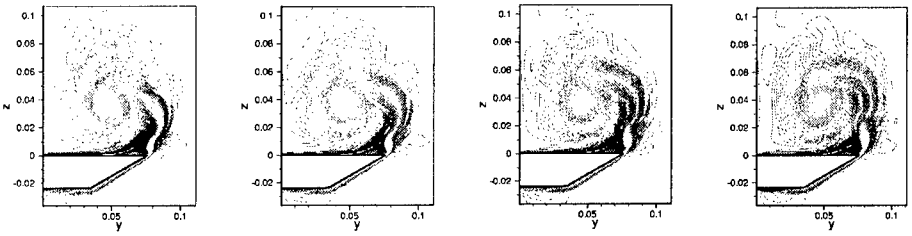
Among the small-scale vortical structures shedding from the leading-edge, there are two types of vortices, distinguished by the direction of rotation or by the sign of axial vorticity. Those vortices whose rotating direction is the same as the primary vortex are named as the A-family vortices, which are corresponding to a positive axial vorticity component. The vortices rotating in the opposite direction as the primary vortex are called the B-family vortices and have a negative axial vorticity component. The A-family vortices are stronger than the B-family vortices, which can be recognized from the contours of the axial vorticity in Figure 10.

In Figure 10(a), a bulge is observed on the leading-edge shear layer. The bulge grows in size as it moves away from the leading edge, as shown in Figure 10(b), (c), and (d). This process is corresponding to the generation and shedding of the A-family vortex. Because the B-family vortices are very

weak, the shedding process of B-family vortices is not clear in Figure 10. However, in colored animations (not shown here), the pairing of the A-family and B-family vortices can be observed. A more detailed study reveals that the B-family vortex comes from the shedding of the secondary vortex.



(a) $t = 55.54L/U_\infty$ (b) $t = 55.68L/U_\infty$ (c) $t = 55.81L/U_\infty$ (d) $t = 55.95L/U_\infty$



(e) $t = 56.09L/U_\infty$ (f) $t = 56.23L/U_\infty$ (g) $t = 56.37L/U_\infty$ (h) $t = 56.51L/U_\infty$

Figure 10. Contours of axial vorticity of different time on a cross section at $x = 0.88L$. Angle of attack $\alpha = 12.5°$, $Re = 1.96 \times 10^5$, $Ma = 0.1$

In Figure 10, frame (a) resembles frame (g). So frames (a) through (g) show one period of vortex shedding. The small-scale vortical structures shedding from the leading-edge are in turn captured by the primary vortex and feeding into the rolling-up process of the primary vortex. After leaving the leading-edge, both A- and B-family vortices experience severe deformation as they are stretched and captured by the primary vortex. The flow pattern inside the core of the primary vortex resembles that of the spiral instability mode, which is also observed in the experiment (Rieley & Lowson, 1998). In the numerical simulation, these small-scale vortical structures dissipate quickly as they are leaving the leading-edge and entering the central region of the primary vortex. But in the experiment the spiral instability can evolve into transition. The fast dissipation of the spiral mode in the numerical simulation can be attributed to the insufficiency of resolution. Because grids are clustered near the wall and near the leading-edge of delta wing, in the areas far away from the wall the resolution is relatively low. The stretching of the small-scale vortical structures is not depicted clearly, especially between the symmetrical plane and the core of the primary vortex.

As it is shown in Figure 10, the grid resolution in the areas far from the wall is not high enough. In the third case, the resolution has been increased in this area. The grid number is $180 \times 250 \times 120$. Because the Reynolds number is the same as the second case, the solution of case 2 has been interpolated to the mesh of case 3 and used as the initial field.

The contours of the instantaneous axial vorticity on selected cross-section are displayed in Figure 11. The cross-sectional view of the contours of instantaneous axial vorticity at $x = 0.88L$ is shown in Figure 12. Small-scale vortical structures are shedding from the leading edge. The pairing of small-scale vortices rotating in the opposite direction can also be recognized. Along the outer edge of the primary vortex, the structures are stretched as they are wrapped into the the vortex core. Compared with case 2, the higher resolution grid has clearly captured the small-scale structures as well as the phenomenon of vortex stretching. Although the stretched the vortical structures which can be considered as disturbance, are wrapped into the primary vortex, the flow in the core area is stable. No breakdown of the primary vortex has been observed in the computational result.

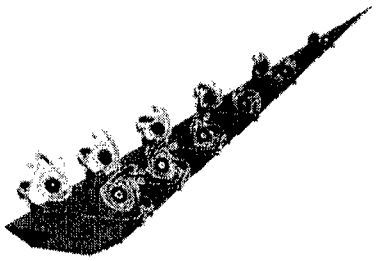


Figure 11. The instantaneous distributions of the axial vorticity on various cross sections. Angle of attack $\alpha = 12.5°$, $Re_c = 1.96 \times 10^5$, $Ma = 0.1$. The grid is $180 \times 250 \times 120$.

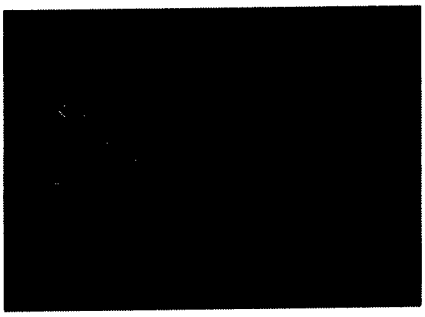


Figure 12. Cross-sectional view of the contours of instantaneous axial vorticity at $x = 0.88L$, Angle of attack $\alpha = 12.5°$, $Re_c = 1.96 \times 10^5$, $Ma = 0.1$. The grid is $180 \times 250 \times 120$.

In Figure 13, the limiting streamlines on the suction side of the delta wing are displayed. The attachment line along the symmetric line of the delta wing represents the attachment of the primary vortex. The position of the separation line indicates the location where the secondary vortex rolls up. The attachment line near the leading edge is cause by the attachment of the secondary vortex. The computational result agrees well with the schematic representations of the flow separation over a high swept delta wing (Delery, 2001). A spatial wandering of the separation line and the attachment line associated with the secondary vortex is also observed in the computational results.

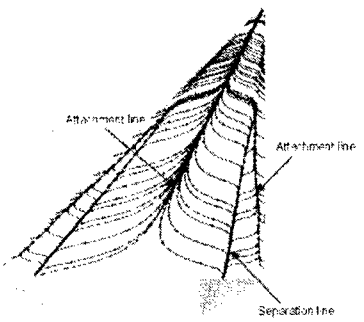


Figure 13. Instantaneous limiting streamline on the suction side of a delta wing. Angle of attack $\alpha = 12.5°$, $Re_c = 1.96 \times 10^5$, $Ma = 0.1$. The grid is $180 \times 250 \times 120$.

4.2. VORTEX SHEDDING NEAR THE LEADING-EDGE

Because the small-scale vortical structures are shedding continuously from the leading-edge, the area near the leading-edge is of particular interest in present work. The detailed pictures of vortex-shedding near the leading-edge is shown in Figure 14, where the projected streamline and contours of axial vorticity of various instance on a cross-section at $x = 0.88L$ are displayed. Through (a) to (h) in Figure 14, the pattern of projected streamline exhibits a periodic feature. Actually, figures (a) to (g) fit in one period of variation. In Figure 14(a), there is a secondary vortex attaching on the suction surface of delta wing. The strong leading-edge shear layer is shown by dark color of the contours of axial vorticity. Near the leading-edge, the shear layer is concentrated in a narrow area. In Figure 14(b), at $t = 55.68L/U_\infty$, a small vortex shown by the projected streamline appears near the leading-edge over the free shear layer. In the same picture, a small bulge appears on the shear layer. The generation of this small vortex can be attributed to the Kelvin-Helmholtz instability. Therefore, the small vortex is named as the Kelvin-Helmholtz (K-H) type vortex. At the same time, the secondary vortex, which was attaching on the wing surface at $t = 55.54L/U_\infty$, moves away from the wall. As the K-H type vortex grows, the secondary vortex is pushed further away from the wall. From $t = 55.81L/U_\infty$ to $t = 55.95L/U_\infty$, (Figure 14(c) to (d)) the secondary vortex moves upward and begins to separate from the wall, which is corresponding to the B-family vortex, whose rotating direction is opposite to the primary vortex. Therefore, the B-family vortex comes from the shedding of the secondary vortex. The generation of the leading-edge K-H type vortex also causes the deformation of the shear layer, which is visible from the contours of the axial vorticity in Figure 14(b), (c), and (d). The bulge on the contours of axial vorticity is corresponding to the K-H type vortex.

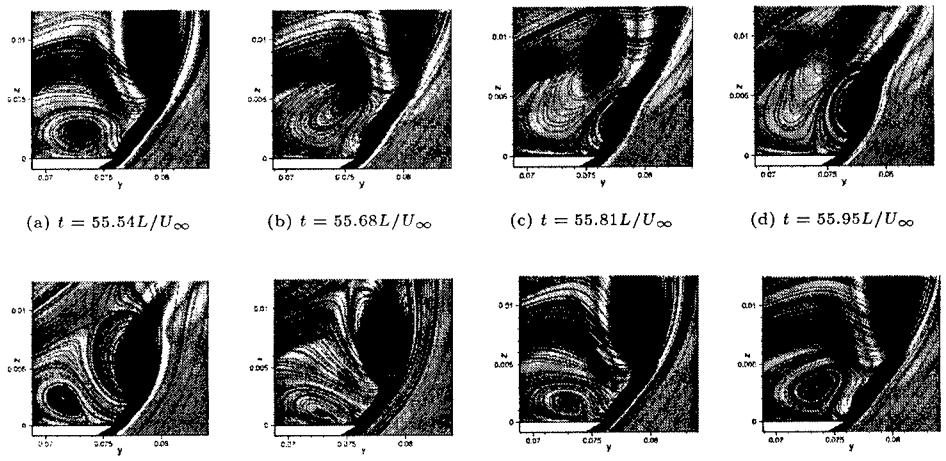
In Figure 14(d), the secondary vortex almost disappears and the K-H type vortex is still attached to the leading-edge. In Figure 14(e) and (f), the K-H type vortex grows in size until it reaches the edge of the primary vortex. Another vortex appears at the same location of the secondary vortex, actually it is a new secondary vortex. The K-H type vortex gradually moves upward and sheds from the leading-edge, and comes out to be the A-family vortex, whose rotating direction is the same as the primary vortex. It is obviously that the A-family vortex originates from the K-H type leading-edge vortex. The last two frames are the periodic repeating of frames (a) and (b) in Figure 14.

The vortex-shedding near the leading-edge is a periodic process. The interaction between the secondary vortex and the leading-edge shear layer generates a K-H type vortex. As this K-H type vortex grows, the induced flow pushes the secondary vortex away form the wall, and ultimately leads to the shedding of the B-family vortex. The K-H type vortex grows in size as the secondary vortex shows up again near the wall. The induced flow pushes the K-H type vortex away form the wall and leads to the shedding of the A-family vortex. So the A-family vortex originates from the Kelvin-Helmholtz instability of shear flow near the leading-edge. The B-family vortex originates from the secondary vortex. The period of vortex shedding is between $0.89L/U_\infty$ and $0.98L/U_\infty$. The scale of the K-H type leading-edge vortex and the secondary vortex is about $0.005L$.

The interpretation of the above phenomena is based on the Kelvin-Helmholtz instability of cross-sectional two-dimensional flow. Considering many cross-sections simultaneously, the period of vortex shedding is the same, there is only phase difference between one cross-section and the other. From a three-dimensional point of view, the A- and B-family vortices become vortex tubes, which are oblique to the axial direction.

The time series of three components of the instantaneous velocity at a location near the leading-edge ($x = 0.88L$, $y = 0.076L$, $z = 0.0094L$) are recorded and shown in Figure 15, 16, and 17. This probe point locates on the cross-section shown in Figure 10 and Figure 14, so that the velocity signals can be interpreted in accordance with the two-dimensional vortex shedding pictures. The signals of the three components of velocity are all periodic functions of time. The axial velocity u has two local maximums and two local minimums within a period. There are only one local maximum and one local minimum within a period for the signals of the spanwise velocity v and the vertical velocity w. The phase difference between v and w is approximately $\pi/2$, which can be interpreted as a result of the small-scale vortical structure passing through the probe.

In order to compare the axial velocity signal with the vortex and shedding pictures in Figure 14, a part of Figure 15 has been enlarged and



(a) $t = 55.54L/U_\infty$ (b) $t = 55.68L/U_\infty$ (c) $t = 55.81L/U_\infty$ (d) $t = 55.95L/U_\infty$

(e) $t = 56.09L/U_\infty$ (f) $t = 56.23L/U_\infty$ (g) $t = 56.37L/U_\infty$ (h) $t = 56.51L/U_\infty$

Figure 14. Projected streamline and contours of axial vorticity of different time on a cross section at $x = 0.88L$. Angle of attack $\alpha = 12.5°$, $Re = 1.96 \times 10^5$, $Ma = 0.1$

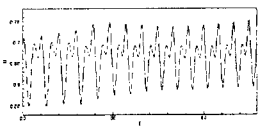


Figure 15. Instantaneous axial velocity at a location of $x = 0.88L$, $y = 0.076L$, $z = 0.0094L$

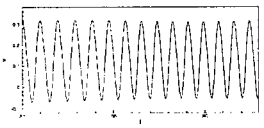


Figure 16. Instantaneous spanwise velocity at a location of $x = 0.88L$, $y = 0.076L$, $z = 0.0094L$

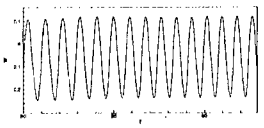


Figure 17. Instantaneous vertical velocity at a location of $x = 0.88L$, $y = 0.076L$, $z = 0.0094L$

shown in Figure 18, where those points with the same time as the frames of Figure 14 have been marked with the same letter through (a) to (g). In Figure 18, one period starts at point (a) and ends at point (g). Compared with Figure 14, it has been found that the local minimum at point (d) with a smaller axial velocity value is corresponding to the B-family vortex. As the B-family vortex moves through the probe point, as shown in Figure 14(c) and (d), the axial velocity u decreases from point (c) to point (d) and reaches its local minimum in Figure 18. Then the axial velocity recovers as the B-family vortex leaves the probe point. It is followed by the shedding of an A-family vortex from the leading-edge. Before the central part of the A-family vortex reaches the probe point, the axial velocity u signals recorded by the probe increases from point (e) to (f) in Figure 18. Then it decreases again from (f) to (g) as the core of the A-family vortex moves through the probe. Therefore, the local minimum at point (g) is associated with the A-family vortex. The local minimum at point (g) has a

relatively larger value of axial velocity compared with the local minimum at point (d), which is related to the B-family vortex. The center of both A- and B-family vortices is low-momentum region. Since the B-family vortex originates from the shedding of the secondary vortex near the suction surface of the delta wing, and it brings fluid with lower axial velocity, the central part of the B-family vortex has a lower momentum. The A-family vortex comes from the shedding of leading-edge K-H type vortex. It brings fluid from the free shear layer, which has a relatively larger momentum. In Figure 18, the local maximum at point (b) is corresponding to frame (b) of Figure 14, where both the A- and B-family vortices have not separated from the delta wing. The signals of the spanwise and the vertical velocity can be interpreted in a similar way. In Figure 17, the local maximum is corresponding to the passing of a B-family vortex, where the vertical velocity is positive. The local minimum is corresponding to the passing of an A-family vortex, where the vertical velocity is negative. Thus the period of velocity signals reflects the elapsed time at which the A- and B-family vortices are shedding from the delta wing. Thus the period of vortex-shedding can be measured as the distance between the peaks of local maximums or local minimums on the signals of three velocity components.

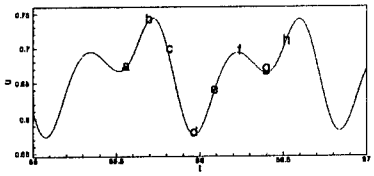


Figure 18. Instantaneous axial velocity at location $x = 0.88L$, $y = 0.076L$, $z = 0.0094L$

In order to estimate the vortex-shedding period more accurately, power spectrums of velocity fluctuations are calculated based on the velocity signals and shown in Figure 19, 20, and 21. The velocity fluctuation is calculated as the difference between the instantaneous velocity and the time-averaged mean velocity. There are two peaks in the spectrum of the axial velocity fluctuation shown in Figure 19. The frequency of the first peak is $1.086U_\infty/L$ and $2.31U_\infty/L$ for the second peak. There is only one peak in the spectrum of the spanwise and vertical velocity fluctuation. The peak frequency is $1.086U_\infty/L$, which is the same as the first peak of the u' spectrum in Figure 19. This peak frequency value $f = 1.086U_\infty/L$ represents the frequency of vortex shedding, the corresponding period is $T = 0.9208L/U_\infty$. The higher frequency in Figure 19, corresponding to a time period of $T = 0.433L/U_\infty$, reflects the elapsed time between the shedding of a A-family vortex and a B-family vortex, which is approximately half the period of the shedding of a single A- or B-family vortex.

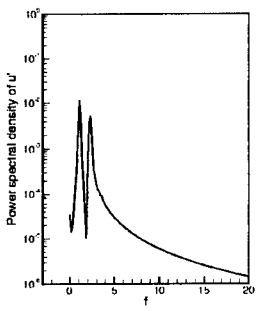


Figure 19. Power spectrum density of u' at location $x = 0.88L$, $y = 0.076L$, $z = 0.0094L$

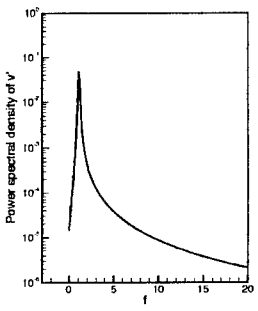


Figure 20. Power spectrum density of v' at location $x = 0.88L$, $y = 0.076L$, $z = 0.0094L$

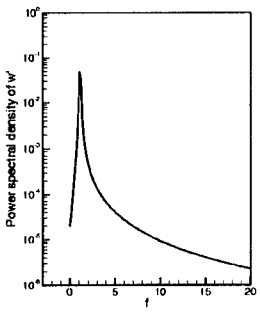
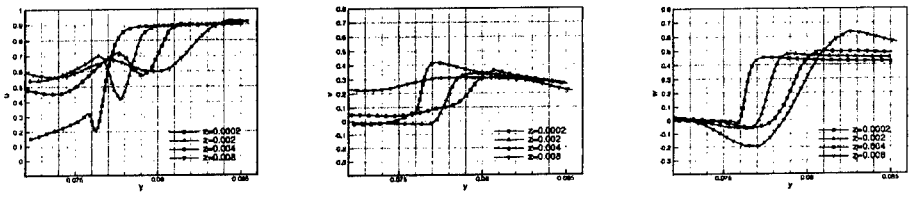


Figure 21. Power spectrum density of w' at location $x = 0.88L$, $y = 0.076L$, $z = 0.0094L$

4.3. TIME-AVERAGED RESULT

The time-averaged velocity profiles distributed on a spanwise line above the suction surface of the delta wing on a cross section at $x = 0.88L$ is shown in Figure 22. The distance between the spanwise line and the wing surface is denoted by the vertical coordinate z in Figure 22. These results are in good agreement with the experiments carried out by Rieley & Lowson (1998). As it was stated by Rieley & Lowson (1998), the axial velocity profile indicates the windward boundary layer separation. The inflection point on the axial velocity profile is similar to the Kelvin-Helmholtz instability in plane mixing layers. In Figure 22(b), the spanwise velocity profile near the surface (z=0.0002L) changes sign near $y = 0.0746L$, which is corresponding to the re-attachment point of the secondary vortex. The inflection points on profiles of the vertical velocity component in Figure 22(c) are corresponding to the edge of the leading-edge shear layer. The inflection point moves outboard as the distance from the wing surface increases. The negative part of the vertical velocity is corresponding to the secondary vortex. The secondary vortex is still visible in the time-averaged results. The evidence of vortex shedding has been removed by the temporal average procedure. The point of inflection on the velocity profile is associated with inviscid instability. Rayleigh's inflection point theorem, studying the instability of a two-dimensional velocity profile based on the linear normal mode approach, points out that disturbance can be amplified at the point of inflection. The physical interpretation of the theorem was given by Lin (1945). The restoring mechanism will force a fluid particle displaced vertically in either direction to return to its starting position. But at the point of inflection the restoring mechanism is not present and disturbance can grow. In the flow around the slender delta wing, the situation is more

complex. On the two-dimensional cross section plane, which is vertical to the axial direction, a strong shear layer is observed near the leading-edge, as shown in Figure 14(a). The existence of the secondary vortex increases the strength of the shear layer and provides more chance for the generation of the Kelvin-Helmholtz instability.



(a) Axial velocity (b) Spanwise velocity (c) Vertical velocity

Figure 22. Variations in the three components of time-averaged velocity at the leading-edge with increasing distance from the wing surface within on a cross section at $x = 0.88L$

In Figure 23 the contours of time-averaged pressure on cross sections at $x = 0.31L$, $0.45L$, $0.59L$, $0.73L$, $0.88L$ are displayed. the lowest pressure appears at the center of the primary vortex. The small-scale vortical structures are smeared out by the time-average process. The profiles of time-averaged velocity and pressure along a vertical line passing through the center of the primary vortices are displayed in Figure 24 and 25. The fluid at the center of the primary vortex experiences a acceleration between $x = 0.31L$ and $x = 0.73L$. The pressure decrease along the axial direction within the same region. The large axial velocity excess in the center of the primary vortex is an important feature of the delta wing velocity field. In the experiment, the axial velocity at the center of the primary vortex can reach $1.3U_\infty$, which is smaller than the value predicted by the computation. The vertical position of the vortex center can be identified by the maximum of the velocity profiles. As the size of the primary vortex grows along the axial direction the distance between the vortex center and the wing surface also increases. Near the wing surface, a large slope on the velocity profile is observed at each cross section.

5. Conclusions

Numerical simulation has been carried out to simulate the flow separation around a slender flat-plate delta wing at 12.5° angle of attack. Two Reynolds number have been selected. At a lower Reynolds number of 5×10^4, the flow is stable and dominated by a pair of leading-edge primary vortices. At a higher Reynolds number of 1.96×10^5, the computational results indicate the unsteady instability. The small-scale vortical structures

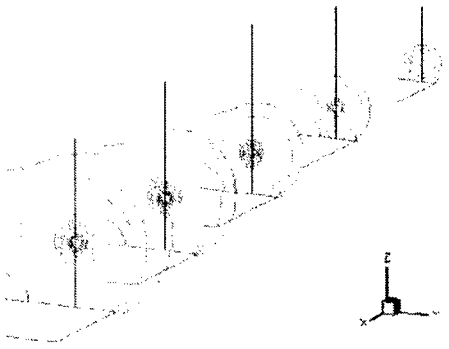


Figure 23. Contours of time-averaged pressure on selected cross sections.

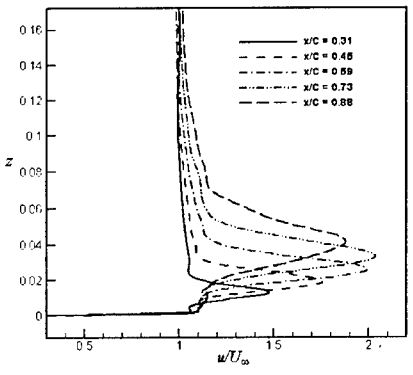


Figure 24. Profiles of time-averaged axial velocity along a vertical line passing through the center of the primary vortex.

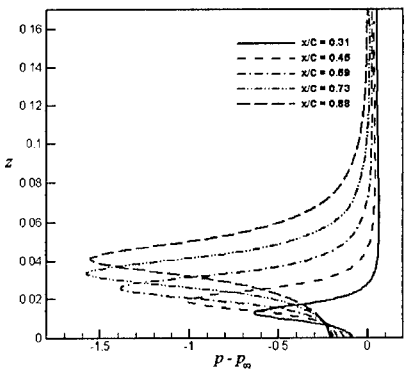


Figure 25. Profiles of time-averaged pressure along a vertical line passing through the center of the primary vortex.

are shedding from the leading-edge. It has been found that the shedding of the small-scale vortical structures originates not only from the Kelvin-Helmholtz type instability of the leading-edge shear layer, but also from the separation of the secondary vortex form the wing surface, as a result of the interaction between the secondary shear layer and the leading-edge shear layer. The vortex pairing of the small-scale structures are observed. The periods of vortex shedding are obtained from the time series of velocity components. The distributions of the time-averaged velocity near the suction surface of the delta wing obtained from the computational results agree well with those from the experiment of Rieley & Lowson (1998). But the steady small-scale vortical structures which indicate the steady instability observed in the experiment have not been found in the current computational results.

Acknowledgments

This work was supported by Air Force Office of Scientific (AFOSR) research grant monitored by Dr. L. Sakell and Dr. Thomas Beutner. The authors are grateful for AFOSR's sponsorship of this research work. The authors also would like to thank DoD HPCC for providing computer resources.

References

1. Agrawal, S., Barnett, R. M., and Robinson, B. A. 1992. Numerical investigation of vortex breakdown on a delta wing. *AIAA Journal*, **30**(3), pp.584–591.
2. Cipolla, K. M., Liakopoulos, A., and Rockwell, D. O. 1998. Quantitative imaging in proper orthogonal decomposition of flow past a delta wing. *AIAA Journal*, **36**(7), pp.1247–1255.
3. Cipolla, K. M., and Rockwell, D. 1998. Small-scale vortical structures in crossflow plane of a rolling delta wing. *AIAA Journal*, **36**(12), pp.2276–2278.
4. Delery, J. M. 2001. Robert Legendre And Hener Werle: Toward the Elucidation of Three-dimensional Separation. *Annu. Rev. Fluid Mech.*, **33**, pp.129–154.
5. Gad-el-Hak, M., and Blackwelder, R. F. 1985. The discrete vortices from a delta wing. *AIAA Journal*, **23**(6), pp.961–962.
6. Gordnier, R. E., and Visbal, M. R. 1994. Unsteady vortex structure over delta wing. *Journal of Aircraft*, **31**(1), pp.243–248.
7. Honkan, A., and Andreopoulos, J. 1997. Instantaneous three-dimensional voritcity measurements of vortical flow over a delta wing. *AIAA Journal*, **35**(1), pp.1612–1620.
8. Jiang, L., Shan, H, Liu, C., Visbal, M. R., 1999. Non-reflecting boundary condition in curvilinear coordinates, *Second AFOSR International Conference on DNS/LES*, Rutgers, New Jersey, June 7-9.
9. LeLe, S. K. 1992. Compact finite difference schemes with spectral-like resolution. *J. Comput. Phys.* **103**, pp.16-42.
10. Lowson, M. V. 1988. The three dimensional vortext sheet structure on delta wings. *AGARD CP* 438, Paper 11.
11. Modiano, D. L., and Murman, E. M. 1994. Adative computations of flow around a delta wing with vortex breakdown. *AIAA Journal*, **32**(7), pp.1545–1547.
12. Riley, A. J., and Lowson, M. V. 1998. Development of a three-dimensional free shear layer. *J. Fluid Mech.*, **369**, pp.49–89.
13. Payne, F. M., Ng, T. T., Nelson, R. C., and Shiff, L. B. 1988. Visualization and wake surveys of vortical flow over a delta wing. *AIAA Journal*, **26**(2), pp.137–143.
14. Spekreijse, S.P. (1995) Elliptic grid generation based on Laplace equations and algebraic transformation. *J. Comp. Phys.*, **118**, pp.38–61
15. Visbal, M. R., and Gordnier, R. E. 1995. Origin of computed unsteadiness in the shear layer of a delta wing. *Journal of Aircraft*, **32**(5), pp.1146–1148.
16. Visbal, M. R. 1995. Computational and physical aspects of vortex breaksown on delta wings. *AIAA Paper* 94-2317
17. Visser, K. D., and Nelson, R. C. 1993. Measurements of circulation and vorticity in the leading-edge vortex of a delta wing. *AIAA Journal*, **31**(1), pp.104–111.
18. Winant, C. D, and Browand, F. K. 1974. Vortex pairing: the mechanism of turbulent mixing-layer growth at moderate Reynolds number. *J. Fluid Mech.*, **63**, pp.237–255.
19. Yoon, S., Kwak D. 1992. Implicit Navier-Stokes solver for three-dimensional compressible flows, *AIAA Journal* **30**, pp.2653-2659

A REVIEW OF MODERN DEVELOPMENTS IN LARGE EDDY SIMULATION OF TURBULENT REACTIVE FLOWS

PEYMAN GIVI
Department of Mechanical and Aerospace Engineering
University at Buffalo, SUNY
Buffalo, NY 14260-4400

Abstract. An overview is presented of recent developments and contributions in large eddy simulation (LES) of turbulent reactive flows. The foundation of some of the recently proposed subgrid scale (SGS) closures for such simulations is presented, along with a discussion of their capabilities and limitations. The scope of the review is limited to physical modeling. In doing so, only issues pertaining to additional complexities caused by chemical reactions are discussed. That is, the challenges associated with "general" LES of non-reactive flows are not considered, even though all of these challenges are indeed present (and in most cases are a lot more complex) in reactive flows. It is recognized that numerical algorithms and computational procedures play a significant role in (any) LES. However, this review does not deal with these issues except for cases wherein the actual numerical-computational methodology is directly coupled with the procedure by which LES is conducted. The SGS closure based on the recently developed "filtered density function" (FDF) method is described in a greater detail. This is due to more familiarity of this reviewer with this closure; it does not imply that other closures are less effective.

1. Introduction

In the late 1980's, I was preparing a review article on large scale numerical simulations of turbulent reactive flows. The intent was to provide a survey of the contributions made to both direct numerical simulation (DNS) and large eddy simulation (LES). However, when that article was finally published (Givi, 1989), its content was heavily biased towards DNS. This was not intentional, it just reflected the state of progress on LES of turbu-

lent combustion at that time. But with all of the enthusiasm for DNS in the combustion community, the limitations of such simulations were well recognized (even with the most optimistic predictions of growth in supercomputer technology). It was also clear that the future of large scale simulations of practical turbulent reacting flows would heavily depend on the development of LES. Therefore, it was quite easy to predict that LES would receive significant attention in computational predictions of turbulent reacting flows in the 1990's and into the next (present) century.

Now, at the time of writing this article (Summer 2001), while struggling to meet the deadline for its submission(!) I am not surprised by the extent of the contributions in developing subgrid scale (SGS) models or by the magnificent work on LES of a variety of turbulent reacting flow systems. In fact, I admit that the rate of these developments has been a lot faster than my capability to absorb, or in some cases even follow, the details of the proposed methodologies. In addition, the page-limit restrictions under which this is being prepared, preclude describing the details of the wide variety of currently available closures; similarly, citation of the relevant references cannot even be done exhaustively. Fortunately, many aspects of SGS closures and LES of reacting turbulence have recently been discussed in several excellent tutorial and review articles (Cook and Riley, 1998a; Candel *et al.*, 1999; Bilger, 2000; Branley and Jones, 2000; Menon, 2000; Peters, 2000; Pope, 2000; Luo, 2001; Poinsot and Veynante, 2001). Therefore, in the present review I concentrate on some of the major issues related to my area of research within this field.

2. Starting Equations

Large eddy simulation involves the use of the spatial filtering operation (Sagaut, 2001)

$$\langle Q(\mathbf{x},t)\rangle_\ell = \int_{-\infty}^{+\infty} Q(\mathbf{x}',t)\mathcal{G}(\mathbf{x}',\mathbf{x})d\mathbf{x}', \tag{1}$$

where $\mathcal{G}$ denotes the filter function of width Δ_G, and $\langle Q(\mathbf{x},t)\rangle_\ell$ represents the filtered value of the transport variable $Q(\mathbf{x},t)$. In variable density flows it is convenient to consider the Favré filtered quantity,

$$\langle Q(\mathbf{x},t)\rangle_L = \langle \rho Q\rangle_\ell / \langle \rho\rangle_\ell. \tag{2}$$

We consider spatially & temporally invariant and localized filter functions, $\mathcal{G}(\mathbf{x}',\mathbf{x}) \equiv G(\mathbf{x}'-\mathbf{x})$ with the properties $G(\mathbf{x}) = G(-\mathbf{x})$, and $\int_{-\infty}^{\infty} G(\mathbf{x})d\mathbf{x} = 1$. Moreover, we only consider "positive" filter functions for which all the moments $\int_{-\infty}^{\infty} x^m G(x)dx$ exist for $m \geq 0$.

To set the framework, we consider the transport equations of chemically reacting flows. To isolate the effects of chemical reaction in the simplest way, we consider single-phase (gaseous) combustion in a low Mach number flow with negligible radiative heat transfer and viscous dissipation. We also assume that Newton's law of viscosity, Fourier's law of heat conduction and Fick's law of mass diffusion are applicable. Therefore, the primary transport variables are the density ρ, the velocity vector u_i, $i = 1,2,3$ along the x_i direction, the pressure p, the species' mass fractions Y_α, and the total specific enthalpy h. All of the mass fractions and the enthalpy are grouped into the scalar array $\boldsymbol{\phi}(\mathbf{x},t) \equiv [\phi_1, \phi_2, \ldots \phi_\sigma] \equiv [Y_1,\ Y_2, \ldots, Y_{N_s}, h]$ of size $\sigma = N_s + 1$ where N_s denotes the total number of species. Application of the filtering operation to the equations of continuity, momentum, enthalpy (energy) and species mass fraction equations gives

$$\frac{\partial \langle\rho\rangle_\ell}{\partial t} + \frac{\partial \langle\rho\rangle_\ell \langle u_i\rangle_L}{\partial x_i} = 0, \tag{3}$$

$$\frac{\partial \langle\rho\rangle_\ell \langle u_j\rangle_L}{\partial t} + \frac{\partial \langle\rho\rangle_\ell \langle u_i\rangle_L \langle u_j\rangle_L}{\partial x_i} = -\frac{\partial \langle p\rangle_\ell}{\partial x_j} + \frac{\partial \langle\tau_{ij}\rangle_\ell}{\partial x_i} - \frac{\partial T_{ij}}{\partial x_i}, \tag{4}$$

$$\frac{\partial \langle\rho\rangle_\ell \langle\phi_\alpha\rangle_L}{\partial t} + \frac{\partial \langle\rho\rangle_\ell \langle u_i\rangle_L \langle\phi_\alpha\rangle_L}{\partial x_i} = -\frac{\partial \langle J_i^\alpha\rangle_\ell}{\partial x_i} - \frac{\partial M_i^\alpha}{\partial x_i} + \langle\rho S_\alpha\rangle_\ell, \tag{5}$$

where t represents time, and the filtered reaction source terms are denoted by $\langle\rho S_\alpha\rangle_\ell = \langle\rho\rangle_\ell \langle S_\alpha\rangle_L$. The viscous stress tensor and the mass/heat fluxes are denoted by τ_{ij}, and J_i^α, respectively. At low Mach numbers and heat release rates, by neglecting the viscous dissipation and thermal radiation the source terms in the enthalpy equation can be assumed to be negligible. Thus, $S_\alpha = S_\alpha(\boldsymbol{\phi})$. The terms $T_{ij} = \langle\rho\rangle_\ell(\langle u_i u_j\rangle_L - \langle u_i\rangle_L \langle u_j\rangle_L)$ and $M_i^\alpha = \langle\rho\rangle_\ell(\langle u_i\phi_\alpha\rangle_L - \langle u_i\rangle_L \langle\phi_\alpha\rangle_L)$ denote the SGS stress and the SGS mass flux, respectively. Equations (3)-(5) are coupled through the equation of state.

3. Closure Methodologies

For non-reacting flows the SGS closure is associated with T_{ij} and M_i^α (Canuto, 1994; Ciofalo, 1994; Lesieur and Metais, 1996). In reacting flows, an additional model is required for the filtered reaction rate $\langle S_\alpha\rangle_L$. This modeling is the subject of primary concern in this review.

One of the first contributions in LES of reactive flows, similar to that in LES of non-reacting flows, was made in atmospheric sciences (Schumann, 1989). In this work, the effects of SGS scalar fluctuations (as appear in the chemical source term) are assumed negligible, *i.e.* $\langle\hat{S}_\alpha(\boldsymbol{\phi})\rangle_L \approx \hat{S}_\alpha(\langle\boldsymbol{\phi}\rangle_L)$. This assumption is compatible with that made in some of the more recent contributions (Boris *et al.*, 1992; Fureby and Grinstein, 1999), in which it

is argued that all of the essential SGS contributions are included in the numerical discretization procedure.

Modeling of the scalar fluctuations has been the subject of broad investigations in Reynolds averaged simulations (RAS) for over five decades, resulting in a variety of closure strategies (Libby and Williams, 1980; Libby and Williams, 1994). Within the past 10 years or so, almost all of these closures have been considered for LES. Examples: the eddy-break up models (Fureby and Lofstrom, 1994; Candel *et al.*, 1999), moment methods (Frankel *et al.*, 1993), the flamelet concept (Cook *et al.*, 1997; Cook and Riley, 1998b; De Bruyn Kops *et al.*, 1998; DesJardin and Frankel, 1998; DesJardin and Frankel, 1999; Pitsch and Steiner, 2000; Ladeinde *et al.*, 2001), the linear eddy model (LEM) (McMurtry *et al.*, 1992; Menon and Calhoon, 1996; Kim *et al.*, 1999; Menon, 2000), the conditional moment method (CMM) (Bushe and Steiner, 1999; Steiner and Bushe, 2001), and many others (Sykes *et al.*, 1992; Galperin and Orszag, 1993; Smith and Menon, 1996; Im *et al.*, 1997; McGrattan *et al.*, 1998; Thibaut and Candel, 1998; Battaglia *et al.*, 2000; Collin *et al.*, 2000). In addition, several of the closures previously developed for LES of non-reacting flows, have been extended for use in reacting flow simulations (DesJardin and Frankel, 1998; Jaberi and James, 1998).

The probability density function (PDF) methods have proven particularly useful in RAS (O'Brien, 1980; Pope, 1985; Dopazo, 1994; Fox, 1996; Pope, 2000). The systematic approach for determining the PDF is by means of solving its transport equation. An alternative approach is based on *assumed* methods in which the shape of the PDF is specified *a priori.* This has been pursued in several studies in most of which it is assumed that the thermo-chemical variables depend only on the mixture fraction, *e.g.* infinitely fast reaction, equilibrium chemistry. Therefore, the PDF is univariate (Madnia and Givi, 1993; Cook and Riley, 1994; Réveillon and Vervisch, 1996; Branley and Jones, 1997; Jiménez *et al.*, 1997; Mathey and Chollet, 1997; DesJardin and Frankel, 1998; DesJardin and Frankel, 1999; Forkel and Janicka, 2000; Kempf *et al.*, 2000). For LES of non-equilibrium reactive flows, it is necessary to assume the joint PDF of multi-scalars (Frankel *et al.*, 1993). Consistent with popular methods of generating univariate (Leemis, 1986) and multivariate (Johnson and Kotz, 1972) distributions, all of the assumed SGS scalar PDFs in the contributions cited above are based on the first and the second order moments. The PDFs generated in this way offer sufficient flexibility and are affordable for large scale simulations. However, it is now well understood that the "true" PDF strongly depends on the actual physics of mixing in a given flow condition (Jaberi *et al.*, 1996). Therefore, there is a need to determine such PDFs in a more systematic manner.

The "filtered density function" (FDF) methodology introduced by Pope (1990) provides the framework for fundamental developments of the PDF based SGS closures. This method provides a means of determining the PDF from its own transport equation. For the scalars' array $\boldsymbol{\phi}(\mathbf{x},t)$ the FDF, denoted by P_L, is defined as (Pope, 1990)

$$P_L(\boldsymbol{\psi};\mathbf{x},t) = \int_{-\infty}^{+\infty} \zeta\left[\boldsymbol{\psi},\boldsymbol{\phi}(\mathbf{x}',t)\right] G(\mathbf{x}'-\mathbf{x})d\mathbf{x}', \tag{6}$$

$$\zeta\left[\boldsymbol{\psi},\boldsymbol{\phi}(\mathbf{x},t)\right] = \prod_{\alpha=1}^{\sigma} \delta[\psi_\alpha - \phi_\alpha(\mathbf{x},t)], \tag{7}$$

where δ denotes the delta function and $\boldsymbol{\psi}$ denotes the composition domain of the scalar array. The term $\zeta[\boldsymbol{\phi}-\boldsymbol{\psi}(\mathbf{x},t)]$ is the "fine-grained" density (Lundgren, 1967; O'Brien, 1980; Pope, 1985; Dopazo, 1994). In variable density flows, it is convenient to consider the "filtered mass density function" (FMDF), denoted by F_L, as

$$F_L(\boldsymbol{\psi};\mathbf{x},t) \equiv \int_{-\infty}^{+\infty} \rho(\mathbf{x}',t)\zeta\left[\boldsymbol{\psi},\boldsymbol{\phi}(\mathbf{x}',t)\right] G(\mathbf{x}'-\mathbf{x})d\mathbf{x}'. \tag{8}$$

The integral property of the FDF and FMDF is such that

$$\int_{-\infty}^{+\infty} P_L(\boldsymbol{\psi};\mathbf{x},t)d\boldsymbol{\psi} = 1, \quad \int_{-\infty}^{+\infty} F_L(\boldsymbol{\psi};\mathbf{x},t)d\boldsymbol{\psi} = \langle\rho(\mathbf{x},t)\rangle_\ell. \tag{9}$$

For further discussions, it is useful to define the mass weighted conditional filtered mean of the variable $Q(\mathbf{x},t)$,

$$\langle Q(\mathbf{x},t)|\boldsymbol{\psi}\rangle_\ell \equiv \frac{\int_{-\infty}^{+\infty} \rho(\mathbf{x}',t)Q(\mathbf{x}',t)\zeta\left[\boldsymbol{\psi},\boldsymbol{\phi}(\mathbf{x}',t)\right] G(\mathbf{x}'-\mathbf{x})d\mathbf{x}'}{F_L(\boldsymbol{\psi};\mathbf{x},t)}. \tag{10}$$

Therefore, when Q can be completely described by the compositional variable, *i.e.* $Q(\mathbf{x},t) \equiv \hat{Q}(\boldsymbol{\phi}(\mathbf{x},t))$, we have $\langle Q(\mathbf{x},t)|\boldsymbol{\psi}\rangle_\ell = \hat{Q}(\boldsymbol{\psi})$. Also,

$$\int_{-\infty}^{+\infty} \langle Q(\mathbf{x},t)|\boldsymbol{\psi}\rangle_\ell F_L(\boldsymbol{\psi};\mathbf{x},t)d\boldsymbol{\psi} = \langle\rho(\mathbf{x},t)\rangle_\ell\langle Q(\mathbf{x},t)\rangle_L. \tag{11}$$

The transport equation for $F_L(\boldsymbol{\psi};\mathbf{x},t)$ is obtained by multiplying the transport equation for the fine grained density by the filter function $G(\mathbf{x}'-\mathbf{x})$ and integrating over $\mathbf{x}'$ space (Gao and O'Brien, 1993; Colucci *et al.*, 1998; Réveillon and Vervisch, 1998; Jaberi *et al.*, 1999; Jaberi, 1999; Zhou and Pereira, 2000; Tong, 2001),

$$\frac{\partial F_L(\psi;\mathbf{x},t)}{\partial t}+\frac{\partial[\langle u_i(\mathbf{x},t)|\psi\rangle_\ell F_L(\psi;\mathbf{x},t)]}{\partial x_i}=-\frac{\partial[\hat{S}_\alpha(\psi)F_L(\psi;\mathbf{x},t)]}{\partial\psi_\alpha}$$

$$+\frac{\partial}{\partial\psi_\alpha}\left[\left\langle\frac{1}{\hat{\rho}(\phi)}\frac{\partial J_i^\alpha}{\partial x_i}|\psi\right\rangle_\ell F_L(\psi;\mathbf{x},t)\right]. \tag{12}$$

The first term on the RHS is due to chemical reaction and is in a closed form. This demonstrates the primary advantage of the FDF methodology. However, the SGS convection (the second term on the LHS) and SGS mixing (the second term on the RHS) must be modeled. One of the most challenging issues in FDF is associated with closure of the mixing term. This has been the subject of broad investigations in PDF modeling (Pope, 1985; Pope, 2000). In Eq. (12) the effects of mixing are displayed through the "conditional expected diffusion" of the scalars, but can also be represented in the form of the "conditional expected dissipation" (O'Brien, 1980; Pope, 1985). The closure for this can be via any of the ones currently in use in PDF methods (Pope, 2000). In the absence of a clearly superior model, the linear mean square estimation (LMSE) model (O'Brien, 1980) has been used in almost all of previous LES based on FDF (Colucci *et al.*, 1998; Jaberi *et al.*, 1999; Garrick *et al.*, 1999; James and Jaberi, 2000; Zhou and Pereira, 2000). With $J_i^\alpha=-\gamma\frac{\partial\phi_\alpha}{\partial x_i}$, this model is

$$\frac{\partial}{\partial\psi_\alpha}\left[\left\langle-\frac{1}{\hat{\rho}}\frac{\partial}{\partial x_i}\left(\gamma\frac{\partial\phi_\alpha}{\partial x_i}\right)|\psi\right\rangle_\ell F_L\right] = \frac{\partial}{\partial x_i}\left[\gamma\frac{\partial(F_L/\langle\rho\rangle_\ell)}{\partial x_i}\right] + \frac{\partial}{\partial\psi_\alpha}\left[\Omega_m(\psi_\alpha-\langle\phi_\alpha\rangle_L)F_L\right], \tag{13}$$

where $\Omega_m(\mathbf{x},t)$ is the "frequency" of mixing within the subgrid and must be modeled. The convective term can be modeled as

$$\langle u_i|\psi\rangle_\ell F_L=\langle u_i\rangle_L F_L-\gamma_t\frac{\partial(F_L/\langle\rho\rangle_\ell)}{\partial x_i}, \tag{14}$$

where γ_t is the SGS diffusion coefficient and must be specified. Equation (14) is in accord with that often used in conventional LES (Moin *et al.*, 1991; Canuto, 1994; Ciofalo, 1994; Lesieur and Metais, 1996). With this formulation, obviously the resolved hydrodynamic field must be determined by other means. This problem can be circumvented by considering the joint velocity-scalar FMDF,

$$\mathcal{F}_L(\mathbf{v},\psi,\mathbf{x};t)\equiv\int_{-\infty}^{+\infty}\rho(\mathbf{x}',t)\xi\left[\mathbf{v},\mathbf{u}(\mathbf{x}',t),\psi,\phi(\mathbf{x}',t)\right]G(\mathbf{x}'-\mathbf{x})d\mathbf{x}', \tag{15}$$

$$\xi[\mathbf{v}, \mathbf{u}(\mathbf{x},t), \boldsymbol{\psi}, \boldsymbol{\phi}(\mathbf{x},t)] = \prod_{k=1}^{3} \delta[v_k - u_k(\mathbf{x},t)] \prod_{\alpha=1}^{\sigma} \delta[\psi_\alpha - \phi_\alpha(\mathbf{x},t)], \quad (16)$$

where $\mathbf{v}$ denotes the composition domain of the random velocity vector, and $\xi[\mathbf{v}, \mathbf{u}(\mathbf{x},t), \boldsymbol{\psi}, \boldsymbol{\phi}(\mathbf{x},t)]$ is the fine-grained velocity-scalar density. Most recent work in this regard consider the transport of the velocity FDF (VFDF) (Gicquel, 2001) and the joint velocity-scalar FDF (VSFDF) (Drozda, 2001). The operational procedure is similar to that developed previously for PDF methods (Pope, 1985; Pope, 1994; Pope, 2000).

The closure problems as noted above are not particular to the FDF; all of the other schemes require similar modelings. For example, in the limit of equilibrium chemistry all of the statistics of the reacting fields are related to those of the mixture fraction. The FMDF of the mixture fraction can be obtained from the solution of Eq. (12) with $S = 0$. So, there is still a need for modeling of the mixing term. Even in cases where the FMDF is assumed, its distribution is parameterized with the low order moments of the mixture fraction. As indicated above, the first two moments are typically used for this parameterization. Therefore, there is a need for closure of the "total SGS dissipation" as appears in the second moment (SGS variance) equation. Several means of dealing with this closure problem are available (Girimaji and Zhou, 1996; Pierce and Moin, 1998; Cook and Bushe, 1999; Jiménez *et al.*, 2001; De Bruyn Kops and Riley, 2001).

The above problem is a bit more complex when the SGS chemical reaction is assumed to be in the "flamelet" regime (Peters, 2000). In this case, even with the one-dimensional flamelet model, the thermo-chemical variables are parameterized by the mixture fraction and its rate of dissipation (Cook *et al.*, 1997; Cook and Riley, 1998b; De Bruyn Kops *et al.*, 1998; DesJardin and Frankel, 1998; Cook and Riley, 1998b). Therefore, there is a need for *a priori* specification of the joint FDF of the mixture fraction and its dissipation. A review of different methods of dealing with this issue is available (Cook and Riley, 1998a). Equation (12) with $S = 0$ indicates that there is a dependence between the FDF of the mixture fractions and the conditional expected diffusion (and the conditional expected dissipation). This dependency is not considered in most previous contributions, but is the subject of current investigations (DesJardin *et al.*, 2001).

Modeling of the conditional expected dissipation is also required in the conditional moment method (Bushe and Steiner, 1999; Steiner and Bushe, 2001). This issue has been recognized at the early stages of developments of CMM in RAS (Bilger, 2000). With this model, the conditional filtered mean values of the thermo-chemical variables (LHS of Eq. (10)) are obtained by their modeled transport equation. This is obviously computationally less demanding that solving the FDF transport equation. But in order to

determine the actual filtered quantities, the distribution of the mixture fraction FDF must be specified.

An important issue in regard to FDF is associated with the numerical solution of its transport equation. The Lagrangian Monte Carlo scheme (Pope, 1985) has proven particularly useful for this purpose. In this scheme, the FDF is represented via an ensemble of computational elements or particles. Transport of these particles and the change in their properties are modeled by a set of stochastic differential equations (SDEs) (Soong, 1973). The diffusion process (Gardiner, 1990) has proven effective for this purpose. The coefficients in the Langevin equation governing this process are set in such a way that the resulting Fokker-Planck equation (Risken, 1989) is equivalent to the FDF transport equation. Therefore, the Monte Carlo solution of the SDEs represent the solution of the FDF in the probabilistic sense. This procedure has proven successful for simulating PDF in a variety of systems (Grigoriu, 1995). However, one must be careful in performing stochastic simulations in conjunction with modern CFD solvers. Many of the advanced discretization routines developed for solving deterministic differential equations may not be applicable, or may have to be significantly modified to be suitable for solving SDEs (Kloeden and Platen, 1995).

Implementation of LEM is also based on stochastic representation of the flow. In its original development in RAS (Kerstein, 1988), the processes of molecular diffusion, chemical reaction and turbulent convection are considered separately. This is achieved by a reduced one-dimensional (linear) description of the scalar field, which makes it possible to resolve the flow scales even for flows with relatively high Reynolds, Schmidt and Damköhler numbers. The interpretation of the one-dimensional domain is dependent on the particular flow under consideration. In this way, the processes of molecular diffusion and chemical reaction are taken into account exactly, but the effects of convection are modeled. This is achieved by "random rearrangement" (or stirring) events in such a way that the displacements of fluid elements result in a diffusivity equal to the "turbulent diffusivity." For LES, this procedure is followed within each of the computational cells, and stirring is performed to yield the desired SGS diffusivity. Menon and colleagues have made extensive use of LEM for LES of a wide variety of reacting flows. A recent review is available (Menon, 2000).

4. Acknowledgment

I am honored to have the opportunity to collaborate with Professor Stephen B. Pope (Cornell University) on FDF and PDF methods, and I am grateful to him and Professor Larry T.T. Soong (SUNY-Buffalo) for teaching me most of what I know about stochastic processes. I am indebted to my

current Ph.D. students, Mr. Tomasz G. Drozda, Mr. Reza Haji-Sheikhi and my former students and collaborators, Dr. Virgil Adumitroaie (Currently at CFD Research Inc.), Dr. Paul J. Colucci (Fluent Inc.), Professor Steve H. Frankel (Purdue University), Professor Sean C. Garrick (University of Minnesota), Dr. Laurent Y.M. Gicquel (CERFACS, Toulouse), Professor Farhad A. Jaberi (Michigan State University), Dr. Sunil James (Rolls-Royce Co.) and Professor Cyrus K. Madnia (SUNY-Buffalo) for their leaderships in all of our previous/ongoing LES work. Our current research in LES/FDF is being sponsored by the U.S. Air Force Office of Scientific Research under Grant F49620-00-1-0035 (Program Manager: Dr. Julian M. Tishkoff), the NASA Langley Research Center under Grant NAG-1-2238 (Technical Monitor: Dr. J. Philip Drummond), and the NASA Glenn Research Center under Grant NAG-3-2225 (Technical Monitor: Dr. Uday Hegde). Acknowledgment is also made to the Donors of the Petroleum Research Funds administrated by the American Chemical Society for their support under Grant ACS-PRF 36981-AC9. Computational resources are provided by the NCSA at the University of Illinois at Urbana, and by the CCR at SUNY-Buffalo.

References

Battaglia, F., McGrattan, K. B., Rehm, R. G., and Baum, H. R. (2000). Simulating fire whirls. *Combustion, Theory, and Modelling* **4**, 123–138.

Bilger, R. W. (2000). Future progress in turbulent combustion research. *Prog. Energy Combust. Sci.* **26**, 367–380.

Boris, J. P., Grinstein, F. F., Oran, E. S., and Kolbe, R. L. (1992). New insights into large eddy simulations. *Fluid Dyn. Res.* **10**, 199–238.

Branley, N. and Jones, W. P. (1997). Large eddy simulation of a turbulent non-premixed flame. In *Proceedings of the Eleventh Symposium on Turbulent Shear Flows*, pages 21.1–21.6, Grenoble, France.

Branley, N. and Jones, W. P. (2000). Large eddy simulation of turbulent flames. In *European Congress on Computational Methods in Applied Science and Engineering*, pages 1–23. Barcelona, Spain.

Bushe, W. K. and Steiner, H. (1999). Conditional moment closure for large eddy simulation of nonpremixed turbulent reacting flows. *Phys. Fluids* **11**, 1896–1906.

Candel, S., Thevenin, D., Darabiha, N., and Veynante, D. (1999). Progress in numerical combustion. *Combust. Sci. and Tech.* **149**, 297–337.

Canuto, V. M. (1994). Large eddy simulation of turbulence : A subgrid scale model including shear, vorticity, rotation, and buoyancy. *The Astro. Phys. Journal* **428**, 729–752.

Ciofalo, M. (1994). Large eddy simulation : A critical survey of models and applications. In *Advances in Heat Transfer*, pages 321–419. Academic Press, New York, NY. Vol 25.

Collin, O., Ducros, F., Veynate, D., and Poinsot, T. (2000). A thickened flame model for large eddy simulation of turbulent premixed combustion. *Phys Fluids* **12**, 1843–1863.

Colucci, P. J., Jaberi, F. A., Givi, P., and Pope, S. B. (1998). Filtered density function for large eddy simulation of turbulent reacting flows. *Phys. Fluids* **10**, 499–515.

Cook, A. W. and Bushe, W. K. (1999). A subgrid-scale model for the scalar dissipation rate in nonpremixed combustion. *Phys. Fluids* **11**, 746–749.

Cook, A. W. and Riley, J. J. (1994). A subgrid model for equilibrium chemistry in turbulent flows. *Phys. Fluids* **6**, 2868–2870.

Cook, A. W. and Riley, J. J. (1998a). Progress in subgrid-scale combustion modeling. In Hafez, M. and Oshima, K., editors, *Computational Fluid Dynamics Review 1998*, pages 914–931. World Scientific, Singapore.

Cook, A. W. and Riley, J. J. (1998b). Subgrid scale modeling for turbulent reacting flows. *Combust. Flame* **112**, 593–606.

Cook, A. W., Riley, J. J., and Kosály, G. (1997). A laminar flamelet approach to subgrid-scale chemistry in turbulent flows. *Combust. Flame* **109**, 332–341.

De Bruyn Kops, S. M. and Riley, J. J. (2001). Mixing models for large-eddy simulation of nonpremixed turbulent combustion. *ASME Journal of Fluids Engineering* **123**, 1–6.

De Bruyn Kops, S. M., Riley, J. J., Kosály, G., and Cook, A. W. (1998). Investigation of modeling for non-premixed turbulent combustion. *Combust. Flame* **60**, 105–122.

DesJardin, P. E. and Frankel, S. H. (1998). Large eddy simulation of a turbulent nonpremixed reacting jet: Application and assessment of subgrid-scale combustion models. *Phys. Fluids* **10**, 2298–2314.

DesJardin, P. E. and Frankel, S. H. (1999). Two-dimensional large eddy simulation of soot formation in the near-field of a strongly radiating nonpremixed acetylene-air turbulent jet flame. *Combust. Flame* **119**, 121–132.

DesJardin, P. E., Smith, T. M., and Roy, C. J. (2001). Numerical simulations of a methanol pool fire. AIAA Paper AIAA-01-0636.

Dopazo, C. (1994). Recent developments in PDF methods. In Libby and Williams (1994), chapter 7, pages 375–474.

Drozda, T. G. (2001), Consistency assessment of velocity-scalar filtered density function for large-eddy simulation of turbulent flows. M.S. Thesis, Department of Mechanical and Aerospace Engineering, State University of New York at Buffalo, Buffalo, NY.

Forkel, H. and Janicka, J. (2000). Large-eddy simulation of a turbulent hydrogen diffusion flame. *Flow, Turbulence and Combustion* **65**, 163–175.

Fox, R. O. (1996). Computational methods for turbulent reacting flows in chemical process industry. *Revue De L'Institut Francais Du Petrole* **51**, 215–246.

Frankel, S. H., Adumitroaie, V., Madnia, C. K., and Givi, P. (1993). Large eddy simulations of turbulent reacting flows by assumed PDF methods. In Ragab, S. A. and Piomelli, U., editors, *Engineering Applications of Large Eddy Simulations*, pages 81–101. ASME, FED-Vol. 162, New York, NY.

Fureby, C. and Grinstein, F. F. (1999). Monotonically integrated large eddy simulation of free shear flows. *AIAA J.* **37**, 544.

Fureby, C. and Lofstrom, C. (1994). Large-eddy simulations of bluff body stabilized flames. In *Proceedings of 25th Symp. (Int.) on Combustion*, pages 1257–1264. The Combustion Institute, Pittsburgh, PA.

Galperin, B. and Orszag, S. A., editors. (1993). *Large Eddy Simulations of Complex Engineering and Geophysical Flows*. Cambridge University Press, Cambridge, England.

Gao, F. and O'Brien, E. E. (1993). A large-eddy simulation scheme for turbulent reacting flows. *Phys. Fluids A* **5**, 1282–1284.

Gardiner, C. W. (1990). *Handbook of Stochastic Methods*. Springer-Verlag, New York, NY.

Garrick, S. C., Jaberi, F. A., and Givi, P. (1999). Large eddy simulation of scalar transport in a turbulent jet flow. In Knight, D. and Sakell, L., editors, *Recent Advances in DNS and LES*, volume 54 of *Fluid Mechanics and its Applications*, pages 155–166. Kluwer Academic Publishers, The Netherlands.

Gicquel, L. Y. M. (2001), *Velocity Filtered Density Function for Large Eddy Simulation of Turbulent Flows*. Ph.D. Dissertation, Department of Mechanical and Aerospace Engineering, State University of New York at Buffalo, Buffalo, NY.

Girimaji, S. S. and Zhou, Y. (1996). Analysis and modeling of subgrid scalar mixing using numerical data. *Phys. Fluids* **8**, 1224–1236.

Givi, P. (1989). Model free simulations of turbulent reactive flows. *Prog. Energy Combust. Sci.* **15**, 1–107.

Grigoriu, M. (1995). *Applied Non-Gaussian Processes.* Prentice-Hall, Englewood Cliffs, NJ.

Im, H. G., Lund, T. S., and Ferziger, J. H. (1997). Large eddy simulation of turbulent front propagation with dynamic subgrid models. *Phys. Fluids* **9**.

Jaberi, F. A. and James, S. (1998). A dynamic similarity model for large eddy simulation of turbulent combustion. *Phys. Fluids* **10**, 1775–1777.

Jaberi, F. A., Miller, R. S., Madnia, C. K., and Givi, P. (1996). Non-Gaussian scalar statistics in homogeneous turbulence. *J. Fluid Mech.* **313**, 241–282.

Jaberi, F. A., Colucci, P. J., James, S., Givi, P., and Pope, S. B. (1999). Filtered mass density function for large eddy simulation of turbulent reacting flows. *J. Fluid Mech.* **401**, 85–121.

Jaberi, F. A. (1999). Large eddy simulation of turbulent premixed flames via filtered mass density function. AIAA Paper 99-0199.

James, S. and Jaberi, F. A. (2000). Large scale simulations of two-dimensional non-premixed methane jet flames. *Combust. Flame* **123**, 465–487.

Jiménez, J., Liñán, A., Rogers, M. M., and Higuera, F. J. (1997). *A Priori* testing of subgrid models for chemically reacting non-premixed turbulent flows. *J. Fluid Mech.* **349**, 149–171.

Jiménez, J., Ducros, F., Cuenot, B., and Bédat, B. (2001). Subgrid scale variance and dissipation of a scalar field in large eddy simulations. *Phys. Fluids* **13**, 1748–1754.

Johnson, N. L. and Kotz, S. (1972). *Distributions in Statistics: Continious Multivariate Distributions.* John Wiley and Sons, New York, NY.

Kempf, A., Forkel, H., Chen, J. Y., Sadiki, A., and Janicka, J. (2000). Large-eddy simulation of a counterflow configuration with and without combustion. *Proceedings of the Combustion Institute* **28**, 35–40.

Kerstein, A. R. (1988). A linear eddy model of turbulent scalar transport and mixing. *Combust. Sci. and Tech.* **60**, 391–421.

Kim, W.-W., Menon, S., and Mongia, H. C. (1999). Large-eddy simulation of a gas turbine combustor flow. *Combust. Sci. and Tech.* **143**, 25–62.

Kloeden, P. E. and Platen, E. (1995). *Numerical Solution of Stochastic Differential Equations*, volume 23 of *Applications of Mathematics, Stochastic Modelling and Applied Probability.* Springer-Verlag, New York, NY.

Ladeinde, F., Cai, X., Sekar, B., and Kiel, B. (2001). Application of combined LES and flamelet modeling to methane, propane, and jet-A combustion. AIAA Paper 2001-0634.

Leemis, L. M. (1986). Relations among common univariate distributions. *American Statistician* **40**, 143–146.

Lesieur, M. and Metais, O. (1996). New trends in large eddy simulations of turbulence. *Ann. Rev. Fluid Mech.* **28**, 45–82.

Libby, P. A. and Williams, F. A., editors. (1980). *Turbulent Reacting Flows*, volume 44 of *Topics in Applied Physics.* Springer-Verlag, Heidelberg.

Libby, P. A. and Williams, F. A., editors. (1994). *Turbulent Reacting Flows.* Academic Press, London, England.

Lundgren, T. S. (1967). Distribution functions in the statistical theory of turbulence. *Phys. Fluids* **10**, 969–975.

Luo, K. H. (2001). DNS and LES of turbulence-combustion interactions. In Geurts, B. J., editor, *Modern Simulation Strategies for Turbulent Flow*, chapter 14, pages 263–293. R. T. Edwards, Inc., Philadelphia, PA.

Madnia, C. K. and Givi, P. (1993). Direct numerical simulation and large eddy simulation of reacting homogeneous turbulence. In Galperin and Orszag (1993), chapter 15, pages 315–346.

Mathey, F. and Chollet, J. P. (1997). Large eddy simulation of turbulent reactive flows. In *Proceedings of the Eleventh Symposium on Turbulent Shear Flows*, pages 16.19–16.24,

Grenoble, France.
McGrattan, K. B., Baum, H. R., and Rehm, R. G. (1998). Large eddy simulation of smoke movement. *Fire Safety Journal* **30**, 161–178.
McMurtry, P. A., Menon, S., and Kerstein, A. R. (1992). A linear eddy sub-grid model for turbulent reacting flows: Application to hydrogen-air combustion. In *Proceedings of 24th Symp. (Int.) on Combustion*, pages 271–278. The Combustion Institute, Pittsburgh, PA.
Menon, S. and Calhoon, W. H. (1996). Subgrid mixing and molecular transport modeling in a reacting shear layer. In *Proceedings of 26th Symp. (Int.) on Combustion*, pages 59–66. The Combustion Institute, Pittsburgh, PA.
Menon, S. (2000). Subgrid combustion modelling for large-eddy simulations. *Int. J. Engine Research* **1**, 209–227.
Moin, P., Squires, W., Cabot, W. H., and Lee, S. (1991). A dynamic subgrid-scale model for compressible turbulence and scalar transport. *Phys. Fluids A* **3**, 2746–2757.
O'Brien, E. E. (1980). The probability density function (PDF) approach to reacting turbulent flows. In Libby and Williams (1980), chapter 5, pages 185–218.
Peters, N. (2000). *Turbulent Combustion*. Cambridge University Press, Cambridge, UK.
Pierce, C. D. and Moin, P. (1998). A dynamic model for subgrid-scale variance and dissipation rate of a conserved scalar. *Phys. Fluids* **10**, 3041–3044.
Pitsch, H. and Steiner, H. (2000). Large eddy simulation of a turbulent piloted methane/air diffusion flame (Sandia flame D). *Phys. Fluids* **12**, 2541–2554.
Poinsot, T. and Veynante, D. (2001). *Theoretical and Numerical Combustion*. R. T. Edwards, Inc., Philadelphia, PA.
Pope, S. B. (1985). PDF methods for turbulent reactive flows. *Prog. Energy Combust. Sci.* **11**, 119–192.
Pope, S. B. (1990). Computations of turbulent combustion: Progress and challenges. In *Proceedings of 23rd Symp. (Int.) on Combustion*, pages 591–612. The Combustion Institute, Pittsburgh, PA.
Pope, S. B. (1994). Lagrangian PDF methods for turbulent flows. *Ann. Rev. Fluid Mech.* **26**, 23–63.
Pope, S. B. (2000). *Turbulent Flows*. Cambridge University Press, Cambridge, UK.
Réveillon, J. and Vervisch, L. (1996). Response of the dynamic LES model to heat release. *Phys. Fluids* **8**, 2248–2250.
Réveillon, J. and Vervisch, L. (1998). Subgrid-scale turbulent micromixing: Dynamic approach. *AIAA J.* **36**, 336–341.
Risken, H. (1989). *The Fokker-Planck Equation, Methods of Solution and Applications*. Springer-Verlag, New York, NY.
Sagaut, P. (2001). *Large Eddy Simulation for Incompressible Flows*. Springer, New York.
Schumann, U. (1989). Large eddy simulation of turbulent diffusion with chemical reactions in the convective boundary layer. *Atmospheric Environment* **23**, 1713–1726.
Smith, T. M. and Menon, S. (1996). The structure of premixed flames in a spatially evolving turbulent flow. *Combust. Sci. and Tech.* **119**, 77–106.
Soong, T. T. (1973). *Random Differential Equations in Science and Engineering*. Academic Press, New York, NY.
Steiner, H. and Bushe, W. K. (2001). Large eddy simulation of a turbulent reacting jet with conditional source-term estimation. *Phys. Fluids* **13**, 754–759.
Sykes, R. I., Henn, D. S., Parker, S. F., and Lewellen, W. S. (1992). Large-eddy simulation of a turbulent reacting plume. *Atmospheric Environment* **26**, 1713–1726.
Thibaut, D. and Candel, S. (1998). Numerical study of unsteady turbulent premixed combustion: Application to flashback simulation. *Combustion and Flame* **113**, 53–65.
Tong, C. (2001). Measurements of conserved scalar filtered density function in a turbulent jet. *Phys. Fluids* **13**, 2923–2937.
Zhou, X. Y. and Pereira, J. C. F. (2000). Large eddy simulation (2D) of a reacting plan mixing layer using filtered density function. *Flow, Turbulence and Combustion* **64**, 279–300.

COMPUTATIONAL CONSTRAINS ON LARGE EDDY SIMULATION OF INHOMOGENEOUS TURBULENT COMPLEX GEOMETRY FLOWS

OLEG V. VASILYEV
Department of Mechanical and Aerospace Engineering,
University of Missouri-Columbia
Columbia, MO 65211, USA
VasilyevO@missouri.edu

1. Introduction

In large eddy simulation (LES) of turbulent flows the dynamics of the large scale structures are computed, while the effect of the small scale turbulence is modeled. The differential equations describing the space-time evolution of the large scale structures are formally derived by applying a low-pass filter with non-uniform filter width to the Navier-Stokes equations. For an incompressible flow the non-dimensional equations describing the evolution of large scale structures take the following form:

$$\frac{\partial \overline{u}_i}{\partial x_i} = -\left[\frac{\partial u}{\partial x_i}\right], \tag{1}$$

$$\frac{\partial \overline{u}_i}{\partial t} + \frac{\partial \overline{u_i u_j}}{\partial x_j} = -\frac{\partial \overline{p}}{\partial x_i} + \frac{1}{Re}\frac{\partial^2 \overline{u}_i}{\partial x_j \partial x_j} - \left[\frac{\partial u_i u_j}{\partial x_j} + \frac{\partial p}{\partial x_i} - \frac{1}{Re}\frac{\partial^2 u_i}{\partial x_j \partial x_j}\right], \tag{2}$$

where the square bracket denotes the commutation operator given by

$$\left[\frac{\partial F}{\partial x_i}\right] = \overline{\frac{\partial F}{\partial x_i}} - \frac{\partial \overline{F}}{\partial x_i}. \tag{3}$$

The filtered convective term $\overline{u_i u_j}$ is unknown in LES and is typically decomposed into the convective term $\overline{u}_i \overline{u}_j$ that can be computed and the remainder, called sub-grid scale (SGS) stress, which should be modelled:

$$\overline{u_i u_j} = \overline{u}_i \overline{u}_j - \underbrace{\left(\overline{u}_i \overline{u}_j - \overline{u_i u_j}\right)}_{\tau_{ij}}. \tag{4}$$

In order to derive LES equations from Eqs. (1), (2), and (4) the following three key assumptions are made:

1. The differentiation and filtering operations commute.
2. The shape of the low-pass filter is known.
3. The modeled subgrid scale stress corresponds to the low-pass filter used in deriving LES equations.

With these assumptions we obtain the classical LES equations

$$\frac{\partial \overline{u}_i}{\partial x_i} = 0, \tag{5}$$

$$\frac{\partial \overline{u}_i}{\partial t} + \frac{\partial \overline{u}_i \overline{u}_j}{\partial x_j} = -\frac{\partial \overline{p}}{\partial x_i} + \frac{1}{Re}\frac{\partial^2 \overline{u}_i}{\partial x_j \partial x_j} + \frac{\partial \tau_{ij}}{\partial x_j}. \tag{6}$$

Ironically, all three assumptions used in derivation of Eqs. (5)-(6) are very often violated, perhaps as a result of addressing other very important problems related to numerical methods. However, recent advancement in numerical algorithms and hardware, has necessitated a careful and systematic examination of this issue. The main objective of this paper is to present a way for LES to be consistent, *i.e.* satisfy all these assumptions.

2. Implicit Filtering

Due to the lack of a straightforward and robust filtering procedure for inhomogeneous flows, most large eddy simulations performed to date have not made use of explicit filtering. The nearly universal approach for LES in complex geometries is to argue that the finite support of the computational mesh together with the low-pass characteristics of the discrete differencing operators effectively act as a filter (Rogallo and Moin, 1984; Lund, 1997), *i.e.*

$$\left.\frac{\delta u}{\delta x}\right|_i = \frac{u_{i+1} - u_{i-1}}{2\Delta x} = \frac{d}{dx}\int_{x_{i-1}}^{x_{i+1}} u dx = \left.\frac{d\overline{u}}{dx}\right|_i, \tag{7}$$

where $\delta/\delta x$ and d/dx are respectively finite difference and the exact (analytical) derivative operators. This procedure is commonly referred as implicit filtering since an explicit filtering operation never appears in the solution procedure. Although the technique of implicit filtering has been used extensively in the past, there are several compelling reasons to adopt a more systematic approach. Foremost of these is the issue of consistency. While it is true that discrete derivative operators have a low-pass filtering effect, the associated filter acts only in one spatial direction in which the derivative is taken. This fact implies that each term in the Navier-Stokes equations is acted on by a distinct one-dimensional filter and the actual equations being

solved are

$$\frac{\partial \widetilde{\overline{u}_1}^{x_1}}{\partial x_1} + \frac{\partial \widetilde{\overline{u}_2}^{x_2}}{\partial x_2} + \frac{\partial \widetilde{\overline{u}_3}^{x_3}}{\partial x_3} = 0, \tag{8}$$

$$\frac{\partial \overline{u}_i}{\partial t} + \frac{\partial \widetilde{\overline{u}_i \overline{u}_1}^{x_1}}{\partial x_1} + \frac{\partial \widetilde{\overline{u}_i \overline{u}_2}^{x_2}}{\partial x_2} + \frac{\partial \widetilde{\overline{u}_i \overline{u}_3}^{x_3}}{\partial x_3} = -\frac{\partial \widetilde{\overline{p}}^{x_i}}{\partial x_i} + \frac{\partial \widetilde{\tau_{i1}}^{x_1}}{\partial x_1} + \frac{\partial \widetilde{\tau_{i2}}^{x_2}}{\partial x_2} + \frac{\partial \widetilde{\tau_{i3}}^{x_3}}{\partial x_3} + \frac{1}{Re}\left[\frac{\partial^2 \widehat{\overline{u}_i}^{x_1}}{\partial^2 x_1} + \frac{\partial^2 \widehat{\overline{u}_i}^{x_2}}{\partial^2 x_2} + \frac{\partial^2 \widehat{\overline{u}_i}^{x_3}}{\partial^2 x_3}\right], \tag{9}$$

where $\widetilde{(\cdot)}^{x_i}$ and $\widehat{(\cdot)}^{x_i}$ are the effective one-dimensional filters associated with the first and second difference operators respectively. Thus, there is no way to derive the discrete equations through the application of a single three-dimensional filter. Considering this ambiguity in the definition of the filter, it is nearly impossible to make detailed comparisons of LES results with filtered DNS or experimental data.

The second significant limitation of the implicit filtering approach is the inability to control numerical error. Without an explicit filter, there is no direct control of the energy in the high frequency portion of the spectrum. Significant energy in this portion of the spectrum coupled with the non-linearities in the Navier-Stokes equations can produce significant aliasing error. Furthermore, all discrete derivative operators become rather inaccurate for high frequency solution components and this error interferes with the dynamics of the small scale eddies. This error can be particularly harmful when the dynamic model is used (Germano *et al.*, 1991; Ghosal *et al.*, 1995), since it relies entirely on information contained in the smallest resolved scales.

3. Explicit Filtering

The difficulties associated with the implicit filtering approach can be alleviated by performing an explicit filtering operation as an integral part of the solution process (Ghosal, 1996; Vasilyev *et al.*, 1998). By damping the energy in the high frequency portion of the spectrum it is possible to reduce or eliminate the various sources of numerical error that dominate this frequency range. Explicit filtering reduces the effective resolution of the simulation, but allows the filter size and shape to be chosen independently of the mesh spacing. In addition explicit filtering provides the means for both assessing and minimizing the effects of numerical error in practical simulations.

In order to illustrate the explicit filtering procedure further, consider a discrete time integration applied to the LES Eqns. (5)-(6):

$$\overline{u}_i^{n+1} = \overline{u}_i^n + \Delta_L \overline{u}_i^{n+1} + \Delta_{NL} \overline{u}_i^{n+1}, \tag{10}$$

where $\Delta_L \overline{u}_i^{n+1}$ and $\Delta_{NL} \overline{u}_i^{n+1}$ are incremental velocity fields resulted from the time integration of linear and non-linear terms respectively. The incremental velocity field $\Delta_{NL} \overline{u}_i^{n+1}$ has frequencies beyond the characteristic frequency that defines $\overline{u}_i$ and thus should be filtered. This additional filtering should be explicitly performed at the end of each time step. Thus the modified time integration procedure can be schematically written as

$$\overline{u}_i^{n+1} = \overline{u}_i^n + \Delta_L \overline{u}_i^{n+1} + \overline{\Delta_{NL} \overline{u}_i^{n+1}}. \tag{11}$$

Note that the frequency content of each term on the right-hand side of Eq. (11) is limited to the bar level. Thus in advancing from time level n to $n+1$, the frequency content of the solution is not altered. This fact implies that the additional filtering of the non-linear terms is sufficient to achieve an explicit filtering of the velocity field for all time.

The explicit filtering procedure (11) automatically implies an alternative form of LES equations (Vasilyev *et al.*, 1998)

$$\frac{\partial \overline{u}_i}{\partial t} + \frac{\partial \overline{\overline{u}_i \overline{u}_j}}{\partial x_j} = -\frac{\partial \overline{p}}{\partial x_i} + \frac{1}{Re} \frac{\partial^2 \overline{u}_i}{\partial x_j \partial x_j} + \frac{\partial \overline{\tau}_{ij}}{\partial x_j}, \tag{12}$$

where $\overline{\tau}_{ij}$ denotes the alternative SGS stress

$$\overline{\tau}_{ij} = \overline{\overline{u}_i \overline{u}_j} - \overline{u_i u_j}. \tag{13}$$

A possible drawback of this new formulation is that the Eq. (12) is not Galilean invariant unless a sharp cut-off filter is utilized (Vasilyev *et al.*, 1998). Non-Galilean invariance follows from the appearance of the term $c_j \partial(\overline{\overline{u}}_i - \overline{u}_i)/\partial x_j$, where c_j is the uniform translation velocity of the moving frame of reference. The error is seen to be proportional to the difference between the singly and doubly filtered velocity. This difference will be zero for a sharp cutoff filter, but will not vanish in the general case. The spectral content of the error is proportional to $\hat{G}(\mathbf{k})(1-\hat{G}(\mathbf{k}))$ where $\hat{G}(\mathbf{k})$ is the filter transfer function and $\mathbf{k}$ is the wave vector. This fact implies that the error is only generated in the wavenumber band where $\hat{G}(\mathbf{k})$ differs significantly from 0 or 1. Thus it is possible to minimize the error by constructing the explicit filter to be as close as possible to a sharp cut-off.

It turns out that non-Galilean invariance of Eq. (12) is not an issue if one adapts the correct physical interpretation of inhomogeneous turbulent complex geometry flows. We recall that if the filter width is non-uniform in one or more directions, it automatically implies that the LES equations *should not* be Galilean invariant in these directions (Ghosal, 1999). To ensure Galilean invariance in homogeneous directions of the flow one may use sharp cut-off filters in these directions.

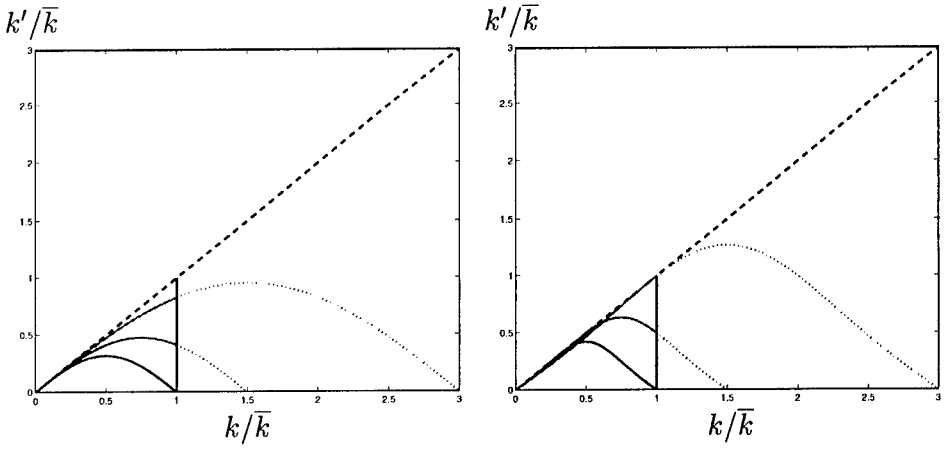


Figure 1. Modified wave-number diagram for the second (left) and fourth (right) order schemes. The vertical solid line represents the effective resolution of the explicitly filtered simulations, *i.e.* fixed cut-off frequency $\overline{k}$. The dashed line is the exact distribution that is achieved with a pseudo spectral method.

It is worthwhile to note that the use of explicit filtering provides the means for reducing the various sources of numerical error that become most severe for length scales on the order of the mesh size. By damping the high frequency portion of the solution, it is possible to control the adverse effects of numerical error. In particular, if the filter width is held fixed as the mesh is refined, the velocity field will converge to the true solution of LES equations (5) and (12). This should be contrasted to the conventional approach where the mesh is refined without the use of an explicit filter. In the latter case, additional length scales are added each time the mesh is refined, and thus the process converges to a direct numerical simulation (DNS) rather than to an LES.

It is very illustrative to consider the effect of explicit filtering on the accuracy of the solution and the computational cost associated with it in terms of modified wavenumber analysis (Lund and Kaltenbach, 1995). For simplicity let us consider the case when we filter the periodic signal given on a uniform mesh with grid size Δ_g. Then explicit filtering can be viewed as refining the mesh but keeping the same frequency content ($k \leq \overline{k}$) determined by the primary filter width Δ. The modified wavenumber diagrams for these simulations are shown in Fig.1. The solid vertical line denotes the fixed effective resolution, while the curves to the left of this line show the modified wavenumber distributions for the various values of filter width to grid ratios Δ/Δ_g. When no filter is applied (the case $\Delta/\Delta_g = 1$) considerable truncation error is evident for the upper half of the wavenumber range. As the ratio Δ/Δ_g is increased, the situation improves and the modified wavenumber slowly approaches the analytical

distribution for $k \leq \overline{k}$. Note that with the increase of the ratio Δ/Δ_g the computational cost associated with the implementation of explicit filtering also increases. Thus, in order for explicit filtering to be cost effective, the higher order schemes need to be used, since they provide the comparable modified wavenumber dependence in the range $k \leq \overline{k}$ with considerably smaller filter width to grid ratios then the lower order schemes.

In summary, the use of explicit filtering results in a LES that satisfies assumptions 2 and 3 that are used in the derivation of the LES equations. However, in order to realize the benefits of explicit filtering and satisfy assumption 1, it is necessary to develop discrete filtering operators that commute with numerical differentiation. This will be discussed next.

4. Construction of Commutative Filters

In order to realize the benefits of explicit filtering, it is necessary to develop robust and straightforward discrete filtering operators that commute with numerical differentiation. Recently a new class of *commutative* filters for both structured (Vasilyev *et al.*, 1998) and unstructured (Marsden *et al.*, 2000) grids has been developed. With these filters the differentiation and filtering operations commute to an *a priori* specified order of filter width.

We begin by discussing the continuous filtering operation and then extend it to discrete filtering. Let us consider a three dimensional field $\phi(\mathbf{x})$ ($\mathbf{x} = (x_1, x_2, x_3)^{\mathrm{T}}$) defined in a three-dimensional domain $\mathbf{D}$. The most general continuous filtering operation in physical space can be written as

$$\overline{\phi}(\mathbf{x}) = \int_{\mathbf{D}} G(\mathbf{x}, \mathbf{y})\, \phi(\mathbf{y}) d^3\mathbf{y}, \tag{14}$$

where $G(\mathbf{x}, \mathbf{y})$ is the location dependent three-dimensional filter function. The filtering operation (14) can be substantially simplified if there exists a function $\boldsymbol{\xi} = \mathbf{f}(\mathbf{x})$ and its inverse $\mathbf{x} = \mathbf{F}(\boldsymbol{\xi})$ that maps the physical domain $\mathbf{D}$ into a rectangular domain $\Omega = [\alpha_1, \beta_1] \times [\alpha_2, \beta_2] \times [\alpha_3, \beta_3]$. In this case the filtering operation can be defined the following way: given an arbitrary function $\phi(\mathbf{x})$ we obtain the new function $\psi(\boldsymbol{\xi}) = \phi(\mathbf{F}(\boldsymbol{\xi}))$ defined in the domain Ω, the function $\psi(\boldsymbol{\xi})$ is then filtered using a sequence of three one-dimensional filters. It can be shown (Vasilyev *et al.*, 1998) that the commutation error of filtering and differentiation operations in three spatial dimensions is given by

$$\left[\frac{\partial \phi}{\partial x_k}\right] \equiv \overline{\frac{\partial \phi}{\partial x_k}} - \frac{\partial \overline{\phi}}{\partial x_k} = \mathrm{O}(\Delta_1^n, \Delta_2^n, \Delta_3^n), \tag{15}$$

provided that the filter moments $M_i^k(\xi)$ of filters G_i ($i = 1, \ldots, 3$) exist and they satisfy the following properties:

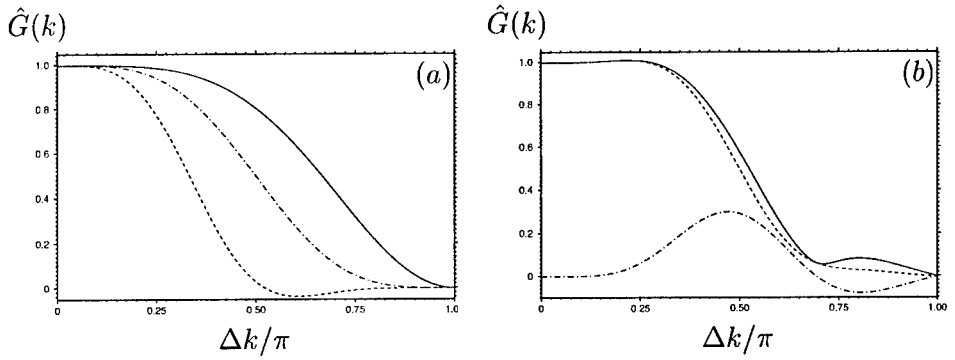


Figure 2. (a) Fourier transform $\hat{G}(k)$ of the symmetric discrete filters with three vanishing moments and different linear constraints. (b) Real, imaginary, and absolute value of $\hat{G}(k)$ of the asymmetric discrete filter with three vanishing moments.

$$M_i^0(\xi_i) = 1 \text{ for } \xi_i \in [\alpha_i, \beta_i], \tag{16}$$

$$M_i^k(\xi_i) = 0 \text{ for } k = 1, \ldots, n-1 \text{ and } \xi_i \in [\alpha_i, \beta_i]. \tag{17}$$

Also it can be shown that the commutation error in the homogeneous directions is exactly zero.

The discrete filtering operation is defined as

$$\overline{\phi}_j = \sum_{l=-K_j}^{L_j} \mathrm{w}_l^j \phi_{j+l}, \tag{18}$$

where w_l^j are the filter coefficients chosen to satisfy the zero-moment requirements (16), (17) and possibly additional constraints. Examples of discrete symmetric and asymmetric filters are shown in Fig. 2.

The discrete commutative filter construction theory can be easily extended to the case when mapped space does not exist, *e.g.* when unstructured meshes are used. In this case there is no choice, but to construct filters in the physical domain. In this case it can be shown (Marsden *et al.*, 2000) that for a smoothly varying filter width, the local commutation error in three dimensions is given by

$$\left[\frac{\partial \phi}{\partial x_1}\right] = O\left(\Delta_1^i(\mathbf{x})\Delta_2^j(\mathbf{x})\Delta_3^k(\mathbf{x})\right), \qquad i+j+k=n \tag{19}$$

provided that filters moments $M^{ijk}(\mathbf{x}) = -\int_\Psi \eta_1^i \eta_2^j \eta_3^k G(\boldsymbol{\eta}, \mathbf{x})\, d^3\boldsymbol{\eta}$ exist and satisfy the following constrains:

$$M^{ijk}(\mathbf{x}) = \begin{cases} 1 & i,j,k = 0 \\ 0 & 0 < i+j+k < n \end{cases} \tag{20}$$

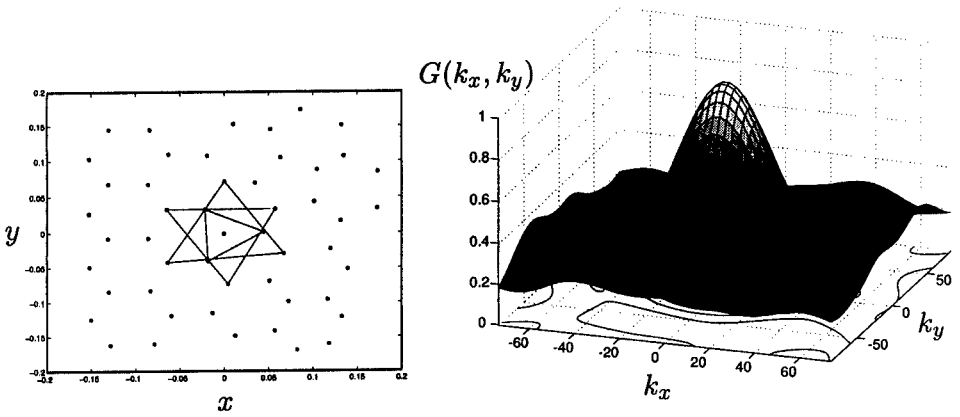


Figure 3. Example of filter constructed with triangles on an unstructured grid and the corresponding transfer function.

Greater predictability and ease of implementation can be gained by using interpolation based filters that are constructed by evaluating either interpolating polynomials (Marsden *et al.*, 2000) or least square interpolants (Haselbacher, 2001) at the desired locations. The n^{th} polynomial construction automatically guarantees an n^{th} order commutation error. To control the shape and other properties of the discrete filters, filters can be constructed as a linear combination of many polynomial based filters, while preserving the commutation properties of the filter.

In general, with an n^{th} order numerical scheme, the filtering operation must commute to order n. Most of the unstructured mesh codes are second order accurate, thus a discrete filter based on first order polynomial interpolation is sufficient to achieve second order commutation error. A two-dimensional discrete filter based on first order polynomial interpolation can be constructed using a triangle of three points surrounding the point (x_0, y_0) where we want the filtered value. A triangle is chosen because in two dimensions three points are needed for exact reconstruction of a first order polynomial. Weights are calculated by fitting a polynomial to the vertices of the triangle, and are then used to find a weighted average at the central point (x_0, y_0). With this method, the same number of points are used in the filter for any point on the mesh. Figure 3 shows an example of a 2-D filter constructed from three triangles. To achieve flexibility in filter width, each triangle as well as the central point is assigned a weight β_i, which applies equally to all vertices of the triangle. The value of β_i can be varied from 0 to 1 as long as the sum total is 1. The optimum value of β for the central point is $1/2$ because this results in a transfer function with a well defined peak and low pass filter shape.

5. Spectrum of Commutation Error

Leading order commutation error analysis described in the previous section can be viewed as a practical tool for constructing discrete filters that commute with finite difference operators to an *a priori* specified order of filter width. However, the leading order error analysis by itself is not enough to guarantee that the commutation error is negligible compared to the subgrid scale stress, since it does not use any information about spectral content of the analyzed signal (Ghosal, 1996; Ghosal, 1999). Due to the presence of significant energy in the high frequency portion of the LES spectrum, the commutation error could be considerable and in some cases even comparable with the subgrid scale stresses. The existence of inhomogeneous directions in the flow precludes the use of the standard Fourier analysis. In this section we present a recently developed mathematical tool that can be used to analyze the *local spectrum* of the commutation error and its dependence on the filter shape and the non-uniformity of the filter width.

We begin by introducing the local spectrum analysis in one-dimensional space and then extend it to three spatial dimensions. Let us consider a one dimensional filter of constant shape but variable width. The continuous filtering operation can be written as

$$\overline{\phi}(x) = \frac{1}{\Delta(x)} \int_{-\infty}^{\infty} G\left(\frac{x-y}{\Delta(x)}\right) \phi(y) dy. \tag{21}$$

Substituting the Fourier integral

$$\phi(x) = \frac{1}{2\pi} \int_{-\infty}^{\infty} \hat{\phi}\,(k)\, e^{i\kappa x} dk \tag{22}$$

into Eq. (21), changing the order of integration, and integrating the resulting equation with respect to y we obtain the following equation:

$$\overline{\phi}(x) = \frac{1}{2\pi} \int_{-\infty}^{\infty} \hat{G}\left(\Delta\,(x)\, k\right) \hat{\phi}(k)\, e^{ikx}\, dk, \tag{23}$$

where $\hat{G}\,(\kappa)$ is the Fourier transform of the filter function given by

$$\hat{G}\,(\kappa) = \int_{-\infty}^{\infty} G(\xi) e^{-i\kappa\xi} d\xi. \tag{24}$$

Now comparing Eqs. (22) and (23) we can see that the structure of the equations is the same. Thus, the *local* Fourier transform can be defined as

$$\hat{\overline{\phi}}(k, x) = \hat{G}\,(\Delta\,(x)\, k)\, \hat{\phi}(k). \tag{25}$$

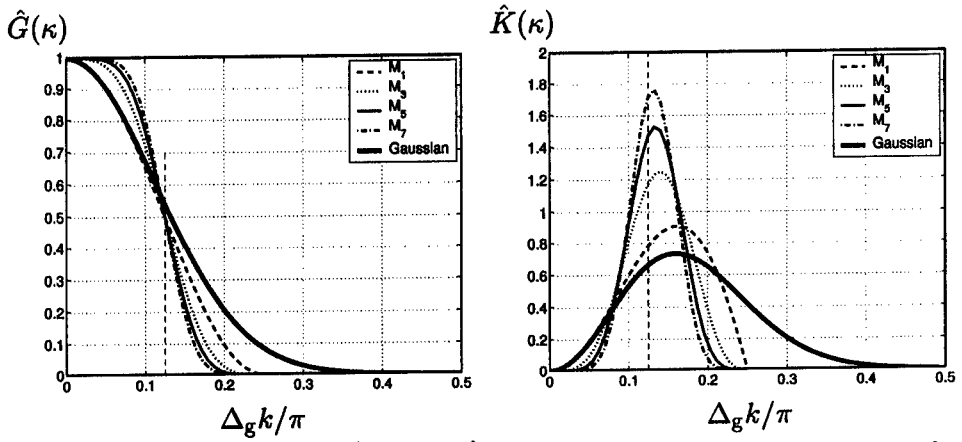


Figure 4. Transfer functions $\hat{G}(\kappa)$ and $\hat{K}(\kappa)$ for a variety of filters. M_n denotes the discrete filter with n vanishing moments.

Now the meaning of the local Fourier transform is clear, it refers to the location in space where the transform is taken and reflects the fact that the filter width is a function of location. Performing analogous analysis for commutation error it can be shown that

$$\left[\frac{d\phi}{dx}\right] = \frac{\Delta'(x)}{\Delta(x)} \frac{1}{2\pi} \int_{-\infty}^{\infty} \hat{K}(\kappa)\, \hat{\phi}(k) e^{ikx} dk, \tag{26}$$

where $\kappa = \Delta(x)\, k$ and the transfer function $\hat{K}(\kappa)$ is defined by

$$\hat{K}(\kappa) = -\kappa \frac{d\hat{G}(\kappa)}{d\kappa}. \tag{27}$$

Now the effect of filtering is clearly seen: filter width stretching affects the amplitude of the commutation error, while the filter shape and width affect the spectrum. The effect of the filter shape on the spectrum of commutation error is demonstrated in Fig. 4, where transfer functions $\hat{G}(\kappa)$ and $\hat{K}(\kappa)$ are shown for a variety of filters. It is important to note that the closer the filter to the sharp cut-off, the more localized the spectrum of commutation error. Also note that the commutation error is exactly zero, when the width of the filter is constant throughout the domain.

The one-dimensional analysis can be easily extended to three spatial dimensions. In particular, it can be shown that for three dimensional filters of constant shape and variable width the commutation error is given by

$$\left[\frac{\partial \phi}{\partial x_i}\right] = \sum_{l=1}^{3} \frac{1}{\Delta_l(\mathbf{x})} \frac{\partial \Delta_l(\mathbf{x})}{\partial x_l} \frac{1}{(2\pi)^3} \int_{-\infty}^{\infty} \hat{K}_l(\boldsymbol{\kappa})\, \hat{\phi}(\mathbf{k}) e^{i\mathbf{k}\mathbf{x}} d^3\mathbf{k}, \tag{28}$$

where $\Delta_i(\mathbf{x})$ is the filter width in the x_i direction, $\mathbf{k} = (k_1, k_2, k_3)^{\mathrm{T}}$ and $\boldsymbol{\kappa} = (\Delta_1(\mathbf{x})k_1, \Delta_2(\mathbf{x})k_2, \Delta_3(\mathbf{x})k_3)^{\mathrm{T}}$ are three dimensional wave vectors,

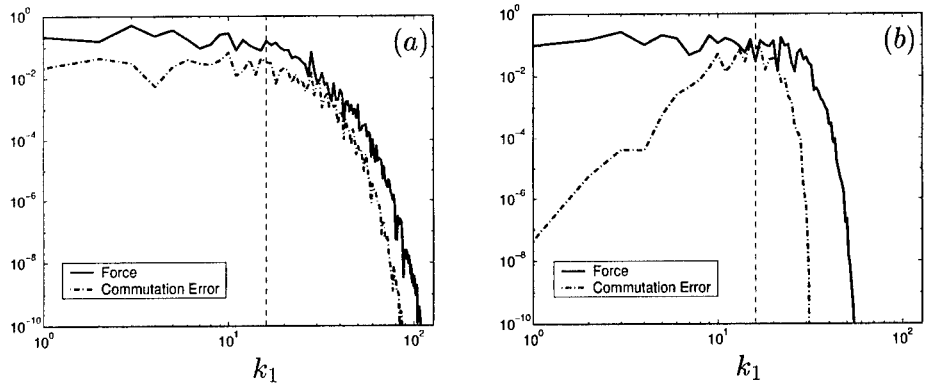


Figure 5. One-dimensional spectrum of the exact SGS force, $\partial\tau_{11}/\partial x_1$, and local one-dimensional spectrum of the commutation error for forced isotropic turbulence at $Re_\lambda = 168$ for (a) Gaussian and (b) M_7 filters.

$\hat{\phi}(\mathbf{k})$ is the Fourier transform of function $\phi(\mathbf{x})$, $\hat{G}(\mathbf{k})$ is the Fourier transform of the filter function, and the transfer function $\hat{K}_l(\boldsymbol{\kappa})$ is defined by

$$\hat{K}_l(\boldsymbol{\kappa}) = -\kappa_l \frac{\partial \hat{G}(\boldsymbol{\kappa})}{\partial \kappa_l}. \tag{29}$$

To demonstrate the effect of commutation error in LES, we consider the results of 256^3 direct numerical simulation of forced homogeneous turbulence at $Re_\lambda = 168$ (Jimenez and Wray, 1993). Figure 5 shows the one-dimensional spectrum of the exact SGS force, $\partial\tau_{11}/\partial x_1$, and the local one-dimensional spectrum of commutation error for the Gaussian and the discrete M_7 filter. These two filters are chosen because the Gaussian filter is smooth, while the M_7 filter is close to the sharp cut-off filter. The exact SGS force is obtained by filtering the DNS data. Note that the local spectrum of the commutation error shown in Fig. 5 does not take into account the grid stretching factor. The results confirm strong dependence of the spectrum of commutation error on the filter shape: the spectrum is global for smooth filters like Gaussian, while for filters, that are close to the sharp cut-off, the spectrum is localized.

6. Conclusions

In this paper we presented a systematic approach for large eddy simulation to be consistent, *i.e.* to satisfy all the assumptions used in the derivation of the LES equations. We demonstrated that a solution, consistent with the true filtered Navier-Stokes equations, can be achieved by means of explicit filtering. We have shown that explicit filtering not only provides the means for both assessing and minimizing the effects of numerical error in

practical simulations, but also allows the filter shape and size to be chosen independently of the computational mesh. Having the ability to control the filter shape opens whole new horizons in LES modelling, since it makes it feasible to look at SGS modelling and filtering as one inseparable issue. The success of explicit filtering strongly depends on the ability to construct discrete filters that commute with differentiation. We have described the general theory of construction of such filters and developed a tool for assessing the local spectrum of the commutation error.

Although tremendous progress has recently been made in the development of the explicit filtering approach, a lot of fundamental research needs to be done before researchers and engineers can take full advantage of this new mathematical tool. Among the issues which definitely need to be addressed in the near future are the development of the SGS models that correspond to specific filters and their subsequent verification with experimental and DNS results.

Acknowledgements

The author would like to thank Thomas Lund and Daniel Goldstein for their input and helpful comments.

References

Germano, M., U. Piomelli, P. Moin, and W. Cabot (1991), A dynamic subgrid-scale eddy viscosity model. *Phys. Fluids A* **3**(7), 1760–1765.

Ghosal, S. (1996), An analysis of numerical errors in large eddy simulations of turbulence. *J. Comp. Phys.* **125**, 187–206.

Ghosal, S. (1999), Mathematical and Physical Constraints on Large-Eddy Simulation of Turbulence. *AIAA Journal* **37**(4), 425–433.

Ghosal, S., T. S. Lund, P. Moin, and K. Akselvoll (1995), A dynamic localization model for large-eddy simulation of turbulent flows. *J. Fluid Mech.* **286**, 229–255.

Haselbacher, A. (2001), Discrete Filtering on Unsructured Grids Based on Least-Square Gradient Reconstruction. In: *Proceedings of the Third AFOSR International Conference on DNS/LES.*

Jimenez, J. and A. A. Wray (1993), The structure of intense vorticity in isotropic turbulence. *J. Fluid Mech.* **255**, 65–90.

Lund, T. S. (1997), On the use of discrete filters for large eddy simulation. *Center for Turbulence Research Annual Research Briefs* pp. 83–95.

Lund, T. S. and H.-J. Kaltenbach (1995), Experiments with explicit filtering for LES using a finite-difference method. *Center for Turbulence Research Annual Research Briefs* pp. 91–105.

Marsden, A., O. Vasilyev, and P. Moin (2000), Construction of commutative filters for LES on unstructured meshes. *Center for Turbulence Research Annual Research Briefs* pp. 179–192.

Rogallo, R. and P. Moin (1984), Numerical simulation of turbulent flow. *Ann. Rev. Fluid Mech* **16**, 99–137.

Vasilyev, O., T. Lund, and P. Moin (1998), A general class of commutative filters for LES in complex geometries. *J. Comp. Phys.* **146**, 105–123.

NUMERICAL SIMULATIONS USING THE IMMERSED BOUNDARY TECHNIQUE

UGO PIOMELLI AND ELIAS BALARAS
Department of Mechanical Engineering
University of Maryland
College Park, MD 20742 - USA

Abstract. The immersed-boundary method can be used to simulate flows around complex geometries within a Cartesian grid. This method has been used quite extensively in low Reynolds-number flows, and is now being applied to turbulent flows more frequently. The technique will be discussed, and three applications of the method will be presented, with increasing complexity, to illustrate the potential and limitations of the method, and some of the directions for future work.

1. Introduction

The increase in computer speed achieved over the last few years has made computational fluid dynamics increasingly useful and widespread as a tool to analyze and design flow configuration. Complex geometries, however, present an obstacle even to present-day computers, since the use of body-fitted meshes (structured or unstructured) significantly increases the cost of a calculation in terms of both computational speed and memory requirements.

An alternative method that may be cost-efficient in many situations is the "immersed-boundary" method. This technique is based on the introduction of body forces distributed throughout the flow that mimic the effect that a solid body would have on the fluid. This approach allows the use of codes in Cartesian coordinates, which present significant advantages, in terms of speed, accuracy and flexibility, over codes that employ body fitted grids.

This idea has been widely used in hæmo-dynamics and bio-fluids engineering: two- and three-dimensional calculations of the flow in the heart

were reported by Peskin [13, 14] and McQueen and Peskin [8, 9]. In these calculations the motion of the boundary was determined by the fluid itself, so that the boundary had to be modeled as a set of elements linked by springs. In cases in which the boundary motion is known *a priori*, the problem can be significantly simplified.

Goldstein *et al.* [4] proposed a feedback forcing mechanism that forces the fluid velocity u_i to approach the velocity of the solid boundary, V_j, on the boundary itself. Consider the incompressible Navier-Stokes equations:

$$\frac{\partial u_j}{\partial x_j} = 0, \tag{1}$$

$$\frac{\partial u_i}{\partial t} + \frac{\partial}{\partial x_j}(u_j u_i) = -\frac{1}{\rho}\frac{\partial p}{\partial x_i} + \nu \nabla^2 u_i + f_i. \tag{2}$$

Goldstein *et al.* [4] assigned a force field

$$f_i(x_{s,i}, t) = \alpha_f \int_0^t [u_i(x_{s,i}, t) - V_i(x_{s,i}, t)]\, dt' + \beta_f [u_i(x_{s,i}, t) - V_i(x_{s,i}, t)], \tag{3}$$

where α_f and β_f are two negative constants, and $x_{s,i}$ are the coordinates of the solid surface. The net effect of this force is to tend to annihilate the velocity difference $u_i - V_i$. The flow, in fact, responds to the forcing as a damped oscillator (see [4] and [3] for an in-depth discussion of this issue); the frequency of the oscillator is $\propto |\alpha_f|^{1/2}$, whereas its damping coefficient is $\propto \beta_f / |\alpha|^{1/2}$. This implies that, in order to enforce the no-slip condition effectively, α_f and β_f must have large magnitudes (larger than the highest frequency in the flow), which may make the equations stiff.

Recently, Mohd-Yusof [11] proposed the "direct forcing method," which assigns a force field given by

$$f_i = \frac{\partial}{\partial x_j}(u_j u_i) + \frac{1}{\rho}\frac{\partial p}{\partial x_i} - \nu \nabla^2 u_i + \frac{V_i - u_i}{\Delta t}, \tag{4}$$

(where the dependence on $x_{s,i}$ and t has been omitted). This forcing imposes directly the desired velocity on the immersed boundary, and has the advantage (over the feedback forcing method) that it does not require significant reductions in the allowable time-step. It was extensively tested in a staggered finite-difference code by Fadlun *et al.* [3], who derived an interpolation scheme to be used when the boundary does not coincide with a grid line. Verzicco *et al.* [15] applied this method to the large-eddy simulation of high Reynolds number turbulent flows by calculating the flow inside an IC engine.

In the present paper additional applications of this method will be presented, and the potential and limitations of the technique, as well as issues

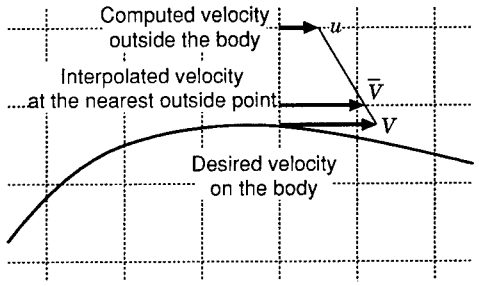


Figure 1. Interpolation method used to apply the forcing.

that require further study, will be discussed. After a brief review of the governing equations and of the numerical scheme used, three test cases will be shown: a low Reynolds-number flow over a cylinder in the presence of a moving surface (Wannier [16] flow), the flow over a circular cylinder at low Reynolds number, and the bypass transition on a flat plate caused by the interaction between the boundary layer and the wake of a circular cylinder.

2. Problem formulation

Governing the flow are the incompressible Navier-Stokes equations (1–2). The flow solver is a standard 2nd-order accurate method on a staggered mesh [1]. The fractional time-step method [2, 6] is used and a 2nd-order accurate Adams-Bashforth method is employed for the time advancement. A non-reflecting boundary condition [12] is used at the outflow, and periodic boundary conditions in the spanwise direction. The inflow and free-stream conditions depended on the case studied.

The direct forcing (4) was used. Since the immersed body does not follow a grid line the interpolation method proposed by Fadlun *et al.* [3] is used. The forcing is imposed not at the surface itself, but at the first point outside it (see Fig. 1) and the solid body velocity in (4) is replaced with the velocity $\overline{V_i}$ obtained by a linear interpolation between the computed fluid velocity outside the body, u_i, and the desired body velocity V_i. This method has several advantages: first, it has been shown to be fully second-order accurate in time [3]; therefore, it is consistent with the second-order differencing scheme used by the solver; secondly, since it assumes that the velocity profile is linear near the body, it implies homogeneous Neumann boundary conditions for the pressure (see the Appendix in [3] for a full discussion of this issue). This last feature is very important in the framework of fractional time-step methods, since it implies that the corrector step does not result in a modification of the body velocity imposed through the forcing in the Helmholtz step. On the other hand, the assumption that the velocity

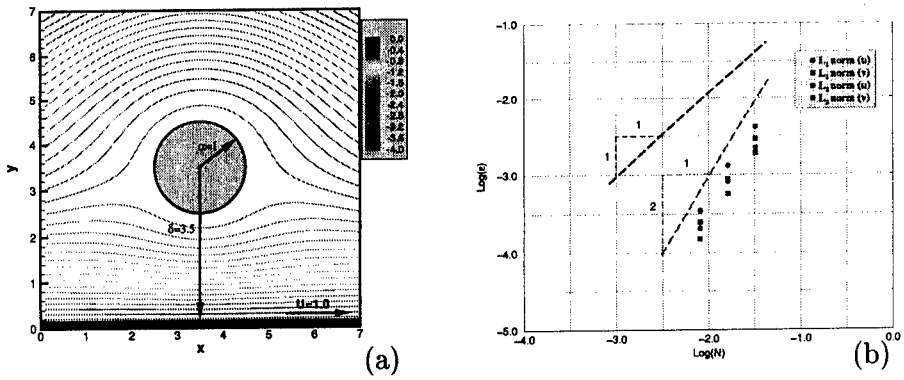


Figure 2. Wannier flow test case (Wannier 1950). (a) Computational domain and computed streamlines; (b) L_1 and L_2 norms of the error, ϵ, for u and v velocity components. N is the total number of grid points.

profile is linear over the first two layers of cells outside the immersed body requires the use of a very fine mesh in the vicinity of the body.

3. Results and discussion

3.1. WANNIER FLOW

A straightforward way to verify the accuracy of the proposed methodology is to compute a flow containing a curved immersed boundary for which an analytical solution exists. The case considered here is the Stokes flow around a cylinder in the vicinity of a moving wall (see Fig. 2). An analytical solution for this case was derived by Wannier [16]. The streamlines for this flow are shown in Fig. 2a. Three computations on gradually finer uniform grids (32×32, 64×64, and 128×128) were conducted. The L_1 and L_2 norms of the error (the difference between the computed and analytical solution) are shown in Fig. 2b as a function of the total number of points N. The error decreases with a -2 slope indicating that the proposed methodology is second order accurate.

3.2. FLOW OVER A CIRCULAR CYLINDER

The next test case examined is the flow over a circular cylinder at $Re_D = U_\infty D/\nu = 300$ (where D is the cylinder diameter and U_∞ the free-stream velocity). Two calculations will be compared: a 2D one that used 400×200 points in the $xz-$plane, and a 3D one, with the same mesh in the $xz-$plane, and 48 points in y. The computational domain was $60 \times 2\pi \times 30$, and the cylinder center was at $x_c = 10$, $z_c = 15$ (all lengths are made dimensionless by D, all velocities by U_∞). The grid was stretched both in the $x-$ and

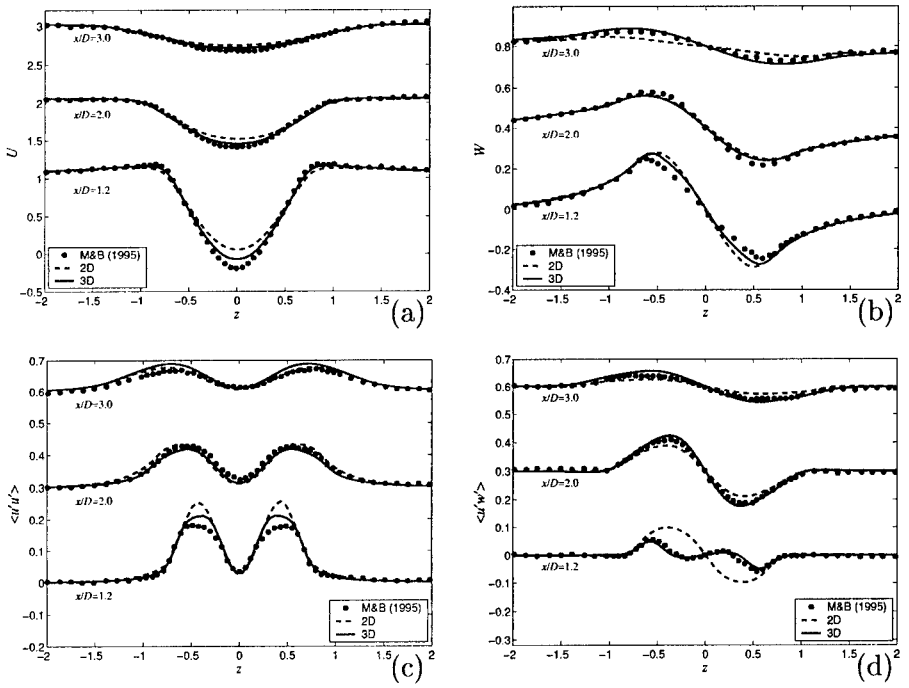


Figure 3. Flow over a circular cylinder, $Re_D = 300$. Velocity statistics. (a) U, (b) W, (c) $\langle u'u' \rangle$, (d) $\langle u'w' \rangle$. Reference data from Ref. [10].

$z-$directions; the last 1/6 of the domain (which required only 10 grid points in x) formed a sponge region, used to minimize the upstream propagation of disturbances due to the convective outflow conditions. A uniform velocity profile was imposed at the inlet, and slip-wall conditions were applied at $z = 0$ and $z = 30$.

The velocity statistics are shown in Fig. 3. Here and in the following the angle brackets denote averaging in time and in the spanwise direction. The 3D calculation is in very good agreement with the reference data by Mittal and Balachandar [10]. At this Reynolds number, three-dimensionality is observed in the wake, which is evidenced in the visualization in Fig. 4, which shows iso-surfaces of the second invariant of the velocity-gradient tensor,

$$Q = -\frac{1}{2}\frac{\partial u_i}{\partial x_j}\frac{\partial u_j}{\partial x_i} = -\frac{1}{2}\left(S_{ij}S_{ij} - \Omega_{ij}\Omega_{ij}\right), \tag{5}$$

(where $\overline{\Omega}_{ij}$ is the anti-symmetric part of the velocity gradient tensor). The condition $Q > 0$ identifies effectively the regions of coherent vorticity [5].

Figure 4 shows the formation of an instability on the initially 2D rollers, and the presence of quasi-streamwise rib vortices joining the rollers. The

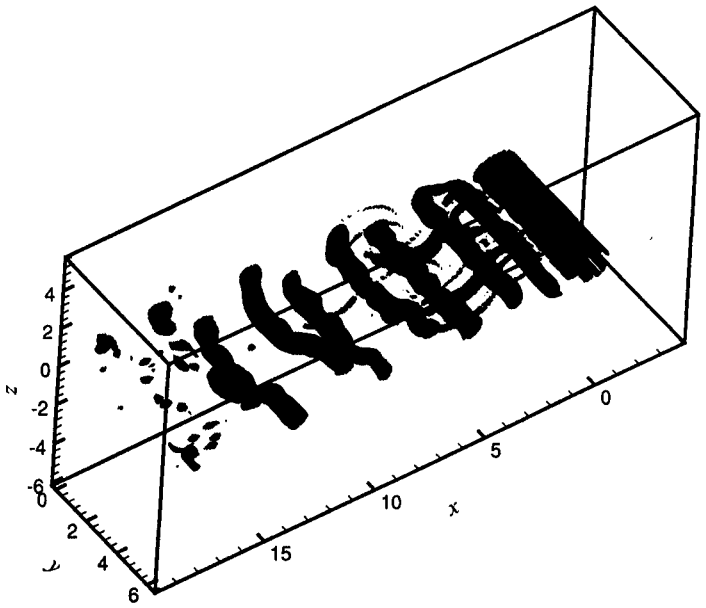


Figure 4. Flow over a circular cylinder, $Re_D = 300$. Isosurfaces of $Q = 0.6$.

magnitude of the spanwise Reynolds stresses $\langle v'v' \rangle$. in this calculation, however, remained significantly smaller than the other two normal components, which allowed the 2D calculation to give reasonable results.

The effects of the grid resolution near the obstacle are shown in Fig. 5. The cell Reynolds number is defined as

$$Re_c = \frac{(\Delta x^2 + \Delta z^2)\,(u^2 + w^2)}{\nu}, \tag{6}$$

where u and w are the instantaneous velocities, and Δx and Δz the grid spacings. If the mesh is insufficiently fine ($Re_c > 30$), some oscillations can be observed that initiate along lines at $\pm 45^o$ on the cylinder (they are especially visible in the w contours, Fig. 5b). Refining the grid, thus reducing Re_c reduces the size of this oscillation (Figs. 7a and b). Two-dimensional interpolation schemes that use both the points indicated by the diamonds and those indicated by squares in Fig. 6 to determine $\overline{V}_i$ have also been found (Verzicco, private communication, 2001) to reduce the amplitude of these oscillations.

3.3. WAKE/BOUNDARY-LAYER INTERACTION

Wakes interact with laminar boundary layers in many applications of engineering interest, for example on the leading edge of multi-component

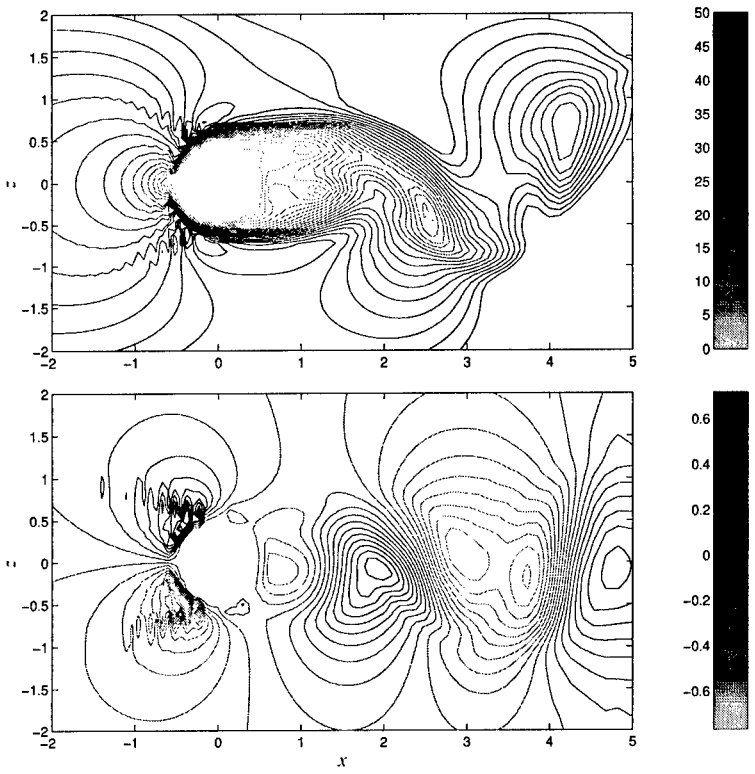


Figure 5. Flow over a circular cylinder, $Re_D = 300$. Coarse (200×100) 2D calculation. (a) Contours of the cell Reynolds number; (b) contours of w.

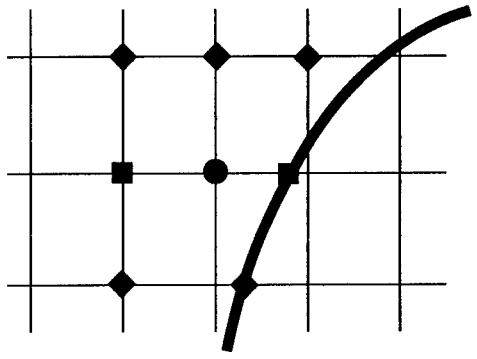


Figure 6. One-dimensional *vs.* two-dimensional interpolation stencils.

airfoils, or inside turbo-machinery. The interaction of the turbulent eddies present in the wake with the boundary layer itself then becomes a primary driver of the transition process in the boundary layer itself, and may lead

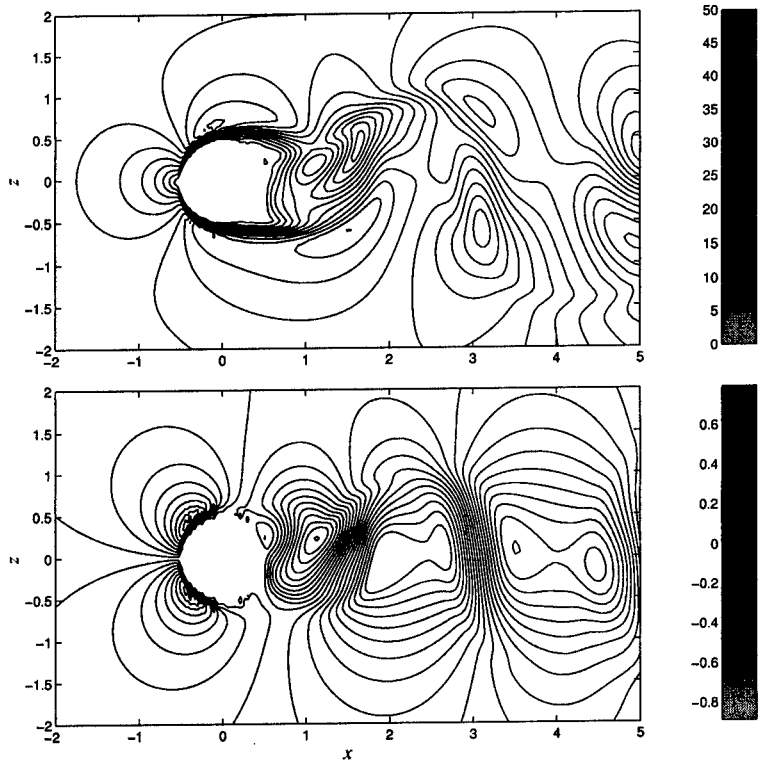


Figure 7. Flow over a circular cylinder, $Re_D = 300$. Fine (400 × 200) 2D calculation. (a) Contours of the cell Reynolds number; (b) contours of w.

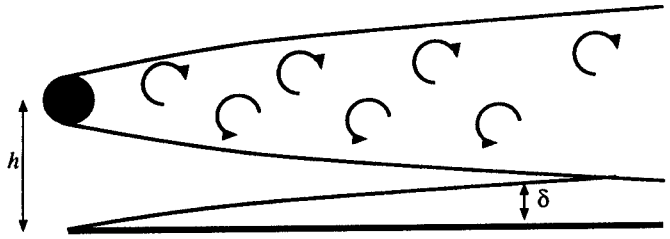


Figure 8. Sketch of the wake/boundary-layer configuration.

to transition to turbulence at fairly low Reynolds numbers.

The configuration examined in the present study is sketched in Fig. 8. A circular cylinder, with its axis normal to the stream is placed above a flat plate. The cylinder center is at $x_c = 10$, $z_c = 3.2$, immediately above the leading-edge of the plate, which was also at $x_c = 10$. As in the previous case, distances are normalized by D, velocities by U_∞. The computational

domain was $60 \times 2\pi \times 20$. As for the cylinder calculation, the grid was stretched both in the $x-$ and $z-$directions and a sponge region was used. The Reynolds number based on cylinder diameter was 385. The configuration corresponds to Case 1 in the experimental paper by Kyriakides *et al.* [7], who observed significant velocity fluctuations in the boundary layer, starting from a point approximately six diameters downstream of the cylinder. These fluctuations are generated by the large-scale convective motion of the vortices, and do not die down after the wake has weakened, but develop into a turbulent boundary layer despite the fact that the Reynolds number is very low.

The distribution of the streamwise Reynolds stress, $\langle u'u' \rangle$, as a function of x is shown in Fig. 9. A sudden increase of $\langle u'u' \rangle$ can be observed to begin at $x = 8$, indicating the beginning of transition. This result is consistent with the observations of Kyriakides *et al.* [7], who defined the onset of transition as "the $x-$location where the velocity signal at the same height above the plate loses its sinusoidal character", and found that transition occurs at $x = 7.4$.

The velocity profiles, shown in Fig. 10a at several locations, initially resemble a Blasius profile merging into a wake near the cylinder. As the wake widens and interacts with the boundary layer, a logarithmic layer begins to establish itself, indicative of transition towards turbulent flow. This transitional behavior is also observed in the trace of the Reynolds stress tensor, q^2 (equal to twice the turbulent kinetic energy), which in the latter sections establishes a turbulent-like distribution, with a peak of magnitude $7 - 8\tau_w$ at $z^+ \simeq 10 - 12$. It should be noted that this quasi-turbulent state is achieved at very low Reynolds number: the boundary-layer thickness δ (defined as the distance above the plate at which the first maximum of the velocity profile occurs) is approximately 50-70 wall units.

A visualization of the flow is shown in Fig. 11. The structure of the

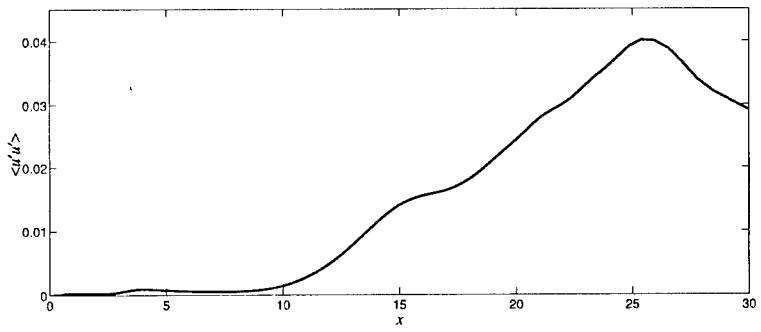


Figure 9. Wake/boundary-layer interaction. $\langle u'u' \rangle$ distribution at $z = 0.18$.

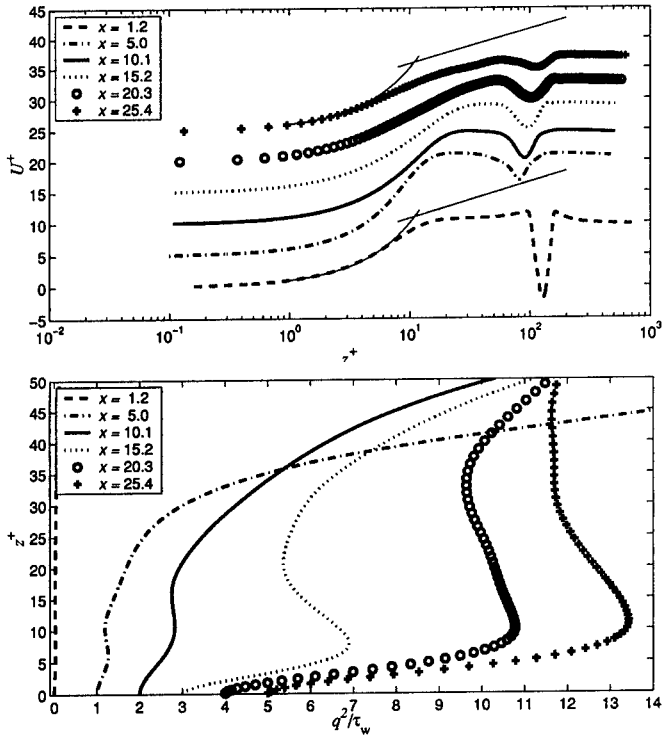


Figure 10. Wake/boundary-layer interaction. Turbulent statistics. Top: mean velocity profile; bottom: $q^2 = \langle u_i' u_i' \rangle$.

cylinder wake is similar to that highlighted in Fig. 4, with strong spanwise rollers that exhibit 3D instabilities and eventually break up, and smaller quasi-streamwise vortices in the braid region. The contours of streamwise velocity fluctuation u' on a plane parallel to the wall show significant levels of fluctuations, especially near kinks in the rollers belonging to the lower row. Quasi-streamwise streaks are formed around $x = 15$, whose spacing is approximately 100 wall units.

4. Conclusions

The immersed-boundary technique has been presented and discussed. Illustrative results from three simulations indicate the potential of this technique, which allows the calculation of flows around complex geometries without requiring a body-fitted grid.

If appropriate interpolation methods are used when the body does not coincide with a grid line, the method is second-order accurate. However, some care must be taken in the discretization of the flow field, especially in

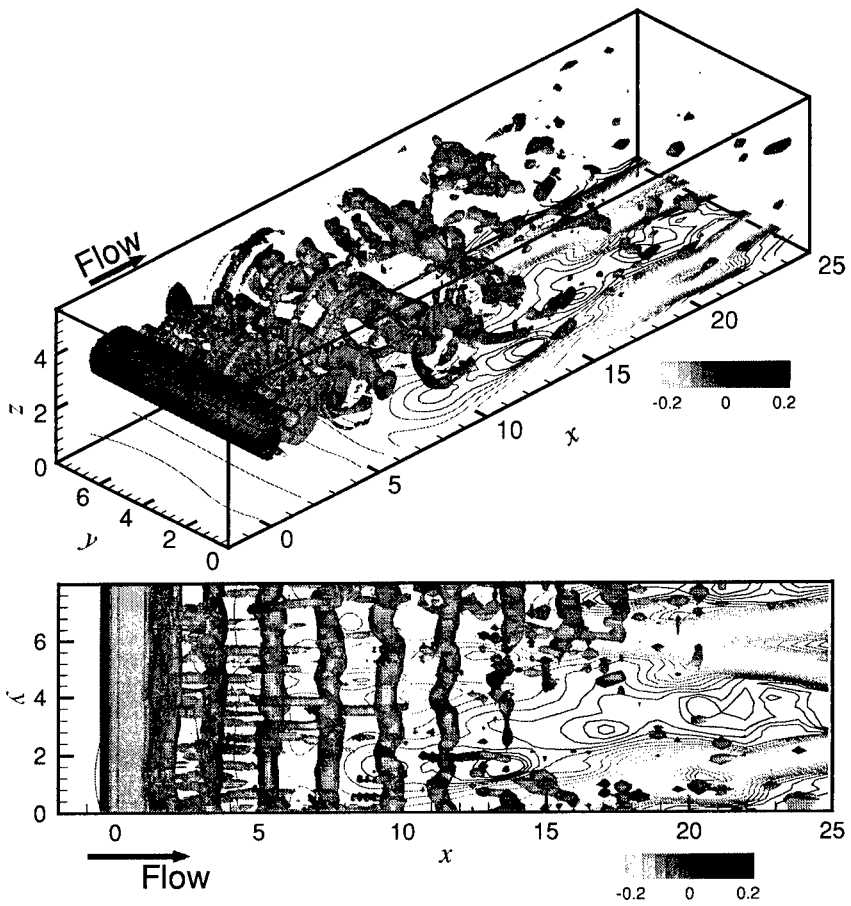


Figure 11. Wake/boundary-layer interaction. Isosurfaces of $Q = 0.4$ and contours of u' in the $z = 0.18$ plane. Top: perspective view; bottom: view from above.

the vicinity of the body. We have observed the development of numerical oscillations when the cell Reynolds-number exceeded values of approximately 30. These oscillations did not grow or change position in time, and their effect on the flow field downstream of the obstacle was limited in the cases studied. This was observed, for instance, in calculations of the flow around the cylinder at $Re_D = 3500$ were carried out in which the grid could not be sufficiently refined to satisfy the cell-Reynolds-number requirement. However, it is not known whether these oscillations might give rise to instabilities in other geometries, or at higher Reynolds numbers. The development of more accurate, multi-dimensional interpolation schemes might be beneficial in this respect. The use of multi-block methods, or embedded grids, could also alleviate this problem.

If these numerical schemes can be overcome, the immersed boundary

method appears to be a useful tool for the simulation of flows in complex geometries at moderate or high Reynolds numbers. This is confirmed by the increasing number of studies using this method that are appearing in the literature.

Acknowledgments

Research supported by the NASA Langley research Center under Grant NAG12285 monitored by Drs. Craig L. Streett and Meelan M. Choudhari.

References

1. Balaras, E. 1995 *Ph. D. Thesis*, EPFL (Federal Institute of Technology–Lausanne, Switzerland).
2. Chorin, A.J. 1968 *Math. Comput.* **22**, 745.
3. Fadlun, E.A., Verzicco, R., Orlandi, P., Mohd-Yusof, J. 2000 *J. Comput. Phys.* **161** 35.
4. Goldstein, D., Handler. R. Sirovich, L. 1993 *J. Comput. Phys.* **105**, 354–366.
5. Hunt, J.C.R., Wray, A.A. and Moin, P. 1988 In *Center for Turbulence Research, Proc. Summer Program 1988*, 193.
6. Kim, J. and Moin, P. 1985 *J. Comput. Phys.* **59** 308.
7. Kyriakides N.K., Kastrinakis, E.G., Nychas, S.G., Goulas, A. 1996 *Proc. Inst. Mech. Eng.* **210**, 167.
8. McQueen, D.M., Peskin, C.S. 1989 *J. Comput. Phys.* **82** 289.
9. McQueen D.M., Peskin, C.S. 1997 *J. Supercomput.* **11** 213.
10. Mittal, R. and Balachandar, S. 1995 *Phys. Fluids* **7**, 1841.
11. Mohd-Yusof, J. 1997 in *CTR Annu. Res. Briefs 1997*, NASA Ames/Stanford University, 317.
12. Orlanski, I. 1976 *J. Comput. Phys.* **21**, 251.
13. Peskin, C.S. 1972 *J. Comput. Phys.* **10** 252.
14. Peskin, C.S. 1977 *J. Comput. Phys.* **25** 220.
15. Verzicco, R., Mohd-Yusof, J., Orlandi, P., Haworth, D. 2000 *AIAA J.* **38** 427.
16. Wannier, G. H. 1950 *Quart. Applied Mathematics* **8** 1.

RECENT DEVELOPMENT AND APPLICATIONS OF WENO SCHEMES

CHI-WANG SHU
Division of Applied Mathematics, Brown University
Providence, RI 02912, USA. E-mail: shu@cfm.brown.edu

Abstract. This paper is a summary of the author's talk given in the Third AFOSR International Conference on DNS/LES (TAICDL), held at the University of Texas at Arlington on August 5-9, 2001. In this paper we briefly present the general ideas of high order accurate weighted essentially non-oscillatory (WENO) schemes, and describe the similarities and differences of the two classes of WENO schemes: finite volume schemes and finite difference schemes. We also briefly mention two recent developments of WENO schemes, namely a technique to treat negative linear weights and a class of high order central WENO schemes.

1. Introduction

This paper is a summary of my talk given in the Third AFOSR International Conference on DNS/LES (TAICDL), held at the University of Texas at Arlington on August 5-9, 2001. In this paper we briefly present the general ideas of high order accurate weighted essentially non-oscillatory (WENO) schemes, and describe the similarities and differences of the two classes of WENO schemes: finite volume schemes and finite difference schemes. We also briefly mention two recent developments of WENO schemes, namely a technique to treat negative linear weights and a class of high order central WENO schemes.

High order accurate weighted essentially non-oscillatory (WENO) schemes have been developed to solve a hyperbolic conservation law

$$u_t + \nabla \cdot f(u) = 0. \tag{1.1}$$

The first WENO scheme was constructed in [19] for a third order finite volume version in one space dimension. In [11], third and fifth order finite dif-

ference WENO schemes in multiple space dimensions are constructed, with a general framework for the design of the smoothness indicators and nonlinear weights. Later, second, third and fourth order finite volume WENO schemes for 2D general triangulation have been developed in [5] and [9]. Very high order finite difference WENO schemes (for orders between 7 and 11) have been developed in [1]. Central WENO schemes have been developed in [13], [14], [15] and [22]. A technique to treat negative linear weights in WENO schemes has been developed in [23]. In this conference, Jiang, Shan and Liu presented their new results on developing compact WENO schemes.

WENO schemes are designed based on the successful ENO schemes in [8, 26, 27]. Both ENO and WENO schemes use the idea of adaptive stencils in the reconstruction procedure based on the local smoothness of the numerical solution to automatically achieve high order accuracy and non-oscillatory property near discontinuities. ENO uses just one (optimal in some sense) out of many candidate stencils when doing the reconstruction; while WENO uses a convex combination of all the candidate stencils, each being assigned a nonlinear weight which depends on the local smoothness of the numerical solution based on that stencil. WENO improves upon ENO in robustness, better smoothness of fluxes, better steady state convergence, better provable convergence properties, and more efficiency. For a detailed review of ENO and WENO schemes, up to the time when these notes were published, we refer to the lecture notes [24, 25].

WENO schemes have already been widely used in applications. Some of the examples include dynamical response of a stellar atmosphere to pressure perturbations [4]; shock vortex interactions and other gas dynamics problems [6], [7]; incompressible flow problems [28]; Hamilton-Jacobi equations [10]; magneto-hydrodynamics [12]; underwater blast-wave focusing [16]; the composite schemes and shallow water equations [17], [18], real gas computations [20], wave propagation using Fey's method of transport [21]; etc. In this conference and in this volume, we have seen several new developments and applications of WENO schemes for DNS/LES of turbulence flows.

The organization of this paper is as follows. In section 2 we discuss two different formulations of WENO schemes, namely the finite volume formulation and the finite difference formulation, and point out their similarities and differences, both in one dimension and in multiple space dimensions. In section 3 we briefly describe two recent developments of WENO schemes, namely the technique to treat negative linear weights [23] and the very high order central WENO schemes [22].

2. Finite volume and finite difference WENO schemes

A finite volume scheme for a conservation law such as (1.1) approximates an integral version of it. Let's use the one dimensional example

$$u_t + f(u)_x = 0 \tag{2.1}$$

to illustrate the ideas. Suppose $\{I_i = [x_{i-\frac{1}{2}}, x_{i+\frac{1}{2}}]\}$, $i = 1, ..., N$, is a partition of the computational domain, and $\Delta x_i = x_{i+\frac{1}{2}} - x_{i-\frac{1}{2}}$. If we integrate the PDE (2.1) in the cell I_i, we obtain

$$\frac{d\bar{u}_i(t)}{dt} + \frac{1}{\Delta x_i}\left[f(u(x_{i+\frac{1}{2}}, t)) - f(u(x_{i-\frac{1}{2}}, t))\right] = 0 \tag{2.2}$$

where

$$\bar{u}_i(t) = \frac{1}{\Delta x_i}\int_{I_i} u(x,t)dx$$

is the cell average of u in cell I_i. Notice that (2.2) is *not* a scheme yet, rather it is still an exact identity satisfied by the exact solution of the PDE (2.1). This is the starting point, though, for designing a finite volume scheme.

A semi-discrete (discrete in the spatial variable only) finite volume scheme for (2.1) is an ODE system for the cell averages $\{\bar{u}_i(t)\}$, $i = 1, ..., N$. In order to obtain such a scheme, we would need the following reconstruction procedure:

Procedure 2.1: Reconstruction. Obtain accurate point values $\{u(x_{i+\frac{1}{2}}, t)\}$, $i = 0, ..., N$, from the given cell averages $\{\bar{u}_i(t)\}$, $i = 1, ..., N$.

Notice that we have ignored possible problems at the boundary. We thus assume the data is either periodic or compactly supported. Boundary conditions can be treated in a stable and high order fashion depending on the type of boundary conditions.

WENO is simply a specific reconstruction procedure. Let us demonstrate the fifth order version. For this purpose, the approximation of $\{u(x_{i+\frac{1}{2}}, t)\}$ uses the information of five cell averages, from the stencil $\{I_{i-2}, I_{i-1}, I_i, I_{i+1}, I_{i+2}\}$. This stencil is not symmetric with respect to the point $x_{i+\frac{1}{2}}$ of the reconstruction. There is one more cell to the left than to the right. Thus this reconstruction is good for upwinding. The procedure consists of the following steps:

1. We break the final stencil

$$\mathcal{T} = \{I_{i-2}, I_{i-1}, I_i, I_{i+1}, I_{i+2}\} \tag{2.3}$$

into the following three smaller stencils:

$$\mathcal{S}_1 = \{I_{i-2}, I_{i-1}, I_i\}, \qquad \mathcal{S}_2 = \{I_{i-1}, I_i, I_{i+1}\}, \qquad \mathcal{S}_3 = \{I_i, I_{i+1}, I_{i+2}\}.$$

Notice that each small stencil contains the "target cell" I_i.

2. We construct three polynomials $p_j(x)$ of degree at most two, with their cell averages agreeing with that of the function u in the three cells in each stencil $\mathcal{S}_j$. We also construct a polynomial $Q(x)$ of degree at most four, with its cell averages agreeing with that of the function u in the five cells in the larger stencil $\mathcal{T}$. The three lower order approximations to $u(x_{i+1/2})$, associated with $p_j(x)$, in terms of the given cell averages of u, are given by:

$$\begin{aligned} p_1(x_{i+1/2}) &= \frac{1}{3}\bar{u}_{i-2} - \frac{7}{6}\bar{u}_{i-1} + \frac{11}{6}\bar{u}_i, \\ p_2(x_{i+1/2}) &= -\frac{1}{6}\bar{u}_{i-1} + \frac{5}{6}\bar{u}_i + \frac{1}{3}\bar{u}_{i+1}, \\ p_3(x_{i+1/2}) &= \frac{1}{3}\bar{u}_i + \frac{5}{6}\bar{u}_{i+1} - \frac{1}{6}\bar{u}_{i+2}. \end{aligned} \tag{2.4}$$

The coefficients in front of the $\bar{u}$ could be derived by Lagrange polynomials or by solving a small 3×3 linear system, from the condition that the quadratic polynomial $p_j(x)$ has the same cell averages as the given $\bar{u}$ in the relevant stencil. See [24] for details. Each of the $p_j(x_{i+1/2})$ in (2.4) is a third order approximation to $u(x_{i+1/2})$. The fifth order approximation to $u(x_{i+1/2})$, associated with $Q(x)$, is given by:

$$Q(x_{i+1/2}) = \frac{1}{30}\bar{u}_{i-2} - \frac{13}{60}\bar{u}_{i-1} + \frac{47}{60}\bar{u}_i + \frac{9}{20}\bar{u}_{i+1} - \frac{1}{20}\bar{u}_{i+2}. \tag{2.5}$$

3. We find three constants, also called linear weights,

$$\gamma_1 = \frac{1}{10}, \qquad \gamma_2 = \frac{3}{5}, \qquad \gamma_3 = \frac{3}{10}, \tag{2.6}$$

such that

$$Q(x_{i+1/2}) = \gamma_1\, p_1(x_{i+1/2}) + \gamma_2\, p_2(x_{i+1/2}) + \gamma_3\, p_3(x_{i+1/2})$$

for all possible given data $\bar{u}_j$, $j = i-2, i-1, i, i+1, i+2$. This is to say, the higher order reconstruction $Q(x_{i+1/2})$ can be written as a linear combination of three lower order reconstructions $p_j(x_{i+1/2})$. The linear weights given in (2.6) depend on local geometry and order of accuracy, but not on $\bar{u}_j$. If some of these linear weights are negative, special techniques must be used and will be described in next section.

4. We compute the smoothness indicator, denoted by β_j, for each stencil $\mathcal{S}_j$, which measures how smooth the function $p_j(x)$ is in the target cell I_j. The smaller this smoothness indicator β_j, the smoother the function $p_j(x)$ is in the target cell. In most of the currently used WENO schemes the following smoothness indicator [11] is used:

$$\beta_j = \sum_{l=1}^{2} \int_{I_i} \Delta x^{2l-1} \left(\frac{d^l}{dx^l} p_j(x) \right)^2 dx \tag{2.7}$$

for $j = 1, 2, 3$, for this fifth order case. These smoothness indicators are quadratic functions of the cell averages in the stencil. For this fifth order case they can be worked out as follows:

$$\begin{aligned}
\beta_1 &= \frac{13}{12}\left(\bar{u}_{i-2} - 2\bar{u}_{i-1} + \bar{u}_i\right)^2 + \frac{1}{4}\left(\bar{u}_{i-2} - 4\bar{u}_{i-1} + 3\bar{u}_i\right)^2 \\
\beta_2 &= \frac{13}{12}\left(\bar{u}_{i-1} - 2\bar{u}_i + \bar{u}_{i+1}\right)^2 + \frac{1}{4}\left(\bar{u}_{i-1} - \bar{u}_{i+1}\right)^2 \\
\beta_3 &= \frac{13}{12}\left(\bar{u}_i - 2\bar{u}_{i+1} + \bar{u}_{i+2}\right)^2 + \frac{1}{4}\left(3\bar{u}_i - 4\bar{u}_{i+1} + \bar{u}_{i+2}\right)^2
\end{aligned} \tag{2.8}$$

5. We compute the nonlinear weights based on the smoothness indicators:

$$\omega_j = \frac{\tilde{\omega}_j}{\sum_l \tilde{\omega}_l}, \qquad \tilde{\omega}_j = \frac{\gamma_j}{(\varepsilon + \beta_j)^2} \tag{2.9}$$

where γ_j are the linear weights determined in step 3 above, and ε is a small number to avoid the denominator to become 0. Typically, we can take $\varepsilon = 10^{-6}$ in all the computations. The final WENO approximation or reconstruction is then given by

$$R(x_{i+1/2}) = \omega_1\ p_1(x_{i+1/2}) + \omega_2\ p_2(x_{i+1/2}) + \omega_3\ p_3(x_{i+1/2}) \tag{2.10}$$

With this WENO reconstruction procedure, a finite volume WENO scheme is now ready. We give here a very brief summary of all the steps of a WENO finite volume scheme applied to (2.1) in the one dimensional scalar case for the positive wind $f'(u) \geq 0$. More details can be found in, e.g., [11, 24, 25]. The algorithm consists of the following steps:

1. Given the cell averages $\bar{u}_i$ for all cells I_i for time level n (starting from time level 0 which is the initial condition);
2. Reconstruct the point values $u^-_{i+1/2}$ for all cell boundaries $x_{i+1/2}$ using the reconstruction procedure detailed above. That is, we use (2.10) with ω_j defined by (2.9), using γ_j given by (2.6) and β_j given by (2.8). The superscript "$-$" in $u^-_{i+1/2}$ refers to the fact that the reconstruction has a stencil (2.3) biased to the left relative to the location $x_{i+1/2}$. This is upwinding according to the wind direction $f'(u) \geq 0$.
3. Form the residue for time level n in the method-of-lines ODE

$$\frac{d\bar{u}_i}{dt} = \frac{1}{\Delta x}\left(f(u^-_{i+1/2}) - f(u^-_{i-1/2})\right),$$

and move to time level $n+1$ by a high order TVD Runge-Kutta method [26].

Next we describe the setup of a finite difference scheme for solving (2.1). A semi-discrete finite difference scheme for (2.1) is an ODE system for the point values $\{u_i(t)\}$, $i = 1, ..., N$, where $u_i(t)$ approximate the point values of the solution $u(x_i, t)$. We also insist on a *conservative* approximation to the derivative $f(u)_x$ in the form of

$$f(u)_x|_{x=x_i} \approx \frac{1}{\Delta x}\left(\hat{f}_{i+1/2} - \hat{f}_{i-1/2}\right) \tag{2.11}$$

where $\hat{f}_{i+1/2}$ is the numerical flux, which typically is a Lipschitz continuous function of several neighboring values of u_j around x_i.

At a first glance, the finite difference scheme has nothing in common with the finite volume scheme described above, as they approximate different values of the solution. However, the following observation, first introduced in [27], establishes a close relationship between the two. If we identify a function $h(x)$ by

$$f(u(x)) = \frac{1}{\Delta x}\int_{x-\frac{\Delta x}{2}}^{x+\frac{\Delta x}{2}} h(\xi)d\xi, \tag{2.12}$$

where we have suppressed the t dependency of the function as we are interested now only at spatial discretizations, then by just taking derivatives on both sides of the above equality we obtain

$$f(u(x))_x = \frac{1}{\Delta x}\left[h\left(x + \frac{\Delta x}{2}\right) - h\left(x - \frac{\Delta x}{2}\right)\right].$$

This means that we only need to take the numerical flux as

$$\hat{f}_{i+1/2} = h(x_{i+1/2}). \tag{2.13}$$

If we could get an approximation to $h(x)$ to high order accuracy, the conservative approximation to the derivative in (2.11) would also be of the same high order of accuracy. Notice that (2.12) can be written as

$$f(u_i) = \bar{h}_i,$$

i.e. we are given the cell averages of h (since we know the point values u_i, hence also $f(u_i)$, in a finite difference scheme) and we would need to reconstruct its point values $h(x_{i+1/2})$ for the numerical flux (2.13). But this is *exactly the same* reconstruction problem in Procedure 2.1 above for finite volume schemes!

Thus for one space dimension, the finite difference and finite volume schemes share the same reconstruction procedure, applied in different contexts (on cell averages of u for the finite volume schemes, and on point

values of $f(u)$ for the finite difference schemes). They involve the same complexity and cost. Finite difference schemes are more restrictive in the situations that they can be applied, as they only work for uniform or smooth varying meshes and a flux splitting (for upwinding) must be smooth.

However, for multiple space dimensions, there are essential differences between these two classes of methods, when the order of accuracy is at least three. While finite difference schemes can still be applied in a dimension-by-dimension fashion (*not* dimension splitting!), i.e. computing $f(u)_x$ along a x-line with fixed y using the procedure above, and likewise for $g(u)_y$, then adding them together to form the residue, finite volume schemes of third order or higher must involve multi-dimensional reconstructions from cell averages to point values and then numerical integrations to get the numerical fluxes along the boundaries of cells. The details of these reconstructions can be found in, e.g., [24, 25, 9, 23]. As such, the operation count and CPU time for a finite volume scheme is around two to four times more expensive in two dimensions and around five to nine times more expensive in three dimensions, compared with a finite difference scheme of the same order of accuracy, see, e.g. [3] for such a comparison for ENO schemes. In return, the finite volume schemes do allow more flexibility in their applications. They can be applied in arbitrary triangulations and do not require smoothness of the meshes. On the other hand, finite difference schemes can only be applied to uniform rectangular or smooth curvilinear coordinates.

3. Two recent developments of WENO schemes

In this section we briefly describe two recent developments in WENO schemes. The first is a technique to treat negative linear weights in [23]. The second is a class of high order central WENO schemes in [22].

3.1. A TECHNIQUE TO TREAT NEGATIVE LINEAR WEIGHTS

As we can see from the previous section, a key idea in the WENO reconstruction is to write a high order reconstruction as a linear combination of several lower order reconstructions. The combination coefficients, also called linear weights, are determined by local geometry and order of accuracy. In many cases these linear weights are positive, such as in (2.6). However there are also situations where some of them become negative. For example, if we have exactly the same setting as in the previous section but now we seek the reconstruction not at the cell boundary but at the cell center x_i, as needed by the central schemes with staggered grids [13], [22], then step 1 would stay the same as above; step 2 would produce

$$p_1(x_i) = -\frac{1}{24}\bar{u}_{i-2} + \frac{1}{12}\bar{u}_{i-1} + \frac{23}{24}\bar{u}_i,$$

$$p_2(x_i) = -\frac{1}{24}\bar{u}_{i-1} + \frac{13}{12}\bar{u}_i - \frac{1}{24}\bar{u}_{i+1}, \tag{3.1}$$
$$p_3(x_i) = \frac{23}{24}\bar{u}_i + \frac{1}{12}\bar{u}_{i+1} - \frac{1}{24}\bar{u}_{i+2}.$$

Each of them is a third order reconstruction to $u(x_i)$. The fifth order reconstruction to $u(x_i)$, associated with $Q(x)$, is given by:

$$Q(x_i) = \frac{3}{640}\bar{u}_{i-2} - \frac{29}{480}\bar{u}_{i-1} + \frac{1067}{960}\bar{u}_i - \frac{29}{480}\bar{u}_{i+1} + \frac{3}{640}\bar{u}_{i+2}. \tag{3.2}$$

Step 3 would produce the following weights:

$$\gamma_1 = -\frac{9}{80}, \qquad \gamma_2 = \frac{49}{40}, \qquad \gamma_3 = -\frac{9}{80}.$$

Notice that two of them are negative. The smoothness indicators in step 4 will remain the same. This time, the WENO approximation, when naively applied, leads to unstable results because of the negative linear weights. As an example, in Fig. 3.1, left, we show the results of using a fourth order finite volume WENO scheme [9] on a non-uniform triangular mesh, for solving the two dimensional Burgers equation:

$$u_t + \left(\frac{u^2}{2}\right)_x + \left(\frac{u^2}{2}\right)_y = 0 \tag{3.3}$$

in the domain $[-2,2] \times [-2,2]$ with an initial condition $u_0(x,y) = 0.3 + 0.7\sin\left(\frac{\pi}{2}(x+y)\right)$ and periodic boundary conditions. We can see that serious oscillation appears near the shock in the numerical solution once the shock has developed. The oscillation eventually leads to instability and blowing up of the numerical solution for this example.

A simple splitting technique of treating negative weights in WENO schemes is developed by Shi, Hu and Shu in [23]: we first split the linear weights into two groups

$$\tilde{\gamma}_i^+ = \frac{1}{2}\left(\gamma_i + 3\left|\gamma_i\right|\right), \qquad \tilde{\gamma}_i^- = \tilde{\gamma}_i^+ - \gamma_i, \qquad i = 1,2,3$$

and scale them by

$$\sigma^{\pm} = \sum_{j=1}^{3} \tilde{\gamma}_j^{\pm}; \qquad \gamma_i^{\pm} = \tilde{\gamma}_i^{\pm}/\sigma^{\pm}, \qquad i = 1,2,3.$$

For the simple example of fifth order WENO reconstruction to $u(x_i)$, the split linear weights are, before the scaling,

$$\tilde{\gamma}_1^+ = \frac{9}{80}, \ \tilde{\gamma}_1^- = \frac{9}{40}, \qquad \tilde{\gamma}_2^+ = \frac{49}{20}, \ \tilde{\gamma}_2^- = \frac{49}{40}, \qquad \tilde{\gamma}_3^+ = \frac{9}{80}, \ \tilde{\gamma}_3^- = \frac{9}{40}.$$

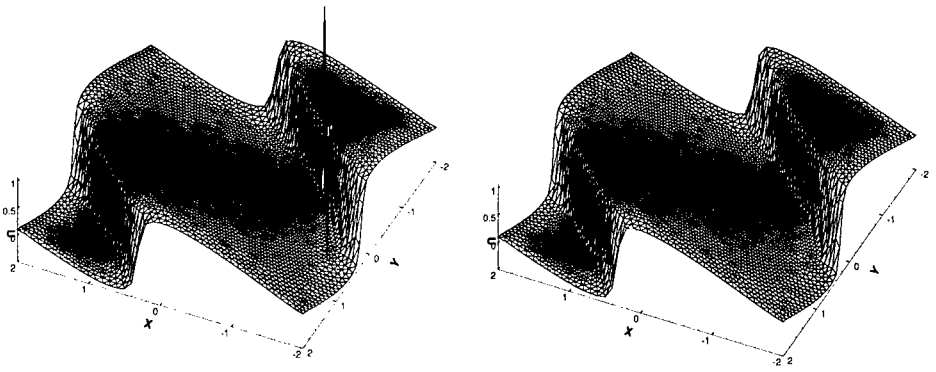


Figure 3.1. 2D Burgers' equation. Left: fourth order WENO result at $t = 0.473$, CFL=0.2, without any special treatment for the negative linear weights; Right: fourth order WENO solution at $t = 5/\pi^2$, CFL=0.2, with the treatment for the negative linear weights.

The WENO reconstruction is now performed on each group separately, by computing the nonlinear weights (2.9) separately for $\omega_j^{\pm}$ with the same smoothness indicators β_j in (2.7). The final WENO reconstruction is then taken as σ^+ times the reconstruction using the group of positive weights minus σ^- times the reconstruction using the group of negative weights. The key idea of this decomposition is to make sure that every stencil has a significant representation in both the positive and the negative weight groups. Within each group, the WENO idea of redistributing the weights subject to a fixed sum according to the smoothness of the approximation is still followed as before. For more details, we refer to [23].

We notice that, as the most expensive part of the WENO procedure, namely the computation of the smoothness indicators (2.7), has not changed, the extra cost of this positive/negative weight splitting is very small. However this simple and inexpensive change makes a big difference to the computations. In Fig. 3.1, right, we show the result of the approximation to the Burgers equation, now using WENO schemes with this splitting treatment. We can see clearly that the results are now as good as one would get from WENO schemes having only positive linear weights.

3.2. HIGH ORDER CENTRAL WENO SCHEMES

In [22] a class of fourth and eighth order central WENO (CWENO) schemes have been constructed and the role of local characteristic decompositions on eliminating spurious oscillations is demonstrated. We will give a brief description of such schemes here.

The notations are the same as before, plus the new one for staggered cells $I_{i+\frac{1}{2}} = [x_i, x_{i+1}]$. Let Δt be the time step, $u_i^n = u(x_i, t^n)$ denotes the point values, and $\overline{u}_i^n = \frac{1}{\Delta x}\int_{I_i} u(x,t^n)dx$, $\overline{u}_{i+\frac{1}{2}}^n = \frac{1}{\Delta x}\int_{I_{i+\frac{1}{2}}} u(x,t^n)dx$ represent the cell averages at time t^n on the cells I_i and $I_{i+\frac{1}{2}}$, respectively. The CWENO scheme approximates the cell averages at time t^{n+1} based on their values at time t^n with staggered space grids. We integrate (2.1) over the region $I_{i+\frac{1}{2}} \times [t^n, t^{n+1}]$, to get an equivalent formulation:

$$\overline{u}_{i+\frac{1}{2}}^{n+1} = \overline{u}_{i+\frac{1}{2}}^{n} - \frac{1}{\Delta x}\left[\int_{t^n}^{t^{n+1}} f(u(x_{i+1},t))dt - \int_{t^n}^{t^{n+1}} f(u(x_i,t))dt\right] \tag{3.4}$$

What we want to do is to find approximations of the cell averages $\overline{u}_{i+\frac{1}{2}}^n$ and the two integrals in (3.4). Thus the algorithm consists of two major steps to evolve from $\{\overline{u}_i^n\}$ to $\{\overline{u}_{i+\frac{1}{2}}^n\}$:

1. The approximation of $\overline{u}_{i+\frac{1}{2}}^n$ from the knowledge of $\{\overline{u}_i^n\}$ by a WENO reconstruction. Notice that

$$\overline{u}_{i+\frac{1}{2}}^n = \frac{1}{\Delta x}\int_{x_i}^{x_{i+1}} u(x,t^n)dx = \frac{1}{\Delta x}\left[\int_{x_i}^{x_{i+\frac{1}{2}}} u(x,t^n)dx + \int_{x_{i+\frac{1}{2}}}^{x_{i+1}} u(x,t^n)dx\right],$$

   hence we only need to reconstruct $\frac{1}{\Delta x}\int_{x_{i-\frac{1}{2}}}^{x_i} u(x,t^n)dx$ for all i because

$$\frac{1}{\Delta x}\int_{x_i}^{x_{i+\frac{1}{2}}} u(x,t^n)dx = \overline{u}_i^n - \frac{1}{\Delta x}\int_{x_{i-\frac{1}{2}}}^{x_i} u(x,t^n)dx \tag{3.5}$$

   by conservation. The WENO reconstruction for this step is very similar to Procedure 2.1.
2. The approximation of $\int_{t^n}^{t^{n+1}} f(u(x_i,t))dt$. If the time step Δt is subject to a restrictive CFL condition $\Delta t \le \frac{\Delta x}{2}\max|f'(u)|$, we can assume that $u(x_i,t)$ is smooth, since the discontinuities starting at t^n from the staggered grid points $x_{i-\frac{1}{2}}$ and $x_{i+\frac{1}{2}}$ have not reached the cell boundary x_i yet. Hence no Riemann solvers are needed and the time integrals can be evaluated with a quadrature formula to high order accuracy. Notice that this is equivalent to a Lax-Friedrichs scheme and the same effect can also be achieved without a staggered mesh by just using a Lax-Friedrichs building block, such as those WENO finite difference schemes in [11], [1] where the Lax-Friedrichs building blocks are used and no Riemann solvers are needed either. We could for example use

a three point Gauss quadrature, obtaining

$$\int_{t^n}^{t^{n+1}} f(u(x_i,t))dt \approx \Delta t \sum_{l=1}^{3} \alpha_l f(u(x_i, t^n + \Delta t \tau_l))$$

where α_l and τ_l are the weights and knots of the Gauss quadrature, respectively. Now what we want to do is to find the approximation of the point values $u(x_i, t^n + \Delta t\tau_l)$ from the cell averages $\{\overline{\mu}_j^n\}$. This can be achieved by solving the ODE at the grid points $x = x_i$:

$$\begin{cases} \frac{du(x_i,t)}{dt} = -(f(u))_x|_{x_i} \\ u(x_i, t^n) \approx \mu^n \end{cases} \tag{3.6}$$

with μ^ncomputed by a WENO reconstruction from the cell averages $\{\overline{\mu}_j^n\}$, very similar to Procedure 2.1 above. The ODE (3.6) is solved by a Runge-Kutta method to obtain the approximation of $u(x_i, t^n+\Delta t\tau_l)$, with the aid of natural continuous extension (NCE) for (3.6), [29], see [2] and [22] for details.

Acknowledgment: The author's research has been partially supported by ARO grant DAAD19-00-1-0405, NSF grants DMS-9804985 and ECS-9906606, and AFOSR grant F49620-99-1-0077.

References

1. D. Balsara and C.-W. Shu, *Monotonicity preserving weighted essentially non-oscillatory schemes with increasingly high order of accuracy*, J. Comput. Phys., v160 (2000), pp.405-452.
2. F. Bianco, G. Puppo and G. Russo, *High-order central schemes for hyperbolic systems of conservation laws*, SIAM J. Sci. Comput., v21 (1999), pp.294-322.
3. J. Casper, C.-W. Shu and H.L. Atkins, *Comparison of two formulations for high-order accurate essentially nonoscillatory schemes*, AIAA J., v32 (1994), pp.1970-1977.
4. L. Del Zanna, M. Velli and P. Londrillo, *Dynamical response of a stellar atmosphere to pressure perturbations: numerical simulations*, Astron. Astrophys., v330 (1998), pp.L13-L16.
5. O. Friedrichs, *Weighted essentially non-oscillatory schemes for the interpolation of mean values on unstructured grids*, J. Comput. Phys., v144 (1998), pp.194-212.
6. F. Grasso and S. Pirozzoli, *Shock-wave-vortex interactions: Shock and vortex deformations, and sound production*, Theor. Comp. Fluid Dyn., v13 (2000), pp.421-456.
7. F. Grasso and S. Pirozzoli, *Shock wave-thermal inhomogeneity interactions: Analysis and numerical simulations of sound generation*, Phys. Fluids, v12 (2000), pp.205-219.
8. A. Harten, B. Engquist, S. Osher and S. Chakravarthy, *Uniformly high order essentially non-oscillatory schemes, III*, J. Comput. Phys., v71 (1987), pp.231–303.
9. C. Hu and C.-W. Shu, *Weighted Essentially Non-Oscillatory Schemes on Triangular Meshes*, J. Comput. Phys., v150 (1999), pp.97-127.
10. G. Jiang and D.-P. Peng, *Weighted ENO schemes for Hamilton-Jacobi equations*, SIAM J. Sci. Comput., v21 (2000), pp.2126-2143.

11. G. Jiang and C.-W. Shu, *Efficient implementation of weighted ENO schemes*, J. Comput. Phys., v126 (1996), pp.202–228.
12. G. Jiang and C.-C. Wu, *A high order WENO finite difference scheme for the equations of ideal magnetohydrodynamics*, J. Comput. Phys., v150 (1999), pp.561-594.
13. D. Levy, G. Puppo and G. Russo, *Central WENO schemes for hyperbolic systems of conservation laws*, Math. Model. Numer. Anal. (M^2AN), v33 (1999), pp.547-571.
14. D. Levy, G. Puppo and G. Russo, *Compact central WENO schemes for multidimensional conservation laws*, SIAM J. Sci. Comput., v22 (2000), pp.656-672.
15. D. Levy, G. Puppo and G. Russo, *A third order central WENO scheme for 2D conservation laws*, Appl. Numer. Math. v33 (2000),415–421.
16. S. Liang and H. Chen, *Numerical simulation of underwater blast-wave focusing using a high-order scheme*, AIAA J., v37 (1999), pp.1010-1013.
17. R. Liska and B. Wendroff, *Composite schemes for conservation laws*, SIAM J. Numer. Anal., v35 (1998), pp.2250-2271.
18. R. Liska and B. Wendroff, *Two-dimensional shallow water equations by composite schemes*, Int. J. Numer. Meth. Fl., v30 (1999), pp.461-479.
19. X.-D. Liu, S. Osher and T. Chan, *Weighted essentially non-oscillatory schemes*, J. Comput. Phys., v115 (1994), pp.200–212.
20. P. Montarnal and C.-W. Shu, *Real gas computation using an energy relaxation method and high order WENO schemes*, J. Comput. Phys., v148 (1999), pp.59-80.
21. S. Noelle, *The MoT-ICE: a new high-resolution wave-propagation algorithm for multidimensional systems of conservation laws based on Fey's method of transport*, J. Comput. Phys., v164 (2000), pp.283-334.
22. J. Qiu and C.-W. Shu, *On the construction, comparison, and local characteristic decomposition for high order central WENO schemes*, J. Comput. Phys., submitted.
23. J. Shi, C. Hu and C.-W. Shu, *A technique of treating negative weights in WENO schemes*, J. Comput. Phys., to appear.
24. C.-W. Shu, *Essentially non-oscillatory and weighted essentially non-oscillatory schemes for hyperbolic conservation laws*, in *Advanced Numerical Approximation of Nonlinear Hyperbolic Equations*, B. Cockburn, C. Johnson, C.-W. Shu and E. Tadmor (Editor: A. Quarteroni), Lecture Notes in Mathematics, volume 1697, Springer, 1998, pp.325-432.
25. C.-W. Shu, *High order ENO and WENO schemes for computational fluid dynamics*, in *High-Order Methods for Computational Physics*, T.J. Barth and H. Deconinck, editors, Lecture Notes in Computational Science and Engineering, volume 9, Springer, 1999, pp.439-582.
26. C.-W. Shu and S. Osher, *Efficient implementation of essentially non-oscillatory shock capturing schemes*, J. Comput. Phys., v77 (1988), pp.439-471.
27. C.-W. Shu and S. Osher, *Efficient implementation of essentially non-oscillatory shock capturing schemes, II*, J. Comput. Phys., v83 (1989), pp.32-78.
28. J. Yang, S. Yang, Y. Chen and C. Hsu, *Implicit weighted ENO schemes for the three-dimensional incompressible Navier-Stokes equations*, J. Comput. Phys., v146 (1998), pp.464-487.
29. M. Zennaro, *Natural continuous extensions of Runge-Kutta methods*, Math. Comp., v46 (1986), pp.119-133.

WEIGHTED COMPACT SCHEME

LI JIANG, HUA SHAN, CHAOQUN LIU
Department of Mathematics
University of Texas at Arlington,
Arlington, Texas, U.S.A.

Abstract.

In this paper a new class of finite difference schemes - the Weighted Compact Schemes are proposed. According to the idea of the WENO schemes, the Weighted Compact Scheme is constructed by a combination of the approximations of derivatives on candidate stencils with properly assigned weights so that the non-oscillatory property is achieved when discontinuities appear. The primitive function reconstruction method of ENO schemes is applied to obtain the conservative form of the Weighted Compact Scheme. This new scheme not only preserves the characteristic of standard compact schemes and achieves high order accuracy and high resolution using a compact stencil, but also can accurately capture shock waves and discontinuities without oscillation. Numerical examples show the new scheme is very promising and successful.

1. Introduction

Recently compact schemes have been widely used in the simulation of complex flows, especially in the direct numerical simulation of turbulent flows (Jiang *et al.*, 1999; Shan *et al.*, 1999; Visbal *et al.*, 1998). Standard finite difference schemes have explicit forms and need to be at least one point wider than the desired approximation order. It is also difficult to find suitable and stable boundary closure for high order schemes. Compared to the standard finite difference approximations, the compact schemes can achieve higher order accuracy without increasing the stencil width. As the compact schemes have implicit forms and involve derivative values of neighboring grid points, additional free parameters can be used not only to improve the accuracy but also to optimize the other properties such as resolution and

stability. The resolution is the largest wave number that can be accurately represented by the scheme. Many complex flows possess a large range of time and space scales. The resolution characteristic of the scheme is essentially important in complex flow simulations. A family of centered compact schemes proposed by Lele (1992) have been proved to have spectral-like resolution. Though the advantages of compact schemes are obvious, there are still difficulties in using them to solve problems involving shock waves or discontinuities. When they are used to differentiate a discontinuous function, the computed derivative has grid to grid oscillation. Compact schemes for filtering are always used together with compact schemes for derivatives to eliminate numerical oscillations (Jiang *et al.*, 1999; Shan *et al.*, 1999; Visbal *et al.*, 1998), but even filtering can not reduce oscillations near the discontinuities. Adams (1996) proposed the hybrid compact-ENO scheme for shock-turbulent interaction problems, in which the upwind-biased compact schemes are coupled with ENO schemes. A detection algorithm is used to identify cells containing large gradients, and then the flux derivative at the faces of such cells is computed with ENO schemes. In this approach, the detecting procedure is very time consuming.

In the present work, a new class of compact schemes which we call the Weighted Compact Schemes, are developed. The building blocks of the Weighted Compact Schemes are the standard compact schemes, which also have centered and biased forms. The Weighted Compact Scheme is a hybrid of different forms of standard schemes. The hybrid idea comes from the WENO schemes (Liu *et al.*, 1994; Jiang *et al.*, 1996). The ENO (Harten *et al.*, 1987; Shu *et al.*, 1988, 1989) and WENO schemes have been applied quite extensively in many different fields. Most of the problems involving shocks, discontinuities and rich structures. The success of the ENO and WENO schemes are so attractive, that the basic methodology inspires the idea of developing the Weighted Compact Scheme. The ENO schemes choose the smoothest stencil to pick one interpolating polynomial for the ENO reconstruction, while the WENO schemes use a convex combination of interpolating polynomials on all candidate stencils to achieve the essentially non-oscillatory property, at the same time additional one order of accuracy is obtained. Thus, WENO schemes remove all the stencil choosing procedures in ENO which is very time consuming. In WENO schemes (Jiang *et al.*, 1996), each of the candidate stencils is assigned a weight that determines the contribution of this stencil to the final approximation of the numerical flux. The weights are defined in such a way that in smooth regions it approaches certain optimal weights to achieve a higher order of accuracy; in regions near discontinuities, the stencils that contain the discontinuities are assigned a nearly zero weight. According to this method, the Weighted Compact Scheme is constructed by the combination of the ap-

proximations of derivatives on candidate stencils. Here the finite difference approximations of derivatives are combined together to form a new finite difference approximation, while in WENO schemes interpolating functions are combined. The general idea of the Weighted Compact Scheme is the following, on each candidate stencil, for a given accuracy order, there is a corresponding finite difference compact scheme. According to the smoothness of each stencil, a weight is assigned to each finite difference approximation obtained by compact schemes. The hybrid of these standard schemes, with corresponding weights, forms the new scheme - the Weighted Compact Scheme. The weights are defined in such a way that the stencils, including discontinuities, have less contribution to the final scheme. Thus, the oscillations near discontinuities can be avoided, while high order accuracy and high resolution properties of compact schemes can still be preserved in the smooth region.

Another problem while using compact schemes is the conservation property of the schemes. Conservation property is especially important in solving problems involving shocks. Nonconservative methods usually generate large errors near the shock. Lele (1992) developed conservative formulations of the finite difference compact scheme by constructing the near boundary schemes in such a way that the discrete form of global conservation is satisfied. This approach is applicable when the scheme coefficients are constant. Davis (1998) applied the primitive function reconstruction method of ENO schemes to a compact scheme to maintain the conservation. In the present work, this method is applied with the new scheme to achieve the conservation.

In section 2 the general idea of the Weighted Compact Scheme is described in detail. The method of applying the new scheme in a conservative form is given. In section 3 we apply the new scheme to solving several typical equations. The problems involving shocks, discontinuities and fine structures are simulated. The numerical results are given.

2. Weighted Compact Scheme

2.1. BASIC FORMULATION

For simplicity, we consider a uniform grid. The independent variable at the node j is $x_j = h(j-1)$ for $1 \leq j \leq N$ and the function value at the nodes $f_j = f(x_j)$ is given. The finite difference approximation f'_j to the first derivative of the function f on the nodes can be written in the following general form while the finite difference compact scheme (Lele, 1992) is used.

$$\beta_- f'_{j-2} + \alpha_- f'_{j-1} + f'_j + \alpha_+ f'_{j+1} + \beta_+ f'_{j+2}$$

$$= \frac{1}{h}(b_- f_{j-2} + a_- f_{j-1} + c f_j + a_+ f_{j+1} + b_+ f_{j+2}) \tag{1}$$

For a given point j, three candidate stencils containing this point are defined as follows:

$$S_0 = (x_{j-2}, x_{j-1}, x_j), \quad S_1 = (x_{j-1}, x_j, x_{j+1}), \quad S_2 = (x_j, x_{j+1}, x_{j+2}).$$

On each stencil a finite difference compact scheme is derived in the form of Eq.(1) by matching the Taylor series coefficients to various orders. When the following coefficients are used:

$$\begin{aligned}
&S_0: \quad \beta_- = \vartheta,\ \alpha_- = 2\vartheta + 2,\ b_- = -\tfrac{5}{2}\vartheta - \tfrac{1}{2},\ a_- = 2\vartheta - 2,\ c = \tfrac{1}{2}\vartheta + \tfrac{5}{2};\\
&S_1: \quad \alpha_- = \tfrac{1}{4},\ \alpha_+ = \tfrac{1}{4},\ a_- = -\tfrac{3}{4},\ a_+ = \tfrac{3}{4},\ c = 0;\\
&S_2: \quad \beta_+ = \vartheta,\ \alpha_+ = 2\vartheta + 2,\ b_+ = \tfrac{5}{2}\vartheta + \tfrac{1}{2},\ a_+ = -2\vartheta + 2,\ c = -\tfrac{1}{2}\vartheta - \tfrac{5}{2},
\end{aligned} \tag{2}$$

where ϑ is a free parameter. In this work, we set $\vartheta = 0$ to get a tridiagonal form. This parameter can also be used to improve the accuracy or optimize the scheme. The sacrifice would be increase the computer time. Those coefficients which are not listed are set to zero. Then, the schemes corresponding to stencils S_0 and S_2 are third order one-sided finite difference schemes, and the scheme corresponding to S_1 is a fourth order centered scheme. As compact schemes have implicit forms, each scheme is represented by an equation in the form of Eq.(1) with coefficients defined in (3) . These three equations are denoted as F_0, F_1, F_2. Then a specific weight is assigned to each equation, and a new scheme is obtained by a summation of the equations.

$$F = C_0 F_0 + C_1 F_1 + C_2 F_2 \tag{3}$$

where, C_0, C_1, C_2 are weights and satisfy $C_0 + C_1 + C_2 = 1$. If the weights are properly chosen, the new scheme can achieve a higher order accuracy because the additional free parameters are introduced. If we set:

$$C_0 = C_2 = \frac{1}{18 - 24\vartheta}, \quad C_1 = \frac{8 - 12\vartheta}{9 - 12\vartheta} \tag{4}$$

the new scheme given by Eq. (3) is at least a sixth order centered compact scheme. The procedure described above implies that the sixth order centered compact scheme can be represented by a combination of three lower order schemes.

Obviously, the scheme F is a standard finite difference compact scheme and cannot avoid the oscillation near discontinuities. In order to achieve non-oscillatory property, the method of the WENO scheme (Jiang *et al.*,

1996) is introduced to determine the new weight for each stencil. The weights are determined according to the smoothness of the function on each stencil. Following the WENO method, the new weights are defined as (Jiang *et al.*, 1996):

$$\omega_k = \frac{\gamma_k}{\sum_{i=0}^{2} \gamma_i} \quad \gamma_k = \frac{C_k}{(\epsilon + IS_k)^p} \tag{5}$$

where ϵ is a small positive number which is used to prevent the denominator becoming zero. p is an important parameter to control the weight. At present time, it is set as a constant. IS_k is the smoothness measurement which is defined according to WENO (Jiang *et al.*, 1996):

$$\begin{aligned} IS_0 &= \frac{13}{12}(f_{j-2} - 2f_{j-1} + f_j)^2 + \frac{1}{4}(f_{j-2} - 4f_{j-1} + 3f_j)^2 \\ IS_1 &= \frac{13}{12}(f_{j-1} - 2f_j + f_{j+1})^2 + \frac{1}{4}(f_{j-1} - f_{j+1})^2 \\ IS_2 &= \frac{13}{12}(f_j - 2f_{j+1} + f_{j+2})^2 + \frac{1}{4}(f_{j+2} - 4f_{j+1} + 3f_j)^2 \end{aligned} \tag{6}$$

where, the two terms on the right side can be regarded as the measurements of the curvature and the slope respectively at a certain point. Through the Taylor expansion, it can be easily proved that in smooth regions new weights ω_k satisfy:

$$\omega_k = C_k + O(h^2) \ \ and \ \ \omega_2 - \omega_0 = O(h^3). \tag{7}$$

The new scheme is then formed using these new weights:

$$F = \omega_0 F_0 + \omega_1 F_1 + \omega_2 F_2. \tag{8}$$

The leading error of F is also a combination of the errors of the original schemes F_i, which is as following:

$$(\frac{1}{12}\omega_0 - \frac{1}{12}\omega_2) f^{(4)} h^3 + (-\frac{1}{15}\omega_0 + \frac{1}{120}\omega_1 - \frac{1}{15}\omega_2) f^{(5)} h^4. \tag{9}$$

When Eq. (7) is satisfied, the leading error of the new scheme can be written as $O(h^6)$. Obviously, this new scheme is of sixth-order accuracy and has the high resolution property as the centered sixth-order compact scheme in smooth regions. But in the regions containing discontinuities, the smoothness measurement IS_k of the non-smooth stencil is large compared to that of the smooth stencil, thus the non-smooth stencil is assigned a small weight and have less contribution to the final scheme so that the non-oscillatory property is achieved.

With the new weights ω_k, the new finite difference compact scheme Eq. (8) is written in the form of Eq. (1). The coefficients of the final Weighted Compact Scheme are given as follows:

$$\begin{aligned}
&\beta_- = \vartheta\omega_0,\ \alpha_- = (2\vartheta+2)\omega_0 + \frac{1}{4}\omega_1,\\
&\alpha_+ = (2\vartheta+2)\omega_2 + \frac{1}{4}\omega_1,\ \beta_- = \vartheta\omega_2,\\
&b_- = (-\frac{5}{2}\vartheta - \frac{1}{2})\omega_0,\ a_- = (2\vartheta-2)\omega_0 - \frac{3}{4}\omega_1,\\
&c = (\frac{1}{2}\vartheta + \frac{5}{2})\omega_0 - (\frac{1}{2}\vartheta + \frac{5}{2})\omega_2,\\
&a_+ = (-2\vartheta+2)\omega_2 + \frac{3}{4}\omega_1,\ b_+ = (\frac{5}{2}\vartheta + \frac{1}{2})\omega_2.
\end{aligned}$$

As ω_k is dependent on the smoothness measurement calculated by local function values, the scheme coefficients are various from point to point. The free parameter ϑ can be used to optimize the scheme when the properties of high resolution, and stability are concerned. If $\vartheta = 0$, the scheme is tridiagonal. Though in the above description the sixth-order Weighted Compact Scheme is selected as an example, the method can be extended to a general form.

2.2. CONSERVATIVE FORMULATION

The conservation property of the scheme is very important in shock wave capturing, since it imposes a constraint on the solution error. In the work of Davis (1998), the reconstruction method developed by Shu and Osher (1989) for the ENO scheme was used together with the Pade scheme to achieve the conservation. As we already mentioned in the previous section, the coefficients of our new scheme are not constant. So the finite difference scheme itself is not conservative. However, conservation can be obtained when the Weighted Compact Scheme is applied together with ENO reconstruction method. Below, we give the description of this method. For 1-D conservation laws:

$$u_t(x,t) + f_x(u(x,t)) = 0. \tag{10}$$

When a conservative approximation to the spatial derivative is applied, a semi-discrete conservative form of Eq. (10) is as follows:

$$\frac{du_j}{dt} = -\frac{1}{\Delta x}\left(\hat{f}_{j+\frac{1}{2}} - \hat{f}_{j-\frac{1}{2}}\right), \tag{11}$$

$\hat{f}_{j+\frac{1}{2}}$ and $\hat{f}_{j-\frac{1}{2}}$ are numerical flux functions at the cell interfaces. Δx is the grid size of the uniform grid. In order to achieve the high order accuracy, the numerical flux should be defined in such a way that the difference of the numerical flux is a high order approximation of the derivative f_x. According to the ENO reconstruction procedure (Shu *et al.*, 1989), it has been approved that the primitive function of $\hat{f}$ at the cell interfaces can be exactly calculated by the given point values f_j. If H is the primitive function of $\hat{f}$, then:

$$H(x_{j+\frac{1}{2}}) = \Delta x \sum_{i=-\infty}^{j} f_i. \tag{12}$$

Obviously, the numerical flux $\hat{f}$ at the cell interfaces is the derivative of its primitive function H. i.e:

$$\hat{f}_{j+\frac{1}{2}} = H'_{j+\frac{1}{2}}. \tag{13}$$

As the values of the function H have already been obtained at the cell interfaces, the approximations of the derivatives of H at the cell interfaces are calculated directly by the Weighted Compact Scheme presented in Section 1. Thus, the Weighted Compact Scheme is applied to the primitive function instead of the function itself. In this way, the conservation property is achieved.

3. Numerical Examples

The prospects of the Weighted Compact Scheme can be seen from our applications of the tridiagonal sixth-order scheme described in section 1 to some model equations and test examples. According to our experience, when the reconstruction method is adopted, the function f in Eq.(10) is used to define the smoothness IS_k instead of using primitive function H. The parameter p in Eq. (5) is set as $p = 1$. For all of the following examples, the fourth order Runge-Kutta scheme (Shu *et al.*, 1988) is used for time integration.

3.1. CONVECTION EQUATION

We first solve the one-dimensional convection equation with several initial functions.

$$\begin{aligned} &u_t + u_x = 0, \qquad -1 \le x \le 1 \\ &u(x,0) = u_0(x), \qquad \textit{periodic with a period of } 2. \end{aligned} \tag{14}$$

N	L_∞ error	L_∞ order	L_1 error	L_1 order
20	4.39E-5		1.19E-5	
40	1.05E-6	5.38	2.37E-7	5.64
80	2.70E-8	5.28	4.23E-9	5.81
160	5.94E-10	5.50	6.35E-11	6.05
320	1.14E-11	5.70	7.15E-13	6.47

TABLE 1. Errors of the numerical solution with $u_0(x) = sin(\pi x)$ at $t = 1$, Weighted Compact Scheme

N	L_∞ error	L_∞ order	L_1 error	L_1 order
20	1.48E-5		9.46E-6	
40	2.26E-7	6.03	1.44E-7	6.02
80	3.57E-9	5.98	2.27E-9	5.98
160	5.88E-11	5.92	3.74E-11	5.92
320	1.07E-12	5.78	5.73E-13	6.02

TABLE 2. Errors of the numerical solution with $u_0(x) = sin(\pi x)$ at $t = 1$, Standard Compact Scheme

The first initial function is $u_0(x) = sin(\pi x)$. The second one is $u_0(x) = sin^4(\pi x)$. The L_1 and L_∞ errors are listed in Table 1 to Table 3. N is the number of grid points. Table 1 and 2 are the results for the first initial function and are obtained respectively by the Weighted Compact Scheme and the standard compact scheme. This data shows that the Weighted Compact Scheme is capable of achieving sixth-order accuracy as the standard compact scheme. Table 3 lists the result for the second initial function. Compared to the results (Jiang *et al.*, 1996) obtained by WENO scheme, this Weighted Compact Scheme achieves higher order accuracy with the same stencils.

The third to fifth initial functions are:

$$(3)\quad u_0(x) = \begin{cases} 1, & -\frac{1}{5} \le x \le \frac{1}{5}; \\ 0, & otherwise, \end{cases}$$

N	L_∞ error	L_∞ order	L_1 error	L_1 order
20	3.73E-2		1.16E-2	
40	4.54E-3	3.03	1.17E-3	3.31
80	5.37E-4	3.07	5.54E-5	4.04
160	7.08E-6	6.25	7.98E-7	6.12
320	4.84E-8	7.19	6.99E-9	5.98
640	2.65E-10	7.51	7.61E-11	6.52

TABLE 3. Errors of the numerical solution with $u_0(x) = sin^4(\pi x)$ at $t = 1$

$$(4)\quad u_0(x) = \begin{cases} \left[1 - (\frac{10}{3}x)^2\right]^{\frac{1}{2}}, & -\frac{3}{10} \le x \le \frac{3}{10}; \\ 0, & otherwise, \end{cases}$$

$$(5)\quad u_0(x) = e^{-300x^2}.$$

Figure 1 is the result of the standard compact scheme for the initial function (3). The solution is seriously damaged by wiggles generated near the discontinuities. Figures 2-4 illustrate the results obtained by the Weighted Compact Scheme for initial functions (3), (4), and (5). There is no obvious numerical oscillation observed in the regions near the discontinuities, and good resolution has been achieved.

3.2. BURGERS' EQUATION

The Weighted Compact Scheme is applied to the nonlinear Burgers' equation. With the given initial condition, the exact solution will develop to a moving shock wave.

$$u_t + (\frac{1}{2}u^2)_x = 0, \qquad -1 \le x \le 1 \tag{15}$$
$$u(x,0) = \frac{1}{2} + sin(\pi x), \qquad periodic\ with\ a\ period\ of\ 2.$$

At $t = 0.15$ the solution is still smooth. The L_∞ and L_1 errors are listed in Table 4. The scheme also has about sixth-order accuracy for the nonlinear problem.

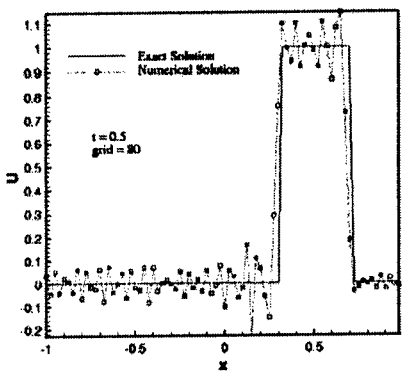


Figure 1. Solution of standard compact scheme

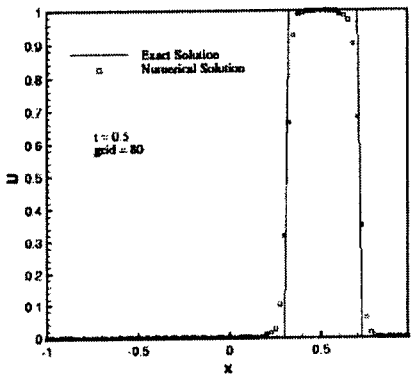


Figure 2. The solution at $t = 0.5$

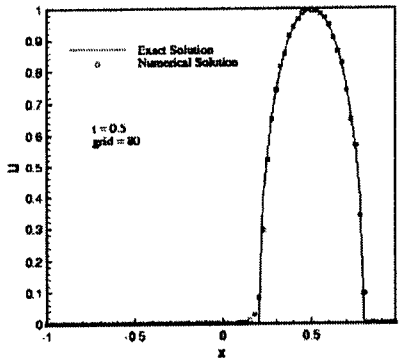


Figure 3. The solution at $t = 0.5$

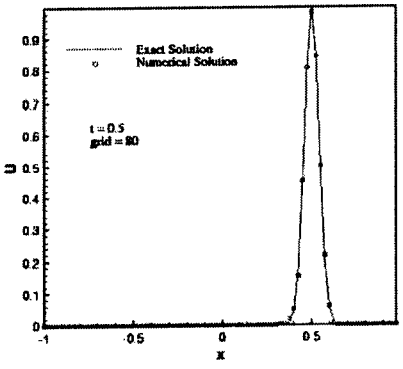


Figure 4. The solution at $t = 0.5$

N	L_∞ error	L_∞ order	L_1 error	L_1 order
80	4.45E-5		3.63E-6	
160	1.75E-6	4.67	4.85E-8	6.23
320	4.41E-8	5.31	9.49E-10	5.85

TABLE 4. Errors of the numerical solution of Burgers' equation. $t = 0.15$

Fig. 5 and Fig. 6 show the wave at $t = 0.3183$ and $t = 0.55$. At $t = 0.3183$ the wave becomes steep and the shock starts to form. At $t = 0.55$ the discontinuity appears and is accurately captured by the scheme without obvious oscillation.

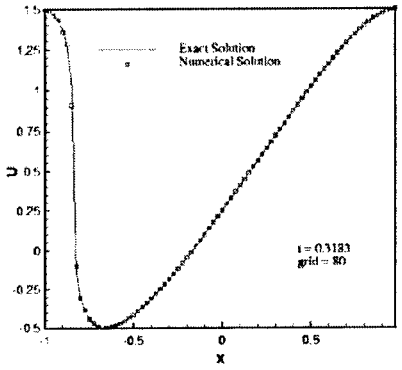


Figure 5. The solution to the Burgers' equation at $t = 0.3138$

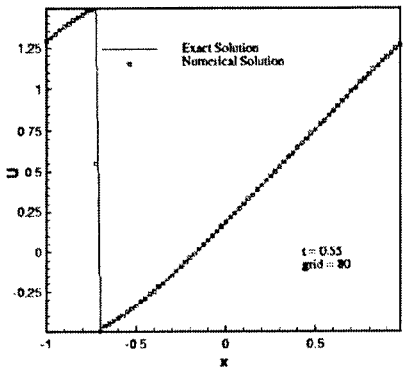


Figure 6. The solution to the Burgers' equation at $t = 0.55$

3.3. 1D EULER EQUATION

We apply our scheme to 1D Euler equation of gas dynamics

$$\begin{aligned} &\frac{\partial U}{\partial t} + \frac{\partial F}{\partial x} = 0 \\ &U = (\rho, \rho u, E)^T \\ &F = (\rho u, \rho u u + p, u(E+p))^T. \end{aligned} \tag{16}$$

The first example is the typical one-dimensional shock tube problem. The initial conditions are chosen so that the solution contains a shock, contact discontinuity and a rarefraction wave. They are given as follows:

$$U_0 = \begin{cases} (1,0,1), & x < 0; \\ (0.125,0,0.1), & x \geq 0, \end{cases}$$

The distributions of pressure, density,velocity and energy are shown in Fig. 7. The shock wave and contact discontinuity are accurately captured.

The second example is to simulate the interaction between shock wave and fluctuations. The calculation starts with the initial field as follows:

$$U_0 = \begin{cases} (3.857143, 2.629369, 10.33333), & x < -4; \\ (1 + 0.2sin(5x), 0, 1), & x \geq -4. \end{cases}$$

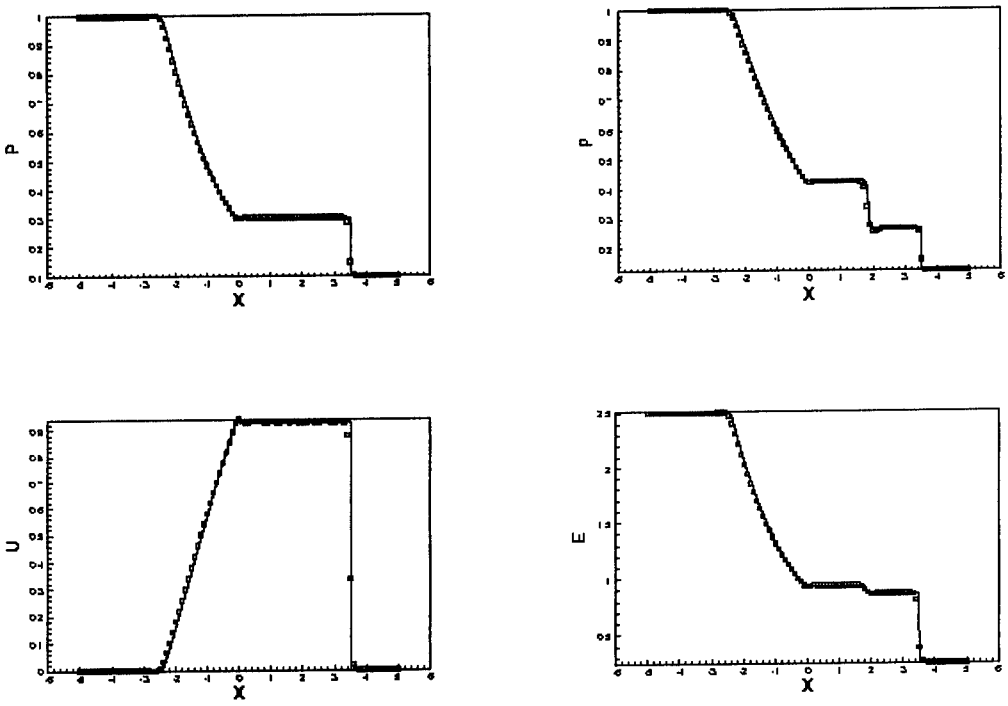


Figure 7. The solutions to the shock-tube problem at $t = 2$, $N = 100$

In this example, the shock is moving into a density fluctuation field and interacts with the fluctuation. This problem requires non-oscillatory scheme with high resolution to resolve the fine structures. In Fig. 8, the solid line represents the numerical solution obtained using the present scheme with a fine grid of $N = 1600$. This is regarded as the exact solution. The results obtained with $N = 400$ compared well with the exact solution. These results show that the present schemes are capable of resolving fine structures with high frequency. No serious oscillation appears near the shock area.

3.4. 2D EULER EQUATION

Finally, we apply the Weighted Compact Scheme to investigate a 2D shock-turbulence interaction problem(Adams,1996; Shu,1989). 2D Euler equations are written as

$$\frac{\partial U}{\partial t} + \frac{\partial F}{\partial x} + \frac{\partial G}{\partial y} = 0 \tag{17}$$

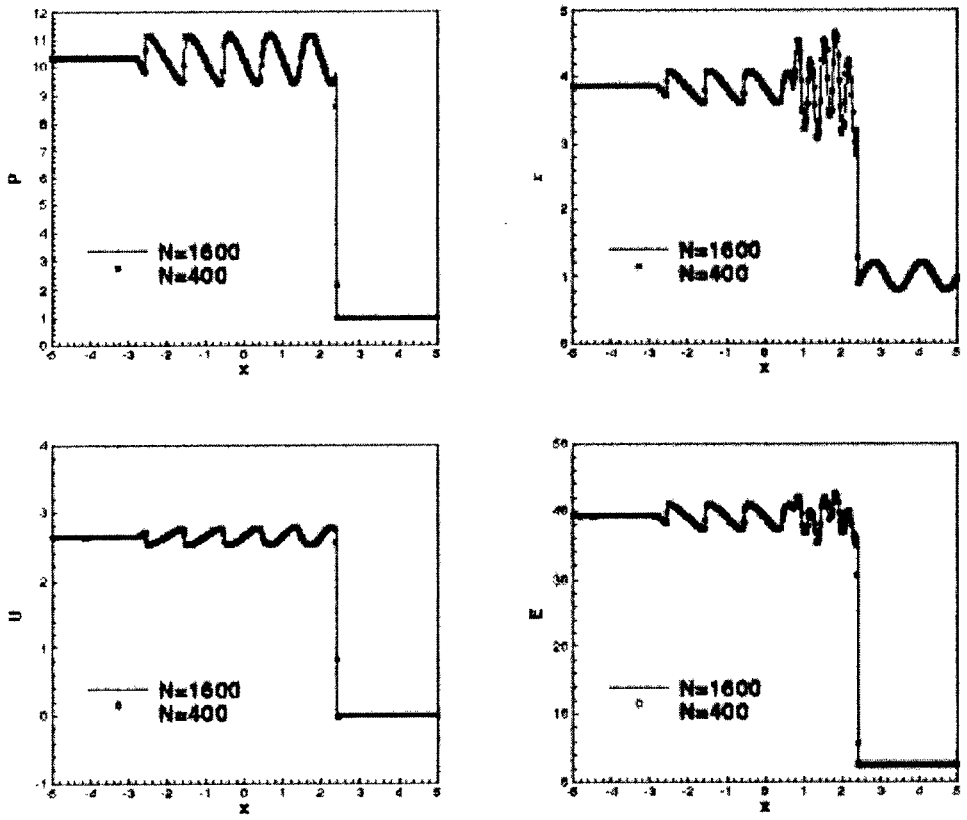


Figure 8. The solutions to the shock-fluctuation interaction problem at $t = 1.8$, $N = 400$

$$U = (\rho, \rho u, \rho v, E)^T$$
$$F = (\rho u, \rho uu + p, \rho uv, u(E + p))^T$$
$$G = (\rho u, \rho vu, \rho vv + p, v(E + p))^T$$

where $E = \frac{p}{\gamma - 1} + \frac{1}{2}\rho(u^2 + v^2)$. The computational domain is given by $-1.5 < x < 1.5$, $-1 < y < 1$. At time $t = 0$, a Mach 8 shock at $x = -1$ is moving in the positive x direction into a vorticity fluctuation field. The initial condition for pre-shock field is specified with vorticity fluctuation as

$$u_1 = -c_1 sin\theta cos(xkcos\theta + yksin\theta)$$
$$v_1 = c_1 cos\theta cos(xkcos\theta + yksin\theta)$$
$$\rho_1 = 1$$
$$p_1 = 1$$

where c_1 is the speed of sound, $k = 2\pi$, $\theta = \frac{1}{6}$. The initial post-shock state can be derived from shock relations.

$$u_2 = \frac{2(M_s^2 - 1)}{(\gamma + 1)M_s^2} u_s$$
$$v_2 = 0$$
$$\rho_2 = \frac{(\gamma + 1)M_s^2}{2 + (\gamma - 1)M_s^2} \rho_1$$
$$p_2 = (1 + \frac{2\gamma(M_s^2 - 1)}{\gamma + 1}) p_1$$

where $u_s = M_s c_1$ is the shock propagation velocity, and M_s is the shock Mach number.

Fig.3.4-3.4 display the results obtained on different grids. The shock front is clearly shown by the pressure contour lines. After the vorticity fluctuations strike the shock, the shock front develops ripples and the vorticity fluctuations are amplified. The results are similar compared with those obtained by Shu (1989) and Adams (1996). This example shows again that the Weighted Compact Scheme can be used for shock-turbulence interaction problems.

4. Conclusions

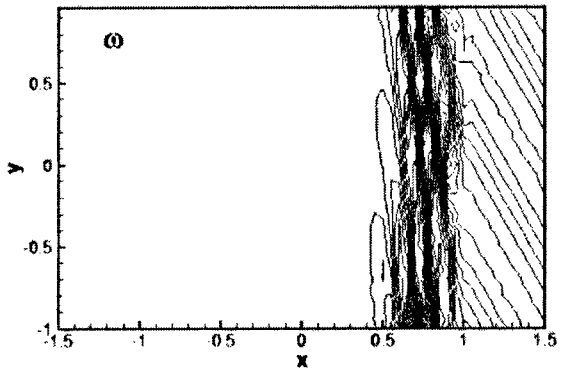
The conservative Weighted Compact Scheme developed in this work has been successfully applied to several one dimensional typical problems involving discontinuities, shock waves, and shock-fluctuation interaction. High order accuracy, high resolution, and non-oscillation are achieved by using compact stencil. This new scheme will be further applied to multi-dimensional flows with shock-turbulence interactions.

Acknowledgments

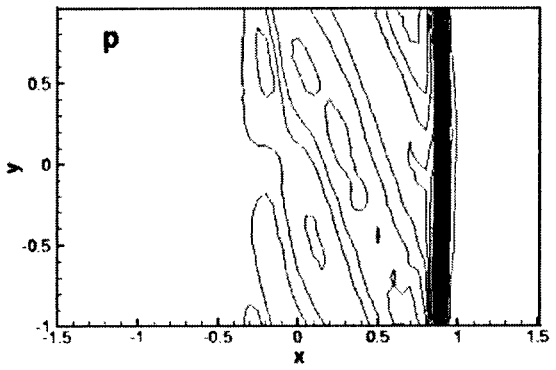
This work was supported by Air Force Office of Scientific (AFOSR) research grant monitored by Dr. L. Sakell and Dr. Thomas Beutner. The authors are grateful for AFOSR's sponsorship of this research work. The authors also would like to thank DoD HPCC for providing computer resources.

References

1. Adams, N.A. and Shariff, K., (1996), A high-resolution hybrid compact-ENO scheme for shock-turbulence interaction problems, *J. Comput. Phys.*, **127**, pp.27-51.
2. Davis, S. F., (1998), Shock capturing with Pade method, *Applied Mathematics and Computation*, **89**, pp.85-98.
3. Harten, A., Engquist, B., Osher, S. and Charavarthy, S., (1987), Uniformly high order accurate essentially non-oscillatory scheme, III, *J. Comput. Phys.*,**71**, pp.231-303.



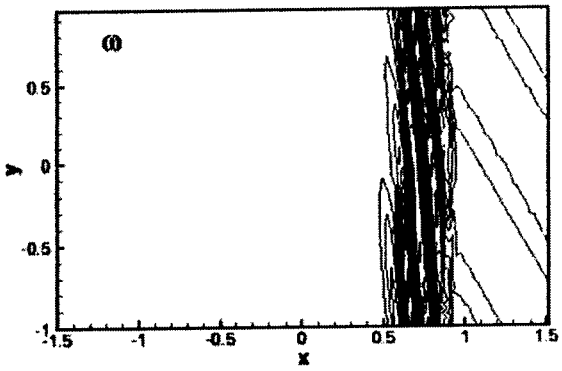
Contours of vorticity



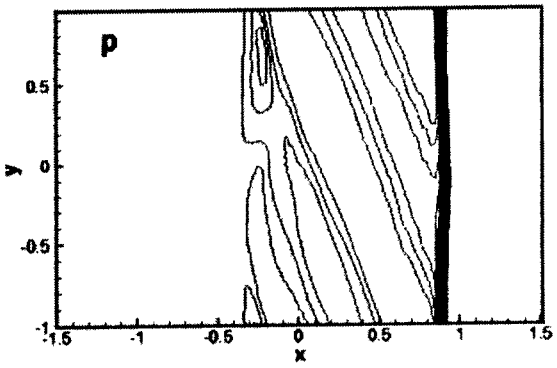
Contours of pressure

Figure 9. Grid=60 × 40,t=0.2

4. Jiang, G. S. and Shu, C. W., (1996), Efficient implementation of weighted ENO scheme. *J. Comput. Phys.*, **126**, pp.202-228.
5. Jiang, L., Shan, H. and Liu, C., (1999), Direct numerical simulation of boundary-layer receptivity for subsonic flow around airfoil, *The Second AFOSR International Conference on DNS/LES*, Rutgers, New Jersey, June 7-9.
6. Lele, S. K., (1992), Compact finite difference schemes with spectral-like resolution. *J. Comput. Phys.*, **103**, pp.16–42.
7. Liu, X. D., Osher, S. and Chan, T., (1994), Weighted essentially non-oscillatory schemes, *J. Comput. Phys.*, **115**, pp.200-212.
8. Shan, H., Jiang, L., Zhao, W. and Liu, C., (1999), Large eddy simulation of flow transition in a supersonic flat-plate boundary layer. *AIAA Paper* 99-0425.
9. Shu, C. W. and Osher, S., (1988), Efficient implementation of essentially non-oscillatory shock-capturing schemes , *J. Comput. Phys.*, **77**, pp.439-471.
10. Shu, C. W. and Osher, S., (1989), Efficient implementation of essentially non-oscillatory shock-capturing schemes II, *J. Comput. Phys.*, **83**, pp.32-78.



Contours of vorticity



Contours of pressure

Figure 10. Grid=120 × 80,t=0.2

11. Visbal, M. R. and Gaitonde, D. V., (1998), High-order accurate methods for unsteady vortical flows on curvilinear meshes, *AIAA Paper* 98-0131.

HIGH-ORDER DISCONTINUOUS GALERKIN METHODS: SIMULATION OF COIL FLOWS

I. PIVKIN, R.M. KIRBY AND G.E. KARNIADAKIS
Division of Applied Mathematics
Brown University

Abstract.

We have developed spectral methods in the discontinous Galerkin framework appropriate for simulations of high-speed flows in complex-geometry domains. In this paper we present details of the stability of the method and demonstrate the importance of over-integration for strongly nonlinear problems. We then present results from the application of the method to stability studies of supersonic and subsonic flows in a Chemical Oxygen Iodine Laser (COIL) device.

1. Introduction

Finite volume methods have been very successful in simulating steady high-speed flows but they are rather inefficient for unsteady flow simulations, and especially for direct or large eddy simulations of turbulent and transitional compressible flows. Discontinuous Galerkin Methods (DGM) [1], when combined with high-order discretizations as in [2], offer some of the advantages of finite volume methods and lead to numerical solutions with significantly reduced numerical dispersion and dissipation. In summary, high-order DGM are:

- High-order finite volumes applied to structured or unstructured meshes.
- Flux-based, and thus maintain conservativity which is important for correct shock location and long-time integration.
- L_2-stable, and thus they do not require explicit flux limiters.
- Robust as they employ Riemann solvers.

The particular DGM implementation we have developed employs an *orthogonal* polynomial basis of different order in each element. The discon-

tinuous basis is orthogonal, hierarchical, and maintains a tensor-product property even for non-separable domains [3, 4].

Unlike pseudo-spectral (collocation) methods used often for incompressible flow simulations, in our spectral DGM approach the number of quadrature points and the number of degrees of freedom (i.e., modes) are decoupled in each element. Specifically, it is a super-collocation method combined with Galerkin projections in an element-wise fashion. This is very important for the treatment of nonlinear terms as this approach offers the possibility of *dealiasing* on arbitrarily non-uniform grids. We discuss this issue in detail in the next section, where we show that simple *quadrature-modes rules* can be derived by considering the long-term (asymptotic) stability of DGM.

In the last section, we apply DGM to three-dimensional supersonic and subsonic flows in a Chemical Oxygen Iodine Laser (COIL) configuration. The flow field of a COIL typically contains multi-phase flow (oxygen, iodine and helium) as well as chemical reactions [5], but here we consider the stability of cold (helium) flow. Due to the importance of COILs in military and industrial uses, there has been a lot of research focused on them during the last decade [6, 7, 8]. Recent two-dimensional simulations have shown that the supersonic COIL flow is unsteady although corresponding preliminary simulations have shown substantially reduced temporal variations [9]. In the current work, we consider both supersonic as well as subsonic conditions on different grids and with p-refinement to address more systematically the question of unsteadiness. Our results show that the strong compressibility and the symmetric crossflow stabilize the supersonic nozzle flow, in contrast with the subsonic cases.

2. Discontinuous Galerkin Method - DGM

We consider the non-dimensional compressible Navier-Stokes equations, which we write in compact form as

$$\vec{U}_t + \nabla \cdot \mathbf{F} = Re_\infty^{-1} \nabla \cdot \mathbf{F}^\nu \quad \text{in } \Omega \tag{1}$$

where $\mathbf{F}$ and $\mathbf{F}^\nu$ correspond to inviscid and viscous flux contributions, respectively, and Re_∞ is the reference Reynolds number. Here the vector $\vec{U} = [\rho, \rho u_1, \rho u_2, \rho u_3, \rho e]^t$ with $\mathbf{u} = (u_1, u_2, u_3)$ the local fluid velocity, ρ the fluid density, and e the total energy. Splitting the Navier-Stokes operator in this form allows for a separate treatment of the inviscid and viscous contributions, which, in general, exhibit different mathematical properties.

To give an overview of the formulation we first apply DGM to the linear two-dimensional equation for advection of a conserved quantity u

$$\frac{\partial u}{\partial t} + \nabla \cdot \mathbf{F}(u) = 0, \tag{2}$$

where $\mathbf{F}(u) = (f(u), g(u), h(u))$ is the *flux* vector which defines the transport of $u(\mathbf{x}, t)$. We start with the variational statement of the standard Galerkin formulation of (2) by multiplying by a test function v and integrating by parts

$$\int_\Omega \frac{\partial u}{\partial t} v \, dx + \int_{\partial\Omega} v \, \hat{n} \cdot \mathbf{F}(u) \, ds - \int_\Omega \nabla v \cdot \mathbf{F}(u) \, dx = 0. \tag{3}$$

The solution $u \in \mathcal{X}$ (approximation space) satisfies this equation for all $v \in \mathcal{V}$ (test space), where $\mathcal{X}$ may contain discontinuous functions. The discrete space $\mathcal{X}^\delta$ contains polynomials within each "element," but zero outside the element. Here the "element" is, for example, an individual triangular region T_i in the computational mesh applied to the problem. Thus, the computational domain $\Omega = \bigcup_i T_i$, and T_i, T_j overlap only on edges.

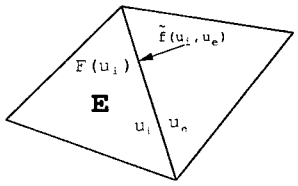


Figure 1. Interface conditions between two adjacent triangles.

Each element (E) is treated separately, giving a variational statement (after integrating by parts once more):

$$\frac{\partial}{\partial t}(u, v)_E + \int_{\partial T_E} v(\tilde{f}(u_i, u_e) - \boldsymbol{F}(u_i)) \cdot \mathbf{n} \, ds + (\nabla \cdot \boldsymbol{F}(u), v)_E = 0, \tag{4}$$

where $\boldsymbol{F}(u_i)$ is the flux of the interior values. Computations on each element are performed separately, and the connection between elements is a result of the way boundary conditions are applied. Here, boundary conditions are enforced via the numerical surface flux $\tilde{f}(u_i, u_e)$ that appears in equation (4). Because this value is computed at the boundary between adjacent elements, it may be computed from the value of u given at either element. These two possible values are denoted here as u_i in the interior of the element under consideration and and u_e in the exterior (see figure 1). Upwinding considerations dictate how this flux is computed.

In the more complicated case of a hyperbolic system of equations, an approximate Riemann solver should be used to compute a value of f, g, h (in three-dimensions) based on u_i and u_e. Specifically, we compute the flux $\tilde{f}(u_i, u_e)$ using upwinding, i.e.

$$\tilde{f}(u) = R\Lambda^+ L u_i + R\Lambda^- L u_e$$

where A (the Jacobian matrix of F) is written in terms of the left and right eigenvectors, i.e. $A = R\Lambda L$ with Λ containing the corresponding eigenvalues in the diagonal; also, $\Lambda^{\pm} = (\Lambda \pm |\Lambda|)/2$. Alternatively, we can use a standard Lax-Friedrichs flux

$$\tilde{f}(u) = \frac{1}{2}(f(u_e) + f(u_i)) - \frac{1}{2}R|\Lambda|L(u_e - u_i).$$

In order to solve the compressible Navier-Stokes equations we also need to treat the second-order terms. This is done similarly by introducing auxiliary fluxes and constructing a system of first-order equations that we treat similarly as the advection equation above. The difference is in the choice of the numerical fluxes at the interface, which we have taken here to be the arithmetic mean of the fluxes from adjoint elements. However, other choices are possible that can affect the computational complexity and the accuracy [1].

With regard to the trial basis we employ Jacobi polynomials with variable weights as reported in [2]. The degree of polynomial can be varied from one element to the other but interpolation along edges or elemental faces should involve the higher order polynomial in order to maintain conservativity. The DGM method is L_2-stable but in practice instabilities may arise in under-resolved or marginally resolved simulations. Such instabilities were first reported in [2] where a slight over-integration seem to provide long-time integration stability. In the next section, we revisit this issue and provide more details on over-integration for both quadratic as well as cubic nonlinearities.

2.1. STABILITY AND OVER-INTEGRATION

To understand the ramifications of under-integration of nonlinear terms, we performed the following test:

1. Initialize a single element spanning $[-1, 1]$ and containing 16 modes.
2. Initialize all the modal coefficients to one.
3. Evaluate the modal representation on a set of quadrature points q.
4. Pointwise square the values at the quadrature points.
5. Pre-multiply the set of points (as a vector) by the collocation derivative matrix of the appropriate size (rank $q \times q$).
6. Project back to modal coefficients by discrete inner products using Gaussian integration.

The procedure above mimicks the "physical space" or pseudo-spectral evaluation of the term $\frac{\partial u^2}{\partial x}$ commonly used in spectral methods for evaluating nonlinear terms. This test was chosen because even in its simplicity it

models the order of nonlinearity that occurs in the solution of the incompressible Navier-Stokes equations. All modes are set to one to mimick a case in which an element has under-resolved or marginally resolved the solution within the element. In the test above, the only unspecified parameter is the number of quadrature points q to be used. In using Gauss-Lobattto points, the value of q is taken to be one more than the number of modes M (in this case then $M = 16$ and $q = 17$) [2], but this value is appropriate for the inner products corresponding to linear terms. For a quadratic or cubic nonlinearities more quadrature points are required. The ramifications of under-integration of this form are shown in figure 2. The figure on the left was obtained for quadratic nonlinearity ($\frac{\partial}{\partial x}u^2$) and the figure on the right was obtained for a cubic nonlinearity ($\frac{\partial}{\partial x}u^3$). The difference in the modal coefficients at the conclusion of the algorithm above for different values of q is provided. We observe that for the quadratic nonlinearity, once $\frac{3}{2}M$ quadrature points are used, the difference in the modal values do not change. Similarly for the cubic nonlinearity, once $2M$ quadrature points are used, the difference in the modal values do not change.

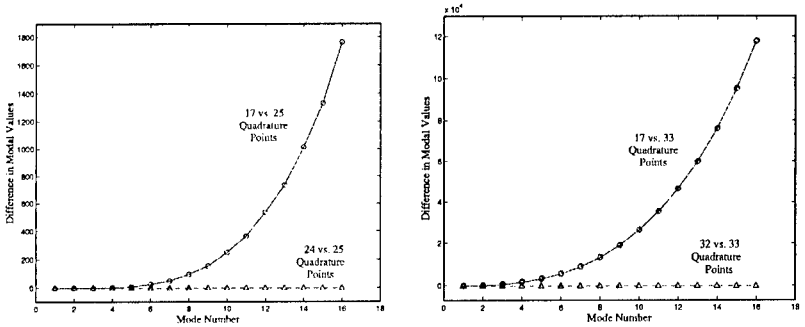


Figure 2. Comparison of the difference in modal coefficients when different numbers of quadrature points are used. Quadratic nonlinearity on the left and cubic nonlinearity on the right.

If figure 3 we plot the difference between using the $\frac{3}{2}M$ rule and $2M$ rule (left and right figures, respectively) versus $M + 2$ rule for chosing the number of quadrature points q. Observe that for small number of modes the two regions overlap or may be sufficiently close that using $M + 2$ will not lead to aliasing instabilities. This may be an explanation of the results shown in [2] in which over-integration by one point was sufficient to stabilize the flow simulation.

To further test the integration of the nonlinear terms, we chose to solve viscous Burgers equation with $\nu = 10^{-5}$. Five equally spaced elements spanning $[-1, 1]$ were used, each one having 16 modes. We have found

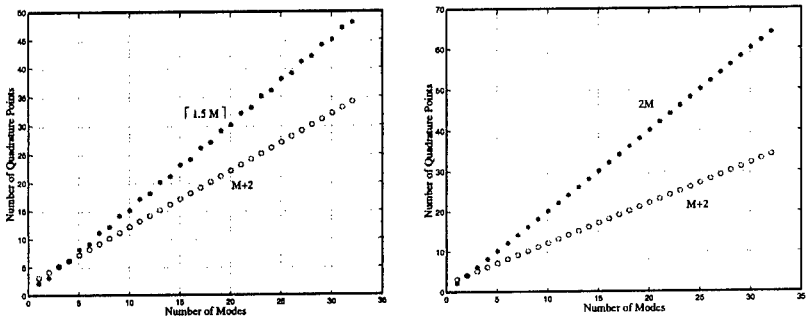


Figure 3. Difference between using the $\frac{3}{2}M$ rule and $2M$ rule (left and right figures, respectively) versus $(M+2)$ rule for chosing the number of quadrature points q.

that when using 17, 19 and 21 quadrature points, the solution is unstable (measured by the L_2 norm). Once the number of quadrature points reaches 24 ($\frac{3}{2}M$, where M is the number of modes), the L_2 norm of the solution does not change.

3. Simulation of COIL Flows

The chemical oxygen iodine laser (COIL) is a very powerful laser, capable of producing megawatts of continuous power at short wavelengths ($1315\,nm$). There are two distinct types of COIL configurations, depending on the characteristic flow velocity of the constituent gases. In the first one, the *supersonic lasers*, the velocities are of the order of $400\,m/s$ or higher while in the second type, the *subsonic lasers*, the characteristic velocities are an order of magnitude lower. There has been some uncertainty regarding the stability of the COIL flows, especially in the supersonic regime. Two-dimensional computations show that the flow is unstable to small perturbations and becomes oscillatory with frequency of about $40\,Khz$ [9]. On the other hand, preliminary three-dimensional simulations reported recently in [9] show only extremely small time variations in amplitude. Unfortunately, there are not enough experimental measurements or flow visualizations to document the stability of the COIL flows, especially in the supersonic nozzle (the so-called RADICL nozzle). In this work, we study the stability of COIL flows via direct numerical simulations based on the DGM spectral/hp element method and the code NEKTAR described in the previous section; see also [1, 4].

An overview of the supersonic flow in the central part of the nozzle is shown in figure 4. There is a strong intercation between the incoming almost uniform flow and the crossflow emanating from the six nozzles. The

SUPERSONIC (CASE A)

Inflow		Pipes		Outflow	
Density	0.013066498	Density	0.039323356	Density	0.001355714
U-velo	153.3355557	U-velo	442.6130539	U-velo	1208.084843
V-velo	0	V-velo	0	V-velo	0
W-velo	0	W-velo	0	W-velo	0
Energy	12209.51111	Energy	53746.82174	Energy	1158.745548
Mach	0.152511337	Mach	0.38	Mach	3.264908

SUBSONIC (NO PIPES) (CASE B)

Inflow		Pipes		Outflow	
Density	0.013066498	Density	0	Density	0.0130896
U-velo	153.3355557	U-velo	0	U-velo	121.480094
V-velo	0	V-velo	0	V-velo	0
W-velo	0	W-velo	0	W-velo	0
Energy	29697.27213	Energy	0	Energy	29727.77876
Mach	0.097424	Mach	0	Mach	0.077138

SUBSONIC (PIPES) (CASE C)

Inflow		Pipes		Outflow	
Density	0.013066498	Density	0.039323356	Density	0.013445426
U-velo	153.3355557	U-velo	0	U-velo	121.480094
V-velo	0	W-velo	50.95079845	V-velo	0
W-velo	0	W-velo	0	W-velo	0
Energy	29697.27213	Energy	119387.5174	Energy	30553.32435
Mach	0.097424	Mach	0.2427434	Mach	0.077138

INCOMPRESSIBLE (CASE D)

Inflow		Pipes		Outflow	
U-velo	2.003558732	U-velo	0	U-velo	0
V-velo	0	V-velo	17.40503091	V-velo	0
W-velo	0	W-velo	0	W-velo	0

geometry and dimensions of the entire device are shown in figure 5. This three-dimensional "slice" is repeated twenty times (in the direction perpendicular to the page) in order to make the entire device, so there are 20 large diameter nozzles and 40 small diameter nozzles in the COIL device. We simulate only one slice, as shown in the figure, and apply periodic boundary conditions along the third direction. A typical mesh employed in the supersonic case is shown in figure 6. It consists of 10,224 hexahedra

elements with 8 layers in the z- (periodic) direction of variable order as shown in the figure. The subsonic cases were simulated with similar meshes but with 7,312 hexahedra of constant polynomial order $p = 3$. The incompressible case was simulated on a mesh consisted of 3,066 tetrahedra with polynomial order $p = 6$.

The specific flow conditions we consider are described in table 3 (all units in metric system). We have simulated in detail the following four cases: (A) Supersonic flow corresponding to experimental case described as "9257cf11" in experiments with helium; (B) Subsonic flow without transverse (secondary) flow; (C) Subsonic flow; and (D) Incompressible flow. In all cases, the geometry remains identical and so is the primary incoming flow. Only the energy input and mass flowrate from the side pipes varies in cases (2) and (3), corresponding to zero and approximately one-eighth of the primary flow, respectively. In cases (A) and (D) the secondary flow is approximately one-fourth of the primary flow.

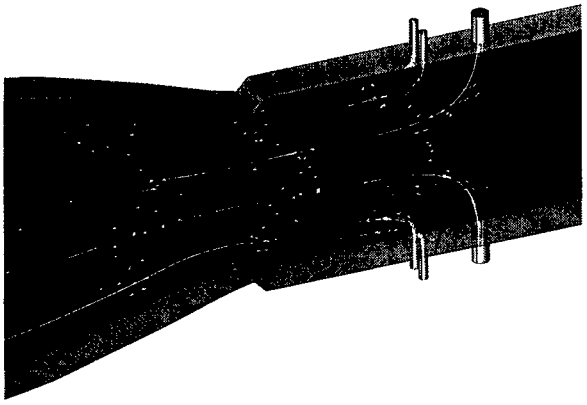


Figure 4. Streamlines in the central portion of the RADICL supersonic nozzle.

Based on systematic direct numerical simulations, we have concluded that unsteadiness is *suppressed* in the supersonic conditions similar to the ones employed in the experiments. A typical plot of Mach contours is shown in figure 7. Pressure distribution along the wall of the COIL as well as along the centerline of the COIL are shown in figure 8. Clearly, there is very good agreement of the high-order DGM results with available experimental data for the wall pressure in contrast with corresponding finite volume simulations performed here on the same mesh of figure 6 but with $p = 1$. These results were obtained from converged (in-time) simulations of the supersonic nozzle. To further examine the stability of the supersonic flow we in-

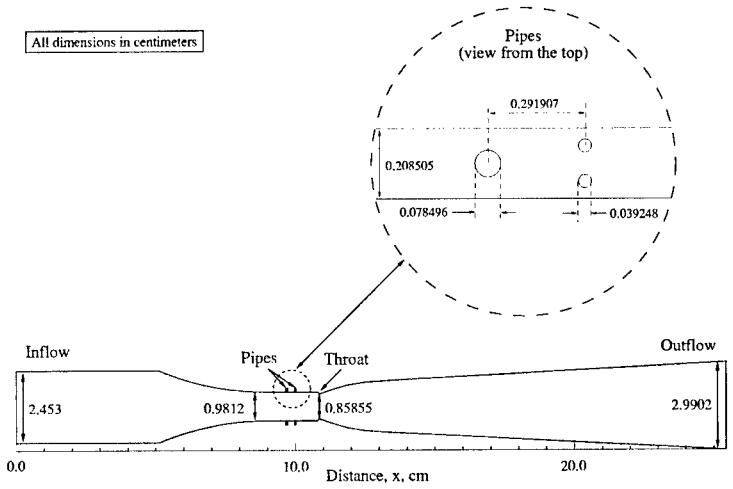


Figure 5. Geometry and dimensions of the COIL device.

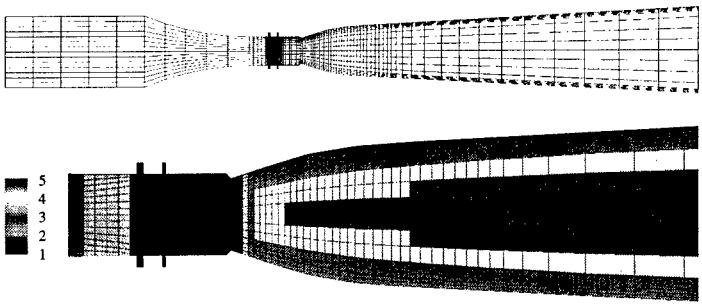


Figure 6. Mesh showing the macro-elements and corresponding polynomial order in the central part of the COIL (supersonic case).

troduced an abrupt and rather large perturbation into the flow in the form of forces in all three directions corresponding to $-8,322\,m/s^2$, $8,322\,m/s^2$ and $8,322\,m/s^2$ along the x-(streamwise), y-(crossflow) and z-(periodic)

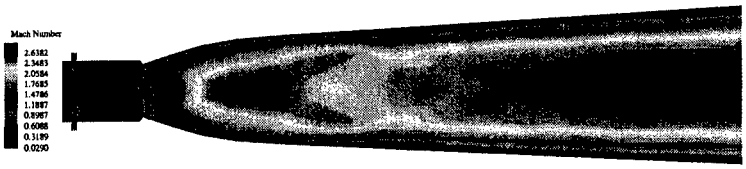


Figure 7. Mach contours in the supersonic RADICL nozzle.

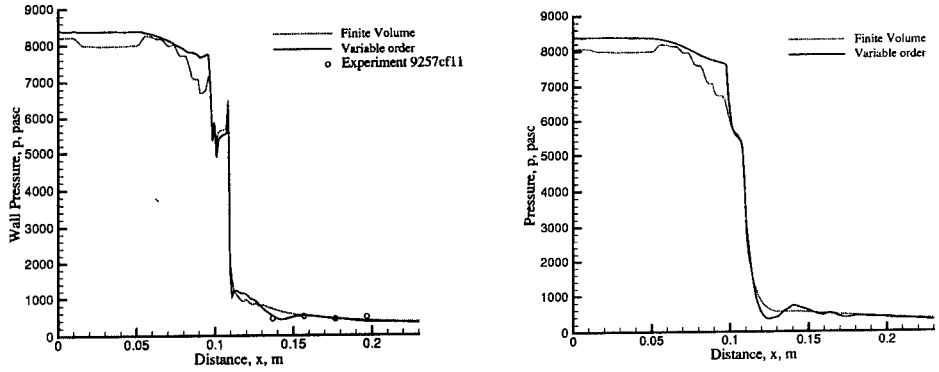


Figure 8. Pressure distribution along the wall and along the centerline for the supersonic case.

directions, respectively. This forcing was imposed for $2.39 \times 10^{-4}\, ms$ and subsequently it was removed while the simulation continued. A typical result of the response in the y-momentum is shown in figure 9. We see that indeed the flow returns to steady state within a short time interval.

Unlike the supersonic case, both subsonic cases we simulated converged to time-dependent flows while the incompressible flow transitioned to a turbulent state. A typical result is shown in figure 10 that plots Mach contours of the subsonic case with crossflow; a large scale unsteadiness is present. This is shown more clearly in figure 11 where we plot the time-histories of the y-momentum of both subsonic cases. The case without crossflow shows a stationary time-periodic flow whereas the subsonic flow with crossflow exhibits an additional modulation associated with the large scale unsteadiness. Therefore, it seems that the effect of crossflow is to suppress unsteadiness.

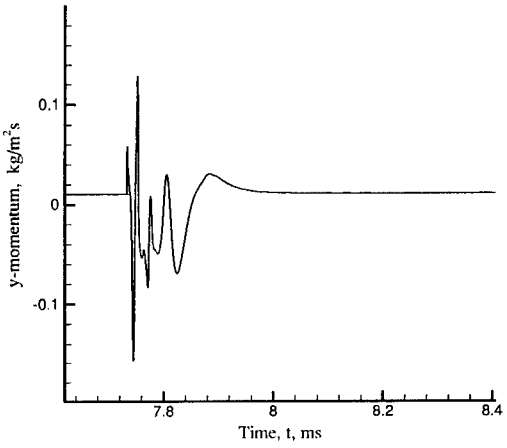


Figure 9. Time history of y-momentum for the supersonic nozzle.

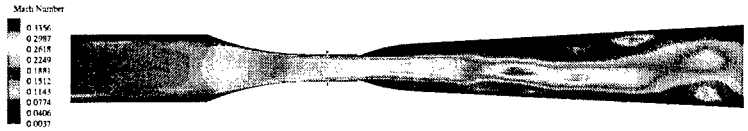


Figure 10. Mach contours for the subsonic case with crossflow.

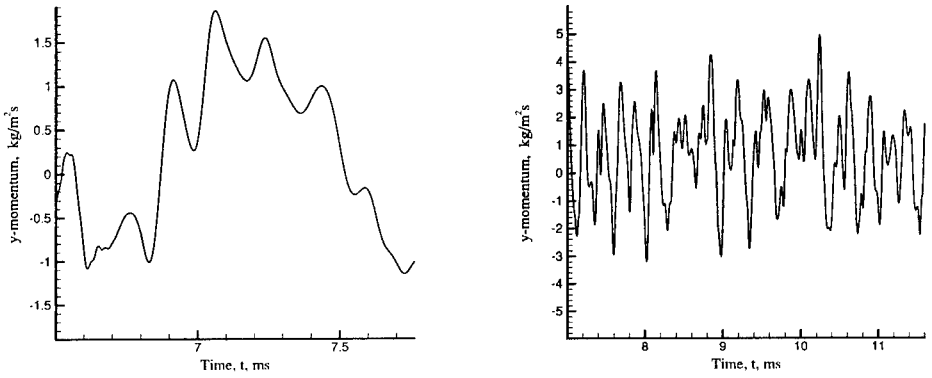


Figure 11. Time-history of y-momentum for the two subsonic cases, with crossflow (left), and without crossflow (right).

Finally, we conclude by commenting on the computational cost of the simulations. All simulations were run using an MPI-based parallel version of the method presented here with the partitioning based on a multi-level graph approach provided by the METIS software [10]. Specifically, the supersonic simulation was run on the IBM Power 3 with 0.6 seconds per time step on 80 processors, the subsonic simulations were run on the IBM Power 3 with 0.2 seconds per time step on 80 processors, and the incompressible simulation was run on the IBM SP 604e (silver nodes) with 10.7 seconds per time step on 64 processors.

Acknowledgments

This work was supported by AFOSR and computations were done on the TCASV Brown IBM SP3 and NPACI, and on the SGI O 2000 at NCSA. We would like to thank R. Canfield, T. Madden, J. Shang and J. Miller for useful discussions related to COILs.

References

1. B. Cockburn, G.E. Karniadakis, and C.-W. Shu. *Discontinuous Galerkin Methods: Theory, Computation and Applications.* Springer, 2000.
2. I. Lomtev, R.M. Kirby, and G.E. Karniadakis. A discontinuous Galerkin ALE method for viscous compressible flows in moving domains. *J. Comp. Phys.*, 155:128–159, 1999.
3. M. Dubiner. Spectral methods on triangles and other domains. *J. Sci. Comp.*, 6:345, 1991.
4. G.E. Karniadakis and S.J. Sherwin. *Spectral/hp Element Methods for CFD.* Oxford University Press, 1999.
5. J.H. Miller, J.S. Shang, R.F. Tomaro, and W.Z. Strang. Computation of COIL nozzle flowfields with transonic injection. In *AIAA-2000-2575*, 2000.
6. G.D. Hager, L.J. Watkins, R.K. Meyer, D.E. Johnson, L.J. Bean, and D.L. Loverro. A supersonic Chemical Oxygen-Iodine Laser. Technical report, Air Force Weapons Lab Technical Report 87-45, Kirtland AFB, NM, 1988.
7. M. Hishida, N. Azami, K. Iwamoto, W. Masuda, F.T. Atsuta, and M. Muro. Flow and optical fields in a supersonic flow Chemical Oxygen-Iodine Laser. In *AIAA 97-2391*, June 1997.
8. B.D.Barmashenko, D. Furman, E. Bruins, and S. Rosenwake. Iodine dissociation and small signal gain in supersonic COILS. In *AIAA 99-3427*, June 1999.
9. J.H. Miller, J.S. Shang, and T.J. Madden. Parallel computation of Chemical Oxygen/Iodine Laser flowfield. In *AIAA 2001-2869, 32nd Plasmadynamics and Lasers Conference, Anaheim, CA*, June 2001.
10. G. Karypis and V. Kumar. METIS: Unstructured graph partitioning and sparse matrix ordering system version 2.0. Technical report, Department of Computer Science, University of Minnesota, Minneapolis, MN 55455, 1995.

COUPLING DNS WITH POLYMER MODELS FOR FLOW CONTROL

RONALD D. JOSLIN
Applied Research Laboratory/Computational Mechanics Division
The Pennsylvania State University, State College, PA

Abstract
This paper discusses the coupling of polymer models with direct numerical simulation (DNS) toward understanding, modeling, and controlling turbulent boundary layer flows for drag reduction. Experiments have demonstrated that a dilute polymer solution injected into a turbulent flow can result in up to 80% drag reduction. Pipe, channel, and flat plate experiments are summarized to highlight similarities and differences in the flows associated with the polymer-induced drag reduction process. Constitutive and kinetic approaches to polymer modeling are then discussed with their respective couplings to DNS.

1. Introduction
Discussions concerning our physical understanding of the fluid dynamics phenomena we call turbulence are extremely controversial mainly because of our lack of irrefutable evidence to explain the flow. However, a couple of schools of thought have formed to explain the flow. One explanation follows a statistical evolution of flow based on averaged quantities and a that of energy cascades.[1] The second view describes turbulence within a deterministic coherent structures process that can be described by dynamical systems or flow stability analysis.[2] More recently, a workshop was held on the subject to further discuss the essence of turbulence.[3] These two schools still exist but with added insight brought about by research on the topic. Now, one school can be described as a *parent-offspring* vortex mechanism whereby the parent (initial) vortex interacts with the wall to induce secondary (offspring) vortices. The second mechanism involves a *flow instability* cyclic process, whereby streamwise vortices collect low speed streaks that cause inviscidly unstable velocity profiles. These views on turbulence serve as an introduction to this paper which focuses on the complex phenomena of non-Newtonian turbulent flows and flow control.

Specifically, our non-Newtonian flows are viscoelastic fluids.[4] The study of these flows involve both material science and fluid mechanics because it requires an understanding of rheological and mechanical properties and complex fluid flows. The rheological properties of the material determine the manner of deformation (or flow) subject to forces; the imposed deformation leads to internal stresses in the material. Typically this material flow, albeit non-

Newtonian, can be considered in many cases as a continuum flow. Such material flows may include toothpaste, paint, blood, oil, cookie dough, soap solutions, and cosmetic flows. Here, for brevity, we will "glaze over" all details associated with particular materials and their properties and resulting influence of these properties on the resulting fluid dynamics. Here, our focus is on non-Newtonian turbulent polymer/water solutions from the fluid mechanics point of view for viscous drag reduction.

This paper is not intended to be a review or summary of the many important papers that have used polymer solutions for skin friction drag reduction. The reader can refer to a bibliography for some 4900 publications on the topic[5] and the excellent texts by Bird et al.[6,7] Instead, only some of the key physical phenomena found from the various experiments will be emphasized for benefit of the modeling activities. All researchers currently agree that the mechanism for drag reduction by polymers remains illusive.

1.1 Polymer Pipe Experiments:

Although many studies of particles and polymers in fluids were documented well before the observations of Toms[8] in 1948, skin friction reductions associated with dilute polymer solutions in turbulent pipe flow are typically referred to as Toms phenomena. By looking at the number of publications since Toms observation, it is clear that much progress has been made toward the understanding of the phenomena. There are some commonly observed features in such flows that are highlighted in this introduction.

For pipe flows, a significant advancement was made by Virk,[9,10] whereby experimental data was analyzed to arrive at a universal asymptote (that is applicable for all polymer solutions). This asymptote reflects the maximum drag reduction possible for pipe flows. Three connected regions across the pipe were identified. The "viscous" zone near the wall was postulated to be essentially the same for both Newtonian and non-Newtonian flows. Near the center of the pipe, the "Newtonian turbulent" zone is shifted upward with increased drag reduction. Finally, the "interactive" (or buffer) zone connects the two other zones and is extended upward with increased drag reduction. Maximum drag reduction occurs when the interactive zone extends to the pipe axis. Concerning turbulence statistics, laser Doppler velocimetry measurements (rms) show that the axial velocity component increased, the radial velocity component decreased, and the Reynolds stress decreased, while the peak profile moved away from the wall.[11] The movement of the peak corresponds to an increase in the size of the buffer region.

Finally, pipe drag reduction can take two forms.[12] This discussion so far has focused on homogeneous drag reduction. The second form is termed heterogeneous and involves drag reduction associated with injecting polymer

solutions into the core of the pipe. Little mixing is observed and the drag reduction is not associated with polymers influencing the wall region.

1.2 Polymer Channel Flow Experiments:

Particle image velocimetry measurements showed a 40% drag reduction in channel flow[13] using only 3.5 wppm (weight-part-per-million) solution and suggested that the streamwise vorticies are enlarged as a result of the addition of polymers. The streamwise fluctuation levels increased for low-drag reductions and decreased for high-drag reduction test cases. The increased drag reduction was achieved by increasing the polymer concentration.[14] Other experiments[15] showed increased streamwise velocity fluctuations and decreased Reynolds stress levels. With drag reduction, the bursting rate per unit area decreased and a total absence of small scale structure was observed during a burst event.[16] Measurements[17] indicate that the near-wall streaks can double, triple and even quadruple in spanwise extent and therefore the spanwise scaling indicates an increase in the size of the large-scale structures. Drag reduction phenomena for the channel is very much like the pipe flow problem. Experiments in the channel showing variation in concentration recorded a 69% drag reduction and velocity profiles that closely approached Virk's ultimate asymptote.[14]

1.3 Polymer Turbulent Flat Plate Experiments:

The flat plate boundary layer flow has many characteristics comparable to the pipe and channel flows. These include an increase in the streamwise rms velocity, decrease in the wall-normal rms velocity, and decrease in the Reynolds stress for polymer solutions.[18-20] However, the flat plate flow is an external flow so diffusion plays a significant role in the degradation of polymer-induced drag reduction. The drag reduction is decreased with distance downstream because of the movement of polymers away from the wall. The polymer concentration was shown to exponentially decrease with downstream distance.[21] For the boundary layer, initial, intermediate, transition and final zones can be outlined to classify the polymer-induced effects in the flow.[22] The initial zone is near the injector and is a region of large concentration gradients. Next, the intermediate zone has self-similar concentration profiles and lasts approximately 18 boundary-layer thicknesses downstream of the initial zone. The transition zone has non-similar concentration profiles and an increasing diffusion layer. Beginning about 60 boundary layer thicknesses downstream of the initial zone, the final zone has self-similar concentration profiles but the amount of drag reduction is continually decreasing with downstream distance. So although there are similarities between the pipe, channel and boundary layer, the boundary layer has an increased complexity because of diffusion.

1.4 Benefits:

Experimental results using polymers have demonstrated a drag reduction of 40-70% in turbulent pipe flows[23,24] and 50-70% for flows on flat plates.[18,25] The success in pipe flows has resulted in over 80 projects using polymers for oil pipe

lines; the Trans Alaskan Pipeline uses polymers to reduce the required number of pumping stations from 12 to 10 to move oil over 1200 km.[23] For external flow applications, the projected benefits of drag reduction are enormous for military and commercial ships. For example, let us estimate the benefits to the M/V AIVIK, which operates around the world. The ship is over 109 m long, weighs some 7000 metric tons fully loaded, and has a top speed of 13 kts. With a 50% reduction in the drag, the speed of the vehicle increases to approximately 17-18 kts. A trip of 13,000 miles (say New York to South Africa) would take 26 days instead of 35 days, which saves 9 days (25%) in transport time. In addition there would be a fuel savings of 20-25%, somewhat offset by the polymer system.

1.5 Mechanisms for Drag Reduction:

As two schools exist to explain the physics of turbulent flows, two leading postulations exist for drag reduction caused by dilute polymer solutions. The first maintains that unraveling and elongation of the polymer chain (extension) is the key process affecting the turbulence and results in a drag reduction. The second claims that elasticity is the mechanism, whereby the stress of a viscoelastic fluid generally is not in phase with the strain rate. As with turbulence alone, no conclusive evidence exists (as yet) to support either postulation.

2. DNS

Some good analytical correlations with the experimental data have been developed for polymer solutions. However, for brevity and to remain in alignment with the focus of this conference, we proceed directly to the link between polymer models and direct numerical simulations (DNS).

The Navier-Stokes equations can be implemented in numerous forms.[26] Here, the velocity-pressure equations in full form are simply listed, including the affect of polymer models. The Navier-Stokes equations are given as

$$\frac{\partial u_i}{\partial x_i} = 0, \quad \rho\frac{\partial u_i}{\partial t} + \rho u_j \frac{\partial u_i}{\partial x_j} = -\frac{\partial p}{\partial x_i} + \frac{\partial}{\partial x_i}(\tau_{ij}) + F \qquad (1)$$

Any equation that assigns values to τ_{ij} is a *constitutive* equation; F may be a polymer-induced body force. The constitutive equation can be decomposed into Newtonian and non-Newtonian (polymer) contributions, such that $\tau_{ij} = \tau_{ij}^N + \tau_{ij}^P$. There are many publications documenting the DNS solutions and therefore we proceed directly into the polymer modeling activity.

3. Polymer Models

Implementation of constitutive models with DNS has a complexity similar to the coupling of the DNS with optimal control theory.[27] DNS and optimal control theory involves Navier-Stokes equations and an equal number of adjoint Navier-Stokes equations combined with a simple optimality condition equation. This leads to a system of nine equations that can be solved for a limited number of applications because of the extreme computational cost. The cost may increase by a factor of 2-10 compared with the DNS cost alone. The DNS and polymer models have similar issues associated with increased complexity and computational cost combined with some model parameters that may be extremely difficult to correlate with experiments. In this section, Eulerian and Lagrangian approaches to modeling polymer flows are highlighted. Some of our preliminary results are also discussed where the primary focus here is the assessment of the cost of the models. Our ultimate goal is coupling the models with DNS to study the turbulent flat plate boundary layer drag reduction phenomena.

3.1 *Constitutive Models:*

Constitutive models for polymer/water solutions have been formulated using stress tensor transport equations to predict the impact of polymers on turbulence within an Eulerian construction (similar to the Navier-Stokes framework). For non-Newtonian fluid flows, the simplest relationship between the shear stress and strain rate is given by a power-law model, $\tau_{ij}^{p} = \kappa \dot{\gamma}_{ij}^{n}$. For a Newtonian fluid, $n=1$; for a pseudoplastic (e.g., polymer solution), $n<1$; and for a dilatant (e.g., corn starch and water solution), $n>1$. For the Newtonian flow, the slope of the curve simply becomes the viscosity $\kappa = \mu$. The impact of the nonlinear (non-Newtonian behavior) for a polymer solution is elevated viscosity near the wall and shear thinning.

Polymeric fluids are often referred to as viscoelastic fluids because such fluids are associated with nonlinear effects and time-dependent properties. Such fluids typically have memory effects. Hence, continuum polymeric fluid models should accommodate terms which retain past states. However, approaches which model dilute solutions of polymers in water may not require the retention of all terms (memory) of past states. In our research a host of models ranging from low to high fidelity, linear to nonlinear, and pseudo-steady to those retaining past states (memory) of the solution are being compared for use in simple steady to fully turbulent flows.

A breadth of models have been used to describe the polymer flows, primarily associated with viscoelastic steady or simple oscillatory flows which have numerous industrial applications.[28] The general classes of these models can be

summarized as generalized Newtonian, linear viscoelastic, and kinetic.[6] Generalized Newtonian constitutive models are low-fidelity models that simply modify the shear stress in a nonlinear manner. These are valid for steady shear flows only, but have often been used for many different steady and unsteady flows. Slightly higher in fidelity, the linear viscoelastic models incorporate some measure of elastic effects on the flow. This is achieved by introducing a relaxation time t_1. The Maxwell model is probably the most famous of these constitutive equations. The model states that the stress at time t is related to the rate of strain at time t and all prior times, with a decay of the influence of all other past times. These models cannot describe the shear-rate dependence of viscosity, nonlinear normal stress phenomena, nor large-displacement small-strain phenomena. The models neglect past kinetic events. However, such models can give shear-rate dependent viscosity.

The Oldroyd 8-constant model[29] for the constitutive equation can be implemented to represent many models. The full form is

$$\tau + \lambda_1 \tau_{(1)} + \frac{\lambda_3}{2}(\dot{\gamma}\cdot\tau + \tau\cdot\dot{\gamma}) + \frac{\lambda_5}{2} tr(\tau)\dot{\gamma} + \frac{\lambda_6}{2}(\tau:\dot{\gamma})\delta \qquad (4)$$

$$= -\eta_0\left(\dot{\gamma} + \lambda_2 \gamma_{(2)} + \lambda_4\{\dot{\gamma}\cdot\dot{\gamma}\} + \frac{\lambda_7}{2}\{\dot{\gamma}:\dot{\gamma}\}\delta\right)$$

where λ_{1-7} are time constants and η_0 is the zero-shear-rate viscosity. For $\lambda_{1-7} = 0$, the Newtonian model is recovered; for $\lambda_{3-7} = 0$, the convected Jeffreys model (or Oldroyd-B) is obtained; for $\lambda_{2-7} = 0$, the convected Maxwell model is obtained. So, many different models may be explored through this one general 8-constant model.

The turbulent flow of interest is time-dependent, extremely dynamic, and non-homogeneous. The extrapolation and enhancements of the various non-Newtonian models to predict and understand the drag reduction associated with polymer solutions is our goal. Previous work with the power-law class of models (a viscous anisotropic model) relying on elongated polymers aligned always parallel to the velocity field, showed drag reduction and turbulent statistics that were in qualitative agreement with the pipe flow experiments.[11] For a Maxwell class of models, a viscoelastic anisotropic model showed drag reduction and turbulent statistics in qualitative agreement with experiments for pipe flow, except the peak of the rms velocities moved toward the wall; the simpler viscous anisotropic model was in better agreement with experiments.[11] The comparison between the various models and complex issues associated with numerical stability and boundary/initial conditions will be left to a future paper; however, in section 3.3, a brief discussion is given concerning the cost of these models linked with DNS.

3.2 *Kinetic Models:*

For polymer-induced turbulent drag reduction, the kinetic models track the macromolecule polymer dynamics through a Lagrangian framework coupled with the Eulerian DNS. Because this is a coupled problem, the flow transports and stretches/deforms the polymers, and the polymers in turn affect the viscosity, shear, and turbulence production phenomena. Because the polymers can have different scales than the turbulence, multiple time and spatial scales exist for the coupled polymer-turbulent flow. Typically the spatial scales for polymers are orders of magnitude smaller than the turbulent flow scales. Although the time-evolution process for polymer motion may be much smaller than turbulence, there appears to be an overlap region that is important to realize drag reduction.

An important parameter in characterizing macromolecule-type drag reduction is related to the polymer relaxation time t_l. Experiments[30] using laser-light scattering suggest that the polymers stretch out in the turbulent flow when sufficient stress (due to high strain rate) is encountered in the flow. A significant drag reduction is observed when this stretching process occurs. It has been suggested that a polymer-eddy interaction occurs when the relaxation time of the polymer is comparable to the small-scale eddy turnover time. The relaxation time is related to the molecular weight of the polymer. For low concentrations this interaction of polymer and turbulence leads to drag reduction and for high concentrations drag reduction primarily results from the viscous effects of polymer solutions. However, only small concentrations are required for drag reduction and, to minimize system penalties, small concentrations are clearly the goal. For non-Newtonian fluids (viscoelastic), the Deborah number[31,32] (De) becomes important and is defined as the ratio of elastic to viscous time scales. The Deborah number is defined as $De = t_1/T = \dot{\varepsilon} t_1$ where t_1 is the largest time constant for the slowest molecular motion (relaxation time), T is the time constant of the flow system, or solution, and $\dot{\varepsilon}$ is the elongation rate. For $De \to 0$, the flow system behaves as a Newtonian fluid, and for $De \to \infty$ the fluid behaves like a Hookean-elastic solid. Typically for polymer solutions, $t_1 \approx 10^{-3} s$ for dilute solutions and $t_1 \approx 10^{3} s$ for concentrated solutions. For the turbulent boundary layer, the characteristic time scale of the flow is approximately $T = \delta/U_\infty$ (boundary layer thickness/free-stream velocity). Rheological measurements have clearly shown that the elongation rate $\dot{\varepsilon}$ is a very useful parameter in examining the viscoelastic behavior of polymer solutions. Essentially, when $\dot{\varepsilon}$ increases and reaches a critical value $\dot{\varepsilon}_c$, the properties of the polymer dramatically change in that the polymers experience a "fully-stretched chain state." Experiments with simple flows suggest this to occur near $De \approx 1$. The dependence of this critical elongation rate has been shown to relate to the monomer chain length N and molecular weight M as

$\dot{\varepsilon}_c \propto N^a \propto M^a$. For good solvents, a=-1.8 has been suggested and a=-2.3 has been found using Monte Carlo simulation techniques.

As the strain rate reaches a second critical point, the stretched out chain ruptures. This rupture process has been shown to be a function of molecular weight in steady shear flow[33] (and will most likely be related to the specific polymer as well). Computationally, a rupture analysis may be investigated by either varying the maximum distance of the beads prior to a "rupture" and/or analyzing the local strain rate versus molecular weight versus peak forces for the polymers.
A widely used model in the Lagrangian framework is referred to as the "dumbbell model." The kinetic force balance equations are in general represented by multiple beads (mass foci) connected by springs (resistive force). A promising yet simple bead-spring model is the FENE (finite-extensible nonlinear elastic) model (or variation thereof). The transport equation for this model operates in a Lagrangian reference frame, and hydrodynamic force corrections are added. So, all macromolecules must be tracked in the simulation.

Here, we use the rigid-mass and elastic dumbbell models to assess the relative importance of the elongation/stretching process for the polymer macromolecules. These models are sufficiently complex to capture the decrease in viscosity with strain rate, which will be important for the turbulent boundary layer flow. Although the polymer may be modeled with a number of beads, a two-bead dumbbell model would have masses (m_1, m_2) with radii (a_1, a_2) located by position vectors (r_1, r_2) relative to the origin of the laboratory reference frame. The dynamic state of a dumbbell can be instantaneously specified with the position vectors and the velocities of the bead.

Instead of developing constitutive models, the Lagrangian approach tracks individual macromolecule polymers, assessing the two-way coupling effects of flow on polymer and polymer on flow. An equation of motion for each bead of the macromolecule can be given as

$$\frac{\partial r}{\partial t} = u_p, \qquad m\frac{\partial u_p}{\partial t} = -\zeta(u_p - u) - k_b T\frac{\partial}{\partial r}(\ln \Psi) + F$$
$$\frac{\partial \Psi}{\partial t} = -(R\cdot\nabla u)\cdot\frac{\partial \Psi}{\partial R} + \frac{2k_bT}{\zeta}\frac{\partial}{\partial R}\cdot\frac{\partial \Psi}{\partial R} + \frac{2}{\zeta}\frac{\partial}{\partial R}\cdot F\Psi \qquad (5)$$

where k_b is the Boltzman constant, T is the temperature, R is the configuration vector between two adjacent beads, and ζ is the friction coefficient for a single bead. Following Stoke's law, this becomes $\zeta = 6\pi\mu a$. The scalar distribution function ψ is a sum of contributions from the hydrodynamic force, the Brownian motion force, the force through the internal resistance, and force due to collisions.[34] Initially, we will take the internal behavior of the macromolecule as

governed by the finite extendable nonlinear elastic (FENE) dumbbell model.[7] The force law relationship for the flexible macromolecule is

$$F = \frac{KR}{1-(R/R_0)^2} \qquad (6)$$

where R_o is the maximum distance the beads can displace (or elongate), and $K=k_bT/N^{6/5}a^2$ is the spring constant as a function of temperature T and number of monomers N. Alternate internal force law relationships will be investigated in a future paper.

After solving equations (5-6), the non-Newtonian stress contribution can be determined from

$$\tau^P = -n\langle RF\rangle + nk_bT\delta \text{ with } \langle RF\rangle = \int_V RF\Psi \qquad (7)$$

where n is the number density of dumbbells and $\langle RF\rangle$ is the volume-average value of the dynamical quantity RF. The terms on the right are from tension in the connectors and bead motion, respectively. The forces acting on the macromolecule act within the distribution function equation as well.

Using the FENE construct, a constitutive model has been developed and evaluated for turbulent channel flow.[35,36] The model qualitatively agreed with experiments, indicating that extensional viscosity plays a role in drag reduction. Key results of the model included an increase in the streamwise rms velocity and decrease in the wall-normal and spanwise rms velocities, in addition to a decrease in the streamwise vorticity fluctuations. The model also predicted an increase in the size of the mean streamwise vortex structure consistent with the experiments. These non-Newtonian computations within the constitutive approach can require 15 times the computational cost of turbulent simulations alone.[35] In a different study using a Lagrangian-particle tracking approach, turbulent channel flow simulation results with the FENE model indicated that the polymer chain unravels to about 87% of the fully extended length and is oriented at about 7° to the flow direction.[13] This later result will be useful in the validation of our investigations.

3.3 *Costs Polymer Model:*

In this section, preliminary cost estimates are provided for both the constitutive model and macromolecule. For this paper, extra stress tensor transport equations are implemented and cost estimates are provided for the Giesekus, FENE-P, and convective Jeffreys models. Table 1 shows the cost of the non-Newtonian models normalized by the DNS cost for a 32x32x32 grid on a 500MHz Beowolf single processor. Because the non-Newtonian models add six additional equations, the cost increases to slightly more than a factor of two over the DNS computational cost. The difference in the cost of various models results from any simplifications that may arise in equation (4).

Table 1. Normalized computational cost of constitutive equations (courtesy of Nathan Grube).

non-Newtonian model	Cost
DNS/Giesekus	2.28
DNS/FENE-P	2.35
DNS/Convected Jeffreys	3.23

For the Lagrangian evolution equations (5-6), Table 2 displays the time required for tracking the macromolecule evolution in a stationary fluid using a 333 MHz processor. For a given number of monomers, there is a one-to-one cost increase with the increase in the number of polymers after 100 polymers are modeled. These initial results for a simplified force model (internal forces and sinusoidal imposed force) yields some insights into the cost with number of polymers and monomers compared with the fully coupled system. The diffusion equation implementation has increased the cost of computation three-fold over model problem cost (Table 2). Note, that no optimization of the code has been attempted at this point.

The true cost of the macromolecule model coupled with the DNS approach for the turbulent boundary layer flow problem will depend on the molecular weight, number of monomers in the model, the flow Reynolds number, concentration of polymers, etc. We can get a preliminary estimate of the polymer requirements for this problem by selecting an initial test case. Choose a Reynolds number based on displacement thickness (δ^*) of 1000. The domain has $100\delta^*$, $20\delta^*$, and $20\delta^*$ for the streamwise, wall-normal, and spanwise directions. Assuming the polymer has a molecular weight of 1 million, a density of 2 g/cm^3, a concentration of 1%, the simulation must track approximately 1 million polymers. Although more complete information on the polymer properties is needed to refine this estimate, this simple analysis combined with the computational cost estimate below indicates that it should be feasible to solve this complex Eulerian/Lagrangian system.

Table 2: Computation time for polymer systems (courtesy of Scott Austin).

# Polymer Masses	# Polymers	Computation Time (sec)
2	10^0	0.371E-03
	10^1	0.117E-02
	10^2	0.998E-02
	10^3	0.953E-01
	10^4	0.953E+00
	10^5	0.956E+01
3	10^0	0.398E-03
	10^1	0.155E-02
	10^2	0.134E-01
	10^3	0.133E+00
	10^4	0.135E+01
	10^5	0.174E+02
5	10^0	0.430E-03
	10^1	0.221E-02
	10^2	0.206E-01
	10^3	0.199E+00
	10^4	0.204E+01
	10^5	0.203E+02

4. Conclusions

This paper has summarized the experimental observations associated polymer-induced drag reduction in turbulent pipe, channel, and flat plate flows. With drag reduction, the 'interactive" (or buffer) region increases in extent and moves away from the wall, the streamwise rms velocity increases, the wall-normal (radial) rms velocity decreases and the Reynolds stress decreases. Furthermore, the large-scale structures increase in size.

The discussion has focused on coupling DNS and polymer models toward understanding, modeling, and controlling turbulent boundary layer flows for drag reduction. Preliminary estimates suggest that a factor of 2 or more time is required to compute the non-Newtonian problem.

Acknowledgement

This material is based upon work supported by the DARPA under Contract No. MDA972-01-C-001, Dr. Parney Albright, Program Manager. This research is being conducted jointly with Dr. Thomas S. Chyczewski, Mr. Nathan Grube, and Mr. Scott Austin at PSU/ARL.

References

[1]Lesieur, M. (1987) Turbulence in Fluids: Stochastic and Numerical Modelling. Kluwer Academic Publishers Group: Boston.

[2]Panton, R. L. (1999) Self-sustaining mechanisms of wall turbulence – A review. AIAA Paper 99-0552, January 1999.

[3]Panton, R. L. (ed) (1997) Self-Sustaining Mechanisms of Wall Turbulence. Computational Mechanics Publications, Boston.

[4]Darby, R. (1976) Viscoelastic Fluids: An Introduction to their Properties and Behavior. Marcel Dekker: New York.

[5]Nadolink, R. H., Haigh, W. W. (1995) Bibliography of skin friction reduction with polymers and other boundary-layer additives. *Appl. Mech. Rev.*, Vol. 48, No. 7, July, pp. 351-460.

[6]Bird, R. B., Armstrong, R. C., Hassager, O. (1987) Dynamics of Polymeric Liquids. Vol.1 Fluid Mechanics. John Wiley & Sons: New York.

[7]Bird, R. B., Hassager, O., Armstrong, R. C., Curtiss, C. F. (1977) Dynamics of Polymeric Liquids. Vol. 2. Kinetic Theory. John Wiley & Sons: New York.

[8]Toms, B. A. (1948) Some observations on the flow of linear polymer solutions through straight tubes at large Reynolds numbers. *Proc. 1st Int. Congress on Rheol.*, pp. 135-141.

[9]Virk, P. S., Mickley, H. S., Smith, K. A. (1970) The ultimate asymptote and mean flow structure in Toms' phenomena. *Trans. ASME J. Appl. Mech.*, Vol. 37, June, pp. 488-493.

[10]Virk, P. S. (1975) Drag reduction fundamentals. *AIChE J.*,Vol. 21, No. 4, July, pp. 625-656.

[11]Den toonder, J. M. J., Hulsen, M. A., Kuiken, G. D. C., Nieuwstadt, F. T. M. (1997) Drag reduction by polymer additives in a turbulent pipe flow: Numerical and laboratory experiments. *J. Fluid Mech.*, Vol. 337, April 25, pp. 193-231.

[12]Hoyer, K. W., Gyr, A. (1996) Heterogeneous drag reduction concepts and consequences. *FED-Vol. 237*, II, pp. 151-158.

[13]Massah, H., Liu, Z. C., Hanratty, T. J., Adrian, R. J., A. (1996) Report on PIV measurements in a drag-reducing turbulent flow. *FED-Vol. 239*, pp. 101-108.

[14]Warholic, M. D., Massah, H., Hanratty, T. J. (1999) Influence of drag-reducing polymers on turbulence: Effects of Reynolds number, Concentration, and mixing. *Exp. Fluids,* Vol. 27, pp. 461-472.

[15]Walker, D. T., Tiederman, W. G. (1990) Turbulent structure in a channel flow with polymer injection at the wall. *J. Fluid Mech.*, Vol. 218, pp. 377-403.

[16]Walker, D. T., Tiederman, W. G., Luchik, T. S. (1986) Optimization of the injection process for drag-reducing additives. *Exp. Fluids*, Vol. 4, No. 2, pp. 114-120.

[17]Donohue, G.L., Tiederman, W. G., Reischman, M. M. (1972) Flow visualization of the near-wall region in a drag-reducing channel flow. *J. Fluid Mech.*, Vol. 56, No. 3, pp. 559-575.

[18]Fontaine, A. A., Petrie, H. L., Brungart, T. A. (1992) Velocity profile statistics in a turbulent boundary layer with slot-injected polymer. *J. Fluid Mech.,*Vol. 238, pp. 435-466.

[19]Petrie, H. L., Fontaine, A. A. (1996) Comparison of turbulent boundary layer modifications with slot-injected and homogeneous drag-reducing polymer solutions. *FED-Vol. 237,* pp. 205-210.

[20]Hoyt, J.W. (1998) Polymer Solution Effects on Turbulent Friction Mechanisms. *Proc. Int. Symp. on Seawater Drag Reduction.* pp. 1-5.

[21]Vdovin, A. V., Smolyakov, A. V. (1982) Turbulent diffusion of polymers in a boundary layer. *Zh. Prikl. Mekh. Tekh. Fiz.*, Vol. 4, pp. 98-104. (Trans. UDC 532.526, 1982, Plenum, pp. 526-531)

[22]Poreh, M., Cermak, J. E. (1964) Study of diffusion from a line source in a turbulent boundary layer. *Int. J. Heat Mass Transfer*, Vol. 7, pp. 1083-1095.

[23]Motier, J. F., Chou, L.-C., Kommareddi, N. (1996) Commercial Drag Reduction Past, Present, and Future. *FED-Vol. 237,* pp. 229-234.

[24]Gasljevic, K., Matthys, E. F. (1996) Field test of a drag-reducing surfactant additive in a hydronic cooling system. *FED-Vol. 237,* pp. 249-260.

[25]Petrie, H. L., Brungart, T. A., Fontaine, A. A. (1996) Drag reduction on a flat plate at high Reynolds number with slot-injected polymer solutions. *FED-Vol. 237,* pp. 3-9.

[26]Joslin, R. D. (2001) Using DNS for Active Flow Control. AIAA Paper 2001-2544.

[27]Joslin, R. D., Gunzburger, M. D., Nicolaides, R. A., Erlebacher, G., Hussaini, M.Y. (1997) Self-contained automated methodology for optimal flow control. *AIAA J.,* Vol. 35, No. 5, May, pp. 816-824.

[28]Schleiniger, G., Weinacht, R. J. (1991) Steady Poiseuille flows for a Giesekus fluid. *J. Non-Newtonian Fluid Mech.,* Vol. 40, pp. 79-102.

[29]Oldroyd, J. G. (1958) Non-Newtonian effects in steady motion of some idealized elasticoviscous fluids. *Proc. Roy. Soc. London A*, Vol. 245, pp. 278-297.

[30]Bhat, S. K. P., Pal, K., Chopra, S. (2000) A study of intermittency and drag reduction in turbulence by dynamic laser light scattering. *Exp. Fluids,* Vol. 28, pp. 160-164.

[31]Bird, R. B. (1965) Experimental tests of generalized Newtonian models containing a zero-shear viscosity and a characteristic time. *Can. J. Chem. Eng.*, Vol. 43, No 3, pp. 161-168.

[32]Reiner, M., The Deborah Number. *Physics Today,* 17, January 1964: 62.

[33]Keller, A., Odell, J. A. (1985) The extensibility of macromolecules in solution; A new focus for macromolecular science. *Coll. & Poly. Sci.*, Vol. 263, pp. 181-201.

[34]Van den Brule, B. H. A. A. (1993) Brownian dynamics simulation of finitely extensible bead-spring chains. *J. Non-Newtonian Fluid Mech.*, Vol. 47, pp. 357-378.

[35]Sureshkumar, R., Beris, a. N. (1997) Direct numerical simulation of the turbulent channel flow of a polymer solution. *Phys. Fluids,* Vol. 9, No. 3, March, pp. 743-755.

[36]Beris, A. N., Dimitropoulos, C. D., Sureshkumar, R., Handler, R. D. (2000) Direct numerical simulations of polymer-induced drag reduction in viscoelastic turbulent channel flows. *XIIIth Int. Congr. Rheol.,* Cambridge, UK, pp. 2.190-192.

DIRECT NUMERICAL SIMULATION OF TRANSITION IN COMPRESSIBLE FLOWS

N. A. Adams
ETH Zürich, Institute of Fluid Dynamics,
ETH Zentrum, CH-8092 Zürich, Switzerland
Nikolaus.Adams@ethz.ch

Abstract In this paper we present first results on the transition of the separated boundary layer along a compression ramp at Mach 5 as an example for today's capabilities of direct numerical simulation of transition in complex shear flows. The computational method is based on the 5th order hybrid compact-ENO method of Adams and Shariff, 1996. The flow parameters of the considered configuration are adjusted to an experimentally feasible configuration. The shock-induced laminar separation extends for about 20 incoming-boundary-layer thicknesses. We find that for the two-dimensional solution following a two-dimensional second mode instability imposed at inflow the unsteady fluctuations with respect to the mean remain small upto rather large excitation levels of the inflow disturbance. No indications for a global instability of the two-dimensional steady solution have been found so far. Even at large inflow-disturbance excitation levels the two-dimensional flow exhibits a split into a nearly steady solenoidal part and an unsteady acoustic part. If in addition to the second mode an unstable first oblique mode is imposed at inflow, streamwise vortices are generated in the detached shear layer.

1. Introduction

An example for the importance of transition in aerodynamic configurations is the effectiveness of control surfaces of re-entry vehicles whose flight corridor passes through a regime of comparably low Reynolds number (Muylaert and Berry, 1998; Berry et al., 1999). Also, down-sized experimental vehicles or rescue vehicles can exhibit laminar or transitional flows along most of their body surface during re-entry since at supersonic and hypersonic speed transition is delayed. For incompressible boundary layers transition mechanisms are fairly well understood (Kleiser and Zang, 1991; Kachanov, 1994). Transition in compressible boundary-

layers was subject of intense investigations in the recent past (Thumm et al., 1990; Pruett and Zang, 1992; Pruett et al., 1995; Pruett and Chang, 1995; Pruett and Chang, 1998; Eißler and Bestek, 1996; Adams and Kleiser, 1996; Mielke, 1999; Mielke and Kleiser, 1999, e.g.). To our knowledge only very few initial studies have been performed so far on transition in supersonic boundary layers with shock-boundary-layer interaction (Pagella et al., 2000; Lawal and Sandham, 2001). Linearized theories for compressible turbulence (Kovasznay, 1953) and shock-turbulence interaction (Ribner, 1953; Ribner, 1954) were early theoretical developments. From these it is known that the interaction with a shock-wave couples the otherwise independent linear modes (vorticity mode, acoustic mode, entropy mode).

The laminar base flow along a supersonic compression ramp with sufficiently large deflection exhibits an area of separated flow which is considerably larger than that for turbulent flow (Adamson and Messiter, 1980). Simplified linear stability analysis such as for zero-pressure gradient boundary layers cannot be performed for the compression ramp flow. The dominant transition mechanisms for this configuration are unknown. For separated flows a global eigenmode analysis was proposed by Theofilis et al., 2000.

With the numerical study, for which we present first results in this paper, we assume that transition takes place in a low-noise environment. We expect that receptivity near the leading edge initiates a "natural" transition through the most unstable linear eigenmodes of the laminar attached boundary layer. The flow parameters of our setup are adjusted to that of a planned experiment (see section 2) which is a generic model for the flow encountered near the body flap of a re-entry vehicle. For a flat-plate boundary-layer at high free-stream Mach numbers two instability modes of different character coexist, the first-mode instability which is of vorticity character, and the second-mode (or Mack-mode) instability which is of mixed vorticity-acoustic type (Mack, 1984; Mack, 1990). Whereas the former is oblique, i.e. it travels downstream at an angle with respect to the freestream, the dominant second mode instability is two-dimensional. The relevance of the second mode for laminar-turbulent breakdown is unclear at present (Stetson and Kimmel, 1992; Pruett and Chang, 1998, e.g.). It is known that these two types of instabilities behave differently with respect to boundary-layer non-parallelity (El-Hady, 1991) and wall-heating (Mack, 1984).

A two-dimensional second mode instability cannot initiate transition without a secondary instability mechanism which most likely follows a subharmonic or H-type route (Pruett and Zang, 1992; Adams and Kleiser, 1996). For the first mode a secondary instability mechanism is

Parameter	Value	Comment
M_∞	5	
Re_{δ_0}	5967	at inflow
Re_{δ_1}	4319	at inflow
δ_1^*	$6.84 \cdot 10^{-4}$	$[m]$, at inflow
T_∞^*	83.33	$[K]$
T_W	$4.8\ T_\infty^*$	
S^*	$110.4K$	
U_∞^*	915	$[m/s]$
p_∞^*	945	$[Pa]$

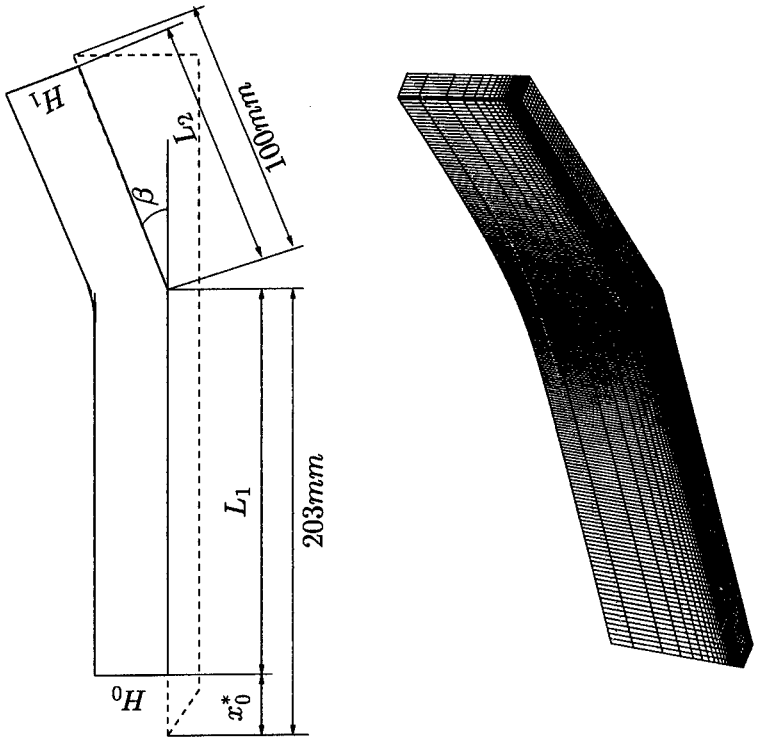
Table 1. Flow parameters.

not required (Thumm et al., 1990; Adams and Kleiser, 1993). Since prior to reattachment the mean streamlines are curved, also a Görtler instability can exist.

2. Problem formulation

We adapt the flow parameters to an experimental setup proposed in a preliminary version of the Stage I Report of the RTO Working Group 10 on "Technologies for Propelled Hypersonic Flight", Subgroup 3 "CFD Validation for Hypersonic Flight", Version January 7, 2000, data set number 2, heated hollow cylinder flare, by B. Chanetz and J, P, Davis. In the final version of this report (Knight, 2000) this proposed experimental data set unfortunately has been discarded. It appears, however, to be a suitable candidate for DNS. The flow parameters are given in table 1, quantities with a star superscript are dimensional, other quantities are non-dimensionalized by the displacement thickness at inflow δ_1 and free-stream quantities. The situation of the computational domain with respect to the experiment is indicated in figure 1(a), the corresponding geometrical parameters are given in table 2. The computational domain is indicated by a solid frame, the experimental-model contours are indicated by a dashed line. Whereas the experimental model is a hollow-cylinder flare combination we neglect the spanwise curvature and use a plane compression ramp as computational representation. To avoid the leading-edge singularity the computational domain starts at a distance x_0^* downstream of the leading edge. We set the wall temperature equal to the adiabatic-wall temperature of the incoming laminar boundary layer. The incoming boundary layer profiles are taken from a similarity solution, figure 2.

To achieve consistency with the free-stream conditions, the wall-normal component $w(z)$ of the similarity solution is ramped exponentially to



(a) Sketch of the setup, ——— computational domain, - - - - model contour.

(b) Computational mesh, not every grid is line shown.

Figure 1. Compression ramp configuration.

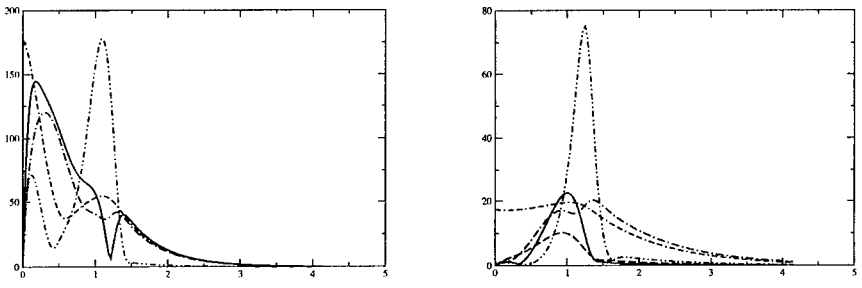
Parameter	Value	Comment
x_0^*	$2.53 \cdot 10^{-2}$	$[m]$, distance from l.e.
L_1	260	
L_2	147	
β	15°	
H_0	60	
H_1	60	
L_x	357	
L_y	12.6	

Table 2. Geometric parameters.

Parameter	First mode	Second mode
α_r	0.4828	2.2061
α_i	−0.0064	−0.0123
β	1	0
ω	0.4	2

Table 3. Eigenvalues of first and second mode instability.

zero outside of the boundary layer. For the similarity solution we perform a spatial linear stability analysis assuming parallel flow. We pick a second mode near its maximum spatial growth rate with the eigenvalues given in table 3. The amplitude distribution of the second mode is shown in figure 3(a). The phase velocity of the second mode is $c_{Phase} = 0.91$ so that the mode travels with almost the free-stream velocity. It is of vorticity character above the relative sonic layer and of acoustic character below (Mack, 1990). An unstable first mode is given



(a) Second mode: ——$10 \cdot u'(z)$, —·—$10 \cdot w'(z)$, ·---· $\rho'(z)$, ——··——$100 \cdot p'(z)$.

(b) First mode: ——$u'(z)$, , —·—$10 \cdot w'(z)$, ·---· $\rho'(z)$, ——··——$100 \cdot p'(z)$.

Figure 3. Amplitude distributions.

by the parameters in table 3, where the frequency was chosen to be an integer fraction of the second mode frequency. The amplitude distribution of the first mode is shown in figure 3(b). The first mode travels downstream with a phase velocity of $c_{Phase} = 0.83$. Near the critical layer z_{cr}, where $u(z_{cr}) = c_{Phase}$, the density fluctuations have maximum amplitude.

The fundamental equations solved are the conservation equations for mass, momentum and energy in generalized coordinates

$$\frac{\partial}{\partial t}\frac{U}{J} + \frac{\partial}{\partial \xi}\frac{F_E}{J} + \frac{\partial}{\partial y}\frac{G_E}{J} + \frac{\partial}{\partial \zeta}\frac{H_E}{J} = \frac{\partial}{\partial \xi}\frac{F_S}{J} + \frac{\partial}{\partial y}\frac{G_S}{J} + \frac{\partial}{\partial \zeta}\frac{H_S}{J} \quad ,$$

where the conservative variables are $U = \{\rho,\ \rho u,\ \rho v,\ \rho w,\ E\}$, with $E = p/(\gamma - 1) + \rho(u^2 + v^2 + w^2)/2$. Considering only essentially two-dimensional configurations we limit the coordinate generalization to the (x, z)-plane. The physical space (x, y, z) is mapped onto the computational space (ξ, η, ζ) which is Cartesian and equi-spaced. The convective and diffusive fluxes are detailed in Adams, 1998.

At the inflow all dependent variables are imposed. At the no-slip wall all velocities are set to zero and the wall temperature is prescribed. At the outer truncation plane Dirichlet boundary conditions fixing all variables at their free-stream values are imposed. At the outflow plane inviscid non-reflecting boundary conditions of Thompson, 1987, are applied.

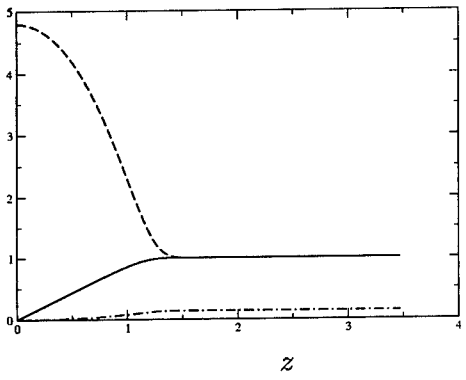


Figure 2. Similarity solution for the incoming boundary layer: ——$u(z)$, - - - -$T(z)$, —·—$10 \cdot w(z)$.

The mapping of the rectangular, evenly spaced computational mesh onto the physical mesh as shown in figure 1(b) is outlined in Adams, 1998. The mapping parameters are adjusted so that about half of the wall-normal grid points are located at $z \leq 6$. Grid points are condensed in streamwise direction towards the corner. The corner itself is smoothed so that it can be resolved on the mesh, curvature radius at the corner is 0.5, whereas the curvature radius of the upper truncation plane is 50.

A family of symmetric compact finite difference schemes with spectral-like resolution has been introduced by Lele, 1992. They are being widely used for direct numerical simulation of transitional and turbulent shear flows (Adams and Kleiser, 1996; Pruett et al., 1995, e.g.) and aeroacoustic problems. As with spectral schemes symmetric compact schemes are sensitive to boundary condition formulation and aliasing errors. The latter is of particular concern for the discretization of convective terms

in the Euler or Navier-Stokes equations, where triple products appear in the conservative form of the momentum equations.

In this study we use compact upwind schemes for the discretization of convection terms, a class of which has been derived from a generalized formulation of compact schemes by Adams and Shariff, 1996, and Adams, 1998. The schemes have a centered stencil but become upwind biased due to non-symmetric coefficients. The upwind biasing introduces a certain amount of numerical dissipation at non-resolved wave numbers which allows to contain aliasing errors. At discontinuities, the scheme is coupled to a high-order essentially non-oscillatory scheme (Shu and Osher, 1989) as described in Adams and Shariff, 1996, and in Adams, 1998.

DNS codes are required to resolve all scales appearing in a flow problem. For that reason it is necessary to perform two different kind of tests, the first of which is to assess how well fluctuations about a mean flow are represented, the second is to see how well the mean flow itself can be computed. Concerning the first, results from linear stability theory can be used as a reference. For the second, comparison with steady-state computations and experimental results for laminar compression ramp flow should be sufficient, in this case the ENO-scheme is active around the shock. These tests have been successfully applied to the the present numerical method. The results are documented in Adams, 1998.

3. Simulation results

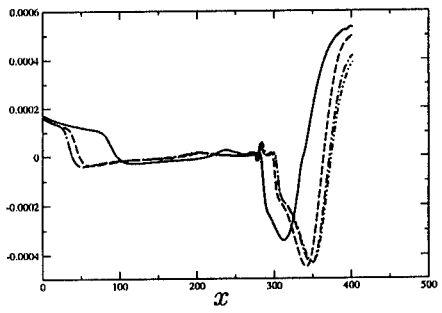
The analysis of transition in shear flows requires to accurately establish the steady base flow first. Although for compression-corner flows with separation it is not clear *a priori* that a steady two-dimensional solution exists, such a solution was found for our flow configuration. Since all computations were performed with explicit time integration without convergence acceleration, the steady-state computations were rather time consuming. After the steady-state solution was established, two-dimensional inflow disturbances were created by superimposing a second Mack mode at a sufficiently large amplitude, resulting in an unsteady two-dimensional flow. The separate analysis of this two-dimensional solution which cannot exhibit laminar-turbulent break down, is helpful to distinguish the effects of the two-dimensional Mack mode from the three-dimensional setting where both first and second mode instabilities are active. Eventually, the two-dimensional steady solution is perturbed by superimposing a combination of first and second mode instability.

Set	N_x	N_z
2D	400	100
2DF	1000	140
2DFF	1500	180
2DFFF	2000	240

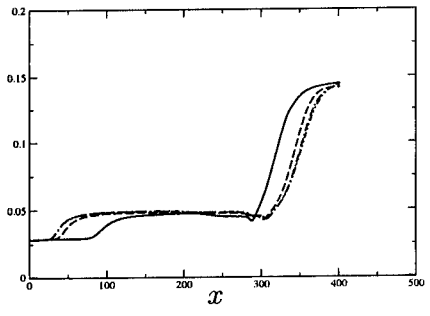
Table 4. Mesh resolution for different data sets of the steady flow solution.

3.1 Steady flow

As initial data we use a laminar flat plate boundary layer similarity solution along the ramp surface, developing as if there was no streamwise pressure gradient. In the exterior of the boundary layer an inviscid Euler solution for the compression-ramp flow is imposed. The initial evolution is computed by a 3rd order ENO scheme with a Roe flux formulation with entropy fix (Shu and Osher, 1989), which is more dissipative than the CUVB scheme used eventually for the later stages (Adams and Shariff, 1996; Adams, 1998). In figure 4 we show the evolution of the skin friction coefficient and the wall pressure from the initial distribution. For each of the resolutions given in table 4 the corresponding steady state solution is shown. It is obvious that the length of the laminar separation depends strongly on the numerical diffusion introduced by the discretization and on the mesh resolution. With the last refinement levels 2DFF and 2DFFF an almost mesh independent solution is achieved.

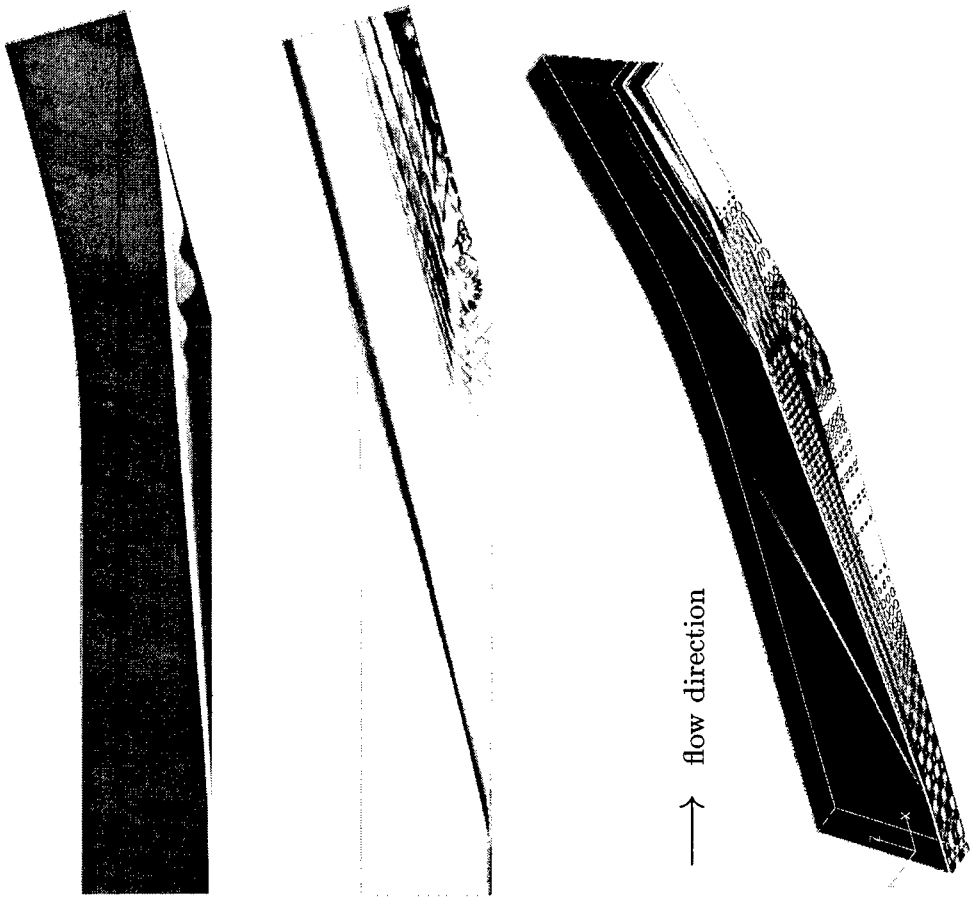


(a) C_f with increasing mesh resolution, ——set 2D, - - - -set 2DF, —·—set 2DFF, ——··——set 2DFFF.



(b) p_W with increasing mesh resolution, ——set 2D, - - - -set 2DF, —·—set 2DFF, ——··——set 2DFFF.

Figure 4. Evolution of the steady-state skin friction coefficient and the wall pressure.



(a) ω_y, grey scales from light -0.2 to dark 0.2.

(b) $|\nabla p|$, grey scales from dark 0 to light 0.003.

(c) Iso-surface of $|\omega_x| = 4.7 \cdot 10^{-4}$: grey shaded, $|\nabla \rho|$ in the computational planes $\eta = 1$, $\xi = 1$: grey coded between 0 and 0.2, contours of $|\omega_x|$ in the plane $\zeta = 0$: grey coded between 0 and $1 \cdot 10^{-4}$.

Figure 5. Steady spanwise-vorticity distribution (a), instantaneous pressure-gradient magnitude (b), and instantaneous visualization at time $t = 372$ after imposing the inflow perturbation (c).

3.2 Two-dimensional unsteady flow

For the unsteady two-dimensional solution we have further increased the spatial resolution to $N_x = 5000$ and $N_z = 320$ cells, for which the

solution can be considered as converged. A reasonable estimate for the amplitude reached by the most unstable linear eigenmodes at inflow is $\max(u')/U_\infty \simeq 10^{-4}$. Given the streamwise growth rates, this is the amplitude roughly reached by the most unstable eigenmodes growing from low-level noise near the leading edge. Since the maximum amplitude of the density eigenfunction is about one order of magnitude larger than that of the streamwise velocity eigenfunction for both first and second mode, one can expect that at a larger amplitude linear theory is no longer a good approximation. We found, however, that imposing the second mode instability scaled with $\max(u')/U_\infty \simeq 10^{-4}$ had no visible effect on the solution. The imposed second mode instability in fact turned out to be stable in the attached part of the spatially growing boundary layer. This behavior is consistent with the finding of El-Hady, 1991, that boundary-layer non-parallelity stabilizes a two-dimensional second mode, compared with the result for parallel flow. The second mode instability neither was able to trigger an instability in the detached shear layer. Only at a significantly increased amplitude of $\max(u')/U_\infty = 0.05$ the flow unsteadiness became significant with considerable excursions of skin friction and surface pressure from the mean. It is found that the instability creates mainly acoustic waves traveling downstream while being reflected back and forth between the detached shear layer and the wall. The solenoidal flow structure remains almost steady. An instantaneous ω_y distribution is almost indistinguishable from the steady state solution in figure 5(a). The acoustic component, however, is highly unsteady, as a snapshot of pressure-waves indicates shown in figure 5(c).

3.3 Three-dimensional unsteady flow

Since in three-dimensions a similarly fine resolution as in the two-dimensional unsteady case is unaffordable, we have chosen the streamwise resolution as $N_x = 3000$ and the wall-normal resolution as $N_z = 180$. This leaves room for a spanwise-domain size of two first-mode spanwise wavelengths, discretized with $N_y = 90$ points. In this case we can consider the resolution being somewhat finer than case 2DFF of section 3.1 as sufficient, albeit not fully mesh independent. The three-dimensional simulations are in progress and we can only show preliminary instantaneous results in this paper. The final results will be published elsewhere. For the present results at time $t = 372$ after imposing the inflow perturbation, the inflow disturbance has not yet reached the outflow plane. The instantaneous skin friction coefficient C_f and the instantaneous surface pressure show only a weak unsteadiness near the corner and near boundary-layer reattachment. An snapshot of the flow

at $t = 372$ shows the generation of streamwise vortices from the first mode instability in the detached shear layer, figure 5(c).

4. Concluding remarks

This paper presents first results of an ongoing research project, final results will be presented elsewhere. The author acknowledges the Swiss Center for Scientific Computing for providing CPU time on its NEC SX-5 computer.

References

Adams, N. A. (1998). Direct numerical simulation of turbulent compression corner flow. *Theor. Comp. Fluid Dyn.*, 12:109–129.

Adams, N. A. and Kleiser, L. (1993). Numerical Simulation of Fundamental Breakdown of a Laminar. *AIAA Journal*, 93-5027.

Adams, N. A. and Kleiser, L. (1996). Subharmonic transition to turbulence in a flat plate boundary layer at Mach number 4.5. *J. Fluid Mech.*, 317:301–335.

Adams, N. A. and Shariff, K. (1996). A high-resolution hybrid compact-ENO scheme for shock-turbulence interaction problems. *J. Comp. Phys.*, 127:27–51.

Adamson, T. C. and Messiter, A. F. (1980). Analysis of two-dimensional interactions between shock waves and boundary layers. *Annu. Rev. Fluid Mech.*, 12:103–138.

Berry, S. A., T. J. Horvath, B. R. H., Thompson, R. A., and H. H. Hamilton II (1999). X-33 hypersonic boundary layer transition. *AIAA-paper*, 99-3560.

Eißler, W. and Bestek, H. (1996). Spatial Numerical Simulation of Linear and Weakly Nonlinear Instabilities in Supersonic Boundary Layers. *Theoret. Comput. Fluid Dynamics*, 8:219–235.

El-Hady, N. M. (1991). Nonparallel instability of supersonic and hypersonic boundary layers. *Phys. Fluids*, A 3(9):2164–2178.

Kachanov, Y. (1994). Physical Mechanisms of Laminar-Boundary-Layer Transition. *Annu. Rev. Fluid Mech.*, 26:411–482.

Kleiser, L. and Zang, T. (1991). Numerical Simulation of Transition in Wall-Bounded Shear Flows. *Annu. Rev. Fluid Mech.*, 23:495–537.

Knight, D. (2000). RTO Working Group 10, "Technologies for Propelled Hypersonic Flight", Subgroup 3, "CFD Validation for Hypersonic Flight", Stage I Report. http://coewww.rutgers.edu/~wg10/report.pdf.

Kovasznay, L. S. G. (1953). Turbulence in supersonic flow. *J. Aero. Sci.*, 20:657–682.

Lawal, A. A. and Sandham, N. D. (2001). Direct simulation of transonic flow over a bump. In Geurts, B. J., Friedrich, R., and Metais, O., editors, *Direct and Large-Eddy Simulation IV*. Kluwer Academic Publishers.

Lele, S. K. (1992). Compact finite difference schemes with spectral-like resolution. *J. Comp. Phys.*, 103:16–42.

Mack, L. (1984). Boundary-Layer Linear Stability Theory. *AGARD Report No. 709*, pages 3-1 to 3-81.

Mack, L. (1990). On the inviscid acoustic-mode instability of supersonic shear flows. Part I: Two-dimensional waves. *Theor. Comput. Fluid Dyn.*, 2:97–123.

Mielke, C. (1999). *Numerische Untersuchungen zur Turbulenzentstehung in dreidimensionalen kompressiblen Grenzschichtströmungen.* PhD thesis, ETH Zürich, Diss. Nr. 13344.

Mielke, C. and Kleiser, L. (1999). Investigation of transition to turbulence in a 3D supersonic boundary layer. In *Proceedings of the IUTAM Symposium on Laminar–Turbulent Transition.*

Muylaert, J. and Berry, W. (1998). Aerothermodynamics for space vehicles - ESA's activities and the challenges. *ESA bulletin*, 96.

Pagella, A., Rist, U., and Wagner, S. (2000). Numerical investigations of small-amplitude disturbances in a laminar boundary layer with impinging shock waves. In *Proceedings of the 12. DGLR Fach-Symposium AG Stab.*

Pruett, C. D. and Chang, C.-L. (1995). Spatial direct numerical simulation of high-speed boundary layer flows – part II: transition on a cone in Mach 8 flow. *Theor. Comp. Fluid Dyn.*, 7:397–424.

Pruett, C. D. and Chang, C.-L. (1998). Direct numerical simulation of Hypersonic boundary–layer flow on a flared cone. *Theoret. Comput. Fluid Dynamics*, 11:49–67.

Pruett, C. D. and Zang, T. (1992). Direct numerical simulation of laminar breakdown in high-speed, axisymmetric boundary layers. *Theor. Comp. Fluid Dyn.*, 3:345–367.

Pruett, C. D., Zang, T., Chang, C.-L., and Carpenter, M. H. (1995). Spatial direct numerical simulation of high-speed boundary-layer flows – part I: algorithmic considerations and validation. *Theor. Comp. Fluid Dyn.*, 7:49–76.

Ribner, H. S. (1953). Convection of a pattern of vorticity through a shock wave. Technical Report TN 2864, NACA.

Ribner, H. S. (1954). Shock-turbulence interaction and the generation of noise. Technical Report TN 3255, NACA.

Shu, C.-W. and Osher, S. (1989). Efficient implementation of essentially non-oscillatory shock-capturing schemes, II. *J. Comput. Phys.*, 83:32–78.

Stetson, K. and Kimmel, R. (1992). On Hypersonic Boundary-Layer Stability. *AIAA Paper*, 92-0737.

Theofilis, V., Hein, S., and Dallmann, U. (2000). On the origins of unsteadiness and three-dimensionality in a laminar separation bubble. *Phil. Trans. R. Soc. Lond. A*, 358:3229–3246.

Thompson, K. W. (1987). Time dependent boundary conditions for hyperbolic systems. *J. Comput. Phys.*, 68:1–24.

Thumm, A., Wolz, W., and Fasel, H. (1990). Numerical simulation of spatially growing three–dimensional disturbance waves in compressible boundary layers. In Arnal, D. and Michel, R., editors, *Laminar–Turbulent Transition IUTAM Symposium Toulouse, France, 1989*, pages 303–308. Springer Verlag.

LARGE EDDY SIMULATION OF SUPERSONIC TURBULENT FLOW IN EXPANSION-COMPRESSION CORNER

DOYLE KNIGHT and HONG YAN
Rutgers - The State University of New Jersey
Piscataway, NJ 08854

ALEXANDER ZHELTOVODOV
Institute of Theoretical and Applied Mechanics
630090 Novosibirsk, Russia

Abstract A Large Eddy Simulation (LES) methodology has been developed for supersonic turbulent flows with strong shock boundary layer interaction. Results are presented for an expansion-compression corner at Mach 3 and compared with experimental data.

Introduction

The interaction of shock waves and turbulent boundary layers is a common and important phenomenon in aerodynamics, and has been studied extensively (Settles and Dolling, 1990; Zheltovodov, 1996). Conventional Reynolds-averaged Navier-Stokes methods have been unable to accurately predict separated shock wave turbulent boundary layer interactions (Knight and Degrez, 1998). Recently, Large Eddy Simulation (LES) and Direct Numerical Simulation (DNS) have been applied to shock wave turbulent boundary layer interactions with significant success. Examples include Adams, 1998, Urbin et al., 1999, Rizzetta et al., 2000 and Rizzetta and Visbal, 2001.

The objective of this paper is to assess the capability of our LES methodology to accurately predict the flowfield in a supersonic expansion-compression corner (Fig. 1). This configuration is reminiscent of aerodynamic configurations wherein a supersonic boundary layer is subjected to an initial expansion followed by a subsequent compression. Interest in this configuration is due in part to the stabilizing influence of the expansion (Dussauge and Gaviglio, 1987; Zheltovodov et al., 1987; Zhel-

tovodov and Schuelein, 1988; Smith and Smits, 1997; Stephen et al., 1998; Zheltovodov et al., 1990b). The first systematic combined experimental and numerical study of an expansion-compression corner by Zheltovodov et al., 1992 and Zheltovodov et al., 1993 showed that several different turbulence models (including $k-\epsilon$, $q-\omega$ and several modifications thereto) did not accurately predict the separation and attachment positions, and distributions of surface skin friction and heat transfer. We therefore seek to ascertain the capability of LES to predict this flowfield.

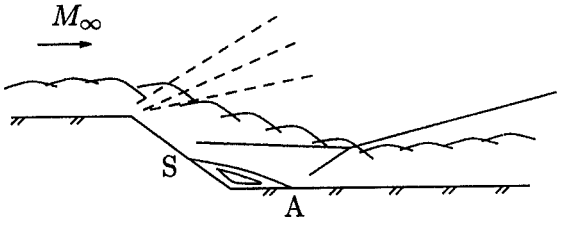


Figure 1. Expansion-compression corner

Governing Equations

The governing equations are the spatially filtered, Favre-averaged compressible Navier-Stokes equations. The spatial filtering removes the small scale (*subgrid scale*) fluctuations, while the three dimensional, time dependent large scale (*resolved scale*) motion is retained. For an arbitrary function $\mathcal{F}(x_i,t)$, the ordinary and Favre-filtered variables $\overline{\mathcal{F}}(x_i,t)$ and $\widetilde{\mathcal{F}}(x_i,t)$ are

$$\overline{\mathcal{F}}(x_i,t) = \int_D G(x_i-\xi_i,\Delta)\,\mathcal{F}(\xi_i,t)\,d\xi_i \quad \text{and} \quad \widetilde{\mathcal{F}}(x_i,t) = \frac{\overline{\rho\mathcal{F}}}{\bar{\rho}} \tag{1}$$

where G is the filter function, and Δ is a measure of the filter width and is related to the computational mesh size.

The filtered governing equations using Cartesian tensor notation are

$$\frac{\partial\bar{\rho}}{\partial t} + \frac{\partial\bar{\rho}\tilde{u}_i}{\partial x_i} = 0 \tag{2}$$

$$\frac{\partial\bar{\rho}\tilde{u}_i}{\partial t} + \frac{\partial\bar{\rho}\tilde{u}_i\tilde{u}_j}{\partial x_j} = -\frac{\partial\bar{p}}{\partial x_i} + \frac{\partial\mathcal{T}_{ij}}{\partial x_j} \tag{3}$$

$$\frac{\partial\bar{\rho}\tilde{e}}{\partial t} + \frac{\partial}{\partial x_j}\left(\bar{\rho}\tilde{e}+\bar{p}\right)\tilde{u}_j = \frac{\partial\mathcal{H}_j}{\partial x_j} \tag{4}$$

$$\bar{p} = \bar{\rho}R\tilde{T} \tag{5}$$

where x_i represents the Cartesian coordinates ($i = 1, 2, 3$), $\bar{\rho}$ is the mean density, $\tilde{u}_i$ are the Cartesian components of the filtered velocity and $\bar{p}$ is the mean pressure. The total stress tensor $\mathcal{T}_{ij} = \tau_{ij} + \bar{\sigma}_{ij}$ where the Subgrid Scale (SGS) stress τ_{ij} and viscous stress $\bar{\sigma}_{ij}$ are

$$\begin{aligned} \tau_{ij} &= -\bar{\rho}\left(\widetilde{u_i u_j} - \tilde{u}_i \tilde{u}_j\right) \\ \bar{\sigma}_{ij} &= \mu(\tilde{T})\left(-\frac{2}{3}\frac{\partial \tilde{u}_k}{\partial x_k}\delta_{ij} + \frac{\partial \tilde{u}_i}{\partial x_j} + \frac{\partial \tilde{u}_j}{\partial x_i}\right) \end{aligned} \tag{6}$$

where $\mu(\tilde{T})$ is the molecular viscosity. The sum of the heat flux plus work done by the stresses is $\mathcal{H}_j = Q_j + \bar{q}_j + \mathcal{T}_{ij}\tilde{u}_i$ where the SGS and molecular heat fluxes are

$$Q_j = -c_p \bar{\rho}\left(\widetilde{u_j T} - \tilde{u}_j \tilde{T}\right) \quad \text{and} \quad \bar{q}_j = \kappa(\tilde{T})\frac{\partial \tilde{T}}{\partial x_j} \tag{7}$$

where $\kappa(\tilde{T})$ the molecular thermal conductivity. The form of $\mathcal{H}_j$ was proposed by Knight et al., 1998 and found to provide an accurate model of SGS turbulent diffusion in decaying compressible isotropic turbulence (Martin et al., 1999). The total energy $\bar{\rho}\tilde{e}$ and SGS turbulence kinetic energy $\bar{\rho}k$ per unit volume are

$$\bar{\rho}\tilde{e} = \bar{\rho}c_v\tilde{T} + \tfrac{1}{2}\bar{\rho}\tilde{u}_i\tilde{u}_i + \bar{\rho}k \quad \text{and} \quad \bar{\rho}k = \tfrac{1}{2}\bar{\rho}\left(\widetilde{u_i u_i} - \tilde{u}_i\tilde{u}_i\right) \tag{8}$$

Closure of the system of equations (2) to (5) requires specification of a model for the subgrid scale stress τ_{ij} and heat flux Q_j. There are two basic approaches (Ghosal, 1999), namely, 1) the explicit specification of an SGS model, and 2) the Monotone Integrated Large Eddy Simulation (MILES) method. In first approach, an explicit mathematical model for τ_{ij} and heat flux Q_j is defined (*e.g.*, the Smagorinsky model). Examples are presented in the recent reviews of Galperin and Orszag, 1993 and Lesieur and Métais, 1996. In the second approach, the SGS model is inherent in the numerical algorithm (Boris et al., 1992; Oran and Boris, 1993; Grinstein, 1996; Grinstein and Fureby, 1998; Fureby and Grinstein, 2000). Fureby and Grinstein, 1999 showed that MILES introduces a tensor eddy diffusivity into the equivalent SGS stress, in contrast to the isotropic eddy diffusivity of the standard explicit Smagorinsky-type SGS models.

The no-slip condition is applied at solid (impermeable) boundaries. The downstream boundary condition for supersonic flows is typically a zero gradient condition on the conservative flow variables ($\bar{\rho}$, $\bar{\rho}\tilde{u}_i$, $\bar{\rho}\tilde{e}$). Periodic boundary conditions are usually employed for the spanwise boundaries with the requirement that the spanwise domain is large compared to the energy containing eddies of the flow and the flowfield is statistically homogeneous in the spanwise direction. The farfield boundary

condition for supersonic flows is typically a Riemann condition allowing waves to leave the computational domain without reflection. The inflow boundary condition for boundary layers is a time-dependent boundary layer profile obtained by the rescaling method originally developed by Lund et al., 1998 for incompressible boundary layers and extended to compressible boundary layers by Urbin and Knight, 1999. The initial condition is typically obtained by linear interpolation from a previous simulation at comparable Mach and Reynolds numbers.

Numerical Algorithm

The governing equations (2) to (5) are solved using a unstructured grid of tetrahedra. The finite volume algorithm is second order accurate in space and time. The inviscid fluxes are computed using Godunov's method with the left and right states at each face reconstructed using a second order Least Squares method (Okong'o and Knight, 1998a). The stencil of cells employed for reconstruction is isotropic except in the vicinity of shock waves where an ENO-like anisotropic stencil is employed (Chernyavsky et al., 2001). The MILES methodology is employed (*i.e.*, $\tau_{ij} = 0$, $Q_j = 0$). The molecular viscous stresses and heat flux are obtained using a discrete version of Gauss' Theorem (Okong'o and Knight, 1998a). The temporal integration is performed by using a second-order accurate Runge-Kutta method. The code is parallelized using domain decomposition with the Message Passing Interface (MPI). The flow variables are non-dimensionalized using the incoming boundary layer thickness δ, and incoming freestream velocity U_∞, density ρ_∞, static temperature T_∞ and molecular viscosity μ_∞.

The code has been validated for a variety of turbulent flows by comparison with experiment and Direct Numerical Simulation (DNS). Examples include decay of isotropic turbulence (Knight et al., 1997; Knight et al., 1998), incompressible channel flow (Okong'o and Knight, 1998b; Okong'o et al., 2000), supersonic turbulent boundary layer (Urbin et al., 1999; Urbin and Knight, 1999; Yan et al., 2000; Urbin and Knight, 2001), and supersonic compression corner (Urbin et al., 1999; Urbin et al., 2000; Yan et al., 2000; Chernyavsky et al., 2001). The supersonic boundary layer results are summarized in the next section.

Flat Plate Boundary Layer

Urbin and Knight, 2001 performed an LES of an adiabatic Mach 3 boundary layer. A detailed grid refinement study was performed to ascertain the required grid resolution in the viscous sublayer, logarithmic and outer regions of the boundary layer. The computed mean veloc-

ity profile, expressed in Van Driest transformed notation, is shown in Fig. 2. The profile shows excellent agreement with the logarithmic region of the Law of the Wall. The computed adiabatic wall temperature is within 3% of the empirical formula $T_{aw} = T_\infty \left(1 + \frac{1}{2}(\gamma - 1) Pr_{t_m} M_\infty^2\right)$ where $Pr_{t_m} = 0.89$ is the mean turbulent Prandtl number. The computed friction velocity u_τ is within 5% of the correlation obtained from the combined Law of the Wall and Wake. The computed normalized Reynolds shear stress $< \rho >< u''v'' > /\tau_w$, shown in Fig. 3, shows excellent agreement with the experimental data.

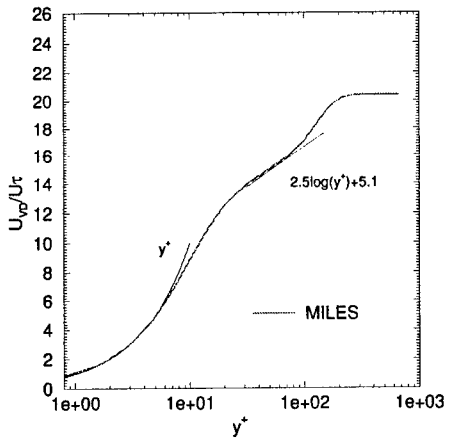


Figure 2. Mean Van Driest velocity

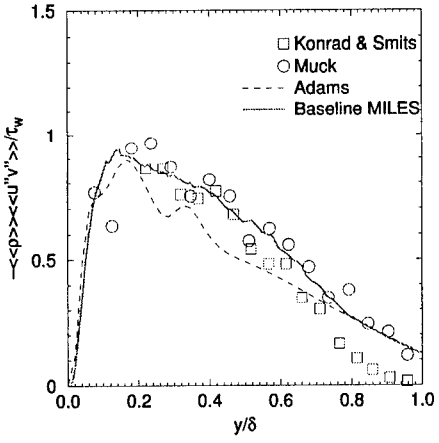


Figure 3. Reynolds shear stress

Expansion-Compression Corner

Details of Computation

The flowfield configuration is shown in Fig. 1. An incoming Mach 3 adiabatic equilibrium turbulent boundary layer of height δ expands over a 25° corner followed by a 25° compression. The distance along the expansion surface is 7.1δ (*i.e.*, the vertical distance between the two horizontal surfaces is 3δ, and the horizontal distance between the expansion and compression corners is 6.43δ).

The Cartesian coordinates x, y and z are aligned in the incoming streamwise, transverse and spanwise directions with the origin at the inflow boundary. The computational domain is $L_x = 24.0\delta$, $L_y = 3.4\delta$, and $L_z = 1.925\delta$. The expansion corner is located at 4δ from the inflow boundary. The grid consists of $253 \times 35 \times 57$ nodes in the x, y and

z directions, respectively, forming 479,808 hexahedra which are subdivided into five tetrahedra each. Thus, the total number of tetrahedra is 2,399,040. The grid is stretched in the y direction with spacing 0.008δ at the wall and a geometric stretching factor of 1.154. The grid is concentrated in the streamwise direction in the neighborhood of the expansion and compression corners. The details are shown in Table 1 where $\Delta y^+ = \Delta y u_\tau / \nu_w$ where ν_w is the computed kinematic viscosity at the wall, $u_\tau = \sqrt{\tau_w / \rho_w}$ is the friction velocity, τ_w is the computed wall shear stress and ρ_w is the computed density at the wall. The grid is consistent with the resolution requirements for the LES code established by Urbin and Knight, 2001.

Table 1. Details of Grid

Name	Δx^+	Δy^+ at the wall	Δz^+	$\Delta x/\delta$	$\Delta y/\delta$ at $y = \delta$	$\Delta z/\delta$	Tetras
Computed	20.9	1.67	7.1	0.1	0.14	0.034	2,399,040

The inflow boundary condition is obtained from a separate flat plate boundary layer computation. All the quantities are averaged in time and in the spanwise direction and denoted by $< f >$. The time averaging period is set to three times the flow-through time, where one flow-through time is defined as the time for the freestream flow to traverse the computational domain. The averaging is performed once the initial transient has decayed (*i.e.*, after four flow-through times). The details are presented in Urbin et al., 1999.

Experiments

Experimental data has been obtained by Zheltovodov et al., 1987, Zheltovodov and Schuelein, 1988, and Zheltovodov et al., 1990a and presented in part in tabular form in Zheltovodov et al., 1990b for the expansion-compression corner at Mach 3 and several Reynolds numbers Re_δ based on the incoming boundary layer thickness δ. The experimental conditions are listed in Table 2, where FPBL and ECC imply flat plate boundary layer and expansion-compression corner, respectively. The LES was performed at a lower Reynolds number ($Re_\delta = 2 \times 10^4$) than the experiment ($Re_\delta = 4.4 \times 10^4$ to 1.94×10^5) for reasons of computational cost. Additional LES cases will be performed at higher Reynolds numbers.

Table 2. Details of Experiments and Computation

Cases	Mach	Re_δ	References
ECC	2.9	4.07×10^4	Zheltovodov et al., 1990a
ECC	2.9	6.76×10^4	Zheltovodov et al., 1990a
ECC	2.9	8.0×10^4	Zheltovodov et al., 1990a
ECC	2.9	1.94×10^5	Zheltovodov et al., 1987; Zheltovodov et al., 1990b
ECC	2.88	2.0×10^4	Present computation
FPBL	2.88	1.33×10^5	Zheltovodov et al., 1990b

Results

The structure of the flowfield is shown in Figs. 4 and Fig. 5 which display the mean static pressure and streamlines at $z = \delta$. The flow expands around the first corner, and recompresses at the second corner through a shock which separates the boundary layer as evident in Fig. 5. The flowfield structure is in good agreement with the results of Zheltovodov et al., 1987; Zheltovodov and Schuelein, 1988; Zheltovodov et al., 1990a and Zheltovodov et al., 1990b which are shown qualitatively in Fig. 1.

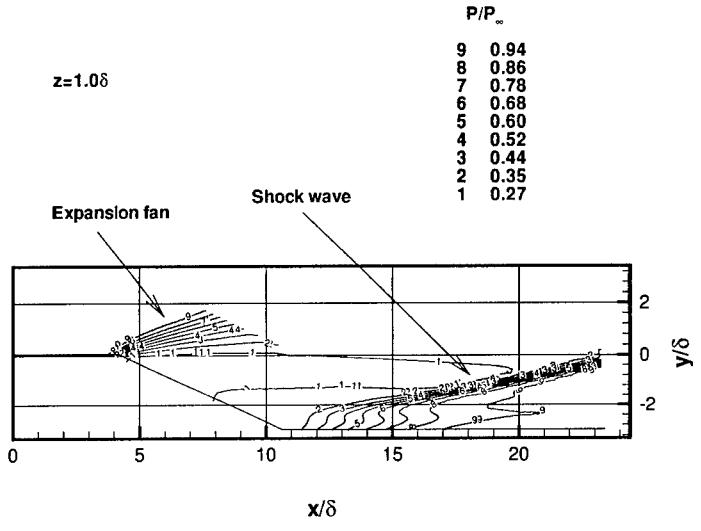


Figure 4. Mean static pressure (S is separation, A is attachment)

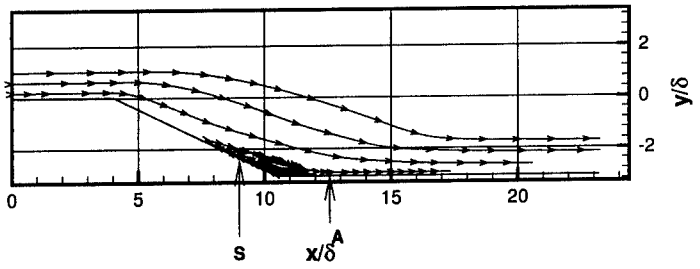


Figure 5. Mean streamlines (S is separation, A is attachment)

The mean velocity profiles in the x-direction are shown in Fig. 6 at $x = 2\delta$ and $x = 6\delta$, where x is measured from the inflow along the direction of the inflow freestream velocity (Fig. 4). The abscissa is the component of velocity locally parallel to the wall, and the ordinate is the distance measured normal to the wall. The first profile is upstream of the expansion corner which is located at $x = 4\delta$, and the second is downstream of the expansion fan and upstream of the separation point. The computed mean velocity profile at the first location is slightly fuller than the experiment. This is consistent with the experimentally observed dependence of the exponent n in the power-law $U/U_\infty = (y/\delta)^{1/n}$ on the Reynolds number. The second profile shows a significant acceleration of the flow in the outer portion of the boundary layer due to the expansion.

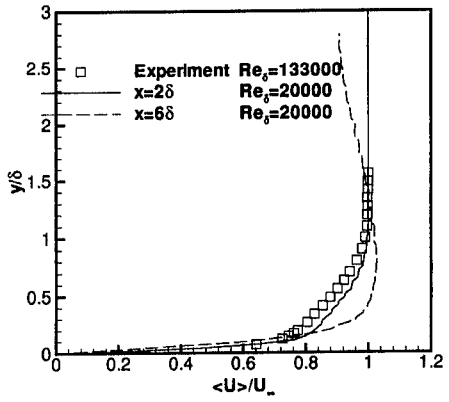


Figure 6. Mean velocity

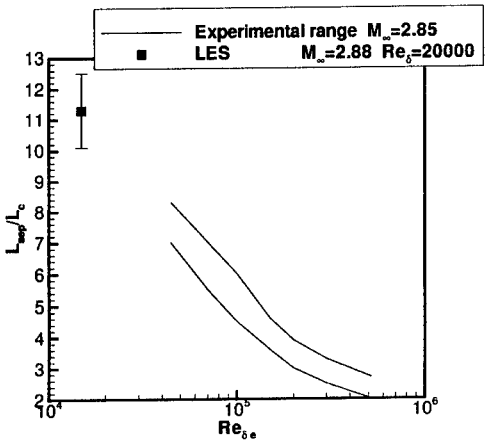


Figure 7. Separation length

Zheltovodov and Schuelein, 1988 and Zheltovodov et al., 1993 developed an empirical correlation for the separation length (defined as the minimum distance between the mean separation and attachment points on the wall) in the expansion-compression corner interaction. The scaled separation length L_{sep}/L_c is observed experimentally to be a function of Re_δ where the characteristic length (L_c) is defined by

$$L_c = \delta_e (p_2/p_{pl})^{3.1}/M_e^3 \tag{9}$$

where δ_e is the incoming boundary layer thickness (upstream of the expansion corner), p_2 is the pressure after the shock in inviscid flow, p_{pl} is the plateau pressure from the empirical formula $p_{pl} = p_e(\frac{1}{2}M_e + 1)$ where p_e and M_e are the static pressure and freestream Mach number upstream of the compression corner and downstream of the expansion fan. In the computation, the location is taken to be $x = 6\delta$. The values of M_e and p_2 have been computed using inviscid theory. Also, $Re_{\delta e} = 1.8 \times 10^4$ for LES ($Re_{\delta e} = \rho_e U_e \delta_e/\mu_e$, where ρ_e, U_e and μ_e are computed using inviscid theory). The experimental data correlation of Zheltovodov and Schuelein, 1988 and the computed result[1] for the scaled separation length is shown in Fig. 7. The computed value is consistent with a linear extrapolation of the expermental data.

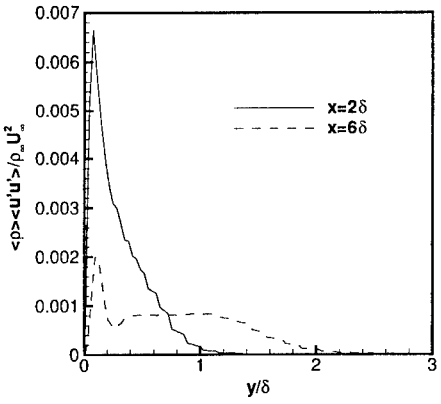


Figure 8. Reynolds streamwise stress

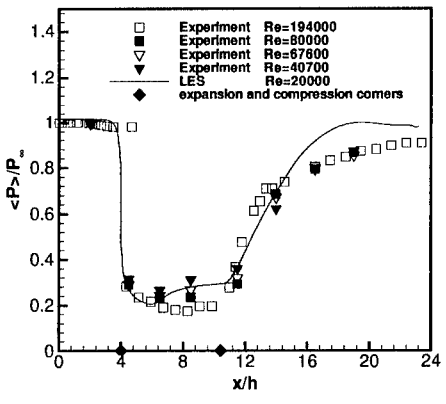


Figure 9. Surface pressure

The surface pressure profile in Fig. 9 displays a pressure plateau on the compression face generated by the separation bubble. The exper-

[1]The uncertainty in the computed value of L_{sep}/L_c is associated with the uncertainty in determining δ_e. We have used the streamwise Reynolds stress ($< \rho >< u'u' >$) to determine δ_e (Fig. 8), where u' is the fluctuating velocity parallel to the wall.

iments exhibit a trend of increase in the size of the pressure plateau region with decreasing Reynolds number. The experimental data at the lowest Reynolds number ($Re_\delta = 4.1 \times 10^4$) shows close agreement with the computed results for $Re_\delta = 2 \times 10^4$ for the location, extent and magnitude of the pressure plateau. Moreover, the shape of the experimental pressure plateau shows little variation for $Re_\delta \leq 6.8 \times 10^4$, thus suggesting that the computed pressure plateau region (for $Re_\delta = 2 \times 10^4$) is accurate. The computed recovery of the surface pressure is more rapid than in the experiment, however.

The computed and experimental mean skin friction coefficient $c_f = \tau_w / \frac{1}{2}\rho_\infty U_\infty^2$ are shown in Fig. 10. The computed separation and attachment points are evident. The skin friction rises rapidly downstream of attachment. The computed results at $Re_\delta = 2 \times 10^4$ are in close agreement with the experimental data at $Re_\delta = 8.0 \times 10^4$ and 1.94×10^5 in the region downstream of reattachment.

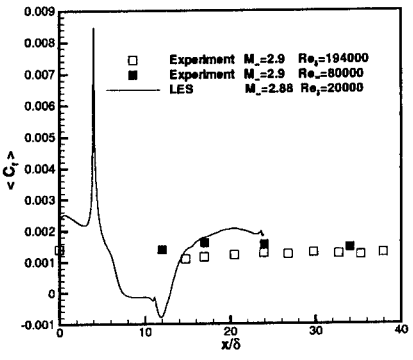


Figure 10. Skin friction coefficient

Summary

An unstructured grid Large Eddy Simulation methodology has been validated for complex compressible turbulent flows. The methodology is based on the MILES concept wherein the inherent dissipation of the monotone inviscid flux algorithm provides the energy transfer from the resolved to the subgrid scales. The methodology has been validated by comparison with experiment for a variety of supersonic turbulent flows including a turbulent boundary layer and an expansion-compression corner at Mach 3.

Acknowledgments

The research is supported by AFOSR Grant No. F49620-99-1-0008 monitored by R. Herklotz, L. Sakell, J. Schmisseur and S. Walker.

References

Adams, N. (1998). Direct Numerical Simulation of Turbulent Compression Ramp Flow. *Theoretical and Computational Fluid Dynamics*, 12:109–129.

Boris, J., Grinstein, F., Oran, E., and Kolbe, R. (1992). New Insights into Large Eddy Simulation. *Fluid Dynamics Research*, 10:199–228.

Chernyavsky, B., Yan, H., and Knight, D. (2001). Analyses of Some Numerical Issues in Compressible LES. AIAA Paper 2001-0436.

Dussauge, J. and Gaviglio, J. (1987). The Rapid Expansion of a Supersonic Turbulent Flow: Role of Bulk Dilatation. *Journal of Fluid Mechanics*, 174:81–112.

Fureby, C. and Grinstein, F. (1999). Monotonically Integrated Large Eddy Simulation of Free Shear Flows. *AIAA Journal*, 37:544–556.

Fureby, C. and Grinstein, F. (2000). Large Eddy Simulation of High Reynolds Number Free and Wall Bounded Flows. AIAA Paper No. 2000-2307.

Galperin, B. and Orszag, S., editors (1993). *Large Eddy Simulation of Complex Engineering and Geophysical Flows*. Cambridge University Press.

Ghosal, S. (1999). Mathematical and Physical Constraints on Large Eddy Simulation of Turbulence. *AIAA Journal*, 37(4):425–433.

Grinstein, F. and Fureby, C. (1998). Monotonically Integrated Large Eddy Simulation of Free Shear Flows. AIAA Paper No. 98-0537.

Grinstein, F. F. (1996). Dynamics of Coherent Structures and Transition to Turbulence in Free Square Jets. AIAA Paper No. 96-0781.

Knight, D. and Degrez, G. (1998). Shock Wave Boundary Layer Interactions in High Mach Number Flows – A Critical Survey of Current CFD Prediction Capabilities. AGARD AR-319, Volume 2.

Knight, D., Zhou, G., Okong'o, N., and Shukla, V. (1997). Large Eddy Simulation of Compressible Flows Using Unstructured Grids. In *First AFOSR Conference on DNS/LES*. Louisiana Tech University.

Knight, D., Zhou, G., Okong'o, N., and Shukla, V. (1998). Compressible Large Eddy Simulation Using Unstructured Grids. AIAA Paper 98-0535.

Lesieur, M. and Métais, O. (1996). New Trends in Large-Eddy Simulations of Turbulence. In *Annual Review of Fluid Mechanics*, volume 28, pages 45–82. Annual Reviews, Inc.

Lund, T., Wu, X., and Squires, K. (1998). Generation of Turbulent Inflow Data for Spatially- Developing Boundary Layer Simulations. *Journal of Computational Physics*, 140:233–258.

Martin, M., Piomelli, U., and Candler, G. (1999). A Priori Tests of SGS Models in Compressible Turbulence. 3rd ASME/JSME Joint Fluids Engineering Conference.

Okong'o, N. and Knight, D. (1998a). Accurate Three-Dimensional Unsteady Flow Simulation Using Unstructured Grids. AIAA Paper 98-0787.

Okong'o, N. and Knight, D. (1998b). Compressible Large Eddy Simulation Using Unstructured Grids: Channel and Boundary Layer Flows. AIAA Paper 98-3315.

Okong'o, N., Knight, D., and Zhou, G. (2000). Large Eddy Simulations Using an Unstructured Grid Compressible Navier-Stokes Algorithm. *International Journal of Computational Fluid Dynamics*, 13:303–326.

Oran, E. and Boris, J. (1993). Computing Turbulent Shear Flows - A Convenient Conspiracy. *Computers in Physics*, 7(5):523–533.

Rizzetta, D. and Visbal, M. (2001). Large Eddy Simulation of Supersonic Compression Ramp Flows. AIAA Paper 2001-2858.

Rizzetta, D., Visbal, M., and Gaitonde, D. (2000). Direct Numerical and Large-Eddy Simulation of Supersonic Flows by a High-Order Method. AIAA Paper 2000-2408.

Settles, G. and Dolling, D. (1990). Swept Shock / Boundary-Layer Interactions - Tutorial and Update. AIAA Paper 90-0375.

Smith, D. and Smits, A. (1997). The Effects of Successive Distortion on a Turbulent Boundary Layer in a Supersonic Flow. *Journal Fluid Mechanics*, 351:253–288.

Stephen, A., Mo, S., and Gregory, S. (1998). The Effects of Expansion on the Turbulence Structure of Compressible Boundary Layers. *J. Fluid Mechanics*, 367:67–105.

Urbin, G. and Knight, D. (1999). Compressible Large Eddy Simulation using Unstructured Grid: Supersonic Boundary Layer. In *Recent Advances in DNS and LES*, pages 443–458, Kluwer Academic Publishers.

Urbin, G. and Knight, D. (2001). Large Eddy Simulation of a Supersonic Boundary Layer Using an Unstructured Grid. *AIAA Journal*, 39(8):1288–1295.

Urbin, G., Knight, D., and Zheltovodov, A. (1999). Compressible Large Eddy Simulation Using Unstructured Grids: Supersonic Turbulent Boundary Layer and Compression Corner. AIAA Paper 99-0427.

Urbin, G., Knight, D., and Zheltovodov, A. (2000). Large Eddy Simulation of Supersonic Compression Corner Part I. AIAA Paper 2000-0398.

Yan, H., Urbin, G., Knight, D., and Zheltovodov, A. (2000). Compressible Large Eddy Simulation using Unstructured Grid: Supersonic Boundary Layer and Compression Ramps. In *10th International Conference on Methods of Aerophysical Research*, pages 215–224, Novosibirsk, Russia.

Zheltovodov, A. (1996). Shock Waves / Turbulent Boundary Layer Interactions - Fundamental Studies and Applications. AIAA Paper 96-1977.

Zheltovodov, A., Borisov, A., Knight, D., Horstman, C., and Settles, G. (1992). The Possibilities of Numerical Simulation of Shock Waves / Boundary Layer Interaction in Supersonic and Hypersonic Flows. In *Proceedings of the International Conference on Methods of Aerophysical Research. Part 1*, pages 164–170. Russian Academy of Sciences, Siberian Division, Novosibirsk.

Zheltovodov, A., Mecler, L., and Schuelein, E. (1987). Pecularities of Development of Separated Flows in Compression Corners After the Expansion Fans. ITAM Preprint 10-87. In Russian.

Zheltovodov, A. and Schuelein, E. (1988). Peculiarities of Turbulent Separation Development in Disturbed Boundary Layers. *Modelirovaniye v Mekchanike*, 2(1):53–58. Novosibirsk (in Russian).

Zheltovodov, A., Schuelein, E., and Horstman, C. (1993). Development of Separation in the Region of Interaction of Shock Wave with Turbulent Boundary Layer Disturbed by Expansion. *Journal of Applied Mechanics and Technical Physics*, 3:58–68. in Russian.

Zheltovodov, A., Trofimov, V., Filippova, E., and Takovlev, Y. (1990a). Influence of Turbulence Change on the Heat Exchange Under the Conditions of Supersonic Separated Flows. In *Abstracts: IUTAM Symposium on Separated Flows and Jets*, pages 273–274. USSR Academy of Sciences, Siberian Division, Novosibirsk.

Zheltovodov, A., Trofimov, V., Schuelein, E., and Yakovlev, V. (1990b). An Experimental Documentation of Supersonic Turbulent Flows in the Vicinity of Forward- and Backward-Facing Ramps. ITAM Report 2030.

DNS OF HYPERSONIC BOUNDARY LAYER STABILITY AND TRANSITION USING HIGH-ORDER NONUNIFORM-GRID SCHEMES

XIAOLIN ZHONG
Mechanical and Aerospace Engineering Department
University of California, Los Angeles, CA 90095

Abstract

High-order schemes are necessary for the DNS of stability and transition of hypersonic boundary layers because lower-order schemes do not have a sufficient accuracy level to compute small flow details. Currently, the main limiting factor in the application of high-order schemes is the numerical instability of high-order boundary closure schemes. In a previous AIAA paper (2001-0437), we presented a family of high-order nonuniform-grid finite-difference schemes with stable boundary closures for multi-dimensional flow simulations. In this paper, the high-order nonuniform-grid schemes (up to 11th order) are applied to the numerical simulation of the receptivity of hypersonic boundary layers to freestream disturbances over a blunt leading edge. The stability and numerical accuracy of the new high-order nonuniform-grid schemes are evaluated for computing the nonlinear 2-D Navier-Stokes equations for hypersonic flow simulations.

1. Introduction

The prediction of laminar-turbulent transition in hypersonic boundary layers is a critical part of the aerodynamic design and control of hypersonic vehicles. The transition process is a result of the nonlinear response of laminar boundary layers to forcing disturbances, which can originate from many difference sources including free stream disturbances, surface roughness and vibrations. In an environment with weak initial disturbances, the path to transition consists of three stages: 1) receptivity, 2) linear eigenmode growth or transient growth, and 3) nonlinear breakdown to turbulence. Due to the complexity of transient hypersonic flow fields including the instability and receptivity process, an effective approach to studying hypersonic boundary

layer stability and receptivity is the direct numerical simulation of the full Navier-Stokes equations. In (1) and (2), we presented and validated a new fifth-order upwind finite difference shock fitting method for the direct numerical simulation of hypersonic flows with a strong bow shock. The use of the high-order shock-fitting scheme makes it possible to obtain highly accurate mean flow and unsteady solutions, which are free of spurious numerical oscillations behind the bow shock. The method has been subsequently validated and applied to numerical studies of receptivity and stability of many two and three-dimensional hypersonic boundary-layer flows.

The application of high-order finite-difference schemes have recently received much attention in many areas of flow simulations, including the direct numerical simulation (DNS) of transitional and turbulent flows[2; 3; 4; 5], and other areas. High-order schemes are necessary in such flow simulations because lower-order schemes do not have sufficient accuracy to compute small flow details. Currently, most high-order finite-difference schemes are derived on uniformly spaced grid points. The schemes are applied to a nonuniform grid by a coordinate transform from the nonuniform physical domain to a uniform computational domain. The main limiting factor in the application of high-order schemes is the numerical instability of high-order boundary closure schemes[6; 7]. For example, Carpenter et al.[6] showed that for a sixth-order inner compact scheme, only a third-order boundary scheme can be used without introducing instability. Consequently, the order of accuracy of numerical schemes used in most practical DNS studies is often limited to 6th-order or lower in the interior and 4th-order or lower on the boundary closure schemes because of the numerical instability of boundary closure schemes. It is necessary to overcome the instability of boundary closure schemes in order to have wide applications of arbitrarily high-order schemes to practical multi-dimensional flow simulations.

In Ref. (8), we showed that it is possible to use high-order (11th or higher order) explicit and compact finite difference schemes with stable boundary closures for high accurate numerical simulation of incompressible and compressible flows. We proposed a simple and effective way to overcome the instability in arbitrarily high-order finite difference schemes with boundary closure schemes. It was shown that the numerical instability of high-order boundary schemes is a result of the use of uniform computational grids in applying high-order schemes. An effective way to overcome the instability for arbitrary high-order finite difference schemes with boundary closure schemes is to use the high-order schemes directly in a nonuniform stretched grid without coordinate transformation. The coefficients of the high-order schemes are determined based on polynomial interpolation in the physical nonuniform grids. The amount of grid stretching is determined to maintain the stability of the overall schemes. The new high-order (up to 12-th

order) schemes have been analyzed and tested in computing a linear wave equation with oscillatory boundary conditions. It was found the high-order schemes are stable and produce a much higher degree of accuracy than lower order schemes. It is not clear, however, if the accuracy and stability of the high-order non-uniform grid schemes can be maintained when they are applied to simulation of complex multidimensional flow fields using the nonlinear Navier-Stokes equations. The purpose of this paper is to apply the new high-order schemes to the DNS of the receptivity and stability of hypersonic boundary layer flows over a 2-D blunt body. The stability and numerical accuracy are quantitatively evaluated based on the numerical solutions.

2. Governing Equations

The governing equations for DNS of hypersonic flows are the unsteady two or three-dimensional Navier-Stokes equations in the following conservation-law form (for 2-D cases):

$$\frac{\partial U^*}{\partial t^*} + \frac{\partial F^*{}_j}{\partial x_j^*} + \frac{\partial F^*{}_{vj}}{\partial x_j^*} = 0 \tag{1}$$

where superscript "$*$" represents dimensional variables. The vector of the conservative flow variables is $U^* = \{\rho^*,\ \rho^* u_1^*,\ \rho^* u_2^*,\ e^*\}$ The gas is assumed to be thermally and calorically perfect. The viscosity and heat conductivity coefficients are calculated using Sutherland's law together with the assumption of a constant Prandtl number.

3. Coordinate Mapping in Shock Fitting Simulations

Numerical simulations for hypersonic flows over a blunt leading edge are carried out using the high-order nonuniform-grid schemes presented in (8) with a shock fitting treatment for the bow shock. The unsteady bow shock shape and shock oscillations are calculated as part of the computational solution. The high-order nonuniform grid schemes are applied to the governing equations using a coordinate transformation. The spatially discretized equations are advanced in time using a low-storage Runge-Kutta scheme of up to third order.

The computational domain for a shock-fitting method used in computating steady and unsteady 2-D viscous hypersonic flow over blunt bodies is shown in Fig. 1. The governing equations are solved in a general curvilinear coordinates $(\xi,\ \eta,\ \tau)$ along body fitted grid lines. The computational domain in (x, y) between the bow shock and the body is transformed into a square domain in $(\xi, \eta) \in [-1, 1] \times [-1, 1]$. The governing equations (1)

are transformed into the computational domain (ξ, η, τ) resulting in:

$$\frac{1}{J}\frac{\partial U}{\partial \tau} + \frac{\partial E'}{\partial \xi} + \frac{\partial F'}{\partial \eta} + + \frac{\partial E'_v}{\partial \xi} + \frac{\partial F'_v}{\partial \eta} + U\frac{\partial(\frac{1}{J})}{\partial \tau} = \frac{W}{J} \tag{2}$$

where J is the Jacobian of the coordinate transformation.

For viscous flow simulations, the physical computational domain between the bow shock and the body (Fig. 1) is mapped to a square in two steps: 1) (x, y, t) to (X, Y, τ), and 2) (X, Y, τ) to (ξ, η, τ), following Kopriva[9]. First, the physical space is mapped to a square by the follow relation:

$$X = \frac{2s(x,y)}{S} - 1 \quad Y = \frac{2h(x,y)}{H(x,y,t)} - 1 \tag{3}$$

where s is the local surface length, S is total surface length in the computational domain, h is the local normal distance of point (x, y) to the body surface, and H is the local shock height. For unsteady flow, $H(x, y, t)$ is a function of time because of the shock motion. This transformation maps the physical space to a square $(X, Y) \in [-1, 1] \times [-1, 1]$. Second, the (X, Y) space is mapped to a square in (ξ, η) space in order to introduce more grid points near the wall to resolve the boundary layer structure better. A hyperbolic tangent stretching[9] is used in the wall-normal direction as follows:

$$Y = 2\frac{[1 - \tanh(\sigma)]^{\frac{\eta+1}{2}}}{1 - \tanh(\sigma\frac{\eta+1}{2})} - 1 \tag{4}$$

where σ is the stretching parameter. The value of σ is chosen to be 0.75 in this paper. This combined transformation maps the physical space in (x, y) to a square space in $(\xi, \eta) \in [-1, 1] \times [-1, 1]$.

4. Interior High-Order Schemes with Stable Boundary Closure

The governing equations (2) in (ξ, η) space are discretized using the high-order nonuniform-grid finite difference schemes[8] in the square computational domain. In this paper, the grid spacing in the (ξ, η) space is given by the following stretching function[10]:

$$\xi_i = \frac{\sin^{-1}(-\alpha\cos(\pi i/N))}{\sin^{-1}\alpha} \quad \eta_j = \frac{\sin^{-1}(-\alpha\cos(\pi j/M))}{\sin^{-1}\alpha} \tag{5}$$

where the parameter α is used to change the stretching of the grid points, i and j are grid index numbers. The high-order nonuniform-grid scheme

applies a finite difference approximation directly to the grid points in the (ξ, η) space. The coefficients are derived from a Lagrange polynomial interpolation. For the case of an N-point grid stencil with a distribution of grid points with coordinates ξ_i, the $N-1$ degree interpolation polynomial is:

$$P_n(\xi) = \sum_{j=1}^{N} l_j(\xi)\, u_j \tag{6}$$

where u_j is the variables at the node points, and

$$l_j(\xi) = \prod_{l=1, l\neq j}^{n} (\xi - \xi_l) \;/\; \prod_{l=1, l\neq j}^{n} (\xi_j - \xi_l) \tag{7}$$

The derivative at a grid point ξ_i can be calculated by differentiating the above polynomial as: $u_i' = \sum_{j=1}^{N} b_{i,j}\, u_j$, where the coefficients $b_{i,j}$ in the derivatives are different for different grid points with index i. Hence, once the ξ_i locations of the stencil are known the coefficients for the finite difference formulas for a high-order scheme in a nonuniform grid can be calculated explicitly using the above formulas. The coefficients at the boundary closure scheme are derived using the same formula by specifying one-sided grid stencils. The derivatives at all grid points, including the interior and boundary points, can be combined into the following vector formula: $\boldsymbol{u}' = \boldsymbol{A}\boldsymbol{u}$, where $\boldsymbol{u}$ is a vector of variables and $\boldsymbol{A}$ is a banded coefficients matrix, which can be computed once and for all at the beginning of a calculation.

4.1. BOUNDARY CONDITIONS

The boundary condition at the bow shock is computed by a shock fitting method described in (2). On the wall, the physical non-slip condition for velocities ($u = v = 0$), and isothermal ($T = T_w$) or adiabatic condition are used. A characteristic equation is used to compute pressure on the wall. For flow conditions at the symmetrical center line, the conditions $v = 0$ and zero gradient for all other variables are used. For exit conditions, a simple extrapolation condition is used because the flow is supersonic outside the boundary layer.

5. Receptivity of Mach 15 Flow Over A Parabola

We apply the new high-order nonuniform grid schemes to compute the receptivity process of Mach 15 flows over a parabolic blunt leading edge. The receptivity mechanism provides important initial conditions of amplitude, frequency, and phase of instability waves in the boundary layers. The same

test case has been studied by Zhong[11] using a fifth-order shock fitting scheme. The receptivity problem is an ideal case to test the stability and accuracy of the new schemes because it involves both steady and unsteady flow simulation in a viscous hypersonic flow field. The unsteady flow field contains complex interactions between a number of waves of different length scales.

Specifically, the receptivity of a two-dimensional boundary layer to free stream acoustic waves in hypersonic flow past a parabolic leading edge at zero angle of attack is considered. The free stream disturbances are assumed to be weak monochromatic planar acoustic waves with wave fronts normal to the center line of the body. The flow is characterized by a free stream Mach number M_∞ and a Reynolds number Re_∞. The forcing frequency of the free stream acoustic wave is represented by a dimensionless frequency F defined as $F = 10^6 \frac{\omega^* \nu^*}{U_\infty^{*2}}$. We can also define a Strouhal number S using the nose radius by $S = \frac{\omega^* r^*}{U_\infty^*}$.

The flow conditions of the current computational case are as follows. $M_\infty = 15$, $T_\infty^* = 192.989\ K$, $p_\infty^* = 10.3\ Pa$, $\gamma = 1.4$, $Pr = 0.72$, $R^* = 286.94\ Nm/kgK$, $Re_\infty = 6026.6$, $T_w^* = 1000K$, $r^* = 0.0125\ m$, $d^* = 0.1\ m$, and $\epsilon = 5 \times 10^{-4}$ to 10^{-1}. The nondimensional frequency is $k_\infty = 15$, and $F = 2655$, $S = 2$. Two sets of grids are used to compute both steady and unsteady flow solutions of the full Navier-Stokes equations: a coarse 31×51 grid and a finer 51×91 grid. The computational grid of 31×51 is shown in Fig. 1. For each grid, the flow solutions are simulated using a nonuniform grid scheme of different orders. Specifically, the orders are 1st, 3rd, 5th, 7th, 9th, and 11th order. The grid stretching parameter α in Eq. (5) is 0.6, which has been found to be stable for the various order schemes computed.

5.1. STEADY BASE FLOW SOLUTIONS

The steady base flow solutions of the Navier-Stokes equations for the Mach 15 flow over the blunt leading edge are obtained first by advancing the solutions to a steady state without freestream perturbations. The physical characteristics of the solutions of this flow problem have been discussed in detail in (2). The main focus of this paper is to evaluate the numerical stability and accuracy of high-order nonuniform grid schemes at different orders and different grid resolutions.

Figure 2 shows the Mach number contours and velocity vectors for steady base flow solutions using the 11th-order nonuniform-grid scheme. The results computed by the 11th-order scheme are very smooth for this relatively coarse grid. Figure 3 shows five sets of pressure contours for steady base flow solutions using five nonuniform-grid schemes of the 1st, 3rd, 5th, 9th, and 11th order using the same 31×51 grid. The first order scheme

produces very large errors. The accuracy improves substantially by the use of the third order scheme. As the order increases further, the accuracy improves further and the numerical solution approaches the exact solution. Since there is no analytical solution available, we evaluate the numerical accuracy by comparing the present solutions with those of an 11th order scheme using a finer 51×91 grid. Figure 4 shows such accuracy evaluation for the surface distribution of vorticity using nonuniform-grid schemes of different orders. The lower figure shows the comparison near the minimum vorticity point. Again the figure shows the improvement of numerical accuracy as the order of the method increases. The 11th-order scheme using the coarse grid is very close to the results of fine grid of the same order. Similar trends in the numerical accuracy of the results are also shown in the pressure and surface heating rates distribution (Figs. 5 and 6).

Figures 7 and 8 show a quantitative assessment of the numerical accuracy of the schemes of different orders by plotting the relative errors of pressure and heating rates at the stagnation point. For a fixed grid resolution, the numerical accuracy of the schemes improves as the order of the schemes increases. The improvement is dramatic when the order is low. As the order increases, the improvement in accuracy becomes smaller. At very high-order, there is very little improvement in accuracy by increasing the order further, because it has reached the limit of the grid resolution. When a finer grid is used, the high-order schemes lead to further improvement of accuracy. Therefore, the accuracy of high-order schemes can be improved substantially by increasing the order of the schemes, but for a given grid resolution there is a limiting order of the schemes, beyond which the accuracy of the solutions can not be improved further unless the grid is further refined. For the current 2-D Navier-Stokes equations over a blunt body, the limiting order for the 31×51 grid is about 5th order, while the limit for the finer 51×91 grid is 9th order.

Overall, the stead-flow results show that the high-order nonuniform grid schemes are stable for very high-order (up to 11th order)schemes. Such high order solutions are not possible using a conventional uniform grid scheme because of numerical instability. The high-order nonuniform-grid schemes can produce highly accurate numerical solutions.

5.2. UNSTEADY FLOW SOLUTIONS

Having obtained the steady solution, the receptivity of the hypersonic boundary-layer in the Mach 15 flow over the parabola is studied by numerical simulation using the high-order schemes. The high-order nonuniform-grid schemes are used to compute the unsteady solutions induced by freestream acoustic waves. The forcing waves induce boundary layer waves inside the

boundary layers. The unsteady calculations are carried out until the solutions reach a periodic state in time. Temporal Fourier analysis is carried out on local perturbations of unsteady flow variables after a time periodic state has been reached. The Fourier transform for the real disturbance functions lead to:

$$q'(x,y,t) = \Re\{\sum_{n=0}^{N} |q_n(x,y)|\ e^{i[-n\omega_0 t+\phi_n(x,y)]}\} \tag{8}$$

where $n\omega_0$ is the frequency of the n-th wave mode, $q'(x,y,t)$ represents any perturbation variables. The boundary layer waves contain the fundamental wave mode, which has the same frequency F as the forcing acoustic waves. At the same time, due to the nonlinear interaction, the wave field also contains higher harmonics of the fundamental frequency, nF, where $n = 0$ represents mean distortion, $n = 1$ represents the fundamental mode, $n = 2$ represents the second harmonics of two times the fundamental frequency, etc. The higher harmonics have smaller wave lengths and orders of magnitude smaller amplitudes. For example, the wavelength of $n = 2$ mode is about half of that of the $n = 1$ fundamental mdoe.

The results presented here are those for the case of freestream frequency of $F = 2655$ and nondimensional freestream forcing wave amplitude of $\epsilon = 0.001$. The unsteady solutions are computed by the new nonuniform grid schemes of different orders. Figure 9 shows the instantaneous pressure and temperature perturbation contours. The solution is obtained by the 9th order scheme using a 51×91 grid. The results show a very smooth wave solution. In response to the perturbations of the forcing waves in the freestream, the unsteady flow field produces boundary layer wave modes of fundamental frequencies and their harmonics. In the present case, the higher harmonics are several orders of magnitudes weaker than the fundamental modes. Figure 10 shows the Fourier harmonics of the induced wave. It shows the Fourier amplitudes of pressure perturbation and their real parts along the parabola surface. The solution is obtained by the 7th order schemes using a 51×91 grid. In the figure, $n = 0, 1, 2, 3$, corresponds to mean flow distortion, fundamental mode, second harmonic, and third harmonic. The figures show that the high-order schemes are able to capture these modes with a relatively coarse grid. Notice that there are about 27, 18, and 9 grid points per period for the first ($n = 1$), the second ($n = 2$), and third harmonic ($n = 3$), respectively. The amplitudes of these three harmonics are in the order of 10^1, 10^{-1}, and 10^{-3} for the first, second, and third harmonics. The figures show that the 7th-order scheme captures all these modes well.

The results of wave harmonics obtained by different order schemes of the same grid are compared in Figs. 11 to 13. The results shows that the funda-

mental mode is captured very well by all three schemes of 5th, 7th, and 9th order. For second harmonics ($n = 2$), however, the 5th-order scheme is not as accurate, while the 7th and 9th order produce almost the same results. Similarly, the 5th-order scheme under predicts the mean flow distortion ($n = 0$ mode) caused by nonlinear wave interaction. Therefore, the 9th-order scheme produces more accurate results than the 5th-order scheme for the transient flow field when the length scale is small for the high harmonics and the mean flow distortion due to nonlinear interactions.

Similar to the steady solution case, it is necessary to have suffucient grid resolution for the flow length scale in order to have good accuracy. The corresponding unsteady flow have also been computed by using a relatively coarse 31×51 grid. Figure 14 shows the Fourier amplitudes of pressure perturbation along the parabola surface for the same case. The solution is obtained by the 9th order scheme using a 31×51 grid. The results show that the high-order schemes capture the fundamental mode very well, but cannot capture the higher harmonics accurately because of the coarser grid.

6. Conclusion

The high-order nonuniform grid schemes have been applied to 2-D hypersonic flow simulations using the nonlinear Navier-Stokes equations. Stable numerical solutions have been obtained for the receptivity of Mach 15 flow over a parabola. The accuracy of both steady and unsteady solutions obtained by using different orders of the schemes and different grid resolutions have been evaluated. The results show the new nonuniform grid schemes are stable and are able to produce highly accurate results.

Acknowledgments

This work was sponsored by AFOSR, USAF, under AFOSR Grant #F49620-00-1-0101. The views and conclusions contained herein are those of the author and should not be interpreted as necessarily representing the official policies or endorsements either expressed or implied, of AFOSR or the U.S. Government.

References

1. Zhong, X., *AIAA paper 97-0755*, 1997.
2. Zhong, X., *Journal of Computational Physics*, Vol. 144, August 1998, pp. 662–709.
3. Lele, S. K., *Journal of Computational Physics*, Vol. 103, 1992, pp. 16–42.
4. Pruett, C. D., et al., *Theoretical and Comp. Fluid Dynamics*, Vol. 7, 1995, pp. 49–76.
5. Mahesh, K., *Journal of Computational Physics*, Vol. 145, pp. 332–358, 1998.
6. Carpenter, M. H., et al., *J. of Comp. Physics*, Vol. 108, 1993, pp. 272–295.
7. Abarbanel, S. S., et al., *J. of Comp. Physics*, Vol. 160, pp. 42–66, 2000.
8. Zhong, X. and Tatineni, M., *AIAA Paper 2001-0437*, 2001.
9. Kopriva, D. A., *AIAA Journal*, Vol. 31, No. 7, 1993, pp. 1235–42.
10. Kosloff, D. and Tal-Ezer, H., *J. of Comp. Physics*, Vol. 104, pp. 457–469, 1993.
11. Zhong, X., *AIAA paper 97-0756*, January 1997.

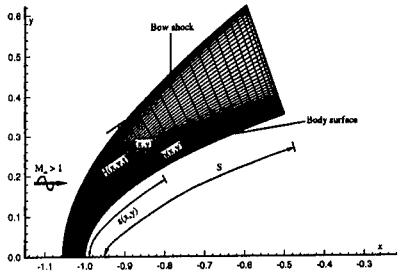


Figure 1. Computational grid for hypersonic flow over a blunt leading edge where the bow shock shape is obtained as the numerical solution for the upper grid line boundary.

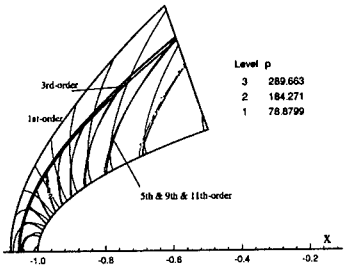


Figure 3. Pressure contours for steady base flow solutions using five nonuniform-grid schemes of the following orders: 1st, 3rd, 5th, 9th, 11th order schemes (31 × 51 grid).

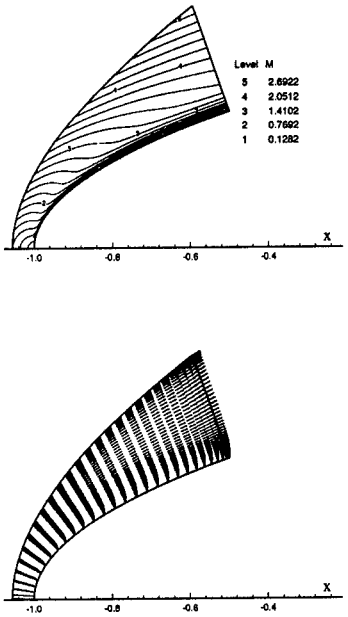


Figure 2. Mach number contours and velocity vectors for steady base flow solutions using the 11th-order nonuniform-grid scheme (31 × 51 grid).

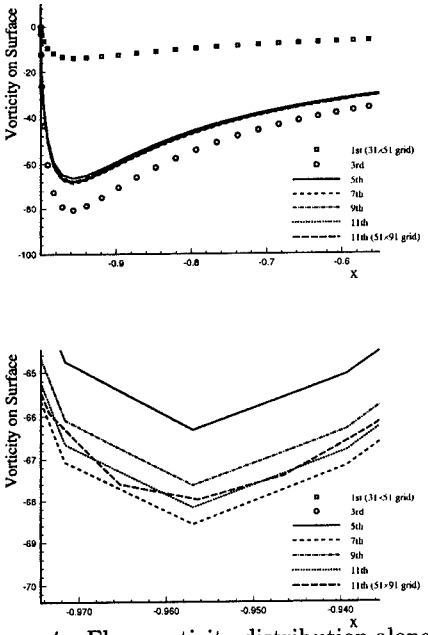


Figure 4. Flow vorticity distribution along parabola surface for steady base flow solutions using nonuniform-grid schemes of the following orders: 1st, 3rd, 5th, 9th, 11th order schemes using 31 × 51 grid and a case of 11th order using a finer grid of 51 × 91. Lower figure shows the comparison near the minimum vorticity point.

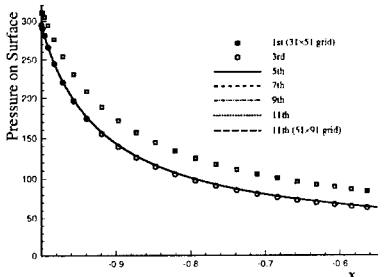


Figure 5. Stead pressure distributions along parabola surface using nonuniform-grid schemes of different orders at 31×51 and different grids.

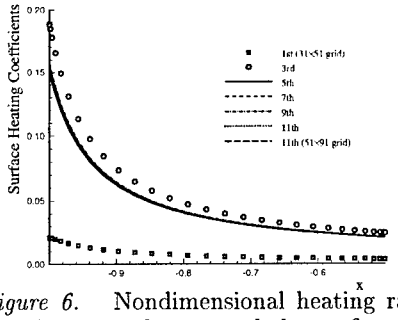


Figure 6. Nondimensional heating rates distributions along parabola surface for steady base flow solutions using nonuniform-grid schemes of different orders and different grids.

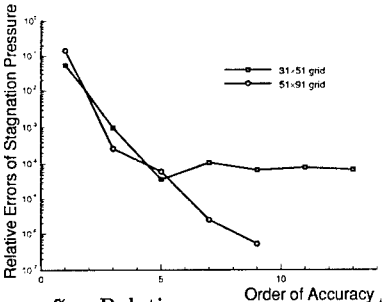


Figure 7. Relative pressure errors at the stagnation point for steady base flow solutions using nonuniform-grid schemes of different orders and different grids.

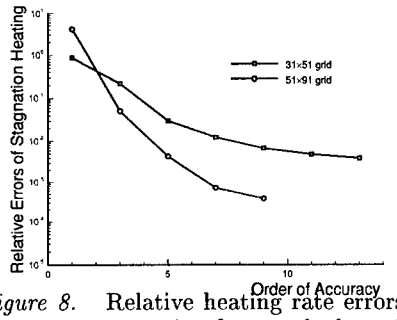


Figure 8. Relative heating rate errors at the stagnation point for steady base flow solutions using nonuniform-grid schemes of different orders and different grids.

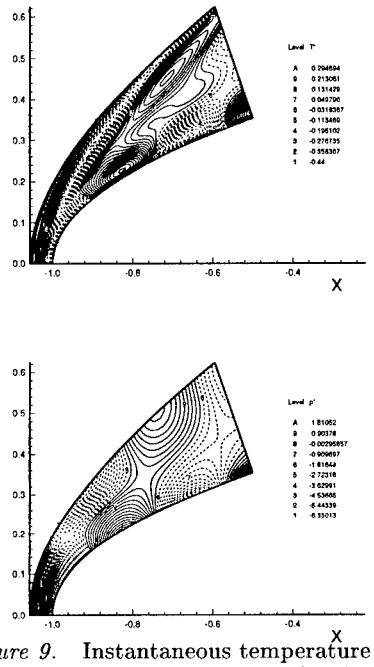


Figure 9. Instantaneous temperature and pressure perturbation contours for the case of freestream acoustic wave of $F = 2655$ and wave amplitude of 0.001. The solution is obtained by the 9th order schemes using 51×91 grid.

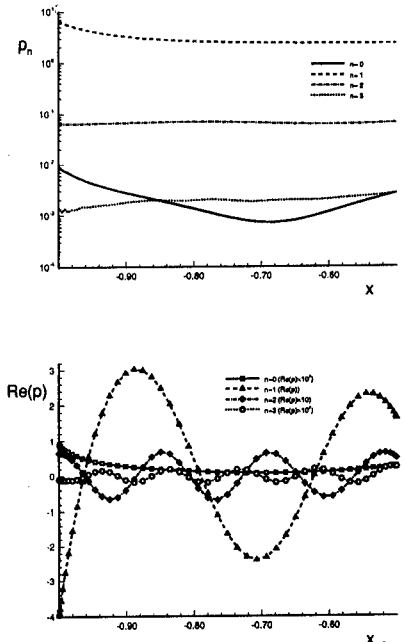


Figure 10. Fourier amplitudes of pressure perturbation and their real part along parabola surface. The solution is obtained by the 7th order schemes using 51×91 grid. In the figure, $n = 0, 1, 2, 3$, corresponds to mean flow distortion, fundamental mode, second harmonic, and third harmonic.

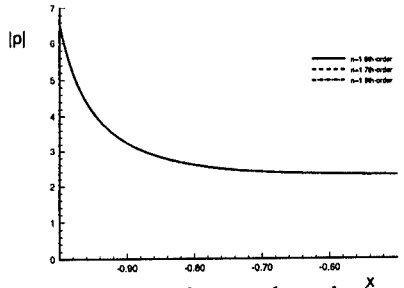


Figure 11. Fundamental mode ($n = 1$) pressure perturbation amplitudes along parabola surface. The solution is obtained by the 5th, 7th, and 9th order schemes using 51×91 grid.

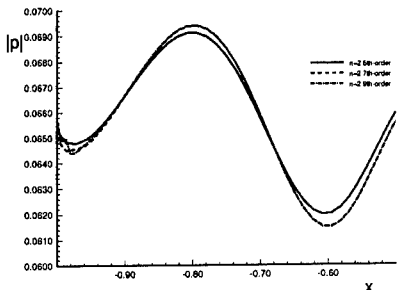


Figure 12. Second harmonic ($n = 1$) pressure perturbation amplitudes along parabola surface. The solution is obtained by the 5th, 7th, and 9th order schemes using 51×91 grid.

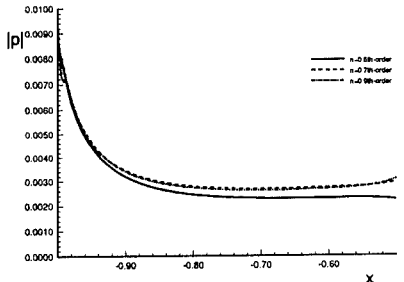


Figure 13. Mean flow distortion ($n = 0$) for pressure perturbation amplitudes along parabola surface. The solution is obtained by the 5th, 7th, and 9th order schemes using 51×91 grid.

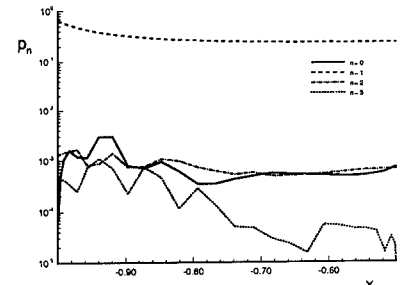


Figure 14. Fourier amplitudes pressure perturbation along parabola surface. The solution is obtained by the 9th order schemes using the coarser 31×51 grid.

DIRECT NUMERICAL SIMULATION OF TURBULENCE USING SYMMETRY-PRESERVING DISCRETIZATION

R.W.C.P. VERSTAPPEN AND A.E.P. VELDMAN
Research Institute for Mathematics and Computing Science, University of Groningen
P.O.Box 800, 9700 AV Groningen, The Netherlands
e-mail: verstappen@math.rug.nl, veldman@math.rug.nl

Abstract. We propose to perform turbulent flow simulations in such a manner that the difference operators do have the same symmetry properties as the underlying differential operators, *i.e.* the convective operator is represented by a skew-symmetric matrix and the diffusive operator is approximated by a symmetric, positive-definite matrix. Such a symmetry-preserving discretization of the Navier-Stokes equations is stable on any grid, and conserves the total mass, momentum and kinetic energy (when the physical dissipation is turned off). Its accuracy is tested for a turbulent channel flow at Re=5,600 (based on the channel width and the mean bulk velocity) by comparing the results to those of physical experiments and previous numerical studies. This comparison shows that with a fourth-order, symmetry-preserving method a $64 \times 64 \times 32$ grid suffices to perform an accurate direct numerical simulation.

1. Introduction

The smallest scales of motion in a turbulent flow result from a subtle balance between convective transport and diffusive dissipation. In mathematical terms, the balance is an interplay between two differential operators differing in symmetry: the convective derivative is skew-symmetric, whereas diffusion is governed by a symmetric, definite operator. With this in mind, we have developed a spatial discretization method which preserves the symmetries of the balancing differential operators. That is, convection is approximated by a skew-symmetric discrete operator, and diffusion is discretized by a symmetric, definite operator. Second-order and fourth-order

versions have been developed thus far, applicable to structured nonuniform grids. The resulting semi-discrete representation conserves energy exactly in the absence of physical dissipation. For finite Reynolds numbers, *i.e.* in the presence of physical dissipation, the kinetic energy of any discrete solution decreases unconditionally in time. Therefore, a symmetry-preserving, spatial discretization is stable on any grid, and we need not add an artificial demping mechanism that will inevitably interfere with the subtle balance between convection and diffusion at the smallest length scales. This forms our motivation to investigate symmetry-preserving discretizations for direct numerical simulation (DNS) of turbulent flow. Because stability is not an issue, the main question becomes how accurate is a symmetry-preserving discretization, or stated otherwise, how coarse may the grid be for a DNS? We will address this question in Section 2 by evaluating the results for a turbulent flow in a channel at Re=5,600. We will kick off by sketching the main lines of symmetry-preserving discretization (Section 1). For a more detailed discussion, we refer to Verstappen and Veldman (1998, 2002). Conservation properties of numerical schemes for the Navier-Stokes equations are currently also pursued at other research institutes, see e.g. Hyman *et al.* (1992), Morinishi *et al.* (1998), Vasilyev (2000), Twerda (2000) and Ducros *et al.* (2000).

2. Symmetry-preserving discretization

The temporal evolution of the discrete velocity vector $\boldsymbol{u}_h$ is governed by a finite-volume discretization of the incompressible Navier–Stokes equations:

$$\boldsymbol{\Omega}\frac{\mathrm{d}\boldsymbol{u}_h}{\mathrm{d}t} + \boldsymbol{C}(\boldsymbol{u}_h)\,\boldsymbol{u}_h + \boldsymbol{D}\boldsymbol{u}_h - \boldsymbol{M}^*\boldsymbol{p}_h = \boldsymbol{0} \qquad \boldsymbol{M}\boldsymbol{u}_h = \boldsymbol{0}, \tag{1}$$

where the vector $\boldsymbol{p}_h$ denotes the discrete pressure, $\boldsymbol{\Omega}$ is a (positive-definite) diagonal matrix representing the sizes of the control volumes, $\boldsymbol{C}(\boldsymbol{u}_h)$ is built from the convective flux contributions through the control faces, $\boldsymbol{D}$ contains the diffusive fluxes, and $\boldsymbol{M}$ is the coefficient matrix of the discretization of the integral form of the law of conservation of mass. The coefficient matrices $\boldsymbol{C}(\boldsymbol{u}_h)$ and $\boldsymbol{D}$ are constructed such that

$$\boldsymbol{C}(\boldsymbol{u}_h) + \boldsymbol{C}^*(\boldsymbol{u}_h) = \boldsymbol{0}, \qquad \boldsymbol{D} + \boldsymbol{D}^* \text{ positive-definite.} \tag{2}$$

The symmetry condition on the coefficient matrix $\boldsymbol{C}(\boldsymbol{u}_h)$ reflects that $\boldsymbol{C}(u_h)$ represents a discrete gradient operator: its null space consists of the constant vectors (provided that the consistency condition $\boldsymbol{C}(\boldsymbol{u}_h)\,\boldsymbol{1} = \boldsymbol{0}$ is satisfied) and $\boldsymbol{C}(\boldsymbol{u}_h)$ is skew-symmetric like a first-order differential operator. The coefficient matrix $\boldsymbol{D}$ of the discrete diffusive operator inherits its positive-definiteness from the underlying diffusive, differential operator $-\nabla\cdot\nabla/\mathrm{Re}$.

The semi-discretization (1)–(2) is conservative and stable. The total mass is trivially conserved, and the same holds for the total amount of momentum (provided that the discretization is exact for $\boldsymbol{u}_h = \mathbf{1}$). The evolution of the discrete energy $\boldsymbol{u}_h^* \boldsymbol{\Omega} \boldsymbol{u}_h$ of any solution $\boldsymbol{u}_h$ of (1)–(2) is governed by

$$\begin{aligned} \frac{\mathrm{d}}{\mathrm{d}t}(\boldsymbol{u}_h^* \boldsymbol{\Omega} \boldsymbol{u}_h) &\overset{(1)}{=} -\boldsymbol{u}_h^*(\boldsymbol{C} + \boldsymbol{C}^*)\boldsymbol{u}_h - \boldsymbol{u}_h^*(\boldsymbol{D} + \boldsymbol{D}^*)\boldsymbol{u}_h + \underbrace{2\boldsymbol{p}_h^* \boldsymbol{M} \boldsymbol{u}_h}_{=0} \\ &\overset{(2)}{=} -\boldsymbol{u}_h^*(\boldsymbol{D} + \boldsymbol{D}^*)\boldsymbol{u}_h \leq 0, \end{aligned} \tag{3}$$

where we have used the skew-symmetry of $\boldsymbol{C}(\boldsymbol{u}_h)$. The right-hand side is zero if and only if $\boldsymbol{u}_h = \mathbf{0}$, or $\boldsymbol{D} + \boldsymbol{D}^* = \mathbf{0}$. Thus, the energy is conserved if the diffusion is turned off. Note that the pressure term $\boldsymbol{M}^* \boldsymbol{p}_h$ in (1) does not affect the evolution of the total kinetic energy (on condition that $\boldsymbol{M}\boldsymbol{u}_h = \mathbf{0}$), because the discrete pressure gradient is represented by the transpose of the coefficient matrix $\boldsymbol{M}$ of the incompressibility constraint.

With diffusion (that is for $\boldsymbol{D} \neq \mathbf{0}$) the right-hand side of (3) is negative for all $\boldsymbol{u}_h \neq \mathbf{0}$ provided that $\boldsymbol{D} + \boldsymbol{D}^*$ is positive-definite. So, the energy of the discrete system (1) decreases in time if (2) is satisfied. The semi-discrete system (1) is stable under this symmetry condition: a solution of (1) can be obtained on any grid, and there is no need to add an artificial damping mechanism to stabilize the spatial discretization.

Since these favorable conservation and stability properties are directly related to the symmetries of the coefficient matrices in (1), we want to construct these matrices such that they fulfil (2). To illustrate the way in which this may be achieved, we consider the approximation of the first-order derivative in one spatial dimension. The traditional method maximizes the (formal) order of the local truncation error. On a stencil consisting of three points, this leads to the second-order approximation

$$\partial_x u(x_i) \approx \tfrac{1}{2}\Omega_i^{-1}\left(r_i^{-1}u_{i+1} - (r_i^{-1} - r_i)u_i - r_i u_{i-1}\right), \tag{4}$$

where

$$\Omega_i^{-1} = \tfrac{1}{2}(x_{i+1} - x_{i-1}) \qquad \text{and} \qquad r_i = (x_{i+1} - x_i)/(x_i - x_{i-1}).$$

The essence of our method is that the first-order derivative $\partial_x u(x_i)$ is approximated by a discrete operator $\boldsymbol{\Omega}^{-1}\boldsymbol{C}$, where the coefficient matrix $\boldsymbol{C}$ is skew-symmetric:

$$\partial_x u(x_i) \approx \tfrac{1}{2}\Omega_i^{-1}(u_{i+1} - u_{i+1}). \tag{5}$$

The two ways of discretization are illustrated in Figure 1.

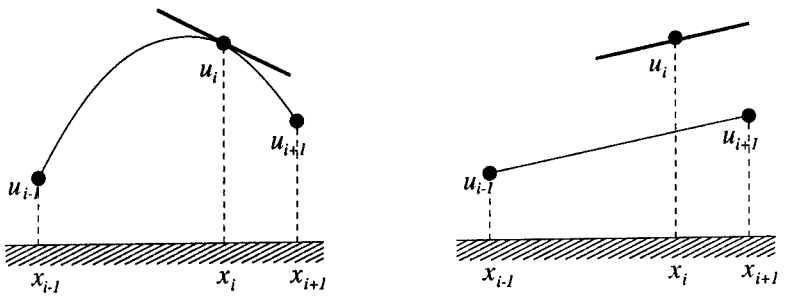


Figure 1. Two ways of approximating $\partial_x u$. In the left-hand figure the derivative is approximated by means of a Lagrangian interpolation, that is by Eq. (4). In the right-hand figure the symmetry-preserving discretization (5) is applied.

As the diagonal-entry of operator in the right-hand side of (4) is non-zero for $r_1 \neq 1$, the standard discretization method breaks the skew-symmetry on a nonuniform grid. Consequently, the standard method does not conserve the energy and is not conditionally stable on nonuniform meshes.

The local truncation error of the symmetry-preserving discretization

$$\tau_h(x_i) = \tfrac{1}{2}(\delta x_{i+1} - \delta x_i)\partial_{xx}u(x_i) + \mathcal{O}(\delta x_{\max}^2), \tag{6}$$

is first-order, unless the grid is (almost) uniform. Given stability, a sufficient condition for second-order accuracy of the discrete solution u_i is that the local truncation error $\boldsymbol{\tau}_h$ be second order. Then the error $\boldsymbol{\epsilon}_h$ in the solution $\boldsymbol{u}_h$, given by $\boldsymbol{\Omega}^{-1}\boldsymbol{C}\boldsymbol{\epsilon}_h = \boldsymbol{\tau}_h$, is second-order. Yet, this is not a necessary condition, as is emphasized by Manteufel and White (1986). They have proven that the symmetry-preserving approximation yields second-order accurate solutions on uniform as well as on nonuniform meshes, even though its local truncation error $\boldsymbol{\tau}_h$ is formally only first-order on nonuniform meshes.

The accuracy of the basic scheme (5) may be improved by means of a Richardson extrapolation, just like in Antonopoulos-Domis (1981). This results into the following, fourth-order accurate discretization:

$$\partial_x u(x_i) \approx \tfrac{1}{2}\Omega_i^{-1}\left(-u_{i+2} + 8u_{i+1} - 8u_{i-1} + u_{i-2}\right),$$

where

$$\Omega_i = \tfrac{1}{2}\left(-x_{i+2} + 8x_{i+1} - 8x_{i-1} + x_{i-2}\right).$$

The diffusive operator undergoes a similar treatment, leading to

$$\Omega_i \partial_{xx}u(x_i) = 8\left(\frac{u_{i+1}-u_i}{x_{i+1}-x_i} - \frac{u_i - u_{i-1}}{x_i - x_{i-1}}\right) - \left(\frac{u_{i+2}-u_i}{x_{i+2}-x_i} - \frac{u_i - u_{i-2}}{x_i - x_{i-2}}\right).$$

Next, we will compare the symmetry-preserving discretization with the traditional discretization methods based on Lagrange interpolation (minimizing local truncation error) for a steady-state solution of the convection-diffusion equation

$$\partial_t u + \bar{u}\partial_x u - \partial_{xx} u/\mathrm{Re} = 0.$$

Since on uniform grids the methods are equal, we choose an example with a boundary-layer character, requiring grid refinement near the outflow boundary $x = 1$. This is achieved by imposing the boundary conditions $u(0,t) = 0$ and $u(1,t) = 1$. The parameters are set equal to $\bar{u} = 1$ and $\mathrm{Re} = 1,000$.

Grid refinement has been carried out on an exponentially stretched grid, with half the grid points in the thin boundary layer of thickness $10/\mathrm{Re}$ near $x = 1$. Four discretization methods have been investigated:

- The traditional Lagrangian second-order method (2L) and its fourth-order counterpart (denoted by 4L) where we have implemented exact boundary conditions to circumvent the problem of a difference molecule that is too large near the boundary;
- The second-order (2S) and fourth-order (4S) symmetry-preserving methods.

We form the vector $\boldsymbol{u}_{\mathrm{exact}}$ by restricting the analytical solution to the grid points, and monitor the global discretization error defined by $||\boldsymbol{u}_h - \boldsymbol{u}_{\mathrm{exact}}||_h$ (where the norm is the kinetic energy norm). Figure 2 shows the global error as a function of the mean mesh size $1/N$, where N is the number of grid points.

A number of observations can be made.

- For all grid sizes the Lagrangian discretization appears to be less accurate than its symmetry-preserving alternative.
- For coarser grids the 4th-order Lagrangian method is not even as accurate as its 2nd-order Lagrangian relative. Similar observations have been made frequently, and this explains why thusfar 4th-order discretization has not been very popular.
- The symmetry-preserving methods already behave nicely on coarse grids. They display a regular monotone behaviour upon grid refinement. Moreover, the discretization error of 4S (2S) picks up its final slope at much coarser grids then 4L (2L). As in turbulent-flow simulations one will always have to cope with limitations on the affordable number of grid points, methods that are less sensitive in this respect are preferable.
- Also note that for a given accuracy (say 10^{-5}), the grid size of the 4th-order symmetry-preserving method can be chosen roughly three times larger than that of the 4th-order Lagrangian method!

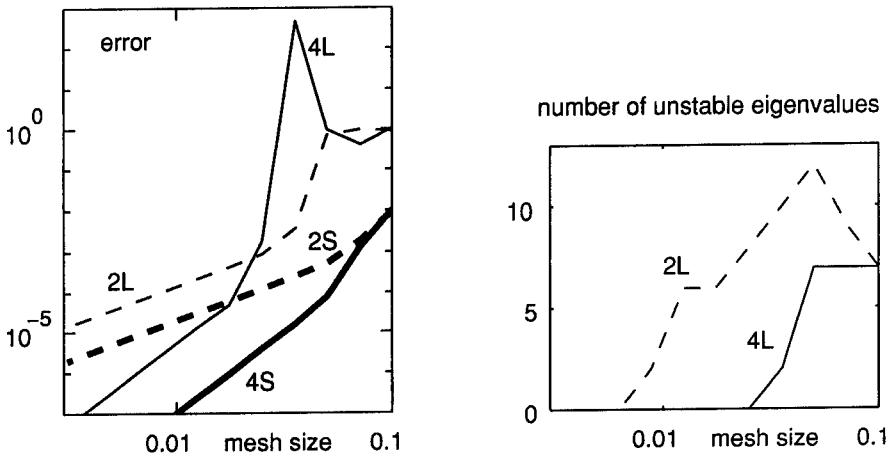


Figure 2. The left-hand figure shows the global error as a function of the mean mesh size on an exponential grid with half of the grid points inside a boundary layer of thickness 10/Re. Four methods are shown: 2L and 4L (2nd- and 4th-order Lagrangian), 2S and 4S (2nd- and 4th-order symmetry-preserving). The right-hand figure depicts the number of eigenvalues of the Lagrangian methods 2L and 4L located in the unstable halfplane. Only the Lagrangian methods are shown, since the symmetry-preserving discretization keeps all the eigenvalues in the stable halfplane.

– The fourth-order Lagrangian method nearly breaks down for $N = 28$ where the stretching factor is 0.72 (which is not extreme). This is due to an eigenvalue moving from the unstable half plane (for low values of N), towards the stable half plane (for higher N), which crosses the imaginary axis close to the origin, making the coefficient matrix almost singular. When one or more eigenvalues of the coefficient matrix are located in the unstable halfplane, the corresponding time-dependent, semi-discrete system is unstable, and can not be integrated in the time domain. In the above examples we have computed the discrete steady-state by a direct matrix solver to avoid this problem.

For details concerning the application to the three-dimensional, incompresible Navier-Stokes equation, we refer to Verstappen and Veldman (1998, 2002). On a uniform grid, the second order scheme proposed by Harlow and Welsh (1965) preserves the symmetries of the convective and diffusive operator. In outline, we have generalized Harlow and Welsh's scheme to nonuniform meshes in such a manner that the symmetries are not broken, and apply Richardson extrapolation to improve the order of accuracy. A variant of our approach for collocated grids has been developed at Delft University (Twerda, 2000).

3. A challenging test-case: turbulent channel flow

In this section, the symmetry-preserving discretization is tested for turbulent channel flow. The Reynolds number is set equal to Re = 5,600 (based on the channel width and the bulk velocity), a Reynolds number at which direct numerical simulations have been performed by several research groups; see Kim *et al.* (1987), Gilbert and Kleiser (1991), Kuroda *et al.* (1995). In addition we can compare the numerical results to experimental data from Kreplin and Eckelmann (1979).

As usual, the flow is assumed to be periodic in the stream- and spanwise direction. Consequently, the computational domain may be confined to a channel unit of dimension $2\pi \times 1 \times \pi$, where the width of the channel is normalized. All computations presented in this section have been performed with 64 (uniformly distributed) streamwise grid points and 32 (uniformly distributed) spanwise points. In the lower-half of the channel, the wall-normal grid points are computed according to

$$y_j = \frac{\sinh(\gamma j/N_y)}{2\sinh(\gamma/2)} \qquad \text{with} \quad j = 0, 1, ..., N_y/2,$$

where N_y denotes the number of grid points in the wall-normal direction. The stretching parameter γ is taken equal to 6.5. The grid points in the upper-half are computed by means of symmetry.

The temporal integration of (1) is performed with the help of a one-leg method that is tuned to improve its convective stability (Verstappen and Veldman, 1997). The non-dimensional time step is set equal to $\delta t = 1.25\ 10^{-3}$. Mean values of computational results are obtained by averaging the results over the directions of periodicity, the two symmetrical halves of the channel, and over time. The averaging over time starts after a start-up period. The start-up period as well as the time-span over which the results are averaged, 1500 non-dimensional time-units, are identical for all the results shown is this section. Figure 3 shows a comparison of the mean velocity profile as obtained from our fourth-order symmetry-preserving simulation ($N_y = 64$) with those of other direct numerical simulations. Here it may be stressed that the grids used by the DNS's that we compare with have typically about 128^3 grid points, that is 16 times more grid points than our grid has. Nevertheless, the agreement is excellent.

To investigate the convergence of the fourth-order method upon grid refinement, we have monitored the skin friction coefficient C_f as obtained from simulations on four different grids. We will denote these grids by A, B, C and D. Their spacings differ only in the direction normal to the wall. They have $N_y = 96$ (grid A), $N_y = 64$ (B), $N_y = 56$ (C) and $N_y = 48$ (D) points in the wall-normal direction, respectively. The first (counted from

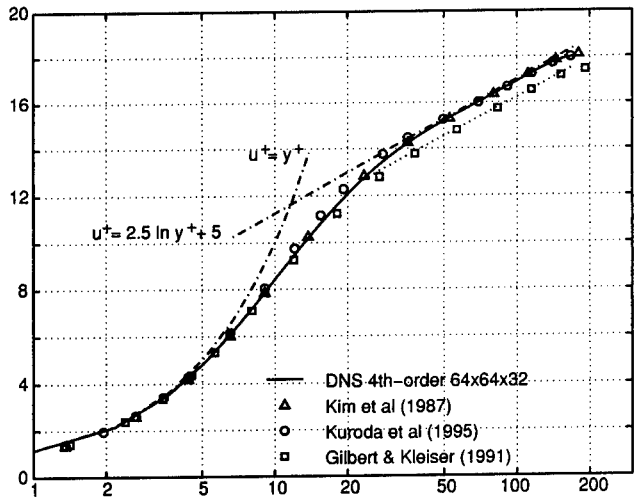


Figure 3. The mean streamwise velocity u^+ versus y^+. The dashed lines represent the law of the wall and the log law. The markers represent DNS-results that are taken from the ERCOFTAC Database.

the wall) grid line used for the convergence study is located at $y_1^+ \approx 0.95$ (grid A), $y_1^+ \approx 1.4$ (B), $y_1^+ \approx 1.6$ (C), and $y_1^+ \approx 1.9$ (D), respectively. Figure 4 displays the skin friction coefficient C_f as function of the fourth

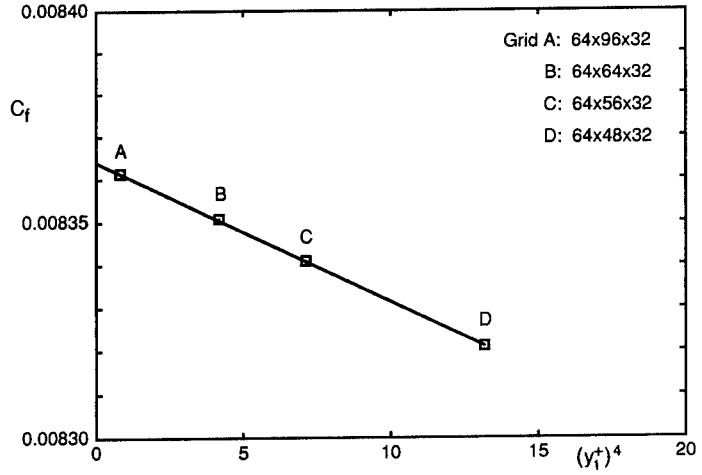


Figure 4. Convergence of the skin friction coefficient C_f upon grid refinement. The figure displays C_f versus the fourth power of the first grid point y_1^+.

power of y_1^+. The convergence study shows that the discretization scheme is indeed fourth-order accurate (on a nonuniform mesh). This indicates that the underlying physics is resolved when 48 or more grid points are used in the wall normal direction. In terms of the local grid spacing (measured by y_1^+), the skin friction coefficient is approximately given by $C_f = 0.00836 - 0.000004(y_1^+)^4$. The extrapolated value at $y_1^+ = 0$ lies in between the C_f reported by Kim *et al.* (1987) ($C_f = 0.00818$) and Dean's correlation of $C_f = 0.073\ Re^{-1/4} = 0.00844$ (Dean, 1978).

The convergence of the fluctuating streamwise velocity near the wall ($0 < y^+ < 20$) is presented in Figure 5. Here, we have added results obtained on three still coarser grids (with $N_y = 32$, $N_y = 24$ and $N_y = 16$ points in the wall-normal direction, respectively), since the results on the grids A, B, C and D fall almost on top of each other. The coarsest grid, with only $N_y = 16$ points to cover the channel width, is coarser than most of the grids used to perform a large-eddy simulation (LES) of this turbulent flow. Nevertheless, the $64 \times 16 \times 32$ solution is not that far off the solution on finer grids, in the near wall region. Further away from the wall, the turbulent fluctuations predicted on the coarse grids ($N_y \leq 32$) become too high compared to the fine grid solutions, as is shown in Figure 6.

The solution on the $64 \times 24 \times 32$, for example, forms an excellent starting point for a large-eddy simulation. The root-mean-square of the fluctuating streamwise velocity is not far of the fine grid solution, and viewed through physical glasses, the energy of the resolved scales of motion, the coarse grid ($N_y = 24$) solution, is convected in a stable manner, because it is conserved by the discrete convective operator. Therefore, we think that the symmetry-preserving discretization forms a solid basis for testing sub-grid scale models. The discrete convective operator transports energy from a resolved scale of motion to other resolved scales without dissipating any energy, as it should do from a physical point of view. The test for a sub-grid scale model then reads: does the addition of the dissipative sub-grid model to the conservative convection of the resolved scales reduce the error in the computation of u_{rms}.

The results for the fluctuating streamwise velocity u_{rms} are compared to the experimental data of Kreplin and Eckelmann (1979) and to the numerical data of Kim *et al.* (1987) in Fig. 7. This comparison confirms that the fourth-order, symmetry-preserving method is more accurate than the second-order method. With 48 or more grid points in the wall normal direction, the root-mean-square of the fluctuating velocity obtained by the fourth-order method is in close agreement with that computed by Kim *et al.* (1987) for $y^+ > 20$ (Figure 7 shows this only for y^+ up to 40; yet, the agreement is also excellent for $y^+ > 40$). In the vicinity of the wall ($y^+ < 20$), the velocity fluctuations of the fourth-order simulation method

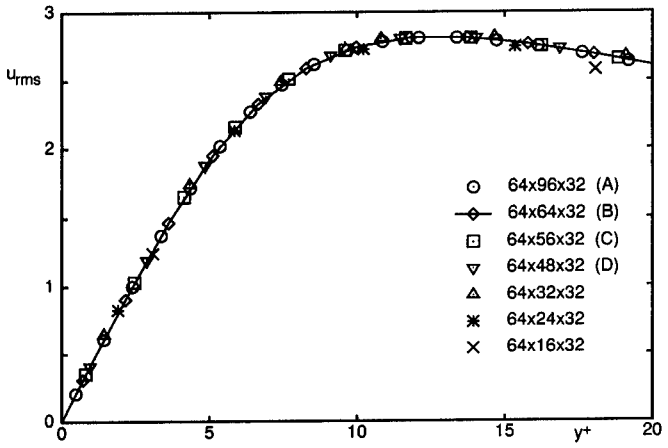


Figure 5. The root-mean-square velocity fluctuations normalized by the wall shear velocity as function of the wall coordinate y^+ on various grids for $y^+ \leq 20$. The markers correspond to the results obtained in the grid points. The solution on grid B is also represented by a continuous line.

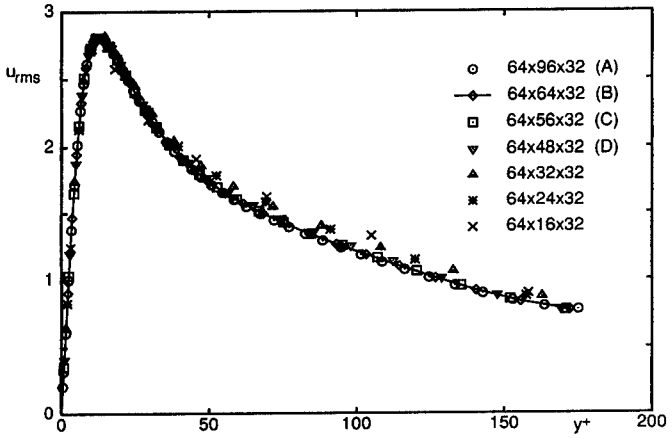


Figure 6. The root-mean-square velocity fluctuations normalized by the wall shear velocity for $y^+ \leq 200$ on various grids.

fit the experiment data nicely, even up to very coarse grids with only 24 grid points in the wall-normal direction. However, the turbulence intensity

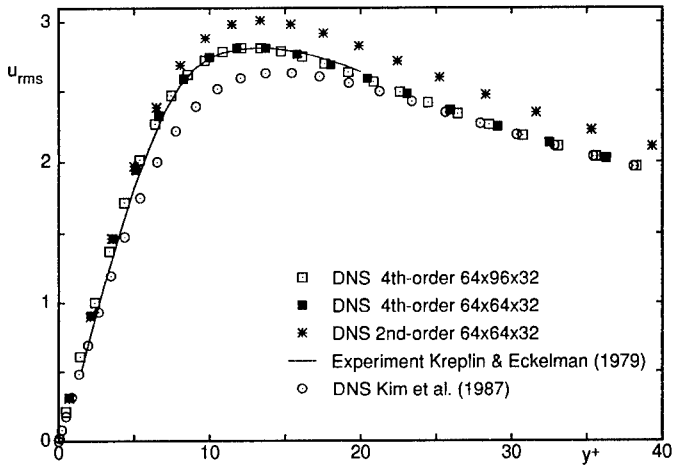


Figure 7. Comparison of the mean-square of the streamwise fluctuating velocity as function of y^+.

in the sublayer ($0 < y^+ < 5$) predicted by the simulations is higher than that in the experiment. According to the fourth-order simulation the root-mean-square approaches the wall like $u_{\text{rms}} \approx 0.38y^+$ ($N_y = 64$). The exact value of this slope is hard to pin-point experimentally. Hanratty *et al.* (1977) have fitted experimental data of several investigators, and thus came to 0.3. Most direct numerical simulations yield higher values. Kim *et al.* (1987) and Gilbert and Kleiser (1991) have found slopes of 0.3637 and 0.3824 respectively, which is in close agreement with the present findings.

So, in conclusion, the results of the fourth-order symmetry-preserving discretization agree better with the available reference data than those of its second-order counterpart, and with the fourth-order method a $64 \times 64 \times 32$ grid suffices to perform an accurate DNS of a turbulent channel flow at Re=5,600.

References

Antonopoulos-Domis, M. (1981) Large-eddy simulation of a passive scalar in isotropic turbulence. J. Fluid Mech. **104**, 55–79

Dean, R. B. (1978) Reynolds number dependence of skin friction and other bulk flow variables in two-dimensional rectangular duct flow. J. Fluids Engng. **100**, 215–223

Ducros, F., Laporte, F., Soulères, T., Guinot, V. Moinat, P. and Caruelle, B. (2000) High-order fluxes for conservative skew-symmetric-like schemes in structured meshes: application to compressible flows. J. Comp. Phys. **161**, 114–139

Gilbert, N. and Kleiser, L. (1991) Turbulence model testing with the aid of direct numerical simulation results. Proc. Turb. Shear Flows 8, Paper 26-1

Hanratty, T. J., Chorn, L. G. and Hatziavramidis, D. T. (1977) Turbulent fluctuations in the viscous wall region for Newtonian and drag reducing fluids. Phys. Fluids **20**, S112

Harlow, F. H. and Welsh, J. E. (1965) Numerical calculation of time-dependent viscous incompressible flow of fluid with free surface. Phys. Fluids **8**, 2182–2189

Hyman, J. M., Knapp, R. J., and Scovel, J. C. (1992) High order finite volume approximations of differential operators on nonuniform grids. Physica D **60**, 112–138

Kim, J., Moin, P. and Moser, R. (1987) Turbulence statistics in fully developed channel flow at low Reynolds number. J. Fluid Mech. **177**, 133–166

Kreplin, H. P. and Eckelmann, H. (1979) Behavior of the three fluctuating velocity components in the wall region of a turbulent channel flow. Phys. Fluids **22**, 1233–1239

Kuroda, A., Kasagi, N. and Hirata, M. (1995) Direct numerical simulation of turbulent plane Couette-Poisseuille flows: effect of mean shear rate on the near-wall turbulence structures. In: F. Durst et al. (Eds.) Proc Turb. Shear Flows, Springer-Verlag, Berlin, 241–257

Manteufel, T. A. and White, Jr., A.B. (1986) The numerical solution of second-order boundary value problems on nonuniform meshes. Math. of Comp. **47**, 511–535

Morinishi, Y., Lund, T. S., Vasilyev, O. V. and Moin, P. (1998) Fully conservative higher order finite difference schemes for incompressible flow. J. Comp. Phys. **143**, 90–124

Twerda, A. (2000) Advanced computational methods for complex flow simulation. Delft University of Technology, PhD thesis.

Vasilyev, O .V. (2000) High order finite difference schemes on non-uniform meshes with good conservation properties. J. Comp. Phys. **157**, 746–761

Verstappen, R. W. C. P. and Veldman, A. E. P. (1997) Direct numerical simulation of turbulence at lower costs. J. Engng. Math. **32**, 143–159

Verstappen, R. W. C. P. and Veldman, A. E. P. (1998) Spectro-consistent discretization of Navier-Stokes: a challenge to RANS and LES. J. Engng. Math. **34**, 163–179

Verstappen, R. W. C. P. and Veldman, A. E. P. (2002) Symmetry-preserving discretization of turbulent flow, submitted to J. Comp. Phys.

DNS OF INCOMPRESSIBLE FLOWS USING LATTICE BOLTZMANN METHOD

NOBUYUKI SATOFUKA

Department of Mechanical and System Engineering,
Kyoto Institute of Technology,
Matsugasaki, Sakyou-ku, Kyoto 606-8585, JAPAN

Abstract

Numerical simulations using the lattice Boltzmann method are presented for the two- and three-dimensional decaying homogeneous isotropic turbulence for low, medium and high Reynolds numbers. Time history of global statistical quantities, wave number spectra, and vorticity contour plots are compared with those of the higher-order method of lines. Comparisons between the square lattice and the triangular (FHP) lattice models are also performed. It is found that the lattice Boltzmann method is able to reproduce the dynamics of decaying turbulence and could be an alternative for solving the Navier-Stokes equations. Computational costs of the lattice Boltzmann method is less than half of that of the 10th-order method of lines.

1. Introduction

The rapid development and introduction of new supercomputer systems over the last decade has opened new opportunities for numerical studies of incompressible fluid flows. The direct numerical simulations of turbulence is one of such problems. So far almost all direct simulations of turbulence has been carried out by either spectral[1] or pseudo spectral[2,3] approximation to spatial derivatives. However, these methods which require the use of series are global in character so that they are quite unsuitable for complex geometry problems and for parallel computing. Therefore, the development of more flexible and efficient methods is hoped for in the simulations of turbulence.

We have proposed a new higher-order method based on a method of lines (MOL) approach[4-7] and demonstrated that results obtained by the method were comparable to those using the pseudospectral method with less than one sixth of the computational time in direct simulation of two-dimensional homogeneous isotropic turbulence on 513×513 grid points.

In the later half of the 80's, a novel technique called Lattice Gas Automata (LGA) for solving the Navier-Stokes equations was developed. Since the first two-dimensional model representing incompressible Navier-Stokes equations was proposed by Frisch, Hasslacher, and Pomeau (FHP) in 1986[8], LGA have attracted much attention as promising methods for solving a variety of partial differential equations and modeling physical phenomena. The basic idea of LGA methods is to represent the fluid as an ensemble of interacting low-order bit-computers situated at regularly spaced lattice nodes. In the FHP model, the underlying lattice is a close-packed equilateral triangular lattice with nodes at triangle vertices, each node has a seven-bit state with the first bit specifying the existence or not of a particle at rest at the lattice node and the remaining six bits specifying the presence or not of a particle traveling at an angle $\vartheta_j = (\pi/3)j$ $(0 \leq j \leq 6)$ along the legs of the triangular lattice. Each particle (except a rest particle) moves one lattice distance in one fundamental time interval. After the particles propagate they then interact according to certain collision rules. Although the LGA method has provided a fast and efficient way for solving partial differential equations, there exist some fundamental problems in this method in simulating realistic fluid flows obeying the Navier-Stokes equations. Besides its intrinsic noisy character which makes the computational accuracy difficult to achieve, it contains certain properties even in the fluid limit. The lattice gas fluid momentum equations cannot be reduced to the Navier-Stokes equations because of two fundamental problems. The first is the non-Galilean invariance property due to the density dependence of the convection coefficient. This limits the validity of the LGA method only a strict incompressible region. Second the pressure has an explicit and unphysical velocity dependence. To avoid some of those inherent problems, several lattice Boltzmann (LB) models have been proposed[9-15]. The main feature of the LB method is to replace the particle occupation variables n_i (Boolean variables) by the single-particle distribution functions (real variables) $f_i = \langle n_i \rangle$, where $\langle\ \rangle$ denotes a local ensemble average, in the evolution equation, i.e., the lattice Boltzmann equation. The LB method as a numerical scheme was first proposed by McNamara and Zaretti[9]. In their model, the form of collision operator is the same as in the LGA, written in terms of distribution functions and completely neglecting the effect of correlations between particles. Higuera, Jimenez, and Succi[10,11] introduced a linearized collision operator that is a matrix and has no correspondence to

the detailed collision rules. Statistical noise is completely eliminated in both models; however, the other problems remain, since the equilibrium distribution is still Fermi-Diracs. The LB model proposed by Chen et al[12,13] and Qian et al[14,15] abandons Fermi-Dirac statistic and applies the single relaxation time approximation first introduced by Bhatnager, Gross, and Krook in 1954[16], to greatly simplify the collision operator. This model is called the lattice BGK (LBGK) model.

This paper organized as follows. In section 2 the lattice Boltzmann methods simulating the Navier-Stokes equations are discussed. The lattice Boltzmann simulation of two-dimensional homogeneous isotropic turbulence is presented in section 3. Three-dimensional homogeneous isotropic turbulence is presented in section 4. Accuracy and efficiency of the lattice Boltzmann method in comparison with the conventional higher-order MOL approach are also discussed. The final section contains concluding remarks.

2. Lattice Boltzmann Method

2.1. SQUARE LATTICE MODEL

In this section an outline is given of the LB methods with BGK model for the collision operator. A square lattice with unit spacing is used on which each node has eight nearest neighbors connected by eight links as shown in Fig.1. Particles can only reside on the nodes and move to their nearest neighbors along these links in the unit time. Hence, there are two types of moving particles. Particles of type 1 move along the axes with speed $|\mathbf{e}_{1,i}| = 1$ and particle of type 2 move along the diagonal directions with speed $|\mathbf{e}_{2,i}| = \sqrt{2}$. Rest particles with speed zero are also allowed at each node. The occupation of the three types of particles is represented by the single-particle distribution function, $f_{\sigma i}(\mathbf{x}, t)$, where subscripts σ and i indicate the type of particle and the velocity direction, respectively. When $\sigma = 0$, there is only f_{01}. The distribution function, $f_{\sigma i}(\mathbf{x}, t)$, is the probability of finding a particle at node $\mathbf{x}$ and time t with velocity $\mathbf{e}_{\sigma i}$. According to Bhatnagar, Gross, and Krook (BGK), the collision operator is simplified using the single time relaxation approximation. Hence, the lattice Boltzmann BGK (LBGK) equation (in lattice unit) is

$$f_{\sigma i}(\mathbf{x} + \mathbf{e}_{\sigma i}, t + 1) - f_{\sigma i}(\mathbf{x}, t) = -\frac{1}{\tau}[f_{\sigma i}(\mathbf{x}, t) - f^{(0)}_{\sigma i}(\mathbf{x}, t)] \qquad (1)$$

where $f^{(0)}_{\sigma i}(\mathbf{x}, t)$ is the equilibrium distribution at $\mathbf{x}, t$ and τ is the single relaxation time which controls the rate of approach to equilibrium. The density per node, ρ , and the macroscopic velocity, $\mathbf{u}$, are defined in terms of the particle distribution function by

$$\rho = \sum_{\sigma} \sum_{i} f_{\sigma i}, \quad \rho \mathbf{u} = \sum_{\sigma} \sum_{i} f_{\sigma i} \mathbf{e}_{\sigma i} \qquad (2)$$

A suitable equilibrium distribution can be chosen in the following form for particles of each type

$$f_{01}^{(0)} = \rho\alpha - \frac{2}{3}\rho\mathbf{u}^2 \tag{3}$$

$$f_{1i}^{(0)} = \rho\beta + \frac{1}{3}\rho(\mathbf{e}_{1i}\cdot\mathbf{u}) + \frac{1}{2}\rho(\mathbf{e}_{1i}\cdot\mathbf{u})^2 - \frac{1}{6}\rho\mathbf{u}^2 \tag{4}$$

$$f_{2i}^{(0)} = \rho\frac{(1-4\beta-\alpha)}{4} + \frac{1}{12}\rho(\mathbf{e}_{2i}\cdot\mathbf{u}) + \frac{1}{8}\rho(\mathbf{e}_{2i}\cdot\mathbf{u})^2 - \frac{1}{24}\rho\mathbf{u}^2 \tag{5}$$

The relaxation time is related to the viscosity by

$$\nu = \frac{2\tau-1}{6} \tag{6}$$

where ν is the kinematic viscosity measured in lattice units. In ref.[17], Hou et al used the value of $\alpha = 4/9$ and $\beta = 1/9$.

The equilibrium populations are determined by assuming that they can be expressed as a power series in velocity and density of the form:

$$f_{\sigma i}^{(0)} = A_{\sigma i}(\rho) + B_{\sigma i}(\rho)\mathbf{e}_{\sigma i}\cdot\mathbf{u} + C_{\sigma i}(\rho)(\mathbf{e}_{\sigma i}\cdot\mathbf{u})^2 + D(\rho)_{\sigma i}\mathbf{u}^2 \tag{7}$$

A Chapman-Enskog procedure is then applied to determine the macroscopic behavior of this model. The values of $A_{\sigma i}$, $B_{\sigma i}$, $C_{\sigma i}$ and $D_{\sigma i}$ are chosen so that the macroscopic behavior matches the Navier-Stokes equations to as high an order as possible. The resulting continuity and momentum equations follow.

$$\frac{\partial\rho}{\partial t} + \frac{\partial\rho u_\beta}{\partial x_\beta} + O(\varepsilon^2) = 0 \tag{8}$$

$$\rho\frac{\partial u_\alpha}{\partial t} + \rho u_\beta\frac{\partial u_\alpha}{\partial x_\beta} = -\frac{\partial p}{\partial x_\alpha} + \frac{\partial}{\partial x_\beta}\left(\mu\left(\frac{\partial u_\beta}{\partial x_\alpha} + \frac{\partial u_\alpha}{\partial x_\beta}\right)\right) + O(\varepsilon^2) + O(M_\alpha^3) \tag{9}$$

Characteristic dimensionless parameters are the Mach number, $M_a = \sqrt{3}U/c$ where U is a characteristic macroscopic flow speed and $c = 1$ in lattice units, the Knudsen number which is proportional to $\varepsilon = c\tau/L$ where L is a macroscopic flow length, and the Reynolds number, $Re = \rho UL/\mu$.

2.2. TRIANGULAR (FHP) LATTICE MODEL

Another lattice model commonly used in two-dimensional LB simulation is a triangular lattice (FHP) model. There are two types of particles on each node of the FHP model: rest particles and moving particles with unit velocity $\mathbf{e}_i$ along six directions as shown in Fig.2. The equilibrium distributions for the FHP model are given as,

$$f_0^{(0)} = d_0 - \rho\mathbf{u}^2 = \rho\alpha - \rho\mathbf{u}^2 \tag{10}$$

$$f_i^{(0)} = d + \frac{1}{3}\rho\left[(\mathbf{e}_i \cdot \mathbf{u}) + 2(\mathbf{e}_i \cdot \mathbf{u})^2 - \frac{1}{2}\mathbf{u}^2\right]$$
$$= \frac{\rho - \rho\alpha}{6} + \frac{1}{3}\rho\left[(\mathbf{e}_i \cdot \mathbf{u}) + 2(\mathbf{e}_i \cdot \mathbf{u})^2 - \frac{1}{2}\mathbf{u}^2\right] \tag{11}$$

where α is an adjustable parameter. If the ratio of rest and moving particles is defined as $\lambda = d_0/d$, the pressure is determined by the isothermal equation of state,

$$p = 3d = \frac{(1-\alpha)\rho}{2} = \frac{3}{\lambda+6}\rho \tag{12}$$

and the speed of sound is

$$c_s^2 = \frac{1-\alpha}{2} = \frac{3}{\lambda+6} \tag{13}$$

The viscosity is related to the relaxation time through an equation of the form

$$\nu = \frac{2\tau - 1}{8} \tag{14}$$

2.3. CUBIC LATTICE MODEL

A cubic lattice[17] with unit spacing is used on which each node has fourteen nearest neighbors connected by fourteen links. Particles can only reside on the nodes and move to their nearest neighbors along these links in the unit time as shown in Fig.3. Hence, there are two types of moving particles. Particles of type 1 move along the axes with speed $|\mathbf{e}_{1,i}| = 1$ and particle of type 2 move along the links to the corners with speed $|\mathbf{e}_{2,i}| = \sqrt{3}$. Rest particles with speed zero are also allowed at each node.

A suitable equilibrium distribution can be chosen in the following form for particles of each type

$$f_{01}^{(0)} = \rho\alpha - \frac{2}{3}\rho\mathbf{u}^2 \tag{15}$$

$$f_{1i}^{(0)} = \rho\beta + \frac{1}{3}\rho(\mathbf{e}_{1i} \cdot \mathbf{u}) + \frac{1}{2}\rho(\mathbf{e}_{1i} \cdot \mathbf{u})^2 - \frac{1}{6}\rho\mathbf{u}^2 \tag{16}$$

$$f_{2i}^{(0)} = \rho\frac{(1-4\beta-\alpha)}{4} + \frac{1}{12}\rho(\mathbf{e}_{2i} \cdot \mathbf{u}) + \frac{1}{8}\rho(\mathbf{e}_{2i} \cdot \mathbf{u})^2 - \frac{1}{24}\rho\mathbf{u}^2 \tag{17}$$

Values of $\alpha = 2/9$ and $\beta = 1/9$ are used. The relaxation time is related to the viscosity by

$$\tau = \frac{6\nu + 1}{2} \tag{18}$$

where ν is the kinematic viscosity measured in lattice units.

3. Two-dimensional Homogeneous Isotropic Turbulence

3.1. INITIAL AND BOUNDARY CONDITIONS

The initial condition of the vorticity is randomly determined by satisfying the relation,

$$E(k) = \frac{1}{2} \sum_{|k'-k| \leq 1/2} | \tilde{\omega}(k_1, k_2) |^2 / k'^2 = \frac{2}{3} k \exp\left(-\frac{2}{3}k\right) \qquad (19)$$

where ω denotes the vorticity in the Fourier space, $k'^2 = k_1^2 + k_2^2$, and k_1 and k_2 are the wave numbers. The periodic boundary conditions are imposed in the x and y directions. The computational domain is square, $(0,0) \leq (x,y) < (2\pi, 2\pi)$.

3.2. LOW REYNOLDS NUMBER SIMULATION

In order to compare the results of the LBGK method with those of the MOL, numerical simulation using the square lattice model is carried out for a low Reynolds number. The kinematic viscosity is chosen as $\nu = 0.01$. The number of lattice nodes is 129×129 (129 lattice nodes and 128 lattice units in one side). In this case, the initial integral scale Reynolds number R_L corresponds to $R_L = 31.9$, which is expressed as $R_L = \Omega/\nu\eta^{\frac{1}{3}}$. Ω and η denote the total energy and the enstrophy dissipation rate, which are defined as

$$\Omega = \int_0^\infty E(k)dk, \quad \eta = 2\nu \int_0^\infty k^4 E(k)dk \qquad (20)$$

Perhaps the most striking verification of the accuracy of the LBGK method is found in the direct comparison of contour plots of vorticity between the LBGK method and higher-order MOL at the same physical time. Fig.4 displays comparison of vorticity contours at $t = 2.0$ between the square lattice BGK method (solid line) and 10th-order MOL (dashed line). The vorticity distribution is extremely similar down to detailed structure in the two simulations. Simulation by using the triangular (FHP) lattice BGK method is also performed for the same initial condition on lattice nodes. In Fig.5 comparison of vorticity contour plots at is shown between the square lattice (solid line) and the FHP lattice (dashed line). Once again, the plots from the two methods show excellent agreement. In order to investigate the behavior of statistical quantities, time history of (a) the total energy Ω, (b) the enstrophy Q and (c) the enstrophy dissipation rate η is shown in Fig.6, where the enstrophy Q is defined as $Q = \int_0^\infty k^2 E(k)dk$. Here Ω and Q are inviscid invariants, and therefore are monotonically decreasing in this dissipative simulation. The solid line, dotted line, and dashed line indicate to these quantities for the square lattice model, FHP lattice model, and

10th-order MOL, respectively. What is evident in Fig.6 is that the LBGK method tracks the higher-order MOL closely with respect to evolutions of Ω, Q and η. Wave number spectra of the total energy are also compared in Fig.7 which clearly displays the excellent match between the three methods. In the simulation of low Reynolds number case, no significant difference is observed between the square and triangular lattice models for this resolution.

3.3. HIGH REYNOLDS NUMBER SIMULATION

As a large-scale direct numerical simulation of high Reynolds number homogeneous isotropic turbulence, simulation for the case with $\nu = 0.0001$ is carried out. This corresponds to the initial integral scale Reynolds number $R_L = 25500$. The number of lattice nodes is 1025×1025. Fig.8 shows comparison of vorticity contour plots at $t = 3.0$ between the square lattice BGK method and the 10th-order MOL. Although slight difference in vorticity contours is noticeable at late time, strikingly similar features can be found for the LBGK simulation, as compared with the solutions by the 10th-order MOL.

Time history of (a) the total energy Ω and (b) the enstrophy dissipation rate η is shown in Fig.9. Since Reynolds number is much higher than the previous case, decrease in Ω is much less than observed in Fig.6(a). In contrast to Ω and Q which are monotonically decreasing in these cases, η can be amplified, as much as dissipated, and not monotonic as shown in Fig.9(b). Wave number spectra of $k^3E(k)$ at $t = 3.0$ are compared in Fig.10. From this figure it is seen that two methods yield quite a similar answer in terms of the statistical behavior of the flow. With the present lattice of 1025×1025 nodes, the inertial range of two-dimensional turbulence can be resolved. The spectrum shown in Fig.10 indicates that there is a range of wave number $k \leq 50$ for which $k^3E(k)$ is roughly constant so that $E(k)$ is proportional to k^{-3}.

Computational cost of the LBGK method for this high Reynolds number simulation on SGI POWER ONYX 10000 is compared in table 1 with that of the 10th-order MOL. As far as efficiency is concerned, the LBGK method requires less than half CPU time per characteristic time of that of the MOL.

4. Three-dimensional Homogeneous Isotropic Turbulence

4.1. INITIAL AND BOUNDARY CONDITIONS

Three-dimensional decaying turbulence is simulated with a random initial condition having the energy spectrum;

$$E(k) = 16\sqrt{2/\pi}\nu_0^2 k_{max}^{-5} k^4 \exp\left[-2(k/k_{max})^2\right] \tag{21}$$

where we set $\nu_0 = 1.0$ and the peak wave number $k_{max} = 4.75683$ for low Reynolds number case and $k_{max} = 2.37841$ for medium Reynolds number one. The periodic boundary conditions are imposed in the x, y and z directions. The computational domain is a cube, $0 \leq (x, y, z) \leq 2\pi$.

4.2. LOW AND MEDIUM REYNOLDS NUMBER SIMULATIONS

Numerical simulations are carried out for two cases. In the first case the kinematic viscosity is chosen as $\nu = 0.01189$. The initial integral scale and micro scale Reynolds number is $30 \sim 45$ which corresponds to low Reynolds number simulation. In the medium Reynolds number case $\nu = 0.0025$ is chosen which corresponds the initial integral scale and micro scale Reynolds number=340. The number of lattice nodes is $65 \times 65 \times 65$.

Contour surface of the enstrophy at $t = 0.5$ for the cubic LBGK method and the MOL for $\nu = 0.01189$ are shown in Fig.11(a) and (b) respectively. The enstrophy Ω is defined as

$$\Omega(x, y, z) = \frac{1}{2}(\omega_x^2 + \omega_y^2 + \omega_z^2) \tag{22}$$

Plot value is $\Omega_{plot} = 150$. Contour surface of the enstrophy computed by two methods are almost indistinguishable. Time history of the total energy and the enstrophy for medium Reynolds number are compared in Fig.12(a) and (b). The former is monotorically decreasing while the latter is amplified. Wave number dependence of energy spectrum $E(k)$ at $t = 0.7$ is also compared in Fig.13. From these figures it is seen that two methods yield quite a similar results in terms of the statistical behavior of the flow. Computational cost of the LBGK method for low Reynolds number simulation on a SGI POWER ONYX 10000 is also compared in Table 1 with that of the 10th-order MOL. As far as efficiency is concerned, the LBGK method requires 26% less CPU time than that of the MOL. Comparison between the cubic LBGK method and the MOL shows that the cubic LBGK method can be an alternative for solving the Navier-Stokes equations.

5. Conclusions

Two- and three-dimensional simulations of decaying homogeneous isotropic turbulence using the LBGK method have shown that the method is as accurate as the conventional method using the same lattice size. The LBGK method is able to reproduce the dynamic of decaying turbulence and could be an alternative for solving the Navier-Stokes equations. Further investigation is needed on the accuracy and efficiency of cubic LBGK model.

References

1. J.R.Herring, S.A.Orszag, R.H.Kraichman, and D.G.Fox, J. Fluid Mech., 66, (1974) 417.
2. D.GFox, and S.A.Orszag, L. Comp. Phys., 11, (1973) 612.
3. B.Fornberg, 1997, J. Comp. Phys., 25, (1997) 1.
4. N.Satofuka and H.Nishida, BAIL III, Boole Press, (1984), 291.
5. N.Satofuka and H.Nakamura and H.Nishida, Lecture Notes in Physics 218, Springer-Verlag, Berlin, (1984), 475.
6. H.Nishida and N.Satofuka, International Journal for Numerical Method in Engineering 34, (1992) 637.
7. H.Nishida and N.Satofuka, Finite Elements in Analysis and Design 16 (1994) 285.
8. U.Frisch, B.Hasslacher and Y.Pomeau. Phys. Rev. Lett. 56, (1986) 1505.
9. G.McNamara and G.Zanetti, Phys. Rev. Lett. 61, (1988) 2332.
10. F.Higuera and J.Jimenez, Europhys, Lett. 9, (1989) 663.
11. F.Higuera and S.Succi, Europhys, Lett. 8, (1989) 517.
12. S.Chen, H.Chen, D.Martinez, and W.H.Matthaeus. Phys. Rev. Lett. 67, (1991) 3776.
13. H.Chen, S.Chen, and W.H.Matthaeus, Phys. Rev. A 45, (1992) 5539.
14. Y.Qian, Ph.D. thesis. de I'Universit e Pierre et Marie Curie. January 1990.
15. Y.Qian, D.d'Humieres, and P. Lallemand, Europhys. Lett. 17(6), (1992) 479.
16. P.L.Bhatnagar, E.P.Gross, and M.Krook. Phys. Rev. 94, (1954) 511.
17. S.Hou, Q.Zou, S.Chen, G.Doolen, and A.C.Cogley. Journal of computational physics. 118, (1995) 329.
18. N.Satofuka, in: Numerical Properties and Methodologies in Heat Transfer, edited by T.M.Shin, Hemisphere, Washington, DC, (1983) 97.

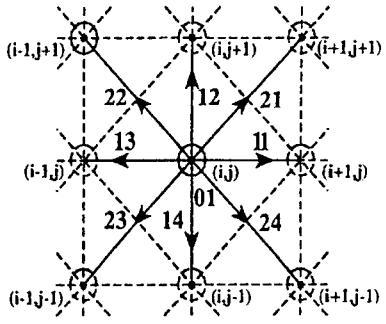


Figure 1. Square lattice model

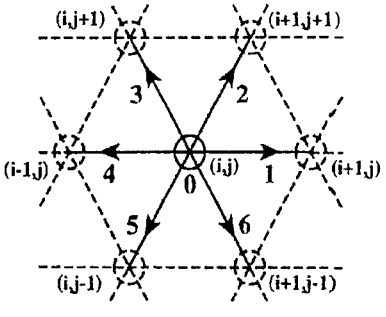


Figure 2. Triangular lattice model

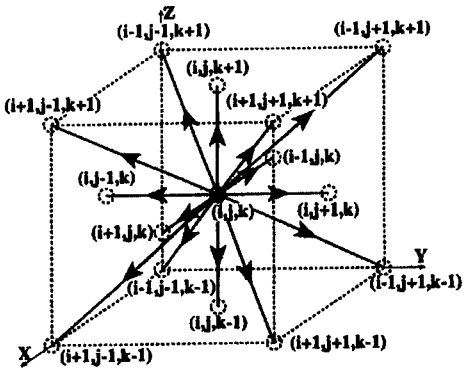


Figure 3. Cubic lattice model

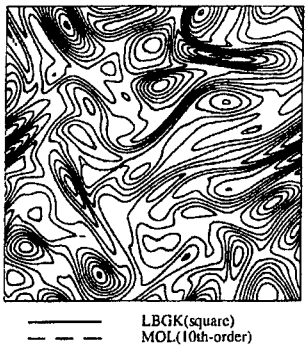


Figure 4. Comparison of vorticity countours between LBGK(square) and MOL(10th-order) at $t = 2.0$, $\nu = 0.01$

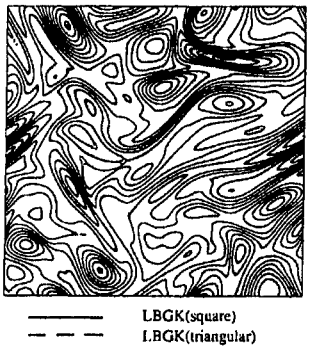


Figure 5. Comparison of vorticity countours between LBGK(square) and LBGK(triangular) at $t = 2.0$, $\nu = 0.01$

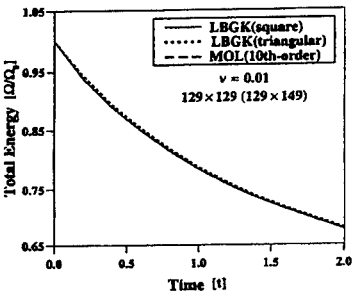


Figure 6(a). Time history of total energy Ω computed by LBGK(square), LBGK(triangular) and MOL(10th-order) for $\nu = 0.01$

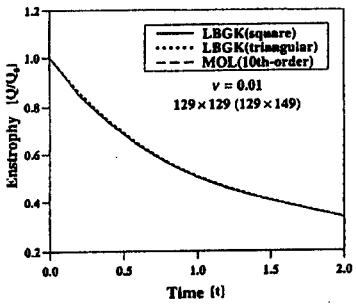


Figure 6(b). Time history of enstrophy Q computed by LBGK(square), LBGK(triangular) and MOL(10th-order) for $\nu = 0.01$

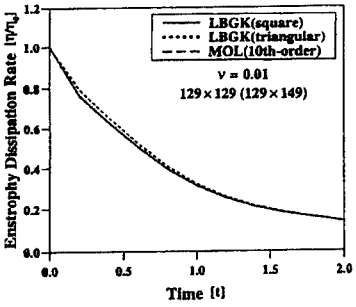


Figure 6(c). Time history of enstrophy disspation rate η computed by LBGK(square), LBGK(triangular) and MOL(10th-order) for $\nu = 0.01$

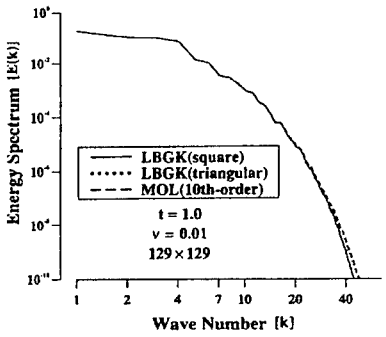


Figure 7. Wave number dependence of energy spectrum $E(k)$ computed by LBGK(square), LBGK(triangular) and MOL(10th-order) at $t = 1.0$, $\nu = 0.01$

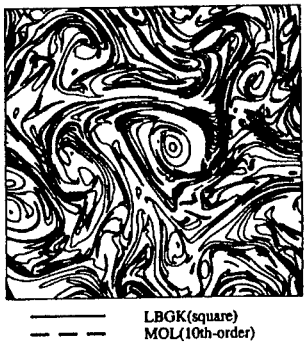


Figure 8. Comparison of vorticity countours between LBGK(square) and MOL(10th-order) at $t = 3.0$, $\nu = 0.0001$

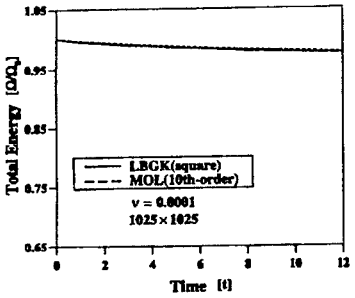


Figure 9(a). Time history of total energy Ω computed by LBGK(square) and MOL(10th-order) for $\nu = 0.001$

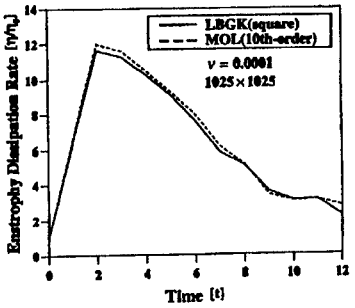


Figure 9(b). Time history of energy dissipation rate η computed by LBGK(square) and MOL(10th-order) for $\nu = 0.001$

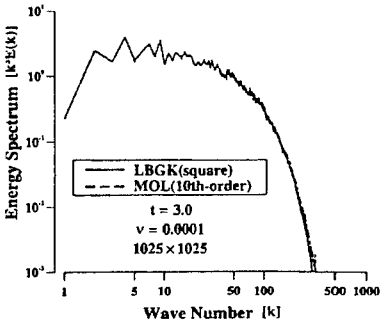


Figure 10. Wave number dependence of energy spectrum $k^3E(k)$ computed by LBGK(square) and MOL(10th-order) at $t = 3.0$, $\nu = 0.0001$

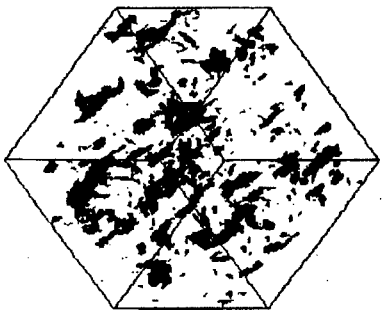


Figure 11(a). Enstorophy contours at $t = 0.5$ for the cubic LBGK method

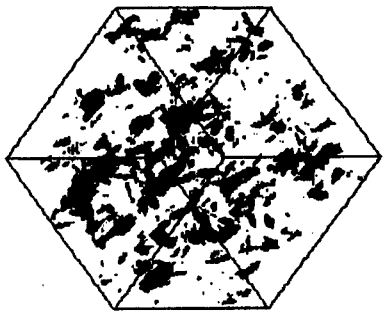


Figure 11(b). Enstorophy contours at $t = 0.5$ for the MOL

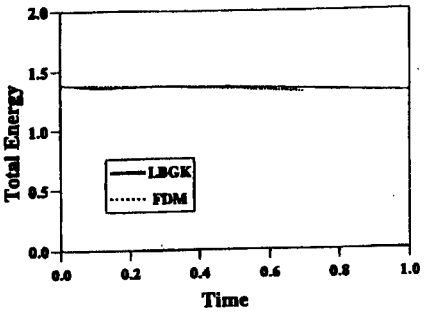


Figure 12(a). Time history of total energy computed by LBGK(cubic) and MOL for $\nu = 0.0025$

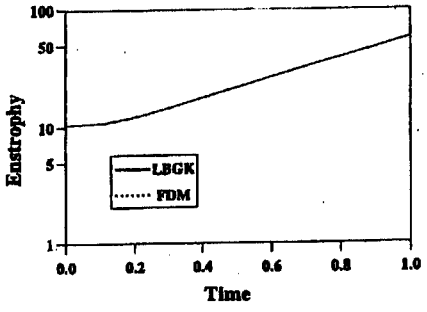


Figure 12(b). Time history of enstrophy computed by LBGK(cubic) and MOL for $\nu = 0.0025$

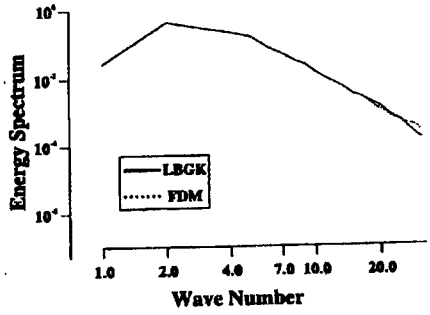


Figure 13. Wave number dependence of spectrum $E(k)$ at $t = 0.7$

TABLE 1. Comparison of computational cost

two-dimension		three-dimension	
LBGK(square)	MOL(10th-order)	LBGK(square)	MOL(10th-order)
$\sqrt{\langle u^2 \rangle} = 0.04$	$\Delta t = 0.001$	$\sqrt{\langle u^2 \rangle} = 0.01$	$\Delta t = 0.01$
4047[time step]	1000[time step]	1019[time step]	100[time step]
$t = 1.0$	$t = 1.0$	$t = 1.0$	$t = 1.0$
63006 < 1 >	136639 < 2.17 >	8686[sec] < 1 >	10924[sec] < 1.26 >
15.47[sec/time step] < 1 >	136.64[sec/time step] < 8.83 >	8.52[sec/time step] < 1 >	109.24[sec/time step] < 12.82 >

TOWARD THE DE-MYSTIFICATION OF LES

C.D. PRUETT
Department of Mathematics & Statistics
MSC 7803
James Madison University
Harrisonburg, VA 22807

1. Introduction

Some 35 years have elapsed since large-eddy simulation (LES) was introduced as a computational tool for weather modeling (Lilly, 1966). Because direct numerical simulation (DNS) will remain prohibitively expensive well into the foreseeable future for high-Reynolds-number flow, LES continues to hold great promise for simulating flows of engineering interest. However, despite the attention the method has received over the past decades, and despite important recent developments (e.g., the notions of "explicit" filtering and localized or "dynamic" modeling (Germano *et al.*, 1992)), LES has been slow to mature as a predictive tool. In contrast, parabolized stability equation (PSE) methodology, for example, which originated in the mid 1980's (Bertolotti *et al.*, 1992), matured quickly and is now ready for use by the aerospace industry for transition prediction.

In the author's view, the relatively slow adaptation of LES as a predictive tool arises not from any fundamental flaw in the idea itself but most likely from misconceptions that widely permeate the practice of LES. The current paper addresses three pervasive misconceptions, each of which reveals a lack of clarity regarding the properties of digital filters and the relationship between the grid filter and the subgrid-scale (SGS) model.

2. Misconception 1: Grid Filtering is a Mere Formality

From an otherwise excellent recent text on turbulent flows (Mathieu and Scott, 2000) comes the following quote:

> Note that, if one forgets that the $\hat{U}_i$ is supposed to represent the filtered velocity field, the filter plays *absolutely no role* (emphasis added) in the final LES

equations, which can be understood in terms of adding a subgrid viscosity term to the Navier-Stokes equations, without introducing the notion of filtering.

The mistake here is confuse *formal* invariance under filtering operations with *quantitative* invariance. To be precise, the grid-filtered Navier-Stokes equations are given as follows:

$$\frac{\partial \overline{u}_k}{\partial t} + \frac{\partial(\overline{u}_k\overline{u}_l)}{\partial x_l} = -\frac{\partial \overline{p}}{\partial x_k} + \frac{1}{Re}\frac{\partial^2 \overline{u}_k}{\partial x_l \partial x_l} + \frac{\partial \tau_{kl}}{\partial x_l} \quad (1)$$

$$\tau_{kl} \equiv \overline{u}_k\overline{u}_l - \overline{u_k u_l} \quad (2)$$

Whereas the *form* of Eq. 1 is independent of the filter, the *value* of the residual stress τ_{kl} is not.

To illustrate, suppose that grid filtering is applied at a wavenumber cut-off k_c *greater than* the Kolmogorov wavenumber k_η (Fig. 1). Then, in effect, one conducts fully resolved DNS rather than LES, in which case, for all practical purposes $\tau_{kl} = 0$. As written, Eq. 2 is missing a parameter. In reality, $\tau_{kl} = \tau_{kl}(k_c)$. That is, the exact residual stress depends first and foremost upon the cut-off of the grid filter. What else does it depend upon? Figure 2 compares *exact* residual stresses computed from *a priori* analyses of isotropic turbulence (Pruett and Adams, 2000) by filtering with two different grid filters: one of 2nd-order, the other of 4th-order. The correlation between the *exact* residual stresses, which differ in both distribution and amplitude, is only 0.5! Thus, at minimum, τ_{kl} depends upon both the cut-off and the order of the grid filter. Can the dependence of the residual stress upon the filter be fully characterized?

Yes. A filter is completely characterized in terms of its transfer function $H(\xi)$, which expresses the action of the filter on the Fourier harmonic $\exp(\imath kx)$, where $\xi = k\Delta x$. That is, if the filter is represented by the parameterized (Δ) convolution integral $\bar{u}(x) = \int_{-\infty}^{-\infty} G(x'-x,\Delta)u(x')dx'$, then H is the Fourier transform of the kernel G, and G is its inverse transform. For example, consider the top-hat filter whose kernel is

$$G(x,\Delta) = \begin{cases} 1/\Delta & \text{if } |x| \le \Delta/2 \\ 0 & \text{otherwise} \end{cases} \quad (3)$$

Trapezoidal-rule quadrature over a filter width of $\Delta = 2\Delta x$ results in the discrete 3-point top-hat filter of weights [1/4,1/2,1/4], whose transfer function is

$$H(\xi) = \frac{1+\cos(\xi)}{2} = 1 - \frac{x^2}{2(2!)} + \frac{x^4}{2(4!)} - \ldots \quad (4)$$

Alternately, the action of a filter can be examined by Taylor-series expansion of a filtered field in terms of the un-filtered field and its derivatives.

For example,

$$\bar{u}(x) = u(x) + a_2 u''(x)\Delta x^2 + a_4 u^{(4)}(x)\Delta x^4 + ... \tag{5}$$

(Because we have presumed G to be symmetric, the expansion has only even-ordered terms.) For convenience, the factorials in the expansion have been absorbed into the coefficients a_{2m}. A filter is said to be of order $2m$ if a_{2m} $(m > 0)$ is the first non-vanishing coefficient. Equations 4 and 5 carry the same information in different guises, which becomes apparent if Eq. 5 is applied to the function $u(x) = \exp(\imath kx)$, from whence it follows

$$a_{2m} = \frac{(-1)^m H^{(2m)}(0)}{(2m)!} \tag{6}$$

Thus, the coefficients of Eq. 5 are completely determined by derivatives of the filter's transfer function. For the three-point top-hat filter, for example, $a_{2m} = \frac{1}{2(2m)!}$.

Now let G_x and G_y be discrete filters in the x and y dimensions, whose Taylor coefficients are a_{2m} and b_{2m}, respectively. For two-dimensional filtering, suppose $\bar{u} = G_y(G_x((u))$. By two-fold expansion, one obtains the following expression for the *exact* residual stress:

$$\begin{aligned}
-\tau_{kl} = {} & 2a_2 \frac{\partial u_k}{\partial x}\frac{\partial u_l}{\partial x}\Delta x^2 + 2b_2 \frac{\partial u_k}{\partial y}\frac{\partial u_l}{\partial y}\Delta y^2 \\
& + \left[4a_4 \frac{\partial u_k}{\partial x}\frac{\partial^3 u_l}{\partial x^3} + (6a_4 - a_2^2)\frac{\partial^2 u_k}{\partial x^2}\frac{\partial^2 u_l}{\partial x^2} + 4a_4 \frac{\partial^3 u_k}{\partial x^3}\frac{\partial u_l}{\partial x}\right]\Delta x^4 \\
& + \left[\frac{\partial u_k}{\partial x}\frac{\partial^3 u_l}{\partial x \partial y^2} + \frac{\partial u_k}{\partial y}\frac{\partial^3 u_l}{\partial x^2 \partial y} + 2\frac{\partial^2 u_k}{\partial x \partial y}\frac{\partial^2 u_l}{\partial x \partial y} + \frac{\partial^3 u_k}{\partial x \partial y^2}\frac{\partial u_l}{\partial x} + \frac{\partial^3 u_k}{\partial x^2 \partial y}\frac{\partial u_l}{\partial y}\right] \\
& \times 2a_2 b_2 \Delta x^2 \Delta y^2 \\
& + \left[4b_4 \frac{\partial u_k}{\partial y}\frac{\partial^3 u_l}{\partial y^3} + (6b_4 - b_2^2)\frac{\partial^2 u_k}{\partial y^2}\frac{\partial^2 u_l}{\partial y^2} + 4b_4 \frac{\partial^3 u_k}{\partial y^3}\frac{\partial u_l}{\partial y}\right]\Delta y^4 \\
& + O(h^6) \quad \text{where } h \in \{\Delta x, \Delta y\}
\end{aligned} \tag{7}$$

Eq. 7 is completely general; it is valid for *any* grid filters G_x and G_y whose coefficients are known, provided the associated Taylor series converge. The issue of convergence is addressed in Vasilyev *et al.* (1998) and Pruett *et al.* (2001). In short, convergence is guaranteed for positive symmetric filters.

We conclude that *the exact SGS-stress tensor is completely determined by the grid filter, as expressed through derivatives of its transfer function.*

3. Misconception 2: Any Model Goes with Any Filter

In the conventional practice of LES, the grid filter and the SGS-model are often selected independently, as observed by Piomelli *et al.* (1988). In

contrast, previous discussion reveals the filter, the exact SGS stresses, and the model to be fundamentally interrelated.

To be specific, Fig. 3 compares the transfer functions of filters of selected orders. The order of a filter is related to the flatness (i.e., the number of vanishing derivatives) of its transfer function at $\xi = 0$. Spectral filters, characterized by a sharp cut-off in Fourier space, act with infinite order. From Eq. 7, it follows that the leading term of τ_{kl} is of order h^{2m} if the grid filter itself is of order $2m$ ($m \geq 1$).

The most common models for LES are of eddy-viscosity type (Mathieu and Scott, 2000), of which the Smagorinsky model ($M1$) is the most familiar. Because $M1$ is scaled by h^2, it is consistent only with filters of (first or) second order. In particular, $M1$ is inconsistent with spectral filters. Even when used in conjunction with second-order filtering, the Smagorinsky model correlates poorly with exact (E) residual stresses, as observed in experiments by Liu *et al.* (1994) and computational studies by Pruett and Adams (2000). Typically $C(E, M1) \leq 0.2$, as suggested in Fig. 4. In contrast, similarity ($M2$) and gradient ($M3$) models perform considerably better in *a priori* analyses. Typically, $C(E, M2) > 0.8$ and $C(E, M3) \approx 0.6$, respectively (Liu *et al.*, 1994; Pruett and Adams, 2000).

The many well-known deficiencies of the Smagorinsky model help to explain, in physical terms, its poor performance. Among these, $M1$ is overly dissipative, which undermines its successful application to laminar-turbulent transition, and it is isotropic, which limits its applicability in the near-wall region. However, from a mathematical perspective, the deficiency of $M1$ is apparent: formally it doesn't match the leading-order terms of Eq. 7. In contrast, $M3$ matches at leading order term and $M2$ matches at leading order and partially matches beyond that. The author is led to concur with Leonard (1997) that the Smagorinsky model has "little justification" beyond some nice properties.

To conclude, further advancement of LES requires that more attention be devoted to filter-model consistency, to models that have greater fidelity to Eq. 7 (for example, similarity models) than does the Smagorinsky model, and/or to promising new mathematical techniques such as deconvolution (Domaradzki and Saiki, 1997; Stolz and Adams, 1999) that avoid explicit modeling.

4. Misconception 3: Fixed-Width Filters are Fine for LES

Whereas the wavenumber k^* and the grid increment Δx^* are dimensional quantities with dimensions $[1/L]$ and $[L]$, respectively, their product $\xi = k^* \Delta x^*$ is dimensionless. (Here, asterisks denote dimensional quantities.) Several problems in LES result from a failure to non-dimensionalize.

To be specific, the maximum wavenumber $k^*_{\max}$ in a simulated flow is determined by *physical* considerations. For fully resolved DNS, $k^*_{\max} \geq k^*_\eta$, where k^*_η, the Kolmogorov wavenumber, depends solely on Reynolds number. For LES, $k^*_{\max} \approx k^*_c$, where k^*_c lies in the inertial range of the energy spectrum (Fig. 1). Either way, physics determines $k^*_{\max}$.

On the other hand, the grid increment Δx^* is mandated by *numerical* considerations, that is, by the resolution necessary to resolve the smallest eddies *for the numerical scheme of choice.* For example, for Fourier and Chebyshev spectral, and fourth- and second-order finite-difference (FD) schemes, respectively,

$$\begin{aligned} \Delta x^* &= \pi/k^*_{\max} \quad \text{(Fourier spectral)} \\ \Delta x^* &= 2/k^*_{\max} \quad \text{(Chebyshev spectral)} \\ \Delta x^* &= \pi/(6k^*_{\max}) \quad \text{(4th-order FD)} \\ \Delta x^* &= \pi/(16k^*_{\max}) \quad \text{(2nd-order FD)} \end{aligned} \tag{8}$$

For the spectral schemes, the stated resolution results from application of the Nyquist criterion. For the FD schemes, resolution is based upon the author's computational experience (Pruett *et al.*, 1995).

A fixed-width filter (e.g., the 3-point top-hat filter) has the disadvantage that its cut-off is "hardwired" to the grid increment Δx^*. In contrast, a tunable filter permits the cut-off k^*_c to be adjusted independently of Δx^*. Figure 6 presents the transfer functions of a family of one-parameter second-order filters of Pade type (Lele, 1992), as functions of their dimensionless cut-off $\xi_c = k^*_c \Delta x^*$, where, by definition, $H(\xi_c) = 1/2$. The filter is continuously adjustable over its entire domain of cut-off values $0 < \xi_c \leq \pi$, which represent varying levels of numerical dissipation. In particular, $\xi_c = \pi$ provides no dissipation, and $\xi_c \approx 0$ provides maximum dissipation. The fixed-width top-hat filter corresponds to the particular value $\xi_c = \pi/2$.

What then are the problems with fixed-width filters? First, for FD numerical schemes, allowing the dissipation of the filter to be set by the grid increment virtually guarantees that the unintended truncation error of the numerical scheme will contaminate the intended dissipation of the filter.

Second, suppose we wish to compare LES against the results of *a priori* analysis from fully resolved DNS at, say, twice the grid resolution of the LES. For specificity, presume that both methods exploit Fourier spectral methods. The comparison, of course, should occur at the same physical cut-off in wavenumber space (Fig. 1). Thus $(k^*_c)_{\text{DNS}} = (k^*_c)_{\text{LES}}$. However, because $(\Delta x^*)_{\text{LES}} = 2(\Delta x^*)_{\text{DNS}}$, for the same physical cut-off, the dimensionless cut-offs must have the ratio $(\xi_c)_{\text{DNS}}/(\xi_c)_{\text{LES}} = 1/2$. Without a tunable filter, the comparison cannot be made at the same physical cut-off.

Third, *Ad hoc* attempts at tuning the three-point top-hat filter, for example, can have unintended consequences. By naively extending the filter

width Δ^* from $2\Delta x^*$ to $4\Delta x^*$, the transfer function changes from low-pass to U-shaped (Fig. 5). It is therefore highly preferable to begin with a tunable low-pass filter whose behavior is suitable at all values of dissipation (cut-off). The Pade filter shown in Fig. 6, for example, is such a filter.

To summarize, in LES, the dimensional cut-off k_c^* is determined by physical considerations, but the grid resolution Δx^* is mandated by numerical ones. Tunable (one-parameter) filters permit the cut-off and resolution to be specified independently, according to their respective criteria.

Conclusion

Most SGS models for LES have been developed on the basis of physical rather than mathematical considerations. However, it is shown that the *exact* residual stress is completely determined by the *mathematical* properties of the grid filter; that is, by its order, its cut-off wavenumber, and the shape of its transfer function.

References

Bertolotti, F., Herbert, Th., and Spalart, P.R., (1992) Linear and Nonlinear Stability of the Blasius Boundary Layer, *J. Fluid Mech.*, **242**, pp. 441-474.

Domaradzki, J.A., and Saiki, E.M., (1997) A Subgrid-Scale Model Based on the Estimation of Unresolved Scales of Turbulence, *Phys. Fluids A*, **9**, pp. 2148-2164.

Germano, M., Piomelli, U., Moin, P., and Cabot, W.H. (1991) A Dynamic Subgrid-Scale Eddy Viscosity Model, *Physics of Fluids A*, **3**, pp. 1760-1765.

Lele, S.K., (1992) Compact Finite Difference Schemes with Spectral-Like Resolution, *J. Comput. Phys.*, **103**, pp. 16-42.

Leonard, A. (1997) Large-Eddy Simulation of Chaotic Convection and Beyond, AIAA Paper No. 97-0204.

Lilly, D.K. (1966) *NCAR Manuscript 123*, Natl. Center for Atmospheric Res., Boulder, CO.

Liu, S., Meneveau, C., and Katz, J. (1994) On the Properties of Similarity Subgrid-Scale Models as Deduced from Measurements in a Turbulent Jet, *J. Fluid Mech.*, **275**, pp. 83-119.

Mathieu, J., and Scott, J. (2000). *An Introduction to Turbulent Flow*, Cambridge University Press.

Piomelli, U., Moin, P., and Ferziger, J.H. (1988) Model Consistency in Large-Eddy Simulation of Turbulent Channel Flow, *Phys. Fluids A*, **31**, pp. 1884-1891.

Pruett, C.D., Zang, T.A., Chang, C.-L., and Carpenter, M.H., (1995) Spatial Direct Numerical Simulation of High-Speed Boundary-Layer Flows–Part I: Algorithmic Considerations and Validation, *Theoret. Comput. Fluid Dynamics*, **7**, pp. 49-76.

Pruett, C.D., and Adams, N.A., (2000) *A Priori* Analyses of Three Subgrid-Scale Models for One-Parameter Families of Filters, *Phys. Fluids A*, **12**, pp. 1133-1142.

Pruett, C.D., Sochacki, J.S., and Adams, N.A. (2001) On Taylor-Series Expansions of Residual Stress, *Phys. Fluids A*, to appear.

Stolz, S., and Adams, N.A., (1999) An Approximate Deconvolution Procedure for Large-Eddy Simulation, *Phys. Fluids A*, **11**, pp. 1699-1701.

Vasilyev, O.V., Lund, T.S., and Moin, P. (1998) A General Class of Commutative Filters for LES in Complex Geometries, *J. Comput. Phys.*, **146**, pp. 82-104.

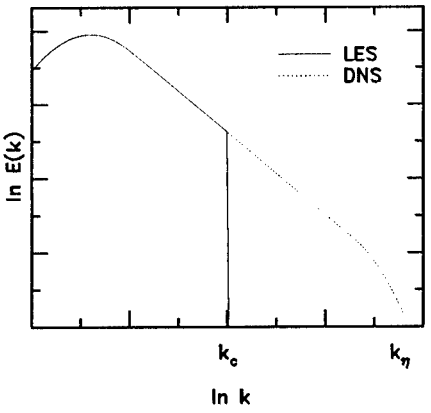


Figure 1. DNS vs. idealized LES.

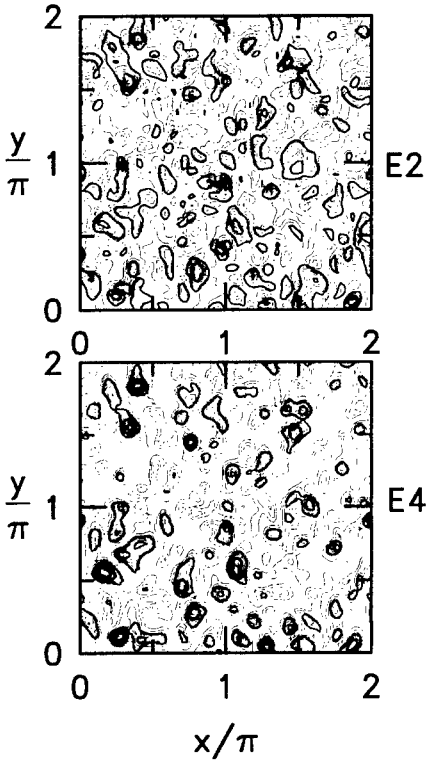


Figure 2. Exact SGS stresses from grid filters of 2nd- ($E2$) and 4th-order ($E4$).

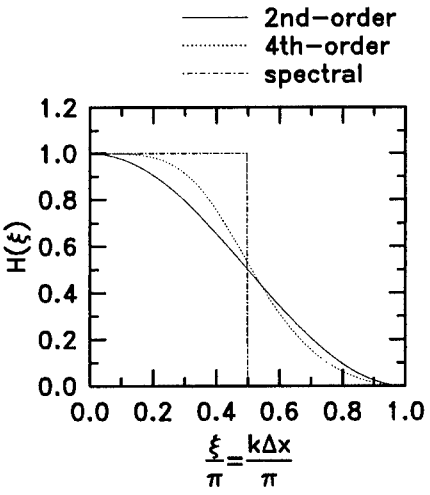


Figure 3. Filters of differing orders.

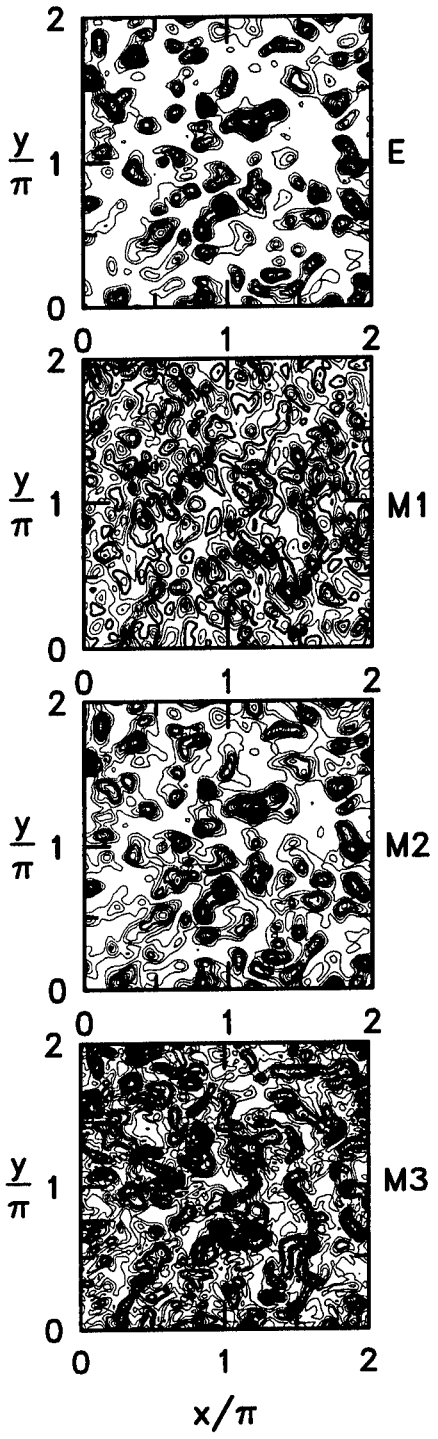


Figure 4. Planar contours of exact (E) and modeled ($M1$-Smagorinsky, $M2$-similarity, $M3$-gradient) SGS stresses (τ_{11} component).

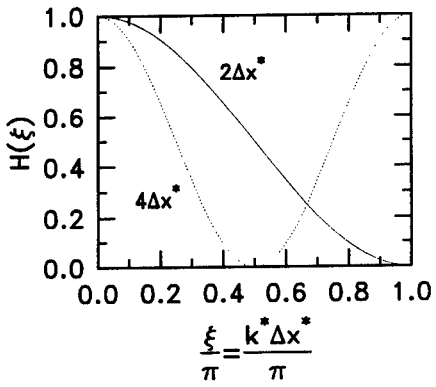


Figure 5. Transfer functions of three-point top-hat filters.

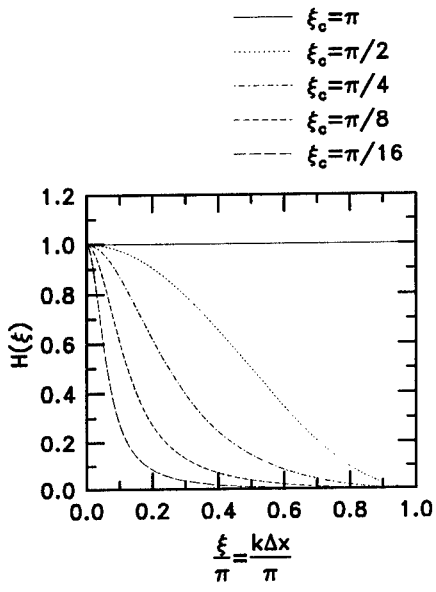


Figure 6. Transfer functions of one-parameter family of Pade filters.

RESIDUAL SCALE DEPENDENCE AND PDE FILTERS

G. PANTELIS
School of Aerospace, Mechanical and Mechatronic Engineering, University of Sydney, NSW, 2006, Australia.

1. Introduction

In [1] and [2] the filter operation acting upon nonlinear partial differential equations (PDE) is examined by way of a PDE filter on a domain involving space/time and an additional dimension associated with a space scale parameter. Under this approach it is possible to obtain an estimate for the error associated with the equations satisfied by the filtered solutions of the microscopic scale PDE given any approximation of the residuals. This provides a condition of consistency. The PDE filter approach suggests approximations for the residuals that are independent of empirical, or arbitrary, parameters.

Here the main points of [1] and [2] are presented with some additional issues addressed. An attempt is made to remain within a setting of general nonlinear PDE systems. The filtered equations of reactive turbulent flows are presented as an example.

2. Macroscopic Equations

Let $\Omega \subseteq \mathbf{R^3}$, $T = (0, t_0)$ and $\eta \in I = (0, \eta_0)$, where $t_0 > 0$ and $0 < \eta_0 << 1$. Define $M \subset \mathbf{R^n}$ such that $M = \Omega \times T \times I$. If $\Omega \subset \mathbf{R^3}$ is bounded we denote the boundary of Ω by $\partial\Omega$. The summation convention of repeated upper and lower indices is adopted and for convenience the following ranges for the indicated indices should be assumed throughout: $a, b, c, d \in \{1, ..., n-2\}$; $i, j, k, l \in \{1, ..., n-1\}$; $p, q, r, s \in \{1, ..., n\}$. Here n $(= 5)$ is the dimension of M and under this convention $(x^a) = (x^a)_{1 \le a \le 3} = (x, y, z)$, $x^{n-1} = t$, $x^n = \eta$. Hence we write, Ω has a coordinate system (x^a), $\Omega \times T$ has a coordinate system $(x^i) = (x^a, t)$ and M has a coordinate system $(x^p) = (x^i, \eta)$. The Greek indices are within the range: $\alpha, \beta, \gamma, \delta \in \{1, ..., N\}$, and are associated with the dependent variables, u^α,

where N denotes the number of dependent variables. Throughout we shall work with nondimensional variables.

The scale parameter η is defined by

$$\eta = \beta\epsilon^2/2 \tag{1}$$

where $\epsilon = l/L$ represents the ratio of the microscopic length scale l (smallest resolvable characteristic length scale) and the macroscopic length scale of the domain L. The parameter β (> 0) is chosen to control the rate of damping of fluctuations in the dependent variables. In most practical applications, ϵ represents a characteristic grid size for a (nondimensional) spatial discretization.

The set of smooth functions on M will be denoted by $F(M)$. For any $f \in F(M)$ the comma followed by a subscript $f_{,p}$ will indicate the partial derivative of f with respect to the coordinate x^p. It should be noted that much of the work that follows could be relaxed by replacing the smoothness condition to one of differentiability of some finite order. It will be useful to introduce a subset $\hat{F}(M) \subset F(M)$ which is defined as follows:

Definition 1. Any $f \in \hat{F}(M)$ has the following properties:

(i) $f \in F(M)$

(ii) For any $u^\alpha \in F(M)$, $f = \text{fn}(u^\alpha, u^\alpha_{,i}, u^\alpha_{,ij})$.

Property (ii) of the definition states that any member of $\hat{F}(M)$ can be expressed in a functional form explicitely independent of x^p, $u^\alpha_{,n}$ and $u^\alpha_{,np}$. It should be pointed out that $\hat{F}(M)$ is introduced here only to avoid some notational difficulties. In [2] the ideas that follow are more conveniently developed in the setting of contact manifolds where some of the restrictions introduced here can be avoided.

For any $u^\alpha \in F(M)$ let $\varphi^\alpha \in F(M)$ be defined by

$$\varphi^\alpha = (\frac{\partial}{\partial\eta} - L)u^\alpha \tag{2}$$

where L is an elliptic differential operator on Ω.

Define the vector field operator

$$U = L(u^\beta)\partial_\beta + (L(u^\beta))_{,i}\partial^i_\beta + (L(u^\beta))_{,ij}\partial^{ij}_\beta \tag{3}$$

with the notation

$$\partial_\beta = \frac{\partial}{\partial u^\beta}, \quad \partial^i_\beta = \frac{\partial}{\partial u^\beta_{,i}}, \quad \partial^{ij}_\beta = \frac{\partial}{\partial u^\beta_{,ij}} \tag{4}$$

A calculation shows that

$$(\frac{\partial}{\partial\eta} - U)f = Wf, \qquad f \in \hat{F}(M) \tag{5}$$

where

$$W = \varphi^{\alpha}\partial_{\alpha} + \varphi^{\alpha}_{,i}\partial^{i}_{\alpha} + \varphi^{\alpha}_{,ij}\partial^{ij}_{\alpha} \tag{6}$$

The PDE filter is defined as follows:

Definition 2. Any $u^{\alpha} \in PDEF\{L, \tilde{f}^{\alpha}, \tilde{u}^{\alpha}\}$ has the following properties:

(i) $u^{\alpha} \in F(M)$, $\tilde{u}^{\alpha} \in F(\Omega \times T)$ and

$$u^{\alpha}|_{\eta=0} = \tilde{u}^{\alpha} \tag{7}$$

(ii) $L : F(M) \to F(M)$ is an elliptic operator on Ω and

$$(\frac{\partial}{\partial \eta} - L)u^{\alpha} = 0, \qquad (x^{p}) \in M \tag{8}$$

(iii) $\tilde{f}^{\alpha} \in \hat{F}(M)$ vanishes at $\eta = 0$, i.e.

$$\tilde{f}^{\alpha}|_{\eta=0} = \tilde{f}^{\alpha}(\tilde{u}^{\beta}, \tilde{u}^{\beta}_{,i}, \tilde{u}^{\beta}_{,ij}) = 0 \tag{9}$$

In Definition 2 the $\tilde{u}^{\alpha}(x^{a}, t)$ are exact solutions of the equations that describe the system at the microscopic scale. These are expressed in the form of the PDE system (9) defined on $\Omega \times T$. ¿From the prescribed data $u^{\alpha}|_{\eta=0} = \tilde{u}^{\alpha}(x^{a}, t)$ we can generate a one parameter family of fields $u^{\alpha}(x^{a}, t, \eta)$ on M by integrating (8) with respect to the scale parameter η. The operator L must be chosen such that the integration of (8), with respect to η, will damp out fluctuations in each $\tilde{u}^{\alpha}$ that cannot be resolved on each scale associated with the parameter η. We will refer to $u^{\alpha}(x^{a}, t, \eta)$ for $\eta > 0$ generated by (8) as the filtered fields associated with solutions of the system of PDE (9). The existence of each $\tilde{u}^{\alpha} \in F(\Omega \times T)$ (coupled with suitable boundary conditions for the filtered fields on $\partial\Omega$ if Ω is bounded) is sufficient to guarantee the existence of the filtered fields $u^{\alpha} \in PDEF\{L, \tilde{f}^{\alpha}, \tilde{u}^{\alpha}\}$.

An effective filter in its simplest form can be obtained using the space Laplace operator

$$L = \delta^{cd}\frac{\partial^{2}}{\partial x^{c}\partial x^{d}} \tag{10}$$

where $\delta^{cd} = 1$ if $c = d$ and $\delta^{cd} = 0$ if $c \neq d$. For demonstration purposes we assume (10) throughout. It should be noted that here we are employing space filters. Definition 2 could be easily modified to include space and/or time filters. The simplest time only filter can be obtained by setting $L = \partial^{2}/\partial t^{2}$.

If $\Omega = \mathbf{R^3}$ and each $\tilde{u}^{\alpha} \in F(\Omega \times T)$ is bounded on $\Omega \times T$ then the filtered fields obtained from the integration of (8) with respect to η subject

to the initial data (7) yields the Gaussian filter

$$u^\alpha(x^a,t,\eta)=\int_\Omega G(x^a-z^a,\eta)\widetilde{u}^\alpha(z^a,t)dz^1dz^2dz^3 \tag{11}$$

where

$$G(x^a,\eta)=(4\pi\eta)^{-3/2}exp[-\delta_{ab}x^ax^b/(4\eta)] \tag{12}$$

Here the Gaussian filter is expressed in normalized form so that

$$\int_\Omega G(x^a-z^a,\eta)dz^1dz^2dz^3=1 \tag{13}$$

For the case of bounded Ω we must impose boundary conditions for the filtered fields on $\partial\Omega$. The PDE filter, as it is defined here, will still be effective in damping out irresolvable fluctuations provided suitable boundary conditions can be imposed.

As η is increased from 0 each $\widetilde{f}^\alpha \in \widehat{F}(M)$ may deviate from 0. We introduce

$$f^\alpha=\widetilde{f}^\alpha+r^\alpha \tag{14}$$

for some residual $r^\alpha \in F(M)$ such that

$$r^\alpha|_{\eta=0}=0 \tag{15}$$

Let $e^\alpha \in F(M)$ be defined by

$$e^\alpha=(\frac{\partial}{\partial\eta}-L)r^\alpha-\sigma^\alpha \tag{16}$$

where $\sigma^\alpha \in F(M)$ is given by

$$\sigma^\alpha=(L-U)\widetilde{f}^\alpha \tag{17}$$

¿From (14), (16) and (17) is obtained

$$e^\alpha=(\frac{\partial}{\partial\eta}-L)f^\alpha-W\widetilde{f}^\alpha \tag{18}$$

If $u^\alpha \in PDEF\{L,\widetilde{f}^\alpha,\widetilde{u}^\alpha\}$ then $\varphi^\alpha=0$ and the vector field operator W vanishes. Hence for $u^\alpha \in PDEF\{L,\widetilde{f}^\alpha,\widetilde{u}^\alpha\}$

$$(\frac{\partial}{\partial\eta}-L)f^\alpha=e^\alpha \tag{19}$$

¿From (9) and (15) we have

$$f^\alpha|_{\eta=0}=0 \tag{20}$$

Consider first the case $\Omega = \mathbf{R^3}$. We see that each f^α satisfies the initial value problem (19)-(20), where η replaces the traditional role taken by time and t appears only as a parameter. If each $e^\alpha \in F(M)$ is bounded on M the solution to this initial value problem can be obtained in the explicit form (see Lecture 8 [3])

$$f^\alpha(x^a, t, \eta) = \int_0^\eta \int_\Omega G(x^a - z^a, \eta - \xi) e^\alpha(z^a, t, \xi) dz^1 dz^2 dz^3 d\xi \tag{21}$$

Thus for consistency we need to generate residuals r^α such that, through the identity (16), each e^α is rendered sufficiently small.

If Ω has a boundary, $\partial\Omega$, then we can assume that given some prescription of u^α and r^α (and/or their spatial gradients) on the boundary $\partial\Omega$ we can set $f^\alpha|_{\partial\Omega} = 0$. This along with the system (19)-(20) defines an initial boundary value problem satisfied by each f^α. For an estimate of the consistency error we can replace the expression (21) by some inequality. For instance in terms of the $L_2(\Omega)$-norm, $\| \cdot \|$, we can obtain, for each $\alpha \in \{1, ..., N\}$, $\eta \in I$ and $t \in T$,

$$\| f^\alpha(\cdot, \eta) \| \leq \int_0^\eta \| e^\alpha(\cdot, \xi) \| e^{-\lambda(\eta - \xi)} d\xi \tag{22}$$

for some $\lambda > 0$. The inequality also holds for the case $\lambda = 0$.

If $e^\alpha = 0$ on M then the residuals r^α are known exactly. Thus, on M, the filtered fields of the solutions of the PDE (9) and the exact residuals $r^\alpha \in F(M)$ satisfy the system

$$\widetilde{f}^\alpha + r^\alpha = 0 \tag{23}$$

$$(\frac{\partial}{\partial \eta} - L) r^\alpha - \sigma^\alpha = 0 \tag{24}$$

where σ^α is given by (17). These are the exact macroscopic equations for the filtered fields $u^\alpha \in PDEF\{L, \widetilde{f}^\alpha, \widetilde{u}^\alpha\}$. Written in this form it is clear where the difficulties arise in constructing subgrid scale models for general nonlinear PDE systems (9). In application one desires the solution computed only on some slice $M|_{\eta = const}$. The presence of the term $\partial r^\alpha / \partial \eta$ makes the solution of (24) impractical and some approximation for the residuals needs to be introduced. The task is to generate r^α such that e^α is minimzed in (16). The relationship (21) (or (22)) gives an estimate of how close (23) is satisfied by the filtered fields $u^\alpha \in PDEF\{L, \widetilde{f}^\alpha, \widetilde{u}^\alpha\}$ given any approximation of the residuals r^α.

3. Approximation of the Residuals

We consider an approximation to (24), presented in [1] and [2], that is valid for any slice $M|_{\eta = const}$ for $0 < \eta \leq \eta_0$. Assume $r^\alpha \in F(M)$, such that

$r^\alpha|_{\eta=0} = 0$, satisfy on M

$$(\frac{1}{\eta} - L)r^\alpha - \sigma^\alpha = 0 \tag{25}$$

for some $u^\alpha \in F(M)$, not necessarily in $PDEF\{L, \widetilde{f}^\alpha, \widetilde{u}^\alpha\}$, and σ^α given by (17). A calculation based on (15), (16) and (25) gives

$$e^\alpha = \frac{\partial r^\alpha}{\partial \eta} - \frac{1}{\eta}(r^\alpha - r^\alpha|_{\eta=0}) = \frac{\eta}{2}\frac{\partial^2 r^\alpha}{\partial \eta^2}|_{\eta=\xi}, \qquad \xi \in (0, \eta) \tag{26}$$

If $\partial^2 r^\alpha / \partial \eta^2$ can be suitably bounded then we have $e^\alpha = O(\eta)$. ¿From (21) (or (22)) it follows that $f^\alpha = O(\eta^2)$ for $u^\alpha \in PDEF\{L, \widetilde{f}^\alpha, \widetilde{u}^\alpha\}$.

In general any $u^\alpha \in PDEF\{L, \widetilde{f}^\alpha, \widetilde{u}^\alpha\}$ will not satisfy (23) exactly on M if the residuals are not exact, i.e. they do not satisfy (24). In application one generates $u^\alpha \in F(M)$ by enforcing (23) and introducing some approximation for the residuals r^α (for example obtained from (25)). In such a case each u^α can only approximate members of $PDEF\{L, \widetilde{f}^\alpha, \widetilde{u}^\alpha\}$.

4. Approximation of the Filtered Fields

Let $u^\alpha \in F(M)$ satisfy (i) and (iii) of Definition 2 and be generated from (23) given some approximation of the residuals r^α (for example through (25)). Let $\bar{u}^\alpha \in PDEF\{L, \widetilde{f}^\alpha, \widetilde{u}^\alpha\}$. Since u^α is not a member of $PDEF\{L, \widetilde{f}^\alpha, \widetilde{u}^\alpha\}$ there exists $\varphi^\alpha \in F(M)$ satisfying (2) and we have

$$(\frac{\partial}{\partial \eta} - L)(u^\alpha - \bar{u}^\alpha) = \varphi^\alpha \tag{27}$$

Consider first the case Ω is unbounded (i.e. $\Omega = \mathbf{R^3}$). If $\varphi^\alpha \in F(M)$ is bounded on M then we obtain

$$(u^\alpha - \bar{u}^\alpha)(x^a, t, \eta) = \int_0^\eta \int_\Omega G(x^a - z^a, \eta - \xi)\varphi^\alpha(z^a, t, \xi) dz^1 dz^2 dz^3 d\xi \tag{28}$$

For the case where Ω has a boundary $\partial\Omega$ we assume that $u^\alpha|_{\partial\Omega} = \bar{u}^\alpha|_{\partial\Omega}$. As before, in terms of the $L_2(\Omega)$-norm we can obtain, for each $\alpha \in \{1, ..., N\}$, $\eta \in I$ and $t \in T$,

$$\| (u^\alpha - \bar{u}^\alpha)(\cdot, \eta) \| \leq \int_0^\eta \| \varphi^\alpha(\cdot, \xi) \| e^{-\lambda(\eta - \xi)} d\xi \tag{29}$$

for some $\lambda > 0$. The inequality also holds for the case $\lambda = 0$. Both (28) and (29) suggest that convergence of the approximations of the filtered fields rests upon the boundedness of φ^α.

A calculation based on (16), (17) and (23) gives

$$W\widetilde{f}^{\alpha} = -e^{\alpha} \tag{30}$$

If the residuals r^{α} are exact, then $e^{\alpha} = 0$ and $W\widetilde{f}^{\alpha} = 0$. For this to hold for arbitrary $\widetilde{f}^{\alpha}$ we must have $W = 0$ (the zero operator). Hence $\varphi^{\alpha} = 0$ and $u^{\alpha} \in PDEF\{L, \widetilde{f}^{\alpha}, \widetilde{u}^{\alpha}\}$. If each r^{α} is not exact then each u^{α}, generated from (23), will not be a filtered field and each φ^{α} will not vanish everywhere on M. Suppose that approximations for the residuals, r^{α}, can be found rendering each $e^{\alpha} = O(\delta(\eta))$, where δ is an order function with respect to η such that $lim_{\eta \to 0}\delta(\eta) = 0$. The problem is then transformed into one of establishing the rate at which the operator W tends to the zero operator as $\eta \to 0$.

5. Example: Reactive Flows

The ideas of the previous sections are developed in the context of general nonlinear PDE. For demonstration purposes we assume an incompressible fluid. The $\widetilde{f}^{a}$ are associated with the three fluid momentum equations and $\widetilde{f}^{n-1}$ is associated with the continuity or fluid mass conservation equation. The system is augmented with $\widetilde{f}^{n-1+A}$ $(A = 1, ..., Q)$ associated with Q mass balance equations for the Q chemical components. In this case we have $N = n - 1 + Q$ and

$$u^{a} = v^{a}, \quad u^{n-1} = p, \quad u^{n-1+A} = \omega^{A}, \quad (A = 1, ..., Q) \tag{31}$$

where v^{a} $(1 \leq a \leq 3)$ correspond to the fluid velocity components, p the fluid pressure and ω^{A} $(A = 1, ..., Q)$ are the mass fractions of the chemical components. We can write the functions $\widetilde{f}^{\alpha} \in \widehat{F}(M)$ corresponding to the equations of motion of an incompressible fluid and chemical component mass balance as

$$\begin{aligned} \widetilde{f}^{a} &= v^{a}_{,t} + (v^{b}v^{a} + \delta^{ab}p - \delta^{bc}v^{a}_{,c}/Re)_{,b} \\ \widetilde{f}^{n-1} &= v^{b}_{,b} \\ \widetilde{f}^{n-1+A} &= \omega^{A}_{,t} + (v^{b}\omega^{A} - \kappa\delta^{bc}\omega^{A}_{,c})_{,b} + \xi^{A} \end{aligned} \tag{32}$$

where Re is the Reynolds number, κ is a coefficient associated with molecular diffusion of the chemical components in the fluid medium and $\xi^{A} = \xi^{A}(\omega^{1}, ..., \omega^{Q})$ are the chemical source terms. It should be mentioned that to regard (9) under the prescription (32) as an exact description of the system at $\eta = 0$ is not entirely true since the fluid viscous and chemical diffusion terms are only approximate models of nonlinear effects ocurring at even smaller scales. For the sake of this demonstration we shall regard

this formulation as representing the exact microscopic equations at $\eta = 0$. We should note that the viscous and diffusion terms are linear and do not contribute to the residuals under filtering.

A calculation based on (17) and (32) leads to

$$\begin{aligned} \sigma^a &= 2\delta^{cd}(v^b_{,c}v^a_{,d})_{,b} \\ \sigma^{n-1} &= 0 \\ \sigma^{n-1+A} &= 2\delta^{cd}(v^b_{,c}\omega^A_{,d})_{,b} + \Xi^A \end{aligned} \tag{33}$$

where

$$\Xi^A = (L - U)\xi^A \tag{34}$$

is left in the generic form since we have not specified the source terms ξ^A as explicit functions of the chemical components. We can assume that the source terms $\xi^A \in \widehat{F}(M)$.

The identities (33) provide the source terms that appear in the system (23)-(24) (or the approximate system (23), (25)). Since $\sigma^{n-1} = 0$ we can set $r^{n-1} = 0$ in (16) and hence the continuity equation will be invariant under filtering, i.e. $\widetilde{f}^{n-1} = 0$ on M. It is seen that each σ^a, for the incompressible case, depend only on the velocities and their spatial partial derivatives. The corresponding residuals, r^a, will model the influence of the residual stress/strain of the turbulent fluid.

The source terms σ^{n-1+A} can be decomposed into two parts

$$\sigma^{n-1+A} = \sigma^{n-1+A}_{disp} + \sigma^{n-1+A}_{reac} \tag{35}$$

where σ^{n-1+A}_{disp} is associated with dispersion and σ^{n-1+A}_{reac} is associated with the reaction kinetics. In the absence of reaction source terms (i.e. when $\xi^A = 0$) each σ^{n-1+A}_{reac} vanish and the residuals, r^{n-1+A}, will model the influence of the dispersion of the chemical components in the flow field.

References

1. Pantelis, G. (1999) Generation of a one-parameter family of residuals for the filtered equations of fluid motion, *Recent Advances in DNS/LES*, D. Knight and L. Sakell (Eds.), Kluwer, pp. 341–348
2. Pantelis, G. (2000) The filter operation on nonlinear PDE, *Int. J. of Mathematics, Game Theory and Algebra*, **11 no. 2**.
3. Sobolev, S.L. (1964) Partial Differential Equations of Mathematical Physics, Pergamon Press.

A STUDY OF THE EFFECT OF SMOOTH FILTERING IN LES

GIULIANO DE STEFANO
Dipartimento di Ingegneria Aerospaziale,
Seconda Universitá di Napoli
81031 Aversa, Italy
Giuliano.DeStefano@unina2.it

AND

OLEG V. VASILYEV
Department of Mechanical and Aerospace Engineering,
University of Missouri-Columbia
Columbia, MO 65211, USA
VasilyevO@missouri.edu

Abstract. The large eddy simulation equations of turbulent flows are formally derived by applying a low-pass filter to the Navier-Stokes equations. As a result the subgrid-scale stress tensor strongly depends on the assumed filter shape, which causes a subgrid scales model to be filter dependent. Depending on the choice of the filter, the corresponding model should satisfy very different requirements in terms of large scale dynamics and kinetic energy budget. In this paper, it is demonstrated that the assumed filter shape can have a significant effect in terms of spectral content and physical interpretation of the solution.

1. Introduction

The large eddy simulation (LES) equations of turbulent flows are formally derived by applying a low-pass filter to the Navier-Stokes equations. The resulting equations have the same structure as the original ones plus additional terms, called subgrid scale (SGS) stresses. The success of the LES approach clearly depends on the ability of the SGS model to accurately represent the effect of the unresolved scales on the resolved ones. However, both the definition of resolved scales and the model for the SGS stress ten-

sor, $\tau_{ij} = \overline{u_i u_j} - \bar{u}_i \bar{u}_j$, strongly depend on the assumed filter shape. If the low-pass filter is exactly the sharp cut-off or close to it, then there is a clear separation of scales into large (resolved) and small (unresolved) ones and SGS stresses represent the effect of small scales on large ones. However, if the filter is smooth (like Gaussian or top-hat filter) then the boundary between resolved and unresolved scales is not well defined and the resulting SGS stresses represent the effect of small as well as large scales interactions.

The present paper is mainly aimed at demonstrating the importance of looking at filtering and SGS modeling as one inseparable issue and to provide LES practitioners a reference for interpreting the results of their simulations. Moreover, the knowledge of how the filter shape affects LES solution is of great importance in constructing efficient and consistent turbulence models. Thus, the objective of the present study is to establish the general framework for looking at the effect of the filter shape on large scale dynamics and energy transfer.

2. Theoretical Accomplishments

In this section the effect of the filter shape is briefly studied from a theoretical point of view. For a deeper analysis one can see in the related paper by the authors (De Stefano & Vasilyev, 2001). For simplicity reasons we consider one-dimensional (1D) homogeneous flow governed by the viscous Burgers equation, originally proposed as a model equation for turbulence (Burgers, 1974),

$$\frac{\partial u}{\partial t} + u\frac{\partial u}{\partial x} = \nu \frac{\partial^2 u}{\partial x^2}. \tag{1}$$

Despite the simplicity of this model, the analysis and subsequent conclusions drawn from it are applicable for the general LES.

By filtering Eq.(1) one obtains the following LES equation describing the evolution of the filtered field:

$$\frac{\partial \overline{u}}{\partial t} + \overline{u}\frac{\partial \overline{u}}{\partial x} = \nu \frac{\partial^2 \overline{u}}{\partial x^2} - \frac{1}{2}\frac{\partial \tau}{\partial x}, \tag{2}$$

where $\tau = \overline{u^2} - \overline{u}^2$ stands for the SGS stress, that must be modeled in order to close the problem.

From a physical point of view, one would like to follow the dynamics of flow structures down to a given size, *i.e.* to solve the velocity field up to a certain characteristic wave-number. Thus, the most natural choice for the filter function is the sharp cut-off filter in Fourier space. This way, the velocity fluctuation does not contain resolved wave-numbers components and the resolved velocity field has a clear physical meaning. On the

contrary, smooth filters provide an overlapping between resolved and unresolved scales and the physical interpretation of the large-eddy field is more obscure. The influence of the filter shape on the SGS stress is very clear if one looks at its spectral content

$$\hat{\tau}(\kappa) = \int_{\kappa'+\kappa''=\kappa} \left[\hat{G}(\kappa) - \hat{G}(\kappa')\hat{G}(\kappa'')\right] \hat{u}(\kappa')\hat{u}(\kappa'')d\kappa', \tag{3}$$

where $\hat{G}$ stands for the filter transfer function. When a sharp cut-off (say at wavenumber κ_c) is applied, the SGS stress spectrum exactly accounts for the effect of small scales ($|\kappa| \leq \kappa_c$) on large ones. For a smooth filter, one can define a characteristic wave-number $\overline{\kappa}$ so that scales at $|\kappa| \leq \overline{\kappa}$ are referred to as large ones. In this case the SGS stress accounts not only for the effect of small scales, but also for the effect of filtering on large ones. It is illustrative to consider a velocity field with no Fourier components beyond $\overline{\kappa} = \kappa_c$. In this case, according to Eq. (3), the SGS stress for the spectral cut-off vanishes while, for a smooth filter, the same equation provides a non-zero SGS stress, being $\hat{G}(\kappa' + \kappa'') \neq \hat{G}(\kappa')\hat{G}(\kappa'')$.

The effect of the smoothness of the filter appears also evident by considering the kinetic energy budget in wave-numbers space

$$\frac{\partial \mathcal{E}}{\partial t} = -2\nu\kappa^2\mathcal{E} + \mathcal{T} + \mathcal{P}, \tag{4}$$

where $\mathcal{E}$ is the resolved field energy density, $\mathcal{T}$ the energy transfer among different resolved wave-numbers and $\mathcal{P}$ a source term due to the interaction between resolved and unresolved eddies. When the sharp cut-off filter is adopted, $\mathcal{P}$ exactly represents the energy transfer between large and small scales while, for smooth filters, it must also account for large scales interactions. In the illustrative example considered, the sharp cut-off filter does not alter the energy transfer, since $\mathcal{P} = 0$, while any smooth filtering results in a drain of energy, since $\mathcal{P}$ no longer vanishes.

3. Numerical Experiments

In this section the results from numerical experiments are presented confirming the strong effect of the filter shape on LES with explicit filtering. First, we report some results dealing with the numerical simulation of a 1D freely decaying turbulent flow, governed by the Burgers equation (1), in terms of temporal evolution of energy and dissipation; for a deeper analysis one can see in (De Stefano & Vasilyev, 2001). Then, some preliminary result about the numerical simulation of isotropic turbulence are shown. In particular, the effect of the filter shape on the energy spectrum of the flow is discussed.

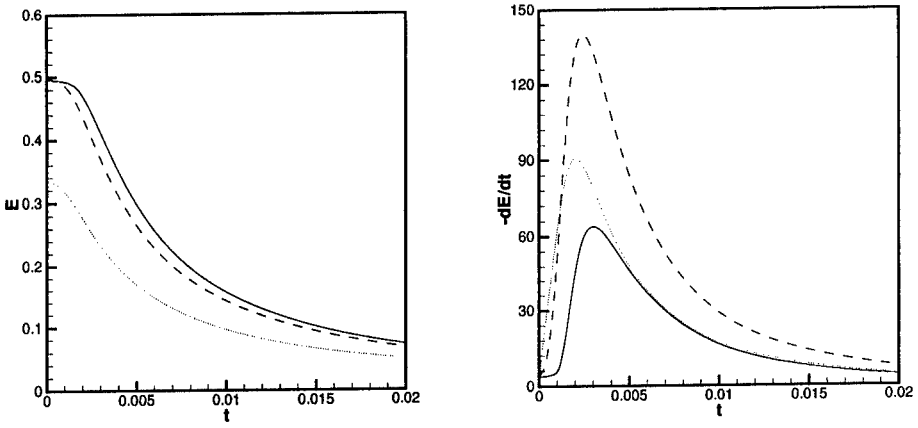


Figure 1. Temporal evolution of total energy E and dissipation $d\mathrm{E}/dt$ for *perfect* LES, for both sharp cut-off (- - -) and top-hat (·····) filters, together with those for DNS (———).

Herein a top-hat filter is used as an example of smooth filters. It is worth noting that when comparing LES results for different filters, one needs to consider these latter corresponding to the same filter width. Thus, it is important to use consistent filter width definitions. In this paper, for the smooth filter, we adopt the definition according to which the filter width is taken to be proportional to the inverse wave-number where the filter transfer function falls to 0.5 (Lund, 1997), that is $\overline{\kappa} = \kappa_c = \pi/\Delta$, being Δ the common filter width. LES runs are performed with the aid of the so-called *perfect* SGS model, an ideal model constructed by definition upon the DNS data, assumed as the exact solution. Then, in order to mimic a real SGS model, in which it is hard to model large scales, this ideal model is modified by taking the effect of large scales out, but leaving the small scales one intact. This is achieved by treating the modeled stress with a high-pass filter, whose Fourier transform is $1 - \hat{G}(\kappa)$, where $\hat{G}(\kappa)$ corresponds to a sharp low-pass discrete filter (Vasilyev *et al.*, 1998) with filter width $\widetilde{\Delta}$. Note that with the increase of the ratio $\widetilde{\Delta}/\Delta \geq 1$ more scales are left intact and the *perfect* LES model is approached.

3.1. BURGERS SOLUTION

The numerical solution of the 1D homogeneous Burgers problem is obtained integrating in time Eq. (1) with periodic boundary conditions. In order to

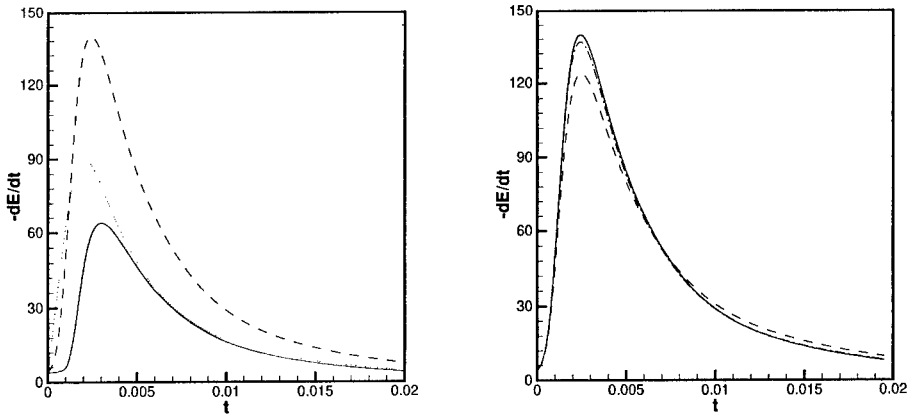


Figure 2. Sharp cut-off filtering: temporal evolution of total energy $\mathbf{E}$ and dissipation $d\mathbf{E}/dt$ for *perfect* LES (———) and altered LES with different ratios $\widetilde{\Delta}/\Delta$: 2 (- - -), 3 (— · —), and 4 (·····).

minimize the influence of truncation and aliasing errors, the numerical integration is carried out with the aid of a high-order non-dissipative numerical method and a sufficiently fine grid. LES simulation with *perfect* SGS stress results in the energy spectra identical to the filtered DNS solution regardless of the filter used (De Stefano & Vasilyev, 2001). The temporal evolution of the total flow energy and dissipation are shown in Fig. 1: in case of sharp cut-off filtering, the solution keeps a high fraction of the energy content of the flow, while, for smooth filtering, a large part of it is lost, even in the ideal case. Due to the perfect modeling and the very good numerics exploited this loss of energy exactly accounts for the effect of smooth filtering on LES solution.

Results for 1D LES with altered SGS model are presented in Fig. 2 and 3. Altering the *perfect* SGS model causes a wrong evolution of total energy: the dissipation provided by the model is not enough and kinetic energy decays less in time with respect to the ideal case. For LES with top-hat filtering this effect is more important and the energy content of the flow is clearly badly represented.

3.2. ISOTROPIC TURBULENCE SIMULATION

In order to extend the 1D results to a real turbulent flow, some numerical test dealing with three-dimensional isotropic forced turbulence at $Re_\lambda \cong 70$

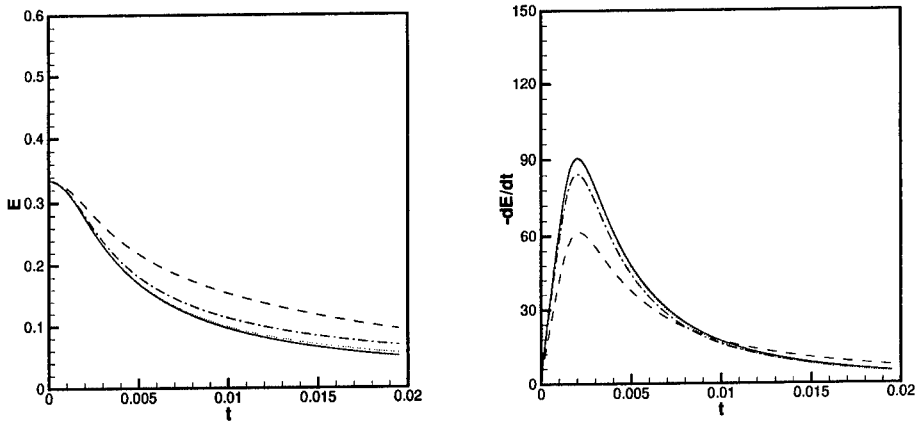


Figure 3. Top-hat filtering: temporal evolution of total energy $\mathbf{E}$ and dissipation $d\mathbf{E}/dt$ for *perfect* LES (———) and altered LES with different ratios $\widetilde{\Delta}/\Delta$: 2 (– – –), 3 (— · —), and 4 (·····).

are presented. The Navier-Stokes equations are solved with the convective term in rotational form and numerical simulation, both DNS and LES, are performed using a de-aliased pseudo-spectral code (Ruetsch & Maxey, 1991).

The DNS is conducted in the wave-numbers range $|\kappa| \leq 36$, while time integration is carried out till a statistical stationary field is reached. The simulation is further advanced in time, storing each N time steps the *perfect* SGS stress, where N is the integer ratio of LES to DNS time steps.

LES with both sharp cut-off and top-hat explicit filtering are conducted in the range $|\kappa| \leq 16$. The filter width is chosen such that the characteristic wave-number $\overline{\kappa} = 12$ is in the inertial range. In order to avoid generation of frequencies beyond the characteristic frequency $\overline{\kappa}$ we adopted an alternative SGS stress definition $\tau_{ij} = \overline{u_i u_j} - \overline{\overline{u}_i \overline{u}_j}$ suggested by Vasilyev *et al.* (1998).

The energy spectra corresponding to LES with *perfect* SGS model agree quite well with the filtered DNS ones, as illustrated in Fig. 4. For comparison the spectra of LES without any model are also reported. This fact is not surprising, since we provide *perfect* SGS model which gives us the exact dynamics and energy transfer. Moreover, as it is expected, the application of a smooth filter strongly affects the shape of the spectrum. In other words, for this kind of filter, even when LES is conducted with the ideal SGS model, the resolved field loses some important features of the *real* field. In particular, the slope corresponding to the inertial range is clearly

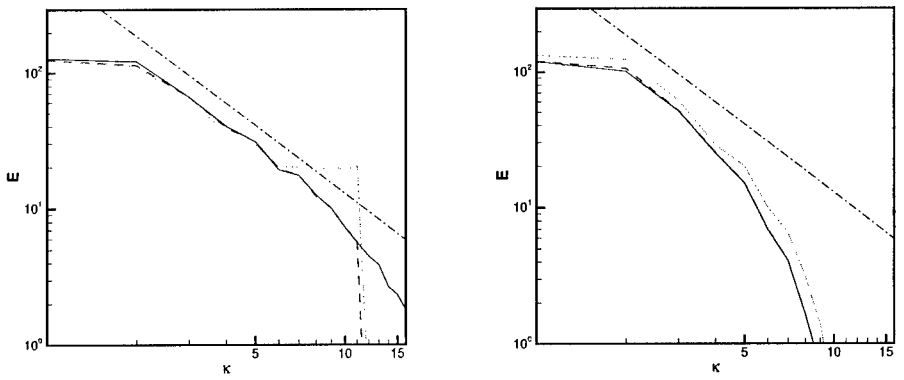


Figure 4. Energy spectra for filtered DNS (———), *perfect* LES (- - -) and LES without any model (·····) , for both sharp cut-off (left) and top-hat (right) filters. There is also shown the ideal slope of the inertial range $-5/3$ (— · —).

misrepresented.

The energy spectra corresponding to LES with altered SGS modeling are presented in Fig. 5. For sharp cut-off filtering, according to (3), the SGS stress has a very little contribution from large scales; thus, the altered *perfect* model appears to work well, even for $\widetilde{\Delta}/\Delta = 1$. The same is no longer true for smooth filtering, for which, even for high $\widetilde{\Delta}$ one cannot recover a good spectrum.

4. Concluding remarks

In this study we carried out some numerical experiments in order to address the influence of the filter shape in LES with explicit filtering. It is worth noting that the analysis was conducted not by means of *a priori* tests, as often made in similar studies, but performing actual LES with SGS models obtained by filtering DNS time series. Due to the good numerics adopted, the pure effect of filtering on actual LES solution was illustrated. In order to mimic a real simulation, the ideal SGS model was altered by filtering out the contribution of large scales on it. In the future, different SGS models used for LES simulations will be tested. Numerical results presented in this paper have clearly demonstrated the importance of considering SGS modeling and filtering as an inseparable issue. In particular, it was shown that if LES is based on smooth filter, then SGS model should also model the effect of the filter on large scales, *i.e.* forces (stresses) produced by interaction of large scales which are filtered out. The same is for energy cascade:

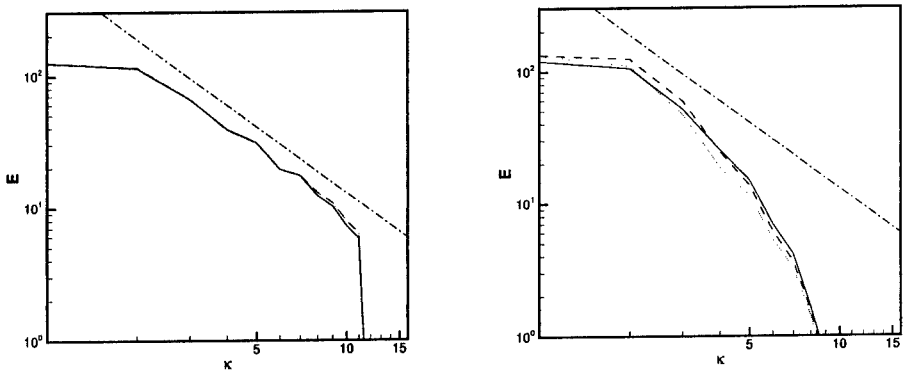


Figure 5. Energy spectra for LES with altered *perfect* SGS model. For sharp cut-off filtering (left), plots refer to $\widetilde{\Delta}/\Delta = 1$ (- - -) and 2 (·····) while, for top-hat filtering, they refer to $\widetilde{\Delta}/\Delta = 2$ (·····) and 4 (- - -). Perfect LES spectra are also shown (———).

SGS model should remove (or add) energy at the resolved scales due to the simple fact that filtering procedure removes them. Thus, depending on the smoothness of the filter, the corresponding SGS model should satisfy very different requirements in terms of large scale dynamics and kinetic energy budget. This contradicts the basic motivation behind LES: to resolve large scales and model unresolved ones. One should not model the interaction of resolved scales, otherwise it will be hard to see the difference between unsteady RANS and LES. However, unless one considers homogeneous turbulence, it is difficult, if not impossible, to adopt an implicit or explicit sharp cut-off filter. Then, the next best choice is to minimize the effect of filter on large scales dynamics and energy transfer. This can be achieved by making the filter as close to sharp cut-off as possible.

References

De Stefano, G. and Vasilyev, O.V. (2001) Sharp cut-off vs. smooth filtering in LES, To appear in *Phys. Fluids.*

Burgers, J.M (1974) The nonlinear diffusion equation, *Reidel Publishing Company.*

Lund, T.S. (1997) On the use of discrete filters for large eddy simulation, *Annual Research Briefs, Center for Turbulence Research, NASA Ames/Stanford Univ.*, 83-95.

Vasilyev, O.V., Lund, T.S. & Moin, P. (1998) A general class of commutative filters for LES in complex geometries, *J. Comp. Phys.*, **146**, 105-123.

Ruetsch G. R. & Maxey, M. R. (1991), Small-scale features of the vorticity and passive scalar fields in homogeneous isotropic turbulence. *Phys. Fluids.* **3** 1587-1597.

CHARACTERIZATION OF OPTIMAL LES IN TURBULENT CHANNEL FLOW

R. D. MOSER, S. VOLKER AND P. VENUGOPAL
Department of Theoretical and Applied Mechanics
University of Illinois at Urbana-Champaign
Urbana, IL 61801 USA

Abstract. The application of large eddy simulation (LES) to wall-bounded turbulent flows has be hindered by the failure of current subgrid models in the strongly inhomogeneous region very near the wall. This is the LES wall modeling problem. To address this a new modeling approach called optimal LES modeling is applied to a turbulent channel flow. Ideal LES is an LES evolution that is guaranteed to produce correct statistics and accurate short-time dynamics, and optimal LES is a minimum error approximation to it. By constructing optimal models that produce correct *a priori* estimates of important statistical quantities, it is shown that for inhomogeneous flows, the subgrid model must represent Reynolds stress spatial transport, in addition to transfer to small scales. Resulting models are found to perform particularly well in LES.

1. Introduction

Large eddy simulation (LES) is a promising simulation technique in which only the large scales of a turbulent flow are simulated and the effects of the small scales are modeled. A variety of subgrid models have been developed, and using these models, LES has been successfully applied in a variety of flows (see Lesieur & Métais, 1996; and Meneveau and Katz, 2000, for reviews). Unfortunately, the near-wall region of a wall-bounded turbulent flow causes difficulties for LES, primarily due to the strong inhomogeneity of the turbulence in this region, which results in a violation of the subgrid homogeneity and isotropy on which most models are predicated. In essence, there is "large-scale" turbulence that is actually smaller than the filter scale.

A new approach to large eddy simulation model formulation (optimal LES) has been developed (Langford and Moser, 1999), which does not rely on subgrid homogeneity or isotropy. Optimal LES is the formal approximation of what we

call the "ideal LES," which is the best possible deterministic LES evolution. In this paper, the optimal LES technique is applied to the turbulent flow in a channel, to begin to address the problem of near-wall LES modeling. In the following subsections the optimal LES approach will be briefly described.

1.1. FILTERING AND IDEAL LES

The large scales to be simulated in an LES are defined through a spatial filter denoted $\widetilde{\cdot}$. For the filter to be useful in the LES context, it cannot be invertible (Langford and Moser, 1999). That is, it must discard information, so that the (formally infinite-dimensional) space of Navier-Stokes solutions will be mapped to a smaller-dimensional space that can be practically represented on a computer. If an invertible filter were used, the dynamics of the filtered system would be identical to the dynamics of the unfiltered system; only the variables describing it would be different. Often the explicit filter used in an LES is invertible (e.g. Gaussian or top-hat), but the numerical discretization (e.g. Fourier truncation or point sampling) invariably introduces non-invertability. In this case we include the discretization as part of the filter.

With an uninvertible filter, the LES state information (the large-scale field) is insufficient to determine either the unfiltered field or the evolution of the filtered field; thus the need for a model. There are in general many possible evolutions of a given filtered field, depending which of an infinite number of subgrid fields is present. In the absence of subgrid information, the large-scale evolution can be considered to be stochastic, and an intuitively reasonable LES evolution would be the average of all the possible large-scale evolutions. This is written mathematically as the conditional average:

$$\frac{\mathrm{d}w}{\mathrm{d}t} = \left\langle \widetilde{\frac{\mathrm{d}u}{\mathrm{d}t}} \middle| \widetilde{u} = w \right\rangle, \tag{1}$$

where the LES field is w, and u is a real turbulent field. It has been shown (Langford and Moser, 1999) that this is the unique LES evolution that guarantees accurate one-time statistics *and* minimizes error of the large-scale dynamics. Because this is all one could wish for in an LES, this evolution is called *ideal* LES.

It is customary to write the LES equations as the Navier–Stokes operators operating on the filtered field:

$$\frac{\partial \widetilde{u}_i}{\partial t} = -\frac{\partial \widetilde{u}_i \widetilde{u}_j}{\partial x_j} - \frac{\partial \widetilde{p}}{\partial x_i} + \frac{1}{\mathrm{Re}} \frac{\partial^2 \widetilde{u}_i}{\partial x_j \partial x_j} + M_i, \tag{2}$$

where

$$M_i = -\frac{\partial \tau_{ij}}{\partial x_j} + C_i, \qquad \tau_{ij} = \widetilde{u_i u_j} - \widetilde{u}_i \widetilde{u}_j, \tag{3}$$

and C_i is a term that arises when the filter does not commute with spatial differentiation. The ideal subgrid model ($\mathbf{m}$) for the the subgrid term ($\mathbf{M}$) is then written:

$$\mathbf{m}(w) = \Big\langle \mathbf{M}(u) \Big| \widetilde{u} = w \Big\rangle, \tag{4}$$

1.2. OPTIMAL LES

The ideal LES defined above has all the features one could wish for in an LES model, but unfortunately it cannot be determined directly. The statistical information embodied in the conditional average of the ideal LES is so tremendous that it is unlikely that the ideal model for a given flow or filter could ever be found exactly. Still, one can approximate the ideal model, and indeed, subgrid modeling can be considered to be the problem of approximating the conditional average that defines the ideal model. The term *optimal LES* is used to describe formulations that most closely approximate ideal LES within some class. Optimal models are defined using stochastic estimation, as originally proposed by Adrian (1990). Stochastic estimation is a well-established method for approximating conditional averages (Adrian, 1977; Adrian and Moin, 1988; Adrian et al., 1989).

In stochastic estimation, a vector of random fields Y is approximated linearly in terms of a vector of "event" fields $E(\mathbf{x})$. The stochastic estimate is then written:

$$y_i(\mathbf{x}) = \langle Y_i \rangle + \int_{\mathcal{D}} L_{ij}(\mathbf{x}, \mathbf{x}') E'_j(\mathbf{x}') \mathrm{d}\mathbf{x}', \tag{5}$$

where $\langle \cdot \rangle$ is the average and $Y' = Y - \langle Y \rangle$.

The estimation kernel L_{ij} is determined from the two-point cross correlations of $E'(\mathbf{x})$ and Y' from:

$$\langle E'_i(\mathbf{x}') Y'_j(\mathbf{x}) \rangle = \int_{\mathcal{D}} L_{jk}(\mathbf{x}, \mathbf{x}'') \langle E'_i(\mathbf{x}') E'_k(\mathbf{x}'') \rangle \mathrm{d}\mathbf{x}'', \tag{6}$$

for all i, j and $\mathbf{x}'$. Nonlinear estimates are obtained by including nonlinear quantities as part of of the event vector.

In what follows, optimal LES models are devised for the turbulent channel flow using stochastic estimation to approximate the ideal model. In Section 2, the the channel flow and subgrid term are characterized, and two optimal models are described in Section 3 and Section 4. Finally, concluding remarks are provided in Section 5.

2. LES of Turbulent Channel Flow

Optimal LES requires as input the two-point correlations that appear in (6). The correlation data was determined from the direct numerical simulation data of Moser *et al* (1999), at $Re_\tau = 590$.

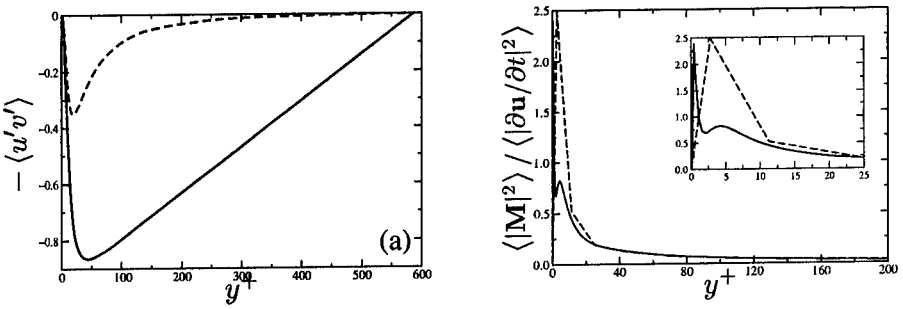


Figure 1. Magnitude of the subgrid force; (a) subgrid contribution to mean Reynolds stress (– – – –) and total Reynolds stress (solid); and (b) mean-square subgrid force fluctuations, normalized by mean-square velocity time derivative fluctuations.

For simplicity we consider a Fourier cut-off filter in the homogeneous directions parallel to the wall. The cut-off wavenumbers in the streamwise and spanwise directions are $k_x h = 16$ and $k_z h = 32$, where h is the channel half-width. This results in an LES representation with 32 modes in the filtered directions, compared to 384 in the DNS. The LES grid spacing is then 116 and 58 wall units in the streamwise and spanwise directions respectively. This is a coarse filter for this flow, which results in a significant model term, as shown in Figure 1. The model terms accounts for as much as 70% of $\widetilde{\partial u_i'/\partial t}$ near the wall and 30% of the mean Reynolds stress. This is representative of the high-Reynolds number wall modeling problem, but with such a large contribution to Reynolds stress, Smagorinsky-based subgrid models must fail (Jiménez and Moser, 1999).

One further complication that arises due to the inhomogeneity in the channel flow is that large quantities of statistical data are required to represent the two-point correlation in the inhomogeneous y direction (Balachandar and Najjar, 2000); more statistical samples than are available from the DNS. To reduce the data required, we only consider estimates that are local in y, though this introduces limitations on the veracity of the resulting models (Volker, 2000).

3. Optimal LES with Directly Estimated Subgrid Terms

Perhaps the most straight-forward way to formulate an optimal LES of the channel flow is to directly estimate the fluctuating subgrid force in terms of the velocity and its y derivatives. In this case the estimate reads

$$m_i(x,y,z) = \langle M_i \rangle + \int_{x,z} L_{ij}(x-x',y,z-z') E_j(x',y,z')\,dx'\,dz' \qquad (7)$$

where the integrals are in x and z only, since the estimates are local in y. This local direct estimate of the subgrid force has been used as a model in an LES. Some representative results are shown in Figure 2. Clearly, the optimal model has not done a particularly good job. The mean velocity is in poor agreement with

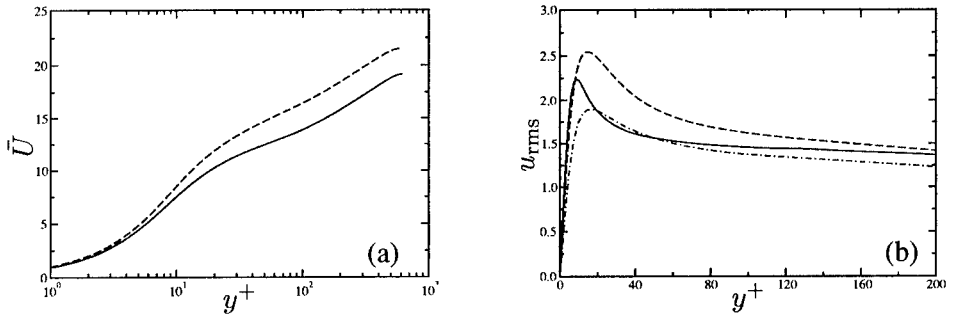


Figure 2. LES results in the channel at $Re_\tau = 590$; (a) mean velocity profiles, and (b) rms streamwise velocity. Shown are the data from the LES (———), DNS (– – –) and filtered DNS (– · – · –).

the DNS, primarily because the wall shear stress (C_f) is over predicted by 11%. The rms streamwise velocity near the wall is also over-predicted compared to the filtered DNS quantity.

The reason for this poor performance can be found by examining the interchange of energy between the resolved and subgrid scales. This is given by $\langle u_i M_i \rangle$, which is plotted in Figure 3. Note that near the wall ($y^+ < 10$), this quantity is positive, indicating energy transfer into the resolved scales. Because of the linearity of the model, this leads to exponential growth of resolved scale fluctuations, until some other effect limits that growth (e.g. nonlinearity). However, this energy transfer term is suggestive of *transport* in the y direction as observed by Häertel & Kleiser (1998). In their analysis, the subgrid energy transfer is rewritten:

$$\langle \tilde{u}_i M_i \rangle = \left\langle \tilde{u}_i \frac{\partial \tau_{ij}}{\partial x_j} \right\rangle = \frac{\partial \langle \tilde{u}_i \tau_{ij} \rangle}{\partial x_j} - \frac{1}{2} \langle S_{ij} \tau_{ij} \rangle , \tag{8}$$

where the first term on the right-hand side represents subgrid transport in y and the second term represents local energy transfer between resolved and subgrid scales (subgrid dissipation for short). These contributions are also shown in Figure 3. Note that the transport term is responsible for the near-wall peak in $\langle \tilde{u}_i M_i \rangle$. The subgrid dissipation term is negative near the wall, though there is a region of true energy transfer to resolved scales farther from the wall.

Since w_i is one of the estimation event variables, the quantity $\langle w_i M_i \rangle$ is predicted exactly by the optimal model, in the *a priori* sense. But, because the estimates are local in y, they do not correctly represent the transport component of this term. To represent the subgrid transport and dissipation terms exactly in the *a prior* sense, we must construct the estimates such that $\langle \tilde{u}_i \tau_{ij} \rangle$ and $\langle S_{ij} \tau_{ij} \rangle$ are recovered (Volker, 2000). Taking advantage of homogeneity in the x and z directions, this can be accomplished by writing M_i as

$$M_i = \rho_i + \frac{\partial \gamma_i}{\partial x_2} \qquad \text{where} \qquad \rho_i = -\frac{\partial \tau_{i1}}{\partial x_1} - \frac{\partial \tau_{i3}}{\partial x_3}, \qquad \gamma_i = -\tau_{i2}, \tag{9}$$

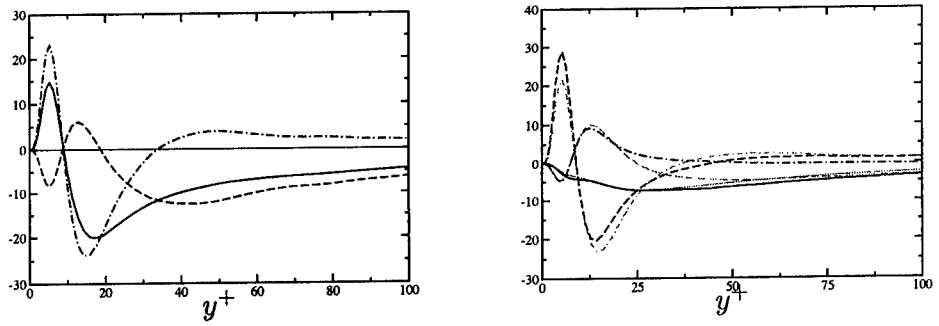


Figure 3. Contributions to the transfer of energy from the resolved scales (left); total energy transfer (———), subgrid dissipation (— — —), subgrid transport (- · - · -). Also, (right) contributions of ρ_i and γ_i to subgrid energy transfer computed *a posteriori* from LES realizations (black), and *a priori* from DNS (grey); $\langle u_i \rho_i \rangle$ (———), $-\langle \gamma_i \partial u_i / \partial x_2 \rangle$ (— — —) $\langle \partial \gamma_i u_i / \partial x_2 \rangle$ (- · - · -)

and estimating ρ_i and γ_i in terms of u_i and $\partial u_i / \partial y$. The total subgrid energy transfer then becomes

$$\langle u_i M_i \rangle = \langle u_i \rho_i \rangle + \left\langle u_i \frac{\partial \gamma_i}{\partial x_2} \right\rangle = \underbrace{\langle u_i \rho_i \rangle - \left\langle \gamma_i \frac{\partial u_i}{\partial x_2} \right\rangle}_{\text{dissipation}} + \underbrace{\left\langle \frac{\partial u_i \gamma_i}{\partial x_2} \right\rangle}_{\text{transport}} \tag{10}$$

where each of the terms on the right hand side are represented exactly *a priori.*

The *a priori* contributions of the individual terms in (10) to the total subgrid energy transfer are shown in Figure 3. Note that it is the dissipation term involving γ that is responsible for the augmentation of energy in the resolved scales. Because of the structure of this term, it will not produce unchecked exponential growth, as occurs when M is estimated directly.

4. Optimal LES with Subgrid Transport Estimated

An LES based on the local estimation of ρ and γ with event data consisting of the velocities and their y derivatives was performed. The results are shown in Figure 4 for mean and rms velocities. The difficulties with the mean velocity, and over-prediction of C_f are now gone. For the rms velocities, the LES are now much closer to the values from the filtered DNS, though there are still some minor discrepancies. A variety of other statistical quantities, including spectra and two-point correlations are in reasonably good agreement with those of the filtered DNS (Volker, 2000).

Given the apparent importance of the energy transfer and transport terms, the *a posteriori* prediction of these quantities in the LES are of some importance. They are shown in black in Figure 3. The agreement with the *a priori* results (grey) is reasonably good, suggesting that ensuring that a model is *a priori* accurate of for these quantities will lead to reasonable predictions.

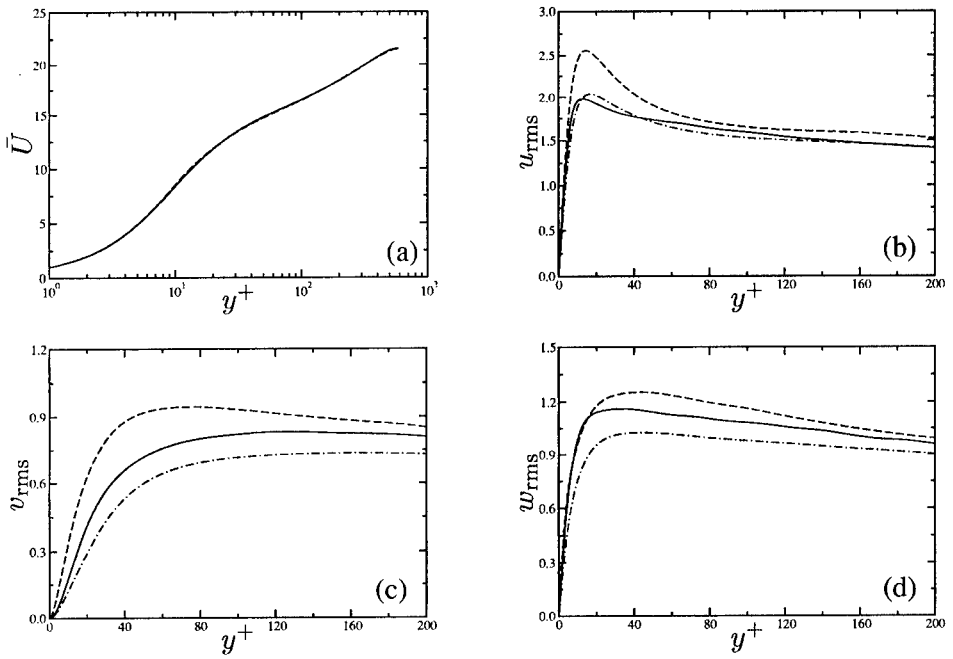


Figure 4. Channel LES using optimal estimation of ρ and γ (see (9)); (a) mean velocity profile, (b) rms streamwise velocity fluctuations, $u_{\rm rms}$, (c) rms wall-normal velocity fluctuations, $v_{\rm rms}$, and (d) rms spanwise velocity fluctuations, $w_{\rm rms}$. Shown are data from the LES (———), the DNS (— — —) and the filtered DNS (- · - · -).

5. Discussion and Conclusions

In both isotropic turbulence (Langford, 2000) and the channel flow, a properly constructed optimal LES model produces very good simulations. But, the experience with the channel flow suggests that what makes a "properly constructed" optimal model is not necessarily obvious. What seems to be important is that the optimal models *a priori* reproduce essential statistical properties of the filtered turbulence, such as the "dissipation" of resolved scale energy (i.e. transfer to subgrid scales) and the subgrid contribution to energy transport. The optimal models actually *a priori* represent more than just these energy dynamic terms. For example in isotropic turbulence, they *a priori* represent the dynamics of the two-point correlation tensor (Langford and Moser, 1999).

In the channel, a global linear optimal model would also reproduce all subgrid contributions to the two-point correlation dynamics. However, we were not able to construct a global estimate, because of the limited statistical data available. The estimates we built, were designed to represent the energy transport term, as well as the dissipation, but they also reproduce the subgrid contribution to transport and dissipation terms in the resolved-scale Reynolds stress transport equations. Only the velocity-pressure-gradient term in the Reynolds stress equations is not reproduced *a priori*. We speculate that a model that also reproduces this term

would further improve LES performance, and that a global model that reproduces 2-point correlation dynamics would do even better.

The optimal models developed here rely on extensive correlation data that we obtained from DNS. Clearly, these models would not be practical if such detailed data were required for each flow in which one wishes to perform an LES. It is thus necessary to generalize models such as those devised here to be applicable in a broad range of applications.

Acknowledgements

The research reported here has been supported by NSF and AFOSR through grant CTS-9616219, NSF grant CTS-001435 and AFOSR grant F49620-01-1-0181, and by the Center for Simulation of Advanced Rockets, which is funded by the Department of Energy through University of California grant B341494. This support is gratefully acknowledged.

References

Adrian, R. (1977). On the role of conditional averages in turbulence theory. In Zakin, J. and Patterson, G., editors, *Turbulence in Liquids*, pages 323–332. Science Press, Princeton, New Jersey.

Adrian, R. (1990). Stochastic estimation of sub-grid scale motions. *Appl. Mech. Rev.*, 43(5):214–218.

Adrian, R., Jones, B., Chung, M., Hassan, Y., Nithianandan, C., and Tung, A. (1989). Approximation of turbulent conditional averages by stochastic estimation. *Phys. Fluids*, 1(6):992–998.

Adrian, R. and Moin, P. (1988). Stochastic estimation of organized turbulent structure: homogeneous shear flow. *J. Fluid Mech.*, 190:531–559.

Balachandar, S. and Najjar, F. (2000). Optimal two-dimensional models for wake flow. Technical Report TAM Report No. 931, UILU-ENG-2000-6006, Theoretical and Applied Mechanics, University of Illinois.

Härtel, C. and Kleiser, L. (1998). Analysis and modelling of subgrid-scale motions in near-wall turbulence. *J. Fluid Mech.*, 356:327–352.

Jiménez, J. and Moser, R. D. (1999). LES: Where are we and what can we expect. *AIAA J.*, 38:605–612.

Langford, J. and Moser, R. (1999). Optimal LES formulations for isotropic turbulence. *J. Fluid Mech.*, 398:321–346.

Langford, J. A. (2000). *Toward Ideal Large-Eddy Simulation.* PhD thesis, University of Illinois at Urbana-Champaign.

Lesieur, M. and Métais, O. (1996). New trends in large-eddy simulations of turbulence. *Annu. Rev. of Fluid Mech.*, 28:45–82.

Meneveau, C. and Katz, J. (2000). Scale-invariance and turbulence models for large-eddy simulation. *Annu. Rev. of Fluid Mech.*, 32:1–32.

Moser, R., Kim, J., and Mansour, N. (1999). Direct numerical simulation of turbulent channel flow up the re_τ=590. *Phys. Fluids*, 11(4):943–945.

Volker, S. A. (2000). *Optimal Large Eddy Simulation of Turbulent Channel Flow.* PhD thesis, University of Illinois at Urbana-Champaign.

PHYSICS-PRESERVING TURBULENT CLOSURE MODELS

SGS Flux Vectors of Mass and Energy

LIQIU WANG
Department of Mechanical Engineering
The University of Hong Kong, Hong Kong

Abstract. Both necessary and sufficient conditions are derived in a systematic, rigorous way for a subgrid-scale (SGS) flux vector model to preserve the frame-indifference of the vector and to satisfy both the principle of material frame indifference (PMFI) and the second law of thermodynamics. This leads to the results either confirming the previous intuitive arguments or offering new insights into turbulence modelling, and is of significance in clarifying some controversies in the literature, examining how well existing models preserve the physics, and developing new models.

1. Introduction

SGS stresses and fluxes of mass and energy are believed to be quantities determined by filtered large-scale velocity and mass fraction/temperature fields in the large eddy simulation (LES). Based on this fundamental, intrinsic belief, various approaches have been proposed to relate SGS stresses and fluxes to the filtered large-scale fields, so-called SGS turbulence modelling. The readers are referred to Ciofalo (1994), Mason (1994), Lesieur & Métais (1996) and Sagaut (2001) for some recent excellent reviews and discussions of this important topic. While some LES results based on some commonly used models seem encouraging, they fail to meet either one or both of two natural fundamental requirements for turbulence models: preserving the fundamental properties of the quantities being modeled and satisfying some classical principles.

The modelling of the SGS flux vectors of mass and energy consists of replacing them by constitutive equations expressing them as functions of filtered large-scale fields of velocity and mass fraction/temperature. While such constitutive equations may take different forms such as algebraic and differential, it appears to be a basic requirement to preserve the properties

which the flux vectors hold by their definition. Such a property is the frame-indifference (Fureby & Tabor 1997, Ghosal 1999, Wang 2001). It follows from the definition of the SGS flux vectors and states that they remain the same directed line element under a change of frame. The issue concerned with whether a model guarantees this property is referred as the invariance in the literature.

While the first requirement focuses on the properties of the SGS flux vectors themselves, the second requirement emphases on their *function relation* with the filtered large-scale fields. Such function relations are required to satisfy some classical principles including the PMFI and the second law of thermodynamics (Fureby & Tabor 1997, Ghosal 1999, Wang 1997, 1999, 2001). The PMFI requires that the function relation is the same for every observer, i.e. in every frame of reference. The second law of thermodynamics, on the other hand, states that the flux is always from high concentration to low concentration. Note that the realizability for the Reynolds and SGS stresses also comes from the second law of thermodynamics (Wang 1999, 2001).

The motivation for the present work comes from the desire to derive *both* necessary and sufficient condition in a systematic, rigorous way for a SGS flux model to preserve the frame-indifference of SGS flux vectors and to satisfy both the PMFI and the second law of thermodynamics. Unlike the works in the literature, no intuitive assumption is introduced in the derivation; the independent variables are chosen properly; the PMFI and the frame indifference of SGS flux vectors are clearly distinguished. This leads to some conclusive results. Among them, some confirm the previous intuitive arguments, and others form new insights to SGS turbulence modelling.

2. Principle of Material Frame-Indifference and Second Law of Thermodynamics

Consider a class of constitutive relations which relate the passive SGS flux vector $\mathbf{q}$ of mass or energy to its arguments $\theta, O.P., \bigtriangledown\theta, \mathbf{v}, \mathbf{L}$, i.e.,

$$\mathbf{q} = \mathbf{f}(\theta, O.P., \bigtriangledown\theta, \mathbf{v}, \mathbf{L}). \tag{1}$$

Here $\mathbf{f}$ is a vector-valued function. θ is the concentration of a property. It is the mass fraction of a species for the case of SGS flux of mass, and the temperature when $\mathbf{q}$ is the SGS flux of energy. $O.P.$ denotes the other scalar-valued thermophysical parameters which are independent of $\mathbf{v}$ and $\mathbf{L}$ and are typically the local thermodynamic state variables. $\bigtriangledown\theta$ is the gradient of θ. $\mathbf{v}$ is the filtered velocity vector. $\mathbf{L}$ is the velocity gradient tensor of $\mathbf{v}$, a second order tensor-valued variable.

In sharp contrast with that in the literature, we choose $\mathbf{L}$ as an independent variable instead of its symmetric part $\mathbf{D}$ (the velocity strain tensor) and skew part $\mathbf{W}$ (the vorticity tensor) because $\mathbf{D}$ and $\mathbf{W}$ can not be regarded as independent. We do not include k, l or ε as the independent variables. The exclusion of the explicit dependence of $\mathbf{q}$ on time t and position vector $\mathbf{r}$ comes from the fact that they affect $\mathbf{q}$ through θ, $O.P.$, $\bigtriangledown\theta$, $\mathbf{v}$ and $\mathbf{L}$.

The relation (1) satisfies both principle of determinism and principle of local action since we assume that $\mathbf{q}$ at a point and a time instant is a function of its arguments at that point and that instant.

The principle of frame-indifference requires that $\mathbf{f}$ is the same for every observer, i.e.

$$\mathbf{q}^* = \mathbf{f}(\theta^*, O.P.^*, (\bigtriangledown\theta^*)^*, \mathbf{v}^*, \mathbf{L}^*) \tag{2}$$

in which superscript $*$ represents the quantities observed by another observer $*$.

The second law of thermodynamics states that $\mathbf{q}$ is always from high concentration to low concentration. This requires that: (1) $\mathbf{f}$ changes its sign if $\bigtriangledown\theta$ changes the sign, i.e.,

$$\mathbf{f}(\theta, O.P., -\bigtriangledown\theta, \mathbf{v}, \mathbf{L}) = -\mathbf{f}(\theta, O.P., \bigtriangledown\theta, \mathbf{v}, \mathbf{L}), \tag{3}$$

and (2) the projection of the $\mathbf{f}$ on $\bigtriangledown\theta$ is negative semi-definite, i.e.,

$$\mathbf{f} \cdot \bigtriangledown\theta \leq 0. \tag{4}$$

2.1. NECESSARY CONDITIONS FOR REQUIREMENTS (2) AND (3)

2.1.1. $\mathbf{q} - \mathbf{v}$ *relation*

Theorem 1. $\mathbf{f}$ *is independent of* $\mathbf{v}$.

Proof From the principle of observer transformations (Geankoplis 1983, Truesdell 1991),

$$\left.\begin{array}{lll} \theta^* = \theta, & (O.P.)^* = O.P., & \mathbf{q}^* = \mathbf{Q}(t)\mathbf{q}, \\ (\bigtriangledown\theta^*)^* = \mathbf{Q}(t)\bigtriangledown\theta, & \mathbf{L}^* = \mathbf{Q}(t)\mathbf{L}\mathbf{Q}^T(t) + \dot{\mathbf{Q}}(t)\mathbf{Q}^T(t), & \\ \mathbf{r}^* = \mathbf{Q}(t)\mathbf{r} + \mathbf{c}(t), & \mathbf{v}^* = \frac{d\mathbf{r}^*}{dt} = \dot{\mathbf{Q}}(t)\mathbf{r} + \mathbf{Q}(t)\mathbf{v} + \dot{\mathbf{c}}(t), & \end{array}\right\} \tag{5}$$

where $\mathbf{Q}$ is an arbitrary rotation tensor, $\mathbf{r}$ a position vector of material point, $\mathbf{c}(t)$ an arbitrary vector-valued function of time t, and a dot over a letter indicates a time derivative. In (5), we have used the frame indifference of $\mathbf{q}$.

By making use of (1) and (5), (2) yields (suppressing t)

$$\mathbf{f}(\theta, O.P., \mathbf{Q}\nabla\theta, \dot{\mathbf{Q}}\mathbf{r} + \mathbf{Q}\mathbf{v} + \dot{\mathbf{c}}, \mathbf{Q}\mathbf{L}\mathbf{Q}^T + \dot{\mathbf{Q}}\mathbf{Q}^T) = \mathbf{Q}\mathbf{f}(\theta, O.P., \nabla\theta, \mathbf{v}, \mathbf{L}), \quad \forall \mathbf{Q} \text{ and } \mathbf{c}. \tag{6}$$

Since (6) holds for all $\mathbf{Q}$, it must be true for $\mathbf{Q} = \mathbf{1}$. Take $\mathbf{Q} = \mathbf{1}$, then $\dot{\mathbf{Q}} = \mathbf{0}$. Equation (6) reduces to

$$\mathbf{f}(\theta, O.P., \nabla\theta, \mathbf{v} + \dot{\mathbf{c}}, \mathbf{L}) = \mathbf{f}(\theta, O.P., \nabla\theta, \mathbf{v}, \mathbf{L}) \quad \forall \dot{\mathbf{c}}. \tag{7}$$

This implies that $\mathbf{f}$ is independent of velocity $\mathbf{v}$.

By applying Theorem 1, (1) and (6) reduce to

$$\mathbf{q} = \mathbf{f}(\theta, O.P., \nabla\theta, \mathbf{L}), \tag{8}$$

$$\mathbf{f}(\theta, O.P., \mathbf{Q}\nabla\theta, \mathbf{Q}\mathbf{L}\mathbf{Q}^T + \dot{\mathbf{Q}}\mathbf{Q}^T) = \mathbf{Q}\mathbf{f}(\theta, O.P., \nabla\theta, \mathbf{L}) \quad \forall \mathbf{Q}. \tag{9}$$

2.1.2. $\mathbf{q} - \mathbf{L}$ *relation*

Note that $\mathbf{L}$ can be uniquely decomposed into a symmetric tensor $\mathbf{D}$ (velocity strain tensor) and a skew tensor $\mathbf{W}$ (vorticity tensor). Expression (9) may, then, be rewritten as

$$\mathbf{f}(\theta, O.P., \mathbf{Q}\nabla\theta, \mathbf{Q}\mathbf{D}\mathbf{Q}^T + \mathbf{Q}\mathbf{W}\mathbf{Q}^T + \dot{\mathbf{Q}}\mathbf{Q}^T) = \mathbf{Q}\mathbf{f}(\theta, O.P., \nabla\theta, \mathbf{L}) \quad \forall \mathbf{Q}. \tag{10}$$

Theorem 2. *For rotation tensor* $\mathbf{Q}(t) = exp[\hat{\mathbf{\Omega}}(t-\tau)]\hat{\mathbf{Q}}$, *we can, at any instant* τ, *pick* $\mathbf{Q}(\tau)$ *and* $\mathbf{Q}(\tau)\mathbf{Q}^T(\tau)$ *to be arbitrary, independent rotation and skew tensors, respectively. Here* $\hat{\mathbf{Q}}$ *is any time-independent rotation tensor, and* $\hat{\mathbf{\Omega}}$ *any time-independent skew tensor.*

Proof As $\hat{\mathbf{\Omega}}$ is a time-independent skew tensor, $exp[\hat{\mathbf{\Omega}}(t-\tau)]$ is thus a rotation tensor for any fixed time τ and all time t. Since both $\hat{\mathbf{Q}}$ and $exp[\hat{\mathbf{\Omega}}(t-\tau)]$ are rotation tensors, $\mathbf{Q}(t) = exp[\hat{\mathbf{\Omega}}(t-\tau)]\hat{\mathbf{Q}}$ is also a rotation tensor for all time t. Also,

$$\mathbf{Q}(\tau) = \hat{\mathbf{Q}}, \tag{11}$$

$$\dot{\mathbf{Q}}(\tau)\mathbf{Q}^T(\tau) = \hat{\mathbf{\Omega}}\mathbf{Q}(\tau)\mathbf{Q}^T(\tau) = \hat{\mathbf{\Omega}}. \tag{12}$$

They are clearly independent rotation and skew tensors if $\hat{\mathbf{Q}}$ and $\hat{\mathbf{\Omega}}$ are any time-independent rotation and skew tensors, respectively.

Theorem 3. $\mathbf{L}$ *affects* $\mathbf{q}$ *only through velocity strain tensor* $\mathbf{D}$.

Proof To prove this, choose $\mathbf{Q}(t)$ defined in Theorem 2 as the rotation tensor in (10) while for any instant τ, $-\mathbf{Q}\mathbf{W}\mathbf{Q}^T\,|_\tau$ is used as the skew

tensor $\hat{\mathbf{\Omega}}$, i.e. $\hat{\mathbf{\Omega}} = -\mathbf{Q}\mathbf{W}\mathbf{Q}^T \mid_\tau$ (Such a $\hat{\mathbf{\Omega}}$ do a skew tensor since $\hat{\mathbf{\Omega}}^T = -\mathbf{Q}\mathbf{W}^T\mathbf{Q}^T \mid_\tau = \mathbf{Q}\mathbf{W}\mathbf{Q}^T \mid_\tau = -\hat{\mathbf{\Omega}}$). Then at time $t = \tau$, (10) yields

$$\mathbf{f}(\theta, O.P., \hat{\mathbf{Q}}\bigtriangledown\theta, \hat{\mathbf{Q}}\mathbf{D}\hat{\mathbf{Q}}^T) = \hat{\mathbf{Q}}\mathbf{f}(\theta, O.P., \bigtriangledown\theta, \mathbf{L}) \quad \forall\hat{\mathbf{Q}}. \tag{13}$$

As this is true for all rotation tensor $\hat{\mathbf{Q}}$, it must hold for $\hat{\mathbf{Q}} = \mathbf{1}$. Let $\hat{\mathbf{Q}} = \mathbf{1}$, (13) yields

$$\mathbf{f}(\theta, O.P., \bigtriangledown\theta, \mathbf{L}) = \mathbf{f}(\theta, O.P., \bigtriangledown\theta, \mathbf{D}), \tag{14}$$

or

$$\mathbf{q} = \mathbf{f}(\theta, O.P., \bigtriangledown\theta, \mathbf{D}). \tag{15}$$

2.1.3. $\mathbf{q}$-$\bigtriangledown\theta$ *relation*

Expression (15) and the principle of frame-indifference together yield

$$\mathbf{q}^* = \mathbf{f}(\theta^*, (O.P.)^*, (\bigtriangledown\theta^*)^*, \mathbf{D}^*) \tag{16}$$

By making use of (5), (15) and $\mathbf{D}^* = \mathbf{Q}\mathbf{D}\mathbf{Q}^T$ (Truesdell 1991), (16) leads to

$$\mathbf{f}(\theta, O.P., \mathbf{Q}\bigtriangledown\theta, \mathbf{Q}\mathbf{D}\mathbf{Q}^T) = \mathbf{Q}\mathbf{f}(\theta, O.P., \bigtriangledown\theta, \mathbf{D}) \quad \forall\mathbf{Q}. \tag{17}$$

Also the second law of thermodynamics [Eq.(3)] requires that

$$\mathbf{f}(\theta, O.P., -\bigtriangledown\theta, \mathbf{D}) = -\mathbf{f}(\theta, O.P., \bigtriangledown\theta, \mathbf{D}). \tag{18}$$

Since the velocity strain tensor $\mathbf{D}$ is a real, symmetric tensor, it has three real eigenvalues. The three eigenvalues can be distinct, identical, or two of them can be identical. In the present work, we focus on the case that the three eigenvalues are distinct. Similar results may be obtained for the other two cases.

Theorem 4. $\bigtriangledown\theta, \mathbf{D}\bigtriangledown\theta, \mathbf{D}^2\bigtriangledown\theta$ *are linearly independent if three eigenvalues of* $\mathbf{D}$ *are distinct.*

Proof Let μ_k and $\mathbf{f}_k$ $(k = 1, 2, 3)$ to be the eigenvalues and eigenvectors of $\mathbf{D}$. $\mathbf{D}$ may be represented, in its spectral form, as

$$\mathbf{D} = \sum_{k=1}^{3} \mu_k \mathbf{f}_k \otimes \mathbf{f}_k. \tag{19}$$

The linear independence of $\mathbf{f}_k (k = 1, 2, 3)$ allows us to write $\bigtriangledown\theta$ as

$$\bigtriangledown\theta = (\bigtriangledown\theta)_j \mathbf{f}_j \tag{20}$$

in which $(\bigtriangledown\theta)_j = \bigtriangledown\theta \cdot \mathbf{f}_j$.

Suppose that $\nabla\theta, \mathbf{D}\nabla\theta$ and $\mathbf{D}^2\nabla\theta$ are linearly dependent for all $\mathbf{D}$ and $\nabla\theta$, there are α, β and γ which are not all zero, such that

$$\alpha\nabla\theta + \beta\mathbf{D}\nabla\theta + \gamma\mathbf{D}^2\nabla\theta = \mathbf{0}. \tag{21}$$

Substituting (19) and (20) into (21) yields

$$\sum_{k=1}^{3}(\alpha + \beta\mu_k + \gamma\mu_k^2)(\nabla\theta)_k\mathbf{f}_k = 0, \tag{22}$$

which implies, as $\mathbf{f}_k$ $(k = 1, 2, 3)$ are linearly independent,

$$(\alpha + \beta\mu_k + \gamma\mu_k^2)(\nabla\theta)_k = 0, \quad (k = 1, 2, 3). \tag{23}$$

For arbitrary $\nabla\theta$, $(\nabla\theta)_k$ need not be zero, so

$$\alpha + \beta\mu_k + \gamma\mu_k^2 = 0, \quad (k = 1, 2, 3) \tag{24}$$

that requires that $\alpha = \beta = \gamma = 0$ for distinct μ_k, contrary to the hypothesis. Theorem 4 has, thus, been proved.

Applying Theorem 4 to the SGS flux vector, we have

$$\begin{aligned}\mathbf{f}(\theta, O.P., \nabla\theta, \mathbf{D}) &= \phi_0(\theta, O.P., \nabla\theta, \mathbf{D})\nabla\theta + \phi_1(\theta, O.P., \nabla\theta, \mathbf{D})\mathbf{D}\nabla\theta \\ &+\phi_2(\theta, O.P., \nabla\theta, \mathbf{D})\mathbf{D}^2\nabla\theta,\end{aligned} \tag{25}$$

and

$$\begin{aligned}\mathbf{f}(\theta, O.P., -\nabla\theta, \mathbf{D}) &= -\phi_0(\theta, O.P., -\nabla\theta, \mathbf{D})\nabla\theta \\ &-\phi_1(\theta, O.P., -\nabla\theta, \mathbf{D})\mathbf{D}\nabla\theta - \phi_2(\theta, O.P., -\nabla\theta, \mathbf{D})\mathbf{D}^2\nabla\theta.\end{aligned} \tag{26}$$

Substituting (25) and (26) into (18) leads to

$$\begin{aligned}&[\phi_0(\theta, O.P., \nabla\theta, \mathbf{D}) - \phi_0(\theta, O.P., -\nabla\theta, \mathbf{D})]\nabla\theta \\ &+[\phi_1(\theta, O.P., \nabla\theta, \mathbf{D}) - \phi_1(\theta, O.P., -\nabla\theta, \mathbf{D})]\mathbf{D}\nabla\theta \\ &+[\phi_2(\theta, O.P., \nabla\theta, \mathbf{D}) - \phi_2(\theta, O.P., -\nabla\theta, \mathbf{D})]\mathbf{D}^2\nabla\theta = 0\end{aligned} \tag{27}$$

which implies, since $\nabla\theta, \mathbf{D}\nabla\theta$ and $\mathbf{D}^2\nabla\theta$ are linearly independent,

$$\phi_i(\theta, O.P., \nabla\theta, \mathbf{D}) = \phi_i(\theta, O.P., -\nabla\theta, \mathbf{D}), \quad (i = 0, 1, 2). \tag{28}$$

To satisfy this requirement, take

$$\phi_i(\theta, O.P., \nabla\theta, \mathbf{D}) = \psi_i(\theta, O.P., \nabla\theta \otimes \nabla\theta, \mathbf{D}), \quad (i = 0, 1, 2). \tag{29}$$

Then (25) and (29) result in

$$\mathbf{f}(\theta, O.P., \mathbf{Q}\nabla\theta, \mathbf{Q}\mathbf{D}\mathbf{Q}^T) = \mathbf{Q}(\hat{\psi}_0\nabla\theta + \hat{\psi}_1\mathbf{D}\nabla\theta + \hat{\psi}_2\mathbf{D}^2\nabla\theta) \tag{30}$$

in which,

$$\hat{\psi}_i = \psi_i(\theta, O.P., \mathbf{Q}\nabla\theta \otimes \mathbf{Q}\nabla\theta, \mathbf{QDQ}^T),$$

and

$$\mathbf{Qf}(\theta, O.P., \nabla\theta, \mathbf{D}) = \mathbf{Q}(\psi_0\nabla\theta + \psi_1\mathbf{D}\nabla\theta + \psi_2\mathbf{D}^2\nabla\theta). \tag{31}$$

By making use of (30) and (31), (17) yields

$$(\hat{\psi}_0 - \psi_0)\nabla\theta + (\hat{\psi}_1 - \psi_1)\mathbf{D}\nabla\theta + (\hat{\psi}_2 - \psi_2)\mathbf{D}^2\nabla\theta = \mathbf{0} \tag{32}$$

that implies, by Theorem 4,

$$\psi_i(\theta, O.P., \mathbf{Q}\nabla\theta \otimes \mathbf{Q}\nabla\theta, \mathbf{QDQ}^T) = \psi_i(\theta, O.P., \nabla\theta \otimes \nabla\theta, \mathbf{D}) \quad \forall\mathbf{Q}. \tag{33}$$

Theorem 5. *Suppose*

$$\psi(\theta, O.P., \mathbf{Qb} \otimes \mathbf{Qb}, \mathbf{QBQ}^T) = \psi(\theta, O.P., \mathbf{b} \otimes \mathbf{b}, \mathbf{B}), \quad \forall\mathbf{b} \text{ and } \mathbf{B},$$

then

$$\psi(\theta, O.P., \mathbf{a} \otimes \mathbf{a}, \mathbf{A}) = \psi(\theta, O.P., \mathbf{b} \otimes \mathbf{b}, \mathbf{B})$$

whenever $J_k(\mathbf{a}, \mathbf{A}) = J_k(\mathbf{b}, \mathbf{B})$ $(k = 1, 2, \cdots, 6)$. *Here*

$$J_1(\mathbf{a}, \mathbf{A}) = tr\mathbf{A}, \quad J_2(\mathbf{a}, \mathbf{A}) = \tfrac{1}{2}[(tr\mathbf{A})^2 - tr(\mathbf{A}^2)], \quad J_3(\mathbf{a}, \mathbf{A}) = det\mathbf{A},$$
$$J_4(\mathbf{a}, \mathbf{A}) = \mathbf{a} \cdot \mathbf{Aa}, \quad J_5(\mathbf{a}, \mathbf{A}) = \mathbf{a} \cdot \mathbf{A}^2\mathbf{a}, \quad J_6(\mathbf{a}, \mathbf{A}) = \mid \mathbf{a} \mid,$$

a *and* **b** *are two arbitrary vectors,* **A** *and* **B** *are two arbitrary symmetric tensors.*

Proof Since $J_k(\mathbf{a}, \mathbf{A}) = J_k(\mathbf{b}, \mathbf{B})$ $(k = 1, 2, 3)$, tensors **A** and **B** have same eigenvalues. Let μ_k be their eigenvalues, **A** and **B** may be written as,

$$\mathbf{A} = \sum_{k=1}^{3} \mu_k \mathbf{e}_k \otimes \mathbf{e}_k, \quad \mathbf{B} = \sum_{k=1}^{3} \mu_k \mathbf{f}_k \otimes \mathbf{f}_k$$

where $\mathbf{e}_k$ and $\mathbf{f}_k$ $(k = 1, 2, 3)$ are eigenvectors of **A** and **B**, respectively. Define

$$\mathbf{Q} = \mathbf{e}_k \otimes \mathbf{f}_k$$

that is a rotation tensor, and

$$\mathbf{e}_i = \mathbf{Qf}_i, \quad \mathbf{A} = \mathbf{QBQ}^T, \quad \mathbf{A}^2 = \mathbf{QB}^2\mathbf{Q}^T, \quad (i = 1, 2, 3). \tag{34}$$

By applying $J_k(\mathbf{a}, \mathbf{A}) = J_k(\mathbf{b}, \mathbf{B})$ $(k = 4, 5, 6)$, we have

$$\sum_{k=1}^{3}(\mathbf{b} \cdot \mathbf{f}_k)^2 = \sum_{k=1}^{3}(\mathbf{Q}^T\mathbf{a} \cdot \mathbf{f}_k)^2, \qquad \sum_{k=1}^{3}\mu_k(\mathbf{b} \cdot \mathbf{f}_k)^2 = \sum_{k=1}^{3}\mu_k(\mathbf{Q}^T\mathbf{a} \cdot \mathbf{f}_k)^2,$$
$$\sum_{k=1}^{3}\mu_k^2(\mathbf{b} \cdot \mathbf{f}_k)^2 = \sum_{k=1}^{3}\mu_k^2(\mathbf{Q}^T\mathbf{a} \cdot \mathbf{f}_k)^2. \tag{35}$$

This implies, for the distinct μ_k $(k = 1, 2, 3)$,

$$(\mathbf{Q}^T\mathbf{a} \mp \mathbf{b}) \cdot \mathbf{f}_k = 0, \quad (k = 1, 2, 3). \tag{36}$$

Note that $\mathbf{f}_k$ $(k = 1, 2, 3)$ are linearly independent, then $\mathbf{a} = \pm\mathbf{Qb}$, $\mathbf{a} \otimes \mathbf{a} = \mathbf{Qb} \otimes \mathbf{Qb}$. By hypothesis,

$$\psi(\theta, O.P., \mathbf{b} \otimes \mathbf{b}, \mathbf{B}) = \psi(\theta, O.P., \mathbf{Qb} \otimes \mathbf{Qb}, \mathbf{QBQ}^T) = \psi(\theta, O.P., \mathbf{a} \otimes \mathbf{a}, \mathbf{A})$$

in which $\mathbf{A} = \mathbf{QBQ}^T$ [(34)] and $\mathbf{a} \otimes \mathbf{a} = \mathbf{Qb} \otimes \mathbf{Qb}$ are used. Therefore,

$$\psi(\theta, O.P., \mathbf{b} \otimes \mathbf{b}, \mathbf{B}) = \psi[\theta, O.P., J_k(\mathbf{b}, \mathbf{B})], \quad (k = 1, 2, \cdots, 6) \tag{37}$$

if

$$\psi(\theta, O.P., \mathbf{Qb} \otimes \mathbf{Qb}, \mathbf{QBQ}^T) = \psi(\theta, O.P., \mathbf{b} \otimes \mathbf{b}, \mathbf{B}), \quad \forall \mathbf{b} \text{ and } \mathbf{B}. \tag{38}$$

The converse is also true since $J_k(\mathbf{Qb}, \mathbf{QBQ}^T) = J_k(\mathbf{b}, \mathbf{B})$ $(k = 1, 2, \cdots, 6)$.

Theorem 6. *The necessary condition for the constitutive process (1) to satisfy requirements (2) and (3) is*

$$\mathbf{q} = \mathbf{f}(\theta, O.P., \nabla\theta, \mathbf{D}) = (\phi_0\mathbf{1} + \phi_1\mathbf{D} + \phi_2\mathbf{D}^2)\nabla\theta$$

where

$$\phi_i = \phi_i[\theta, O.P., J_k(\nabla\theta, \mathbf{D})], \quad (i = 0, 1, 2;\ k = 1, 2, \cdots, 6).$$

Proof Applying Theorem 5 to (33) yields

$$\psi_i(\theta, O.P., \nabla\theta \otimes \nabla\theta, \mathbf{D}) = \psi_i[\theta, O.P., J_k(\nabla\theta, \mathbf{D})]. \tag{39}$$

This, with (25) and (29), leads to

$$\mathbf{q} = \mathbf{f}(\theta, O.P., \nabla\theta, \mathbf{D}) = (\phi_0\mathbf{1} + \phi_1\mathbf{D} + \phi_2\mathbf{D}^2)\nabla\theta \tag{40}$$

where

$$\phi_i = \phi_i[\theta, O.P., J_k(\nabla\theta, \mathbf{D})], \quad (i = 0, 1, 2;\ k = 1, 2, \cdots, 6).$$

If the three eigenvalues of $\mathbf{D}$ are not distinct, we can still obtain (40) with $\phi_1 = \phi_2 = 0$ (for the case of three identical eigenvalues) or $\phi_2 = 0$ (for the case of two identical eigenvalues) by the similar method. Therefore, (40) is valid for all cases.

2.2. SUFFICIENCY OF (40) FOR REQUIREMENTS (2) AND (3)

Suppose (40) holds, then

$$\begin{aligned}
&\mathbf{f}(\theta^*, O.P.^*, (\bigtriangledown\theta^*)^*, \mathbf{v}^*, \mathbf{L}^*) = \{\phi_0(\theta^*, O.P.^*, J_k((\bigtriangledown\theta^*)^*, \mathbf{D}^*))\mathbf{1} \\
&+\phi_1(\theta^*, O.P.^*, J_k((\bigtriangledown\theta^*)^*, \mathbf{D}^*))\mathbf{D}^* + \phi_2(\theta^*, O.P.^*, J_k((\bigtriangledown\theta^*)^*, \mathbf{D}^*))\mathbf{D}^{*2}\} \\
&(\bigtriangledown\theta^*)^* = \{\phi_0(\theta, O.P., J_k(\mathbf{Q}\bigtriangledown\theta, \mathbf{QDQ}^T))\mathbf{Q1Q}^T + \phi_1(\theta, O.P., J_k(\mathbf{Q}\bigtriangledown\theta, \\
&\mathbf{QDQ}^T))\mathbf{QDQ}^T + \phi_2(\theta, O.P., J_k(\mathbf{Q}\bigtriangledown\theta, \mathbf{QDQ}^T))\mathbf{QD}^2\mathbf{Q}^T\}\mathbf{Q}\bigtriangledown\theta \\
&= \mathbf{Q}\{\phi_0(\theta, O.P., J_k(\mathbf{Q}\bigtriangledown\theta, \mathbf{QDQ}^T))\mathbf{1} + \phi_1(\theta, O.P., J_k(\mathbf{Q}\bigtriangledown\theta, \mathbf{QDQ}^T)) \\
&\mathbf{D} + \phi_2(\theta, O.P., J_k(\mathbf{Q}\bigtriangledown\theta, \mathbf{QDQ}^T))\mathbf{D}^2\}\mathbf{Q}^T\mathbf{Q}\bigtriangledown\theta \\
&= \mathbf{Qf}(\theta, O.P., \bigtriangledown\theta, \mathbf{v}, \mathbf{L}) = \mathbf{q}^*, \quad (k = 1, 2, \cdots, 6)
\end{aligned} \tag{41}$$

in which Eq.(5), $\mathbf{D}^* = \mathbf{QDQ}^T$ and $J_k(\mathbf{Q}\bigtriangledown\theta, \mathbf{QDQ}^T) = J_k(\bigtriangledown\theta, \mathbf{D})$ $(k = 1, 2, \cdots, 6)$ are used.

Also, if (40) holds,

$$\begin{aligned}
&\mathbf{f}(\theta, O.P., -\bigtriangledown\theta, \mathbf{v}, \mathbf{L}) = \{\phi_0(\theta, O.P., J_k(-\bigtriangledown\theta, \mathbf{D}))\mathbf{1} \\
&+\phi_1(\theta, O.P., J_k(-\bigtriangledown\theta, \mathbf{D}))\mathbf{D} + \phi_2(\theta, O.P., J_k(-\bigtriangledown\theta, \mathbf{D}))\mathbf{D}^2\}(-\bigtriangledown\theta) \\
&= -\{\phi_0(\theta, O.P., J_k(\bigtriangledown\theta, \mathbf{D}))\mathbf{1} + \phi_1(\theta, O.P., J_k(\bigtriangledown\theta, \mathbf{D}))\mathbf{D} \\
&+\phi_2(\theta, O.P., J_k(\bigtriangledown\theta, \mathbf{D}))\mathbf{D}^2\}(\bigtriangledown\theta) = -\mathbf{f}(\theta, O.P., \bigtriangledown\theta, \mathbf{v}, \mathbf{L}), (k = 1, 2, \cdots, 6)
\end{aligned} \tag{42}$$

in which $J_k(-\bigtriangledown\theta, \mathbf{D}) = J_k(\bigtriangledown\theta, \mathbf{D})$ $(k = 1, 2, \cdots, 6)$ are used. Equations (41) and (42) establish the sufficiency of (40) for (2) and (3).

2.3. PROPERTIES OF ϕ_I $(I = 0, 1, 2)$ AND BOTH NECESSARY AND SUFFICIENT CONDITIONS FOR INEQUALITY (4)

Both necessity and sufficiency of (40) for Eqs.(2) and (3) are established in §2.1 and §2.2. Here we analyze some fundamental properties of ϕ_i $(i = 0, 1, 2)$, and develop both necessary and sufficient conditions for inequality (4).

Rewrite Eq.(40) as

$$\mathbf{q} = -\mathbf{K}\bigtriangledown\theta, \tag{43}$$

with

$$\mathbf{K} = -(\phi_0\mathbf{1} + \phi_1\mathbf{D} + \phi_2\mathbf{D}^2) = \varphi_0\mathbf{1} + \varphi_1\mathbf{D} + \varphi_2\mathbf{D}^2. \tag{44}$$

Here $\mathbf{1}$ is a unit (identity) tensor, and

$$\varphi_i = -\phi_i \quad (i = 0, 1, 2). \tag{45}$$

$\mathbf{K}$ has two fundamental properties: (1) it is a real-valued tensor on the ground of practical transport processes, and (2) it is a symmetric tensor due to the symmetry of velocity strain tensor $\mathbf{D}$.

Let λ_j and f_j $(j = 1, 2, 3)$ be the three eigenvalues of $\mathbf{D}$ and $\mathbf{K}$, respectively. Since $\mathbf{K}$ is related to $\mathbf{D}$ through Eq.(44),

$$f_j = \varphi_0 + \varphi_1 \lambda_j + \varphi_2 \lambda_j^2, \quad (j = 1, 2, 3). \tag{46}$$

Because $\mathbf{D}$ and $\mathbf{K}$ are real-valued symmetric tensors, λ_j and f_j $(j = 1, 2, 3)$ must be real-valued, i.e.,

$$\overline{f}_j = f_j, \quad (j = 1, 2, 3), \tag{47}$$

$$\overline{\lambda}_j = \lambda_j, \quad (j = 1, 2, 3). \tag{48}$$

By Eq.(46),

$$\overline{f}_j = \overline{\varphi}_0 + \overline{\varphi}_1 \overline{\lambda}_j + \overline{\varphi}_2 \overline{\lambda}_j^2, \quad (j = 1, 2, 3). \tag{49}$$

By making use of Eqs.(47) and (48), Eq.(49) leads to

$$f_j = \overline{\psi}_0 + \overline{\varphi}_1 \lambda_j + \overline{\varphi}_2 \lambda_j^2, \quad (j = 1, 2, 3). \tag{50}$$

This, with Eq.(46), yields

$$(\varphi_0 - \overline{\varphi}_0) + (\varphi_1 - \overline{\varphi}_1)\lambda_j + (\varphi_2 - \overline{\varphi}_2)\lambda_j^2 = 0, \quad (j = 1, 2, 3), \quad \forall \lambda_j \in R \tag{51}$$

which indicates that

$$\varphi_i = \overline{\varphi}_i \quad (i = 0, 1, 2). \tag{52}$$

Therefore, φ_i $(i = 0, 1, 2)$ must be real-valued.

Substituting Eq.(43) into inequality (4) yields

$$\nabla\theta \cdot \mathbf{K} \nabla\theta \geq 0, \qquad \forall \nabla\theta, \tag{53}$$

which implies that $\mathbf{K}$ is positive semi-definite. Note also that $\mathbf{K}$ is, in practice, an invertible tensor, it must be positive definite. The same conclusion may be obtained by noting that the equal sign in (4) is only for reversible processes and transport processes are irreversible.

The necessary and sufficient condition for a symmetric tensor to be positive definite is that all of its eigenvalues are positive definite. Both necessary and sufficient condition for inequality (4) is, thus,

$$\varphi_0 + \varphi_1 \lambda_j + \varphi_2 \lambda_j^2 > 0, \quad (j = 1, 2, 3), \quad \forall \lambda_j \in R. \tag{54}$$

Two necessary conditions of (54) can be easily obtained by considering cases of $\lambda_j = 0$ and $\mid \lambda_j \mid \to \infty$, respectively, as

$$\varphi_0 > 0, \tag{55}$$

$$\varphi_2 > 0. \tag{56}$$

Dividing (54) by φ_0, we can rearrange (54) into an alternative form

$$(1 + \frac{\varphi_1 \lambda_j}{2\varphi_0})^2 + (\frac{\varphi_2}{\varphi_0} - \frac{\varphi_1^2}{4\varphi_0^2})\lambda_j^2 > 0 \quad \forall \lambda_j \in R. \tag{57}$$

This yields another necessary condition, by setting $\lambda_j = -2\varphi_0/\varphi_1$,

$$\varphi_1^2 - 4\varphi_0\varphi_2 < 0. \tag{58}$$

Conversely, it is easy to show that (55), (56) and (58) are also the sufficient conditions of (54).

The detailed expressions of φ_0, φ_1 and φ_2 are material-dependent and need to be determined through experiments. Once they are determined, Eq. (43) can serve as the SGS flux model that is properly invariant and satisfies the second law of thermodynamics.

3. Concluding Remarks

For a class of turbulence flows for which the SGS flux vector can be described by Eq.(1), both necessary and sufficient conditions are derived in a systematic, rigorous way for the invariance, the PMFI and the second law of thermodynamics. This leads to a general model (43) with three real-valued functions φ_i $(i = 0, 1, 2)$ satisfying (55) (56) and (58). Any specific model satisfying (43), (55), (56) and (58) is properly invariant and satisfies the second law of thermodynamics while the model violating these conditions is not. The work is believed to be important both for developing the specific, physics-preserving models and for clarifying some confusion in the literature by noting that the previous works employ an intuitive approach with the focus on only obtaining the sufficient condition.

Acknowledgments: Financial support from the Outstanding Young Researcher Award 2000-2001, the CRCG of the University of Hong Kong is gratefully acknowledged.

References

Ciofalo, M. (1994) Large-eddy simulation: a critical survey of models and applications, *Advances in Heat Transfer* **25**, 321-419.

Fureby, C. and Tabor, G. (1997) Mathematical and physical constraints on large-eddy simulations, *Theoret. Comput. Fluid Dynamics*, **9**, 85-102.

Geankoplis, C. J. (1983) *Transport Processes: Momentum, Heat, and Mass.* Allyn and Bacon Inc., Boston.

Ghosal, S. (1999) Mathematical and physical constraints on large-eddy simulation of turbulence, *AIAA Journal* **37**, 425-433.

Lesieur, M. and Métais, O. (1996) New trends in large-eddy simulations of turbulence, *Annu. Rev. Fluid Mech.* **28**, 45-82.

Mason, P.J. (1994) Large-eddy simulation: a critical review of the technique, *Q. J. R. Meteorol Soc.* **120**, 1-26.

Sagaut, P. (2001) *Large Eddy Simulation for Incompressible Flows.* Springer, Berlin.

Truesdell, C. (1991) *A First Course in Rational Continuum Mechanics.* Academic Press, New York.

Wang, L. (1997) Frame-indifferent and positive-definite Reynolds stress-strain relation, *J. Fluid Mech.* **352**, 341-358.

Wang, L. (1999) Second law of thermodynamics and Arithmetic-mean–geometric-mean inequality, *Int. J. Modern Physics B* **13**, 2791-2793.

Wang, L. (2001) Physical Constraints of Turbulence Modeling. invited book chapter in *Progress and Perspectives in Turbulence* (ed. by J. J. Wang *et al.*), pp. 189-207. Science, Beijing.

LARGE EDDY SIMULATION USING COMPLETE FOURTH ORDER DIFFERENCE METHOD AND VORTICITY-VECTOR POTENTIAL FORMULATION IN GENERALIZED COORDINATES

HIROSHI TOKUNAGA AND KAZUNORI OKUDA
Department of Mechanical & System Engineering
Kyoto Institute of Technology
Matsugasaki, Sakyo-ku, Kyoto 606-8585, JAPAN
e-mail: tokunaga@ipc.kit.ac.jp

Abstract. The vorticity-vector potential formulation and the fourth-order difference method are combined with LES with dynamic subgrid scale model. The new sharp cut off filtering is devised, which has the fourth order accuracy. The present computational method is validated for the simulation of transition in channel. The channel flow with two rows of transverse riblet is computed by the present method and is shown that the drag reduction is attained after the turbulet field developes fully on the riblet surface. It is also found that the transverse riblet has the same effect as the suction.

1. Introduction

Recently, the large eddy simulation is devoted to study the turbulence phenomena with complex geometric configulations such as turbulence over the airfoil (Weber et al 2000) and the turbulence flow in motored piston-cylinder assembly (Verzicco et al 2000). In conducting these simulations accurately, it is crucially important to use the accurate large eddy simulation technique in the generalized coordinate system. The accurate filtering technique is also important as well as accurate computational method. The dynamic subgrid scale model (Germano et al 1991) should be adopted in these simulations. It has also to be considered the importance of the formulation method in dealing with incompressible turbulent flow. The fractional step method has been widely used as the formulation method since the regular grid is applicable and the continuity equation of the velocity field is satisfied sufficiently.

Although, the vorticity-vector potential method has been used in the early stage of the large eddy simulations (Mansour *et. al.*, 1979), this method was replaced to the fractional step method due to the difficulty on applicating the wall boundary conditions adequately. However, recently this problem has been dramatically solved by the research works of the present author (Tokunaga, 1992; Shimada *et. al.*, 1991; Tokunaga *et. al*, 1991; Tokunaga, 1999). The fourth order accurate difference method has been also combined to this formulation in the frame work of the dynamic subgrid scale model.

The present author conducts the research works on the drag reduction of the transverse riblet by making use of the large eddy simulation technique which consists of the fourth order difference method, fourth order accurate sharp-cut-off filter, dynamic subgrid scale model and the vorticity-vector potential formaulation in the curved coordinate system.

It has to be pointed out at first the direct numerical simulation over riblet (Choi *et. al.*, 1994) about research works of turbulent drag reduction. However, another studies exist on numerical simulations of the turbulent drag reduction, such as the linear feedback control (Cortelezzi *et. al.*, 1999) as well as the transverse riblet (Tokunaga and Yamauchi, 1997; Tokunaga, 1999; Manuilovich, 1994; Liu *et. al*, 1994; Mochizuki *et. al*, 1994). The present author showed that the concave transverse riblet has the significant effect for drag reduction since the streak structure of wall bounded turbulence is blocked by the concave transverse riblet and the turbulence is weakened as the suction (Tokunaga, 1999). The suction is used as an effective means for laminarizing the flow along airfoil and reducing the drag, in which the slotted surface is accompanied for delaying the transition and reducing the drag, although this apparatus includes the complex mechanical arrangements (Bobbit *et. al*, 1991).

In the present paper, we intend to verify more precisely the drag reduction effect by conducting the large eddy simulation of the turbulence over the two rows of transverse riblet in the periodic domain of the streamwise direction. The computaional grid cinsists of $129 \times 85 \times 65$ where the curved coordinate is used.

2. Governing Equations

We adopt the fourth order accurate sharp-cut-off filter which is able to be applied to the generalized body fitted coordinate system since the constant width $\delta_{min}/2$ is used as shown in Fig. 1, where $\delta_{min}/2$ denotes the minimum grid spacing in the generalized coordinate, and therefore the filtering and differentiation process is comutable each other with respect to the order. The dynamic subgrid scale is used and the integration in the box filtering

is performed analytically by approximating the turbulent field with the second order Lagrage interpolation both on the basic and test filtering. The integration is performed by the Simpson's rule, so that the fourth order accuracy is assured.

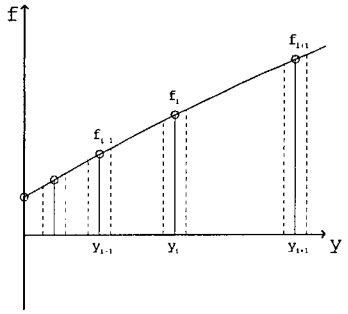


Figure 1. Filtering process

The vorticty-vector potential formulation is applied to the equation of LES with dynamic subgrid scale model. , The vorticity ω is defined as

$$\omega = \nabla \times \mathbf{u}. \tag{1}$$

The vorticity transport equation is derived by taking the rotation of the Navier-Stokes equation with the SGS model. After introducing the vector potential

$$\mathbf{u} = \nabla \times \psi, \tag{2}$$

the Poisson equations are also derived as

$$\Delta\psi_i = -\omega_i, \tag{3}$$

where the solenoidal condition is assumed for the vector potential

$$\frac{\partial \psi_j}{\partial x_j} = 0. \tag{4}$$

These equations are transformed to the generalized coordinate ξ and η from x_1 and x_2.

The vortcicity-vector potential method was validated for the numerical simulation of 180° curved duct with the circular section and the transition simulation in a plane channel (Tokunaga et al 1991).

3. Computational Methods

In order to compute accurately the shear flow turbulence, the fourth order difference method is used. In this case, the first and second derivative, for example, are discretized in the ξ-direction as

$$\left.\frac{\partial \omega}{\partial \xi}\right|_{ijk} = (-\omega_{i-2,j,k} - 8\omega_{i+1,j,k} - 8\omega_{i+1,j,k} + \omega_{i+2,j,k})/(12\ \Delta\ \xi), \quad (5)$$

$$\left.\frac{\partial^2 \omega}{\partial \xi^2}\right|_{ij,k} = (-\omega_{i-2,j,k} + 16\omega_{i-1,j,k} - 30\omega_{i,j,k} + 16\omega_{i+1,j,k} - \omega_{i+2,j,k})$$
$$/(12\ \Delta\ \xi^2),$$

where $\Delta\xi$ represents the grid interval in the ξ-direction The derivative in η- and z-direction as well as the cross derivative are also differenced in the same way, and finally the set of the ordinary differential equations (ODEs) is led.

$$\frac{\mathrm{d}\vec{\omega}}{\mathrm{d}t} = \vec{F}(\vec{\omega}), \quad (6)$$

$$\vec{\omega} = (\omega_{1,2,1}\omega_{2,2,1}, ..., \omega_{I,J-1,K})^T, \quad (7)$$

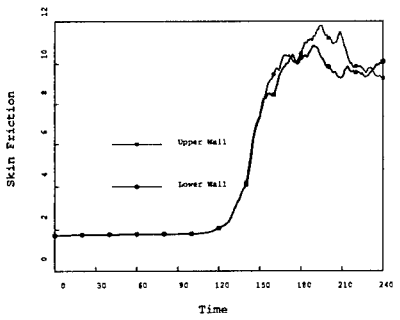
where I, J and K denote the number of grid points in ξ, η and z direction. For time-stepping in the set of ODEs, we apply the TVD Runge-Kutta method with the third order accuracy.

The same discretization procedure is adopted for the Poisson equation for the vector potential, where the point Jacobi is used in ξ and z direction while the SOR method is only applied in η direction, since the computation is performed by Fujitsu FACOM VPP-800/63 of the architecture of pipeline with the huge length. The convergence of the Poisson equation gives a significant influence on the turbulent field and insufficient relaxation weakens the turbulence, so that we adopt the five hundreds relaxations as maximum.

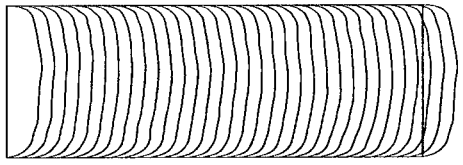
4. Transition Simulation in Channel Flow

In order to validate the present computational method, the transition process in channel flow is simulated. The Renolds number is $Re = 8,000$, and the initial condition consists of the Poiseuille flow with 2% amplitude 2-D and .02% amplitude 3-D T-S waves, which is the standard case (Germano et al 1991).

The time evolution of the wall shear stress is depicted in Fig. 2 (a), where the wall shear is depicted both on the lower and upper wall. The transition occurs at $t = 180$ due to the impuritt of the initial condition. The figure 2 (b) shows the streamwise velocity distribution average in the



(a) Time evolution of skin friction



(b) Averaged streamwise velocity distribution

@@

Figure 2. Time evolution of skin friction on channel wall srafaces (a) and streamwise velocity distribution averaged in spanwise direction (b)

spanwise direction, which shows that the turbulent flow fully developes.

5. Numerical Simulation of Channel Flow with Two Rows of Transverse Riblet

Since the possiblity of drag reduction has been already suggested in the single row of transverse riblet in the periodic domain (Tokunaga, 1999), we investigate the drag reduction in two rows of transverse riblet which is shown in Fig. 3.

The Reynolds number $Re = U_{max} 2\delta/\nu$ is chosen as 8,000 and the height of the transverse riblet $\kappa = -0.03$ which are the same in LES of the single row of transverse riblet.

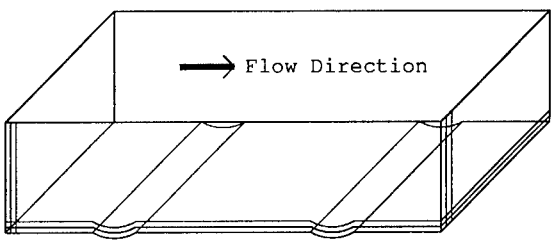
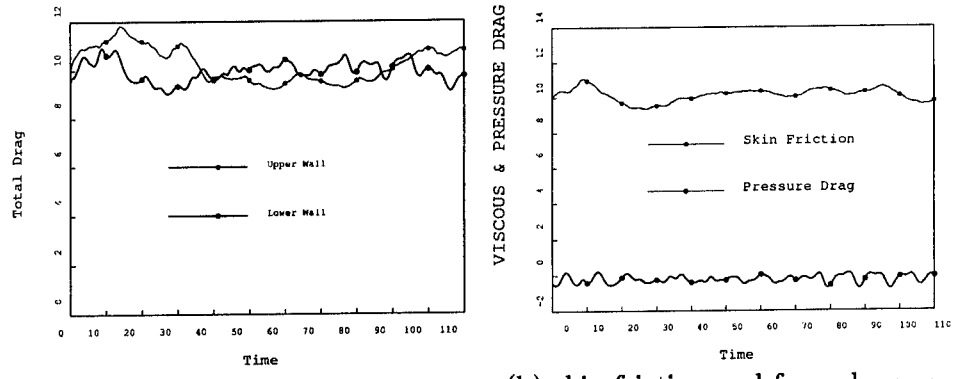


Figure 3. Transverse riblet

The initial turbulent field is initiated by adopting incidently the fully developed channel turbulent flow, which is obtained in the previous chapter, to the channel with two transverse riblets in order to elucidate the robustness of the present computational method. The computational time is 17 hours to proceed 10 non-dimensional time by making use of single vector processor of Fujitsu VPP-800/63 which is the parallel super computer with 63 processors at the maximum performance 504 GFlops . Figure 4 (a) and (b) depict the time history of the total drag at the lower and upper wall, as well as the skin friction and pressure drag at the lower wall. In the present paper, the total drag denotes the sum of the skin friction and pressure drag.

It is shown that the darg on the flat upper wall exceeds the total drag on the lower riblet surface after the initial channel turbulent field fits to the geometry of two rows of transverse riblet. It is also shown that the form drag is too small compared with the wall shear. From this point of view, it is concluded that the transverse riblet has potential as the device of drag reduction.



(a) total drag on riblet and flat wall

(b) skin friction and form drag on riblet wall

@@

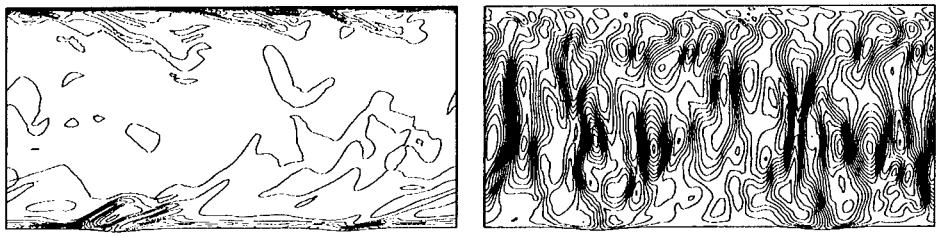
Figure 4. Time history of total drag (a), skin friction and form drag (b)

6. Turbulent Field on Riblet Surface

In this section, we investigate the mechanism of drag reduction from visualizing the turbulet field on the riblet surface. Figure 5 (a) shows the contours of the spanwise vorticity, where it is found that the turbulet vortices are

attracted to the transverse riblet and weakened. The effect is the same as the suction used in the drag reduction device.

In Fig. 5 (b), we show the contours of the velocity normal to the wall which is averaged in the spanwise direction. It is depicted the average velocity directs to the riblet surface. Therefore, it is thought that the transverse riblet has the same effect as the suction.



(a) Contours of spanwise vorticity (b) Contours of the normal velocity

Figure 5. Contours of spanwise vorticity on $x - y$ plane ($k = 9$) at $t = 110$ (a) and velocity normal to the wall average in spanwise direction (b)

The iso-surface of the spanwise vorticty is depicted in Fig. 6. It is found that the streak structure on the upper flat surface is smooth and strong, while the one on the riblet surface is blocked on the two rows of riblets and weakened.

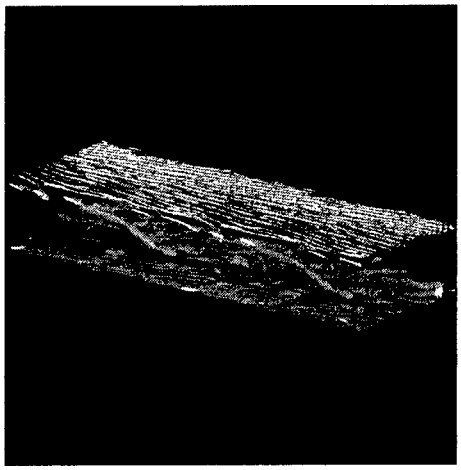


Figure 6. Iso surfaces of streamwise vorticity

7. Conclusions

The complete fourth order accurate method is presented for LES in the vorticity-vector potential formulation and LES is performed for channel flow with two lows of transverse riblets. As results, the following conclusions are obtained.

(1) It is shown that the channel transition simulation is successfully carried out by the present computational method.

(2) It is found that the total drag is reduced after the turbulet field developes fully on the riblet surface.

References

Bobbit, P. J., Harvey, W. D., Harris, C. D. and Brooks, Jr., C. W. (1991), *Natural Laminar Flow and Laminar Flow Control, eds., Barnwell, R. W. and Hussaini, M., Y., Springer-Verlag,* , pp. 247-411

Choi, H., Moin, P. and Kim J. (1994), *J. Fluid Mech.*, **Vol. 262**, pp. 75-110

Cortelezzi, L., Lee, K. H., Kim, J. and Speyer, J. L. (1999), *Int. J. Comp. Fluid Dyn.*, **Vol. 11**, pp. 79-92

Germano, M., Piomelli, U., Moin, P. and Cabot, W. H. (1991) *Phys. Fluids*, **Vol. 29**, pp. 1760-1765

Liu, Z., Liu, Z., Liu, C. and McCormick, S. (1994), *Int. J. Num. Meth. Fluids*, **Vol. 19**, pp. 23-40

Mansour, N. N., Moin, P., Reynolds, W. C., Ferziger, J. H. (1979), *Turbulent Shear Flows I, Springer-Verlag, Berlin*, pp. 386-401

Manuilovich, S. V. (1994), *Theor. Comput. Fluid Dynamics*, , pp. 31-47

Mochizuki, S., Kameda, T. and Osaka, H. (1997), *Proc. of Int. Conf. Fluid Engg., JSME Centenial Grand Conf., Tokyo, JSME*, **No. 97-203**, pp. 1655-1666

Shimada, M., Tokunaga, H., Satofuka, N. and Nishida, H. (1991), *JSME Int. J.* , **Vol. 34**, pp. 109-114

Tokunaga, H., Yoyeda, K. and Satofuka, N. (2000), *Proc. of AIAA 10th Computational Fluid Dynamics Conference, Honolulu, HI, AIAA*, , pp. 937-946

Tokunaga, H. (1999), *37th AIAA Aerospace Sciences Meeting and Exibit, Reno, NV, AIAA Paper 99-0424*, , pp. 1-10

Tokunaga, H. (1992) *Annual Research Briefs, Center for Turbulence Research, Stanford Univ./NASA Ames*, pp. 171-184

Tokunaga, H. and Yamauchi (1997), *Int. J. Num. Meth. Fluids*, **Vol. 25**, pp. 1107-1117

Verzicco, R., Yusof, J. M-. Orlandi P. and Haworth, D. (2000), *AIAA J.*, **Vol. 38**, pp. 427-433

Weber, C. and Ducros, F. (2000), *Int. J. Comp. Fluid Dyn.*, **Vol. 13**, pp. 327-355

A 3D CHANNEL FLOW SIMULATION AT $RE_\tau = 180$ USING A RATIONAL LES MODEL

P. FISCHER AND T. ILIESCU
Mathematics and Computer Science Division
Argonne National Laboratory
9700 S. Cass Ave., Argonne, IL 60439

Abstract. This paper presents numerical results obtained by applying an LES model based on a rational (subdiagonal Padé) approximation in the wave number space. We used a spectral element code to test this LES model and the Smagorinsky model with Van Driest damping in the numerical simulation of a 3D channel flow at $Re_\tau = 180$. The corresponding results were compared with the fine DNS simulation of Moser, Kim, and Mansour.

1. Introduction

Introduced in 1970 by Deardorff [4], Large Eddy Simulation (LES) is one of the most promising approaches to the numerical simulation of turbulent flows. LES has a rich history, being successfully developed and applied to a wide range of applications by the engineering and geophysics communities.

LES is based on the idea that the large scales in the flow are essential, being responsible for the important engineering quantities (heat transfer, mixing, etc.), whereas the small scales are important because of their effect on the large scales. Another important assumption in LES is that the small scales of turbulence are more isotropic and more universal than the large scales.

The usual LES starts by convoluting the Navier-Stokes equations (NSE) with a spatial filter g_δ:

$$\overline{\mathbf{u}}_t + \nabla \cdot (\overline{\mathbf{u}}\overline{\mathbf{u}}) - Re^{-1}\Delta\overline{\mathbf{u}} + \nabla\overline{p} = \overline{\mathbf{f}}, \tag{1}$$

where $\overline{\mathbf{u}} = g_\delta * \mathbf{u}$ is the variable of interest. The filtered NSE (1) do not form a closed system, and most LES research has been directed at modeling the subgrid-scale (SGS) stress

$$\tau = \overline{\mathbf{u}}\overline{\mathbf{u}} - \overline{\mathbf{u}}\,\overline{\mathbf{u}}. \tag{2}$$

Arguably the most popular class of SGS models is the eddy viscosity type, based on (variants of) Smagorinsky's model [24],

$$\tau = -(C_s\delta)^2\,|\nabla^s\overline{\mathbf{u}}|\,\nabla^s\overline{\mathbf{u}}, \tag{3}$$

where δ is the radius of the filter and $\nabla^s \overline{\mathbf{u}} = \frac{1}{2}(\nabla \overline{\mathbf{u}} + \nabla \overline{\mathbf{u}}^T)$. Smagorinsky proposed (3) with C_s a constant, but the most successful models have been those in which C_s is computed dynamically (the dynamic subgridscale eddy viscosity model [9] and its variants).

Other successful LES models include the scale-similarity models, the mixed models (scale-similarity models coupled with an eddy-viscosity model to properly dissipate energy), and the RNG models.

Despite its undeniable achievements, LES still poses numerous challenges, many of them at a very fundamental level. One of these challenges is the need for more mathematical consistency, which would provide the means for sounder mathematical and numerical analysis for the corresponding LES models. Other fundamental challenges are the LES boundary conditions, the influence of the filter on the SGS model, commutation errors in filtering, numerical errors, and numerical validation. A growing current of opinion in the LES community favors the need for new approaches that could answer these fundamental challenges.

The LES model used in this paper is based on an approximation rather than a physical analogy. This model has evolved in several steps. First, in 1974 Leonard [16] developed a continuum model of $\overline{\overline{\mathbf{u}}\,\overline{\mathbf{u}}}$

$$\overline{\overline{\mathbf{u}}\,\overline{\mathbf{u}}} = \overline{\mathbf{u}}\,\overline{\mathbf{u}} + \frac{\delta^2}{4\gamma}\Delta(\overline{\mathbf{u}}\,\overline{\mathbf{u}}) + O(\delta^4), \tag{4}$$

where δ is the radius of the filter and γ is a parameter in the Gaussian filter. Next, in 1979 Clark, Ferziger, and Reynolds [3] developed an analogous model for the "cross terms" $\overline{\overline{\mathbf{u}}\mathbf{u}'} + \overline{\mathbf{u}'\overline{\mathbf{u}}}$, where $\mathbf{u}' := \mathbf{u} - \overline{\mathbf{u}}$ represents the turbulent fluctuations. The approach used in the derivation of these models involved taking the Fourier transform of the corresponding terms, approximating the Fourier transform of the Gaussian filter $\hat{g}_\delta$, dropping the terms of order $O(\delta^4)$ and, finally, taking the inverse Fourier transform of the resulting approximations. Noticing that the approximation by Taylor series of $\hat{g}_\delta$ actually *increases* the high wave number components, Galdi and Layton [8] developed a new LES model based on a rational ((0,1) Padé) approximation of $\hat{g}_\delta$, which preserves the decay of the high wave number components. The resulting LES model, which will be called in the sequel the "Rational" LES model, reads as follows:

$$\begin{cases} \mathbf{w}_t - Re^{-1}\Delta\mathbf{w} + \nabla\cdot(\mathbf{w}\mathbf{w}) + \nabla q + \nabla\cdot\left[\left(-\frac{\delta^2}{4\gamma}\Delta + I\right)^{-1}\left(\frac{\delta^2}{2\gamma}\nabla\mathbf{w}\nabla\mathbf{w}\right)\right] = \overline{\mathbf{f}} & \text{in } \Omega, \\ \mathbf{w}(\mathbf{x},0) = \overline{\mathbf{u}}_0(\mathbf{x}) & \text{in } \Omega, \\ \text{Boundary Conditions} & \text{on } \partial\Omega, \end{cases}$$

where $(\mathbf{w}, q)$ are proposed as an approximation to $(\overline{\mathbf{u}}, \overline{p})$, $\Omega \subseteq \mathbb{R}^d$ $(d = 2, 3)$, and

$$(\nabla\mathbf{w}\nabla\mathbf{w})_{i,j} = \sum_{l=1}^{d} \frac{\partial \mathbf{w}_i}{\partial \mathbf{x}_l}\frac{\partial \mathbf{w}_j}{\partial \mathbf{x}_l}. \tag{5}$$

A sound mathematical analysis [2] and the first steps for a numerical validation [12] were provided for the "Rational" LES model (5) coupled with a Smagorinsky model with a very small coefficient C_s (for alternatives to the Smagorinsky model, see [14]).

This paper presents numerical results for the "Rational" LES model (5) applied to the 3D channel flow test problem at a Reynolds number based on the wall shear velocity $Re_\tau = 180$.

2. Numerical Setting

The 3D channel flow (Figure 1) is one of the most popular test problems for the investigation of the wall bounded turbulent flows. We will compare our numerical results with the extensive data existing for this test problem (both Direct Numerical Simulation (DNS) and LES). The computational domain is periodic in the streamwise (x) and spanwise (z) directions, and the pressure gradient that drives the flow is adjusted dynamically to maintain a constant mass flux through the channel. We selected the periodic domain sizes (x and z) as $L_x = 2\pi$, $L_z = \frac{4}{3}\pi$, and we chose unity as the channel half-width ($\delta_{channel} = 1$). We employed in our calculations a $40 \times 49 \times 40$ quadrature grid. The length scale δ is computed as $\delta = \sqrt[3]{\Delta_x\ \Delta_z\ \Delta_y(y)}$, where Δ_x and Δ_z are twice the largest spaces between the Gauss-Lobatto-Legendre (GLL) points in the x and z directions, respectively, and $\Delta_y(y)$ is inhomogeneous and is computed as an interpolation function that is zero at the wall and is twice the normal meshsize for the elements near the wall and for those in the center of the channel. For the "Rational" LES model (5) we chose $\gamma = 6$ (the usual choice for the Gaussian filter).

We compared the "Rational" LES model (5) with the Smagorinsky model with Van Driest damping (see [18]). The Smagorinsky model with Van Driest damping is obtained by modifying the usual Smagorinsky model (3) to reduce the eddy viscosity in the near-wall region

$$\tau = -[C_s\delta(1 - exp(-y^+/A^+))]^2\ |\nabla^s\overline{\mathbf{u}}|\ \nabla^s\overline{\mathbf{u}}, \tag{6}$$

where $y^+ = (\delta_{channel} - |y|)u_\tau/\nu$ is the nondimensional distance from the wall, C_s is the Smagorinsky constant, and A^+ is a constant. Here u_τ is the wall-shear velocity, $u_\tau = \sqrt{\tau_{wall}/\rho}$, in which ρ is the density, and τ_{wall} is the wall-shear. In our calculations we made the usual choices: $C_s = 0.1$ and $A^+ = 25$.

The numerical simulations were performed using a spectral element code based on the $\mathbb{P}_N - \mathbb{P}_{N-2}$ velocity and pressure spaces introduced by Maday and Patera [17]. The domain is decomposed into $8 \times 10 \times 8$ elements, as shown in Figure 2. The velocity is continuous across element interfaces and is represented by Nth-order tensor-product Lagrange polynomials based on the GLL points. The pressure is discontinuous and is represented by tensor-product polynomials of degree $N - 2$. Time stepping is based on an operator-splitting of the discrete system, which leads to separate convective, viscous, and pressure subproblems without the need for ad-hoc pressure boundary conditions. A filter, which removes 5% of the highest velocity mode, is used to stabilize the Galerkin formulation [7]. Details of the discretization and solution algorithm are given in [5], [6].

We applied initial conditions consisting of the parabolic mean flow (Poiseuille flow), on which a 2D Tollmien-Schlichting (TS) mode of 2% amplitude and a 3D TS mode of 1% amplitude were superimposed.

In our numerical experiments we considered, as a first step, homogeneous boundary conditions for the "Rational" LES model (5). The mathematical and numerical investigation of more realistic (slip-with-friction) boundary conditions in the LES context began in [22], [13].

The numerical results include plots of the following time- and plane-averaged quantities: the mean streamwise velocity $\ll \overline{u} \gg$, the x,y-component of the Reynolds stress $\ll u'v' \gg$, and the

rms values of the streamwise $\ll u'u' \gg$, wall-normal $\ll v'v' \gg$, and spanwise $\ll w'w' \gg$ velocity fluctuations, where $< \cdot >$ denotes plane (xz) averaging, $\ll \cdot \gg$ denotes time and plane (xz) averaging, the fluctuating quantities f' are calculated as $f' = f - \ll f \gg$, and a "+" superscript denotes the variable in wallunits.

3. Results and Conclusions

These numerical results were the basis for *a posteriori* tests: we compared them with the fine DNS simulation of Moser, Kim and Mansour [19].

Figure 3 shows the mean streamwise velocity; note the almost perfect overlapping of the results corresponding to the two methods ("Rational" LES and Smagorinsky model with Van Driest damping). The same behavior can be observed in the x, y-component of the Reynolds stress in Figure 4, with a slight improvement for the "Rational" LES model.

Figures 5–7, containing the rms values for the three velocity components, merit a more detailed discussion.

The rms values of the streamwise velocity fluctuations in Figure 5 show a better (closer to the fine DNS benchmark results in [19]) behavior for the "Rational" LES model. Near the wall this improvement is clearer, the two models performing similarly away from the wall.

Figure 6 shows the rms values of the wall-normal velocity fluctuations. Here, the Smagorinsky model with Van Driest damping performs slightly better near the wall, and consistently better between the near-the-wall region and the center of the channel. Toward the center of the channel, the "Rational" LES model performs slightly better.

The rms values of the spanwise velocity fluctuations in Figure 7 are consistently better for the "Rational" LES model, with the exception of a very short portion close to the center of the channel.

In conclusion, the "Rational" LES model performs better near the wall (with the exception of the rms values of the wall-normal velocity fluctuations), whereas the Smagorinsky model with Van Driest damping performs better closer to the center of the channel (with the exception of the rms values of the spanwise velocity fluctuations). The two models are comparable in accuracy.

Further research should be directed at the investigation of additional terms accounting for the discarded $O(\delta^4)$ terms in the "Rational" LES model, as well as to the influence of the length scale δ in the spectral element implementation of the "Rational" LES model.

4. Acknowledgments

This work was supported in part by the Mathematical, Information, and Computational Sciences Division subprogram of the Office of Advanced Scientific Computing Research, U.S. Dept. of Energy, under Contract W-31-109-Eng-38.

We thank Prof. R. Moser for helpful communications that improved this paper.

References

1. Aldama, A.A. (1990) *Filtering Techniques for Turbulent Flow Simulation*. Lecture Notes in Engineering **56**, Springer-Verlag, ed. by C. A. Brebbia and S. A. Orszag.
2. Berselli, L.C., Galdi, G.P., Layton, W.J. and Iliescu, T. (2001) Mathematical Analysis for a Large Eddy Simulation Model, preprint

3. Clark, R. A., Ferziger, J.H. and Reynolds, W.C. (1979) Evaluation of Subgrid Scale Models Using an Accurately Simulated Turbulent Flow, *J. Fluid Mech.* **91**, pp. 1–16
4. Deardorff, J.W. (1970) A Numerical Study of Three-Dimensional Turbulent Channel Flow of Large Reynolds Numbers, *J. Fluid Mech.* **41**, pp. 453–480
5. Fischer, P.F. (1997) An Overlapping Schwarz Method for Spectral Element Solution of the Incompressible Navier-Stokes Equations, *J. of Comp. Phys.* **133**, pp. 84–101
6. Fischer, P.F., Miller, N.I. and Tufo, H.M. (2000) An Overlapping Schwarz Method for Spectral Element Simulation of Three-Dimensional Incompressible Flows, in *Parallel Solution of Partial Differential Equations*. Springer-Verlag, ed. by P. Björstad and M. Luskin, pp. 159-181.
7. Fischer, P.F. and Mullen, J.S. (2001) Filter-Based Stabilization of Spectral Element Methods *Comptes rendus de l'Académie des sciences Paris, t. 332, -Série I - Analyse numérique*, pp. 265–270
8. Galdi, G.P. and Layton, W.J. (2000) Approximating the Larger Eddies in Fluid Motion II: A Model for Space Filtered Flow, *Math. Methods and Models in Applied Sciences* **10**, pp. 343–350
9. Germano, M., Piomelli, U., Moin, P. and Cabot, W. (1991) A Dynamic Subgridscale Eddy Viscosity Model, *Phys. Fluids A* **3**, pp. 1760–1765
10. Geurts, B.J. (1997) Inverse Modeling for Large-Eddy Simulation, *Phys. Fluids* **9**, pp. 3585–3587
11. Hughes, T.J.R., Oberai, A.A. and Mazzei, L. (2001) Large Eddy Simulation of Turbulent Channel Flows by the Variational Multiscale Method, *Phys. Fluids* **13**, pp. 1784–1799
12. Iliescu, T., John, J., Layton, W.J., Matthies, G. and Tobiska L. (2001) A Numerical Study of a Class of LES Models, preprint.
13. Iliescu, T., John, J. and Layton, W.J. (2001) Convergence of Finite Element Approximation of Large Eddy Motion, preprint.
14. Iliescu, T. and Layton, W.J. (1998) Approximating the Larger Eddies in Fluid Motion III: The Boussinesq Model for Turbulent Fluctuations, *An. St. Univ."Al. I. Cuza"* **44**, pp. 245–261
15. Kim, J., Moin, P. and Moser, R. (1987) Turbulence Statistics in Fully Developed Channel Flow at Low Reynolds Number, *J. Fluid Mech.* **177**, pp. 133–166
16. Leonard, A. (1974) Large Eddy Simulation of Turbulent Fluid Flows, *Adv. in Geophysics* **18A**, pp. 237–248
17. Maday, Y. and Patera, A.T. (1989) Spectral Element Methods for the Navier-Stokes Equations, in *State of the Art Surveys in Computational Mechanics*, ASME, New York, ed. by A. K. Noor, pp. 71–143
18. Moin, P. and Kim, J. (1982) Numerical Investigation of Turbulent Channel Flow, *J. Fluid Mech.* **118**, pp. 341–377
19. Moser, D.R., Kim, J. and Mansour, N.N. (1999) Direct Numerical Simulation of Turbulent Channel Flow up to $Re_\tau = 590$, *Phys. Fluids* **11**, pp. 943–945
20. Piomelli, U. (1993) High Reynolds Number Calculations Using the Dynamic Subgrid-Scale Stress Model, *Phys. Fluids A* **5**, pp. 1484–1490
21. Sagaut, P. (2001) *Large Eddy Simulation for Incompressible Flows*. Springer Verlag, Berlin.
22. Sahin, N. (2001) New Perspectives on Boundary Conditions for Large Eddy Simulation, preprint.
23. Sarghini, F., Piomelli, U. and Balaras, E. (1999) Scale-Similar Models for Large-Eddy Simulations, *Phys. Fluids* **11**, pp. 1596–1607
24. Smagorinsky, J. (1963) General Circulation Experiments with the Primitive Equation: I The Basic Experiment, *Mon. Wea. Rev.* **91**, pp. 216–241
25. Stolz, S., Adams, N.A. and Kleiser, L. (2001) An Approximate Deconvolution Model for Large-Eddy Simulation with Application to Incompressible Wall-Bounded Flows, *Phys. Fluids* **13**, pp. 997–1015

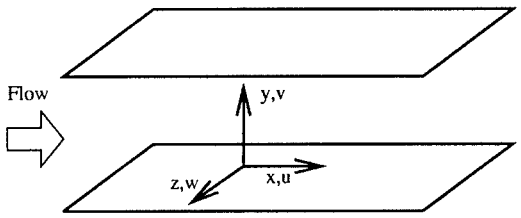


Figure 1. Problem setup for the channel flow.

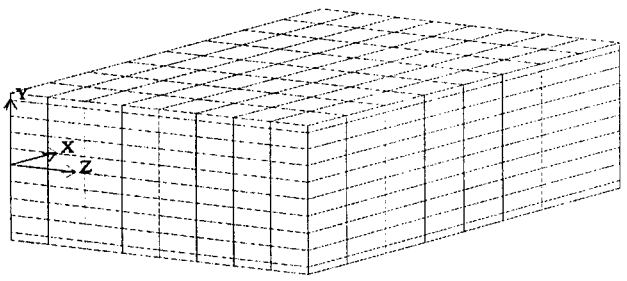


Figure 2. Spectral element mesh.

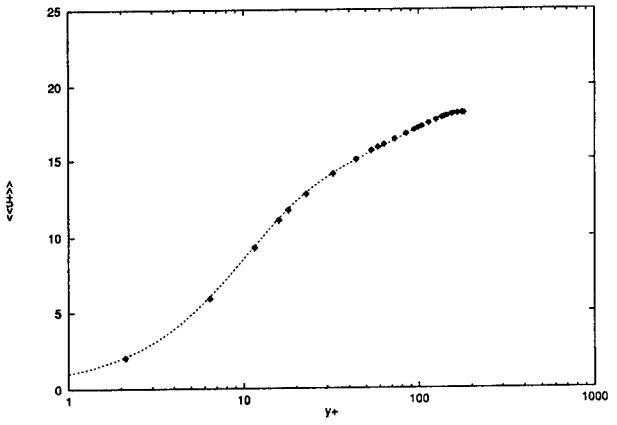


Figure 3. Mean streamwise velocity; ... fine DNS, ◇ Smagorinsky with Van Driest damping, + "Rational" LES.

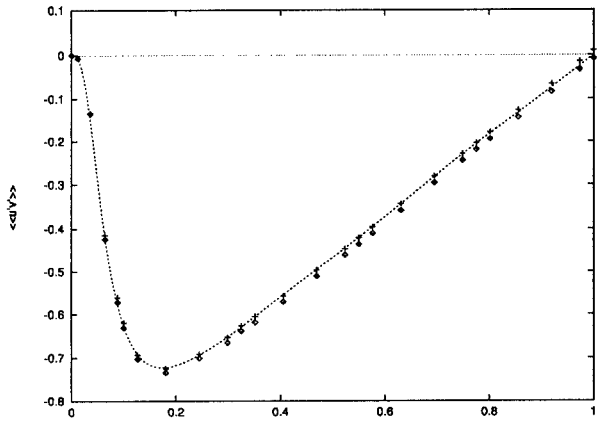


Figure 4. x, y-component of the Reynolds stress; ... fine DNS, $\diamond$ Smagorinsky with Van Driest damping, + "Rational" LES.

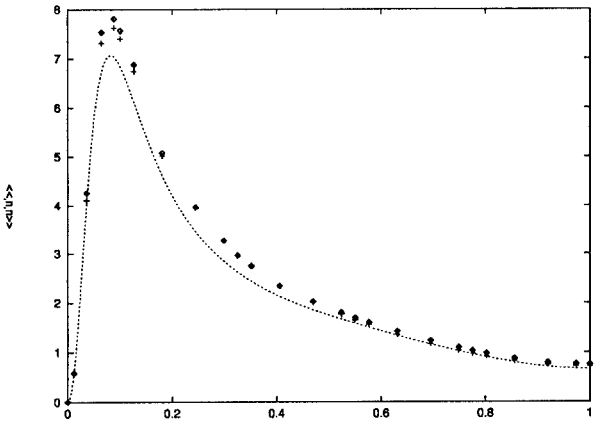


Figure 5. rms values of streamwise velocity fluctuations; ... fine DNS, $\diamond$ Smagorinsky with Van Driest damping, + "Rational" LES.

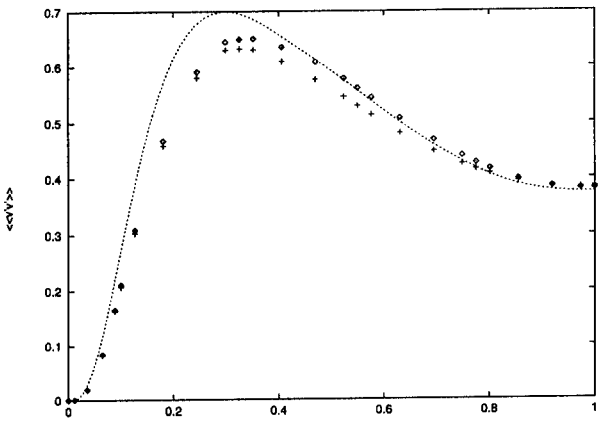


Figure 6. rms values of wall-normal velocity fluctuations; ... fine DNS, ◇ Smagorinsky with Van Driest damping, + "Rational" LES.

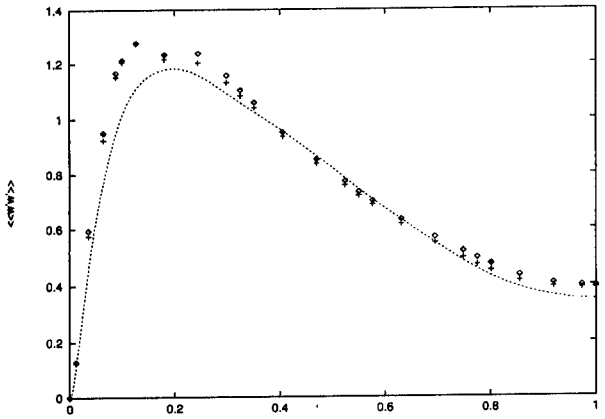


Figure 7. rms values of spanwise velocity fluctuations; ... fine DNS, ◇ Smagorinsky with Van Driest damping, + "Rational" LES.

DISCRETE FILTERING ON UNSTRUCTURED GRIDS BASED ON LEAST-SQUARES GRADIENT RECONSTRUCTION

A. HASELBACHER
Center for Simulation of Advanced Rockets
University of Illinois at Urbana-Champaign
Urbana, IL 61801

1. Introduction

The equations for Large-Eddy Simulation (LES) of turbulent flows are formally derived by applying a low-pass filter to the Navier-Stokes equations. In doing so, it is often tacitly assumed that the filtering and differentiation operations commute. This assumption is invalid if the filter width is not uniform—as is the case if wall-bounded flows are computed—unless special filter operators are constructed, see, e.g, Vasilyev *et al.* (1998).

Recent work by Marsden *et al.* (2000) resulted in a framework for the construction of filters on unstructured grids which commute with differentiation to a potentially arbitrarily high order. They also demonstrated a filter operator with a second-order commutation error. However, their method appears to be quite complicated in its construction, particularly in three dimensions and near boundaries. Furthermore, it is dependent on geometric comparisons with user-specified parameters.

The goal of the present work is to develop a simpler filtering method than that of Marsden *et al.* (2000). The new filtering method is based on the following observation: The conditions for filtering a function to a given order of commutation error derived by Vasilyev *et al.* (1998) are formally identical to the conditions for reconstructing the gradient of a function to a given order of truncation error. In other words, the construction of filtering operators may be reinterpreted as the construction of—suitably reformulated—gradient-reconstruction methods. This apparently trivial observation has important consequences because the reconstruction of gradients is central to many flow-solution methods on unstructured grids and is well understood, see Haselbacher and Blažek (2000).

2. Least-Squares Gradient Reconstruction

The least-squares gradient-reconstruction procedure originally developed by Barth (1991) is based on approximating the variation along an edge linking vertices 0 and i by a truncated Taylor series, e.g., for a linear approximation,

$$\phi_i = \phi_0 + (\nabla\phi)_0 \cdot \Delta\mathbf{r}_{0i}, \tag{1}$$

where $\Delta\mathbf{r}_{0i} = \mathbf{r}_i - \mathbf{r}_0$ and $\mathbf{r} = \{x, y\}^t$. The application of Eq. (1), or corresponding higher-order approximations, to all edges incident to vertex 0 gives a system of linear equations for the derivatives at vertex 0,

$$\mathbf{A}\mathbf{x} = \mathbf{b}, \tag{2}$$

where $\mathbf{A}$ is a $d_0 \times n_0$ matrix of geometrical terms, $\mathbf{x}$ is an n_0–vector containing derivatives, and $\mathbf{b}$ is a d_0–vector of function values, with n_0 being the number of derivatives reconstructed and d_0 denoting the degree of vertex 0. Since there are usually more incident edges than derivatives, Eq. (2) is solved for $\mathbf{x}$ in a least-squares fashion.

A general closed-form solution of Eq. (2) can be derived through the QR-decomposition of $\mathbf{A}$ using the Gram-Schmidt process. In the following, we denote by $\mathbf{a}_i$ and $\mathbf{q}_i$ the ith column vector of the matrices $\mathbf{A}$ and $\mathbf{Q}$, respectively, and by r_{ij} the ijth element of the upper triangular matrix $\mathbf{R}$. There is no summation over repeated indices. The general solution is

$$\mathbf{x} = \mathbf{W}^t\mathbf{b}, \tag{3}$$

where $\mathbf{W}$ is a $d_0 \times n_0$ matrix with column vectors $\mathbf{w}_i$ given by

$$\mathbf{w}_i = c_{ii}\mathbf{q}_i + \sum_{k=i+1}^{n_0} c_{ik}\, c_{kk}\, \mathbf{q}_k, \tag{4}$$

with

$$\mathbf{q}_i = c_{ii}\left(\mathbf{a}_i + \sum_{j=1}^{j<i} c_{ji}\,\mathbf{a}_j\right). \tag{5}$$

The geometrical quantities c_{ij} are defined as

$$c_{ii} = r_{ii}^{-1} \tag{6}$$

$$c_{ij} = -\left(c_{ii}\, r_{ij} + \sum_{k=i+1}^{j-1} c_{ik}\, c_{kk}\, r_{kj}\right) \quad \text{for} \quad j > i \leq n_0, \tag{7}$$

where

$$r_{ij} = \frac{1}{r_{ii}}\left(\mathbf{a}_i \cdot \mathbf{a}_j - \sum_{k=1}^{i-1} r_{ki}\, r_{kj}\right) \quad \text{for} \quad j \geq i \leq n_0. \tag{8}$$

The general closed-form solution allows the reconstruction of derivatives to an arbitrarily high order of accuracy on unstructured grids.

3. Least-Squares Filtering

The least-squares gradient-reconstruction method can be turned into a filtering method by modifying Eq. (1), so that ϕ_0 is no longer a point value, but represents a filtered value $\overline{\phi}_0$,

$$\phi_i = \overline{\phi}_0 + (\nabla\phi)_0 \cdot \Delta\mathbf{r}_{0i}. \tag{9}$$

The effect of this modification is that the filtered value $\overline{\phi}_0$ is appended to the vector of unknowns $\mathbf{x}$. The resulting system of equations can be solved using the method described in Section 2. This leads to an expression for the filtered value in the form of a weighted sum,

$$\overline{\phi}_0 = \sum_{i=1}^{d_0} \omega_{0i}\phi_i. \tag{10}$$

The accuracy of the filtering operation is determined by the order of the derivatives included in the gradient reconstruction. For example, linear gradient reconstruction leads to a second-order accurate expression for the filtered value, with weights given by

$$\omega_{0i} = \frac{1}{r_{33}^2}\left(1 - \frac{r_{23}}{r_{22}}\Delta y_{0i} + \frac{r_{12}r_{23} - r_{13}r_{22}}{r_{11}r_{22}}\Delta x_{0i}\right). \tag{11}$$

It is easily verified that Eq. (11) leads to two vanishing moments,

$$\sum_{i=1}^{d_0} \omega_{0i}\Delta\mathbf{r}_{0i} = \mathbf{0},$$

which is merely a consequence of its second-order accuracy.

The spectral behaviour of Eq. (10) can be improved if the unfiltered value ϕ_0 is also included in the stencil,

$$\overline{\phi}_0 = \omega_{00}\phi_0 + (1 - \omega_{00})\sum_{i=1}^{d_0} \omega_{0i}\phi_i. \tag{12}$$

This modification does not degrade the accuracy of Eq. (10).

The remainder of this work is based upon Eq. (12) and investigates linear and quadratic filter functions. For both functions, the stencil is extended to include an additional layer of vertices beyond the nearest neighbours. In

the interior, this gives a stencil of 18 vertices for $\omega_{00} = 0$ or 19 vertices for $\omega_{00} \neq 0$. The motivation for extending the support is twofold. First, having two layers of vertices allows the introduction of two parameters β and γ, which can be used to weight the contributions to Eq. (10) of the inner and outer layers, respectively. Together with ω_{00}, these additional degrees of freedom may be used to optimize damping of high-wavenumber components or to achieve a specified filter width. Second, the nearest-neighbour stencil leads to a singular matrix $\mathbf{A}$ for the quadratic filter function on uniform grids, thus necessitating the use of additional points in the stencil.

One advantage of the new filtering method is that it allows reusing data structures and geometric weights already employed to compute gradients in the flow-solution method. Furthermore, it is easily extended to three dimensions and does not require special treatment at boundaries beyond ensuring—as for interior vertices—that the degree of a given vertex is greater than the number of derivatives reconstructed at that vertex.

4. Determination of Filter Width

In the present work, the filter width is determined from the polar moment of the filter transfer function,

$$J_{xy} = \int_0^{\pi/\Delta} \int_0^{\pi/\Delta} \left(k_x^2 + k_y^2\right) G(k_x, k_y)\, dk_x\, dk_y, \tag{13}$$

where $\mathbf{k} = \{k_x, k_y\}^t$ is the wave-number vector, $G(k_x, k_y)$ is the filter transfer function, and Δ is the grid spacing. In one dimension, this reduces to the second moment of the filter transfer function, whose use in determining the filter width was originally suggested by Lund (1997). In this section, we assume the grid spacing to be uniform.

The ratio of the filter width Δ_f to the grid spacing may be computed from the relation

$$\alpha \equiv \frac{\Delta_f}{\Delta} = \left(\frac{\pi^5}{8 J_{xy} \Delta^4}\right)^{\frac{1}{4}}. \tag{14}$$

The constants in Eq. (14) were chosen such that it gives the correct width for the Fourier cut-off filter.

Figure 1(a) depicts the transfer function for the linear filter function with $\omega_{00} = 1/5$ and $\beta = \gamma = 1$. While high wave-numbers are damped well, the transfer function deviates quickly from unity for low to moderate wave-numbers, and, as such, is a poor representation of the Fourier cut-off filter. Numerical evaluation of Eq. (13) gives $\alpha = 1.40$.

The transfer function for the quadratic filter function with $\omega_{00} = 1/2$ and $\beta = \gamma = 1$ is shown in Fig. 1(b). Compared to the linear filter function, the quadratic filter function is a good approximation to the Fourier cut-off filter for low to moderate wave-numbers. For higher wave-numbers, preferred directions can be discerned which are aligned with the edges in the grid. For the quadratic filter function, Eq. (13) gives $\alpha = 1.12$.

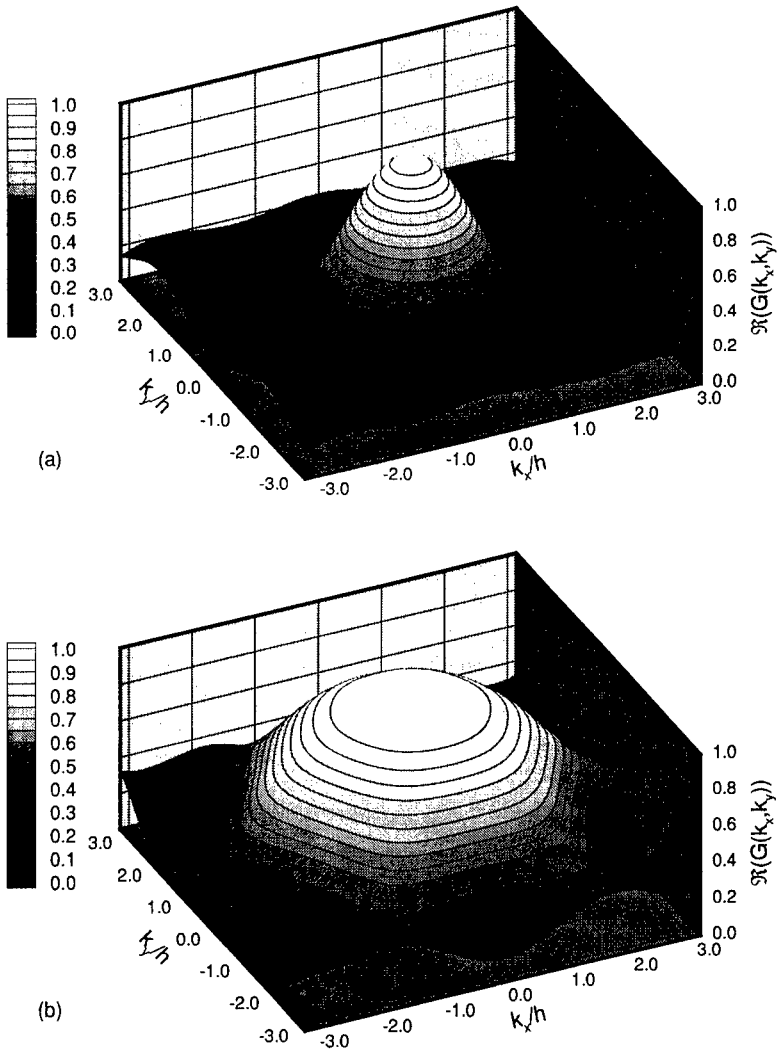


Figure 1. Transfer functions for filter functions on uniform grids and $\beta = \gamma = 1$. (a) Linear filter function with $\omega_{00} = 1/5$ and (b) quadratic filter function with $\omega_{00} = 1/2$.

5. Commutation Error

Marsden *et al.* (2000) proved that a filter with $p-1$ vanishing moments is needed to achieve a commutation error of order p for smoothly varying filter widths in one dimension. An equivalent statement is that the filter must be accurate to order p to achieve a commutation error of order p for smoothly varying filter widths. For grids with arbitrarily varying filter widths, the commutation error will drop below p. It is thus necessary to construct filter operators of order $p+1$ to obtain commutation errors of order p on arbitrary unstructured grids. We are interested in this general case since unstructured grids rarely satisfy smoothness constraints. To obtain a second-order commutation error, we thus require quadratic filtering.

The order of the commutation error is computed by carrying out a grid-refinement study using an analytic function for the unfiltered field. Five uniform triangular grids were generated for a hexagonal domain, containing 271, 1141, 4681, 18961, and 76321 vertices. The interior vertices were subsequently distorted by random amounts of a given fraction of the grid spacing in both coordinate directions. In the results presented below, this fraction was taken to be 0.35. The distorted grid with 1141 vertices is shown in Fig. 2.

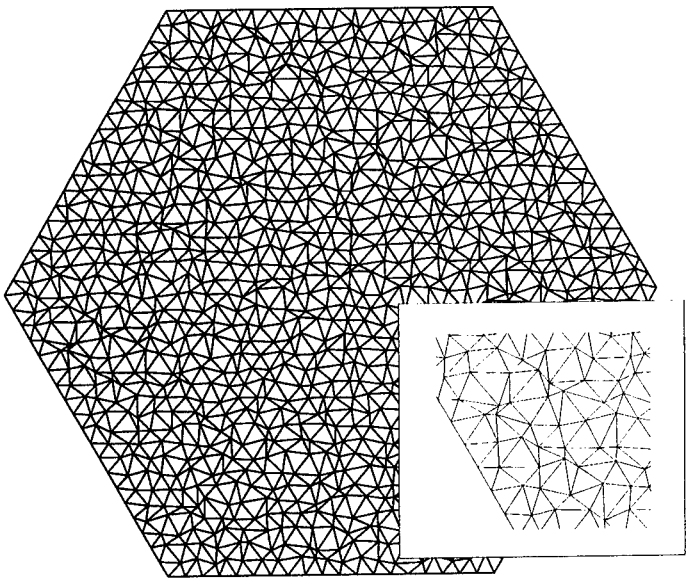


Figure 2. Distorted grid with 1141 vertices. Inset shows detail of distorted grid.

The commutation error is defined in terms of the discrete divergence,

$$E_c = \left(\overline{\frac{\delta u}{\delta x}} + \overline{\frac{\delta v}{\delta y}} \right) - \left(\frac{\delta \overline{u}}{\delta x} + \frac{\delta \overline{v}}{\delta y} \right), \tag{15}$$

where $\delta(\cdot)/\delta x$ represents the discrete gradient operator in the x–coordinate direction. The function chosen in the present study is

$$\left\{ \begin{matrix} u \\ v \end{matrix} \right\} = \left\{ \begin{matrix} \cos(\pi x)\sin(\pi y) \\ \sin(\pi x)\cos(\pi y) \end{matrix} \right\}. \tag{16}$$

In computing the commutation-error norms, only the vertices were included whose gradients or filtered values were not affected by boundary effects. Effects of one-sided stencils arising from the presence of boundaries will be studied in future work. It was verified that commutation errors were identically zero for arbitrary functions on uniform grids.

The variation of the L_2-norms of the commutation error with grid refinement is shown in Fig. 3. Note that the commutation error is about an order of magnitude smaller than the truncation error of the divergence operator. The order of accuracy of the filtering operator, the divergence operator, and the order of the commutation error were computed from a linear least-squares curve fit for the finest four grids. The slopes were determined to be 3.05, 1.96, and 2.17, respectively. It is thus verified that the commutation error obtained with the new quadratic filtering method on a randomly distorted unstructured grid is of second order.

The ultimate test for commutation will be to specify a uniform filter width on a randomly distorted grid using the parameters ω_{00}, β, and γ and to check for zero commutation error. This is an objective of future work.

6. Conclusions

A new filtering method for unstructured grids was presented. Closed-form expressions were given which allow the construction of filtering operators of arbitrarily high order. The new filtering method is easily constructed, does not require special treatment at boundaries, and allows reusing data structures and geometric terms needed by the flow-solution method without filtering. Linear and quadratic filter functions were studied. A grid-refinement study on randomly distorted grids demonstrated a commutation error of second order.

Acknowledgement

This research is funded by the U.S. Department of Energy through the University of California under Subcontract number B341494.

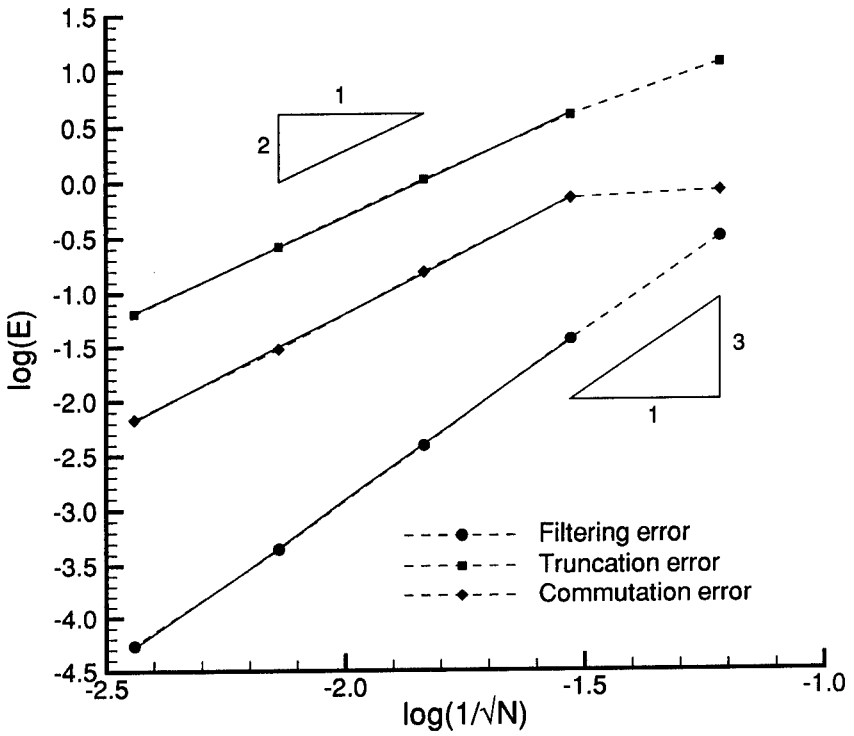


Figure 3. Variation of L_2–norm of errors with grid refinement. Solid lines represent linear curve fits to data, and N denotes the number of vertices.

References

Barth T.J. (1991), A 3D Upwind Euler Solver for Unstructured Meshes, *AIAA Paper 91-1548*, 10th Computational Fluid Dynamics Conference, Honolulu, HI, June 1991

Haselbacher A. and Blažek J. (2000), On the Accurate and Efficient Discretisation of the Navier-Stokes Equations on Mixed Grids, *AIAA J.*, **38** (11), 2094–2102

Lund T.S. (1997), On the Use of Discrete Filters for Large-Eddy Simulation, *Annual Research Briefs 1997*, Center for Turbulence Research, Stanford University, 83–95

Marsden A., Vasilyev O.V., and Moin P. (2000), Construction of Commutative Filters for LES on Unstructured Meshes, *Annual Research Briefs 2000*, Center for Turbulence Research, Stanford University, 179–182

Vasilyev O.V., Lund T.S., and Moin P. (1998), A General Class of Commutative Filters for LES in Complex Geometries, *J. Comp. Phys.*, **146**, 82–104

PERFORMANCE OF SUBGRID FLAMELET MODEL IN LES OF REACTING, TURBULENT FLOWS

XIAODAN CAI AND FOLUSO LADEINDE
Aerospace Research Corporation, L.I.
P.O. Box 1527
Stony Brook, NY 11790-0609

Abstract. Large eddy simulation (LES) with a flamelet-based chemistry model has been evaluated through *a priori* and *a posteriori* tests in both decaying homogeneous turbulence and spatially-developing mixing layers. The present flamelet-LES approach involves a series of models, among which are the models for the PDF of mixture-fraction ($f(z)$) and the conditional filtered dissipation rate ($\widetilde{\chi}_{st}$). We test three models for $f(z)$: a) $\delta-$PDF ($f(z) = \delta\left(\widetilde{Z}\right)$), b) $\beta-$PDF, c) Gaussian PDF; and two models for $\widetilde{\chi}_{st}$. The Gaussian PDF model consistently performs almost as well as the $\beta-$PDF, and may provide an alternative approach to the $\beta-$PDF method. This point is important to the LES simulations since the calculation of Gaussian function is much cheaper than that of $\beta-$function. Furthermore, it may be said from the error analyses that the counterflow model for $\widetilde{\chi}_{st}$ has average performance in its present form and that a phenomenological model in the form of Eq. (6) exists with an optimum value of a parameter C_3 to produce a better result. The *a posteriori analysis* shows a satisfactory performance of the flamelet model within the context presented in this paper.

1. Introduction

Large eddy simulation (LES) constitutes an attractive approach for numerical simulation of turbulent reacting flows. The basic idea of LES is to calculate the large-scale energy-containing eddies and use a subgrid model for the small scales. The large-scale structures resolved by LES are effective entrainers and play a role in bringing various reactive gas pockets into contact before the reactants are mixed by molecular diffusion, prior to reaction. Hence, the entrainment rates induced by the large-scale structures will

determine the overall reaction rates in a turbulent reacting flow, and are sometimes crucial to the understanding of flame behavior, especially when combustion instabilities occur[1]. LES is thus regarded as a favorable tool in combustion applications, better than the traditional Reynolds-Averaged Navier-Stokes (RANS) turbulent models which are limited to the description of the mean flow field.

However, relatively few studies have addressed LES of reacting flows. Modeling subgrid combustion activities encounters great challenges. Unlike the aerodynamic problem, the use of the similarity assumption for the small-scale mixing and dissipation processes in reactions leads to unresolved terms which are related to the heat release. In addition, a more serious problem for LES combustion models is that the chemical reactions almost always take place within the unresolved subgrid scales. For example, an approximate model neglecting subgrid scale contributions, i.e., writing the reaction rates as an Arrhenius law in terms of the filtered quantities, significantly misrepresents the combustion dynamics[2]. The modeling tasks are then as challenging as in RANS applications.

The current practice in modeling the subgrid combustion activities generally follows the concepts and the techniques once developed for RANS applications. They include the direct methods, such as the extended version of the Eddy-Break-Up model[2], the Linear-Eddy model[3], the Transported Probability Density Function (TPDF) method[4] and the Conserved Scalar method, such as the flamelet approach[5]. Some new models based on the similarity concept have also been suggested[6]. Until recently, the focus was on *a priori* testing of the applicability of combustion models in LES[7]; the evaluation of the models by *a posteriori* testing is not as common, except in the studies of Menon and his co-workers[8] and Pitsch and Steiner[9].

The basic procedure for the flamelet-LES model used in the present paper is contained in Cook and Riley[7]. However, the present paper uses this technique within the framework of a generalized curvilinear coordinate system to permit the calculation of turbulent combustion in realistic systems which usually have complex geometries. The main contribution of the present paper is in the investigation of the various model assumptions used for the calculation of the mixture-fraction dissipation rate and its PDF. Both the *a priori* and *a posteriori* testing through direct numerical simulation (DNS) and LES of turbulent non-premixed flames are reported.

2. Subgrid Flamelet Models

The generalized curvilinear coordinate formulation for the large-eddy simulation follows Jordan[11], where the full Navier-Stokes equations are transformed prior to filtering. The filtered reaction rate is approximated by the

laminar flamelet model. That is, in the unresolved subgrid scales, combustion takes place in a thin layer in the vicinity of the surface of stoichiometric mixture fraction where its local gradient is sufficiently high. Therefore, the combustion in a turbulent flow is represented by a statistical ensemble of such laminar flamelets. At each grid point, the filtered reaction rate is therefore modeled as

$$\overline{\dot{\omega}_i}(\mathbf{x}) = \iint \dot{\omega}_i(Da, Ze, Ce, P_0, Y_{i1}, Y_{i2}, T_1, T_2; Z, \chi_s) \cdot f(Z, \chi_s; \mathbf{x})\, dZ d\chi_s. \tag{1a}$$

The mass fraction is also modeled in a similar fashion:

$$\overline{Y_i}(\mathbf{x}) = \iint Y_i(Da, Ze, Ce, P_0, Y_{i1}, Y_{i2}, T_1, T_2; Z, \chi_s) \cdot f(Z, \chi_s; \mathbf{x})\, dZ d\chi_s. \tag{1b}$$

In the above equations, $\dot{\omega}_i$ and Y_i are the reaction rates and species mass fractions obtained from the steady-state laminar flamelet calculations[5]. The input to the flamelet calculations includes the free-stream values of species concentrations (Y_{i1}, Y_{i2}) and temperatures (T_1, T_2), and the stoichiometric dissipation rates, which have to be modeled from the LES calculations. The normalized parameters Da, Ze and Ce are, respectively, the Damkhōler number, Zeldovich number, and the Heat Release parameter.

The joint probability density function of the mixture fraction and its dissipation rate, $f(Z, \chi_s)$, contains the statistical information on the flamelets in a turbulent flow. Statistical independence is assumed for the mixture fraction (Z) and its scalar dissipation rate (χ_s):

$$f(Z, \chi_s; \mathbf{x}) = f(Z; \mathbf{x}) \cdot f(\chi_s; \mathbf{x}).$$

As most reactions occur around the flame sheet, which is close to the stoichiometric surface in a statistical sense, it is reasonable to assume that

$$f(\chi_s; \mathbf{x}) = \delta(\widetilde{\chi}_{\mathbf{st}}), \tag{2}$$

and $f(Z; \mathbf{x})$ is usually modeled by the $\beta-$form PDF:

$$f(Z; \mathbf{x}) = \frac{Z^{a-1}(1-Z)^{b-1}}{B(a,b)}, \tag{3}$$

where $a = \widetilde{Z} \cdot \left[\frac{\widetilde{Z}(1-\widetilde{Z})}{<Z''^2>} - 1\right]$, $b = a(\frac{1}{\widetilde{Z}} - 1)$, and $B(a,b) = \frac{\Gamma(a+b)}{\Gamma(a)+\Gamma(b)}$. This paper compares the performance of $\beta-$form PDF model with that of a Gaussian PDF:

$$f(Z; \mathbf{x}) = \left(\frac{1}{2\pi < Z''^2 >}\right)^{1/2} \exp\left(-\frac{\left(Z - \widetilde{Z}\right)^2}{2 < Z''^2 >}\right). \tag{4}$$

Similarity assumption[7] has been used to model the filtered mixture fraction variance and dissipation rate for the *a posteriori* test which, respectively, are

$$\widetilde{Z''^2} = \widetilde{Z^2} - \tilde{Z}^2 \simeq C_1 \left[\widehat{(\tilde{Z})^2} - \left(\hat{\tilde{Z}} \right)^2 \right],$$

and

$$\tilde{\chi} \simeq C_2 \cdot D \frac{\partial \tilde{Z}}{\partial x_i} \frac{\partial \tilde{Z}}{\partial x_i}.$$

The symbol "$\hat{}$" implies test-level filtering. The constants $C_1 \simeq 1.3$ and $C_2 \simeq 1.1$ have been chosen from direct numerical simulations that were carried out as part of the present study. For the *a priori* test, they are obtained directly from the DNS data. Cook and Riley[7] proposed the use of the counterflow assumption to close the conditional filtered dissipation rate ($\tilde{\chi}_{st}$) with the above filtered dissipation rate, i.e.,

$$\tilde{\chi}_{st} \simeq \tilde{\chi} \frac{\exp\left\{-2\left[erfc^{-1}\left(2Z_{st}\right)\right]^2\right\}}{\int_0^1 \exp\left\{-2\left[erfc^{-1}\left(2Z\right)\right]^2\right\} f(Z) dZ}. \tag{5}$$

However, it is argued that the counterflow structure is rarely found in realistic turbulent reacting flows. For example, recent DNS of turbulent, reacting mixing layers[22] found that the chemical reaction occurs typically in a shear-type stretching mode instead of a counterflow structure, even though the concept of laminar flamelets was still applicable in this case. A mapping-closure approach has been attempted by the current authors[23] to replace the counterflow model. However, little improvement has been found. One phenomenological model that has been used in RANS modeling is evaluated in this paper but within the framework of the flamelet-LES procedure being reported on. The phenomenological model takes the form

$$\tilde{\chi}_{st} \simeq C_3 \tilde{\chi}. \tag{6}$$

3. Numerical Procedures

Both DNS and LES are performed to evaluate the subgrid models through *a priori* and *a posteriori* testings. The numerical methods employed to solve the DNS/LES equations are the compact schemes for the spatial derivatives and the classical fourth-order Runge-Kutta scheme for the time integration. This is combined with a high-order filtering procedure[10] in order to suppress numerical instabilities arising from the unsolved scales, mesh non-uniformities and boundary conditions. It must be noted that this filtering

operation has a much weaker attenuation effect on the Fourier amplitudes of ϕ_i than the LES filters so that this effect won't mask the the effect of the LES filter. The LES filter scheme uses the Simpson's averaging scheme. To account for the boundary effects, the Navier-Stokes Characteristic Boundary Condition (NSCBC)[14] is extended to the generalized curvilinear coordinate system in the present work. The steady flamelet equations are solved by the Newton-Raphson method, as described in Ladeinde *et al*[15].

A single-step, irreversible chemical reaction of the type

$$F + rO \longrightarrow (r+1)\,P, \tag{7}$$

is used, where r represents the mass stoichiometric ratio of oxidizer to fuel, and is related to the stochiometric value of mixture-fraction by $Z_{st} = [1 + r \cdot Y_{F,1}/Y_O]^{-1}$. For methane/air combustion, which is represented by Case 2, $r = 4$ and $Z_{st} = 0.055$. The reaction rate assumes the form

$$\dot{\omega}_r = \rho^2 \cdot Da \cdot Y_1 Y_2 \cdot \exp\left(-\frac{Ze}{T}\right).$$

The two-dimensional calculations in this work are able to capture the essential features of the reaction mechanism. The test cases are listed in Table 1. Case 1 and Case 2 involve decaying homogeneous turbulence with initial Reynolds number of $Re_0 = 250$. The initial field for Z is random with a pseudo double-delta probability distribution[17]. The initial fields for the mass fractions of the reacting species are then generated from Z assuming the fast-limit reaction. The smallest turbulent scales under the Reynolds number of 250 are fully resolved by the DNS grids for Case 1 and Case 2. Case 3 involves a spatially-developing mixing layer with an inflow Reynolds number of 720 (based on vorticity thickness). The convective Mach number is 0.125 with a ratio of slow- to fast-stream velocity 0.5. Both the initial velocity field and the initial mixture-fraction field use the hyperbolic tangent profile, and the initial mass fraction fields for the reacting species are generated from Z, assuming the fast-limit reaction distribution. The inflow conditions are generated by superposition of small perturbations on the mean field. To facilitate the formation of roll-up structures, the perturbations are generated from the fundamental modes ($\omega_0 = 1.3198$) obtained from linear-stability analysis[24]. The DNS grids for Case 3 have a resolution of 25η (η is the Kolmogorov length scale), which seems fine enough for the mixing layer turbulent flows[20] when the large-scale structures dominate the flow behaviors. LES was carried out for Case 1 and Case 3 but not for Case 2. However, Case 2 was used in the evaluation of the flamelet model (Figure 1).

Table 1. Test Cases.

Test	Flow Type	Z_{st}	Da	Ze	Ce	DNS Grid	LES Grid
Case 1	Homogeneous	0.5	10	0	0	133×133	35×35
Case 2	Homogeneous	0.055	10	0	0	133×133	N/A
Case 3	Mixing Layer	0.5	10	5	1.0	375×99	186×49

4. Evaluation of Models

Flamelet Calculation: Prior to the *a priori* and *a posteriori* analyses of model performance, flamelet calculations are carried out to obtain the values of $\dot{\omega}_i$ and Y_i for the integrals in Eq. (1). The calculations are performed in the mixture-fraction space[15]. Note that the parameters Da, Ze and Ce, are required for the flamelet calculations. The values of $\dot{\omega}_i$ and Y_i from the flamelet calculation are then constructed in the form of a look-up table (indexed by $\widetilde{Z}, < Z''^2 >, \tilde{\chi}$) to facilitate the LES calculations. Figure 1 shows the product mass fraction results from the flamelet calculations for Case 1 and Case 2. The effects of conditional scalar dissipation rate on species distribution appear to be significant for the chemistry model in Eq. (7), especially around the stoichiometric values of the mixture-fraction. This result implies that the scalar dissipation rate model has significant effects on the filtered reaction rates and filtered mass fractions of product around their maximum values, which occur close to the stoichiometric value in mixture fraction space. However, it is noted that the same chemistry model has been used by DesJardin and Frankel[6] but with the erroneous assumption that the concentrations of the species were independent of the scalar dissipation rate.

a priori analysis: Data sets from the DNS for the three cases are used to evaluate the accuracy of the flamelet models. To proceed with the analysis, the DNS data is filtered by the Simpson's scheme onto coarse grid-points ($\Delta_{DNS} = C \cdot \Delta_c$, where Δ_{DNS} is DNS grid-spacing and Δ_c is the coarse-grid spacing). The "exact" values for $\overline{Y_p}$, $\overline{\dot{\omega}_f}$, $\widetilde{Z}$, $\widetilde{Z''^2}$ and $\tilde{\chi}$ are used to represent their corresponding filtered quantities on the coarse grid point. The last three quantities are then used to obtain the model values for $\overline{Y_p}$ and $\overline{\dot{\omega}_f}$ using the flamelet model described above. Since the grid-coarsening factor, C, determines the number of sampled DNS points in each LES grid point, it may affect the statistical properties of the embedded flamelets. Therefore, we test two levels of this parameter: $C = 2$ and $C = 4$.

Figure 2 shows the contour maps of product mass-fraction obtained from DNS for Case 1 (eddy-turn-over time of 4.0, Figure 2(a)) and Case 3

(evolution time of 208, Figure 2(b)). The contour maps evidently show that the fine flow-structures are suitably resolved, and therefore can be used to evaluate the flamelet chemistry model.

It is noted that the present flamelet-LES approach involves a series of models, among which are the models for the PDF of mixture-fraction ($f(z)$) and the conditional filtered dissipation rate ($\widetilde{\chi}_{st}$). We test three models for $f(z)$: a) $\delta-$PDF ($f(z) = \delta\left(\widetilde{Z}\right)$, b) $\beta-$PDF (Eq. 3), c) Gaussian PDF (Eq. 4); and two models for $\widetilde{\chi}_{st}$ (Eq. 5 and Eq. 6). The errors from these models have been evaluated by two criteria, $\sum \frac{(X_{model}-X_{exact})^2}{X^2_{exact}}$ and $\sum \frac{(X_{model}-X_{exact})^2}{(X^2_{exact})_{\max}}$, where X represents $\overline{Y_p}$ or $\overline{\dot{\omega}_f}$. As Criterium 2 puts more weight on the large values, it is considered to be more suitable for evaluating the model performance in the sense that the model has more significant effects on the behaviors of $\overline{Y_p}$ and $\overline{\dot{\omega}_f}$ around their maximum values, which are discussed at the beginning of this section. Figures 3(a), 3(b), and 3(c) present the model errors for $\overline{\dot{\omega}_f}$ for Cases 1, 2 and 3, respectively, with grid-coarsening factor $C = 2$. Figure 3(d) shows the model errors for $\overline{\dot{\omega}_f}$ with $C = 4$ (Case 1). The values of C_3 for the counterflow model in the figures represent an averaged quantity over the whole domain since the counterflow model for $\widetilde{\chi}_{st}$ produces a local C_3 value at each grid point. From these figures we see that the errors for the Gaussian PDF model and the $\beta-$PDF are much smaller than those for $\delta-$PDF. The improvement in the Gaussian PDF and $\beta-$PDF prediction increases with increasing values of C. Since the use of $\delta-$PDF implies that there is no local PDF model for the mixture fraction on each LES grid point, the improvement in the Gaussian PDF and $\beta-$PDF predictions suggests that the use of some subgrid PDF models, even though simple, will be very helpful in LES calculations, a point consistent with the results obtained by Jimenez *et al.*[21] It is also observed that the Gaussian PDF model consistently performs almost as well as the $\beta-$PDF, although the latter is used more often in the literature. The results here suggest that the use of the Gaussian PDF is equally acceptable. This point is important since the Gaussian function is much cheaper to calculate than the β function. Furthermore, it can be seen from Figure 3 that the $\widetilde{\chi}_{st}$ model also has a strong effect in comparison to the Gaussian and $\beta-$PDF models. The graphs clearly show that an optimal C_3 value exists for each case. It may be said that the performance of the counterflow model is modest in comparison to the performance of the phenomenological models in Eq. (6). This point is strengthened by Figure 4, which shows the correlation between the exact and modeled values of $\overline{\dot{\omega}_f}$ in the form of scatter plots for the three cases. Here, the results from the counterflow model for $\widetilde{\chi}_{st}$ are compared with those from Eq. (6) using the optimal value of coefficient C_3.

a posteriori analysis: The *a posteriori* tests are considered to be the

ultimate tests of model performance in the sense that the model is evaluated only after it has been implemented in the large-eddy simulation. Figure 5(a) shows the correlation between the DNS and LES values of $\overline{Y_p}$ (Case 1) in the form of scatter plots. It appears from this figure that the LES-flamelet procedure, along with the assumptions in Eq. (3) and Eq. (6), is capable of generating accurate results. Further evidence comes from a comparison of the growth rates of momentum thickness θ in the DNS and the LES-flamelet calculations for the spatially-developing mixing layers (Figure 5(b)). The LES-flamelet model gives better results compared to those without the model. However, owing to the combined effects of numerical discretization in space and time, and averaging[13], *a posteriori* tests of the mixing layer flows do show some scatter for the correlation between the DNS and LES values of $\overline{Y_p}$.

5. Conclusions

We have shown satisfatory performance of a flamelet-LES procedure for decaying homogeneous turbulence and the spatially-developing mixing layer. The chemical reaction used in the tests has a moderate Damkhöler number and a reasonable Zeldovich number but with weak heat release. The laminar-flame structures of the chemical reactions are strongly dependent on the conditional scalar dissipation-rate and are thus very sensitive to the model for this quantity.

We use the *a priori analysis* to compare the model values of $\overline{Y_p}$ and $\overline{\dot{\omega}_f}$ with their corresponding "exact" values from DNS data sets. The error analyses prove that the use of some subgrid models for the PDF of mixture-fraction, even though simple, yields accurate LES calculations, which is consistent with the observations of Jimenez *et al.*[21] We also see in this study that the Gaussian PDF model consistently shows a comparable performance to the more common β−PDF, and may provide an alternative approach. This point is important because the Gaussian function is much cheaper to calculate than the β function. Furthermore, it may be said from the error analysis that the counterflow model shows only a moderate performance

The *a posteriori analysis* confirms the observation that the performance of the flamelet-LES procedure consistent with the model assumptions in this paper appears to be satisfactory. However, owing to the combined effects of numerical discretization in space and time, and averaging, *a posteriori* tests of the mixing layer flows show some scatter for the correlation between the DNS and LES values of $\overline{Y_p}$.

References

1. 1. McManus, K.R., Poinsot, T. and Candel, S., *Progress in Energy and Combustion Science*, Vol. 19, p.1-29 (1993).
2. 2. Candel, S., Thevenin, D., Darabiha, N., and Veynante, D., *Combust. Sci. and Tech.*, Vol.149, pp. 297-337 (1999)
3. 3. Kerstein, A.R., *Combust. Sci. and Tech.*, Vol.60, pp.391 (1988)
4. 4. Gao, F. and O'Brien, E. E., *Phys. Fluids* A, 5, pp. 1282-1284, (1993)
5. 5. Peters, N., *Prog. Energy Combust. Sci.*, Vol. **10,** p. 319-339 (1984).
6. 6. DesJardin, P.E. and Frankel, S.H., *Phys. Fluids* Vol. 10(9), pp.2298-2314 (1999).
7. 7. Cook, A. W. and Riley, J. J. *Combustion and Flame* 112:593, (1998).
8. 8. Chakravarthy, V.K. and Menon, S. In "Recent Advances in DNS and LES", (D. Knight and L. Sakell, Eds.), Kluwer Academic Publishers, pp. 85-98 (1999).
9. 9. Pitsch, H. and Steiner, H., *Phys. Fluids* Vol. 12(10), pp.2541-2554 (2000).
10. 10. Visbal, M.R. and Gaitonde, D.V., AIAA Paper 98-0131, January 199108.
11. 11. Jordan, S.A., *J. Comp. Phys.* Vol.148, pp.322-40 (1999).
12. 12. Janicka, J. and Peters, N., *19th Symposium (international) on Combustion*, the Combustion Institute, Pittsburg, pp. 367-374 (1982).
13. 13. Meneveau, C. and Katz, J., *Annu. Rev. Fluid Mech.* 32:1-32 (2000).
14. 14. Poinsot, T.J. and Lele, S.K., *J. Comp. Phys.* **101**, pp.104-129 (1992).
15. 15. Ladeinde, F., Cai, X. and Sekar, B. paper 2000-GT-144, IGTI Congress and Exhibition, Munich, Germany (2000).
16. 16. Ladeinde, F., O'Brien, E.E., Cai, X., Liu, W., *Phys. Fluids* **8** (11) (1995) 2848-2857.
17. 17. Mell, W.E., Nilsen, V., Kosaly, G. and Riley, J.J., *Phys. Fluids* **6** (3) (1994), 1331-1356.
18. 18. Piomelli U, Moin P, and Ferziger JH, *Phys. Fluids* **31** (A) (1988), 1884-1891.
19. 19. Ribault, C.L., Sarkar, S. and Stanley, S.A., *Phys. Fluids* **11** (10) (1999) 3069-3083.
20. 20. Freund, J.B., Moin, P. and Lele, S., Department of Mechanical Engineering, Stanford University, Report No. TF-72.
21. 21. Jimenez, J., Linan, A., Rogers, M. and Higuera, F., *J. Fluid Mech.* (1997), vol.349, pp.149-171.
22. 22. Miller, R.S., Madnia, C.K. and Givi, P. "Structure of a turbulent reacting mixing layer," Comb. Sci. and Tech. (1994) Vol. 99(3), 1.
23. 23. Cai, X.D., Ladeinde, F. and Sekar, B. "Some issues in the use of laminar flamelet model in LES", Bulletin of the American Physics Society, Vol. 44 (8), P.45, 1999.
24. 24. Michalke, A., "On the invisid instability of the hyperbolic-tangent velocity profile", *J. Fluid Mech.* **19**, 543-56 (1964).

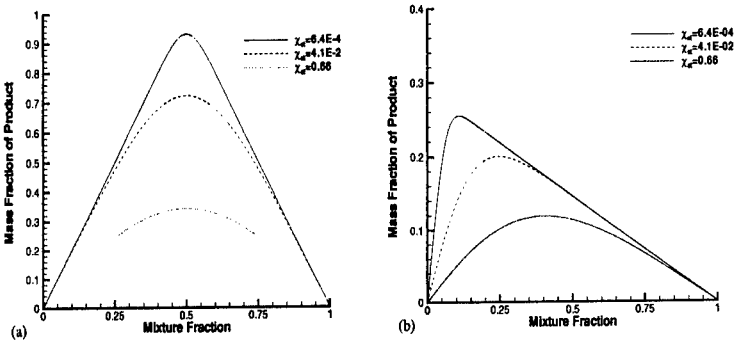


Figure 1. Flamelet results for Case 1 (a) and Case 2 (b), showing the effects of different values of χ_{st}

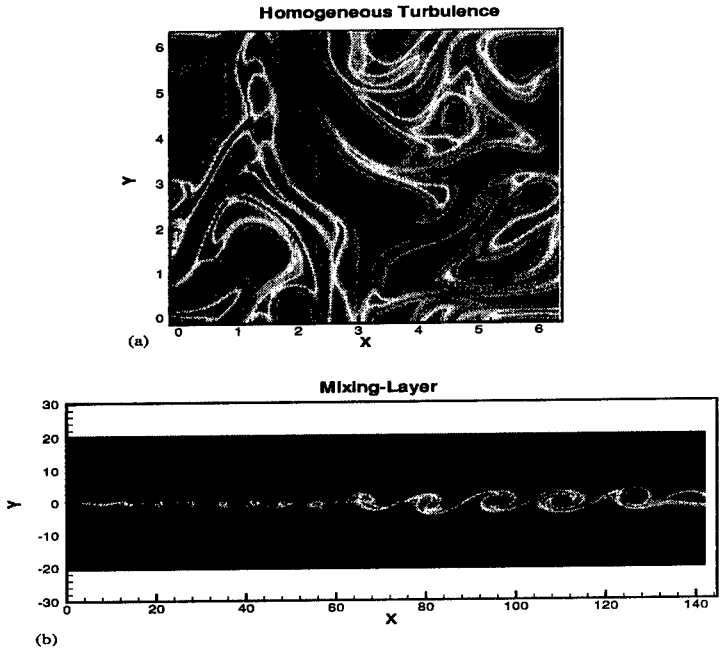


Figure 2. Contour maps of product mass-fraction at time of: a) $t = 4.0$ (Case 1); b) $t = 208$ (Case 3).

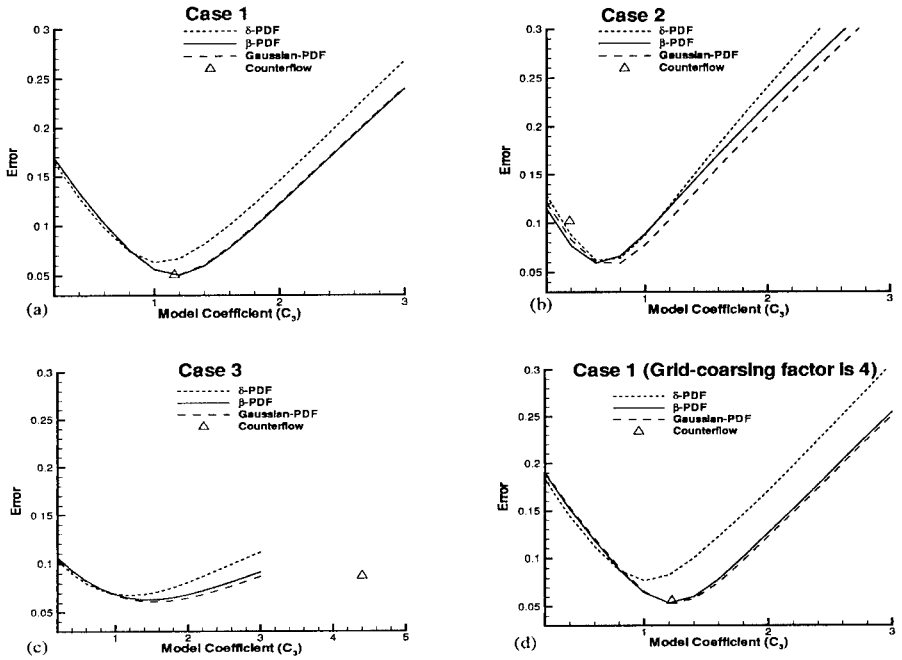


Figure 3. The effect of Coefficient C_3 on the model errors of $\overline{\dot{\omega}_f}$ for the three cases ((a)-(c)), with $C = 2$. The error plot in Figure 3(d) is for Case 1 with $C = 4$.

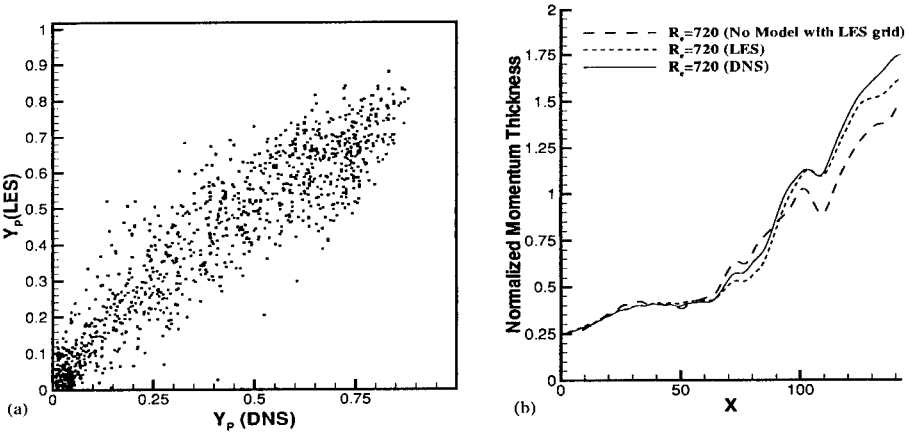


Figure 5. *a posteriori* tests of model performance: a) the correlation between DNS and LES values of $\overline{Y_p}$ in the form of scatter plots for Case I; b) comparison of the growth rates of the momentum thickness θ from DNS and flamelet-LES calculations.

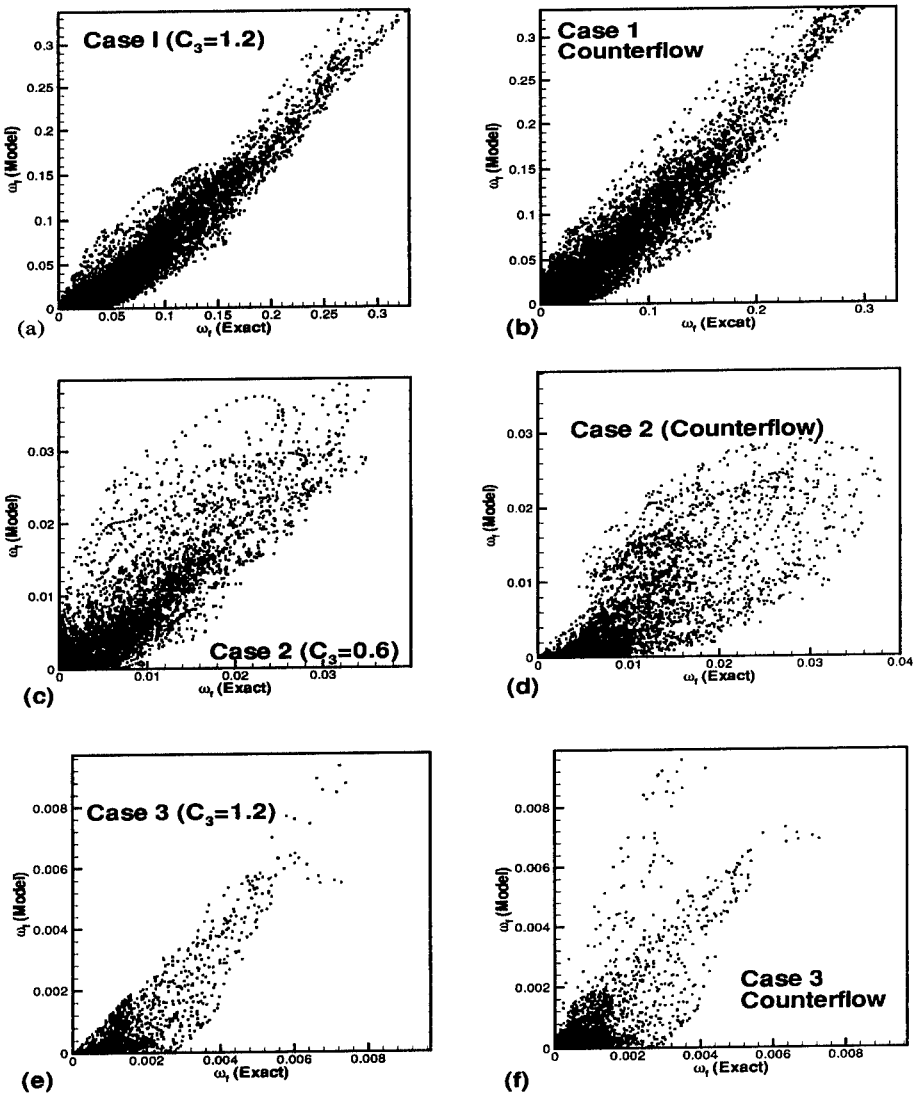


Figure 4. The correlation between the exact and modeled values of $\overline{\dot{\omega}_f}$ in the form of scatter plots. Figure 4(a), (c), and (e) use Eq. (6) with the values of C_3 as shown while Figure 4(b), (d), and (f) use the Counterflow model for $\widetilde{\chi}_{st}$.

A DYNAMIC PROCEDURE FOR CALCULATING THE TURBULENT KINETIC ENERGY

B. KNAEPEN, O. DEBLIQUY AND D. CARATI
Universté Libre de Bruxelles, Boulevard du Triomphe, Campus Plaine - CP.231, 1050 Brussels, Belgium

Abstract. We propose a dynamic model based on the Germano identities to evaluate the subgrid scale energy $<\overline{k}>$ in LES as a function of the large scale velocity field only. Contrary to traditional transport equation for $\overline{k}$, this model does not require any additional equation and provide a very simple first approximation for $\overline{k}$.

1. Introduction

The aim of LES is to make predictions about turbulent flows which are not accessible by DNS. Therefore, it is important to establish correspondence rules between the physical quantities predicted by LES and their actual measured values. These correspondence rules are also useful when assessing the performance of LES subgrid models through the comparison with resolved DNS, although in that context it may be possible to filter the DNS fields down to the LES scales to produce the desired comparison.

A detailed discussion of how to establish these correspondence rules can be found in (Winckelmans *et al*, 2001). Here we focus our attention to one of most fundamental one: the relation between the total energy (density) of the turbulent fluid and the resolved LES energy density. It can be written as,

$$E = E_R + E_{sgs}, \tag{1}$$

where E denotes the total energy, E_R the resolved LES energy and E_{sgs} is the subgrid-scale energy. This last quantity is traditionally not available in LES and thus needs to be reconstructed to evaluate the total energy density from the LES energy density. As shown in (Winckelmans *et al*, 2001), E_{sgs} is also required to reconstruct the full Reynolds stress tensor.

In order to calculate E_{sgs}, a transport equation can be introduced. Although quite effective (Debliquy *et al*, 2001), this method has however two side effects. First, to close the transport equation in terms of filtered quantities, one needs further modelling efforts. Second, the resolution of the extra equation increases the computation requirements.

In this paper, we propose a different approach and show how an estimate of the subgrid scale energy E_{sgs} can be obtained using the Germano identities and a model for the energy spectrum. We also produce some numerical results to illustrate the method.

2. Modelling the turbulent kinetic energy

For an incompressible, Boussinesq flow, the Navier-Stokes equations for the LES field $\overline{u}_i$ read,

$$\partial_t \overline{u}_i + \partial_j(\overline{\overline{u}_j \overline{u}_i}) = -\partial_i \overline{p} + \nu \triangle \overline{u}_i - \partial_j \overline{\tau}_{ij}. \tag{2}$$

One of the essential difficulty of LES consist in modelling the unknown subgrid-scale stress tensor $\overline{\tau}_{ij} \equiv \overline{u_i u_j} - \overline{\overline{u}_i \overline{u}_j}$ which appears in the filtered Navier-Stokes equations. Note that since our numerical code is fully dealiased we have, for consistency, expressed (2) only in terms of filtered quantities, including $\overline{\tau}_{ij}$.

Like any second-order symmetric tensor, $\overline{\tau}_{ij}$ may be decomposed into an isotropic part and a trace-free part:

$$\overline{\tau}_{ij} = \frac{2}{3}\overline{k}\delta_{ij} + \overline{\tau}^*_{ij}, \tag{3}$$

where $\overline{\tau}^*_{ij} = \overline{\tau}_{ij} - \frac{1}{3}\overline{\tau}_{rr}\delta_{ij}$ and

$$\overline{k} = \frac{1}{2}\overline{\tau}_{rr} \tag{4}$$

$$= \frac{1}{2}(\overline{u_i u_i} - \overline{\overline{u}_i \overline{u}_i}). \tag{5}$$

Traditionally, $\overline{k}$ is known in the literature as the turbulent kinetic energy. However, this name might be misleading and one must be careful about the interpretation of $\overline{k}$. To be more precise, let us denote by u_i the non-filtered velocity and by u'_i the subgrid scale part of u_i. We then have $u_i = \overline{u}_i + u'_i$ and we can define three *local* energy densities: 1) $e = \frac{1}{2}u_i u_i$; 2) $e_R = \frac{1}{2}\overline{u}_i \overline{u}_i$; 3) $e_{sgs} = \frac{1}{2}u'_i u'_i$. At this stage, it might be tempting to identify the turbulent kinetic energy $\overline{k}$ with $\overline{e}_{sgs}$. However, only their space average are identical. Indeed, locally we have:

$$\overline{k} = \overline{e}_{sgs} + \overline{\overline{u}_i u'_i}. \tag{6}$$

Therefore, $\overline{k}$ does not represent the *local* contribution of the small scales to the energy budget. To add to this, we also recall that $\overline{k}$ is in general not even positive definite for arbitrary grid filters (e.g. projectors).

Usually, modelling $\overline{k}$ is not an issue in the case of incompressible LES since one can define a modified pressure, $\overline{p}' = \overline{p} + \frac{2}{3}\overline{k}$ which is obtained by enforcing the continuity condition $\partial_i \overline{u}_i = 0$. However, this does not apply to the compressible case and as we exposed in the introduction, the knowledge of $< \overline{k} >$ might be very useful for real flow predictions and comparison with DNS.

To proceed, we follow the steps of (Germano *et al*, 1991) and introduce a second coarser filter called the test-filter which we denote by $\cdot\hat{\cdot}\cdot$. In the sequel all the filters considered will be sharp Fourier cut-offs. Therefore, the "grid+test" filter, denoted $\widetilde{\cdots}$ is equivalent to the test-filter: $\widetilde{\cdots} = \widehat{\overline{\cdots}} = \overline{\widehat{\cdots}}$ The filtered velocity $\widetilde{u}_i$ then satisfies the following equation:

$$\partial_t \widetilde{u}_i + \partial_j(\widetilde{\widetilde{u}_i \widetilde{u}_j}) = -\partial_i \widetilde{p} + \nu \triangle \widetilde{u}_i - \partial_j \widetilde{T}_{ij}, \tag{7}$$

where $\widetilde{T}_{ij} \equiv \widetilde{u_i u_j} - \widetilde{\widetilde{u}_i \widetilde{u}_j}$ is the subgrid-scale stress tensor at the combined grid+test filter level. The Germano identity states that $\widetilde{T}_{ij}$ and $\widetilde{\tau}_{ij}$ are related by,

$$\widetilde{L}_{ij} = \widetilde{T}_{ij} - \widetilde{\tau}_{ij}, \tag{8}$$

where,

$$\widetilde{L}_{ij} = \widetilde{\overline{u}_i \overline{u}_j} - \widetilde{\widetilde{u}_i \widetilde{u}_j}, \tag{9}$$

is the Leonard tensor.

For any quantity we have the following property,

$$< F > = < \overline{F} > = < \widetilde{F} >, \tag{10}$$

where the bracket $< \cdots >$ denotes space average: $< F > = \frac{1}{V} \int d^3x F(x)$. Indeed, for any filter $G(y)$ ($\overline{\cdots}$) we have $\int d^3y G(y) = 1$ so that:

$$< \overline{F} > = \frac{1}{V} \int d^3x \overline{F}(x) \tag{11}$$

$$= \frac{1}{V} \int d^3x \int d^3y G(x-y) F(y) \tag{12}$$

$$= \frac{1}{V} \int d^3y F(y) \int d^3z G(z) \tag{13}$$

$$= \frac{1}{V} \int d^3x F(x) = < F > \tag{14}$$

where we have used the change of variable: $z = x - y$.

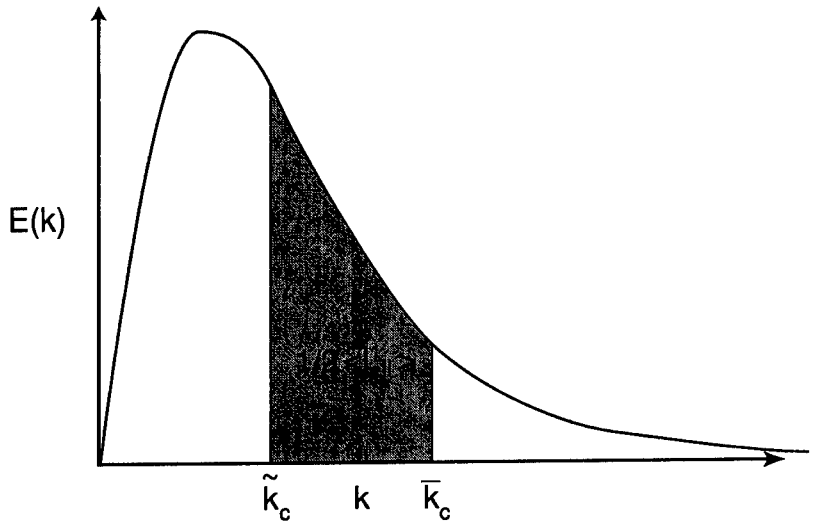


Figure 1. Space average of Leonard tensor. $\overline{k}_c$ and $\widetilde{\overline{k}}_c$ denote respectively the cut-offs at grid and grid-and-test levels.

Using property (10) and the trace of equation (9) we get the relation,

$$< \widetilde{L}_{ii} >=< \overline{u}_i\overline{u}_i > - < \widetilde{u}_i\widetilde{u}_i >, \tag{15}$$

which states that the space average of the Leonard tensor is equal to twice the difference of the energy at grid level and grid+test level. Another way of getting this relation is by taking the trace of (8). Denoting by $\widetilde{K}$ the turbulent kinetic energy density at grid+test level, we obtain, $< \widetilde{L}_{ii} > = 2(< \widetilde{K} > - < \overline{k} >)$, which has of course the same interpretation. Figure 1 illustrates the situation.

The above considerations allow us to write,

$$< L_{ii} >= 2 \int_{\widetilde{k}_c}^{\overline{k}_c} E(k)dk, \tag{16}$$

where $\overline{k}_c$ and $\widetilde{k}_c$ denote respectively the cut-offs at grid and grid+test levels. The energy spectra $E(k)$ is defined so that, $E = \int_0^\infty E(k)dk$.

The next step in the analysis is to introduce a model for the energy spectra. To begin with, let us suppose that $\overline{k}_c$ and $\widetilde{k}_c$ lie in the inertial range which is assumed to be represented by $E(k) = C_K \epsilon^{2/3} k^{-\frac{5}{3}}$ where C_K is the Kolmogorov constant and ϵ is the global dissipation which is usually not known in LES simulations. We propose here to estimate $C_K \epsilon^{\frac{2}{3}}$

by substituting $E(k)$ in (16). After straightforward algebra one gets:

$$C_K \epsilon^{\frac{2}{3}} = \frac{< \widetilde{L}_{ii} >}{3(\widetilde{k_c}^{-\frac{2}{3}} - \overline{k}_c^{-\frac{2}{3}})}. \tag{17}$$

If we now extend the inertial range to infinity (which is the main approximation so far) we finally get a dynamic expression for the mean turbulent kinetic energy:

$$< \overline{k} > = \int_{\overline{k}}^{\infty} E(k)dk \tag{18}$$

$$= \frac{< \widetilde{L}_{ii} >}{2(\frac{\overline{k}_c}{\widetilde{k}_c})^{\frac{2}{3}} - 1} \tag{19}$$

$$= \frac{< \widetilde{L}_{ii} >}{2(\frac{\widetilde{\Delta}}{\overline{\Delta}})^{\frac{2}{3}} - 1}, \tag{20}$$

where $\overline{\Delta}$ and $\widetilde{\Delta}$ denote respectively the width of the grid and grid+test filters. The last equation is written to stress that the model is also suited to the physical formulation approach. Indeed, we only used spectral considerations to establish the model but the final result does not require the spectral formulation. We stress that the expressions (19) and (20) are indeed dynamic since they can be evaluated during the simulation. Usually they do not represent any further computational effort since $\widetilde{L}_{ii}$ is often already required by dynamic eddy-viscosity models.

In the next section we present some results based on our estimate of $< \overline{k} >$.

3. Numerical results

To test model (19), we have build a 256^3 DNS database of isotropic decaying turbulence. The initial condition is build according to Rogallo's prescription (Rogallo, 1981) using the spectra of the Comte-Bellot-Corrsin (Comte-Bellot and Corrsin, 1971) experiment at stage 2. The initial random phases of the velocity fields are correlated by time-stepping 100 times the flow and maintaining the spectra constant.

The initial condition of the DNS has then been filtered down to 32^3 modes and two kind of LES have been performed. The first one is denoted LES/KOL. It is based on an eddy-viscosity model with Kolmogorov scaling: $\overline{\tau}^*_{ij} = -2C\epsilon^{\frac{1}{3}}\overline{\Delta}^{\frac{4}{3}}\overline{S}_{ij}$, where $\overline{S}_{ij} = \frac{1}{2}(\partial_i\overline{u}_j + \partial_j\overline{u}_i)$; the constant C is evaluated using the dynamic procedure. The second LES run is denoted LES/Transport. It is also based an eddy-viscosity model but this time, the

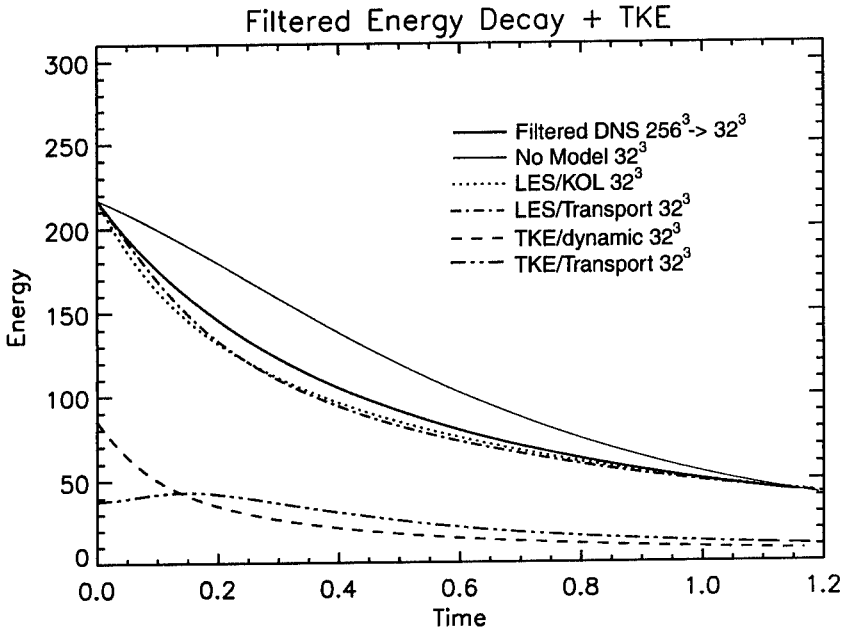


Figure 2. Filtered energy and average turbulent kinetic energy decays.

viscosity is scaled with the turbulent kinetic energy: $\overline{\tau}^*_{ij} = -2C\overline{k}_+^{\frac{1}{2}}\overline{\Delta S}_{ij}$, where the constant C is also evaluated using the dynamic procedure and $k_+ = k$ for $k > 0$ and $k = 0$ otherwise. The essential difference is that here $\overline{k}$ is not evaluated using the diagnostic (19) but is simulated using the transport equation due to Speziale (Speziale, 1991); the details of this LES simulation can be found in (Debliquy *et al*, 2001). For completeness, we have also performed a 32^3 unresolved DNS to emphasize the roles of the LES models.

In Figure 2 we plot 1) the energy decay of the 32^3 modes resolved by the LES ($E_R =< e_R >$ in the terminology described above) for the different models used; 2) the subgrid-scale energies predicted by model (19) (dynamic TKE) and by the turbulent kinetic transport equation (transport TKE). From the graph we observe a good agreement between the filtered DNS and the two LES which produce very similar results for the resolved energy. The importance of the subgrid-scale models is stressed by the "No Model curve". The average turbulent kinetic energies predicted by the two LES models are quite different initially but tend to get closer to each other later.

In Figure 3 we plot the decay of the total energy. For the two LES, the curves correspond to the sum of the resolved energies and the average

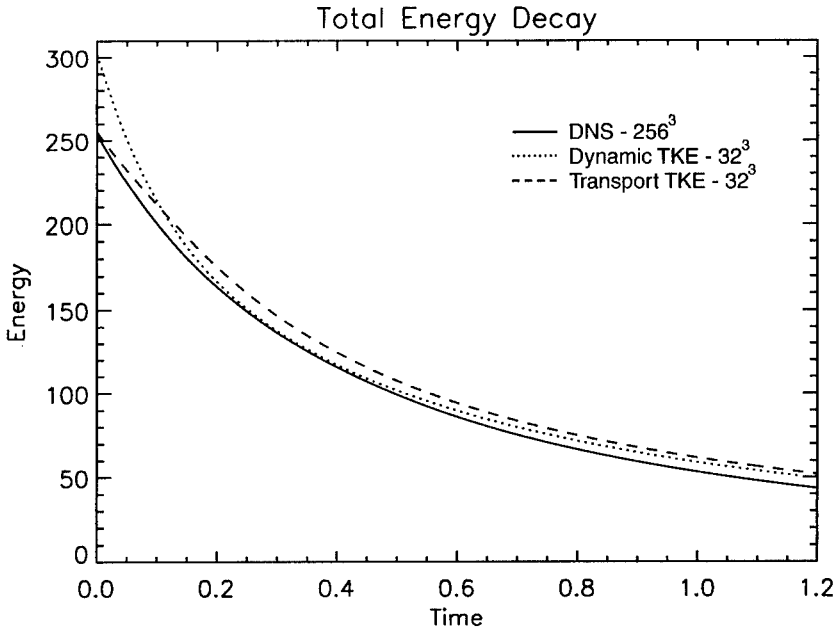


Figure 3. Reconstruction of total DNS energy.

turbulent kinetic energies presented in Figure 2. Initially, model (19) tend to overestimate quite seriously the subgrid scale energy. Later, the behavior is much more satisfactory and even slightly better than than the one of the LES/Transport model. The initial precise match between the DNS and the LES/Transport model is of course natural since the initial condition for $\overline{k}$ is in that case computed from the DNS. The test for model (19) is thus much more severe. The initial overestimate of $\overline{k}$ by model (19) may be due to two causes. The first one is the choice of the model for the energy spectrum. Indeed, the resolution of our DNS does not allow a clear inertial range and extending the later to infinity may be a crude oversimplification. The second source of error might come from the dynamic procedure itself. It has been observed already that this procedure takes some time to settle and predict appropriate values. This is probably due to the fact that a filtered DNS field is badly correlated as an initial condition for an LES. Bearing these in mind, the prediction of model (19) are nevertheless satisfactory and show that the expression for $<\overline{k}>$ is a useful first approximation when no DNS is available, and if we want to avoid an additional transport equation for $\overline{k}$.

4. Summary and conclusion

In this article we have derived a dynamic expression to estimate the subgrid scale energy E_{sgs} of a turbulent flow from the resolved LES scales. The knowledge of E_{sgs} can then be used to reconstruct the complete Reynolds stress and in particular the total energy from the LES field.

We have presented numerical result which indicate that the estimate we propose for E_{sgs} is satisfactory and rivals the performance of a direct evaluation obtained from a transport equation.

References

G. Winckelmans, H. Jeanmart and D. Carati "On the comparison between Reynolds stresses from large-eddy simulation with those from direct numerical simulation" submitted to Phys. Fluids.

O. Debliquy, B. Knaepen and D. Carati "A dynamic subgrid-scale model based on the turbulent kinetic energy" in "Direct and Large-Eddy Simulation Workshop 4" editors, B. Geurts, R. Friedrich and O. Metais, p. 58–61, University of Twente, Enschede, The Netherlands (2001).

M. Germano, U. Piomelli, P. Moin and W. H. Cabot "A dynamic subgrid-scale eddy viscosity model" *Phys. Fluids A* **3**(7), 1760–1765 (1991).

R. Rogallo "Numerical experiments in homogeneous turbulence" NASA technical Memorandum 81315 NASA, Ames Research Center (1981).

G. Comte-Bellot and S. Corrsin "Simple eulerian time correlation of full- and narrow-band velocity signals in grid-generated, 'isotropic' turbulence" *J. Fluid Mech.* **48 part 2**, 273–337 (1971).

C. Speziale "Analytic methods for the development of reynolds-stress closures in turbulence" *Ann. Rev. Fluid Mech.* **23**, 105–157 (1991).

GENERATION OF TURBULENT INFLOW DATA WITH A PRESCRIBED SHEAR-STRESS PROFILE

A. SPILLE-KOHOFF AND H.-J. KALTENBACH

Hermann-Föttinger Institut für Strömungsmechanik
Technische Universität Berlin, Sekretariat HF 1
Straße des 17. Juni 135, D-10631 Berlin, Germany

1. Background and objectives

Simulation of spatially developing turbulent flows using DNS or LES requires specification of unsteady inflow data. Several methods for generating turbulent inflow data for wall-bounded flows have been proposed which introduce a temporal periodicity (e.g. [1, 2, 11, 13]) on a time-scale of $\mathcal{O}(10)\ \delta_{99}/U_\infty$ that can interfere with low–frequency flow dynamics. This might not be an issue in a spatially evolving mixing layer, since it was found by [9] that the temporal correlation introduced by the inflow generation decayed quickly with streamwise distance from the domain inlet. However, in flows involving separation from a smooth surface it has been observed that the periodicity of the inflow signal can trigger the unsteady behavior of the detachment point of a separation bubble [1].

Other inflow generation methods which are based on specification of random numbers at the inlet plane avoid the issue of temporal periodicity [7, 8]. However, they are known to require an extended spatial development region to reach equilibrium and the integral properties of the developing boundary layer are difficult to control with this approach.

Here, we propose a new method which avoids certain drawbacks of the former approaches. The method is based on random numbers and therefore avoids long-range temporal correlations. By introducing body forces in the framework of closed-loop control we are able to (i) accelerate the adjustment process towards equilibrium turbulence and to (ii) precisely control integral properties of the boundary layer.

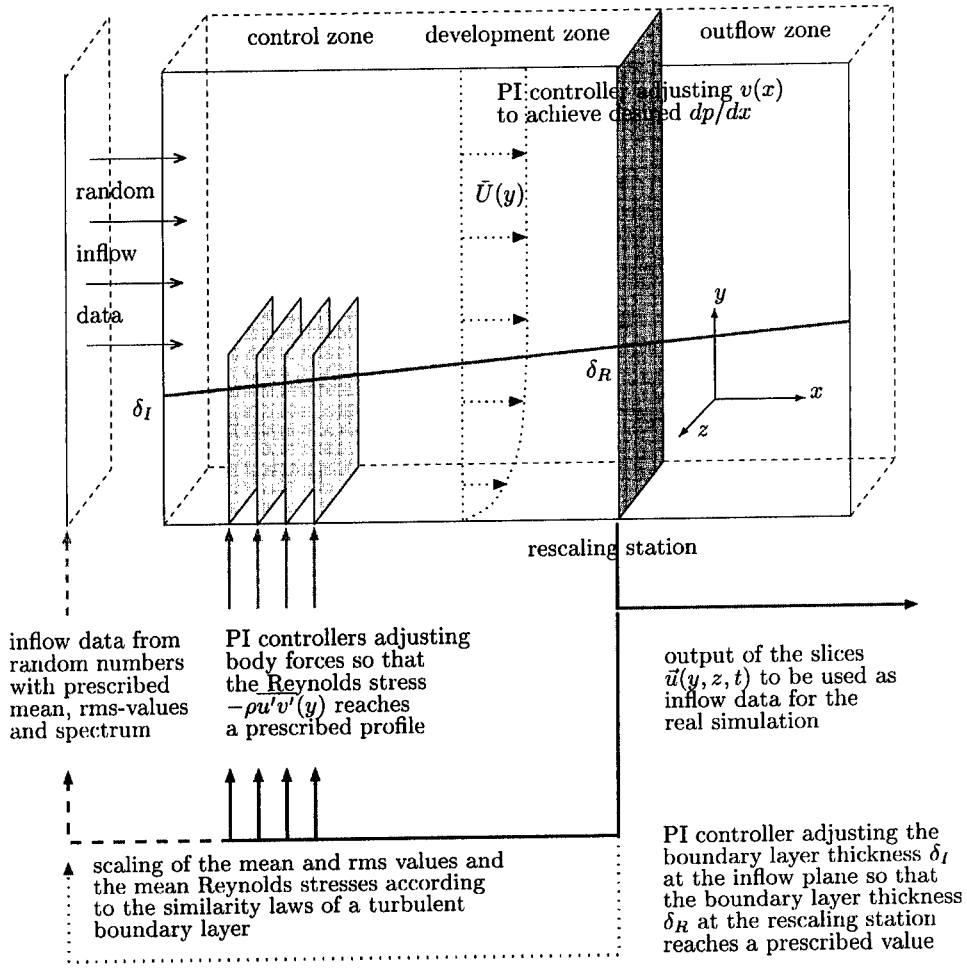


Figure 1. Sketch of the computational domain and outline of individual steps of the method.

2. Method

Similarly to [11], we demonstrate the proposed new inflow generation method for a Navier-Stokes simulation (DNS or LES) of a spatially developing turbulent boundary layer in a rectangular computational domain, see Fig. 1. At the inlet plane, we specify mean flow $U(y), V(y)$ and superimposed fluctuations $u'(y,z,t), v'(y,z,t), w'(y,z,t)$, generated from random Fourier coeffi-

cients similarly to [7]. The amplitudes of the coefficients follow a prescribed spectrum ($k < k_p: \ E(k) \sim k^2$; $k > k_p: \ E(k) \sim k^{-5/3}$) and the profiles of $u'_{rms}(y), v'_{rms}(y), w'_{rms}(y)$ match those obtained after time-averaging and rescaling the instantaneous flow obtained at the "rescaling station", which is located at x_R at the end of the development zone. Since it is impossible to provide *a priori* the correct phase relation between individual Fourier modes, turbulence decays downstream of the inlet plane.

In the control zone the flow is subject to a body force f acting in the wall-normal direction according to

$$\frac{\partial \vec{u}}{\partial t} + (\vec{u} \cdot \vec{\nabla})\, \vec{u} = -\vec{\nabla} p + \frac{1}{Re} \Delta \vec{u} + f \vec{e}_y.$$

The rationale behind this approach is the observation that $-\overline{v'v'}dU/dy$ forms the dominant production term in the balance equation for the shear stress $-\rho\overline{u'v'}$. The body forces act simultaneously in several x,z-planes which are $\mathcal{O}(1)\delta_{99}$ apart in the streamwise direction.

The magnitude of the body force at a streamwise location x_0 is adjusted via a PI–controller with the goal to achieve a prescribed shear-stress profile $g(x_0, y)$. The target shear stress $g(x_0, y)$ is obtained by upstream extrapolation based on a similarity hypothesis using the mean stress $-\rho\overline{u'v'}^{\,z,t}(y)$ at the rescaling station as in Lund's method [11]. Here, $\overline{()}^{\,z,t}$ denotes averaging in the spanwise direction and over $\mathcal{O}(10)\delta_{99}/U_\infty$ in time. The use of a "rescaling" station is not mandatory, since the target profile $g(x_0, y)$ might also come from an experiment or from a RANS calculation – possibly carried out simultaneously with the LES.

The input of the PI controller at the location x_0, the error signal e, is computed as

$$e(y,t) = -\rho\overline{u'v'}^{\,z,t}(x_0, y, t) - g(x_0, y)\,.$$

With the amplitude

$$r(y,t) = \alpha\, e(y,t) + \beta \int_0^t e(y,t')\,\mathrm{d}t',$$

the instantaneous body force is computed as

$$f(x_0, y, z, t) = r(y,t)[u(x_0, y, z, t) - \overline{u}^{\,z,t}(x_0, y)].$$

In order to prevent stimulation of unrealistic large shear stress 'events', f is only applied if the following constraints for the instantaneous, local correlation $u'v'(x_0, y, z, t)$ and the fluctuations $u'(x_0, y, z, t)$ and $v'(x_0, y, z, t)$ are met:

$$|u'| < 0.6\, U_\infty, \ |v'| < 0.4\, U_\infty, \ u'v' < 0 \quad \text{and} \quad |u'v'| > 0.0015\, U_\infty^2.$$

The parameters α, β of the PI controllers are chosen in order to decrease the error signal sufficiently fast without causing instabilities.

A closed-loop controller is used to control the boundary layer thickness δ_I at the domain inlet until δ_{99} at the rescaling station reaches a target value δ_R. Similarly, $v(x)$ at the top of the domain is adjusted via a feedback loop in order to obtain a desired streamwise pressure gradient, e.g. $dp/dx \approx 0$. The adjustment times for reaching approximately steady values are of $\mathcal{O}(100)\delta_{99}/U_\infty$.

The incompressible Navier-Stokes equations for primitive variables u, v, w, p are solved on a staggered mesh. The non-linear term is discretized in the skew-symmetric form, guaranteeing conservation of kinetic energy in the absence of viscosity [12, 6, 5]. Spatial derivatives in the wall-parallel directions (x, z) including the pressure gradient and the continuity equation are approximated with 6th-order compact (Hermitian) differences. Explicit second order differences are used in the non-equidistant wall-normal direction. The pressure Poisson equation is solved via Fourier transform in the spanwise periodic direction and via cosine transform in the streamwise direction where the pressure satisfies a von Neumann boundary condition. At the outflow plane we specify a convective outflow boundary condition. The Smagorinsky model accounts for the sub-grid-stresses with the model constant determined via the dynamic procedure [4] in the formulation of Lilly [10]. The test filter is approximated with the trapezoidal rule, filtering is limited to the wall-parallel directions, and the ratio of test and grid filter width is $\widehat{\Delta}/\Delta = 2.0\sqrt{3/2}$.

3. Results

The method has been applied in an LES in a domain of size $18\delta_0 \times 3.5\delta_0 \times 2.2\delta_0$. The reference length δ_0 corresponds approximately to the 99%-thickness of the boundary layer at the "rescaling" station which is located at $x_R = 12\delta_0$. There, integral properties of the turbulent boundary layer are $\theta/\delta_0 = 0.129$, $\delta^*/\delta_0 = 0.187$, $c_f = 0.00353$, and $H_{12} = 1.44$. This corresponds to $Re_\theta = 1816$, $Re_{\delta^*} = 2616$, and $Re_\tau = u_\tau \delta_{99}/\nu = 780$. The domain is discretized into $144 \times 55 \times 48$ cells. At the rescaling station, the grid spacing normalized in wall-units is $\Delta x^+ = 98$, $\Delta y^+_{min} \approx 1.2$, and $\Delta z^+ = 36$. Body forces act at three stations located at $x/\delta_0 = 2$, 3.75, and 5.5. In the wall-normal direction they are limited to the region $0.05 < y/\delta_0 < 0.5$. Results are compared with the random-phase method of [7] where no adjustment by body forces takes place.

Fig. 2 and 3 show the results in terms of 'streamwise' evolution of skin friction coefficient $c_f = \rho u_\tau^2/(0.5U_\infty^2)$, shape factor $H_{12} = \delta^*/\theta$ and velocity derivative skewness coefficient $S_{\partial u/\partial x} = \overline{(\partial u/\partial x)^3}/\overline{(\partial u/\partial x)^2}^{1.5}$.

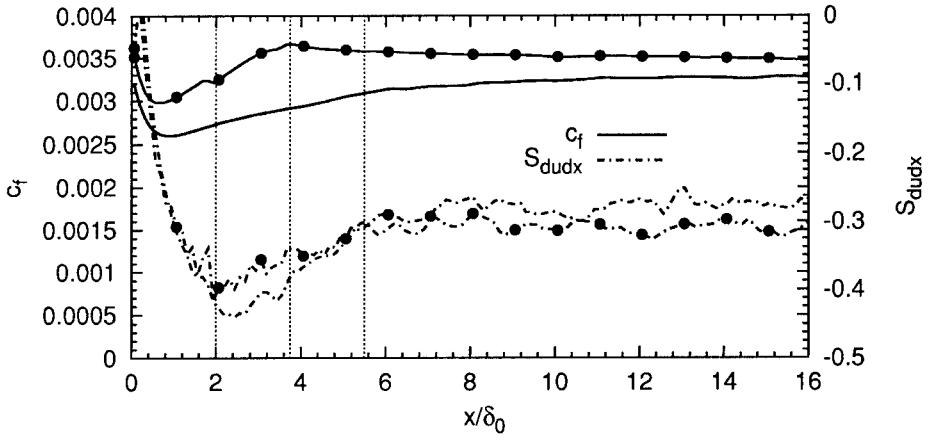


Figure 2. Streamwise development of friction coefficient c_f (left axis) and velocity derivative skewness $S_{\partial u/\partial x}$ (right axis). Lines corresponding to the forced case are marked with additional dots. Vertical lines denote the three forcing locations.

Inflow generation by random numbers causes a strong deviation of statistics from equilibrium values due to the lack of proper correlations. Obviously, with body forces the development length needed for reaching a statistical equilibrium is shortened considerably. This can be seen from the quicker recovery of c_f and $S_{\partial u/\partial x}$, the latter being an indicator for the onset of non-linear energy transfer. Comparison with experimental data in Fig. 3 reveals, that the auxiliary body forces are beneficial for driving the boundary layer closer to an equilibrium state.

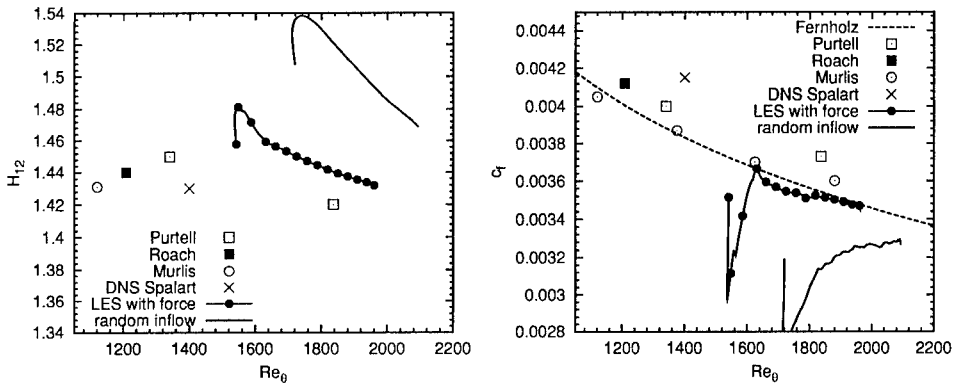


Figure 3. Shape factor H_{12} and skin friction coefficient c_f as function of Re_θ. For comparison we include DNS and experimental data, for the references see Fernholz & Finley (1996).

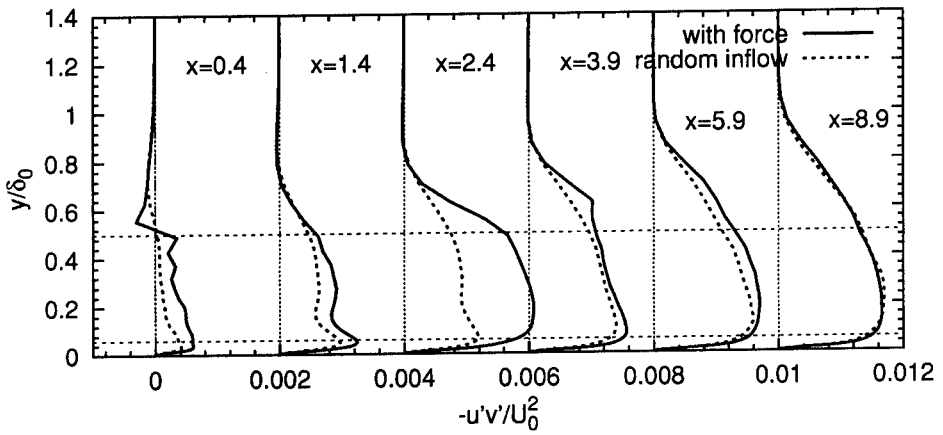


Figure 4. Profiles of shear stress $-\rho\overline{u'v'}$ at several stations as indicated in the plot for the new method (———) and the random method (----). Horizontal lines indicate the zone in which the body forces act.

Fig. 4 shows the streamwise development of the shear-stress profile. Ahead of the first forcing station, shear-stresses are too small due to lack of proper correlation between u' and v' fluctuations at the domain inlet. Without body forces, recovery of the profiles proceeds quicker near the wall than in the outer part of the boundary layer. The addition of body forces at $x/\delta_0 = 2$ has some influence on the flow upstream. At $x/\delta_0 = 2.4$ we observe the largest difference between forced and unforced cases. The forcing at the first station results in an overshoot in the shear-stress magnitude. As a consequence, body-forces at the second station – located at $x/\delta_0 = 3.75$ – counteract the wall-normal fluid motion, thereby reducing the shear-stress to the desired levels. The amplitude of the force decreases nearly an order of magnitude from the first to the last station.

Downstream of the forcing zone the flow recovers into an equilibrium state. The mean flow profile follows the standard log-law, see Fig. 5. We observe a pronounced wake which does not seem to be connected with the forcing since it is also visible in the unforced case. Rms-profiles of the resolved velocity fluctuations are in good agreement with DNS data.

For a coarse-grid DNS at $R_\theta \approx 340$ carried out in a domain of size $10\delta_{99} \times 3\delta_{99} \times 3\delta_{99}$, the new method was compared with Lund's [11] approach. The rescaling station was located at $x_R/\delta_{99} = 6.3$. Power spectra recorded inside and outside the boundary layer are shown in Fig. 6. Whereas Lund's method exhibits peaks at frequencies U_∞/x_R and its higher harmonics, spectra from the new method are smooth in the low-frequency range. Thus, the proposed method is capable of generating inflow turbulence without introducing a quasi-periodicity at low frequencies.

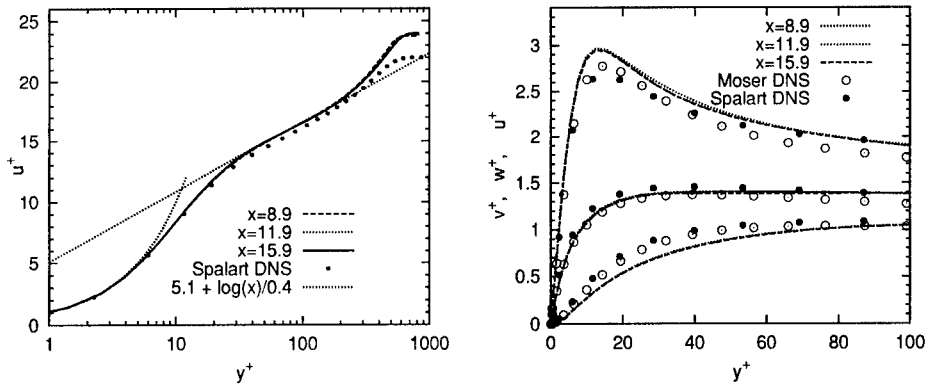


Figure 5. Mean flow profile and turbulence statistics scaled in inner variables at several downstream locations.

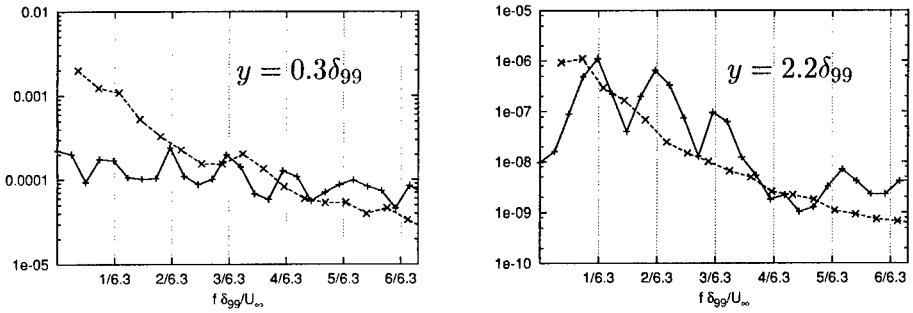


Figure 6. Power spectra Φ_{uu} at x_R inside (left) and outside (right) of the boundary layer using Lund's method (———) and the new approach (·····) for a coarse-grid DNS at $R_\theta \approx 340$.

4. Conclusions and perspectives

We propose a new method for the generation of turbulent inflow data which avoids a long-range temporal correlation in the artificial velocity signal. It turns out that the method is fairly robust with respect to several of the parameters which can be chosen. These include the spectrum of the random turbulence introduced at the domain inlet, the streamwise extent of the control zone, the number of x, z-planes where body-forces are applied, the streamwise spacing between stations, and the vertical extent of the forcing zone.

The method is not restricted to equilibrium situations since turbulence is forced to follow a prescribed target profile. The method is capable to both enhance and damp existing fluctuations in order to achieve a desired target, e.g. the shear stress $\overline{u'v'}$. The method can easily be extended to

consider other targets such as $\overline{U}$ or rms profiles. Possibly, the occurence of "adverse" forces at later stations could be avoided entirely by correcting only part of the "error" at the first station.

Similar strategies might be applied in the context of hybrid RANS/LES approaches, where zones exist in which the grid is too coarse for resolving a sufficient range of energy containing eddies, e.g. near the wall. There, the generation of "supporting" stresses induced by body forces might be useful in order to achieve a smooth transition between regions which are modeled via RANS and via LES, respectively.

Acknowledgements

Part of this work was funded by DFG within Sfb 557. Computer time was provided by the Konrad-Zuse-Zentrum (ZIB), Berlin.

References

1. Adams, K.: 1997, 'DNS of shock boundary-layer interaction — preliminary results for compression ramp flow'. In: *CTR Annual Research Briefs 1997.* pp. 329–338.
2. Chung, Y. M. and H.-J. Sung: 1997, 'Comparative study of inflow conditions for spatially evolving simulation'. *AIAA Journal* **35**, 269–274.
3. Fernholz, H. H. and P. J. Finley: 1996, 'The incompressible zero-pressure gradient turbulent boundary layer: an assessment of the data'. *Prog. Aerosp. Sci.* **23**, 245–311.
4. Germano, M., U. Piomelli, P. Moin, and W. H. Cabot: 1991, 'A dynamic subgrid-scale eddy viscosity model'. *Phys. Fluids A* **3**, 1760–1765, Erratum: 3128.
5. Kaltenbach, H.-J. and D. Driller: (to appear)a, 'LES of wall-bounded turbulence based on a 6th-order compact scheme'. In: R. Friedrich, O. Metais, and B.J.Geurts (eds.): *Direct and Large-Eddy Simulation IV.* Dordrecht, The Netherlands.
6. Kaltenbach, H.-J. and D. Driller: (to appear)b, 'Phase-error reduction in LES using a compact scheme'. In: R. Friedrich and W. Rodi (eds.): *Proceedings of EUROMECH Colloquium 412 "LES of complex transitional and turbulent flows", Munich, October 2000.* Dordrecht, The Netherlands.
7. Le, H., P. Moin, and J. Kim: 1997, 'Direct numerical simulation of turbulent flow over a backward-facing step'. *J. Fluid Mech.* **330**, 349–374.
8. Lee, S., S. Lele, and P. Moin: 1992, 'Simulation of spatially evolving turbulence and the applicability of Taylor's hypothesis in compressible flow'. *Phys. Fluids* **A4**, 1521–1530.
9. Li, N., E. Balaras, and U. Piomelli: 2000, 'Inflow conditions for large-eddy simulations of mixing layers'. *Phys. Fluids* **12**, 935.
10. Lilly, D. K.: 1992, 'A proposed modification of the Germano subgrid-scale closure method.'. *Phys. Fluids A4* **3**, 633–635.
11. Lund, T. S., X. Wu, and K. D. Squires: 1998, 'Generation of turbulent inflow data for spatially-developing boundary layer simulations'. *J. Comp. Phys.* **140**, 233–258.
12. Morinishi, Y., T. Lund, O. Vasilyev, and P. Moin: 1998, 'Fully conservative higher order finite difference schemes for incompressible flow'. *J. Comp. Phys.* **143**, 90–124.
13. Na, Y. and P. Moin: 1998, 'Direct numerical simulation of a separated turbulent boundary layer'. *J. Fluid Mech.* **374**, 379–405.

VELOCITY FILTERED DENSITY FUNCTION FOR LARGE EDDY SIMULATION OF A TURBULENT MIXING LAYER

L.Y.M. GICQUEL AND P. GIVI
Department of Mechanical and Aerospace Engineering
University at Buffalo, SUNY
Buffalo, NY 14260-4400

F.A. JABERI
Department of Mechanical Engineering
Michigan State University
East Lansing, MI 48824-1226

AND

S.B. POPE
Sibley School of Mechanical and Aerospace Engineering
Cornell University
Ithaca, NY 14853-1301

Abstract. The "velocity filtered density function" (VFDF) methodology is employed for large eddy simulation (LES) of a three-dimensional, temporally developing, turbulent mixing layer. A transport equation is derived for the VFDF in which the effects of the subgrid scale (SGS) convection appear in closed form. The unclosed terms in this equation are modeled. A system of stochastic differential equations (SDEs) which yields statistically equivalent results to the modeled VFDF transport equation is proposed. These SDEs are solved numerically by a Lagrangian Monte Carlo procedure. The VFDF results are compared with those obtained via several existing SGS closures and with data obtained by direct numerical simulation (DNS) of the mixing layer.

1. Introduction

The probability density function (PDF) approach has proven useful for large eddy simulation (LES) of turbulent reacting flows (Pope, 2000; Poinsot

and Veynante, 2001). The formal means of conducting such LES is by consideration of the "filtered density function" (FDF) which is essentially the filtered fine-grained PDF of the transport quantities (Pope, 1990). In all previous contributions, the FDF of the "scalar" quantities is considered (Pope, 1990; Gao and O'Brien, 1993; Colucci *et al.*, 1998; Réveillon and Vervisch, 1998; Garrick *et al.*, 1999; Jaberi *et al.*, 1999; James and Jaberi, 2000; Zhou and Pereira, 2000; Tong, 2001). The objective of the present work is to extend the methodology for LES of the velocity field.

2. Formulation

We consider a constant (unit) density, three-dimensional temporally developing mixing layer. The primary transport variables are the velocity vector, $u_i(\mathbf{x},t)$ $(i=1,2,3)$, and the pressure, $p(\mathbf{x},t)$, field. Large eddy simulation involves the spatial filtering operation (Guerts, 2001; Sagaut, 2001)

$$\langle f(\mathbf{x},t)\rangle_L = \int_{-\infty}^{+\infty} f(\mathbf{x}',t)G(\mathbf{x}'-\mathbf{x})d\mathbf{x}', \tag{1}$$

where $G(x)$ denotes a spatially and temporally invariant, localized and positive filter function (Vreman *et al.*, 1994) of length Δ_L, and $\langle f(\mathbf{x},t)\rangle_L$ represents the filtered value of the transport variable $f(\mathbf{x},t)$. The application of the filtering operation to the instantaneous equations describing transport of the variables in space and time (t) yields

$$\begin{gathered}\frac{\partial\langle u_i\rangle_L}{\partial x_i}=0,\\ \frac{\partial\langle u_j\rangle_L}{\partial t}+\frac{\partial\langle u_i\rangle_L\langle u_j\rangle_L}{\partial x_i}=-\frac{\partial\langle p\rangle_L}{\partial x_j}+\frac{\partial\langle\sigma_{ij}\rangle_L}{\partial x_i}-\frac{\partial\tau_L(u_i,u_j)}{\partial x_i}.\end{gathered} \tag{2}$$

For a Newtonian fluid the viscous stress tensor σ_{ij} is represented by $\sigma_{ij}=\nu\left(\frac{\partial u_i}{\partial x_j}+\frac{\partial u_j}{\partial x_i}\right)$, with ν denoting the (constant) kinematic viscosity. The term $\tau_L(u_i,u_j)=\langle u_iu_j\rangle_L-\langle u_i\rangle_L\langle u_j\rangle_L$ denotes the generalized SGS stresses (Germano, 1992). The "velocity filtered density function" (VFDF), denoted by P_L, is formally defined as (Pope, 1990)

$$\begin{gathered}P_L(\boldsymbol{v};\mathbf{x},t)=\int_{-\infty}^{+\infty}\varrho\left[\boldsymbol{v},\boldsymbol{u}(\mathbf{x}',t)\right]G(\mathbf{x}'-\mathbf{x})d\mathbf{x}',\\ \varrho\left[\boldsymbol{v},\boldsymbol{u}(\mathbf{x},t)\right]=\prod_{i=1}^{3}\delta[v_i-u_i(\mathbf{x},t)],\end{gathered} \tag{3}$$

where δ denotes the delta function and $\boldsymbol{v}$ is the velocity state vector. The term $\varrho[\boldsymbol{v},\boldsymbol{u}(\mathbf{x},t)]$ is the "fine-grained" density (O'Brien, 1980; Pope, 1985;

Pope, 2000), and Eq. (3) defines the VFDF as the *spatially filtered* value of this density. With the condition of a positive filter kernel (Vreman *et al.*, 1994), P_L has all the properties of the PDF (Pope, 1985). The transport equation for the VFDF is obtained by applying the filter to the equation governing the evolution of fine-grained density (Gicquel, 2001). The effects of SGS convection in physical space appear in a closed form in this equation. However, the convective effects in the velocity space due to SGS pressure gradient and SGS diffusion need to be modeled. For closure of these terms, the generalized Langevin model (GLM) (Haworth and Pope, 1986; Pope, 1994) is employed,

$$\begin{aligned}\frac{DP_L}{Dt} &= -\frac{\partial}{\partial x_k}\left[(v_k - \langle u_k\rangle_L)P_L\right] + \frac{\partial\langle p\rangle_L}{\partial x_i}\frac{\partial P_L}{\partial v_i} - \frac{\partial\langle\sigma_{ik}\rangle_L}{\partial x_k}\frac{\partial P_L}{\partial v_i} \\ &\quad - \frac{\partial}{\partial v_i}\left[\, G_{ij}\,(v_j - \langle u_j\rangle_L)\,P_L\,\right] + \frac{1}{2}\,C_0\,\varepsilon\,\frac{\partial^2 P_L}{\partial v_i \partial v_i},\end{aligned} \tag{4}$$

where $\frac{D}{Dt} = \frac{\partial}{\partial t} + \langle u_k\rangle_L \frac{\partial}{\partial x_k}$, and the two terms G_{ij} and ε jointly represent the SGS pressure-strain and SGS dissipation,

$$G_{ij} = -\,\omega\left(\frac{1}{2} + \frac{3}{4}C_0\right)\delta_{ij},\;\; \varepsilon = C_\varepsilon\, k^{3/2}/\Delta_L,\;\; \omega = \varepsilon/k. \tag{5}$$

In this model ω is the SGS mixing frequency, $k = \frac{1}{2}\tau_L(u_i, u_i)$ is the SGS kinetic energy, and ε is the SGS dissipation rate. In Reynolds averaged simulations, typically $C_\varepsilon \approx 1$, and $C_0 \approx 2.1$.

In addition to VFDF, three other LES are conducted with (1) no SGS model, (2) the Smagorinsky SGS closure (Smagorinsky, 1963), and (3) the dynamic Smagorinsky (Germano *et al.*, 1991; Germano, 1992; Lilly, 1992) model. The no model refers to the case in which the contribution of the SGS is completely ignored, *i.e.* $\tau_L(u_i, u_j) = 0$.

3. Numerical Solution Procedure

The solution of the VFDF transport equation provides all the statistical information pertaining to the velocity vector. The most convenient means of solving this equation is via the Lagrangian Monte Carlo scheme (Pope, 1985; Pope, 1994). To do so, the general diffusion process is considered via the following system of stochastic differential equations (SDEs) (Pope, 1985; Haworth and Pope, 1986),

$$\begin{aligned} d\mathcal{U}_i(t) &= \left[\left(-\frac{\partial\langle p\rangle_L}{\partial x_i} + \frac{\partial\langle\sigma_{ik}\rangle_L}{\partial x_k}\right) + G_{ij}\,(\mathcal{U}_j(t) - \langle u_j\rangle_L)\right]\,dt + \sqrt{C_0\varepsilon}\,dW_i^v(t) \\ d\mathcal{X}_i(t) &= \mathcal{U}_i(t)\,dt, \end{aligned} \tag{6}$$

where $\mathcal{X}_i$ and $\mathcal{U}_i$ are probabilistic representations of the position and the velocity, respectively; and W_i^v denotes independent Wiener-Lévy processes (Karlin and Taylor, 1981). The corresponding Fokker-Planck equation for this diffusion process is the same as the VFDF transport equation. With the Lagrangian description, the VFDF is represented by an ensemble of Monte Carlo particles. Each of these particles carries information pertaining to its velocity and position. This information is updated via temporal integration of Eq. (6). The statistics are evaluated by consideration of the ensemble of particles in a "finite volume" centered at a spatial location. This finite volume is characterized by a cubic box of length Δ_E containing N_E Monte Carlo particles.

The "mean field solver" is based on the "compact parameter" finite difference scheme (Carpenter, 1990) with a fourth order spatial accuracy and a second order symmetric predictor-corrector sequence for time discretization. All the finite difference operations are conducted on fixed and equally sized grid points with spacings Δ. The transfer of information from these points to the location of the Lagrangian particles is conducted via interpolation. The mean-field solver also determines the filtered velocity field. That is, there is a "redundancy" in the determination of the first filtered moments as both the finite difference and the Monte Carlo procedures provides the solution of this field. This redundancy is actually very useful in monitoring the accuracy of the simulated results (Jaberi *et al.*, 1999; Muradoglu *et al.*, 1999). The DNS and all the other LES (via the no-model, Smagorinsky, and the dynamics Smagorinsky) are conducted with the same finite-difference scheme.

4. Results

Simulations are conducted of a three-dimensional (3D) temporally developing mixing layer. This layer consists of two parallel streams traveling in opposite directions with the same speed (Moser and Rogers, 1992). A hyperbolic tangent profile is utilized to assign the velocity distribution at the initial time. The coordinates x, y, z denote the streamwise, cross-stream, and spanwise directions, respectively. The flowfield is initialized with a procedure somewhat similar to that considered previously (Vreman *et al.*, 1997) which results in the formation of two successive vortex pairings and strong three-dimensionality. Simulations are conducted on 193^3 and 33^3 points for DNS and LES, respectively. For filter, a top-hat function of width $\Delta_L = 2\Delta$ is used. No attempt is made to investigate the sensitivity of the results to the filter function (Vreman *et al.*, 1994) or the size of the filter. Simulations are conducted with $C_\varepsilon = 1$, $C_0 = 2.1$, $\Delta_E = \Delta/2$, $N_E = 40$, and with a uniform "weight" (Pope, 1985) of the Monte Carlo particles.

Figures 1 and 2 show the contours of the spanwise and the streamwise components of the vorticity field, respectively. By this time, the flow has gone through several pairings and exhibits strong 3D effects. This is evident by the formation of large scale spanwise rollers with presence of counter-rotating streamwise vortex pairs in all the simulations. The results via the no-model indicate too many small-scale structures which clearly are not captured accurately on the coarse grid. The amount of SGS diffusion with the Smagorinsky model is very significant at initial times. Due to this dissipative characteristics of the model, the predicted results are too smooth and only contain the large scale structures. The vortical structures as depicted by the dynamic Smagorinsky and the VFDF are very similar and predict the DNS results better than the other two models. But both models yield less fine structures as compared to DNS. The Reynolds averaged values of the simulated data (not shown) also indicate the dissipative nature of the Smagorinsky model resulting in a slow growth of the layer. As a result, this model does not predict the spread and the peak value of the resolved Reynolds stresses. The VFDF predicts both the spread and the peak values reasonably well, except for small C_ε values. In this case, the amount of energy in the resolved scale decreases too much in favor of the increase of the SGS stress.

5. Acknowledgments

This work is sponsored by the U.S. Air Force Office of Scientific Research under Grant F49620-00-1-0035 to SUNY-Buffalo and Grant F49620-00-1-0171 to Cornell University. Dr. Julian M. Tishkoff is the Program Manager for both these grants. Additional support for the work at SUNY-Buffalo is provided by the NASA Langley Research Center under Grant NAG-1-2238 with Dr. J. Philip Drummond as the Technical Monitor. Acknowledgment is also made to the Donors of the Petroleum Research Funds administrated by the American Chemical Society for their support under Grant ACS-PRF 36981-AC9. Computational resources are provided by the NCSA at the University of Illinois at Urbana and by the CCR at SUNY-Buffalo.

References

Carpenter, M. H. (1990). A high-order compact numerical algorithm for supersonic flows. In Mortron, K. W., editor, *Proc. 12th International Conference on Numerical Methods in Fluid Dynamics*, volume 371 of *Lecture Notes in Physics*, pages 254–258. Springer-Verlag.

Colucci, P. J., Jaberi, F. A., Givi, P., and Pope, S. B. (1998). Filtered density function for large eddy simulation of turbulent reacting flows. *Phys. Fluids* **10**, 499–515.

Gao, F. and O'Brien, E. E. (1993). A large-eddy simulation scheme for turbulent reacting flows. *Phys. Fluids A* **5**, 1282–1284.

Garrick, S. C., Jaberi, F. A., and Givi, P. (1999). Large eddy simulation of scalar trans-

port in a turbulent jet flow. In Knight, D. and Sakell, L., editors, *Recent Advances in DNS and LES*, volume 54 of *Fluid Mechanics and its Applications*, pages 155–166. Kluwer Academic Publishers, The Netherlands.

Germano, M., Piomelli, U., Moin, P., and Cabot, W. H. (1991). A dynamic subgrid-scale eddy viscosity model. *Phys. Fluids* **A3**, 1760–1765.

Germano, M. (1992). Turbulence: The filtering approach. *J. Fluid Mech.* **238**, 325–336.

Gicquel, L. Y. M. (2001), *Velocity Filtered Density Function for Large Eddy Simulation of Turbulent Flows*. Ph.D. Dissertation, Department of Mechanical and Aerospace Engineering, State University of New York at Buffalo, Buffalo, NY.

Geurts, B. J., editor. (2001). *Modern Simulation Strategies for Turbulent Flow*. R. T. Edwards, Inc., Philadelphia, PA.

Haworth, D. C. and Pope, S. B. (1986). A generalized Langevin model for turbulent flows. *Phys. Fluids* **29**, 387–405.

Jaberi, F. A., Colucci, P. J., James, S., Givi, P., and Pope, S. B. (1999). Filtered mass density function for large eddy simulation of turbulent reacting flows. *J. Fluid Mech.* **401**, 85–121.

James, S. and Jaberi, F. A. (2000). Large scale simulations of two-dimensional non-premixed methane jet flames. *Combust. Flame* **123**, 465–487.

Karlin, S. and Taylor, H. M. (1981). *A Second Course in Stochastic Processes*. Academic Press, New York, NY.

Lilly, D. K. (1992). A proposed modification of the Germano sub-grid closure method. *Phys. Fluids* **A 4**, 633–635.

Moser, R. D. and Rogers, M. M. (1992). The three-dimensional evolution of a plane mixing layer: the Kelvin-Helmholtz rollup. *J. Fluid Mech.* **243**, 183–226.

Muradoglu, M., Jenny, P., Pope, S. B., and Caughey, D. A. (1999). A consistent hybrid-volume/particle method for the PDF equations of turbulent reactive flows. *J. Comp. Phys.* **154**, 342–371.

O'Brien, E. E. (1980). The probability density function (PDF) approach to reacting turbulent flows. In Libby, P. A. and Williams, F. A., editors, *Turbulent Reacting Flows*, chapter 5, pages 185–218. Springer-Verlag, Heidelberg.

Poinsot, T. and Veynante, D. (2001). *Theoretical and Numerical Combustion*. R. T. Edwards, Inc., Philadelphia, PA.

Pope, S. B. (1985). PDF methods for turbulent reacting flows. *Prog. Energy Combust. Sci.* **11**, 119–192.

Pope, S. B. (1990). Computations of turbulent combustion: Progress and challenges. In *Proceedings of 23rd Symp. (Int.) on Combustion*, pages 591–612. The Combustion Institute, Pittsburgh, PA.

Pope, S. B. (1994). Lagrangian PDF methods for turbulent flows. *Ann. Rev. Fluid Mech.* **26**, 23–63.

Pope, S. B. (2000). *Turbulent Flows*. Cambridge University Press, Cambridge, UK.

Réveillon, J. and Vervisch, L. (1998). Subgrid scale turbulent micromixing: dynamic approach. *AIAA J.* **36**, 336–341.

Sagaut, P. (2001). *Large Eddy Simulation for Incompressible Flows*. Springer, New York.

Smagorinsky, J. (1963). General circulation experiments with the primitive equations. I. The basic experiment. *Monthly Weather Review* **91**, 99–164.

Tong, C. (2001). Measurements of conserved scalar filtered density function in a turbulent jet. *Phys. Fluids* **13**, 2923–2937.

Vreman, B., Geurts, B., and Kuerten, H. (1994). Realizability conditions for the turbulent stress tensor in large-eddy simulation. *J. Fluid Mech.* **278**, 351–362.

Vreman, B., Geurts, B., and Kuerten, H. (1997). Large-eddy simulation of the turbulent mixing layer. *J. Fluid Mech.* **339**, 357–390.

Zhou, X. Y. and Pereira, J. C. F. (2000). Large eddy simulation (2D) of a reacting plan mixing layer using filtered density function. *Flow, Turbulence and Combustion* **64**, 279–300.

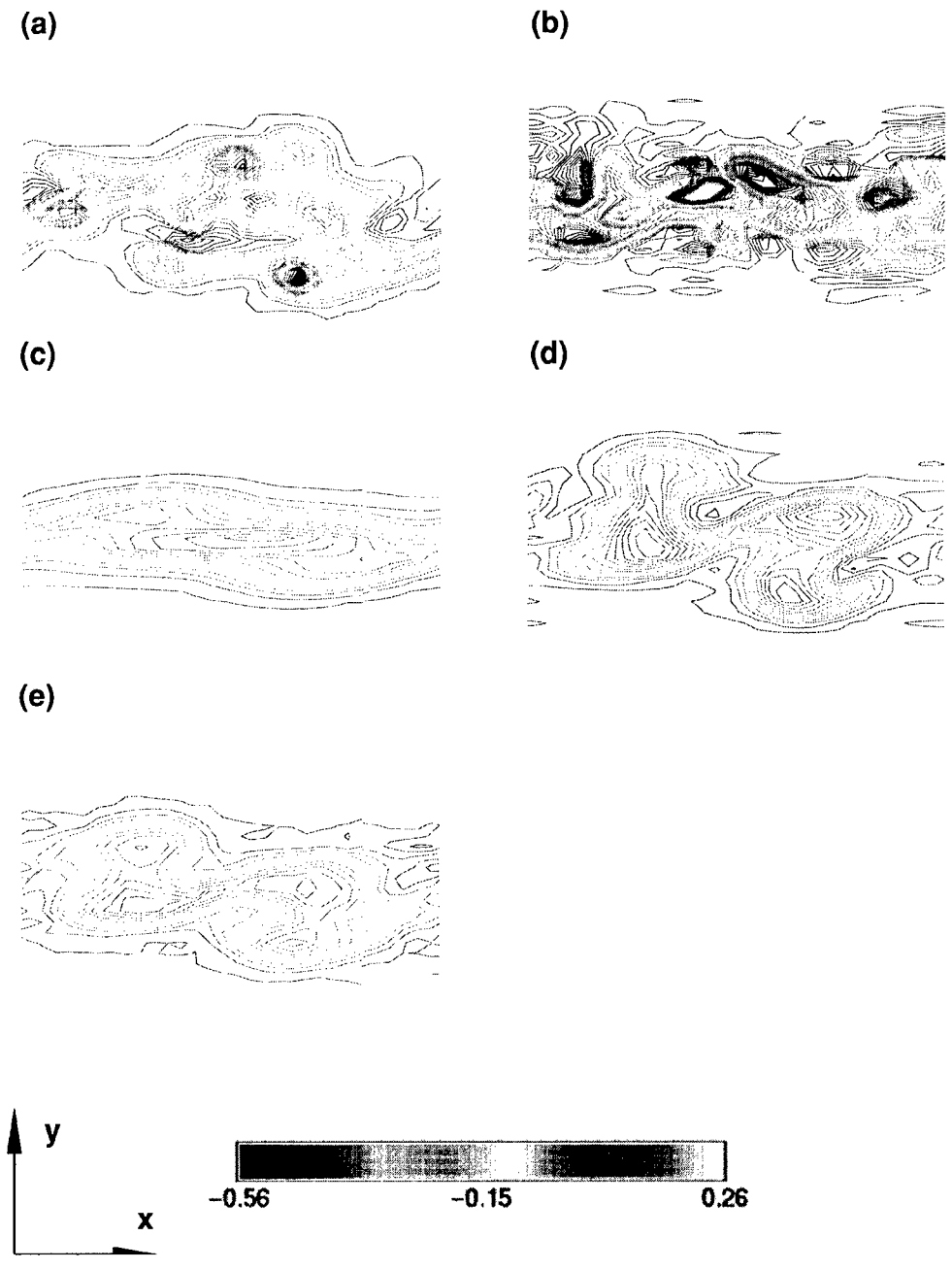


Figure 1. Contour plots of the spanwise component of the vorticity. (a) Filtered DNS, (b) no model, (c), Smagorinsky model, (d) dynamic Smagorinsky model, (e) VFDF.

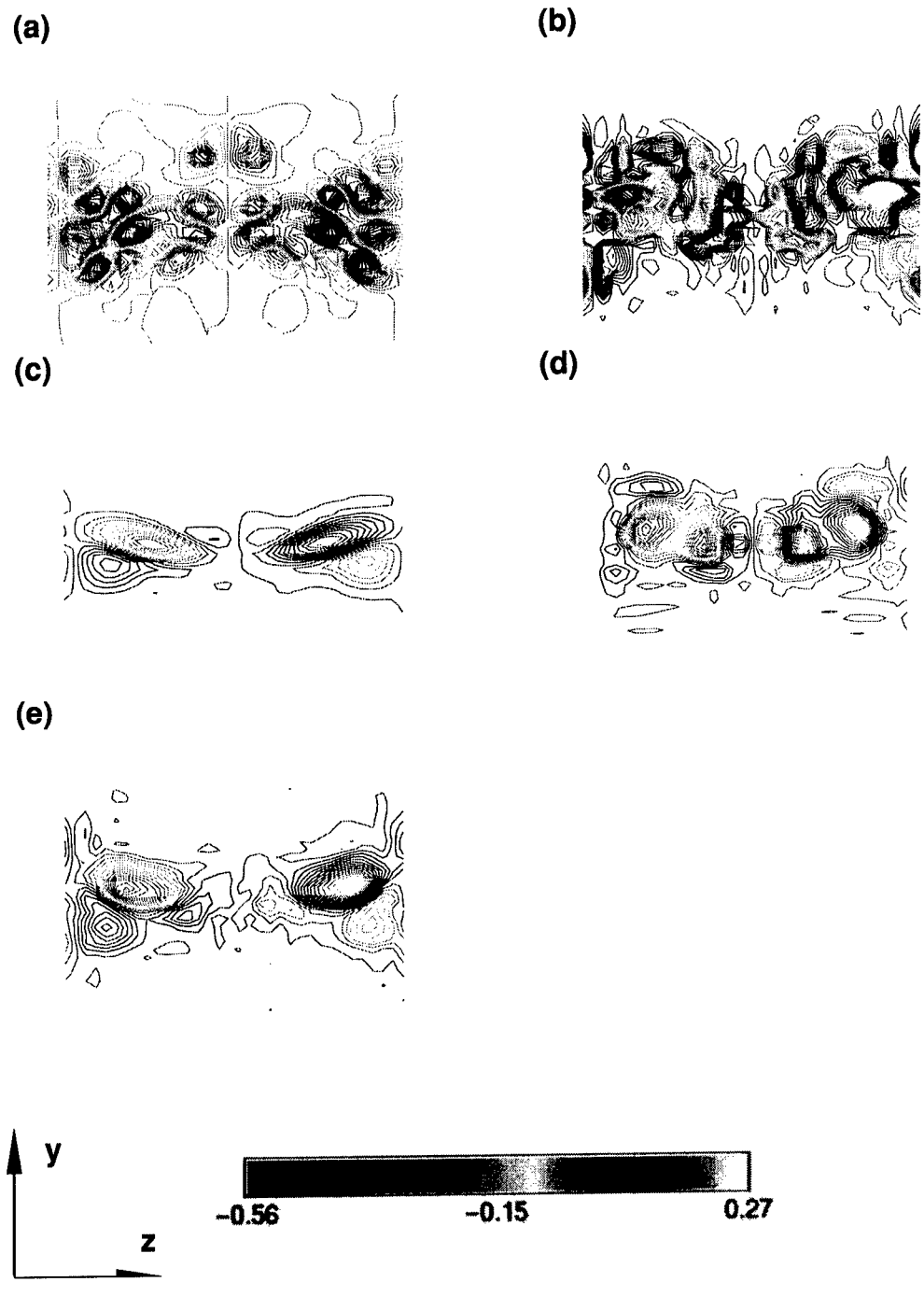


Figure 2. Contour plots of the streamwise component of the vorticity vector. (a) Filtered DNS, (b) no model, (c) Smagorinsky model, (d) dynamic Smagorinsky model, (e) VFDF.

A NEW DYNAMIC SGS MODEL FOR LARGE EDDY SIMULATION OF PARTICLE-LADEN TURBULENT FLOWS

KANGBIN LEI
Computer and Information Division, Advanced Computing Center
The Institute of Physical and Chemical Research (RIKEN)
2-1, Hirosawa, Wako-shi, Saitama 351-0198, Japan
lei@riken.go.jp

NOBUYUKI TANIGUCHI
Super Computing Division, Information Technology Center
University of Tokyo
2-11-16, Yayoi, Bunkyo-Ku, Tokyo, 113-8658, Japan
taniguchi@cc.u-tokyo.ac.jp

TOSHIO KOBAYASHI
The 2nd Department, Institute of Industrial Science
University of Tokyo
4-6-1, Komaba, Meguro-ku, Tokyo 153-8505, Japan
kobaya@iis.u-tokyo.ac.jp

Abstract

The paper presents a new dynamic SGS model of two-way coupling for large eddy simulation of particle-laden turbulent flow. The advantage of this new model is that coupling of fluid-particles SGS components was taken into account and at the same time the coefficient of proposed SGS model can be optimized by Germano's (1991) dynamic procedure[1]. To investigate the capability of this model, numerical simulations of particle-laden turbulent flow at Re=644 in a vertical channel were performed using this new dynamic SGS model. By comparing the calculation results with that using single-phase SGS models which didn' t consider coupling of SGS components the role of particles SGS components played in the turbulence modulation of fluid flow was clarified for particle-laden channel turbulent flows. In addition, the subgrid-scale stresses obtained using the proposed model vanish at wall boundary, and have the correct asymptotic behavior in the near-wall region of the turbulent boundary.

1. Introduction

In large eddy simulation of single-phase turbulent flows, one major deficiency of the Smagrinsky[2] subgrid-scale stress models is their inability to represent correctly with a single universal constant to different turbulent fields in rotating

or sheared flows, near solid walls, or in transitional regimes. Usually additional modifications to the Smagorinsky model were made in the near-wall region to force the subgrid-scale stresses to vanish at the wall boundary with a standard Van Driest[3] damping function. The dynamic SGS model proposed by Germano[1] et al. (1991) overcomes these deficiencies by locally calculating the eddy viscosity coefficient to reflect closely the sate of the flow. In large eddy simulation of multi-phase turbulent flows, it is being expected that the fluid turbulence modulation SGS model can be evaluated by Germano's dynamic procedure as in the single-phase turbulent flows.

In particle-laden turbulent flow, a kind of multi-phase turbulent flows that occur in a wide range of engineering and scientific research, interaction of particles and gas-phase turbulent carrier flow is a problematic research topic of both fundamental importance and practical interest. In addition, it is the most interesting problem in developing numerical simulation models. A two way coupling SGS model was present by Yuu[4] (1997), in which coupling of fluid-particles SGS component was considered. However, the model coefficient was simply decided in the same way as previous works for the single-phase turbulent flows.

We present here a new dynamic SGS model for two way coupling LES of particle-laden turbulent flow based on Yuu' s SGS model. The couplings of fluid-particles SGS component on fluid turbulence modulation in LES was taken into account and at the same time the coefficient of proposed SGS model can be dynamically decided by assuming that the small scales are in equilibrium, so that energy production, dissipation and interaction of fluid-particles are in balance.

The main objective of this paper is to introduce this model and at the same time to report the results of investigation about the capability and limitation of present SGS mode in predicting the fluid turbulence modulation for particle-laden turbulent flows through numerical simulations, which were performed in downward particle-laden turbulent flows at Re=644 in a vertical channel using Van Driest wall function model and the proposed new dynamic SGS model.

2. Improvement of Two Way Coupling SGS model

For dilute particle-laden turbulent flow, in which particle volume fraction is very small but the particle mass loading is large, momentum equations governing transport of the large eddies was oriented by filtering the incompressible Navier-Stokes equations with the particle source term, where the Leonard and Cross terms were neglected.

$$\frac{\partial \overline{u}_i}{\partial t}+\frac{\partial}{\partial x_j}(\overline{u}_i\overline{u}_j)=-\frac{1}{\rho_f}\frac{\partial \overline{p}}{\partial x_i}+\frac{\mu}{\rho_f}\frac{\partial^2 \overline{u}_i}{\partial x_j \partial x_j}-\frac{\partial \tau_{ij}}{\partial x_j}-F[N(\overline{u}_i-\overline{u}_{pi})+\overline{n'u_i'}-\overline{nu_{pi}'}] \quad (1)$$

The effect of the SGS on the resolved eddies in EQ (1) is represented by SGS stress $\tau_{ij}=\overline{u_iu_j}-\overline{u}_i\overline{u}_j$. In this work, τ_{ij} is parameterized using an eddy viscosity

hypothesis expressed by EQ (2), and the particles turbulent dispersion flux terms $\overline{n'u_i'}$ and $\overline{n'u_{pi}'}$ adopt gradient dispersion model as presented in EQ (3) and EQ (4).

$$\tau_{ij} - \frac{1}{3}\delta_{ij}\tau_{kk} = -2\nu_T \bar{S}_{ij} \tag{2}$$

$$\overline{n'u_i'} = -\nu_{TS}\frac{\partial N}{\partial x_i} \tag{3}$$

$$\overline{n'u_{pi}'} = -\nu_{TP}\frac{\partial N}{\partial x_i} \tag{4}$$

Here, the viscosity taking into account fluid particles interactions needs to be parameterized.

The governing equation of kinetic energy for subgrid-scale flow considering the interaction of fluid and particles can be derived as follow.

$$\frac{Dk}{Dt} = \frac{\partial k}{\partial t} + \bar{u}_j\frac{\partial k}{\partial x_j} = -\overline{u_i'u_j'}\bar{S}_{ij} - \frac{\partial}{\partial x_j}\left(\frac{1}{2}\overline{u_j'u_i'u_i'} + \frac{1}{\rho_f}\overline{u_j'p} - \nu\frac{\partial k}{\partial x_j}\right) - \nu\overline{\frac{\partial u_i'}{\partial x_j}\frac{\partial u_i'}{\partial x_j}} - F[\overline{N(u_i'u_i' - u_iu_{pi}')} + \overline{n'u_i'}(\bar{u}_i - \bar{u}_{pi}) + \overline{nu_i'(u_i' - u_{pi}')}] \tag{5}$$

From EQ (5), however, the third order fluctuating terms were neglected, Yuu[4] (1997) proposed a two way coupling SGS model applying a local equilibrium assumption expressed as EQ (6) that energy production, dissipation and interaction of fluid-particles are in balance.

$$2\nu_T\bar{S}_{ij}\bar{S}_{ij} - C_\varepsilon k^{3/2}\Delta^{-1} - 2NF\frac{1-b}{aT_{Li}+1}k + F\frac{\nu_T}{\sigma_s}\frac{\partial N}{\partial x_i}(\bar{u}_i - \bar{u}_{pi}) = 0 \tag{6}$$

From EQ (6), the viscosity taking into account of fluid-particles interaction was derived and expressed as EQ (7)

$$\nu_T = C_{\nu T}C_\varepsilon^{1/3}\Delta\left[\frac{-A_2 + \sqrt{A_2^2 + 4A_1(A_3 + A_4)}}{2A_1}\right] \tag{7}$$

Where $A_1 = C_\varepsilon\Delta^{-1}$ $A_2 = 2NF\dfrac{1-b}{aT_{Li}+1}$

$$A_3 = 2C_{\nu T}C_\varepsilon^{1/3}\Delta\bar{S}_{ij}\bar{S}_{ij} \quad A_4 = FC_{\nu T}C_\varepsilon^{1/3}\frac{\Delta}{\sigma_s}\frac{\partial N}{\partial x_i}(\bar{u}_i - \bar{u}_{pi})$$

$$T_{Li} = \frac{L_e}{(2k/3)^{1/2}} = \frac{\alpha_1}{C_\varepsilon}\frac{\Delta}{(\frac{2}{3}k)^{1/2}} \tag{8}$$

However, it is difficult to decide the coefficient $C_{\nu T}$ dynamically in Yuu' s model because the filter width Δ are mixed in EQ (7). In this study, we take the place of EQ (6) T_{Li} with EQ (8) and get EQ (9) as follows

$$2\nu_T\bar{S}_{ij}\bar{S}_{ij}-C_\varepsilon k^{3/2}\Delta^{-1}-2NF\frac{1-b}{a\dfrac{\alpha_1}{C_\varepsilon}\dfrac{\Delta}{(\frac{2}{3}k)^{1/2}}+1}k+F\frac{\nu_T}{\sigma_s}\frac{\partial N}{\partial x_i}(\bar{u}_i-\bar{u}_{pi})=0 \quad (9)$$

The SGS turbulence energy k can be modeled as follows according to dimensional analysis

$$k=\frac{C_\nu}{C_\varepsilon^{2/3}}\Delta^2(2\bar{S}_{ij}\bar{S}_{ij})=\frac{C_\nu}{C_\varepsilon^{2/3}}\Delta^2|\bar{S}|^2 \quad (10)$$

Substitution of EQ (10) into the third term denominator of EQ (9) and put it in order, the new eddy viscosity is then given by

$$\nu_T=C_{\nu T}^{3/2}\Delta^2\left[\frac{|\bar{S}|^2+\dfrac{F}{\sigma_s}\dfrac{\partial N}{\partial x_i}(\bar{u}_i-\bar{u}_{Pi})}{1+\dfrac{2NF(1-b)}{\sqrt{3/2}\alpha_1 a+\sqrt{C_\nu C_\varepsilon}|\bar{S}|}}\right]^{1/2} \quad (11)$$

Because the filter width Δ appears at only one place in the EQ (11) similar to the standard Smagrinsky model of single-phase turbulent flows, the coefficient $C_{\nu T}$ of proposed model can be easily decided by Germano's (1991) dynamic procedure.

3. A proposal of new dynamic SGS model of Two Way Coupling

Now substitute EQ (11) into EQ (2) to get the new dynamic eddy viscosity subgrid-scale stress expressed as EQ (12), which takes into account of the interaction of particles-fluid SGS components in LES.

$$\begin{aligned}\tau_{ij}&=\overline{u_iu_j}-\bar{u}_i\bar{u}_j\\&=-2\nu_T\bar{S}_{ij}=-2C_{\nu T}^{3/2}\Delta^2\left[\frac{|\bar{S}|^2+\dfrac{F}{\sigma_S}\dfrac{\partial N}{\partial x_i}(\bar{u}_i-\bar{u}_{Pi})}{1+\dfrac{2FN(1-b)}{\sqrt{3/2}\alpha_1 a+\sqrt{C_\nu C_\varepsilon}|\bar{S}|}}\right]^{\frac{1}{2}}\bar{S}_{ij}\\&=-2(C_{ms}\Delta)^2 g(\bar{u}_i,\bar{u}_{Pi},N)\bar{S}_{ij}\end{aligned} \quad (12)$$

According to the Germano's dynamic procedure [1], the test filter level SGS stress can be defined as

$$\begin{aligned}T_{ij}&=\overline{\bar{u}_i\bar{u}_j}-\tilde{\bar{u}}_i\tilde{\bar{u}}_j=-2C_{\nu T}^{3/2}\Delta_S^2\left[\frac{|\tilde{\bar{S}}|^2+\dfrac{F}{\sigma_S}\dfrac{\partial\tilde{N}}{\partial x_i}(\tilde{\bar{u}}_i-\tilde{\bar{u}}_{Pi})}{1+\dfrac{2F\tilde{N}(1-b)}{\sqrt{3/2}\alpha_1 a+\sqrt{C_\nu C_\varepsilon}|\tilde{\bar{S}}|}}\right]^{\frac{1}{2}}\tilde{\bar{S}}_{ij}\\&=-2(C_{ms}\Delta_S)^2 g(\tilde{\bar{u}}_i,\tilde{\bar{u}}_{Pi},\tilde{N})\tilde{\bar{S}}_{ij}\end{aligned} \quad (13)$$

Where, Δ is the characteristic filter width associated with the grid level filtering operator, and Δ_S is the filter width associated with the test level filtering operator. Considering the similarity between the SGS stresses at the grid and test levels, which are modeled using the same functional expression, it was assumed that the coefficient C_{vT} or C_{mS} in EQ (12) and EQ (13) are same, then grid filter stress τ_{ij}, test filter stress T_{ij} and resolved turbulent stress can be related in algebraic relation EQ (14)

$$T_{ij} - \tilde{\tau}_{ij} = \tilde{\overline{u}}_i \overline{u}_j - \tilde{\overline{u}}_i \tilde{\overline{u}}_j = 2C_{vT}^{3/2} \Delta [\overline{g(\overline{u}_i, \overline{u}_{pi}, N)} \overline{S}_{ij} - \alpha^2 g(\tilde{\overline{u}}_i, \tilde{\overline{u}}_{Pi}, \tilde{N}) \tilde{\overline{S}}_{ij} \qquad (14)$$

From EQ (14), $C_{vT}(x, y, z, t)$ can be obtained in principle. The quantity in square brackets, however, can become zero, which would make C_{vT} indeterminate or ill-conditioned. For the channel flow, therefore, it was assumed that C_{vT} is only a function of y and t. The average of both sides of EQ (14) are taken over a plane parallel to the wall to yield

$$C_{mS} = C_{vT}^{3/4} = \left[\frac{< \tilde{\overline{u}}_i \overline{u}_j - \tilde{\overline{u}}_i \tilde{\overline{u}}_j >}{2\Delta^2 < \overline{g(\overline{u}_i, \overline{u}_{Pi}, N)} \overline{S}_{ij} - \alpha^2 g(\tilde{\overline{u}}_i, \tilde{\overline{u}}_{Pi}, \tilde{N}) \tilde{\overline{S}}_{ij} >} \right]^{\frac{1}{2}} \qquad (15)$$

The new dynamic eddy viscosity subgrid-scale stress model, which takes into account of the interaction of particles-fluid SGS components in LES, is then given by

$$\tau_{ij} = \left[\frac{< \tilde{\overline{u}}_i \overline{u}_j - \tilde{\overline{u}}_i \tilde{\overline{u}}_j >}{\alpha^2 g(\tilde{\overline{u}}_i, \tilde{\overline{u}}_{Pi}, \tilde{N}) \tilde{\overline{S}}_{ij} - \overline{g(\overline{u}_i, \overline{u}_{Pi}, N)} \overline{S}_{ij}} \right] g(\overline{u}_i, \overline{u}_{Pi}, N) \overline{S}_{ij} \qquad (16)$$

4. Simulation overview

4.1 Calculation of fluid phase

The particle-laden turbulent flows between plane channels driven by uniform pressure gradient and particles gravity were calculated by large eddy simulations at Reynolds numbers based on friction velocity and channel half-width of 644. Van Driest damping function model and dynamic SGS models with (the present model) or without (Germano's model) couplings of SGS components were applied respectively. The governing equation EQ (1) and continuity equation were solved numerically by SMAC method on a staggered grid. Second-order central difference scheme was used for the advection and diffusion terms, and second-order Adams-Bashforth method was adopted for time advancement. The Poisson equation for pressure was solved using ICCG method. The flow was resolved using $32 \times 64 \times 32$ grid points in the x, y and z directions, respectively. The channel domain for the calculation was $\pi\ \delta \times 2\ \delta \times \pi\ \delta / 2$. For fully developed channel flow, periodic boundary conditions for the dependent variables were applied in the streamwise and spanwise directions, whereas the no-slip condition was applied on the channel walls.

4.2 Calculation of particle phase

The motion of particles was integrated using second-order Adams-Bashform in time, and third -order Lagrange polynomials were used to interpolate the fluid velocity to the particle position since it is only by chance that a particle is located at a grid point where the Eulerian velocity is available. For particles that moved out of the channel in the streamwise or spanwise directions, the periodic boundary conditions were used to introduce them into the computational domain. The channel walls were perfectly smooth and a particle was assumed to contact the wall when its center was one radius from the wall. Elastic collisions were assumed for particles contacting the wall.

The initial condition of single phase Eulerian velocity field was given by a statistically developed solution. Then the particles were assigned to random locations throughout the cannel, where the initial particle velocity was assumed to be the same as the fluid velocity at the particle location. Similar to the fluid flow, statistics of the particle velocity were averaged over two homogeneous directions, both channel halves and time. To distinguish the effect of two way coupling, the 70 μ m Copper particles were blended at mass loading ratio1.0.

5. Calculation results

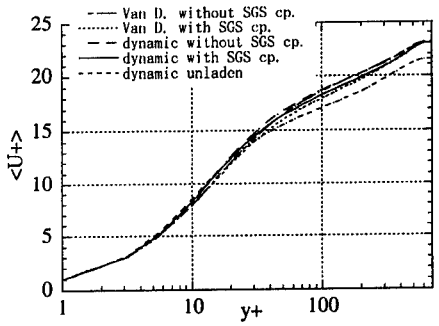


Figure 1. Profile of streamwise mean velocity of fluid

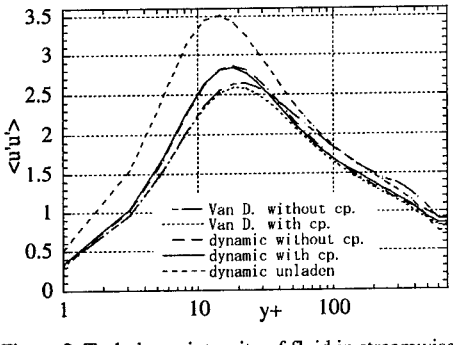


Figure 2. Turbulence intensity of fluid in streamwise

The numerical simulations were carried out using Van Driest wall function and the present dynamic SGS model, while the SGS coupling was taken into account or not respectively. The streamwise mean velocities of fluid are shown in Figure 1, the root-mean-square velocity fluctuations of fluid in streamwise are shown in Figure 2. As may be observed in figures above, in spite of the SGS coupling is taken into account or not, the mean velocities are predicted larger, and the root-mean-square velocity fluctuations are also slightly larger using proposed dynamic SGS models than using Van Driest wall function. Since this characteristic is similar to single-phase turbulent flow using standard dynamic SGS model, we can say that the present SGS model has proper asymptotic behavior near the wall without the use of *ad hoc* damping function in case of multiphase turbulent flow. As shown in Figure 2, the turbulence intensities of

particle-laden flow are clearly decreased than ones of particle-unladen flow for the coupling of GS components of particle-laden flow, but the turbulence intensities of particle-laden flow are hardly decreased when the SGS coupling was taken into account.

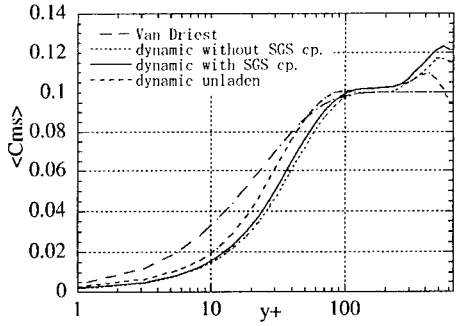


Figure 3. Profile of mean model coefficients

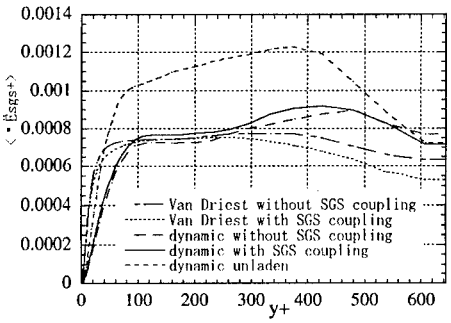


Figure 4. Profile of mean SGS eddy viscosity

The eddy viscosity model coefficients that were calculated by proposed dynamic SGS model are shown in Figure 3. In the channel buffer region, the dynamic SGS model coefficient of particle-laden flow is smaller than that of particle-unladen flow. On the contrary, in the channel center area, the former is higher than the latter. Since the effects of two-way coupling of GS and SGS components correspond the profile of turbulence intensity of fluid in wall normal, the coefficient of proposed dynamic SGS model obtains the correct asymptotic behavior in the near-wall region. In logarithm law region(y+$\sim$100), where concentration of the local particles is lowest, the proposed model obtains the fittest value Cm$\sim$0.1 in single-phase channel turbulent flows. It reflects the local structure of small eddies, showing that the capability of proposed model is validated.

The mean distributions of eddy viscosity are shown in Figure 4. In the near-wall region (y+<30), as the effects from SGS component to GS component are relatively small, the distribution of model coefficients correspond the profile of eddy viscosity as they are. While in the logarithm law region, though the model coefficients are roughly same, the effect of two-way coupling of GS components is significant, which may result from the difference of strain velocity S. As a result of taking into account of two-way coupling of SGS component, the model coefficients become bigger, which is agreed with the tendency that dissipation of turbulence is enhanced in high frequency.

The cascade profile of GS turbulence energy with or without SGS component coupling is shown in Figure 5, the energy cascade becomes slightly stronger owing to SGS coupling as expected. This indicates that the contribution of SGS component to GS component is shown as dissipation of GS component. According to this simulation result, the efficiency of presented dynamic two-way coupling SGS Model is verified. Intriguingly, contrary to the conjecture of Yamamoto[5] et al. (1998), the spatial spectra of fluctuation energy becomes a

little stronger with SGS coupling than that without it as shown in Figure 6.

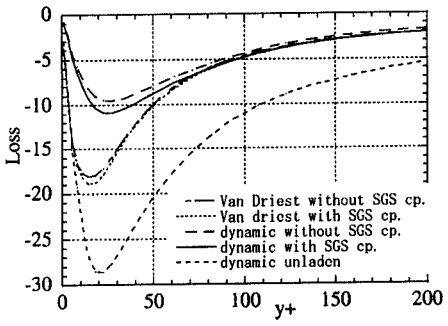


Figure 5. Cascade Profile of GS turbulence energy

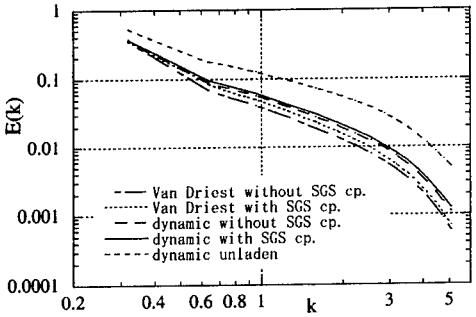


Figure 6. Streamwise spatial spectra of fluctuation enegy at y+=5

6. Concluding remarks

(1) A new dynamic SGS model has been proposed for two way coupling LES of particle-laden turbulent flow based on Yuu' s SGS model, in which the couplings of fluid-particles SGS component on fluid turbulence modulation was taken into account and at the same time the coefficient of proposed SGS model can be dynamically obtained as the calculations progress rather than input *a priori*.

(2) As a result of taking into account of two-way coupling of SGS component, the dynamic model coefficients become bigger, and in the channel buffer region, the proposed dynamic model coefficient of particle-laden flow is smaller than that of particle-unladen flow, on the contrary, the former is higher than latter in the channel center area.

(3) Numerical simulation results using the new dynamic model proposed reflected the local structure of small eddies of particle-laden, showing that the capability of proposed model was validated.

Reference

1. Germano, M., Piomelli, U., Moin, P., & Cabot, W.H., (1991) A dynamic subgrid-scale eddy viscosity model, *Phys. Fluids*, A3, pp.1760-1765.
2. Smagorinsky, J., (1963) General circulation experiments with the primitive equations, I. The basic experiment, *Mon. Weather Rev.*, Vol.91, No.3, pp.99-164.
3. Van Driest, E. R., (1956) On turbulent flow near a wall, *J. Aeronaut. Sci.*, Vol.23, pp.1007 -1011,
4. Yuu, S., (1997) Effects of particle existences on low and high Reynolds number gas-particle jets, *ISAC'97 High Performance Computing on Multiphase Flows*, pp.67-73.
5. Yamamoto, Y., Tanaka, T., & Tsuji, Y., (1998) LES of gas-particle turbulent channel flow (The effect of inter-particle collision on structure of particle distribution), *Proceedings of 3rd International Conference on Multiphase Flow (CD-ROM)*, Paper 518, pp.1-7.

EVALUATION OF TIME AND SPACE SCALES IN A SPATIALLY DEVELOPING 3D TURBULENT INCOMPRESSIBLE MIXING LAYER BY USING LES

S. PELLERIN, A. DULIEU, C. TENAUD, L. TA PHUOC
L.I.M.S.I. - UPR CNRS 3251
BP 133, F-91403 Orsay Cedex, France

Abstract

The spatial development of a 3D turbulent incompressible mixing layer is computed by using Large Eddy Simulation (LES). The time and space fluctuations of velocity components lead to the energy spectra. We can then to highlight the characteristic scales in both time and space. The energy spectra in time are in agreement with the turbulence theory and show two significant dimensionless frequencies; the largest one encountered for all the variables corresponds to the creation of main rolls. On the energy spectra in space, we can observe also two spanwise scales, one of them is found everywhere in the flow while the other one is representative of the phenomena inside the mixing zone.

Key words: Turbulence, Mixing layer, LES, Time and space scales.

1. Introduction

In incompressible flows, a mixing layer develops at the confluence of two parallel flows with different velocities, from the trailing edge of a flat plate (fig. 1.a). Instabilities then grow and eddy structures appear in the mixing zone, such as Kelvin-Helmoltz rolls, aligned with spanwise direction. A second instability creates other streamwise vortices (*braids*), observed between main structures. We study the spatial development of a 3D turbulent incompressible mixing layer, at a high turbulent Reynolds number. Therefore, control methods and flow reconstruction methods such as POD approach, require good unsteady descriptions of spatially developed flows.

The Reynolds number $\mathcal{R}_e = 3.5 \times 10^4$ is based on the velocity difference $U_{high} - U_{low}$ ($U_{high} = 42.8$ m/s and $U_{low} = 25.2$ m/s) and on the value of the

vorticity thickness experimentaly mesured at a reference section in the similarity zone, as $\delta_\omega(x_0) = 0.03$ m.

The mixing layer development is computed with a LES code, using a velocity-vorticity formulation. The influence of the subgrid model has been previously studied (Lardat *et al.* , 1998). It was also pointed out that the upstream condition has a significant influence on the quality of the results (Pellerin *et al.* , 1999). The velocity and the Reynolds stress tensor profiles show self-similarity behavior and a good agreement with the reference experiment data (Delville, 1994).

Coherent structures have been visualized in this simulation and a study of the energy spectra in time and space, associated to this turbulent mixing layer computed by LES, would be able to find their time and space characteristics and are analyzed in order to recover the classic properties of the turbulence phenomena. Energy spectra are represented in appropriate y positions, to highlight the time and space characteristic scales of the flow. Our numerical results are compared to experimental ones and to the well known theoretical behaviors.

2. Numerical method : LES

We use a velocity-vorticity formulation of the Navier-Stokes equations. In LES, the exact field ϕ is split into a filtered variable $\overline{\phi}$ and a subgrid variable ϕ'. The incompressible vorticity transport equation can then be written as:

$$\frac{\partial \overline{\omega}}{\partial t} - \nabla \times (\overline{v} \times \overline{\omega}) = -\frac{1}{\mathcal{R}_e} \nabla \times (1 + \nu_t) \nabla \times \overline{\omega} \quad ; \quad \overline{\omega} = \nabla \times \overline{v} \tag{1}$$

where $\overline{v}$ and $\overline{\omega}$ correspond to the filtered variables, resolved on the grid. The subgrid effects are based on the Taylor theory by means of a subgrid model using an eddy viscosity, ν_t, related to the macroscopic quantities. The filtered velocity and pressure fields are obtained by a projection method (Lardat *et al.* , 1997).

A mixed scale subgrid model is used here (Ta Phuoc, 1994):

$$\nu_M = \left[(C_S \Delta)^2 \|\omega\| \right]^\alpha \left[C_B \Delta \sqrt{|k'|} \right]^{1-\alpha} \tag{2}$$

where k' corresponds to a kinetic energy associated to the subgrid cell. Note that we obtain classical vorticity and TKE models for special values of the α exponent (0 and 1 respectively). C_S and C_B correspond to the Smagorinsky and the Bardina constants respectively. Following several simulations, we choose $\alpha = 0.5$ which leads to the better results for this kind of problem. The advantage of this model is to dump smoothly the eddy viscosity in the regions where all the scales are well resolved.

The upstream condition corresponds to the mean velocities, according to experimental values (Delville, 1994). A rather high white noise is superimposed on this condition in order to obtain a correct development of the mixing layer (Pellerin *et al.* , 1999).

At the outlet surface, a convective transport hypothesis is applied (viscous effects neglected). The vorticity tangential components are calculated using an extrapolation along the characteristics. The outlet propagation velocity $\overline{v_x}$ is deduced from vorticity, taking into account the mass flux conservation over this surface. In the inhomogeneous direction (y), a slip condition is imposed at the lower and upper surfaces. A periodicity condition is used for the spanwise direction (z).

A staggered M.A.C. grid is used for the spatial discretization (inhomogeneous grid in y). Time and space derivatives are estimated by second order schemes. The LES code used has been vectorized and reaches very good performances, the use of FFT allowing speed improvement (for homogeneous directions). For example, on a NEC-SX5 with a maximal performance of 8 GFlops (IDRIS-CNRS, Orsay), we obtain for a classical run about 5 GFlops (7×10^{-7} sec./time step/point).

3. Statistical study of the turbulent mixing layer

Vorticity thickness, velocity and stress tensor components

Solving unsteady Navier Stokes filtered equations for incompressible flows, we obtain then the unsteady velocity components. The figure 1.b shows the evolution in time (for 3000 time steps) of the flow direction component u, for three positions over the shear direction y. This variable has a strong turbulent behavior inside the mixing layer (at $y = 0$ on the figure) and very low variations outside of it (at $y = \pm\delta_\omega$ here).

Therefore, mean values are computed over a large integration time over 9000 time steps. Using a reference time of $\delta_\omega(x_0)/\left(U_{high} - U_{low}\right)$, this interval corresponds to a dimensionless time of 61.7. We then obtain the mean velocity values and also the Reynolds stress tensor components. The mean values in time are next averaged over the transversal direction z to compare with experimental data.

The characteristic lenght of this flow is the vorticity thickness $\delta_\omega(x)$ which increases linearly with the flow direction x. Turbulent structures in the mixing layer can be observed for $y \in [-\frac{\delta_\omega}{2}, +\frac{\delta_\omega}{2}]$, where y is the shear direction. The vorticity thickness is calculated from the mean longitudinal velocity $\langle\overline{u}\rangle$:

$$\delta_\omega(x) = \left[\langle\overline{u}\rangle_{max} - \langle\overline{u}\rangle_{min}\right] / \left(\frac{\partial \langle\overline{u}\rangle}{\partial y}\right)_{max} \tag{3}$$

The self similarity behavior is recovered when using the dimensionless parameters δ_ω and $\Delta U = U_{high} - U_{low}$. The velocity profiles show a good self-similarity behavior (fig. 2.a). While it is more difficult to converge the Reynolds stress tensor components, the resolved profiles are similar and show the quality of our simulation (fig. 2.b), using the mixing scale subgrid model and an appropriate upstream perturbation. All the results agree with experimental ones.

Energy spectra computation

Energy spectra in time and space are computed from velocities, which can be stored through the calculation and on the 3D grid. There are about two million points in the mesh. Therefore, we select for storage five vertical positions y, such as the center of the mixing layer $y = 0$, its up and down boundaries $y = \pm\ \delta_\omega/2$ and two positions outside of the mixing layer, $y = \pm\ \delta_\omega$. It is well known that these are the right positions to exhibit the characteristical scales. In addition, special values of the longitudinal x locations are selected inside the self-similarity zone, where the mixing layer is fully developed. In conclusion, the velocity storage is performed for all time steps and for all spanwise direction points, for these particular (x, y) locations (these positions are represented on figure 1.a).

The Kintchine's theorem about random steady functions (Chassaing, p46, 2000) allows to obtain the energy spectra using a Fourier transformation for velocity fluctuations. The energy spectra in time as functions of frequencies f are computed with a common vectorized FFT. The same procedure is followed in space, for the transversal direction z. The energy spectra in space are represented as function of the wave numbers k_z.

4. Energy spectra results and characteristic scales

For a normalized representation, we use the dimensionless wave numbers $k_{za}(x) = k_z * \delta_\omega$ and the dimensionless frequencies $f_a(x) = \frac{f\delta_\omega}{U_{ref}}$. We choose for the reference velocity $U_{conv} = (U_{high} + U_{low})/2$, according to the Taylor's hypothesis. Energy spectra are then plotted as function of the (local) dimensionless frequencies f_a and the (local) dimensionless wave numbers kz_a.

Some characteristic dimensionless frequencies or wave numbers can be identified and correspond to the characteristic scales in time and space. For time energy spectra, the characteristic scale is found for the maximal value, just before the theoretical fall down. Spatial evolutions are controled by a spatial scale which is a wave length, obtained by $\Lambda_z = 1/k_z$ and unsteady phenomena are characterized by a time scale $T = 1/f$.

Energy spectra in space, associated to the spanwise direction z, are presented on figure 3 for u_x, u_y and u_z velocity components, as function of the dimensionless wave numbers. Spectra are plotted for two different x locations. For every y position in the mixing layer, we find equivalent evolutions for both x positions. Spectra have maximal values in the center of the mixing layer, at $y = 0$ and decrease from the center to ouside. Outside of the mixing zone, energy spectra present very small intensities. Therefore, energy is localized in the mixing layer where the velocity gradient is representative of the flow behavior.

A first characteristic spatial scale is encountered in energy spectra for all velocities. Its value is about 0.15-0.18 and coincides with the largest scale (wave length) observed experimentally, equal to 0.15. This scale is representative of turbulent

phenomena everywhere in the flow for u_y and u_z velocities (figs. 3.a and 3.b) and outside of the mixing layer for u_x (fig 3.a).

We find a second spatial scale in u_x energy spectra, which characterizes the spatial evolution inside the mixing layer. This scale is 0.5 at the boundaries of the shear zone ($\pm\ \delta_\omega/2$) and stabilizes itself at 0.65 in $y = 0$. The u_y energy spectra show also this characteristic scale, because of divergence free effects. In these spectra, this scale is clearly visible only in the center of the mixing layer, at $y = 0$, and is equal to 0.7. This second scale has been estimated experimentally to be equal to 0.5.

Therefore, the characteristic spatial scales obtained numerically are in good agreement with experimental results, which means that the spatial behaviors must be rather well simulated. The main conclusion is the highlight of two characteristic scales for u_x, one representing phenomena inside the mixing layer and the other outside of the mixing zone.

The characteristic spatial scale representative of phenomena inside the mixing layer, $kz_a = kz * \delta_\omega \simeq 0.5 - 0.65$, can be associated to the wave lenght $\Lambda_z \simeq [1.54 - 2.]\ \delta_\omega$. This spanwise scale characterizes the spacing between two successive secondary structures (braids). We recover approximatively experimental results of Bernal and Roshko for the equivalent problem.

Figure 4.a represents the time energy spectra for u_x velocity, using as self-similarity parameter, the dimensionless frequency $\frac{f\delta_\omega}{U_{conv}}$. Inside the mixing layer, from the center $y = 0$ to the frontiers $y = \pm\ \delta_\omega/2$, energy spectra have equivalent evolutions and are similar for the three different chosen positions x. A characteristic scale f_a less than 0.2 is clearly found and aggrees with the experimental value of 0.15 observed by Delville (1995). An other time scale expresses the behavior outside the mixing layer. The value of this scale compares well quantitatively with the experimental one equal to 0.3.

Energy spectra for u_y is plotted on figure 4.b. Everywhere within the flow, for all y positions, the same scale is representative of turbulent phenomena, about 0.3. We don't represent here energy spectra for the transversal velocity u_z because we find the same behavior as u_y. In addition, these two velocities have energy spectra which do not depend on the x position.

The main characteristic time scale $f_a \simeq 0.3$ can be associated to a longitudinal wave lenght $\Lambda_x = T * U_{conv}$, which controls longitudinal space evolutions. We can then write $\Lambda_x = 3.33\ \delta_\omega$. This longitudinal lenght represents the spacing between two successive spanwise vertices (Kelvin-Helmoltz instabilities). If we consider the ratio between the transversal wave lenght Λ_z and the longitudinal one, $\Lambda_z/\Lambda_x \simeq 0.46 - 0.6$ which compare quantitatively well with the experimental value of 2/3 usually found.

On figures 4.a and 4.b, the decrease of curves after their maximal values (characteristic scale in time), have at least over one decade a correct slope of approximatively - 5/3, according to the well known theoretical slope of the energy cascade.

5. Conclusion

A 3D spatially developed mixing layer is studied numerically using LES. Energy spectra are computed in order to highlight the characteristic scales in both time and space. Two spanwise scales are found; one is encountered everywhere in the flow and the other is representative of the spanwise spacing between braids. In addition, two dimensionless frequencies are observed on energy spectra in time, which behave well. The largest frequency corresponds to Kelvin-Helmoltz instabilities.

Acknowledgements

The authors would like to acknowledge J. Delville from C.E.A.T. of Poitiers, France, for his collaboration concerning his experimental results. The authors would also acknowledge the support of I.D.R.I.S.-C.N.R.S (Orsay, France), where the calculations have been performed on a NEC-SX5.

References

Bertagnolio, F. (1996) Thèse de Doctorat de l'Université Pierre et Marie Curie, Paris 6.

Chassaing, P. (2000) *Turbulence en mécanique des fluides*, Cépaduès Editions, Toulouse.

Delville, J. (1994) Characterization of the organization in shear layers via the proper orthogonal decomposition, *Applied Scientific Research*, **53**, pp. 263-281.

Delville, J. (1995) *La décomposition orthogonale et l'analyse de l'organisation tridimentionnelle d'écoulements turbulents cisaillés libres*, Thèse de Doctorat de l'Université Pierre et Marie Curie, Paris 6.

Lardat, R. 1997 Thèse de Doctorat de l'Université d'Orsay, Paris 11.

Lardat, R., Dulieu, A., Ta Phuoc, L. and Tenaud, C. (1998) L.E.S. of a spatially developing 3-D incompressible mixing layer with velocity-vorticity formulation, 16^e *ICNMFD*, Arcachon, France.

Lardat, R., Bertagnolio, F. et Daube, O. (1997) La formulation vitesse-tourbillon en maillage décalé : une méthode de projection, *C.R.Ac.Sc.*, **324, II b**, pp. 747-753.

Pellerin, S., Dulieu, A., Ta Phuoc, L. and Tenaud, C. (1999) Incompressible 3-D mixing layer using LES : Influences of subgrid scale models and of upstream perturbations, *ISCFD'99*, Bremen, Germany. Proceedings published in a Special Issue of *Computational Fluid Dynamics Journal*, **9**, no.1, April 2001.

Ta Phuoc, L. (1994) Aérodynamique instationnaire turbulente - Aspects numériques et expérimentaux, *Journée Thématique DRET*, Paris, France.

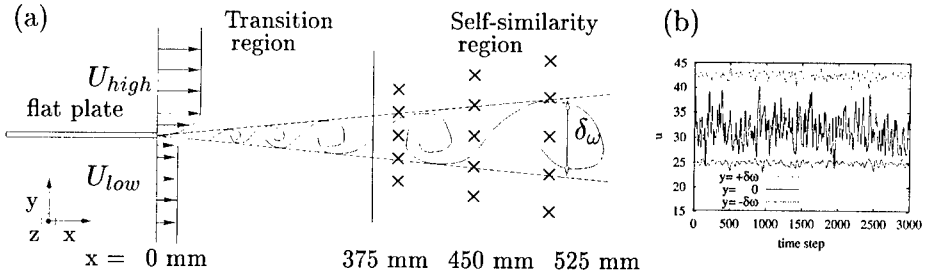


Figure 1. (a) Spatially developing mixing layer geometry. The mixing phenomena establishes behind the trailing edge of a flat plate, at the confluence of two different velocity turbulent flows; $\times$: (x, y) storage locations for energy spectra computation; (b) Longitudinal velocity u inside the mixing layer at $y = 0$ and outside at $y = +\delta_\omega$ ($u \simeq U_{high} = 42.8$ m/s) and $y = -\delta_\omega$ ($u \simeq U_{low} = 25.2$ m/s), evolution for 3000 time steps.

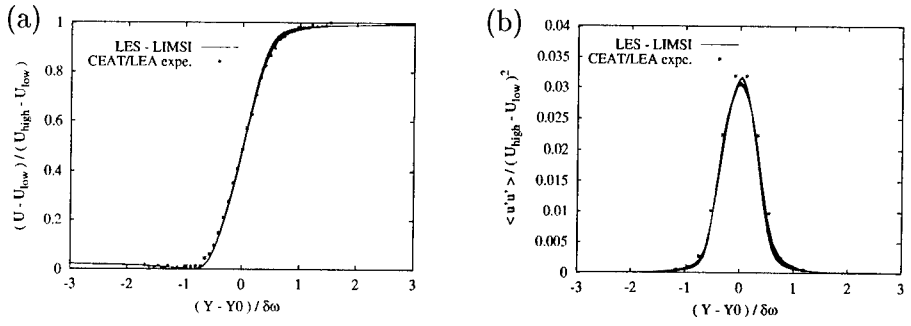


Figure 2. Superposition of profiles (at ten streamwise locations) versus the self-similarity parameter $(y - y_0)/\delta_\omega$. (a) u_x mean velocity; (b) first component of the Reynolds stress tensor, $< \overline{u}'^2 >$. L.E.S. performed using mixed scale model and white noise perturbation of 7.5% U_{high}.

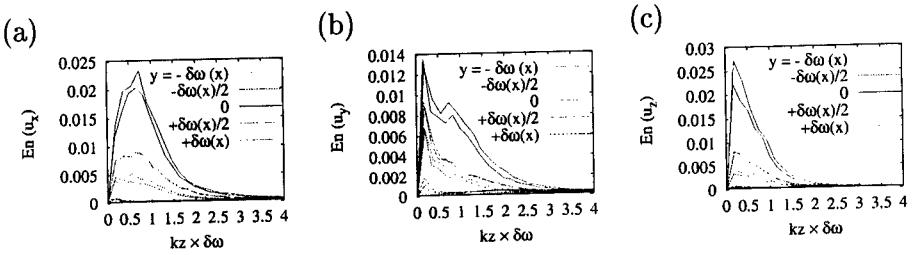


Figure 3. Spatial energy spectra for the spanwise direction z, inside and outside the mixing layer, for two x locations from the flat plate, 450 mm and 525 mm: (a) energy spectra for u_x velocity, which show two characteristic scales in space; (b) energy spectra for u_y velocity; (c) energy spectra for u_z velocity.

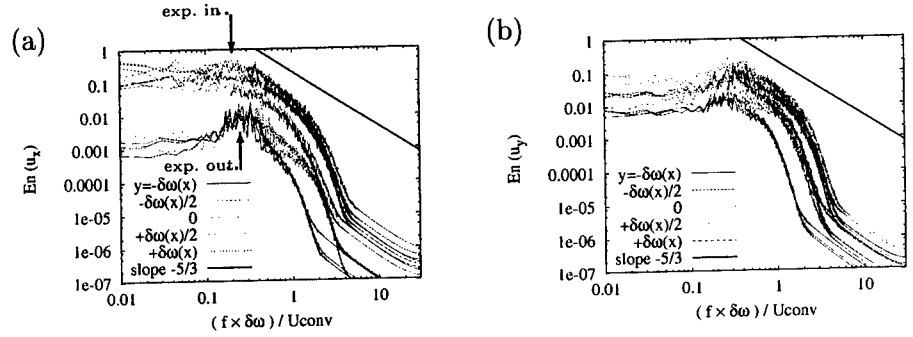


Figure 4. Time energy spectra inside and outside the mixing layer, for three x locations from the flat plate, 375 mm, 450 mm and 525 mm : (a) energy spectra for u_x velocity, which show two characteristic scales in time; (b) energy spectra for u_y velocity, with only one characteristic scale.

LARGE EDDY SIMULATION OF ROTATING TURBULENT CONVECTION USING THE SUBGRID SCALE ESTIMATION MODEL

SHARI J. KIMMEL
Department of Mechanical Engineering and Mechanics,
Lehigh University,
Bethlehem, PA 18015-3085

AND

J. ANDRZEJ DOMARADZKI
Department of Aerospace and Mechanical Engineering,
University of Southern California,
Los Angeles, California 90089-1191

Abstract. A large eddy simulation with the estimation subgrid scale model was used to simulate rotating convective flows up to a Rayleigh number of 8.4×10^6. The flow fields demonstrated expected qualitative properties of rotating flow including radially oriented convective plumes. The Nusselt number and mean temperature profiles show the decreased mixing due to rotation and agree well with DNS results. For higher Rayleigh numbers, including truncated Navier- Stokes dynamics resulted in better agreement with DNS.

1. Introduction

Turbulent convective flows under the influence of strong rotation are important in the study of geophysical flows. In the arctic regions, convection and other buoyancy effects drive large scale thermohaline circulations and convective processes which ultimately influence global oceanic circulations. The purpose of the current research is to apply turbulent simulations to rotating turbulent convection in order to better understand convective geophysical flows. The evolution of turbulent convective structures has been studied both experimentally (Fernando *et al.*, 1991; Coates *et al.*, 1995)

and numerically, including DNS (Julien *et al.*, 1996) and LES with a constant eddy viscosity model (Jones & Marshall, 1993). Initially the growth of buoyant plumes are dominated by convection. When they reach a transition depth h_c (Fernando *et al.*, 1991), the plumes are constrained horizontally due to the rotation. In addition, high rotation causes the plumes to elongate in the radial direction and the distance between plumes to decrease.

The subgrid scale estimation model has been used successfully in both high Reynolds number flows (Domaradzki & Saiki, 1997) and turbulent convection (Kimmel & Domaradzki, 2000). In this study, we have examined the estimation model applied to convective, rotating flows. The incompressible Navier-Stokes equations are spatially filtered to yield the large eddy simulation (LES) equations for rotating turbulent convection. Spatial filtering applied to $f(x)$ is defined by the relation

$$\overline{f}(x) = \int f(x')G(x,x')dx', \tag{1}$$

where G is a given filter function. The LES equations to be solved are

$$\frac{\partial \overline{u}_j}{\partial x_j} = 0 \tag{2}$$

$$\frac{\partial \overline{u}_i}{\partial t} + \frac{\partial \overline{u}_i \overline{u}_j}{\partial x_j} + \sqrt{Ta} Pr\, \overline{u}_j \epsilon_{ij3} = -\frac{\partial P}{\partial x_i} + Pr \frac{\partial^2 \overline{u}_i}{\partial x_j \partial x_j} - \frac{\partial}{\partial x_j}\tau_{ij} + Pr\, Ra \overline{T} \delta_{i3} \tag{3}$$

$$\frac{\partial \overline{T}}{\partial t} + \frac{\partial \overline{u}_j \overline{T}}{\partial x_j} = \frac{\partial^2 \overline{T}}{\partial x_j \partial x_j} - \frac{\partial}{\partial x_j}\tau_{\theta j}. \tag{4}$$

In these equations, the flow is assumed to be incompressible, consistent with the Boussinesq approximation, and dependent only on the vertical component of rotation.

The Rayleigh number is defined as

$$Ra \equiv \frac{\alpha g \Delta T H^3}{\nu \kappa},$$

and the Prandtl number as

$$Pr \equiv \nu/\kappa,$$

where ΔT is the temperature difference between the upper and lower surfaces, α is the volumetric thermal expansion coefficient, g is the acceleration due to gravity, and ν and κ are the molecular viscosity and diffusivity,respectively. The equations are nondimensionalized using diffusivity κ and the depth of the flow H. The Taylor number (Ta), which represents the ratio of rotational forces to viscous forces, is defined as

$$Ta \equiv \frac{4\Omega^2 H^4}{\nu^2}.$$

In the estimation model, the subgrid scale stress tensor is computed directly from the definition using the approximated unfiltered velocity field (Domaradzki & Saiki, 1997). An estimate $\tilde{u}_i$ of the unfiltered velocity is obtained by expanding the resolved large scale velocity field, $\overline{u}_i$, to subgrid scales two times smaller than the grid scale. The estimation procedure consists of two steps. The first step utilizes properties of a top-hat filtering operation and the representation of the velocity field in terms of Fourier series. For the second step, the phases associated with the computed smaller scales are adjusted in order to correspond to the small scale phases generated by nonlinear interactions of the large scale field. Once the estimate $\tilde{u}_i$ of the full field u_i is known, the subgrid scale stress tensor is computed directly from the definition

$$\tau_{ij} = \overline{\tilde{u}_i \tilde{u}_j} - \overline{\tilde{u}}_i \overline{\tilde{u}}_j. \tag{5}$$

For convective flows the subgrid scale heat flux $\tau_{\theta i}$ is computed in a similar manner (Kimmel & Domaradzki, 2000).

Finally, to obtain a $\tilde{u}_i$ velocity field that obeys continuity, truncated Navier-Stokes dynamics are imposed by advancing the velocity field in time on the expanded mesh using the large eddy simulation equations without the terms that account for the interactions between the resolved scales and the subgrid scales (Domaradzki *et al.*, 2000). The current study is the first application of the estimation subgrid scale model in an LES of rotating turbulent Rayleigh-Bénard convection. Horiuti (1999) shows that, unlike dynamic models, estimation subgrid scale model with truncated Navier-Stokes dynamics obeys transformation rules required for the subgrid scale stress tensor in a noninertial frame of reference, and the LES results agree well with DNS data for rotating, homogeneous turbulence.

2. Numerical Simulations

LES of rotating turbulent convection between two parallel plates were performed in a three-dimensional rectangular domain. The boundary conditions are periodic in the horizontal direction. No-slip velocity and constant temperature boundary conditions are imposed on the top and bottom boundaries. The convection is driven by an unstable temperature gradient in the vertical direction. The simulations and relevant parameters for this study are shown in Table 1. Case R3t includes the truncated Navier-Stokes dynamics. The LES results shown here were computed using a resolution of 32x32x64, the same vertical resolution as a DNS but one quarter of the horizontal resolution. Exact Nusselt numbers are from DNS results for rotating (Julien *et al.*, 1996) and nonrotating (Kerr, 1996) turbulent convection. The

Rossby number, which is expressed as

$$Ro = \left(\frac{Ra}{PrTa}\right)^{1/2}, \tag{6}$$

measures the importance of rotation. These results were computed on a grid of 32x32x65 for a Rossby number of 0.75, and a Prandtl number of 1. At this Rossby number both buoyancy and rotational effects are important, and the LES correctly reproduces many qualitative features of experimental and DNS results for rotating convection.

TABLE 1. Parameters for LES simulations

case(LES)	Ra	Ta	Nu	Exact Nu
E2	$2.5\text{x}10^6$	0	13	11
R2	$2.5\text{x}10^6$	$4.5\text{x}10^6$	11	10
E3	$1.0\text{x}10^7$	0	19	16.6
R3	$8.4\text{x}10^6$	$1.5\text{x}10^7$	16	14.6
R3t	$8.4\text{x}10^6$	$1.5\text{x}10^7$	13.5	14.6

A measure of the amount of heat transfered between the two plates can be estimated using the Nusselt number which is the ratio of the total heat transfer to the conductive heat transfer. It is defined as

$$Nu = \frac{Q}{\kappa \Delta T/H}$$

where Q is heat flux between the upper and lower surfaces. Since the heat transfer depends on molecular transport and convective transport as a result of fluid motion, the Nusselt number has two components:

$$Nu = \frac{-\kappa d < T > /dz + < w'T' >}{\kappa \Delta T/H}, \tag{7}$$

the latter of which includes both the resolved and subgrid scale heat transfer. The fluctuating temperature T' and vertical velocity w' are variations from the mean

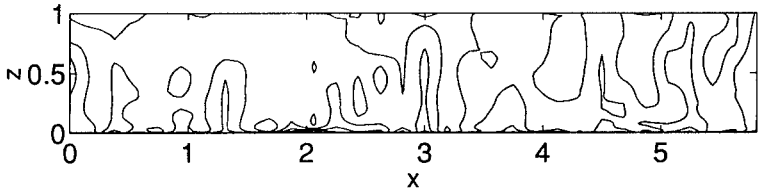
$$T' = T - < T >,$$

$$w' = w - < w >,$$

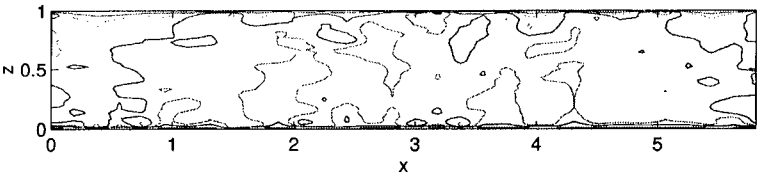
where $< \ldots >$ denotes a horizontally averaged quantity. The decreased mixing between the two plates is demonstrated by less heat transfer and

a smaller Nusselt number then the corresponding nonrotating flow. The Nusselt number from the simulation which includes the truncated Navier-Stokes dynamics has better agreement with the exact DNS results.

The influence of rotation on a turbulent convective flow is demonstrated for the temperature field by comparing LES data with results from an equivalent nonrotating flow (Kimmel & Domaradzki, 2000) in Figure 1 for vertical contours and in Figures 2 and 3 for horizontal planes. In both cases, the rotation causes the thermals to elongate in both the vertical direction and the horizontal direction perpendicular to the direction of rotation, as has been demonstrated experimentally (Rossby, 1969).



(a) $Ra = 8.4\text{x}10^6$, $Ta = 1.50\text{x}10^7$



(b) $Ra = 1.0\text{x}10^7$, $Ta = 0.0$ (nonrotating)

Figure 1. Temperature contours from LES data in a vertical plane through center of the domain for rotating and nonrotating turbulent convection.

The LES can correctly reproduce the steeper slope of the mean temperature gradient for nonrotating flow than for rotating flow. As shown in Figure 4, the agreement between the LES and DNS is very good for $Ra = 2.5\text{x}10^6$. In Figure 5, mean temperature profiles for simulations at $Ra = 8.4\text{x}10^6$ are shown. For the case, the slope of the mean temperature profile from the LES with truncated Navier-Stokes dynamics agrees better with the DNS results than the simulation without it. The difference between the results from these different simulations should be more significant at higher Rayleigh numbers.

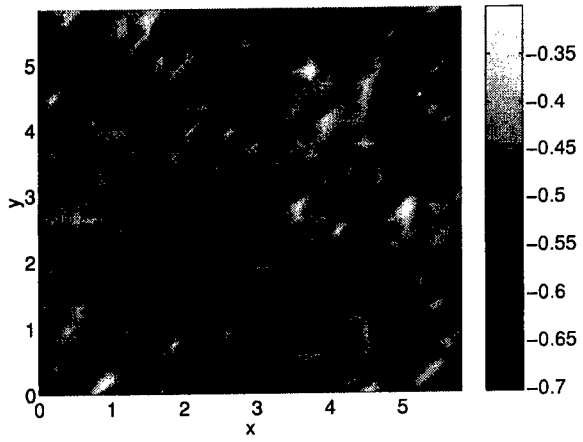


Figure 2. Gray scale plot of the fluctuating temperature in a horizontal plane through the center of the domain for $Ra = 8.4\text{x}10^6$ and $Ta = 1.5\text{x}10^7$.

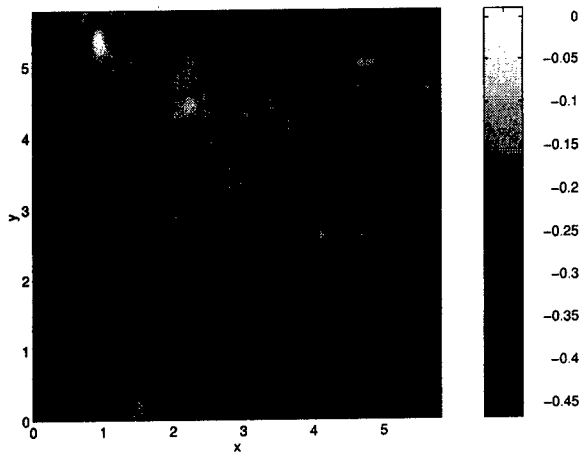


Figure 3. Gray scale plot of the fluctuating temperature in a horizontal plane through the center of the domain for $Ra = 8.4\text{x}10^6$ and $Ta = 0$.

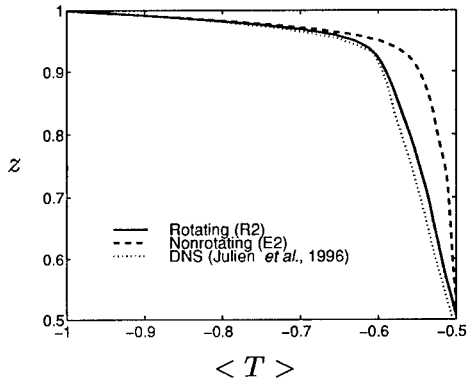


Figure 4. Comparison of mean temperature profile for rotating and nonrotating convective flow.

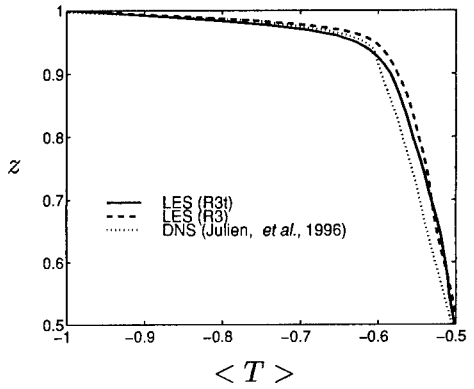


Figure 5. Comparison of LES vertical mean temperature profile with DNS results for $Ra = 8.44\text{x}10^6$, $Ta = 1.7\text{x}10^7$ for LES with (R3t) and without (R3) truncated Navier-Stokes dynamics

3. Summary

The estimation model was used to simulate rotating turbulent convection, and good agreement with DNS results was seen. However, better agreement between the LES and DNS for $Ra = 8.4\text{x}10^6$ and $Ta = 1.5\text{x}10^7$ is seen for the mean temperature profiles and Nusselt number when truncated Navier-Stokes dynamics is also applied. This improved version of the estimation model should result in improved results for strongly rotating convective flows at higher Rayleigh numbers.

4. Acknowledgements

This work was supported by the NSF Grant CTS-0075076.

References

Coates, M.J., G.N. Ivey & R.J. Taylor. 1995: Unsteady,Turbulent Convection into a Rotating Linearly Stratified Fluid: Modeling Deep Ocean Convection. *Journal of Physical Oceanography.* **25**,3032.

Domaradzki, J.A. and E.M. Saiki. 1997: A subgrid-scale model based on the estimation of unresolved scales of turbulence. *Phys. Fluids*, **9**, 2148.

Domaradzki, J.A., K.C. Loh, and P.P. Yee. 2000: Large eddy simulations using the subgrid-scale estimation model and truncated Navier-Stokes dynamics. *Journal of Fluid Mechanics.*,submitted.

Fernando, H.J.S., R.R. Chen Chen & D.L. Boyer. 1991:Effects of rotation on convective turbulence. *Journal of Fluid Mechanics.* **228**, 513.

Horiuti, K. 1999:Transformation properties of subgrid-scale models in a frame of reference undergoing rotation. *J. Fluid Mech.*,submitted.

Jones, Helen & John Marshall. 1993: Convection with Rotationin a Neutral Ocean: A Study of Open-Ocean Deep Convection. *Journal of Physical Oceanography.* **23**, 1009.

Julien, K., S. Legg, J. McWilliams, and J Werne. 1996: Rapidly rotating turbulent Rayleigh-Bénard convection. *Journal of Fluid Mechanics*, **322**, 243.

Kerr., R. 1996: Rayleigh number scaling in numerical convection. *Journal of Fluid Mechanics*, **310**, 139.

Kimmel, S.J. and J.A. Domaradzki. 2000: Large eddy simulations of Rayleigh-Bénard convection using subgrid scale estimation model. *Phys. of Fluids*, **12**, 169.

Maxworthy, T. & Narimousa, S. 1994: Unsteady, Turbulent Convection into a Homogeneous Rotating Fluid, with Oceanographic Applications. *Journal of Physical Oceanography.* **24**, 865.

Rossby, H.T. 1969: A study of Bénard convection with and without rotation. *Journal of Fluid Mechanics*, **36**, 309.

NUMERICAL ANALYSIS OF LARGE EDDY SIMULATION

A. DUNCA
Department of Mathematics, University of Pittsburgh, Pittsburgh, PA 15260, U.S.A.; ARDST21@pitt.edu

V. JOHN
Faculty of Mathematics, Otto-von-Guericke-University, Magdeburg, Germany; john@mathematik.uni-magdeburg.de
http://www-ian.math.uni-magdeburg.de/~home/john

W. J. LAYTON
Department of Mathematics, University of Pittsburgh, Pittsburgh, PA 15260, U.S.A., wjl@pitt.edu,
http://www.math.pitt.edu/~wjl

AND

N. SAHIN
Department of Mathematics, University of Pittsburgh, Pittsburgh, PA 15260, U.S.A.; NISST6@pitt.edu

Abstract. We have focused upon the development and validation of finite element methods for LES of turbulent flows in settings in which interaction with (possibly geometrically complex) boundaries are important. New results are presented in Section 2 on closure and convolution on bounded domains. Similarly, new near wall models were required; our method for developing these is described and one from our work is presented in Section 3. The difficulties in closure and wall modelling suggest a second approach: direct simulation of large eddy motion. We give an extension of this approach to nonlinear, equilibrium flows - a step closer to turbulence for an approach not requiring wall models or closure models.

1. Introduction

There is a natural interplay between Finite Element CFD and LES for topics such as: closure models, near wall models, and FEM postprocessing by

local averaging. Because of their geometric flexibility *and* their flexibility with respect to continuum models and linear or nonlinear boundary conditions, FEM's are a natural discretization in the LES of flows with complex boundaries. Adaptivity, highly developed for FEM's, has interesting potential for LES without modelling error. For example, using extensions of work in (John and Layton, 2001) reported in Section 4, a CFD mesh can be designed so that local averages of an inaccurate approximate flow field approximate the true local velocity averages with assured accuracy.

This paper surveys some of our work developing a mathematical foundation for finite element LES and presents some new results and extensions of this work. Many of the reports cited herein are available at http://www.math.pitt.edu/~wjl.

Consider therefore the turbulent flow of an incompressible fluid in three dimensions, bounded by walls and driven by a body force $f(x,t)$. The velocity-pressure (u,p) satisfy the Navier Stokes equations, given by:

$$u_t + \text{div}(uu) - 2Re^{-1}\text{div}\ (\mathbb{D}(u)) + \text{grad}p = f(x,t), \text{ and } \text{div}u = 0, \quad (1)$$

in a domain Ω complemented by boundary and initial conditions

$$u = 0 \text{ on walls, and } u(x,0) = u_0(x),$$

where $\mathbb{D}(u) = (\text{grad } u + \text{grad } u^t)/2$ is the velocity deformation tensor. Picking a length scale δ and an associated averaging kernel $g_\delta(x) := \delta^{-3}g(x/\delta)$, where $g(x)$ is a mollifier satisfying certain properties, local velocity and pressure averages are frequently defined by convolution with $g(x), \overline{u} := g_\delta * u, \overline{p} := g_\delta * p$, etc., where all functions are, when necessary, extended by 0 off the flow domain to compute the required average.

For compactness, we will only discuss herein the case of constant averaging radius δ. Alternate approaches include a variational definition of the large eddies (Layton, 1999), (Hughes *et al.*, 2001), and differential filters, introduced by Germano in the 1980's, wherein (in effect) $\delta = \delta(x) \to 0$ as x approaches walls in a manner intrinsic to the NSE and the domain's geometry, (Layton and Lewandowski, 2001).

2. Convolution on Bounded Domains and Closure

With constant averaging radius, δ, convolution operators commute with differential operators *in the absence of boundaries.* With boundaries, extra terms arise which are often overlooked. For example, filtering (1) with $g_\delta(x)$ on a bounded domain gives the following space filtered equations for $\overline{u} := g_\delta * u, \overline{p} := g_\delta * p$ (see (Dunca *et al.*, 2001))

$$\overline{u}_t + \text{div}(\overline{u}\ \overline{u}) - 2Re^{-1}\text{div}(\mathbb{D}(\overline{u})) + \text{grad}\overline{p} + \text{div}(\mathbb{T}(u)) = \overline{f} + A_\delta(\sigma), \quad (2)$$

where σ is the stress of the unknown flow and $\mathbb{T}(u) := \overline{uu} - \overline{u}\,\overline{u}$ is the Reynolds stress tensor. A direct calculation in (Dunca *et al.*, 2001) using the theory of distributions reveals that

$$A_\delta(\sigma) := \int_{\partial\Omega} g_\delta(x-s)(\sigma\cdot\hat{n})(s)ds, \quad \sigma := 2Re^{-1}\mathbb{D}(u) - pI,$$

which can be interpreted as a boundary stress distribution smeared out onto the entire flow domain. Since the $A_\delta(\sigma)$ term in (2) is normally neglected, it might be hoped to be negligible. Unfortunately, this is not the case, as is seen in the following result, (Dunca *et al.*, 2001).

Proposition. *Let* $||w||_{L^p} := (\int_{\mathbb{R}^3} |w|^p dx)^{1/p}, 1 \le p < \infty$ *denote the usual* L^p *norm,* $1 \le p < \infty$ *and* $||w||_{L^\infty} := \operatorname{ess\,sup}_{x\in\mathbb{R}^3} |w|$. *Then for* $1 \le p \le \infty$

$$||A_\delta||_{L^p} \to 0 \text{ as } \delta \to 0.$$

if and only if the normal stress is identically zero on the boundary of the flow domain

$$\sigma\cdot\hat{n} \equiv 0 \text{ on the boundary.} \ \square$$

The proof of this result is moderately technical but the importance of the result is clear: *the term* $A_\delta(\sigma)$ *cannot be omitted if the boundary influences the flow!*

It is well-known that (2) are *not closed* for periodic problems due (only) to the Reynolds stress tensor $\mathbb{T}(u)$ and numerous LES models have been developed to model $\mathbb{T}(u)$, see, e.g., (Iliescu and Layton, 1998), (Berselli *et al.*, 2001), (Layton, 2000), (Galdi and Layton, 1999), (Layton and Lewandowski, 2001) for our work on closure. For flows with real walls or other boundaries, (2) are not closed due to both $\mathbb{T}(u)$ and the "smeared" wall stress operator $A_\delta(\sigma)$. More detailed understanding of $A_\delta(\sigma)$ is necessary to model correctly the interaction of large eddies with walls; see (Dunca *et al.*, 2001) for first steps.

3. Near Wall Models: Boundary Conditions for LES

Either modeling or omitting the smeared wall stress term $A_\delta(\cdot)$, boundary conditions are still required for the large eddies $\overline{u}$ and simply imposing $\overline{u} = 0$ at walls is inconsistent, see (Galdi and Layton, 1999), Figure 1. This inconsistency is intuitively clear: a tornado, as an example of a large eddy, does move/slip along the ground.

What are then the correct boundary conditions? Motivated by this example of a tornado, we have explored no-penetration and slip-with-friction conditions (see, e.g., (Navier, 1823) and (Maxwell, 1879) for antecedents) for $\overline{u}$:

$$\overline{u} \cdot \hat{n} = 0 \text{ and } \beta_j \, \overline{u} \cdot \hat{\tau}_j + t(\overline{u}) \cdot \hat{\tau}_j = 0 \text{ on walls,} \tag{3}$$

where $\hat{n}, \tau_1, \tau_2$ are unit normal and tangent vectors to the wall (Layton, 2001), and t is the Cauchy stress or traction vector. The effective friction coefficient β for the large eddies is calculated explicitly in (Sahin, 2000) and (John *et al.*, 2001)

$$\beta = \beta(\delta, Re) \text{ or } \beta = \beta(\delta, |\overline{u} \cdot \hat{\tau}_j|) : \text{ large eddy friction coefficient.}$$

The conditions (3) thus allow both linear and nonlinear near wall models. For turbulent channel flow, the linear model, based on a global Reynolds number, seems to suffice. However, for flows in complex geometries, the local Reynolds number, related to the slip velocity $|\overline{u} \cdot \hat{\tau}_j|$, varies greatly from recirculation zones to mean stream regions. Thus, the nonlinear model seems necessary.

The friction laws in (Sahin, 2000), (John *et al.*, 2001) are calculated using boundary layer theory, with different results for different types of turbulent layers. For example, for a power law layer the linear wall model's effective friction coefficient is as follows. Let $\Gamma[\cdot]$ denote the usual gamma function and $\Gamma[\cdot, \cdot]$ the incomplete gamma function, $\eta = 0.21 Re^{-1}$ and $Z := \eta/\delta$

$$\beta(\delta, \eta) = \frac{Re^{-1} Z^{1/7} [7\Gamma[\frac{15}{14}] - \frac{1}{2}\Gamma[\frac{1}{14}, Z^2]]}{2\sqrt{\pi}\delta^2 [Z^{1/7}\{\Gamma[\frac{4}{7}] - \Gamma[\frac{4}{7}, Z^2]\} + \sqrt{\pi}(1 - \text{ erf}(Z))]}.$$

A very good (and simple) approximation is given (to 4 decimal places) by the effective friction coefficient:

$$\beta(\delta, Re) \cong Re^{-1}\delta^{-2} 1.22 e^{-0.008/Z}. \tag{4}$$

From this simple formula we see that:

- As $\delta \to 0$, for fixed Re, the friction $\beta \to \infty$, i.e., the boundary conditions (3) reduce to no slip.
- As $Re \to \infty$ for fixed δ, the friction coefficient $\beta \to 0$, i.e., the boundary conditions (3) reduce to free-slip and no-penetration, as appropriate for the Euler equations.

To explain the nonlinear friction laws we note that for a power law layer (and other profiles as well), the slip speed, $s := \sqrt{|\overline{u} \cdot \hat{\tau}_1|^2 + |\overline{u} \cdot \hat{\tau}_2|^2}$ is a monotone increasing function of Re for δ fixed. Expressing this as

$s = g(Re), g'(Re) > 0$ implies that the inverse function $g^*(\cdot)$ of $g(\cdot)$ exists. We can then write $Re = g^*(s)$. Inserting this inverted relation into (4) yields nonlinear friction laws:

$$\beta_j(\delta, g^*(|\overline{u} \cdot \hat{\tau}_j|)) \cong 1.22\delta^{-2} g^*(|u \cdot \hat{\tau}_j|) e^{-0.0090/g*(|\overline{u}\cdot\hat{\tau}_j|)}.$$

This program can be carried out for different types of turbulent boundary layer profiles, see (John *et al.*, 2001) for detailed formulas.

4. Numerical Errors in LES

With closure models and boundary conditions selected, convergence of a chosen numerical method to the model's solution must be considered, e.g. (John and Layton, 2000), (Iliescu *et al.*, 2000), (Layton, 1996). For example, in (John and Layton, 2000) convergence for a FEM discretization of the Smagorinsky model is proven to be *uniform in Re*, as is often reported in practical simulations but hitherto unproven. This work does *not* address the modelling error itself however.

In recent work, we have devised new algorithms which give computable bounds on *both the modelling and the numerical errors*, (John and Layton, 2000). This work was begun in (John and Layton, 2001) for (linear) Stokes flow. Our current work, reported in this section, has extended those new methods to the (nonlinear) equilibrium NSE - a step closer to the true problem.

The approach is simple to describe: the fluid velocity is directly approximated and then postprocessed by local averaging, giving $g_\delta * u^h$ as an approximation to $\overline{u} = g_\delta * u$. One key is that the finite element mesh is adapted within the calculation so that $g_\delta * u^h$ *approximates* $\overline{u}$ *with assured accuracy*, even when u^h is a bad approximation to u. The second key is that the averaging radius δ must be taken smaller than the local meshwidth of the refined mesh, $\delta << O(h)$. These new a posteriori estimators are given in (John and Layton, 2000) (and a new report in preparation). With these new estimators, the error is also concentrated in high frequencies and killed by postprocessing. Thus, the error in the large eddies is typically far smaller than the overall error, as in the following theorem.

Theorem. *Let the equilibrium NSE be solved by the FEM with finite element spaces satisfying the usual stability and local-polynomial degree k approximation conditions. Let the NSE solution be nonsingular with linearized dual H^{k+1}-regular. Then, the error in the large eddies $||g_\delta * u^h - \overline{u}||_{L^2}$ is related to (and much smaller than), the error in the velocity ($||\nabla(u - u^h)||$) and pressure ($||p - p^h||$) by, for any $\epsilon > 0$:*

$$||g_\delta * u^h - \overline{u}||_{L^2} \leq C\left\{\left(Re^{-1} + \sqrt{h}\right)\left(\frac{k}{\delta}\right)^k \delta ||\nabla(u - u^h)||_{L^2}\right.$$

$$+\left(\frac{h}{\delta}\right)^k \delta\left(||p-p^h||_{L^2}+||\nabla\cdot(u-u^h)||_{L^2}\right)$$
$$+\left(\frac{h}{\delta}\right)^k \delta||\nabla(u-u^h)||_{L^2}^2+\delta^{\frac{1}{2}-\epsilon}||u-u^h||_{L^2}^2\Big\}. \ \square$$

This theorem also gives analytical guidance for relating δ and h. However, the related mesh-adaptation strategy is the most important practical contribution of this theory.

Acknowledgement: The work of the second author was partially supported by the DAAD (Deutsche Akademische Austauschdienst). The work of the first, third and fourth authors was partially supported by NSF grants DMS9972622, INT9814115 and INT9805563.

References

A. Dunca, V. John, and W.J. Layton. Estimates of the commutation error in the space averaged Navier-Stokes equations. Technical report, 2001.

L.C. Berselli, G.P. Galdi, T. Iliescu, and W.J. Layton. Mathematical analysis for a new large eddy simulation model. Technical report, 2001.

G.P. Galdi and W.J. Layton. Approximating the larger eddies in fluid motion II: A model for space filtered flow. *M^3AS*, 10:343–350, 2000.

T.J.R. Hughes, A.A. Oberai, and L. Mazzei. Large eddy simulation of turbulent channel flows by the variational multiscale method. *Phys. of Fluids*, 13:1784–1799, 2001.

T. Iliescu, V. John, and W.J. Layton. Convergence of finite element approximations of large eddy motion. Submitted, currently under review, 2000.

T. Iliescu and W.J. Layton. Approximating the larger eddies in fluid motion, III: the Boussinesq model for turbulent fluctuation. *Analele Stin. Ale Univ. "Al. I. Cuza" Iasi, T. XLIV, ser. mat.*, pages 245–261, 1999.

V. John and W.J. Layton. Analysis of numerical errors in large eddy simulation. Submitted, currently under review, 2000.

V. John and W.J. Layton. Approximating the larger eddies in fluid motion, I: direct simulation for the Stokes problem. *Computing*, 66:269–287, 2001.

V. John, W.J. Layton, and N. Sahin, 2001. Report in preparation.

W. Layton. Approximating the larger eddies in fluid motion, IV: kinetic energy balance of scale similarity models. *Math. and Computer Modeling*, 31:1–7, 2000.

W.J. Layton. Analysis of a scale-similarity model of the motion of large eddies in turbulent flows. To appear in J. Math. Anal. Appls., 2001.

W.J. Layton. What are $\hat{n}$ and $\hat{\tau}$ in Navier's slip law? Technical report, Dept. of Mathematics, University of Pittsburgh, 2001.

W.J. Layton. On nonlinear subgrid scale models for viscous flow problems. *SIAM J. Sci. Computing*, 17:347–357, 1996.

W.J. Layton. A connection between subgrid scale eddy viscosity and mixed methods. To appear in Appl. Math. and Computing, 1999.

W.J. Layton and R. Lewandowski. Analysis of an eddy viscosity model for large eddy simulation of turbulent flows. Technical report, 2001.

J.C. Maxwell, 1879. Phil. Trans. Royal Society.

C.L.M.H. Navier. Mémoire sur les lois du mouvement des fluides. *Mém. Acad. Royal Society*, 6:389–440, 1823.

N. Sahin. New perspectives on boundary conditions for large eddy simulation. Submitted, currently under review, 2000.

ADAPTIVE NUMERICAL-DISSIPATION/FILTER CONTROLS FOR HIGH ORDER NUMERICAL METHODS

H. C. YEE
NASA Ames Research Center, Moffett Field, CA 94035, USA

AND

B. SJÖGREEN
Department of Numerical Analysis and Computer Sciences, KTH, 100 44 Stockholm, Sweden

Abstract.[1] Proper control of the numerical-dissipation/filter to accurately resolve all relevant multiscales of complex flow problems while still maintaining nonlinear stability and efficiency for long-time numerical integrations poses a great challenge to the design of numerical methods. The required type and amount of numerical-dissipation/filter are not only physical problem dependent, but also vary from one flow region to another. An approach for the automatic detection of different flow features as distinct sensors to signal the appropriate type and amount of numerical-dissipation/filter for non-dissipative high order schemes is proposed. These scheme-independent sensors are capable of distinguishing shocks/shears, turbulent fluctuations and spurious high-frequency oscillations. In addition, these sensors are readily available as an improvement over existing grid adaptation indicators. The same shock/shear detector that is designed to switch on the shock/shear numerical dissipation can be used to switch off the entropy splitting form of the inviscid flux derivative [31] in the vicinity the discontinuous regions to further improve nonlinear stability and minimize the use of numerical dissipation. The rest of the sensors in conjunction with the local flow speed and Reynolds number can also be used to adaptively determine the appropriate entropy splitting parameter for each flow type/region. The goal of this paper is to further improve nonlinear stability, accuracy and efficiency of long-time numerical integration of complex shock/turbulence/acoustics interactions and numerical combustion. The minimization of employing very fine grids to overcome the production of spurious numerical solution and/or instability due to under-resolved grids is also sought [29, 6].

1. Motivation and Objective

When employing finite time steps and finite grid spacings in the long-time integration of multiscale complex nonlinear fluid flows, nonlinear instability commonly occurs and the use of a numerical-dissipation/filter is unavoidable. Aside from acting as a post-processor step, most filters serve as some form of numerical dissipation. Without loss of generality, "numerical-dissipation/filter" is, hereafter, referred to as "numerical dissipation" unless otherwise stated. The required type and amount of numerical dissipation can vary drastically from one flow region to another (within the same problem) and are highly problem dependent. This is particularly

[1]Proceedings of the Third AFOSR International Conference on DNS/LES, Arlington, Texas, August 4-9, 2001. Part of this work was carried out while the second author was a visiting scientist with RIACS, NASA Ames Research Center.

true for unsteady high-speed turbulence and/or combustion problems. For this type of problem, it is of paramount importance to have proper control on the type and amount of numerical dissipation in regions where it is needed but nowhere else. Inappropriate type and/or amount can be detrimental to the integrity of the computed solution, especially for problems with no known analytical solution and/or experimental data for comparison.

The linear and nonlinear numerical dissipation presently available is either built into the numerical scheme or added on to the existing scheme. The built-in numerical dissipation schemes are, e.g., upwind, flux corrected transport (FCT), total variation diminishing (TVD), essentially non-oscillatory (ENO), weighted ENO (WENO), and hybrid schemes (e.g., those that switch between spectral and high-order shock-capturing schemes). The built-in nonlinear numerical dissipation in TVD, ENO and WENO schemes was designed to capture accurately discontinuities and high gradient flows while hoping to maintain the order of accuracy of the scheme away from discontinuities.

There exist different specialized linear and nonlinear filters to post process the numerical solution after the completion of a full time step of the numerical integration. Since they are post processors, the physical viscosity, if it exists, is taken into consideration. The main design principle of linear filters is to improve nonlinear stability, under-resolved grids [6] and de-aliasing of smooth flows, while the design principle of nonlinear filters is to improve the nonlinear stability and accuracy near discontinuities as well. See, for example, the present proceedings and [9, 6, 7, 27] for forms of linear filters, and see [30, 31, 21] for forms of nonlinear filters. For direct numerical simulation (DNS) and large eddy simulation (LES), there are additional variants of the filter approach.

For the last decade, CPU intensive high order schemes with built-in nonlinear dissipation have been gaining in popularity in DNS and LES for long-time integration of shock-turbulence interactions. Unfortunately, these built-in dissipations cannot clearly distinguish shocks/shears, from turbulent fluctuations and/or spurious high-frequency oscillations. In [30, 31, 21], it was shown that these built-in numerical dissipation are more dissipative and less accurate than the nonlinear filter approach of [30, 31, 21] with a similar order of accuracy. It was also shown that these nonlinear filters can also suppress spurious high-frequency oscillations. However, a subsequent study of Sjögreen & Yee [23] showed that the high order linear filter can sustain longer time integration more accurately than the nonlinear filter for low speed smooth flows. In other words, for the numerical examples that were examined in [23], the high order linear filter can remove high-frequency oscillations producing nonlinear instability better than the second-order nonlinear filter. Higher than third-order nonlinear filters might be able to improve their performance or might outperform the high order linear filters at the expense of more CPU time and added complexity near the computational boundaries. These findings prompted the design of switching on and off or blending of different filters to obtain the optimal accuracy of high order spatial difference operator as proposed in Yee et al. and Sjögreen & Yee [31, 21]. The missing link of what was proposed in [31, 21] is an efficient, automated and reliable set of appropriate sensors that are capable of distinguishing shocks/shears, from turbulent fluctuations and/or spurious high-frequency oscillations for a full spectrum of flow speeds and Reynolds numbers.

The present paper is a sequel to [30, 31, 21]. The objective here is to propose an adaptive procedure employing appropriate sensors to switch on the desired numerical dissipation where needed and leave the rest of the region free of numerical dissipation contamination while at the same time improving nonlinear stability of the entire numerical process. In addition, the minimization of employing very fine grids to overcome the production of spurious numerical solutions and/or instability due to under-resolved grids is sought [6]. It was shown in [17, 8, 31, 21] that conditioning the governing equations via entropy splitting of the inviscid flux derivatives [31] can improve the over all stability of the numerical approach for smooth flows. Therefore, the same shock/shear detector that is designed to switch on the shock/shear numerical dissipation can be used to switch off the entropy splitting form of the inviscid flux derivative in the vicinity the

discontinuous regions to further improve nonlinear stability and minimize the use of numerical dissipation. The rest of the sensors, in conjunction with the local flow speed and Reynolds number, can also be used to adaptively determine the appropriate entropy splitting parameter for each flow type/region. These sensors are readily available as an improvement over existing grid adaptation indicators. If applied correctly, the proposed adaptive numerical dissipation control is scheme independent, and can be a stand alone option for many of the favorite schemes used in the literature. Although the proposed adaptive procedure is scheme independent, we prefer a complete treatment of the numerical approach in the following framework:

1. For stability considerations, condition the governing equations before the application of the appropriate numerical scheme.
2. For consistency, compatible schemes that posses stability properties similar to those of the discrete analogue of the continuum are preferred.
3. For the minimization of numerical dissipation contamination, efficient and adaptive numerical dissipation control to further improve nonlinear stability and accuracy should be used.
4. For practical considerations, the numerical approach should be efficient and applicable to general geometries. An efficient and reliable dynamic grid adaptation should be used if necessary. Note that the computation of the illustrative examples used such a numerical approach [30, 31, 28, 21, 8, 16].

A brief summary of (1)-(3) is discussed in the next three sections. Some representative examples to illustrate the performance of the approach are given in Section 5.

2. Conditioning of the Governing Equations

Traditionally, conditioning the governing partial differential equations (PDEs) usually referred to rewriting the governing equations in an equivalent set of PDEs in order to prove the stability and/or well-posedness of the PDEs. When numerical methods are used to solve PDEs that are nonlinear, it is well-known that different equivalent forms of the governing equations might exhibit different numerical stability, accuracy and/or spurious computed solutions, even for problems containing no shock/shear discontinuities. There are many conditioned forms of the governing equations proposed in the literature. Different conditioned forms of the convection fluxes and the viscous fluxes have been proposed for the incompressible and compressible Navier-Stokes equations. Here we mention a few which are precursors of the so called entropy splitting of the compressible Euler equations [31]. If a method-of-lines approach is used to discretize these equations, the entropy splitting reduces to the splitting of the convection flux derivatives.

The splitting of the convection terms (for both the compressible and incompressible Navier-Stokes equations) into a conservative part and a non-conservative part has been known for a long time. In the DNS, LES and atmospheric science simulation literature, it is referred to as the skew-symmetric form of the momentum equations [1, 14, 2, 35]. It consists of the mean average of the conservative and non-conservative (convective form [35]) part of the momentum equations. The spatial difference operator is then applied to the split form. From the numerical analysis standpoint, the Hirt and Zalesak's ZIP scheme [12, 34] is equivalent to applying central schemes to the non-conservative momentum equations (convective form of the momentum equations). MacCormack [15] proposed the use of the skew-symmetric form for problems other than DNS and LES. Harten [10] and Tadmor [26] discussed the symmetric form of the Euler equations and skew-adjoint form of hyperbolic conservation laws, respectively. Although the derivation in these works is different, the ultimate goal of using the split form is almost identical. This goal is to improve nonlinear stability, minimize spurious high-frequency oscillations and robustness of the numerical computations. See [33, 23] for a historical consolidation of these approaches. The canonical splitting used by Olsson & Oliger [17] is a mathematical tool to prove the existence of a generalized energy estimate for a symmetrizable system of conservation laws. For the ther-

mally perfect gas compressible Euler equations, the transformation consists of a convex entropy function that satisfies a mathematical entropy condition. The mathematical entropy function, in this case, can be a function of the physical entropy. Therefore, the resulting splitting was referred to as **entropy splitting** for ease of reference by Yee et al. [31]. The entropy splitting can be viewed as the more general form which provides L_2 stability proof of the nonlinear Euler equations with physical boundary conditions included.

Consider a general nonlinear system of conservation laws,

$$U_t + F(U)_x = 0, \quad a \le x \le b. \tag{2.1}$$

If the conservation law has an entropy function, it can be transformed into a symmetric conservation law in terms of a new variable W. The change of variables $\partial U/\partial W$ is symmetric and positive definite, and the new Jacobian $\partial F/\partial W$ is symmetric. If furthermore U and F are homogeneous in W of degree β, which is the case for the thermally perfect gas Euler equations for any $\beta \neq -1$, the formulas become simple. In that case we insert the change of variables into the conservation law, and define the split form of the flux derivative [17]

$$U_t + \frac{\beta}{1+\beta} F_x + \frac{1}{1+\beta} F_W W_x = 0, \tag{2.2}$$

with β a splitting parameter ($\beta = \infty$ recovers the original conservative form). Here $\beta \neq -1$ and, for a perfect gas, $\beta > 0$ or $\beta < \frac{\gamma}{1-\gamma}$. The theory only gives the range of β and does not give any guidelines on how to choose β for the particular flow. The vectors F_W and W can be cast as functions of the primitive variables and β. From the study of [31], β is highly problem dependent. Multiplying the above equation by W (where $(\mathbf{p}, \mathbf{q})$ denotes the scalar or inner product of the vectors $\mathbf{p}$ and $\mathbf{q}$), gives

$$-(1+\beta)(W, U_t) = \beta(W, F_x) + (W, F_W W_x) = \beta(W, F_x) + (F_W W, W_x). \tag{2.3}$$

Integration by parts in space gives

$$(1+\beta)(W, U_t) = -[W^T F_W W]_a^b \tag{2.4}$$

from which we obtain the estimate

$$\begin{aligned} \tfrac{d}{dt}(W, U_W W) = \; & (W_t, U_W W) + (W, (U_W W)_t) = (U_t, W) + \beta(W, U_t) = \\ & (1+\beta)(W, U_t) = -[W^T F_W W]_a^b. \end{aligned} \tag{2.5}$$

In order to have an energy estimate, the boundary term $[W^T F_W W]_a^b$ should be of the sign that makes the time derivative of the norm negative. For stability the entropy norm $(W, U_W W)$ should be bounded.

3. Discrete Analogue of the Continuum

For ease of reference, "scheme" or more precisely "interior scheme" here generally refers to spatial difference schemes for the interior grid points of the computational domain, whereas "boundary scheme" is the numerical boundary difference operators for grid points near the boundaries. However, without loss of generality, we also adopt the conventional terminology of denoting "scheme" interchangeably as either the "combined interior and boundary scheme" or just the "interior scheme" within the context of the discussion. Before 1994, rigorous stability estimates for accurate and appropriate boundary schemes associated with fourth-order or higher spatial interior schemes were the major stumbling block in the theoretical development of combined interior and boundary schemes for nonlinear systems of conservation laws. Olsson [18] proved

that an energy estimate can be established for second-order central schemes. To obtain a rigorous energy estimate for high order central schemes, one must apply the scheme to the split form of the inviscid governing equation. A discrete analogue of the continuum using a semi discrete approach can be written as

$$\frac{dU_j(t)}{dt} = -\frac{\beta}{1+\beta} DF(U_j) - \frac{1}{1+\beta} F_W(U_j) DW_j. \tag{3.1}$$

Here, D is a difference operator, having the summation by parts (SBP) property [18, 25]. The estimate

$$\frac{d}{dt}(W, U_W W)_h = -W_J^T F_W(W_J) W_J + W_1^T F_W(W_1) W_1 \tag{3.2}$$

in the discrete scalar product follows in the same way as for the PDE with indices 1 and J the end points of the computational domain, and h the grid spacing. Here the SBP satisfying difference operator, for example, consists of central difference interior operators of even order together with the corresponding numerical boundary operators that obey the discrete energy estimate. See Olsson and Strand for forms of the SBP boundary operators [18, 25].

For the full discretization of the problem, we should discretize in time in such a way that the discrete energy estimate also holds. The obvious solution would be to discretize in time in a skew symmetric way, in a manner similar to the spatial discretization, e.g.,

$$\frac{\beta}{1+\beta} D_t U_j^n + \frac{1}{1+\beta} U_W(W_j^n) D_t W_j = -\frac{\beta}{1+\beta} DF(U_j^n) - \frac{1}{1+\beta} F_W(W_j^n) DW_j^n. \tag{3.3}$$

However, it turns out that the SBP property of the time difference quotient leads to a problem which is coupled implicitly in the time direction. To solve it we have to solve a nonlinear system of equations for all time levels in the same system, leading to an impractically large computational effort. Furthermore, numerical experiments shown in Sjögreen & Yee [23] indicated that a bounded L^2 entropy norm $(W, U_W W)_h$ does not necessarily guarantee a well behaved numerical solution for long-time integrations. In other words, L^2 stability does not necessarily guarantee an accurate solution. In practical computations, the classical Runge-Kutta time discretizations using the method-of-lines approach (which we used for our numerical experiments) works well, but we have not been able to prove a time discrete entropy estimate for this method. In addition, numerical experiments shown in [23] indicate that the time discrete problem does not have a decreasing entropy norm for all values of β. Numerical experiments in Yee et al. [31, 19] also indicate the wide variations of the β value for a full spectrum of flow problems. For example, if a constant β is used for problems containing shock waves, a very large value of β is needed. Otherwise diverge solution or wrong shock location and/or shock strength are obtained. With these findings, employing a constant β (within the allowable range of β) throughout the entire computational domain is not advisable unless the flow problem is a simple smooth flow. Studies in [31, 21] indicate that the split form of the inviscid flux derivatives does help in minimizing the use of numerical dissipation. What is needed is adaptive control of the β parameter from one flow region to another as well as from one physical problem to another.

We would like to point out that for non-homogeneous physical boundary conditions, it is important to impose these boundary conditions to maintain the SBP property. For a nonlinear symmetrizable system of conservation laws that contain time-dependent physical boundary conditions, an extra complication arises, especially if a multistage Runge-Kutta method is used. See Johansson [13] for a discussion.

4. Adaptive Numerical Dissipation Control

For smooth flows, entropy splitting does significantly improve the stability of the computation, but does not completely remove all nonlinear instabilities, especially for long-time wave

propagations, computation of turbulent statistics, and spurious numerical solutions and spurious oscillations due to under-resolved grids [29, 6]. Furthermore, the entropy splitting was developed for smooth solutions. Additional difficulties from shock wave formation are the oscillatory behavior of the centered difference interior scheme, and the fact that the nonconservative terms might lead to inconsistent behavior at shocks/shears [31, 21, 23]. We propose to enhance the above conditioning of the equations with an advanced numerical dissipation model, which includes nonlinear sensors to detect shocks/shears and other small scale features, and spurious oscillation instability due to under-resolved grids. Furthermore, we will use the detector to switch off the entropy splitting at shocks/shears and adjust the entropy splitting parameter with the aid of local Mach number and Reynolds number in smooth region as discussed earlier. The advanced numerical dissipation model can be used: (Option I) as part of the scheme, (Option II) as an adaptive filter control after the completion of a full time step of the numerical integration or (Option III) as a combination of Options I and II (e.g., high order nonlinear dissipation (with sensor control) using Option I and nonlinear filter (with a different sensor control) using Option II).

Due to space constraints, we concentrate here on an adaptive procedure that can distinguish three major computed flow features to signal the correct type and amount of numerical dissipation needed in addition to controlling the entropy splitting parameter. The major flow features and numerical instability are (a) shocks/shears , (b) turbulent fluctuations , and (c) spurious high-frequency oscillations. The procedure can be extended if additional refinement or classification of flow types and the required type of numerical dissipation is needed. There exist different detection mechanisms in the literature for the above three features. These detectors are not mutually exclusive and/or are too expensive for practical applications. We believe that the multiresolution wavelet approach proposed in Sjögreen & Yee [21] is capable of detecting all of these flow features, resulting in three distinct sensors. If chosen properly, one multiresolution wavelet basis function might be able to detect all three features. For an optimum choice, one might have to use more than one type of wavelet basis functions but at the expense of an increase in CPU requirements. Some incremental studies into the use of entropy splitting and the application of these sensors were illustrated in [31, 21, 22, 24, 23, 16]. Here, additional tools are illustrated together with highlights of some examples. An adaptive numerical dissipation model illustrating some of the proposed ideas will be described in the next section. Full implementation of the complete treatment of the numerical approach (including grid adaptation) discussed in Section 1 to complex realistic multiscale problems is in progress.

5. Numerical Examples

This section illustrates the power of entropy splitting, the difference in performance of linear and nonlinear (with sensor controls) filters and the combination of both types of filters with adaptive sensor controls. We use the same notation as in [30, 31, 22]. The artificial compression method (ACM) and wavelet filter schemes using a second-order nonlinear filter with sixth-order spatial central interior scheme for both the inviscid and viscous flux derivatives are denoted by ACM66 and WAV66. See [30, 31, 22] for the forms of these filter schemes. The same scheme without filters is denoted by CEN66. The scheme using the fifth-order WENO for the inviscid flux derivatives and sixth-order central for viscous flux derivatives is denoted by WENO5. Computations using the standard fourth-order Runge-Kutta temporal discretization are indicated by appending the letters "RK4" as in CEN66-RK4. ACM66 and WAV66 use the Roe's average state and the van Leer limiter for the nonlinear numerical dissipation portion of the filter. The wavelet decomposition is applied in density and pressure, and the maximum wavelet coefficient of the two components is used. The nonlinear numerical dissipation is switched on wherever the wavelet analysis gives a Lipschitz exponent [21] less than 0.5. Increasing this number will reduce oscillations, at the price of reduced accuracy (see [21] for other possibilities). Computations

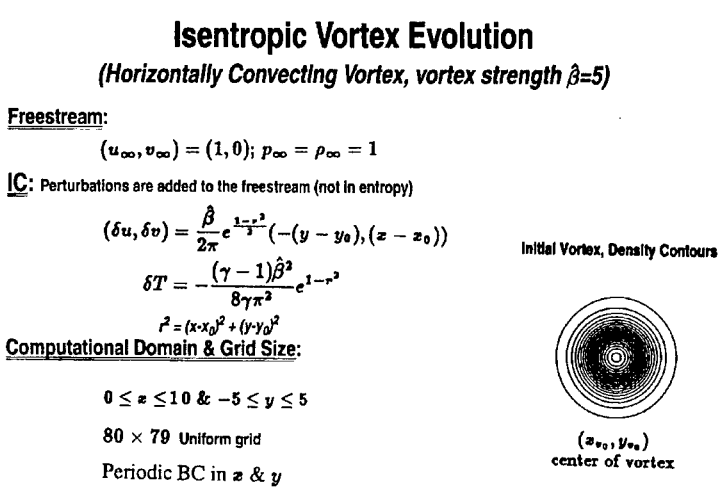


Figure 5.1. Vortex convection problem description.

using entropy splitting are indicated by appending the letters "ENT" as in WAV66-RK4-ENT. Computations using an eighth-order linear dissipation filter are indicated by appending the letters "D8" as in WAV66-RK4-D8. In order not to introduce additional notation, inviscid flow simulations are designated by the same notation, with the viscous terms not activated.

5.1. A 2-D VORTEX CONVECTION MODEL [30, 31, 21, 23]

The onset of nonlinear instability of long-time numerical integration, the benefit of the entropy splitting and the difference in performance of linear and nonlinear numerical dissipations in improving nonlinear stability for a horizontally convecting vortex (see Fig. 5.1) can be found in in [30, 31, 21, 23]. We summarize the result here.

To show the onset of nonlinear instability, the 2-D perfect gas compressible Euler equations are approximated by CEN66-RK4 with periodic boundary conditions imposed using a 80×79 grid with the time step $\Delta t = 0.01$. Since this is a pure convection problem, the vortex should convect without any distortion if the numerical scheme is highly accurate and non-dissipative. Although CEN66-RK4 is linearly stable, the test problem is nonlinear and instability eventually sets in. Almost perfect vortex preservation is observed for up to 5 periods of integrations (5 times after the vortex has convected back to the same position - time = 50). Beyond 5 periods the solution becomes oscillatory, and blows up before the completion of 6 periods. The blow up is associated with an increase in entropy [23]. If we instead use the entropy-split form of the approximation (CEN66-RK4-ENT) with a split parameter $\beta = 1$, almost perfect vortex preservation for up to 40 periods can be obtained. The computation remains stable for up to 67 periods before it breaks down. The time history of the L^2 entropy norm and density contours of the solution after 5, 10, 30 and 67 periods using CEN66-RK4-ENT is shown in Figs. 5.2 and 5.3. The norm is decreasing, although the instabilities break down the solution after 67 periods. Using the second-order nonlinear filter without splitting (ACM66-RK4 or WAV66-RK4), the solution remains stable beyond 67 periods. However, the numerical solution gradually starts to diffuse after 20 periods. If we use the nonlinear filter in conjunction with entropy splitting (ACM66-RK4-ENT or WAV66-RK4-ENT), almost perfect vortex preservation can be obtain for up to 120 periods using a split parameter $\beta = 1$ [31].

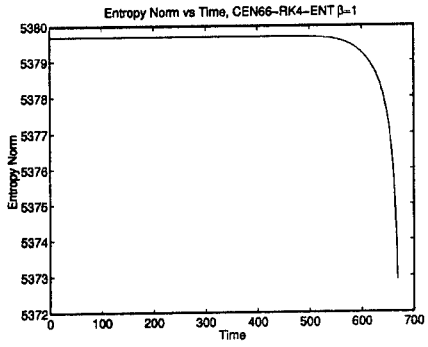


Figure 5.2. Entropy norm history of CEN66-ENT: entropy split parameter $\beta = 1$ and 80×79 grid.

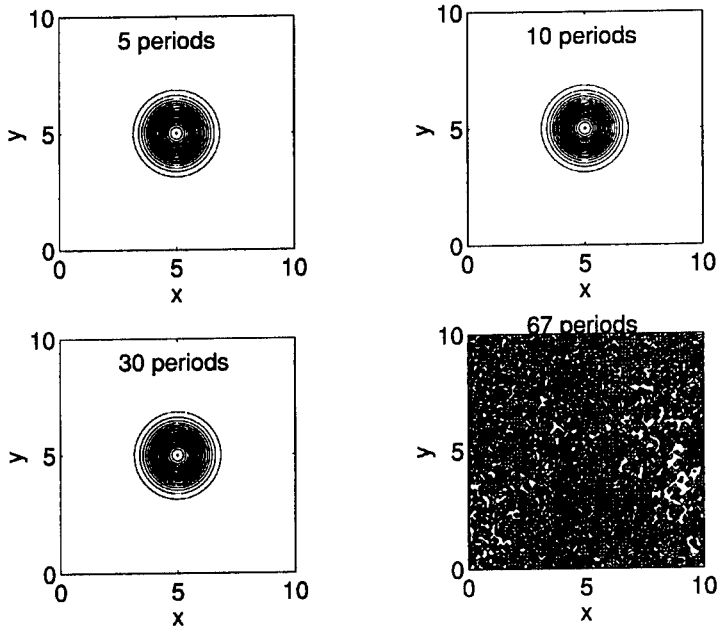


Figure 5.3. Density Contours of CEN66-ENT: entropy split parameter $\beta = 1$ and 80×79 grid.

The density contours of the solution after 5, 10, 200 and 300 periods for the unsplit ($\beta = \infty$) computation using the eighth-order linear dissipation (CEN66-RK4-D8) are shown in Fig. 5.4. The linear dissipation term $(-dh^7(D_+D_-)^4U_j)$ with grid spacing h was added to the sixth-order base scheme to discretize the convection terms. The parameter d is a given constant ($d = 0.0002$) and is scaled with the spectral radius of the Jacobian of the flux function, and D_+ and D_- are the

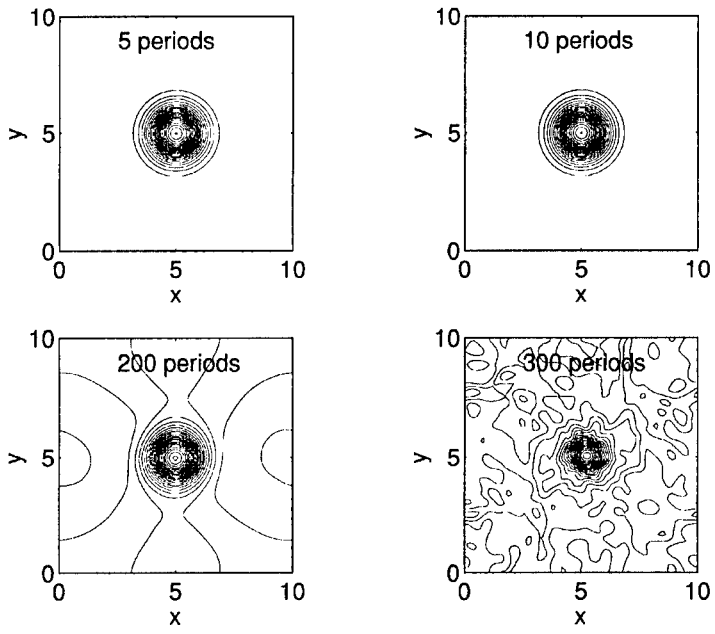


Figure 5.4. Density contours of CEN66-RK4-D8 using 80 × 79 grid.

forward and backward difference operators, respectively. This numerical dissipation is applied as part of the scheme and not as a post processing filter. The computation can be run for 300 periods without breakdown. However, serious degradation of accuracy occurs after 250 periods. For this particular problem, the CEN66-RK4-D8 out performed the ACM66-RK4-ENT and WAV66-RK4-ENT using $\beta = 1$. Perhaps using a higher than third-order nonlinear filter might improve the performance of the ACM66-RK4-ENT and WAV66-RK4-ENT at the expense of an increase in CPU.

5.2. DNS OF 3-D COMPRESSIBLE TURBULENT CHANNEL FLOW [19]

To obtain an accurate turbulent statistics, very long-time integration and highly accurate methods are required for this DNS computation. This numerical example illustrates the power of entropy splitting. The computation employed the SBP-satisfying boundary difference operator with the fourth-order central interior scheme applied to the split form of the inviscid flux derivatives CEN44-RK4-ENT with $\beta = 4$. The fluid mechanics of this 3-D wall bounded isothermal compressible turbulent channel flow has been studied in some detail by Coleman et al. [4]. They showed that the only compressibility effect at moderate Mach numbers comes from the variation of fluid properties with temperature. They used a uniform body force term to drive the flow, but recommended the constant pressure gradient approach which was adapted by Sandham & Yee [19]. For simplicity, the fixed pressure gradient problem rather than the constant mass flow problem was solved using fixed fluid properties. Thus only the wall shear stress and mass flow rate vary during the simulation. A Mach number of 0.1 is chosen, based on friction velocity and sound speed corresponding to the fixed wall temperature. Channel half

width h, friction velocity u_τ, wall temperature and bulk (integrated) density are the normalizing quantities for non-dimensionalization with a Reynolds number of 180. Grid refinement studies (three grids) were conducted and comparisons were made with results from incompressible flow spectral method calculations using the same computational box size and the finest of the three grids. Very good agreement was obtained. In addition, using the same uniform body force term, computational box and grid size as in Coleman et al., excellent agreement was also obtained with the Coleman et al. spectral compressible Navier-Stokes computation. What is interesting is that this simulation did not require filtering, upwinding, or additional numerical dissipation for shock free compressible turbulence computations. Moreover, this high order method can be efficiently extended to general geometries [28]. Using CEN44-RK4-ENT ($\beta = 4$) together with a so called Laplacian viscous term formulation, Sandham & Yee [19] demonstrated a robustness down to very coarse resolutions, comparable with the best incompressible turbulent flow solvers incorporating de-aliasing and skew-symmetric formulation of the convection terms. For the same 3-D problem, WENO5 is more than six times as expensive yet more diffusive than the present scheme using the same temporal discretization. Without the use of the entropy splitting of the inviscid flux derivatives and Laplacian right hand side formulation, using the same CFL number, the CEN44-RK4 solutions diverge for all three grids before meaningful turbulence statistics can be obtained. In view of the spurious high-frequency-oscillation-producing nonlinear instability nature of central schemes and the past experience in incompressible turbulence simulations, in the absence of entropy splitting and Laplacian formulation, the present calculations might not even be possible with much higher resolution grid.

For the performance of ACM66-RK4, WAV66-RK4 and WENO5-RK4 on a spatially or a time-developing mixing layer problem containing shock waves, see [31, 21].

5.3. MULTISCALE COMPLEX UNSTEADY VISCOUS COMPRESSIBLE FLOWS [22, 24]

Extensive grid convergence studies using WAV66-RK4 and ACM66-RK4 for two complex highly unsteady viscous compressible flows are given in [22, 24]. The first flow is a 2-D complex viscous shock/shear/boundary-layer interaction. This is the same problem and flow conditions studied in Daru & Tenaud [5]. The second flow is a supersonic viscous reacting flow concerning fuel breakup. More accurate solutions were obtained with WAV66-RK4 and ACM66-RK4 than with WENO5-RK4, which is nearly three times as expensive. To illustrate the performance of these nonlinear filter schemes, the first model is considered. The ideal gas compressible full Navier-Stokes equations with no slip BCs at the adiabatic walls are used. The fluid is at rest in a 2-D box $0 \le x, y \le 1$. A membrane with a shock Mach number of 2.37 located at $x = 1/2$ separates two different states of the gas. The dimensionless initial states are

$$\rho_L = 120, \quad p_L = 120/\gamma; \qquad \rho_R = 1.2, \quad p_R = 1.2/\gamma, \tag{5.1}$$

where ρ_L, p_L are the density and pressure respectively, to the left of $x = 1/2$, and ρ_R, p_R are the same quantities to the right of $x = 1/2$. $\gamma = 1.4$ and the Prandtl number is 0.73. The two Reynolds numbers considered are 200 and 1000. The viscosity is assumed to be constant and independent of temperature, so Sutherland's law is not used. The velocities and the normal derivative of the temperature at the boundaries are set equal to zero. This is done by leaving the value of the density obtained by the one sided difference scheme at the boundary unchanged, and updating the energy at the boundary to make the temperature derivative equal to zero.

At time zero the membrane is removed and wave interaction occurs. An expansion wave and a shock are formed initially. Then, a boundary layer is formed on the lower boundary behind the right going waves. After reflection, the left going shock wave interacts with the newly formed boundary layer, causing a number of vortices and lambda shocks near the boundary layer. Other kinds of layers remain after the shock reflection near the right wall. The complexity of this highly unsteady shock/shear/boundary-layer interactions increases as the Reynolds number increases.

For illustration, here we show the difficult case of Reynolds number $Re = 1000$. The computations stop at the dimensionless time 1 when the reflected shock wave has almost reached the middle of the domain, $x = 1/2$. The numerical results discussed here are at time 1 with uniform Cartesian grid spacings as described by Daru and Tenaud. Due to symmetry, only the lower half of the domain is used in the computations; symmetry BCs are enforced at the boundary $y = 1/2$. Figure 5.5 shows the comparison of a second-order MUSCL using a second-order Runge-Kutta method (MUSCL-RK2) with WAV66-RK4, ACM66-RK4 and WENO5-RK4 using a 1000×500 grid. Comparing with the converged solution of WAV66-RK4 and ACM66-RK4 using 3000×1500 (see bottom of figure) and 4000×2000 grids (see [22]), one can conclude that WAV66-RK4 exhibits the most accurate result among the 1000×500 grid computations. We note that, for this Reynolds number, the unsteady problem is extremely stiff, requiring very small time steps and very long-time integrations before reaching the dimensionless time of 1.

5.4. AN ADAPTIVE NUMERICAL DISSIPATION MODEL FOR 1-D SHOCK-TURBULENCE INTERACTIONS

In classical CFD codes, a second order accurate base method is used together with two constant strength linear numerical dissipation terms. One linear fourth-order dissipation is used everywhere except near shocks/shears/steep-gradients to remove nonlinear instabilities. It does not affect the second order accuracy of the base scheme. The second dissipation term is a second-order linear dissipation, which affects the order of accuracy, but is only switched on near discontinuities, and/or steep unresolved gradients using a gradient sensor. The sensor used cannot distinguish the different flow features distinctly and is not accurate enough for turbulent statistics and long-time acoustic computations, unless extreme grid refinement is employed.

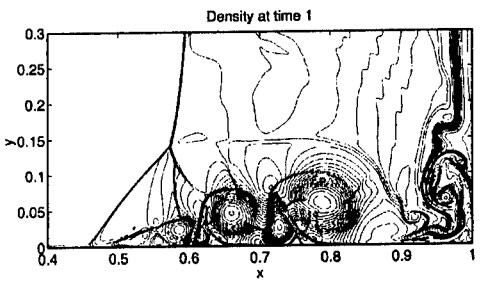
In analogy with the aforementioned classical methods, a more advanced numerical dissipation model with improved flow feature extraction sensors for high order central schemes is proposed. Here, we consider a dissipation model with two parts. One part is a nonlinear filter ([30]) and the second part is a high order linear numerical dissipation term modified at boundaries to become a semi-bounded operator, see [20, 23]. The wavelet dissipation control sensor developed in [21] is used as the flow feature detector. The sensor is computed from the wavelet estimate of the Lipschitz exponent α of the density and pressure in the flow field. Below we present a filter model for 1-D shock/turbulence interactions.

A Filter Model: Using a suitable wavelet basis function, the final result of the wavelet computation is a quantity, S_j, which is near zero at points x_j where the solution is smooth and near one where the solution is discontinuous. S_j depends on the Lipschitz regularity exponent of the solution. We define the filter numerical flux of the numerical dissipation operator as $H^d_{j-1/2}$.

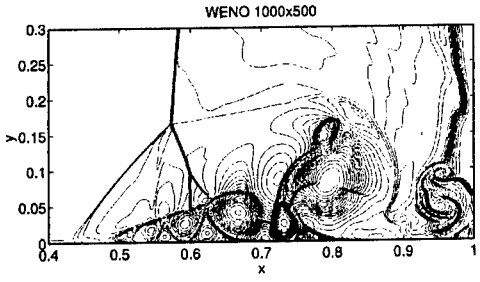
$$H^d_{j-1/2} = \max(S_j, S_{j-1}) F^*_{j-1/2} + d_j[1 - \max(S_j, S_{j-1})](h^6 D_+(D_+D_-)^3 U_j, \qquad (5.2)$$

where $F^*_{j-1/2}$ is the flux function corresponding to the dissipative portion of a shock-capturing scheme (e.g., second order accurate TVD scheme) [30]. The first part of the filter stabilizes the scheme at shock/shear locations. The second part is an eighth-order filter which improves nonlinear stability away from shock/shear locations. Analogous eighth-order filters can be used if a sixth-order compact spatial base scheme is used [7, 27]. We switch on the high order part of the filter when we switch off the nonlinear filter. The physical quantity (e.g., local Mach number) can be used to determine the d_j parameter of this high order dissipation term.

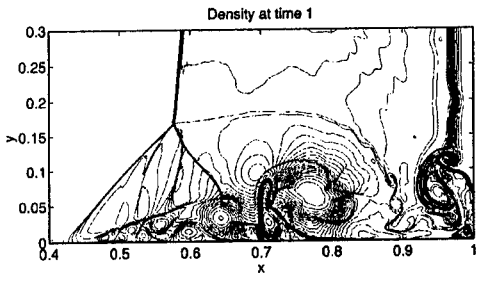
To further increase stability properties, it is possible to use the sensor to switch on and off the entropy splitting and adjust the value of the entropy splitting parameter according to flow type and region. For this problem, however, we believe a constant $\beta = 1$ away from the shock waves is sufficient. After the completion of a full time step computation using the sixth-order



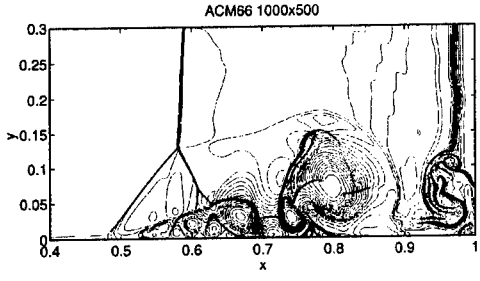
(a) MUSCL-RK2, 1000 × 500 grid



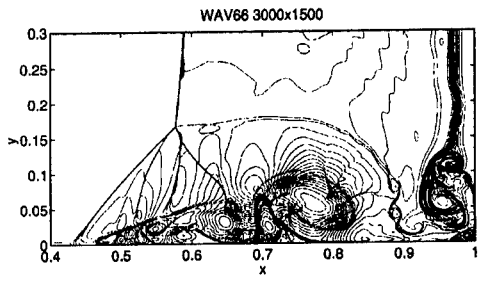
(b) WENO5-RK4, 1000 × 500 grid



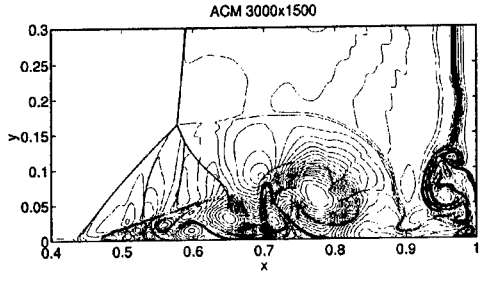
(c) WAV66-RK4, 1000 × 500 grid



(d) ACM66-RK4, 1000 × 500 grid



(e) WAV66-RK4, 3000 × 1500 grid



(f) ACM66-RK4, 3000 × 1500 grid

Figure 5.5. Comparison: MUSCL-RK2, WAV66-RK4, WAV66-RK4 and WENO5-RK4 for $Re = 1000$. Density contours using 1000 × 500 and 3000 × 1500 grids.

base scheme (denoting the solution by $\widehat{U}_j$), we filter this solution by

$$U_j^{n+1} = \widehat{U}_j + \frac{\Delta t}{h}[H^d_{j+1/2} - H^d_{j-1/2}]. \tag{5.3}$$

Here the filter numerical fluxes $H^d_{j\pm 1/2}$ are evaluated at $\widehat{U}$.

The Wavelet Sensor: The wavelet sensor estimates the Lipschitz exponent of a grid function f_j (e.g., the density and pressure). The Lipschitz exponent at a point x is defined as the largest

α satisfying

$$\sup_{h\neq 0}\frac{|f(x+h)-f(x)|}{h^{\alpha}}\leq C, \tag{5.4}$$

and this gives information about the regularity of the function f where small α means poor regularity. For a C^1 wavelet function ψ with compact support, α can be estimated from the wavelet coefficients, defined as

$$w_{m,j} =< f,\psi_{m,j} >= \int f(x)\psi_{m,j}(x)dx, \tag{5.5}$$

where

$$\psi_{m,j} = 2^m\psi\Big(\frac{x-j}{2^m}\Big) \tag{5.6}$$

is the wavelet function $\psi_{m,j}$ on scale m located at the point j in space. This definition gives a so called redundant wavelet, which gives (under a few technical assumptions on ψ) a non-orthogonal basis for L^2. It is possible to prove that the coefficients $\max_j |w_{m,j}|$ in a neighborhood of j_0 decay as $2^{m\alpha}$ as the scale is refined, where α is the Lipschitz exponent at j_0. In practical computation, we have a smallest scale, determined by the grid size. We evaluate $w_{m,j}$ on this scale, m_0, and a few coarser scales, m_0+1, m_0+2, and estimate the Lipschitz exponent at the point j_0 by a least square fit to the line [21]

$$\max_{j \text{ near } j_0} \log_2|w_{m,j}| = m\alpha_{j_0} + c. \tag{5.7}$$

For the numerical experiments, the wavelet coefficient $w_{m,j}$ is computed numerically by a recursive procedure, which is a second-order B-spline wavelet or a modification of Harten's multiresolution scheme [21]. The sensor we use in the computations is

$$S_j = \tau(\alpha_j), \tag{5.8}$$

where

$$\tau(\alpha_j) = \begin{cases} 1 & \alpha_j \leq 0.5 \\ 0 & \alpha_j > 0.5. \end{cases} \tag{5.9}$$

The dissipative model (5.2) is used to solve a simple, yet difficult, 1-D compressible inviscid shock-turbulence interaction problem with initial data consisting of a shock propagating into an oscillatory density. The initial data are given by

$$(\rho_L,\ u_L,\ p_L) = (3.857143,\ 2.629369,\ 10.33333) \tag{5.10}$$

to the left of a shock located at $x=-4$, and

$$(\rho_R,\ u_R,\ p_R) = (1+0.2*\sin(5*x),\ 0,\ 1) \tag{5.11}$$

to the right of the shock where u is the velocity. Fig. 6.6 show the comparison between a second-order MUSCL-RK2 with a sixth-order central scheme and the aforementioned numerical dissipation model using RK4 as the time discretization (WAV66-RK4-D8). The parameter $d = 0.002$ is scaled with the spectral radius of the Jacobian of the flux function. Note that the eighth-order dissipation is a filter, and is different from the CEN66-D8 used in Section 5.1 where the dissipation is part of the scheme. Solution using a second-order uniformly non-oscillatory (UNO) scheme on a 4000 uniform grid is used as the reference solution (solid lines on the first three subfigures). The bottom of the right figures show the density and Lipschitz exponent distribution for the WAV66-RK4-D8 using 400 grid points. Comparing our result with the most accurate computation found in the literature for this problem, the current approach is highly efficient

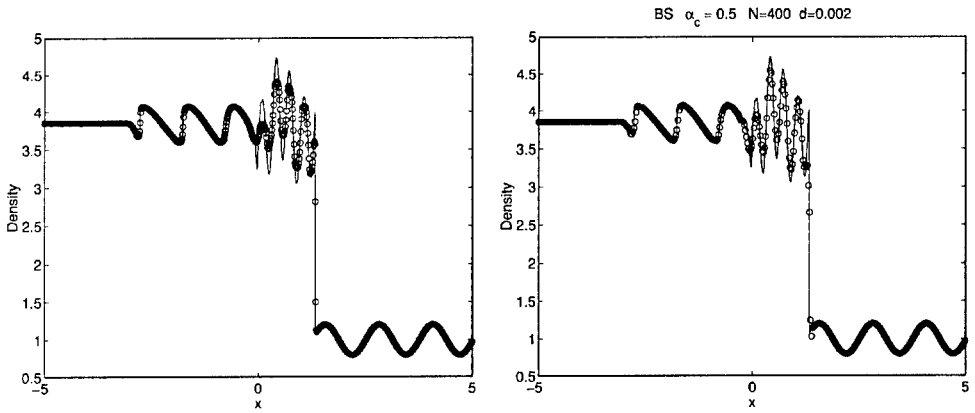
and accurate using only 800 grid points without grid adaptation or very high order shock-capturing scheme. For the present computation, the WAV66-RK4-D8 consumed only slightly more CPU than the second-order scheme MUSCL-RK2. With the eighth-order dissipation filter turned off (i.e., only the nonlinear filter remains - WAV66-RK4), the computation is not very stable unless a finer grid and smaller time step is used. Turning on the entropy splitting away from the shocks helps to reduce the amount of the eighth-order dissipation coefficient [33].

6. Concluding Remarks

A general framework for the design of an adaptive low dissipative high order scheme is presented. The approach is applicable to a wide spectrum of flow problems. However the demand on the overall numerical approach for nonlinear stability and accuracy is much more stringent for long-time integration of complex multiscale shock/shear/turbulence/acoustics interactions and numerical combustion problems. Robust classical numerical methods for less complex flow physics are not suitable or practical for such applications. The present approach is designed expressly to address such flow problems and computational challenges. The incremental studies to illustrate the performance of the approach are summarized. Extensive testing and full implementation of the approach is forthcoming. The results shown so far are very encouraging.

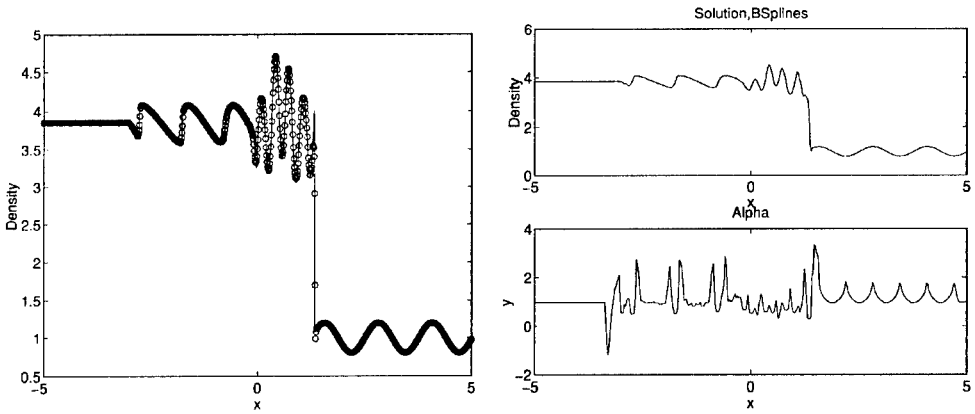
References

1. A. Arakawa, *Computational Design for Long-Term Numerical Integration of the Equations of Fluid Motion: Two-Dimensional Incompressible Flow. Part I*, J. Comput. Phys., **1** (1966), pp. 119–143.
2. G. A. Blaisdell, *Numerical Simulation of Compressible Homogeneous Turbulence*, PhD Thesis, Stanford University, 1991.
3. M.H. Carpenter, J. Nordstrom and D. Gottlieb, *A Stable and Conservative Interface Treatment of Arbitrary Spatial Accuracy*, ICASE Report 98-12, 1998.
4. G.N. Coleman, J. Kim, J. and R. Moser *A Numerical Study of Turbulent Supersonic Isothermal-Wall Channel Flow, J. Fluid Mech.* **305**, (1995), pp. 159-183.
5. V. Daru and C. Tenaud, *Evaluation of TVD High Resolution Schemes for Unsteady Viscous Shocked Flows*, Computers Fluids, **30** 89–113 (2000).
6. P.F. Fischer and J.S. Mullen, *Filter-Based Stabilization of Spectral Element Methods*, Argonne National Lab. Report, August 4, 1999.
7. D.V. Gaitone and M.R. Visbal, *Further Development of a Navier-Stokes Solution Procedure Based on Higher-Order Formulas*, AIAA Paper 99-0557, Reno, NV, 1999.
8. M. Gerritsen and P. Olsson, *Designing an Efficient Solution Strategy for Fluid Flows*, J. Comput. Phys. **129** 245–262 (1996).
9. D. Gottlieb and J.S. Hesthaven, *Spectral Methods for Hyperbolic Problems*, J. Comput. Applied Math., **128**, 83-131 (2001).
10. A. Harten, *On the Symmetric Form of Systems for Conservation Laws with Entropy*, J. Comput. Phys. **49**, 151-164 (1983).
11. A. Harten, *Multiresolution Algorithms for the Numerical Solution of Hyperbolic Conservation Laws*, Comm. Pure Appl. Math., **48**, 1305 (1995).
12. C.W. Hirt, *Heuristic Stability Theory for Finite-Difference Equations*, J. Comput. Phys., **2** (1968), pp. 339-355.
13. M. Johansson, *Loss of High Order Spatial Accuracy due to Boundary Error Caused by Runge-Kutta Time Integration*, Technical report 2000-013, Dept. Info. Tech., Uppsala University, May 2000.
14. H.-O. Kreiss and J. Oliger, *Comparison of accurate methods for the integration of hyperbolic equations*, Tellus, **24** (1972), pp. 199-215.
15. R.W. MacCormack, *Numerical Solution of the Interaction of a Shock Wave with a Laminar Boundary Layer*, Proceedings of the 2nd Intern. Conf. on Num. Meths. in Fluid Dynamics, (1971), pp. 151-163.
16. B. Müller and H.C. Yee, *Entropy Splitting for High Order Numerical Simulation of Vortex Sound at Low Mach Numbers*, Proceedings of the 5th Internat. Conf. on Spectral and High Order Methods, Uppsala, Sweden, June 11-15, 2001.
17. P. Olsson and J. Oliger, *Energy and Maximum Norm Estimates for Nonlinear Conservation Laws*, RIACS Technical Report 94.01 (1994).
18. P. Olsson, *Summation by Parts, Projections, and Stability. III*, RIACS Technical Report 95.06 (1995).
19. N. D. Sandham and H.C. Yee, *Entropy Splitting for High Order Numerical Simulation of Compressible Turbulence*, RIACS Technical Report 00.10, June 2000, NASA Ames Research Center; Proceedings of the First International Conference on CFD, July 10-14, 2000, Kyoto, Japan.
20. B. Sjögreen, *High Order Centered Difference Methods for the Compressible Navier-Stokes Equations*, J.



(a) MUSCL-RK2, 800 grid

(b) WAV66-RK4-D8, 400 grid



(c) WAV66-RK4-D8, 800 grid

(d) Density & Lipschitz Exponent Distributions, WAV66-RK4-D8, 400 grid

Figure 6.6. Comparison and Lipschitz exponent distribution of WAV66-RK4-D8, second-order B-spline wavelet.

Comput. Phys., **117** (1995), pp. 67–78.

21. B. Sjögreen and H. C. Yee *Wavelet Based Adaptive Numerical Dissipation Control for Shock-Turbulence Computation*, RIACS Report 01.01, NASA Ames research center (Oct 2000).
22. B. Sjögreen and H. C. Yee, *Grid Convergence of High Order Methods for Multiscale Complex Unsteady Viscous Compressible Flows*, RIACS Report 01.06, April, 2001, NASA Ames Research Center; AIAA 2001-2599, Proceedings of the 15th AIAA CFD Conference, June 11-14, 2001, Anaheim, CA.
23. B. Sjögreen and H.C. Yee *On Entropy Splitting, Linear and Nonlinear Numerical Dissipations and Long-Time Integrations*, Proceedings of the 5th Internat. Conf. on Spectral and High Order Methods, Uppsala, Sweden, June 11-15, 2001.
24. B. Sjögreen and H. C. Yee, *Low Dissipative High Order Numerical Simulations of Supersonic Reactive Flows*, RIACS Report 01-017, NASA Ames Research Center (May 2001); Proceedings of the ECCOMAS Computational Fluid Dynamics Conference 2001, Swansea, Wales, UK, September 4-7, 2001.
25. B. Strand, *Summation by Parts for Finite Difference Approximations for d/dx*, J. Comput. Phys. **110** (1994), pp. 47–67.

26. E. Tadmor, *Skew-Self Form for Systems of Conservation Laws*, J. Math. Anal. Appl., **103** (1984), pp. 428–442.
27. R. Vichnevetsky, *Numerical Filtering for Partial Differencing Equations*, Numerical Applications Memorandum, Rutgers University, NAM 156 (1974).
28. M. Vinokur and H.C. Yee, *Extension of Efficient Low Dissipative High Order Schemes for 3-D Curvilinear Moving Grids*, NASA TM 209598, June 2000.
29. H.C. Yee, P.K. Sweby, *Dynamics of Numerics & Spurious Behaviors in CFD Computations*, 7th ISCFD Conference, Sept. 15-19, 1997, Beijing, China, RIACS Technical Report 97.06, June (1997).
30. H. C. Yee, N. D. Sandham, and M. J. Djomehri, *Low Dissipative High Order Shock-Capturing Methods Using Characteristic-Based Filters*, J. Comput. Phys., **150**, 199 (1999).
31. H.C. Yee, M. Vinokur, and M.J. Djomehri, *Entropy Splitting and Numerical Dissipation*, NASA Technical Memorandum 208793, August, 1999, NASA Ames Research Center; J. Comput. Phys., **162**, 33 (2000).
32. H.C. Yee, B. Sjögreen, N.D. Sandham and A. Hadjadj, *Progress in the Development of a Class of Efficient Low Dissipative High Order Shock-Capturing Methods*, RIACS Technical Report 00.11, June, 2000; Proceedings of the CFD for the 21st Century, July 15-17, 2000 Kyoto, Japan.
33. H.C. Yee and B. Sjögreen, *Designing Adaptive Low Dissipative High Order Schemes for Long-Time Integrations*, RIACS Technical Report, in preparation (2001). An invited chapter for *Turbulent Flow Computation*," (eds. D. Drikakis & B. Geurts), Kluwer Academic Publisher.
34. S.T. Zalesak, *High Order "ZIP" Differencing of Convective Terms*, J. Comput. Phys., **40** (1981), pp. 497-508.
35. T. A. Zang, *On the Rotation and Skew-Symmetric Forms for Incompressible Flow Simulations*, Appl. Numer. Math., **7** (1991), pp. 27–40.

LARGE EDDY SIMULATION OF SUPERSONIC COMPRESSION CORNER USING ENO SCHEME

HONG YAN, DOYLE KNIGHT
Department of Mechanical and Aerospace Engineering
Rutgers - The State University of New Jersey
Piscataway, N.J. 08854-8058, USA

AND

ALEXANDER A. ZHELTOVODOV
Institute of Theoretical and Applied Mechanics
Russian Academy of Sciences - Siberian Branch
Novosibirsk 630090, Russia

1. Abstract

A Large Eddy Simulation of a 25° compression corner at $M = 2.88$ and $Re_\delta = 2 \times 10^4$ is performed using an Essentially Non Oscillatory (ENO) scheme. The Favre filtered compressible Navier-Stokes equations are solved using a Monotone Integrated Large Eddy Simulation (MILES) technique on an unstructured grid of tetrahedral cells. The mean flow variables and turbulent shear stress at the incoming flow are in good agreement with experiment and DNS. The separation length scaled by the characteristic scale [27, 31] shows agreement with the experiment. No pronounced pressure plateau is observed compared with experiment at higher Reynolds number.

2. Introduction

Supersonic flow over a compression corner is a classic problem embodying all the difficulties of viscous/inviscid interactions, compressibility and turbulence. A full understanding of this configuration is important for efficient aerodynamic and propulsion design. An extensive effort [1, 3, 4, 6, 7, 8, 10, 11, 15, 16, 17, 18, 20, 21, 22, 24, 25, 26, 27, 29, 30, 31, 32] has been focused on the study of this flow. However, traditional RANS meth-

ods have not accurately predicted the heat transfer and skin friction coefficient[3, 4, 10, 18, 29, 30] in cases with large flow separation. In addition, the scaled seperation length proposed in [27, 31] shows a significant deviation from the experimental range in Fig. 1. A Very Large Eddy Simulation by Hunt [11] for a 24° Mach 2.8 compression corner at $Re_\delta = 10^6$ revealed that the size of the separation bubble correlates strongly with the shock wave position. A DNS of 18° Mach 3 compression corner at $Re_\theta = 1685$ implemented by Adams [1] indicated the effect of compressibility on the turbulence structure in the interaction area. Rizzetta *et al.* [16, 17] performed a DNS and LES of 18° compression corner and made full comparison with DNS results by Adams [1].

This paper implements an ENO scheme for a 25° compression corner at Mach 2.88 and $Re_\delta = 2 \times 10^4$ to assess the capability of LES to accurately predict the turbulence characteristics.

3. Methodology

The Monotone Integrated Large Eddy Simulation technique [2] is used to solve the Favre-filtered compressible Navier-Stokes equations. The inviscid fluxes are computed using the second order Godunov's method and the viscous fluxes and heat transfer are obtained by application of Gauss' Theorem to each face. An ENO scheme has been developed for the unstructured grid. Our LES code is parallelized using domain decomposition in spanwise direction with Portable Message Passing Interface Model Implementation `Mpich`. The details are presented in [5, 14].

Allowing x, y and z to denote the streamwise, transverse and spanwise directions, respectively, the computational domain is $L_x = 16.0\delta$, $L_y = 3.4\delta$, and $L_z = 1.925\delta$. The grid consists of $213 \times 35 \times 57$ nodes in the x, y and z directions, respectively. The reference quantities for nondimensionalization are length δ (the incoming boundary layer thickness), velocity U_∞, density ρ_∞, static temperature T_∞ and molecular viscosity μ_∞ (where the subscript ∞ denotes the freestream conditions upstream of the compression corner). The tetrahedral grid is employed and stretched in the y direction with a spacing of 0.008δ at the wall and the stretching factor of 1.154. The grid is concentrated around the compression corner. The details of the grid are shown in Table 1, wherein $\Delta y^+ = \Delta y/\eta$ with the inner length scale $\eta = \nu_w/u_\tau$ (ν_w is the kinematic viscosity at the wall, $u_\tau = \sqrt{\tau_w/\rho_w}$ is the friction velocity, τ_w is the wall shear stress and ρ_w is the density at the wall). The theoretical values of u_τ and ν_w are obtained from the combined Law of the Wall and Wake evaluated at $y = \delta$ and the power law of the relationship between temperature and kinematic viscosity, respectively.

TABLE 1. Details of Grids

Name	Mach	Δx^+	Δy^+ at the wall	Δz^+	$\Delta x/\delta$	$\Delta y/\delta$ at $y = \delta$	$\Delta z/\delta$	Tetras
Theoretical value	2.88	24	1.9	8.1	0.1	0.14	0.034	
LES	2.88	20.9	1.67	7.1	0.1	0.14	0.034	2,018,240

The inflow condition is obtained from a separate flat plate boundary layer computation. The non-slip boundary condition is used to the adiabatic wall. All the flow variables shown in the figures are averaged in time and the spanwise direction. The time averaging period is set to three times the flow-through time, where one flow-through time is defined as the time for the freestream flow to traverse the computational domain. The details are presented in [21].

4. Results

The oncoming flow characteristics are illustrated by the mean flow variables in Fig. 3 and Fig. 4 and the Reynolds shear stress in Fig. 5. The comparisons with experiments [28] and DNS show good agreement.

Fig. 2 shows the pressure contour distribution at $x - y$ plane of $z = 1.0\delta$. A strong separation and attachment shock wave is formed at the compression corner leading to the higher pressure level after the shock. The strong adverse pressure gradient causes the skin friction coefficient to decrease dramatically and the flow separates. Downstream of the corner, the overall increase in pressure and the decrease in Mach number cause the skin friction coefficient to recover.

The computational results are shown in Fig. 6–Fig. 8 along with experimental data. The skin friction coefficient in Fig. 6 is compared with the experiment at higher Reynolds number of $Re_\delta = 63560$. According to the Law of the Wall and Wake, the friction velocity is decreased with the increase in Reynolds number, leading to the higher skin friction coefficient in the computation. The time and spanwise averaged surface pressure profile along the streamwise direction is compared with experiment at higher Reynolds number in Fig. 7 and the pressure plateau is not observed. The difference between the predicted and experimental surface pressure profile may be attributable to the difference in Reynolds number.

The effect of Reynolds number on the separation length is plotted in

Fig. 8. In this figure, the separation length is measured by connecting the separation and attachment points at which the time and spanwise averaged skin friction coefficients go to zero and then scaled by the characteristic length (L_c) proposed by Zheltovodov and Schuelein [27, 31]

$$L_c = \delta(p_2/p_{pl})^{3.1}/M_\infty^3 \tag{1}$$

where δ is the incoming boundary layer thickness, p_2 is the pressure after the shock in inviscid flow, p_{pl} is the plateau pressure obtained by the empirical formula $p_{pl} = p_\infty(0.5M_\infty + 1)$ [33] and M_∞ is the Mach number in the uniform flow. Some LES and DNS results by other researchers are also plotted in Fig. 8 for comparison. Our LES successfully predicts the consistent trend with the experiment.

5. Conclusion

A 25° supersonic compression corner at Mach 2.88 and $Re_\delta = 2 \times 10^4$ has been simulated using an Essentially Non Oscillatory (ENO) scheme. The mean quantities in the incoming equilibrium flow show good agreement with experiment. The separation length is consistent with the extrapolated experimental trend. Computations at higher Reynolds number are in progress.

6. Acknowledgement

The research is supported by AFOSR under grant No. F49620-99-1-0008 monitored by Drs. Robert Herklotz, Len Sakell, John Schmisseur and Steve Walker.

References

1. Adams, N. A. (2000) Direct Simulation of the Turbulent Boundary Layer along a Compression Ramp at $M = 3$ and $Re_\theta = 1685$, *J. Fluid Mech.*, **Vol. 420, pp. 47–83**
2. Boris, J., Grinstein, F., Oran, E. and Kolbe R. (1992) New Insights into Large Eddy Simulation, *Fluid Dynamics Research*, **Vol. 10, pp. 199–228**
3. Borisov, A. V., Zheltovodov, A. A., Badekas, D. and Narayanswami, N. (1995) Computational Study of Supersonic Turbulent Separated Flows in the vicinity of Inclined Steps, *J. Applied Mechanics and Technical Physics*, **Vol. 36, No. 3, pp. 68–80** (in Russian)
4. Borisov, A. V., Zheltovodov, A. A., Maksimov, A. I., Fedorova, N. N. and Shpak, S. I. (1996) Verification of Turbulence Models and Computational Methods of Supersonic Separated Flows, *8th International Conference on Methods of Aerophysical Research, Institute of Theoretical and Applied Mechanics, Russian Academy of Sciences, Novosibirsk, Russia*
5. Chernyavsky, B., Yan, H. and Knight, D. (2001) Analyses of Some Numerical Problems in LES, *AIAA Paper 2001-0436*

6. Dolling, D. S. and Murphy, M. T. (1983) Unsteadiness of the Separation Shock Wave Structure in a Supersonic Compression Ramp Flowfield, *AIAA J.*, **Vol. 23, No. 12, pp. 1628–1634**
7. Dolling, D. S. (1983) Fluctuating Loads in Shock Wave/Turbulent Boundary Layer Interaction: Tutorial and Update, *AIAA Paper 93-0284*
8. Erengil, M. E. and Dolling, D. S. (1991) Correlation of Separation Shock Motion with Pressure Fluctuations in the Incoming Boundary Layer, *AIAA J.*, **Vol. 29, No. 11, pp. 1868–1877**
9. Horstman, C C and Hung, C M. (1977) Reynolds Number Effects on Shock-Wave Turbulent Boundary-Layer Interaction - A Comparison of Numerical and Experimental Results, *AIAA paper 77-42*
10. Horstman, C. C. and Zheltovodov, A. A. (1994) Numerical Simulation of Shock Waves/Expansion Fans – Turbulent Boundary Layer Interaction, *Proc: Int. Conference on the Methods of Aerophysical Research, Novosibirsk, Part II*, **pp. 118–125**
11. Hunt, D. (1995) A Very Large Eddy Simulation of an Unsteady Shock Wave/Turbulent Boundary Layer Interaction, *AIAA Paper 95-2212*
12. Konrad, W. and Smits, W. (1998) Turbulence Measurements in a Three-Dimensional Boundary Layer in Supersonic Flow, *J. Fluid Mech.*, **Vol. 372, pp. 1–23**
13. Muck, K., Spina, E. and Smits, A. (1984) Compilation of Turbulence Data for an 8 degree Compression Corner at Mach 2.9, *Tech. Rep. Report MAE-1642, Princeton University*
14. Okong'o, N. and Knight, D. (1998) Compressible Large Eddy Simulation Using Unstructured Grids: Channel and Boundary Layer Flows, *AIAA Paper 98-3315*
15. Ong, C. and Knight, D. (1987) Hybrid MacCormack and Implicit Beam-Warming Algorithms for a Supersonic Compression Corner, *AIAA J.*, **Vol. 25, No. 3, pp. 401–407**
16. Rizzetta, D. P., Visbal, M. R. and Gaitonde, D. V. (2000) Direct Numerical and Large-Eddy Simulation of Supersonic Flows by a High-Order Method, *AIAA Paper 2000-2408*
17. Rizzeta, D. and Visbal, M. (2001) Large-Eddy Simulation of Supersonic Compression Ramp Flows, *AIAA Paper 2001-2858*
18. Settles, G. S., Fitzpatrick, T. J. and Bogdonoff, S. M. (1979) Detailed Study of Attached and Separated Compression-corner Flowfields in High Reynolds Number Supersonic Flow, *AIAA J.*, **Vol. 17, pp. 579–585**
19. Shang, J S and Hankey Jr, W L. (1975) Numerical Solution for Supersonic Turbulent Flow over a Compression Corner, *AIAA J.*, **Vol. 13, No. 10, pp. 1368–1374**
20. Unalmis, O. H. and Dolling D. S. (1994) Decay of Wall Pressure Field and Structure of a Mach 5 Adiabatic Turbulent boundary Layer, *AIAA Paper 94-2363*
21. Urbin, G., Knight, D. and Zheltovodov, A. A. (1999) Compressible Large Eddy Simulation using Unstructured Grid: Supersonic Turbulent Boundary Layer and Compression Corner, *AIAA Paper 99-0427*
22. Urbin, G., Knight, D. and Zheltovodov, A. A. (2000) Large Eddy Simulation of a Supersonic Compression Corner Part I, *AIAA Paper 2000-0398*
23. Visbal, M and Knight, D. (1984) The Baldwin-Lomax Turbulence Model for Two-Dimensional Shock-Wave/Boundary-Layer Interactions, *AIAA J.*,**Vol. 22, No. 7, pp. 921–928**
24. Wilcox, D. C. (1990) Supersonic Compression Corner Applications of a Multiscale Model for Turbulent Flows, *AIAA J.*, **Vol. 28, No. 7, pp. 1194–1198**
25. Yan, H., Urbin, G., Knight, D. and Zheltovodov, A. A. (2000) Compressible Large Eddy Simulation Using Unstructured Grid: Supersonic Boundary Layer and Compression Ramps, *10th International Conference on Methods of Aerophysical Research, Institute of Theoretical and Applied Mechanics, Russian Academy of Sciences, Novosibirsk, Russia*
26. Zheltovodov, A. A. and Yakovolev, V. (1986) Stages of Development, Gas Dy-

namic Structure and Turbulence Characteristics of Turbulent Compressible Separated Flows in the Vicinity of 2-D Obstacles, *Preprint No 27-86, Institute of Theoretical and Applied Mechanics, USSR Academy of Sciences* (in Russian)

27. Zheltovodov, A. A. and Schuelein, E. (1987) The Peculiarities of Turbulent Separation Development in Disturbed Boundary Layers, *Modeling in Mechanics*, **Vol. 2, No. 1, pp. 53–58** (in Russian)
28. Zheltovodov, A. A., Trofimov, V. M., Schuelein, E. and Yakovlev, V. N. (1990) An Experimental Documentation of Supersonic Turbulent Flows in the Vicinity of Sloping Forward- and Backward-Facing Ramps, *Rep No 2030, Institute of Theoretical and Applied Mechanics, USSR Academy of Sciences*
29. Zheltovodov, A. A., Borisov, A. V., Knight, D. D., Horstman, C. C. and Settles, G. S. (1992) The Possibilities of Numerical Simulation of Shock Waves/Boundary Layer Interaction in Supersonic and Hypersonic FLows, *Proc: Int. Conference on the Methods of Aerophysical Research, Novosibirsk, Part I*, **pp. 164–170**
30. Zheltovodov, A. A. and Horstman, C. C. (1993) Experimental and Numerical Investitgation of 2-D Expansion/Shock Wave – Turbulent Boundary Layer Interaction, *Preprint No 2-93, Institute of Theoretical and Applied Mechanics, Russian Academy of Sciences, Novosibirsk*
31. Zheltovodov, A. A., Schuelein, E. and Horstman, C. C. (1993) Development of Separation in the Region where a Shock Interacts with a Turbulent Boundary Layer Perturbed by Rarefaction Waves, *J. Applied Mechanics and Technical Physics*, **Vol. 34, No. 3, pp. 58–68**
32. Zheltovodov, A. A. (1996) Shock Waves / Turbulent Boundary Layer Interaction - Fundamental Studies and Applications, *AIAA Paper 96-1977*
33. Zukoski, E. E. (1967) Turbulent Boundary Layer Separation in front of a Forwrad Facing Step, *AIAA J.*, **Vol. 5, No. 10, pp. 1746–1753**

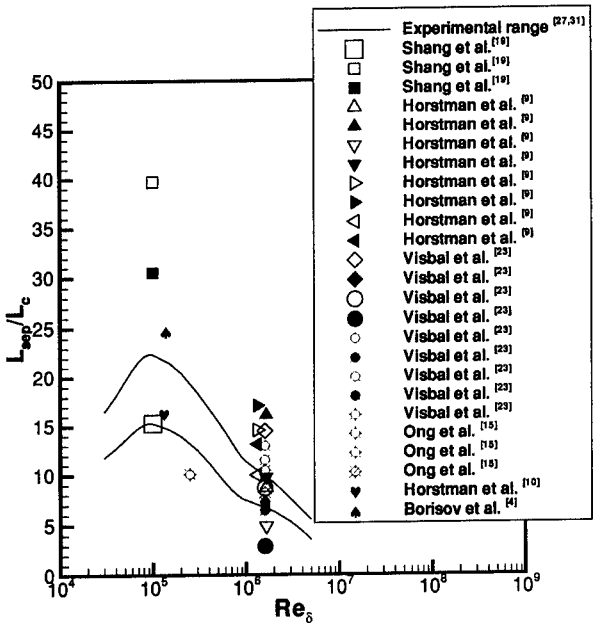


Figure 1. Separation length for RANS

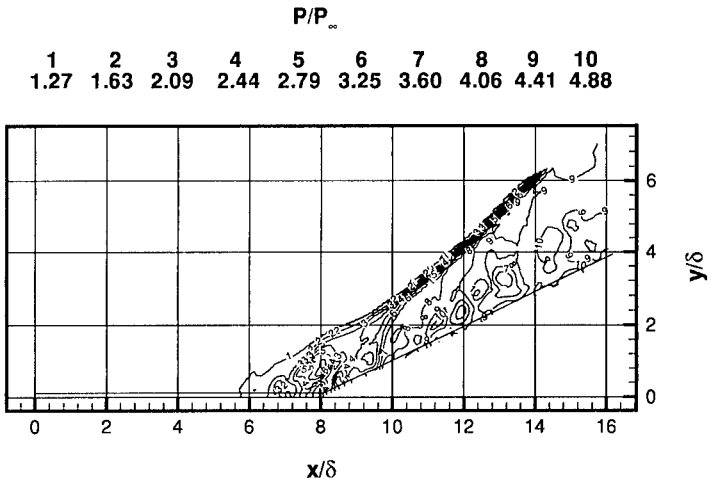


Figure 2. Instantaneous pressure contour

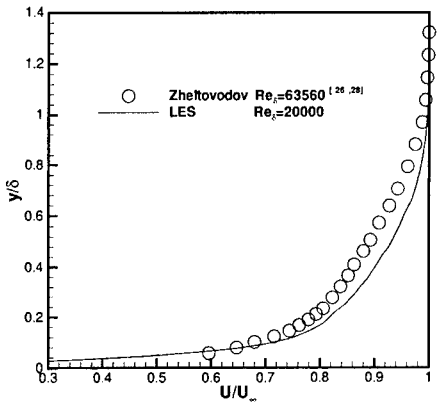


Figure 3. Mean streamwise velocity

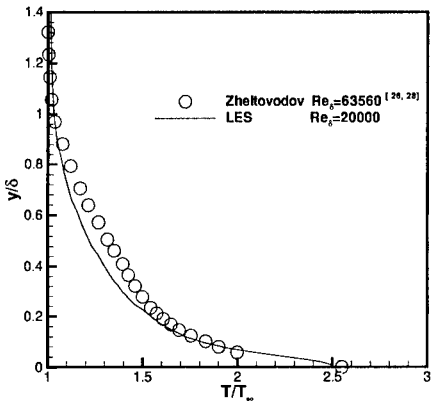


Figure 4. Mean temperature

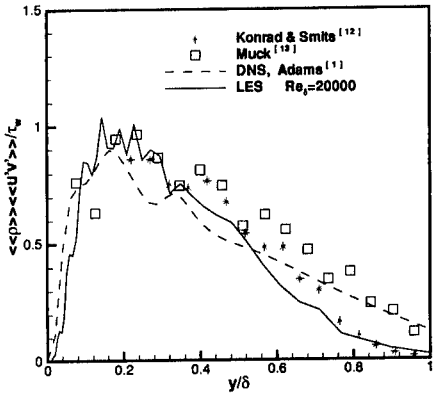


Figure 5. Reynolds shear stress

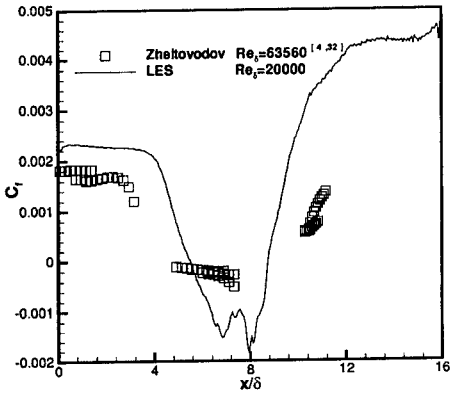


Figure 6. Skin friction coefficient

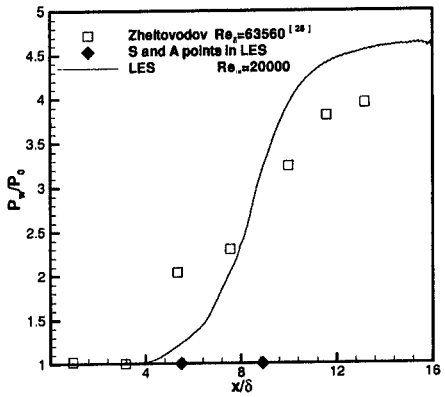


Figure 7. Surface wall pressure

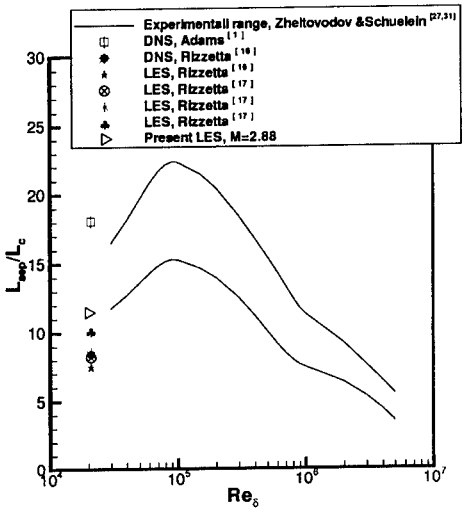


Figure 8. Separation length for LES and DNS

FILTERING BOUNDARY CONDITIONS FOR LES AND EMBEDDED BOUNDARY SIMULATIONS

A. DAS AND R. D. MOSER
Department of Theoretical and Applied Mechanics
University of Illinois at Urbana-Champaign
104 S. Wright St., Urbana IL, 61801

1. Introduction

In the Large Eddy Simulation (LES) of turbulence, we simulate the spatially filtered velocity field. The governing equations are obtained by applying a spatial filter to the Navier-Stokes equations. The set of filtered equations are solved numerically to obtain the solution in terms of filtered quantities. Though successful LES have been performed for several different flows (Lesieur and Métais, 1996; Meneveau and Katz, 2000), LES for wall bounded flows posses some critical challenges (Piomelli et al., 1989; Balaras et al., 1996). Some of the difficulties in LES modeling of wall bounded flows are due to the strong inhomogeneity of the turbulence, the scaling of the largest scales near the wall, and the strong filter inhomogeneity commonly employed to accommodate the boundary conditions. Because of these issues, many of the reported LES of wall bounded flows have no filtering at all in the wall normal direction. The problem associated with strong filter inhomogeneity can be thought of as arising from the inconsistency of the requirement to represent a sharp boundary in a simulation which resolves only large scales.

In a different context, immersed boundary methods are promising tools for treating complex geometries in fluid dynamics simulations. In these methods the irregular boundary is embedded in a regular grid and a forcing term is included to account for the embedded boundary. This forcing is such that a prescribed velocity is achieved at the given surface boundary. The forcing is nonzero only in the neighborhood of the boundary (few grid points near the wall), but due to incompressibility of the flow, the forcing affects the entire flow field. The forcing can be considered to be singular field in the computational domain. The concept was implemented by Peskin

(1972) to simulate flow around heart valves, and Goldstein et. al. (1993) used this technique to simulate flows in complex geometries using a pseudo spectral method. Due to the global nature of the expansion functions used in the spectral methods, discontinuities produce Gibbs phenomenon in the flow field. According to Goldstein et. al. (1993), this oscillation does not corrupt the flow field as the flow evolves in time. Mohd-Yusof (1997,1998) used a different expression for the forcing to remove the severe time step restriction of the method developed by Goldstein et. al. (1993). This approach was used by Verzicco et. al. (1998) to perform an LES in complex geometries. However, in immersed boundary techniques it is in general difficult to preserve higher order accuracy and high resolution as is generally required in turbulent simulations. This difficulty mainly arises due to the presence of discontinuities at the boundaries.

These two related observations lead us to propose a new approach for embedding boundaries in the context of LES. In this approach, we treat the wall by 'filtering through it'. A homogeneous or nearly homogeneous filter is applied to the flow field including the embedded boundary. As a result, the boundary is no longer a sharp interface, but is diffused across the filter width. To recover a Direct Numerical Simulation (DNS), the filter width is made small enough to resolve all relevant scales of motion, but remains finite so that the boundary is not a sharp interface. In LES, the scale on which the boundary is resolved is consistent with the resolved scales of motion.

2. Governing equations and numerical methods

To illustrate the concept of 'filtering through the wall', we consider the heat equation on $y \in [-1, 1]$. In the computational domain, we include a buffer region outside the boundaries, where the velocities are zero.

$$\frac{\partial u}{\partial t} = \frac{\partial^2 u}{\partial y^2} \qquad |y| \leq 1 \tag{1}$$

$$u = 0 \qquad |y| > 1 \tag{2}$$

These two equations can be combined by introducing a Heaviside function $H(y)$.

$$\frac{\partial u}{\partial t} = H(y)\frac{\partial^2 u}{\partial y^2} \qquad -L \leq y \leq L$$

where

$$H(y) = \begin{cases} 1 & : \quad |y| \leq 1 \\ 0 & : \quad \text{otherwise} \end{cases}$$

A homogeneous filter is applied on the domain $-L$ to L, including the boundary. For any function f, the filtered function $\tilde{f}$ is obtained by

$$\tilde{f} = \int_{-L}^{L} G(x-\xi) f(\xi) d\xi \tag{3}$$

where G is the filter kernel. The resulting filtered equation is

$$\frac{\partial \tilde{u}}{\partial t} = \frac{\partial^2 \tilde{u}}{\partial y^2} + G(y-1)\frac{\partial u}{\partial y}(1) - G(y+1)\frac{\partial u}{\partial y}(-1)$$

$$-L \leq y \leq L$$

The boundary term, b is defined:

$$b = G(y-1)\frac{\partial u}{\partial y}(1) - G(y+1)\frac{\partial u}{\partial y}(-1)$$

which includes the unfiltered derivatives at the boundary. These are not known from the simulated filtered field. We propose to estimate the stress by applying a suitable constraint on the field in the buffer domain, $|y| > 1$. The boundary terms obtained by this technique are similar to the forcing term used by (Goldstein et al., 1993) except the forcing is distributed in the domain according to the filter kernel.

Now consider the Navier-Stokes equations for incompressible flows and apply a similar technique. After filtering the equations and taking account of the filtered boundary, the filtered equations are

$$\frac{\partial \tilde{u}_i}{\partial x_i} = 0$$

$$\frac{\partial \tilde{u}_i}{\partial t} + \tilde{u}_j \frac{\partial \tilde{u}_i}{\partial x_j} = -\frac{\partial \tilde{p}}{\partial x_i} + \frac{1}{Re}\frac{\partial}{\partial x_j}\frac{\partial}{\partial x_j}\tilde{u}_i + b_i$$

where b_i is the boundary term. This boundary term is expressed as

$$b_i(\mathbf{x}) = \int_{\partial R} \sigma_{ij}(\mathbf{x}') n_j G(\mathbf{x}-\mathbf{x}')\, d\mathbf{x}'$$

where σ is the stress at the boundary, including pressure and viscous stress, ∂R is the boundary of the fluid region R and n_j is the unit normal to the surface.

In simulating wall bounded turbulent flow, a large number of grid points are required to resolve the near wall layer, as a result, in many practical applications it would be difficult to apply an LES that resolves the wall layer. In many LES of wall bounded flows, approximate boundary conditions are used to model the effect of the wall layer (Balaras et al., 1996).

The approximate boundary conditions are prescribed in terms of the wall shear stress, so wall stresses must be determined in terms of the resolved velocities.

In the present formulation, the unfiltered wall stresses are also required, and for analogues reason. Even though the boundary, or the flow near it is not resolved in LES, it is necessary to represent the transfer of momentum from the flow to the wall, which is governed by the wall stresses. In the current description, in which the unfiltered velocity is zero in the buffer domain, the wall stress is the surface forcing required to ensure that momentum is not transfered to the buffer domain. That is, that the velocity remains zero. This suggests a technique for determining the wall stress. Instead of defining a force to make the velocity zero at the boundary as in Mohd-Yusof (1997), we choose σ_{wall} to minimize the transport of momentum to the exterior domain. To this end, the wall stresses at each time step is defined by minimizing

$$E = \int_{\mathcal{B}} |\tilde{\mathbf{u}}|^2 + \alpha \left| \frac{\partial \tilde{\mathbf{u}}}{\partial t} \right|^2 d\mathbf{x} \tag{4}$$

where the integral is over the buffer domain. The $|\tilde{\mathbf{u}}|^2$ term forces the energy in the buffer domain to be small, and the $\alpha \left| \frac{\partial \tilde{\mathbf{u}}}{\partial t} \right|^2$ term ensures that the transfer of energy into the domain is small. The constant α controls the balance between these two competing requirements and is set to a value of order Δt^2. In the Fourier spectral method employed in section 3 for the channel flow, this minimization is straight forward since it can be done independently for each (k_x, k_z) wavenumber, resulting in a 6-parameter optimization in $(\sigma_{xy}, \sigma_{yy}, \sigma_{zy})$.

3. Results and Discussion

In this section, we present the results of two numerical tests of the filtered boundary technique.

In both cases, a plane channel flow is simulated. Periodic boundary conditions are applied in streamwise (x) and spanwise (z) directions, and in the wall normal direction (y), a buffer region outside the wall is included, and periodicity is imposed in the buffer region as well. A Fourier cutoff filter is applied in the wall normal direction effectively filtering the wall, and a Fourier spectral method is used. A low storage second-order Runga-Kutta method is used to time discritize the nonlinear terms and the viscous terms are treated using an integrating factor.

3.1. THE EVOLUTION OF SMALL AMPLITUDE DISTURBANCES

In this test, evolution of a linear stability mode is illustrated. The exact solution in this case has the form:

$$u(x,y,t) = (1-y^2) + \epsilon Re\{\psi_y(y)e^{i(\alpha x-\omega t)}\}, \tag{5}$$

$$v(x,y,t) = \epsilon Re\{i\alpha\psi(y)e^{i(\alpha x-\omega t)}\}, \tag{6}$$

where ψ is the Orr-Sommerfeld eigenfunction (appropriately normalized), ω is the complex frequency (eigenvalue), α is the prescribed wave number, and ϵ is the perturbation amplitude. The simulation was performed with $\alpha = 1$ at Reynolds numbers $Re_c = 10000$. For this case, the most unstable mode has eigenvalue $\omega = 0.23752649 + i0.00373967$. An initial condition was constructed from the eigenfunction with the most unstable mode and then filtered. Two cases were run, with 64 and 256 Fourier modes in the wall normal direction. A total of 20 "points" are in the buffer domain outside of the channel ($|y| > 1$).

The exact unfiltered pressure fluctuations are formally zero in the exterior, resulting in a discontinuity in pressure, and the resulting Gibbs phenomenon in the filtered pressure is shown in figure 1c. The wall normal pressure gradient appears in the v-momentum equation, and this quantity is dominated by the filtered delta function at the boundary and the resulting Gibbs phenomenon (figure 1d). Yet the Gibbs phenomenon in velocity perturbations in figure 1a and 1b is imperceptible. The reason is that the terms b_v (figure 1e) has exactly the same structure as the pressure gradient and cancel the Gibbs phenomenon (figure 1f). The role of the boundary terms in the momentum equation is thus clear. They regularize the stress discontinuities at the wall (both pressure and viscous stresses).

In these tests, the intent is to use a filter width sufficiently fine that the only input is the filtering of the boundary (i.e. a "DNS").

The average growth rate (ω_i, imaginary part of the complex frequency) of the disturbance was measured as a function of time. For $\alpha = 1$, the complex frequency (ω) is given by

$$\omega = -i(1/\hat{v})(d\hat{v}/dt) \tag{7}$$

Due to errors introduced in the initial conditions, there is a transient before the asymptotic growth rate is reached. The solution with 64 grids in y direction under predicts the growth rate (.00286091) and this is apparently due to inadequate resolution in the domain. The growth rate of the disturbance is correctly reproduced by the simulation with $N_y = 256$ (.00374844 vs. the value from linear theory .00373967).

This is a severe test for the filtered boundary approach, since the Fourier spectral method behaves poorly in presence of discontinuities and because

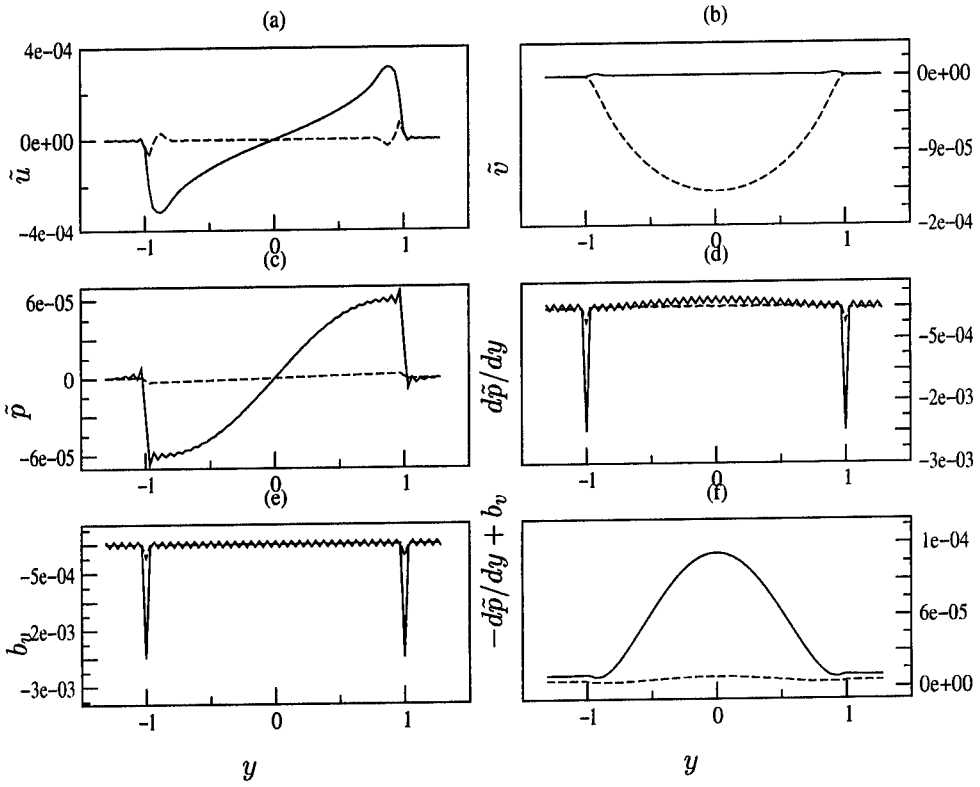


Figure 1. Effect of the boundary terms in the test of evolution of small disturbances in a channel flow. (a) filtered u velocity, (b) filtered v velocity, (c) filtered pressure, (d) pressure gradient, (e) boundary term for v equation, (f) pressure gradient + boundary term. — real part, - - - imaginary part.

the growth rate is very sensitive. But, the boundary terms precisely account for the poor behavior of the filter and provides a good representation of the filtered eigenfunction.

3.2. TURBULENT FULLY DEVELOPED CHANNEL FLOW

To demonstrate the applicability of this technique in simulating turbulent flow, a fully developed channel flow is computed on a $64 \times 128 \times 64$ grid with 20 point in the buffer region. Based on the wall shear velocity u_τ and channel half-width δ, the Reynolds number

$$Re_\tau = \frac{u_\tau \delta}{\nu} \tag{8}$$

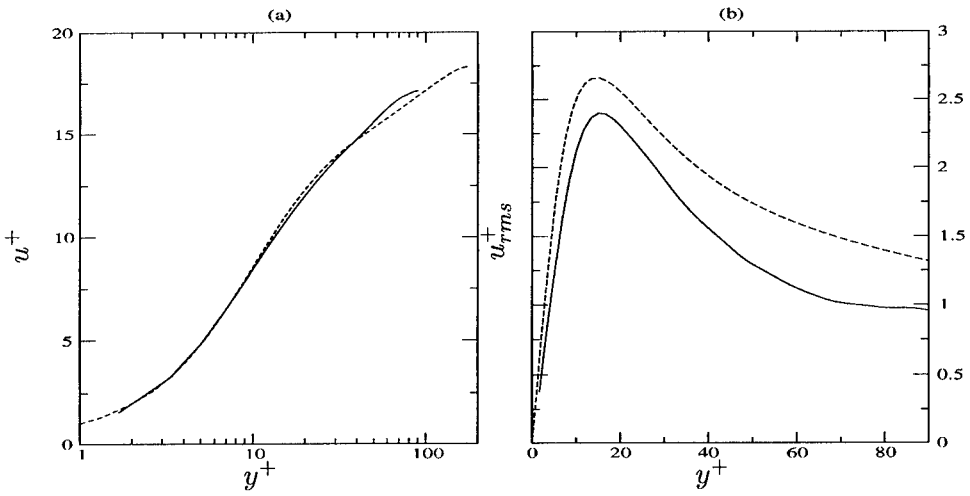


Figure 2. (a)Mean velocity, (b)u_{rms}, normalized by wall shear stress. — present simulation Re_τ 90, - - - Kim et. al. (1987) Re_τ 180.

of this flow is 92.23. The corresponding Reynolds number based on the centerline velocity and channel half-width is 1485. The streamwise and spanwise dimensions of the channel are $4\pi\delta$ and $4/3\pi\delta$ respectively. The flow field was initialized by spatially filtering a DNS flow field obtained at $Re_\tau = 180$ by Kim et al. (1987).

The governing equations were integrated until the mean flow reached statistical equilibrium (approximately $4\delta/u_\tau$). Instantaneous results are shown at non dimensional time 7. The mean velocity distribution normalized by the wall shear velocity is shown in figure 2a, along with the data reported by (Kim et al., 1987) at $Re_\tau = 180$. Also shown in figure 2b is the streamwise turbulent intensity. Note that the computed peak is 9.84% lower than the $Re_\tau = 180$ case, and this is not a low Reynolds number effect (Keefe et al., 1992). The cause of this low peak in u_{rms} is not clear at this point, but the near wall resolution may be responsible. In other ways, the turbulence near the wall is consistent with expectations for wall bounded flows. For example, familiar flow structures (streaks, inclined shear layers) are present near the wall and are approximately of the expected scale.

4. Conclusion

A new approach for treating boundaries in the context of LES, especially extended boundaries, was developed, and applied to the computation of turbulent channel flow. In this representation, the issue of highly inhomogeneous filtering near a wall in LES is obviated, since homogeneous filters

can be used since the boundary itself is filtered. In this formulation, the unfiltered stresses at the wall are required, and are obtained from a minimization of perturbations in the buffer domain.

The method was successfully tested in the evolution of a Tollmien-Schlichting wave in a channel flow. Also a low Reynolds number fully developed turbulent channel was simulated. The new approach is promising for the treatment of boundaries in LES, and the application of optimal LES (Langford and Moser, 1999) to the filtered boundary formulation is planned.

References

Balaras, E., Benocci, C., and Piomelli, U. (1996). Two-layer approximate boundary conditions for large-eddy simulations. *AIAA Journal*, 34:1111–1119.

Goldstein, D., Handler, R., and Sirovich, L. (1993). Modeling a no-slip flow boundary with an external force field. *J. Comp. Phys.*, 105:354–366.

Keefe, L., Moin, P., and Kim, J. (1992). The dimension of attractors underlying periodic turbulent Poiseuille flow. *J. Fluid Mech.*

Kim, J., Moin, P., and Moser, R. (1987). Turbulence statistics in fully developed channel flow at low reynolds number. *J. Fluid Mech.*, 177:133–166.

Langford, J. A. and Moser, R. D. (1999). Optimal les formulations for isotropic turbulence. *J. Fluid Mech.*, 398:321–346.

Lesieur, M. and Métais, O. (1996). New trends in large-eddy simulations of turbulence. *Annu. Rev. Fluid Mech.*, 28:45–82.

Meneveau, C. and Katz, J. (2000). Scale-invariance and turbulence models for large-eddy simulation. *Ann. Rev. Fluid Mech.*, 32:1–32.

Mohd-Yusof, J. (1997). Combined immersed-boundary/b-spline methods for simulations of flow in complex geometries. Technical Report Annual Research Briefs, Center for Turbulence Research, Stanford University.

Mohd-Yusof, J. (1998). Development of immersed boundary methods for complex geometries. Technical Report Annual Research Briefs, Center for Turbulence Research, Stanford University.

Peskin, C. S. (1972). Flow patterns around heart valves: A numerical method. *J. Comp. Phys.*, 10:252–271.

Piomelli, U., Ferziger, J., Moin, P., and Kim, J. (1989). New approximate boundary conditions for large eddy simulations of wall-bounded flow. *Phys. Fluids A*, 1.

Verzicco, R., Mohd-Yusof, J., Orlandi, P., and Haworth, D. (1998). Les in complex geometries using boundary body forces. Technical Report Annual Research Briefs, Center for Turbulence Research, Stanford University.

A COMPARISON OF ADAPTIVE MESH REFINEMENT APPROACHES FOR LARGE EDDY SIMULATION

Sorin M. Mitran
Department of Applied Mathematics
University of Washington
Box 352420, Seattle, WA, 98195-2420, USA
mitran@amath.washington.edu

Abstract A number of approaches to the problem of using adaptive mesh refinement in large eddy simulations are considered and tested. These include unstructured and structured adaptive grids, various treatments of the convective terms and a number of flow diagnostic procedures. The approaches are exemplified on a rotating channel flow.

Introduction

An important aspect in applying large eddy simulation (LES) to technologically interesting flows is the control of the computational costs involved. Complex flows usually present a variety of regions in which different resolutions are called for. Moreover, these regions are not static in the course of the flow evolution. Adaptive mesh refinement is a natural candidate for keeping computational costs down in these types of applications. In this paper a number of approaches are compared in an effort to provide information on the benefits of applying adaptive mesh refinement techniques to LES computations. A first comparison is made between an unstructured grid algorithm and a structured grid algorithm. The same computational procedures are implemented in both codes and comparable resolutions are achieved on a moderately complex flow. The results are compared to one another and a direct numerical simulation (DNS) to permit evaluation of grid quality effects. An additional comparison is made between various criteria of controlling the mesh adaptation. A variety of flow feature diagnostic procedures are allowed to control placement of additional grid points. These include

comparison to predictor steps on coarser grids and refinement according to local values of vorticity.

1. Adaptive Mesh Refinement for LES

1.1 General observations

Adaptive mesh refinement (AMR) [5] has shown itself to be a powerful technique in the computation of flows with dynamic localized structures that require much greater resolution than that needed for most areas of the flow. AMR has been widely applied to flows involving shocks or chemical reactions. There has been less work in the area of applying AMR to turbulent flow. AMR is not suitable for turbulent flows in which fine resolution is required everywhere. There are however a number of flows in which small-scale structures appear and then drive the overall flow. Such structures have limited spatial and temporal extent. The streaks that appear in the boundary layer of channel flow are an example. The overall accuracy of the flow computation is sacrificed if the grid resolution is not fine enough to capture the streaks. Extending the fine grid required to resolve wall streaks to the entire domain is prohibitively expensive. The situation bears some resemblance to those in which AMR has been applied with success.

There is however a significant difference between standard AMR applications and turbulent flow. In standard AMR the computational grids are set up quite frequently, every few time steps. The standard technique used to identify regions in which additional resolution is required is to compare predictions on a coarser and finer grid and use Richardson extrapolation to estimate whether the local truncation error is within acceptable limits. This implicitly assumes that the finest grids in the computation can achieve enough resolution so that the asymptotic error estimates based upon the formal order of accuracy of the numerical method are valid. In the context of turbulence computations this is equivalent to stating that the finest grids can achieve DNS-like resolution. This is prohibitive and a modification of AMR to account for unresolved scales of motion is necessary.

Previous work has also sought to address the problem of differentiating between scales that should be resolved and others that can be economically modeled. An early idea due to Voke [18] was to use multiple meshes as a tool in accelerating convergence to a quasi-steady state. The Dynamic Multilevel (DML) method of Dubois, Jauberteau and Temam [7] can be seen as an alternative to LES. Instead of modeling subgrid stresses using a physical model, in DML the small scales are computed less accurately using lower-order schemes with larger time steps. Terra-

col, Sagaut and Basdevant [16] have suggested freezing the small scales while a number of time steps are taken on the coarser grids. In order not to lose small-scale dynamics, they suggest a periodic prolongation of the large-scale velocity fields using small-scales stored from previous time steps. Both the large and small scales are advanced in time for a few steps after which a new large scale velocity field is obtained by filtering. This procedure raises the question of the equilibrium between small and large scales during the prolongation stage. This step of the algorithm might effectively act as an external, non-physical excitation. Quéméré, Saguat and Couaillier [15] presented a procedure in which patched grids of different resolutions were used in a channel flow. They show that considerable economy may be obtained by using fine grids only in the wall region but also remark that numerical artefacts arose at the grid boundaries.

1.2 Governing equations

The governing equations are the filtered, compressible Navier-Stokes equations for an ideal gas

$$\frac{\partial \bar{U}}{\partial t} + \frac{\partial \bar{F}_1}{\partial x_1} + \frac{\partial \bar{F}_2}{\partial x_2} + \frac{\partial \bar{F}_3}{\partial x_3} = 0\,,$$

$$\bar{U} = \left[\begin{array}{cccc} \bar{\rho} & \bar{\rho}\tilde{u}_1 & \bar{\rho}\tilde{u}_2 & \bar{\rho}\tilde{u}_3 \end{array}\quad \bar{\rho}\tilde{e}\right]^T,$$

$$\bar{F}_i = \left[\begin{array}{c} \bar{\rho}\tilde{u}_i \\ \bar{\rho}\tilde{u}_i\tilde{u}_1 + \bar{p}\delta_{i1} - \tau_{i1} - \mu\tilde{S}_{i1} \\ \bar{\rho}\tilde{u}_i\tilde{u}_2 + \bar{p}\delta_{i2} - \tau_{i2} - \mu\tilde{S}_{i2} \\ \bar{\rho}\tilde{u}_i\tilde{u}_3 + \bar{p}\delta_{i3} - \tau_{i3} - \mu\tilde{S}_{i3} \\ (\bar{\rho}\tilde{e} + \bar{p})\tilde{u}_i - Q_i - \mu\tilde{S}_{ij}\tilde{u}_j - k\dfrac{\partial\theta}{\partial x_i} \end{array}\right],$$

with $\bar{}$ denoting grid filtering, and $\tilde{}$ density-weighted averaging. The filtered equation of state is $\bar{p} = \bar{\rho}R\tilde{T}$, the diagonal term of the subgrid-stress tensor is neglected [8], the resolved energy is

$$\bar{\rho}\tilde{e} = \bar{\rho}c_v T + \frac{1}{2}\bar{\rho}\left(\tilde{u}_1^2 + \tilde{u}_3^2 + \tilde{u}_3^2\right),$$

the Sutherland relation for constant Prandtl $\mathrm{Pr} = c_p\mu(\theta)/k(\theta) = 0.7$ is applied, and the system is closed with variable density eddy-viscosity and diffusivity models

$$\tau_{ij} = \bar{\rho}\nu_t\tilde{S}_{ij}, \quad Q_i = \bar{\rho}\frac{\nu_t}{\mathrm{Pr}_t}\frac{\partial\theta}{\partial x_i}.$$

1.3 Filtering procedures

The general multi-level filtering framework proposed by Germano [9] is adopted. Each grid level has an associated filter operation G_n. Filters from the same family (i.e. top hat in the applications presented here) are used at all levels. Filtered variables may be defined at each grid level by $\langle\phi\rangle_n(\mathbf{x},t) = (G_n * \phi)(\mathbf{x},t)$. The coarsest grid level is denoted by 0 and the finest existent at a given space-time locale by L. The Navier-Stokes equations from above, $\partial_t U + N(U) = 0$ become

$$\partial_t \langle U\rangle_n + N(\langle U\rangle_n) = -T_n$$

after filtering. The closure procedure parallels that presented for a single filtering operation in the previous section.

1.4 Flow feature diagnostics

Standard AMR is typically viewed as a black box that may applied to the solution of any time varying problem that exhibits localized features. The criterion governing grid refinement is mathematical in nature and typically does not include any physical knowledge about the particular problem being solved. On the other hand, most multi-level techniques that have been proposed for turbulence simulation rely heavily upon physical modeling of the subgrid scale effects. For instance, in DML [7] the freezing of the small scales when taking coarse grid time steps is justified by the different characteristic times in which small and larger scale turbulence achieves local equilibrium. The point of view espoused in this paper is that probably both ingredients are required in order to achieve a successful algorithm. The particular method studied here is a combination of *a posteriori* error analysis combined with physical analysis.

Initially the standard technique of error estimation based upon Richardson extrapolation [5] was tried. This was unsatisfactory as it led to a rapid increase in the overall number of points. A resolution typical of DNS was set up by this procedure. The approach that was successful consists of a combination of error estimation and physical reasoning. Recently, Adjerid et al. [1] have analyzed the error of a class of discontinuous Galerkin methods applied to hyperbolic problems that include the standard finite volume schemes typically used in compressible fluid computations. Essentially, the procedure recognizes that for a given polynomial approximation of the solution of degree p over an element of extent h, the discretization error is generally $O(h^{p+1})$. At certain points within the element, that correspond to the roots of the difference of two Legendre polynomials, the error is $O(h^{p+2})$. For details the reader is

directed to [1]. The different spatial orders of accuracy permit a rapid *a posteriori* estimate of the accuracy achieved on the cells at any one particular grid level. Rather than obtaining the error estimate by comparison to a test integrating in time on a coarser grid, only the results from a trial time step on the current grid level is required.

Changing the mathematical error estimation method is not enough. Tests using the *a posteriori* error estimate again led to excessive refinement and consequent loss of economy of computation. An examination of the flow field showed that this occurred even in regions where the fluid turbulence was essentially isotropic and suitable for modeling by the subgrid scale terms. A physical correction of the error estimator was therefore added. In the regions flagged for refinement by the error estimator two physical indicators were computed: the enstrophy $|\nabla \times \vec{u}|$ and the scalar product of the local velocity and vorticity $|(\nabla \times \vec{u}) \cdot \vec{u}|$. Only when one of the physical indicators exceeded a threshold value was the region subject to refinement. In effect the physical indicators act to discriminate interesting dynamics that includes prominent vortex tubes from that of locally near-isotropic turbulence. The cutoff value was determined by numerical experimentation. This is unsatisfactory and further analysis is underway to establish a more rational procedure of establishing a cutoff value. Other indicators suggested by coherent structure eduction procedures are also undergoing tests.

1.5 Communication between grids

An important aspect in a multilevel algorithm is to establish procedures for communication of data between grids on various levels. This involves two operations: (1) a prolongation operation P from coarse to fine grids and; (2) a restriction operation R from fine to coarse grids. Standard AMR typically uses a linear interpolation to define P and a cell averaging procedure to define R. A modification of these procedures was found to be necessary in the context of applying AMR to LES. The prolongation operator is applied whenever new fine grids are generated. Generally there is significant overlap between the new fine grids and previously generated grids at the same level since coherent structures that require better resolution are advected with the mean flow. In order not to lose dynamic content (high frequency contributions), fine grids are first initialized to previously computed values at the same grid level in areas of grid overlap. The prolongation operator is only applied to newly created fine grids, at level l say, where no grids of level l existed previously. Straightforward linear interpolation was found to induce excessive subgrid cell excitation. This had the effect of increasing the

number iterations in the pseudo-time variable (see below) required to achieve convergence at a given physical time step. Faster convergence was achieved by using the truncation of the dispersion relation from the Navier-Stokes equations to the wavenumbers resolvable on the newly created grid. This relation was used to define the newly resolvable spectral content by assuming that the energy spectrum follows a power law. The power law coefficient was taken to depend on the region of the spectrum, i.e. a quadratic interpolation of the power law coefficient from $m = 4$ in the energy containing eddy region to $m = -5/3$ in the inertial range.

A number of previous multi-level turbulence simulations (e.g. [15]) mentioned difficulties at the boundaries between coarse and fine grids due to the effect of averaging. Simple averaging was found to have the same effect in the computations carried out here. However, conservative fix-ups [5], [4] in which the more accurately computed fluxes on fine grids are used to update adjoining coarse grid values was found to work well.

2. Numerical Methods

2.1 Unstructured Grid Algorithm

The unstructured grid algorithm uses an embedded tetrahedral grid approach implemented as an octal tree structure (OCTLES - Octal Tree Large Eddy Simulation code) [13]. There are several options for treating the convective terms from the Navier-Stokes equations. These include multi-dimensional fluctuation splitting [6], second order reconstruction and approximate Riemann solvers along the cell interface normal direction [17] and multi-dimensional wave propagation techniques [12]. The convective terms are advanced in time explicitly. Diffusive terms are treated implicitly. A pseudo-time stepping technique [3] is used within each physical time step to solve the resulting implicit system. Subgrid-scale turbulent stresses are included using the dynamic model [10]. An interesting feature of this application of the dynamic model is that subgrid-scale stresses are computed for each grid pair between the coarsest, initial grid and the finest grid present. This has been observed to speed up the convergence of the pseudo-time iterations required to determine the contribution of the viscous terms. The code has been validated [14] by comparison to a number of test cases proposed in [2]. Grid adaptation is carried out by recursive subdivision of an initial tetrahedral grid.

2.2 Structured Cartesian grid algorithm

An alternative to the complicated program structures required for unstructured girds is to use embedded Cartesian grids [5]. The grid generation procedures are much simpler in this case, but the problem of boundary representation appears for general geometries. In order to test the AMR-LES procedures, sample computations have been performed only in a rectangular geometry. The computer code for this approach (BEARCLAW -Boundary Embedded Adaptive Refinement Conservation Law) allows for a number of treatments of the convective and source terms. These parallel those presented in the unstructured grid case. The BEARCLAW code may be freely downloaded from `www.washington.edu/~claw`.

3. Applications

3.1 Stationary and rotational channel flow

The above procedures are now tested on channel flow. Both a stationary channel and one rotating along an axis in the spanwise mean flow direction are considered. The AMR-LES results are compared to DNS results [11]. The half channel width, bulk velocity Reynolds number is $\mathrm{Re} = U_b h/\nu = 2900$. The rotating channel has a Rossby number $Ro = 2\Omega h/U_b = 0.5$. The second order wave propagation algorithms of [12] are used to treat the convective terms in both the structured and unstructured computations presented here. A comparison between the DNS results and those obtained by the two AMR methods is presented in fig. 1-2 for the turbulent stress. An initial, coarsest level, grid of dimensions $32x32x32$ was used. A tetrahedral grid was obtained by splitting each hexahedron of the regular Cartesian grid in six tetrahedra. The AMR results are within 1% of the DNS results for the stationary channel flow. Both the structured and unstructured methods perform similarly on this case. This is thought to result from the overall symmetry of the flow and the fact that the tetrahedral grid was obtained by destructuring the Cartesian grid. It is apparent from fig. 1 that the AMR algorithms place finer resolution in the high shear regions closer to the walls. When rotation is applied the AMR-LES methods exhibit lower accuracy. The maximum error observed in the turbulent stress was 2.4%. Also, the loss of symmetry imposed by the rotation led to different grid placement in the unstructured algorithm with respect to the Cartesian algorithm. Higher error levels were observed for the tetrahedral grid algorithm. Instantaneous vorticity plots of the flow computed by the Cartesian AMR-LES method are presented in fig. 3-4. It may

be observed that the AMR procedure captures the rich dynamics of the near-wall region and the relaminarization which occurs on the rotating channel suction side.

4. Conclusions

An adaptive mesh refinement methodology for large eddy simulation has been proposed. LES in itself reduces the dynamic complexity of simulating fluid turbulence. It is asserted that adaptive refinement may offer further reductions of the degrees of freedom that need to be resolved. The AMR-LES algorithm proposed here differs from standard AMR algorithms. There are always some dynamics taking place at the unresolved scale, so the usual error estimation procedures used to add mesh points do not carry over directly. Rather, a combined strategy incorporating both numerical estimates and physical flow features is applied. The overall effect is to employ greater grid resolution in regions in which the subgrid effects relative to grid level l are diagnosed as involving significant deviations from isotropic turbulence. In regions in which the indicator suggests that subgrid fluctuations are isotropic in nature, a standard dynamic, eddy-viscosity model is used to provide closure terms. Full testing of the method is still in progress and shall be reported at a later date.

Acknowledgments

This research was supported in part by the National Science Foundation through grant DMS-9803442, and the Department of Energy through grant DE-FG03-00ER2592. The author also gratefully acknowledges the support and encouragement offered by Randall J. LeVeque.

References

[1] S. Adjerid, L. Krivodonova, J. Flaherty, and K. Devine. An a posteriori error estimate for the discontinuous galerkin method for hyperbolic problems. *Comp. Meth. Appl. Mech. Engrng.*, (to appear).

[2] AGARD. A selection of test cases for the validation of large-eddy simulations of turbulent flows. Technical Report 345, AGARD, 1998.

[3] A. Arnone, M.-S. Liou, and L. Povinelli. Integration of Navier-Stokes equations using dual time stepping and a multigrid method. *AIAA J.*, 33:985–990, 1995.

[4] M. Berger and R. LeVeque. Adaptive mesh refinement using wave-propagation algorithms for hyperbolic systems. *SIAM J. Num. Analysis*, 35:2298–2316, 1998.

[5] M. J. Berger and J. Oliger. Adaptive mesh refinement for hyperbolic partial differential equations. *J. Comp. Phys.*, 53:484–512, 1984.

[6] H. Deconinck, R. Struijs, H. Bourgois, H. Paillere, and P. Roe. Multidimensional upwind methods for compressible flows. *AGARD*, R-787, 1992.

[7] T. Dubois, F. Jauberteau, and R. Temam. *Dynamic Multilevel Methods and the Numerical Simulation of Turbulence.* Cambridge University Press, Cambridge, 1999.

[8] G. Erlebacher, M. Hussaini, C. Speziale, and T. Zang. Toward the large-eddy simulation of CompressibleTurbulent flows. *J. Fluid Mech.*, 238:155–185, 1992.

[9] M. Germano. Turbulence: the filtering approach. *J. Fluid Mech.*, 238:325–336, 1992.

[10] M. Germano, U. Piomelli, P. Moin, and W. Cabot. A dynamic subgrid-scale eddy viscosity model. *Phys. Fluids*, A 3:1760, 1991.

[11] R. Kristoffersen and H. Andersson. Direct simulations of low-reynolds-number turbulent flow in a rotating channel. *J. Fluid Mech.*, 256:163–197, 1993.

[12] R. LeVeque. Wave propagation algorithms for multidimensional hyperbolic systems. *J. Comp. Phys.*, 131:327–353, 1997.

[13] S. Mitran, D. Caraeni, and D. Livescu. Large eddy simulation of unsteady rotor-stator interaction in a centrifugal compressor. In *33rd*

AIAA/ASME/SAE/ASEE Joint Propulsion Conference and Exhibit, New York, 1997. AIAA.

[14] S. Mitran and P. Cizmas. LES calibration of a turbulent potential model for turbomachinery flows. In *AIAA/ASME/SAE/ASEE Joint Propulsion Conference and Exhibit*. AIAA Paper 2000-3203, 2000.

[15] P. Quéméré, P. Sagaut, and V. Couailler. Une méthode multidomaine/multirésolution avec application à la simulation des grandes échelle. *Comptes rendus de l'Académie des sciences - Série IIb - Mécanique*, 328:87–90, 2000.

[16] M. Terracol, P. Sagaut, and C. Basdevant. A multilevel / multiresolution approach for large-eddy simulation. In *European Congree on Computational Methods in Applied Sciences and Engineering (ECCOMAS 2000)*, 2000.

[17] V. Venkatakrishnan. Perspective on unstructured grid flow solvers. *AIAA J.*, 34:533–547, 1996.

[18] P. Voke. Multiple mesh simulation of turbulent flow. Technical Report QMW EP-1082, Queen Mary and Westfield College, University of London, 1990.

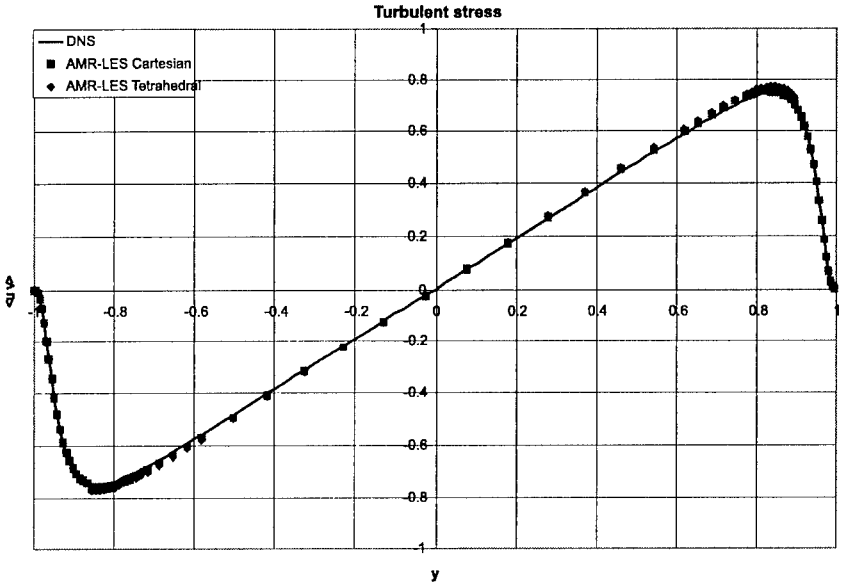


Figure 1. Comparison between DNS computation (line)[11], Cartesian grid AMR (squares) and tetrahedral grid AMR (diamonds). The turbulent stress along the channel span. Notice the larger grid spacing close the channel centerline and the smaller grid spacing near the walls.

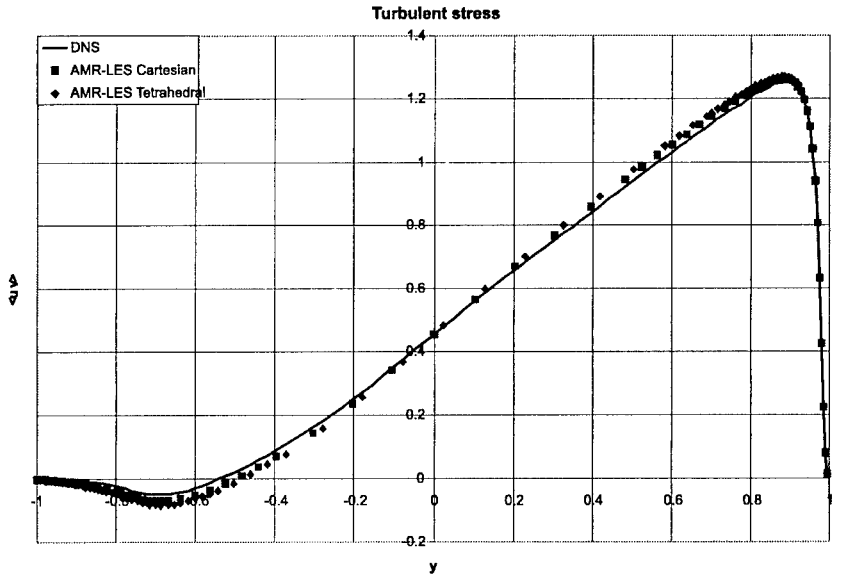


Figure 2. Similar to previous figure but for rotating channel, $Ro = 0.5$.



Figure 3. Isovorticity surfaces computed using Cartesian AMR, stationary channel.

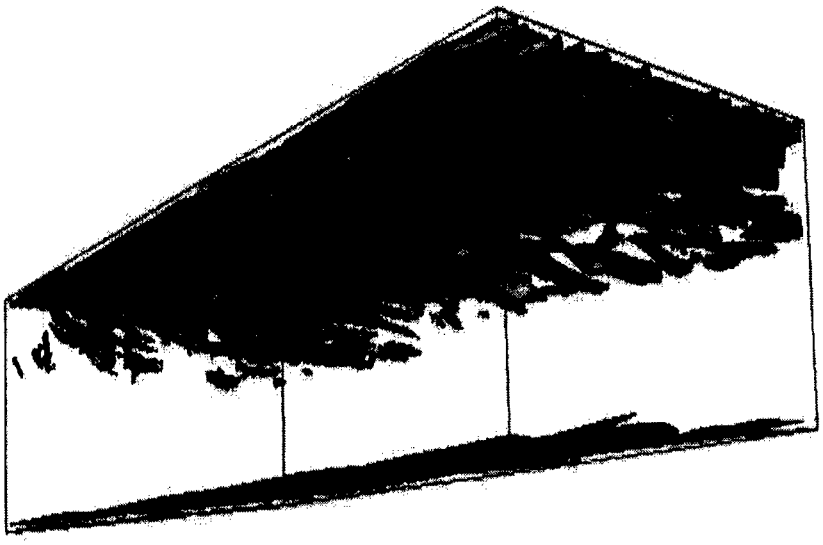


Figure 4. Isovorticity surfaces computed using Cartesian AMR, rotating channel $Ro = 0.5$.

AN EFFECTIVE FOURTH ORDER FINITE VOLUME METHOD FOR DNS/LES ON NON-UNIFORM GRID

P. IANNELLI, F. M. DENARO, G. DE STEFANO
Dipartimento di Ingegneria Aerospaziale
Seconda Università di Napoli, Aversa, Italia

Abstract

This paper is concerned with the development of a fourth order Finite Volume scheme for the numerical solution of the incompressible Navier-Stokes equations on non-uniform grids. In fact, the use of non-uniform computational grids is inevitable in handling non-homogeneous flow computations, while numerical simulation of turbulent flows demand for higher order schemes. The effective high order accuracy is obtained by reformulating the momentum equation in terms of a fourth order deconvolved velocity field. Both a proper integration and flux reconstruction is implemented for the space discretization. A Fractional Time-Step method for the pressure-velocity de-coupling is adopted and a second order semi-implicit scheme is used for the time integration. Particular attention has been devoted in developing congruent time-accurate intermediate boundary conditions for the predictor step.

1. Introduction

Direct Numerical Simulations (DNS) as well as Large Eddy Simulation (LES) demand for accurate and efficient numerical schemes due to the wide range of length scales involved in a turbulent flow. In fact, low order methods show high numerical errors in the smallest resolved scales. As a matter of fact, for a long time, the numerical simulation of turbulent flows has been carried out by means of second order Finite Difference (FD) central scheme since, from the LES point of view, one performs an implicit application of the *top-hat* spatial filter. Moreover, LES on non-uniform grids were initially performed in a straightforward manner without taking into account for the existing commutation error, while only recently the correct equations for LES on non-uniform grids were analysed [1] and much more importance was given to the correlation between numerical errors and modelling ones (e.g.: [2]). More recently, conservative fourth order FD schemes were proposed over both staggered and co-located non-uniform grids (e.g.: [3]).

As it regards with the Finite Volume (FV) method, the integral form of the Navier-Stokes equations appears the most opportune by a physical point of view, allowing mass and momentum to be *a-priori* conserved. In this framework, an evolution equation for the volume-averaged field $\bar{\mathbf{v}}$ is solved, obtaining a second order approximation for the point-wise velocity $\mathbf{v}$, even by adopting higher-order

fluxes integration. Very recently, a fourth order FV compact scheme was proposed in [4], where a deconvolution technique was proposed in order to recover fourth-order accuracy from the volume averaged velocity field. Actually, such procedure was applied only in a post-processing step while the solved variable remains the second order averaged one.

On the contrary, in this paper, we follow the approach already introduced in the framework of the so-called Implicit Structural Models [5, 6]. In that approach, a modified integral equation, governing the evolution of an effective fourth-order variable, is obtained by means of a de-convolution procedure applied on the original FV equations. Following such guidelines, the development of a high order FV scheme on non-uniform grid is illustrated in the framework of the Fractional Time-Step (FTS) method for pressure-velocity de-coupling. The spatial discretization is performed according to the Simpson integration rule while proper Lagrange interpolation is used for the fluxes reconstruction. The time integration is performed by means of the semi-implicit Adams-Bashforth/Crank-Nicolson (AB/CN) scheme. Finally, time-accurate boundary conditions to be associate to the predictor equation were developed in a manner consistent with the adopted time integration. The proposed method has been validated in the numerical simulation of both the two-dimensional Taylor decaying vortex solution and a time evolving mixing layer.

2. Deconvolved Navier Stokes Equations On Non-Uniform Grids

Consider the Navier-Stokes equations for incompressible isothermal flows in a bounded domain V, written in integral non-dimensional form over a Finite Volume (FV) $\Omega(\mathbf{x})\subseteq V$, centred in $\mathbf{x}$, whose boundary is denoted by $\partial\Omega(\mathbf{x})$:

$$\int_{\partial\Omega(\mathbf{x})} \mathbf{n}\cdot\mathbf{v}\; dS = 0 \quad , \tag{1}$$

$$\frac{\partial \bar{\mathbf{v}}}{\partial t} + \frac{1}{|\Omega(\mathbf{x})|}\int_{\partial\Omega(\mathbf{x})} \mathbf{n}\cdot\mathbf{F}\, dS = \mathbf{0} \tag{2}$$

being $\bar{\mathbf{v}}$ the local volume averaged velocity, $|\Omega(\mathbf{x})|$ the measure of the FV, $\mathbf{n}$ the local unit vector outward to the boundary $\partial\Omega$ and $\mathbf{F}$ the momentum flux tensor, expressed as $\mathbf{vv} + \mathbf{I}p - \underline{\nabla}\mathbf{v}/\mathrm{Re}$. A proper initial field $\mathbf{v}_0$ and boundary conditions $\mathbf{v}_b$ on ∂V must be associated to the system (1)-(2).

Following the formulation proposed in [5], an *m-th* order Taylor expansion for $\mathbf{v}$ around the FV centre $\mathbf{x}$ is performed, being m an even integer. Owing to the cell symmetry, one gets (for sake of brevity, time dependence is omitted):

$$\bar{\mathbf{v}}(\mathbf{x}) = \left(I_{\mathbf{x}} - R_{\mathbf{x}}^{(m)}\right)\mathbf{v} + O\left(h^{m+2}\right) \equiv G_{\mathbf{x}}^{(m)}\,\mathbf{v} + O\left(h^{m+2}\right) \tag{3}$$

being h a linear extension of the FV, e.g. $h=|\Omega(\mathbf{x})|^{1/3}$. The differential operator $R_{\mathbf{x}}^{(m)} \equiv -\sum_{l=1}^{m} \frac{1}{l!} \sum_{l_1+l_2+l_3=l} C_{l_1,l_2,l_3}(\mathbf{x})\, D_{\mathbf{x}}^{(l_1,l_2,l_3)}$ was introduced, being $D_{\mathbf{x}}^{(l_1,l_2,l_3)} = \partial_{x_1}^{l_1}\partial_{x_2}^{l_2}\partial_{x_3}^{l_3}$ the

l-th order three-dimensional derivative in a Cartesian reference system and $C_{l_1,l_2,l_3}(\mathbf{x}) = \frac{1}{|\Omega(\mathbf{x})|}\prod_{k=1}^{3}\int_{\Omega(\mathbf{x})}(x'_k - x_k)^{l_k}d\mathbf{x}'$ the coefficients of the moments of the Taylor expansion terms. By truncating and inverting Eq.(3), one obtains the m-th order de-convolved velocity $\tilde{\mathbf{v}}(\mathbf{x}) \equiv \left[G_{\mathbf{x}}^{(m)}\right]^{-1}\bar{\mathbf{v}}$, whose properties in both physical and Fourier space were analysed in [5]. If the inverse operator $\left[G_{\mathbf{x}}^{(m)}\right]^{-1}$ is applied on Eq.(2), one gets an evolution equation for the de-filtered field $\tilde{\mathbf{v}}$, but commutation terms appear for non-uniform grids. Herein, in order to avoid the explicit computation of such terms, the LHS of Eq.(2) is simply re-written, so that:

$$G_{\mathbf{x}}^{(m)}\frac{\partial\tilde{\mathbf{v}}}{\partial t} = \mathbf{I}_{conv} + \mathbf{I}_{diff} + \mathbf{I}_{press} \tag{4}$$

with

$$\mathbf{I}_{pres} = -\frac{1}{|\Omega(\mathbf{x})|}\int_{\partial\Omega(\mathbf{x})} dS\,\mathbf{n}\cdot\mathbf{I}p \quad ; \mathbf{I}_{conv} = -\frac{1}{|\Omega(\mathbf{x})|}\int_{\partial\Omega(\mathbf{x})} dS\,\mathbf{n}\cdot\mathbf{vv} \quad ; \tag{5}$$

$$\mathbf{I}_{diff} = \frac{1}{\mathrm{Re}\,|\Omega(\mathbf{x})|}\int_{\partial\Omega(\mathbf{x})} dS\,\mathbf{n}\cdot\underline{\nabla}\mathbf{v} \equiv \frac{1}{\mathrm{Re}}D\mathbf{v}\,;\; D \equiv \frac{1}{|\Omega(\mathbf{x})|}\int_{\partial\Omega(\mathbf{x})} dS\,\mathbf{n}\cdot\underline{\nabla}(\bullet)$$

As a matter of fact, from the LES point of view, Eq. (4) should be supplied with a suitable Sub-Grid Scales (SGS) model, in order to express the RHS in terms of the resolved variable $\tilde{\mathbf{v}}$. However, in this paper, we just consider $\mathbf{F}(\mathbf{v}) \approx \mathbf{F}(\tilde{\mathbf{v}})$ without addressing this issue. In the framework of Implicit Structural Models [6], this can be interpreted as an LES approach for the *top-hat* filtered variable, supplied by a sort of generalized scale similarity SGS model. Finally, the de-convolution order is fixed to $m=2$ ($G_2 \equiv G_{\mathbf{x}}^{(2)}$) in order to get $\tilde{\mathbf{v}}$ representing an effective fourth-order approximation to the point-wise velocity field.

3. A Fourth Order Deconvolution-based Scheme on Non-Uniform Grids

In this section, a fourth order FV method is developed for 2-D flows simulation on Cartesian non-uniform grids. The de-coupling between the velocity and the pressure gradient is performed according to the FTS method [7], while the semi-implicit Adams-Bashforth/Crank-Nicolson second order scheme is adopted for the time integration. Furthermore, let us assume the computational domain $V = [0, L_1]\times[0, L_2]$. Owing to its computational simplicity, a co-located arrangement of the variables was adopted, hence the flux vectors defined onto the face-nodes must be approximated in terms of the balanced variables in the FV centre nodes.

3.1. Two-Dimensional Grid Definition

The grid points (see Fig.1) are uniformly distributed in x-direction (supposed to

be a stream-wise direction), i.e., $x_i = (i-1)h_1 + h_1/2$, with $h_1=L_1/N_1$ the step size, $i=1,...N_1$, being N_1 the number of FVs in x- direction. The y-direction (supposed to be a normal wall one) has non-uniform grid spacing obtained by means of an 1-D mapping $y = Y(\zeta)$, being ζ the independent variable in the computational domain. This latter is uniformly discretized by a step size $H=L_2/N_2$, being N_2 the number of FVs in y-direction. Furthermore, for each FV the face co-ordinates $y_j^- = Y(\zeta_j)$ and $y_j^+ = Y(\zeta_{j+1})$, are defined for $j=1,..\ N_2$ and thus, the FV grid node results $y_j = (y_j^- + y_j^+)/2$, being $y_j^- = y_{j-1}^+$ for grid construction. The mesh size in y-direction is defined as $h_2(j) = y_j^+ - y_j^- = Y(\zeta_{j+1}) - Y(\zeta_j)$ having assumed a smooth mapping ($h_2/H = O(1)$) so that, the FV definition is $\Omega_{ij} \equiv [x_i - h_1/2; x_i + h_1/2] \times [y_j - h_2(j)/2; y_j + h_2(j)/2]$. It is noteworthy that one can simply express the face co-ordinates as $x_i^{\pm} = x_i \pm h_1/2$, $y_j^{\pm} = y_j \pm h_2(j)/2$.

3.2. The FTS Procedure and The Discrete Time Integration

In Eqs.(1) and (4) the diffusive terms along the y-direction are integrated in time by means of the Crank-Nicolson scheme, while the Adams-Bashforth one is adopted for all the other terms. In the present FTS method (*pressure-free projection method*), first an equation for a non-solenoidal vector $\mathbf{v}^*$ is obtained by integrating Eq.(4) and eliminating the pressure term:

$$\left(G_2 - \frac{\Delta t}{2\,\mathrm{Re}} D_y\right)\mathbf{v}^* = \left[G_2 + \frac{\Delta t}{2\,\mathrm{Re}}(D_y + 3D_x)\right]\mathbf{v}^n + \frac{\Delta t}{2}\left(3\mathbf{I}_{conv}^n - \frac{1}{\mathrm{Re}} D_x \mathbf{v}^{n-1} - \mathbf{I}_{conv}^{n-1}\right) \quad (6)$$

$$\text{in } V$$

$$\mathbf{v}^* = \mathbf{v}_b^* \qquad \text{on } \partial V$$

$$D_x \equiv \frac{1}{|\Omega(\mathbf{x})|}\int_{y^-}^{y^+} d\eta \left(\left.\frac{\partial}{\partial \xi}\right|_{x^+} - \left.\frac{\partial}{\partial \xi}\right|_{x^-}\right) \quad ; \quad D_y \equiv \frac{1}{|\Omega(\mathbf{x})|}\int_{x^-}^{x^+} d\xi \left(\left.\frac{\partial}{\partial \eta}\right|_{y^+} - \left.\frac{\partial}{\partial \eta}\right|_{y^-}\right)$$

In the previous relations, the operator D was split as $D = D_x + D_y$, along the Cartesian directions, being $x^{\pm}$ and $y^{\pm}$ the face co-ordinates of Ω. Observe that the de-convolution procedure does not increase the computational cost since a semi-implicit procedure has been adopted for the time integration. Therefore, the LHS will simultaneously take into account for both deconvolution and time integration

The predicted velocity field $\mathbf{v}^*$ must be corrected by means of a pure gradient field according to:

$$\mathbf{v}^{n+1} \equiv \mathbf{v}^* - \underline{\nabla}\phi \quad . \quad (7)$$

Therefore, once the vector field $\mathbf{v}^*$ was computed, the continuity constraint is enforced at the new time level t^{n+1} by means of the *projection* step:

$$D\phi = \frac{1}{|\Omega(\mathbf{x})|}\int_{\partial\Omega(\mathbf{x})} \mathbf{n}\cdot\mathbf{v}^*\, dS \quad ; \quad \frac{\partial\phi}{\partial n} = \mathbf{n}\cdot\left(\mathbf{v}^* - \mathbf{v}_b^{n+1}\right) \text{ on } \partial V \tag{8}$$

associated to the proper normal boundary conditions.

3.3. Fourth Order Spatial Discretization

The achievement of a real fourth order space accuracy is obtained by means of the Simpson integral discretization along with explicit Lagrangian interpolation for the fluxes discretization. Although, at the same accuracy, a Lagrangian polynomial involves a wider stencil than a Hermitian interpolation (as recently proposed in [4]), the former approach remains simply applicable in the non-uniform direction. The operator $G_2 = I_{\mathbf{x}} + \frac{h_1^2}{24}\frac{\partial^2}{\partial\xi^2}\Big|_{\mathbf{x}'=\mathbf{x}} + \frac{h_2^2(y)}{24}\frac{\partial^2}{\partial\eta^2}\Big|_{\mathbf{x}'=\mathbf{x}}$ is discretized to fourth order accuracy by considering second order central difference formulas for the spatial derivatives. Having deconvolved the velocity field to fourth order accuracy, the integral fluxes in Eqs.(6) and (8) are congruently discretized by means of the Simpson formula. In such a way, one has, as an example, for the net flux along x-direction:

$$\int_{y_j^-}^{y_j^+}\left[f\left(x_i^+,\eta\right) - f\left(x_i^-,\eta\right)\right]d\eta = \frac{h_2}{6}\left(f_{i,j^+} + 4f_{i,j} + f_{i,j^-}\right)\Big|_{i^-}^{i^+} - \frac{h_1 h_2^5}{2880}\frac{\partial^5 f}{\partial\xi\partial\eta^4}\Big|_{i,j} + \ldots \tag{9}$$

wherein, the face-node unknowns (see Fig.1) are expressed in terms of the grid nodes values. A high-order Lagrangian interpolation procedure is adopted by factorising the function along each direction and approximating both the factors by means of two third degree polynomials, i.e.: $f(x,y) \cong \hat{f}(x,y) = L_1(x)L_2(y)$. This way, one obtains a global 25 grid-nodes computational molecule.

3.4. Boundary Conditions

The original system (1), (4) was de-coupled in the separate prediction (6) and projection (8) equations. The solution of this latter, together with Eq. (7), allows the intermediate velocity $\mathbf{v}^*$ to be corrected by imposing the exact normal velocity component $\mathbf{n}\cdot\mathbf{v}_b^{n+1}$ on ∂V. Since the projection can not correct the tangential velocity component, this latter must be congruently assigned for solving Eq.(6). In this paper we propose a procedure for assigning time accurate boundary conditions. In fact, by taking the limit of Eq.(6) for vanishing grid spacing ($G_2 \to I$ for $h \to 0$) and projecting it along the direction tangential to the boundary, one gets:

$$\left(v_t^* - \frac{\Delta t}{2\mathrm{Re}}\frac{\partial^2 v_t^*}{\partial y^2}\right)_{\partial V} = \left(v_t^n + \frac{\Delta t}{2\mathrm{Re}}\frac{\partial^2 v_t^n}{\partial y^2}\right)_{\partial V} + \tag{10}$$

$$-\frac{\Delta t}{2}\mathbf{t}\cdot\left\{\underline{\nabla}\cdot\left[(3\mathbf{vv})^n - (\mathbf{vv})^{n-1}\right] - \frac{1}{\mathrm{Re}}\left(3\frac{\partial^2\mathbf{v}^n}{\partial x^2} - \frac{\partial^2\mathbf{v}^{n-1}}{\partial x^2}\right)\right\}_{\partial V}$$

When properly spatially discretized, Eq.(10) provides the correct second order time accurate solution on the frontier, as illustrated in the next section.

4. Numerical Results

The adopted test case is the classical 2-D Taylor decaying vortex solution at Re=1. The error estimations are performed in the computational domain $V=[-\pi, \pi]\times[-\pi, \pi]$, by taking the L_∞ norm of the difference between the x-component of the exact and numerical velocity field. In a first test, for bi-periodical boundary conditions, the effect of the de-averaging procedure was studied, having used the fourth-order flux integration (9). The resulting errors, computed after 100 time steps ($\Delta t=10^{-4}$), are shown in Fig.2 versus the normalised grid size in a double logarithmic scale, for both uniform and non-uniform grids. It can be noted that only in the presence of the de-averaging procedure (m=2) an effective fourth order accuracy is reached in computing unsteady solutions. The space accuracy is also checked for Dirichelet boundary conditions in the y-direction, as illustrated in Fig.3 on both uniform and non-uniform grids. Moreover, the correctness of the proposed boundary conditions (10) is analysed from the results in Fig.4, where the time accuracy tests is reported. A single time integration was conducted in order to avoid stability problems when working with high time steps. The errors are reported versus the used time step, showing a third order slope according to the fact we are evaluating the direct error on a single time step, that corresponds to a second-order local truncation error.

Finally, the procedure was tested for a time evolving mixing layer. The initial configuration is the same adopted in [9], i.e. a hyperbolic tangential velocity profile $u(y) = u_\infty \tanh 2y/\delta_1$ (being $2\ \delta_1$ the initial vorticity thickness) submitted to a white noise perturbation plus a deterministic sine perturbation at $k_4=(2\pi/\lambda_a)$ with $\lambda_a=7\,\delta_1$. Kelvin-Helmholtz instabilities lead to the development of vortices which in a later stage roll-up and merge. This is a good example for the tendency of 2D turbulence to transfer energy from small to large scales thus requiring an accurate numerical simulation. The preliminary results of this study are reported in Fig.s 5 for a 128^2 computational grid on a domain $V=[0, 4\lambda_a]\times[-2\lambda_a, 2\lambda_a]$ at $\mathrm{Re} = u_\infty \delta_1 / \nu = 250$ showing the salient features of backscatter transfer energy and the appearance of a k^{-4} range according to the LES performed in [9].

References

1. S. Ghosal, P.Moin, The basic equations for the large eddy simulation of turbulence flows in complex geometry *J. Comp. Phys.*, 118, 1995.
2. A. G. Kravchenko, P. Moin, On the effect of numerical errors in Large Eddy Simulations of turbulent Flows. *J. Comp. Phys.*, 131, 1997.
3. Y. Morinishi, T.S. Lund, O. V. Vasilyev, P. Moin, Fully Conservative Higher Order Finite Difference Schemes for Incompresible Flow. *J. Comp. Phys.*, 143, 90-124, 1998.

4. J. M. C. Pereira, M. H. Kobayashi, J. C. F. Pereira, A fourth order accurate finite volume compact method for the incompressible Navier-Stokes solutions, J. Comp. Physics, in press, 2001.
5. G. De Stefano, F.M. Denaro, G. Riccardi, High order filtering for control volume flow simulations, *Int. J. Num. Methods in Fluids*, 37, 2001.
6. P. Sagaut, Large Eddy Simulation for incompressible flows. An introduction. (pp.198-200), Springer, 2001.
7. A. J. Chorin, Numerical Solution of the Navier-Stokes Equations, *Math. Comp.*, 22, 745-762, 1968.
8. J. Kim, P. Moin, Application of A Fractional-Step Method to Incompressible Navier-Stokes Equations, *J. Comp. Phys.*, 59, 308-323, 1985.
9. M. Lesieur, C. Staquet, P. Le Roy, P. Comte, The mixing layer and its coherence examined from the point of view of two-dimensional turbulence, *J. Fluid Mech.*, 192, 1986.

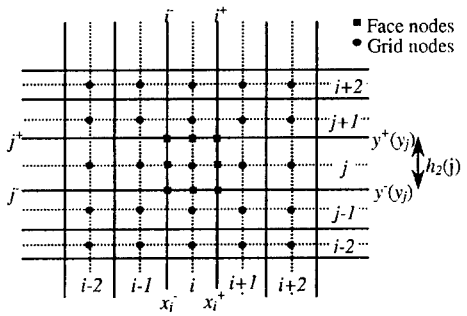


Figure 1: description of the adopted 2-D grid, non-uniform in the y- direction. For each j-th finite volume, the vertical flux section is centred with respect to the node j i.e., $y^{\pm}(y_j)=y_j\pm h_2(j)/2$. The unknown variables u, v, p are co-located on the grid nodes (•).

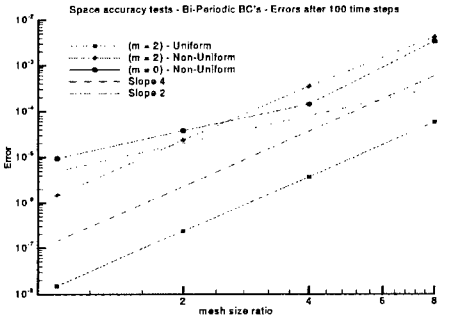


Figure 2: Space accuracy tests with Bi-periodic boundary conditions applied. Effects of the de-averaging procedure on the accuracy. Errors computed after 100 time steps on both uniform and non-uniform grids.

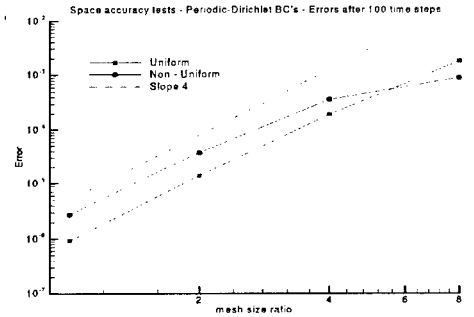


Figure 3: Space accuracy tests with Periodic-Dirichlet boundary conditions applied. Errors computed after 100 time steps on both uniform and non-uniform grids.

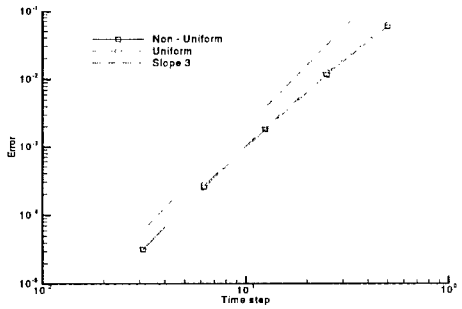


Figure 4: Time accuracy tests. Errors computed after one time steps on both uniform and non-uniform grids of 60^2 CV's.

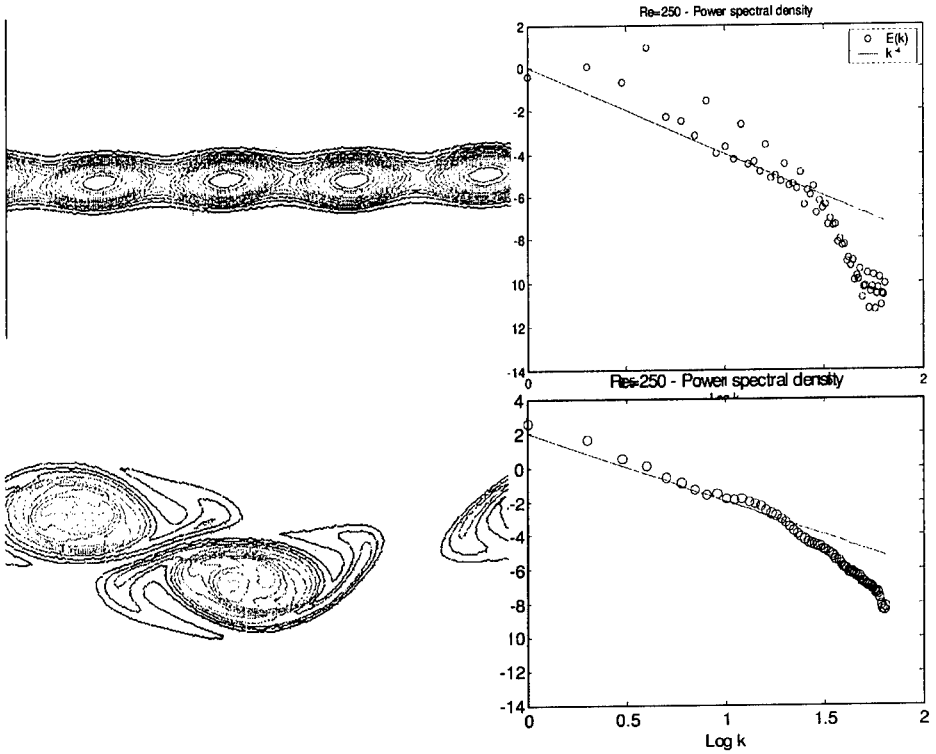


Figure 5: Time evolving mixing layer; isovorticity contours are on the left column while the one-dimensional energy spectra are on the right for $t = 35\delta_1 / u_\infty$ and $t = 65\delta_1 / u_\infty$

LARGE EDDY SIMULATIONS OF COMPLEX TURBULENT FLOWS USING IMMERSED BOUNDARY METHOD

MAYANK TYAGI, SUMANTA ACHARYA
Mechanical Engineering Department
Louisiana State University, Baton Rouge, LA

Abstract

Large eddy simulations (LES) are performed for two representative complex geometry problems of particular interest to turbomachinery flows. First problem studied is the flow field inside a trapped-vortex combustor. Second problem is the unsteady interaction of rotor blade with stator blade wake field. The representation of complex geometry is done using immersed boundary method (IBM). Two different implementations are presented for the body force terms.

1. Introduction

Simulation of turbulent flows in complex geometries is a daunting task. LES can formally alleviate the issue of ever-increasing resolution demand for high Reynolds number flow. However, complex geometries pose the problem of commutation errors on curvilinear grids. Moreover, the representation of moving geometries using either sliding meshes or regenerating the mesh becomes overwhelmingly complicated in complex situations. IBM relies upon the body force terms added in the momentum equations to represent the geometry on a fixed Cartesian mesh (Peskin, 1977, Mohd.-Yusof, 1996, Glowinski et al., 1994, Fadlun et al. 2000, Kellog, 2000). This formulation is simple and ideally suited for the moving geometries involving no-slip walls with prescribed trajectories and locations.

2. Governing Equations

In the immersed boundary method, the complex geometrical features are incorporated by adding a forcing function in the governing equations. The forcing function is zero everywhere except at the surface where the influence of the solid boundaries is assigned (Subscript Γ).

$$\frac{\tilde{u}-u^n}{\Delta t}=\frac{3}{2}\left(C^n+D^n\right)-\frac{1}{2}\left(C^{n-1}+D^{n-1}\right)+f$$

$$f=[\frac{u_\Gamma^{n+1}-u^n}{\Delta t}-\frac{3}{2}\left(C^n+D^n\right)+\frac{1}{2}\left(C^{n-1}+D^{n-1}\right)]\delta(\vec{x}-\vec{x}_\Gamma)$$

$$\frac{u^{n+1}-\tilde{u}}{\Delta t}=-\nabla p^{n+1}$$

where the convective terms are represented by C and the diffusion terms are represented by D. In case of highly refined meshes, it may be necessary to treat some directions implicitly for diffusion terms (generally using Crank-Nicholson scheme).

$$C = -(u \cdot \nabla)u, D = \frac{1}{\mathrm{Re}} \nabla^2 u$$

To obtain the pressure Poisson equation, take the divergence of the second step and enforce the continuity condition for the velocity field at the next time step

$$\nabla^2 p = \frac{\nabla \cdot \tilde{u}}{\Delta t} - \nabla \cdot f - \frac{\nabla \cdot u^{n+1}}{\Delta t}$$

$$\because \nabla \cdot u^{n+1} = 0$$

$$\Rightarrow \nabla^2 p = \frac{\nabla \cdot \tilde{u}}{\Delta t} - \nabla \cdot f$$

Therefore, the Poisson equation for pressure can be solved prior to the second step in the time-split scheme. The spatial discretization is performed using fourth order central difference schemes. For the two problems studied, two different implementations for the body force terms are presented. The trapped-vortex combustor is a complicated but stationary geometry and hence, interpolation on only one-side of the geometry is adequate. However, for moving rotor blade the interpolation is performed on both sides of the curved surface.

CASE A: *Forcing at only one side of the immersed boundary (inside the virtual solid)*

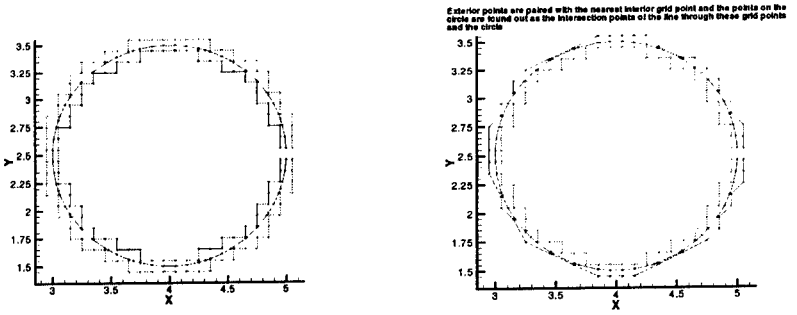


Figure 1 Identification of the circular boundary on uniform 2-D cartesian mesh and evaluation of the nearest exterior point corresponding to each identified interior point

Let Δ be the mesh spacing and δ be the distance of the forcing point from the immersed surface. Therefore, we apply the linear interpolation/extrapolation among the forced point, point on the immersed surface and the point just outside the virtual solid. Let V_d be the desired velocity at the point on the immersed

surface and V_c be the computed velocity in the region of interest. Therefore, the velocity at the forcing point V_{im} is given by

$$[V_c - V_d]/[\Delta - \delta] = [V_d - V_{im}]/[\delta]$$
$$V_{im} = V_d\,[\Delta]/[\Delta - \delta] - V_c\,[\delta]/[\Delta - \delta]$$

Clearly, In the limit δ going to zero, i.e. the forcing point approaching the point on the immersed surface, we retrieve the limit V_{im} approaching V_d. However, In the limit δ approaching mesh spacing Δ, we have V_c approaching V_d. V_{im} is ill-defined because it is the difference between V_d and V_c with very large coefficients. For such coefficients, V_c is set equal to V_d.

CASE B: *Forcing at both sides of the immersed boundary (inside the virtual solid and at the very first point outside the virtual solid)*

Let Δ be the mesh spacing and δ be the distance of the forcing point from the immersed surface. Therefore, we apply the linear interpolation/extrapolation among the forced points, point on the immersed surface and the computed point just outside the virtual solid (Figure 2). Let V_d be the desired velocity at the point on the immersed surface and V_c be the computed velocity in the region of interest. Therefore, the velocity at the internal forcing point V_{int} is given by

$$[V_c - V_d]/[2\Delta - \delta] = [V_d - V_{int}]/[\delta]$$
$$V_{int} = V_d\,[2\Delta]/[2\Delta - \delta] - V_c\,[\delta]/[2\Delta - \delta]$$

Similarily, the velocity at the external forcing point V_{ext} is given by

$$[V_c - V_d]/[2\Delta - \delta] = [V_{ext} - V_d]/[\Delta - \delta]$$
$$V_{ext} = V_d\,[\Delta]/[2\Delta - \delta] + V_c\,[\Delta - \delta]]/[2\Delta - \delta]$$

Clearly, in the limit δ going to zero, i.e. the internal forcing point approaching the point on the immersed surface, we retrieve the limit V_{int} approaching V_d and V_{ext} approaching $[V_d + V_c]/2$. Moreover, In the limit δ approaching mesh spacing Δ, we have V_{ext} approaching V_d . V_{int} is defined as $[2V_d - V_c]$ as it should be by reflection condition. Thus, the forcing remains physical for all positions of the immersed surface between the grid interfaces. For moving boundary implementation, it will be important for another reason. It avoids reflected velocities to show up in the region of interest.

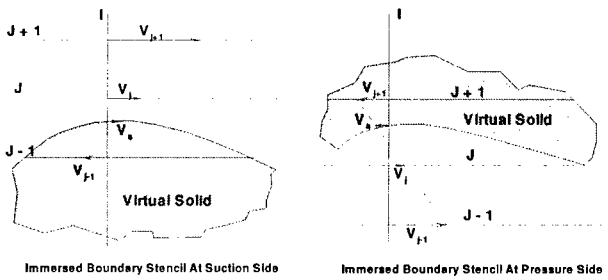


Figure 2 Identification of the interpolation stencils for a moving rotor blade.

3. Trapped Vortex Combustor

3.1 Problem Description

A uniform cartesian grid of 92×57×117 points is used for a domain containing the upper half of the TV combustor. All the dimensions are selected to approximate the experimental setup of Mancilla (2001) within Cartesian geometry. Ratio of air injection velocity to the mainflow velocity is 2.2. Reynolds number based on the annular mainflow velocity and air hole dimension (D) is 3400 for these simulations. The radii of the forebody, the connecting tube, the afterbody and the outer shell are 24.5D, 3.7D, 23D and 27.5D respectively. The lengths of the forebody, the connecting tube and the afterbody are 12D, 30D and 12D respectively. The periodicity of the geometry is exploited by putting half of the jet injections around the bottom of the computational domain with the boundary conditions obtained by the rotational symmetry about the axial direction. At the inflow, fully developed laminar profile along with fluctuations is prescribed. The fluctuations are assumed to be Gaussian and are calculated using Box-Muller algorithm. At the walls, no slip boundary conditions are imposed using immersed boundary method. Uniform injections of air and fuel are applied at the respective holes on the afterbody. Periodic boundary conditions are applied in the spanwise (z) direction. At the outflow, a non-reflective convective scheme is applied to convect away the flow structures out of the computational domain without any spurious reflections. The wave speed is calculated to maintain the mass flux balance in the whole domain.

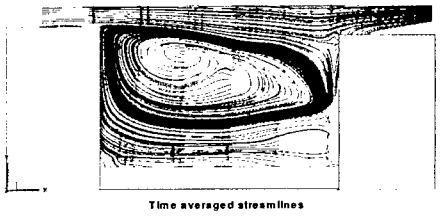
3.2 Results

The three-dimensional simulations showed that the vorticity magnitude of the trapped vortex in the cavity changes due to vortex stretching mechanism that is absent in the two-dimensional simulations done by other researchers (Katta and Roquomore, 1996 and Stone and Menon, 2000). The motion of the trapped vortex is unsteady inside the cavity as observed experimentally as well as numerically (Mancilla, 2001). Unsteady dynamics of the coherent structures inside the cavity is a slower process as compared to the separation region over the afterbody and the mixing layer region behind the forebody lip. The ingestion of annular mainflow in front of the afterbody separation region is the main mechanism of the flow entrainment inside the cavity. The mixture in the cavity is ejected radially outwards due to the pressure gradients there. The instantaneous axial and radial locations of the TV are different at different meridional planes. However, time-averaged streamtrace patterns seem to converge towards a TV with simpler geometrical features.

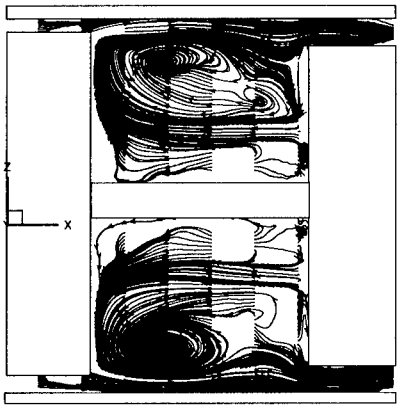
TIME AVERAGED FLOW FIELD

The streamtraces are presented at the meridional planes $\theta = 90°$, 0° and 180° (figure 3). At $\theta = 90°$, the large recirculation region is formed between the annular mainflow and the fuel injections. The unsteadiness of the mixing layer

and the motion of TV inside the cavity has been averaged out. At $\theta = 0°$ and 180°, the streamtraces are asymmetric implying that a longer averaging period is needed to completely eliminate the slow variations. Moreover, the axisymmetry is also absent at these meridional planes. The TV is a doughnut shaped structure inside the cavity. The pitch of the spiral formed by streamtraces close to the meridional plane $\theta = 90°$ is largest. The azimuthal motion of the streamtraces along the surface of the TV is absent in all the previous 2-D studies. However, the core of the TV is mostly irrotational.



(a)



(b)

Figure 3 Streamtraces at (a) $\theta = 90°$ (b) $\theta = 0°$ and 180° (tracers are released along radial positions at several axial locations).

TURBULENT STRESSES (No Figures)

At $\theta = 90°$, the turbulent shear stress $u'v'$ inside the cavity is mostly generated by the production terms ($u'u'.\partial V/\partial x$ and $v'v'.\partial U/\partial y$) around the mixing layer region. The high axial momentum fluctuations of the fluid parcels are correlated with radially inward fluctuations around the mixing layer region. This implies the turbulent mixing and diffusion is enhanced between the cavity and annular mainflow by this stress component. The shear stress is also large along the jet injections. However, the levels of turbulent stresses indicate that flow is mostly laminar close to the forebody and connecting tube junction. At $\theta = 0°$ and 180°, the turbulent shear stress $u'w'$ inside the cavity is mostly generated by the production terms ($u'u'.\partial W/\partial x$ and $w'w'.\partial U/\partial z$) around the jets in the cavity and the mixing layer region. This distribution indicates enhanced mixing of fluid parcels inside the core of TV. The distribution of $u'w'$ near the jet injections is dictates the radial spread of the jets along the axial direction in the cavity. At X/D = 40.8, the radial fluctuations are high at different azimuthal or meridional planes. The normal stress $u'u'$ is mostly negligible due to suppression

of fluctuations normal to the face of the afterbody. The only significant levels are above the afterbody in the annular region. The distribution of the shear stress $v'w'$ along the jets is primarily due to turbulent production ($v'v'.\partial W/\partial y$ and $w'w'.\partial V/\partial z$). The distribution in the annular region seems to attain the periodicity between the fuel injections. It can be expected that the modeling of the shear stress tensor components using an eddy viscosity approximation may work here since the shear stress components depend on the corresponding mean strain rate tensor components only.

4. Unsteady Stator-Rotor Interactions

4.1 Problem Description

The inherent unsteadiness of a turbomachinery flow field created by relative motion between stationary blades (stator) and the rotating blades (rotor), requires the designer to account for three-dimensional as well as unsteady effects. The unsteadiness is caused by (a) the interaction of the rotor airfoils with the wakes and passage vortices generated by upstream airfoils, (b) the relative motion of the rotors with respect to the stators (potential effect), and (c) the shedding of vortices by the airfoils because of the blunt trailing edges (Rai and Madavan, 1990, Saxer and Giles, 1994). Computation of such flows is complicated by relative motion between rotor and stator airfoils and the periodic transition of the flow from laminar to turbulent. Unsteady simulations have been performed using multitudes of approximations such as unsteady RANS, "average-passage" approach and "mixing-plane" approach. These calculations have been performed invariably using "sliding mesh" techniques requiring further modeling of "apparent stresses" and "phase-lagged" interface conditions (Sharma et al., 1994). In the present study, we utilize LES with moving IBM to simulate unsteady stator-rotor interactions. Though, the calculation is performed for incompressible fluid at a low Reynolds number, it demonstrates the strength of the method by avoiding all ad-hoc assumptions pertaining to RANS modeling and sliding meshes. A uniform Cartesian grid of 302×202×11 points is used for a domain of the size 3D×1D×0.1D, where D is the chord length of the rotor airfoil. Choice of a small spanwise dimension may not allow larger physical scales and hence may not be desirable. The geometry of the airfoils is taken from the numerical study of Kelecy et al (1995). The airfoil profile is approximated by the cubic spline surfaces. The airfoil is divided into leading edge, trailing edge, pressure surface and suction surface to ensure that immersed boundary conditions are enforced on enough grid points to realize the geometry. Uniform flow field is specified at the inflow. Periodic boundary conditions are applied in the direction of rotor motion (y) and the spanwise (z) direction. Reynolds number base on the inflow velocity and rotor chord length is 5000. At the outflow, a non-reflective convective scheme is applied to convect away the flow structures out of the computational domain without any spurious reflections. The wave speed is calculated to maintain the mass flux balance in the whole domain.

4.2 Results

Four snapshots of the instantaneous vorticity field are shown in figure 4 at time instants T apart (=0.12τ, where τ is the non-dimensional time scale). There is a separation region on the suction side of the stator. The trailing edge vortices of the stator blade impact on the suction side of the rotor blade near its leading edge. The trailing edge vortices of the rotor and the vortices formed due to the interaction of stator wake and suction-side boundary layer are shed into the passage flow and convected out of the domain.



a) t_0



b) $t_0 + T$



c) $t_0 + 2T$



d) $t_0 + 3T$

Figure 4 Instantaneous snapshots of vorticity component at time a) $t = t_0$, b) $t = t_0+T$, c) $t = t_0+2T$ and d) $t = t_0+3T$.

5. Concluding Remarks

The merit of immersed boundary method (IBM) for simulating moving complex geometries on Cartesian mesh has been demonstrated. High order of accuracy of discretization schemes is retained which is very important for LES. The problems studied are a) Trapped vortex combustor (TVC) and b) Stator-rotor interactions in a transonic turbine stage. In TVC case study, mixing inside an annular cavity is analyzed. In stator-rotor case study, the superiority of this method is demonstrated over existing methodologies such as sliding meshes. Moreover, the ad-hoc modeling for the "apparent stresses" is not needed in the realms of LES. In future, a zonal refinement treatment of the immersed boundaries will be implemented to capture the essential near wall physics to render this method with predictive capabilities.

References

Fadlun, E., Verzicco, R., Orlandi, P. and Yusof, J. M. (2000), Combined immersed-boundary finite-difference methods for three-dimensional complex flow simulations, *J. Comp. Phy.*, Vol. 161, pp. 35-60.

Glowinski, R., Pan, T.-W. and Periaux, J. (1994), A ficitious domain method for unsteady incompressible viscous flow modeled by Navier-Stokes equations, *Contemporary Mathematics*, Vol. 157, pp. 421-431.

Katta, V.R. and Roquemore, W.M. (1996), Numerical studies on trapped-vortex combustor, *AIAA 96-2660.*

Kelecy, F.J., Griffin, J.W. and Delaney, R.A. (1995), The effect of vane-blade spacing on transonic turbine stage performance, *AGARD-CP-571*, Paper # 5.

Kellogg, S.(2000), Immersed boundary methods with applications to flow control, *M.S. Thesis*, Rice University, TX.

Mancilla, P.C. (2001), Flame stability in a trapped-vortex spray-combustor, *M.S. Thesis*, Louisiana State University, LA.

Peskin, C. S. (1977), Numerical analysis of blood flow in the heart, *J. Comp. Phy.*, Vol. 25, pp. 220-252.

Rai, M.M. and Madavan, N.K. (1990), Multi-airfoil Navier-Stokes simulations of turbine rotor-stator interaction, *J. Turbomachinery*, Vol. 112, pp. 377-384.

Saxer, A.P. and Giles, M.B. (1994), Predictions of three-dimensional steady and unsteady inviscid transonic stator/rotor interaction with inlet radial temperature nonuniformity, *J. Turbomachinery*, Vol. 116, pp. 347-357.

Sharma, O.P., Ni, R.H. and Tanrikut, S. (1994). Unsteady flows in turbines – Impact on design procedure, *AGARD-LS-195*, Paper # 5.

Stone, C. and Menon, S. (2000), Simulation of Fuel-Air Mixing and Combustion in a Trapped-Vortex Combustor, *AIAA Paper No.00-0478*, 38th AIAA Aerospace Sciences Meeting and Exhibit, Reno, NV.

Yusof, J. Mohd. (1996), Interaction of massive particles with turbulence, *Ph.D. Dissertation*, Cornell University.

NUMERICAL EFFICIENCY OF EXPLICIT AND IMPLICIT METHODS WITH MULTIGRID FOR LARGE EDDY SIMULATION

S. ERTEM-MÜLLER AND M. SCHÄFER
Darmstadt University of Technology, Department of Numerical Methods in Mechanical Engineering,
Petersenstr. 30, 64287 Darmstadt, Germany

Abstract. In this paper the accuracy and efficiency of a finite-volume multigrid solver for Large Eddy Simulation (LES) is investigated. The spatial discretization method employed is a second-order accurate central differencing scheme. For time discretization of the momentum equations the implicit second-order Crank-Nicolson method and the explicit second-order Adams-Bashforth method are considered. The influences of the two time discretizations, choice of grid size and time-step size and multigrid performance on the numerical accuracy and computational efficiency are discussed.

1. Introduction

Due to the foreseeable progresses in the performance of computer systems, it can be expected, that in the near future the Large Eddy Simulation (LES) will become more important and applicable also in industrial practice. However, efficient numerical algorithms designed for modern parallel computer architectures with facilities to allow the modeling of complex geometries are another crucial issue in the application of LES. In this way it will be possible to achieve a sufficient numerical resolution and geometrical flexibility also to deal with complex practical problems within reasonable computing times.

Numerical aspects such as spatial and temporal discretization, solution algorithms and resolution requirements , and modeling aspects such as subgrid scale models are effecting the accuracy and efficieny of the simulations. Due to the enormous computational requirements for LES, there can

be found few systematic investigations about the above mentioned aspects. Despite that different groups have organized LES workshops for specified test cases, it was difficult to come to any definite conclusions about the performance of different applied numerical methods as well as the varying subgrid scale models.

In this study the accuracy and performance of a finite-volume multigrid solver for LES is investigated. The main focus of the present contribution will relate to the following aspects with respect to their influences on the numerical accuracy and computational efficiency of the considered approach: comparison of the explicit/implicit methods, choice of grid size and time-step size and multigrid performance.

For this an already well investigated turbulent channel flow will be considered for comparison to other results from the literature.

2. Numerical Procedure

The governing equations for an incompressible flow are given by

$$\frac{\partial \bar{u}_i}{\partial x_i} = 0, \tag{1}$$

$$\frac{\partial(\rho\bar{u}_i)}{\partial t} + \frac{\partial(\rho\overline{u}_i\overline{u}_j)}{\partial x_j} = -\frac{\partial \bar{p}}{\partial x_i} + \frac{\partial}{\partial x_j}\left[\mu\left(\frac{\partial \bar{u}_i}{\partial x_j} + \frac{\partial \bar{u}_j}{\partial x_i}\right)\right] - \frac{\partial \tau_{ij}}{\partial x_j}, \tag{2}$$

where $\bar{u}_i$ are the velocity components of the resolved scales with respect to the Cartesian coordinates x_i, $\bar{p}$ is the corresponding pressure, μ is the viscosity, ρ is the density and t is the time. The subgrid scale stresses

$$\tau_{ij} = \rho\left(\overline{u_i u_j} - \overline{u}_i\overline{u}_j\right) \tag{3}$$

are modeled by the Smagorinsky model [1] and the dynamic Germano model [2] to close the problem. In order to stabilize the dynamic model, the negative values for the parameter C_s of the underlying Smagorinsky model are clipped.

The basic flow solver is the FASTEST-3D code (INVENT Computing, Erlangen) [3] with extensions for LES. The solver is based on a fully conservative finite-volume method for solving the incompressible Navier-Stokes equations on a non-staggered, cell-centered grid arrangement. The spatial discretization method employed is a second-order accurate central differencing scheme for block-structured non-orthogonal boundary-fitted grids. For time discretization of the momentum equations we consider two different approaches: the implicit second-order Crank-Nicolson method and the explicit second-order Adams-Bashforth method. Both methods define

approximations $\bar{u}_h^n$ and $\bar{p}_h^n$ to the solution of the continuous problem at the time levels $t_n = n\Delta t \quad (n = 1, 2, ...)$, where the parameter h is a measure for the spatial resolution and $\Delta t > 0$ is the time-step size.

Within the implicit method, for each time-step, assuming that the unknowns at the time level t_{n-1} have already been computed, the unknowns at the time level t_n have to be determined as the solution of a nonlinear algebraic system. For this a nonlinear full approximation multigrid scheme with a pressure-correction smoother is employed [4].

The smoothing procedure is based on a variant of the well-known SIMPLE algorithm proposed by Patankar and Spalding [5]. The determination of $\bar{u}_h^n$ and $\bar{p}_h^n$ is done in several steps. In the first step, after the calculation of the turbulent viscosity, an intermediate approximation to $\bar{u}_h^n$ is obtained by solving the discrete momentum equations with the pressure term, the source term and the matrix coefficients formed with values of the previous iteration. In the second step, corrections $\Delta\bar{p}_h^n$ and $\Delta\bar{u}_h^n$ are sought to obtain the new pressure $\bar{p}_h^n$ and the new velocity $\bar{u}_h^n$ exactly satisfying the continuity equation. By considering a modified discrete momentum equation together with the discrete continuity equation, an equation for the pressure correction $\Delta\bar{p}_h^n$ is derived, where a selective interpolation technique is used for making the cell face velocities dependent on the nodal pressure, which is necessary to avoid oscillatory solutions that may occur owing to the non-staggered grid arrangment[6]. To improve the diagonal dominance in the pressure-correction equation the contributions due to grid non-orthogonality are neglected. The smoothing iteration step is completed by correcting the velocity components and the pressure. To ensure convergence, for the velocity components and the pressure an under-relaxation in the variant suggested by Patankar [7] is employed. For the solution of the linear system of equations the Strongly Implicit Procedure (SIP) of Stone [8] is used. The global outer multigrid procedure is implemented as a nonlinear full approximation scheme, in which the above pressure-correction scheme acts as the smoother. The different grid levels are visited following the standard V-cycle approach, where second-order interpolation is employed for the grid transfers. This procedure is repeated till convergence is reached.

Within the explicit method, first the turbulent viscosity and the velocity $\bar{u}_h^n$ are calculated explicitly from the unknowns at the time level t_{n-1}. Then the pressure correction equation is derived using the modified discrete momentum equation together with the discrete continuity equation. The corresponding resulting linear system is solved by a linear multigrid method. The computation of the time level t_n is completed by correcting the velocity components and the pressure. In Figure 1 a schematical flow diagram of both methods is given.

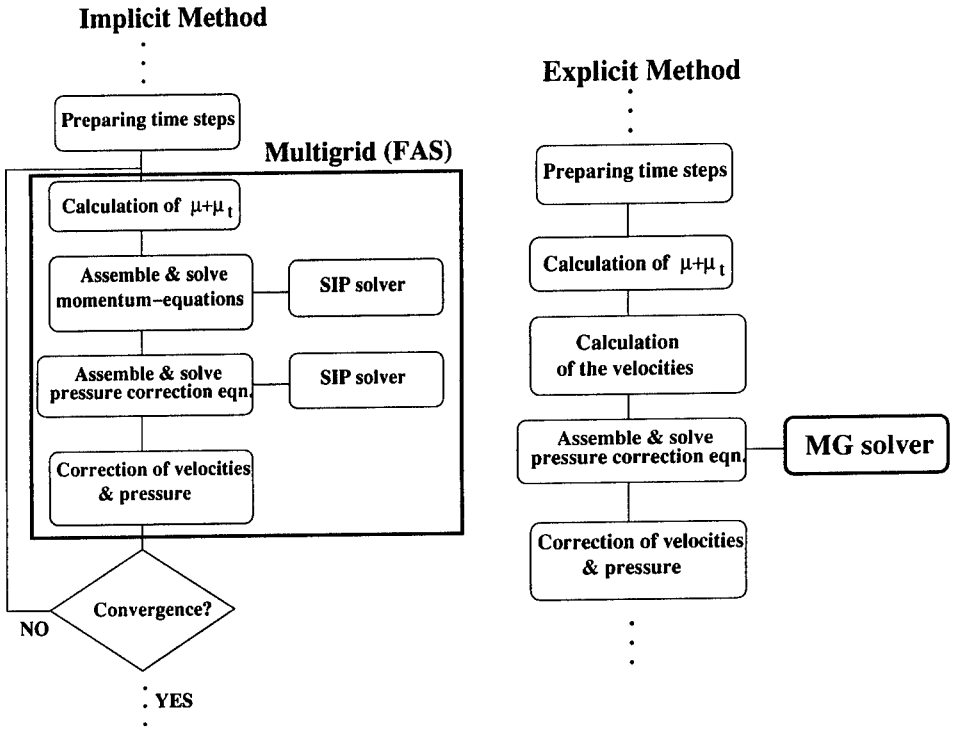


Figure 1. Flow diagram of implicit/explicit methods.

3. Numerical Results

The following investigations concern the accuracy and the numerical efficieny of the methods given in the previous section. All computations were carried out on a Compaq AlphaServer ES40 667 MHz.

As a test case the turbulent flow between two parallel plates seperated by a distance 2δ is investigated. The flow is driven by a uniform streamwise pressure gradient. The Reynolds number $Re_\tau = 395 \quad (Re_b = 6875)$ based on half-width and friction (or bulk) velocity is considered. Since the streamwise and spanwise directions (i.e. x and z) are formally infinite, periodic boundary conditions are used for the simulation of a finite domain. The computational domain has the dimensions $2\pi\delta \times 2\delta \times \pi\delta$ which are considered to be large enough to avoid adverse effects of the periodic boundary conditions. Initial conditions with random fluctuations are given to assure turbulence. Three different grids with $64 \times 32 \times 32$, $96 \times 48 \times 48$ and $128 \times 64 \times 64$ control volumes (CVs) are employed in x, y, z directions. The grids are equidistant in streamwise and spanwise directions where in the wall-normal direction a geometric progression is used for the grid density. The first point away from the wall is at $y^+ \approx 9.25$ for the coarse grid,

$y^+ \approx 6.17$ for the medium grid and $y^+ \approx 4.62$ for the fine grid. Before starting the computation of mean values and statistics of the flow, the simulations are carried out until the numerical solution reached a statistically steady state. All data are computed from the appropriate quantities and averaged in the homogeneous spatial directions x and z and in time. The averages in time are taken over 200 s in each case. The results are compared to the DNS data given in [9].

First, a validation of the applied subgrid models is carried out. In Figure 2 (left) a comparison of the mean velocity profile U_m normalized by the friction velocity u_τ in the normalized half channel width is given. The results

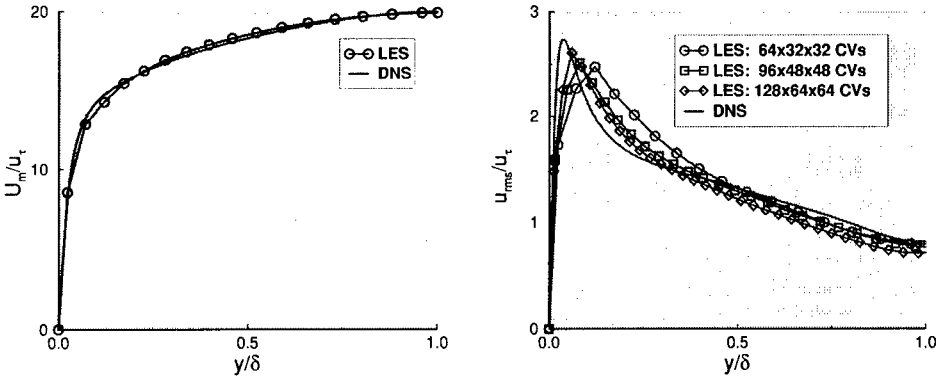


Figure 2. Comparison of mean velocity profile (left) and rms velocity profile (right) between LES and DNS.

calculated with the finest grid and the Germano model correspond well with the reference data. Figure 2 (right) shows the root mean square u_{rms} of the velocity in streamwise direction normalized by the friction velocity u_τ in normalized half channel width for three grids with the Smagorinsky model. Compared with the DNS data the LES results for the coarse grid show slightly lower fluctuations. However, the overall agreement is satisfactory and with grid refinement the profile approaches the reference data.

Next, the numerical efficiencies of the explicit and implicit methods are investigated. Figure 3 shows the comparison of both methods without the multigrid solver for CFL=0.5, where the computational time per time-step against the number of CVs is plotted. The CFL-number is defined by

$$\mathrm{CFL} = \max_{\mathrm{CV}} \left[\sum_{i=1}^{3} \bar{u}_i / \Delta x_i \right] \cdot \Delta t \,,$$

where the maximum is taken over all control volumes (CV). It is observed that without a multigrid solver the implicit method is more efficient than

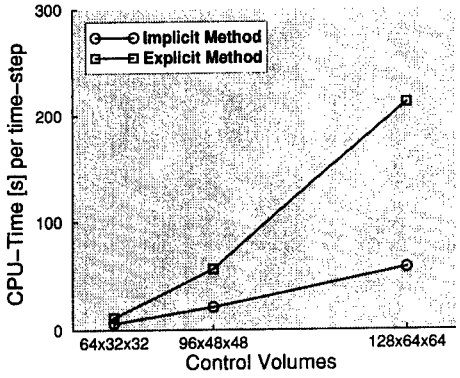


Figure 3. Comparison of explicit and implicit methods without the multigrid solver for CFL=0.5 with varying grid size.

the explicit method, where the differences in CPU-time increase with grid refinement. This is due to the fact, that within the explicit method, the pressure-correction equation has to be solved very exactly, since it is solved only once. Thus the CPU-time for solving the linear system without the multigrid solver is very high and the computational effort increases rapidly when the grid is refined.

In Figure 4 the computational time per time-step against the number of CVs for both methods with the multigrid solver for the same CFL-number is plotted. The multigrid approach yields an acceleration for both methods. The acceleration for the explicit method is much higher as for the implicit method, such that the explicit method becomes superior to the implicit one.

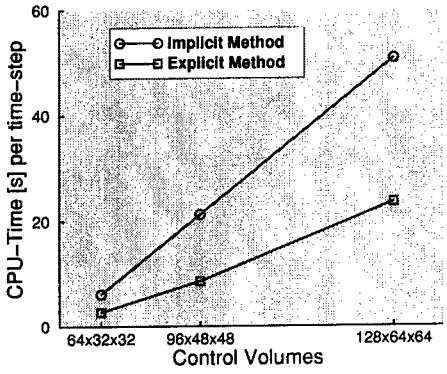


Figure 4. Comparison of explicit and implicit methods with the multigrid solver for CFL=0.5 with varying grid size.

Since there exists no strict time-step limitation, of course, with the implicit method computations with higher CFL numbers are possible. In Figure 5 the computing times against the number of CVs are plotted for the implicit method using CFL=6 and the explicit method using CFL=0.5. It can be seen that even in this comparison the explicit method still turns out to be slightly more efficient. In order to see how the time-step size is effecting the results of the computations, in Figure 6 the root mean square values u_{rms} of the velocity in streamwise direction normalized by the friction velocity u_τ in the normalized half channel width for the coarse grid with the Smagorinsky model is shown for different CFL-numbers. The computations with a larger time-step size (CFL=6) overpredict the streamwise fluctuations when compared with the smaller time-step size (CFL=0.5). Further test computations have shown that using even larger time-step sizes (e.g. CFL=10) yield rather poor results, such that for the considered test case CFL=6 can be viewed as the maximum value to achieve physically reasonable results.

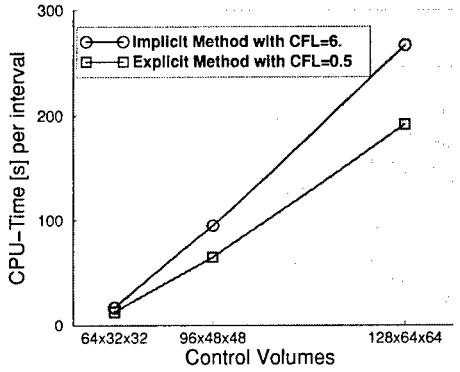


Figure 5. Comparison of explicit and implicit methods with the multigrid solver for different CFL-numbers and varying grid size.

4. Conclusions

The numerical accuracy and efficieny of explicit and implicit methods with and without multigrid for Large Eddy Simulation has been investigated. For the comparisons the simple well known turbulent channel flow is considered. Without using the multigrid solver, the computational requirement for the explicit method increases very rapidly with increasing number of grid points, such that in this case the implicit method is superior. However, when employing the multigrid solver, a high acceleration for the explicit method can be realized, which makes the method more efficient than the implicit one. It has been shown, that with the implicit method it is possible

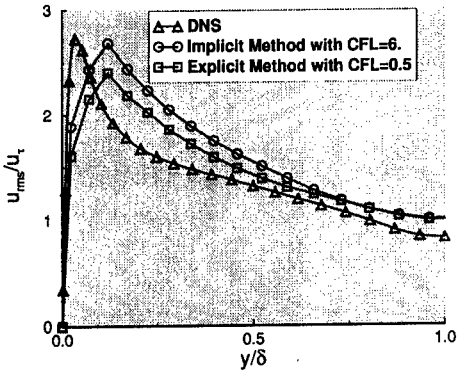


Figure 6. Comparison of rms velocity profile for different CFL-numbers.

to achieve also for CFL>1 physically reasonable results, but comparing the overal computational performance the explicit method still turned out to be superior.

Of course, it would be of interest, if the findings for the considered geometrically very simple test case will also be confirmed for problems in more complex geometries. The situation may change in such cases, when it is necessary to use more irregular grids with higher variations of control-volume sizes. Here, the advantages of the implicit method, where there is no need to adjust the time-step size to the smallest control volumes, can become more dominant. Corresponding investigations will be a topic of forthcoming work.

References

1. J. Smagorinsky, General circulation experiments with the primitive equations, I, the basic experiment, *Mon. Weather Rev.*, **91**, pp. 99–165 (1963).
2. M. Germano, U. Piomelli, P. Moin and W. H. Cabot, A dynamic subgrid-scale eddy viscosity model, *Phys. Fluids*, **A 3(7)**, pp.1760–1765 (1991).
3. FASTEST, Software for Computational Fluid Dynamics, *INVENT Computing GmbH, Erlangen* (1997).
4. F. Durst and M. Schäfer, A Parallel Blockstructured Multigrid Method for the Prediction of Incompressible Flows, *Int. J. for Num. Meth. in Fluids*, **22**, pp. 549–565 (1996).
5. S. Patankar and D. Spalding, A calculation procedure for heat, mass and momentum transfer in three dimensional parabolic flows, *Int. J. Heat Mass Transfer*, **15**, pp. 1787–1806 (1972).
6. C. Rhie and W. Chow, Numerical study of the turbulent flow past an airfoil with trailing edge seperation, *AIAA Journal*, **21**, pp. 1525–1532 (1983).
7. S. Patankar, *Numerical Heat Transfer and Fluid Flow*, Hemisphere (1980).
8. H. L. Stone, Iterative solution of implicit approximations of multidimensional partial differential equations, *SIAM J. Numer. Anal.*, **5**, pp. 530–558 (1968).
9. R. D. Moser, J. Kim and N. N. Mansour, Direct Numerical Simulation of Turbulent Channel up to $Re_\tau = 590$, *Physics of Fluids*, **11**, pp. 943–945 (1999).

LARGE-EDDY SIMULATION OF SQUARE JET

X. ZHOU AND D. D. KNIGHT
Department of Mechanical and Aerospace Engineering
Rutgers University
98 Brett Road
Piscataway, NJ 08854-8058
USA

Abstract. We present a large-eddy simulation (LES) of the near-field of a low-Mach number square jet. The filtered governing equations of compressible flows are solved using the approximate Riemann solver of Roe for the convective fluxes and an application of Gauss' theorem for the viscous fluxes on an unstructured grid of tetrahedral cells. The LES is performed with the Monotone Integrated LES (MILES) for the subgrid scale model. A square jet at a Mach number of 0.3 and a Reynolds number of 3,200 is simulated. Axis-rotation occurs and is caused by Biot-Savart self-induction associated with nonuniform shear-layer curvature at the exit. Complex vortex topologies and interaction between vortex rings and rib vortices are observed downstream. Mean properties are in good agreement with the Direct Numerical Simulation (DNS) results of Grinstein et al. (1995).

1. Introductions

Turbulent round and plane jets are simple inhomogeneous flows that can be served to verify models for complex flows and have been experimentally and numerically studied extensively [1, 2]. Recently, noncircular jets have been gained much interest in passive control due to their enhanced jet mixing properties [3, 4, 5, 6, 7].

In the past, Reynolds-Averaged Numerical Simulations (RANS) have often been employed for the investigation of jet flows. However, this kind of traditional method cannot give a clear picture of the unsteady behaviour and the results are too sensitive to the turbulence models used. The advantage of Direct Numerical Simulation (DNS) [8] and Large Eddy Simulation

(LES) [9] in being able to capture a wide range of spatial scales and temporal scales is of great value for fundamental and applied studies. LES is a good alternative to DNS which is more expensive for high Reynolds number flows. One of the practical uses of LES is to predict the transition and subsequent turbulent mixing (or spreading) process that occurs in spatially developing flows.

As is well known, a free jet is subject to Kelvin-Helmholtz instability which, in turn, means that the flow experiences an exponentially growing instability and results in rolling up of vortices, pairing and merging processes. Linear instability analyses have confirmed this growth. The subsequent breakdown of the large-scale vortical structures is followed by the advent of spreading by the secondary three-dimensional instability mechanism. Vortex dynamics are also expected to be important in the control of noncircular jets instability, transition from laminar to turbulence and the jet development further downstream. Grinstein and DeVore [3] showed a transition to turbulence in free square jets characterized by the dynamics of vortex rings and braid vortices and observed a larger entrainment rate compared to round jets. The underlying mechanism for the enhanced entrainment is the self-induced axis-rotation or axis-switching resulting from Biot-Savart deformation of vortex rings caused by non-uniform azimuthal curvature at the jet exit. Foss and Zaman [10] and Zaman [11] analyzed the influence of jet geometry on the characteristics of spreading in subsonic and supersonic flows. They observed a substantial increase of jet spreading when tabs were inserted at the nozzle which induced streamwise vortex pairs.

The objective of this research is to validate the present MILES methodology using an unstructured grid for a subsonic square jet. First, the implementation techniques of solving the governing equations are discussed briefly using an approximate Riemann solver of Roe's method and the SGS model for the unresolved small scales in the LES. Secondly, a square jet at a Reynolds number of 3,200 and a Mach number of 0.3 is simulated. Temporal evolutions are visualized to characterize the dynamics of deforming vortex rings, ribs and their interactions. Statistical quantities are quantified and compared with the DNS results of Grinstein et al [3].

2. Governing equations

The present LES method is based on solving the 3-D time-dependent nondimensional filtered transport equations for mass, momentum and energy and the state equation of ideal gas for fully compressible flows in an unstructured grid of tetrahedral cells using a cell-centered finite volume formation. Following are the nondimensionalized governing equations and the reference

quantities are: velocity U_∞, static temperature T_∞, density ρ_∞, length scale L and viscosity μ_∞, resulting in a Mach number of $M_\infty = U_\infty/\sqrt{\gamma R T_\infty}$ and a Reynolds number of $Re = \rho_\infty U_\infty L/\mu_\infty$.

$$\frac{\partial \overline{\rho}}{\partial t} + \frac{\partial}{\partial x_j}(\overline{\rho}\tilde{u}_j) = 0 \tag{1}$$

$$\frac{\partial(\overline{\rho}\tilde{u}_i)}{\partial t} + \frac{\partial(\overline{\rho}\tilde{u}_i\tilde{u}_j)}{\partial x_j} = -\frac{\partial \overline{p}}{\partial x_i} + \frac{\partial \tau_{ij}}{\partial x_j} + \frac{\partial \overline{\sigma}_{ij}}{\partial x_j} \quad (i = 1,2,3) \tag{2}$$

$$\frac{\partial(\overline{\rho}\,\tilde{e})}{\partial t} + \frac{\partial(\overline{\rho}\,\tilde{e} + \overline{p})\,\tilde{u}_j}{\partial x_j} = \frac{\partial}{\partial x_j}\left(Q_j + \overline{q}_j + (\tau_{ij} + \overline{\sigma}_{ij})\tilde{u}_i\right) \tag{3}$$

$$\overline{p} = \frac{\overline{\rho}\tilde{T}}{\gamma M_\infty^2} \tag{4}$$

where summation over the three coordinate directions is implied in terms with repeated indices, $\tilde{u}_i = \overline{\rho u_i}/\overline{\rho}$, and $\tilde{e} = \overline{\rho e}/\overline{\rho}$ are the Favre-filtered velocity and total energy, $\overline{p}$ is the pressure, $\overline{\rho}\tilde{e} = \overline{p}/(\gamma-1) + \frac{1}{2}\tilde{u}_k\tilde{u}_k$ is the total energy. $q_j = \frac{\mu}{RePr(\gamma-1)M^2}\frac{\partial \tilde{T}}{\partial x_j}$ is the molecular heat flux, where $Pr = 0.72$ is the molecular Prandtl number. The dimensionless molecular viscosity is dependent on temperature, $\mu = T^n$, where $n = 0.76$. The subgrid scale (SGS) stress is $\tau_{ij} = \overline{\rho\, u_i\, u_j} - \overline{\rho}\,\tilde{u}_i\,\tilde{u}_j$, the SGS heat transfer is $Q_j = \overline{\rho}(\widetilde{u_j T} - \tilde{u}_j\,\tilde{T})$, and the molecular viscous stress is $\overline{\sigma}_{ij} = \frac{\mu}{Re}[-\frac{2}{3}\frac{\partial \tilde{u}_k}{\partial x_k}\delta_{ij} + (\frac{\partial \tilde{u}_i}{\partial x_j} + \frac{\partial \tilde{u}_j}{\partial x_i})]$. The SGS terms τ_{ij} and Q_j are modeled by the MILES method ($\tau_{ij} = 0$ and $Q_j = 0$) to account for the unresolved small scale turbulence [12]. Although many advanced SGS models have been developed, the simple models such as the MILES are widely used.

The inviscid fluxes are computed by an approximate Riemann solver of Roe's flux difference splitting method [13], and Gauss' theorem is applied for the viscous fluxes and heat transfer. A second-order Runge-Kutta scheme is used for the time marching, and the time step is determined such that the total CFL (Courant-Friedrichs-Lewy) number is less than 1.0. The gradients of each variable $(\overline{\rho}, \overline{\rho}\tilde{u}, \overline{\rho}\tilde{v}, \overline{\rho}\tilde{w}, \overline{\rho}\tilde{e})$ in a cell are computed using Least Squares (LS) method of Singular Value Decomposition (SVD), where eight neighboring stencil cells are used. More details of the numerical procedure can be found in Ref. [14, 15].

The present MILES method has been validated for several benchmark problems. In Okong'o, Knight and Zhou [14], good agreement was achieved for the energy spectrum in an isotropic turbulent flow; also, the comparisons with the DNS and experiment were good for a channel flow. A LES of a supersonic flat plate boundary layer was successfully validated by comparing with experimental and theoretical results [16].

3. Details of Computation

A free square jet of width D at Reynolds number of 3,200 and Mach number of 0.3 is studied. The grid consists of $65 \times 65 \times 65$ hexahedral cells in an unstructured grid covering a computational domain of $5D$ in the streamwise direction and $\pm 3D$ along the transverse directions. Each hexahedral cell is divided into five tetrahedral cells, yielding a total of 1.3M tetrahedra. A uniform grid is used along the streamwise direction with the hexahedral grid spacing of $\Delta x/D = 0.078$, which is larger than 0.04 used by Grinstein et al. in their DNS [3]. The grids are stretched along the other two directions and the minimum grid spacings are $\Delta y/D = \Delta z/D = 0.0375$. The imposed boundary conditions include inflow, outflow and wall boundaries. At the inflow, the streamwise velocities are prescribed as

$$u = U[1 + A\sin(2\pi f t)] \tag{5}$$

and

$$\begin{aligned} U = 0.5\, U_\infty\, [1 - \tanh[b_2(2|y|/D - D/(2|y|))] \times \\ 0.5\, U_\infty\, [1 - \tanh[b_2(2|z|/D - D/(2|z|))], \end{aligned} \tag{6}$$

where $A = 0.02$ is the perturbation amplitude, f is the forcing frequency ($f = 0.5$), $b_2 = 0.25 R_{\frac{1}{2}}/\theta$, where $R_{\frac{1}{2}}/\theta = 40$, $R = D/2$ and θ is the momentum thickness. Zero-gradient condition is imposed at the outlet and symmetry boundary conditions are used at the side walls.

4. LES Results

4.1. VORTEX DYNAMICS AND TOPOLOGY

The iso-surfaces of the total vorticity $\omega = \sqrt{\omega_x^2 + \omega_y^2 + \omega_z^2}$ corresponding to $\omega = 0.25\omega_{peak}$ are shown in Fig. 1. Azimuthal nonuniformities make the evolution of the jet shear layer more complicated relative to circular jets. Close to the jet exit, a smooth square vortex sheet can be observed, and subsequently rolled-up vortex-ring structures form due to shear-layer Kelvin-Helmholtz instability. However, the vortex rings further downstream deform to non-planar shape due to self-induction mechanism caused by azimuthal nonuniformities. The deformed vortex rings are connected with the four corners of the initial square sheet by ribs. The hairpin braid vortices aligned with the corners progress faster in the diagonal direction than the others, "which results in redistribution of energy between azimuthal and streamwise vortices" [5]. Further downstream, the jet development is characterized by the strong interaction between vortex rings and braid vortices, which leads to a final breakdown of the large-scales coherent structures

and transition to the turbulent flow. The self-induced deformation of the rings and rib pair were explained to be the leading mechanism for larger entrainment properties in non-circular jets relative to circular jets [7]. "The interactions between the streamwise vortices and the vortex rings is reminiscent of the interaction between ribs and spanwise rollers in the mixing layer" [7]. Mixing of jets with surroundings can be enhanced through controlling the formation, development and interaction of large-scale coherent structures passively.

Fig. 2 shows the instantaneous crosswise vorticity $\omega_z = \partial v/\partial x - \partial u/\partial y$ contours at a central $x-y$ plane. Rolled-up structures can be observed near the base, and subsequently symmetrical counterrotating toroidal structures form in the shear layer which are then followed by their stretching and deformation. The organized structures can be broken down into smaller eddies further downstream. Evidently, the MILES model can capture the transition process. Large-scale vortex rings dominate in the near-field and the small vortices dominate downstream after the breakdown. The spatial spreading can be clearly observed downstream as the jet spreads by entraining mass from the surrounding nonvortical fluid.

Fig. 3 (a-d) shows the contours of instantaneous streamwise vorticity, $\omega_x = \partial v/\partial z - \partial w/\partial y$, across the $y-z$ planes of $x/D = 1$, 2, 3 and 4. Quite different behaviour can be observed at different axial positions. Vortex shears with some rounded-corners are stretched and thickened but still keep the initial square shape at the position of $x/D = 1$. The jet cross section switches axis 45° relative to that of the jet nozzle at the axial location of $x/D = 2, 3$ due to self-induced velocity around the corners by the presence of streamwise vorticity. The flow structure develops into a irregular shape further downstream at $x/D = 4$.

4.2. JET MIXING AND ENTRAINMENT

The statistical quantities are obtained by averaging over 5 forcing cycles after a statistically stationary state has been reached after an elapsed dimensionless physical time of 10.

The centerline distributions of the mean axial velocity by LES compared with the DNS results of Grinstein et al. [3] are plotted in Fig. 4. The mean velocity initially decays within the first 1.5 diameters and subsequently shows a slight increase due to the periodic roll-up by the sinusoidal forcing. The decay after 3.2 diameters is the result of turbulent mixing. In general, the agreement between present MILES and previous DNS results are good.

The corresponding centerline r.m.s. velocities u'/U_c are shown in Fig. 5. Note that close to the inflow plane the r.m.s. of velocity fluctuations is about 2 percent and corresponds to the imposed disturbance level. In the

potential core region, the r.m.s. velocity decreases slightly with increasing axial distance which shows a tendency to remain laminar with low turbulence intensities. Beyond the end of the potential core, the fluctuations of velocity increase very rapidly, which indicates the appearance of the secondary-instability mechanism which leads to the final breakdown of the large vortex structures. Due to insufficient length scale in the streamwise direction, the self-similar behaviour has not been achieved. However, it can be seen that the agreement between MILES and DNS is very good for the transient square jet.

5. Conclusions

A subsonic free square jet of Mach 0.3 and Reynolds number of 3,200 has been investigated by the MILES using an unstructured grid. Self-induced axis-switching occurs due to azimuthal non-uniformity at the exit. Complex vortex topologies and interaction between vortex rings and rib vortices are observed downstream. The mean properties are in good agreement with the DNS results of Grinstein et al. [3].

6. Acknowledgment

The research was supported by the Air Force Office of Scientific Research (AFOSR) under grant F49620-99-1-0008 monitored by Robert Herklotz, John Schmisseur, Len Sakell and Steve Walker. The calculations were conducted on a cluster parallel computer with 16 processors in Rutgers University.

References

1. Panchapakesan, N. R. and Lumley, J. L., Turbulence Measurements in Axisymmetric Jets of Air and Helium. Part 1. Air Jet (1993) *J. Fluid Mech.*, **Vol. 246**, pp. 197-223
2. Rodi, W., Turbulence Models and Their Application in Hydraulics-A State of the Art Review (1980), IAHR, Delft
3. Grinstein, F. F., Gutmark, E. and Parr, T. Near Field Dynamics of Subsonic Free Square Jets. A Computational and Experimental Study (1995), *Physics of Fluids*, **Vol. 7 no. 6**, pp. 1483–1497
4. Grinstein, F. F. and Kailasanath, K. (1995) Three-dimensional Numerical Simulations of Unsteady Reactive Square Jets, *Combustion and Flame*, **Vol. 100**, pp. 2–10
5. Grinstein, F. F. Vortex Dynamics and Entrainment in Rectangular Free Jets (2001) *J. Fluid Mech.*, **Vol. 437**, pp. 69–101
6. Gutmark, E. J. and Grinstein, F. F., Flow Control with Noncircular Jets (1999) *Annu. Rev. Fluid Mech.*, **Vol. 31**, pp. 239–272
7. Grinstein, F. F. and DeVore C. R., Coherent Structure Dynamics in Spatially-Developing Square Jets (1992) *AIAA-92-3441*

8. Boersma, G. J., Brethouwer, G. and Nieuwstadt, F. T. M., A numerical investigation on the effect of the inflow conditions on the self-similar region of a round jet (1996) *Phys. Fluids*, **Vol. 8**, pp. 899–909
9. Le Ribault, C., Sarkar, S. and Stanley, S. A., Large eddy simulation of a plane jet (1999) *Phys. Fluids*, **Vol. 11**, pp. 3069–3083
10. Foss, J. K. and Zaman, K.B.M.Q., Large- and Small-scale Vortical Motions in a Shear Layer Perturbed by Tabs (1999) *J. Fluid Mech.*, **Vol. 382**, pp. 307–329
11. Zaman, K.B.M.Q., Spreading Characteristics of Compressible Jets From Nozzles of Various Geometries (1999) *J. Fluid Mech.*, **Vol. 383**, pp. 197–228
12. Fureby, C., On Subgrid Scale Modeling in Large Eddy Simulations of Compressible flow (1996) *Phys. Fluids*, **Vol. 5**, pp. 1301–1311
13. Hirsch, C., Numerical Computation of Internal and External Flows - Volume 2: Computational Methods for Inviscid and Viscous Flows, Wiley (1997), pp. 204–210
14. Okong'o, N., Knight, D. and Zhou, G., Large Eddy Simulations Using an Unstructured Grid Compressible Navier-Stokes Algorithm (2000) *Int. J. Computational Fluid Dynamics* , **Vol. 13 no. 13**, pp. 303-326
15. Urbin, G., Knight, D. and Zheltovodov, A., Compressible Large Eddy Simulation Using Unstructured Grid: Supersonic Turbulent Boundary Layer and Compression Corner (2000) *AIAA 2000-0427*
16. Urbin, G. and Knight, D., Large Eddy Simulation of a Supersonic Boundary Layer Using an Unstructured Grid (2001) *AIAA J.*, **Vol. 39 no. 7**, pp. 1288–1295

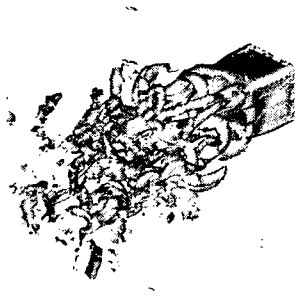


Figure 1. Instantaneous isosurfaces of total vorticity $\omega = 0.25\omega_{peak}$.

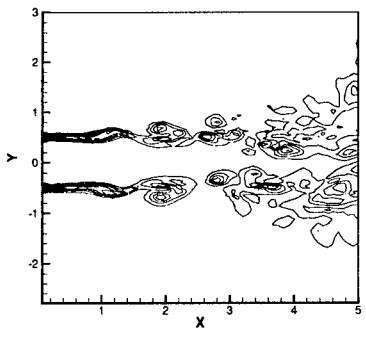


Figure 2. Instantaneous streamsise vorticity contours at the $x - y$ centre-plane.

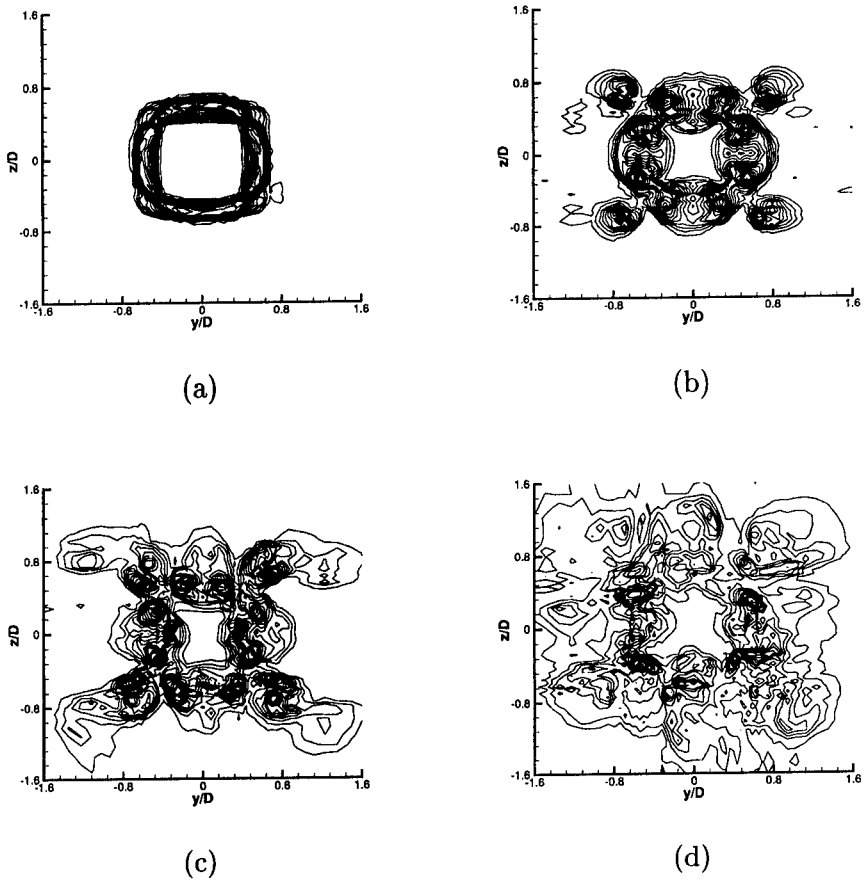


Figure 3. Instantaneous streamwise vorticity contours across the $y - z$ planes at x/D = (a) 1, (b) 2, (c) 3 and (d) 4.

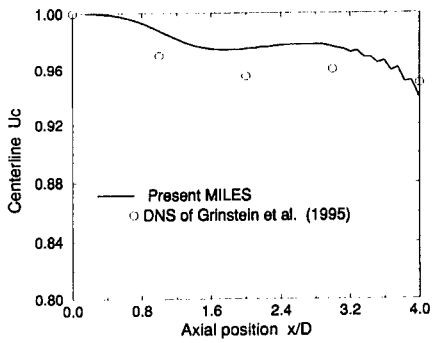


Figure 4. Centerline profiles of the mean velocity.

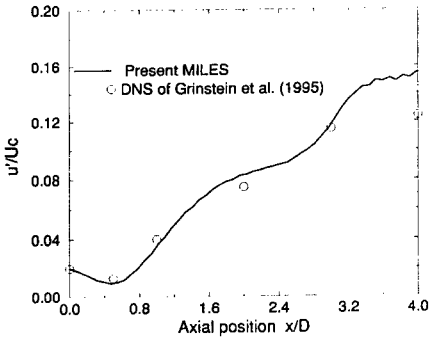


Figure 5. Centerline profiles of the r.m.s. axial velocity.

EFFICIENT LARGE-EDDY SIMULATIONS OF LOW MACH NUMBER FLOWS USING PRECONDITIONING AND MULTIGRID

BAMDAD LESSANI[1] JAN RAMBOER [1] CHRIS LACOR [1]

[1] *Department of Fluid Mechanics, Vrije Universiteit Brussel, Pleinlaan 2, 1050 Brussel, Belgium*

Abstract

In the present paper an implicit time accurate approach combined with multigrid and preconditioning is used for the large-eddy simulation of low Mach number flows. It will be shown that the present approach allows an efficiency gain of a factor 4 to 7 compared to the use of a purely explicit approach. The efficiency varies according to the test case, grid clustering, physical time step and requested residual drop.

1 Introduction

Preconditioning is widely used as a convergence accceleration tool for low Mach number flows. This technique, however, is not time accurate excluding its straightforward use for unsteady problems. Multigrid on the other hand is one of the most efficient convergence acceleration tools. In practice, most multigrid applications are for steady state problems. The dual time-stepping approach can be used for time accurate problems and has the advantage that non-time accurate tools such as preconditioning, multigrid, residual smoothing and local time stepping can be used in a time accurate context. In the present paper the use of these methods is extended towards large-eddy simulations of low Mach number flows.

The LES code is an extension of the finite volume Reynolds Averaged Navier-Stokes (RANS) solver EURANUS, [1]. EURANUS contains an efficient multigrid solver based on the Full Approximation Storage (FAS) scheme for flows ranging from low subsonic up to hypersonic, [2][3]. The Runge-Kutta scheme acts as a smoother for the multigrid. For low Mach number flows, the efficiency of multigrid strongly depends on the stiffness of the equation and the ability of the smoother to damp the high frequency errors. The stiffness is removed with the preconditioning technique which was applied successfully to different steady and unsteady RANS flows, [4][2], and in the present paper will be used in the LES context. A central second-order finite volume spatial discretization is used in the LES code. Fourth-order artificial dissipation is added to increase the high frequency damping of the smoother. In order to avoid laminarization of the flow, the artificial dissipation is only added to the continuity equation but not to the momentum and energy equations. According to our experience, this also suffices to guarantee a good overall convergence. As mentioned above, dual time-stepping is used to update the equations in time. The physical time derivative is discretized either by a backward differencing method or by a trapezoidal scheme. Numerical experiments show that the trapezoidal scheme is more flexible and allows bigger time steps as compared to the backward differencing.

The Smagorinsky model is used for subgrid-scale modeling. Both the classical model and the dynamic model, [7], are available in the code.

2 Mathematical Formulation

The preconditioning procedure in the framework of dual time-stepping can be formulated as, [2]:

$$\frac{1}{\beta^2}\frac{\partial \overline{p}}{\partial \tau}+\frac{\partial \overline{\rho}}{\partial t}+\frac{\partial \overline{\rho}\tilde{u}_i}{\partial x_i}=0 \tag{1}$$

$$\frac{(1+\alpha)\tilde{u}_i}{\beta^2}\frac{\partial \overline{p}}{\partial \tau}+\overline{\rho}\frac{\partial \tilde{u}_i}{\partial \tau}+\frac{\partial \overline{\rho}\tilde{u}_i}{\partial t}+\frac{\partial \overline{\rho}\tilde{u}_i\tilde{u}_j}{\partial x_j}=-\frac{\partial \overline{p}}{\partial x_i}+\frac{\partial \widetilde{\sigma_{ij}}}{\partial x_j}-\frac{\partial \tau_{ij}}{\partial x_j} \tag{2}$$

$$(\frac{\alpha\tilde{u}_i^2+\tilde{H}-\beta^2}{\beta^2})\frac{\partial \overline{p}}{\partial \tau}+\overline{\rho}\frac{\partial \tilde{H}}{\partial \tau}+\frac{\partial \overline{\rho}\tilde{E}}{\partial t}+\frac{\partial(\overline{\rho}\tilde{E}\tilde{u}_j+\overline{p}\tilde{u}_j)}{\partial x_j}=\frac{\partial \widetilde{\sigma_{ij}}\tilde{u}_i}{\partial x_j}-\frac{\partial \tilde{q}_j}{\partial x_j}-\frac{\partial Q_j}{\partial x_j} \tag{3}$$

Where τ is the pseudo-time, t the physical time and $\widetilde{\sigma_{ij}}$, τ_{ij} respectively the filtered stresses and SGS stresses:

$$\widetilde{\sigma_{ij}}=\tilde{\mu}(\frac{\partial \tilde{u}_i}{\partial x_j}+\frac{\partial \tilde{u}_j}{\partial x_i}-\frac{2}{3}\frac{\partial \tilde{u}_k}{\partial x_k}\delta_{ij}) \tag{4}$$

$$\tau_{ij}=\bar{\rho}(\widetilde{u_iu_j}-\tilde{u}_i\tilde{u}_j)=-\mu_t(\frac{\partial \tilde{u}_i}{\partial x_j}+\frac{\partial \tilde{u}_j}{\partial x_i}-\frac{2}{3}\frac{\partial \tilde{u}_k}{\partial x_k}\delta_{ij}) \tag{5}$$

The subgrid-scale heat-flux Q_i is defined as:

$$Q_i=\bar{\rho}c_p(\widetilde{Tu_i}-\tilde{T}\tilde{u}_i) \tag{6}$$

It is modeled using an eddy diffusivity SGS model:

$$Q_i=-\frac{\mu_t c_p}{Pr_t}\frac{\partial \tilde{T}}{\partial x_i} \tag{7}$$

$\mu_t=\rho C\Delta^2|\tilde{S}|$, and $Pr_t=0.5$ or is calculated dynamically. β and α are the preconditioning parameters. α is taken as a constant around -1, and β can be defined locally as, [9],

$$\beta=Min(Max(\sqrt{u_iu_i},\frac{\nu}{\Delta},\frac{l}{\pi\Delta t}),c) \tag{8}$$

With Δ the smallest cell length, l the biggest characteristic dimension of the domain, Δt the physical time step and c the speed of sound. In the present LES calculations Δt is rather small, due to physical restrictions, such that $\frac{l}{\pi\Delta t}$ is the dominant term in (8). As a result, β will be constant on the whole field.

By applying the finite volume method to (1), (2) and (3), they can be written in matrix form as follows:

$$\Gamma^{-1}\frac{\partial Q\Omega}{\partial \tau}+\frac{\partial U\Omega}{\partial t}=Res \tag{9}$$

Written out fully:

$$\begin{bmatrix} \frac{1}{\beta^2} & 0 & 0 & 0 & 0 \\ \frac{(1+\alpha)\tilde{u}_1}{\beta^2} & \overline{\rho} & 0 & 0 & 0 \\ \frac{(1+\alpha)\tilde{u}_2}{\beta^2} & 0 & \overline{\rho} & 0 & 0 \\ \frac{(1+\alpha)\tilde{u}_3}{\beta^2} & 0 & 0 & \overline{\rho} & 0 \\ \frac{\alpha\tilde{u}_i^2+\tilde{H}-\beta^2}{\beta^2} & 0 & 0 & 0 & \overline{\rho} \end{bmatrix} \begin{bmatrix} \overline{p}_{,\tau}\Omega \\ \tilde{u}_{1,\tau}\Omega \\ \tilde{u}_{2,\tau}\Omega \\ \tilde{u}_{3,\tau}\Omega \\ \tilde{H}_{,\tau}\Omega \end{bmatrix} + \begin{bmatrix} \overline{p}_{,t}\Omega \\ (\overline{\rho}\tilde{u}_1)_{,t}\Omega \\ (\overline{\rho}\tilde{u}_2)_{,t}\Omega \\ (\overline{\rho}\tilde{u}_3)_{,t}\Omega \\ (\overline{\rho}\tilde{E})_{,t}\Omega \end{bmatrix} = - \begin{bmatrix} \int \overline{\rho}\tilde{u}_jn_jdS \\ \int(\overline{\rho}\tilde{u}_j\tilde{u}_1+\overline{p}\delta_{1j}+\tau_{1j}-\widetilde{\sigma_{1j}})n_jdS \\ \int(\overline{\rho}\tilde{u}_j\tilde{u}_2+\overline{p}\delta_{2j}+\tau_{2j}-\widetilde{\sigma_{2j}})n_jdS \\ \int(\overline{\rho}\tilde{u}_j\tilde{u}_3+\overline{p}\delta_{3j}+\tau_{3j}-\widetilde{\sigma_{3j}})n_jdS \\ \int((\overline{\rho}\tilde{E}+\overline{p})\tilde{u}_j+\tilde{q}_j+Q_j-\widetilde{\sigma_{ij}}\tilde{u}_i)njdS \end{bmatrix} \tag{10}$$

The physical time derivative ($\frac{\partial U\Omega}{\partial t}$) is discretized with a multi-step scheme:

$$\Gamma^{-1}\frac{\partial Q\Omega}{\partial \tau} = -\frac{\beta_1}{\Delta t}U\Omega + S^n + \gamma_1 Res(U) \tag{11}$$

where S^n is the source term defined as:

$$S^n = -\frac{\beta_0}{\Delta t}(U^n\Omega) - \frac{\beta_{-1}}{\Delta t}(U^{n-1}\Omega) - \frac{\beta_{-2}}{\Delta t}(U^{n-2}\Omega) + \gamma_2 Res(U^n) \tag{12}$$

by multiplying both sides of (11) by Γ

$$\frac{\partial Q\Omega}{\partial \tau} = \Gamma(-\frac{\beta_1}{\Delta t}U\Omega + S^n + \gamma_1 Res(U)) \tag{13}$$

Now a Runge-Kutta method can be used to reach the steady state in pseudo-time. For stability reasons the $\frac{\beta_1}{\Delta t}U$ term is treated implicitly within the Runge-Kuta cycle, for example the i stage is written as,

$$Q^i + \alpha_i \Delta\tau\Gamma\frac{\beta_1 U^i}{\Delta t} = Q^0 + \alpha_i\frac{\Delta\tau}{\Omega}\Gamma(S^n + \gamma_1 Res(U^{i-1})) \qquad i = 1, q \tag{14}$$

after some algebraic manipulations,

$$Q^i = Q^0 + (I + \Gamma\alpha_i\Delta\tau\frac{\beta_1}{\Delta t}\frac{\partial U}{\partial Q})^{-1}\alpha_i\frac{\Delta\tau}{\Omega}\Gamma(-\frac{\beta_1 U^{i-1}\Omega}{\Delta t} + S^n + \gamma_1 Res(U^{i-1})) \tag{15}$$

Calculation of $(I+\Gamma\alpha_i\Delta\tau\frac{\beta_1}{\Delta t}\frac{\partial U}{\partial Q})^{-1}$ in a general compressible case is computationally very expensive. For the sake of simplicity, incompressibility is assumed for the evaluation of $\frac{\partial U}{\partial Q}$. The matrix equals,

$$(I + \Gamma\alpha_i\Delta\tau\frac{\beta_1}{\Delta t}\frac{\partial U}{\partial Q})^{-1} = \begin{bmatrix} 1 & 0 & 0 & 0 & 0 \\ 0 & \frac{1}{1+\alpha_i\frac{\beta_1\Delta\tau}{\Delta t}} & 0 & 0 & 0 \\ 0 & 0 & \frac{1}{1+\alpha_i\frac{\beta_1\Delta\tau}{\Delta t}} & 0 & 0 \\ 0 & 0 & 0 & \frac{1}{1+\alpha_i\frac{\beta_1\Delta\tau}{\Delta t}} & 0 \\ 0 & 0 & 0 & 0 & \frac{1}{1+\alpha_i\frac{\beta_1\Delta\tau}{\Delta t}} \end{bmatrix} \tag{16}$$

This simplification seems to be accurate enough and has not brought any convergence problem for the test cases considered so far.

3 Results

The efficiency of the dual time-stepping method depends on the number of inner iterations (n_1) and the ratio of the physical time step to the time step of a purely explicit scheme ($n_2 = \frac{\Delta t}{\Delta\tau}$). The gain achieved will be n_2/n_1. As a result, the main goal is to choose the physical time step (Δt) as large as possible and make the number of inner iterations (n_1) as small as possible.

This section is divided into three parts, the first part is about the method of discretizing the physical time derivative and its effect on the maximum allowable time step (Δt), in the second part the beneficial effect of preconditioning and multigrid on the requested number of inner iterations is demonstrated and finally some LES results of the channel, cavity and circular cylinder flows are presented.

3.1 Relation Between the Time Integration and the Physical Time Step

It is a well known fact that the backward differencing scheme unlike the trapezoidal scheme has a dissipation error proportional to the time step. In order to see this effect and its influence on the LES results a channel flow at $Re_\tau = 180$ with a mesh of $33 \times 33 \times 65$ points in the x, y and z directions is considered. The time derivative is discretized either with a backward differencing ($\beta_1 = 1.5$, $\beta_0 = -2$, $\beta_{-1} = 0.5$, $\beta_{-2} = 0.0$, $\gamma_1 = 1.$ and $\gamma_2 = 0.0$) or a trapezoidal scheme ($\beta_1 = 1.$, $\beta_0 = 0.0$, $\beta_{-1} = -1$, $\beta_{-2} = 0.0$, $\gamma_1 = 0.5$ and $\gamma_2 = 0.5$) Figures (1) and (2) show the mean velocity profile and the turbulence intensities calculated with the backward differencing scheme and the trapezoidal scheme, respectively.

The trapezoidal scheme is much more flexible than the backward differencing for large time steps. By increasing the time step, the results start deviating from the reference solution (obtained with an explicit time accurate Runge-Kutta method) at $\Delta t = 0.005$ for the backward differencing and at $\Delta t = 0.02$ for the trapezoidal scheme. This behavior is in accordance with the flat plate boundary layer results of Weber *et al.*[11]. The results are also compared with the DNS data of Kim *et al.*[12], the discrepancy between the LES and DNS results is due to the use of a second-order scheme used for the spatial discretization on a relatively coarse mesh. By using higher order methods more accurate results can be obtained, [10].

3.2 The Effect of Preconditioning on Multigrid

The success of multigrid depends on the ability of the smoother to remove the high frequency errors which cannot be supported on coarser meshes. For low Mach number flows preconditioning is necessary to remove the stiffness of the equations and to increase the high frequency damping ability of the smoother.

A test was carried out on the channel flow at $Re_\tau = 180$, M=0.06 with a mesh of $33 \times 33 \times 33$ points. Figure (3) shows part of the convergence graph for four combinations of multigrid and preconditioning. The number of inner iterations is fixed to 50.

When preconditioning is not used there is almost no difference between single grid and multigrid, but when preconditioning is activated multigrid becomes quite efficient.

When both preconditioning and multigrid are switched off, the residual drop of the first momentum equation is around one order of magnitude, and for the continuity equation is less than two. When both preconditioning and multigrid are used, the residual drops are more than four and three orders of magnitude for the first momentum and continuity equations, respectively. Due to the addition of artificial dissipation, the multigrid works more efficiently for the continuity equation than for the first momentum equation in which the artificial dissipation is switched off. For these calculations $\alpha = -1$ and β is globally defined as $\beta^2 = 3.V_{cent}^2$, where V_{cent} is the velocity at the centerline of the channel. A three-level V-sawtooth multigrid is used.

3.3 Some LES Results

In all calculations a second-order central discretization is used in space and a second-order trapezoidal scheme in time. A five-stage Runge-Kutta scheme, $\alpha = \{\frac{1}{4}, \frac{1}{6}, \frac{3}{8}, \frac{1}{2}, 1\}$, $\beta = \{1, 0, 0.56, 0, 0.44\}$ with three evaluations of dissipation, [6], is used as the smoother for the multigrid. A three-level V-sawtooth multigrid with a first order prolongation and quadratic restriction is used.

3.3.1 Channel Flow

The rotating and non-rotating channel flows are considered. For the non-rotating channel flow, a mesh of $33 \times 33 \times 65$ points is used in the x, y and z directions, the streamwise, normal and spanwise dimensions are $4\pi \times 2 \times 2\pi$. Uniform meshes with spacing $\Delta x^+ = \frac{\Delta x u_\tau}{\nu} \simeq 71$ and $\Delta z^+ = \frac{\Delta z u_\tau}{\nu} \simeq 18$ are used in the streamwise and spanwise directions. A non uniform mesh with cosinus distribution is

used in the wall-normal direction. The first mesh point away from the wall is at $y^+ = \frac{\Delta y u_\tau}{\nu} \simeq 0.87$ and the maximum spacing (at the centerline of the channel) is 18 wall units. The Reynolds number based on the friction velocity is $Re_\tau = 180$ and the Mach number at the centerline is $M = 0.06$. A dynamic procedure, [7], is used to calculate the Smagorinsky coefficient and the turbulent Prandtl number. For this calculation $\alpha = -1$ and $\beta^2 = 3.U^2_{center}$.

For the rotating channel flow, the same mesh is used and the results of the non-rotating channel were used as the initial solution. The rotation number is equal to $Ro = 0.01$. The rotation number based on the bulk mean velocity (U_m), angular velocity (Ω) and channel half width (h) is,

$$Ro = \frac{2\Omega h}{U_m} \tag{17}$$

The turbulence intensities are shown in Fig. (4), the results are compared with the DNS data of Kim *et al.*[12] and Kristoffersen *et al.* [13].

The physical time step is around 200 times bigger than the time step of a purely explicit method, the residual drop of the continuity equation is fixed to -2.5 and this requires almost 50 inner iterations. The gain achieved is roughly equal to $\frac{200}{50} = 4$.

3.3.2 Cavity Flow

A lid driven cavity flow is considered as another example to test the ability of the present approach. The flow is driven by the top wall, $z = h$, in the x direction moving with a velocity $U = 1$. The Reynolds number is $Re = \frac{Uh}{\nu} = 10000$ where h is the dimension of the cube. A 33^3 mesh is used with a cosinus distribution of the mesh points. Starting from a stagnant flow, the flow is fully developed after $32h/U$, after which statistics were collected during a period of $32h/U$. The mean velocity profiles along the vertical and horizontal symmetry lines and the statistics of the fluctuating field are shown in Fig. 5. The agreement between the experiment, [14], and simulation is satisfactory. A Smagorinsky model with damping near the wall is used for subgrid scale modeling. For this calculation $\alpha = -1$ and $\beta^2 = 10.U^2$. The physical time step (Δt) is around 1000 times bigger than the maximum time step allowed by the stability condition of an explicit scheme in a compressible flow. In almost 130 inner iterations the residual of the continuity equation drops four orders of magnitude. As a rough estimation, and without taking into account the extra work of the multigrid, the implicit approach is around $1000/130 \simeq 7.5$ times faster than a purely explicit approach.

3.3.3 Circular Cylinder

The cylinder has a diameter of D and a spanwise length of πD at a Reynolds number of $Re_D = 3900$. In the plane normal to the cylinder axis, an O-type grid with 49×81 points is used with 81 points on the surface and 49 points in the radial direction, 33 grid points is used over the spanwise length of πD. The mesh is clustered near the wall to ensure $y^+ < 1$ for the first grid point. A Smagorinsky model with damping near the wall is used for subgrid-scale modeling. For this calculation $\alpha = -1$ and $\beta^2 = 3.U^2_\infty$. The flow statistics are compared with the experimental data of Lourenco and Shih, taken from, [16]. Statistics were accumulated over $T = 60D/U_\infty$. The distribution of the pressure coefficient c_p and the friction coefficient c_f on the cylinder are plotted in Fig. 6. In the same figure the mean streamwise velocity component along the centerline is shown.

Figure 7 shows the velocity fluctuations at $X = \frac{x - x_l}{x_l} = -0.0806$, with x_l the location where the time averaged streamwise velocity component is zero.

The residual drop of the continuity equation is fixed to -2. which is obtained after 100 inner iterations. The physical time step of the implicit method is around 400 times bigger than the time step of the explicit one. The implicit method is $\frac{400}{100} = 4$ times faster than the explicit method.

4 Conclusions

Preconditioning and multigrid have been used for large-eddy simulation of low Mach number flows. A dual time-stepping approach was used to keep the time accuracy of the simulation. The channel and cavity flows as well as the flow around a circular cylinder have been considered to test the ability of the method. It was shown that the present method was 4 to 7 times faster than a purely explicit approach. The efficiency varies according to the test case, grid clustering, physical time step and requested residual drop.

5 Aknowledgments

This research work was partially funded by the Flemish Science Foundation (FWO) under the grant G.0170.98. This support is gratefully acknowledged.

References

[1] Lacor C., Zhu Z. W. and Hirsch Ch.,"*A New Family of Limiters within the Multigrid/Multiblock Navier-Stokes Code EURANUS*", AIAA/DGLR 5th International Aerospace Planes and Hypersonics Technologies Conference, AIAA 93-5023, 1993.

[2] Hirsch Ch. and Hakimi N., "*Preconditioning Methods for Time-Marching Navier-Stokes Solvers*", Solution Techniques for Large-Scale CFD Problems, CMAS, John Wiley and Sons, pp. 333-353, 1995.

[3] Zhu Z. W., Alavilli P., Lacor C., and Hirsch Ch., "*Efficiency and Robustness of Multigrid Methods for Hypersonic Flows*", AIAA 97-0342, 1997.

[4] Hirsch Ch. and Hakimi N., "*Preconditioning Methods for Time-Marching Navier-Stokes Solvers*", International Workshop on Solution Techniques for Large-Scale CFD Problems, 26-28 Sep, CERCA, Montral, Quebec, Canada, 1994.

[5] Darmofal D. L. and Van Leer B., "*Local Preconditioning of the Euler Equations: A Characteristic Interpretation*", Von Karman Lecture Series 1999-03, March 8-12, 1999.

[6] Jameson A., "*Time Dependent Calculations Using Multigrid, With Applications to Unsteady Flows past Airfoils and Wings*", AIAA 91-1596, 1991.

[7] Germano M., Piomelli U., Moin P. and Cabot W. H., "*A Dynamic Subgrid-Scale Eddy Viscosity Model*", Physics of Fluids A, **3**, 1991.

[8] Piomelli U. and Liu J.,"*Large-Eddy Simulation of Rotating Channel Flows Using a Localized Dynamic Model*, Physics of Fluids, **7**, 1995.

[9] Venkateswaran S. and Merkle L., "*Analysis of Preconditioning Methods for the Euler and Navier-Stokes Equations*", Von Karman Lecture Series, 1999-03, March 8-12,1999.

[10] Smirnov S., Lacor Ch. and Baelmans M., "*A Finite Volume Formulation for Compact Scheme with Applications to LES*", AIAA 2001-2546.

[11] Weber C., Ducros F., and Corjon A., "*Assessment of Implicit Time Accurate Integration for LES*", AIAA 99-3355, pp. 866-876.

[12] Kim J., Moin P. and Moser R., "*Turbulence Statistics in Fully Developed Channel Flow at Low Reynolds Number*", Journal of Fluid Mechanics, 177, 133-166.

[13] Kristoffersen R., Andersson H. I., "*Direct Numerical Simulations of Low-Reynolds Number Turbulent Flow in a Rotating Channel*", Journal of Fluid Mechanics, 256, 163-197.

[14] Prasad A. K. and Koseff J. R., "*Reynolds Number and End-Wall Effects on a Lid Driven Cavity Flow*", Physics of Fluids, **1**, 1989.

[15] Leriche E. and Gavrilakis S., "*Direct Numerical Simulation of the Flow in a Lid-Driven Cubical Cavity*", Physics of Fluids, **12**, 2000.

[16] Kravchenko A. G. and Moin P., "*Numerical Studies of Flow Over a Circular Cylinder at Re_D = 3900*", Physics of Fluids, **12**, 2000.

[17] Breuer M., "*Large Eddy Simulation of the Subcritical Flow Past a Circular Cylinder: Numerical and Modeling Aspect*", International Journal for Numerical Methods in Fluids, **28**, 1998.

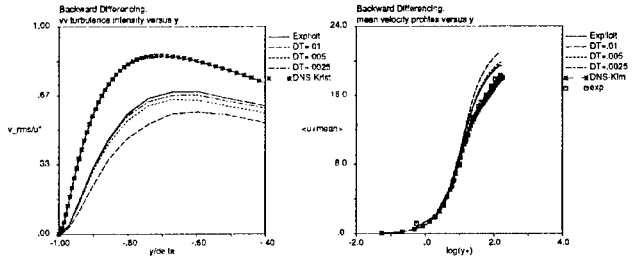


Figure 1: Effect of the time step with the backward-differencing

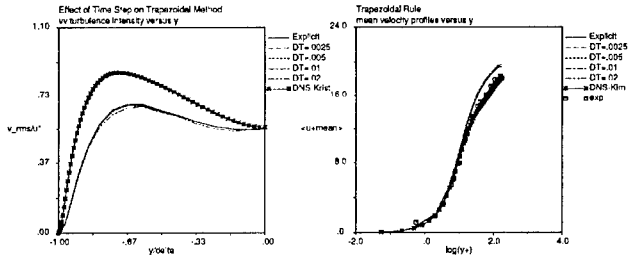


Figure 2: Effect of the time step with the trapezoidal scheme

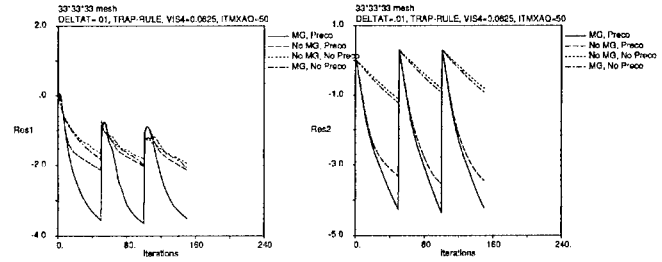


Figure 3: The effect of preconditioning on multigrid for the channel flow calculation with a fixed number of inner iterations, left: continuity equation, right: first momentum equation

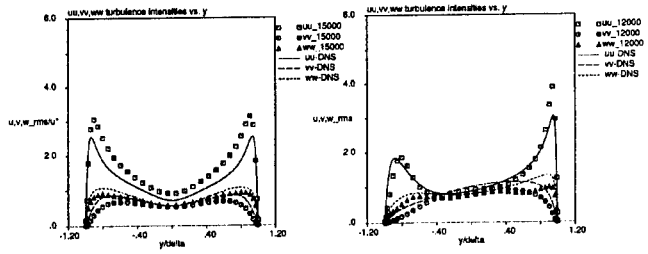


Figure 4: Turbulence intensities, left: non rotating channel flow, right: rotating channel flow

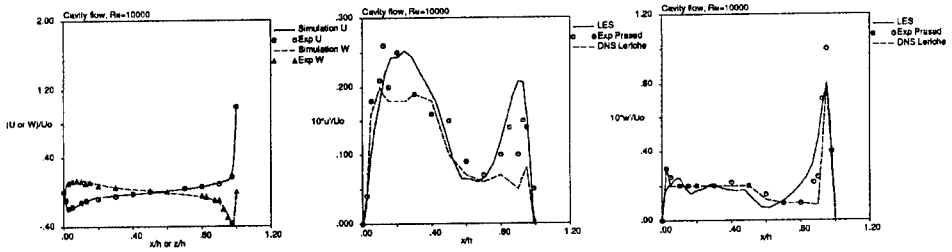


Figure 5: (left): mean velocity profile along two symmetry lines, (middle): $10\sqrt{u'u'}/U$, (right): $10\sqrt{w'w'}/U$, lines are used for the simulation data and markers for experimental data.

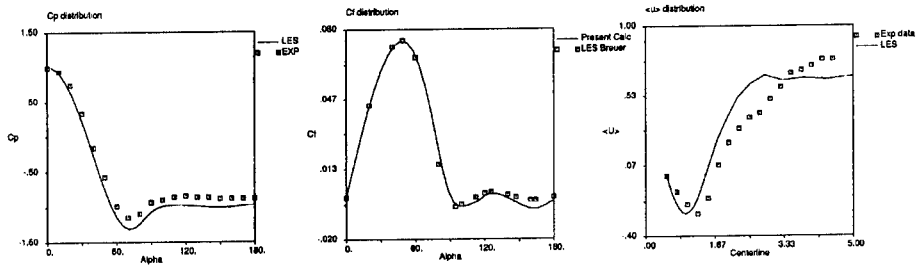


Figure 6: (left): c_p distribution, (middle): c_f distribution, $\circ$ LES of Breuer [17] (right): mean streamwise velocity, c_p and $< u >$ are compared with the experiment of Lourenco and Shih [16]

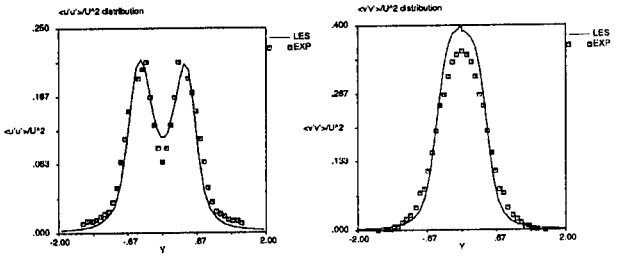


Figure 7: (left): velocity fluctuations at $X = \frac{x-x_l}{x_l} = -0.0806$, $\diamond$, experiment of Lourenco and Shih [16]

CRITICAL COMPARISON OF THE COLLOCATED AND STAGGERED GRID ARRANGEMENTS FOR INCOMPRESSIBLE TURBULENT FLOWS

FREDERIC N. FELTEN AND THOMAS S. LUND

Department of Mechanical and Aerospace Engineering
University of Texas at Arlington,
Box 19018, Arlington, TX 76019-0018

E-mail: felten@uta.edu, lund@uta.edu

Abstract. The collocated-mesh scheme is often favored over the staggered-mesh scheme for turbulence simulation in complex geometries due to its slightly simpler form in curvilinear coordinates. The collocated mesh scheme does not conserve kinetic energy however, and few careful checks of the impact of these errors have been made. In this work, analysis is used to identify two sources of kinetic energy conservation error in the collocated-mesh scheme: (1) interpolation errors arising from second-order linear interpolation and (2) pressure errors. It is shown that the interpolation error can be eliminated through the use of a first-order accurate centered interpolation operator with mesh-independent weights. The pressure error can not be eliminated and it is shown to scale as $O(\Delta t^2 \Delta x^2)$. The effects of the conservation errors is investigated numerically by performing simulations of turbulent channel flow as well as inviscid simulations of the flow over an airfoil. The channel flow results are compared with those of a staggered-mesh code. Neither the second-order interpolation error nor the pressure error appear to lead to significant error in the channel where the Cartesian mesh is stretched in only one direction. The airfoil simulations performed in curvilinear coordinates show a much greater sensitivity to the interpolation errors. The second-order centered interpolation lead to severe numerical oscillations, while the kinetic energy-conserving first-order centered interpolation produce solutions that are almost as smooth as those obtained with a second-order upwind interpolation. These results suggest that numerical oscillations can be controlled in curvilinear coordinates through the use of properly-constructed non-dissipative centered interpolations.

1. Introduction

Numerical Simulation of turbulent flows, using either Direct Numerical Simulation (DNS) or Large Eddy Simulation (LES), requires high-fidelity numerical methods. For incompressible flow, it is highly desirable to have a scheme that conserves mass, momentum, and kinetic energy. In practice, it is rather difficult to satisfy these three constraints simultaneously and one is often faced with the need to give up strict conservation. For computations in Cartesian coordinates, the staggered-mesh scheme is most often used since it is fully-conservative in this case. The extension of the scheme to curvilinear coordinates is not entirely straightforward however, and many researchers have opted for simpler formulations. Formost among these is the so-called collocated-mesh scheme, which has been used by a number of investigators (Peric, 1985), (Peric *et al.*, 1988), (Zang *et al.*, 1994), (Ye *et al.*, 1998), (Armenio and Piomelli, 2000), who were interested in performing LES in complex geometries using body-fitted grids.

Morinishi *et al.* (1998) analyzed the conservation properties of several finite-difference schemes for both staggered and collocated grid arrangements. By restricting the analysis to Cartesian uniform meshes, Morinishi *et al.* showed that staggered-mesh methods can be made fully-conservative, whereas collocated-mesh methods will always contain an energy conservation error of the form $O(\Delta t^m \Delta x^n)$. On curvilinear meshes the collocated-mesh scheme may also develop a second kinetic energy conservation error due to interpolation errors. Like the others before us, we were motivated to use the collocated-mesh scheme for complex flow LES due to it simpler form. Before doing this, however, we wanted to perform analysis and numerical experiments to investigate the impact of the kinetic energy conservation errors. We were also concerned with the prevalence of upwind interpolations used by prior investigators when performing LES with the collocated-mesh scheme in curvilinear coordinates. Any serious problems stemming from the kinetic energy conservation errors, or from the use of upwind interpolations would be grounds for us to reject the collocated-mesh scheme and simply code the staggered-mesh scheme in curvilinear coordinates.

The objective of this paper is twofold: (1) to clearly state the source of the conservation errors through analysis, and (2) to compare the performance of the two schemes for LES of turbulent channel flow, and for the inviscid flow over an airfoil.

2. Analysis

First we define an interpolation operator that approximates the function ϕ at an arbitrary position x^*, which lies between the mesh points x and

$x + \Delta x$

$$\phi(x^*) \simeq \overline{\phi}^x \equiv (1-w)\phi(x) \; + \; w\phi(x+\Delta x). \tag{1}$$

This formula is second order accurate if $w = (x^* - x)/\Delta x$ and is first order accurate otherwise. It is useful to rewrite the interpolation operator as the sum of two operators; one with the mesh-independent weights and a second containing the mesh information:

$$\overline{\phi}^x = \underbrace{\frac{1}{2}[\phi(x) + \phi(x+\Delta x)]}_{\overline{\phi}^{x^0}} \; + \; \underbrace{\left(w - \frac{1}{2}\right)\Delta x}_{r} \frac{\delta\phi}{\delta x}, \tag{2}$$

where $\delta\phi/\delta x = (\phi_{i+1} - \phi_i)/\Delta x$.

In addition, we define a special interpolation operator for the product of ϕ and ψ:

$$\widehat{\phi\,\psi}^x = \frac{1}{2}\phi(x)\;\psi_i(x+\Delta x) \; + \; \frac{1}{2}\psi(x)\;\phi(x+\Delta x). \tag{3}$$

The following identity involving these two interpolation operators will be needed later on in the paper

$$\phi\,\frac{\delta\left(\psi\cdot\overline{\phi}^{x^0}\right)}{\delta x} = \frac{1}{2}\frac{\delta\left(\psi\cdot\widehat{\phi\phi}^x\right)}{\delta x} + \frac{1}{2}\phi\phi\,\frac{\delta\psi}{\delta x}. \tag{4}$$

2.1. STAGGERED GRID SYSTEM

The staggered mesh arrangement in Cartesian coordinates is shown in figure 1. The velocity components U_i (or U, V, W) are distributed around the pressure points p. This layout has the advantage that, when multiplied by the cell face area, the velocity components give the exact volume fluxes, F_i. This feature leads to a simplified mass balance computation and results in fully-coupled velocity and pressure fields.

2.2. COLLOCATED GRID SYSTEM

The collocated-mesh arrangement in Cartesian coordinates is shown in figure 2. The velocity components u_i (or u, v, w) are stored with the pressure p at the cell center. In addition, volume fluxes, f_i, are defined at the cell face in a manner analogous to the staggered-mesh system. The volume fluxes are not solution variables, but rather are determined through interpolation of the cell-centered u_i values plus a projection operation that guarantees exact conservation of mass (Rhie and Chow, 1983). Use of the

mass-conserving volume fluxes results in a pressure equation identical to that in the staggered-mesh system and thus also leads to fully-coupled velocity and pressure fields. The only drawback of the collocated-mesh scheme is that cell-center values, u_i, are only approximately divergence free. This feature leads to a kinetic energy conservation error as discussed below.

2.3. KINETIC ENERGY CONSERVATION

2.3.1. *Staggered-grid system*

When properly-formulated, the second-order staggered-mesh scheme should conserve mass, momentum, and kinetic energy, irrespective of the underlying coordinate system. In developing higher-order schemes, Morinishi *et al.* (1998) first reviewed the conservation properties of several existing schemes cast in uniform Cartesian coordinates. They were able to show that all correctly-coded second-order accurate forms of the non-linear terms (divergence, advective, rotational, and skew-symmetric) are equivalent numerically and fully-conservative. Later Vasilyev (2000) extended the work of Morinishi *et al.* to the case of non-uniform Cartesian meshes. In this work, Vasilyev advocated the use of a mapping to uniform computational space where grid-independent difference and averaging operators could be used. In spite of this, he chose to analyze the divergence form of the non-linear terms in physical space. He found that such a formulation does not conserve kinetic energy due to a lack of commutivity between the average and difference operators. This error can be dispensed with by choosing to work with the non-linear term written in the uniform computational space. The transformation is quite simple in the case of a non-uniform Cartesian mesh, and the fully-conservative formulation can be written as

$$\frac{\delta F_j}{\delta \xi_j} = 0, \tag{5}$$

$$\frac{\delta U_i}{\delta t} + \frac{1}{\overline{\mathcal{V}}^{\xi_i}} \frac{\delta}{\delta \xi_j} \left(\overline{U_i}^{\xi_j} \overline{F_j}^{\xi_i} \right) + \frac{\delta p}{\delta x_i} + (\text{visc})_i = 0, \tag{6}$$

where $\mathcal{V}$ is the cell volume, F_i is the volume flux, ξ_i is a computational space with unit displacements, and $(\text{visc})_i$ are the viscous terms. The commutation error discussed by Vasilyev does not appear in this formulation since both the average and difference operations are performed in the uniform computational space. The only subtle point is that this formulation requires an average of the physical velocity components in the computational space (i.e. $\overline{U_i}^{\xi_j}$). Although this operation is easy to code (weights of 1/2), it results in a an approximation that is only first order accurate. This same issue arises in the collocated mesh scheme and will be discussed in more detail below.

2.3.2. *Collocated-grid system*

The mass and momentum conservation equations for the collocated-mesh system in curvilinear coordinates are

$$\frac{\delta f_j}{\delta \xi_j} = 0, \tag{7}$$

$$\frac{\delta u_i}{\delta t} + J\frac{\delta}{\delta \xi_j}\left(\overline{u_i}^{\xi_j} f_j\right) + J\frac{\delta}{\delta \xi_j}\left(\overline{J^{-1}\xi_i^j p}^{\xi_j}\right) + (\text{visc})_i = 0, \tag{8}$$

where $\xi_i^j = \frac{\delta \xi_j}{\delta x_i}$ and J^{-1} is the jacobian of the transformation.

In the case of the collocated layout, the pressure term is primarily responsible for the lack of kinetic energy conservation. The convective terms may or may not conserve kinetic energy depending on the details of the interpolation operator. Note that the interpolation $\overline{u_i}^{\xi_j}$ suggests interpolating the physical velocity u_i in the computational space ξ_j. While this is a first order accurate approximation (since it makes no account for the physical distances), it results in a kinetic energy conserving formulation. In order to retain second order accuracy, it is tempting to compute mesh-dependent weighting factors and make use of Eq. (2) for the interpolation. This attempt for higher accuracy actually spoils kinetic energy conservation. To see this, we first write the interpolation operator in the convective terms in the form of Eq. (2) and dot the result with the velocity vector to get

$$u_i\frac{\delta}{\delta \xi_j}\left(\overline{u_i}^{S_j} f_j\right) = u_i\frac{\delta}{\delta \xi_j}\left(\overline{u_i}^{S_j^0} f_j + r_j\frac{\delta u_i}{\delta S_j} f_j\right). \tag{9}$$

where S_j is the physical distance measured along the mesh direction ξ_j. Note the trivial equivalence: $\overline{(\cdot)}^{S_j^0} \equiv \overline{(\cdot)}^{\xi_j}$.

Now making use of Eq. (4), Eq. (9) becomes

$$u_i\frac{\delta}{\delta \xi_j}\left(\overline{u_i}^{S_j} f_j\right) = \frac{1}{2}\frac{\delta}{\delta \xi_j}\left(\widehat{u_i u_i}^{S_j} f_j\right) + \frac{1}{2}u_i^2\frac{\delta f_j}{\delta \xi_j} + u_i\frac{\delta}{\delta \xi_j}\left(r_j\frac{\delta u_i}{\delta S_j} f_j\right). \tag{10}$$

The first term on the right hand side is in divergence form and is thus conservative. The second term vanishes due to the continuity relation. The final term represents the kinetic energy error arising from the interpolation. This term vanishes when $r_j = 0$, which corresponds to mesh-independent weights of $1/2$ in Eq. (2).

The kinetic energy conservation property of the pressure term is analyzed in a similar fashion by starting with the interpolation in the form of

Eq. (2):

$$u_i \frac{\delta}{\delta \xi_j}\left(\overline{J^{-1}\xi_i^j p}^{S_j}\right) = u_i \frac{\delta}{\delta \xi_j}\left(\overline{J^{-1}\xi_i^j p}^{S_j^0}\right) + u_i \frac{\delta}{\delta \xi_j}\left(r_j \frac{\delta}{\delta S_j}\left(J^{-1}\xi_i^j p\right)\right),$$

$$= \frac{\delta}{\delta \xi_j}\left(\overline{J^{-1}\xi_i^j p}^{S_j^0}\,\overline{u_i}^{\xi_j}\right) - p\frac{\delta}{\delta \xi_j}\left(J^{-1}\xi_i^j \overline{u_i}^{\xi_j}\right) + u_i \frac{\delta}{\delta \xi_j}\left(r_j \frac{\delta}{\delta S_j}\left(J^{-1}\xi_i^j p\right)\right). \quad (11)$$

Using the Rhie and Chow (1983) interpolation defined as

$$f_j = J^{-1}\xi_i^j\left(\overline{u_i}^{\xi_j} - \Delta t \frac{\delta p}{\delta \xi_j}\delta_{ij}\right)$$

Eq.(11) becomes

$$u_i \frac{\delta}{\delta \xi_j}\left(\overline{J^{-1}\xi_i^j p}^{S_j}\right) = \frac{\delta}{\delta \xi_j}\left(\overline{J^{-1}\xi_i^j p}^{S_j^0}\,\overline{u_i}^{\xi_j}\right) - p\frac{\delta f_j}{\delta \xi_j} - p\Delta t \frac{\delta^2}{\delta \xi_i \delta \xi_j}\left(J^{-1}\xi_i^j p\right) + u_i \frac{\delta}{\delta \xi_j}\left(r_j \frac{\delta}{\delta S_j}\left(J^{-1}\xi_i^j p\right)\right) \quad (12)$$

The first term on the right hand side is in divergence form and is thus conservative. The second term vanishes due to the continuity relation. The remaining two terms are the kinetic energy error arising from the fact that the cell-center velocities do not conserve mass exactly. The final term vanishes in the case of a first order interpolation ($r_j = 0$).

The pressure error terms are added to the convective error term to form $(E_{ke})_{coll}$, the total error in kinetic energy conservation for the collocated-mesh arrangement:

$$(E_{ke})_{coll} = \underbrace{u_i \frac{\delta\left(r_j\left(f_j \frac{\delta u_i}{\delta \xi_j} + \frac{\delta\left(J^{-1}\xi_i^j p\right)}{\delta S_j}\right)\right)}{\delta \xi_j}}_{\text{Interpolation Errors}} \underbrace{- p\Delta t \frac{\delta^2\left(J^{-1}\xi_i^j p\right)}{\delta \xi_j\, \delta \xi_i}}_{\text{Pressure Error}}. \quad (13)$$

This analysis shows that there are two sources of kinetic energy conservation error for the collocated-mesh scheme. The interpolation error will be present if second order, mesh-dependent weighting factors are used. It can be eliminated by choosing first order fixed weights of 1/2 ($r_j = 0$). Veldman and Verstappen (1992), (1998) recognized the conservation error associated with mesh-dependent averaging weights and opted for constant weights of

1/2, in the case of a non-transformed staggered mesh system. Although the pressure error can not be eliminated, it can be reduced to $O(\Delta t^2)$ through the use of the Van Kan scheme (van Kan, 1986). In this formulation, one effectively projects with $\delta p = p^{n+1} - p^n \simeq (\partial p/\partial t)\Delta t$ instead of p in Eq. (12) and thus the terms proportional to p in Eq. (13) are reduced by a factor of Δt.

There are two important questions regarding the kinetic energy errors: (1) are the pressure errors strong enough to de-stabilize the scheme, and (2) does the kinetic energy violation due to second order interpolations negate any increase in accuracy over the first order (kinetic energy conserving) interpolations? We will explore these questions in the following section where the numerical experiments are discussed.

3. Numerical results

3.1. TURBULENT CHANNEL FLOW

The influence of the two sources of kinetic energy conservation error are evaluated through LES of plane channel flow at $Re_\tau = 400$, based on the channel half width and friction velocity. Two computer codes are used; one is based on the second-order staggered-mesh arrangement in the form of Eq. (6) and the other is based on the second-order collocated-mesh arrangement. In either case, finite differences are used only in the streamwise and wall-normal directions and Fourier collocation is used in the spanwise direction. This arrangement allows for more efficient convergence studies since it is only necessary to vary the mesh spacings in the x and y directions in order to investigate the effects of the numerical error. Both codes make use of a third-order Runge-Kutta explicit time marching scheme. The spanwise direction is de-aliased at no computational expense through the use of mesh shifting (Rogallo, 1981). This is done in concert with the multi-step Runge-Kutta scheme. The pressure Poisson equation is solved directly via Fourier transforms in x and z and tri-diagonal inversion in y direction.

Three mesh resolutions and several time step sizes are investigated in order to study the effect of the discretization and the time stepping errors (see Table 1). The computational domain is $8\delta \times 2\delta \times 2\delta$, where δ is the channel half width. The subgrid-scale stresses are modeled using the Smagorinsky (1963) model in conjunction with a Van-Driest type wall-damping function. The results are compared with the DNS data of Moser *et al.* (1999) for $Re_\tau = 395$. For the convergence studies, the time step was held fixed for the three mesh resolutions. This time step corresponds to a viscous $CFL = 1.5$ on mesh C. Cases were also run at larger time steps for meshes A and B.

Figure 3 shows the mean velocity profiles for the three mesh resolutions.

As expected, both the staggered and collocated results improve as the resolution is increased. The staggered-mesh results are consistently closer to the DNS data at all resolutions, and a very good agreement is achieved in the sublayer and log region on the finest mesh (case C). The collocated-mesh results are also reasonably accurate on mesh C.

Since the collocated mesh scheme in conjunction with the Van Kan scheme (van Kan, 1986) has a kinetic energy conservation error that scales like Δt^2, we investigated the possibility that the differences in Figure 3 are from this source. The time step was reduced by 50% on mesh C, and increased by 400% on mesh B. In either case, the results were almost invariant to changes in the time step. This leads us to believe that the energy conservation errors in the collocated mesh scheme do not have a visible impact on the results.

Figure 4 shows a comparison of the the turbulent velocity fluctuations. For the sake of clarity, only results for u_{rms} and v_{rms}, for cases A and C are shown. Once again the staggered-mesh results are superior to the collocated-mesh at all resolutions. The DNS data were not filtered and thus some of the apparent difference between the LES and DNS is due to the unresolved energy in the LES. This effect should be minimal on mesh C. The differences between the two schemes on the finest mesh (C) are minor and either method produces reasonable results at this resolution. The velocity fluctuation profiles are also rather insensitive to changes in the time step.

The rate of convergence of the LES results to the DNS data was investigated by forming the rms difference between the LES and DNS mean velocity profiles:

$$E_{rms} = \sqrt{\frac{1}{2\delta}\int_0^{2\delta} (U_{LES} - U_{DNS})^2 \, dy} \tag{14}$$

Figure 5 shows the E_{rms} for both mesh arrangements as a function of the grid resolution. The two grid arrangements behave similarly, showing something close to second order convergence between the finest two meshes. The Collocated mesh scheme appears to converge at a slightly higher rate, which is consistent with the generally poorer results on the coarser meshes. The collocated mesh scheme also has a slightly smaller rms error as compared with the staggered mesh scheme, even though Figure 3 would suggest the opposite. The reason for this is that Figure 3 is plotted on a log scale, which emphasizes the near-wall region.

The convergence results suggest that the first order momentum interpolations do not have a visible impact on the convergence rate at these resolutions. This may be due to the fact that the interpolation error is multiplied by the factor $(w - 1/2)$ where w is the averaging weight required

for second order accuracy. For relatively coarse, but smooth meshes, the difference $(w - 1/2)$ is of the order of the mesh spacing, and thus one will not see the effect of the first-order interpolation until the mesh is refined further.

We also investigated the use of the second order interpolation weights. The results were similar to those shown in Figures 3 and 4, but with a general small degradation in accuracy. We attribute the degradation to the kinetic energy conservation error. More exacting tests of the interpolation scheme will be presented in the following section where the flow around an airfoil is simulated on a curvilinear mesh.

3.2. INVISCID FLOW AROUND AN AIRFOIL

The inviscid two-dimensional flow over a NACA-0012 airfoil at zero angle of attack has been considered to test the behavior of the collocated mesh arrangement in curvilinear coordinates. An O-mesh containing 50×30 grid-points with the outer boundary placed at four chords is used for the study. The mesh is stretched in both the radial and azimuthal directions in order to better resolve the flow near the leading and trailing edges.

The simulation are performed using three different momentum interpolation operators: (1) the first-order centered interpolation ($w = 1/2$), (2) the second-order centered interpolation ($w = s^*/\Delta s$), and (3) the second-order upwind interpolation (QUICK-type (Leonard, 1979)).

Figure 6 shows the distribution of the pressure coefficient along the airfoil for the three operators considered. The results for the first order centered and second order upwind interpolations are in good agreement with the results of a potential flow analysis. The results for the second-order centered interpolation, on the other hand, show strong oscillations. More insight can be gained from a comparison of the streamwise velocity contours shown in Figure 7. As expected, the dissipative second-order upwind interpolation gives the smoothest solution. On the opposite extreme, the second-order centered interpolation produces a flow field that is obscured by numerical oscillations. The first-order centered interpolation, on the other hand gives a reasonably smooth solution that is comparable to the upwind interpolation. These results are rather significant since they imply that numerical oscillations can be controlled without resort to dissipative upwind schemes. This is particularly important for turbulence simulation where the effects of dissipation have a large negative impact on the solution.

4. Conclusions

We have shown that, in general, the collocated-mesh scheme violates kinetic energy conservation due to two sources: (1) interpolation errors and

(2) pressure errors. The first of these can be eliminated through the use of mesh-independent centered interpolation operators. Although these operators are formally only first order accurate, they are multiplied by geometric terms that are of the order of the mesh spacing for practical computations. We observed second order convergence under mesh refinement for typical LES meshes used in turbulent channel flow. The kinetic energy conservation errors associated with second-order centered interpolations were shown to lead to fairly severe numerical oscillations in a test case involving the inviscid flow around an airfoil computed in curvilinear coordinates. The oscillations could be controlled either by switching to a kinetic energy-conserving first-order centered interpolation, or by switching to a second-order upwind interpolation. We favor the centered interpolation approach for turbulence simulation since it is non-dissipative. This work suggests that the use of upwind interpolations may be unnecessary when the collocated-mesh scheme is applied in curvilinear coordinates, which would significantly increase the fidelity of the numerical method for LES applications.

It does not appear possible to eliminate the second source of kinetic energy conservation error (pressure error). It is possible, however, to limit the size of this error to $O(\Delta t^2 \Delta x^2)$. We could not discern any evidence of this error in turbulent channel flow simulations, where its magnitude was varied by a factor of 16 through time step refinement. These results suggest that pressure term is probably not a serious issue for LES where reasonably fine meshes and small time steps are required for general accuracy purposes.

Our overall conclusion is that the collocated-mesh scheme behaves rather similar to the staggered-mesh scheme, provided that the correct interpolation operators are used. Given its slightly simpler form in curvilinear coordinates, the collocated-mesh scheme may be a better overall choice for LES in complex geometries.

References

Armenio, V. and Piomelli, U. (2000) A Lagrangian mixed subgrid-scale model in generalized coordinates, *Flow, Turbulence and Combustion*, **Vol. 65**, pp. 51–81

Leonard, B. P. (1979) A stable and accurate convection modeling procedure based on quadratic upstream interpolation, *Comput. Meth. Appl. Mech. Engrg.*, **Vol. 19**, pp. 59–98

Moser, R. D., Kim, J. and Mansour, N. N. (1999) Direct numerical simulation of turbulent channel flow up to $Re_\tau = 590$, *Phys. Fluids*, **Vol. 11. 4**, pp. 943–945

Morinishi, Y., Lund, T.S., Vasilyev, O.V. and Moin, P. (1998) Fully conservative higher order finite difference schemes for incompressible flow, *J. Comput. Phys.*, **Vol. 143**, pp. 90–124

Peric, M. (1985) A finite volume method for the prediction of three-dimensional fluid flow in complex ducts, PhD Thesis, University of London.

Peric, M., Kessler, R. and Scheuerer, G. (1988) Comparison of finite-volume numerical methods with staggered and collocated grids, *Computers & Fluids*, **Vol. 16. 4**, pp. 389–403

Rhie, C. M., and Chow, W. L. (1983) A numerical study of the turbulent flow past an isolated airfoil with trailing edge separation, *AIAA J.*, **Vol. 21. 11**, pp. 1525–1532

Rogallo, R. S.(1981) Numerical experiments in homogenous turbulence, *NASA Tech. Memo.*, **81315**

Smagorinsky, J. (1963) General circulation experiments with the primitive equations, part I: the basic experiment, *Monthly Weather Rev.*, **Vol. 91**, pp. 94–164

van Kan, J. (1986) A second-order accurate pressure correction method for viscous incompressible flow, *SIAM J. Sci. Stat. Comput.*, **Vol. 7**, pp. 870–891

Vasilyev, O.V. (2000) High order finite difference schemes on non-uniform meshes with good conservation properties, *J. Comput. Phys.*, **Vol. 157**, pp. 746–761

Veldman, A.E.P. and Rinzema, K. (1992) Playing with non-uniform grids, *J. Eng. Math.*, **Vol. 26**, pp. 119–130

Verstappen, R.W.C.P. and Veldman, A.E.P. (1998) Spectro-consistent discretization of Navier-stokes: A challenge to RANS and LES, *J. Eng. Math.*, **Vol. 34**, pp. 163–179

Ye, J., McCorquodale, J.A. and Barron, R.M. (1998) A Three-dimensional hydrodynamic model in curvilinear coordinates with collocated grid, *Int. J. Numer. Methods Fluids*, **Vol. 28**, pp. 1109–1134

Zang, Y., Street, R.L. and Koseff, J.R. (1994) A Non-staggered grid, fractional step method for time-dependent incompressible Navier-Stokes equations in curvilinear coordinates, *J. Comput. Phys.*, **Vol. 114**, pp. 18–33

TABLE 1. Mesh spacings used for the LES of turbulent plane channel flow.

Case	N_x	N_y	N_z	Δx^+	Δy^+	Δz^+	$\Delta t \cdot u_\tau/\delta$
A	16	16	32	200	4∼127.15	25	1.36×10^{-3}
B	32	32	32	100	2∼62.63	25	1.36×10^{-3}
C	64	64	32	50	1∼30.91	25	1.36×10^{-3}

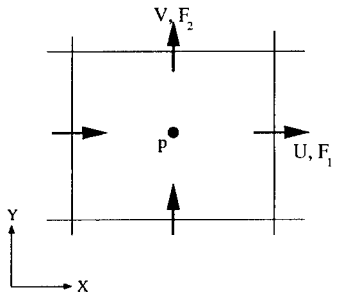


Figure 1. Staggered mesh arrangement in two-dimensional plane.

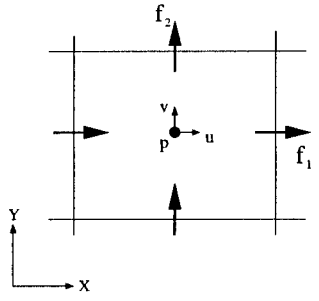


Figure 2. Collocated mesh arrangement in two-dimensional plane.

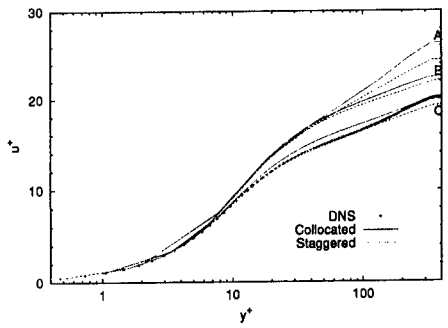


Figure 3. Convergence of the mean velocity profile.

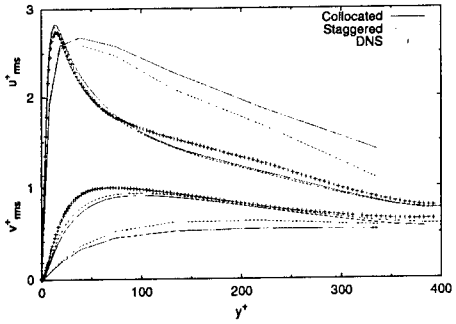


Figure 4. Convergence of the velocity fluctuations.

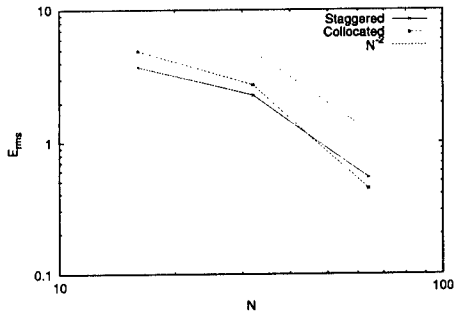


Figure 5. Convergence history as a function of the mesh resolution.

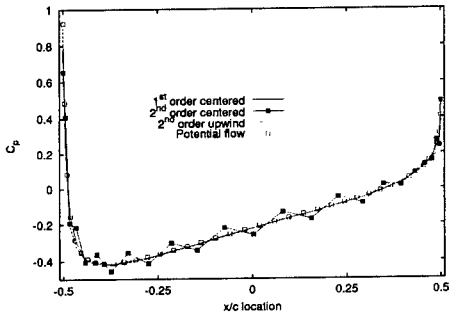


Figure 6. Inviscid NACA-0012 airfoil flow: pressure coefficient distribution.

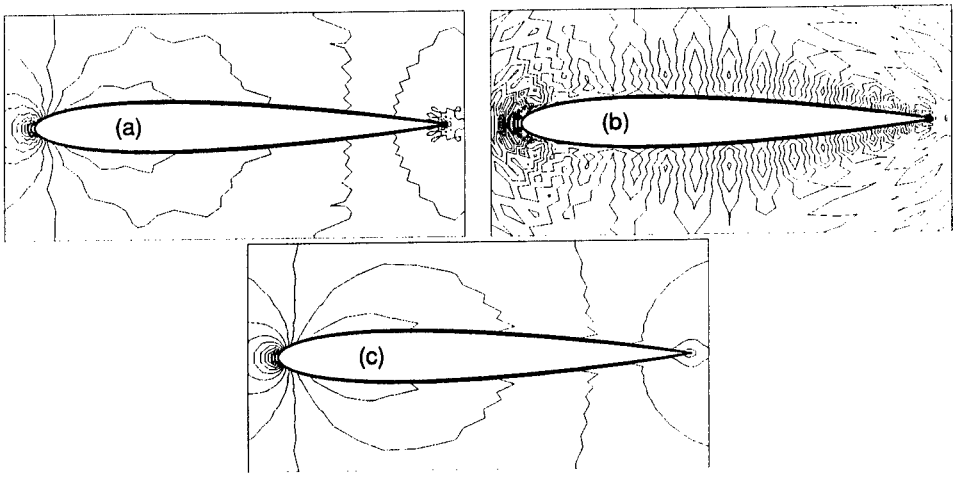


Figure 7. Streamwise velocity contours for the airfoil flow. (a) First-order centered interpolation, (b) Second-order centered interpolation, and (c) Second-order upwind interpolation.

LARGE EDDY AND DETACHED EDDY SIMULATIONS USING AN UNSTRUCTURED MULTIGRID SOLVER

DIMITRI J. MAVRIPLIS
ICASE
NASA Langley Research Center, Hampton, VA, USA
JUAN PELAEZ
Department of Aerospace Engineering
Old Dominion University, Norfolk, VA, USA
AND
OSAMA KANDIL
Department of Aerospace Engineering
Old Dominion University, Norfolk, VA, USA

1. Introduction

This work is concerned with the development of an efficient parallel Large Eddy Simulation (LES) and Detached Eddy Simulation (DES) capability using unstructured meshes. The advantages of unstructured meshes include flexible modeling of complex geometries, adaptive meshing capabilities, and homogeneous data structures well suited for massively parallel computer architectures. On the other hand, unstructured mesh techniques require additional computer resources as compared to cartesian or structured mesh methods, and the achievable accuracy of the particular unstructured mesh discretization must be carefully considered. The approach developed in this work is based on an existing steady-state unstructured mesh solver which relies on agglomeration multigrid for rapid convergence and has been shown to scale well on inexpensive personal computer (PC) clusters as well as on massively parallel supercomputers using thousands of processors [1]. A vertex-based discretization is used, where the flow variables are stored at the vertices of the mesh, and a single edge-based data structure capable of handling combinations of tetrahedra, hexahedra, prism and pyramids is employed. Spatial discretization is achieved through a central-difference control-volume formulation with scaled matrix-based artificial dissipation

derived from an upwind Roe-Rieman solver. This discretization is second-order accurate in space. The baseline steady-state solver is extended to an unsteady Reynolds-Averaged Navier-Stokes (URANS) solver, using a second-order accurate three-point backwards difference time discretization [2]. At each physical time-step, the parallel agglomeration multigrid algorithm is employed to drive the non-linear (unsteady) residual to convergence. The agglomeration algorithm automatically constructs coarse levels in a pre-processing phase, based on the graph of the original fine grid. A preconditioned multi-stage iterative scheme is then used on each grid level to drive the multigrid algorithm. Jacobi (point-wise) preconditioning is used in isotropic regions of the grid, while line preconditioning is used in highly stretched regions of the grid such as near walls where high grid stretching is required to resolve thin boundary layers [3]. The steady and unsteady RANS solver employs the one equation turbulence model of Spalart and Allmaras [4]. The extension from RANS to LES and DES is achieved through the modification of the length scale definition d in the Spalart-Allmaras turbulence model. In the original model, d is taken as the distance at a given grid point to the closest wall. In the DES extension proposed by Spalart [5], this length scale is replaced by:

$$d_{DES} = min(d, C_{DES}, \Delta x) \tag{1}$$

where d represents the original closest-wall length scale, C_{DES} represents a model constant taken as 0.65, and Δx represents a measure of the local grid spacing. For unstructured meshes, Δx is taken as the maximum edge length touching a given vertex. In regions far removed from walls, this modification to the turbulence model emulates a simple Smagorinsky model for LES, while reverting in a smooth manner to the well-established Spalart-Allmaras RANS model in near wall boundary-layer regions.

The resulting solution methodology is nominally second-order accurate in space and in time. We avoid the construction of higher-order accurate spatial operators in order to be able to retain all the discretization, solution, and parallelization techniques previously developed in the steady-state solver context. However, extra care must be taken to avoid excessive numerical diffusion from the second-order discretization from dominating the turbulence eddy viscosity levels in LES regions. With this in mind, the individual convective and numerical dissipative terms of the discretization are evaluated separately, and a (constant) scaling factor is applied to the dissipative terms which provides the option for reducing these terms from their nominal values obtained when the scheme is written as an upwind Roe-Rieman solver.

The agglomeration multigrid algorithm, which is used here as a non-linear implicit solver in time, removes any stability restrictions on the per-

missible time-step size, thus allowing the time-step choice to be determined solely by accuracy considerations. While the desirable time-step size in LES regions may be small enough to obviate the need for a fully implicit solver, in the DES mode very high Courant numbers will almost always be encountered in boundary layer regions, where the solver reverts to a RANS behavior, thus making the availability of an implicit solver essential.

In the following sections, the solver is validated first in unsteady RANS mode for the flow over a circular cylinder. Validation in the LES regime is then undertaken by computing the decay of isotropic turbulence in a periodic box. Finally, the flow over a sphere is simulated in DES mode and compared with experiment and with an equivalent simulation using the solver in an unsteady RANS mode.

2. Unsteady RANS Flow Over a Circular Cylinder

The flow around a circular cylinder is a well- known case, which has been widely studied computationally and experimentally. This case is used as the basis for validation of the unsteady RANS solver, and for assessing grid resolution and time-step requirements for accurately predicting the vortex shedding frequency observed in the cylinder flow. Two different meshes of 252,000 and 631,000 grid points and three different time-steps of 0.5, 0.25 and 0.1 were used. The time-step is non-dimensionalized as $t = t_o U_{inf}/d$ where d is diameter of the cylinder and U_{inf} is the freestream velocity.

The one equation Spalart-Allmaras turbulence model [4] was used for all calculations in fully turbulent mode. In all cases the agglomeration multigrid strategy was used with four levels. The Mach number is 0.2 and the Reynolds number is 1200 for this case. All runs were performed in parallel using 16 processors of an Intel 500 MHz Pentium III PC cluster.

The computational domain in the plane normal to the cylinder span has an aspect ratio of 1 and a side length of 100 cylinder diameters. A span of two cylinder diameters is employed, and inviscid (slip velocity) boundary conditions are applied at the end-walls.

Table 1 shows the Strouhal Numbers computed for each mesh and each time-step of the cylinder flow simulations. Convergence is achieved as the time-step is reduced and the mesh size increased. A second-order accurate convergence behavior is observed as the time-step is reduced, validating the accuracy of the three-point backwards difference scheme used to discretize the time-step. From the smallest time step results, the solution can be seen to be grid converged, at least with respect to the prediction of the vortex shedding frequency. The computed Strouhal number compares very well to the experimental value of St = 0.21.

3. LES Simulation of Isotropic Decaying Turbulence

In order to validate the solver in the LES mode, the simulation of decaying homogeneous isotropic turbulence is computed and the energy spectra of the flow field are compared with experimental results from Comte-Bellot and Corrsin [6]. Strelets [7] has performed similar computations which were used to calibrate the value of the C_{DES} model constant. In the present work, we are mainly concerned with assessing the impact of numerical dissipation on solution accuracy, since the scheme is only second-order accurate. Therefore, the value of C_{DES} is held constant at 0.65 for all computations, which is the value recommended by Strelets [7]. Artificial dissipation levels are varied by prescribing different values of the dissipation scaling parameter, and by varying the grid resolution. In addition, simulations with and without the turbulence model eddy viscosity are performed to assess the effect of the turbulence model on overall solution accuracy, and to determine whether the the levels of eddy viscosity dominate the artificial dissipation.

The computational domain consists of a cube with periodic boundary conditions. Because no wall regions are present, the DES model operates in the LES mode throughout the domain regardless of grid resolution. Computations are performed on a coarse and a fine grid, which are constructed as unstructured cartesian grids with 32 and 64 hexahedral cells, respectively, in each dimension of the cubic domain.

In order to compare with the experimental values from [6], the flow field in the computational domain must be initialized as a solenoidal field with a prescribed energy spectrum corresponding to that measured at the initial test section in the experiments (up to the cutoff value of the wave number corresponding to the grid size). The initial eddy viscosity field must then be obtained by preconverging the turbulence model with the flow-field held frozen. Once the initialization is complete, the flow field is advanced in time using the implicit time-stepping procedure described above. A time-step of 0.01 is employed, where time is non-dimensionalized as $t = t_o(1.5u'^2)^{1/2}/L$, where L is the box length, and u' represents the initial rms average velocity fluctuation. The resulting flow fields at t = 0.87 and t= 2.0 are postprocessed to obtain the energy spectra, which are then compared with corresponding experimental data.

Figure 1 illustrates the computed spectra on both grids at two time levels for the nominal value of the artificial dissipation scaling factor, i.e. the value generally employed for steady-state calculations in RANS mode. Clearly, the finer scales decay more rapidly than in the experimental values. When the same simulations are performed with the eddy viscosity turned off, little difference in the energy spectra is observed, suggesting that the eddy viscosity values are overwhelmed by the levels of artificial dissipation.

In Figure 2, the same computations are performed with a lower scaling of the artificial dissipation terms (0.25 of the nominal value). Substantially better agreement is observed at all scales, although the finest scales are still dissipated faster than in the experimental results. However, reasonably good agreement is obtained up to k=10 for the fine grid, and both grids agree reasonably well at lower wave numbers. When the eddy viscosity is omitted in these cases, agreement with experiment degrades, particularly at the lower wave numbers where the dissipation is lower than observed experimentally.

4. DES Flow Over a Sphere

The current solver is applied in DES mode to predict the flow around a sphere. A Mach number of 0.2 was prescribed, while the Reynolds number was set to 10^4, corresponding to the sub-critical regime (laminar boundary layer separation), which is similar to the computations performed in [8], which provides a comparative basis for our results. An unstructured mesh of 767,000 vertices is employed, in a cubic computational domain of 100 sphere diameters in total length. At the surface of the sphere, the normal grid spacing is 10^{-4} sphere diameters.

Two different time-steps of 0.1 and 0.05 are used, where the time-step is non-dimensionalized as shown in equation (1). Four multigrid levels are used, and each physical time-step is solved with 25 multigrid cycles, resulting in a two order of magnitude reduction in the residuals. All runs were performed on a cluster of thirty-two 800 MHz Pentium III PCs, for which the convergence of a physical time-step could be achieved in approximately 6 minutes of wall clock time.

This case has been computed in both DES and URANS mode, using the Spalart-Allmaras turbulence model without modification in the latter case. The time history of the drag coefficient is shown in Figure 3 and reveals important differences between URANS and DES. The mean value of the drag coefficient in both cases is close to the experimentally reported value of 0.40 from Schlichting [9]. However, the URANS simulation appears to damp out most of the oscillations present in the DES run, while the DES runs show a very chaotic oscillatory pattern quite similar to the solutions obtained by Constantinescu et al. [8]. Spectral analysis of the time-dependent drag coefficient history reveals a peak corresponding to a Strouhal number of 0.1 which is not in agreement with the values 0.18 to 0.2 reported experimentally [8]. This may be due to an insufficiently long time history sample, since less than three full periods of this frequency are present in our sample.

In Figure 4, the average surface pressure computed using DES is seen to provide superior agreement with experimental results at Re=165,000

reported by Achenbach [10] in the separated region over the URANS results, and are in agreement with the results reported by Constantinescu [8]. The average computed separation angle of 81^o in the DES case compares reasonably to experimental vale of 82.5^o .

5. Conclusions and Further Work

This work prepresents initial efforts at developing and validating a fully implicit parallel LES/DES solver based on unstructured meshes. In the near future, we intend to pursue further validation studies on both basic flows using finer grids and time-steps, and more complex geometries such as flow over bluff body components of aerospace vehicles. Efficiency improvement are also under consideration through the use of higher-order time-stepping procedures and Krylov acceleration methods. This work has been supported by AFOSR under the management of Dr. Len Sakell.

References

[1] D. J. Mavriplis and S. Pirzadeh. Large-scale parallel unstructured mesh computations for 3D high-lift analysis. *AIAA Journal of Aircraft*, 36(6):987–998, 1999.

[2] J. Pelaez, D. J. Mavriplis, and O. Kandil. Unsteady analysis of separated aerodynamic flows using an unstructured multigrid algorithm. AIAA Paper 2001-0860, January 2001.

[3] D. J. Mavriplis. Multigrid strategies for viscous flow solvers on anisotropic unstructured meshes. *Journal of Computational Physics*, 145(1):141–165, September 1998.

[4] P. R. Spalart and S. R. Allmaras. A one-equation turbulence model for aerodynamic flows. *La Recherche Aérospatiale*, 1:5–21, 1994.

[5] P. R. Spalart, W-H. Jou, M. Strelets, and S. R. Allmaras. Comments on the feasibility of LES for wings and on a hybrid RANS/LES approach. Paper presented at the First AFOSR International Conference on DNS and LES, Louisiana Tech University, Ruston, Louisiana, August 1997.

[6] G. Comte-Bellot and S. Corrsin. Simple Eulerian time correlation of full- and narrow-band velocity signals in grid generated isotropic turbulence. *Journal of Fluid Mechanics*, 48(2):273–337, 1971.

[7] M. Strelets. Detached eddy simulation of massively separated flows. AIAA Paper 2001-0879, January 2001.

[8] G. S. Constantinescu and K. D. Squires. LES and DES investigations of turbulent flow over a sphere. AIAA Paper 2000-0540, January 2000.

[9] H. Schlichting. *Boundary Layer Theory.* McGraw-Hill, New York, USA, 1979. Seventh Edition.

[10] E. Achenbach. Experiments on the flow past spheres at very high Reynolds numbers. *Journal of Fluid Mechanics*, 54(3):565–575, 1972.

TABLE 1. Computed Strouhal Number for Various Grid Sizes and Time Steps for RANS Flow over Circular Cylinder

Grid Size (points)	Time Step = 0.5	Time Step = 0.25	Time Step = 0.1
0.252 million	0.19249	0.20304	0.20833
0.631 million	0.19379	0.20408	0.20833

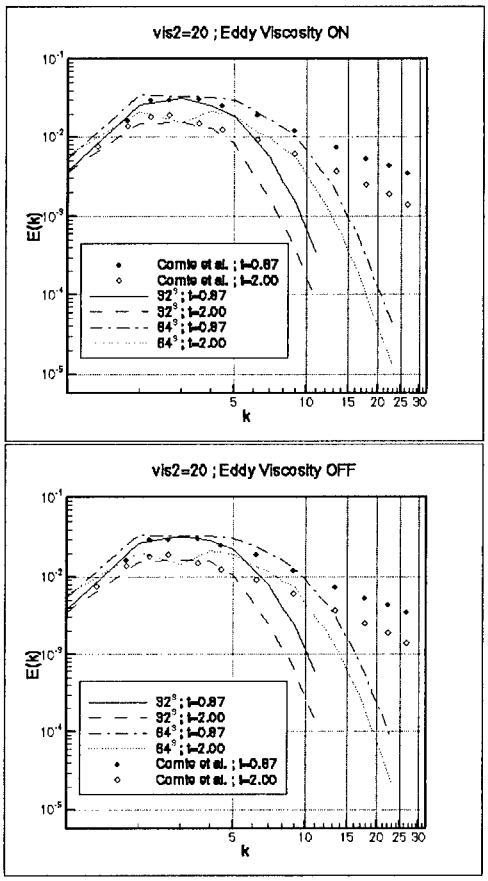


Figure 1. Comparison of Computed and Measured Energy Spectra for Nominal Artificial Viscosity Levels with Eddy Viscosity (LEFT) and Without Eddy Viscosity (RIGHT)

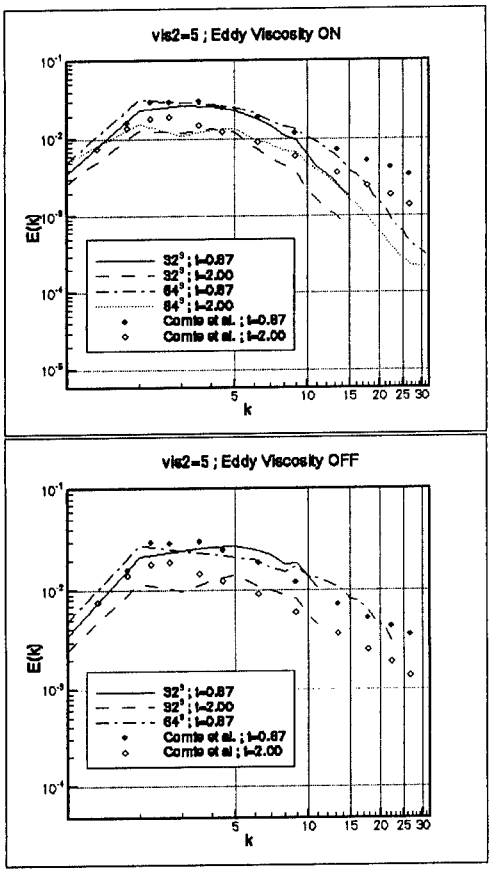


Figure 2. Comparison of Computed and Measured Energy Spectra for Reduced Artificial Viscosity Levels with Eddy Viscosity (LEFT) and Without Eddy Viscosity (RIGHT)

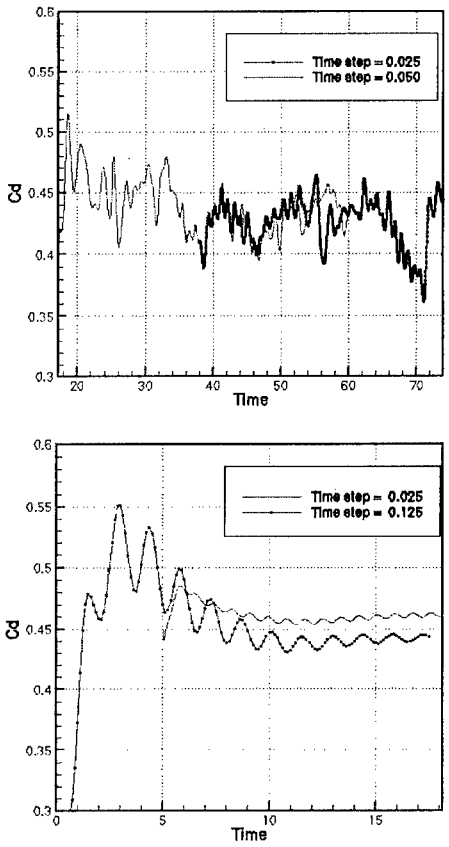


Figure 3. Comparison of Computed Drag Coefficients for Sphere using DES (LEFT) and URANS (RIGHT)

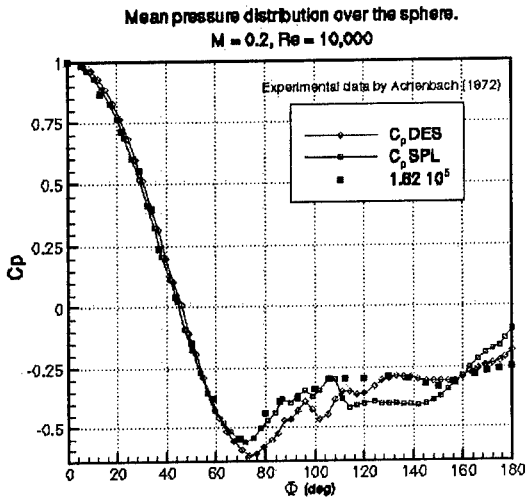


Figure 4. Comparison of Computed Average Surface Pressure Coefficient using DES and URANS versus Experimental Data

TRUNCATION ERROR REDUCTION METHOD FOR POISSON EQUATION

CHAOQUN LIU[¶] AND JIAN XIA[§]
Department of Mathematics,
University of Texas at Arlington,
Arlington, TX 76019-0408, USA

Abstract

A new so-called truncation error reduction method (TERM) is developed in this work. This is an iterative process which uses a coarse grid (2h) to estimate the truncation error and then reduces the error on the original grid (h). The purpose is to use multigrid and simple stencils for high-order accuracy.

1. Introduction

The driven force for this work is to develop a new method which can use simple stencils with multigrid method for high order accuracy. The multigrid (Brandt, 1984) was originally used to accelerate the convergence for elliptic systems. The work here is to use multigrid for high-order accuracy with a simple stencil which allows to achieve high-order accuracy with much fewer points than the traditional finite schemes. The high-order scheme is particularly important for direct numerical simulation (Orszag, S. A. & Patterson, G. S., 1972; Moine and Mahesh, 1998) and the large eddy simulation (LES) (Lilly, 1966; Leseiur & Metais, 1996).

Let us take a look at the problem with coarse grid DNS from the mathematical point of view. Here, the coarse grid DNS means to use a grid which is acceptable by currently available computers. The problem with the coarse grid DNS is really caused by the truncation error while the mesh size 'h' and time step 'k' are not small enough. There are resolution problems with coarse grid DNS as well, of course. Before we can reduce the truncation error, we need to give an estimation which is given by an iterative process including a coarse grid discretization and a coarse-to-fine grid interpolation.

We use the Poisson equation as a test case to check the TERM method and

[¶] Professor of Mathematics
[§] Post-doctoral Research Associate

will use this method for CFD late.

2. Truncation errors reduction methods for Poisson equation

Let us take a look at the following Poisson equation:

$$\frac{\partial^2 u}{\partial x^2}+\frac{\partial^2 u}{\partial y^2}=-k^2\pi^2\left(\sin(k\pi x)+\cos(k\pi y)\right) \tag{1}$$

$$u(0,y)=\cos(k\pi y); \qquad u(1,y)=\cos(k\pi y); \tag{2}$$

$$u(x,0)=1+\sin(k\pi x); \qquad u(x,1)=(-1)^k+\sin(k\pi x)$$

The exact solution is $\sin(k\pi x)+\cos(k\pi y)$. We adopt a standard second order central difference scheme with uniform grids, $\Delta x=\Delta y=h$, and obtain a finite difference scheme:

$$\frac{u^h_{i-1,j}-2u^h_{i,j}+u^h_{i+1,j}}{h^2}+\frac{u^h_{i,j-1}-2u^h_{i,j}+u^h_{i,j+1}}{h^2}+\tau^h_{i,j}=s_{i,j} \tag{3}$$

where u is the exact solution and $s_{i,j}=-k^2\pi^2\sin(k\pi x_i)-k^2\pi^2\cos(k\pi x_i)$.

This finite difference scheme will give an exact solution if we can find the exact truncation error, $\tau^h_{i,j}$, which has a second order, $O(h^2)$. We all know it is difficult to find the exact truncation error, but we can try to give a more accurate estimate by an iterative process which can be described as follows.

1. Assume $\tau^{h,0}_{i,j}=0$, do one or two times Gauss-Seidel iterations, multigrid (Brandt, 1984) may be much faster, to get an approximation $u^{h,1}_{i,j}$.
2. Find the approximation on the coarse grid $u^{2h,1}_{i2,j2}=I^{2h}_h u^{h,1}_{i1,j1}$. In our case, a simple injection is used for I^{2h}_h (or $u^{2h,1}_{i2,j2}=u^{h,1}_{i1,j1}$).
3. Estimate the truncation error on the coarse grid:

$$\tau_{i,j}^{2h,1} = s_{i,j} - \frac{u_{i-1,j}^{2h} - 2u_{i,j}^{2h} + u_{i+1,j}^{2h}}{(2h)^2} - \frac{u_{i,j-1}^{2h} - 2u_{i,j}^{2h} + u_{i,j+1}^{2h}}{(2h)^2} \quad (4)$$

4. Estimate the truncation error on the fine grid:

$$\tau_{i1,j1}^{h,1} = \frac{1}{4} \times I_{2h}^{h} \tau_{i2,j2}^{2h,1} \quad (5)$$

where I_{2h}^{h} should have same or higher order than the finite difference scheme and we should use 1/16 instead of 1/4 in the formula if we use a fourth-order scheme.

5. Get a revised finite difference scheme on the fine grid:

$$\frac{u_{i-1,j}^{h} - 2u_{i,j}^{h} + u_{i-1,j}^{h}}{h^2} + \frac{u_{i,j-1}^{h} - 2u_{i,j}^{h} + u_{i,j+1}^{h}}{h^2} + \tau_{i,j}^{h,1} = s_{i,j} \quad (6)$$

6. Go to step 1 and start a new loop until $\| \tau^{h,n+1} - \tau^{h,n} \| <$ tolerance

This method can be extended with some changes to other flow problems which are usually non-linear and time-dependent.

3. Numerical test for Poisson equation with different grids

A number of numerical tests by using this truncation error reduction method (TERM) for different grids (8x8, 16x16, 32x32, 64x64, 128x128) and different k (1, 2, 3, 4, 8, 16) have been conducted.

Table 1 compares the numerical results with the exact solution. The comparison shows the error ratio of coarse grid 2h over fine grid h for standard second order central difference scheme, $\left\| u - u^{2h} \right\| / \left\| u - u^{h} \right\|$, is near 4, which shows the numerical scheme has a second order accuracy (Burden & Faires, 1996). By using the TERM method , the accuracy has been significant increased. First we find the error ratio is nearly 16, which shows we got a fourth order accuracy with second order stencils. From Table 1, we can find a solution with a grid of 16x16 by the new method can get same results as one obtained with a grid of 64x64 by the standard central difference scheme. It shows we can save the grids or the computer memory by 16 times for this 2-d Poisson equation. The

computation time can be saved almost 100 times. Similar conclusion can be found with other grids and different wave number k. More encouraging, the method shows a same achievement when the wave number becomes higher. It still can improve the results when we have only three points for one wave (see the cases of 8x8 for k=4 and 16X16 for k=8). It provides a high potential which could be used for coarse grid DNS for a more accurate numerical simulation for transitional turbulent flow.

Figure 1-4 show the L_2 norm of errors between the numerical solution and exact solution against the standard central difference method and the TERM method for different grids. It clearly shows that the new method increases the accuracy significantly and has potential for more accurate coarse grid simulation. For 2-D, the new method saves at least 16 times in grid point numbers and much more in CPU time. We can anticipate it will save at least 64 times in the number of grid points for 3-D problems.

4. Conclusion

The new so-called truncation error reduction method (TERM) can significant increase the accuracy of numerical solution for Poisson equation for different wave numbers. It shows TERM can use coarse grids to achieve much more accurate numerical solution than the standard finite difference scheme for Poisson equations. It can save hundreds times in memory and computational time. Potentially, the method may be used for fluid dynamics and for coarse grid DNS.

References

[1] Brandt, Multigrid techniques: Guide with applications in fluid dynamics, GMD, St. Augustine, 1984.

[2] Burden R. L. & Faires, J. D., Numerical Analysis, Brooks/Cole, 1996.

[3] Lesieur, M. & Metais, O., New trends in large-eddy simulations of turbulence. Ann. Rev. Fluid Mech. Vol 28, pp45-82, 1996.

[4] Lilly, D. K., NCAR Manuscript 123, National Center for Atmospheric Res., Boulder, Co. (1966).

[5] Moin, P. & Mahesh, K., Direct numerical simulation: a tool in turbulent research, Annu. Rev. Fluid Mech., Vol 30, pp539-578, 1998.

[6] Orszag, S. A. & Patterson, G. S., Numerical simulation of three-dimensional

Analytic Solution $u(x, y) = \sin k\pi x + \cos k\pi y$		IMAX = 8 JMAX = 8	IMAX = 16 JMAX = 16	IMAX=32 JMAX=32	IMAX=64 JMAX=64	IMAX=128 JMAX=128
k=1	ERROR (central difference)	3.8297E-003	1.0188E-003	2.6273E-004	6.6712E-005	1.6809E-005
	ERROR (TERM)	7.8555E-004	6.1889E-005	4.3033E-006	2.8284E-007	1.8116E-008
k=2	ERROR (central difference)	3.5781E-002	9.3823E-003	2.4108E-003	6.1159E-004	1.5406E-004
	ERROR (TERM)	9.9472E-003	8.4777E-004	6.0961E-005	4.0573E-006	2.6110E-007
k=3	ERROR (central difference)	9.3301E-002	2.3893E-002	6.1033E-003	1.5461E-003	3.8931E-004
	ERROR (TERM)	4.2942E-002	3.8647E-003	2.8834E-004	1.9441E-005	1.2565E-006
k=4	ERROR (central difference)	1.9922E-001	4.8970E-002	1.2387E-002	3.1303E-003	7.8776E-004
	ERROR (TERM)	1.3625E-001	1.1337E-002	8.7461E-004	5.9764E-005	3.8789E-006
k=8	ERROR (central difference)	1.3273	2.3419E-001	5.5260E-002	1.3733E-002	3.4418E-03
	ERROR (TERM)	6.7739	1.6488E-001	1.2195E-002	8.9128E-004	5.9201E-05
k=16	ERROR (central difference)	91.4400	1.5034	2.5141E-001	5.8164E-002	1.4329E-02
	ERROR (TERM)	92.3567	31.4476	1.8054E-001	1.2681E-002	9.0120E-04

homogeneous isotropic turbulence, Phys. Rev. Lett. Vol 2, pp76-79, 1972.

Table 1. Error comparison between central difference scheme and TERM with different grids and wave numbers

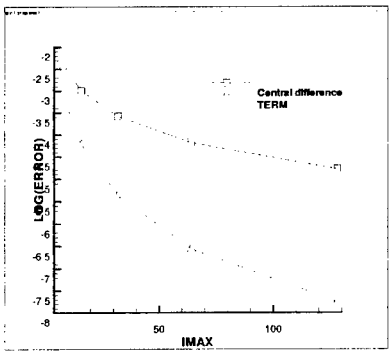


Figure 1: Comparison of errors between standard Central difference scheme and TERM scheme, k=1.

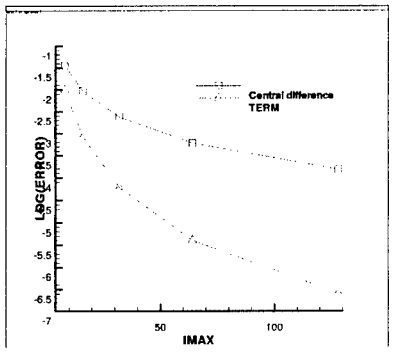


Figure 2: Comparison of errors between standard Central difference scheme and TERM scheme, k=2.

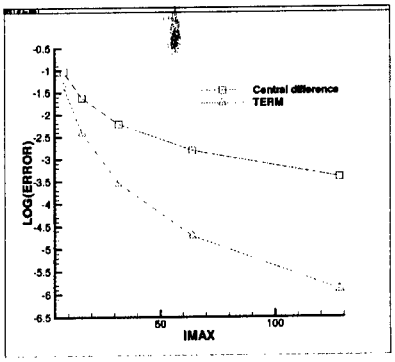


Figure 3: Comparison of errors between standard Central difference scheme and TERM scheme, k=3.

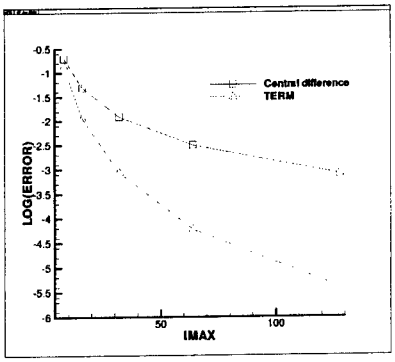


Figure 4: Comparison of errors between standard Central difference scheme and TERM scheme, k=4.

Appendix

We can prove the above TERM method for Poisson equation has fourth order for interior points. For simplicity, we consider the one dimensional case:

$$\frac{\partial^2 u}{\partial x^2} = f \tag{7}$$

Similarly to (3), the standard second order central difference scheme with uniform grids, $\Delta x = h$, can be written as

$$\frac{u_{i-1} - 2u_i + u_{i+1}}{h^2} + \tau_i = f_i \tag{8}$$

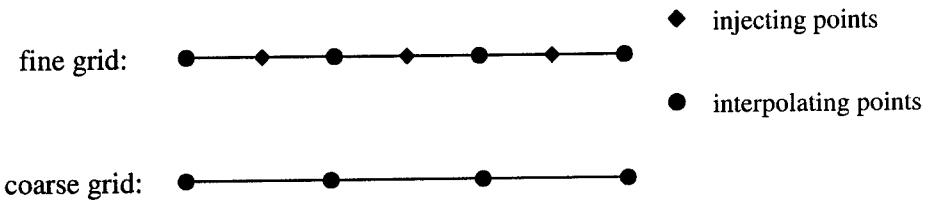


Figure 5 Injecting points and interpolating points

1. Injecting points where the fine grid point coincides with the coarse grid point ($u_i^{2h} = u_{2i}^h$):

On coarse grid

$$\frac{u_{i-2}-2u_i+u_{i+2}}{(2h)^2}+\bar{\tau}_i=f_i \tag{9}$$

Here, $\bar{\tau}_i$ is the truncation error on coarse grid. We have used the following relation between τ_i and $\bar{\tau}_i$

$$\tau_i=\frac{1}{4}\bar{\tau}_i+\tilde{\tau}_i=\frac{1}{4}\left(f_i-\frac{u_{i-2}-2u_i+u_{i+2}}{4h^2}\right)+\tilde{\tau}_i \tag{10}$$

Here, $\tilde{\tau}_i$ is the truncation error for the new scheme. Substitute (10) into (8), we have

$$\frac{-u_{i-2}+16u_{i-1}-30u_i+16u_{i+1}-u_{i+2}}{12h^2}+\tilde{\tau}_i=f_i \tag{11}$$

Using Taylor series, we can find that $\tilde{\tau}_i \sim O(h^4)$ and (11) is a fourth order scheme.

2. Interpolating points where the fine grid point is located between two coarse grid points.

On coarse grid

$$\frac{u_{i-3}-2u_{i-1}+u_{i+1}}{(2h)^2}+\bar{\tau}_{i-1}=f_{i-1} \tag{12}$$

$$\frac{u_{i-1}-2u_{i+1}+u_{i+3}}{(2h)^2}+\bar{\tau}_{i+1}=f_{i+1} \tag{13}$$

Here, $\bar{\tau}_{i-1}$ and $\bar{\tau}_{i+1}$ are the truncation errors on coarse grid. We have used the following relation for $\bar{\tau}_{i-1}, \bar{\tau}_{i+1}$ and τ_i

$$\tau_i=\frac{1}{4}\times\frac{1}{2}\times(\bar{\tau}_{i-1}+\bar{\tau}_{i+1})+\tilde{\tau}_i=\frac{1}{8}\left(f_{i-1}+f_{i+1}-\frac{u_{i-3}-u_{i-1}-u_{i+1}+u_{i+3}}{4h^2}\right)+\tilde{\tau}_i$$

(14)

Here, $\tilde{\tau}_i$ is the truncation error for the new scheme. Substitute (16) into (8), we have

$$\frac{-u_{i-3}+33u_{i-1}-64u_i+33u_{i+1}-u_{i+3}}{24h^2}+\frac{(f_{i-1}-2f_i+f_{i+1})}{6}+\tilde{\tau}_i=f_i \quad (15)$$

We have following relations on the fine grid:

$$\frac{u_{i-2}-2u_{i-1}+u_i}{h^2}-\frac{h^2}{12}u^{(4)}(\xi_{i-1})=f_{i-1} \quad (16)$$

$$\frac{u_{i-1}-2u_i+u_{i+1}}{h^2}-\frac{h^2}{12}u^{(4)}(\xi_i)=f_i \quad (17)$$

$$\frac{u_i-2u_{i+1}+u_{i+2}}{h^2}-\frac{h^2}{12}u^{(4)}(\xi_{i+1})=f_{i+1} \quad (18)$$

Here $x_{i-2}\le\xi_{i-1}\le x_i$, $x_{i-1}\le\xi_i\le x_{i+1}$ and $x_i\le\xi_{i+1}\le x_{i+2}$. Substitute (16), (17), (18) into (15), we have

$$\frac{-u_{i-3}+4u_{i-2}+17u_{i-1}-40u_i+17u_{i+1}+4u_{i+2}-u_{i+3}}{24h^2}+\tilde{\tau}_i-\frac{h^2}{72}(u^{(4)}(\xi_{i-1})-2u^{(4)}(\xi_i)+u^{(4)}(\xi_{i+1}))=f_i \quad (19)$$

Because $$u^{(4)}(\xi_{i-1})-2u^{(4)}(\xi_i)+u^{(4)}(\xi_{i+1})\approx u^{(6)}(\eta_i)h^2 \quad (20)$$

here $x_{i-2}\le\eta_i\le x_{i+2}$. Therefore

$$\frac{h^2}{72}(u^{(4)}(\xi_{i-1})-2u^{(4)}(\xi_i)+u^{(4)}(\xi_{i+1}))\sim O(h^4) \quad (21)$$

Using Taylor series, we can find that $\tilde{\tau}_i\sim O(h^4)$ and (15) is a fourth order scheme.

DIRECT NUMERICAL SIMULATION OF SUPERSONIC TURBULENT RAMP AND STEP FLOW

I. KLUTCHNIKOV AND J. BALLMANN
Mechanics Department
RWTH Aachen, University of Technology
D-52062 Aachen, Germany

Abstract

Direct numerical simulations of compressible fluid flow are performed for subsonic and supersonic channel flow with two symmetrically backward facing steps and for a supersonic compression ramp flow field. Spatial derivatives are represented by a central scheme of high order difference operators (N=2,4,6,8,...) that is used together with artificial dissipation of order N. A two-step Richtmyer scheme is employed for time integration. In regions with steep gradients flux-corrected transport (FCT) according to Boris and Book is applied. Preliminary results are presented for Mach number 1.5 in case of the channel flow and further results for Mach number 2.84 in case of the ramp with a ramp angle of 24 degrees.

1. Introduction

The Reynolds Averaged Navier-Stokes equations (RANS) are often used in connection with various turbulence models to model technical problems of compressible fluid flow, e.g. [1]. But the aptitude of a particular turbulence model for the problem to solve is generally not known beforehand and may even be unsatisfactory. On the other hand, the rapidly growing computer resources offer a promising future to physically more realistic mathematical models like Large-Eddy Simulation (LES) and Direct Numerical Simulation (DNS), see for example [2][3]. Both methods require high order discretization with special treatment of shocks or steep gradients. While LES still needs some modeling to account for the spatially underresolved stresses, DNS should be apt to resolve all turbulent scales without the support of any empirical turbulence modeling. While the method in [3] employs alternating upwinding using compact differences, the method applied in this

paper is based on central high order numerical operators for interpolation and approximation in space in conjunction with a two-step Richtmyer scheme. The method represents an extension of the concept proposed in [4] for the Burgers' equation and the Euler equations to the system of the Navier-Stokes equations for heat conducting compressible fluid flow [5]. Flux-Corrected Transport (FCT) according to Boris and Book has been implemented to account for steep gradients, e.g. in the presence of shocks.

2. Numerical Method

2.1. INTERIOR POINTS OF THE SOLUTION DOMAIN

Denoting by U the set of conserved variables ρ, ρu, ρv, ρw, ρe_{total} and by F^c the fluxes corresponding to the inviscid and by F^d the dissipative part of the fluxes and leaving out body forces and body energy supply the system of Navier-Stokes equations reads

$$U_{,t} + \sum_{r=1}^{3} F_r^c = \sum_{r=1}^{3} F_r^d \tag{1}$$

The equations are integrated with respect to time employing a second order Richtmyer scheme. Space discretization is performed with central high order numerical operators [4][5]. The numerical scheme requires artificial dissipation of the highest order of the scheme for numerical stability in the sense of von Neumann [5]. Using lower index i_r for discretization in the space directions r, $r = 1, 2, 3$ and upper index n for time stepping the set of discretized equations reads

$$\begin{aligned} U_{i_r+1/2}^{n+1/2} &= L_r U_{i_r+1/2}^n - 0.5\lambda_r A_{ri_r+1/2}^n R_r U_{i_r+1/2}^n \\ U_\bullet^{n+1} &= U_\bullet^n - \sum_{r=1}^{3} \lambda_r \{(F_{ri_r+1/2}^{cn+1/2} - F_{ri_r-1/2}^{cn+1/2}) \\ &+ (F_{ri_r+1/2}^{dn} - F_{ri_r-1/2}^{dn}) - (S_r U_{i_r+1/2}^n - S_r U_{i_r-1/2}^n)\} \\ i_r = \{i, j, k\} \quad &, \quad \Delta t/\Delta x_r =: \lambda_r \quad , \quad r = 1, 2, 3 \end{aligned} \tag{2}$$

Therein L_r, R_r, S_r represent the aforementioned high order operators, L_r serving for interpolation, R_r for approximation and S_r for artificial dissipation. A_r is the Jacobian. With coefficients a_m in L_r, b_m in R_r, and d_m in S_r the operators of order N are defined as follows,

$$L_r U_{i_r+1/2} = \sum_{m=1}^{N/2} (-1)^{m+1} a_m (U_{i_r+m} + U_{i_r-m+1}), \tag{3}$$

$$R_r U_{i_r+1/2} = \sum_{m=1}^{N/2} (-1)^{m+1} b_m (U_{i_r+m} - U_{i_r-m+1}), \tag{4}$$

$$S_r U_{i_r+1/2} = \alpha_{i_r+1/2} \sum_{m=1}^{N/2} (-1)^{m+1} d_m (U_{i_r+m} + U_{i_r-m+1}), \tag{5}$$

with $\alpha_{i_r+1/2}$ a prescribed factor for each cell index. The expression for the artificial dissipation of order N is

$$-\alpha \frac{\partial^N U}{\partial x_r^N} \Delta x_r^N = -(S_r U_{i_r+1/2} - S_r U_{i_r-1/2}) \Delta x_r^{-1}, \tag{6}$$

with α a number to be chosen. Optionally, in domains with steep gradients FCT is applied in a self-controlled fashion with the following expressions for the anti-diffusive flux (index ad) and the corrected flux (index cor)

$$F^{c(ad)}_{ri_r+1/2} = F^{c(h)n+1/2}_{ri_r+1/2} - F^{c(l)n+1/2}_{ri_r+1/2}, \quad F^{c(cor)n+1/2}_{ri_r+1/2} = c_{i+1/2} F^{c(ad)}_{ri_r+1/2}. \tag{7}$$

The coefficients a_m, b_m and d_m in Eq. (3), (4), and (5) are depending on the order N which is chosen for the solution [4][5].

2.2. BOUNDARY POINTS

At solid walls the no slip condition is prescribed and walls are assumed thermally adiabatical. The central scheme of order N makes use of N/2 fictitious points by mirror principle. For solution points at artificial boundaries marking the boundary of the computational domain, e.g. at inflow and outflow, also N/2 fictitious points are needed. Different conditions are to be distinguished in the fictitious points there for subsonic and supersonic flow. For subsonic inflow and outflow part of the values in the fictitious points are set using Riemann invariants according to a concept of local simple waves in the sense of gasdynamics while the other part of the values are extrapolated. This way non-physical reflections from the artificial boundary are mostly suppressed.

2.3. APPLICATION PROCEDURE AND VALIDATION

The examples we discuss in this paper would represent two-dimensional flow fields in case of laminar flow. The calculation starts as for laminar flow. On the inflow boundary at a wall a starting boundary layer with parabolic velocity profile is prescribed which may become later on changed as part of the solution because of locally subsonic inflow. At walls the correct boundary conditions are introduced from the first iteration step.

First, some thousands of time steps of the solution are performed for two-dimensional flow. Then during a certain number of time steps a disturbance consisting of two additional velocity components in the cross-plane of the main flow direction is superposed to the boundary condition at the entrance of the solution domain which makes the flow three-dimensional. Thereafter this disturbance is removed.

Numerous and extended validation tests which are not presented in the paper have been conducted for the method [5][11], e.g. comparison was made with analytical solutions of the Burgers' equation, of the 1D Riemann problem for the Euler equations, and of the mean velocity distributions in the viscous layer and the logarithmic layer from turbulent boundary layer theory. Results for compressible flow at Mach number M=0.2 in a straight channel at Reynolds number Re=1750 have been compared with DNS results [6][7] and experimental results at comparable Reynolds numbers [8][9]. Numerical results for a Mach 0.2 flow with Re=2600 through a channel with a backward facing step were compared with experimentally determined values [10] including the Reynolds stresses at different positions behind the step [5][11]. A kind of self-validation is the check of asymptotic convergence with increasing the order N first and then refining the grid. This has been done e.g. in [11] for the flow through a channel with a straight axis and a symmetric jump of the channel height from h on the upstream side to 3h on the downstream side. Data for Mach and Reynolds numbers were M=0.6 and $Re=10^4$. Asymptotic convergence was found for N=8.

3. Simulations of Supersonic Flow Fields

A Mach 1.5 flow through the aforementioned channel with two symmetrical backwards facing steps has been simulated. Static pressure in the flow just before and just behind the steps has the same value p=1. The Reynolds number based on the step height h is $Re=10^4$. The length of the solution domain from the steps to the outflow end is 16h. Number of grid cells in this domain is 256x61x41. Flow is from left to right. Computation is started with given supersonic inflow upstream of the steps including a boundary layer of thickness 0.15h at the upper and lower wall with a parabolic velocity profile. In Fig.(1) results of the density distribution are shown for orders from N=2 up to N=16 for the same physical time t=20 which means 20000 time steps. The flow field is not yet fully established. Comparing the contour lines for the different orders one recognizes that contrary to the subsonic M=0.6 case the order N=8 seems not sufficient for asymptotic convergence. Before the order step from N=14 to 16 the solution exhibits decreasing but still remarkable changes with increasing order. The long time simulation was then conducted with order 16. In Fig.(2) some results obtained so far

are presented. The instantaneous contour lines of Mach number, pressure and density distributions for t=70 show on the inflow side the typical jet behavior for the case of adapted pressure. Then the jet becomes declining more and more, exhibiting vortical structures, local supersonic pockets at vortices and shocklets. The ranges of Mach number are from M=0.1 to M=2.8 and of pressure and density from p=0.3 to p=2.3 and ρ=0.4 to 1.7, respectively. Pressure fluctuations for the time interval from t=40 to t=100 have been recorded in points P_1: $x_1 = 3h$, $x_1 = 2h$, $x_3 = 0$ and P_2: $x_1 = 15h$, $x_2 = 2h$, $x_3 = 0$. The graphs and frequency spectra do not yet represent fully developed turbulent flow. It seems that the computational domain is not long enough to observe the full transition region. Further investigations are necessary. As a second example the supersonic flow over a 24^o ramp is revisited [11] Mach number and Reynolds number are M=2.84 and Re=10^7. According to experiments by Settles [12][13]. results are depicted in Fig.(3). The length of the separation zone is reproduced fairly well by the simulation, and the three-dimensional character of the flow is obvious. The pressure signature in the middle of the corner line is within a range of p=1.9 to p=3.3. The mean pressure is overpredicted in the separation zone but fits fairly well the experimental values outside. The skin friction coefficient fits best the earlier experimental values found by Settles [12] . That agrees with recent results [2].

References

1. Rodi W., Mansour N.N. (1993) Low Reynolds number k-e modeling with the aid of direct simulation data, *J. Fluid Mech. 250*, pp. 509-529
2. Rizzetta, D.P. and Visbal, M.R. (2001) Large-Eddy Simulation of Supersonic Compression-Ramp Flows, *AIAA paper 2001-2858*
3. Fezer A., Kloker M. (1998) Transition Processes in Mach 6.8 Boundary Layers at Varying Temperature Conditions Investigated by Spatial Direct Numerical Simulation, *Notes on Numerical Fluid Mechanics*, **Vol. no. 72**, pp. 138-145
4. Zalesak S.T. (1984) A Physical Interpretation of the Richtmyer Two-Step Lax-Wendroff Scheme, and its Generalization to Higher Spatial Order", *Adv. In Comp. Meth. For Part. Diff. Eq.*, Publ. IMACS, pp. 491-496
5. Klutchnikov, I. (1998) *Direct numerical simulation of turbulent compressible fluid flow.* Habilitation thesis (in Russian), Russian Academy of Sciences, Moscow
6. Kim J., Moin P., Moser R.D. (1987) Turbulence Statistics in Fully Developed Channel Flow at Low Reynolds Number, *J. of Fluid Mech. 177*, pp. 133-166
7. Spalart P.R. (1988) Direct simulation of a turbulent boundary layer up to R=1410, *J. of Fluid Mech. 187*, pp. 61-98
8. Whan G.A., Rothfus R.R. (1959) *Amer. Inst. Chem. Eng. J.*, **Vol. no. 5**, N2, pp. 205-208
9. Patel V.C., Head M.R. (1969) Some Observations on Skin Friction and Velocity Profiles in Fully Developed Pipe and Channel Flows, *J. Fluid Mech.*, **Vol. no. 38**, N1, pp. 181-201
10. Komarov P.L., Polyakov A.F. (1996) *Investigation About the Characteristics of Turbulence and Heat Exchange in a Channel Behind a Backward Facing Step.* Preprint IVTAN N2-396, Moscow, 70p. (in Russian)

11. Klutchnikov I., Ballmann J. (2001) DNS of Turbulent Compresible Fluid Flow with a High Order Difference Method, AIAA paper 2001-2542
12. Settles G.S., Vas I.E., Bogdonoff S.M. (1976) Details of a Shock-Separated Turbulent Boundary Layer at a Compression Corner, *AIAA Journal*, **Vol. 14, No. 12**, pp. 1709-1715
13. Settles G.S., Dodson L.J. (1991) Hypersonic Shock/Boundary-Layer Interaction Database, AIAA paper 1991-1763

4. Figures

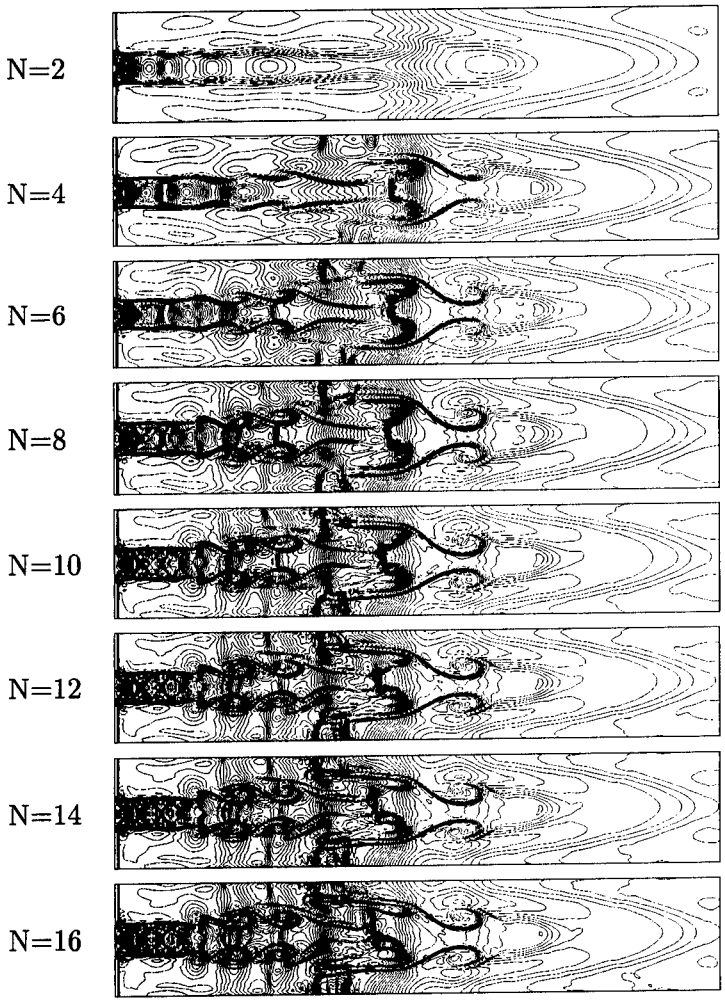


Figure 1. Supersonic flow (M=1.5, Re=10^4) through a channel with two backwards facing steps. Asymptotic convergence check of the instantaneous density field with increasing order, t=20

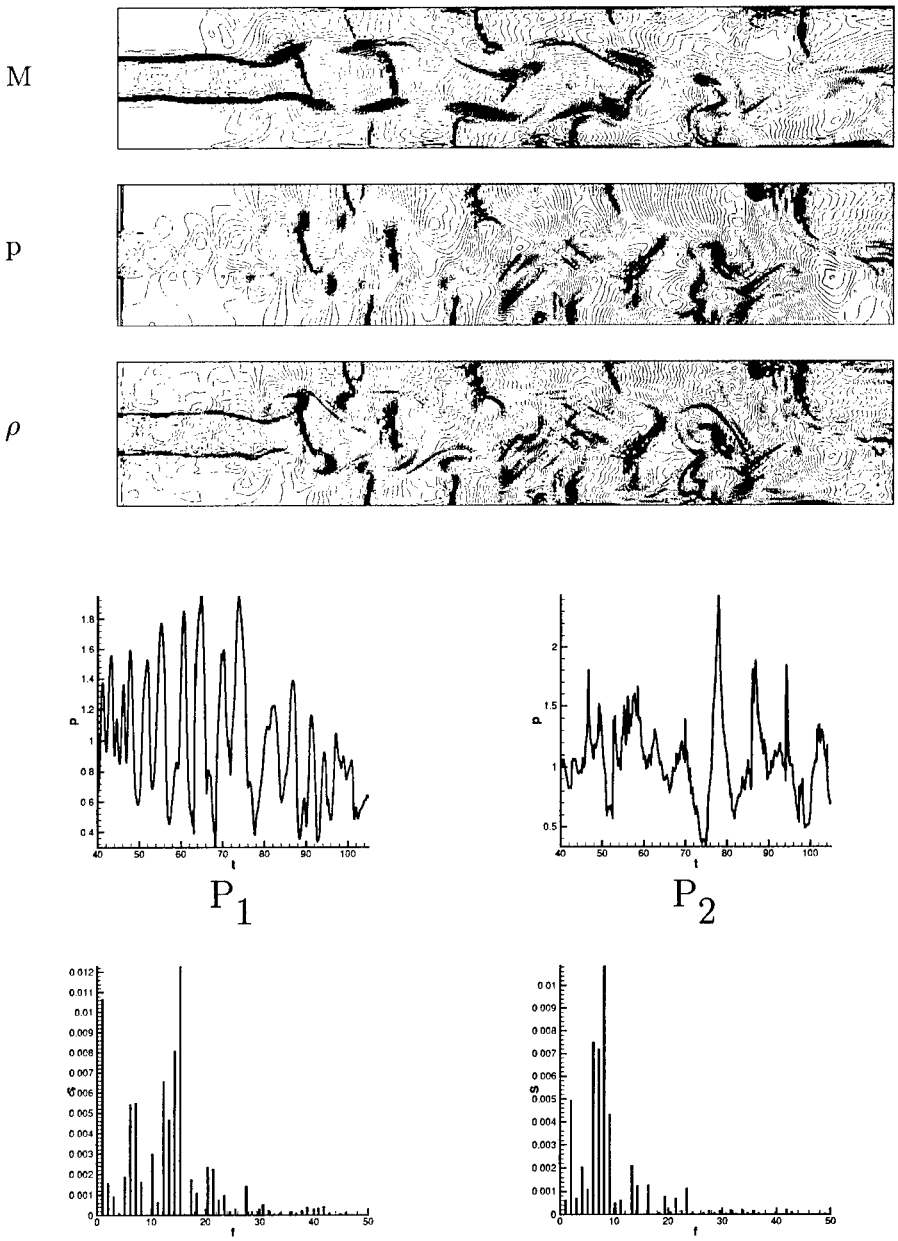


Figure 2. Supersonic channel flow (M=1.5, Re=10^4) , instantaneous contours of Mach number, pressure and density for time t=70 and signatures of pressure over time from t=40 to t=100 in points P_1: $x_1 = 3h$, $x_2 = 2h$, $x_3 = 0$ and P_2: $x_1 = 15h$, $x_2 = 2h$, $x_3 = 0$. Lower figures: respective Fourier spectra

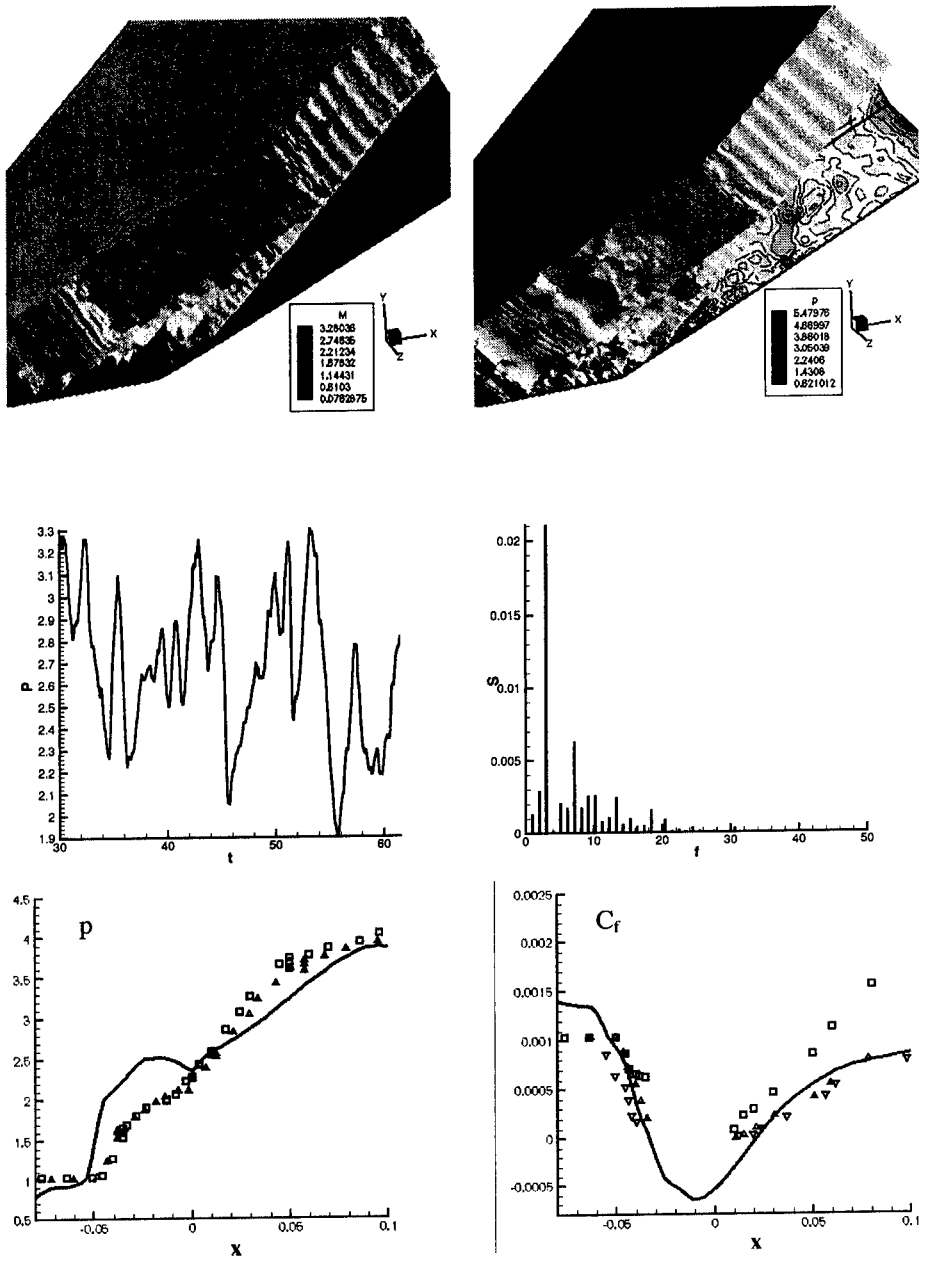


Figure 3. Supersonic flow along a 24° compression ramp (M=2.84, Re=10^7), isosurfaces of M=2.74, 2.5 and 2.05 and p=2.58 and 1.54 (upper figures), graph of pressure signature in the middle point of the corner line for the time interval from t=30 to t=60 and the respective Fourier spectrum (middle figures) and mean wall distributions of pressure p and skin friction coefficient c_f (lower figures). Symbols represent experimental values [12][13]

A MULTIGRID METHOD FOR ELLIPTIC GRID GENERATION USING FINITE VOLUME MEHTOD

SHENG LUO, CHAOQUNLIU, HAUSHAN
Department. of Mathematics, University of Texas at Arlington, Box 19409, Arlington, TX, U.S.A

1. INTRODUCTION

Elliptic and hyperbolic partial differential equations are, at the heart of most mathematical models used in engineering and physics, giving rise to extensive computations. Often the problems that one would like to solve exceed the capacity of even the most powerful computers. On the other hand, the time required is too great to allow inclusion of advanced mathematical models in the design process. Also iterative processes for solving the algebraic equations arising from discretizing partial-differential equations are stalling numerical processes, in which the error has relatively small changes from one iteration to the next. The computer grinds very hard for very small or slow real physical effect with the use of too-fine discretization grids. In this case, in large parts of the computational domain, the mesh size is much smaller than the real scale of solution changes. In particular, convergence of iterative methods for elliptic grid generation based on non-linear grid generation equations is extremely slow.

For the above reason, the authors have worked on the improvement of the non-linear elliptic grid generation. In this paper, the Laplace equation and the algebraic transformation were presented for the domains in 2D and 3D physical space. The second order finite difference scheme was used for the discretization of the grid generating equations. The linear system is solved by the ADI method and the convergence was accelerated by the multigrid FAS scheme. The performance characteristic of the algorithm was discussed and illustrations were made.

2. 2D AND 3D ELLIPTIC GRID GENERATION

The elliptic grid generation method used in this paper is based on the use of a composite mapping [1]. It is a composition of an algebraic transformation and an elliptical transformation based on Laplace equations. The algebraic transformation is a differential one-to-one mapping from computational space onto a parameter space. The parameter space and the computational space are unit squares. The algebraic transformation will only depend on the prescribed boundary grid point distribution. The control functions are defined based on the algebraic transformation. The elliptical transformation is a differential one-to-one mapping from parameter space onto the physical domain. The elliptical transformation depends only on the shape of the domain and is independent of

the prescribed boundary grid point distribution. The composition of these two mappings defines the interior grid point distribution and is a differentiable and one-to-one for 2D domains and surfaces and, probably, also for 3D domains.

2.1 Grid Generation Equations

For 2D problem, the grid generating system of elliptic partial differential equations are as follow:

$$Px_{\xi\xi} + 2Qx_{\xi\eta} + Rx_{\eta\eta} + Sx_{\xi} + Tx_{\eta} = 0 \tag{1}$$

Where

$$P = (x_{\eta}, x_{\eta}), Q = -(x_{\xi}, x_{\eta}), R = (x_{\xi}, x_{\xi}),$$
$$S = PP_{11}^{1} + 2QP_{12}^{1} + RP_{22}^{1}, T = PP_{11}^{2} + 2QP_{12}^{2} + RP_{22}^{2} \tag{2}$$

The control functions are given by

$$P_{11} = -T^{-1}\begin{pmatrix} s_{\xi\xi} \\ t_{\xi\xi} \end{pmatrix}, P_{12} = -T^{-1}\begin{pmatrix} s_{\xi\eta} \\ t_{\xi\eta} \end{pmatrix}, P_{22} = -T^{-1}\begin{pmatrix} s_{\eta\eta} \\ t_{\eta\eta} \end{pmatrix} \tag{3}$$

and the matrix T is defined as $T = \begin{pmatrix} s_{\xi} & s_{\eta} \\ t_{\xi} & t_{\eta} \end{pmatrix}$

The six coefficients of the vectors
$P_{11} = (P_{11}^{1}, P_{11}^{2})^{T}, P_{12} = (P_{12}^{1}, P_{12}^{2})^{T}$ $and P_{22} = (P_{22}^{1}, P_{22}^{2})^{T}$ are called the control functions. The two algebraic equations that define the transformation are given by

$$s = s_{E_3}(\xi)(1-t) + s_{E_4}(\xi)t \tag{4}$$

$$\text{and } t = t_{E_1}(\eta)(1-s) + t_{E_2}(\eta)s \tag{5}$$

The 3D grid generating system is too complicated to describe here. It can be found in [1].

2.2 Discretization Method

Let's use 2D case as an example and consider a uniform rectangular grid of size $(N+1)(M+1)$ defined as $\xi_{i,j} = \xi_i = i/N$, $\eta_{i,j} = \eta_j = j/M$, $i = 0...N; j = 0...M$.

Let $X_{i,j}$ be prescribed on the boundary of this grid. We are going to compute $X_{i,j}$ in the interior of the computational grid based on the solution of the Poisson system defined by Eq.1.

The solution of this system of nonlinear elliptical equations is obtained by Picard iteration.

$$P^{k-1}\mathbf{x}^{k}_{\xi\xi} + 2Q^{k-1}\mathbf{x}^{k}_{\xi\eta} + R^{k-1}\mathbf{x}^{k}_{\eta\eta} + S^{k-1}\mathbf{x}^{k}_{\xi} + T^{k-1}\mathbf{x}^{k}_{\eta} = 0,$$

Where, $P^{k-1} = (\mathbf{x}^{k-1}{}_{\eta}, \mathbf{x}^{k-1}{}_{\eta})$, $Q^{k-1} = -(\mathbf{x}^{k-1}{}_{\xi}, \mathbf{x}^{k-1}{}_{\eta})$, $R^{k-1} = (\mathbf{x}^{k-1}{}_{\xi}, \mathbf{x}^{k-1}{}_{\xi})$,

$S^{k-1} = P^{k-1} P^{1}{}_{11} + 2Q^{k-1} P^{1}{}_{12} + R^{k-1} P^{1}{}_{22}$, $T^{k-1} = P^{k-1} P^{2}{}_{11} + 2Q^{k-1} P^{2}{}_{12} + R^{k-1} P^{2}{}_{22}$.

The six control functions $P^{1}{}_{11}$, $P^{1}{}_{12}$, $P^{1}{}_{22}$, $P^{2}{}_{11}$, $P^{2}{}_{12}$, $P^{2}{}_{22}$ are computed according to the equations given by Eq.2 and by applying second order central difference schemes for the discretizations of $s_{\xi\xi}, s_{\eta\eta}, s_{\xi\eta}, t_{\xi\xi}, t_{nn}$, $t_{\xi\eta}, s_{\xi}, s_{\eta}, t_{\xi}, t_{\eta}$

The arc length normalized variables $(s_{i,j}, t_{i,j})$ at the boundary are computed as follows:

- Compute the distance (l) between succeeding points at the each boundary.
- Define the length of the edge (L) along each boundary as the sum of the distances between succeeding points along that boundary.
- The normalized distance (d) between succeeding points is then given by l/L.
- The arc length normalized variables $s_{i,j}$ and $t_{i,j}$ at the boundary are defined by

$$s_{0,j} = 0, \quad s_{N,j} = 1, \quad j = 0...M, \quad t_{i,0} = 0, \quad t_{i,M} = 1, \quad i = 0...N,$$

$$\text{and } s_{i,0} = s_{i-1,0} + d_{i,0}, \quad s_{i,M} = s_{i-1,M} + d_{i,M}, \quad i = 1...N,$$

$$t_{0,j} = t_{0,j-1} + d_{0,j}, \quad t_{N,j} = t_{N,j-1} + d_{N,j}, \quad j = 1...M.$$

The arc length normalized variables $(s_{i,j}, t_{i,j})$ in the interior of the grid are computed according to the algebraic straight-line transformation given by Eq.(3) and (4). Simultaneously solving the two linear algebraic equations yields $(s_{i,j}, t_{i,j})$.

$$s_{i,j} = s_{i,0}(1 - t_{i,j}) + s_{i,M} t_{i,j}, \quad t_{i,j} = t_{0,j}(1 - s_{i,j}) + t_{N,j} s_{i,j},$$

at each node $(i, j) \in (1...N-1; 1...M-1)$

The steps for an iteration to improve the current approximation x^{k-1} is as follows:

- The coefficients $P^{k-1}, Q^{k-1}, R^{k-1}, S^{k-1}, T^{k-1}$ are computed by applying central difference schemes for the discretization of x_{ξ}^{k-1} and x_{η}^{k-1}. The six control functions remain unchanged during the iterative process.

• Using central difference schemes to discretize $x^k_{\xi\xi}, x^k_{\eta\eta}, x^k_{\xi}, x^k_{\eta}$. The discretization of the mixed derivative using central difference schemes is done in a way described in [2].

• We then obtain a linear system of equations for the unknowns $x^k_{i,j}, i = 0...N; j = 0...M$ with Dirichlet boundary conditions. A Multigrid solver is used to solve this linear system. The solver is called twice to compute the two components $x^k_{i,j}$ and $y^k_{i,j}$.

The initial approximation x^0 is obtained by an algebraic grid generation. The above iterative process is repeated until a required approximation to the solution has been obtained.

The discretization method for 3D problem can also be found in [1].

3. FINITE DIFFERENCE AND FINITE VOLUME METHOD

In this paper, the second order finite difference scheme was used to discretize the equations and the boundary conditions. For 2D problem, Eq. (1) becomes:

$$P\frac{x_{i+1,j} - 2x_{i,j} + x_{i-1,j}}{\Delta x^2} + 2Q\frac{-x_{i-1,j} - x_{i+1,j} - x_{i,j-1} - x_{i,j+1} + x_{i+1,j+1} + x_{i-1,j-1} + 2x_{i,j}}{2\Delta x\Delta y}$$

$$+ R\frac{x_{i,j+1} - 2x_{i,j} + x_{i,j-1}}{\Delta y^2} + S\frac{x_{i+1,j} - x_{i-1,j}}{2\Delta x} + T\frac{x_{i,j+1} - x_{i,j-1}}{2\Delta y} = 0$$

Grids obtained by the nonlinear elliptic Poisson grid generation system defined by Eq.(1) are grid folding free and have an excellent interior gird point spacing distribution. However, the computed grids are in general not orthogonal at the boundary, but we need grids to be orthogonal at the boundary, especially for Navier-Stokes computations. The orthogonality of the gird in a boundary layer is often desired.

The s coordinate in parameter space P satisfies the linear second-order elliptic equation $(Ja^{11}s_\xi + Ja^{12}s_\eta)_\xi + (Ja^{12}s_\xi + Ja^{22}s_\eta)_\eta = 0$. The t coordinate is obtained in the same way. A finite-volume cell-centered nine-point stencil approach is used to obtain the discretized equations for boundary orthogonality of 2D problem and seven-point stencil for that of 3D problem.

4. MULTIGRID TECHNIQUE

As we know, Gauss-Seidel relaxation for solving Eq.6 typically stalls after a few iterations. This is because Gauss-Seidel, though effective for high-frequency errors components, has very little effect on low-frequency components. Multigrid capitalizes on this "smoothing" property of Gauss-Seidel by visiting coarser grids to resolve smooth errors. But the regular multigrid correction scheme is only valid for linear problem. In order to accommodate the nonlinearities in Eq.6, we applied the Full Approximation Scheme (FAS) version of multigrid with bilinear interpolation and full weighting of residuals and approximations.

4.1. Full Approximation Scheme (FAS)

In non-linear problem, the difference $L_h u_h - L_h \bar{u}_h$ can no longer be replaced by $L_h v_h$, where v_h is the truncation error on fine grid. Hence, we introduce a new coarse grid variable u_{2h} defined as $u_{2h} = I_h \bar{u}_h + v_{2h}$, where I_h represents a so-called restriction operator which interpolates fine grid solution variables to the coarse grid and v_{2h} is the truncation error on coarse grid. The coarse grid equation can be written as $L_{2h} u_{2h} - L_{2h} I_h \bar{u}_h = -I_h^{2h} r_h$, I_h^{2h} represents the restriction operator which transfers residuals from fine to coarse grids and r_h is the residue on fine grid. The operators I_h may in principle be different from each other.

It is useful to rewrite the above equation as:

$$L_{2h} \bar{u}_{2h} = S_{2h}, \text{ where } S_{2h} = L_{2h} I_h^{2h} \bar{u}_h - I_h^{2h} r_h .$$

In this form, the coarse gird equation is seen to take on a similar structure to the original fine grid equation, with a modified source term. This enables us to use similar techniques for solving both the coarse and fine grid problems. Once the coarse grid equations have been solved, either exactly or approximately, the fine grid variables are updated as:

$$\bar{u}_h^{new} = \bar{u}_h^{old} + I_{2h}^h (\bar{u}_{2h}^{new} - I_h^{2h} \bar{u}_h^{old})$$

which can also be written as $\bar{u}_h^{new} = \bar{u}_h^{old} + I_{2h}^h v_{2h}$. I_{2h}^h is called interpolation operator.

The FAS method is carried out in the following steps. [4]

- Restrict the current approximation and its fine-grid residual to the coarse grid: $r_{2h} = I_h^{2h}(f_h - L_h(v_h))$ and $v_{2h} = I_h^{2h} v_h$, where f_h is the right-hand term of nonlinear equation system on fine grid.
- Solve the coarse-grid problem $L_{2h}(u_{2h}) = L_{2h}(v_{2h}) + r_{2h}$.
- Compute the coarse-grid approximation to the error: $e_{2h} = u_{2h} - v_{2h}$.
- Interpolate the error approximation up to the fine grid and correct the current fine-grid approximation: $v_h \quad v_h + I_{2h}^h e_{2h}$, where h: the mash space on finest grid, 2h: the mesh space on coarse grid.

4.2. The Solver for Linear Systems

The linear systems were solved by applying *alternating direction implicit* methods (ADI). The basic idea for ADI method is as follows: a complete iteration consists of two scans. The first scan goes from the smallest index number to the largest one from one row to the other followed by the same in the column direction. The second scan is almost the same as the first one, except for going from the largest index number to the smallest one. This method can

increase the convergence rate at the cost of some complication in the computational algorithm. [3]

To illustrate the advantage of FAS method, the author compared ADI method with FAS and ADI method.

5. ILLUSTRATIONS

5.1. For 2-D Case

In Fig. 2(a), the body-fitted C-grid around a NACA 0012 airfoil is displayed. The close-up of mesh near the airfoil is shown in Fig. 2(b) where grids are orthogonal at the boundaries. The mesh is clustered near the wall in the wall-normal direction (η) as well as in the vicinity of the leading and trailing edge of the airfoil in the direction parallel to the wall (ξ). The grid contains 769 points in the ξ direction and 129 points in the η direction.

As seen in the figures, the grid generated is grid folding free and the interior grid point distribution is a good reflection of the prescribed boundary grid point distribution. The initial grid is obtained with algebraic grid generation and is required as the initial solution for the non-linear elliptical Poisson system. The final grid is independent of the initial grid. The quality of the initial grid is unimportant and severe grid folding of the initial grid is allowed.

Fig. 3. shows the Log (residue) vs. Work Units of the ADI and the multigrid method for 2D case. From the figure, the multigrid method reduced the residue significantly, which is faster than the ADI method for the above problem. The multigrid method saves at least 23 times in CPU times (or work unit) than the ADI method.

5.1. For 3-D Case

The geometry of the delta wind, taken from the experimental work of Rieley & Lowson (1998), is shown in Fig. 4. The sweep angle denoted by Λ is 85° and the leading-edge angle denoted by σ is 30°. The chord length is taken as the characteristic length L, such that the non-dimensional chord length is $c = 1.0L$. The non-dimensional thickness of the delta wing is $h = 0.024L$.

In Fig.5, the grids around the delta wind are being shown. The mesh is H-type in the meridian section and C-type in the cross section. The grids are orthogonal on the delta wing surface. The meshes are $129 \times 65 \times 65$, where the sequence of numbers is corresponding to the axial, the spanwise and the wall-normal direction, respectively.

Fig. 6. shows the Log (residue) vs. Work Units of the ADI and the multigrid method for 3D case. Great improvement of convergence speed can also been seen from this figure, although it is not as apparent as that in 2D case. The multigrid method saves at least 2 times in CPU times (or work unit) than ADI method.

6. CONCLUSIONS

The Multigrid method is applied to elliptic partial differential equations. As seen from the illustrations, convergence of the 2D and 3D elliptic grid generation problems is greatly improved by using the multigrid solver, although convergence of three dimensional elliptic grid generation is still not fast enough and need to be improved. Second order central difference schemes used for discretizing the grid generation equations are close to the exact differentiation and provide better grid point distribution.

References

[1] S. P. Spekreuse, *Elliptic Grid Generation Based on Laplace Equations and Algebraic Transformations*, Journal of Computational Physics 118, 38-61, 1995.
[2] Dale A. Anderson, Johe C. Tannehill, *Computational Fluid Mechanics and Heat Transfer*, Hemisphere Publishing Corporation, 1984.
[3] William F. Ames, *Numerical Methods for Partial Differential Equations*, Third Edition, Academic Press, New York, 1992.
[4] William L. Briggs, Van Emden Henson and Steve F. McCormick, A Multigrid Tutorial, Second Edition, Siam, 2000

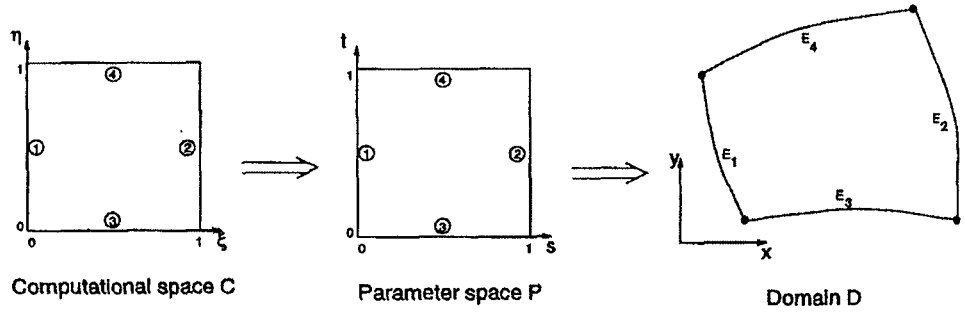


FIG. 1. Transformation from computational (ξ,η) space to a domain D in Cartesian (x, y) space.

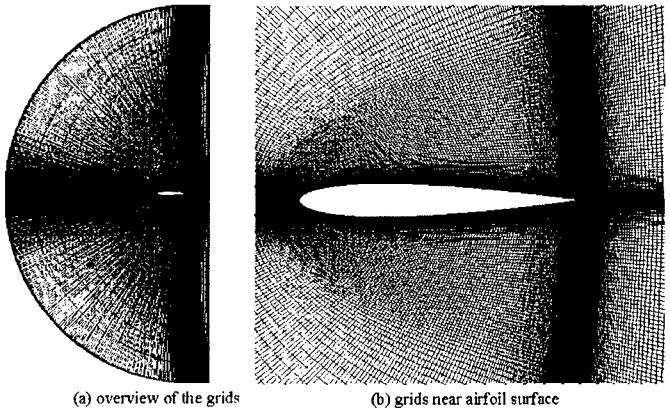


FIG. 2. C-grid around a NACA 0012 airfoil

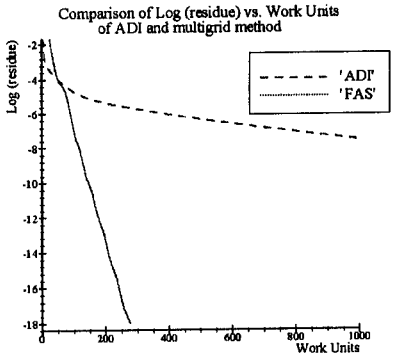


FIG. 3. Comparison of Log (residue) vs. Work Units of ADI and multigrid method in 2D case

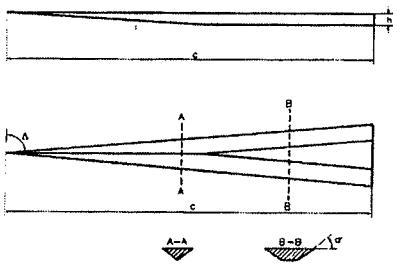


FIG. 4. Schematic of the delta wing

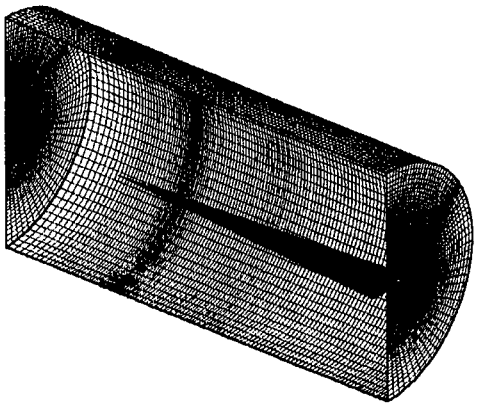


FIG. 5. H-C type grid around a 85°

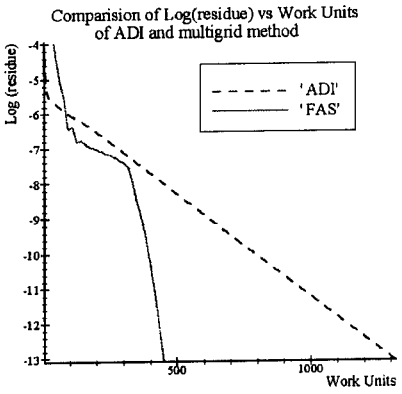


FIG. 6. Comparison of Log(residue) vs. sweep delta wing Work Units of ADI and multigrid method in 3D case

APPLICATION OF HIGH-ORDER COMPACT SCHEME TO INCOMPRESSIBLE TURBULENT FLOW

CHAO-HO SUNG* LI JIANG+ CHAOQUN LIU+

*David Taylor Model Basin, Carderock Division, NSWC, Bethesda, MD 20084

+ Department of Mathematics, University of Texas at Arlington, TX 76019

ABSTRACT

In this work, the high-order central compact scheme is introduced to improve the accuracy of the IFLOW solver. The high-order compact filter is used to reduce non-physical oscillations. To achieve the conservation property of the scheme, the compact scheme is combined with the ENO reconstruction method. The numerical flux at the cell interface is approximated by the derivative of its primitive function which can be exactly calculated. At the boundary, ghost points are constructed. The high-order extrapolation is used to obtain values at the ghost points. Instead of using the one-sided compact scheme, the explicit central difference scheme is applied at the boundary. The results from spatial simulations of trailing vortices have shown obvious improvement in accuracy.

1. INTRODUCTION

The compact schemes have been widely used in numerical simulation of complex flows. It has been shown [1] that the compact scheme can reach high-order accuracy and good small scale resolution with narrow grid stencils.

IFLOW code [2] is designed as a general-purpose production code for the numerical solutions of the incompressible Reynolds-averaged Navier-Stokes equations supplemented by appropriate turbulence models. The numerical methods include multi-block grid structure for complex geometry, artificial compressibility model, explicit one-step multi-stage Runge-Kutta scheme for time stepping, mutigrid, local time-stepping, implicit residual smoothing, optimal precondition, and bulk viscosity damping for convergence acceleration. The second order central difference and finite volume method are used for spatial discretization.

The fourth-order artifical dissipation terms are added to suppress numerical oscillations. The code has been used to analyze many complex flow fields including those around submarine, surface ship, and various parts of each.

In this work, the fourth-order compact finite difference scheme is incorporated into the code to improve the accuracy of the solutions. Instead of using artificial dissipation, the sixth order compact filter is used to reduce non-physical oscillations. To achieve the conservation property of the scheme, the compact scheme is combined with the ENO reconstruction method[3]. The numerical flux at the cell interface is approximated by the derivative of its primitive function which can be exactly calculated. The physical flux at the boundary is used as the boundary condition. To calculate the physical flux, ghost points are constructed by the fourth order extrapolation. The next section presents this method in detail, followed by the test cases and results of calculations.

2. GOVERNING EQUATIONS

The three-dimensional incompressible Reynolds-averaged Navier-Stokes equations based on the artificial compressibility approach can be expressed using the following conservative formulation.

$$P_0^{-1} q_t + F_x + G_y + H_z = 0 \tag{1}$$

where the preconditioned matrix P_0 and the three components of fluxes F, G, and H are defined as

$$P_0^{-1} = \begin{bmatrix} (1+\gamma)\beta^{-2} & \gamma\beta^{-2}u & \gamma\beta^{-2}v & \gamma\beta^{-2}w \\ (1+\alpha+\gamma)\beta^{-2} & 1+\gamma\beta^{-2}u^2 & \gamma\beta^{-2}uv & \gamma\beta^{-2}uw \\ (1+\alpha+\gamma)\beta^{-2} & \gamma\beta^{-2}vu & \gamma\beta^{-2}v^2 & \gamma\beta^{-2}vw \\ (1+\alpha+\gamma)\beta^{-2} & \gamma\beta^{-2}wu & \gamma\beta^{-2}wv & 1+\gamma\beta^{-2}w^2 \end{bmatrix}$$

$$q = \begin{bmatrix} p^* \\ u \\ v \\ w \end{bmatrix}, \quad F = \begin{bmatrix} u \\ u^2 + p^* - \tau_{xx} \\ uv - \tau_{xy} \\ uw - \tau_{xz} \end{bmatrix}, \quad G = \begin{bmatrix} v \\ uv - \tau_{yx} \\ v^2 + p^* - \tau_{yy} \\ vw - \tau_{yz} \end{bmatrix}, \quad H = \begin{bmatrix} w \\ uw - \tau_{zx} \\ wv - \tau_{zy} \\ w^2 + p^* - \tau_{zz} \end{bmatrix}$$

Here p^* is the pressure p divided by a constant density ρ. α, β^{-2} and γ are preconditioning parameters. In this presented work, $\alpha = \gamma = 0$ and

$\beta^{-2} = \max\left(|u|^2, \varepsilon\right)$, $\varepsilon = 0.7$. The Reynolds stresses calculated by turbulence model are given by τ_{ij}, $i, j = x, y, z$.

3. NUMERICAL METHOD

In the old version of IFLOW, a finite volume method is used. The mean flow is descretized by a second-order accurate central difference method with the fourth-order dissipation terms. The turbulent flow is discretized by one of the several upwind schemes. The time step is based on an explicit one-step multi-stage Runge-Kutta method to reach a steady-state solution. Several convergence acceleration techniques including multigrid, local time step, implicit residual smoothing, preconditioning, and bulk viscosity damping have been implemented.

In this work, the fourth-order compact finite difference scheme [1] and the ENO reconstruction method [3] are used to approximate the derivatives of fluxes. To illustrate how to use this method, we choose F_x, the derivative of flux in the x direction, as the example. When a conservative approximation to the spatial derivative is applied, F_x can be expressed as

$$F_x\big|_j = \frac{1}{\Delta x}\left(\hat{F}_{j+\frac{1}{2}} - \hat{F}_{j-\frac{1}{2}}\right) \tag{2}$$

where $\hat{F}_{j+\frac{1}{2}}$ and $\hat{F}_{j-\frac{1}{2}}$ are numerical flux functions at the cell interfaces. In order to achieve the high-order accuracy, numerical fluxes should be defined in such a way that the difference of numerical fluxes is a high-order approximation of the derivative F_x. According to the ENO reconstruction procedure [3], it has been proved that the primitive function of $\hat{F}$ at the cell interfaces can be exactly calculated by the value of F_j at given points. If P is the primitive function of $\hat{F}$, then:

$$\mathrm{P}_{j+\frac{1}{2}} = \Delta x \sum_{i=-\infty}^{j} \hat{F}_i \tag{3}$$

Then the numerical flux $\hat{F}$ at the cell interface can be obtained by taking derivative of its primitive function P,

$$\hat{F}_{j+\frac{1}{2}} = \mathrm{P}'_{j+\frac{1}{2}} \tag{4}$$

The approximations of derivatives of P at cell interfaces are calculated by the fourth-order compact finite difference scheme. G_y and H_z are discretized in the same manner. The sixth order compact filter is used to reduce numerical oscillations.

4.NUMERICAL EXAMPLES

To verify the efficiency of this high-order approach, the development of a trailing vortex is simulated using the k-ω turbulence model. In the first testing problem, a laminar q-vortex solution of Batchelor[2] is used as the inlet flow condition, i.e.

$$V_\theta = V_{\theta 1}(1+\frac{1}{2\alpha})\frac{r_1}{r}\left[1-\exp\left(-\alpha\frac{r^2}{r_1^2}\right)\right] \qquad U-U_\infty = U_D\left(-\alpha\frac{r^2}{d^2}\right)$$

where $r^2 = y^2 + z^2, \alpha = 1.25643, V_{\theta 1} = 0.286,$ $U_D = 0.165,$ and $r_1 = 0.036$. The size of the computational domain is $40\times1\times1$. The inlet is located at x=5. The grid number is $96\times32\times32$. Fig.1 and 2 show the distributions of the streamwise and tangential velocities along a vertical line through the vortex core at different locations in the x direction. The results from the second-order and the fourth-order are displayed in the same figure. Fig.3 shows the contours of vorticity at different x locations. The first row is corresponding to the second-order results, and the second row is of the fourth-order. It can be seen from these results that the high-order compact scheme increases the accuracy of the solutions and has demonstrated a better resolution than second-order scheme.

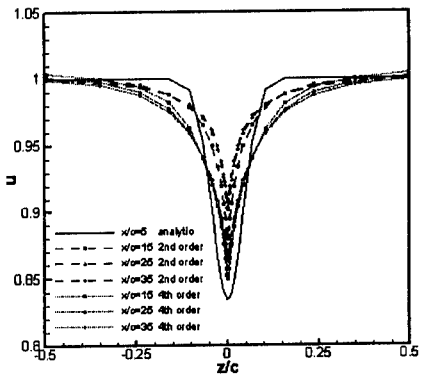


Fig.1 Streamwise velocity

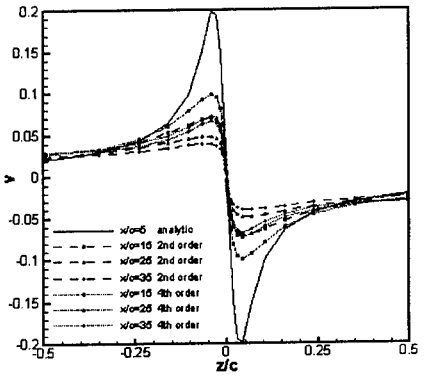


Fig.2 Tangential velocity

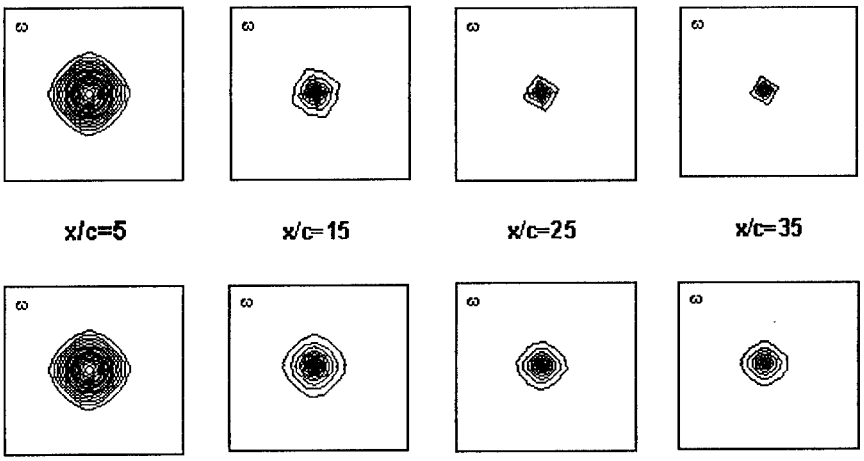


Fig.3 Contours of vorticity at different x locations

In the second testing problem, the experimental data from [2] are used to prescribe the inlet flow. The geometry and flow condition match those in the experiment. The computational domain extends from $x/c=5$ to $x/c=45$ in the streamwise direction. The grid is clustered near the center of the vortex on the cross section. In the streamwise direction the grid is uniform. The grid number is $56\times56\times56$. Experimental data (17×17) at $x/c=5$ are interpolated to the computational grid nodes. The numerical results are compared with experimental data at $x/c=10$. Fig.4 and 5 show the distributions of the streamwise and tangential velocities along a vertical line through the vortex core at different locations in the x direction. The results from the second-order and the fourth-order are compared with the experimental results. It is obvious that the accuracy is improved by using the high-order compact scheme. The large discrepancy between numerical results and experiment data is caused by errors of the interpolated inlet boundary condition, as we find this discrepancy also exists at the sections very close to the inlet boundary.

5.CONCLUSIONS

The fourth-order compact scheme in the conservative form has been incorporated in to the production code IFLOW. The results from the testing cases have shown the improvement in accuracy. The further applications of this method to more complex flows are undertaken.

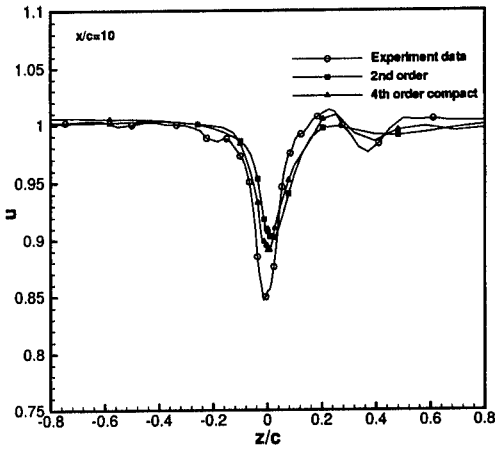


Fig.4 Streamwise velocity

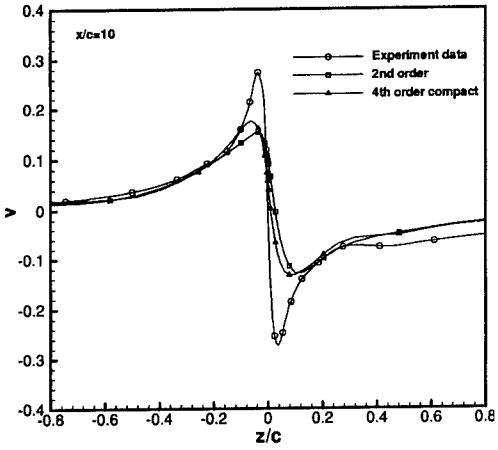


Fig.5 Tangential velocity

References

1. Lele, S.K., Compact finite difference schemes with spectral-like resolution. J.Comput. Phys., 103, pp.16-42, 1992
2. Sung, C.H., Rhee, Bong, Proceedings of the Seventh International Conference on Numerical Ship Hydrodynamics. Nantes, France, July 19-22, 1999.
3. Shu, C. W., Osher, S, Efficient implementation of essentially non-oscillatory shock capturing schemes II, I. Comput. Phys., 83, 32-78, 1989.
4. Devenport, W. J., et al, 1996, The structure and development of a wing-tip vortex. J. Fluid Mech.312,67-106.

HAIRPIN VORTEX FORMATION IN POISEUILLE FLOW DUE TO TWO-HOLE SUCTION

D. B. GOLDSTEIN
Dept. of Aerospace Engineering and Engineering Mechanics
The University of Texas at Austin, Austin, TX 78712

AND

J. COHEN AND V. LEVINSKI
Faculty of Aerospace Engineering
Technion, Israel Institute of Technology, Haifa, Israel, 32000

A virtual-surface DNS is used to examine hairpin formation caused by a pair of suction holes below a laminar wall-bounded flow. The work models an experiment, presently underway, in which quasi-periodic hairpins are to be generated in a laminar plane-Poiseuille flow. We present some brief preliminary studies of vortex dynamics and find both symmetric and antisymmetric modes of shedding. We also examine the effect of inter-hole spacing on hairpin formation.

1. Introduction

A turbulent boundary layer is known to consist mainly of two different kinds of coherent vortical structures: counter-rotating streamwise vortices observed in the near wall region and hairpin-shaped vortices extended across the boundary layer. The hairpin structure consists of a head reaching out into the log layer and long legs trailing behind and below in the buffer layer. There may be many variants on this model since a simple, isolated, symmetric hairpin can be hard to find in experimental or computational fully turbulent boundary layers. Assymetric or one-legged structures are common and a visualization of a high Reynolds number simulation can often look like a confused mass of writhing worms. The hairpin structures extend from a near-wall region of high shear having more stream-aligned structures out into a much lower mean shear region. How each region influences the other remains open to discussion. There has also been much effort exerted in trying to fathom out how such coherent structures self-replicate. In a

turbulent boundary layer the hairpins may form as an instability along the low speed streaks. It is likely, however, is that there are several processes which occur with different frequencies and that if one looks closely, one process blends smoothly into another and becomes only distinguishable by degree.

Levinski and Cohen [6] (LC) proposed a new predictive theoretical model explaining the mechanism leading to the rapid growth of hairpin vortices in shear flows. Malkiel *et al* [7] provided further proof of this theory. LC focused on the evolution of localized disturbances (all dimensions of which are much smaller than the length scale corresponding to variations of the basic velocity shear) and used the fluid impulse integral to characterize this type of disturbance.

Their analysis showed that unidirectional planar shear flows are always unstable with respect to finite-amplitude localized disturbances. Furthermore, the analysis predicts that the initial vortex grows exponentially and that it is inclined at 45° to the basic flow direction. These predictions agree with existing experimental observations concerning the growth of hairpin vortices in laminar and turbulent boundary layers.

The resulting set of coupled equations obtained by Levinski and Cohen [6] describes the dynamics of the localized vorticity disturbance. Accordingly it is governed by two mechanisms: one is the lift-up of the disturbance in the cross-stream direction which stretches the basic spanwise vorticity field and thus generates a disturbance-vorticity component in the cross-stream direction; the other mechanism is associated with the stretching and rotation of this disturbed vortex by the basic shear field. This intensifies the streamwise vorticity component which, in turn, induces an increased cross-stream velocity, thereby enhancing the lift-up effect and closing the feedback loop. Once formed, the hairpin evolves through self-induction in the presence of the mean shear.

Computational modeling of the Couette flow hairpin device was done by Rosenfeld *et al* [9] who suggested hairpin formation due to a shedding of a vortical bridge between the holes. In an ongoing experiment, hairpins are to be generated in a laminar plane-Poiseuille flow by way of suction through a pair of small holes on one wall. Computations of the effect of similar distributed discrete suction holes by Meitz [8] examined how suction alters the stability of quiet flow, Klebanoff modes, and TS waves in a Blasius boundary layer. Meitz's work utilized a prescribed suction profile over the holes with forced spanwise symmetry and emphasized the effects of relatively lower suction levels than examined presently.

We here briefly examine the process through which such quasi-periodic hairpins can develop. There can be different modes of hairpin shedding with hairpins sometimes forming right between the suction holes, if the

flow has slight asymetries, and at other times the hairpins roll up much further downstream. The suction holes obviously alter the mean (parabolic) flow field so whether the hairpins we examine correspond to those in an unperturbed flat plate boundary layer remains to be determined.

2. The Computational Approach

The present work uses an unconventional computational approach – solid surfaces are modeled by applying a body force to the flow to bring the flow to rest on a virtual surface. This approach for creating a virtual solid surface has been shown [1] to be sufficiently flexible and efficient to model laminar and turbulent flow over complicated geometries. That work also discusses the numerical stability of the method. Goldstein *et al* [2] provides a more detailed review of the virtual surface approach as well as grid resolution studies of laminar flow over riblets, an examination of the sensitivity of the solution to various smoothing parameters, and an in depth analysis of turbulent flow over virtual flat and textured plates. Goldstein and Tuan [3] produce exhaustive grid resolution studies showing convergence even in a turbulent flow over a ribbed surface using the same code as used herein.

The basis of the virtual surface model is that the surface being modeled is defined by a set of boundary points which exist within a region spanned by a fixed (Eulerian) mesh on which the flow equations are solved. The boundary points $\mathbf{x}_s$ exert a body force on the fluid such that the flow comes to a desired velocity, $\mathbf{U_{des}}$, on $\mathbf{x}_s$. A key feature of the present approach is that flows around complex boundary geometries are reduced to ones which are fully rectilinear and hence are amenable to spectral methods (we use that of [5] and [4]). The virtual surface approach imposes only a small computational overhead and little in the way of a coding burden. Potential difficulties associated with the singular nature of the force field, addressed in Goldstein *et al* [1,2], are largely overcome by spatial smoothing and spectral filtering. The forcing function $\mathbf{f}(\mathbf{x},t)$ is determined as $\mathbf{f}(\mathbf{x},t) = \alpha \int_0^t \mathbf{\Delta U}(\mathbf{x},t')\mathrm{d}t' + \beta \mathbf{\Delta U}(\mathbf{x},t)$ with $\mathbf{\Delta U} = \mathbf{U} - \mathbf{U_{des}}$ where the quantities α and β are negative constants (see [1]). On an immobile surface $\mathbf{U_{des}} = 0$. The lower surface is a virtual solid surface created with the force field (Fig. 1(a)). The flow is sucked into the holes in the surface due to the reduced pressure in the gap between the virtual surface and the ordinary flow field boundary. This low pressure is maintained by forced blowing ($\mathbf{U_{des}} = (0, v_{blow}, 0)$) out of a spanwise strip in the virtual surface well downstream of the suction holes.

A buffer zone, located immediately downstream of the blowing slot, is used to both maintain the parabolic velocity profile in the bulk of the domain and to absorb the perturbations introduced by the suction and blow-

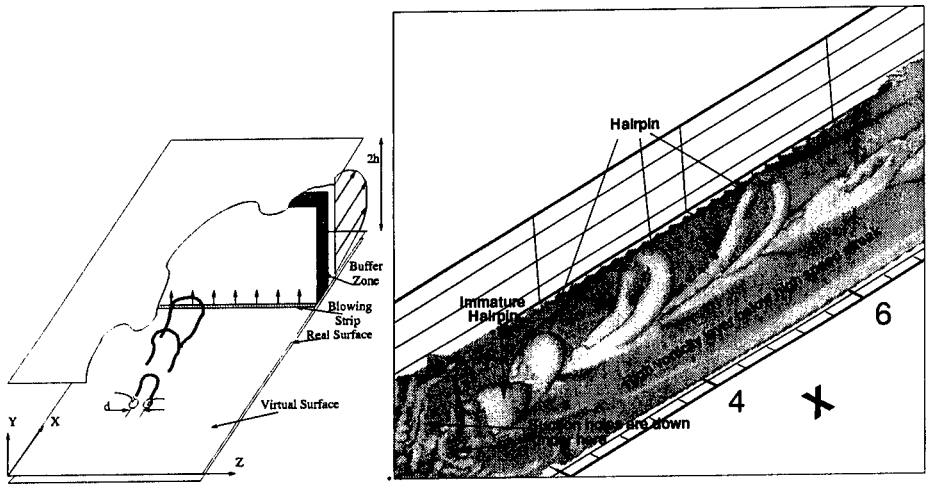


Figure 1. (a) Channel flow configuration for two-hole suction simulations. Channel is periodic in the streamwise (X) and spanwise directions (Z) and bounded by impermeable flat walls in the vertical direction (Y). Flow quantities are represented by Fourier expansions in the horizontal ($X-Z$) plane and a Chebyshev expansion in the wall normal direction. (b) Close-up of instantaneous isosurfaces of vorticity magnitude showing hairpins shedding in the wake of two holes. Flow from lower left.

ing sites. The buffer zone uses the force field to bring the flow to the desired parabolic profile. In order that this accomodation process be gradual, the quantities α and β are made to vary in the buffer region in a smooth manner as $\alpha_{buffer}(x) = 20e^{-120(\Delta i/W)^2}$ and $\beta_{buffer}(x) = 20e^{-12(\Delta i/W)^2}$ where W is the number of cells in the the length of the buffer zone (=25) and Δi the number of cells distant from the center x-plane of the buffer region. The width of the α_{buffer} Gaussian is much narrower than that of the β_{buffer} Gaussian. α_{buffer} is a rather harsh term in that it makes the force adjust itself to completely cancel out the velocity error. This is of use in ensuring the steady mean flow. The β_{buffer} term surrounding the α_{buffer} core region damps nearly all of the temporal fluctuations before they reach the α_{buffer} layer. The present channel dimensions are chosen to be $12.9h$:$2h$:$6.46h$ in x:y:z where h is the channel half-height and the grid is $128 \times 65 \times 128$.

3. Hairpin Formation

Figure 1(b) illustrates the nature of the hairpin vorticies we obtain in our simulations. The channel Reynolds number based on centerline velocity, U_{cl}, and $h(= .9289)$, is 1115. The hole center-to-center spacing, d, is $0.84h$ and the holes are $7.32h$ upstream of the buffer layer. We give the volume flow rate through the holes, Q_{holes} by comparison to the volume which

would flow through the channel cross-sectional area bound by the top and bottom surfaces and the hole centerlines in the absence of suction: dhU_{mean}. That ratio is $dhU_{mean}/Q_{holes} = 5.86$. One incipient hairpin is forming just downstream of the holes and three others are seen further downstream in various stages of evolution. At this low Reynolds number the hairpins of figure 1(b) appear short and stocky. At higher Reynolds numbers the legs become longer and thinner and may develop a kink which evolves, through leg-to-leg reconnection, into two separate hairpins.

The holes continuously pull high speed fluid from well above the surface, down towards the surface. As a result, there is a continuous downflow of fluid both over the holes and in their wake. Figure 2(a), shows a close-up view of iso-vorticity contours in a ZY plane $2d$ downstream of the hole centerline. There is clearly a region of downwash just above each high (ω_z) vorticity streak in the wake of each hole. The head of a hairpin is just passing through the frame at this time.

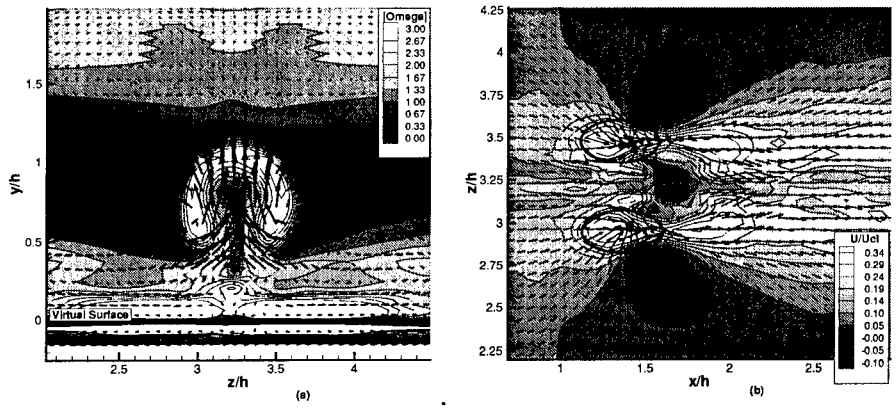


Figure 2. (a) Vorticity magnitude in a ZY plane showing slice of a hairpin head in the wake of two holes and (b) streamwise instantaneous velocity contours in a ZX plane near the suction holes (black ovals). Velocity vectors are also shown.

Figure 2(b) provides contours of the streamwise velocity U just above the virtual surface near the suction holes. It is clear that the holes draw in fluid nearly radially from the front and sides of the holes. The drawing down of high speed fluid from well above the surface creates a region of fluid just over the hole as well as just aft having a high U velocity. Moreover, the suction is strong enough to create a separated reverse flow region outboard of each hole.

We can interpret the flow in terms of the vorticity dynamics schematically shown in figure 3. The hairpins originate upstream of the holes. As

the near-wall spanwise vortex lines in the mean parabolic flow move downstream ahead of the holes, they are pulled into a downstream orientation by the suction thus rotating $-\omega_z$ vorticity into the x direction to create $\pm\omega_x$ vorticity. The vortex lines are strongly stretched, increasing in vorticity, as they are drawn down the holes. These stretched and rotated

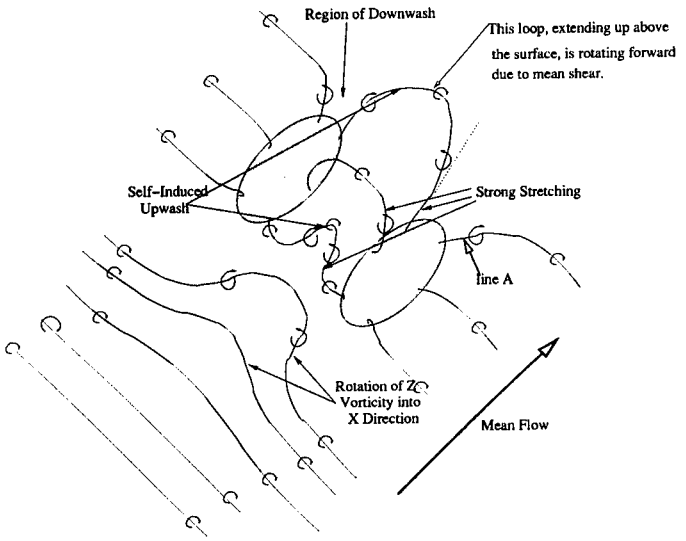


Figure 3. Close-up schematic of vortex line dynamics near suction holes. Note that this is meant to be a 3D perspective view and some of the lines project above the plane of the paper.

vortex lines produce a region of upwash along the centerline, upstream of the holes, that is surrounded by a pair of counter-rotating vorticies of the same orientation as the hairpin legs downstream. Outboard of the holes the downward-dipping highly stretched spanwise vortex lines can produce the regions of reverse flow near the surface. The broken vortex lines drawn down a hole (*e.g.*, line A) lead to a region of downwash behind the hole. That high-speed flow brought down toward the surface subsequently creates a persistent high ω_z vorticity streak in the wake of each hole. There is also a circumferential nest-like ring of high vorticity around each hole (not seen in these figures) caused by the high-speed flow drawn in over the hole rim.

So the looped vortex lines originate in the immediate vicinity of the holes, in a region of large pressure gradients and strong vortex line stretching. The upwash caused by these bent vortex lines between the holes brings low speed fluid away from the surface producing the central low speed

streak. How these vortex lines manage to roll into a thickened discrete hairpin appears to depend on flow symmetry. If the flow is symmetric across the central Z-normal plane between the holes, the central low speed streak and surrounding pair of streamwise vorticies may extend a long distance downstream before the streak becomes unstable and sheds hairpins. Sometimes, however, we find that the low speed streak encounters a spanwise instability directly between the holes. When this occurs (fig. 4), the hairpins roll up and shed just aft of the holes. The shedding can switch between symmetric and asymmetric modes in an apparently random manner for some flow conditions but be locked into one mode for others.

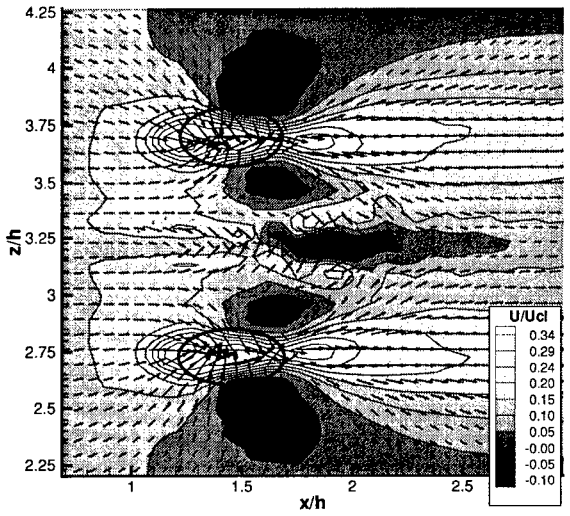


Figure 4. Instantaneous streamwise velocity contours and velocity vectors in a ZX plane near the suction holes. Note that the low speed streak between the holes is not symmetric but undergoes a flapping motion associated with hairpin roll-up immediately downstream of holes. In this case $d = .98h$, $Re = 3717$, and $dhU_{mean}/Q_{holes} = 6.80$

We ran a parametric study of the effect of hole spacing, d, on the nature of hairpin shedding by simply varying d while all other variables were kept constant (Reynolds number = 3717). Meitz [8], referencing Goldsmith (1957), utilizes a non-dimensional parameter for shear, $T = \frac{d^2}{2\nu}\frac{\mathrm{d}u}{\mathrm{d}y}|_{wall}(\frac{d-D}{d})^{1.18}$ where $\frac{\mathrm{d}u}{\mathrm{d}y}|_{wall}$ is the velocity gradient at the wall and D is the hole diameter, and a non-dimensional suction flux, $F = \frac{1}{\nu}\frac{Q_{holes}}{\Delta z}(\frac{d-D}{d})^{0.62}$ where $\frac{Q_{holes}}{\Delta z}$ is the suction flow volume per unit spanwise length. Both Meitz and Goldsmith examined circular uniformly spaced holes while our holes have an

aspect ratio of 2.7 and are nearly isolated pairs. Nonetheless, whether we choose D to be the hole width, hole length, or the geometric mean, our values of T are $O(10^1 - 10^3)$, within the range suggested by Meitz and Goldsmith to produce hairpin shedding if $F >\sim 37$. Yet we find shedding for lower values of F regardless of what D we choose or whether we take $\Delta z = d$ or equal to the domain width. Only for the smallest value of d ($d/h = 0.44$) do we find that the flow becomes steady. As we increase d, we first find low frequency shedding with the hairpins forming symmetrically, well downstream of the holes. For $d \sim 1$, asymetric near-hole shedding also occurs.

Acknowledgment

The computations were performed at the University of Texas Center for High Performance Computing and were supported by AFOSR under grant F49620-98-1-0027 monitored by Dr. Thomas Beutner and through a Lady Davis Fellowship at the Technion.

References

1. D. Goldstein, R. Handler, and L. Sirovich, 1993a, "Modeling a no-slip flow boundary with an external force field," *J. Comp. Phys.* **105**, 354-366.
2. D. Goldstein, R. Handler, and L. Sirovich, 1995, "Direct numerical simulation of turbulent flow over a modelled riblet covered surface," *J. Fluid Mech.*,**302**, 333-376.
3. D. Goldstein and Tuan, T.-C., 1998, "Secondary flow induced by riblets," *J. Fluid Mech.*,**363**, 115-151.
4. R. A. Handler, E. W. Hendricks, and R. I. Leighton, 1989, Low Reynolds Number Calculation of Turbulent Channel Flow: A General Discussion. NRL Memorandum Report 6410, p. 1-103.
5. J. Kim, P. Moin, and R. Moser, 1987, "Turbulence statistics in fully developed channel flow at low Reynolds number," *J. Fluid Mech.*, **177**, 133.
6. V. Levinski and J. Cohen, 1995. "The evolution of a localized vortex disturbance in external shear flows. Part 1. Theoretical considerations and preliminary experimental results," *J. Fluid Mech.*, **289**, pp. 159-177.
7. E. Malkiel, V. Levinski and J. Cohen, 1999. "The evolution of a localized vortex disturbance in external shear flows. Part 2. Comparison with experiments in rotating shear flows," *J. Fluid Mech.*, **379**, pp. 351-380.
8. H. L. Meitz, 1996, *Numerical investigation of suction in a transitional flat-plate boundary layer*, PhD Dissertation, Univ. of Arizona.
9. M. Rosenfeld, J. Cohen and V. Levinski, 1999, "The evolution of hairpin vorticies in rotating shear flows. Numerical Simulations," Proceedings of the 39th Israel Annual Conference on Aerospace Sciences, Israel, Feb. 17-18, pages: 11-19.

DNS OF BOUNDARY LAYER TRANSITION INDUCED BY A COHERENT PERTURBATION

H.C. DE LANGE AND R.J.M. BASTIAANS
Section Energy Technology, Department of Mechanical Engineering
Eindhoven University of Technology, The Netherlands

1. Abstract

Bypass transition of a boundary layer takes place at high main stream turbulence levels. It is governed by the intrusion of non-linear disturbances into the viscous sublayer. In this paper a numerical study is presented in which a spatially developing laminar boundary layer is subdued to large scale (non-linear) disturbances. The (fully compressible) Navier-Stokes equations are solved using direct numerical simulation with a higher order finite difference method on a collocated grid. The results show that the initially smooth disturbance rapidly changes into an arrow-head structure with the characterics of a turbulent spot.

2. Introduction

In the design of turbomachinery the prediction of the boundary layer layer heat transfer is of mayor importance, to since the hot gases from the combustion chamber force an enormous heat flux to the turbine blades. The heat transfer in a boundary layer increases significantly when laminar to turbulent transition occurs. When transition starts it is assumed that so called turbulent spots are initiated in the laminar boundary layer.

Turbulent spots have been first observed by (Emmons, 1951) in a water channel. Most transition models which are used nowadays are based on these turbulent spots. It is supposed that a turbulent spot is a local area of turbulence, that convects in streamwise direction with a mean velocity which is less than the main flow velocity. The leading edge travels faster than the trailing edge and so the turbulent spot grows lengthwise while moving in downstream direction. Furthermore, the spots appear to remain at the same shape so they also grow laterally. At a certain point the spots

start to merge untill the flow is completely turbulent. This is said to be the end of transition.

In general a distinction between natural and bypass transition must be made. At low disturbance levels in the main flow Tollmien-Schlichting waves are initiated at a certain Reynolds number. These waves grow in amplitude and three dimensional waves start to develop. Further downstream the first turbulent spots occur untill transition is completed. This scenario is called natural transition.

For higher turbulence levels bypass transition takes place. It is governed by the direct intrusion of non-linear disturbances into the viscous sublayer, where they initiate turbulent spots. In the spot-formation process both the length scale and the initial strength of the disturbance may be important.

Bypass transition is governed by the forcing of free-stream disturbances on the viscous sublayer. To describe bypass transition the transient growth theory has been developed over the last ten years. It can be modeled using the Parabolised Stability Equations. However, this modelling starts from the amplification of waves or (coherent) structures present in the boundary layer. There are two semi-emperical models ((Johnson, 1999) and (Mayle and Schultz, 1997)) known to describe the initiation for bypass transition starting from the intrusion of free-stream disturbances. In both models, the free-stream disturbances are assumed to intrude via the amplification and subsequent breakdown of laminar modes. The amplification rate is prescribed from emperical relations. The actual formation of turbulent spots (i.e. the onset of transition) has to be introduced through a presumed criterion.

These models result in the well-known intermittency distributions introduced in (Narashima, 1957) or (Johnson, 1994). In the derivation of these intermittency distributions the influence of the initation process only remains in the (empirical) parameter x_t (the streamwise position of the start of transtion). The shape of the distribution is determined by the spot growth- and merge-processes. This means that the theoretical models for natural and bypass transition both lead to these intermittency distributions, since they both lead to rapid non-linear breakdown and, therefore, more or less instantanious spotproduction. In the past numerous experiments have been performed to find Re_{xt} and Re_λ depending on the pressure gradient, turbulence intensity, compressibility, etc.

Recent experiments ((Schook *et al.*, 2001)) show that for low levels of free-stream turbulence the Narashima- and Johnson-intermittency distributions are indeed applicable. However, as the turbulence intensity is raised to levels representative for gasturbine flows, the intermittency distribution changes shape. A closer examination of the experimental conditions (at different levels and length scales of the free-stream turbulence) shows

that the Narashima- and Johnson-intermittency distributions are not found when the turbulence length scale is large compared to the boundary layer thickness.

The shape of the distributions, found at these length scales, suggests that 'spots' grow or shrink depending on both the local boundary layer thickness and the strength of the impinging disturbances. This means that the spots must be created directly from free-stream perturbations. They can not be the result of a initiation process within the boundary layer. Therefore, at these scales the mechanism of direct intrusion of free-stream disturbances dominates the initiation process.

This raises the question of boundary layer selectivity; which properties of a main stream disturbances are descisive for the production of a turbulent spot. In the present study fully compressible direct numerical simulation is used to study this transition mechanism. In this paper a numerical study is presented in which a spatially developing laminar boundary layer on a flat plate is subdued to large scale (non-linear) disturbances.

3. Governing equations

For a compressible flow of an ideal gas, conservation of mass, momentum and entropy can be written as

$$\begin{aligned} \frac{\partial \rho}{\partial t} + \nabla \cdot \rho \mathbf{v} &= 0 \\ \rho \left[\frac{\partial \mathbf{v}}{\partial t} + \mathbf{v} \cdot \nabla \mathbf{v} \right] &= -\nabla p - \nabla \cdot \boldsymbol{\tau} \\ \rho T \left[\frac{\partial s}{\partial t} + \mathbf{v} \cdot \nabla s \right] &= -\nabla \cdot \mathbf{q} - \boldsymbol{\tau} : \nabla \mathbf{v} \end{aligned} \tag{1}$$

with time t, density ρ, the velocity vector $\mathbf{v}$, entropy s, pressure p, stress tensor $\boldsymbol{\tau}$, temperature T and heatflux vector $\mathbf{q}$. The set of equations are closed with the constitutive relations $T = f(\rho, s)$ and $p = \rho RT$.
The use of the entropy s has the advantage that its conservation equation does not contain any acoustic waves. Therefore, only mass and momentum conservation need to be resolved on an acoustic time-scale.

4. Numerical scheme

The equations are solved with a higher order finite difference method on a collocated grid. The time integration uses a third order low storage Runge Kutta scheme, which requires only one additional storage location. A compact (implicit) sixth order scheme due to (?) is used for the spatial discretisation of all non-advective terms. The scheme uses five grid points and

can be evaluated with order N manipulations for N derivatives. Advection is approximated with a fifth order explicit upwind scheme. In this way a stable integration is obtained in which no additional filtering is required.

Characteristic boundary conditions are implemented according to the NSCBC approach of (?). In this approximation local one dimensional waves are used for acoustic and convective transport and supplemented with viscous conditions.

Sub-stepping is used in which acoustic, convective and viscous transport are evaluated in splitted (third and second-order) time evolution. The properties of the numerical scheme are such that it is ideal for parallel processing. Furthermore, the code is optimised for memory access, caching and load balancing. The calculations presented in this paper typically use about 400 CPU hours when run on 16 R10k3-processors (250 Mhz).

5. Problem definition

Initially a Blasius profile ($u_b(y)$, Ma_∞=0.1) is prescribed for Re_{δ^*} equal to 400 (with δ the momentum thickness, this means that the Reynolds-number based on the displacement thickness is approximately 1000). At the inflow boundary the wall normal velocity v is perturbed (similar as in (Breuer and Landahl, 1990), who used a spatially introduced streamwise vorticity) according to:

$$
\begin{aligned}
\frac{\partial \mathrm{v}}{\partial t} &= Af(y)(1-2\phi^2)(1-2\xi^2)\exp(-\phi^2-\xi^2+1/2) \\
\phi &= \frac{t-t_0}{\theta} \qquad \theta = 11\delta^*/U_\infty \qquad t_0 = 6\theta \\
\xi &= \frac{z/L_z - 1/2}{\zeta} \qquad \zeta = 8 \\
f(y) &= u_b(y)(1-y/L_y)^2
\end{aligned}
$$

The computation domain has a height L_y of $20\delta^*$, the length and width are choosen $6L_y$ and $3L_y$, respectively. The lateral length scale agrees with simulations by (Breuer and Landahl, 1990), who found that the resulting perturbation is approximately independent of the spanwise scale. The typical time-integration continues till tU_∞/δ^*=600. In the simulations a uniform grid of 193×65×192.

The flat plate is prescribed by an adiabatic no-slip boundary condition. The upper boundary is acoustically non-reflective. At the inflow the velocity components and entropy are fixed. At the outflow the downstream pressure is fixed. In the spanwise direction the domain is periodic.

6. Results

The initial perturbation results in a checkerboard pattern of (alternating) wall-normal velocity. This leads to three spanwise rows of three alternating negative/positive λ_2-pockets. In the main stream the disturbance is rapidly transferred to the outflow, as shown in figure 1, leaving behind a pattern of alternating positive and negative wall-normal velocity, with a characteristic length scale of δ^*. The formation of this pattern goes hand in hand with combination of the front middle and middle outer regions of negative λ_2 into an arrow-head structure, shown in figure 2. This structure is stretched into a lambda-shaped vortex, situated in the near-wall boundary layer region, below $3\delta^*$. The ratio of leading and trailing edge velocity of the lambda vortex is about 3. Subsequently, a rapid local creation of vortices near the legs is triggered, similar to the observations of (Singer and Joslin, 1994). In the later stages a turbulent spot-like structure is formed.

It is clear that the time-wise introduction of the perturbation on the wall-normal velocity leads to results very similar to those in (Breuer and Landahl, 1990). A difference in both results is the alternating pattern of wall-normal velocity at ther center-line which arises in the Breuer-results. It is not clear it these are caused by the difference in boundary conditions ((Breuer and Landahl, 1990) uses streamwise periodic boundary conditions). The similarity in the results indicates that the formulation of the initial disturbance ($v(t)$ instead of a spatial stream-wise vorticity perturbation) is not important. Instead the development of the initial disturbance into the Λ-vortex and the subsequent production of vorticity at the stretching legs seems to be determined by the perturbation-length scale. Of course, more simulations for different θ and ζ are needed to support this conclusion.

7. Conclusions

The results show that the developed code is suitable for the study of the spot-initiation proces. In the near future, the boundary layer sensitivity will be investigated for different θ and ζ. Furthermore, mode-selection for more random perturbations will be studied. These initial disturbance are placed in the laminar boundary layer. The intrusion mechanism of free-stream disturbances into the viscous sublayer will be the subject of future studies to answer the question of boundary layer selectivity.

References

Breuer, K.S. and Landahl, M.T. (1990) The evolution of a localized disturbance in a laminar boundary layer. Part 2. Strong disturbances *J. Fluid Mech.*, **Vol. no. 220**, pp. 595-621

Emmons, H.W. (1951) The laminar turbulent transition in a boundary layer *J. Aero. Sci.*, **Vol. no. 18**, pp. 490-498

Johnson, M.W. (1994) A bypass transition model for boundary layers *J. of Turbomachinery*, **Vol. no. 116**, pp. 759-764

Johnson, M.W. (1999) A physical model for bypass transition *J. Heat and Fluid flow*, **Vol. no. 20**, pp. 95-104

Lele, S.K., 1992 Compact finite difference schemes with spectral-like resolution *J. Comp. Phys.*, **Vol. no. 103**, pp. 16-42

Mayle, R.E., and Schultz, A. (1997) The path to predicting bypass transition *J. of Turbomachinery*, **Vol. no. 119(3)**pp. 405-411

Narashima, R. (1957) On the distribution of intermittency in the transition region of a boundary layer *J. Aero. Sci.*, **Vol. no. 24**, pp. 711-712

Poinsot, T.J. and Lele, S.K. (1992) Boundary conditions for direct simulations of compressible viscous flows *J. Comp. Phys.*, **Vol. no. 101**, pp. 104-129

Schook, R., Lange, H.C. de, and Steenhoven, A.A. van (2001) Heat transfer measurements in transitional boundary layers *Int. J. Heat and Mass Tr.*, **Vol. no. 44**, pp. 1019-1030

Singer, B.A., and Joslin, R.D. (1994) Metamorphosis of a hairpin vortex into a young turbulent spot *Physics of Fluids*, **Vol. no. 6**, pp. 3724-3736

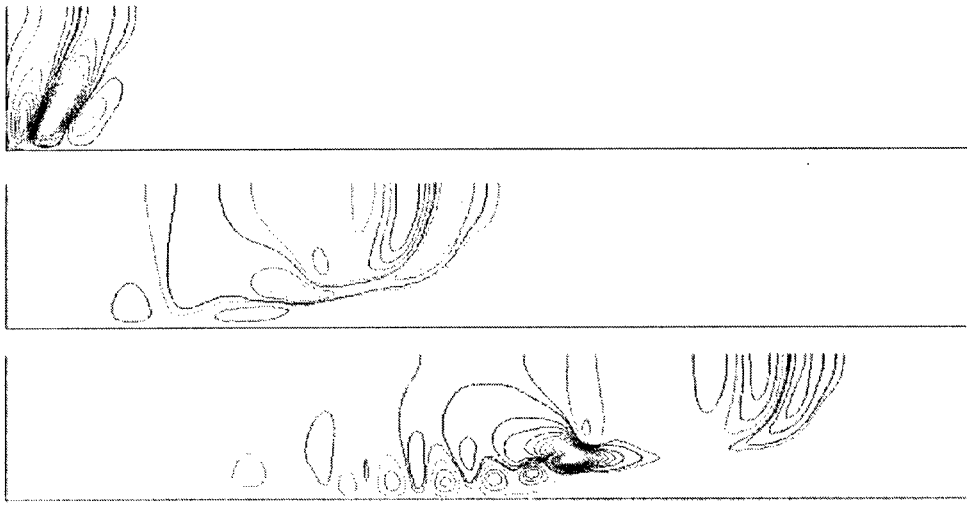


Figure 1. Contours of constant wall normal velocity on the center plane at $t = U_\infty/\delta^* = 98$, 245 and 392

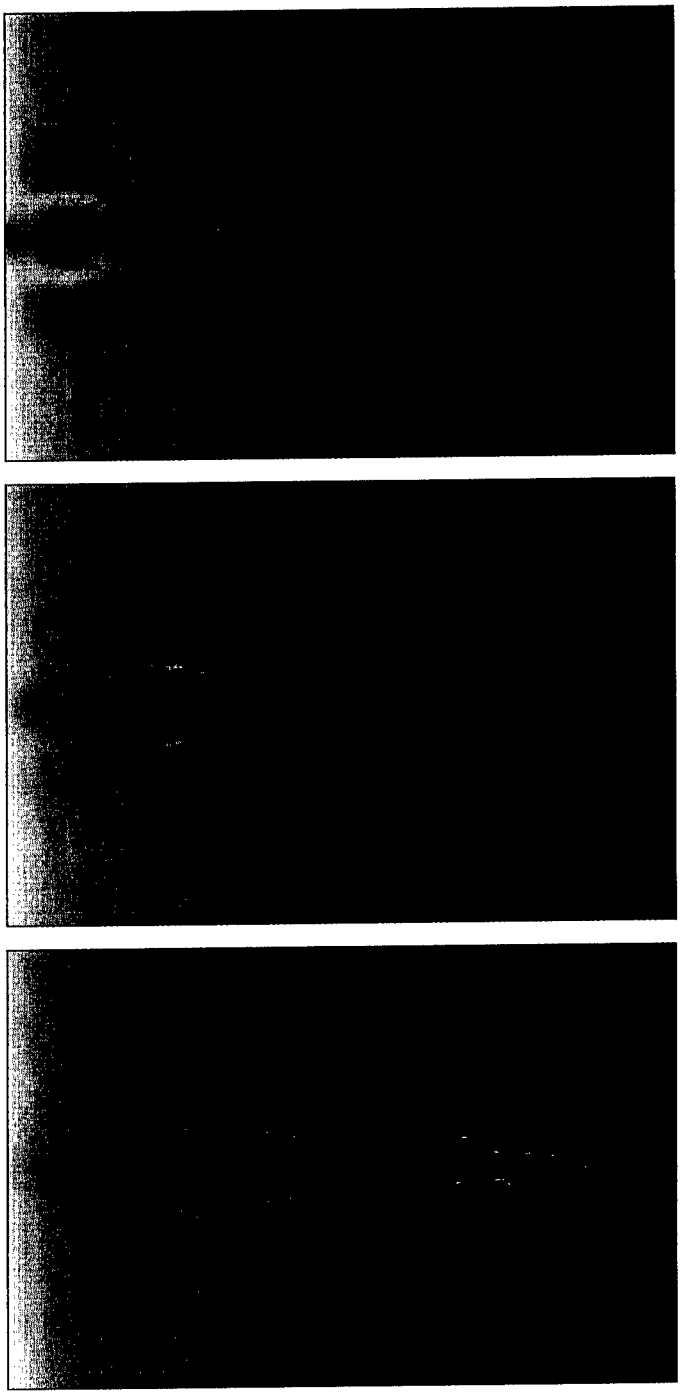


Figure 2. Top view of regions of negative λ_2 and gray scales indicating the entropy on the flat plate at tU_∞/δ^*=245, 392 and 539

MODAL INTERACTIONS IN A BICKLEY JET BY DIRECT NUMERICAL SIMULATION

ROLAND MALLIER AND MICHAEL HASLAM
Department of Applied Mathematics,
University of Western Ontario, London, ON, Canada

Abstract.
We consider interactions between varicose and sinuous oblique disturbances in the Bickley jet, using both nonlinear stability theory (in its nonlinear critical layer form) and direct numerical simulation using a spectral method. Nonlinear stability theory indicates that a (nonlinear) interaction between the modes should occur, and our simulations would seem to support this.

1. Introduction

This study is concerned with three-dimensional transition in plane wakes and jets. Nonlinear stability theory [9, 10] has predicted that modal interactions play an important role in that transition, and in this paper, we will first present an overview of that theory and then present simulations that support the theory.

For the plane wakes and jets considered here, it is well known that there may be two different types of neutral modes with critical layers centred on the inflection points, viz. the sinuous and varicose modes. The plane (Bickley) jet, which has a $\mathrm{sech}^2 y$ velocity profile has been used by numerous authors to provide a good approximation to such a wake behind a bluff body, is somewhat special in that the varicose and sinuous modes have neutral wavenumbers of 1 and 2 respectively, so that the former is the subharmonic of the latter. Several studies have explored the possibility of an interaction between these two modes, and this sort of interaction is the focus of the present study. For two-dimensional disturbances, Kelly [6] used Stuart-Watson type nonlinear stability theory to investigate interactions of this type; however, he found that there was no modal interaction of the type assumed. Later, Leib and Goldstein[8] re-examined the problem for

purely two-dimensional disturbances using a nonlinear-nonequilibrium critical layer, and they found that there was indeed an interaction between the modes. Mallier[9, 10] studied three-dimensional disturbances, since Goldstein[3, 2] had earlier shown that a pair of oblique waves superimposed on a shear layer could interact nonlinearly to give rise to extremely rapid growth, and also[4] that when the oblique waves were inclined at $\pm 60°$, an additional interaction could take place between the oblique waves and a plane wave, so that the growth was faster still; this last mechanism is known as a "resonant triad". Mallier[9] explored the possibility of an interaction between a pair of resonant triads in the Bickley jet, with one triad consisting of a plane sinuous mode together with a pair of oblique sinuous modes inclined at $\pm 60°$ and the other triad consisting of a plane varicose mode together with a pair of oblique varicose modes also inclined at $\pm 60°$; the motivation behind this was to see if the triads could interact so that the growth was more rapid than if only a single triad were present. Mallier found that interactions could occur, and his study essentially covered three stages: a linear stage when the amplitudes of the disturbances were very small, the "parametric resonance" stage[11], and the so-called "fully-coupled" stage[4, 21, 12]. The amplitude equations presented were of course for the third (fully-coupled) stage, but the two earlier stages could be recovered from these equations by rescaling the amplitudes, as discussed in[4]. The study of the fully-coupled stage was a little restrictive in that it was necessary to assume that, in that stage, the varicose oblique modes were larger any of the other waves present which is at odds with the linear theory which says that the linear growth rates of the sinuous modes are larger than those of the varicose modes. This was because in the earlier parametric resonance stage, when it was assumed that all of the waves were of the same order of magnitude, it had been found that the varicose oblique waves underwent very rapid growth while the plane waves and the sinuous oblique waves continued to grow exponentially in a linear fashion. In addition, the coupling in the equations in [9] was a little unusual in that the sinuous triad did not affect the varicose triad, and therefore equations for the varicose triad were simply those for a single resonant triad[4, 21, 12]. However, the sinuous triad was strongly affected by presence of the varicose triad, and furthermore, if the varicose triad was absent the nonlinear terms in the equations for the sinuous triad vanished, leaving only linear equations for those modes. Mallier[10] later studied the case of two pairs of oblique waves superimposed on the Bickley jet at the same angle, $\pm\theta$: one pair was varicose, the other sinuous. Once again, an interaction was found to occur between the modes. In both studies, [9, 10] the end result was a set of highly nonlinear coupled (Hickernell-type[5]) integro-differential evolution equations, the solutions to which had a finite-time singularity. These equa-

tions involved a nonlinear kernel, with the nonlinearity being cubic in[10] and quartic in[9]. Both studies[9, 10] used nonlinear critical layer theory and followed the approach taken earlier by Goldstein[3, 4] for a flow with a single critical layer and a single unstable mode.

The reason these interactions between the varicose and sinuous modes are considered important is that it is possible they can cause extremely rapid nonlinear growth. Unfortunately, at the time the studies mentioned above were performed, there was little if any experimental or numerical evidence to corroborate our analysis, and the situation remains the same today. Some experiments have hinted at interactions, but have not explored it further. Wygnanski *et al.* [23] conducted careful experiments on small deficit (turbulent) wakes and found that the development of some aspects of the flow was dependent on initial conditions, which they attributed to interactions between the varicose and sinuous modes, and other experiments (e.g.[13, 14]) have also suggested that these interactions may take place. We should also mention that very rapid amplification of three-dimensional disturbances has indeed been observed in plane wakes in both experiments (e.g. [1, 19, 20]) and numerical simulations[17, 18], but it is unclear (at least to the present author) how much of that growth is attributable to the Goldstein mechanisms for three-dimensional instability and how much is due to an interaction between the varicose and sinuous modes.

In an attempt to remedy what we perceive as a lack of numerical verification of the theoretical results, we present here some preliminary results from direct numerical simulations of the Bickley jet and compare those results to the predictions of our earlier asymptotic analysis. The outline of the rest of the paper is as follows. In the next section, we review the theory and resulting amplitude equations. After that, we give the details of our numerical method and present the results of our simulations. Finally, we make some concluding remarks.

2. Review of Theory

In [9, 10], we considered the stability of the Bickley jet $\underline{u}_0 = \left(\operatorname{sech}^2 y, 0, 0\right)$ to three-dimensional disturbances, either in the form of two pair of oblique waves,

$$\begin{aligned} & 2\varepsilon A_{11}\tilde{\underline{u}}_{11}e^{i\alpha\cos\theta(x-ct)}\cos\left[\alpha\sin\theta z\right] + c.c. \\ + \quad & 2\varepsilon A_{22}\tilde{\underline{u}}_{22}e^{2i\alpha\cos\theta(x-ct)}\cos\left[2\alpha\sin\theta z\right] + c.c. \end{aligned} \tag{1}$$

or in the form of a pair of resonant triads, consisting of a two pair of oblique waves at ± 60 together with two plane waves,

$$2\varepsilon A_{11}\tilde{\underline{u}}_{11}e^{i\alpha(x-ct)/2}\cos\left[\alpha\sqrt{3}z/2\right] + c.c.$$

$$+ \quad 2\varepsilon A_{22}\tilde{\underline{u}}_{22}e^{2i\alpha(x-ct)/2}\cos\left[\alpha\sqrt{3}z\right] + c.c.$$
$$+ \quad \varepsilon^{4/3}\left[A_{20}\tilde{\underline{u}}_{20}e^{i\alpha(x-ct)} + A_{40}\tilde{\underline{u}}_{40}e^{2i\alpha(x-ct)} + c.c.\right]. \qquad (2)$$

From the linear theory, we know that the Bickley jet has two inflection points at $y = \pm\text{arccosh}\,\sqrt{3/2}$ where $u_0 = 2/3$, and also two neutral modes with $c = 2/3$ which have critical layers centered on the inflection points: a varicose mode with $\alpha = 1$ and $\hat{v} = \text{sech}\, y \tanh y$ [15] and a sinuous mode with $\alpha = 2$ and $\hat{v} = \text{sech}^2 y$ [16]. In the above disturbances, we have either two amplitudes (for the pairs of oblique waves) or four amplitudes (for the resonant triad) and the objective of [9, 10] was to derive amplitude equations for those amplitudes, and examine how they affected each other. In the analysis, it was assumed that the modes were periodic in time and spatially growing, with the wavenumber α taking the neutral value of 1 and phase velocity being perturbed slightly from neutral $c = 2/3 - \mu c_1$. This perturbation from neutral led to a slow time scale $T = \mu t$ on which the amplitudes evolved. For extremely small disturbances, it was found that the growth was linear, with $A_{11}(T) = A_{11}^{(0)}e^{\sigma_{11}X}$ and similar expressions for the remaining modes, but for larger disturbances the evolution was nonlinear; the evolution first became nonlinear when $\varepsilon = \mu^3$. For pairs of oblique waves, it was found that the amplitude equations were (Hickernell-type) integrodifferential equations with a cubic nonlinearity. For the resonant triad, the equations were of a similar form but with a quartic rather than a cubic nonlinearity. In [10], we solved these equations numerically, using Goldstein's numerical scheme [3], and it was found that, as with similar problems, the evolution of the disturbances went through 3 stages: initially, the disturbances grew linearly, until a second finite-amplitude nonlinear stage was reached, and eventually, the oblique waves experienced explosive growth. Goldstein [3] showed that his equations had a singularity after a finite time T_s (or at a finite distance downstream), and was able to fit a structure to it $A \sim a_0(T_s - T)^{-3-i\psi}$. This same structure applies to both modes for the Bickley jet. Although our study did not include viscous effects, other studies for related problems [7, 22] have shown that weak viscosity can delay the onset of this finite time singularity but not eliminate it, so that our results are still meaningful at high Reynolds numbers. The origins of this finite-time singularity are still not entirely clear, but it appears to be connected to the breakdown of the theory and the onset of a new, still more nonlinear stage governed by the full Euler equations.

3. Numerical Simulations

We now turn to our numerical simulations, in which we have employed a standard spectral (Fourier) method. In our computations, we decomposed

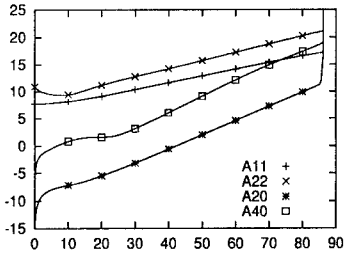


Figure 1. 3D Run1

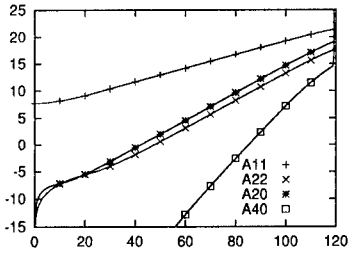


Figure 2. 3D Run2

the velocity into a mean flow and a perturbation, $\underline{u} = (u_0(y), 0, 0) + \tilde{\underline{u}}$, and then assumed that the mean flow is independent of time and the viscosity acts only on the perturbation; in reality, this would require the presence of a body force to counteract the effect of viscosity on the mean flow. The perturbation therefore obeys

$$\begin{aligned} \frac{\partial \tilde{\underline{u}}}{\partial t} &= -\underline{\underline{u}} \bullet \nabla \underline{u} - \nabla p + \frac{1}{\mathrm{Re}} \nabla^2 \tilde{\underline{u}} \\ \nabla \bullet \tilde{\underline{u}} &= 0. \end{aligned} \tag{3}$$

The approach we took was to assume that the flow was periodic in both x (streamwise) and z (spanwise), and use complex Fourier series in those directions. We truncated the y-direction, so that our domain was $-Y \leq y \leq Y$ rather than $-\infty < y < \infty$ and used sines and cosines in that direction. We calculated the nonlinear terms in physical space and derivatives in Fourier

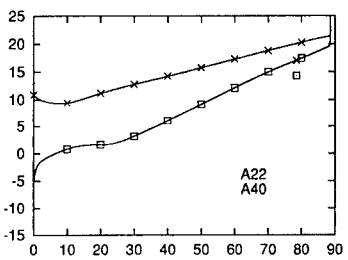


Figure 3. 3D Run3

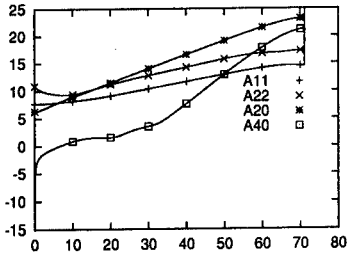


Figure 4. 3D Run4

space, and used a fast fourier transform (FFT) to switch between real and physical space. In our computations, it was necessary to calculate the pressure, which we were able to do by using incompressibility and then inverting a Laplacian,

$$p = -\left(\nabla^2\right)^{-1} \nabla \bullet \underline{NL}; \tag{4}$$

this is fairly easy to do with a Fourier method. For the time-stepping, we used an explicit Adams-Bashforth scheme for the nonlinear terms,

$$\tilde{u}_1 = \tilde{u}_0 + \frac{\delta t}{2}\left(3F_0 - F_{-1}\right), \tag{5}$$

while for the viscous terms, a semi-implicit Adams-Moulton scheme was used,

$$\tilde{u}_1 = \tilde{u}_0 + \frac{\delta t}{2}\left(F_1 + F_0\right). \tag{6}$$

In our simulations, we calculated the energy in each mode,

$$\int_{-Y}^{Y}\int_0^{2\pi/\alpha_x}\int_0^{2\pi/\alpha_z} |\underline{u}_{mn}|^2\, dzdxdy, \tag{7}$$

and compared this to the theoretical amplitude of the disturbance. We should mention however that strictly speaking, therefore, we are not comparing like-with-like, since the two definitions differ slightly. Similarly, our simulations include weak viscosity (a Reynolds number of 1500 was used) which is necessary for numerical stability, while our theory was inviscid. However, as we discussed earlier, studies by other authors have indicated that our theory is applicable to high Reynolds number flows.

3.1. SAMPLE 3D RUNS

In Fig.s 1-4, we present several different runs for the resonant triad, with $\theta = \pi/3$. Each of the runs shown eventually blows up as we lose spectral

decay and the higher harmonics become too large. Paradoxically, this is similar to the reason for the finite-time singularity in Goldstein's amplitude equation. Since the location of the blow-up is different for each of the runs presented, this by itself would indicate that an interaction between the modes is occuring. Our simulations indicate that we are able to capture the nonlinear stage that appeared in the solution to Goldstein's equation, and for the three-dimensional case it would appear that the modes do indeed exert a significant influence on each other; an example of this can be seen in the behavior of A_{11} in Fig.s 1 and 2: the initial conditions for A_{11} were the same in both runs, and the difference in the behaviors of this mode in the two runs is due entirely to nonlinear interactions between the modes. The initial conditions for the runs shown are as follows: in Run 1, A_{20} and A_{40} were initially zero; in Run 2, A_{20}, A_{40} and A_{22} were all originally zero; in Run 3, A_{20}, A_{40} and A_{11} were all originally zero; in Run 4, A_{40} was all originally zero. One point to notice about Run 3 is that since A_{11} and A_{20} were both initially zero, they remain zero: those two modes cannot be generated by the interaction of the other two modes. It is interesting to note in these figures that the behaviour of one mode depends upon which other modes is present, which confirms that there is indeed a strong nonlinear interaction between the modes as suggested by [9, 10].

4. Conclusions

In the preceding sections, we have outlined the theory presented in [9, 10] for nonlinear interactions in the (plane) Bickley jet between the varicose and sinuous modes, and then presented some of the three-dimensional results obtained using DNS. For both the three-dimensional case and also the two-dimensional case [8], the nonlinear theory suggests that there is an interaction between the sinuous modes and the varicose modes. The three-dimensional simulations presented here would appear to confirm that because the behaviour of a mode clearly differs depending upon which other modes are present. This behaviour is quite strong in the three-dimensional case and two-dimensional simulations not presented here indicate that the two-dimensional modes also interact but that the interaction in that case is much weaker. We are currently performing more simulations, although this is a slow process (the turnaround time for 3D runs on the UWO Cray is about 2 months), and we hope to present more complete results at some point in the future.

Acknowledgements

This work was supported by the Natural Sciences and Engineering Council of Canada.

References

1. Corke T.C., Krull J.D., Ghassemi M. (1992) Three-dimensional resonance in far wakes. *J. Fluid Mech.*, Vol.239,pp.99-132.
2. Goldstein M.E. (1994) Nonlinear interaction between oblique waves on nearly planar shear flows. *Phys. Fluids A*, Vol.6,pp.42-65.
3. Goldstein M.E., Choi S.W. (1989) Nonlinear evolution of interacting oblique waves on two-dimensional shear layers. *J. Fluid Mech.*, Vol.207,pp.97-120. Corrigendum (1990). *J. Fluid Mech.*, Vol.216,pp.659-663.
4. Goldstein M.E., Lee S.S. (1992) Fully coupled resonant-triad interaction in an adverse-pressure-gradient boundary layer. *J. Fluid Mech.*, Vol.245,pp.523-551.
5. Hickernell F.J. (1984) Time-dependent critical layers in shear flows on the beta-plane. *J. Fluid Mech.*, Vol.142,pp.431-449.
6. Kelly R.E. (1968) On the resonant interaction of neutral disturbances in two inviscid shear flows. *J. Fluid Mech.*, Vol.31,pp.789-799.
7. Lee S.S. (1997) Generalized critical-layer analysis of fully coupled resonant-triad interactions in a free shear layer. *J. Fluid Mech.*, Vol.347,pp.71-103.
8. Leib S.J., Goldstein M.E. (1989) Nonlinear interaction between the sinuous and varicose instability modes in a plane wake. *Phys. Fluids A*, Vol.1,pp.513-521.
9. Mallier R. (1996) Fully coupled resonant triad interactions in a Bickley jet. *Eur. J. Mech., B/Fluids*, Vol.15,pp.507-526.
10. Mallier R., Haslam M. (1999) Interactions between pairs of oblique waves in a Bickley jet. *Eur. J. Mech., B/Fluids*, Vol.18,pp.227-243.
11. Mallier R., Maslowe S.A. (1994) Parametric resonant triad interactions in a free shear layer. *Canadian Applied Mathematics Quarterly*, Vol.2,pp.91-113.
12. Mallier R., Maslowe S.A. (1994) Fully coupled resonant triad interactions in a free shear layer. *J. Fluid Mech.*, Vol.278,pp.101-121.
13. Sato H. (1970) An experimental study of nonlinear interaction of velocity fluctuations in the transition region of a two-dimensional wake. *J. Fluid Mech.*, Vol.44,pp.741-765.
14. Sato H., Saito H. (1978) Artificial control of laminar-turbulent transition of a two-dimensional wake by external sound. *J. Fluid Mech.*, Vol.67,pp.539-559.
15. Savic P. (1941) On acoustically effective vortex motion in gaseous jets. *Phil. Mag.*, Vol.32,pp.245-252.
16. Savic P., Murphy J.W., The symmetrical vortex sheet in sound sensitive plane jets. *Phil. Mag.*, Vol.34, pp.139-144.
17. Sondergaard R., Mansour N.N., Cantwell B.J. (1994) The effect of initial conditions on the development of temporally evolving planar three dimensional incompressible wakes. *AGARD Conference Proceedings*, **AGARD-CP-551**.
18. Sondergaard R., Cantwell B.J., Mansour N.N. (1997) Direct numerical simulation of a temporally incompressible plane wake: effect of initial conditions on evolution and topology. *Joint Institute for Aeronautics and Acoustics Technical Report*, **JIAA TR 118**, 1997.
19. Williamson C.H.K., Prasad A. (1993) A new mechanism for oblique wave resonance in the 'natural' far wake. *J. Fluid Mech.*, Vol.256,pp.269-313.
20. Williamson C.H.K., Prasad A. (1993) Acoustic forcing of oblique wave resonance in the far wake. *J. Fluid Mech.*, Vol.256,pp.313-341.
21. Wu X. (1992) The nonlinear evolution of high-frequency resonant-triad waves in an oscillatory Stokes layer at high Reynolds number. *J. Fluid Mech.*, Vol.245,pp.553-597.
22. Wu X. (1995) Viscous effects on fully coupled resonant-triad interactions: an analytical approach. *J. Fluid Mech.*, Vol.292,pp.377-407.
23. Wygnanski I., Champagne F., Marasli B. (1986) On the large scale structures in two dimensional, small deficit turbulent wakes. *J. Fluid Mech.*, Vol.168,pp.31-71.

DIRECT NUMERICAL SIMULATION OF TURBULENT FLOW AND HEAT TRANSFER IN A SQUARE DUCT AT LOW REYNOLDS NUMBER

M. PILLER AND E. NOBILE
Dipartimento di Ingegneria Navale, del Mare e per l'Ambiente
Sezione di Fisica Tecnica
University of Trieste, 34127 Trieste - ITALY

Abstract. In this paper, we present the results from Direct Numerical Simulations of turbulent, incompressible flow through a square duct, with an imposed temperature difference between two opposite walls, while the other two walls are assumed perfectly insulated. The mean flow is sustained by an imposed, mean pressure gradient. The most interesting feature, characterizing this geometry, consists in the presence of turbulence-sustained mean secondary motions in the cross-flow plane.

In this study, we focus on weak turbulence, in that the Reynolds number, based on bulk velocity and hydraulic diameter, is about 4450. Our results indicate that secondary motions do not affect dramatically the global parameters, like friction factor and Nusselt number, in comparison with the plane-channel flow. This issue is investigated by looking at the distribution of the various contributions to the total heat flux, with particular attention to the mean convective term, which does not appear in the plane channel flow.

1. INTRODUCTION

In this work, we adopt Direct Numerical Simulation (DNS hereafter) as a convenient tool for studying both the velocity and temperature fields in the presence of solid corners. A square duct is a suitable geometry, in this respect, due to its high degree of symmetry. An imposed pressure drop drives the flow, while the temperature field is generated by the two horizontal walls, kept at constant, different temperatures $\pm T_w$. The vertical walls are assumed perfectly insulated. The Reynolds number, based on hydraulic diameter and bulk velocity, is approximately 4450, while the Prandtl number

is assumed 0.71, representative of air. The Reynolds number Re_τ, based on hydraulic diameter and friction velocity, is 300, as in [1].

From the present simulations, the maximum secondary mean velocity was found to be about 2% of the centerline streamwise velocity. The results clearly indicate that, even though both the heat transfer rate and friction factor are not strongly affected by the presence of mean secondary motions, their effect on the distribution of various quantities within the flow field can not be neglected. For instance, we report the distributions of both the shear stress and the heat flux, at the horizontal walls. Interesting features, clearly connected with the presence of mean secondary motions, characterize these quantities.

2. PROBLEM DEFINITION AND SCALES

The full, time-dependent incompressible Navier Stokes and energy equations are solved directly, without any modelling assumption regarding the turbulent velocity and temperature fields. Simplifying assumptions are made, in that viscous energy dissipation and buoyancy forces are neglected, and the fluid properties are assumed constant. The hydraulic diameter, $D_h = 2h$, the friction velocity, $u_\tau = (-\Delta P\, D_h/4\rho\, \lambda_x)^{1/2}$, and the wall-temperature T_w are used in order to define dimensionless quantities. Domain dimensions are indicated in figure 1, which shows a sketch of the duct. Two simulations have been considered, and they differ in the streamwise domain length, λ_x, which was $4\pi h$ for Case A, and $12\pi h$ for case B. Grids with $200 \times 127 \times 127$ and $600 \times 127 \times 127$ computational cells were used in simulations A and B, respectively, so that the resolution was identical in both cases. The grid spacing was $\Delta x^+ = 9.42$, $\Delta y^+ = \Delta z^+ = 0.45 \div 4.6$. This resolution was judged to be adecquate in [1].

We adopted a second-order, Finite-Volume algorithm in order to solve the flow and energy equations [2]. Decoupling of the continuity from the momentum equations is performed by a classical second-order projection scheme [4]. The computational grid is uniform in the homogeneous, streamwise direction, while an hyperbolic-tangent distribution is adopted in both cross-stream directions.

All data reported here originate from case B. Statistics were acquired over 2 Large Eddy Turnover Times (LETOTS). By using the bulk-velocity reported in table 1, this time interval corresponds to about 1.6 flow-through times.

TABLE 1. Global statistics for Case B, compared with results for the channel flow, and with a DNS for a square duct.

	Case B	Channel [6]	Ref. [1]
Re_b	4453	4560	4410
U_b	14.84	15.2	14.7
f	0.0363	0.035	0.037
Nu	4.89	5.08	

3. RESULTS AND DISCUSSION

Mean secondary motions, shown in figure 2(a), result in four couples of counter-rotating corner-vortices, which carry high-momentum fluid from the core-region toward the corners, and low-momentum fluid away from the walls. The effect of the mean secondary motions on the streamwise velocity distribution is evident, in that isotach lines are bent toward the corners. Weaker vortices, located on both sides of the wall bisectors, were reported in [1], but have not been observed from the mean data of the present simulations. A conditional sampling of the flow field showed the presence of these vortices (figure 2b); the flow field was acquired only when the value of the streamwise vorticity, averaged in the marked box, was smaller than -3.0, in wall units. Since these vortices are highly intermittent, a longer averaging time would be required to capture them in the mean data. At higher Reynolds numbers these vortices have not been observed [3], and therefore they could be a low-Reynolds feature.

Mean temperature profiles at various distances from the left wall are presented in figure 3. The temperature distribution on a wall-bisector compares well with that of the channel flow, at the same Re_τ [6]. The temperature profile at $y^+ = 35$ from the left wall is clearly influenced by the corner vortices, resulting in a more distorted profile than at the wall-bisector. The bending of the temperature profile at $y^+ = 3.3$ indicates the presence of significant turbulent activity at this location. This is quite surprising, since we are well within the viscous sublayer. However, the side-walls are assumed perfectly insulated, thus allowing the temperature fluctuations to extend down to the wall, as can be verified in figure 4(a). Moreover, the w' fluctuations assume large values in the close proximity of the vertical walls, before vanishing at the wall (figure 4b). Thus, the turbulent mixing affects the mean temperature distribution, even in the viscous sublayer on the vertical walls.

Values of the bulk-Reynolds number, Re_b, the mean Nusselt number, Nu and the friction factor, f, are reported in table 1. The friction factor

agrees, to better than 1%, with empirical correlations available for this geometry [5], when the laminar equivalent diameter, $D_l = \left(1+\sqrt{2}\right) h$, is used. The Nusselt number is defined as $Nu = (q_w\, 2h) \,/\, [k\,(\Delta T_w)]$, and can be evaluated from the DNS data as

$$Nu = \frac{1}{2}\left\langle \int_{-1/2}^{+1/2} Re_\tau Pr\, \overline{w\vartheta} - \frac{\partial T}{\partial z} dy \right\rangle$$

where the brackets indicate avaraging along z, and all quantities are dimensionless. The Nusselt number from present simulations is only 3.8% smaller than the Nusselt number evaluated for the channel flow [6].

A possible interpretation of this fact could be that the decrease of turbulent heat transfer ,near the vertical walls, is partially compensated by the mean convective heat flux in the core region. This picture is confirmed by figure 5, which shows the total, the turbulent and the mean convective heat-flux distributions. The gray sfumature corresponds to values from -11.9 (black) to 11.9 (white). The total heat flux ranges from -3.09 to 11.90. The turbulent heat flux assues values between -4.5×10^{-5} and 6.24. For comparison, the turbulent heat flux in the channel flow [6] assumes an almost constant value of 6.4 in the core region, when scaled by the friction velocity and the temperature difference between the walls. The mean convective heat-flux is comprised between -6.05 and 9.95. The mean convective heat-flux is defined as follows:

$$q''_{\mathrm{conv}} = 1/2\, Re_\tau Pr\, (W/u_\tau)\, (T/T_w)$$

Figure 5 suggests that there is a *corridor* through which the heat flows from the bottom toward the top wall. Several *obstacles* tend to reduce this flow. First, the turbulent heat-flux is reduced near the vertical walls, due to the presence of the velocity boundary layer. Second, the corner vortices create mean convective heat fluxes, WT, which *pump* heat in the positive z direction near the horizontal walls bisector, but they also create a negative, mean convective heat flux, near the vertical walls. This effect can be recognized in figure 5(c), where regions of negative mean convective heat-flux appear in correspondence of the corner vortices.

Figures 6 and 7 show the distributions of the mean, total shear stress and heat flux at the bottom wall, respectively. The shear stress vanishes at the vertical walls, due to the presence of stagnation regions at the corners. Three local maxima are evident in the shear-stress profile at the wall. The near-wall peaks are located in the region below the corner-vortices, and are clearly generated by the intense impingement of high-speed fluid, carried from the vortex, against the wall. The local minima are located where the corner vortices carry low-speed fluid away from the wall, toward the core

region. The central peak in the wall shear stress is known to be a low-Reynolds number effect [1]. Clustering and widening of streamwise velocity contours, evident in figure 2, allow an immediate interpretation of the shear-stress behavior. The local heat flux, figure 7, shows a behavior similar to the shear stress. In this case, however, the central maximum is smaller than the side ones. The lateral peaks in the wall heat flux profile are located below regions of high mean convective heat flux, which is advected by the corner vortices and carried toward the bisector of the horizontal wall. This can be appreciated in figure 5(c).

The $\overline{w'\theta'}$ turbulent heat flux decreases near the vertical walls, due to the combined effect of a reduction in the intensity of both w' and θ', as shown in figure 4. Moreover, there is also a loss of correlation between w' and θ', in regions close to the vertical walls, as reported in figure 8, which shows the distribution of $\overline{w'\theta'}/w'\theta'$. In figure 8 black corresponds to 0 and white corresponds to 1. The correlation coefficient is particularly low in correspondence of the corner vortices attached to the vertical walls ($y/2h \approx 0.4$, $z/2h \approx 0.35$). Just below this area there is a region of high correlation coefficient, attached to the horizontal wall. It corresponds to the high heat flux region evidenced in figures 5(a),(c). The loss of correlation of w' and ϑ' close to the vertical walls is an expected feature, considering the different boundary conditions imposed on velocity and temperature.

Streamwise power spectra for both the temperature and the streamwise velocity fluctuations are shown in figure 9. They are normalized in such a way that the area under each curve equals unity. At the centerline the spectral distributions of temperature and velocity fluctuations are very close to each other, in the whole wavenumber range. In the corner region there is still substantial agreement between ϑ' and u' spectra, although the second tend to decay slightly faster. As one might expect, in the corner region both viscosity and molecular conductivity are more effective in damping velocity and temperature fluctuations, and both spectra decay faster than at the centerline, at least in the intermediate range of wavenumbers. At very large wavenumbers the spectra evaluated at both locations collapse on each other; this is quite surprising, since the characteristics of both the velocity and temperature fields are fairly different, in these regions. Aliasing effects show up just in a very-high wavenumber range,which accounts for negligible energy content. This shows that the adopted streamwise resolution was adequate, in order to represent the main features of both the flow and temperature fields.

4. CONCLUDING REMARKS

In this work we presented results obtained from DNS of turbulent forced convection in a square duct. In particular, DNS data for the temperature field were not available before, to the best of our knowledge.

Streamwise power spectra for both streamwise velocity and temperature fluctuations were calculated, at various cross-stream locations. Some peculiar aspects regarding the decay of the highest wave-number components were pointed out.

The influence of mean secondary motions on both the temperature and velocity fields was discussed. The maximum intensity of these motions was found to be about 2% of the maximum mean streamwise velocity. The comparison of the duct flow with the plane-channel flow led to the observation that global parameters, like the Fanning friction-factor and the Nusselt number, are not strongly affected by the presence of the side-walls, while the distribution of the local shear-stress and heat-flux at a wall shows characteristic patterns, whose origin appears to be related to the mean secondary motions.

The present work constitute a base for future investigations, regarding unstably stratified internal flows. We are currently running other simulations for the square-duct flow, in order to investigate the combined influence of mean secondary motions and buoyancy forces, on both the velocity and temperature fields.

AKNOWLEDGEMENTS

Financial support for this research was provided by ENEA – Contract *Settore Calcolo* L.95/95 – and by MURST - Progetto di Ricerca di Interesse Nazionale 1999, "Enhancement techniques in thermofluids", and are gratefully aknowledged. The calculations for case B have been performed on the IBM SP3 at the Centro di Calcolo dell'Università di Trieste.

References

1. Gavrilakis, S. (1992) Numerical simulation of low-Reynolds-number turbulent flow through a straight square duct *J. Fluid Mech.*, **Vol. no. 244**, pp. 104–129.
2. Onesti, L. (1995) *High Performance Parallel Computing on the Cray T3D - CFD Applications*, Batchelor Thesis (*in Italian*), University of Trieste, Italy.
3. Gessner, F.B. and Jones, J.B. (1965) On some aspects of fully-developed turbulent flow in rectangular channels *J. Fluid Mech.*, **Vol. no. 23**, pp. 689–713.
4. Gresho, P.M. (1990) On the theory of semi-implicit projection method for viscous incompressible flow and its implementation via a finite element method that also introduces a nearly consistent mass matrix. Part 1: theory. *Int. J. Numer. Methods Fluids*, **Vol. no. 11**, pp. 587–620.
5. Kakac, S., Shah, R.K. and Aung, W. (1987) *Handbook of Single-Phase Convective Heat Transfer*, Chapter 4, John Wiley and Sons.
6. Iida, O. and Kasagi, N. (2001). Heat transfer of fully developed turbulent channel flowwith iso-thermal walls. *Online database: www.thtlab.t.u-tokyo.ac.jp, case # CH122_PG.WL4*

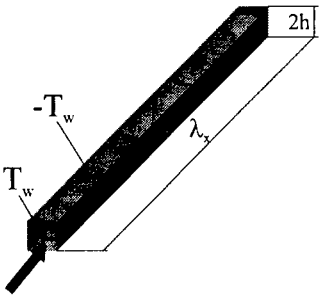


Figure 1. Sketch of the computational domain.

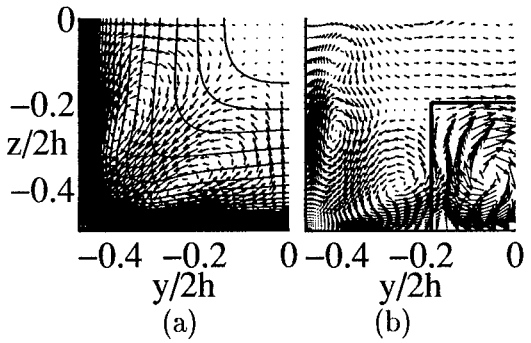


Figure 2. (a) Mean secondary motions and Mean streamwise velocity contours on a cross-stream plane. (b) Conditional sampling of the secondary motions.

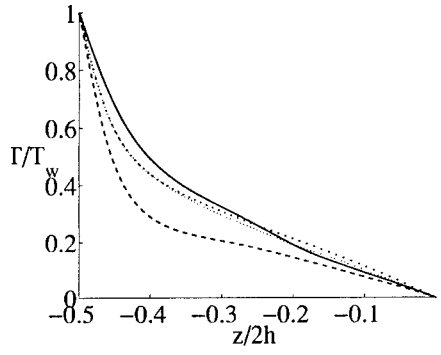


Figure 3. Mean temperature profiles at several distances y_w^+ from a vertical wall. ——: $y_w^+ = 3.3$; − − −: $y_w^+ = 35$; — · —: $y_w^+ = 150$. Data for the plane channel flow [6] are shown as symbols.

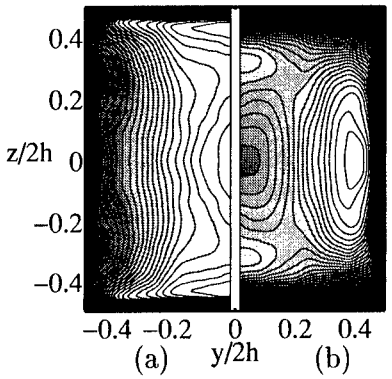


Figure 4. ϑ' (left) and w' (right) fluctuations, scaled by their maximum values. From black to white: 0.0 to 1.0.

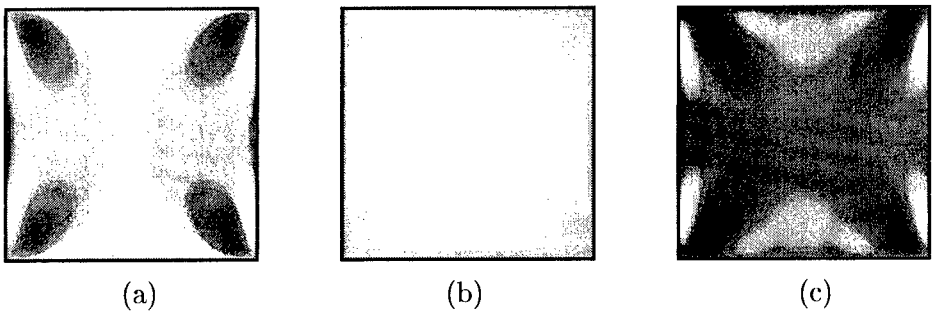


Figure 5. Heat-flux in the z direction. (a): total; (b) turbulent; (c) convective.

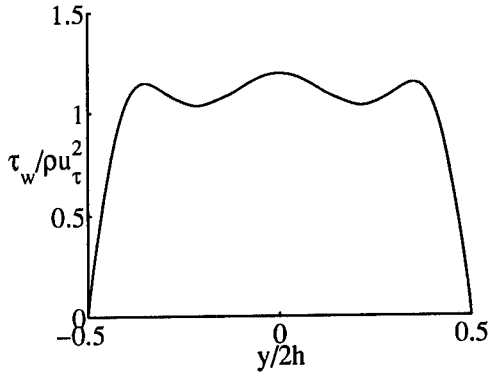


Figure 6. Wall shear-stress.

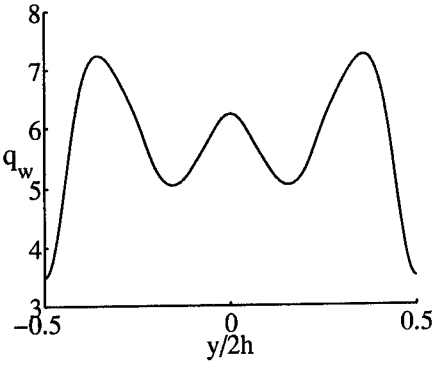


Figure 7. Wall heat-flux.

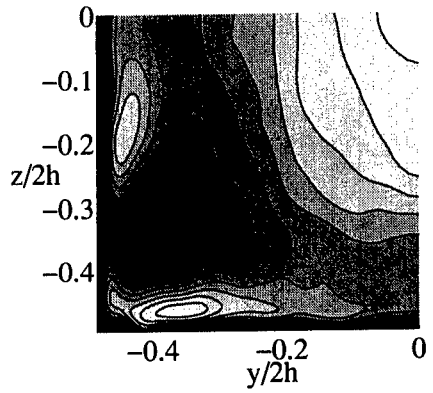


Figure 8. $\overline{v'\vartheta'}/v'\vartheta'$ contours on a cross-flow plane.

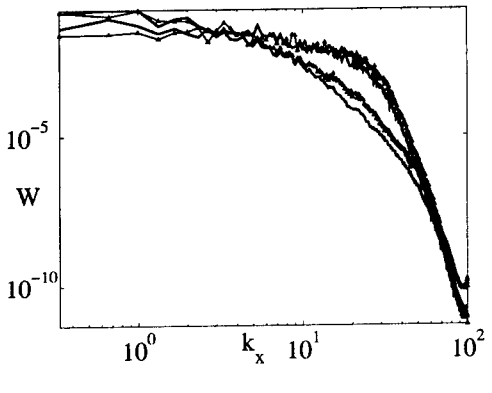


Figure 9. Spectra of streamwise velocity and temperature fluctuations, at the centerline (upper curves) and at $y^+ = z^+ = 15$ (lower curves). Thick solid curves: spectra of streamwise velocity fluctuations. Tiny curves with symbols: spectra of temperature fluctuations.

DIRECT NUMERICAL SIMULATION OF FULLY DEVELOPED FLOW NEAR A FLAT PLATE

V. S. CHELYSHKOV [1] AND CHAOQUN LIU [2]
[1] *Department of Mathematics,*
University of New Orleans, New Orleans, USA;
Institute of Hydromechanics, Kiev, Ukraine
[2] *Department of Mathematics,*
University of Texas at Arlington, Arlington, USA

Abstract

A traditional local approach is applied for simulation of a statistically steady flow near a flat plate. A local flow domain is placed far from the leading edge of the plate. A coupled system of the Prandtl and the Navier-Stokes equations for disturbances is chosen as the governing system of equations. Fully spectral approach is used for space discretization. This helps to avoid prescribing inflow and outflow boundary conditions. Acceptable particular solutions are selected to describe physically adequate phenomenon. A new spectral method for integrating the Cauchy problem is adopted to study the flow evolution.

1. Introduction

The phenomenon of turbulence in lengthy flows involves a large range of space scales. This is the challenge for flow modeling based the full Navier-Stokes equations. The class of external quasi-homogeneous flows related to the boundary layer theory has a quasi-regular nature, it shows that lengthy disturbances carry small amounts of energy in thin layers. The main feature of the boundary layer flows is the existence of laminar regimes of motion that can be described on the basis of the Prandtl equations. Thin laminar flows are unstable and simulation of thin transitional and turbulent flows is usually based on the full Navier-Stokes equations (see, for instance, [8]). The regular approach, however, introduces restrictions on Reynolds numbers because of limitations on computer resources. To weaken the restriction one can use local modeling of quasi-homogeneous external flows. We employ SFM, a coupled system of Prandtl and Navier-Stokes equations for disturbances [5,7] for local modeling of the flow near a flat plate.

First theoretical investigations of stability of laminar boundary layer flows showed the existence of coherent structures in transitional zones of the flows in the form of the Tollmien-Schlichting wave. The existence of local flow structures was confirmed later by experiments for both transitional and turbulent

quasi-regular flows. The local approach is widely used in the thin layer theory. Being the analogy with a channel flow, the approach leads to definition of a local Reynolds number, but it does not answer the question about the scale of flow structure. It also introduces an uncertainty to inflow and outflow boundary conditions because of the weak non-homogeneity of quasi-regular flows. The local approach is not general enough to follow space upwind peculiarities of a flow, but this can be considered as the advantage when simulating lengthy flows for high Reynolds numbers.

The scale of a flow structure is the result of competition of disturbances with random lengths that depend weakly on the external conditions and are determined by the internal nature of a flow, in particular, by the local Reynolds number. Space parameters of coherent structure can be estimated on the basis of numerical experiments. If a flow is unstable to infinitesimal disturbances then there is another possibility to choose the local characteristic size of the flow: one can suppose that scales of coherent flow structures coincide with space scales of the disturbances corresponding to the maximal temporal increments. We apply this *principle of maximal instability* for the near-wall flow modeling.

Turbulence has a self-sustained nature, it arises in flows spontaneously, and its physical existence does not require special conditions. This attribute of turbulence could be considered as the concept for numerical simulation. Actually, a laminar flow can loose its stability due to introduced disturbances at any place of the flow at some moment of time. The disturbances then develop in space and time, and the development does not require any conditions for its support, in particular, inflow boundary conditions. Application of spectral methods is the direct way of realizing this approach numerically. Such an approach allows developing the idea of selection of local particular solutions [3], which capture the adequate phenomenon when extracting them from the problem considered.

Another feature of the numerical procedure applied is the application of a new integration method for the Cauchy problem [2]. The algorithm is the adaptation of the general spectral approach to the Cauchy problem solving. Unknown variables are represented as a sum of preliminary chosen sequence of functions; both the spectral space and the space of original variables are involved in the algorithm construction. The approach leads to the choice of non-uniformly disposed collocation points in a fixed temporal interval and provides an additional flexibility in comparison to traditional methods.

2. Space and Time Discretization Procedures

To this end we developed the results for 2D flow modeling, so the discretization procedure is briefly described in two space dimensions and time.

Let (t, X_0, y) be a non-dimensional time and non-dimensional coordinates with the origin at the leading edge of the plate, and let the local variable x be connected to X_0 by the formulas

$$X_0 = 1 + X, \quad X = \lambda x, \ \lambda = \kappa^2 / \mathrm{Re}, \ \kappa = 1.72078766,$$

where Reynolds number Re is chosen on the basis of thickness of the boundary layer. The neutral stability curve $\mathrm{Re} = \mathrm{Re}(\alpha)$ borders energy-bearing intervals of space scales that support the phenomenon of turbulence in the flow. For a fixed Reynolds number, we can pick up the point (α_m, Re) inside the neutral curve that corresponds to the disturbance with the maximal temporal increment. In accordance with the principle of maximal instability, the parameter $\alpha = \alpha_m$ provides the scale of coherent structure $2\pi / \alpha$, and we study flow in the domain

$$D = \{-\pi / \alpha \le x \le \pi / \alpha \ , \ 0 \le y \le \infty\}.$$

We consider the solution of the problem for *disturbances* $\mathbf{F}^d$ of the laminar flow in the form

$$\mathbf{F}^d = \mathbf{F}^S + \mathbf{F}^f, \quad \overline{\mathbf{F}}^f = 0,$$

where $\mathbf{F}^S = \{u^S, v^S, p^S\}(X_0, y, t)$, $\mathbf{F}^f = \{u^f, v^f/\lambda, p^f\}(x, y, t)$ are slow and fast components of the velocity vector and pressure, bar means $x-$averaging. The Navier-Stokes equations for disturbances $\mathbf{F}^d$ were split in coupled Prandtl and Navier-Stokes equations for the disturbance components $\mathbf{F}^S$ and $\mathbf{F}^f$ in [5,7]; the procedure was specified for smooth periodic function $\mathbf{F}^f$ of the x-variable in the domain D.

The problem statement does not involve unknown inflow and outflow boundary conditions, and we follow the idea of extracting the adequate particular solutions from the governing equations.

The approximation in x-variable is

$$\{u^f, v^f, p^f\}(x, y, t) = \sum_{\substack{|k| \le K \\ k \ne 0}} \{u_k^f, v_k^f, p_k^f\}(y, t) e^{i\alpha x}. \qquad (1)$$

If weak non-homogeneity of the flow is taken into account in the equations for fast disturbances, then the requirement of periodicity of $\mathbf{F}^f$ leads to Gibbs phenomenon of the order of $O(1/\mathrm{Re})$ near the inflow and the outflow boundary

for representation of slow components of the velocity vector. Modes in (1) draw the Orr-Sommerfield eigenfunctions in the development of disturbances.

The linearized Prandtl problem for disturbances also has nontrivial solutions in the absence of upwind boundary conditions. Those modes are proportional to the sequence $\{X_0^{-\nu_j}\}$, $\nu_1 = 1$, $\nu_2 = 1.887$, $\nu_3 = 2.867$, ... in the boundary layer coordinates [9]. It seemed the modes would have to be involved in the phenomenon modeling [7]. However, it has been shown that those eigenfunctions describe solely the peculiarities of damping the slow component of upwind stationary velocity disturbances in the streamwise direction, and they must be excluded from the description of the flow evolution in the case of uncertainty in the inflow boundary conditions [3]. The uncertainty makes the problem under consideration ill posed in terms of slow variables, and we apply the Galerkin-Petrov variant of a spectral method representing the solution in the longitudinal direction in the form

$$u^S = \sum_{j=0}^{J} U_j(\eta,t) X_0^j, \quad v^S = \sum_{j=0}^{J} V_j(\eta,t) X_0^{j-1/2}, \quad \eta = y/\sqrt{X_0}.$$

This removes the possibility of self-excitation of the slow modes. So, interaction of fast disturbances is the only source of excitation of slow ones. Variation of $X_0 = 1 + X$ is small if $\alpha \sim O(1)$, and we can choose functions $X^j, j = 1,...,J$ as the test functions being content with a small value of J, in particular, with $J = 1$, because terms of the order $O(\lambda^2)$ have been removed from the model equations.

The discretization procedure for the problem under consideration in the direction orthogonal to the wall (that is in y-direction) for both slow and fast components of the flow is based on a weak formulation (see, for instance, [4]). Orthogonal exponential polynomials $\mathcal{E}_{ml}(\alpha y)$, $l=1,...,m$ [6] were used as the trial and the test functions.

The finite dimensional dynamic system of equations extracted from the governing equations was integrated in time by a spectral method developed recently in [2]. The method can be summarized as follows.

Let $\mathbf{Y}$ and $\mathbf{F}$ be vector functions with dimension N. We consider the Cauchy problem

$$\mathbf{Y}' = \mathbf{F}(t, \mathbf{Y}(t)), \quad \mathbf{Y}(T_I) = \mathbf{Y}_I \tag{2}$$

in the interval $t \in [T_I, T_I + h]$, $h > 0$, for some prescribed initial value $\mathbf{Y}_I$.

Let $\lambda_m > 0$, $\alpha_n = h/\lambda_m$, $\tau = (t - T_I)/\alpha_n$, $\mathbf{y}(\tau) = \mathbf{Y}(T_I + \alpha_n \tau)$,

$\mathbf{f}(\tau,\mathbf{y}) = \alpha_n \mathbf{F}(T_I + \alpha_n\tau, \mathbf{Y}(T_I + \alpha_n\tau))$. Then problem (2) can be represented as follows

$$\mathbf{y}'(\tau) = \mathbf{f}(\tau, \mathbf{y}(\tau)), \quad \mathbf{y}(0) = \mathbf{Y}_I, \ \tau \in [0, \lambda_{nn}] \tag{3}$$

We look for an approximate solution $\mathbf{y}_n(\tau) \approx \mathbf{y}(\tau)$ to system (3) in the form

$$\mathbf{y}_n(\tau) = \mathbf{Y}_I + \mathbf{f}_0\tau + \sum_{j=1}^{n} \mathbf{a}_{nj}(S_{nj}(\beta_n, \tau) - (-1)^{n-j}\tau), \tag{4}$$

$$S_{nj}(\beta_n, \tau) = \int_0^{\tau} \mathcal{E}_{nj}(\beta_n t)dt$$

that satisfies the initial condition in (3) and the initial condition for the derivative of the unknown variable. Here $\mathbf{a}_{nj}$ are unknown vector coefficients with dimension N, $\beta_n = 1$, $\mathbf{f}_0 = \mathbf{f}(0, \mathbf{Y}_I)$. To find the spectral coefficients $\mathbf{a}_{nj}$ in (4) we consider the discrete form of the problem (3) in the collocation points $\tau_{ns} = \lambda_{ns} / \beta_n$, $s = 1,...,n$; λ_{ns} are the zeros of the polynomial $\mathcal{E}_{n0}(\tau)$, λ_{nn} is the maximal zero. Transformations in the spectral space lead to the discrete analog of the Cauchy problem (2)

$$T_{np} = T_I + \nu_{np} h, \quad \mathbf{Y}_{np} = \mathbf{Y}_n(T_{np}),$$

$$\mathbf{Y}_{np} = \mathbf{Y}_I + \sigma_{np0} h \mathbf{F}(T_I, \mathbf{Y}_I) + h \sum_{s=1}^{n} \sigma_{nps} \mathbf{F}(T_{ns}, \mathbf{Y}_{ns}), \tag{5}$$

in the original variables. Here $p = 1,...,n$, and coefficients $\nu_{np}, \sigma_{np0}, \sigma_{nps}$ can be tabulated for any reasonable n. Resolving the equations (5) leads to a step error of the order of $O(h^{n+1})$ for sufficiently smooth function $\mathbf{F}$, but getting the precise solution is a difficult task. An explicit single-step procedure that provides an approximate solution of the problem (5) has been developed as a trial value. The procedure is based on the property of thickening of the zeros of $\mathcal{E}_{n0}(\tau)$ in the vicinity of $\tau = 0$. This leads to a recurrence algorithm that has the same order as the Euler method, but gives better accuracy when increasing n. It should be mentioned that the algorithm is convenient for the implementation of the adaptive stepsize control.

Detailed description of the method is given in [2]. The method could provide calculations both in the spectral space and in the space of the original variables that gives the opportunity to interpolate unknown variables in

intermediate collocation points. High degree approximations lead to higher storage requirements, but calculations in highly non-uniform disposed points can give an advantage in terms of prediction of the solution and application to stiff problems.

The single-step explicit procedure has been applied for simulation of the flow for $n \leq 16$. The initial data at $t = 0$ should represent an arbitrary disturbance with small amplitude. Following the concept of self-sustained nature of turbulence, one can suppose that the disturbance contains the mode with the maximal temporal increment. So, we can chose the initial guess, considering only one mode at $t = 0$, and the initial data satisfying linearized governing equations can have a moderate amplitude.

3. Flow Simulation Results

Simulation has been performed for $N = 1220$ degrees of freedom and for large Reynolds numbers. Full development of disturbances was provided by integration in a long non-dimensional time interval. The example of the simulation described here corresponds to the turbulent zone of the flow for $\mathrm{Re}_l = 10^6$, in this case the local Reynolds number is equal to 2961.1.

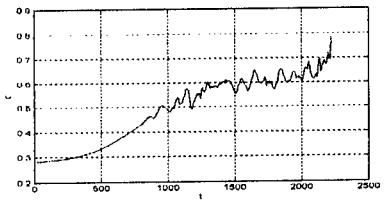


Figure 1. Development of phase speed

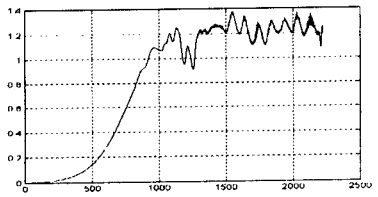


Figure 2. Development of mean friction

Development of the phase speed c in time is shown in Fig. 1. The speed varies from the value that is determined by the linear theory of hydrodynamic stability until a value in the interval (0.6, 0.7). It is found that the phase speed of statistically steady flow is a rather conservative characteristic, it depends weakly on the local Reynolds number. Figure 2 shows the development of the slow component of the skin friction in the point $X_0 = 1$ on the wall. In contrast with the phase speed,

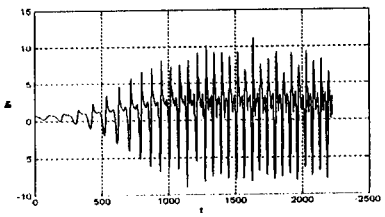


Figure 3. Development of skin friction

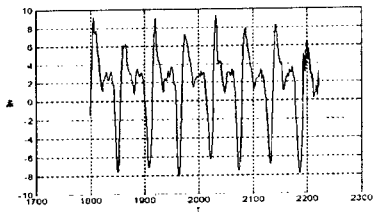


Figure 4. Fully developed skin friction

mean skin friction increases significantly when increasing the distance from the leading edge. It appears that the model employed for the direct numerical simulation demonstrates good results in mean skin friction prediction. This may be the consequence of involving the Prandtl equations for disturbances to the flow description. Fig. 3 shows development of full skin friction on the wall, details of the statistically steady regime of the flow are given in Fig. 4, which is the part of Fig. 3. It is seen that the impulsive injection of fluid into the boundary layer takes approximately 1/5 of the full time in every point of the domain near the wall. This 2D phenomenon correlates with the existence of hairpin vortex structure in 3D boundary layer [1].

Considering Fig. 5 and Fig. 6 one may come to the conclusion about chaotic nature of the flow. The power spectral density is shown in Fig. 5 in logarithmic scale. Two dimensional projection of the attractor of the dynamic system for fully developed flow in delay coordinates with delay $\Delta t = 30$ for full skin friction is shown in Fig. 6. The trajectory with self-intercepts clearly shows the complexity of the phenomenon and demonstrates the nature of the dynamic system extracted.

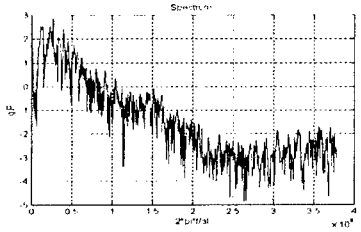


Figure 5. Power spectral density

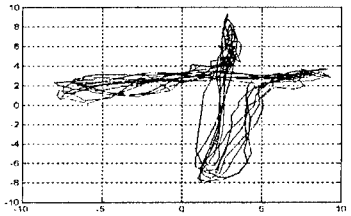


Figure 6. Projection of the attractor in the delay coordinates

It should be mentioned that the dependence of the wall pressure on time is similar to the full skin friction; the spectral analysis shows that the characteristics of the pressure frequency correspond to the appropriate characteristics of the full skin friction, and the pressure phase speed is the same as for the skin friction.

4. Conclusion

The concept of local simulation of flows related to boundary layer problems is adopted in this work. Spectral methods based on selection of appropriate particular solutions are elaborated to overcome the uncertainty in inflow and outflow boundary conditions. The restrictive approach that leads to elimination of lengthy disturbances is used to choose the scale of a coherent structure. Special attention is paid to application of a recently developed spectral method for the initial value problem integration.

Although simulation of 2D flow for big Reynolds numbers can be considered as a methodical one, the results obtained are consistent with turbulence modeling. Heavy nonlinear phenomenon in the near-wall region has a chaotic background. Fluid is pumping away from the wall, and the region of separation moves along the wall taking approximately 1/5 of an exposed time in every point of the segment chosen on the wall. At the same time simulation shows good results for the mean profile of the flow. The phase speed of the flow is in the interval (0.6, 0.7). The parameters are found for $\mathrm{Re}_l = 10^6$.

5. Acknowledgments

This work was supported by Air Force Office of Scientific Research Grant. We thank G. Pantelis for a discussion. One of the authors (VSC) thanks L. Tkachenko for her help in treatment of the simulation results.

References

1. Adrian, R.J., Balachandar, S. (1998) Vortex Packets and the Structure of Wall Turbulence. *Proceedings of the International Symposium on Seawater drag reduction*. 22-23 July 1998, Newport, Rhode Island: pp. 33 - 38.
2. Chelyshkov, V. S. (2000) A Spectral Method for Cauchy Problem Solving. *Proceedings of MCME International Conference. Problems of Modern Applied Mathematics*. N. Mastorakis (Editor), WSES Press, pp. 227-232.
3. Chelyshkov, V.S., Grinchenko, V.T., Liu, C. (1997) Local Approach for Modeling of Quasi-regular Flows. *Proceedings of The First AFOSR International Conference on Direct and Large Eddy Simulation*. C. Liu, Z. Liu (Editors), Greyden Press, Columbus, pp. 265-272.
4. Chelyshkov, V.S. (1994) A Variant of Spectral Method in the Theory of Hydrodynamic stability. *Hydromechanics (Gidromekhanika)*. N 68: pp. 105-109 (in Russian).
5. Chelyshkov, V.S. (1993) The Model of Near-Wall Flow. *Institute of Hydromechanics, NAS of Ukraine, Annual report for 1993*, pp.54-55.
6. Chelyshkov, V.S. (1987) Sequences of Exponential Polynomials, which Are Orthogonal on the Semi-Axis. *Reports of the Academy of Sciences of the Ukraine, (Doklady AN UkSSR)*. ser. A, N 1: pp. 14-17 (in Russian).
7. Grinchenko, V.T., Chelyshkov, V.S. (1995) Transition in the Case of Low Free Stream Turbulence. *Progress and Challenges in CFD Methods and Algorithms AGARD-CP-578*, pp. 26-1--26-9.
8. Li Jiang, Hua Shan, Chaoqun Liu (1999) Direct Numerical Simulation of Boundary Layer Receptivity for Subsonic Flow Around Airfoil. *Recent Advances in DNS and LES*, Doyle Knight and Leonidas Sakell (Editors), Kluwer Academic Publishers, pp. 203-218.
9. Libby, P.& Fox, H. (1963) Some Perturbation Solutions in the Boundary Layer Theory. Part 1. The momentum equation. *J. Fluid Mech.* Vol. 17, N 3, p.433-447.

DIRECT NUMERICAL SIMULATION OF TURBULENT MIXING IN A ROUGH-WALL FLOW

K. TSUJIMOTO, Y. MIYAKE AND N. NAGAI
Department of Mechanical Engineering, Osaka University
2-1, Yamada-oka, Suita, 565-0871 JAPAN

1. Introduction

Rough-wall turbulent flows are more common in engineering application than smooth-wall turbulent flows. Modification of mean flow and turbulence property have been established by enormous experiments. However, details of mechanism of rough-wall turbulence has been understood little because spatial resolution is limited in experiments. Meanwhile, Direct Numerical Simulation (DNS) of a rough-wall turbulent flows which is capable of giving high resolution data requires prohibitively heavy computer power and accordingly, no other DNS data are available than those published by the present authors (Miyake *et al.*, 1999). Our first DNS considered sand-grain roughness whose effect was implemented by profile drag based on Stokes drag and could successfully reproduce experimentally established rough-wall turbulent flow such as downward shift of straight line of logarithmic mean velocity distribution and vanishing of viscous sublayer. It was confirmed that the layer adjacent to the wall up to several tens in wall unit where smooth-wall turbulence exhibits autonomous property independent on the layer above it, is taken over by the layer having property of logarithmic layer, in rough-wall turbulence. While quasi-streamwise vortices play major role to generate high turbulent shear stress in this near-wall layer in smooth-wall turbulent flow, roughness destroy this vortical system and consequently, different mixing system which replaces the role of quasi-streamwise vortices should be found in rough-wall layer. Present work intends to investigate the turbulent mixing in the layer close to the wall of rough-wall turbulence by a DNS of more sound numerical conditions, *i.e.*, without using any model for roughness element.

Table 1. Computational conditions

	Streamwise	Wall normal	Spanwise
Length (wall unit)	$2\pi H$ (942)	$2H$ (300)	πH (471)
Grid number	256	257	128
Reynolds number	$Re_\tau = H\bar{u}_\tau/\nu = 150$		

2. Computational procedure

2.1. CHANNELS

Since implement of a roughness element in the calculation requires enormously high computational power, only one wall is assumed rough and the other, smooth. The configuration of the channel is illustrated in Fig.1. A Cartesian coordinate system is employed, in which x, y, z are streamwise, wall-normal, and spanwise directions, respectively, and the velocity components in the respective directions are denoted by u, v, w.

Computational conditions such as size of computational domain, grid number and Reynolds number are given in Table 1. The global Reynolds number is defined as $Re_\tau = \bar{u}_\tau H/\nu$ where $\bar{u}_\tau$ is global mean friction velocity and is calculated from pressure gradient $d\bar{p}/dx$ by $\bar{u}_\tau = [(H/\rho)(d\bar{p}/dx)]^{1/2}$, H is half channel width and ν and ρ are kinematic viscosity and density, respectively. In the following, superscript($\bar{\ }$) denotes quantities averaged in a plane parallel to the wall (x-z plane), superscript ($'$), fluctuation from this mean and superscript($^+$), non-dimensionalized quantities by $\bar{u}_\tau$ which is mean friction velocity and ν. The spatial discretization is a Fourier series expansion in x and z for the sake of periodicity and a Chebyshev polynomial expansion in the normal direction. Time advancement is done by a semi-implicit method (Crank-Nicolson scheme for viscous term and third order Adams-Bashforth scheme for the convective term).

2.2. ROUGHNESS ELEMENT

The roughness is composed of periodically arranged two-dimensional spanwise ribs whose cross section is a square of a side $h_s^+ = 20$ and separated in streamwise direction by $\Delta x^+ = 118$. The boundary condition on the solid wall is treated rigorously to satisfy non-slip flow. Namely, at each grid point $\boldsymbol{x}_s$ on every rib surface, external force $\boldsymbol{f}_v$ is added so as to make the flow vanishing there. The magnitude of $\boldsymbol{f}_v$ is determined iteratively to satisfy

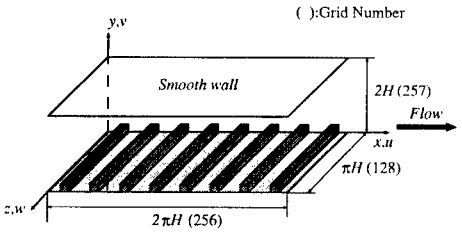


Figure 1. Configuration of a channel with a rough wall of 2-dimensional ribs.

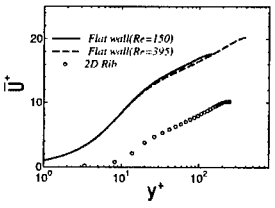


Figure 2. Distribution of mean velocity $\bar{u}^+$ normalized by mean friction velocity $\bar{u}_{\tau,r}$ on the rough wall and ν.

$$\boldsymbol{f}_v(\boldsymbol{x}_s,t) = \alpha_v \int_0^t \boldsymbol{v}(\boldsymbol{x}_s,t')dt' + \beta_v \boldsymbol{v}(\boldsymbol{x}_s,t) \tag{1}$$

where α_v and β_v are negative constants to prevent the computation from instability and in this calculation, they are $\alpha_v = -4\times10^5$ and $\beta_v = -6\times10^2$. These procedures are proposed by Goldstein *et al.* (1995).

3. Results

3.1. MEAN FLOW PROPERTY

Mean velocity distributions are given in Fig.2. In order to make the straight line of logarithmic part parallel to the one established for the ordinary smooth wall, correction of the location of wall surface is required. In this case, upward-shifting by $\Delta y^+ = 7.0$ is needed. Magnitude of the downward shift of the straight lines from the case of the ordinary smooth wall is within the scatter of experimental data (Raupach *et al.*, 1991). Corresponding shear stress distribution is given in Fig.3. The height H_r from the rough-wall where total shear stress vanishes is defined hereafter as the equivalent half width of the rough-wall channel. The width H_r is larger than H because total drag on the rough wall is larger than on the smooth wall. The defect of total shear stress in the layer close to the rough wall found in Fig.3 is covered by pressure drag of ribs. It is noted that local high viscous shear stress $\bar{\tau}_{wr}/\rho = \nu(\partial\bar{u}/\partial y)$ is observed in the layer near the top of the rib surface.

3.2. MODIFICATION OF LARGE-SCALE FLOW

The modification of large-scale flow by rough-wall is considered in this section, since it is substantial for global mixing . Figure 4 shows the ratio of turbulent shear stress $-\overline{u'v'}$ to turbulent kinetic energy k, $r = -\overline{u'v'}/k$.

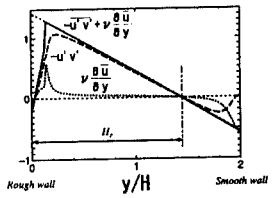


Figure 3. Distribution of shear stress across channel, normalized by overall mean friction velocity $\bar{u}_\tau$ and ν.

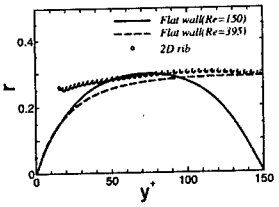
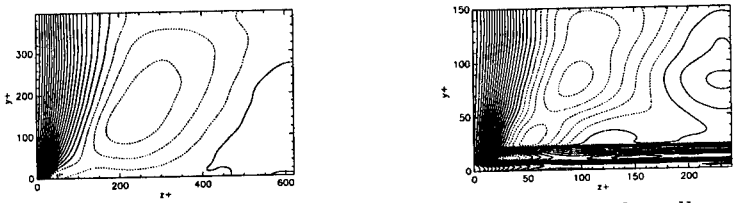


Figure 4. Distribution of structure parameter $r = -\overline{u'v'}/k$.

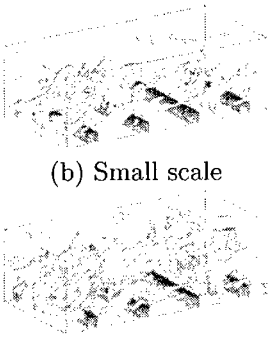


(a) smooth ($Re_\tau = 395$) (b) 2D rough wall

Figure 5. Iso-contour of spanwise correlation factor of streamwise velocity fluctuation.

It is known to be around 0.27 in the logarithmic layer and the larger the Reynolds number, the thicker the constant r-layer. Present simulation shows that the wall roughness makes this layer to reach closer to the wall, as expected.

As mentioned earlier, the profile drag is dominant on the rough wall. However, in the region near the top of the roughness elements, the shear stress must be sustained mostly by turbulent shear flows. Therefore , strong turbulent mixing is required there. While quasi-streamwise vortices play dominant role for strong mixing near the smooth wall, rough-wall is expected to have different mechanism for the strong mixing. Figures 5 show the contour of spanwise correlation of streamwise velocity fluctuation. In place of streaks of mean spanwise separation $\Delta z^+ \sim 100$ which is a distinguished feature of the buffer layer, large scale streaks of much larger mean spanwise separation than in the buffer layer appears. These large-scale streaks are characteristic of wall turbulence of a large Reynolds number and accordingly, of the layer close to the wall near the rough surface. These observation suggests that the turbulence property normally found in the layer away from the wall prevails closer towards the wall in a rough-wall case. Namely it is suggested that a large-scale mixing takes place actively over the roughness.



(b) Small scale

(a) Original

Figure 6. Iso- surface of the second invariance of velocity gradient tensor Q' ($Q'^{+} > 1.8 \times 10^{-4}$).

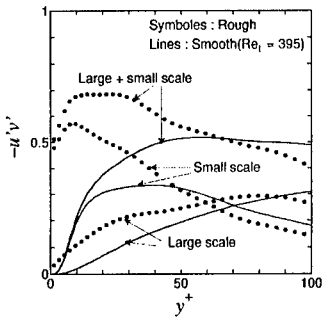
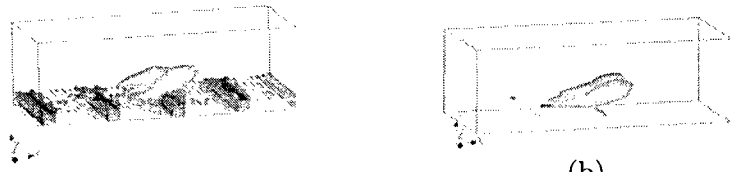


Figure 7. Distribution of separately averaged turbulent shear stress due to large and small-scale flow.

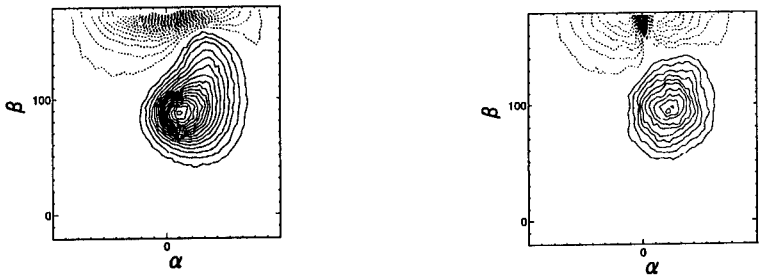


(a) (b)

Fig. 8 Extracted vortex structure LSE with the detector in the plane at $y^{+} = 25$. (a) detector at near the rib, (b) position of detector unconditioned. ($Q'^{+} > 1.8 \times 10^{-4}$).

3.3. TURBULENT MIXING DUE TO COHERENT VORTICES

To investigate the contribution of coherent vortices of different scale to turbulent shear stress, a filter is used to decompose the flow. The decomposing filter is of wavelengths of $\delta_x^{+} \approx 400, \delta_z^{+} \approx 100$ in x, z direction, respectively. Figures 6 compares (a) whole scale flow and (b) large-scale eddies discarded flow, by the iso-surfaces of the second invariance of velocity gradient tensor $Q'^{+} = 1.8 \times 10^{-4}$. It is observed that the coherent flow mainly consists of small-scale eddies of above-defined length. Figure 7 which shows the contribution of each component to turbulent shear stress demonstrates that the shear stress is composed dominantly of the small scale vortices in near-wall region of both smooth- and rough-wall flow, especially in rough-wall flow and that the stress due to small-scale vortices is strongly enhanced over the rough-wall. An alternative way that we attempted to extract the governing event associated with the generation of turbulent shear stress is based on LSE (Linear Stochastic Estimation, Adrian *et al.*, 1988). The extracted



(a) Smooth wall at $Re_\tau = 395$ in $y^+ = 10 \sim 50$

(b) Rough wall in $y^+ = 10 \sim 50$

Figure 9. Contour lines of statistical property of vorticity on $\alpha - \beta$ plane. Solid lines : positive, dotted lines : negative.

structures in positioning the detector in the plane parallel to the wall at $y^+ = 25$ are shown in Fig.8 which demonstrate that streamwise elongated vortices are the key structures and that the key structure does not depend on the position of the detector, as in (b) which is for the detector's position unconditioned. It is also found that the extracted vortices are more tilted from the wall in the rough-wall case than in smooth wall case, though the pictures are not shown here. It is concluded that such a modulation of attitude angle of vortices is substantial in enhancing the turbulence mixing of near-wall layer, in rough-wall flow. In order to know the tilting property of the vortices, weighted average of a quantity $\hat{\phi}$ on the attitude angle of vortex line α, β is defined as,

$$\hat{\phi} = \int_V \int_{\beta-\Delta\beta}^{\beta+\Delta\beta} \int_{\alpha-\Delta\alpha}^{\alpha+\Delta\alpha} \phi(\alpha,\beta) d\alpha d\beta dV \qquad (2)$$

where $\alpha = \tan^{-1}(\omega_y/\sqrt{\omega_x^2+\omega_z^2})$, $\beta = \tan^{-1}(\omega_x/\omega_z)$, $\Delta\alpha = 2.5°$! $\$\Delta\beta = 5°$! %

Figures 9 which shows the average for $\hat{\phi} = \hat{Q}$ gives the peak of Q in α-β map at around $\beta \approx 90°$, which corresponds to streamwise small-scale vortices. In rough wall flow, the peak shifts to larger α than in smooth-wall flow, indicating that the vortex structures inclines more from the wall in average.

3.4. FORMATION OF SMALL-SCALE COHERENT VORTICES OVER THE ROUGHENED WALL

Though small-scale coherent vortices are found to be key structures of turbulence mixing over roughened wall, the well-known coherent vortices found in smooth wall flow are different however, from those of rough-wall flow.

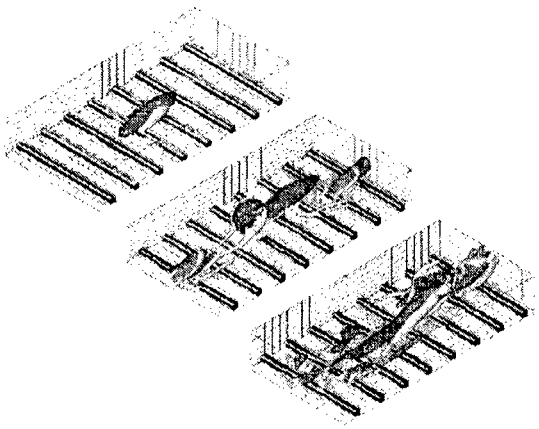


Figure 10. Evolution of a hairpin vortex initially introduced in a laminar flow having velocity distribution of a turbulent flow, T^+ =0, 120, 240. Light color : $Q^+ > 0.0001$, Dark color : $u' < -2$

Visualization of the small-scale coherent vortices demonstrates diversity of vortices. In the region over the top of roughness element, it seems that vortex generation is strongly associated with the flow separation at the upstream corners of roughness elements, *via* a shedding of strong vortex sheets. However, complexity of flow structure does not allow us to trace the evolution of vortices. Therefore, to investigate the fundamental process of vortex formation, an evolution of a single hairpin vortex is traced by conducting numerical simulation in which a laminar flow having mean flow distribution of turbulent flow is assumed and small eddy is introduced in it at an initial time. The introducing baby eddy can be extracted by LSE as proposed by Zhou *et al.*(1996). Figures 10 show the evolution for the non-dimensional time $T^+(= T\bar{u}_\tau^4/\nu^2) = 0, 120, 240$ and depict iso-surfaces of Q^+ and low-speed streaks. The vortex introduced initially is a pair of small quasi-streamwise vortices. At the beginning, the quasi-streamwise vortices grows quickly to a hairpin vortex and extends to further away from the wall. At $T^+ = 120$, the secondary hairpin vortex is born newly at the upstream of primary hairpin vortex, *i.e.*, regeneration is confirmed. At $T^+ = 240$, the group of vortices becomes matured and the size of the originally introduced vortex becomes larger than half width of the channel. Qualitatively, the evolution of vortices in the upper layer from the wall is similar to that of smooth wall case simulated in the previous work (Zhou *et al.*1996,1999 ; Miyake *et al.*, 2000). However, in the layer closest to the wall, a distinct pattern of vortex generation appears. In the smooth wall case, though not shown here, a lot of quasi-streamwise vortex are generated over the flat wall, most probably forming a vortex group. In rough wall case, instead of

such a group of quasi-streamwise vortices around the legs of primaly hairpin vortex, vortex shedding at the upstream corner of roughness elements occurs induced by the vortical flow from upper layer. Although the ordinary regeneration process of smooth wall flow are destroyed in rough wall flow, strong vorticity from not random but fixed position associated with roughness supplements the loss and maintain turbulence. This characterizes the rough-wall turbulence as an alternative way of generating vortices, suggesting that regeneration of quasi-streamwise vortices by themselves is not always unique process.

4. Conclusions

1. The turbulence property normally found in the layer away from the wall prevails close to the wall and large-scale streaks comes closer to the wall. It is suggested that a large-scale mixing takes place over the roughness.
2. The major effect of roughness element is to modify the mechanism of turbulent mixing. Modulation of attitude angle of vortex which is tilted upward from the wall is the key factor in enhancing mixing in near-wall layer over the roughness.
3. On the observation of simplified simulation and the visualized instantaneous flow field of full simulation, further away from the wall, the mechanism of generation of coherent vortices is similar to that of smooth wall case. Closer to the top of roughness, however, quasi-streamwise vortices are not observed. The vortex sheet shedding at the upstream corner of roughness causes the vortex generation. Thus in rough-wall flow, regeneration process of the quasi-streamwise vortices by themselves is suppressed.

References

1. Adrian,R.J. and Moin,P., 1988, "Stochastic estimation of organized turbulent structure: Homogeneous shear flow", *J.Fluid Mech.*, *190*, pp.531-559.
2. Goldstein, D., Handler, R. and Sirovich, L. , 1995 , Direct numerical simulation of turbulent flow over a modeled riblet covered surface. *J. Fluid Mech.*, **302**, 598-606
3. Miyake, Y., Tsujimoto, K. and Agata, Y. , 1999 , A DNS of a turbulent flow in a rough-wall channel using roughness elements model. *JSME Intern.J.*, **43**-2, 233-242
4. Miyake, Y., Tsujimoto, K., Sato, N. and Suzuki, Y. , 2000 , Turbulence Property in the Near-Wall Layer. *Trans JSME ,ser* B **66**-650, 2585-2592 (in Japanese)
5. Raupach, M.R., Antonia, R.A. and Rajagopalan, S. , 1991 , Rough-wall boundary layers. *Appl.Mech.Rev.*, **44**-1, 1-25
6. Zhou,J., Adrian,R.J. and Balanchandar,S., 1996, "Autogeneration of near-wall vortical structures in channel flow", *Phys.Fluids*, **8**-1, pp.288-290.
7. Zhou,J., Adrian,R.J., Balachandar,S. and Kendall,T.M., 1999, "Mechanism for generating coherent packets of hairpin vortices in channel flow", *J.Fluid Mech.*, **387**, pp.353-396.

PARTICLE DISPERSION IN INHOMOGENEOUS TURBULENT FLOW

M.P.B. VEENMAN, J.G.M. KUERTEN AND J.J.H. BROUWERS
Department of Mechanical Engineering
Eindhoven University of Technology, The Netherlands

Abstract

A DNS code based on a spectral-element method is developed. The code is applied to calculate Eulerian space-time velocity correlation functions and to study the possibility to describe the dispersion of particles by a Langevin equation for particle velocity. The preliminary results indicate that it is possible to derive the damping coefficients from the correlation functions.

1. Introduction

Particle dispersion can be described by a Langevin equation, but there is no unique way to determine the coefficients in this equation for inhomogeneous flow. A recently developed theory (Brouwers [1]) predicts that these coefficients are related to the Eulerian space-time correlation function in a moving frame. The frame is moved in time with the local average fluid velocity.
The outline of this paper is as follows. In section 2 the numerical methods for the continuum phase and particles are considered. Next, in section 3 the stochastic theory is explained. Then some preliminary results will be presented and discussed in section 4. Finally, the conclusions are made.

2. Numerical Method

2.1. CONTINUUM PHASE

In this section the numerical method used for DNS of turbulent flow in a cylindrical pipe will be described. The equations to be solved are the Navier-

Stokes equations and continuity equation for incompressible flow. Because of the cylindrical geometry the choice for cylindrical coordinates and cylindrical velocity components is natural. Used are r, ϕ and z for the radial, tangential and axial coordinates and u_r, u_ϕ and u_z for the corresponding velocity components. Then the governing equations can be written in the form:

$$\frac{1}{r}\frac{\partial}{\partial r}(ru_r) + \frac{1}{r}\frac{\partial u_\phi}{\partial \phi} + \frac{\partial u_z}{\partial z} = 0 \tag{1}$$

$$\begin{cases} \dfrac{\partial u_r}{\partial t} + \omega_\phi u_z - \omega_z u_\phi + \dfrac{\partial P}{\partial r} = \dfrac{2}{Re}\left(\Delta u_r - \dfrac{u_r}{r^2} - \dfrac{2}{r^2}\dfrac{\partial u_\phi}{\partial \phi}\right) \\ \dfrac{\partial u_\phi}{\partial t} + \omega_z u_r - \omega_r u_z + \dfrac{1}{r}\dfrac{\partial P}{\partial \phi} = \dfrac{2}{Re}\left(\Delta u_\phi - \dfrac{u_\phi}{r^2} + \dfrac{2}{r^2}\dfrac{\partial u_r}{\partial \phi}\right) \\ \dfrac{\partial u_z}{\partial t} + \omega_r u_\phi - \omega_\phi u_r + \dfrac{\partial P}{\partial z} = \dfrac{2}{Re}\Delta u_z + f \end{cases} \tag{2}$$

Here t denotes time, ω_r, ω_ϕ and ω_z are the cylindrical components of the vorticity, Δ is the Laplace operator and the total pressure P is defined as $P = p + \mathbf{u}^2/2$, where p is the static pressure. The forcing term f is adjusted each time step to ensure a constant mass flow through the pipe demanding

$$f = -\frac{4}{Re}\left.\frac{\partial \overline{u}_z}{\partial r}\right|_{r=R}.$$

The equations have been non-dimensionalized by the radius of the pipe R, the kinematic viscosity ν and the bulk velocity u_B. The Reynolds number is defined as $Re = u_B D/\nu$ where D is the diameter of the pipe.

A finite part of a cylindrical pipe of length L is considered, using periodic boundary conditions in the axial direction. Combined with the natural periodicity in the tangential direction there are two periodic directions and the choice for a spectral method is obvious. In the radial direction an expansion based on Chebyshev polynomials is used. However, the distribution of the Gauss-Lobatto collocation points leads to very small cells near the pipe axis and thus necessitates the use of very small time steps. Therefore, the radial direction is divided into several elements and in each element an expansion into Chebyshev polynomials is adopted. At the interfaces between the elements the solution is required to be C^1. Each component of the solution is thus expanded as:

$$u(r,\phi,z) = \sum_{k_\phi=-M_\phi/2+1}^{M_\phi/2-1} \sum_{k_z=-M_z/2+1}^{M_z/2-1} \tilde{u}_{k_\phi,k_z}(r)\exp(ik_\phi\phi + 2\pi i k_z z/L).$$

In this way a hybrid method appears: Fourier-Galerkin in the two periodic directions and Chebyshev-collocation in the radial direction. Derivatives in the periodic directions can easily be calculated in spectral space, whereas derivatives with respect to r follow from the Chebyshev derivative matrix, see [5]. The reduction on the time step is alleviated further by applying 'mode-reduction' in the central element, i.e. the element near the pipe-axis. Here, only half of the available modes are solved, see e.g. [6]. For these modes the boundary conditions for the velocity and pressure at $r = 0$ are translated to the element interface.

The Navier-Stokes equations are integrated in time using a time-splitting method by [4]. We write the Navier-Stokes equations schematically as

$$\frac{\partial \boldsymbol{u}}{\partial t} + \boldsymbol{N}(\boldsymbol{u}) + \nabla P = \boldsymbol{L}(\boldsymbol{u}) + \boldsymbol{f},$$

where $\boldsymbol{N}$ denotes the nonlinear terms on the left-hand side of (2), $\boldsymbol{L}$ the viscous terms on the right-hand side and $\boldsymbol{f}$ the forcing term. A second-order accurate time-splitting method with constant time step Δt is then given by

$$\begin{cases} \boldsymbol{u}^{n+1/3} = 2\boldsymbol{u}^n - \frac{1}{2}u^{n-1} - \Delta t(2\boldsymbol{N}(\boldsymbol{u}^n) - \boldsymbol{N}(\boldsymbol{u}^{n-1})) + \Delta t\boldsymbol{f} \\ \Delta P^{n+1} = \frac{1}{\Delta t}\nabla \cdot \boldsymbol{u}^{n+1/3} \\ \boldsymbol{u}^{n+2/3} = \boldsymbol{u}^{n+1/3} - \Delta t \nabla P^{n+1} \\ \boldsymbol{u}^{n+1} = \frac{2}{3}u^{n+2/3} + \frac{2}{3}\Delta t\boldsymbol{L}(\boldsymbol{u}^{n+1}). \end{cases} \tag{3}$$

In these formulas the superscript denotes the time level. In the first step the nonlinear terms are treated explicitly. The products of vorticity and velocity are calculated in a pseudo-spectral way, where fast-fourier transforms are used to transform from spectral to physical space. Note that the nonlinear terms have to be calculated only once per time step. The latest result is stored and used again in the next time step. Aliasing is prevented by the 3/2-rule.

In the second step a Poisson equation is solved for the pressure to ensure that the solution after the third step satisfies the continuity equation. A point that requires special attention in this step is the boundary condition for the pressure at the wall of the pipe. Following [4] we employ at $r = R$

$$\frac{\partial P^{n+1}}{\partial r} = -\frac{2}{Re}\left(\frac{1}{r}\frac{\partial^2 u_\phi^{n+1}}{\partial r \partial \phi} + \frac{\partial^2 u_z^{n+1}}{\partial r \partial z}\right),$$

where the solution at the new time level is found by linear extrapolation from the solution at the two previous time levels. In order to obtain a unique solution this boundary condition cannot be used for the $(k_\phi, k_z) = (0, 0)$ mode. Instead the mean pressure at the wall of the pipe is prescribed.

In the final step the linear, viscous terms in the Navier-Stokes equations are treated implicitly. In cylindrical coordinates the viscous parts of the equations for u_r and u_ϕ are coupled, but they can be decoupled by introducing $u_\pm = u_r \pm i u_\phi$. Moreover, the equations for the Fourier modes are completely decoupled, so that a one-dimensional equation for each Fourier mode and each velocity component results. These one-dimensional problems are solved by a direct method. At the wall of the pipe a no-slip boundary condition is applied. At the pipe axis the boundary conditions follow from the requirement that the Cartesian velocity components are regular. This results in $\tilde{u}_z = 0$ for $k_\phi \neq 0$, $\partial \tilde{u}_z / \partial r = 0$ for $k_\phi = 0$, $\tilde{u}_\pm = 0$ for $k_\phi \neq \mp 1$ and $\partial \tilde{u}_\pm / \partial r = 0$ for $k_\phi = \mp 1$.
The calculation is started from a random field superposed on an approximate mean field with the axial velocity component given by a logarithmic velocity profile. The random field is chosen in such a way that it satisfies the continuity equation and that the lowest four Fourier modes in both periodic directions are unequal to zero. In the first time step scheme (3) cannot be applied since only one field is available. A first-order time-splitting scheme is used instead. After a large number of time steps a state of fully-developed turbulence is reached. From that time onwards averaged flow quantities can be calculated.

2.2. FLUID PARTICLES

Fluid particles, e.g. particles without inertia, are tracked using this code. The differential equation for the position of such a particle is given by

$$\frac{d\boldsymbol{x}_i}{dt} = \boldsymbol{u}(\boldsymbol{x}_i, t), \tag{4}$$

where $\boldsymbol{x}_i$ is the particle position of particle i and $\boldsymbol{u}$ are the three components of the particle velocity derived at the particle position. There are several methods to obtain the particle velocity in the interior of a grid cell. A very accurate method is direct summation of the Fourier series expansion, but this is prohibitively expensive. Linear interpolation gives reasonable results for the velocity, but derivatives of the velocity will be very inaccurate. Alternatively, Hermite interpolation in the radial direction and a fourth order accurate Lagrange interpolation scheme in the periodic directions are used, see [7]. This is done in physical space, since the solution is known there each time step to calculate the nonlinear term. An Euler-forward or 2-stage Runge-Kutta method is used to solve eq. (4) numerically and obtain the new particle position. If a particle leaves the computational domain through the axial boundary the periodicity of the velocity is used to determine its velocity. If a particle leaves the pipe at the outer wall it is reintroduced, using an elastic collision with the wall.

3. Stochastic Approach

3.1. DNS

With this code Eulerian space-time velocity correlation functions are calculated. These are defined as

$$R_{ii}(r,\tau) = \overline{u_i'(r,\phi,z,t)u_i'(r,\phi,z+\overline{u_z}(r)\tau,t+\tau)}, \tag{5}$$

where the overhead bar means time- or ensemble-average, u_i are the fluctuating parts of the three velocity components and τ is the time separation. Since ϕ and z are coordinates in homogeneous directions and the turbulence is stationary, the correlation function depends only on r and τ. As can be seen from eq. (5) the frame is moved in streamwise direction with the local average axial velocity. The Fourier transform of eq. (5) gives the spectral density function for the velocity.

3.2. LANGEVIN MODEL

The Langevin equation for particle velocity can be written as (see e.g. Borgas [2] and Wilson & Sawford [3])

$$\dot{v}' + \tau_s^{-1}v' = (C_0\epsilon)^{1/2}w_1(t), \tag{6}$$

where C_0 is the universal Kolomorov constant, ϵ the mean rate of energy dissipation ,$w_1(t)$ a white-noise term and τ_s the correlation time. The damping coefficient in the Langevin equation corresponds to the correlation time τ_s of the Eulerian correlation function. The determination of τ_s from the correlation function is not a trivial process, since several time scales determine the shape of this function. The smallest scales cause the zero-slope at $\tau = 0$. For high Re-numbers this effect decreases and the correlation function could be described by a single exponential function from which the correlation time can easily be determined. However, in our simulations of moderate Re-numbers a separation of time scales is used. This enables us to quantify the small scale effects.

To model the second (small) time scale, smoothing of white-noise is applied (see e.g. Stratonovic [8]), i.e. the rhs of eq. (6) is replaced by the random process $\zeta(t)$ which obeys the equation

$$\tau_\eta\dot{\xi} + \xi = (C_0\epsilon)^{1/2}w_2(t), \tag{7}$$

where τ_η is the Kolmogorov time-scale and $w_2(t)$ another white-noise term. The resulting spectral density of the particle velocity is

$$S_V(\omega) = \frac{C_0\epsilon}{(1+\tau_\eta^2\omega^2)(\tau_s^{-2}+\omega^2)} \tag{8}$$

The white-noise from the original Langevin equation (eq. 6) is no longer lumped into a delta-correlated process. By decreasing the order of the white-noise, viz. applying eq. (7), the real turbulent process is more accurately described. The process is divided into 2 time scales. If $Re \to \infty$, $\tau_\eta \to 0$ and the original Langevin equation is obtained again. In real flows the Reynolds number is never infinite, so *smoothing the white-noise* is a more realistic approach. The corresponding correlation function is the Fourier transform of eq. (8) and reads

$$\overline{v(0)v(t)} = \frac{\sigma_v^2}{1-\frac{\tau_\eta}{\tau_s}}\left(e^{-\frac{t}{\tau_s}} - \frac{\tau_\eta}{\tau_s}e^{-\frac{t}{\tau_\eta}}\right), \tag{9}$$

where the standard deviation σ_v is given by

$$\sigma_v^2 = \frac{1}{2}C_0\frac{\epsilon\tau_s}{(1+\frac{\tau_\eta}{\tau_s})} \tag{10}$$

The spectral density function for the acceleration, $S_A(\omega)$, can be obtained by multiplying eq. (8) with ω^2.

4. Results

The investigated Reynolds number equals 5300 based on the bulk velocity. The number of Fourier-modes in tangential and axial directions equal resp. 128 and 128. 5 Chebyshev elements are used which contain 28, 28, 21, 28 and 7 collocation points resp., where the element near the pipe axis has 7 collocation points. The code has been extensively tested and compared with DNS and experimental results of others ([6], [9], [10] and [11]). The investigated results, e.g. rms of velocity fluctuations, pressure- and vorticity fluctuations, 2-point velocity spectra and the components of the turbulent kinetic energy equation, are in good agreement. These quantities are merely used to check our code and hence the results are not displayed here.
Some preliminary results on particle dispersion will be discussed now. Special emphasis is put on the tangential velocity component. Due to the symmetry of the flow, the Langevin for this component is decoupled from the axial and radial components which are coupled. So, the tangential direction is a truly homogeneous direction.
Figure 1 shows the Eulerian correlation function for the tangential component, denoted by the solid line, at $r/R = 0.4$. Least-Square-Fitting this result to eq. (9), using τ_c and τ_η as fitting parameters, gives the dashed line as shown in figure 1. This indicates that the assumption of two separate time scales is justified and that this simple model is capable to describe the Eulerian statistics. The correlation function from the DNS, see figure

1, is Fourier transformed to obtain the velocity spectrum, $S_V(\omega)$. For the model eq. (8) can be used. Figure 1 shows the results in *log-log* scale and in figure 2 a linear scale is used. Multiplying these spectra with ω^2 gives the acceleration spectrum as indicated in figure 2. The reciprocal calculated values for τ_η and τ_c are also shown (arrows). The time scales are separated by approximately a factor 10. In the limiting process, where $\tau_\eta \to 0$, the spectrum for the acceleration goes to a constant value (dashdot). This is the true *white-noise approximation.* The actual DNS results are far from this limiting process. Still, by using a relatively simply model, a quantification of the 2 time-scales is possible. In the near future we will analyze the remaining radial and axial directions in the same way, in order to obtain all (damping) coefficients for the 3D Langevin equation. The result will be an *accurate* particle dispersion model for inhomogeneous turbulent flow. It also enables us to calculate the universal Kolmogorov constant C_0.

5. Conclusions

A spectral DNS code is developed to calculate the turbulent flow in a cylindrical geometry. Calculated averaged quantities are in good agreement with DNS and experimental results by others. Eulerian space-time velocity correlations, calculated with this code, can be modeled with a Langevin equation. In this way it is possible to derive the damping coefficients for this equation. Due to the relatively moderate Re-number employed, the white-noise approximation is not obtained.

References

1. Brouwers J.J.H., On Diffusion Theory of Stochastic Inhomogeneous Turbulence, *To be published.*
2. Borgas, M.S. and Sawford B.L., A Family of Stochastic Models for Two-Particle Dispersion in Isotropic Homogeneous Stationary Turbulence, *J. Fluid. Mech*, **279**, 69-99, 1994.
3. Wilson, J.D. and Sawford, B.L., Review of Lagrangian Stochastic Models for Trajectories in the Turbulent Atmosphere, *Bound. Lay. Met.*, **78**, 191-210, 1996.
4. Karniadakis, G.E., M. Israeli, and S.A. Orszag, High-order splitting methods for the incompressible Navier-Stokes equations, *J. Comp. Phys.*, **97**: 414-443, 1991
5. Canuto, C., M.Y. Hussaini, A. Quarteroni, and T.A. Zang, *Spectral methods in fluid dynamics*, Berlin, Springer-Verlag, 1988.
6. Loulou, P., *Direct Numerical Simulation of Incompressible Pipe Flow Using a B-Spline Spectral Method*, Ph.D. Thesis, Stanford University, Department of Aeronautics and Astronautics, 1996.
7. Balachandar, S., Maxey, M.R., Methods for Evaluating Fluid Velocities in Spectral Simulation of Turbulence, *J. Comp. Phys.*, **83**, 96-125, 1989.
8. Stratonovich, R.L., *Topics in the Theory of Random Noise*, Gordon and Breach, New York, 1967.
9. Eggels, J.G.M., Unger, F., Weiss, M.H., Westerweel, J., Adrian, R.J., Friedrich, R., Nieuwstadt, F.T.M., Fully Developed Turbulent Pipe Flow: a Comparison Between

Direct Numerical Simulation and Experiment, *J. Fluid. Mech*, **268**, 175-209, 1994.
10. Wagner, C., Hüttl, T.J., Friedrich, R., Low-Reynolds-Number Effects Derived from Direct Numerical Simulations of Turbulent Pipe Flow, *Computers & Fluids*, **30**, 581-590, 2001.
11. Westerweel, J., Draad, A.A., Hoeven, van der J.G.Th, Oord, van J., Measurement of Fully-Developed Turbulent Pipe Flow With Digital Particle Image Velocimetry, *Experiments in Fluids*, **20**, 165-177, 1996.

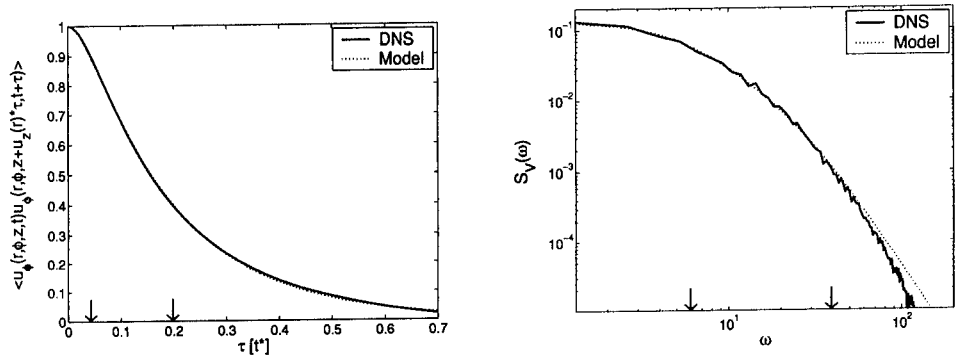


Figure 1. Left: The Eulerian Space-Time correlation function for the tangential velocity component; solid: DNS, dashed: Model. Right: Velocity spectrum; solid: DNS, dashed: Model. In both figures the arrows represent the calculated time-scales.

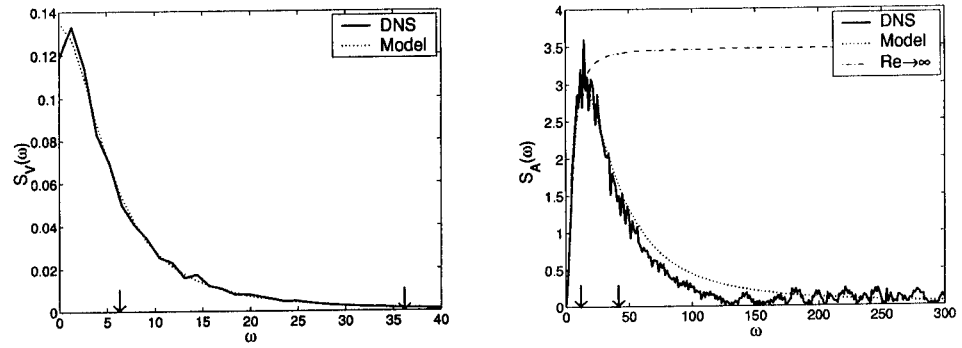


Figure 2. Left: Velocity spectrum; solid: DNS, dashed: Model. Right: Acceleration spectrum; solid: DNS, dashed: Model, dashdot: white-noise approximation. In both figures the arrows represent the calculated time-scales.

DNS OF MULTIPLICITY AND STABILITY OF MIXED CONVECTION IN ROTATING CURVED DUCTS

LIQIU WANG AND TIANLIANG YANG
Department of Mechanical Engineering
The University of Hong Kong, Hong Kong

Abstract. A numerical study is made on the fully-developed bifurcation structure and stability of the mixed convection in rotating curved ducts with the emphasis on the effect of buoyancy force. The rotation can be positive or negative. The fluid can be heated or cooled. The study reveals the rich solution and flow structures and complicated stability features. One symmetric and two symmetric/asymmetric solution branches are found with seventy-five limit points and fourteen bifurcation points. The flows on these branches can be symmetric, asymmetric, 2-cell and up to 14-cell structures. Dynamic responses of the multiple solutions to finite random disturbances are examined by the direct transient computation. It is found that possible physically realizable fully-developed flows evolve, as the variation of buoyancy force, from a stable steady multi-cell state at a large buoyancy force of cooling to the co-existence of three stable steady multi-cell states, a temporal periodic oscillation state, the co-existence of periodic oscillation and chaotic oscillation, a chaotic temporal oscillation, a subharmonic-bifurcation-driven asymmetric oscillating state, and a stable steady 2-cell state at large buoyancy force of heating.

1. Introduction

We study the fully-developed bifurcation-driven multiplicity and dynamic responses of multiple solutions to finite random disturbances numerically by the finite-volume/Euler-Newton continuation and the direct transient computation for the mixed convection in ducts of square cross-section with the streamwise curvature, the spanwise rotation in either positive or negative direction, and the wall heating/cooling [Fig. 1 with (R, Z, φ) as the radial, spanwise and streamwise directions, respectively]. A positive rotation

gives rises to a Coriolis force in the cross plane (RZ-plane) directed along positive R-direction and vice versa. Such flows and transport phenomena find their application in sedimentation field-flow fractionation, aerosol centrifuges, rotating power machinery, rotating heat exchangers, centrifugal material processing and material quality control, medical and chromatographic devices, etc.

Early works on the rotating curved duct flows were constrained to two simplified limiting cases with strong or weak rotations. Ludwieg (1951) developed a solution based on a momentum integral method for the isothermal flow in a square duct with a strong spanwise rotation. Miyazaki (1971, 1973) examined the mixed convection in a curved circular/rectangular duct with spanwise rotation and wall heating by a finite difference method. Because of the convergence difficulties with the iterative method used, Miyazaki's work was constrained to the case of weak curvature, rotation and heating rate. As well, all the works employ a steady model for the fully developed laminar flow with a positive rotation of the duct. Since the solution is only for the asymptotic cases, the secondary flow revealed by these early works consists of only one pair of counter-rotating vortices in the cross-plane. The interaction of the secondary flow with the pressure-driven streamwise flow shifts the location of the maximum streamwise velocity away from the center of the duct and in the direction of the secondary velocity in the middle of the duct.

More comprehensive studies have been made in recent years by Wang & Cheng (1996a) and Daskopoulos & Lenhoff(1990) for a circular tube, Matsson & Alfredsson (1990, 1994) and Guo & Finlay (1991) for a high-aspect-ratio rectangular duct, and Wang & Cheng (1995, 1996b, 1997, 2001), Wang (1997a, b, 1999), Selmi *et al.*(1994) and Selmi & Nandakumar (1999) for the square and rectangular ducts with a low-aspect-ratio. All the works are for the steady fully developed flows. Wang & Cheng (1996a) developed an analytical solution for rotating curved flow with effect of heating or cooling which allows to analyze the solution structure. Detailed flow structures and heat transfer characteristics were examined numerically by Wang & Cheng (1996b) and Wang (1997a, b, 1999). The rotating curved flows were visualized using smoke injection method by Wang & Cheng (1995, 1997, 2001). Daskopoulos & Lenhoff (1990) made the first bifurcation study numerically under the small curvature and the symmetry condition imposed along the tube horizontal central plane. Matsson & Alfredsson (1990) presented the first and comprehensive linear stability analysis. Matsson & Alfredsson (1994) reported an experimental study, by hot-wire measurements and smoke visualization, of the effect of rotation on both primary and secondary instabilities. Using a linear stability theory and spectral method, Guo & Finlay (1991) examined the stability of streamwise oriented vortices

to 2D, spanwise-periodic disturbances (Eckhaus stability). Detailed bifurcation structure and linear stability of solutions was determined numerically by Selmi *et al.* (1994) and Selmi & Nandakumar (1999) without imposing the symmetric boundary conditions.

It is the *relative* motion between bodies that determines the performances such as friction and heat transfer characteristics. The duct rotation introduces both centrifugal and Coriolis forces in the momentum equation describing the *relative* motion of fluids with respect to the duct. For isothermal flows of a constant property fluid, the Coriolis force tends to produce vorticity while the centrifugal force is purely hydrostatic, analogous to the Earth's gravitational field (Wang 2001). When a temperature-induced variation of fluid density occurs for non-isothermal flows, both Coriolis and centrifugal-type buoyancy forces could contribute to the generation of the vorticity (Wang 2001). These two effects of rotation either enhance or counteract each other in a nonlinear manner depending on the direction of duct rotation, the direction of wall heat flux and the flow domain. As well, the buoyancy force is proportional to the square of the rotation speed while the Coriolis force increases proportionally with the rotation speed itself (Wang 1997b). Therefore, the effect of system rotation is more subtle and complicated and yields new, richer features of flow and heat transfer in general, the bifurcation and stability in particular, for non-isothermal flows. While some of such new features are revealed by our recent analytical and numerical works (Wang 1997a, b, 1999, Wang & Cheng 1996a, b), there is no known study on the bifurcation and stability of mixed convection in rotating curved ducts.

The present work is a relatively comprehensive study on the bifurcation structure and stability of multiple solutions for the laminar mixed convection in a rotating curved duct of square cross-section (Fig. 1). The governing differential equations in primitive variables are solved for detailed bifurcation structure by a finite-volume/Euler-Newton continuation method with the help of the bifurcation test function, the branch switching technique and the parameterization of arc-length or local variable. Transient calculation is made to examine in detail the response of every solution family to finite random disturbances. The power spectra are constructed by the Fourier transformation of temporal oscillation solutions to confirm the chaotic flow. We restrict ourself to the hydrodynamically and thermally fully-developed region and two-dimensional disturbances. So far, a detailed 3D numerical computation of flow bifurcation and stability is still too costly to conduct. A 2D model is still useful for a fundamental understanding of rotating curved duct flows. However, our assumption of fully developed flow limits our analysis to the one preserving the streamwise symmetry. There may be further bifurcation to flows that breaks this symmetry and that

cannot be found in the present work.

2. Governing Parameters and Numerical Algorithm

Consideration is given to a hydrodynamically and thermally fully developed laminar flow of viscous fluid in a square duct with the streamwise curvature, the spanwise rotation, and the wall heating or cooling at a constant heat flux (Fig.1). The geometry is toroidal and hence finite pitch effect is not considered. The rotation can be positive or negative at a constant angular velocity. The duct is streamwisely and peripherally uniformly heated or cooled with a uniform peripheral temperature. The properties of the fluid, with the exception of density, are taken to be constant. The usual Boussinesq approximation is used to deal with the density variation. The gravitational force is negligible compared with the centrifugal and Coriolis forces.

Consider a non-inertial toroidal coordinate system (R, Z, ϕ) fixed to the duct rotating with a constant angular velocity about the $O'Z'$ axis, as shown in Fig. 1. We may obtain the governing differential equations, in the form of primitive variables, governing fully-developed mixed convection based on conservation laws of mass, momentum and energy. The boundary conditions are non-slip and impermeable, streamwise uniform wall heat flux and peripherally uniform wall temperature at any streamwise position. The proper scaling quantities for non-dimensionalization are chosen based on our previous experience (Wang & Cheng 1996b). The formulation of the problem is on full flow domain without imposing symmetric boundary conditions to perform a thorough numerical simulation. The readers are referred to Wang & Cheng (1996b) for the details of mathematical formulation of the problem.

The dimensionless governing equations contain five dimensionless governing parameters: one geometrical parameter σ (the curvature ratio defined by a/R_c , the ratio of duct width/height a over the radius of the curvature R_c, representing the degree of curvature), one thermophysical parameter Pr (the Prandtl number, representing the ratio of momentum diffusion rate to that of the thermal diffusion), and three dynamical parameters Dk, $L1$ and $L2$ defined in Wang & Cheng (1996b). The pseudo Dean number Dk is the ratio of the square root of the product of inertial and centrifugal forces to the viscous force and characterizes the effect of inertial and centrifugal forces. $L1$ represents the ratio of the Coriolis force over the centrifugal force, characterizing the relative strength of Coriolis force over the centrifugal force. $L2$ is the ratio of the buoyancy force over the centrifugal force and represents the relative strength of the buoyancy force. A positive (negative) value of $L1$ is for the positive (negative) rota-

tion. A positive (negative) value of $L2$ indicates the wall heating (cooling). In the present work, we set $\sigma = 0.2$ (typically used in cooling systems of rotor drums and conductors of electrical generators) and $Pr = 0.7$ (a typical value for air) to study the effects of three dynamical parameters on the multiplicity and stability. While results regarding the effects of Dk and $L1$ are also available, we focus on the effects of $L2$ at $Dk = 300$ and $L1 = 28$ in the present paper due to limited space.

The governing differential equations are discretized by the finite volume method to obtain discretization equations. The discretization equations are solved for parameter-dependence of velocity, pressure and temperature fields by the Euler-Newton continuation method with the solution branches parameterized by $L2$, the arc-length or the local variable. The starting points of our continuation algorithms are the three solutions at $Dk = 300$, $L1 = 28$ and $L2 = 0$ from our study of the effects of D_k and $L1$. The bifurcation points are detected by the test function developed by Seydel (1994). The branch switching is made by a scheme approximating the difference between branches proposed by Seydel (1994). The dynamic responses of multiple solutions to the 2D finite random disturbances are examined by the direct transient computation. The readers are referred to Wang & Yang (2001) and Yang & Wang (2000) for the numerical details and the check of grid-dependence and accuracy. The computations are carried out on the Super Computer SP2 of The University of Hong Kong.

3. Results and Discussion

3.1. SOLUTION STRUCTURE

The bifurcation structure is shown in Fig.2 for $L2$ values from -20 up to 70 at $\sigma = 0.02$, $Pr = 0.7$, $Dk = 300$ and $L1 = 28$. In Fig.2, the radial velocity component u at $r = 0.9$ and $z = 0.14$ (where the flow is sensitively dependent on $L2$; $r = R/a$ and $z = Z/a$) is used as the state variable, enabling the most clear visualization of all solution branches. Three solution branches, labeled by $AS1$, $AS2$ and $S3$ respectively, are found. Here, S stands for symmetric solutions with respect to the horizontal central plane $z = 0$, and AS indicates that the branch has both symmetric and asymmetric solutions.

Branch $AS1$ has sixty-nine limit points labeled by $AS1^1$ to $AS1^{69}$, eleven bifurcation points connecting its sub-branches denoted by $AS1^{AS1-1}$ to $AS1^{AS1-11}$, two bifurcation points connecting itself to $AS2$ labeled by $AS1^{AS2-1}$ and $AS1^{AS2-1}$, and one bifurcation point connecting itself to $S3$ denoted by $AS1^{S3}$. Branch $AS2$ has four limit points labeled by $AS2^1$ to $AS2^4$. Branch $S3$ is a symmetric solution branch and has two limit points $S3^1$ and $S3^2$. The location of fourteen bifurcation points and seventy-five

limit points is available in Yang (2001). To visualize the details of branch connectivity and some limit/bifurcation points, the locally enlarged state diagrams are also shown in Fig. 2. As Fig. 2 is only 1D projection of 12400 dimensional solution branches, all intersecting points except fourteen bifurcation points should not be interpreted as connection points of branches.

For a large $\mid L2 \mid$ value ($L2 \leq -14.5$ or $L2 \geq 63.1$), the buoyancy force dominant the mixed convection. There is unique flow and temperature field for a specified value of $L2$ in these two ranges. Figure 3 illustrates the secondary flow patterns, the streamwise velocity profiles and temperature profiles at $L2 = -17$ and $L2 = 65$, respectively. In the figure, the stream function, streamwise velocity and temperature are normalized by their corresponding maximum absolute values $\mid \psi \mid_{max}$, w_{max} and t_{max}. A vortex with a positive (negative) value of the secondary flow stream function indicates a counter-clockwise (clockwise) circulation. The readers are referred to Wang & Cheng (1996b) for a detailed discussion of the flow structures shown in Fig.3 in general, their relations with physical mechanisms and driving forces and their effects on the flow resistance and heat transfer in particular.

For a $L2$ value in $-14.5 < L2 < 63.1$, however, we can have multiple solutions. Figure 4 shows typical secondary flow patterns of six solutions (thirty-nine solutions in total) at $L2 = -11.7$. It is observed that the nonlinear competition of driven forces leads to not only a rich solution structure but also complicated flow structures. Therefore, the mixed convection in rotating curved ducts is much more complicated than that available in the literature.

3.2. STABILITY OF MULTIPLE SOLUTIONS

Recognizing that there is no study on dynamic responses of multiple solutions to finite random disturbances in the literature, a relatively comprehensive transient computation is made to examine the dynamic behavior and stability of typical steady solutions with respect to four sets of finite random disturbances with $d = 4\%, 10\%$, 15% and 40% respectively. Here, d is the maximum percentage of disturbing value over the steady value (Wang & Yang 2001).

Seven sub-ranges are identified with each having distinct dynamic responses to the finite random disturbances. The first ranges from $L2 = -20$ to $L2 = -14.5$, where the finite random disturbances lead all steady solutions at any fixed $L2$ to a steady symmetric multi-cell state on $AS1_a$ with the same $L2$. The second covers the range $-14.5 < Dk \leq -13.6$ where there is co-existence of three stable steady symmetric multi-cell states. In the third sub-range $-13.6 < L2 \leq 12.1$, all steady solutions evolve to

a temporal periodic solution. The fourth sub-range is from $L2 = -12.1$ to $L2 = -11.5$ where the solutions response to the finite random disturbances in the form of either periodic oscillation or chaotic oscillation. There is the co-existence of periodic and chaotic oscillations. In the fifth sub-range $-11.5 < L2 \leq -10.5$, all steady solutions evolve to a temporal chaotic solution. The next sub-range $-10.5 < L2 \leq -10.2$ serves as a transition between the chaotic oscillation and the stable steady 2-cell flow. The solutions response to the finite random disturbances in the form of subharmonic-bifurcation-driven asymmetric oscillation. In the last sub-range $L2 > -10.2$, the finite random disturbances lead all steady solutions at any fixed $L2$ to a stable steady symmetric 2-cell state on $AS1_s$ with the same $L2$. A detailed discussion of stability features can be found in Yang (2001).

4. Concluding Remarks

The governing differential equations from the conservation laws are discretized by the finite volume method to obtain discretization equations, a set of nonlinear algebraic equations. The discretization equations are solved for parameter-dependence of flow and temperature fields by the Euler-Newton continuation with the solution branches parameterized by $L2$, the arclength or the local variable. The bifurcation points are detected by the test function. The branch switching is made by a scheme approximating the difference between branches proposed. One symmetric and two symmetric/asymmetric solution branches are found with fourteen bifurcation and seventy-five limit points. Both solution and flow structures are much more richer than those available in the literature.

The dynamic responses of multiple solutions to the 2D finite random disturbances are examined by the direct transient computation. The finite random disturbances are found to lead the steady solutions to a stable steady multi-cell state in $-20 < Dk \leq -14.5$, the co-existence of three stable steady multi-cell states in $-14.5 < L2 \leq -13.6$, a temporal periodic oscillation in $-13.6 < Dk \leq -12.1$, the co-existence of periodic and chaotic oscillating states in $-12.1 < L2 \leq -11.5$, a chaotic oscillation in $-11.5 < L2 \leq -10.5$, a subharmonic-bifurcation-driven asymmetric oscillation in $-10.5 < L2 \leq -10.2$, and a stable steady 2-cell state in $-10.2 < L2 \leq 70$.

Acknowledgments: The financial support from the Research Grants Council of Hong Kong (HKU7086/00E), the Outstanding Young Researcher Award and the CRCG of the University of Hong Kong to LW is gratefully acknowledged.

References

1. Daskopoulos P. & Lenhoff A. M. 1990 Flow in curved ducts: Part 2 rotating ducts. *J. Fluid Mech.* **217**, 575-593.
2. Guo Y. & Finlay W. H. 1991 Splitting, merging and wavelength selection of vortices in curved and/or rotation duct flow due to Eckhaus instability. *J. Fluid Mech.* **228**, 661-691.
3. Ludwieg H. 1951 Die ausgebildete kanalstrmung in einem rotierenden system. *Ing.-Arch. Bd.* **19**, 296-308.
4. Matsson O. J. E. & Alfredsson P. H. 1990 Curvature- and rotation-induced instabilities in channel flow. *J. Fluid Mech.* **210**, 537-563.
5. Matsson O. J. E. & Alfredsson P. H. 1994 The effect of spanwise system rotation on Dean vortices. *J. Fluid Mech.* **274**, 243-265.
6. Miyazaki H. 1971 Combined free and forced convective heat transfer and fluid flow in a rotating curved circular tube. *Int. J. Heat Mass Transfer* **14**, 1295-1309.
7. Miyazaki H. 1973 Combined free and forced convective heat transfer and fluid flow in a rotating curved rectangular tube. *J. Heat Transfer* **95**, 64-71.
8. Selmi M., Nandakumar K. & Finlay W. H. 1994 A bifurcation study of viscous flow through a rotating curved duct. *J. Fluid Mech.* **262**, 353-375.
9. Selmi M. & Nandakumar K. 1999 Bifurcation study of flow through rotating curved ducts. *Physics of Fluids* **11**, 2030-2043.
10. Seydel, R. 1994 Practical Bifurcation and Stability Analysis: From Equilibrium to Chaos. Springer-Verlag, New York.
11. Wang L. 1997a Buoyancy-force-driven transitions in flow structures and their effects on heat transfer in a rotating curved channel. *International Journal of Heat and Mass Transfer* **40**, 223-235.
12. Wang L. 1997b Effect of spanwise rotation on centrifugal instability in rotating curved non-isothermal flows. *Computational Mechanics* **19**, 420-433.
13. Wang L. 1999 Competition of Coriolis instability with centrifugal instability and its effects on heat transfer. *International Journal of Non-linear Mechanics* **34**, 35-50.
14. Wang L. 2001 Physical Constraints of Turbulence Modeling. Invited book chapter in: New Developments and Perspectives in Turbulence (ed. J. J. Wang et al.), Science, Beijing, 189-207.
15. Wang L. & Cheng K. C. 1995 Flow in curved channels with a low negative rotating speed. *Physical Review E* **51**, 1155-1161.
16. Wang L. & Cheng K. C. 1996a Flow transitions and combined free and forced convective heat transfer in a rotating curved circular tube. *International Journal of Heat and Mass Transfer* **39**, 3381-3400.
17. Wang L. & Cheng K. C. 1996b Flow transitions and combined free and forced convective heat transfer in rotating curved channels: the case of positive rotation. *Physics of Fluids* **8**, 1553-1573.
18. Wang L. & Cheng K. C. 1997 Visualization of flows in curved channels with a moderate or high rotation speed. *International Journal of Rotating Machinery* **3**, 215-231.
19. Wang L. & Cheng K. C. 2001 Visualization of Flows in Channels with Curvature and Rotation. Invited book chapter in: Centrifugal Processing (ed. L. L. Regel & W. R. Wilcox), Kluwer Academic/Plenum Publishers, New York (in press).
20. Wang L. & Yang T. 2001 Bifurcation and stability of forced convection in curved ducts. Communicated to *J. Fluid Mech.*
21. Yang T. 2001 Multiplicity and Stability of Flow and Heat Transfer in Rotating Curved Ducts, PhD thesis, Department of Mechanical Engineering, The University of Hong Kong.
22. Yang T. & Wang L. 2000 Microscale flow bifurcation and its macroscale implications in periodic porous media. *Computational Mechanics* **26**, 520-527.

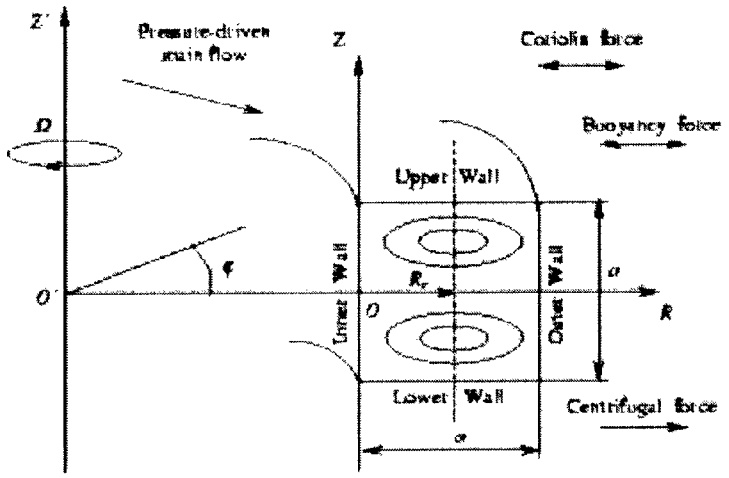
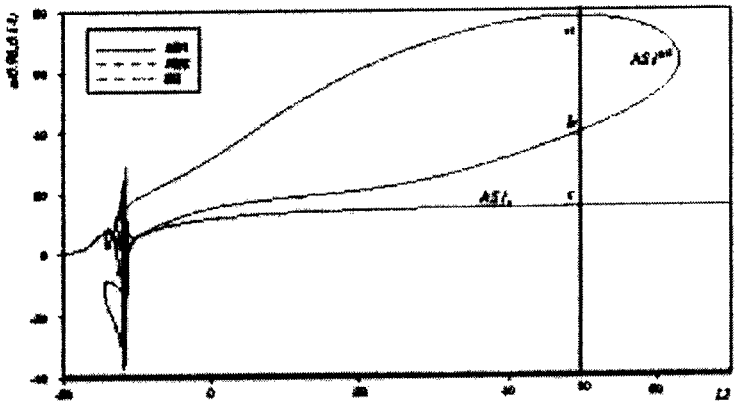
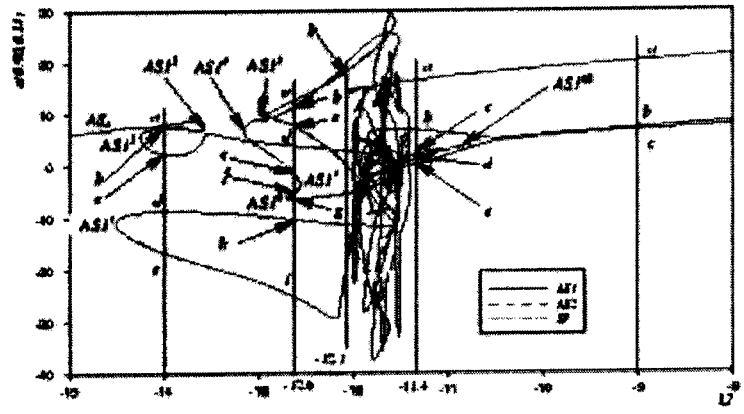


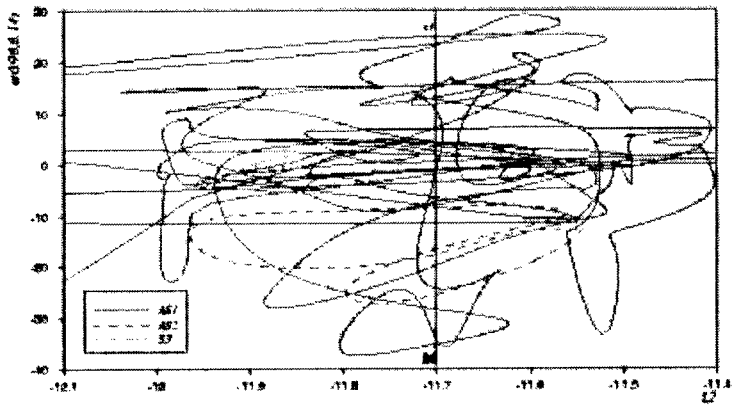
Figure 1. Physical problem and coordinate system



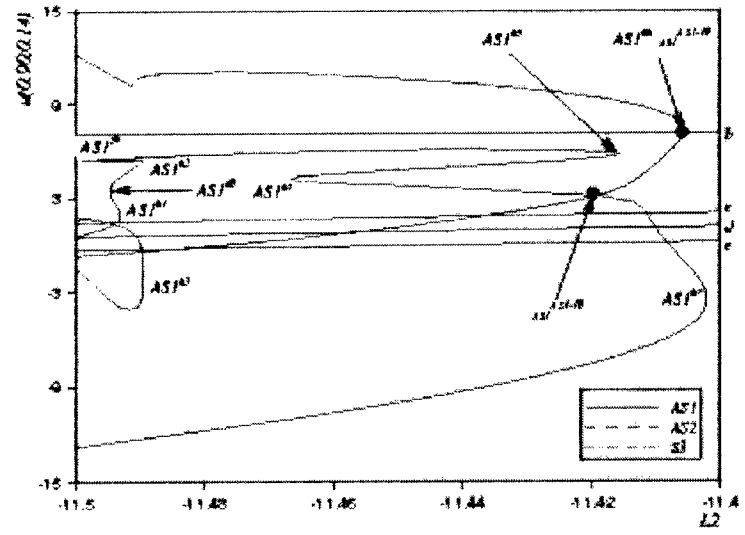
(a) $-20 < L2 < 70$



(b) $-15 < L2 < -8$



(c) $-12.1 < L2 < -11.4$



(d) $-11.5 < L2 < -11.4$

Figure 2. Solution branches and limit/bifurcation points ($\sigma = 0.02$, Pr=0.7, $Dk = 300$ and $L1 = 28$)

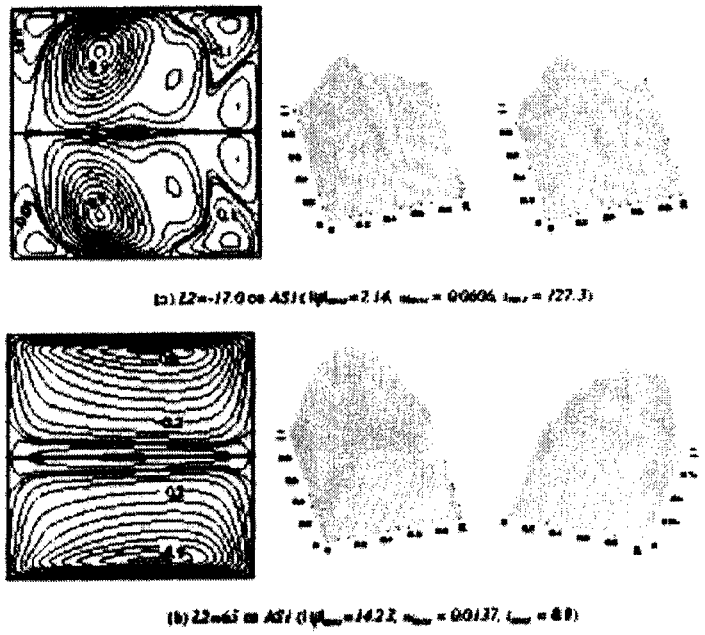


Figure 3. Flow and temperature fields ($\sigma = 0.02$, Pr=0.7, $Dk = 300$ and $L1 = 28$; left: secondary flow, middle: streamwise velocity, right: temperature)

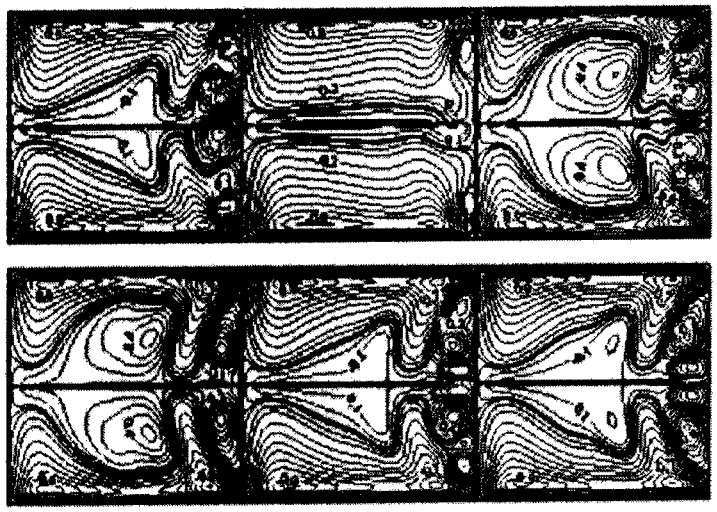


Figure 4. Typical secondary flow patterns of six solutions among thirty-nine solutions at $L2 = -11.7$ ($\sigma = 0.02$, Pr=0.7, $Dk = 300$ and $L1 = 28$)

DIRECT NUMERICAL SIMULATION OF THE FULLY DEVELOPED OPEN-CHANNEL FLOW AT SUBCRITICAL FROUDE NUMBERS

A. NAKAYAMA AND S. YOKOJIMA
Graduate School of Science and Technology, Kobe University
1-1 Rokkodai, Nada, Kobe 657-8501, JAPAN

Abstract. Direct numerical simulation(DNS) of a fully-developed open-channel flow has been carried out for subcritical Froude numbers at a fixed friction-velocity Reynolds number of 180. The free surface is approximated by small-amplitude wave theory. The results are presented emphasizing the effects of the Froude number on turbulence quantities related to the free surface fluctuations. The amplitude of the free-surface fluctuation increases as the square of the Froude number. While statistical quantities involving the vertical velocity component are most influenced by the Froude number but only in the region close to the free surface, quantities related to the pressure fluctuations are influenced over much wider region.

1. Introduction

Turbulent flows in open-channels are important in engineering and environmental applications, but their understanding and prediction are not as satisfactory as those for flows in closed ducts. Turbulence mechanisms near a free surface have been investigated both experimentally and numerically(e.g. Kumar *et al.*, 1998 and Nagaosa, 1999), but no specific methods of modeling in practical engineering calculations are established. It may be noted that the recent advancements of the wall turbulence modeling have been made possible by detailed databases obtained by DNS. DNS for open-channel flows have been reported, but most of these simulations assume that the free surface is a rigid slip surface and its vertical movement is neglected(e.g. Nagaosa, 1999). In the DNS conducted by Komori *et al.*(1993), the Froude number is so small that there are no recognizable differences from the slip-surface flow. Borue *et al.*(1995) applied the linearized free-surface boundary conditions and obtained the dynamics associated with

the turbulence/interface interactions. They did not provide the type of database that would be required to refine and validate turbulence models for open-channel flows. In the present paper, we report the results of DNS of a fully developed turbulent flow in a two-dimensional open channel with deforming free surface approximated by the small-amplitude wave assumption using a finite difference method. We obtain a detailed database of the mean flow and the turbulence quantities for subcritical Froude numbers.

2. Basic Equations and Boundary Conditions

We consider a fully developed incompressible open-channel flow over a flat smooth floor as shown in Fig.1. The governing equations are the Navier-Stokes equations and continuity equation for incompressible fluid with gravitational acceleration g. The boundary conditions are the no-slip condition on the bottom floor($x_2 = 0$), and the free-surface conditions as described in the following. The flow field is supposed to extend infinitely in the streamwise(x_1) and the cross-flow(x_3) directions and the periodic boundary conditions are applied at the boundaries of the finite computational domain. We denote the time mean of instantaneous quantity $\hat{f}$ by $\overline{f}$ or F, the deviation from the mean by f, the root mean square by f^{rms} and the value at $x_2 = a$ by $\hat{f}|_a$. The free surface movement is assumed mild and it can be described by a smooth continuous surface which deforms continuously so that its position can be represented by a single-valued continuous function by $x_2 = \hat{h}(x_1, x_3, t)$. Function $\hat{h}$ satisfies the kinematic condition

$$\frac{\partial \hat{h}}{\partial t} + \hat{u}_1|_{\hat{h}} \frac{\partial \hat{h}}{\partial x_1} + \hat{u}_3|_{\hat{h}} \frac{\partial \hat{h}}{\partial x_3} = \hat{u}_2|_{\hat{h}}, \tag{1}$$

where $\hat{u}_i$ is the instantaneous velocity component in x_i direction. If we assume that the fluid above the free surface has negligible density and the pressure is constant zero, and that the surface tension can also be neglected, the dynamic conditions are that both normal and tangential stresses on the instantaneous free surface are zero. If the displacement of the instantaneous free surface from the mean position and the slopes of the free surface is small, the quantities on it may be replaced by the values on the mean position and the normal and tangential directions may be replaced by the vertical and horizontal directions, respectively, then the first approximation gives

$$\frac{\partial h}{\partial t} + \frac{\partial}{\partial x_1}(\hat{u}_1|_H h) + \frac{\partial}{\partial x_3}(\hat{u}_3|_H h) = \hat{u}_2|_H, \tag{2}$$

$$\nu\left(\frac{\partial \hat{u}_1}{\partial x_2} + \frac{\partial \hat{u}_2}{\partial x_1}\right)\Big|_H = 0, \quad \nu\left(\frac{\partial \hat{u}_3}{\partial x_2} + \frac{\partial \hat{u}_2}{\partial x_3}\right)\Big|_H = 0, \tag{3}$$

$$\hat{P}|_H = -g_2 h + 2\nu \frac{\partial \hat{u}_2}{\partial x_2}\bigg|_H, \tag{4}$$

where $\hat{P} = \hat{p} - g_2 h$, $\hat{p}$ is the instantaneous pressure divided by the density, g_2 is the component of gravitational acceleration in x_2 direction and ν is the kinematic viscosity. Since these boundary conditions are all in terms of the quantities at the mean position of the free surface, the flow calculations can be made with the fixed grid in the region $x_2 < H$.

3. Numerical Methods

The governing equations are solved by a finite difference technique based on the SMAC method on a Cartesian staggered grid. The spatial derivatives are descretized using the second-order conservative difference scheme and time advancing is done by the second-order Adams-Bashforth method. The position of the free surface h is solved by descretizing the spatial derivative terms in Eq.(2) using the fifth-order upwind-shifted interpolation(USI) scheme(Kajishima, 1994) and time advancing by the third-order Adams-Bashforth method. The Poisson equation for pressure is solved by Fourier-transforming the equations in the horizontal directions and the resulting equation is solved by the tri-diagonal algorithm. The calculations were conducted for the Reynolds number Re_τ based on the friction velocity u_τ and the mean flow depth H of 180, which is the same as the closed-channel flow simulation of Moser *et al.*(1999)(MKM) and Yokojima & Nakayama(2000)(YN) for a similar flow with free-slip boundary condition (hereafter referred to as the 'slip channel'). The Froude numbers based on the average velocity and the flow depth are 0.3, 0.6 and 0.9. The number of grid points is 128^3; the spatial resolutions are $\Delta x_1^+ = 9$, $\Delta x_2^+ = 0.27 - 2.71$, $\Delta x_3^+ = 4.5$. Here the superscript $^+$ refers to the nondimensionalized quantities by u_τ and ν. With a time increment of $\Delta t^+ = 0.0114$, about 200,000 time steps are used to obtain the well-converged turbulence quantities averaged over space and time.

4. Results and Discussion

Fig.2 shows properties of the calculated instantaneous flow field for the slip-channel flow at $Fr = 0$ and the present fluctuating free surface computation for $Fr = 0.6$. The figures on the top are the samples of instantaneous flow represented by the iso-surfaces of the streamwise velocity u_1. The instantaneous position of the free surface $\hat{h}$ and the velocity vectors projected in the mean free-surface position are shown in the middle and at the bottom, respectively. The well-known streak structure of the wall turbulence is seen in both cases near the bottom floor and the overall simulation method ap-

pears satisfactory. In $Fr = 0$ case, $\hat{h}$ is not available and the instantaneous pressure at the free surface $\hat{p}|_H$ is shown instead. The surface pressure and h appear to show very a similar trend. The free surface fluctuation and the velocity vectors do not seem to have any prefered directionality and their scales appear to be much larger than the viscous scales of the near-wall flow. These tendencies agree with the results of Thomas & Williams(1995)(TW) who reported preliminary results of a direct simulation using 'volume of fluid' method to track the movement of the free surface. The velocity vectors on the free surface indicate that the flow is generally divergent in the horizontal plane where the upwelling bulges with positive h are seen and convergent in the area the free surface is lower than the average position.

The profiles of computed RMS surface fluctuation are compared with experimental results of Nakayama *et al.*(2000)(EXPN00) and Nakayama (1997)(EXPN97) in Fig.3. The Reynolds numbers of the experiments are indicated in terms of the bulk Reynolds number defined by the average velocity and the mean depth H. It shows that the present DNS results are a little lower than the measurements but show the same increasing trends with respect to Fr and are very close to the results of TW. Though not shown, the computed skewness and flatness factors of h also agree well with those of measurements, which indicates that the small-amplitude approximation used here is appropriate for the DNS of subcritical flows.

Fig.4 shows the computed mean velocity profiles compared with the closed-channel and slip-channel flow simulations. It shows that the velocity profile of the open-channel flow follows the logarithmic distribution up to a point very close to the free surface and it is not influenced very much by the free-surface movements. The distributions of the RMS fluctuations of velocity components and the Reynolds shear stress are shown in Fig.5. It is seen that the distributions of all stress components are very close to the closed-channel results of Moser *et al.*(1999) over most of the channel. The open-channel flow results deviate from the closed channel results in the region $120 < x_2^+ < 180$. Fig.6 is an enlarged plot of $u_2^{\rm rms}$ which is the quantity most sensitively affected by the free surface and Fr. $u_2^{\rm rms}|_H$ increases with roughly square of Fr, which is the same as $h^{\rm rms}$. Fig.7 is a plot of the RMS pressure fluctuation. Unlike the velocity fluctuations, $p^{\rm rms}$ is seen to be influenced by the free surface and the value of Fr throughout the entire channel depth. Since the Reynolds stress component $\overline{u_2^2}$ is most influenced by the Froude number, the terms in the transport equation for this stress are shown in Fig.8. Fig.8(a) is the distribution across the entire channel and Figs.8(b)-(d) show enlarged plots near the free surface for $Fr = 0.3$, 0.6 and 0.9, respectively, each compared with $Fr = 0$ case. It is seen that near the free surface the pressure-strain term, which works like a generation for $\overline{u_2^2}$, drops and the pressure diffusion increases. It is further

seen in the enlarged plots of Figs.8(b)-(d) that the pressure diffusion term changes sharply from loss to gain within about 20 viscous units from the free surface. Its distribution and that of the turbulent diffusion appear to be influenced by Fr over at least upper half of the channel.

5. Conclusions

Direct numerical simulation of a fully developed turbulent flow in a two-dimensional open channel has been successfully performed. The present results with the assumption of small displacement of the free surface from its mean position appear to represent the open-channel flow with subcritical Froude numbers properly, and show the effects due to the moving free surface. Most of the quantities including the mean velocity profiles and the Reynolds stresses in the horizontal directions are not influenced by the free-surface movements. The vertical velocity fluctuation and the pressure fluctuation are the quantities influenced by the free surface. The vertical fluctuation near the free surface increases with Fr in the region very close to the free surface, while the pressure fluctuation is influenced over almost entire depth of the channel. This influence appears to be effected by the readjustment by the pressure diffusion.

References

Borue, V., Orszag, S.A. and Staroselsky, I. (1995) Interaction of surface waves with turbulence: direct numerical simulations of turbulent open-channel flow, *J. Fluid Mech.*, Vol.286, pp.1-23.

Kajishima, T. (1994) Upstream-shifted interpolation method for numerical simulation of incompressible flows, *Trans. JSME B*, Vol.60 No.578, pp.3319-3326 (in Japanese).

Komori, S., Nagaosa, R., Murakami, Y., Chiba, S., Ishii, K. and Kuwahara, K. (1993) Direct numerical simulation of three-dimensional open-channel flow with zero-shear gas-liquid interface, *Phys. Fluids A*, Vol.5 No.1, pp.115-125.

Kumar, S., Gupta, R. and Banerjee, S. (1998) An experimental investigation of the characteristics of free-surface turbulence in channel flow, *Phys. Fluids*, Vol.10 No.2, pp.437-456.

Moser, R.D., Kim, J. and Mansour, N.N. (1999) Direct numerical simulation of turbulent channel flow up to $Re_\tau = 590$, *Phys. Fluids*, Vol.11 No.4, pp.943-945.

Nagaosa, R. (1999) Direct numerical simulation of vortex structures and turbulent scalar transfer across a free surface in a fully developed turbulence, *Phys. Fluids*, Vol.11 No.6, pp.1581-1595.

Nakayama A., Nakase, Y., Yokojima, S. and Fujita, I. (2000) Improvements of two-equation turbulence model with surface fluctuation used as a parameter for calculation of open-channel flows, *J. Applied Mech. JSCE*, Vol.3, pp.745-752 (in Japanese).

Nakayama, T. (1997) Turbulent structures and characteristics of coherent vortices near the free-surface, Master's thesis, Kyoto University (in Japanese).

Thomas, T.G. and Williams, J.J.R. (1995) Turblent simulation of open channel flow at low Reynolds number, *Int. J. Heat Mass Transfer*, Vol.38 No.2, pp.259-266.

Yokojima, S. and Nakayama, A. (2000) Evaluation of turbulence statistics and their budgets in an open-channel flow using direct numerical simulation, *J. Applied Mech. JSCE*, Vol.3, pp.753-762 (in Japanese).

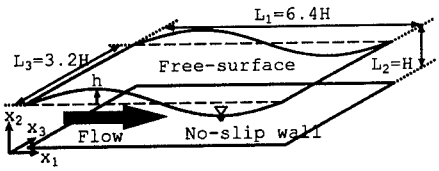
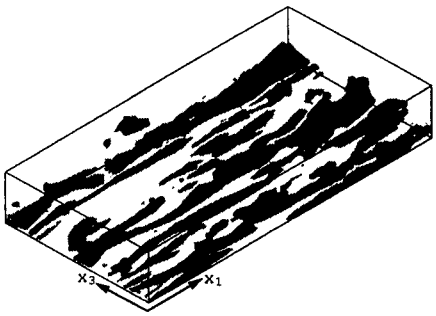
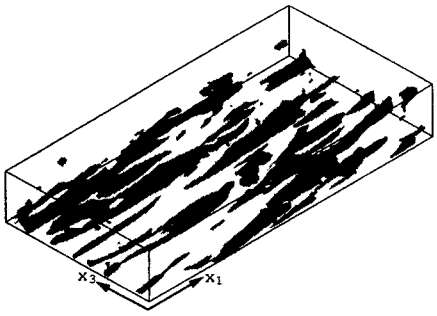


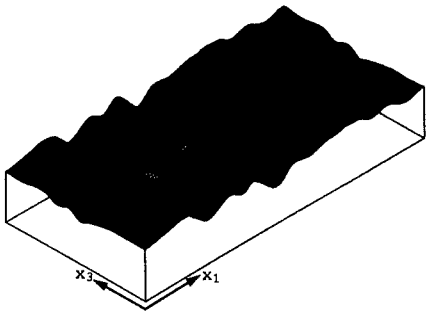
Figure 1. Flow configuration of open-channel flow.



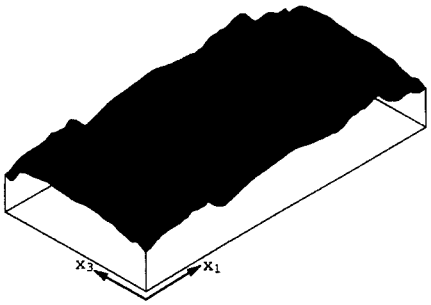
(a) Low-speed streaks, $Fr = 0$



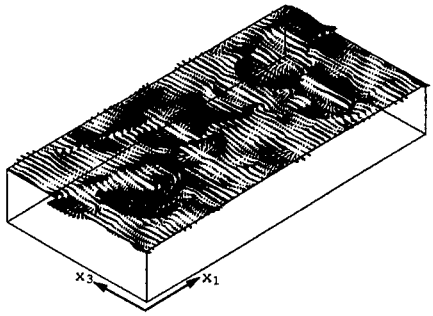
(b) Low-speed streaks, $Fr = 0.6$



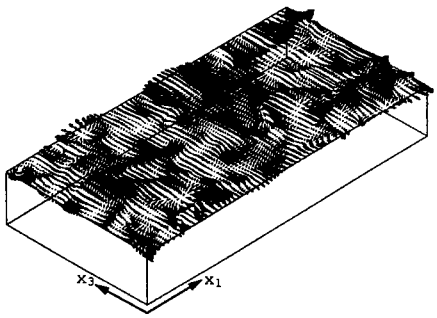
(c) Pressure at $x_2 = H$, $Fr = 0$



(d) Surface height, $Fr = 0.6$



(e) Projected velocity vectors, $Fr = 0$



(f) Projected velocity vectors, $Fr = 0.6$

Figure 2. Instantaneous flow features.

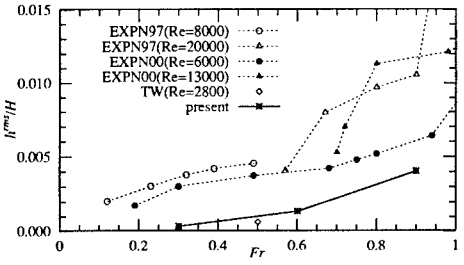


Figure 3. RMS fluctuations of h.

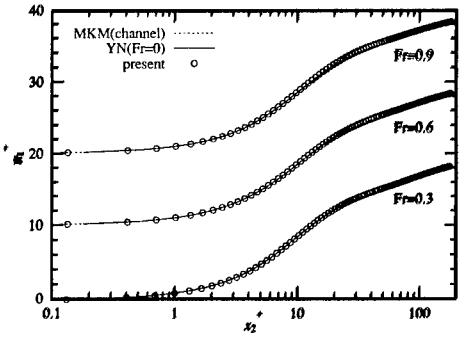
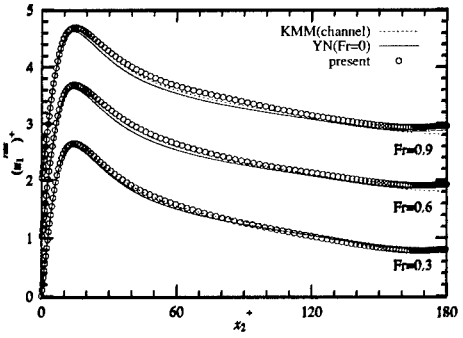
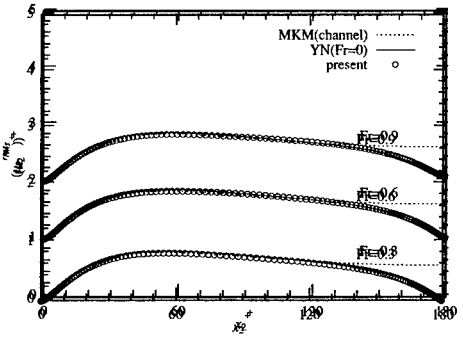


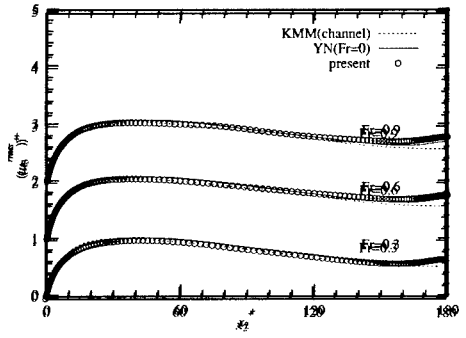
Figure 4. Mean velocity profiles.



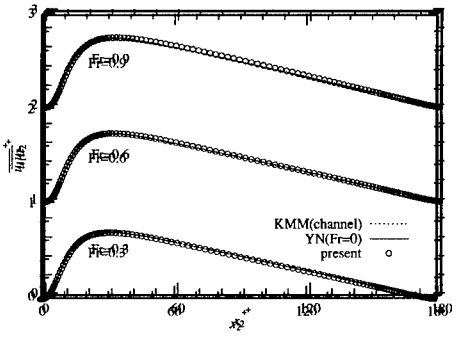
(a) u_1^{rms}



(b) u_2^{rms}



(c) u_3^{rms}



(d) $\overline{u_1 u_2}$

Figure 5. Profiles of turbulence intensities and Reynolds shear stress.

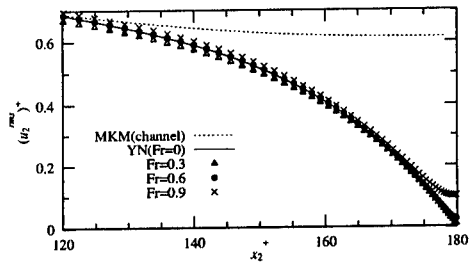


Figure 6. $u_2^{\rm rms}$ near free surface.

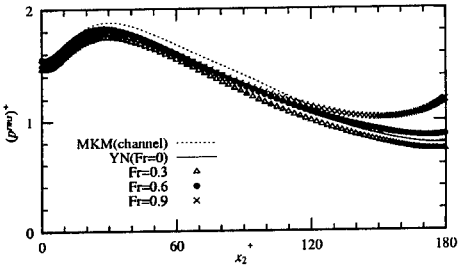
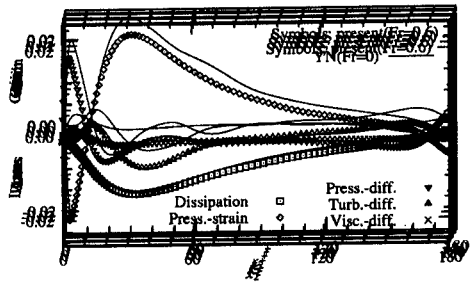
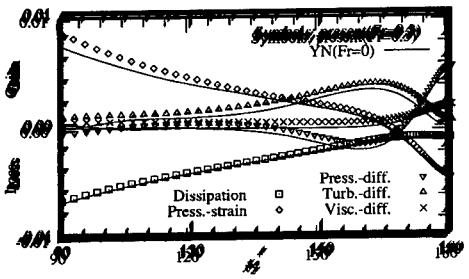


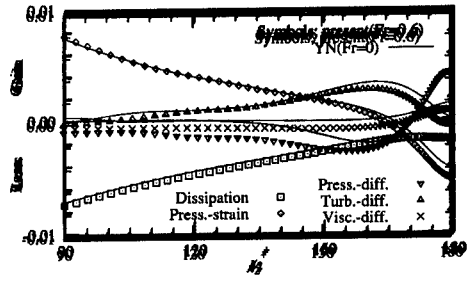
Figure 7. RMS pressure fluctuation.



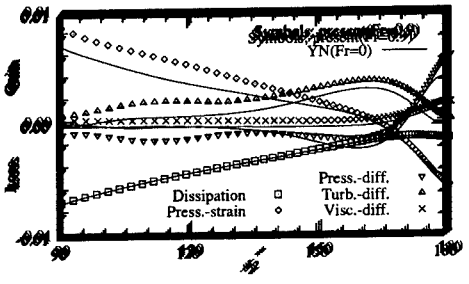
(a) Entire depth, $Fr = 0,\ 0.6$



(b) Near free surface, $Fr = 0,\ 0.3$



(c) Near free surface, $Fr = 0,\ 0.6$



(d) Near free surface, $Fr = 0,\ 0.9$

Figure 8. $\overline{u_2^2}$ budget.

2D-DNS OF QUASI-2D TURBULENCE IN SHALLOW WATER

ROB UITTENBOGAARD, BAS VAN VOSSEN
J.M. Burgers Centre, Delft University of Technology, The Netherlands
WL|Delft Hydraulics, The Netherlands

Abstract

Through a series of cases, we investigate the possibilities of the shallow-water solver Delft3D-Flow of simulating the evolution of (quasi-)2D turbulence in shallow water subjected to internal and external friction and forcing.
This paper presents the simplest case, namely the 2D-DNS of laboratory experiments of freely-evolving 2D turbulence, initiated by a rake in a shallow fresh-water layer on top of a salt-water layer in a square 1*1 m^2 basin (Maassen 2000). Tabeling et al. (1991) report similar experiments in a fluid with a free surface but initiated by vortices counter-rotating in a chessboard arrangement.
Likewise, our depth-averaged free-surface simulations are initiated by random as well as by chessboard vortices. We compare the temporal evolution of the simulated vorticity field in a viscous fluid with observations as well as with simulations of Clercx et al. (1999) dedicated to incompressible 2D turbulence simulation with a rigid lid. Theirs and our simulations agree with the experimentally observed evolution of vorticity into just two vortices with opposite rotation. All simulations neglect the friction at the density interface and exhibit lesser decay of kinetic energy than observed in the experiments of Maassen (2000).

1. Introduction

Based on the hydrostatic-pressure assumption, the shallow-water solver Delft3D-Flow has been extensively used for modeling the depth-averaged or 3D flows in civil-engineering applications.
For better assessment of ship traffic, structural stability, sediment transport, dredging operations and algae blooms, there appears to be a growing interest in simulating more details of the flow such as the temporal and spatial pdpf's of horizontal velocity, bed-shear stress, mixtures of dissolved or suspended constituents etc.
Rather than developing 2D turbulence closures, we prefer resolving and simulating most of the horizontal flow patterns. Although, practical feasibility demands that we maintain modeling the 3D turbulence in the orthodox manner using partial-slip, bed friction and 3D turbulence closures for boundary-layer

type of flows. We define the latter approach as Horizontal Large Eddy Simulation (HLES) acknowledging the particular properties of shallow-water flows. Recently, this HLES approach has been validated against observations of a shallow-water mixing layer (Kernkamp & Uittenbogaard, 2001).
The essential question is whether the available general-purpose shallow-water solver is suitable for HLES, particularly, its numerical dissipation and the accuracy constraints for simulating 2D-turbulence in free-surface flows. This paper deals with these fundamental questions by simulating laboratory experiments of 2D turbulence freely-evolving in a square basin.

2. The shallow-water solver Delft3D-Flow

In depth-averaged mode, Delft3D-Flow solves the following depth-averaged shallow-water equations (SWE) for mass conservation and for the depth-averaged horizontal velocity:

$$\frac{\partial \zeta}{\partial t} + \nabla \cdot (h\underline{u}) = 0 \text{and} \frac{\partial \underline{u}}{\partial t} + \underline{u} \cdot \nabla \underline{u} + g\nabla\zeta = \nu\nabla^2 \underline{u} + \underline{T} - h^{-1} c_f |\underline{u}|\underline{u}. \qquad (1)$$

In (1), $\underline{u}$=(u,v) is the depth-averaged horizontal velocity vector, $h=d+\zeta$ the total depth, d the still-water depth and ζ the free-surface position, both referring to some horizontal reference plane, c_f the bed-friction coefficient, ν the kinematic viscosity and g the magnitude of gravitational acceleration. The bed friction term is the depth average of the force by the Reynolds-shear stress of 3D turbulence without wind. The force vector $\underline{T}$ is due to subgrid-scale stresses. Bed friction and $\underline{T}$ are omitted in this paper but applied by Kernkamp & Uittenbogaard (2001) for simulating a shallow-water mixing layer. The term $g\nabla\zeta$ represents the horizontal gradient of pressure based on the hydrostatic-pressure assumption. On a staggered (Arakawa-C) grid, the horizontal terms in (1) are formulated in curvilinear orthogonal co-ordinates but in this paper we consider just Cartesian (x,y)-(u,v) grids.
The SWE (1) are time integrated by ADI of which the first half time step, from t=nΔt to (n+½)Δt, begins by solving the discretised v-momentum equation:

$$\frac{v^{n+\frac{1}{2}} - v^n}{\frac{1}{2}\Delta t} + u^n D_x^{2^{nd}\,upw}\left\{v^{n+\frac{1}{2}}\right\} + v^n D_y^{2^{nd}\,upw}\left\{v^{n+\frac{1}{2}}\right\} + gD_y^{2^{nd}\,cntrl}\left\{\zeta^n\right\} = 2\nu D_x^{2^{nd}\,cntrl}\left\{D_x^{2^{nd}\,cntrl}\left\{v^n\right\}\right\} + 2\nu D_y^{2^{nd}\,cntrl}\left\{D_y^{2^{nd}\,cntrl}\left\{v^n\right\}\right\} \qquad (2)$$

where D_α is a first-order difference operator with respect to a horizontal Cartesian co-ordinate α=x,y. For the advection terms in (2), D_α is 2nd order

upwind but 2nd order central for pressure as well as stresses. Eq. (2) is implicit for $v^{n+½}$, solved by red-black Jacobi while pressure and twice the Laplacian $\nu\nabla^2 v$ are integrated explicitly. Instead, the discretised u-momentum (3) reads:

$$\frac{u^{n+\frac{1}{2},p+1}-u^{n}}{\frac{1}{2}\Delta t}+u^{n+\frac{1}{2},p+1}D_x^{2^{nd}\,cntrl}\left\{u^{n}\right\}+v^{n+\frac{1}{2}}D_y^{2^{nd}\,cntrl}\left\{u^{n}\right\}+g\frac{h^{n+\frac{1}{2},p}}{h^{n+\frac{1}{2},p+1}}D_x^{2^{nd}\,cntrl}\left\{\zeta^{n+\frac{1}{2},p+1}\right\}=0. \tag{3}$$

Using (3), the new iterate $h^{n+\frac{1}{2},p+1}u^{n+\frac{1}{2},p+1}$, with iteration level p, is expressed into old-time level variables as well as into $\zeta^{n+\frac{1}{2},p+1}$ and subsequently substituted into the following discretised conservation equation:

$$\frac{\zeta^{n+\frac{1}{2},p+1}-\zeta^{n}}{\frac{1}{2}\Delta t}+D_x^{2^{nd}\,cntrl}\left\{h^{n+\frac{1}{2},p+1}u^{n+\frac{1}{2},p+1}\right\}+D_y^{2^{nd}\,cntrl}\left\{h^{n}v^{n}\right\}=0, \tag{4}$$

with h centrally-averaged to (u,v) points yielding a tri-diagonal system in x-direction that is solved by the Thomas algorithm and subsequently iterated on (p) to convergence. Note that the ratio $h^{n+\frac{1}{2},p}/h^{n+\frac{1}{2},p+1}$ in the last term of (3) ensures mass-conservation at every p-iteration. In the subsequent half-time step, the u-momentum equation is formulated and solved as (2) and then the inviscid momentum (3) for v is coupled to (4) while (3) is formulated implicitly in v-component and in y-direction.

For the full time step, the coupled advection-conservation schemes are second-order in time with fourth-order dissipation in space and unconditionally stable (Stelling, 1984). The viscous force is integrated explicitly, invoking a mild time step limitation.

For DNS or LES applications, a disputable disadvantage is that the cyclic combination of 2nd-order upwind and 2nd-order central advection in (2-4) are neither strictly momentum nor strictly energy conserving. On the other hand, however, the tendency of creating velocity wiggles in inviscid simulations using the energy-conserving scheme of Arakawa & Lamb (1981) appear to invoke more dissipation in simulations when viscous stresses are included (Hólm, 1995). Further, the semi-implicit coupling of the pressure $g\zeta$ to the momentum equations (2-3) as well as to the conservation equation (4) tends to conserve the energy stored in the free-surface or compressible velocity modes induced by the velocity-advection operator. Depending on the flow and on the advection scheme, the latter may convert incompressible energy modes into compressible energy modes that are subsequently removed/dissipated by pressure

correction/projection schemes that are customary in fixed-volume incompressible DNS/LES solvers.
This section is concluded by introducing the time-step limitations based on accuracy, rather than stability, of advection and of the long-wave or barotropic (BT) velocity modes on a square mesh with grid size Δx:

$$\Delta t_A = \sigma_A \frac{\Delta x}{\max(|\underline{u}|)}; \Delta t_{BT} = \frac{\sigma_{BT}}{2\sqrt{2}} \frac{\Delta x}{\sqrt{gh}} \rightarrow \frac{\Delta t_A}{\Delta t_{BT}} = 2\sqrt{2} \frac{\sigma_A}{\sigma_{BT}} \frac{\sqrt{gh}}{\max(|\underline{u}|)}. \tag{5}$$

The first criterion originates from the semi-implicit x-advection term in (3) and it demands $\sigma_A<4$ (Stelling, 1984, p. 165). Benqué et al., (1982) proposed the second criterion with $\sigma_{BT}<4\sqrt{2}$ for avoiding aliasing in wave propagation using ADI and staggered grids e.g. over bed topography. For the temporal representation of advected and deforming vortices we believe $\sigma_A<O(0.3)$ would be a proper *space-time consistency criterion.* For Froude numbers $U/g\sqrt{h} > O(0.15)$, using the limitation $\sigma_{BT} < 4\sqrt{2}$, the latter criterion coincides, i.e. $\Delta t_A \approx \Delta t_{BT}$. However, smaller Froude numbers are typical for our applications and then the accuracy of simulating BT modes limits the time step.

3. Some considerations of 2D turbulence with a free surface

For an overview of properties of 2D turbulence, such as the inverse energy cascade related to vortex merging, we refer to e.g. (Lesieur, 1997). For an closed basin with water volume V, this section considers briefly the possible coupling of 2D turbulence (vortical) motions to free-surface (BT) motions. The frictionless SWE (1) then yields the following conservation property (Arakawa & Lamb, 1981):

$$\frac{\partial}{\partial t} \iint h\left\{\tfrac{1}{2}\underline{u}\cdot\underline{u} + \tfrac{1}{2}gh - gd\right\} dx\,dy = 0, \tag{6}$$

where the first term represents the kinetic energy (KE) and the sum of second and third term the potential energy (PE). For a closed basin with horizontal bed (constant d), the third term cancels due to mass conservation. In addition, from the frictionless SWE (1) also follows

$$\frac{D^2\zeta}{Dt^2} - gh\nabla^2\zeta = h\left\{D_{ij}D_{ij} - \omega_z^2\right\} + h\left\{\frac{1}{h}\frac{D\zeta}{Dt}\right\}^2; \frac{D\zeta}{Dt} = \frac{\partial}{\partial t} + \underline{u}\cdot\nabla, \tag{7}$$

with horizontal-strain rate tensor D_{ij} based on $\underline{u}$ and vertical vorticity component ω_z. From the frictionless SWE also follows the conservation of potential vorticity (PV) ω_z / h:

$$\frac{D}{Dt}\left(\frac{\omega_z}{h}\right)=0. \tag{8}$$

A priori (6-8) suggest that 2D turbulence in free-surface flows differs from 2D turbulence in rigid fluid volumes. For example, the LHS of (7) represents the long-wave propagation of a surface perturbation ζ associated with PE in (6) whereas (6) shows that PE is reversibly exchanged with KE. Further, the RHS of (7) acts as source of surface perturbations ζ of which the vertical vorticity obeys (8). Note that (7) is similar to Lighthill's equation for sound generation by turbulence. The RHS of (7) equals the Weiss-function, see e.g. (Basdevant & Philipovitch, 1994), where the last term is due to the vertical strain rate in long waves.

We conclude that *a priori* deviations may exist between the evolution of 2D turbulence simulated with a rigid lid, such as by Clercx et al. (1999), or with the SWE (1). Nevertheless, detailed analysis (Vossen, 2000) of our SWE simulations as well as animations of vorticity combined with surface elevation show that (7) can be approximated well by the rigid-lid counterpart with pressure $g\zeta$:

$$\nabla^2(g\zeta)=\omega_z^2 - D_{ij}D_{ij}. \tag{9}$$

4 Numerical initialisation of 2D turbulence in a free-surface fluid

Clercx et al. (1999) solve the viscous 2D stream function and vorticity equations using 288^2 Chebyshev polynomial expansion and they initiate 2D turbulence by random 64^2 Chebyshev modes that in general do not obey incompressibility. The laboratory experiments of Tabeling et al. (1991) start with 2D chessboard vortices. In both cases, our simulations initiated with a spatially constant ζ show that much PE is generated as freely-propagating waves, see LHS of (7). For a proper comparison with experiments we must initiate the velocity-surface field more carefully as follows. Define, at t=0, the master velocity field as $\underline{u}_0$ either based on 64^2 Chebyshev modes or chessboard vortices. Next, the associated incompressible field $\underline{u}(\underline{x},0)$ is derived from:

$$\underline{u}(\underline{x},0)=\underline{u}_0+\nabla\lambda \text{ with } \nabla^2\lambda=-\nabla\cdot\underline{u}_0, \tag{10}$$

with $\nabla\lambda$ the corrected velocity field such that $\nabla \cdot \underline{u}(\underline{x},0)=0$ holds on the computational grid. For closed boundaries (10) yields less KE in $\underline{u}(\underline{x},0)$ than in $\underline{u}_0$. Likewise, Clercx et al. (1999) report a decrease in KE at their first time step that yields $\nabla \cdot \underline{u}(\underline{x},\Delta t)=0$. With $\underline{u}(\underline{x},0)$ by (10), the initial surface elevation $\zeta(\underline{x},0)$ is obtained from (9) as the quasi-steady approximation to (7). Following this initialisation, our SWE simulations then evolve gradually in time and space without notable wave-like motions.

5. Investigation and estimation of numerical dissipation

In view of (5), the appropriate time step was investigated by inviscid simulations of (1) initialised by Clercx's random 64^2 Chebyshev modes and the procedure given in section 4. Figure 1 presents the temporal evolution of volume-integrated KE in a basin of width W=1m with 1 cm still-water depth and $|u'|$=4 mm/s using 100^2 square grid. In all cases, $\sigma_A \leq 0.24$ holds but Figure 1 shows that only if $\sigma_{BT} < 4\sqrt{2}$ is satisfied then near conservation of KE is obtained. Therefore, $\sigma_{BT} < 4\sqrt{2}$ is applied in all subsequent simulations.

For practical reasons we estimate a numerical viscosity ν_{num}, equivalent to the kinematic viscosity, by

$$\nu_{num} = -\frac{1}{2\Theta}\frac{\partial E_k}{\partial t} \text{ with } E_k = \tfrac{1}{2}\rho\iint h\left(u^2+v^2\right)dx\,dy \text{ and } \Theta = \tfrac{1}{2}\rho\iint h\omega_z^2\,dx\,dy, \quad (11)$$

although the advection operators yield 4th order dissipation. Series of inviscid runs with variations of grids N_p*N_p (N_p= 50, 100, 200, 500), of basin size (1-100m) and initial fields with random Chebyshev polynomials or chessboard vortices (1, 4, 16 and 100) yield the following approximation:

$$\nu_{num} \approx \frac{|u'|\Delta x}{8\sqrt{N_p}} \quad ; \quad N_p = \frac{W}{\Delta x} \quad , \quad (12)$$

with N_p proportional to the resolved band width. Despite the strong temporal merging of vortices (see figure 5), Figure 2 presents an example of the marginal temporal dependence of ν_{num} estimated through (11) and thus suggests its validity as estimator for numerical dissipation.

6. Simulations of 2D turbulence in free-surface experiments

The upper part of figure 5 presents particle tracks observed in a 1*1 m^2 reservoir (Maassen, 2000). Although the top layer floats on a denser salt-water layer, Maassen (2000) notes a significant interfacial friction reducing the effective Reynolds number by a factor 5. The lower part of figure 5 presents the vorticity contours simulated by the shallow-water solver but without interfacial friction. The evolution of vorticity patterns is similated qualitatively well by our shallow-water solver. Due to the uncertainty in modelling the interfacial friction, i.e. c_f in (1), we prefer the comparison with simulations by Clercx et al. (1999) who applied a solver dedicated to this type of experiments.

For Reynolds number Re=2000, Clercx et al. (1999) simulated decaying viscous 2D turbulence with no-slip wall conditions but without bed or interfacial friction. They define Re and the temporal scale T by

$$\mathrm{Re} = \frac{\frac{1}{2}W|u'|}{\nu} \quad ; \quad T = \frac{\frac{1}{2}W}{|u'|} \quad ; \quad \tfrac{1}{2}\Delta y^{+} \approx \frac{\mathrm{Re}}{17N_p} \quad , \tag{13}$$

with W the width of the square basin. For resolving viscous boundary layers with a square grid the last expression in (13) should equal unity and this expression determines that N_p=200 is adequate for a 2D DNS with our shallow-water solver. Figure 3 includes the simulations of Clercx et al. (1999) solved by 288^2 Chebyshev modes and we applied their initial velocity field based on 64^2 Chebyshev polynomials but corrected to an incompressible flow through (10).

Figure 3 presents the relative decay of volume-integrated KE as well as volume-integrated enstrophy, as defined by (11), against time scaled by T defined in (13). Under these conditions, the overall numerical viscosity (12) of the shallow-water solver is estimated to be about 0.2ν. Nevertheless the decay simulated with the shallow-water solver is comparable or even less than simulated by Clercx et al. (1999).

7. Conclusions and discussion

We conclude that the general-purpose shallow-water solver Delft3D-Flow is capable of simulating vortex merging and the decay of 2D turbulence in a viscous fluid without notable numerical diffusion (figure 3). From a simulation point-of-view, the most notable aspect of the free surface in 2D turbulence reads as follows. Animations of vorticity and surface elevations show that most of the free-surface elevations are induced by the Weiss function, RHS in (9). Despite that the free-surface elevations carry marginal available potential energy, compared to kinetic energy, their evolution must be carefully simulated else kinetic energy is generated artificially (Figure 1). The latter demands for the barotropic Courant number $\sigma_{BT}/4\sqrt{2} \le 1$ (figure 1) and it is very restrictive compared to other accuracy and stability conditions for the shallow-water solver

Delft3D-Flow. The reason for the constraint on this typical wave-propagation condition is not clear. We speculate that the Poisson equation (9) is essential and needs to be solved accurately. In SWE, however, the solution of (9) is obtained through (7) and, if σ_{BT} is too large, errors in the rapid propagation of surface perturbations spoil the approximation to (9).

8. Acknowledgments

We appreciated the stimulating discussions with Dr. Clercx and Prof. Van Heijst (Eindhoven University of Technology) as well the patient support of our colleague Dick Verploegh in post-processing the simulation.

References

1. Arakawa, A. & V.R. Lamb 1981 A potential enstrophy and energy conserving scheme for the shallow-water equations. *Monthly Weather Rev.*, vol. 109, pp. 18-36.
2. Basdevant, C. & T. Philipovitch 1994 On the validity of the "Weiss criterion" in two-dimensional turbulence. *Physica D,* 73, pp. 17-30.
3. Benqué, J.P. J.A. Cunge, J. Feuillet, A. Hauguel & F.M. Holly 1982 New method for tidal current computation. *J. Waterway, Port, Coastal and Ocean Div. ASCE,* 73, pp. 396-417.
4. Clercx, H.J.H., S.R. Maasen & G.J.F. van Heijst 1999 Decaying two-dimensional turbulence in square containers with no-slip or stress free boundary conditions. Phys. Of Fluids, vol. 11, no. 3, pp. 611-626.
5. Hólm, E.V. 1996 Energy and enstrophy conservation properties of high-order non-oscillatory advection schemes. *Tellus*, 48A, pp. 122-137.
6. Kernkamp, H.W.J. & R.E. Uittenbogaard 2001 2D-LES of a free-surface mixing layer. *Proc. Direct and Large-Eddy Simulation Workshop 4,* (ed's B.J. Geurts, F. Friedrich & O. Metais), Enschede, The Netherlands, July, pp. 213-216.
7. Lesieur, M. *Turbulence in fluids.* Kluwer, Dordrecht, The Netherlands.
8. Maassen, S.R. 2000 *Self-organisation of confined two-dimensional flows.* Ph.D. Thesis, Eindhoven University of Technology, August.
9. Stelling, G.S. 1984 *On the construction of computational methods for shallow water flow problems.* Rijkswaterstaat communications, No. 35.
10. Tabeling, P., S. Burkhart, O. Cardoso & H. Willaime 1991 Experimental study of freely-decaying two-dimensional turbulence. *Phys. Rev. Letters*, vol. 67, no. 27, pp. 3772-3775.
11. Vossen, van, B. 2000 *Horizontal Large Eddy Simulations; evaluation of flow computations with Delft3D-Flow.* M.Sc.Thesis Delft University of Technology, MEAH-197, Aug.

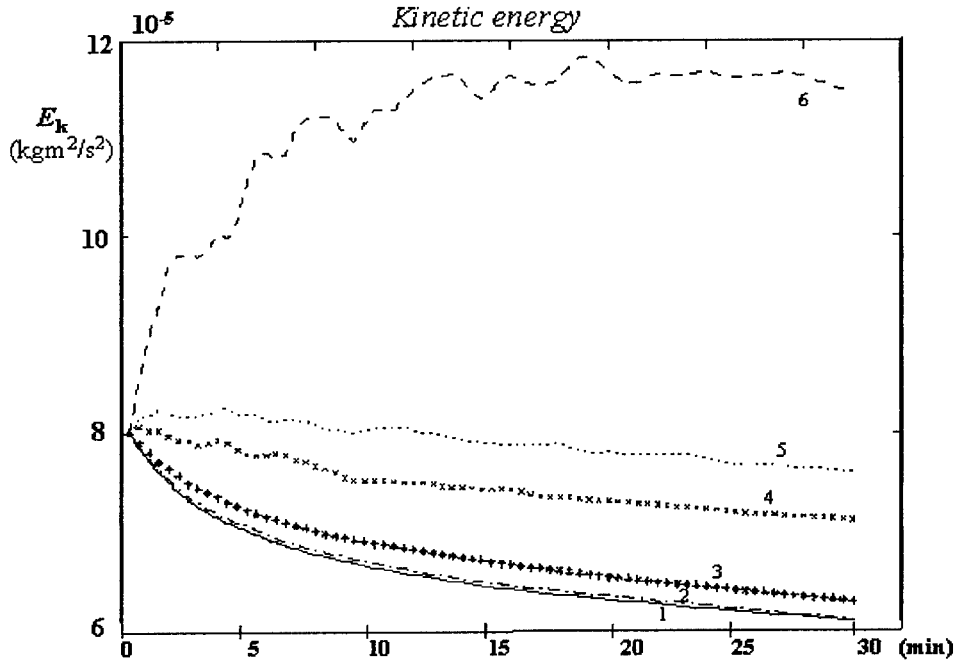


Figure 1. Decay of kinetic energy 100^2 grid, 1*1*0.01 m^3, lu'l=4 mm/s, initial random field, for $\sigma_{BT} / 4\sqrt{2}$ = 9.4 (6) ; 4.8 (5) ; 3.9 (4) ; 1.9 (3) ; 0.94 (2) ; 0.47 (1).

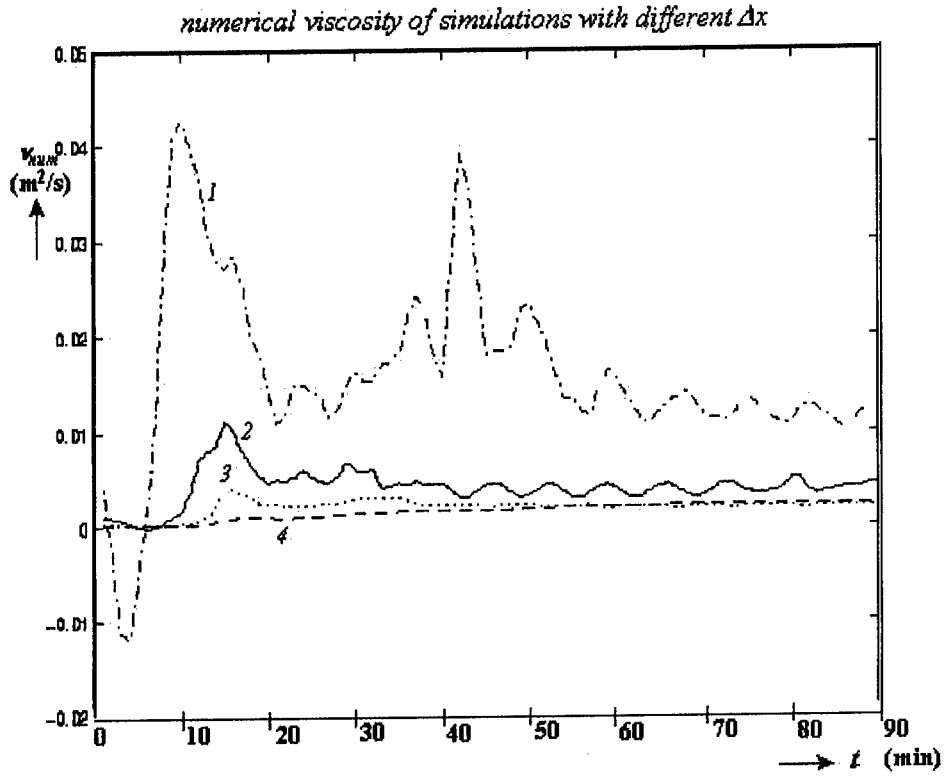


Figure 2. Numerical viscosity, estimated by (11), for 50×50 (1), 100×100 (2), 200×200 (3) and 500×500 (4) grid cells ; 100*100*1 m^3 ; |u'|=0.4 m/s, initialized by 16 chessboard vortices.

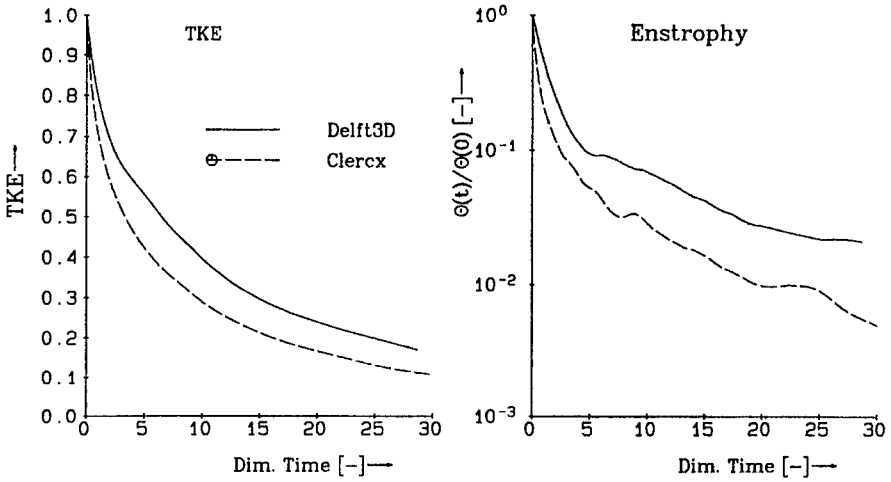


Figure 3. Relative decay of volume-integrated kinetic energy and enstrophy, see (11) of 2D turbulence initiated by a random field at Re=2000 and T=125 s time scale. Comparison between the shallow-water solver (Delft3D) using 200^2 square grid at σ_Λ=0.012 and $\sigma_{BT}/4\sqrt{2}$ =0.47, see (5), with simulations in (Clercx et al., 1999).

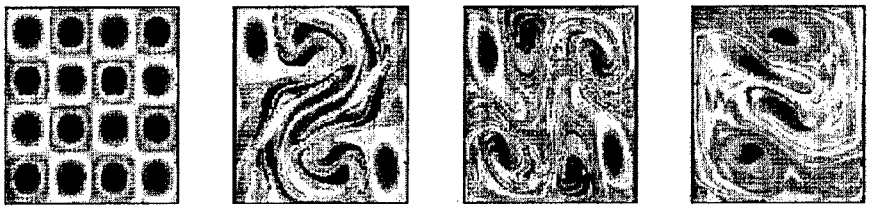


Figure 4. From left to right t= 0 ; 15 ; 20 ; 30 minutes. Evolution of 4*4 chessboard vortices on a 500^2 grid of 100*100*1m^3 ; |u'|=0.4 m/s ; inviscid shallow-water simulation.

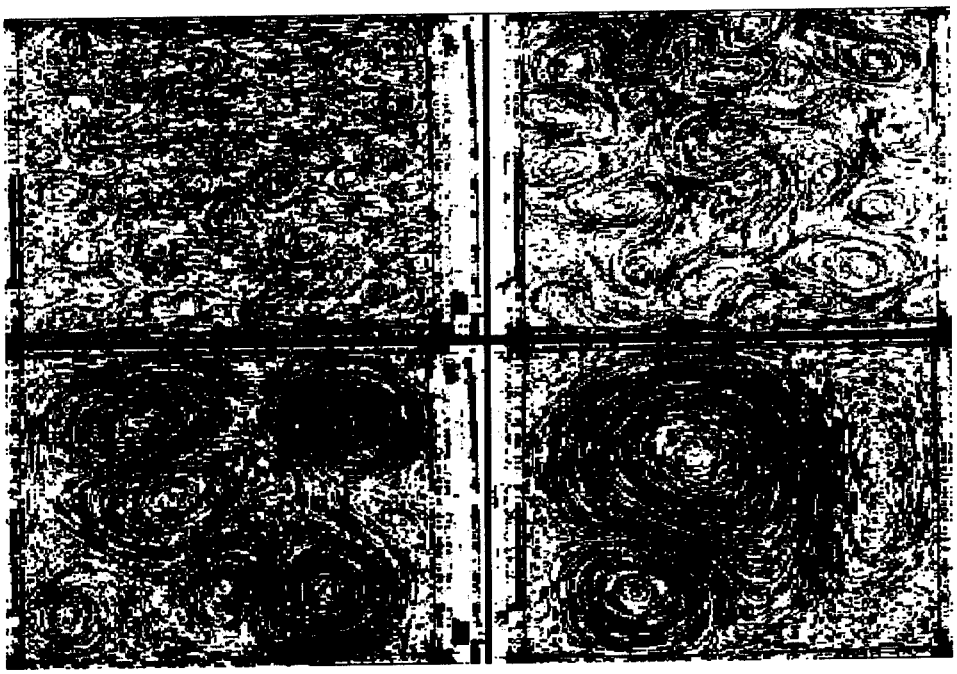
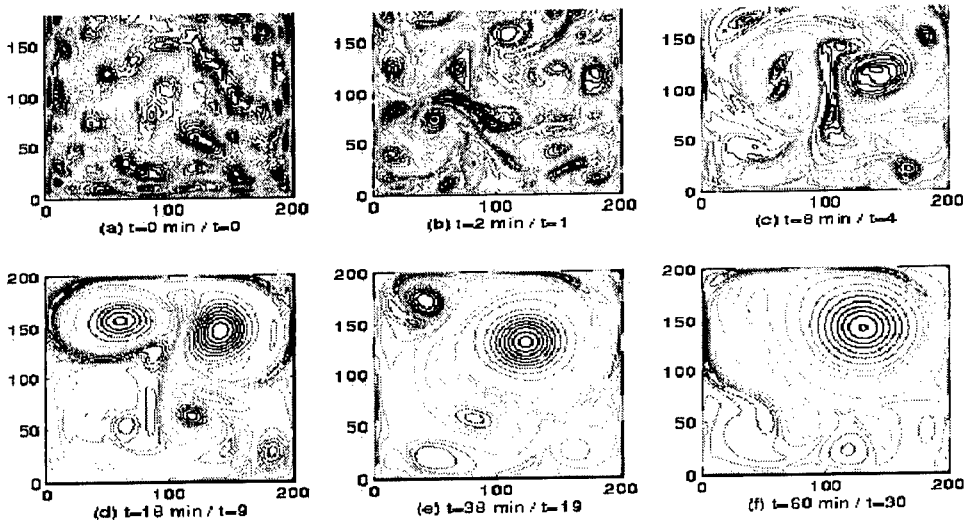


Figure 5. Particle tracks in the free-surface water layer on top of a dense salt layer 10 seconds (up-left), 1 minute (up-right), 5 minutes (down-left) and 50 minutes after passage of a raKE (Maassen, 2000). Below, iso-contours of vertical vorticity, simulated by Delft3D for conditions of figure 3 and similar to observations above.



DIRECT NUMERICAL SIMULATION OF JET NOISE

BENDIKS JAN BOERSMA
J.M. Burgers Centre
Delft University of Technology
Mekelweg 2
2628 CD Delft
The Netherlands
email: b.j.boersma@wbmt.tudelft.nl

Abstract. In this paper we will investigate the sound field of a round turbulent jet with a Mach number of 0.6 based on the jet centerline velocity and the ambient speed of sound. The sound field is obtained by solving a wave equation for the acoustic field. Two different acoustic source terms are used as right hand side of the wave equation. One in which the source term is given by traditional Lighthill stress tensor and a second one in which the source term is based on the vorticity in the fluid.

1. Introduction

A generic flow geometry of aeroacoustical sound production is a turbulent jet. Most people will be familiar with the sound of a jet engine of a commercial airliner. Stricter environmental measures around airports have put strong limitations on the sound that may produced by jets. Although significant sound reduction of these jet engines has been obtained over the last few decades, it is nevertheless required to reduce the sound of jet engines even more in view of the strong growth in air traffic foreseen in the future. The above mentioned jet engine is only one of the examples and other examples are aeroacoustical sound produced by high speed trains, wind noise around buildings, the sound comfort in cars but also ventilator noise in various household appliances. In this study we will focus on sound produced by turbulent jets because this flow is one of the benchmark flows for which a reasonable amount of experimental data is available.

Here we only want to mention the experimental studies which are relevant for this study, for a more detailed overview we refer to Goldstein (1976). Lush (1971) reports acoustic pressure spectra of a Mach 0.3, 0.6 and 0.9 turbulent jet. Mollo-Christensen (1967) also reports spectra for Mach 0.6 and Mach 0.9 turbulent jets and gives detailed information about the directivity of the sound. Unfortunately no information is given on the structure of the flow field. Information on the flowfield of a jet has been presented in various studies see for instance, Panchapekesan & Lumley (1993), and Boersma *et al.* (1998). There is as far as we know, no detailed experimental study in which both the flow field and the acoustic field are presented.

Recently, with increasing computer power, it has become possible to calculate the acoustic field of simple flows using Direct Numerical Simulation (DNS), Colonius *et al.* (1997), Mitchell *et al.* (1999). Direct numerical simulations of high Mach number turbulent jets have been performed by Freund (1998). In these simulations the sound is calculated with help of Kirchhoff surfaces. In low Mach number flows the acoustic amplitudes are very small and it is likely that acoustic equations like the one proposed by Lighthill (1952) or Howe (1975) will give more reliable results which are less contaminated by numerical errors.

In this paper we will focus on a jet with a Mach number of 0.6. We will compare acoustic fields obtained with both the Lighthill and Howe equations.

2. Governing equations

The flow is described by the well known compressible Navier-Stokes equations which can be found in various text books (Bachelor 1967). The equation for conservation of mass reads.

$$\frac{\partial \rho}{\partial t} + \frac{\partial \rho u_i}{\partial x_i} = 0 \tag{1}$$

where ρ is the fluids density and u_i the fluids velocity component in the ith coordinate direction. The equation which describes the conservation of momentum reads

$$\frac{\partial \rho u_i}{\partial t} + \frac{\partial \rho u_j u_i}{\partial x_j} = -\frac{\partial p}{\partial x_i} + \frac{\partial}{\partial x_i}\tau_{ij} \tag{2}$$

In which p is the pressure and τ_{ij} is the viscous stress given by:

$$\tau_{ij} = \mu S_{ij} = \mu\left(\frac{\partial u_i}{\partial x_j} + \frac{\partial u_j}{\partial x_i} - \frac{2}{3}\delta_{ij}\frac{\partial u_i}{\partial x_i}\right) \tag{3}$$

The dynamics viscosity μ is a weak function of the temperature in the gas. For the moment we will neglect this and assume that μ is constant.

For the energy equation in a compressible flow various formulations are possible. Here we choose for a formulation using the total energy, i.e. the sum of temperature and kinetic energy

$$E = \rho C_v T + \frac{1}{2}\rho u_i u_i \tag{4}$$

In which C_v is the specific heat at constant volume and T the temperature. The transport equation for the total energy E reads

$$\frac{\partial E}{\partial t} + \frac{\partial}{\partial x_i} u_i [E + p] = \frac{\partial}{\partial x_i} \kappa \left(\frac{\partial T}{\partial x_i} \right) + \frac{\partial}{\partial x_i} u_i S_{ij} \tag{5}$$

In which κ is the thermal diffusion coefficient, which is again a weak function of the fluids temperature. The formulation of the energy equation given above has the advantage that no source terms appear in the right hand side which would be the case for formulations using the temperature instead of the energy. The temperature T, the pressure p and the density ρ are related to each other by the equation of state

$$p = \rho R T \tag{6}$$

2.1. THE ACOUSTIC FIELD

The acoustic field of the jet can be calculated with help of acoustic analogons like the Lighthill equation (Goldstein 1976):

$$\frac{\partial^2 \rho'}{\partial t^2} + c^2 \frac{\partial^2 \rho'}{\partial x_i^2} = \frac{\partial^2}{\partial x_i \partial x_j} T_{ij}. \tag{7}$$

In which ρ' is the acoustic density of the gas, c the speed of sound and T_{ij} is the Lighthill stress tensor which is given by the following relation

$$T_{ij} = \rho u_i u_j + \mu \left(\frac{\partial u_i}{\partial x_j} + \frac{\partial u_j}{\partial x_i} \right). \tag{8}$$

For turbulent flows the viscous term in the Lighthill stress tensor will be small and T_{ij} can be approximated by $T_{ij} \approx \rho u_i u_j$. Furthermore, if the Mach number is sufficiently small the density ρ can be replaced by the ambient value ρ_∞, resulting in the following equation for the acoustic density fluctuations

$$\frac{\partial^2 \rho}{\partial t^2} + c^2 \frac{\partial^2 \rho}{\partial x_i^2} = \rho_\infty \frac{\partial^2}{\partial x_i \partial x_j} u_i u_j. \tag{9}$$

Another formulation of the wave equation has been proposed by (Howe 1975). In this formulation the Lighthill tensor is expressed in terms of the vorticity and kinetic energy.

$$\frac{\partial^2}{\partial x_i \partial x_j} u_i u_j = \nabla \cdot \nabla \cdot (\underline{uu}) = \nabla \cdot (\underline{\omega} \times \underline{u}) + \nabla^2 \frac{1}{2} u^2 \tag{10}$$

For low Mach number flows the last term in the equation above (the kinetic energy) is neglected (Howe 1975) and we find the following wave equation for the sound

$$\frac{\partial^2 \rho}{\partial t^2} + c^2 \frac{\partial^2 \rho}{\partial x_i^2} = \nabla \cdot (\underline{\omega} \times \underline{u}) \tag{11}$$

3. Numerical method

In the previous section we have presented the governing equation for compressible flow. In this section we will describe how those equations are discretized.

A natural choice for the computation of a round jet would be to use a cylindrical coordinate system. In previous computational studies such systems have been used, Freund (1998), Boersma *et al.* (1998). The problem when dealing with such a coordinate system is the treatment of the singularity at the centerline ($r = 0$) of the coordinate system. In the literature various methods are discussed, for a detailed overview we refer to Mohensi & Colonius (2000). None of these methods are able to retain a high order of numerical accuracy at the axis ($r = 0$) of the system. In physical space this axis will represent the jet centerline. An accurate simulation at the jet centerline is necessary because this is the area where most of the sound will be produced. In view of the problems mentioned above we have decided to use a Cartesian coordinate system for the complete flow domain.

The computational grid in the physical domain is non-uniform. Mapping functions $X_i = \eta_i(x_i)$, with $X_i = i\Delta X$ are used to map differential equation on a uniform grid in the computational domain, i.e.

$$\frac{\partial f}{\partial x} = \frac{\partial f}{\partial X} \frac{\partial X}{\partial x} \tag{12}$$

The mapping function $X_i = \eta_i(x_i)$ is chosen in such a way that $\partial X/\partial x$ can be integrated analytically to obtain the physical distribution of the gridpoints x_i. The derivative $\partial f/\partial X$ has been calculated with a 8th order compact finite difference scheme (Lele 1992):

$$\left.\frac{\partial f}{\partial X}\right|_i = f'_i \tag{13}$$

$$\frac{3}{8}(f'_{i-1} + f'_{i+1}) + f'_i = \frac{25}{32}\frac{f_{i+1} - f_{i-1}}{\Delta X} + \frac{3}{60}\frac{f_{i+2} - f_{i-2}}{\Delta X} - \frac{1}{480}\frac{f_{i+3} - f_{i-3}}{\Delta X}$$

At the boundaries of the computational domain the accuracy of the compact scheme was reduced to third order, (Lele 1992). If we would have used a cylindrical system we would also have to reduce the order at the jet centerline to third order. Which on its turn would give an unreliable prediction of T_{ij}.

All the spatial derivatives in the continuity, momentum and energy equation are discretized with the 8th order approximation given above. The time integration has been performed with a standard 4th order Runga-Kutta method. The time step was fixed and the corresponding CFL number $(u_i \Delta t/\Delta x_i)$was approximately 1.0

Two different computational domains are used, one with a small spatial size for the Navier-Stokes equations and one with a larger spatial size for the wave equations. The Navier-Stokes domain consisted of $160 \times 144 \times 144$ the x, y and z-direction respectively (x is streamwize direction). The wave domain consisted of $320 \times 272 \times 272$ points.

4. Results

In this section we will present results obtained from the Direct Numerical Simulation of the jet and the sound field. For the jet-inflow profile a simple hyperbolic tangent profile of the following form is taken

$$U(r) = Ma\left(\frac{1}{2} - \frac{1}{2}\tanh[20(r - R_0)]\right) \tag{14}$$

In which R_0 is the radius of the jet and Ma the Mach number. The calculations have been continued until they reached a statistically steady state. After the calculations have reached this state they are continued for another 200 acoustic timescales R_0/c to obtain the statistics.

In Figure 1 (left) we show an instantaneous plot of the density field ρ in the jet and in Figure 1 (right) a contour plot of the total energy E in the jet. The figures show that the flow is laminar close to the jet nozzle and starts to become turbulent in the region $10 < x/R_0 < 15$ and becomes gradually fully turbulent farther downstream of the jet nozzle. In Figure 2 we show the mean velocity profiles along the jet centerline. In the region close to the jet orifice the centerline velocity is constant and then suddenly drops. The point were the centerline velocity suddenly drops is the point were most of the sound will be produced.

In Figure 3 (left) an instantaneous plot of the right hand side of equation (9) is shown. In Figure 3 (right) the right hand side of equation (11) has been plotted. Clearly there is a large difference between both source terms close to the jet nozzle. The source terms are large in the region $10 < x/R_0 < 30$, i.e the region in which the flow goes from a laminar to a turbulent state.

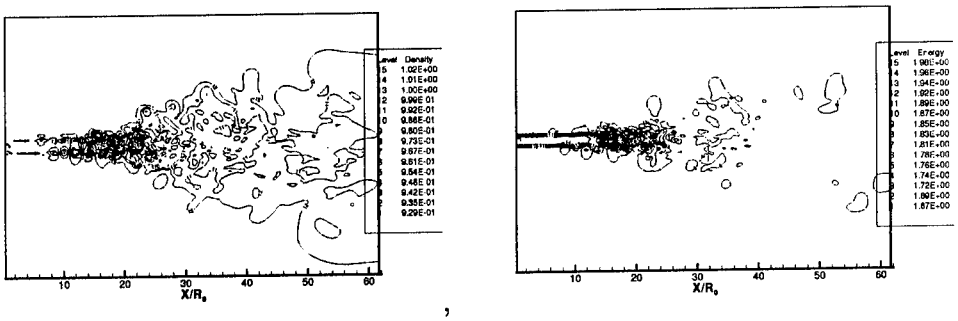


Figure 1. Left: an instantaneous plot of the density in the jet, right: an instantaneous plot of the axial velocity.

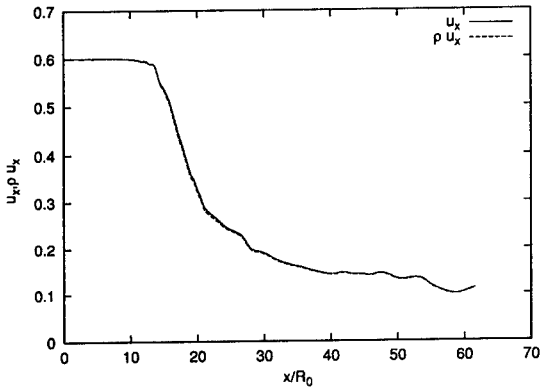


Figure 2. The mean axial velocity and axial flux at the jet centerline as a function of the downstream coordinate.

The difference between the two source terms is due to the removal of the kinetic energy from the right hand side of equation (10) and therefore the difference between the source terms are most pronounced in regions with a relatively large velocity, i.e. the region close to the centerline of the jet.

In Figure 4 the acoustic fields obtained with equations (9) and (11) are shown (the acoustic field is visualized with help of the dillatation $q = \partial\rho'/\partial t$). The sound field obtained with help of the Lighthill equations is very similar to the sound field observed in experiments. For instance, most of the sound is emitted under an angle of approximately 30^o which is also found in the experiments by Lush (1971) and Mollo-Christensen (1967). The second result presented in Figure 4 clearly has a wrong directivaty pattern and too much sound is emitted under and angle of 90^o.

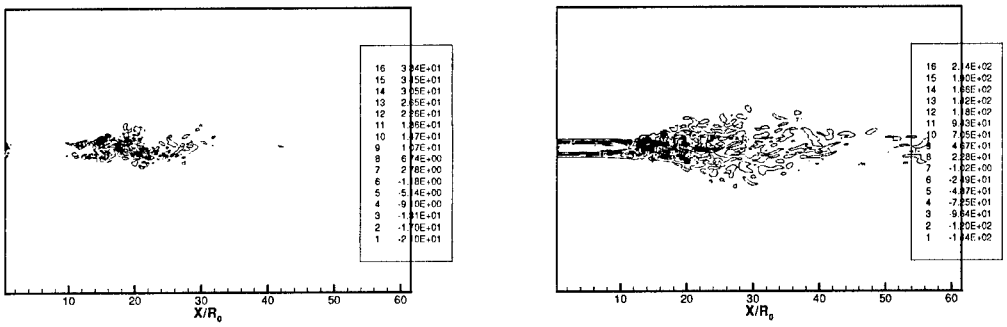


Figure 3. The acoustic source terms. Left: the right hand side of equation (9), Right: the right hand side of equation (11).

5. Conclusion

In this paper we have presented the sound field produced by a turbulent jet using two different acoustic equations. One of these equation is the traditional Lighthill equation which relates the sound to Reynolds stresses in the fluid. The second formulation we have used has been derived by Howe and relates the sound in the fluid to the vorticity. The last formulation is often preferred because it can be used in combination with simple vortex models for the flow, see e.g. Howe (1975).

It has been shown that there is a considerable difference between the source terms in the two formulations. The directivity pattern of the acoustic field obtained with equation (9) is much better than the pattern obtained with equation (11).

References

Batchelor, G.K., 1967, *An introduction to fluid mechanics*, Cambridge University Press.

Boersma, B.J., Brethouwer, G., and Nieuwstadt, F.T.M, 1998, A numerical investigation on the effect of the inflow conditions on the the self-similar region of a round jet, *Physics of Fluids* 10, 899-909.

Colonius, T., Lele, S.K., & Moin, P., 1997, Sound generation in a mixing layer, *J. Fluid Mech*, **330**, 375-409.

Freund, J.B., Lele, S.K., & Moin, P., 1998, Direct simulation of a Mach 1.92 jet and its sound field, AIAA/CEAS paper 98-2291.

Goldstein, M.E., 1976, *Aeroacoustics* McGraw Hill.

Howe, M.S., 1975, Contributions to the theory of aerodynamics sound, with application to excess jet noise and the theory of the flute, *J. Fluid Mech.*,**71**, 625-673.

Lele, S.K., 1992, Compact finite difference schemes with spectral-like resolution, *J. Comp. Phys.* 103, 16-42.

Lighthill, M.J., 1952, On sound generated aerodynamically, *Proc. R. Soc. of London Ser. A*, 211, 564-587.

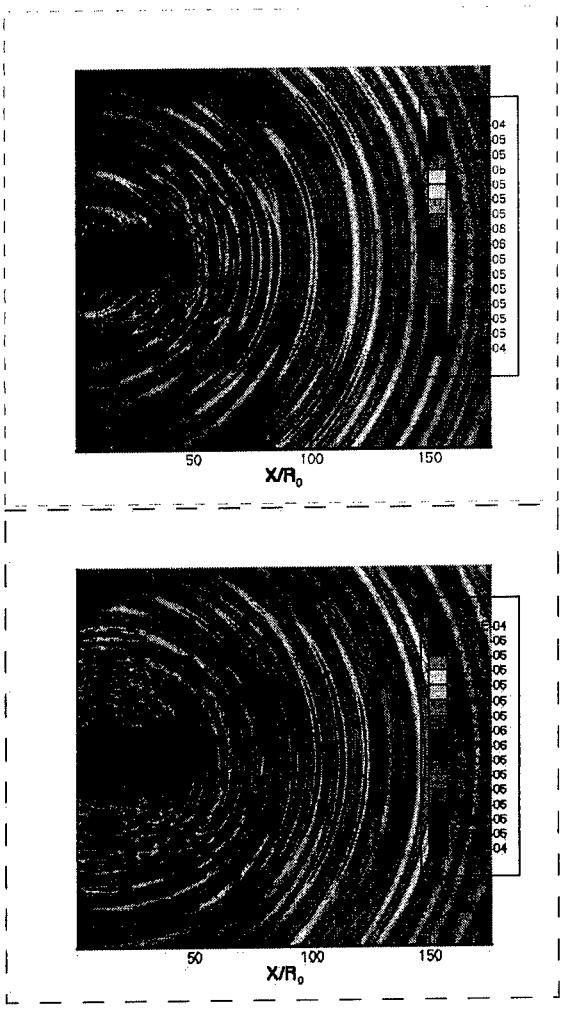


Figure 4. The acoustic field obtained with equation 9 (top) and with help of equation 11 (bottom).

Lighthill, M.J., 1954, On sound generated aerodynamically: II. Turbulence as a source of sound.*Proc. R. Soc. of London, Ser. A*, 222, 1-32.

Lush., P.A., 1971, Measurement of subsonic jet noise and comparison with theory, *J. Fluid Mech.*, **46**, 477-500.

Mitchell, B.E., Lele, S.K., Moin, P., 1999, Direct computation of the sound generated by vortex pairing in an axissymmetric jet, *J. Fluid Mech*, **383**, 113-142.

Mohensi, K. & Colonius, T., 2000, Numerical Treatment of Polar coordinate singularities, *J. Comp. Phys.*, **157**, 787-795.

Mollo-Christensen, E., 1967, Jet noise and shear flow instabilities seen from an experimenter's viewpoint, *J. Appl. Mech.*, **34**, 1-7.

Panchapakesan, N.R., and Lumley, J.L., 1993 *Turbulence measurements in axissymmetric jets of air and helium. Part 1. Air jet*, J. Fluid Mech. i**246**, 197-224.

DIRECT NUMERICAL SIMULATIONS OF HIGH SPEED FLOW OVER CAVITY

A. HAMED, D. BASU, A. MOHAMED AND K. DAS
Department of Aerospace Engineering and Engineering Mechanics
University of Cincinnati, Cincinnati, OH

Abstract

Direct numerical simulations are used to investigate the effect of Mach number on the unsteady flow of an open cavity. The implicit solution is obtained for the compressible Navier-Stokes Equations using compact sixth-order spatial differencing coupled with tenth-order implicit filters. Results for transonic and subsonic flow over a two dimensional cavity are presented for the sound pressure level and pressure fluctuation frequencies.

1. Introduction

Future Strike Aircrafts have a requirement for supersonic release of weapons from internal weapons bays. The associated highly unsteady flow features result in the production of noise levels which are unacceptable for operational and safety considerations. Current generation bay spoilers fail to provide adequate acoustic suppression above Mach one. Some degree of acoustic suppression control has been achieved experimentally by stimulating the shear layer spanning the bay with various actuators (Stanek et al. 2000,2001), however optimizing the performance of these devices requires detailed knowledge of the bay flow field.

Grace (2001) conducted a recent review of computational and experimental studies for flow over cavities. Most of the numerical studies were based on the solution of the time dependent Reynolds-Averaged Navier-Stokes equations (RANS). Colonius et al. (1999) used Direct Numerical Simulations (DNS) to study unsteady subsonic flow over two-dimensional cavities, and predicted transition from the shear layer mode to the wake mode as the Mach number and the cavity length to depth ratio increased. Shieh and Morris (2001) used Detached Eddy Simulations (DES) to study subsonic cavity flow. They predicted the wake mode in the two-dimensional but not in the three-dimensional results, and reported better agreement between the predicted pressure fluctuations' frequency and Rossiter's correlation (1964) for the three-dimensional results. Henderson et al. (2000) pointed out that the challenge is to predict the level of oscillation rather than the frequency of the discrete tones, and

presented experimental results for Sound Pressure Level (SPL) at the cavity floor.

Direct numerical simulations are used in the current investigation to study transonic flow over two-dimensional cavities. The results obtained using high order compact differencing in conjunction with high order non-dispersive filters, are presented for the pressure fluctuations, and sound pressure level spectra at the cavity opening for three Mach numbers. The computed vorticity and Mach number contours illustrate the roll up vortex structure in the shear layer and the shock waves above the shear layer as the free stream Mach number increases.

2. Methodology

Direct numerical solutions were obtained for the full compressible Navier-Stokes equations using FDL2DI, the solver developed by Gaitonde and Visbal (1998). The spatial derivatives are represented by high order (up to six) compact approximation that is used in conjunction implicit compact high order filter (up to ten). The scheme achieves second order temporal accuracy using a time-implicit approximately-factored scheme, and Newton-like subiterations. The solver was thoroughly validated by Visbal and Gaitonde (1998,1999) for subsonic flows, wall jets, and acoustic fields. Rizzetta and Visbal (2001) used the code with a third order Roe upwind biased evaluation of the fluxes in the regions of strong shock waves, to perform Large-eddy simulations of supersonic compression-ramp flows.

In the present investigation a sixth-order compact formula was used in the interior points with fifth and fourth orders near the boundary (C45654), according to Visbal and Gaitonde (1999). Similarly the implicit filtering scheme denoted $F10^{0.3}$- 0.2.4.6.8.10, was tenth order in the interior with a free parameter $\alpha_f = 0.3$. The equations were normalized using the cavity depth, free stream velocity, and free stream density. The unsteady solution was advanced using implicit time marching with a non-dimensional time step of 2.0×10^{-3}. The computational domain for the L/D =2 cavity allowed the laminar boundary layer to develop from uniform free stream conditions at the upstream boundary on the flat plate, which extended 4.95D upstream of the cavity's forward bulkhead. At the upper boundary, which was placed 9.35D above the cavity opening, characteristic conditions were applied for subsonic free stream, and first order extrapolation was applied for supersonic free stream. At the downstream boundary, which was placed at 10.41D behind the rear bulkhead, first order extrapolation was applied. The computational grid included 143x129 points inside the cavity, and 330x95 points on and above the plane of cavity opening. The grid was clustered with a minimum spacing of 1.0×10^{-4} D in the streamwise and normal directions.

4. Results and Discussions

Results are presented for a Re_L = 3,000 based on the cavity length, and L/θ = 52.8, where θ is the momentum thickness of the incoming laminar boundary layer. Sample computational results from the direct numerical simulations are presented for free stream Mach numbers of 1.1, 0.9 and 0.6. The vorticity contours of figure 1 show the roll up vortical structures in the shear layer and the counter rotating vorticity (opposing sign to the boundary layer) near the cavity walls and floor. Figure 1 shows that the vortex size increases with the free stream Mach number, but such large scale shedding as reported by Colonius (1999) for subsonic flow in the wake mode was not observed in the present study. Flow separation upstream of the cavity was not observed in Mach 0.6 and 0.9 cases, and was restricted to a very small region in the case of Mach 1.1. The Mach number contours are presented in figure 2 to show the shock wave structure above the shear layer at different times for Mach 1.1.

The pressure fluctuations at the cavity opening, 0.2 L upstream of the rear bulkhead, are presented in figure 3. The free stream Mach number is seen to have a significant effect on the pressure fluctuations amplitude, which at Mach 1.1 is four times that at Mach 0.6. Figure 4 presents the, SPL spectra, calculated from the pressure fluctuations of figure 3 using 65536 sampled points. The variation in computed SPL at the cavity opening with Mach number is presented in Figure 5. Henderson et al. (2000) presented experimental results for SPL at the cavity floor at Mach 0.85, 0.98, and 1.19. Even though the level was higher in the case of L/D=5 cavity, the variation exhibited similar trends with Mach number. The discrete frequencies determined from the spectra are presented in Figure 6, and compared to Rossiter's modified empirical correlation (Hellar et al. 1970). The correlation, which quantifies the coupling of the acoustic and vorticity fields gives the following equation for feedback frequencies:

$$St_m = \frac{f_m L}{U_\infty} = \frac{m - \alpha}{M_\infty / \sqrt{1 + \frac{\gamma - 1}{2} M_\infty^2} + \frac{1}{k}}$$

Where St_m is the Strouhal number, U_∞, and M_∞ are free stream velocity and Mach number, f_m is the resonant frequency corresponding to the m mode. The constants α, and k were determined experimentally to be 0.25, and 0.57 by Heller et al. (1970) for cavities with L/D greater than four. According to Figure 6, the computed frequencies agree within 6% with Rossiter's equation for the first mode, m=1.

5. Conclusions

The presented results for the unsteady two-dimensional flow over a rectangular cavity demonstrated that the direct numerical simulations captured the flow main features including the vortex shedding, shock waves and coupling of the acoustic and vorticity fields. Further investigations are planned for longer cavity at higher Mach numbers with turbulent upstream boundary layer using Large-eddy simulations.

Acknowledgements

This work was supported by DAGSI, Project Number VA-UC-00-01, Dr. Frank Moore Grant monitor. The authors want to thank Dr. D. Gaitonde for his guidance in using FDL2DI, and Dr. D. Rizzetta for his helpful discussions.

References

Colonius, T., Basu, A. J., and Rowley, C. W. (1999) Numerical Investigation of the Flow Past a Cavity. AIAA 99-1912

Gaitonde, D., and Visbal, M. R., (1998) High-Order Schemes for Navier-Stokes Equations: Algorithm and Implementaion into FL3DI, AFRL-VA-TR-1998-3060.

Gaitonde, D., and Visbal, M. R., (1999) Further Development of a Navier-Stokes Solution Procedures Based on High-Order Formulas, AIAA 1999-0557.

Grace, S. (2001) An Overview of Computational Aeroacoustic Techniques Appliedto Cavity Noise Prediction, AIAA 2001-0510.

Heller, H. H., Holmes, G., and Covert, E. (1970). Flow-Induced Pressure Oscillations in Shallow Cavities, AFFDRL-TR-70-104..

Henderson, J., Badcock, K. J., and Richards, B. E. (2000) Understanding Subsonic and Transonic Open Cavity Flows and Suppression of Cavity Tones," AIAA 2000-0658.

Rizzetta, D. P., and Visbal, M. R. (2001) Large Eddy Simulation of Supersonic Compression-Ramp Flows, AIAA-2001-2858.

Rossitter, J.E. (1964). Wind-Tunnel Experiments on the Flow over Rectangular Cavities at Subsonic and Transonic Speeds. Royal Aircraft Establishment Reports and Memoranda No. 3438.

Shieh, C. M., and Morris, Philip, J. (2001) Comparison of two-and three-dimensional turbulent Cavity Flows, AIAA-2001-0511.

Stanek, M. J., Raman, G., Kibens, V., Ross, J. A., Odedra, J., Peto, J.W. (2000) Control of Cavity Resonance Through Very High Frequency Forcing. AIAA 2000-1905.

Stanek, M. J., Raman, G., Kibens, V., Ross, J. A., Odedra, J., Peto, J.W. (2001) Suppression of Cavity Resonance Using High Frequency Forcing – The Characteristic Signature of Effective Devices, AIAA 2001-2128.

Visbal, M. R. and Gaitonde, D. (1998). Direct Numerical Simulation of a Forced Transitional Plane Wall Jet, AIAA 98-2643.

Visbal, M. R., and Gaitonde, D. (1999) Computation of Aeroacoustic Fields on General Geometries Using Compact Differencing and Filtering Schemes, AIAA 99-3707.

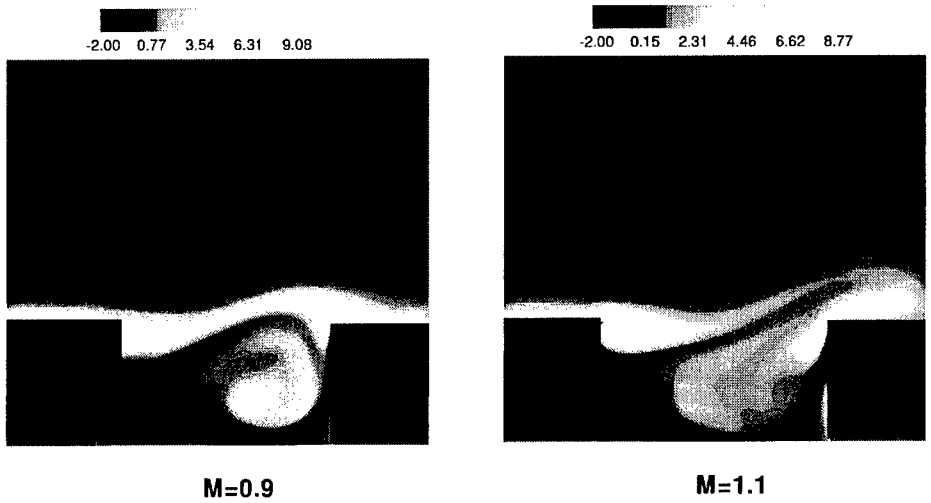


Fig. 1 Vorticity contours

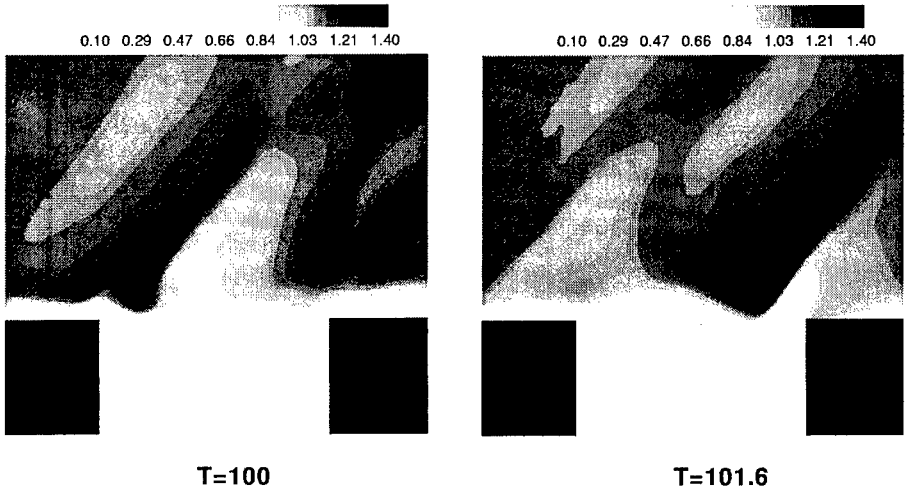


Fig. 2 Mach number contours for freestream Mach number 1.1

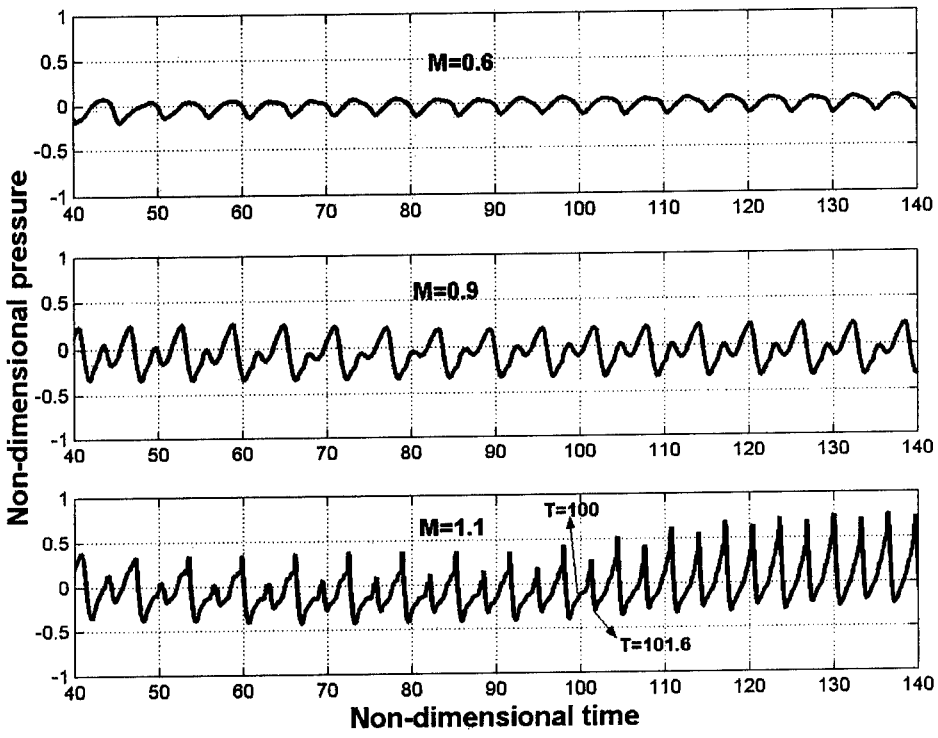


Fig. 3 Perturbation pressure history at cavity opening for different Mach numbers

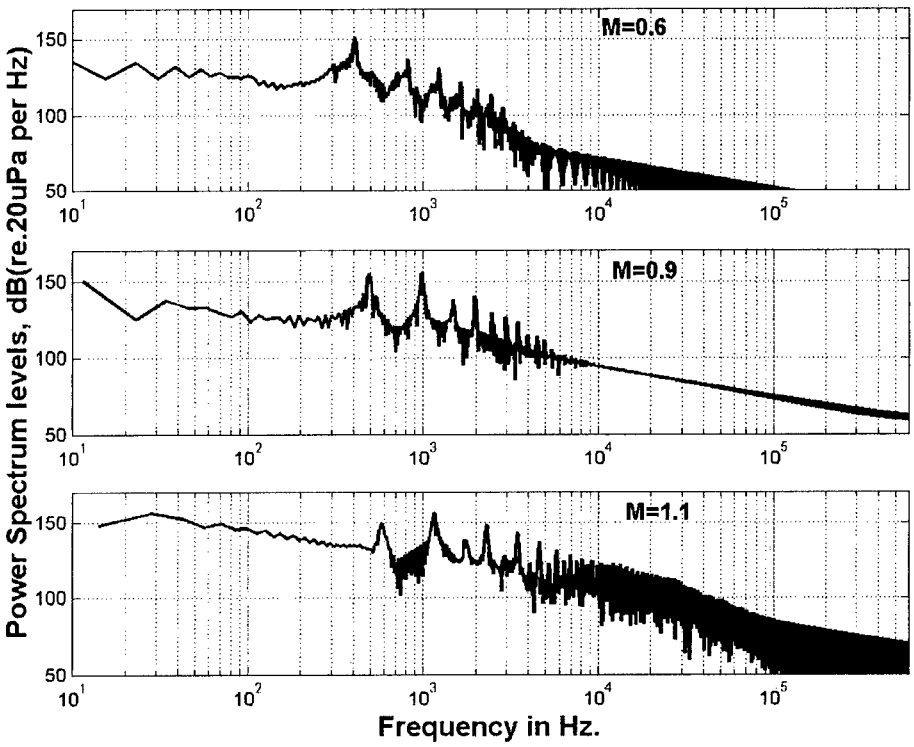


Fig. 4 Sound Pressure level (SPL) spectra for different Mach numbers

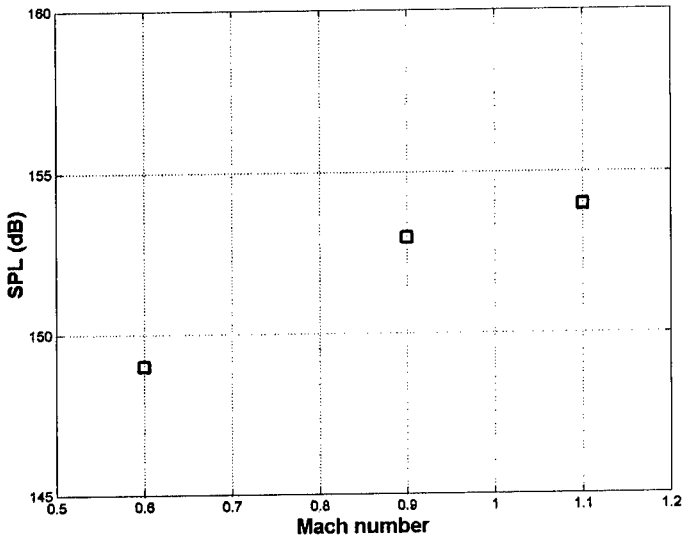


Fig. 5 Variation of sound pressure level with Mach number

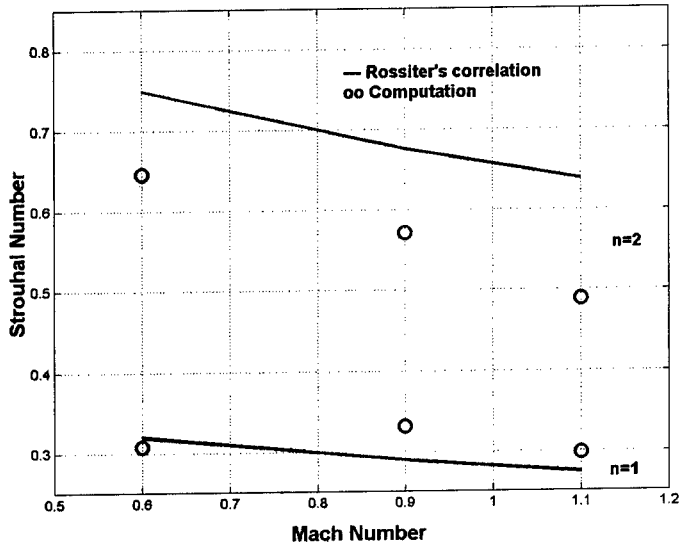


Fig. 6 Comparison of computed discrete frequencies with Rossiter's correlation

FLAME KERNEL INTERACTIONS IN A TURBULENT ENVIRONMENT

K.W. JENKINS AND R.S. CANT
University of Cambridge
CFD Laboratory
Department of Engineering
Trumpington Street
Cambridge
CB2 1PZ
UK

Abstract. Results are presented from a parallel DNS combustion code called SENGA. The code solves a fully compressible reacting flow in three dimensions. High accuracy numerical schemes have been employed which are explicit 10th order central finite differences in space, a third order explicit Runge-Kutta method in time and parallel implementation is achieved through the Message Passing Interface (MPI). Turbulence is generated numerically for a 128^3 simulation with $\mathrm{Re} = 30$ and a 384^3 simulation with $\mathrm{Re} = 130$. Finally, results are presented and discussed for simulations with different initial non-dimensional turbulence intensities ranging from 5 to 23.

1. Introduction

A difficulty that arises in practical turbulent combustion processes, such as the combustor sections of jet engines and internal combustion engines, is the strong coupling between turbulence, chemical kinetics and heat release. These interactions are generally three dimensional and time dependent, and are not easily accessible to experimental investigation. Therefore, to extract valuable information from these and other turbulent flows, highly accurate numerical solutions are required, such as those obtained using Direct Numerical Simulation (DNS).
DNS is now a useful and well established research tool in the field of tur-

bulent combustion. The solution of the full governing equations without the need for any form of turbulence modelling enables the collection of a great deal of information on turbulent flame structure and propagation that is obtainable by no other means. However, to obtain representative simulations, the DNS must be able to resolve the smallest length and time scales applicable to the problem of interest. High resolution and the need to solve in three spatial directions and time comes at a cost, therefore parallel supercomputers are a pre-requisite to carry out these simulations. Due to the high computational costs, it is important to use high accuracy spatial discretisation schemes. The most accurate scheme is the Fourier spectral method, however, these schemes are restricted to problems with periodic boundary conditions which in combustion DNS is a restriction since reactants must be able to enter and products and heat must be able to leave the computational domain. Therefore alternative schemes with spectral like accuracy and non restrictive boundary conditions are required, the most popular scheme for combustion being the compact scheme (Lele, 1992). In the present work, 10th order explicit finite differences are employed. These offer near spectral accuracy along with inflowing and outflowing boundary conditions and are more efficient for parallel implementation. (Prosser and Cant, 1998) compared various spatial schemes applicable to combustion DNS, and showed the explicit scheme to perform well in terms of accuracy when the resolution is known to be sufficient, and in terms of CPU time and storage the explicit schemes proved least expensive on both counts.

Practical combustion problems have chemical and turbulent scales and in most cases it is the smallest chemical scales within the reaction zone of the flame that are of interest, not the smallest turbulent scales. This is true for example in the spark ignition engine where combustion takes place in a reasonably homogeneous mixture of fuel vapour and air, and where the turbulence is of moderate intensity. These kind of systems operate within the laminar flamelet regime of turbulent premixed combustion (Libby and Williams, 1994). Here the thickness of the flame sheet remains smaller than the Kolomogorov scale of turbulence and the Kilmov-Williams criteria is satisfied (Williams, 1985). The flame sheet retains the structure of a laminar flame, even though it is wrinkled by the surrounding turbulence. The flame-turbulence interactions in the present work are in the above regime and therefore the flame structure and not the turbulence defines the resolution requirement. Research in combustion DNS as come a long way in these regimes (Poinsot *et al.*, 1996), especially for planar flames. The present work uses flame kernels in a turbulent environment which have a practical relation to ignition problems. The growth of the flame is laminar once established in the early stages, and then propagates spherically outwards. Its motion is accelerated by flow divergence due to thermal expansion and it

begins to interact with the surrounding turbulence becoming wrinkled and increasing in surface area. Flame kernels in conjuction with non-reflecting outflow boundaries on all faces using the NSCBC formalism (Poinsot and Lele, 1992), allow the flame structure to be observed away from the influence of any boundary impositions.
The aim of the present research is to use a parallel DNS code called SENGA, developed in Cambridge, to study flame kernels in a turbulent environment. The DNS code solves the fully compressible reacting flow equations in three dimensions and time with heat release. The paper is organised as follows. The equations governing the flow are outlined in non-dimensional format, the numerical procedure is explained and finally the simulation method and results are presented for various flame turbulent interactions.

2. Governing Equations

The governing equations that describe the motion of a reacting gas are the three dimensional equations for mass, momentum, energy and a species conservation equation (Williams, 1985). In non-dimensional form these equations become.

$$\frac{\partial \rho}{\partial t} + \frac{\partial \rho u_k}{\partial x_k} = 0 \tag{1}$$

$$\frac{\partial \rho u_i}{\partial t} + \frac{\partial \rho u_k u_i}{\partial x_k} = -\frac{\partial P}{\partial x_k} + \frac{1}{Re}\frac{\partial \tau_{ki} u_i}{\partial x_k} \tag{2}$$

$$\begin{aligned}\frac{\partial \rho E}{\partial t} + \frac{\partial \rho u_k E}{\partial x_k} = & -(\gamma-1)\mathcal{M}^2 \frac{\partial P u_k}{\partial x_k} \\ & + \frac{1}{Re}(\gamma-1)\mathcal{M}^2 \frac{\partial \tau_{ki} u_i}{\partial x_k} \\ & + \frac{\tau}{RePr}\frac{\partial}{\partial x_k}(\lambda \frac{\partial T}{\partial x_k}) \\ & - \frac{\tau}{ReSc}\frac{\partial}{\partial x_k}(\rho D \frac{\partial c}{\partial x_k})\end{aligned} \tag{3}$$

$$\frac{\partial \rho c}{\partial t} + \frac{\partial \rho u_k c}{\partial x_k} = \omega_\alpha + \frac{1}{ReSc}\frac{\partial}{\partial x_k}(\rho D \frac{\partial c}{\partial x_k}) \tag{4}$$

where x and t are the space and time coordinates, ρ is the density, u is the velocity , P is the pressure, E is a stagnation internal energy, c is a reaction progress variable, formulated as a normalised mass fraction and rising monotonically from zero in the unburned state to unity in the fully burned products and τ_{ki} is the viscous stress tensor
The non-dimensional parameters in the above equations are the Mach num-

ber $\mathcal{M}$, the Reynolds Number Re, the Prandtl number Pr and the Schmidt number Sc. For a full description of the non-dimensionisation and the extra terms needed to close the problem, see (Jenkins and Cant, 1999).

3. Numerical Procedure

Turbulent combustion DNS requires spatial schemes with high accuracy. Therefore, all first and second spatial derivatives are discretised using a central 10^{th} order explicit scheme obtained from the central finite difference approximation

$$f_i' = \sum_{j=1}^{m/2} \frac{a_j}{2jh}(f_{i+j} - f_{i-j})$$

where m is the order of the approximation (always even). Values of constants a_j are obtained by expanding in Taylor series and equating coefficients of successive orders in h.

These finite difference approximations have a stencil width of eleven points which implies 5 points are required at the boundary. These boundary points are again treated with explicit finite differences of decreasing accuracy to the boundary. This is covered in detail by (Jenkins and Cant, 1999). Time stepping is carried out by an explicit third order Runge-Kutta method (Wray, 1990). This method requires three sub steps for each main time advancement step and requires only two storage locations, one for the time derivative and one for the dependent variable.

An initial field of isotropic turbulence is generated numerically to satisfy the continuity constraint for incompressible flow. The general requirement for this turbulent field is the specification of an energy spectrum E(k), where k is a wavenumber in the Fourier-space representation of the turbulent velocity field. Various energy specta exist for this work such as (Lee and Reynolds, 1985) which as previously been used by the authors. However, the present work uses the spectrum of (Schumann and Patterson, 1978) after studies showed a slower decay in turbulent kinetic energy compared to Lee and Reynolds. This is of interest, especially for higher turbulence intensity cases, were the flame interacts longer at the higher intensities. Finally, boundary conditions are implemented using the Navier Stokes Characteristic Boundary Conditions (NSCBC) (Poinsot and Lele, 1992) and parallel implementation is achieved through the Message Passing Interface (MPI).

4. Simulation Results

Flame kernel interactions for various turbulent intensities will be presented. Two simulations were undertaken, one with a grid size 384^3 and the other with a grid size 128^3. Both simulations were undertaken using 64 processors on the Hitachi SR2201 at Cambridge University and table 2 shows the problem parameters for each case.

TABLE 1. Simulation Parameters

Case	Re	Pr	Sc	M	β	α	τ	B
128^3	30	0.7	0.7	0.00142	6.0	5.0	0.83	1225.0
384^3	130	0.7	0.7	0.00142	6.0	5.0	0.83	1225.0

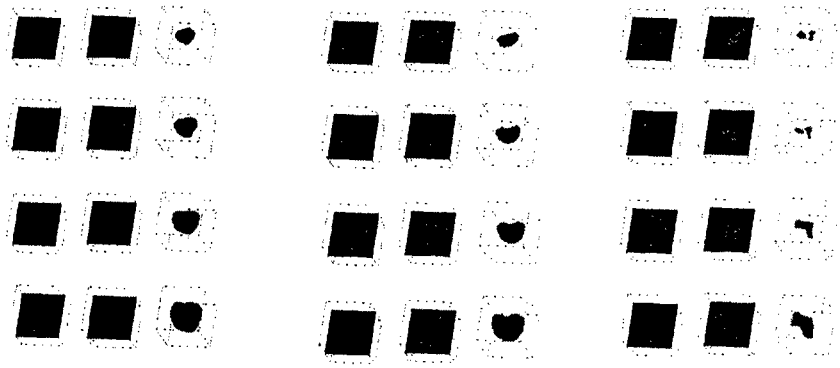
In both cases, the simulations were initialised by a Gaussian distribution of the progress variable c decomposed on the 64 processors with an initial turbulent field. All boundary conditions were non-reflecting outflow types with a time step $\Delta t = 1.0 \times 10^{-6}$ which is restricted by the acoustic Courant stability criteria. Initial studies on small grids (64^3) have been undertaken with $\mathcal{M} = 0.0142$, enabling larger time steps $\Delta t = 1.0 \times 10^{-4}$. Computational performance is reasonable, with the initial turbulent fields taking approximately 8 and 20 minutes to generate for 128^3 and 384^3 simulations respectively, and time stepping takes approximately 15 and 50 seconds for each case. A full parallel performance test can be found in (Jenkins and Cant, 1999).

Figures 1a - 1c show results from initial $\frac{u'}{S_L}$ values of 5, 10 and 23 respectively. In each figure, three sets of results are plotted at 2, 4, 6 and 8 thousand time steps. The left and centre columns show a 2D slice from a laminar and turbulent flame and the right column shows the isosurface of progress variable c, all at the same time levels respectively. The laminar and turbulent flame cases are plotted with progress variable contours ranging from 1 (fully burned) at the centre to 0 (unburned) on the outer contour. In each case the flames can clearly be seen to propagate outwards. As the flames develop the effect of turbulence on them becomes less significant, since the turbulence is decaying. From these figures, an important feature of the flame is clear. Small scale wrinkles in the flame, more noticeable at $\frac{u'}{S_L}$ =23, do not remain. They appear to be smoothed out as the flame propagates. Also evident at high turbulence intensity is the flame breaking up and re-joining as the turbulence decays.

Figures 2a and 2b show a (128^3) flame evolution at the centre x-y plane

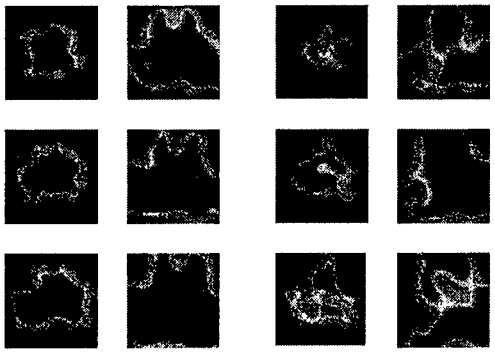
(k=64) and the quarter x-y plane (k=96) over time starting at the top left and going to the bottom right of each figure. Two interesting features occur in these figures, the first being an increase in burned area with time about the initial ignition point and the second is the evidence of holes in the flame due to strain. The holes are more noticeable in figure 2b. Here the image plane is initially at the edge of the flame and as the flame progresses holes and break up are evident. Figure 3 looks at an enlarged portion of the centre plane. Here the flame front is moving to the right and upwards. Velocity vectors are superimposed on to the flame contours to show the effect of flame curvature due to the eddies in the turbulent field. Also at the points of maximum curvature the flame thickness seems to be increasing due to a higher burning rate, since the surface area is increasing.
Finally, figure 4 shows an isosurface of the progress variable at c = 0.8. The image shown is for the inner 8 processors of a 64 processor simulation. This is evident by the rings on each surface due to the flame leaving one processor and joining the next. This is a good indication of the velocity of the parallel implementation as well as visualising in three dimensions the flame surface.

5. Figures



(a) $\frac{u'}{S_L}$=5 (b) $\frac{u'}{S_L}$=10 (c) $\frac{u'}{S_L}$=23

Figure 1. laminar, turbulent and isosurfaces for 3 turbulent cases t = 2k - 8k



(a) Centre Plane (b) Quarter Plane

Figure 2. 2D slice at centre x-y plane and quarter x-y plane

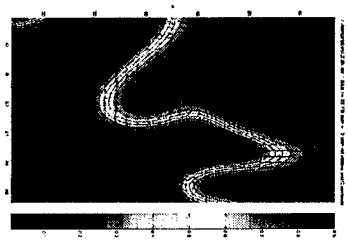


Figure 3. Enlarged 2D slice of progress variable contours and velocity vectors

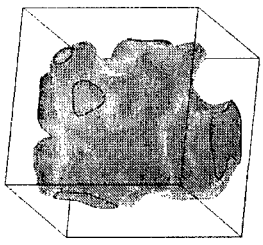


Figure 4. Isosurface of progress variable, c = 0.8

Acknowledgements

This work was supported by EPSRC under research grant number GR/M18256. The authors would also like to thank the High Performance Computing Centre at Cambridge University for their assistance and access to the Hitachi SR2201.

References

Jenkins, K.W., Cant, R.S. (1999) DNS of turbulent flame kernels, Proc. Second AFOSR Conf on DNS and LES, eds (Knight and Sakell), Rutgers University, *Kluwer Academic Publishers* **pp. 192-202.**

Lee, M.J., Reynolds, W.C. (1985) Numerical experiments on structure of homogeneous turbulence, *Technical Report, Dept of Mech Eng, Stanford* **TF-24.**

Lele, S.K. (1992) Compact finite difference schemes with spectral-like resolution, *J. Comp Phys* **Vol 103, pp. 16-42.**

Libby, P.A., Williams, F.A. (1994) Turbulent reacting flows, *Academic press, New York.*

Poinsot, T.J., Candel, S., Trouve, A. (1996) Application of direct numerical simulation to premixed turbulent combustion, *Prog Energy Comb Sci*, **Vol 21, pp. 531-576.**

Poinsot, T.J, Lele, S.K. (1992) Boundary conditions for direct simulations of compressible viscous flows. *J. Comp Phys* **Vol 101, pp. 104-129.**

Prosser, R., Cant, R.S. (1998) Assesment of spatial discretisation schemes for direct numerical simulation of combustion, *Unpublished report, Dept of Engineering, University of Cambridge.*

Schumann, U., Patterson, G.S. (1978) Numerical study of pressure and velocity fluctuations in nearly isotropic turbulence, *J. Fluid Mech* **Vol 88, part 4, pp. 685-709.**

Wiiliams, F.A. (1985) Combustion theory, 2^{nd} ed, *Addison Wesley, Menlo Park, California.*

Wray, A.A. (1990) Minimal storage time advancement schemes for spectral methods, *unpublished report, NASA Ames.*

ANISOTROPY IN REACTING COMPRESSIBLE TURBULENT SHEAR FLOW

D. LIVESCU AND C.K. MADNIA
Department of Mechanical and Aerospace Engineering,
State University of New York at Buffalo,
Buffalo, NY 14260

Abstract.

The structure of reacting compressible homogeneous turbulent shear flow is examined via data generated by direct numerical simulations (DNS). The reaction is modeled as one-step, exothermic, irreversible, and Arrhenius type. The effects of reaction are studied by decomposing the velocity field into its solenoidal and dilatational parts. The heat of reaction significantly enhances the dilatational kinetic energy, while it reduces its solenoidal counterpart. The solenoidal and dilatational large scales (kinetic energy) and small scales (viscous dissipation) anisotropies are investigated for cases with different initial turbulent Mach numbers and Reynolds numbers.

1. Introduction

Homogeneous turbulent shear flow represents one of the simplest anisotropic flows and its study can reveal important aspects of the structure and production of the turbulent fluctuations. Moreover, the recent high Reynolds number experiment of incompressible turbulent shear flow of Shen and Warhaft (2000) indicates that the higher order moments of the velocity field are not consistent with the postulate of local isotropy. Although DNS at high Reynolds numbers are not feasible yet, persistent anisotropy of the higher order moments for incompressible shear flow at moderate Reynolds numbers has been observed earlier in the numerical results of Pumir (1996). Compared to incompressible turbulent shear flow, the compressible turbulent shear flow is much less investigated computationally, although the recent studies of Blaisdell, Mansour & Reynolds (1993), Sarkar (1995) and Hamba (1999) have improved our understanding of the influence of compressibility on the structure and development of the flow. The heat release influence on the turbulent shear flow development has been studied by Livescu, Jaberi & Madnia (2001) (hereinafter, referred to as LJM01). However, the reacting flows usually involve a large amount of heat release and thus are intimately related to the compressibility of the flow. Furthermore, the combined effects of heat release and compressibility

on the structure of the turbulent shear flow have not been studied. The main objective of this study is to examine the influence of heat release and compressibility on the large scale and small scale anisotropies in reacting compressible homogeneous turbulent shear flow.

2. Numerical Methodology and DNS Parameters

In order to assess the coupled influence of compressibility and heat release on the structure of the reacting compressible shear flow, DNS of homogeneous sheared turbulence are performed under reacting (heat-releasing) and nonreacting conditions. The continuity, momentum, energy and species mass fractions transport equations are solved using the spectral collocation method. The coordinate system is moving with the mean velocity which makes necessary a periodic remeshing of the grid in order to avoid errors associated with highly skewed grids. The remeshing procedure is carried out in wavenumber space with explicit removal of the modes affected by aliasing. The aliasing errors associated with the evaluation of the nonlinear terms are controlled by using the skew-symmetric form of the convective terms. In the reacting cases, the chemical reaction is modeled by a single step, exothermic, irreversible, Arrhenius-type reaction. The viscosity varies with the temperature according with a power law and $Le = 1$ in all cases.

The velocity fluctuations are initialized as a random solenoidal, 3-D field with Gaussian spectral density function (with the peak at $k_{0v} = 10$) and unity rms. The initial pressure fluctuations are evaluated from a Poisson equation (except for case 3 for which they are set to zero) and the initial density field has the mean value equal to 1 and no fluctuations. For the reacting cases the scalar fields are initialized as "random blobs", with double-delta PDFs (Overholt & Pope, 1996). Details can be found in LJM01. The variables are time advanced in physical space using a second order accurate Adams-Bashforth scheme. The code developed for this work is based on a fully parallel algorithm and uses the standard Message Passing Interface (MPI).

The cases considered in this study, summarized in table 1, have different values for the initial turbulent Mach number, M_{t_0}, and initial Reynolds number, Re_{λ_0}. All cases have the same value of the mean shear rate $S = \partial\tilde{u}_1/\partial x_2 = 5.1$ ($\tilde{u}_i$ is the mass average of the velocity), which is in the range dominated by nonlinear effects. For each case two simulations, nonreacting and reacting, are performed. All reacting cases have the values of the heat release parameter $Ce = 1.44$, computational Damköhler number $Da = 1100$, and Zeldovich number $Ze = 8$. For an initial mean temperature in the range of temperatures prior to ignition in an IC engine, the values for the pre-exponential constant of reaction K_f, the activation energy E_a, and the heat of reaction $-H^0$, are calculated and they are in the range of values for the elementary reactions for hydrocarbon combustion.

The range of Mach numbers considered extends from the nearly incompressible case 1 to the high Mach number case 3 which is at the upper limit for the numerical method considered. The range of Re_{λ_0} extends to values higher than any considered in previous studies of compressible homogeneous turbulent shear flow. The simulations were monitored to ensure that the integral scales remain much smaller than the box size, all scales of motion are fully resolved and no significant shocklet regions develop. Thus, all simulations were stopped between $St = 18$ and 20, except the nonreacting and reacting case 5 which were stopped at $St = 10.5$

Case #	M_{t_0}	Re_{λ_0}	Grid size
1	0.1	21	128^3
2	0.3	21	128^3
3	0.6	21	128^3
4	0.3	14	64^3
5	0.3	50	256^3
2^+	0.3	21	128^3
5^+	0.3	50	256^3

TABLE 1. Parameters for the DNS cases. $^+$ In these cases S is set to zero at $St = 4$.

and $St = 12.5$, respectively, before strong shocklets can be formed in the flow. Cases with different values of the reaction parameters and mean shear rate have also been examined. Although the results for these cases are not shown here, they agree qualitatively with the results presented in this paper.

3. Results

Due to the presence of the mean velocity gradient, the velocity field, initially isotropic, develops to become anisotropic with $K_1 > K_3 > K_2$, where K_1 is the kinetic energy in the direction of the mean velocity (the only component of the kinetic energy with a production term in its transport equation) and K_2 is the kinetic energy in the direction of the shear. In order to examine quantitatively the degree of anisotropy among the kinetic energy components, the Reynolds stress anisotropy tensor is considered:

$$b_{ij} = \frac{< \rho u_i'' u_j'' >}{< \rho u_k'' u_k'' >} - \frac{1}{3}\delta_{ij} \tag{1}$$

In agreement with the previous nonreacting simulations (Sarkar 1995; Hamba 1999) our results show that the anisotropy among the normal stresses increases with increasing M_{t_0}. However, as figure 1 shows, for the reacting cases the normal stresses anisotropy decreases during the time when the reaction is important ($3 < St < 8$). Similar results are also obtained for reacting mixing layers (Luo 1999). For the case of reacting homogeneous shear flow, it is shown in LJM01 that this decrease can be associated with two effects, a decrease in the solenoidal kinetic energy in the direction of the mean velocity due an enhanced viscous dissipation and an increase in the dilatational part of the kinetic energy in the direction of the mean shear. However, after the reaction is completed ($St > 10$) the normal stresses anisotropy becomes larger than in the nonreacting case. This behavior is related to reduced levels of the pressure strain terms, responsible for the energy redistribution among the kinetic energy components. As the value of the shear rate S is set to zero, the flow starts to return to isotropy (figure 1), although some small persistent anisotropy can be observed for the time range examined.

As explained by LJM01, the solenoidal and dilatational parts of the kinetic energy are influenced differently by the reaction. Therefore, in order to understand the heat release effects, it is more useful to study separately the anisotropy among the dilatational and solenoidal components of the normal Reynolds stresses. We define a measure of the anisotropy of the normal stresses as:

$$a_K^\alpha = \left[(b_{11}^\alpha)^2 + (b_{22}^\alpha)^2 + (b_{33}^\alpha)^2\right]^{1/2} \tag{2}$$

where $b_{ij}^\alpha = < \rho u_i''^\alpha u_j''^\alpha > / < \rho u_k''^\alpha u_k''^\alpha > -1/3\delta_{ij}$, and $\alpha = s$ or d represents the solenoidal or dilatational part, respectively. Helmholtz decomposition is used to split the normal Reynolds stresses into their solenoidal and dilatational components. In the extreme case where $b_{11}^\alpha = 2/3$ and $b_{22}^\alpha = b_{33}^\alpha = -1/3$, $a_K^\alpha = \sqrt{2/3}$ and thus $0 \leq a_K^\alpha \leq \sqrt{2/3}$.

Figure 2 shows that a_K^s increases as M_{t_0} increases, and this can be mainly associated with a decrease in the solenoidal pressure strain terms. For the reacting cases, as shown by LJM01, the heat release influences the solenoidal parts of the normal Reynolds stresses mainly through the viscous terms. Furthermore, the increase in the solenoidal viscous dissipation components is such that the anisotropy among the solenoidal parts of the normal stresses is little affected. As a result, as figure 2 shows, the values of a_K^s for the reacting and nonreacting cases are close during the time when the reaction is important. At later times a_K^s becomes larger for the reacting cases compared to the nonreacting cases, although the difference between the values obtained for the reacting and nonreacting cases decreases with increasing Mach number.

The influence of the initial value of the Reynolds number on the evolution of a_K^s is presented in figure 3(a). As expected, a_K^s decreases with increasing Re_{λ_0} for both nonreacting and reacting cases. After S is set to zero, a_K^s decreases initially, then reaches a quasi-steady state. This persistent (although small) anisotropy decreases with increasing Re_{λ_0} and it is discussed in more detail below.

It is found in LJM01 that the explicit dilatational effects occur predominantly in the direction of the mean velocity gradient in both nonreacting and reacting cases. The role of the reaction is to significantly amplify these effects, during the time when the reaction is important. Consequently, as figure 3(b) shows, the anisotropy among the dilatational components of the normal Reynolds stresses increases by the reaction. By comparing the results presented in figures 3(a) and (b) it can be seen that the anisotropy levels remain higher for a_K^d than for a_K^s after S is set to zero. For clarity, the results obtained for the reacting cases 2^+ and 5^+ are not shown in figure 3(b) but they are consistent with the discussion above. The M_{t_0} influence on the evolution of a_K^d has also been examined but no clear trend has been observed, although it seems that the behavior at small and large values of M_{t_0} is different.

The quantity a_K^α is defined based on the kinetic energy components and thus it can be associated with the anisotropy at large scales. The small scale anisotropy has been studied in detail for incompressible flows for a large range of Re_λ and it is generally agreed that the second order moments are consistent with the requirements of local isotropy postulate (Saddoughi & Veeravalli 1994; Shen & Warhaft 2000; Ferchichi & Tavoularis 2000). Much less is known, however, about the small scale anisotropy in compressible flows or the differences between the small scale behavior of the solenoidal and dilatational velocity fields. Although the values of the Reynolds numbers in the present study are not high enough to address the

issues of the local isotropy postulate, our results can be useful for modeling purposes and to shed some light on the physics of the solenoidal and dilatational fields in turbulent reacting flows.

Consistent with the definitions for the viscous dissipation terms in the transport equations for the solenoidal and dilatational parts of the normal Reynolds stresses provided in LJM01, the measures of the anisotropies of the solenoidal and dilatational dissipations are defined as:

$$a_\epsilon^\alpha = \left[(d_{11}^\alpha)^2 + (d_{22}^\alpha)^2 + (d_{33}^\alpha)^2\right]^{1/2} \tag{3}$$

where $d_{ij}^\alpha = \epsilon_{ij}^\alpha/\epsilon_{kk}^\alpha - 1/3\delta_{ij}$, and ϵ_{ij}^s and ϵ_{ij}^d are the components of the solenoidal and dilatational viscous dissipation tensors, respectively. Figure 4 shows that the solenoidal dissipation anisotropy has a similar dependence on M_{t_0} as a_K^s, for nonreacting as well as for reacting cases. The difference between the late time values of a_K^s and a_ϵ^s for the reacting and nonreacting cases decreases at higher values of M_{t_0}. In order to examine which scales of motion are responsible for this behavior, the three-dimensional power spectra of the solenoidal velocity are examined in figure 5 at $St = 18$. It can be seen that the energy levels are lower at all scales at higher M_{t_0} for both nonreacting and reacting cases. However, for the reacting cases the small and intermediate scales are mostly affected. Since the small scales are more isotropic, the energy decrease at small scales for the reacting cases can be associated with an increase in the anisotropy of the flow. Moreover, for the reacting cases the small scales energy levels decrease more at lower M_{t_0}. As the Reynolds number increases, a_ϵ^s decreases (figure 6a). However, it remains larger for the reacting cases than for the nonreacting cases. For the highest Re_{λ_0} examined, a_ϵ^s becomes very small after S is set to zero.

The dilatational dissipation anisotropy becomes larger than its solenoidal counterpart after the initial development time for both reacting and nonreacting cases (figure 6b). Unlike a_ϵ^s, a_ϵ^d is much larger for the reacting cases than for the corresponding nonreacting cases during the time when the reaction is important, which is consistent with the discussion above about the amplification of the dilatational effects by the reaction in the direction of the mean velocity gradient. After the mean shear rate is set to zero, even for the case with the highest Re_{λ_0} examined, there are still some persistent anisotropy levels. For clarity, the results obtained for the reacting cases 2^+ and 5^+ are not shown in figure 6(b) but they are consistent with the discussion above.

For reacting decaying isotropic turbulence, Jaberi, Livescu & Madnia (2000) show that the heat release increases the dilatational kinetic energy, unlike the solenoidal energy, at all scales. Figure 7 shows that at $St = 6$, which is close to the time when the mean reaction rate peaks for case 5, the dilatational energy is enhanced at all scales by the reaction. As the reaction is completing ($St > 10$), the contributions from the production and pressure dilatation terms to the increase in the dilatational kinetic energy decrease (LJM01). Moreover, due to the higher temperature, the viscous dissipative effects are still significant and the energy in the small dilatational scales becomes less than in the nonreacting case.

In order to understand the persistent anisotropy levels observed in the normal Reynolds stresses after setting S to zero, the three-dimensional power spectra of the solenoidal and dilatational velocities for the nonreacting case 5^+ at different times are examined in figure 8. It can be seen that the solenoidal kinetic energy is affected mostly at intermediate scales after the shear rate is set to zero. Thus

the largest eddies, which are more anisotropic, are little affected during the initial transient time when the flow adapts to the new conditions. However, the intermediate dilatational scales do not decrease their energy during initial transient time after setting $S = 0$, and the largest scales even increase their energy levels. Therefore, it is expected that some persistent dilatational anisotropy levels should remain in the flow after setting $S = 0$. Although these levels are likely to vanish as the Reynolds number increases, it is important to note that they are larger than for the solenoidal motions, suggesting that the return to isotropy could be different for the solenoidal and dilatational fields.

4. Concluding remarks

DNS are conducted of compressible homogeneous turbulent shear flow under reacting (heat releasing) and nonreacting conditions to examine the coupled influence of compressibility and heat release on the structure of the flow. For the reacting cases the chemical reaction is modeled as one step, irreversible, and Arrhenius type. The parameters considered for this study are the initial values of the turbulent Mach number and the Reynolds number. In order to examine the return to isotropy, after significant anisotropy levels are developed in the flow, the value of the mean shear rate is set to zero for cases with different values of Re_{λ_0}.

In order to study the changes in the structure of the flow due to the heat of reaction and compressibility, the velocity field is decomposed into solenoidal and dilatational parts using the Helmholtz decomposition. Anisotropy tensors are defined for each part of the normal Reynolds stresses and also for the solenoidal and dilatational parts of the viscous dissipation. The results show that both the large and small scale anisotropies are affected by compressibility and heat release. However, the small solenoidal scales tend to be more isotropic than their dilatational counterparts for the range of Reynolds numbers examined. This tendency is also maintained after setting the shear rate to zero.

Acknowledgments

This work is sponsored by the American Chemical Society under Grant 35064-AC9. Computational resources were provided by the San Diego Supercomputer Center, National Center for Supercomputer Applications at the University of Illinois Urbana-Champaign, and the Center for Computational Research at the State University of New York at Buffalo.

References

Blaisdell, G. A., Mansour, N. N. & Reynolds, W. C. 1993 Compressibility effects on the growth and structure of homogeneous turbulent shear flows. *J. Fluid Mech.* **256**, 443-485.

Ferchichi, M. & Tavoularis, S. 2000 Reynolds number effects on the fine structure of uniformly sheared turbulence. *Phys. Fluids* **12**, 2942-2953.

Hamba, F. 1999 Effects of pressure fluctuations on turbulence growth in compressible shear flow. Phys. Fluids **11**, 1623-1635.

Jaberi, F. A., Livescu, D. & Madnia, C. K. 2000 Characteristics of chemically reacting compressible homogeneous turbulence. *Physics of Fluids* **12**, 1189-1209.

Livescu, D., Jaberi, F. A. & Madnia, C. K. 2001 Heat release effects on the energy exchange in turbulent reacting shear flow. Accepted for publication in *J. Fluid Mech.*

Luo, K. H. 1999 Combustion effects on turbulence in a partially premixed supersonic diffusion flame. *Combust. Flame* **119**, 417-435.

Pumir, A. 1996 Turbulence in homogeneous shear flow. *Phys. Fluids* **8**, 3112-3127.

Shen, X. & Warhaft, Z. 2000 The anisotropy of the small scale structure in high Reynolds number ($R_\lambda \approx 1000$) turbulent shear flow. *Phys. Fluids* **12**, 2976-2989.

Saddoughi, S. G. & Veeravalli, S. V. 1994 Local isotropy in turbulent boundary layers at high Reynolds number. *J. Fluid Mech.* **268**, 333-372.

Sarkar, S. 1995 The stabilizing effect of compressibility in turbulent shear flows. *J. Fluid Mech.* **282**, 163-186.

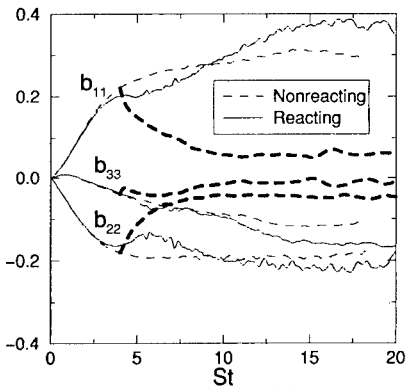


Figure 1: The diagonal components of the anisotropy tensor for case 2 (thin lines) and 2* (thick lines).

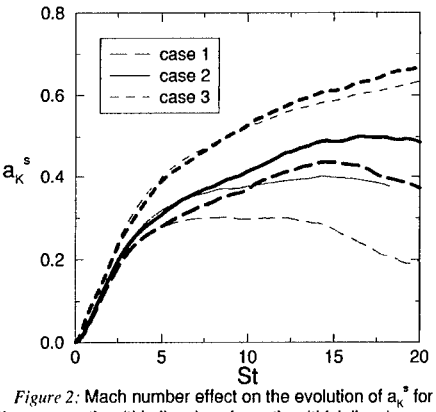
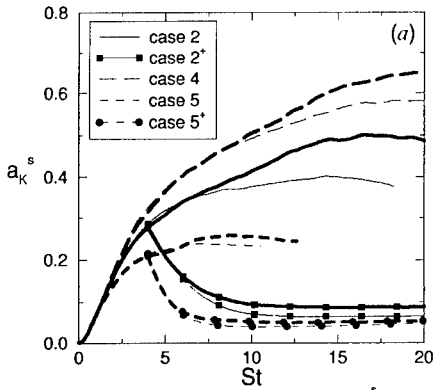


Figure 2: Mach number effect on the evolution of a_K^s for the nonreacting (thin lines) and reacting (thick lines) cases.



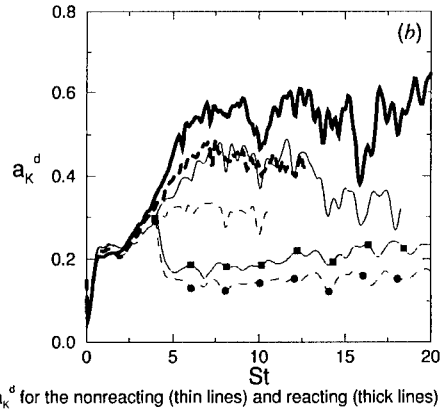


Figure 3: Re influence on the evolution of *a)* a_K^s and *b)* a_K^d for the nonreacting (thin lines) and reacting (thick lines) cases.

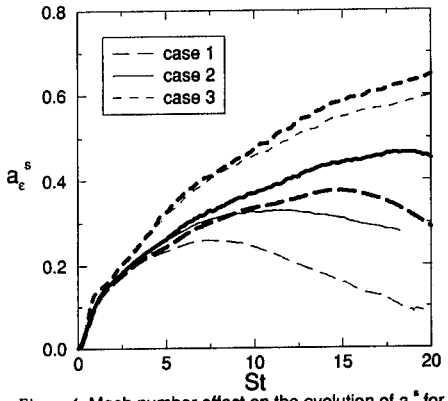


Figure 4: Mach number effect on the evolution of a_ϵ^s for the nonreacting (thin lines) and reacting (thick lines) cases.

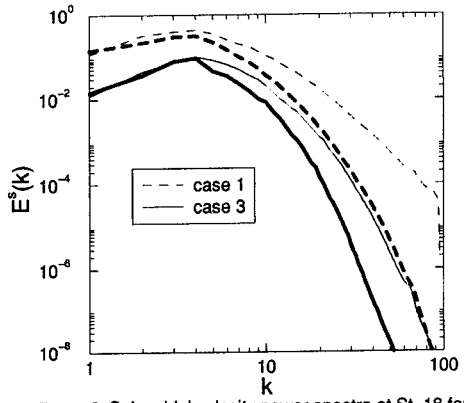
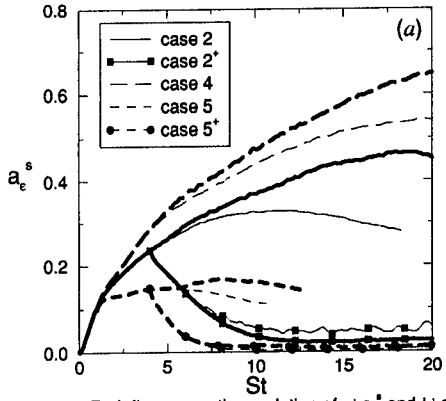


Figure 5: Solenoidal velocity power spectra at St=18 for the nonreacting (thin lines) and reacting (thick lines) cases.



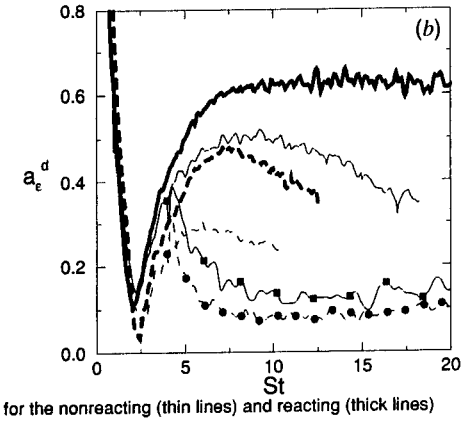


Figure 6: Re influence on the evolution of *a)* a_ϵ^s and *b)* a_ϵ^d for the nonreacting (thin lines) and reacting (thick lines) cases.

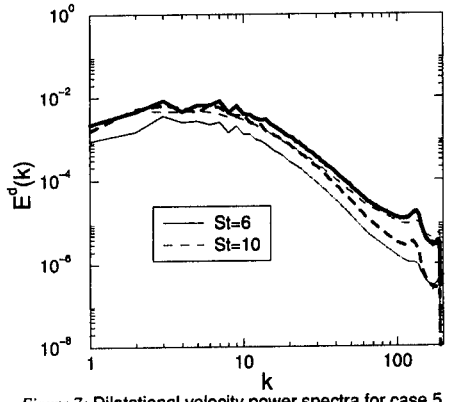


Figure 7: Dilatational velocity power spectra for case 5 nonreacting (thin lines) and reacting (thick lines).

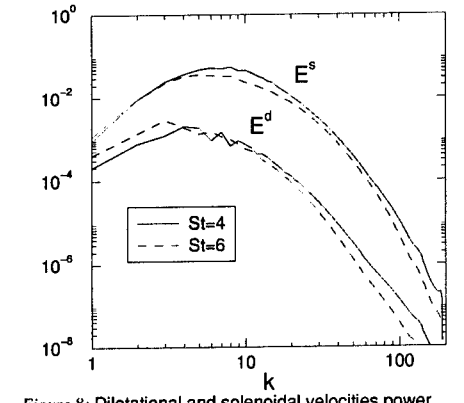


Figure 8: Dilatational and solenoidal velocities power spectra for case 5+.

SIMULATION OF PARTICLE COAGULATION IN TEMPORALLY DEVELOPING MIXING LAYERS

S.C. GARRICK, S. MODEM AND M.R. ZACHARIAH
Department of Mechanical Engineering
University of Minnesota
Minneapolis, MN 55455-0111

AND

K.E.J. LEHTINEN
Department of Physics
Helsinki University
Helsinki, 00014 Finland

Abstract. Direct numerical simulation of coagulating aerosols in two-dimensional, mixing layers are performed. The evolution of the particle field is obtained by utilizing a sectional model to approximate the aerosol general dynamic equation. The sectional model is advantageous in that there are no *a priori* assumptions regarding the particle size distribution. This representation facilitates the capture of the underlying physics in an accurate manner.

1. Introduction

Ultrafine particles play a very important role in a wide variety of physical/chemical phenomena and processes. An important application is the synthesis of nanostructured materials. There are several technologies which can be employed in the manufacture of nanoscale materials (films, particles, *etc.*) Vapor-phase methodologies are by far the most favored because of chemical purity and cost considerations. A key issue in the formation of nanoscale particles is the prevention of hard agglomerates and chemical control. A number of strategies have been attempted to minimize agglomeration(Matsoukas and Friedlander, 1991).

The dynamics of particles in turbulent flows have received some attention. The earlier works were focused on understanding the phenomenon of particle dispersion by turbulence(Riley and Patterson, 1974; Elghobashi, 1991). The influence of particle parameters on collision frequencies in a turbulent particle laden suspension leading to coagulation was considered by Sundaram and Collins (1996), who showed that the magnitude of the minimum particle collision frequency was strongly correlated with the turbulent motions at the integral scale. Reade and Collins (2000) simulated the coagulation and growth of an initially mono-disperse aerosol subject to isotropic turbulence. This work resulted in an improved understanding of the trends in the relative width of the particle size distribution and its dependence on the Stokes number and radial distribution function. However, much of the work performed thus far consider large, micron-scale particles in a Lagrangian manner which use primarily particle tracking methods. The large number of particles needed to represent the underlying physics of particle growth using Lagrangian methods render the computations infeasible for all but inhomogeneous systems.

In this work we consider the growth of nanoscale particles in a compressible, temporally developing mixing layer. The particulate phase will be accounted for using a sectional method which treats the particles in an Eulerian manner(Pyykonen and Jokiniemi, 1999; Garrick *et al.*, 2001). This approach is advantageous in that there are no *a priori* assumptions regarding the nature of the particle size distribution. We intend to use direct numerical simulations to capture the underlying physics of particle growth in a model-free manner(Givi, 1989).

2. Formulation

The flows under consideration are two-dimensional mixing layers and are governed by the compressible Navier-Stokes equations. The transport of the nanoscale particles dispersed is governed by the aerosol general dynamic equation (GDE). The equation is expressed in a discrete form as a population balance on each cluster or particle size. From a practical standpoint however such systems of equations cannot be solved explicitly except for very small particle sizes. Therefore a sectional method is used to represent the particle field as a function of space and time.

This approach effectively divides the particle size distribution into "bins," as illustrated in Fig. 1. The discrete part of the representation models nucleation and molecule-molecule interactions which lead to particle formation. A molecular cluster q_i is comprised of i molecules. Typically molecular clusters grow by the addition of one molecular unit at a time. As particles become larger they are transitioned to the sectional representation,

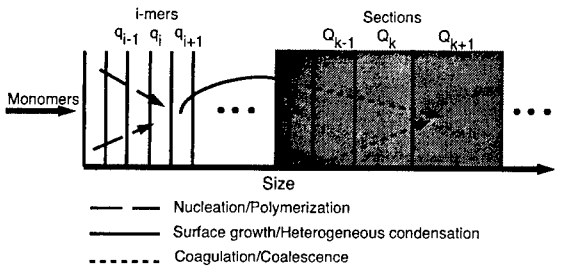


Figure 1. Discrete - sectional representation of particle field.

Q_k, after reaching a cut-off size consisting of M clusters. We consider only large clusters, and particles which typically contain tens of thousands of molecules for which a discrete representation is unnecessary. The GDE is therefore solved as a set of N_s transport equations, one for each section Q_k, $k = 1, 2, \ldots, N_s$(Xiong and Pratsinis, 1993). In adopting this framework we can write the general transport equation for the concentration of particles in the kth section, Q_k:

$$\frac{\partial \rho Q_k}{\partial t} + \frac{\partial \rho Q_k u_j}{\partial x_j} = \frac{\partial}{\partial x_j}\left(\mathcal{D}_Q \frac{\partial Q_k}{\partial x_j}\right) + \omega_k^Q, \tag{1}$$

where $\mathcal{D}_Q$ is the diffusivity

$$\mathcal{D}_Q = k_b T \frac{C_c}{3\pi\mu d_p}, \tag{2}$$

where k_b is the Boltzmann constant, C_c is the Cunningham correction factor, d_p is the particle diameter, and T and μ are the fluid temperature and viscosity, respectively. The source term, ω_k^Q, is given by

$$\omega_k^Q = \frac{1}{2}\sum_{i=1}^{N_s}\sum_{j=1}^{N_s}\beta_{i,j}\chi_{ijk}Q_iQ_j - \sum_{i=1}^{N_s}\beta_{ik}Q_iQ_k. \tag{3}$$

The source term, ω_k^Q, represents the effects of particle-particle interactions: production of Q_k due to collisions of smaller particles; the loss or gain of Q_k by collision with a smaller particle which either moves the resulting particle out of or into section k; the loss of particles in section k as they collide with each other and form larger particles; and the loss of particles in section k due to collisions with larger particles. It should be noted that repeated indices in Eq. 3 do not imply summation but instead infer interactions between

particles in section i and particles in section j. The collision frequency function β_{ij} is given by

$$\beta_{ij} = \left(\frac{3}{4\pi}\right)^{\frac{1}{6}} \left(\frac{6k_bT}{\rho_p}\right)^{\frac{1}{2}} \left(\frac{1}{v_i} + \frac{1}{v_j}\right)^{\frac{1}{2}} \left(v_i^{\frac{1}{3}} + v_j^{\frac{1}{3}}\right)^2, \tag{4}$$

where v_i is the volume of the ith particle, ρ_p is the particle density and χ_{ijk} is given by

$$\chi_{ijk} = \begin{cases} \frac{v_{k+1}-(v_i+v_j)}{v_{k+1}-v_k} & \text{if } v_k \leq v_i + v_j < v_{k+1} \\ \frac{(v_i+v_j)-v_{k-1}}{v_k-v_{k-1}} & \text{if } v_{k-1} \leq v_i + v_j < v_k \\ 0 & \text{otherwise.} \end{cases} \tag{5}$$

The sectional method is discretized in size space such that the volume of particles in two successive sections is doubled, *i.e.* $v_k = 2 \times v_{k-1}$. This scheme allows us to span a volume range of $V = v_1$ to $V = 2^{N_s-1} \times v_1$.

3. Numerical Procedure

The governing transport equations are solved using a hybrid MacCormack based compact difference scheme(Carpenter, 1990; Kennedy and Carpenter, 1994). The numerical scheme used is based on the one-parameter family of dissipative two-four schemes (DCPS)(Carpenter, 1990). The accuracy of the scheme is second order in time, and fourth order in space. All calculations are performed on a rectangular uniformly spaced grid. The computational algorithm uses the message passing interface to execute on parallel computing platforms. The treatment of the particulate phase in a Eulerian manner, as opposed to a Lagrangian one, helps to keep processor-processor communication to a minimum.

4. Results

The flows under consideration are two-dimensional, compressible, shear layers. A schematic is shown in Fig. 2. Periodic boundary conditions are used in the streamwise direction, while the free shear condition is imposed in the cross-stream direction. The gas is air, and the velocity is initialized with a hyperbolic tangent in the cross-stream direction. The Reynolds number is based on the vorticity thickness, δ_ω, and the velocity difference, $\Delta U = U_1 - U_2$, $Re_{\delta_\omega} = \frac{\Delta U \delta_\omega}{\nu}$. Two cases are considered. Case (I), considers particle coagulation in a uniform temperature flow at $T_1 = T_2 = 300K$. Case (II), considers the flow where the temperature of the particle-free stream is $T_1 = 300K$, and the temperature of the

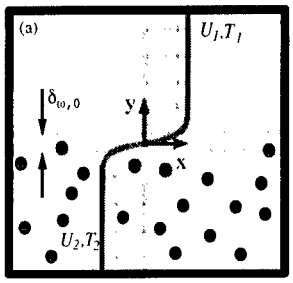


Figure 2. Flow configuration

particle-laden stream is $T_2 = 900K$. Thermophoresis effects are not included in these calculations, but inclusion of such effects pose no additional mathematical or computational difficulties(Pratsinis and Kim, 1989; Pyykonen and Jokiniemi, 1999). Both cases consider an initial volume fraction of $\mathcal{V}_f = 9.4 \times 10^{-8}$. The volume fraction is defined as the ratio of the volume occupied by the particulate phase to that occupied by the fluid. A total of ten sections are solved, *i.e.* $N_s = 10$. This allows for the solution of particles covering a range of 3 orders of magnitude in volume.

Computations are performed on a domain of $2\pi \times 2\pi$ in the streamwise, x, and cross-stream, y, directions on 1500^2 grid points. With this resolution, flows with a Reynolds number of $Re_{\delta_\omega} = 200$ are well resolved. All calculations were performed on a SGI-Origin3800 supercomputer, and each calculation simulated up to a nondimensional time of $t^\star = 14.25$.

Particle concentration profiles obtained from Case (I) are shown in Fig. 3. Cross-stream profiles of Q_1, Q_2, Q_7, and Q_{10}, are obtained by averaging in the streamwise x-direction, at four times. All values of Q are normalized by the initial number of particles in the particle-laden stream, Q_{1_o}. At time $t^\star = 0$, $Q_1/Q_{1_o} = 1$ in the particle-laden stream, and $Q_1/Q_{1_o} = 0$ in the particle free stream. Figure 3a indicates the decrease from the initial Q_1 concentration in the particle-laden stream, and increase in concentration in the initially particle-free stream. As the particles collide, they coagulate to form larger particles, thereby moving out of section 1. The increase in particles in the $y > 0$ region is due to dispersion. As the mixing layer evolves the particle-laden stream is mixed, via convection, with the particle-free fluid. The figure also reveals a peak in Q_1 near the interface of the two streams, the magnitude of which decreases with time. The peak is due to the gradient in Q_1 in the shear region which results in a lower growth rate, in comparison to that observed in the freestream of the initially particle-laden stream. A similar trend is observed in section 2, shown in Fig. 3b. Particles collide and coagulate to form larger particles which can no longer be accommodated in Q_2. The decrease of Q_2 in time is accompanied by

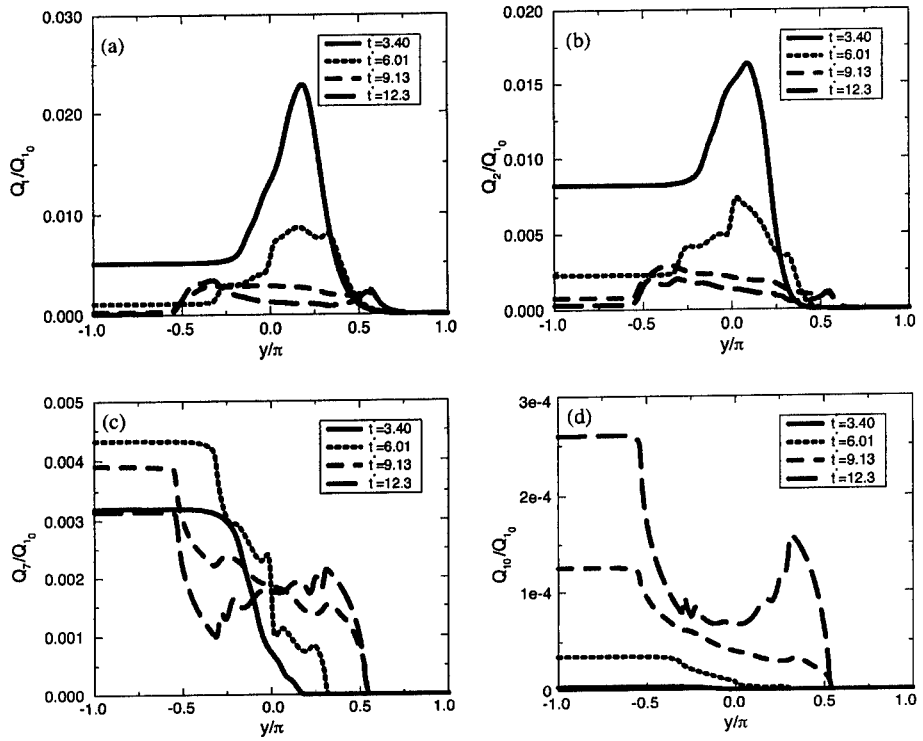


Figure 3. Cross stream variation of particle concentrations, Case (I): (a) Q_1; (b) Q_2; (c) Q_7; (d) Q_{10}.

increases in the higher numbered sections, $Q_k, k = 3, 4, \ldots, 10$. The concentration of particles in section 7 is shown in Fig. 3c. The trend is different from that observed in the first two sections in that the maximum concentration is observed in the initially particle-laden stream. The concentration increases to $Q_7/Q_{1_o} = 0.0044$, at time $t^\star = 6.01$, then begins to decrease. However, the concentration in the initally particle-free stream increases over the same period of time. Near the interface of the two streams there is some overlap of the profiles at later times, $t^\star = 6.01, 9.13$, and 12.3. This "equilibrium" may be attributed to the mixing of the particle-free stream with the particle-laden stream as the vortex develops. The concentration of particles in section 10 is shown in Fig. 3d. The figure reveals that the concentration Q_{10} increases at each y location across the mixing layer. There are fewer Q_{10} particles in the core of the vortex in comparison to the initially particle-laden stream. This further reflects the reduced growth rate observed in the first two sections. Additionally, the concentrations of all sections are seen to spread out into the particle-free stream with time as the flow develops. A qualititative view of the particle field for the isothermal flow, Case (I),

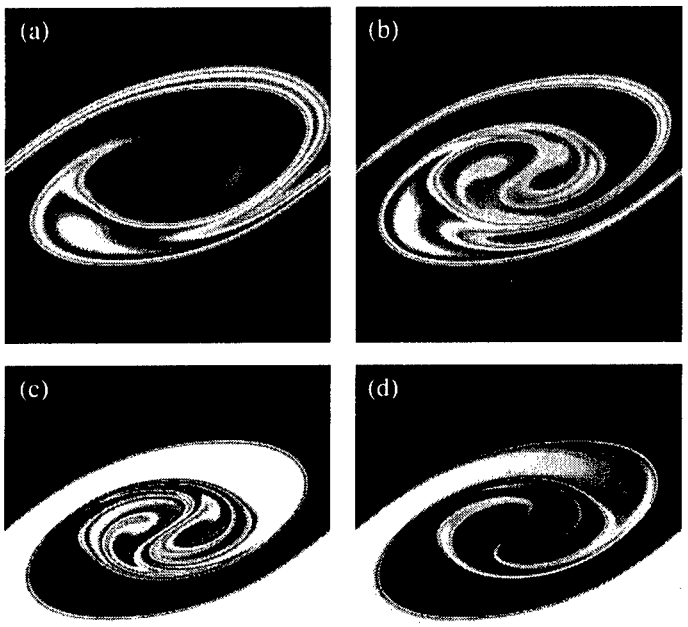


Figure 4. Instantaneous particle concentrations contours, Case (I): (a) Q_1;(b) Q_2; (b) Q_7; (b) Q_{10}.

is presented in Fig. 4. This figure shows instantaneous contours of the concentrations in sections 1, 2, 7, and 10, taken at time $t^\star = 12.3$. In addition to spatial concentration variation, the diffusion effects are also evident. The striation thickness decreases as the particle size increases. This is because larger particles have smaller coefficients of diffusion.

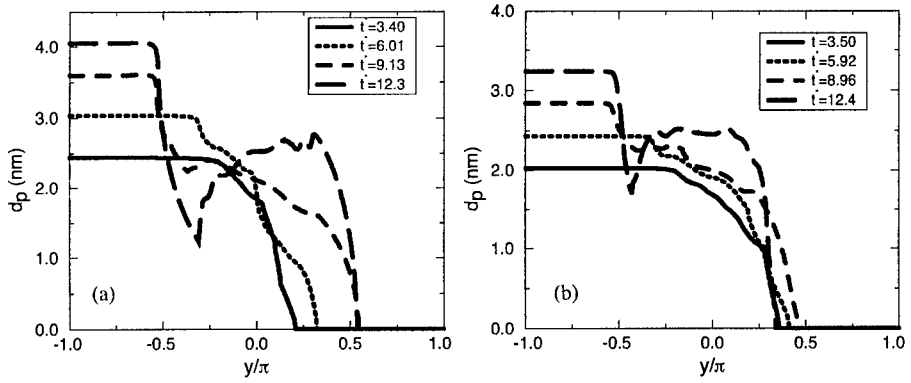


Figure 5. Cross stream variation of mean particle diameter: (a) Case (I); (b) Case (II).

Temperature effects may be observed by considering the average particle size. The average diameter is given by $d_p = (6/\pi\overline{v})^{1/3}$, where the mean volume is given by $\overline{v} = \sum_{i=1}^{N_s} Q_i v_i / \sum_{i=1}^{N_s} Q_i$. The temporal evolution of the mean diameter for Case (I), and Case (II) is shown in Fig. 5. Though the profiles show an overall increase with time, the particle growth rate in Case (II) is less than that in Case (I). Though the temperature of the particle-laden stream is greater, which also means that the rate of collisions is greater, the particles effectively grow at a slower rate. The spread of the profiles indicates mixing of the two streams as the vortices develop.

5. Acknowledgement

The first two authors acknowledge the support of the National Science Foundation under Grant ACI-9982274. Computational resources are provided by the Minnesota Supercomputing Institute.

References

Carpenter, M. H. (1990). A high-order compact numerical algorithm for supersonic flows. In Morton, K. W., editor, *Twelfth International Conference on Numerical Methods in Fluid Dynamics*, volume 371 of *Lecture Notes in Physics*, pages 254–258. Springer-Verlag, New York, NY.

Elghobashi, S. (1991). Particle-laden turbulent flows: Direct simulation and closure models. *Appl.Sci.Res.* **48**, 301–314.

Garrick, S. C., Lehtinen, K. E. J., and Zachariah, M. R. (2001). Modeling and simulation of nanoparticle coagulation in high reynolds number incompressible flows. In *Proc. Joint US Sections Meeting of the Combustion Institute*, Oakland, CA.

Givi, P. (1989). Model free simulations of turbulent reactive flows. *Prog. Energy Combust. Sci.* **15**, 1–107.

Kennedy, C. A. and Carpenter, M. H. (1994). Several new numerical methods for compressible shear-layer simulations. *Appl. Num. Math.* **14**, 397–433.

Matsoukas, T. and Friedlander, S. K. (1991). Dynamics of aerosol agglomerate formation. *Coll. Int. Sci.* .

Pratsinis, S. E. and Kim, K.S. (1989). Particle coagulation, diffusion, and thermophoresis in laminar flows. *J. Aerosol Sci.* **20**, 101.

Pyykonen, J. and Jokiniemi, J. (1999). Compuatational fluid dynamics based sectional aerosol modelling schemes. *J. Aerosol Sci.* **31**, 531–550.

Reade, W. C. and Collins, L. R. (2000). A numerical study of the particle size distribution of an aerosol undergoing turbulent coagulation. *J. Fluid Mech.* **415**, 45–64.

Riley, J. J. and Patterson, G. S. (1974). Diffusion experiments with numerically integrated isotropic turbulence. *Phys. Fluids* **17**, 292–297.

Sundaram, S. and Collins, L. R. (1996). Collision statistics in an isotropic particle-laden turbulent suspension.part 1. direct numerical simulations. *J. Fluid Mech.* **335**, 75–109.

Xiong, Y. and Pratsinis, E. S. (1993). Formation of agglomerate particles by coagulation and sintering part-i. a 2-d solution of the population balance equation. *J. Aerosol Sci.* **24**, 283–300.

NUMERICAL SIMULATION FOR FLOW SEPARATION AROUND A 2-D AIRFOIL

SHUTIAN DENG, CHAOQUN LIU, HUA SHAN
Department of Mathematics
University of Texas at Arlington, Arlington, TX

Abstract

This paper carries out numerical study of the flow separations around NACA 0012 airfoil at large angles of attack. Flow separation introduces two major effects: sudden loss of lift and generation of aerodynamic noise. These two factors are highly concerned on the aircraft designation. This study gives a detail picture of flow separation.

As the problems caused by flow separation are complicated, the spatial and temporal complexity makes it difficult to access by conventional experiment methods. In the presented work, the numerical investigation results from solving the time-dependent Navier-Stockes equations in the generalized curvilinear coordinates. Using a fourth order centered compact scheme for spatial discretization facilitates high resolution of the flow field, which will be neglected if using low-order numerical schemes. To avoid possible non-physical wave reflection, the non-reflecting boundary conditions are used at far-field and outlet boundary.

Complex flow separation, vortex shedding, vortex merging, and vortex paring are observed in the computational results. The main purpose of this paper is to provide more detailed information of the flow separation.

1. Introduction

Flow separation around airfoil receives highly concerned from the researchers. Shih et al.(1992) had pointed out that the understanding of this problem needs to make a step forward from qualitative conjecture to quantitative measurement of the instantaneous flow field. Shih et al (1995) investigated the unsteady flow past a NACA 0012 airfoil in pitching-up motion experimentally. They carried out the experiment at a Reynolds number of 5000 using PIDV method. Instantaneous velocity field data at different times have been obtained over the whole flow field. They drew the conclusion that boundary-layer separation near the airfoil leading edge leads to the formation of a vortical structure. The evolution of the vortex along the upper surface dominates the aerodynamic performance of the airfoil. Complete stall emerges when the boundary layer near the leading edge detaches

from the airfoil, under the influence of the vortex. Furthermore in 1995 they studied the stall process using a water towing tank facility, and found that near the leading edge large vortical structures emerge as a consequence of Van Dommelen and Shen type separation and a local vorticity accumulation. They pointed out that the trailing edge only play a secondary role on the dynamic stall process.

Tenaud & Phuoc (1997) used large eddy simulation (LES) to study this problem. They described that three flow fields can be distinguished according to different flow structures. Near the leading edge, vortex shedding due to separation of the boundary layer is dominant. In the second area, which is the middle part of the upper surface of the airfoil, the eddy structures grow and move downstream. The last field is close to the trailing edge, where the alternate vortices are created.

This work focuses on numerical simulation of flow separation around a NACA 0012 airfoil at a 16 angle of attack. From the previous understanding of experimental and numerical investigation of this problem, it is known that large vortices are generated and shed from the leading edge, thus leads to fluctuation of pressure and the lift lost. But the detail of this process is still unclear, the main purpose of this work is to give detailed picture of flow separation structures using a high-order and high-resolution approach.

2. Basic Equation And Numerical Methods

The governing equations are the two-dimensional compressible Navier-Stocks equations in the generalized curvilinear ξ-η coordinates, and in a conservative form:

$$\frac{1}{J}\frac{\partial Q}{\partial t}+\frac{\partial (E-E_v)}{\partial \xi}+\frac{\partial (F-F_v)}{\partial \eta}=0 \qquad (1)$$

where flux vectors F, E, E_v, F_v are:

$$Q=\begin{bmatrix}\rho\\ \rho u\\ \rho v\\ e\end{bmatrix} \quad E=\frac{1}{J}\begin{bmatrix}\rho U\\ \rho uU+p\xi_x\\ \rho vU+p\xi_y\\ U(e+p)\end{bmatrix} \quad F=\frac{1}{J}\begin{bmatrix}\rho V\\ \rho uV+p\eta_x\\ \rho vV+p\eta_y\\ V(e+p)\end{bmatrix}$$

$$E_v=\frac{1}{J}\begin{bmatrix}0\\ \tau_{xx}\xi_x+\tau_{yx}\xi_y\\ \tau_{xy}\xi_x+\tau_{yy}\xi_y\\ q_x\xi_x+q_y\xi_y\end{bmatrix} \quad F_v=\frac{1}{J}\begin{bmatrix}0\\ \tau_{xx}\eta_x+\tau_{yx}\eta_y\\ \tau_{xy}\eta_x+\tau_{yy}\eta_y\\ q_x\eta_x+q_y\eta_y\end{bmatrix}$$

Where J is the Jacobian of the coordinate transformation, and $\xi_x, \xi_y, \eta_x, \eta_y$ are coordinate transformation metrics. ρ is density, p is pressure, u and v are components of velocity. $U = u\xi_x + v\xi_y$, $V = u\eta_x + v\eta_y$. e is the total energy. The components of viscous stress and heat flux are denoted by $\tau_{xx}, \tau_{yy}, \tau_{xy}$ and q_x, q_y, respectively.

The second order Euler Backward scheme is applied to solve Eq. (1), that is,

$$\frac{3Q^{n+1} - 4Q^n + Q^{n-1}}{2J\Delta t} + \frac{\partial(E^{n+1} - E_v^{n+1})}{\partial\xi} + \frac{\partial(F^{n+1} - F_v^{n+1})}{\partial\eta} = 0 \qquad (2)$$

Q^{n+1} is estimated iteratively as: $Q^{n+1} = Q^p + \delta Q^p$, $\delta Q^p = Q^{p+1} - Q^p$
Flux vectors are linearized by the local Taylor expansion about Q as following:

$$E^{n+1} \approx E^p + A^p \delta Q^p \ , \ F^{n+1} \approx F^p + B^p \delta Q^p$$

Now equation (2) turns into:

$$[\frac{3}{2} I + \Delta t J (D_\xi A + D_\eta B)]\delta Q^p = R \qquad (3)$$

Where $R = -(\frac{3}{2}Q^p - 2Q^n + \frac{1}{2}Q^{n-1}) - \Delta t J [D_\xi (E - E_v) + D_\eta (F - F_v)]^p$

The superscript p stands for iteration step. D_ξ and D_η are partial differential operators in the ξ and η directions, respectively. The right hand side of Eq. (3) is discretized using the fourth-order compact scheme. A sixth-order compact filter is used to depress the numerical oscillation. The left hand side of Eq. (3) is discretized following the LU-SGS method (Yoon & Kwak, 1992). Then the finite difference expression of Eq. (3) can be written as:

$$\left[\frac{2}{3} I + \Delta t J (r_A + r_B) I\right]\delta Q_{i,j}^p = R_{i,j}^p -$$

$$\Delta t J \left[A^- \delta Q_{i+1,j}^p - A^+ \delta Q_{i-1,j}^p + B^- \delta Q_{i,j+1}^p - B^- \delta Q_{i,j-1}^p\right]$$

Where $A^\pm = \frac{1}{2}[A \pm r_A I]$, $B^\pm = \frac{1}{2}[B \pm r_B I]$, and $A = A^+ + A^-$,

$$B = B^+ + B^- , \ A = \frac{\partial E}{\partial Q}, \ B = \frac{\partial F}{\partial Q},$$

$$r_{A,B} = k \max[|\lambda(A,B)|] + \nu ,$$

$$\nu = \max[\frac{\mu}{(\gamma - 1) M_r^2 R_e P_r}, \frac{4}{3}\frac{\mu}{R_e}] .$$

For subsonic flow, u, v, T are prescribed at the upstream boundary, p is obtained by solving the modified N-S equation based on characteristic analysis. On the far-field and out-flow boundary, the non-reflecting boundary conditions are

applied. Adiabatic, non-slipping condition is used for the wall boundary. All equations of boundary conditions are solved implicitly with internal points. Specific details of boundary treatment can be found in Jiang et al. (1999)

3. Grid Generation

A grid generation method first proposed by Spekreijse (1995) is used to generate the C-type grids. The grid generation method is a composite method, which consist of an algebraic transformation and an elliptic transformation. The algebraic transformation maps the computational space onto a parameter space, and the elliptic transformation maps the parameter space onto the physical domain by solving a set of Poisson equations. The orthogonality of grids on the surface and near the boundary is achieved by re-configuration of the algebraic transformation. The grid numbers are 841 in the ξ direction, and 141 in the η direction. The overview of the C-grid and grid near the airfoil surface are displayed in Figure 1(a) and (b).

4. Computational Result

The flow field around an NACA-0012 airfoil is analyzed by solving the Navier-Stocks equations using the finite difference scheme. Flow separation at a large angle of attack ($\alpha = 16^\circ$) has been studied using a high-resolution numerical simulation. In this case, the fluid flow around the airfoil becomes very unstable and different eddy structures are formed in the vicinity of the airfoil. The Reynolds number based on the chord length and the free-stream velocity is 5×10^5, the free stream Mach number is 0.4. The angle of attack is 16 °. During the computation, the flow field is recorded every 1000 time steps, and the time step is approximately $1.768\times10^{-4} L/U_\infty$. Figure 2 shows the contours of the instantaneous spanwise voriticity. The time interval between each of those 15 pictures is about $0.7072L/U_\infty$. From those figures we can see that flow separation process start at the leading edge and the leading edge vortices continue to shed and convect downstream. In Figure 2(c), a separation bubble can be observed on the upper surface of the airfoil near the leading edge. A chain of vortical structures appear on the upper surface of the airfoil, which is more clear in Figure 2(h). The vortices shedding from the leading-edge rotate in the clockwise direction. Near the surface of the airfoil, a layer of reversed vorticity is induced by the vortices shedding from the leading-edge. The interactions between the positive and negative vorticity leads to the vortex pairing. The merging of vortices rotating in the same direction is also observed, e.g. in Figure 2(j). A vortex, which first appears at the trailing edge of airfoil in Figure 2(a), grows as it is carried downstream by the mean flow, as shown in Figure 2(b), (c), and (d). In Figure 2(d), along the shear layer starting from the trailing edge, a series of small vortical structures are generated as a result of the Kelvin-Helmholtz instability. These small structures are also visible in Figure 2(e), (f), (g), and (h).

5. Conclusions

Detailed numerical simulation has been carried out by solving Navier-Stocks equations in the generalized curvilinear coordinates to study the separated flow around an NACA 0012 airfoil at large angle of attack. By using a fourth–order centered compact scheme for spatial discretization, the small–scale vortical structures are resolved, which will dissipate if low-order numerical schemes are used. Non-reflecting boundary conditions are imposed at the far field and outlet boundaries to avoid possible non-physical wave reflection.

The numerical simulation results clearly describe the flow separation process at the upper surface of the airfoil. The phenomena of the leading-edge separation, vortex shedding, vortex merging, vortex pairing, and formation and shedding of large-scale trailing edge vortex are displayed and discussed in detail. The small-scale vortices associated with the Kelvin-Helmholtz instability are also observed along the shear layer near the trailing-edge. These phenomena are in food agreement with the experimental results obtained by Shih, et al (1992,1995) and Yoshifumi et al (1986).

Reference:

[1] L. Jiang, H. Shan, C. Liu and M. R. Visbal 1999. Non-reflecting boundary condition in curvilinear coordinates, Second AFOSR International Conference on DNS/LES, Rutgers, New Jersey, June 7-9

[2] S. K. LeLe 1992. Compact finite difference schemes with spetral-like resolution. Journal of Computational Physics. 103 ,P 16-42

[3] C. Shih, L. Lourenco, L. Van Dommelen and A. Krothapalli 1992. Unsteady flow past an airfoil pitching at a constant rate. AIAA Journal, 30(5), P 1153-1161

[4] C. Shih, L. Lourenco, and A. Krothapalli 1995. Investigation of flow ar leading and trailing edge of pitching-up airfoil. AIAA Journal, 30(5), P 1369-1376

[5] S. P. Spekreijse 1995. Elliptic grid generation based on Laplace equations and algebraic transformation. Journal of Computational Physics. 118 ,P 38-61

[6] C. Tenaud and L. T. Phuoc 1997. Large eddy simulation of unsteady, compressible, separated flow around NACA 0012 airfoil. Lecture Notes in Physics 490, P424-429

[7] J. F. Thompson, Z. U. A. Warsi and C. W. Mastin 1985. Numerical Grid Generation: Foundations and Applications. Elsevier, New York

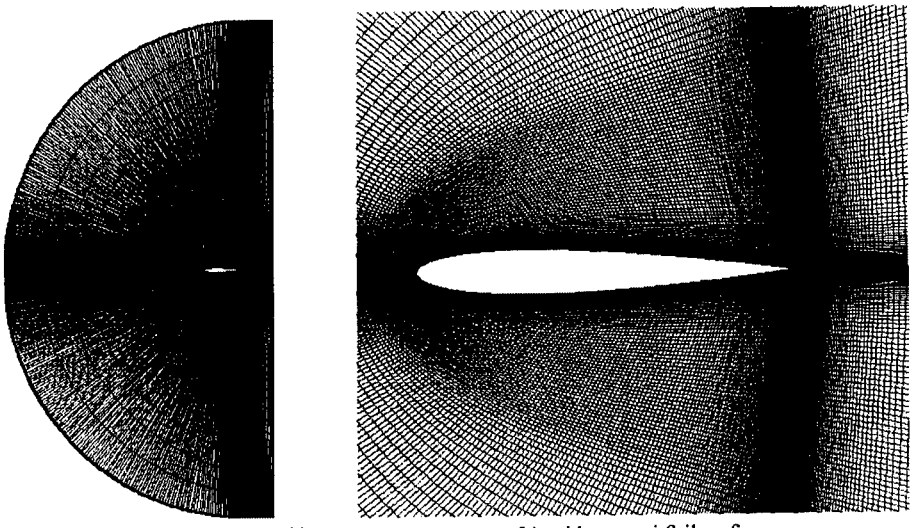
[8] L. Van Dommelen and Shen 1980. The Spontaneous generation of singularity in a separating laminar boundary layer. Journal of Computational Physics.38,P 125-140

[9] L. Van Dommelen and S. J. Cowsley 1990. On the Lagrangian description of unsteady boundary later, Part 1: General theory. J. Fluid Mech., 210 P593-626

[10] J-Z. Wu, X. Lu, A. G. Denny, M. Fan and J-M Wu 1999. Post-stall lfow control on an airfoil by local unsteady forcing. J. Fluid Mech., 371 P 21-58

[11] S. Yoon and D. Kwak 1992. Implicit Navier-Stocks solver for three-dimensional compressible flows. AIAA Journal, 30(5), P 2653-2659

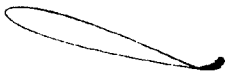
[13] S. P. Spekreijse 1995. Elliptic grid generation based on Laplace equations and algebraic transformation. J. Comp. Phys., 118, P 38-61



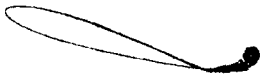
(a) overview of the grids (b) grids near airfoil surface

Figure 1. C-grid around an NACA 0012 airfoil

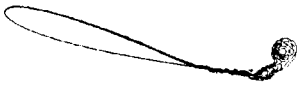
(a)



(b)



(c)



(d)



(e)



(f)



(g)



(h)



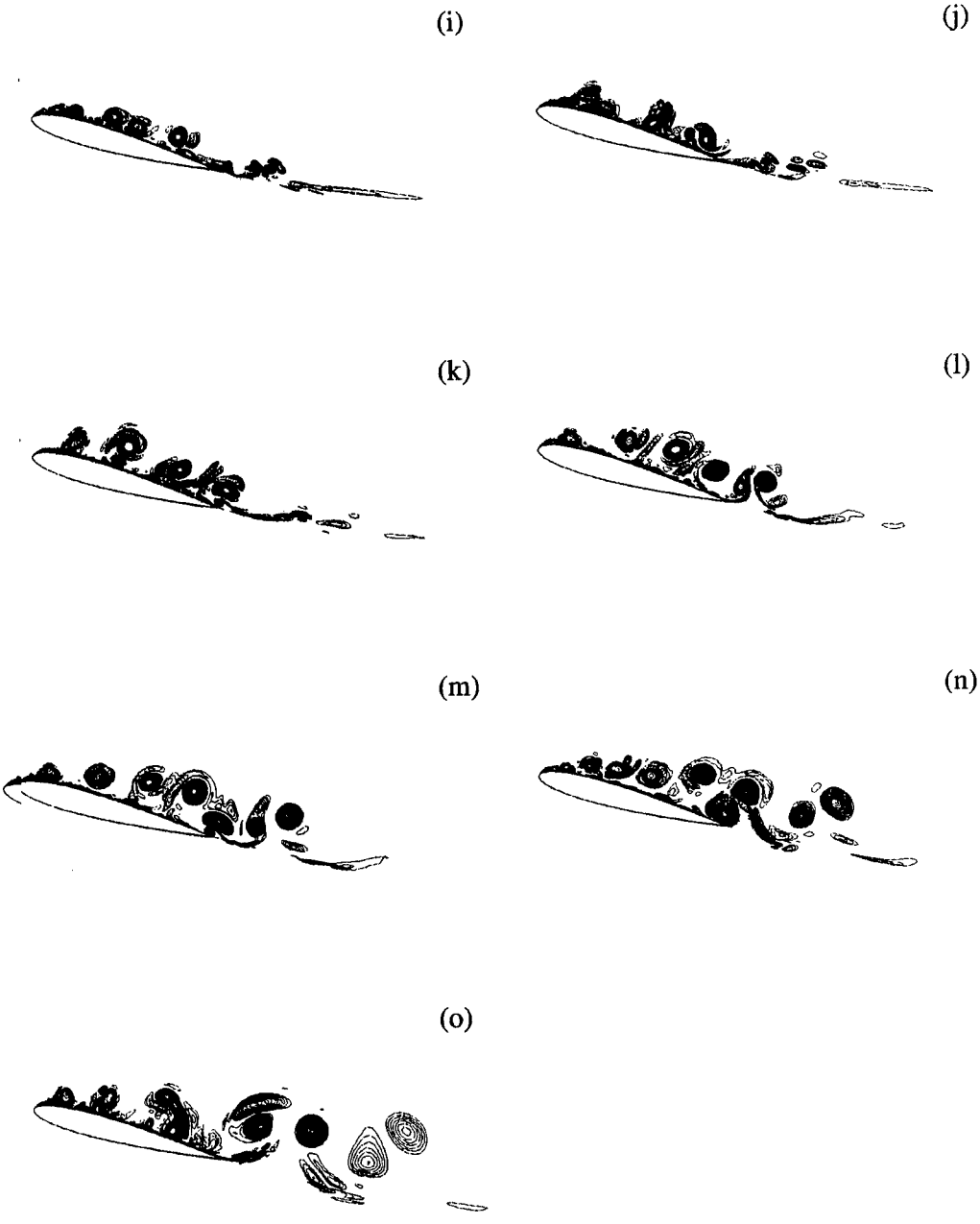


Figure 2. Contours of instantaneous spanwise vorticity at different time

MEASUREMENT AND 3D COMPUTER SIMULATION OF THE CRYSTALLINITY DISTRIBUTION IN INJECTION MOLDED SYNDIOTACTIC POLYSTYRENE

RICHARD D. SUDDUTH, PAVAN K.YARALA
Department of Chemical Engineering
University of Louisiana at Lafayette, Lafayette, LA 70504-4130
QIN SHENG
Department of Mathematics
University of Dayton, Dayton, OH 45469-2316
KEVIN NICHOLS
Dow Chemical Company, Midland, MI 48667

Abstract

Injection molding of semi-crystalline polymers has been one of the most important yet complicated fabrication processes that combines polymer rheology, heat transfer, and crystallization kinetics. 3D mathematical modeling of polymer flow, and computer simulation of distributions of crystallinity in a semi-crystalline polymer in injection molding applications were studied in this project. Our modeling includes the shear stress and thermal conduction in the width direction and will also eventually provide details of the polymer flow in intricate small cavities of changing cross sections. The simulation developed in this study predicted 3D crystallization properties of syndiotactic polystyrene as a function of position in an injection molded part. The predicted crystallinity distributions were effectively described across a profile at various locations along the flex bar as a function of different molding temperatures and different hold times.

1. Introduction

Computer simulations of injection molding of semicrystalline polymer components have been an active area of research [1-6]. The primary goal of this project was to develop 3D computer simulated virtual integrated prototyping (VIP), rather than traditional 2D Hele-Shaw approximations or smaller scale physical trials, to enhance downstream plastics manufacturing-particularly injection molding. Primary semi-crystalline polymers evaluated include polyphyenelene sulfide and syndiotactic polystyrene. Preliminary results from this study have been presented and published elsewhere [7-9]. Several other authors have also published simulation results[10-12]. The simulation results in this study have focused almost exclusively on syndiotactic polystyrene (244,000 Mol. Wt.). The confirmation of our model also involved the

evaluation of injection-molded parts made from syndiotactic polystyrene. The predicted crystallinity distributions were compared with measured values from molded parts.

2. Governing Equations

Let L, W, H be the length, width and thickness of a slit mold region, respectively. We consider the following mass, momentum and energy balance equations:

$$Q = \int_0^W \int_0^H u\,dy\,dx \tag{1}$$

$$0 = \frac{\partial}{\partial y}\left(\eta \frac{\partial u}{\partial y}\right) + \frac{\partial}{\partial z}\left(\eta \frac{\partial u}{\partial z}\right) - \frac{\partial P}{\partial x} \tag{2}$$

$$\rho C_p\left(\frac{\partial T}{\partial t} + u\frac{\partial T}{\partial x}\right) = k\frac{\partial^2 T}{\partial y^2} + k\frac{\partial^2 T}{\partial z^2} + \eta\dot{\gamma}^2 \tag{3}$$

where the heat capacity, C_p, is

$$C_p = C_p' - |\lambda_\infty| \frac{dX}{dT} \tag{4}$$

and u, P, T, k, ρ, C_p', λ_∞, X, η, $\dot{\gamma}$ are velocity, pressure, temperature, thermal conductivity, density, specific heat, heat of crystallization, fraction of crystallinity, viscosity and shear rate, respectively.

Many applications in injection molding require processing polymers at temperatures below the glass transition temperature, T_g, and at temperatures over the melting point, T_m. We propose a new model[13,14] that allows appropriate crystallization results to be obtained over the entire temperature range of processing:

$$\mathrm{Log}_{10}(-\mathrm{Log}_{10} k(T)) = \mathrm{Log}_{10}(-\mathrm{Log}_{10} k_P) + aY + bY^2 + cY^3 + dY^4 + eY^5 + fY^6 \tag{5}$$

where $Y = (T - T_P)^2$, $k(T)$ is the crystallization rate at processing temperature T, k_P is the peak crystallization rate constant, a, b, c, d, e and f are numeric constants and T_P is the peak crystallization temperature.

The sensitivity of k_P and T_P to shear stress, τ, is shown by the following[15]:

$$T_p = T_{pq} + E_{STk}(\tau), \quad \mathrm{Log}_{10} k_P = \mathrm{Log}_{10} k_{pq} + E_{Sk}(\tau) \tag{6}$$

Since the shear stress constants E_{Sk} and E_{STk} for syndiotactic polystyrene were not available for this study, they were assumed to be comparable to those by Hsiung[15] for polyphenylene sulfide based on the data of Haas,et al[16]. On the other hand, the true induction time evaluated must be generated from an equation introduced by Sifleet et al[17].

In our study, the induction time was determined using the following model:

$$t_i = t_{ib}\, e^{c_{ti}(T - T_b)^2} \tag{7}$$

The effect of shear stress, τ , on the induction time was again addressed from the expressions proposed by Hsuing[15] for polyphenylene sulfide as:

$$T_b = T_{bq} + E_{STti}(\tau), \qquad \mathrm{Log}_{10} t_{ib} = \log_{10} t_{ibq} - E_{Sti}(\tau) \tag{8}$$

Values of the constants for E_{STti} and E_{Sti} were evaluated from the data of Hsuing[15] and related studies[16,18-20] for polyphenylene sulfide.

The melt viscosity, η, of the syndiotactic polystyrene was evaluated using the Cross law[21] as a function of shear rate (see Verhoyen et al [22]).

2.1. Fractional Crystallinity System of Integro-Differential Equations

It was known[8,9] that the following system was satisfied by the fractional crystallinity,

$$\frac{\partial X}{\partial t} = exp\left(-I^{n_c}\right) n_c I^{(n_c-1)} \left[K(x, y, t) - K(x, y, t_{cs})\right] \tag{9}$$

$$\frac{\partial X}{\partial x} = exp\left(-I^{n_c}\right) n_c I^{(n_c-1)} \left[\int_{t_{cs}}^{t} \left(\frac{\partial K}{\partial T}\frac{\partial T}{\partial x} + \frac{\partial K}{\partial \tau}\frac{\partial \tau}{\partial x} \right) dt \right] \tag{10}$$

where

$$I = \int_{t_{cs}}^{t} K\left(T(x, y, t), \tau(x, y, t)\right) dt$$

Initial polymer melt temperature T_o was taken as the polymer processing temperature at the shutoff nozzle. It was observed that the degradation of syndiotactic polystyrene is considerably lower if the temperatures were kept below 305°C. The melt temperature was taken to be 305°C. T_o = 305°C while wall temperature, T_w, is a constant.

$$T(x, H, z, t) = T(x, 0, z, t) = T(x, y, W, t) = T(x, y, 0, t) = T_w \tag{11}$$

The following homogeneous velocity on the boundaries of the mold was considered.

$$u(x, H, z, t) = u(x, 0, z, t) = u(x, y, W, t) = u(x, y, 0, t) = 0.0 \tag{12}$$

The melt front of the polymer was considered to be flat and the temperature was assumed to be uniform all over the melt front. The uniform temperature is equal to the centerline temperature at the stream-wise location immediately upstream of the melt front. The curvature and the transverse flows associated with the melt front due to the fountain flow effect were neglected. Thus we have the following equality:

$$T(x_{mf}, y, z, t) = T\left(x_{mf} - \Delta x, \frac{1}{2H}, \frac{1}{2W}, t\right) \tag{13}$$

2.2. Numerical Method

Introduction of the discrete parameters, Δx, Δy, Δz and Δt along x, y, z (i, j, k) direction s and time, t(n), into the energy balance equation yields the following implicit schemes via the parallel splitting algorithm[8,9,23].

$$-\frac{u^{n}_{(i,j,k)}}{\rho C_p'}\frac{1}{\Delta x}T^{n+1}_{1;(i-1,j,k)}+\left(\frac{1}{\Delta t}+\frac{u^{n}_{(i,j,k)}}{\rho C_p'}\frac{1}{\Delta x}\right)T^{n+1}_{1;(i,j,k)}=\frac{1}{\Delta t}T^{n}_{1;(i,j,k)}+\frac{\eta\dot{\gamma}^2}{\rho C_p'}+C$$

$$-\frac{k}{\rho C_p'}\frac{1}{\Delta y^2}T^{n+1}_{2;(i,j-1,k)}+\left(\frac{1}{\Delta t}+\frac{2k}{\rho C_p'\Delta y^2}\right)T^{n+1}_{2;(i,j,k)}-\frac{k}{\rho C_p'}\frac{1}{\Delta y^2}T^{n+1}_{2;(i,j+1,k)}=\frac{1}{\Delta t}T^{n}_{2;(i,j,k)}$$

$$-\frac{k}{\rho C_p'}\frac{1}{\Delta z^2}T^{n+1}_{3;(i,j,k-1)}+\left(\frac{1}{\Delta t}+\frac{2k}{\rho C_p'\Delta z^2}\right)T^{n+1}_{3;(i,j,k)}-\frac{k}{\rho C_p'}\frac{1}{\Delta z^2}T^{n+1}_{3;(i,j,k+1)}=\frac{1}{\Delta t}T^{n}_{3;(i,j,k)}$$

$$C=\frac{\left|f_c\lambda_\infty\right|}{C_p'}\{\exp\left(-I^{n_c}\right)n_cI^{(n_c-1)}\left[K(x,y,t)-K(x,y,t_{cs})\right]+$$

$$u^{n}_{(i,j,k)}\left(\exp\left(-I^{n_c}\right)n_cI^{(n_c-1)}\left[\int_{t_{cs}}^{t}\left(\frac{\partial K}{\partial T}\frac{\partial T}{\partial x}+\frac{\partial K}{\partial \tau}\frac{\partial \tau}{\partial x}\right)dt\right]\right)\}$$

Thus, by applying the parallel splitting algorithm[23], the solution of the energy balance equation can be obtained with a neglectful error as

$$T^{n+1}=1/2(\exp\{\Delta tM_1\}\exp\{\Delta tM_2\}\exp\{\Delta tM_3\}+$$

$$\exp\{\Delta tM_3\}\exp\{\Delta tM_2\}\exp\{\Delta tM_1\})T^{n} \qquad (14)$$

where M_1, M_2 and M_3 are tri-diagonal matrices generated.

4. Computer Program Simulation Results

4.1. Simulation of Crystallinity Distributions at Different Holding Times and Different Locations

Computer simulated crystallinity distributions at a mold temperature of 200°C and an injection speed of 23.2 cc/sec at Location #1 in Figure 1 are summarized in Figures 2 as a function of holding time. In all the figures plotted from the simulation results the direction shown as *Z* direction corresponds to width (1/2 in) of the sample and the direction shown as *Y* direction corresponds to thickness (1/8 in) of the sample. The location indicated as 'entrance' is located near the gate and the location indicated, as Location #3 is located further down the sample along the direction of flow. The third axis in the figures shows the magnitude of the fraction of crystallinity, *X*, developed. The value of $X = 1$ along this axis direction indicates

the maximum crystallinity that can develop at any point. The maximum corresponded to a heat of fusion which was approximately 61.7 percent of the maximum crystallinity possible or $f_c = .617$ giving: $|f_c\ \lambda_\infty| = .617$ (53.2 Joules/gram) = 32.82 Joules/gram.

As shown elsewhere[13,14], the maximum crystallization rate for the syndiotactic polystyrene utilized in this study can be achieved at a temperature of approximately 200°C. A rapid surface crystallinity development at 200°C is indicated in Figure 2 as a function of holding time at location #1. The computer simulated crystallinity at a mold temperature of 200°C and an injection speed of 23.2 cc/sec is also indicated at several different locations in Figure 3 at a holding time of 60 sec.

4.2. Crystallinity Distribution at Two Locations as a Function of Mold Temperature at a Given Holding Time and a Specific Injection Speed

The injection molding we considered was at mold temperatures of 50°C, 90°C, 150°C and 190°C and an injection speed of 23.2 cc/sec. The simulations for these runs are indicated in Figure 4 for location position indicated in Figure 1 as the entrance. Assuming that the mass forming the injection molded polymer bar remained the same independent of the temperature of the mold, then the old mold temperature and new estimated mold temperatures were as follows:

T_{MOLD}, °C	T_{NEW}, °C
50°C	132.3 (135)
90°C	159.4 (160)
150°C	200 (200)
190°C	227.1 (230)

The new computer injection molding simulations for mold temperatures of 135°C, 160°C, 200°C and 230°C are indicated in Figures 5 at the entrance location.

5. Experimental

The syndiotactic polystyrene used in this study was supplied by the Dow Chemical Company and had a molecular weight currently characteristic of the production grade of syndiotactic polystyrene (Mol.wt = 244,000). Most of the experimental details for the crystallinity and injection molding measurements have been reported elsewhere[13,14]. The crystallinity measurements determined at four different mold temperatures (50°C, 90°C, 150°C and 190°C) are summarized in Figures 6 and 7.

Since the maximum crystallization rate was found to occur at approximately 200°C, it was expected that the mold temperature of 190°C would have given the maximum amount of surface crystallinity. However, the maximum surface crystallinity was achieved with a mold temperature of 150°C instead of 190°C. This result strongly suggested that the effective mold temperature at 150°C was probably

nearer to the 200°C as proposed in an earlier section. Comparison of these experimental results with the simulated results in Figures 4 & 5 would also be consistent with this observation.

6. Conclusion

In this study, four mold temperatures (50°C, 90°C, 150°C and 190°C) were experimentally evaluated and compared with computer-simulated results. For the injection molded bar simulated in this study it was found that the maximum crystallinity characteristic of a theoretical mold temperature of approximately 200°C was experimentally achieved at a mold temperature of approximately 150°C at an injection speed of 23.3 cc/min. Using a correction factor approach and local heating it was found that the thermal transfer of energy apparently allows a temperature of approximately 200°C to be achieved in the mold at a mold temperature of 150°C.

By addressing effective computer simulation and appropriate experimental outputs for syndiotactic polystyrene, it has been shown that an optimized control of the injection molding process can be developed for better commercial applications.

Acknowledgements

The Authors gratefully acknowledge the support of this project through grants from the Louisiana Board of Regents and Dow Chemical Company. R. Dugyala significantly contributed to the computer programming in the study as a graduate student in chemical engineering. The authors also acknowledge important support from H. Spence of Ash Industries in preparing injection-molding samples evaluated.

References

1. AI Isayev, Y. Churdpunt and X. Guo (2000) Comparative study of Ziegler-Natta and metallocene based polypropylene in injection molding – simulation and experiment, *Inter. Polymer Processing*, Vol.15, pp. 72-82
2. X. Guo and AI Isayev (2000) Residual stresses and birefringence in injection molding of semicrystalline polymer- Part II: experiment and simulations, *Inter. Polymer Processing*, Vol.14, pp. 387-398
3. S. C. Chen, Y. C. Chen and H. S. Peng (2000) Simulation of injection-compression-molding process. Part II: influence of process characterization on part shrinkage, *J. Appl. Polymer Sci.*, Vol.75, pp. 1640-1654
4. X. Guo, AI Isayev and L. Guo (1999) Crystallinity and microstructure in injection moldings of isotactic polypropylenes. Part I: a new approach to modeling and model parameters, *Polymer Eng. Sci.*, Vol.39, pp. 2096-2114
5. X. Guo, AI Isayev and M. Demiray (1999) Crystallinity and microstructure in injection moldings of isotactic polypropylenes. Part II: simulation and experiment, *Polymer Eng. Sci.* Vol.39, pp. 2132-2149

6. E. J. Holm and H. P. Langtangen (1999) A unified finite element model for the injection molding process, *Computer Meth. Appl. Mech. Eng.*, Vol.178, pp. 413-429
7. R. Sudduth, Q. Sheng, P. K Yarala and R. Dugyala (2000) Measurement and computer simulation of crystallinity in injection molded syndiotactic polystyrene, *Proc. SCC 2000*, University of Southern Mississippi, Hattiesburg, MS
8. Q. Sheng, F. F. Farshad and S. Duan (1999) A simulation of crystallinity gradients developed in slowly crystallizing injection molded polymers via parallel splitting, *Eng. Comput.*, Vol.16, pp. 892-912
9. C-M Hsiung and Q. Sheng (1997) A rectilinear flow model approach to the simulation of injection molding process, *J. Reinforced Plastics & Composites*, Vol.16, pp. 1242-1251
10. Y-W Yu and T-J Liu (1999) A hybrid 3D/2D finite element technique for polymer processing operations, *Polymer Eng. Sci.*, Vol.39, pp. 44-54
11. J-F Hetu, D. M. Gao, Garciea-Rejon and G. Salloum (1998) 3D finite element method for the simulation of filling stage in injection molding, *Polymer Eng. Science*, Vol.38
12. G. A. A. Haagh and F. N. Van DeVosse (1998) Simulation of three-dimensional polymer mould filling processes using a pseudo-concentration method, *Inter. J. Numer. Meth. In Fluids*, Vol.28, pp. 1355-1369
13. R. D. Sudduth, P. K Yarala and Q. Sheng (2001) A comparison of induction time and crystallization rate for syndiotactic polystyrene, accepted for publication in *Polymer Eng. Sci.*
14. R. D. Sudduth, R. Dugyala, Q. Sheng, K. Nichols, and J. Garber (2001) Computer simulation of syndiotactic polystyrene crystallization during injection molding, submitted for publication.
15. C-M Hsiung (1990) *Processing-Structure-Property Relationship and Simulation of Stucture gradients in Injection Molded Semi-crystalline Aromatic Polycondensates*, PHD Thesis, University of Akron
16. T. W. Haas and B. Maxwell (1969) *Polymer Eng. Sci.*, Vol.9, pp. 225
17. W. L. Sifleet, N. Dinos and J. R. Collier (1973) Unsteady-state heat transfer in a crystallizing polymer, *Polymer Eng. Sci*, Vol.13, pp. 10-16
18. J. E. Spruiell and J. White (1975) Structure development during polymer processing: studies of the melt spinning of polyethylene and polypropylene fiber, *Polymer Eng. Sci.*, Vol.15, pp. 660-667
19. R. R. Lagasse and B. Maxwell (1976) An experimental study of the kinetics of polymer crystallization during shear flow, *Polymer Eng. Sci.*, Vol.16, pp. 189-199
20. M. C. Chien and R. A. Weiss (1988) Strain-induced crystallization behavior of poly (Ether-Ether Ketone), *PEEK*, Vol.28, pp. 6-12
21. M. M. Cross (1979) *Rheol. Acta*, Vol.18, pp. 609
22. O. Verhoyen and F. Dupret (1998) A simplified method for introducing the cross viscosity law in the numerical simulation of Hele-Shaw flow, *J. Non-Newtonian Fluid Mech.*, Vol.74, pp. 25-46
23. Q. Sheng , (1989) Solving partial differential equations by exponential splitting, *IMA J. Numer. Anal.*, Vol.9, pp. 199-212

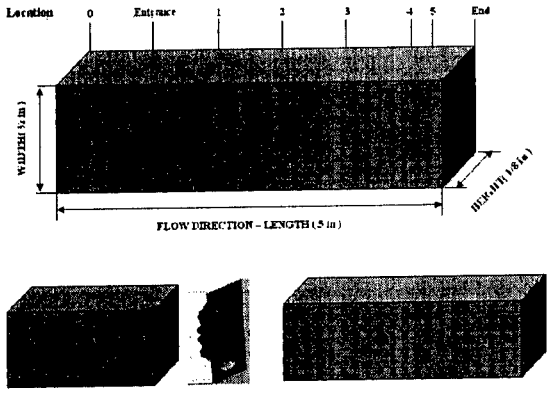


Figure 1 Schematic of Simulated Flex Bar with Locations for Analysis of Cross Sections

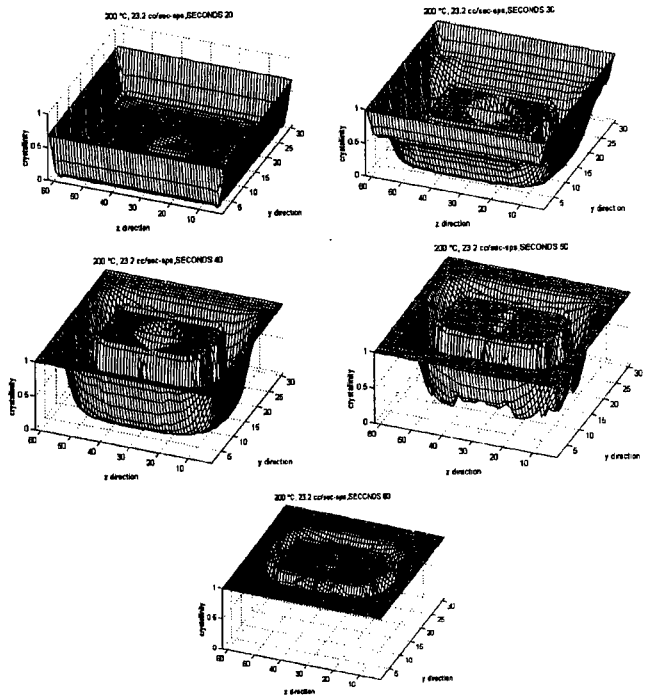


Figure 2 Crystallinity Distributions at a Mold Temperature of 200ºC and Different Mold Times at Location#1

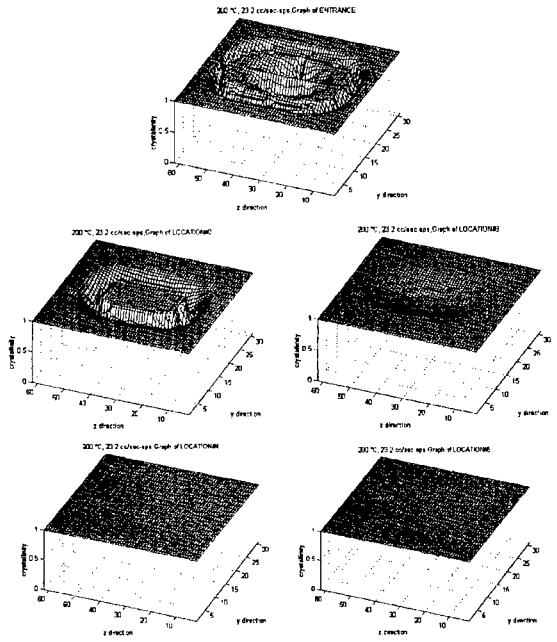


Figure 3 Crystallinity Distribution at Different Locations at a 200°C Mold Temperature after a Hold Time of 60 Seconds

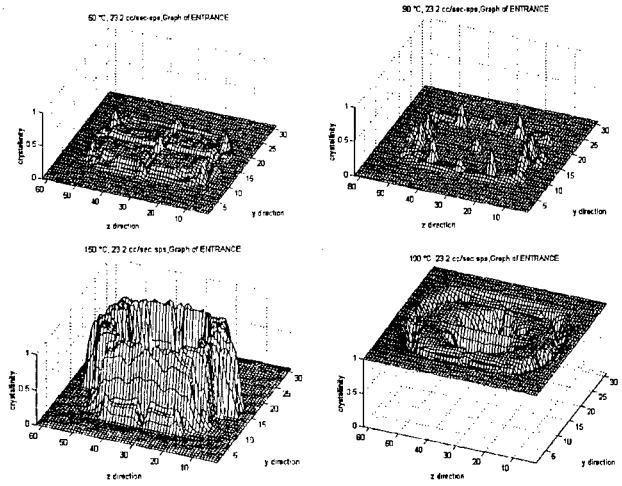


Figure 4 Crystallinity Distributions at the Entrance Location at Four Different Mold Temperatures (50°C, 90°C, 150°C, 190°C)(Injection Speed of 23.2 cc/sec and a Hold Time of 60 sec)

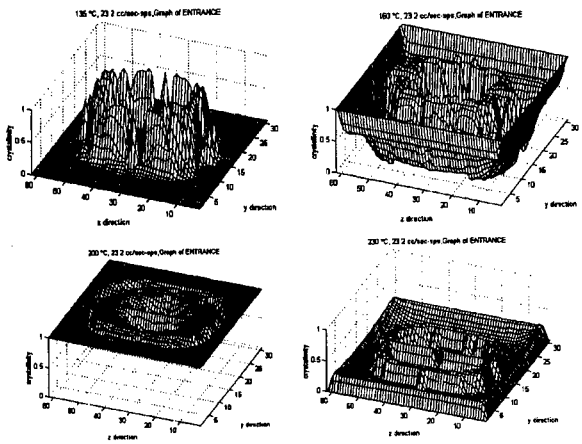


Figure 5 Crystallinity Distributions at the Entrance Location at Four Effective Mold Temperatures (135°C, 160°C, 200°C, 230°C) (Injection Speed of 23.2 cc/sec and a Hold Time of 60 sec)

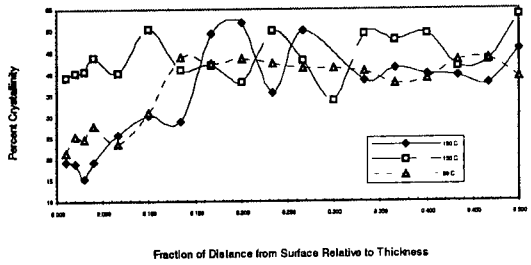


Figure 6 Percent Crystallinity vs Distance from the Surface at Entrance Location for Three Mold Temperatures (90ºC, 150ºC, 190ºC)

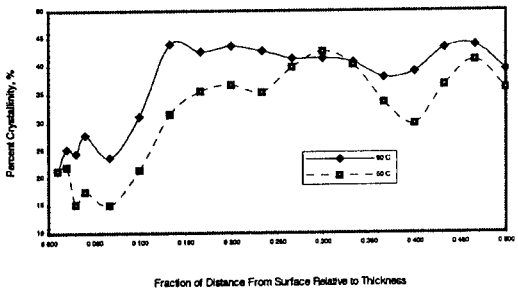


Figure 7 Percent Crystallinity vs Distance from the Surface at Entrance Location and Two Mold Temperatures (50°C, 90°C)

NUMERICAL INVESTEGATION OF BOUNDARY LAYER TRANSITION OVER FLAT-PLATE

KUNLUN LIU, KHOON SENG YEO
AND
CHANG SHU, ZHENGYI WANG

Department of Mechanical Engineering,
National University of Singapore
10 Kent Ridge Crescent, Singapore, 119260

Abstract

This paper presents two numerical cases of disturbed Navier-Stokes equations. In case 1, four order accuracy finite difference is used to investigate the evolution of negative frequency disturbance in Blasius boundary layer, results show us that negative frequency can reduce the streamwise wavelength of T-S wave, and accelerate the transition process. The effect of negative frequency lets to the breakdown of fluid structure becomes more significant. And, in the case two, two order accuracy finite volume method is used, Reynolds number is 900, and dimensionless frequency F is 86 in this case. Results present that the evolution process is more gradual in the positive frequency compare with the negative frequency in case 1. And the pressure contours clearly present a nonlinear interaction and break down process of two λ vortexes.

1. Introduction.

The laminar-turbulent transition is long interested by researchers of fluid dynamics. Stability theory has been developed as a theoretical understand of transition phenomena, its early period is the stage of linear theory, L. Prandtl[1], W. Tollmien and Grohne, D[2], W. Heisenberg[3] and C. C. Lin[4] greatly contributed to it. The character of this period is the development of theoretical work is faster than that of experiment and computation. Up to 1947, by the using of ribbon technique, G. B. Schubauer and H. K. Skramstad[5] successfully got powerful experiment supports of the linear stability theory.

Since the breakthrough in experiment and computation, experiment and computation quickly developed, and quickly beyond the development of theoretical work, because the difficulty in non-linear analysis obstructs its advance. The most important achievements in the stability theory during this period is the discovery of C-type[6], H-type[7,8], K-type[9] and N-type[10, 11] breakdown. C-type breakdown can be explained by triad resonance theory, and H-type

breakdown can be explained by the secondary instability theory. The experiments of Saric and Tomas[12] show that for the different amplitude of T-S wave, fluid will transition on the different breakdown route. When the amplitude of T-S wave range from 0.2% to 0.4%, the flows will present C-type instability, and the amplitude of T-S wave range from 0.4% to 0.6%, H-type instability will appear in flow. When the amplitude of T-S wave is over 0.6%, the k-type instability will appear. Since the secondary instability bases on the assumption that T-S wave is independent with the secondary disturbance, when the amplitude of T-S wave is high enough, this condition can be easily satisfied. This is the reason H-type breakdown happen on the higher amplitude T-S wave conditions compare with C-type breakdown. Since the clear, directly and universal theoretical analysis about Navier-Stokes equation has been unavailable up to now because of the nonlinear difficulty, numerical simulation become the necessary tool to the stability theory. H. Fasel[13, 14], B. J. Bayly & S. A. Orsag[15] and C. Liu & Z. Liu[16] got some excellent numerical simulated results of transition in the different cases.

The purpose of this paper is to present the nonlinear interaction of fluid structure, and effect of frequency to transition.

2. Governing equation and numerical method.

Fluid field is decomposed into two parts: mean flow and disturbance. The mean flow in our cases is Blasius boundary layer. The governing equations become:

$$\frac{\partial u_i}{\partial t}+J[(\frac{\partial u_i(U_1+U_1^0)+u_i^0U_1}{\partial \xi})+(\frac{\partial u_i(U_2+U_2^0)+u_i^0U_2}{\partial \eta})+(\frac{\partial u_i(U_3+U_3^0)+u_i^0U_3}{\partial \varsigma})]+$$

$$(\xi_i\frac{\partial}{\partial \xi}+\eta_i\frac{\partial}{\partial \eta}+\varsigma_i\frac{\partial}{\partial \varsigma})p-\frac{\Delta u_i}{\mathrm{Re}}=0 \qquad (1.1)$$

$$\frac{\partial u_1}{\partial \xi}+\frac{\partial u_2}{\partial \eta}+\frac{\partial u_3}{\partial \varsigma}=0 \qquad (1.2)$$

where u_i are disturbed velocity components, p is disturbed pressure, J is transformation Jacobian, u_i^0 are mean flow velocity components. U_i and U_i^0 are contravariant disturbance velocity components and contravariant mean flow velocity components, and hold:

$$U_1=\frac{1}{J}(u_1\xi_x+u_2\xi_y+u_3\xi_z),\quad U_2=\frac{1}{J}(u_1\eta_x+u_2\eta_y+u_3\eta_z),$$

$$U_3=\frac{1}{J}(u_1\varsigma_x+u_2\varsigma_y+u_3\varsigma_z)$$

$$U_1^0 = \frac{1}{J}(u_1^0\xi_x + u_2^0\xi_y + u_3^0\xi_z),\ U_2^0 = \frac{1}{J}(u_1^0\eta_x + u_2^0\eta_y + u_3^0\eta_z),$$

$$U_3^0 = \frac{1}{J}(u_1^0\varsigma_x + u_2^0\varsigma_y + u_3^0\varsigma_z)$$

Inflow displacement thickness is used as dimensionless constant. The following orthogonal grids are used for the numerical simulation:

$$x = \xi, \qquad y = \frac{y_{\max}\sigma\eta}{\eta_{\max}\sigma + y_{\max}(\eta_{\max} - \eta)}, \qquad z = \varsigma \tag{2}$$

in both case, $y_{\max} = 40$, and $\sigma = 6$. And the grids are homogeneous in the streamwise and spanwise. For preventing the pressure-velocity couple, staggered grid is used.

We simulate two different cases for the description the evolutions and interaction of T-S wave in flat-plate boundary layer transition. The first case focus on the effect of negative frequency disturbance to the transition, we wish numerical results could present the phenomena that the negative frequency disturbance will greatly accelerate the breakdown process. And for this purpose, finite difference method with second-order backward Euler differences in time direction and fourth-order central differences in space direction is used. The inflow is the superposition of solutions of O-S equation, and holds:

$$u_i = \phi(\eta)_i^{2d} e^{i(-\omega t)} + \phi(\eta)_i^{3d} e^{i(-\omega t + \beta\varsigma)} + \phi(\eta)_i^{3d} e^{i(-\omega t - \beta\varsigma)} + C.C. \tag{3.1}$$

$$p = \phi'(\eta)^{2d} e^{i(-\omega t)} + \phi'(\eta)^{3d} e^{i(-\omega t + \beta\varsigma)} + \phi'(\eta)^{3d} e^{i(-\omega t - \beta\varsigma)} + C.C. \tag{3.2}$$

The side condition is periodic, which hold:

$$\phi_{i,j,1} = \phi_{i,j,NK+1}, \qquad \phi_{i,j,NK+2} = \phi_{i,j,2} \tag{4}$$

So every periodic in spanwise direction will be investigated by $K+1$ point. And the length of spanwise is set as:

$$L_k = \frac{2\pi(NK+1)}{\beta K} \tag{5}$$

For avoiding the numerical divergence in the outflow region, the previous work[16] use buffer zone technique in the outflow region. But in case one, we replace the buffer zone technique with the first order upwind scheme, by the numerical dispassion of upwind scheme, the numerical divergence is successfully avoided. The using of upwind scheme bases on the following consider, when the transition happen, the large scale vortex structure will grow up, if the outflow boundary locate at the center of this large scale vortex, the outer flow boundary will hold the symmetric boundary condition, such as

$$\phi_{I-1/2} = \phi_{I+1/2}, \qquad \phi'_{I-1/2} = -\phi'_{I+1/2}$$

where I is the grid of outer boundary. In this condition, we have the following relation:

$$\frac{\partial f}{\partial \xi}=\frac{f^*_{i+1/2}-f^*_{i-1/2}}{\Delta\xi}=\frac{(f_{i+1}-f_{i-1})-|A|_{i+1/2}\Delta U_{i+1/2}+|A|_{i-1/2}\Delta U_{i-1/2}}{\Delta\xi}=\frac{2|A|_{i-1/2}\Delta U_{i-1/2}}{\Delta\xi}$$

So

$$\frac{\partial U}{\partial t}+\frac{\partial f}{\partial \xi}+\frac{\partial p}{\partial \xi}-\frac{\partial^2 f_v}{\mathrm{Re}\,\partial\xi\partial\xi}=\frac{U^{n+1}-U^n}{\Delta t}+\frac{2|A|_{i-1/2}\Delta U_{i-1/2}}{\Delta\xi}+\frac{\partial p}{\partial \xi}-\frac{\partial^2 f_v}{\mathrm{Re}\,\partial\xi\partial\xi} \quad (6)$$

This is obvious that (6) has upwind character; this kind of boundary condition can help to prevent the numerical divergence.

In the second case, the disturbance;

$$u_1=\varepsilon_1^{2d}e^{i(-\omega t)}+\varepsilon_1^{3d}e^{i(-\omega t+\beta\varsigma)}+\varepsilon_1^{3d}e^{i(-\omega t-\beta\varsigma)}+C.C. \quad (7.1)$$

$$u_2=u_3=p=0 \quad (7.2)$$

is introduced on the wall, and the position is $(i',1,k)$. We use this kind of disturbance to simulate the behavior of disturbance, which is excited by a ribbon on the wall. The two order spatial accuracy and two order temporal accuracy SIMPLE method is used.

2. Results and Conclusions.

In the case 1, the Reynolds number 900 and 800 are simulated, and β is 0.1. In this case, we set $\phi_i^{2d}=2\phi_i^{3d}$, the wavelength of (3.1) and (3.2) on the spanwise direction will reduce to its half, $\frac{\beta}{2}$. Therefore, a subharmonic, which holds a half frequency of T-S wave, generates. The numerical grid of case 1 is $160\times36\times32$. Since the early part of transition is a spatial instability dominant, wave number is real, so we assume that the dimensionless frequency is –86, according to analysis of A. H. Nayfeh and A. Padhyen[17], the group speed hold:

$$\frac{\partial\omega}{\partial a}=C_g e^{i\chi}=\frac{d\xi}{dt}\Big|_{(T-S\ wave)} \quad (8)$$

where χ is the phase angel of group speed. Therefore, for the T-S wave, we can get the following formula:

$$\phi(\eta)e^{i(-\omega t+\alpha\xi)}=\phi(\eta)\exp[i(a\xi-\omega\int_{t_0}^{t}dt)]=\phi(\eta)\exp[i(a\xi-\omega\int_{t_0}^{t}\frac{d\xi}{C_g e^{i\chi}})] \quad (9)$$

Our numerical results in case 1 (fig.1~fig.3) proves that in the first 4 or 5 T-S wave, the group speed of T-S wave is homogenous. Therefore, from (9), it obtains that:

$$\phi(\eta)e^{i(-\omega t+\alpha\xi)}=\phi(\eta)\exp[i(a-\omega\left\langle\frac{1}{C_g e^{i\chi}}\right\rangle)\xi] \tag{10}$$

where $\langle\cdot\rangle$ stands for the average in a streamwise wavelength. From (10), we get a formula of streamwise wavelength l_{wave}:

$$l_{wave}=2\pi/(a_{re}-\omega\left\langle\frac{1}{C_g e^{i\chi}}\right\rangle) \tag{11}$$

where a_{re} is the real part of a. Although the wave number of case 1 is negative, the propagation direction of T-S wave and the direction of group speed are still positive, which are along the streamwise. Therefore, the wavelength l_{wave} of case 1 is shorter than the condition of corresponding positive frequency, such as case 2.

Figure 1, 2 and 3 are consequences of case 1, Figure 2 clearly present that, in the second periodic of T-S wave, it breaks into two parts in the spanwise, this is a typical harmonica behavior. As the evolution of T-S wave, structures continuously break down; fluid contour becomes more and more irregular and complex. Turbulence happens. The strength of the amplitude of disturbance in figure 3 is higher than that of figure 1 and figure 2, and $\max(\phi_i^{2d})=0.04$ in figure 3, and $\max(\phi_i^{2d})=0.02$ in figure 1 and figure 2, where ϕ_i^{2d} is the profile of coming flow.

Figure 4 to 11 are numerical result of case 2. In this case, Reynolds number is 900, β is 0.1, and the dimensionless frequency F is 86. But, in case 2, $\phi_i^{2d}=3\phi_i^{3d}$. The numerical grid is $140\times32\times32$. Numerical ribbon sets on the grids $(30,1,k)$. The maximum receptive velocity on the $(30,2,k)$ is 0.005. Results clearly show us an entire interaction process of two λ vortexes. At first, each λ vortex will be stretched by the other, their head will move closely in their propagation direction. In the region $\mathrm{Re}=1200$, two λ vortexes merge together. And, quickly, breakdown happens.

REFRENCE

[1]Prandtl, L. 1931, Über die Entstehung der Turbulenz. *ZAMM*, **11**, 407.

[2]Tollmien, W. and Grohne, D. 1961, *The nature of transition, In: Boundary Layer and Flow Control.* **Vol.2,** Pergamon Press, London.

[3]Heisenberg, W. 1924, Über Stabilität und Turbulenz von Flüssigkeitsströmen. *Ann. D. Phys.* **74,** 577.

[4]Lin, C. C. 1955, The theory of hydrodynamic stability, Cambridge Univ. Press.

[5]Schubauer, G. B., Skramstad, H. H., 1947, Laminar boundary layer oscilliations and stability of laminar flow, NACA Tech. Report No. 909.

[6]Craik, A. D. D. 1971, Non-Linear resonant instability in boundary layers. *J. Fluid Mech.* **50,** 393.

[7]Herbert, Th. 1983, Secondary instability of plane channel flow to subharmonic three-dimensional disturbances. *Phys. Fluids.* **26(4),** 871.

[8]Herbert, Th. 1988, Secondary instability of boundary Layers. *Ann. Rev. Fluid. Mech.* **20,** 487.

[9]Klebanoff, P. S., Tidstrom, K. D. & Sargent, L. M. 1962, The three-dimensional nature of boundary-layer instability. *J. Fluid Mech.* **12,** 1.

[10]Kachanov, Y. S. 1987, On the resonant nature of the breakdown of a laminar boundary layer. *J. Fluid Mech.* **184,** 43.

[11]Kachanov, Y. S. 1994, Physical mechanisms of laminal-boundary-layer transition. *Ann. Rev. Fluid. Mech.* **26,** 411.

[12]Saric, W. S. and Thomas, A. S. W. 1984, Experiments on the subharmonic route to turbulence in boundary layers, *Turbulence and Chaotic Phenomena in Fluids.* (ed. T. Tatsumi), pp. 117~122. North-Holland.

[13]Fasel, H. 1976, Investigation of the stability of boundary layers by a finite differencemodel of the Navier-Stokes equations. *J. Fluid Mech.* **78,** 355.

[14]Fasel, H. and Konzelmann, U. 1990, Non-parallel stability of a flat-plate boundary layer using the complete Navier-Stokes equations. *J. Fluid Mech.* **221,** 311.

[15]Baylay, B. J. and Orszag, S. A. 1988, Instability mechanisms in shear-flow transition. *Ann. Rev. Fluid. Mech.* **26,** 411.

[16]Liu, C. & Liu, Z., 1995, Multigrid mapping and box relaxation for simulation of the whole process of flow transition in 3d boundary layer, *J. Comp. Phy.* **119,** 325.

[17]Nayfeh A. H. and Padhyen A. 1979, *AIAA Jour.* **17.** 1084~1090.

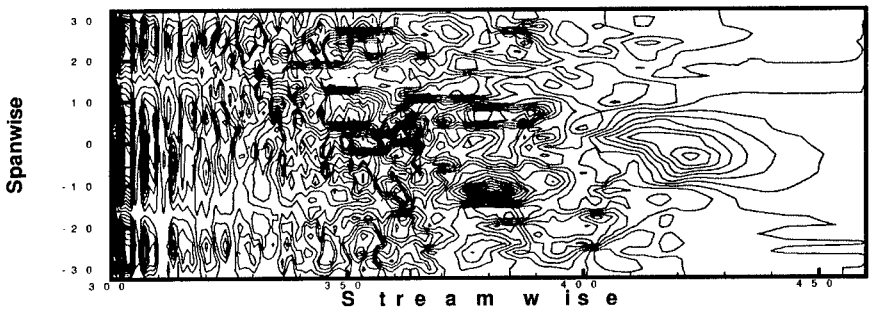


Figure 1, Spanwise velocity contour, Re = 900, F = 86. y = 2.0

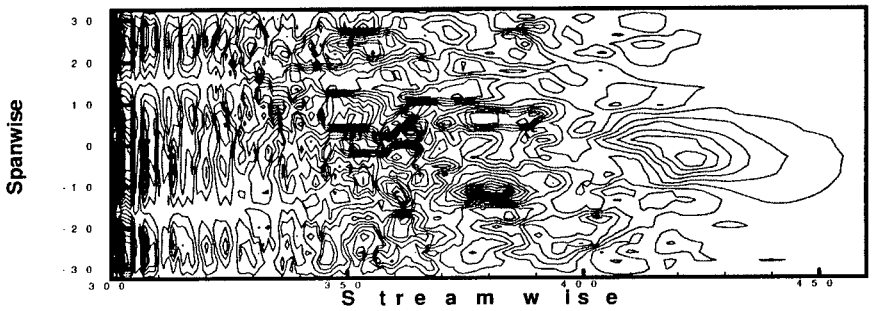


Figure 2, Spanwise velocity contour, Re = 900, F = 86. y = 1.4

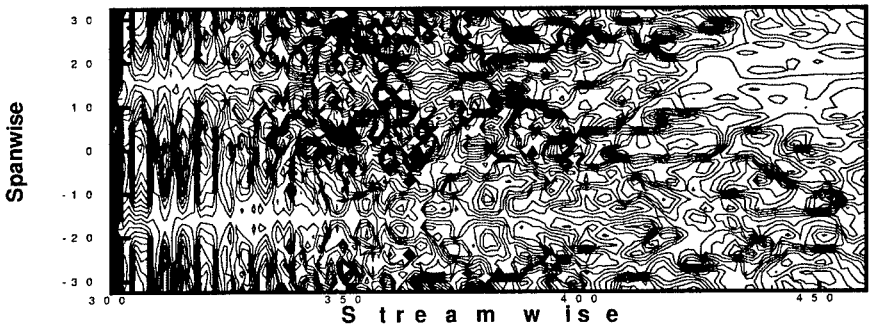


Figure 3, Spanwise velocity contour, Re = 800, F = 86. y = 2.0

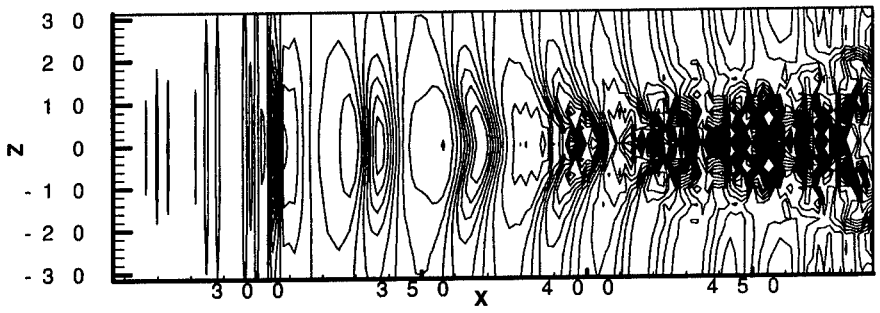


Figure 4, Pressure contour, Re = 900, F = 86. y = 2.0, t = 7T,
Ribbon position x = 303.94

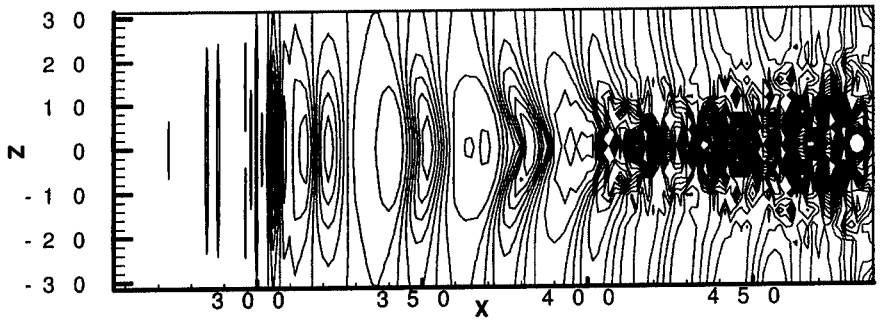


Figure 5, Pressure contour, Re = 900, F = 86. y = 2.0, t = 7.125T,
Ribbon position x = 303.94

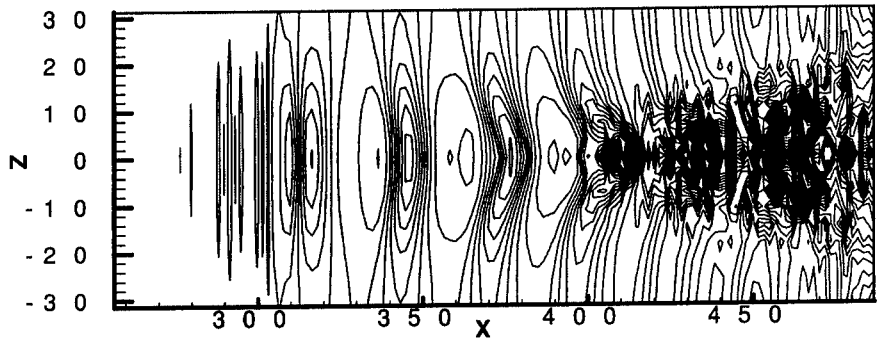


Figure 6, Pressure contour, Re = 900, F = 86. y = 2.0, t = 7. 25T,
Ribbon position x = 303.94

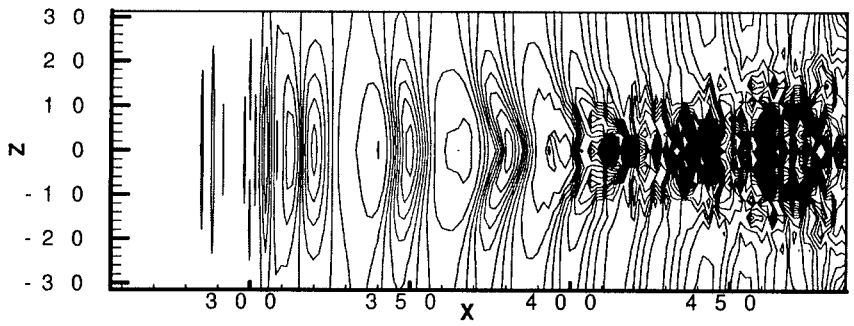


Figure 7, Pressure contour, Re = 900, F = 86. y = 2.0, t = 7. 375T, Ribbon position x = 303.94

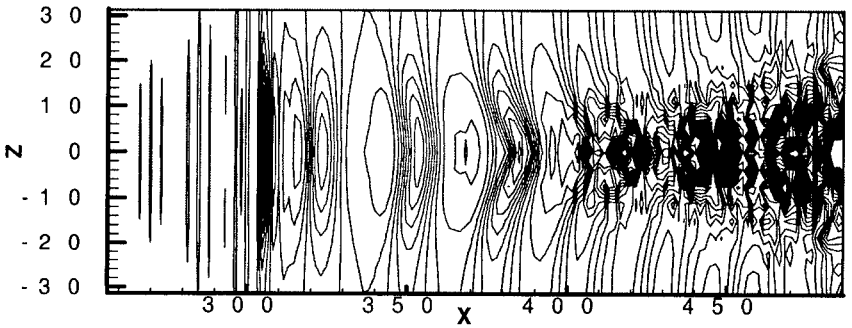


Figure 8, Pressure contour, Re = 900, F = 86. y = 2.0, t = 7. 5T, Ribbon position x = 303.94

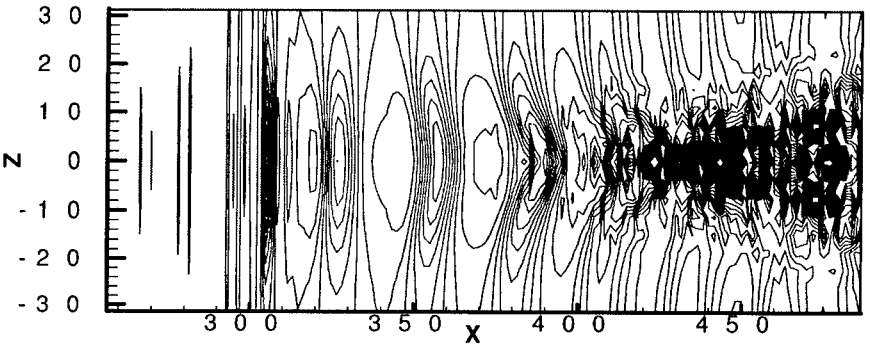


Figure 9, Pressure contour, Re = 900, F = 86. y = 2.0, t = 7. 625T, Ribbon position x = 303.94

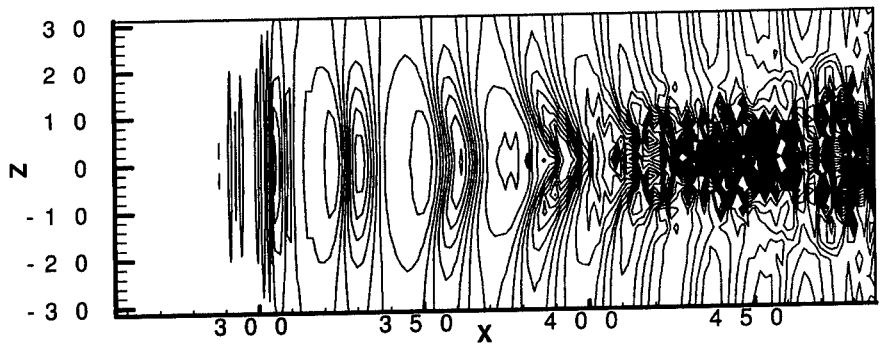


Figure 10, Pressure contour, Re = 900, F = 86. y = 2.0, t = 7. 75T, Ribbon position x = 303.94

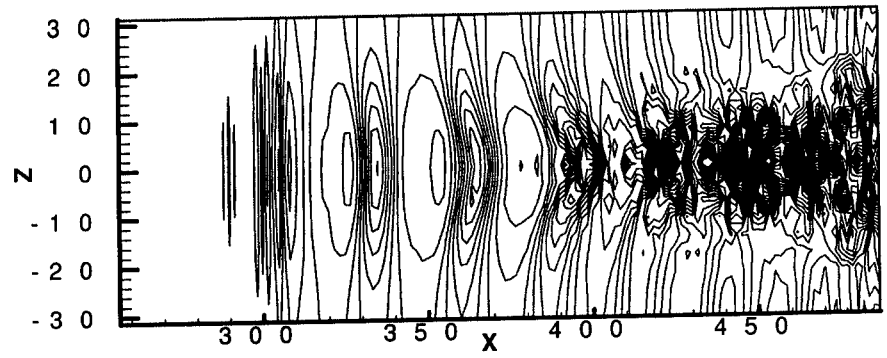


Figure 11, Pressure contour, Re = 900, F = 86. y = 2.0, t = 7. 875T, Ribbon position x = 303.94

DNS OF A STRAINED TURBULENT AXIAL VORTEX

B. ESHPUNIYANI AND G.A. BLAISDELL
School of Aeronautics and Astronautics
Purdue University
West Lafayette, IN 47907-1282

Abstract.

Direct numerical simulations (DNS) of a strained turbulent axial vortex are performed using a b-spline/Fourier spectral DNS code. Extending previous DNS further in time reveals that a global measure of the turbulent kinetic energy (GTKE) decays after growing to a certain extent, contrary to the earlier picture of unbounded growth. This observation leads to a re-investigation of the strained vortex simulations performed by Qin (Qin 1998). It is observed that the GTKE shows unbounded growth after a long period of decay. The Widnall instability seems to have been captured. Large eddy simulations (LES) shall be performed in the near future to study the vortex at higher Reynolds numbers.

1. Introduction

The work presented includes direct numerical simulations (DNS) of a strained turbulent axial vortex. This effort is part of an on-going project on the DNS and LES of turbulent axial vortices with and without the effect of an external strain field. The overall project is motivated by the wake hazard problem for commercial aircraft where the wing-tip vortices behind large aircraft present a serious safety concern for the following aircraft. In order for progress to be made in the prediction and control of these vortices, it will be helpful to have a better understanding of how turbulence within these vortices behaves and how the turbulence affects the distribution of vorticity. Also, current turbulence models do not perform well for strongly rotating flows and the current study provides needed data for the improvement of turbulence models for such flows.

There have been several experimental studies of turbulent vortices, which are discussed in the papers by Devenport *et al.* (1996) and Leweke and Williamson (1998). Numerical simulations of an isolated turbulent axial vortex have been presented in a series of papers by Ragab *et al.* (1995). More recently, DNS have been done by Coppens (1998), Qin (1998) and Blaisdell and Qin (1999), who considered the effects of an external strain field. The effect of strain was included because each vortex of a trailing vortex pair induces a strain field on the opposite vortex. The external strain field causes the streamlines to become elliptical (see figure 1) and introduces an instability (the short wavelength instability is known as the Widnall instability) which affects the development of turbulence within the vortex. A DNS has been done by Orlandi *et al.* (1998) of a trailing vortex pair corresponding to the experiment of Leweke and Williamson.

The objectives of the current study are to re-investigate the simulations of Qin by continuing them for larger times. It is found that the turbulence growth seen by Qin is a transient phenomenon, which is followed by decay. However, ultimately the instability due to strain does take over and the turbulence grows. The appropriate Reynolds number is $Re_\Gamma = \Gamma/\nu$, where Γ is the circulation of the vortex and ν is the kinematic viscosity.

2. Numerical Method

The vortex under consideration is time developing and, therefore, homogeneous in the axial (z) direction. This corresponds to a vortex far downstream, under the approximation that the flow changes slowly in the streamwise direction. Also, the azimuthal direction is naturally periodic. This enables the use of a Fourier spectral method in the streamwise and azimuthal directions. Basis spline polynomials (b-splines) are used in the radial direction. These provide spectral-like accuracy and are C^{k-2} continuous, where k is the order of the splines being used. The current study uses 4^{th} order b-splines. Also, since b-splines have local support on a given interval (see figure 2), they lead to sparse matrices that can be efficiently stored and solved.

Loulou (1996) developed a computer program to study turbulent pipe flow that solves the incompressible Navier-Stokes equations in cylindrical coordinates using a Galerkin formulation with a Fourier spectral method in z and θ and a b-spline method in r. The program was modified by Qin (Qin 1998) to solve the vortex problem and to run on an IBM SP2 parallel computer. This code has been further modified to perform large eddy simulations of a turbulent axial vortex using the dynamic SGS model which is implemented using the approach described in Eshpuniyani and Blaisdell (1999). LES will be performed in the near future, while the current study

focuses on DNS results. The grid used for the DNS presented here contains 96 θ-modes, 160 z-modes and 128 basis splines in the radial direction.

3. Results and discussion

Qin (1998) presented four direct numerical simulations of a strained turbulent axial vortex (see table 1). STRN1 and STRN2 included a wake like axial velocity profile, while STRN3 and STRN4 considered a vortex without any axial flow. Qin observed an unbounded monotonic growth of the global turbulent kinetic energy (GTKE) in STRN2. Here GTKE is the non dimensionalized volume averaged turbulent kinetic energy defined as

$$\mathcal{K} = \frac{1}{\pi R^2 L_z {V_0}^2} \int_0^R \int_0^{2\pi} \int_0^{L_z} k r dz d\theta dr \,, \tag{1}$$

where $V_0 = V_z(r)|_{r=\infty} - V_z(r)\Big|_{r=0}$ is the initial mean axial velocity deficit, R is the radius of the computational domain, L_z is the length of the computational domain in the streamwise direction, and k is the local turbulent kinetic energy per unit mass.

Upon continuing the simulation STRN2, it was discovered that the GTKE eventually decays in a manner similar to the DNS at a lower Reynolds number (STRN1). Thus it was realized that the Widnall instability had not been captured (see figure 3), contrary to the conclusion drawn earlier based on a DNS that was not extended far enough in time. This led to a fresh look at the DNS results by Qin and an inquiry into the possible reasons behind the lack of success in capturing the Widnall instability. As this instability is introduced by the external strain field, the simulations of the strained vortex without an axial wake (STRN3 and STRN4) were revisited in order to study the effect of the strain field without any possible interference from the axial flowfield during the simulation.

The fact that these DNS were carried out at low Reynolds numbers was considered as a possible reason for not capturing the Widnall instability. Hence, DNS of a strained vortex at higher Reynolds numbers were performed. However, eventual decay of GTKE was observed in all these simulations (see figure 4). Here $Re = V_0 R/\nu$ is the computational Reynolds number.

Shariff *et al.*(1994) present the evolution of modal energies for a three-dimensional vortex ring simulation. The evolution of all but a few unstable modes show a striking resemblance to the GTKE behavior in Figure 3. However, after a long period of time the initially stable modes also show unbounded growth. Since a strained vortex has the same short wavelength instability as a vortex ring (Widnall *et al.* 1974), the possibility of a similar phenomenon occurring in the current DNS was explored by extending the

DNS at the largest Reynolds number considered to a longer period of time. It is observed that the GTKE begins to grow exponentially after a long period of decay (see figure 5).

Upon this observation, STRN4 was extended in time to see if the Widnall instability can indeed be captured at the Reynolds numbers considered by Qin. It is observed that the GTKE behaves in a manner similar to the high Reynolds number simulation (see figure 6). The GTKE grows exponentially after a long period of decay. The Widnall instability seems to have been captured.

STRN2 is currently being extended in time to see if the decay of the wake like axial velocity profile eventually stabilizes the flow, as in the case of an isolated vortex (Qin 1998), or whether the Widnall instability dominates.

4. Conclusions

Eventual unbounded growth of global turbulent kinetic energy seems to indicate that the Widnall instability is captured for a strained vortex without axial flow. An interesting feature revealed in these simulations is that the GTKE has a transient growth phase followed by a long period of decay before it grows unbounded. Thus if the simulations are not continued for a long enough time, one may reach a wrong conclusion of eventual decay of turbulence, and misunderstand the flow physics. A previous DNS of a strained vortex with a wake-like initial axial velocity profile is currently being extended in time.

In future work spectra shall be computed to ensure that the simulations are well resolved. Flow visualization shall be carried out to understand the transition process better. Isolated vortex simulations (Qin 1998) show the presence of helical waves during the transition to turbulence, which break down during the re-laminarization process. A similar study shall be performed for the strained vortex simulations.

LES shall be performed to study the vortex at higher Reynolds numbers. The DNS of Qin have a Reynolds number $Re_\Gamma = \Gamma/\nu$ of about $50,000$ which is about three orders of magnitude smaller than that found in the wakes of large commercial aircraft. While LES still cannot reach full scale Reynolds numbers, it will allow the effects of varying Reynolds number to be studied. Also, Reynolds number is particularly important for the case with strain, because viscosity creates a high wave number cut-off for unstable modes. The current DNS are barely able to capture the instability due to strain because the smallest unstable mode has a length scale comparable to the vortex core size. It is desirable to have a wider range of unstable length scales, and this should be achievable with LES.

References

Blaisdell, G.A. and Qin, J.H. (1999), Numerical simulation of a strained turbulent axial vortex, *Turbulence and Shear Flow Phenomena - 1, First International Symposium, September 12-15, 1999, Santa Barbara, California*, pp. 1007-1012.

Coppens, F. (1998), *Simulations Numeriques Sur Le Developpement De La Turbulence Dans Un Tourbillon*, Ph.D. thesis, L'Institut Polytechnique De Toulouse, 3 June 1998.

Devenport, W.J., Rife, M.C., Liapis, S.I. and Follin, G.J. (1996), The structure and development of a wing-tip vortex, *J. Fluid Mech.* **Vol. 312**, pp. 67-106.

Eshpuniyani, B. and Blaisdell, G.A. (1999), Implementation of an SGS model in a B-spline spectral method and LES of a turbulent axial vortex, *Recent Advances in DNS and LES, Proceedings of the Second AFOSR Conference held at Rutgers - The State University of New Jersey, New Brunswick, U.S.A., June 7-9, 1999*, pp. 549-558.

Leweke, T. and Williamson, C.H.K. (1998), Cooperative elliptic instability of a vortex pair, *J. Fluid Mech.* **Vol. 360**, pp. 85-119.

Loulou, P. (1996), *Direct Numerical Simulation of Incompressible Pipe Flow Using a B-spline Spectral Method*, Ph.D. thesis, Department of Aeronautics and Astronautics, Stanford University, June 1996.

Orlandi, P., Carnevale, G.F., Lele, S.K. and Shariff, K. (1998), DNS study of stability of trailing vortices, *Center for Turbulence Research, Proceedings of the Summer Program 1998*, pp. 187-208

Qin, J.H. (1998), *Numerical Simulations of a Turbulent Axial Vortex*, Ph.D. thesis, Department of Aeronautics and Astronautics, Purdue University, December 1998.

Ragab, S.A. and Sreedhar, M.K. (1995), Numerical simulation of vortices with axial velocity deficits, *Phys. Fluids.* **Vol. 7**, pp. 549-558.

Shariff, K., Verzico, R. and Orlandi, P. (1994), A numerical study of three-dimensional vortex ring instabilities: viscous corrections and early nonlinear stage, *J. Fluid Mech.* **Vol. 279**, pp. 351-375.

Widnall, S.E., Bliss, D.B. and Tsai, C. (1974), The instability of short waves on a vortex ring, *J. Fluid Mech.* **Vol. 66**, pp. 35-47.

TABLE 1. Primary case parameters for the strained vortex (see Qin 1998 for a complete description).

Case	Re_Γ	Axial flow
STRN1	19268	wake
STRN2	29428	wake
STRN3	29428	none
STRN4	58836	none

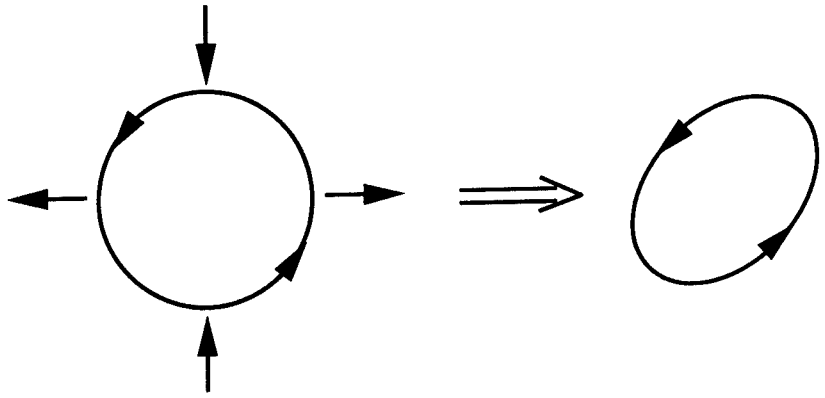


Figure 1. A strained vortex leads to a mean flow with elliptical streamlines.

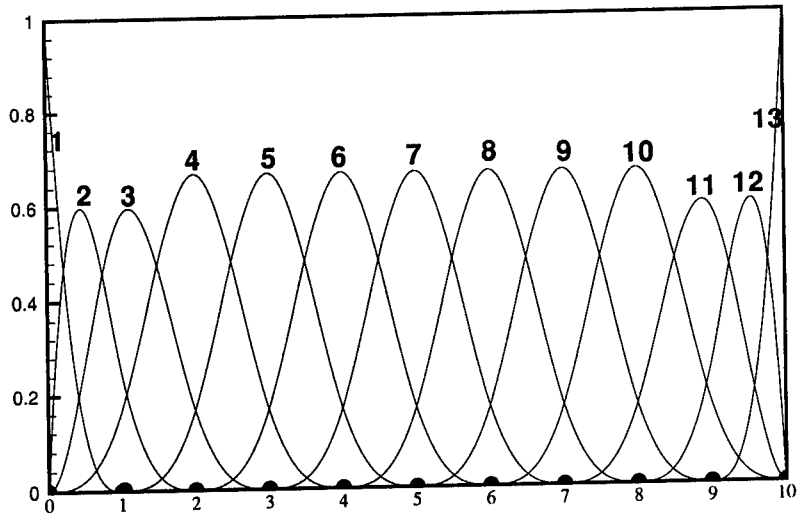


Figure 2. Fourth order B-splines on an 11-knot uniform grid.

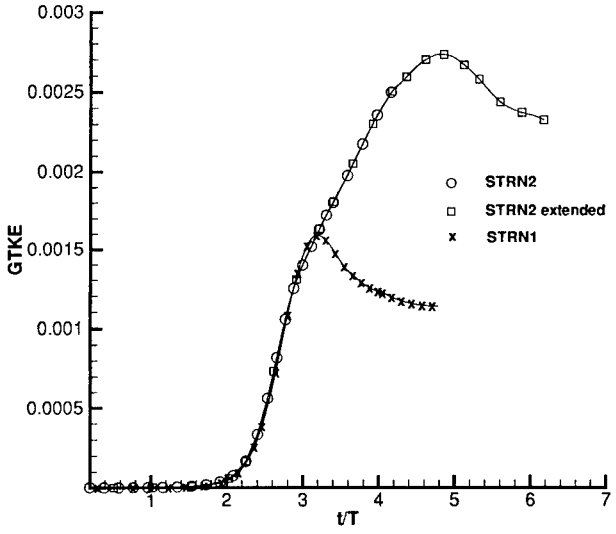


Figure 3. Global turbulent kinetic energy history for STRN 2 by Qin(1998) extended in time.

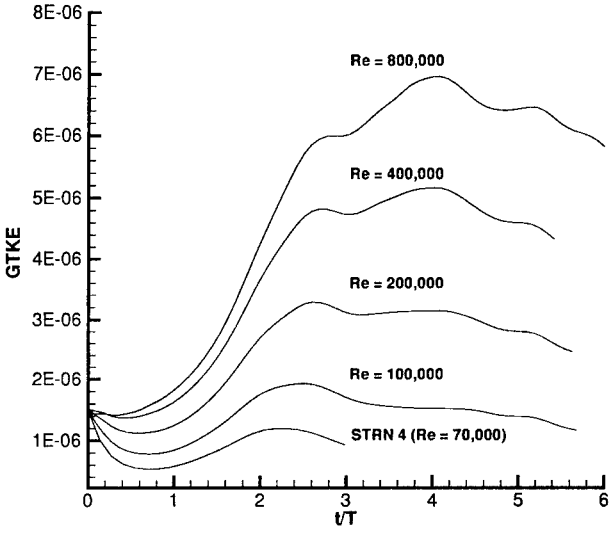


Figure 4. Global turbulent kinetic energy history for a strained vortex without axial flow at higher Reynolds numbers.

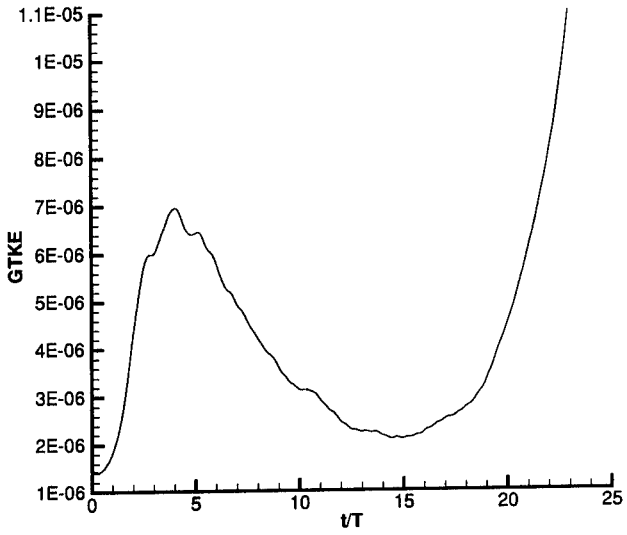


Figure 5. Global turbulent kinetic energy history for a strained vortex without axial flow at Re = 800,000 extended in time.

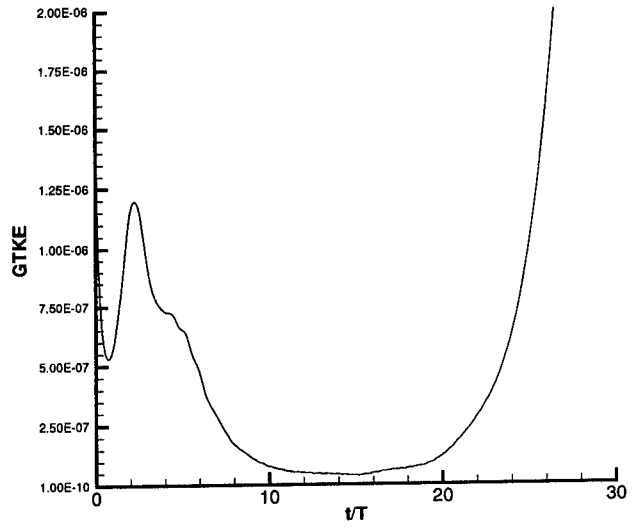


Figure 6. Global turbulent kinetic energy history for STRN4 extended in time.

LARGE-EDDY SIMULATION OF MACH 3.0 FLOW PAST A 24-DEGREE COMPRESSION RAMP

DONALD P. RIZZETTA AND MIGUEL R. VISBAL
Air Force Research Laboratory
Wright-Patterson Air Force Base, Ohio 45433-7521

Abstract.

Large-eddy simulation of the Mach 3.0 flow past a 24 deg compression ramp is performed by a high-order numerical method. Spatial derivatives are represented by a sixth-order compact stencil that is used in conjunction with a tenth-order non-dispersive filter. The scheme employs a time-implicit approximately-factored finite-difference algorithm, and applies Newton-like subiterations to achieve second-order temporal and sixth-order spatial accuracy. In the region of the shock wave, compact differencing of convective fluxes is replaced locally by a third-order Roe upwind-biased evaluation. The Smagorinsky dynamic subgrid-scale model is incorporated in the simulation to account for the spatially under-resolved stresses and heat flux. Comparisons are made with experimental data in terms time-mean surface pressure and skin friction distributions, and with instantaneous surface pressure measurements.

1. Introduction

Large-eddy simulation(LES) of supersonic flows is useful for studying compressibility effects, which can appreciably alter fluid physics. Such studies increase the understanding of turbulence mechanisms and can lead to the development, improvement, and testing of lower-order closure models. Despite remaining computationally intensive, LES also may be beneficial in the design and analysis of high-speed flight vehicles and associated propulsion systems where less sophisticated approaches fail.

Due to their geometric simplicity, supersonic compression-ramp flowfields have been studied extensively, both experimentally and computationally. Characteristics of the unsteady shock-wave motion of such flows

have been observed, measured, and analyzed by Andreopoulos and Muck[1], Smits and Muck[2], Dolling and Murphy[3], and Erengil and Dolling[4, 5], among others. Numerical investigations have typically considered the Reynolds-averaged Navier-Stokes equations used in conjunction with mean turbulence models. These efforts have met with limited success in the prediction of quantities such as heat transfer and skin friction, particularly in situations with large reversed-flow regions[6]. It is believed that this difficulty may be due in part to the disparity between the time-mean and instantaneous shock-system structure. In addition, the models and resultant computations often fail to account for compressibility effects or the three-dimensionality of the flowfield. In an effort to overcome these deficiencies, direct numerical and large-eddy simulations have been carried out by Hunt and Nixon[7], Urbin et al.[8, 9], Adams[10, 11], and Rizzetta et al.[12, 13] The present effort provides a large-eddy simulation for the flow past at 24 deg compression ramp at a freestream Mach number of 3.0 and $Re_\theta = 1696$.

2. Governing Equations

The governing equations are the unsteady three-dimensional compressible Favre filtered Navier-Stokes equations, written in nondimensional variables utilizing a generalized coordinate system, and expressed notationally in the following conservative form

$$\frac{\partial Q}{\partial t} + \frac{\partial}{\partial \xi}(F - \frac{1}{Re}F_v) + \frac{\partial}{\partial \eta}(G - \frac{1}{Re}G_v) + \frac{\partial}{\partial \zeta}(H - \frac{1}{Re}H_v) = 0. \quad (1)$$

All dependent variables may be decomposed into a filtered or large-scale portion, and a subgrid-scale component e.g., $u = \overline{u} + u_{sg}$. It is then convenient for compressible flows to recast the large-scale component in terms of a Favre-averaged variable so that

$$\widetilde{u} = \frac{\overline{\rho u}}{\overline{\rho}}. \quad (2)$$

The subgrid-scale stress and heat flux are provided by

$$\tau_{ij} = -Re\overline{\rho}(\widetilde{u_i u_j} - \widetilde{u}_i\widetilde{u}_j), \quad \mathcal{Q}_i = Re\overline{\rho}(\widetilde{u_i T} - \widetilde{u}_i\widetilde{T}). \quad (3)$$

Following Germano et al.[14], the compressible version of the model is given in trace-free form as

$$\mu_t = ReC\Delta^2\overline{\rho}\widetilde{\mathcal{S}}_M \quad \text{where} \quad \widetilde{\mathcal{S}}_M = \left(2\widetilde{\mathcal{S}}_{ij}\widetilde{\mathcal{S}}_{ij}\right)^{1/2} \quad (4)$$

is the magnitude of the rate-of-strain tensor, and

$$\widetilde{\mathcal{S}}_{ij} = \frac{1}{2}\left(\frac{\partial \xi_k}{\partial x_j}\frac{\partial \widetilde{u}_i}{\partial \xi_k} + \frac{\partial \xi_k}{\partial x_i}\frac{\partial \widetilde{u}_j}{\partial \xi_k}\right). \tag{5}$$

The eddy-viscosity length scale is taken as

$$\Delta = \left(\frac{1}{J}\right)^{1/3} \tag{6}$$

which corresponds to the width of the grid filter in physical space, C is the eddy-viscosity model coefficient, and

$$\tau_{ij} - \frac{1}{3}\tau_{kk}\delta_{ij} = -2\mu_t\left(\widetilde{\mathcal{S}}_{ij} - \frac{1}{3}\widetilde{\mathcal{S}}_{kk}\delta_{ij}\right). \tag{7}$$

For compressible applications, the isotropic part of the stress tensor is obtained according to Yoshizawa[15] from

$$\tau_{kk} = 2C_I\Delta^2\overline{\rho}\widetilde{\mathcal{S}}_M^2. \tag{8}$$

To complete closure of the model, the subgrid-scale heat flux vector is specified in terms of the turbulent Prandtl number as

$$\mathcal{Q}_i = -\left(\frac{\mu_t}{Pr_t}\right)\frac{\partial \xi_j}{\partial x_i}\frac{\partial \widetilde{T}}{\partial \xi_j}. \tag{9}$$

The model coefficients C, C_I, and the turbulent Prandtl number Pr_t are computed as a function of time and space from the energy content of the resolved large-scale structures.

3. Numerical Method

Time-accurate solutions to Eq. 1 were obtained numerically by the implicit approximately-factored finite-difference algorithm of Beam and Warming[16] employing Newton-like subiterations, which may be represented notationally as follows

$$\begin{aligned}&\left[I + \left(\frac{2\Delta t}{3}\right)\delta_{\xi 2}\left(\frac{\partial F^p}{\partial Q} - \frac{1}{Re}\frac{\partial F_v^p}{\partial Q}\right)\right] \times \\ &\left[I + \left(\frac{2\Delta t}{3}\right)\delta_{\eta 2}\left(\frac{\partial G^p}{\partial Q} - \frac{1}{Re}\frac{\partial G_v^p}{\partial Q}\right)\right] \times \\ &\left[I + \left(\frac{2\Delta t}{3}\right)\delta_{\zeta 2}\left(\frac{\partial H^p}{\partial Q} - \frac{1}{Re}\frac{\partial H_v^p}{\partial Q}\right)\right]\Delta Q\end{aligned} \tag{10}$$

$$= -\left(\frac{2\Delta t}{3}\right)\left[\left(\frac{1}{2\Delta t}\right)\left(3Q^p - 4Q^n + Q^{n-1}\right)\right.$$
$$+\delta_{\xi 6}\left(F^p - \frac{1}{Re}F_v^p\right) + \delta_{\eta 6}\left(G^p - \frac{1}{Re}G_v^p\right)$$
$$\left. + \delta_{\zeta 6}\left(H^p - \frac{1}{Re}H_v^p\right)\right].$$

In this expression, which was employed to advance the solution in time, Q^{p+1} is the $p+1$ approximation to Q at the $n+1$ time level Q^{n+1}, and $\Delta Q = Q^{p+1} - Q^p$. The implicit segment of the algorithm incorporated second-order-accurate centered differencing for all spatial derivatives($\delta_{\xi 2}, \delta_{\eta 2}, \delta_{\zeta 2}$), and utilized the diagonalized form of the factorized equations to enhanced efficiency. Temporal and spatial accuracy were maintained by utilizing subiterations within a time step.

A sixth-order tridiagonal subset of Lele's[17] compact difference scheme was used to evaluate the right-hand side of Eq. 10($\delta_{\xi 6}, \delta_{\eta 6}, \delta_{\zeta 6}$), and is illustrated here in one spatial dimension as

$$\alpha\left(\frac{\partial F}{\partial \xi}\right)_{i-1} + \left(\frac{\partial F}{\partial \xi}\right)_i + \alpha\left(\frac{\partial F}{\partial \xi}\right)_{i+1} \tag{11}$$
$$= a\left(\frac{F_{i+1} - F_{i-1}}{2}\right) + b\left(\frac{F_{i+2} - F_{i-2}}{4}\right)$$

$$\text{with} \quad \alpha = 1/3, \quad a = 14/9, \quad b = 1/9. \tag{12}$$

The scheme is used in conjunction with a 10th-order non-dispersive compact spatial filter in order to maintain both stability and accuracy, particularly on stretched curvilinear meshes. The filter is applied to the solution vector sequentially in each of the three computational directions following each subiteration, and is implemented as

$$\alpha_f \check{Q}_{i-1} + \check{Q}_i + \alpha_f \check{Q}_{i+1} = \sum_{n=0}^{5} \frac{a_n}{2}(Q_{i+n} + Q_{i-n}) \tag{13}$$

where $\check{Q}$ is the filtered value of Q. Equation 13 represents a one-parameter family of filters, where numerical values for α_f and the a_n's may be found in Ref.[18]. Repeated application of the spatial filter can result in shock waves that are excessively diffuse. This deficiency is overcome by replacing the compact-differencing of convective derivatives and use of filtering, by Roe's third-order upwind-biased scheme, locally in inviscid regions of shock waves.

4. Results

A computational domain size was taken as

$$L_x = 31.2\delta_0, \quad L_y = 4.7\delta_0, \quad L_z = 2.9\delta_0, \tag{14}$$

where L_x, L_y, L_z, are streamwise, vertical, and spanwise extents respectively, and δ_0 is the height of the incoming boundary layer. The vertical extent L_y corresponds to the domain height at the inflow location. This region was discretized with a nonuniform computational mesh consisting of $(421 \times 151 \times 81)$ points in (i, j, k). At the inflow location, the grid had the following minimum spacings in wall units:

$$\Delta x^+ = 16.8, \quad \Delta y^+ = 1.4, \quad \Delta z^+ = 8.3. \tag{15}$$

Based upon the mean incoming profile, 79 of the 151 vertical grid points were within the boundary layer.

The solution presented here for the Mach 3.0 flow past a 24 deg compression ramp with $Re_\theta = 1696$ represents part of a comprehensive investigation which was performed for supersonic compression-ramp flows. These are described, along with more complete details of the present simulation, in Ref.[13]. Typical instantaneous results at the midspan location are presented in Fig. 1. Mach number contours appear in the left-hand portion of the figure, while the grid structure is indicated to the right. Segments of the grid which are blanked out correspond to mesh points where convective derivatives were obtained via the Roe upwind-biased scheme. In the figure, only every other i-grid and every third j-grid line are displayed. It is evident that the upwind-biased evaluation is confined locally to a small region surrounding the shock wave, so that accuracy of the high-order method is not compromised in other regions of the flowfield.

Although no experimental data exists for the exact flow conditions of the simulation, it is useful to compare to measurements obtained at Reynolds numbers which were several orders of magnitude larger than that of the computation. Spanwise averaged time-mean surface pressure and skin friction coefficient distributions are shown in Fig. 2. The pressure coefficient has been normalized by the inviscid rise to account for variations in the freestream Mach number between the calculation and experiments. Because of the higher Reynolds numbers of the measurements, Cf has been normalized by its value just upstream of the interaction region.

Comparisons of the computed surface pressure standard deviation(s) and skewness(Sk) distributions with the data of Dolling and Murphy[3] appear in Fig. 3. The value of s upstream of the interaction(s_1) has been removed from the standard deviation in order to account for differences in the incoming states between the simulation and the experiment. Apart from

disparities near separation($X/\delta_0 \approx -2.0$), these comparisons are favorable. The disparities are caused by differences in the shock wave motion between the respective results, which will be illustrated subsequently.

The wall pressure intermittency(Γ) and instantaneous pressure time history are displayed in Fig. 4. It is observed that the experimental distributions of Γ have a steeper rise which occurs further downstream than the numerical result. This is due to the more extensive interaction region present in the low Reynolds number large-eddy simulation. Although the time mean level of the computed surface pressure near the separation point is approximately the same as that of the experiment, a very different fluctuating component is indicated. The high frequency oscillations exhibited in the numerical simulation are similar to those of the incoming boundary layer, while the low frequency modes of the experiment correspond to more extensive motion of the shock wave.

5. Summary

Computed surface pressure and skin friction distributions compared reasonably well with experimental data collected at higher Reynolds numbers. Comparisons were also made with statistical quantities extracted from instantaneous unsteady surface pressure measurements.

6. Acknowledgments

The work presented here was sponsored by the U. S. Air Force Office of Scientific Research under Task 2304N402 and was monitored by W. Hilbun and T. Beutner. Computational resources were supported in part by a grant of supercomputer time from the U. S. Department of Defense Major Shared Resource Centers at Stennis Space Center, MS and Aberdeen Proving Ground, MD.

References

1. Andreopoulos, J., and Muck, K. C., "Some New Aspects of the Shock-Wave/Boundary-Layer Interaction in Compression-Ramp Flows," *Journal of Fluid Mechanics*, Vol. 180, July 1987, pp. 405-428.
2. Smits, A. J., and Muck, K.-C., "Experimental Study of Three Shock Wave / Turbulent Boundary Layer Interactions," *Journal of Fluid Mechanics*, Vol. 182, Sept. 1987, pp. 291-314.
3. Dolling, D. S., and Murphy, M. T., "Unsteadiness of the Separation Shock Wave Structure in a Supersonic Compression Ramp Flowfield," *AIAA Journal*, Vol. 23, No. 12, Dec. 1983, pp. 1628-1634.
4. Erengil, E. E., and Dolling, D. S., "Unsteady Wave Structure Near Separation in a Mach 5 Compression Ramp Interaction," *AIAA Journal*, Vol. 29, No. 5, May 1990, pp. 728-735.

5. Erengil, M. E., and Dolling, D. S., "Correlation of Separation Shock Motion with Pressure Fluctuations in the Incoming Boundary Layer," *AIAA Journal*, Vol. 29, No. 11, Nov. 1991, pp. 1868-1877.
6. Settles, G. S., Fitzpatrick, T. J., and Bogdonoff, S. M., "Detailed Study of Attached and Separated Compression Corner Flowfields in High Reynolds Number Supersonic Flow," *AIAA Journal*, Vol. 17, No. 6, June 1979, pp. 579-585.
7. Hunt, D., and Nixon, D., "A Very Large Eddy Simulation of an Unsteady Shock Wave Turbulent Boundary Layer Interaction," AIAA Paper 95-2212, June 1995.
8. Urbin, G., Knight, D., and Zheltovodov, A. A., "Compressible Large Eddy Simulation using Unstructured Grid: Supersonic Turbulent Boundary Layer and Compression Corner," AIAA Paper 99-0427, Jan. 1999.
9. Urbin, G., Knight, D., and Zheltovodov, A. A., "Large Eddy Simulation of a Supersonic Compression Corner Part I," AIAA Paper 2000-0398, Jan. 2000.
10. Adams, N. A., "Direct Numerical Simulation of Turbulent Compression Ramp Flow," *Theoretical and Computational Fluid Dynamics*, Vol. 12, No. 2, Sept. 1998, pp. 109-129.
11. Adams, N. A., "Direct Simulation of the Turbulent Boundary Layer along a Compression Ramp at $M = 3$ and $Re_\theta = 1685$," *Journal of Fluid Mechanics*, Vol. 420, Oct. 2000, pp. 47-83.
12. Rizzetta, D. P., Visbal, M. R., and Gaitonde, D. V., "Direct Numerical and Large-Eddy Simulation of Supersonic Flows by a High-Order Method," AIAA Paper 2000-2408, June 2000.
13. Rizzetta, D. P., and Visbal, M. R., "Large-Eddy Simulation of Supersonic Compression-Ramp Flows," AIAA Paper 2001-2858, June 2001.
14. Germano, M., Piomelli, U., Moin, P., and Cabot, W. H., "A Dynamic Subgrid-Scale Eddy Viscosity Model," *Physics of Fluids A*, Vol. 3, No. 7, July 1991, pp. 1760-1765.
15. Yoshizawa, A., "Statistical Theory for Compressible Turbulent Shear Flows, with the Application to Subgrid Modeling," *Physics of Fluids*, Vol. 29, No. 7, July 1986, pp. 2152-2164.
16. Beam, R., and Warming, R., "An Implicit Factored Scheme for the Compressible Navier-Stokes Equations," *AIAA Journal*, Vol. 16, No. 4, Apr. 1978, pp. 393-402.
17. Lele, S. A., "Compact Finite Difference Schemes with Spectral-like Resolution," *Journal of Computational Physics*, Vol. 103, No. 1, Nov. 1992, pp. 16-42.
18. Gaitonde, D., and Visbal, M. R., "High-Order Schemes for Navier-Stokes Equations: Algorithm and Implementation into FDL3DI," AFRL-VA-WP-TR-1998-3060, Wright-Patterson AFB, OH, Aug. 1998.
19. Settles, G. S., and Dodson, L. J., "Hypersonic Shock/Boundary-Layer Interaction Database: New and Corrected Data," NASA-CR-177638, Apr. 1994.

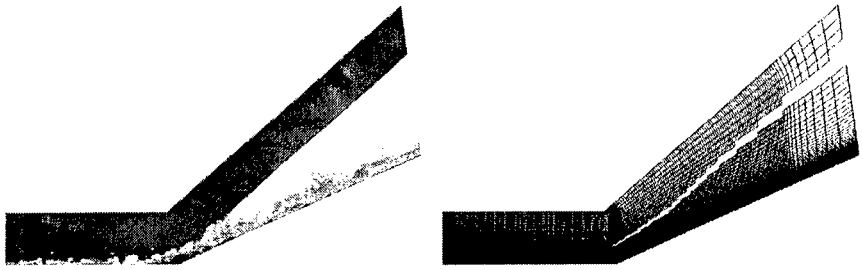


Figure 1. Typical instantaneous Mach number contours and shock-capturing stencils at the midspan location

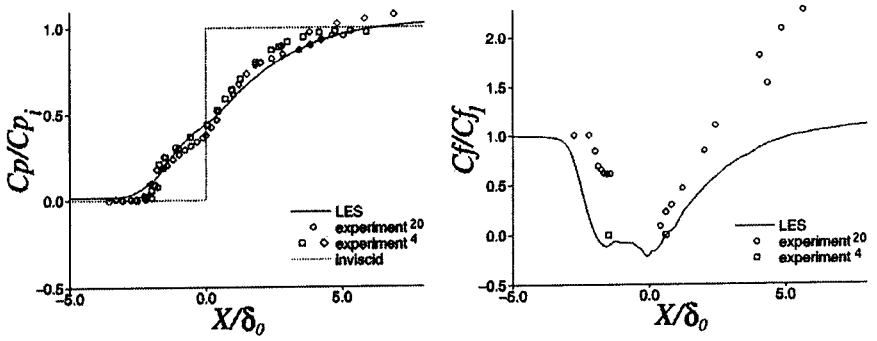


Figure 2. Spanwise averaged time-mean surface pressure and skin friction coefficient distributions

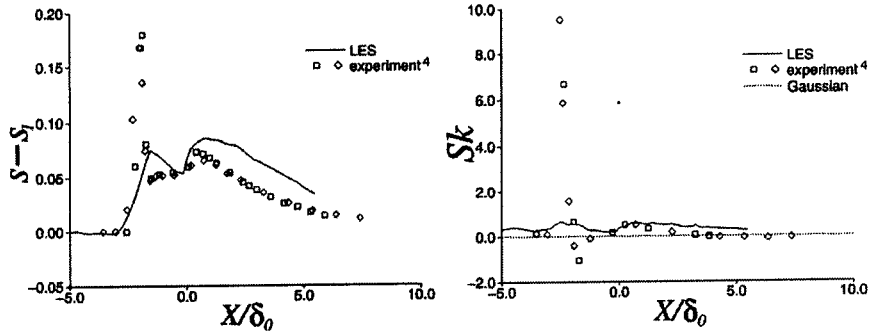


Figure 3. Spanwise averaged surface pressure standard deviation and skewness distributions

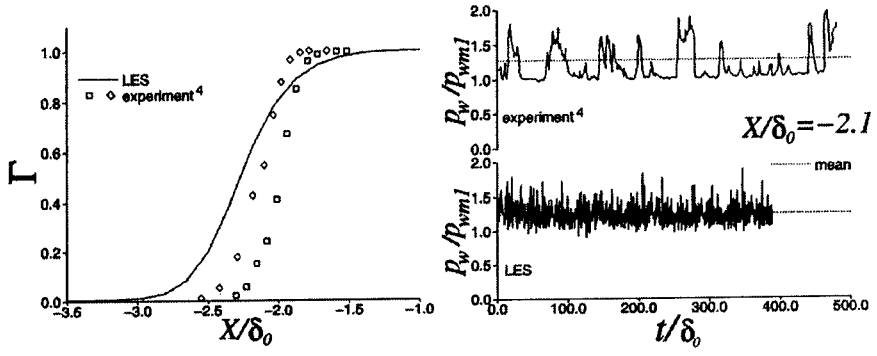


Figure 4. Spanwise averaged surface pressure intermittency distributions and midspan surface pressure time history at $X/\delta_0 = -2.1$

ON THE APPLICATION OF HYBRID RANS-LES AND PROPER ORTHOGONAL DECOMPOSITION TECHNIQUES TO CONTROL OF CAVITY FLOWS

SRINIVASAN ARUNAJATESAN AND NEERAJ SINHA
Combustion Research and Flow Technology, Inc.
(CRAFT Tech) Dublin, PA 18917

LAWRENCE UKEILEY
National Center for Physical Acoustics (NCPA)
University of Mississippi
Oxford, MS

Abstract

Issues pertaining to the application of hybrid RANS-LES modeling and Proper Orthogonal Decomposition (POD) techniques to the development of control strategies for cavity flows are discussed. The criteria for correct and consistent hybrid RANS-LES modeling are outlined – unsteady RANS-LES interfacing and mesh sensitive eddy-viscosity modeling are identified as the main issues. Preliminary calculations of a compression ramp are presented to illustrate our approach for RANS-LES interfacing. Next, a generalized mesh dependent eddy-viscosity modeling procedure is detailed and its applicability is demonstrated through calculations of weapons bay cavity flows. Comparisons with measurements are seen to agree better than earlier "LES" calculations which did not adequately treat the approach boundary layer. The technique is then used to create datasets for developing a POD based model of the cavity flow field. The differences between coupled and uncoupled POD applications to the density and velocity fields are discussed – it is seen that the coupled approach yields a flow field representation that is closer to the parent LES flow field than the uncoupled approach. Finally, a dynamical systems model of the flow field is presented. Applications to control problems are now in progress and will be presented in the future.

1. Introduction

The use of passive controllers to control the aeroacoustics in weapons bay flow fields has been studied in the past with limited success and range of operability, forcing aircraft to reduce speed to deploy stores [1,2]. Active control technology presents a better alternative because of its ability to adapt to the different flow conditions and its potentially larger range of operability. Techniques such as pulsed jets, piezzo activated actuation, and more recently, high

frequency actuation as a control means have been studied [3]. While the search for an optimal controller continues, analysis techniques are sought that can be used to examine the flow field and test out the controller concepts. Towards this end, a joint research effort has been initiated at CRAFT Tech and NCPA to develop a high fidelity lower dimensional model of the weapons bay flowfield combining hybrid RANS-LES modeling and the Proper Orthogonal Decomposition (POD) technique. While modeling based on Large Eddy Simulation (LES) embodies sufficient fidelity to represent the dynamic aeroacoustic environment in a cavity [4], it requires substantive computer resources and consequently, a hybrid RANS-LES method has been developed to minimize cost and maximize computational fidelity. Lumley's Proper Orthogonal Decomposition (POD) methodology [5] is being assessed with the objective of developing a simplified model of cavity flow dynamics. This entails utilization of the numerical simulation data to obtain a simplified eigenfunction representation of the flow that is ideally suited for utilization in a Low Dimensional Model of the cavity to study control alternatives.

In this paper, two aspects of this development effort are presented. In the first part of the paper, we discuss issues pertaining to hybrid RANS-LES modeling for complex flows in general and demonstrate its application to a weapons bay flow field. The issues of interfacing between RANS and LES – an issue not addressed so far in the literature – and mesh sensitive unified turbulence modeling are discussed. In the second part of the paper, we address the development of a reduced order POD based model of the cavity flowfield based on hybrid RANS-LES simulations. Issues pertaining to the coupling of flow field variables are addressed and a general method to develop a lower dimensional dynamical model for the cavity flow field is presented.

2. Hybrid RANS-LES Modeling

In the first of the present series of conferences, Spalart et al. [6] estimated (optimistically) that an LES of a whole aircraft flow field would require about 10^{11} grid points and about 5 million time steps to obtain reasonable solutions. Simulations using just a fraction of that number of grid points are still not possible today. Hybrid RANS-LES methods address this need by combining the cost effectiveness of RANS methods with the accuracy of LES methods. RANS methods compute only the mean flow field while modeling the effects of turbulence entirely. LES methods, on the other hand, resolve most of the energy containing flow scales and model only the small turbulent scales. RANS methods are thus suitable only for steady or at most mildly unsteady flows, while, LES methods perform much better for flowfields with strong unsteadiness. Hybrid RANS-LES methods attempt to take advantage of this fact by resorting to RANS type modeling in steady flow regions and switching to LES type modeling only in regions where it is required (such as regions with strong unsteadiness, separation

or aeroacoustic interactions, etc). However, interfacing RANS and LES regions of the flow fields is not straightforward and requires careful examination.

In order to interface RANS and LES solutions consistently, two different aspects need to be considered. The first one pertains to the fact that the RANS solutions are steady solutions while the LES solutions are unsteady. Hence, when RANS solutions are used as interfacial boundary conditions (either implicitly through unified methods or explicitly by zonal methods) the steady state flow field needs to be augmented with unsteady fluctuations. This has to be done in a manner consistent with the LES resolution at the interface boundary. Secondly, the eddy viscosity that is used to model the effects of the unresolved scales (all turbulent scales in RANS and sub-grid scales in LES) has to be suitably modified to reflect the increased resolution in LES regions. Unless both these conditions are satisfied, truly hybrid RANS-LES interfacing cannot be achieved. In the literature to date, several hybrid approaches [6,7,8,9,10] have been proposed to address the second issue, while the first issue has not received much attention. In all these methods, the eddy viscosity computation is suitably tuned such that a certain extent of mesh dependence is achieved – regions of higher resolution (or LES type regions) see lower values of the turbulent viscosity while regions of lower resolution (or RANS type regions) see higher turbulent viscosities. Thus steady solutions are obtained in regions of lower resolution while a higher level of unsteadiness is sustained in regions of higher resolution.

While this approach is consistent with the general dissipative natures of RANS and LES, it does not reconcile the large differences in the range of structures resolved in the RANS and LES regions. This omission can be unimportant to a large class of problems where the unsteadiness is generated and contained entirely within the LES domain (such as cavity flows, as we will show later), but can be very important for a wide class of problems where the small scales unsteadiness that are not resolved in the RANS regions interact very strongly with the flow structures in the LES regions. In the RANS region, only the mean flow field is resolved and all turbulence is modeled – the structure of the turbulent flow field is represented by increased turbulent diffusivities and kinetic energy, thus capturing the turbulence effect in a statistical sense. However, such a representation does not allow for the unsteady interactions of any flow structures in the RANS regions with any other flow field characteristics in the LES region. Hence, the resulting solution in the LES region cannot capture any of the unsteadiness present in the actual flow field. For such flows, the mean flow field from the RANS solution must be transformed at the interface boundary to re-introduce the unsteadiness in the flow field, so that the LES region will see the proper boundary conditions.

In the next section, we present two example calculations – one of each of the types discussed above. The first calculation is that of a supersonic flow over a

compression corner – this is shown to demonstrate the importance of the unsteadiness re-creation concept discussed earlier. The second flow field, discussed in more detail, is the hybrid simulation of the cavity flow field. In this flow, the effect of the small scale unsteadiness in the upstream boundary layer is small – the flow is dominated by resonant shear layer-acoustic interactions in the cavity. For this flow field, the mesh dependent eddy viscosity modeling methodology is demonstrated.

2.1 Unsteady Interfacing for Hybrid RANS-LES

In this section we present an example of a flowfield where the interaction of the unsteadiness in the "RANS" region of a hybrid simulation strongly affects the "LES" region simulation. This calculation is presented here only as a demonstration of the issue of interfacing – the details are omitted for brevity and will be presented elsewhere. The flow field chosen for this purpose is a Mach 2.88 flow over a compression corner (Fig. 1) – a flat plate boundary layer (with a long run) leads up to a ramp with a turning angle of 8 degrees. Here, results from two calculations are shown - in both these calculations, the upstream approach boundary layer is simulated using RANS (using a k-ε turbulence model) and a short distance upstream of the compression corner the model is switched to LES (a one equation LES model [10] is used). In the first simulation, nothing is done at the interface between the RANS and LES regions, the RANS profile is used as the starting input profile for the LES calculation. In the second simulation, the RANS boundary layer is transformed into an LES boundary layer using the recycling method of Urbin and Knight [11]. The mean boundary layer thickness at the interface location for the two calculations is the same; the only difference is the unsteadiness in the flow field in the second simulation.

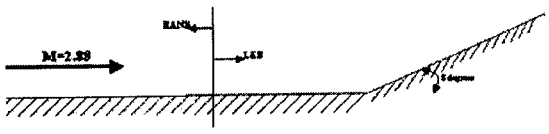


Fig. 1. Schematic of the compression ramp calculation

Figures 2 and 3 show an instantaneous snapshot of the shock structure in the corner – the effect of the unsteadiness is clearly seen in Fig. 3 – the streamwise vortices in the boundary layer wrinkle the shock surface and cause the shock to

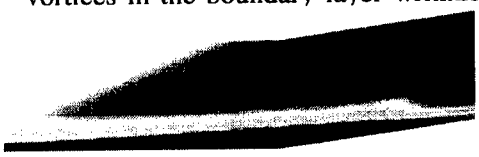


Fig. 2. Instantaneous snap shot from the hybrid calculation without unsteady interfacing.

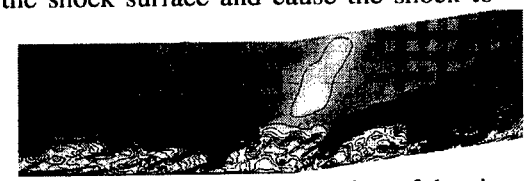


Fig. 3. Instantaneous snap shot of density contours from the hybrid calculation with unsteady interfacing following ref. [11].

constantly move about its mean location. Figure 2 on the other hand does not show any unsteadiness at all – the shock is stationary, and no fluctuations are visible in the flow field. Further, the recirculation length is incorrect and in fact, moves all the way upstream to the inflow boundary before the simulation has to be stopped. The comparison of the surface pressures shows that the second simulation yields much better comparisons with the experimental data and the LES of Yan et al. [12]. This shows that the small structures in the upstream boundary layer can be very important in predicting this flow field. These small scale structures provide the turbulent mixing (diffusion) that keeps the shock stably oscillating around its mean position. In the case of the pure LES, this turbulent diffusion is missing and the shock moves all the way upstream. Therefore, the unsteadiness not only is responsible for providing the shock (and hence the pressure oscillations), it is also responsible for the stability of the flowfield itself.

2.2 Mesh Dependent Turbulence Modeling for Hybrid RANS-LES

In this section we describe a method for introducing a mesh dependence in the computation of the eddy viscosity used in turbulence models. The model is based on the k-ε RANS model and the one-equation subgrid model [10]. As we shall show, the model reduces to the baseline RANS model in regions where the mesh does not permit the resolution of flow structures. As the mesh size decreases in regions of strong flow features, the model reduces to the LES model thereby allowing the user to perform hybrid calculations within a unified framework. Clearly, this is more suited to problems that are not strongly dependent upon the interfacing boundary conditions. To demonstrate the applicability of this model, we apply it to the simulation of a weapons bay flow field – these results are presented in the next section.

As mentioned earlier, several approaches have been proposed to deal with mesh dependent eddy viscosities [6-10]. However, as identified in Reference [8], one drawback of the approaches is that no attempt is made to determine the extent of the local resolution with respect to the overall turbulence levels. A certain grid size will resolve different amounts of energy/turbulence in low and high Reynolds number flows. That this relative difference in the resolution with respect to the local turbulence levels is incorporated into the various hybrid models is not clear. In order to address this issue, we present a different approach here. In this method, the eddy viscosity is still linked to the local mesh size; however, additional effort is spent to characterize the local turbulence levels, so that the amount of net turbulent dissipation used in the momentum and energy balance is consistent with the local mesh size *and* the local turbulent Reynolds number.

The overall approach involves solving the mass, momentum and energy conservation equations using a finite volume framework. In addition to these conservation equations, two additional equations describing the evolution of the

turbulence variables are solved for - one each for the subgrid kinetic energy and the overall turbulent dissipation rate, respectively. These equations are given as follows:

$$\frac{\partial \rho k^{sgs}}{\partial t} + \frac{\partial}{\partial x_i}\left(\rho u_i k^{sgs} - \left(\mu + \frac{\mu_T^{SGS}}{\sigma_k} \right) \frac{\partial k^{sgs}}{\partial x_i} \right) = P_k - \rho \varepsilon^{sgs}$$
$$\frac{\partial \rho \varepsilon}{\partial t} + \frac{\partial}{\partial x_i}\left(\rho u_i \varepsilon - \left(\mu + \frac{\mu_T^{RANS}}{\sigma_\varepsilon} \right) \frac{\partial \varepsilon}{\partial x_i} \right) = P_\varepsilon - D_\varepsilon \tag{1}$$

Here, σ_k, σ_ε, are the modeling constants appearing in the RANS form of the k-ε model. Details of the expressions for the source terms on the right hand side of equation (1) are presented in Ref. [8] and are omitted here for brevity. Note that since the two quantities represent different scale variables, namely, ε represents the large scale variable and k^{sgs} represents the sub-grid scales (SGS), different eddy viscosities are used in the two equations. The momentum and energy equations, however, use the SGS value of the eddy viscosity because that represents the amount of energy that is dissipated from the flow field based on how much of the flow field is resolved. This value blends to the RANS value as the grid is coarsened, as will be shown later.

Once these two variables are available at any flow field location, it is assumed that the local turbulent energy spectrum can be represented using a hybrid form of the energy-inertial-dissipation range spectrum. The form of the spectrum is given as follows,

$$\hat{E}(\hat{k}) = C_e \hat{k}_e^{-5/3} \left(\frac{\hat{k}}{\hat{k}_e} \right)^4 \left(1 + \left(\frac{\hat{k}}{\hat{k}_e} \right)^2 \right)^{-17/6} \exp\left(-\frac{3}{2} \alpha \hat{k}^{4/3} \right) \tag{2}$$

where, α=1.5, $\hat{k} = k\eta$, and $\hat{E} = E/(\upsilon^5 \varepsilon)^{1/4}$. Here, k is the wave number, $\hat{k}_e$ is an energy containing wave number, and C_e is a constant to be determined. The calibration for C_e requires that the integral of the dissipation range spectrum yield the local turbulence dissipation rate. In order for this form to be useful, the independent variables, namely, η the Kolmogorov scale and $\hat{k}_e$, in equation (2) must be related to the flow variables. The Kolmogorov scale is computed from the turbulent dissipation rate and laminar viscosity

Information about the subgrid kinetic energy and the Δ, the local mesh resolution are used to compute the energy containing wave number $\hat{k}_e$.

$$k^{SGS} = \int_{k_\Delta}^{\infty} E(k)\, dk \tag{3}$$

Equation (2) can be solved iteratively to determine $\hat{k}_e$. This completely determines the spectrum in Equation (2) and can then be used to compute the eddy viscosities. The eddy viscosities are computed from expressions similar to the baseline RANS model expressions. The model, it's testing and validations in the RANS and LES limits are described in greater detail in reference [8] and are omitted here for brevity. We now present an application of this modeling to the simulation of cavity flows. As we shall demonstrate the flow field is very amenable to this kind of modeling because the source of the unsteadiness is completely contained in the LES region. The flow field doest not strongly depend on the detailed structure of the approach boundary layer, but only on the momentum thickness.

2.3 Hybrid Simulation of Cavity Flowfield

The case selected for demonstration of the hybrid LES-RANS turbulence model corresponds to an experiment performed by Shaw at the Lockheed Compressible Flow Wind Tunnel (CFWT) [13]. The tests featured a generic 20% rectangular cavity - 36 inches in length with a L/D ratio of 6. Dynamic load spectra were obtained at various locations during these tests. A schematic of the geometry and the dynamic pressure measurement locations is shown in Fig. 4. The case simulated has a freestream Mach number of 1.5 and a Reynolds number of 7 million per foot.

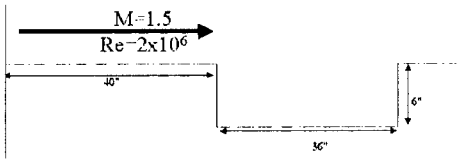


Fig. 4. Schematic of the cavity flow field.

The weapons bay flow field can be visualized as the combination of the two flow fields discussed above – the upstream region of the cavity is a boundary layer flow field, while the flow over the cavity itself is a shear layer flow field. The goal is to achieve a RANS type behavior in the upstream boundary layer region and a LES type behavior in the shear layer region. Hence, the mesh used in the calculations are created with high aspect ratio cells in the boundary layer - the wall normal mesh spacing is fine while the axial spacing is fairly coarse. This permits the shear in the wall normal direction to be adequately resolved, but the high aspect ratio cells do not permit the resolution of the fine scale structures in the buffer region. In the shear layer over the cavity, the mesh is uniformly fine in both the directions. In this

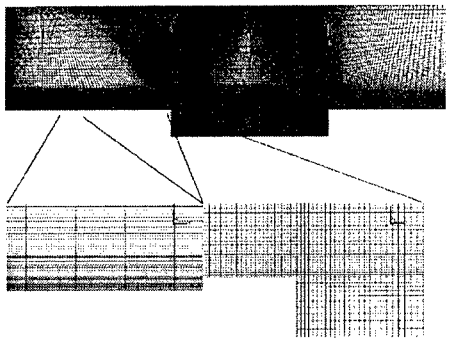


Fig. 5. Mesh used in the hybrid cavity calculation.

region, the evolution of the shear layer disturbances that result in the formation of the shear layer need to be resolved along with the strong gradients in the mean flow. The mesh used in these simulations is shown in Fig. 5. The insets show the cells in the boundary layer and shear layer regions. The wall normal resolution of $\Delta y^+=0.25$ was used in the boundary layer grid and the stretching rate in the boundary layer in the wall normal direction was limited to 4%. In the shear layer region over the cavity, the stretching rates in both directions were kept below 4%.

According to the test measurements, the upstream boundary layer thickness is an inch, which is consistent with one-fifth scaling for a fighter aircraft like the F-111. The dependence of the shear layer over the cavity on the boundary layer thickness has been well documented [14] – the momentum deficit at the leading edge of the cavity is critical for the shear layer development. The feedback mechanism, which determines the pressure and dynamic load fluctuations on the weapons bay floor interacts strongly with the separating boundary layer at the leading edge. Thus it is important that the boundary layer be captured accurately.

Fig. 6 shows a snapshot of the instantaneous contours of vorticity. The basic features of the flow are highlighted in this. The boundary layer upstream of the cavity is steady like a RANS boundary layer, the shear layer over the cavity, on the other hand is seen to be inherently unsteady and dominated by periodic vortex shedding from the separated boundary layer. Examination of the temporal fluctuations in the boundary layer showed that the fluctuations were barely noticeable - apart from the initial transients during start up of the calculation, there are no fluctuations in the boundary layer region upstream of the cavity leading edge. The approach boundary layer is seen to thicken with length as it approaches the cavity – the thickness of the boundary layer measured at the leading edge of the cavity (the last grid point before the cavity leading edge) shows a value of 1.067 inches. This is very close to the thickness measured in the experiments.

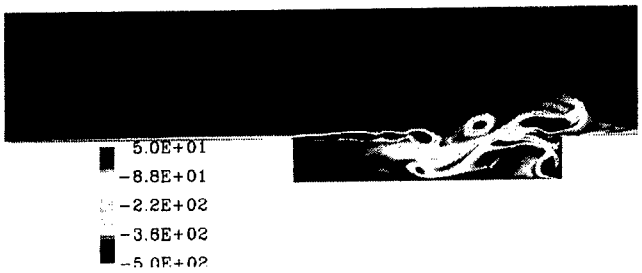


Fig. 6. Vorticity contours over the cavity showing steady RANS like and unsteady LES like regions.

The shear layer over the cavity as seen from above is clearly unsteady. The separated boundary layer becomes unstable and rolls up into vortices. These vortices are convected downstream in the shear layer and impinge upon the aft end of the cavity. This causes a recirculating flow region to be set up inside the cavity forming the feedback loop. The reflected waves interact with the vortex shedding upstream, resulting in the creation of a limit cycle type process. An examination of

the flow variables in the shear layer clearly reveals this. Of particular interest to us is the pressure oscillation in the cavity. The predicted pressure oscillations on the cavity floor are compared with experimental data.

Prior to presenting the dynamic load predictions from the present simulation, Fig. 7(a) shows predictions from a preliminary LES simulation where the entire flow field is modeled through the use of the one equation LES model [10]. The mesh used for this calculation is the same as that used for the hybrid calculation. In the pure LES calculation, the approach boundary layer is not captured correctly. There is no unsteadiness in the boundary layer because the mesh cannot sustain it, however, the thickness at the cavity leading edge and the growth rate are predicted incorrectly by this model. The boundary layer thickness at the cavity leading edge is only 0.48 inches – almost half the experimental value. This adversely effects the shear layer and the whole cavity flow field downstream of the leading edge. The predicted pressure spectra at 25% and 75% cavity length are compared with the wind tunnel data. While the overall comparison with data is reasonable, significant discrepancies can be identified.

In Fig. 7 (b) and (c), the predictions from the hybrid model are shown. The main difference between these two simulations is the boundary layer upstream of the cavity. The difference in the pressure spectra predictions is clear – the hybrid model captures both the modes and the amplitudes of the pressure oscillations very well. The pure LES calculation, on the other hand, while exhibiting the correct trends, shows significant discrepancies with the experimental measurements. This highlights the role of the boundary layer in altering the cavity feedback mechanism and is very significant for control-oriented applications of the simulation methodology.

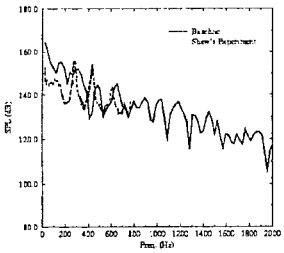


Fig. 7(a). Pressure spectrum from the pure LES at ¼ cavity length location compared with experiment.

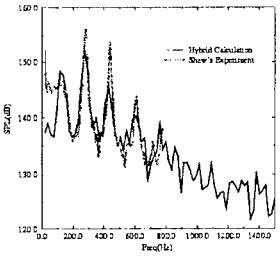


Fig. 7(b). Pressure spectrum from the hybrid RANS-LES at ¼ cavity length location compared with experiment.

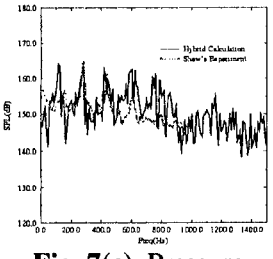


Fig. 7(c). Pressure spectrum from the hybrid RANS-LES at ¾ cavity length location compared with experiment.

In order to illustrate the role of the hybrid model, Fig. 8(a) shows contours of mean eddy viscosity and velocity in the boundary layer upstream of the cavity.

It is clearly seen that as the mesh resolution increases approaching the leading edge of the cavity the eddy viscosity drops, but there is no noticeable difference in the mean velocity contours – the boundary layer thickness and profile itself are not affected. Instead, an increased level of unsteadiness is seen in the boundary layer as the cavity is approached. The oscillations of the shear layer feedback through the subsonic portion of the boundary layer there by.causing oscillations in the flow variables. However, farther upstream, these are wiped out by the eddy viscosity yielding a steady boundary layer there. The time histories of the streamwise velocity at three different locations upstream of the cavity are shown in Fig. 8(b) – at the location farthest from the cavity, the oscillation amplitudes are mild and only low frequencies are seen to exist. However, as the cavity is approached, the amplitude and frequency content of the velocity fluctuations are seen to increase, this corresponds to the reduction in eddy viscosity, showing that the lower turbulent dissipation levels allows greater amounts of unsteadiness to be sustained in the boundary layer. This clearly highlights the role of the hybrid model and shows that the sought behavior has been achieved in the flow field.

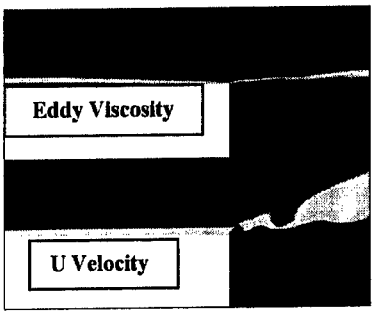


Fig. 8(a). Contours of eddy viscosity and U-velocity over the upstream Boundary layer

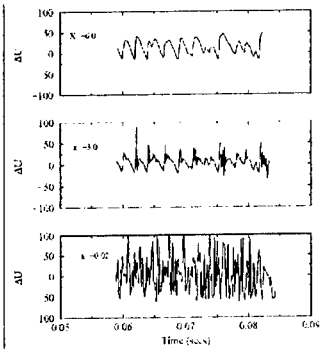


Fig. 8(b). Unsteady histories of velocity in the upstream boundary layer.

So far we have discussed methods of simulating the weapons bay flow field using hybrid techniques. The goal of these simulations is to develop a greater understanding of the flow field dynamics thereby permitting us to control its behavior. However, real time control in the hybrid RANS-LES simulations is still not feasible and hence reduced order models are required to help us examine control strategy alternatives. We now present results from our approach to develop one such model using POD and the simulations described above.

3.0 Proper Orthogonal Decomposition Analysis

The low-dimensional model developed here is derived using modes from the application of the Proper Orthogonal Decomposition to the cavity data set. The basis set of the POD modes are projected onto the governing partial differential equations (PDE) using a Galerkin method. The methodology to derive

the dynamical systems model discussed here is similar to that of Aubry et al [15] and Ukeiley et al [16]. In what follows we will briefly discuss the results of applying the POD to the numerical data-set of the cavity then discuss the formulation of the low-dimensional model. Since the cavity flow field under study is compressible the POD has been applied to both the density and velocity fields.

3.1 Application of the POD

Applications of the POD to the unsteady simulations have been reported in Ukeiley et al [16], Sinha et al [17] and Ukeiley et al [18]. All these applications follow the original work of Lumley [5], which is derived from projecting a candidate structure on the instantaneous field and maximizing in a least square sense. This results in a Fredholm integral equation, the solution of which yields the orthogonal basis vectors and the relative weights of these vectors that optimally describe the chosen field. This was later generalized to the "method of snapshots" by Sirovich [19] where he showed that the eigenfunctions of the POD can be written as linear combination of instantaneous flow fields,

$$\phi_i^n(\vec{x}) = \sum_{k=1}^{M} \psi^n(t_k) u_i(\vec{x}, t_k) \tag{4}$$

and they can be evaluated by solving an intermediate eigenvalue problem. This requires identifying the eigenfunctions of a matrix which is calculated by correlating independent snapshots and integrating over the spatial domain of interest. Significantly, this results in an eigenvalue problem which is of the order of the number of ensembles, and not the number of spatial locations, as with the original formulation. Equation (4) can be solved either independently for each flow variable or through the use of a suitable kernel that combines flow variables. Following Lumley and Poje [21] we have used $w = \left[\{\frac{au_i}{u}\}_{i=1\ldots3}, \{\frac{b\rho}{r}\}_{i=4} \right]; u^2 = \langle u_i u_j \rangle; r^2 = \langle \rho^2 \rangle$ such that a and b satisfy $a^2 \langle u_i u_j \rangle + b^2 \langle \rho^2 \rangle = 2$ thereby modifying equation (4) as

$$\phi_i^n(\vec{x}) = \sum_{k=1}^{M} \psi^n(t_k) w_i(\vec{x}, t_k) \tag{5}$$

The effects of using the modified kernel as opposed to the independent decomposition will be discussed briefly here. Figure 9 shows the convergence of the POD applied to both the density and velocity fields. Approximately 20% of the mean square energy is contained in the in the dominant mode and 70%

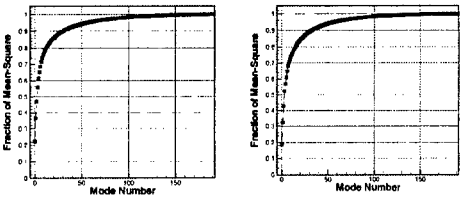


Fig. 9. Convergence of POD for density and u velocity.

in the first eight modes. The spatial structure of the modes is shown in Fig. 10(a) which shows the first 4 POD modes of streamwise velocity. The dominant modes are seen to contain information about the large scale features of the flow while the higher modes contain much of the smaller scale detail in the flow field. The vortical structure seen in the results of the hybrid calculation are seen here through an opposition in sign of eigenfunction across the shear layer. Figure 10(b) shows the modes associated with the density field. As with the velocity field, streamwise aligned waves and waves propagating out of the cavity can be distinctly identified in these modes. Shown in Fig. 11 is the effect of using the coupled formulation as opposed to the uncoupled formulation originally proposed. Here it is seen that that first modes are very different for the two reconstructions, however, as more modes are added, the solutions seem to converge. From a qualitative examination of the flowfields using only one POD mode, it is seen that the coupled application yields a reconstruction that is closer to the original flowfield, in spite of the fact that the first modes from the independent reconstructions actually contained a greater fraction of the mean square energy. Thus this implies that in order to predict the dynamics of the flow field, the coupled application yields better results.

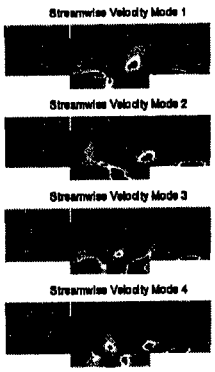


Fig. 10(a). POD modes of the velocity field from the coupled formulation.

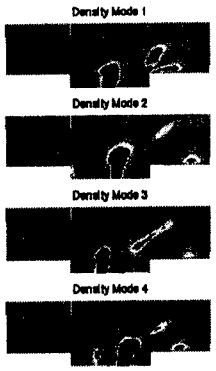


Fig. 10(b). POD models of the density field from the coupled formulation

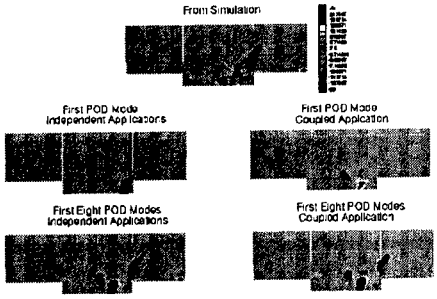


Fig. 11. Comparison of the reconstructed flow field from the coupled and uncoupled POD applications

3.2 Dynamical Systems Model

The system of PDE's for the model developed here consists of the conservation of mass and momentum equations for a compressible fluid and are given by,

$$\frac{\partial \rho}{\partial t} + \rho \frac{\partial u_j}{\partial x_j} + u_j \frac{\partial \rho}{\partial x_j} = 0 \tag{6}$$

$$\rho\frac{\partial u_i}{\partial t}+\rho u_j\frac{\partial u_i}{\partial x_j}=-\frac{\partial p}{\partial t}+\mu\frac{\partial^2 u_i}{\partial x_j\partial x_j}+\frac{1}{3}\mu\frac{\partial^2 u_j}{\partial x_i\partial x_j} \tag{7}$$

In using this system as the governing equations we are assuming a constant total enthalpy flow for the model. The first step in deriving the model equations is to expand out the density and velocity in terms of the POD modes. These representations can be written as follows,

$$\begin{aligned} u_i &= \sum_{n=1}^{N} a^n(t)\phi_i^n(\vec{x}) \\ \rho &= \sum_{l=1}^{N} b^l(t)\psi^l(\vec{x}). \end{aligned} \tag{8}$$

Since only the density and velocity will be expanded in terms of POD modes we will use an Ideal Gas assumption to relate the pressure field in terms of one of the model variables. After substituting in the above relationship the Galerkin projection is performed. The projection takes advantage of the POD basis being orthogonal to simplify the constant matrices. The resulting equations have the form,

$$\frac{\partial b^m}{\partial t}=-\sum_n a^n C1-\sum_l b^l B1-\sum_l\sum_n (b^l-\overline{b^l})(a^n-\overline{a^n})B2-\sum_l b^l B3-\sum_l\sum_n (b^l-\overline{b^l})(a^n-\overline{a^n})B2 \tag{9}$$

for the continuity relationship and,

$$\begin{aligned} \frac{d}{dt}a^m &= -\sum_p\sum_n b^p C3-\sum_n a^n L1-\sum_p\sum_n b^p a^n L2-\sum_p\sum_n a^n a^p Q1 \\ &-\sum_p\sum_n\sum_l b^p a^n a^l Q2+\sum_n\sum_l\overline{a^n a^l}S1+\sum_p\sum_n\overline{b^p a^n}S2+\sum_p\sum_n\sum_l\overline{b^p a^n a^l}S3 \end{aligned} \tag{10}$$

for the Navier-Stokes equations. In the above equations C1-C3, B1-B3, L1, L2, Q1, Q2 and S1-S3 are constant matrices calculated from the POD eigenfunctions. These coefficients relate to the various properties of the governing PDE's. For example, the linear term, L1, contains two parts; the first is viscous dissipation, the second has mean gradients which relates it to production of turbulence. It should be noted that separating the time and spatial dependence allows for the coefficients involving the POD eigenfunctions to be calculated only once since all of the time dependence is in the expansion coefficients.

3.3 Solution Methodology

Based on the results from the application of the POD the low-dimensional model developed will use 8 density and 8 velocity POD modes. This yields a set of 16 ordinary differential equations which need to be solved: 8 from continuity

and 8 from Navier-Stokes. These 16 equations have been programmed into a fourth order Runge-Kutta routine with adaptive time stepping. The routine will be used to integrate the ODE' s to obtain the expansion coefficients a(t) and b(t). Once the time evolution of these coefficients has been obtained they can be projected onto the eigenfunctions to get the time dependent velocity and density fields. This allows us to study both the time evolution of the dominant features and supplies a simple set of ODE' s that can be coupled with an active flow control methodology to determine an optimal flow control situation.

From examining the equations it is apparent that there are several terms that can not be written in terms of the POD modes, such as the temperature, the mean velocities and mean density. The temperature field will be assumed to be a function of space only, i.e., $T = T(\vec{x})$. This means that the temperature field will not be a function of time and in the model the mean value from all of the snapshots will be used. This is consistent with a constant total enthalpy assumption, which also allows us to only use the continuity and Navier-Stokes equations with out the energy equation. For the initial approach both the density and velocity fields will be treated as not being a function of time either. The numerical values used for these parameters will be those from the ensemble average of the snapshots. These values might be high, however, since there is over 80% of the turbulent kinetic energy and mean-square density retained in the model it is a reasonable first step. In the future a model for the mean velocity that more accurately represents an appropriate one for the truncated system and allows feedback from the turbulence can be introduced such as the one discussed in Ukeiley and Glauser, 1995.

Another important aspect of low-dimensional modeling is how to account for the neglected POD modes. To date we have tried to treat this simulation much like the VLES simulations that were used to generate the data used to extract the POD modes. That is to say, the numerical dissipation will be assumed great enough to account for energy lost to the POD modes that have not been included in the model. This is an initial approach and it is envisioned that an extra term to account for the truncated modes, much like what has been classically done, will be added later.

4.0 Conclusions and Future Work

In this paper we have addressed some key issues pertaining to the development and assessment of control strategies for cavity flows. Requirements for hybrid RANS-LES modeling in general have been outlined and demonstrative calculations have shown the need for each one of the components of hybrid modeling. The interfacial boundary condition generation issue was addressed briefly – further enhancements and improvements are being studied and will be presented in the future. The issue of mesh dependent modeling was demonstrated through its application to the cavity problem. In this regard, a more complete three

equation version of this model is being currently studied and will be presented in the future. The technique of POD was shown to be a good candidate for the application to the development of a lower dimensional model for the cavity – convergence of the POD modes was demonstrated along with comparisons to with the Hybrid RANS-LES calculations to show that the model mimics the simulations. The dynamical systems model of the flow field was derived and will be tested and studied in more detail in the future.

References

[1] Shaw, L., Bartel, H., and McAvoy, J., "Acoustic Environment in Large Enclosures With a Small Opening Exposed to Flow," *J. of Aircraft*, Vol. 20, No 3, March 1983.

[2] Shaw, L., "Weapons Bay Acoustic Environment Control," CEAS/AIAA -95-141, 1995.

[3] Stanek, M.J., Raman, G., Kibens, V., Ross, J.A., Odedra, J., Peto, J.W., "Control of Cavity Resonance through Very High Frequency Forcing", AIAA -2000-1905, 2000.

[4] Sinha, N., York, B.J., Dash, S.M., Chidambaram, N., and Findlay, D., "A Perspective on the Simulation of Cavity Aeroacoustics," AIAA Paper No. 98-0286, 1998.

[5] Lumley, J.L., "The Structure of Inhomogeneous Turbulent Flows," *Atmospheric Turbulence and Radio Wave Propagation*, Yaglom and Tatarsky eds. Nauka, Moscow, 166-178, 1967.

[6] Spalart, P.R., Jou, W-H., Strelets, M., and Allmaras, S.R., "Comments on the feasibility of LES for wings, and on a Hybrid RANS/LES approach", Advances in DNS/LES, *First AFOSR International conference in DNS/LES*, Greyden Press, 1997.

[7] Speziale, C.G., "Turbulence Modeling for Time-Dependent RANS and VLES: A Review," *AIAA J.*, Vol. 36, No. 2., p 173, February 1998.

[8] Arunajatesan, S.A. and Sinha, N., "Unified Unsteady RANS-LES Simulations of Cavity Flowfields," AIAA Paper No. 2001-0516, 39th AIAA Aerospace Sciences Meeting, Reno, NV, January 8-11, 2001.

[9] Peltier, L.J., Zajaczkowski, F.J., and Wyngaard, J.C., "A Hybrid RANS/LES Approach to Large-Eddy Simulation of High-Reynolds Number Wall bounded Turbulence," FEDSM2000-11177, 2000.

[10] Arunajatesan, S., Sinha, N., and Menon, S., "Towards Hybrid LES-RANS Computations of Cavity Flowfields", AIAA-00-0401, 38th AIAA Aerospace Sciences Meeting at Reno, NV, Jan 10-13, 2000.

[11] Urbin, G. and D. Knight, "Compressible Large Eddy Simulation Using Unstructured Grid: Supersonic Boundary Layer", Second AFOSR International Conference on DNS and LES, Rutgers University, June 1999. Kluwer Academic Publishers, 1999, pp. 443--458. Accepted for publication in AIAA Journal.

[12] Yan, H., Urbin, G., Knight, D., and Zheltovodov, A., "Compressible Large Eddy Simulation Using Unstructured Grid: Supersonic Boundary Layer and Compression Ramps," 10th Intl Conf. on Methods of Aerophysical Res., Institute of Theoretical and Applied Mechanics, Russ. Acad of Sciences, 2000.

[13] Shaw, L.L., 'High Speed Application of Active Flow Control for Cavity Acoustics", AIAA-00-1926, 2000.
[14] Dix, R.E. and Bauer, R.C., 'Experimental and Predicted Amplitudes In A Rectangular Cavity," AIAA 2000-0472, 38th AIAA Aerospace Sciences Meeting at Reno, NV, Jan. 10-13, 2000.
[15] Aubry, N., Holmes, P., Lumley, J. and Stone, E., 'The Dynamics of Coherent Structures in the Wall region of a Turbulent Boundary Layer", *Journal of Fluid Mechanics*, Vol. 192, 1988, 115-173.
[16] Ukeiley, L., et al. 'Examination of Large Scale Structures in a Turbulent Plane Mixing Layer. Part 2: Dynamical Systems Model," *J. of Fluid Mechanics*, Vol. 441, pp. 67-108, 2001.
[17] Sinha, N, and Arunajatesan, S., and Ukeiley, L., 'High Fidelity Simulation Of Weapons Bay Aeroacoustics Attenuation Using Active Flow Control," Paper No. AIAA-2000-1968, 6th AIAA/CEAS Aeroacoustics Conference, Lahaina, Hawaii, June 12-14, 2000.
[18] Ukeiley, L., Kannepalli, C., Arunajatesan, S. and Sinha, N. 'Low-Dimensional Description of Variable Density Flows". AIAA Paper 2001-0515, 39th AIAA Aerospace Sciences Mtg, Reno, NV, Jan., 2001.
[19] Sirovich, L., "Turbulence and the Dynamics of Coherent Structures," *Quarterly of Applied Math*, 45 (3), 1987.
[20] Lumley, J.L. and Poje, A.J., 'Low-Dimensional Models for Flows with Density Fluctuations", *Physics of Fluids*, Vol. 9, No. 7, 2023-2031, 1997.

LES BASED TRAILING-EDGE NOISE PREDICITON

W. SCHRÖDER, M. MEINKE, R. EWERT AND W.A. EL-ASKARY

Aerodynamisches Institut, RWTH Aachen
Wüllnerstr. 5-7, 52062 Aachen, Germany

Abstract. The paper presents a large-eddy simulation of the flow over a sharp trailing edge. To minimize the computational effort inflow conditions for fully turbulent compressible boundary layers are developed. The LES findings show good agreement with other numerical and experimental data. For the prediction of the trailing-edge noise, acoustic perturbation equations are derived, which are excited by sources determined from results of a compressible flow simulation. Results of acoustic fields are presented for a model problem.

1. Introduction

The interaction of the turbulent boundary layer and the wake in the vicinity of a trailing edge produces noise [6]. For the prediction of the trailing-edge aeroacoustics a two-step approach is proposed. The first step consists of a large-eddy simulation of the compressible flow problem only in the area where the noise is generated, i.e., just in the immediate vicinity of the trailing edge. Since the acoustical and fluid dynamical length scales differ considerably, the acoustic field is computed with a different grid resolution in a second step, using a system of acoustic perturbation equations that describe only the propagation of the acoustic modes. Its computational domain contains not only the trailing-edge region but the entire plate. Source terms, determined from the LES solution, are used to generate the sound in the trailing-edge region. Since only the aft region of the plate geometry is simulated in the LES, appropriate inflow conditions for a turbulent compressible boundary layer are derived. In the second part of the paper the acoustic perturbation equations are briefly introduced and their prediction qualities are discussed based on the flow over a circular cylinder [3]. In an upcoming step the trailing-edge noise will be simulated.

2. LES of the Trailing-Edge Flow

2.1. NUMERICAL METHOD AND CONFIGURATION

A large-eddy simulation is performed to simulate the turbulent compressible flow over a sharp trailing-edge of an adiabatic flat plate. The discretization of the convective fluxes in the governing equations is a second-order accurate AUSM formulation with a central pressure derivative. The viscous stresses are discretized using central differences of second-order accuracy. Furthermore, an explicit 5-step Runge-Kutta time stepping scheme of second-order accuracy is used for the temporal integration. The scheme is described in more detail in [9] where also results of various validation tests are discussed. The flow being simulated corresponds to experiments conducted by the Universities of Dresden and Stuttgart at a Reynolds number based on the freestream velocity and the length of the plate of Re_∞=5.33·10^5 and a Mach number of M=0.15 [10]. The thickness d of the plate is linearly reduced from d=1mm to zero under an angle of 15^o to avoid vortex shedding in the wake. Hot wire measurements are used to determine the mean velocity and turbulence intensities in the boundary layer and the wake. To reduce the computational effort while capturing the essential physics the numerical simulations are conducted in a domain that contains 25% of the total length of the plate. Since the boundary layer is tripped immediately after the leading edge, a fully turbulent boundary layer enters the domain of integration with a thickness of δ_0/d=2.1.

2.2. BOUNDARY CONDITIONS

The domain of integration comprises only the rear part of the flat plate and the wake region. Therefore, a slicing technique is used in which the instantaneous velocity distribution at each time level for the inflow boundary is generated from the simultaneous simulation of a turbulent boundary layer, see Fig. 6. The boundary layer simulation also requires an inlet boundary condition, which is obtained by extending the method of Lund et al. [8] for compressible flows. This technique will be discussed in the next section. At the surface of the plate the no-slip condition and an adiabatic wall is prescribed, at all outflow boundaries non-reflecting boundary conditions with pressure relaxation are applied [11]. Since the pressure relaxation introduces some numerical reflections, a sponge layer zone is added, in which the source terms S are computed as a function of the deviation of the instantaneous from the analytical solution q_a based on the logarithmic wall law $S = \sigma(q(t,\vec{x}) - q_a(\vec{x}))$, where q represents the vector of conservative variables. The parameter σ is computed as a function of the distance from the boundaries and increases from zero to σ_{max} within the sponge layer zone. The value for σ_{max} is chosen to be 0.5, which has been determined in test simulations under the condition to minimize numerical reflections.

2.3. RESCALING METHOD

The slicing technique involves the simulation of an adiabatic flat plate boundary layer. For that purpose the rescaling method of Lund et al. [8] is extended for compressible flows. In a first attempt a constant total enthalpy in the inflow section of the boundary layer was assumed, so that the mean and the fluctuation temperature could be determined by the corresponding velocity quantities. This procedure was called simple temperature rescaling [2]. The results, however, showed quite a discrepancy in the mean streamwise velocity (Fig. 1) and the skin-friction distribution (Fig. 2), which is why a more consistent compressible extension of the rescaling method was derived. The idea of the rescaling method is to decompose all flow field components into a mean and a fluctuating part, and then, to apply an appropriate scaling law to each quantity separately for inner and outer layers. For the velocity components the procedure proposed by Lund et al. [8] is adopted.

To take into account compressibility effects the temperature profile is rescaled as follows. For the mean static temperature T, we locally use Walz's equation $T/T_\infty=1+A(1-U^2/U_\infty^2)$ with $A=0.5(\gamma-1)rM^2$, where r represents the recovery factor and M the freestream Mach number [14]. Furthermore, the temperature fluctuation T' can be calculated assuming a negligible total temperature fluctuation T_t' compared with the static temperature fluctuation. This assumption is valid, since we study subsonic flows at $M=0.4$ and $M=0.15$ in the present work. Following Bradshaw [1], we introduce the static temperature fluctuation

$$\frac{T'(y,z,t)}{T(y,z,t)} = -(\gamma-1)\,M_l^2\,\frac{u_1'(y,z,t)}{u_1(y,z,t)} \quad ,$$

where M_l is the local Mach number. Using the equation of Walz [14] and formulating the rescaling process similar to the velocity we obtain the following equations for the rescaled temperature and its fluctuations

$$T_{in}^{inner}=\beta_s^2 T_{re}(y_{in}^+)+C_1T_\infty \quad \text{and} \quad T_{in}^{outer}=\beta_s^2 T_{re}(\eta_{in})-C_2\frac{U_{re}(\eta_{in})}{U_\infty}T_\infty+C_3T_\infty$$

$$T'^{inner}_{in}=\beta_s^2 T'_{re}(y_{in}^+,z,t) \quad \text{and} \quad T'^{outer}_{in}=\beta_s^2 T'_{re}(\eta_{in},z,t)-C_2\frac{(u_1')_{re}(\eta_{in},z,t)}{U_\infty}T_\infty$$

with $C_1=(1+A)(1-\beta_s^2)$, $C_2=2A\beta_s(1-\beta_s)$, and $C_3=(1-\beta_s)(1+\beta_s+2A\beta_s)$. If the rescaling factor $\beta_s=u_{\tau,in}/u_{\tau,re}$ is assumed to be 1 for the temperature distribution, we arrive at the formulation that was used by Urbin et al. [13] to compute supersonic boundary layers.

The composite distribution that is approximately valid over the entire boundary layer is obtained by forming a weighted average of the inner and outer profile for the velocity and the temperature as was proposed by Lund et al. [8].

The rescaling operation requires the skin friction velocity u_τ and the boundary layer thickness δ, both at the rescaling station and at the inlet. They can be directly determined from the mean velocity profile at the rescaling station, but must be specified at the inlet. It is sufficient to fix δ at the inlet, whereas u_τ for compressible flow at the inlet is evaluated via

$$u_{\tau,in} = u_{\tau,re} \sqrt{\left(\frac{\rho_{(wall)_{re}}}{\rho_{(wall)_{in}}}\right)} \left(\frac{\delta_{1re}}{\delta_{1in}}\right)^{\frac{1}{[2(n-1)]}}$$

where δ_1 is the displacement thickness, $\rho_{(wall)}$ is the local density at the wall, the ratio of which contains the temperature distribution along the surface, and the exponent n is set to n=5. The above relation can be derived from the standard power-law approximations, $c_f \sim Re_x^{1/n}$, $\delta_1/x \sim Re_x^{1/n}$, where c_f is the skin-friction coefficient. Unlike in Lund et al. [8] where the momentum thickness is used we incorporate the displacement thickness in the rescaling formulation. Since the momentum thickness is a non-linear function of the velocity profile, different results are obtained when either the spanwise averaged velocity profile is used to compute the momentum thickness or the momentum thickness is computed locally and then averaged in the spanwise direction.

2.4. RESULTS

To validate the compressible rescaling method we first simulate a boundary layer flow of an adiabatic flat plate for M=0.4 and Re_{δ_o}=14400 (Re_{θ_o}=1400), where δ_o is the boundary layer and θ_o the momentum thickness at the inlet, respectively. The dimensions of the computational domain are $30\delta_0 \times 3.5\delta_0 \times 0.64\delta_0$ in the streamwise, wall normal, and spanwise direction. Furthermore, we evidence the influence of the sponge layer and study the impact of grid resolution by using two different grids, one with approx. 700,000 cells and a finer mesh with approx. 1,350,000 cells.

The mean streamwise velocity profiles are plotted in inner-law scaling in Fig. 1 for both grid resolutions and different rescaling laws. The fine grid profiles based on the new temperature rescaling closely follow the analytic form that consists of the viscous sublayer $y^+ \leq 5$, $u/u_\tau = y^+$, the buffer layer $5.0 < y^+ \leq 30.0$, $u/u_\tau = 5.0 \ln y^+ - 3.05$, and the logarithmic layer $y^+ > 30.0$, $u/u_\tau = 2.5 \ln y^+ + 5.5$. In Fig. 2 the skin friction coefficient is compared with the formula of Falkner $c_f = 0.012/Re_\theta^{\frac{1}{6}}$ [4]. Here, also results of a coarse grid solution using no sponge layer are shown to demonstrate the influence of the formulation of the exit boundary condition. The added source term in the sponge layer damps reflected pressure waves, but also all turbulent fluctuations, so that c_f is progressively reduced in the sponge layer region. c_f is slightly underpredicted on the coarse grid, since the coherent structures

that redistribute the turbulence intensities from the streamwise direction to the wall normal and spanwise directions are not captured accurately with the larger spatial steps. Consequently, this leads to a smaller exchange of momentum, and thus, to a lower wall shear stress on the coarse grid. The turbulence intensities are compared in Fig. 5 with the data of Lund et al. [8] at $Re_\theta = 1850$ for the fine grid. The good agreement of the present results of a compressible boundary layer and the LES of Lund et al. [8] is clearly visible.

Fig. 3 shows the mean temperature distribution in inner-law scaling y^+. The profiles do not coincide perfectly near the inflow section, whereas further downstream the distributions do lie on top of each other up to the beginning of the outer layer at approx. y^+=180. The discrepancy immediately downstream of the inlet probably occurs due to the linear interpolation for corresponding locations at the inlet and rescaling locations and the different grid resolution, which, measured in wall units, is coarser at the inlet than further downstream. Fig. 4 illustrates the mean temperature-velocity relationship. The simulation data fits well with the Walz's quadratic profile for an adiabatic wall [14].

Using the compressible boundary layer solution, a realistic inlet boundary condition is obtained for the turbulent trailing-edge flow. The grid lines at the inflow boundary coincide with those of the boundary layer simulation, such that no interpolation of the instantaneous solution is required. The entire computational mesh to simulate trailing-edge flow is plotted in Fig. 7. It contains 2,250,000 grid points distributed in 19 blocks, 3 blocks of which are used for the flat plate simulation. To evidence the vortical structures in the vicinity of the trailing edge, the wake of the M=0.15 flow is visualized using the λ_2-criterion [7] in Fig. 8. The initially elongated vortex structures above the plate become shorter close to the trailing edge due to the deceleration of the flow.

In Figs. 9 and 10 mean velocity and turbulence intensity profiles in the trailing-edge and near-wake regions are compared with the experimental data from [10]. The agreement of the turbulence intensity between the present LES and the experimental data is fairly good except in the near-wall region where the experimental intensity profiles lack the near-wall peaks that do exist in turbulent boundary layers. This suggests a spatial underresolution or an insufficient high-frequency response of the measuring instrument near the wall.

The time history of the flow induced force on the plate in the vertical direction is plotted in Fig. 11. These fluctuations occur with a regular frequency related to a Strouhal number of about 0.2 based on the plate thickness. Thus, they are obviously associated with a Kelvin-Helmholtz type unsteady motion in the wake of the trailing edge, which can clearly be seen in the spanwise averaged temperature distribution in Fig. 12. Since

the unsteady vorticity in the wake has a vortex axis parallel to the trailing edge, it produces more efficient sound than the turbulent eddies from the boundary layer, which are more aligned with the streamwise direction.

3. Simulation of Aerodynamic Noise

We now turn to the numerical prediction of the acoustic field. The following discussion is a brief summary of the detailed analysis by Ewert et al. presented in [3]. The acoustic perturbation equations (APE) for the simulation of wave propagation are derived by a flow decomposition into acoustic and non-acoustic quantities, based on a filtering of the non-linear and viscous terms of the Navier-Stokes equations in Fourier/Laplace transformed space. The pressure is decomposed into a pseudo-sound pressure $\rho_\infty \phi_v$ and an acoustic perturbation p'. The perturbation density ρ' in general also contains non-acoustic fluctuations. Furthermore, the APE describe the propagation of irrotational velocities u' in an unsteady solenoidal background flow field U.

To compute the acoustic field of a circular cylinder at laminar freestream conditions the following simplifications are introduced. Neglecting the scattering of acoustic waves due to the unsteady mean-flow field, it seems to be acceptable to use a time averaged base flow field $\bar{U}_i$ instead of U_i. Furthermore, for small acoustic quantities the non-linear terms can be dropped. The equations used for the computations read, see [3] for details

$$\frac{\partial \rho'}{\partial t} + \frac{\partial}{\partial x_i}\left(\rho' \bar{U}_i + \rho_\infty u_i\right) = 0 \quad , \quad \frac{\partial u_i}{\partial t} + \frac{\partial}{\partial x_i}\left(\bar{U}_j u_j\right) + \frac{1}{\rho_\infty}\frac{\partial p'}{\partial x_i} = 0 \quad ,$$

$$\frac{\bar{D}p'}{Dt} - c_\infty^2 \frac{\bar{D}\rho'}{Dt} = -\rho_\infty \frac{\bar{D}\Phi v}{Dt} = -\rho_\infty \left(\frac{\partial \phi_v}{\partial t} + \bar{U}_i \frac{\partial \phi_v}{\partial x_i}\right) .$$

The term $\bar{D}\phi_v/Dt$ is computed by solving a Poisson equation with a right hand side determined from an appropriate LES or DNS solution of the compressible flow problem in the region where the noise is generated. The generation of vorticity is prevented completely. $\bar{U}_i$ is determined in the complete acoustic domain e.g. by an Euler or RANS computation. The acoustic field is computed by solving the perturbation equations for the unknowns ρ', u_i, p'.

3.1. NUMERICAL METHOD

For the spatial discretization of the acoustic perturbation equations the fourth-order dispersion relation preserving (DRP) scheme following Tam [12] is applied in generalized curvilinear coordinates. The DRP scheme is also applied to compute the metric terms so that a consistent discrete system is achieved. The temporal integration is performed using the fourth-order alternating two-step low dissipation and low dispersion Runge-Kutta scheme

(LDDRK 5-6). To suppress spurious high frequency waves artificial selective damping has been used. At far field boundaries a sponge layer formulation is used and at the solid walls a ghost point concept is imposed [3].

3.2. RESULTS

The flow around a circular cylinder at a freestream Mach number M=0.3 and a freestream Reynolds number based on the diameter Re_∞=200 is considered. The aeroacoustic sources are determined from a highly resolved compressible flow simulation. The solution of the acoustic perturbation equations with the source term determined by the unsteady flow, is performed on an O-grid with 257 × 161 grid points. The source terms are determined for 43 time levels within one vortex shedding cycle. During the acoustic simulation the time dependent source term for the intermediate time steps is computed using linear interpolation.

The acoustic pressure field $p - \rho_\infty \phi_v$ is shown in Fig. 13. According to the formulation of the acoustic perturbation equations no vorticity is generated by the acoustic simulation, so that no vortex street occurs. The directivity shown in Fig. 14 agrees well with that determined by Guo [5]. Since ϕ_v decays very fast to zero in a certain distance from the noise generating region the computation of the source term, e.g. from the large-eddy simulation, can be restricted to the small part of the total computational domain in which the noise generation occurs.

4. Conclusions

A consistent extension of the rescaling method for incompressible turbulent boundary layers to compressible fluids has been developed. Although only subsonic flows were considered at present, the results indicate that the proposed rescaling of the temperature profile seems to be superior to simpler formulations. An LES of the flow past a sharp trailing edge showed good agreement with experimental data. Furthermore, the acoustic field of the flow over a cylinder was computed using acoustic perturbation equations driven by a source term from the unsteady flow. The study proved the two-step approach to be capable to predict aeroacoustic sound based on a LES of a compressible flow field and will be used to predict trailing-edge noise in the next step.

References

1. P. Bradshaw. Compressible turbulent shear layers. *Ann. Rev. Fluid Mech*, 9:33–54, 1977.
2. R. Ewert, W. El-Askary, M. Meinke, and W. Schröder. Computation of turbulence related noise on the basis of large-eddy simulation. In H. Krner and J. W. Delfs, editors, *Second Aeroacoustics Workshop*. DLR Braunschweig, Oct. 2000.

3. R. Ewert, M. Meinke, and W. Schröder. Comparison of source term formulations for a hybrid CFD/CAA method. Paper 2001-2200, AIAA, 2001.
4. V. M. Falkner. The resistance of a smooth flat plate with turbulent boundary layer. *Aircraft Eng.*, 15:65–68, 1943.
5. Y. P. Guo. Application of the Ffowcs Williams/Hawkings equation to tw o dimensional problems. *J. Fluid Mech.*, 403:201–221, 2000.
6. M. S. Howe. Trailing edge noise at low mach numbers. *J. Sound and Vibration*, 225(2):211–238, 2000.
7. J. Jeong and F. Hussain. On the identification of a vortex. *J. Fluid Mech.*, 285:69–94, 1995.
8. T. S. Lund, X. Wu, and D. Squires. Generation of turbulent inflow data for spatially-developing boundary layer simulations. *J. of Computational Physics*, 140:233–258, 1998.
9. M. Meinke, W. Schröder, E. Krause, and T. Rister. A comparison of second- and sixth-order methods for large-eddy simulations. *Computers and Fluids*, pages –, submitted for publication, 2001.
10. J. Ostertag, S. Guidati, G. Guidati, S. Wagner, A. Wilde, and N. Kalitzin. Prediction and measurement of airframe noise on a generic body. Paper 2000-2063, AIAA, 2000.
11. T. J. Poinsot and S. K. Lele. Boundary conditions for direct simulations of compressible viscous flows. *J. Comput. Phys.*, 101:104–129, 1992.
12. C. Tam and J. Webb. Dispersion-relation-preserving finite difference schemes for computational acoustics. *J. Comput. Phys.*, 107:262–281, 1993.
13. G. Urbin and D. Knight. Compressible large eddy simulation using unstructured grid: supersonic boundary layer. In *Second AFOSR International Conference on DNS/LES, Rutgers University*, pages 1–16, June 7-9 1999.
14. A. Walz. *Boundary layers of flow and temperature.* MIT Press, 1969.

5. Figures

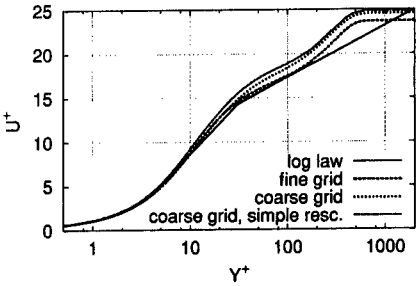


Figure 1. LES of a turbulent boundary layer for Re_{θ_o}=1400 and M=0.4 with a sponge layer. Velocity profiles in comparison with the log law.

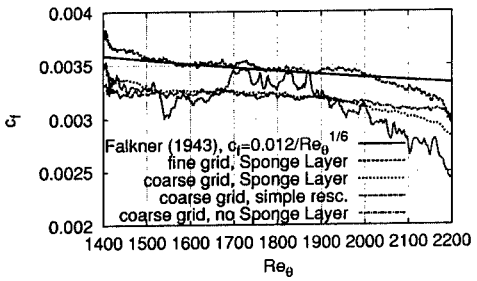


Figure 2. LES of a turbulent boundary layer for Re_{θ_o}=1400 and M=0.4. Skin-friction coefficient in comparison with Falkner's formula.

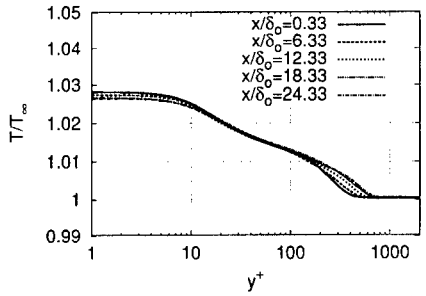


Figure 3. LES of a turbulent boundary layer for Re_{θ_o}=1400 and M=0.4. Temperature profiles at different streamwise locations.

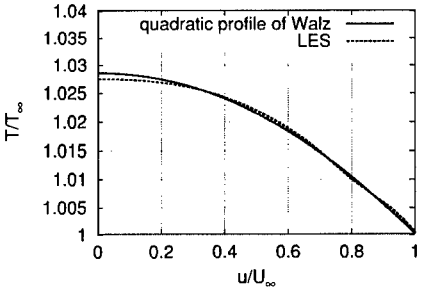


Figure 4. LES of a turbulent boundary layer for Re_{θ_o}=1400 and M=0.4 at Re_θ=1850. Temperature-velocity relationship compared with the profile of Walz [14].

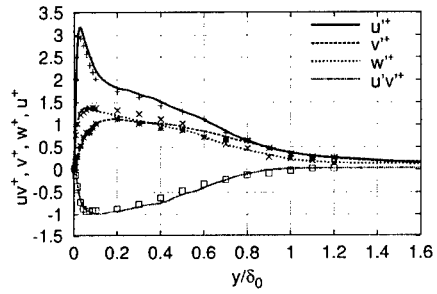


Figure 5. LES of a turbulent boundary layer for Re_{θ_o}=1400 and M=0.4 at Re_θ = 1850. Reynolds stress tensor components for the fine grid in comparison with the data of Lund et al.[8] (Symbols).

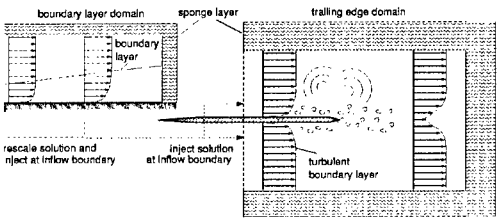


Figure 6. Sketch of the domain of integration for the boundary layer and trailing edge simulation.

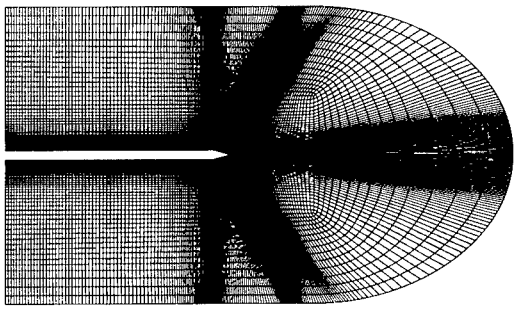


Figure 7. Grid for the LES of a turbulent flow over a sharp trailing edge. 2.25 Million grid points in 19 blocks. Every second grid point is shown.

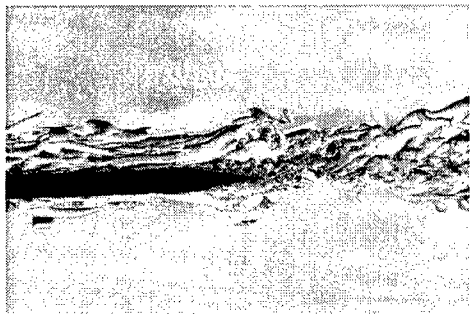


Figure 8. Visualization of the vortex structures in the boundary layer and in the near wake of the turbulent M = 0.15 flow around a sharp trailing edge.

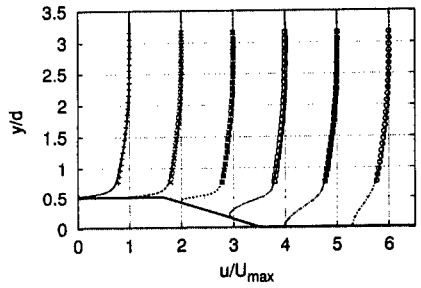


Figure 9. LES of a trailing-edge flow for $Re_\infty = 5.33 \times 10^5$ and M=0.15. Mean velocity profiles in the trailing-edge and the near-wake region compared with experimental data (Symbols).

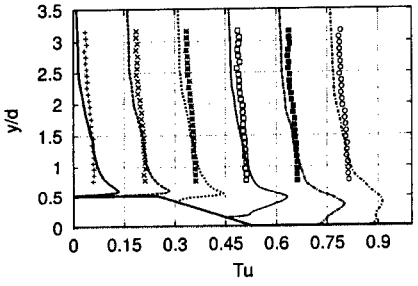


Figure 10. LES of a trailing-edge flow for $Re_\infty = 5.33 \times 10^5$ and M= 0.15. Turbulence kinetic energy profiles in the trailing-edge and the near-wake region compared with experimental data (Symbols).

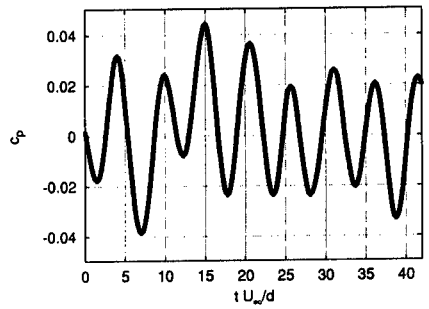


Figure 11. Time history of the surface pressure coefficient

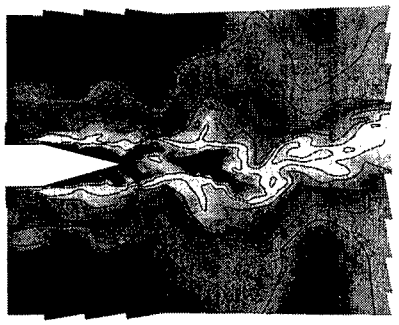


Figure 12. Instantaneous temperature distribution averaged in the spanwise direction.

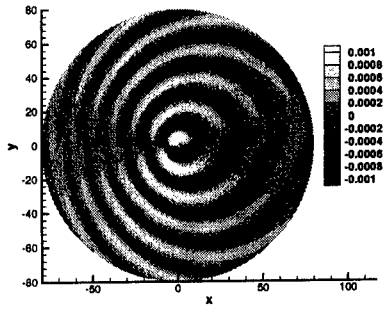


Figure 13. Instantaneous pressure distribution from the CAA solution, source term $-\rho_\infty \bar{D}\phi_v/Dt$.

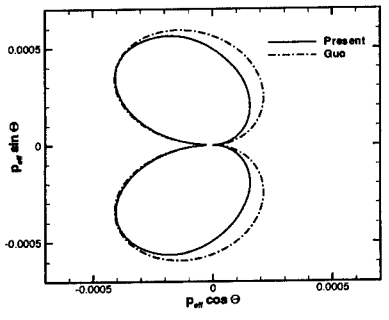


Figure 14. Directivity for the first harmonic frequency in comparison with Guo [5].

LARGE EDDY SIMULATION OF A RIB-ROUGHENED TURBULENT CHANNEL FLOW WITH HEAT TRANSFER AND PROPERTY VARIATIONS

NING MENG AND RICHARD H. PLETCHER

Department of Mechanical Engineering
Iowa State University, Ames, Iowa 50011

Abstract. Turbulent channel flow with a rib-roughened wall has been computed with constant heating rate using large eddy simulation. An implicit, second order accurate finite volume scheme was used to solve the time dependent filtered set of equations to determine large eddies, while a dynamic subgrid-scale model was used to account for the subgrid scale effects. A dynamic Prandtl number was introduced to calculate subgrid scale heat transfer. The effects of strong heating on the rib-roughened wall were investigated and Nusselt numbers were computed and compared with experimental data. The instantaneous plots revealed the influence of turbulent heat transfer on velocity, temperature and vorticity in this particular geometry.

1. Introduction

Engineers are using three different approaches to cope with turbulence. In industry, Reynold average Navier-Stokes (RANS) methods employing two equation models are widely used in a variety of forms. Direct numerical simulation is mainly used in academic research. Large Eddy Simulation (LES) which originated in academia tends to be a more and more useful analysis tool for industry in recent years. Several commercial codes (such as FLUENT and StarCD) have implemented some types of LES models. LES resolves all the energy-carrying large eddies, but models small eddies with length scales smaller than the grid size. This equips LES with the ability to analyze complex three dimensional time dependent flows at a moderate computational cost where RANS simulations usually fail.

The rib-roughened channel flow is a good test case for LES simulation due to its complex flow features, such as flow separations, recirculation zones, and re-attachment. Cooling in gas turbine blades is a potential application for this kind of flow. Early work was done by Ciofalo and Collins [1] for a rib-roughened channel using the Smagorisky model and a commercial CFD code employing an incompressible flow formulation. Yang and Ferziger [2] used a dynamic subgrid-scale model to simulate a turbulent flow over an obstacle the geometry of which is different from Ciofalo's case. Dailey [3] developed a compressible formulation for large eddy simulation and applied it to the simulation of a compressible channel flow with heat transfer. Further, Meng and Pletcher [4] calculated an isothermal flow case similar to that of Ciofalo and Collins but using dynamic SGS model and a finer grid. This paper is a continuation of that research and considers effects of heat transfer and property variations.

2. Problem Description

The problem of interest is the turbulent flow and heat transfer in a two-dimensional plane channel with a periodic array of transverse square ribs on one wall. The simulation was set up such that comparisons could be made to the experimental data of Drain et al. [5] and Bates et al. [6], who made detailed mean and fluctuating velocity measurements. The blockage ratio, which is the ratio of the rib height, h, to channel height, H, was $h/H = 0.2$. The pitch-to-height ratio of the ribs was 7.2, where the pitch, P, is the streamwise spacing of the ribs. This value of pitch-to-height ratio was consistently found empirically to yield the greatest enhancement of heat transfer rates [1]. The nominal Reynolds number based on hydraulic diameter ($D_h = 4\delta$) and bulk velocity was $Re_D = 20,000$.

For simulations with heat transfer, a constant heat flux, $q_w = \frac{q_w^*}{C_p \rho_{ref} U_{ref} T_{ref}}$, was applied to both the lower wall and the upper wall. On the front, top, and back surfaces of the rib, a constant heat flux, $q_{w,rib}$, was applied with a magnitude that was one-third of the heat flux on the lower wall, q_w. Consequently, the total heat added to the ribbed channel was the same as for a smooth channel with no ribs and wall heat flux, q_w. For the simulations presented here, $q_w = 0.002$, and $q_{w,rib} = 0.000667$.

The computational domain only contained one rib. This section was assumed to be embedded in a periodic array of many ribs in a fully developed flow, which permitted the use of periodic or step periodic boundary conditions in the streamwise direction.

2.1. NUMERICAL PROCEDURE

A system of Favre-filtered Navier-Stokes equations was solved using a dynamic sub-grid scale model. The details can be found in Dailey's Ph.D. thesis [3]. The simulations were primarily run with the dual time-stepping LU-SGS scheme with the solution domain divided into 8 blocks for the coarse grid, and 16 blocks for the fine grid. The fine grid simulations were run with 17 processors (one for master node, sixteen for slave nodes) on the IBM-SP2 and required about 10 - 12 hours of wall clock time per 10,000 time steps, depending on the number of subiterations required for each step in physical time.

For the solid walls, including the upper and lower walls and rib surfaces, the no-slip velocity and zero normal pressure gradient boundary conditions were enforced. The wall temperature was determined from the specified heat flux. All solution variables were assumed to be periodic in the z direction, the only homogeneous direction for this flow. In the streamwise direction, the x-momentum, v and w velocities, and periodic component of the pressure, p_p, were assumed to be periodic. The mean pressure gradient parameter was adjusted at each time step to maintain the desired mass flow rate. The temperature was assumed to be stepwise periodic, with ΔT_x given by

$$\Delta T_x = \frac{q_w L_x}{2(\dot{m}/L_y Lz)} \tag{1}$$

where $L_y = 2$ and $L_z = \pi$.

After the turbulent flow was deemed be statistically stationary, the simulation was run another 10,000 time steps to compute the ensemble averaged turbulence statistics.

2.2. GRID AND RUN PARAMETERS

The dimensions of the computational domain were $7.2h \times 5h \times 7.85h$, or $2.88\delta \times 2\delta \times \pi\delta$, in the x, y, z directions, respectively. The coarse grid used $40 \times 32 \times 24$ control volumes, with 8 cells on each surface of the rib. The fine grid consisted of $80 \times 64 \times 48$ control volumes, with 16 cells on each surface of the rib. The fine grid is shown in Fig.1. The nondimensional time step was 0.01.

3. Results

3.1. MEAN AND FLUCTUATING VELOCITY PROFILES

The mean streamwise velocity profiles, normalized by the average bulk velocity on the top of the rib, are depicted in Figs. 2 and 3 at planes A and

B, respectively. Plane A was located mid-way between the ribs, and plane B was located on the middle of the rib top surface. Both experimental data and current simulation results are shown to facilitate the comparison. From these two figures, it can be seen that both coarse-grid results and fine-grid results agree reasonably well with the experimental data in predicting averaged velocity, although fine-grid results are slightly better.

The root-mean-square (rms) of the streamwise velocity fluctuations are shown in Figs. 4 and 5. In the prediction of velocity fluctuations in section A, the fine-grid result shows much better agreement with experimental data, even though both results underestimate the velocity fluctuations to some extent. For section B, the fine-grid result captures precisely the peak value near the top of the rib, and continues to be closer to the experimental data than the coarse-grid result. It seems that the fine grid is necessary to calculate the turbulent statistics, e.g. velocity fluctuations, accurately.

3.2. HEAT TRANSFER PARAMETERS

The local Nusselt number distribution is shown in Fig. 6, compared to the experimental data of Lockett and Collins [7] at two different Reynolds numbers. The distance along the lower wall of the channel, including the rib surfaces, is represented by x, and the location of the lower-front corner of the rib is xle. The normalized Nusselt number distribution, as shown in Fig. 7, used the average Nusselt number as the normalization factor, which is defined as below

$$Nu_{D,avg} = \frac{1}{S}\int_0^S Nu_D(s)ds \tag{2}$$

where S is the distance along the lower wall, including the rib surfaces. The LES prediction of Nusselt number agrees quite well with experimental data. It reproduced the overall streamwise profile of Nu_D, with a local maximum immediately upstream of the rib, a global maximum immediately adjacent to the left-upper corner of the rib, and a local minimum immediately downstream of the rib. The fine grid results performed slightly better than coarse grid ones, in particular, in the prediction of the peak values. In Fig. 7, use of the normalized Nusselt number permits comparison of results obtained from different Reynolds numbers. The examination of the profiles reveals that the LES simulation is in very good agreement with experimental data, except that the maximum value of Nu_D is slightly underestimated. Note that there is an increase of Nusselt number near the trailing edge of the rib for the experimental results ($Re_D = 29,870$), probably due to a recirculation zone that develops on top of the rib at high Reynolds numbers.

3.3. ENSEMBLE AVERAGED AND INSTANTANEOUS CONTOURS

Some ensemble averaged and instantaneous contours for a rib-roughened channel flow with heat transfer are presented in this section.

Figure 8 shows mean velocity vectors with a ensemble averaged contour of u velocity as the background. This plot was created based on the simulation results without heat transfer for the purpose of comparison. A large recirculation zone behind the rib and a smaller recirculation zone in front of the rib are evident. A large fraction of the region between the ribs is in the recirculation zone for the current pitch-to-height ratio. Drain and Martin [5] reported a reattachment length of 4.3h. The present simulation gives a reattachment length of $4.2 - 4.3h$.

A 3D geometric representation of this flow (instantaneous u velocity) is shown in Fig. 9. A cutting plane is located midway in the spanwise direction. The instantaneous velocity contours are very irregular because of the nature of turbulence.

The following figures show the contours of a variety of variables on two cutting planes, which are located at 8% and 92% channel height, respectively, and parallel to the top or bottom walls. Figure 10 reports the instantaneous u velocity. On the top cutting plane, there are streak patterns, which are characteristics for the small-scale turbulent structure near the wall. On the bottom cutting plane, no obvious streak pattern can be found even though there are still some variations of u velocity. The existence of recirculation area before and after the rib is thought to be the reason for this streak deterioration.

The instantaneous temperature is presented in Fig. 11. The top cutting plane is uniformly and moderately heated. The bottom cutting plane, however, has a large cool region upstream of the rib and a small hot region downstream of the rib followed by another cool region.

The magnitude of vorticity is reported in Fig. 12. There exist some streak structures of vorticity on the top cutting plane, but the vorticity is weak and smooth on the bottom cutting plane except a narrow area immediately before the front surface of the rib. The recirculation of flow is not conducive to the formation of streak structure of vorticity.

4. Conclusions

The simulation of turbulent flow and heat transfer of air in a planar channel with transverse square ribs on one wall was attempted. Very good agreement between fine grid results and experimental data were obtained in predicting velocity and velocity fluctuations. Coarse grid results agree well with experimental data in velocity profiles but not as well as the fine grid results in velocity fluctuation profiles. The Nusselt number profiles obtained

from the current simulation agree reasonably well with experimental data which tends to validate the current SGS model for turbulent heat transfer. The instantaneous contours of some important variables, e.g. u velocity, temperature, and vorticity, were presented and analyzed. It is found that the recirculation of flow has a negative impact on the formation of streak structure near the wall.

5. Acknowledgments

This research was supported in part by the Air Force Office of Scientific Research under grants F49620-94-1-0168 and F49620-00-1-0229 and by the National Science Foundation under grants CTS-9414052 and CTS-9806989. The use of computer resources provided by the Minnesota Supercomputing Institute are gratefully acknowledged.

References

1. Ciofalo, M. and Collins, M., 1992, "Large eddy simulation of turbulent flow and heat transfer in plane and rib-roughened channels",*International Journal for Numerical Methods in Fluids*, Vol. 15, pp. 453-489.
2. Yang, K. and Ferziger, J., 1993, "Large eddy simulation of turbulent obstacle flow using a dynamic subgrid-scale model", *AIAA Journal*, Vol. 31, pp. 1406-1413.
3. Dailey, L., 1997, "Large eddy simulation of turbulent flows with variable property heat transfer using a compressible finite volume formulation", Ph.D Thesis, Iowa State University.
4. Meng, N., Pletcher, R., and Simons, T., 1999, "Large eddy simulation of a turbulent channel flow with a rib-roughened wall", AIAA 99-0423, 37th AIAA Aerospace Sciences Meeting and Exhibit, January 11-14, 1999/Reno, NV.
5. Drain, L. and Martin, S., 1985, "Two component velocity measurement of turbulent flow in a ribbed-wall flow channel", *Proceedings of the International Conference on Laser Velocimetry - Advances and Applications*, Manchester, U.K.
6. Bates, C., Yeoman, M., and Wilkes, N., 1983, "Non-intrusive measurements and numerical comparison of the axial velocity components in two-dimensional flow channel for backward-facing step and a rib-roughened surface", Harwell Report AERE-R 10787.
7. Lockett, J. and Collins, M., 1990, "Holographic interferometry applied to rib-roughness heat transfer in turbulent flow", *International Journal of Heat and Mass Transfer*, Vol. 33, pp. 2439-2449.

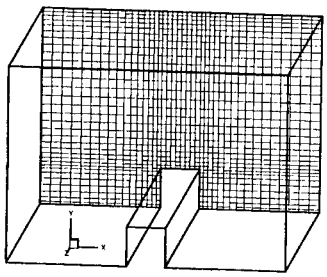


Figure 1. Computational grid for rib-roughened channel flow

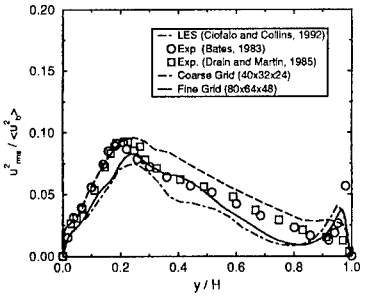


Figure 4. *rms* streamwise velocity fluctuations normalized by bulk velocity for Section A

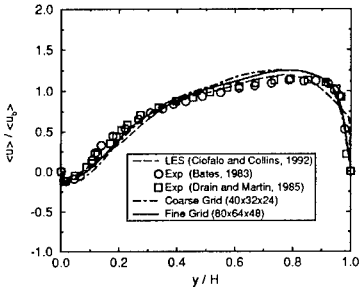


Figure 2. Mean streamwise velocity normalized by bulk velocity for Section A

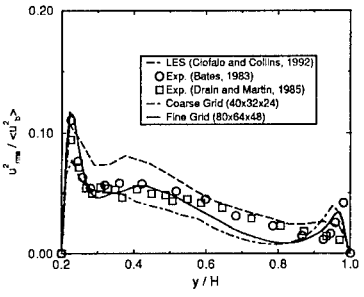


Figure 5. *rms* streamwise velocity fluctuations normalized by bulk velocity for Section B

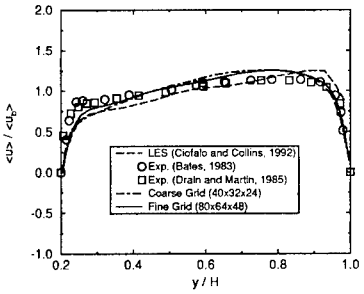


Figure 3. Mean streamwise velocity normalized by bulk velocity for Section B

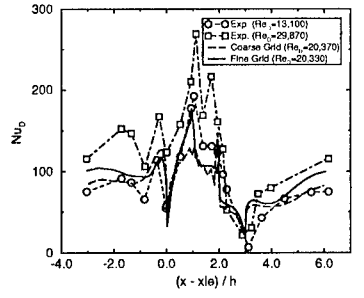


Figure 6. Local Nusselt number compared to experimental data of Lockett and Collins (1990)

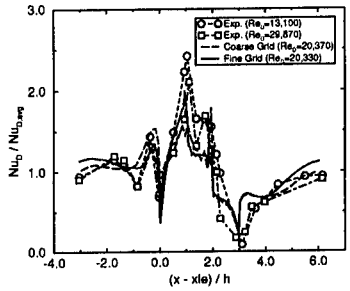


Figure 7. Normalized Nusselt number compared to experimental data of Lockett and Collins (1990)

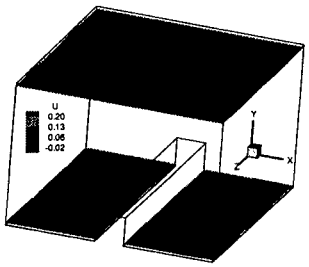


Figure 10. Instantaneous u velocity

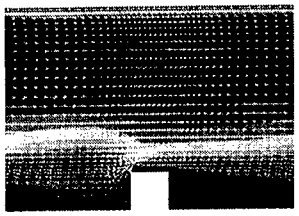


Figure 8. Mean velocity vectors

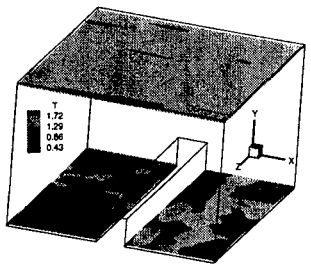


Figure 11. Instantaneous temperature

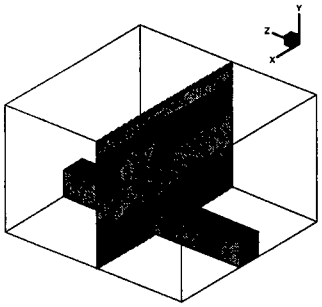


Figure 9. 3D configuration

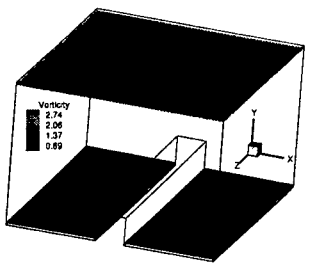


Figure 12. Instantaneous vorticity

LARGE EDDY SIMULATION OF THE TURBULENT FLOW PAST A BACKWARD FACING STEP

Isothermal flow and flows with heat transfer and property variations

RAVIKANTH AVANCHA AND RICHARD PLETCHER
Department of Mechanical Engineering
Iowa State University, Ames IA 50011

Abstract

The heat transfer and fluid mechanics of a turbulent separating and reattaching flow past a single-sided backward-facing step are studied using large eddy simulation. A fully coupled, low Mach number preconditioned, collocated-grid, central differenced, compressible, finite volume formulation was developed to conduct the simulations. A sixth-order compact filter was used to prevent pressure-velocity decoupling. A compressible version of the dynamic subgrid scale model was used to model the effects of the smaller eddies. Navier-Stokes characteristic boundary conditions designed by Poinsot and Lele were used to provide boundary conditions. The isothermal turbulent flow past the step, at a Reynolds number of 5,540 (based on the step height and upstream centerline velocity) and a Mach number of 0.006, was simulated to validate the formulation. Subsequently, the bottom wall downstream of the step was supplied with constant wall heat flux levels of 1.0, 2.0, and 3.0 kW/m^2. The viscous sub-layer played a critical role in controlling the heat transfer rate. Streamwise and wall-normal turbulent heat fluxes were of the same order of magnitude. The Reynolds analogy did not hold in the recirculation region. However, the Stanton number profiles showed a striking similarity with the fluctuating skin-friction profiles.

1. Introduction

Turbulent flows with separation and reattachment, in the presence of heat transfer, occur routinely in aircraft propulsion equipment, such as turbines and combustors, and cause large variations of local heat transfer coefficient as well as augmentation of overall heat transfer. The backward facing step geometry is well suited for investigation into the characteristics of flow separation, reattachment and recovery in the presence of an adverse pressure gradient. Most of the numerical calculations to date for this flow regime with

heat transfer have used two equation turbulence models like the $k-\epsilon$ and $k-\omega$ models with the Reynolds averaged Navier-Stokes (RANS) equations. Existing RANS approaches have not been successful in predicting all the flow features and heat transport mechanisms for this geometry. A summary of benchmark calculations [1] noted that only the results for streamwise velocity and dissipation agreed amongst all contributors, but substantial differences were noted for the wall-normal velocity, skin friction, Nusselt number, and wall temperatures. For the Nusselt number profiles, none of the methods produced a shape similar to the experimental results of [2]. There did not appear to be any consistency in the computed points of maximum Nusselt number and the reattachment point [1]. Many simulations in this study did not include the effects of property variations although large heat flux levels were used. Since RANS methods rely to a great extent on the modeling aspects, large variations in the quality of simulations are observed depending on the model assumptions. Little *ad-hoc* modeling is employed in large eddy simulation (LES), where the three-dimensional unsteady motion of the larger eddies is computed and subgrid-scale modeling is employed to account for the effects of the smaller eddies. Thus, the large eddy simulations presented in this work offer a way to better understand the effects of the heat transfer and property variations in separated flow regions at low speeds.

2. Governing Equations and Subgrid Scale Modeling

The Favre-filtered compressible Navier-Stokes (NS) equations, and the equation of state, in their non-dimensional form are given as:

$$\frac{\partial \overline{\rho}}{\partial t} + \frac{\partial \overline{\rho}\tilde{u}_j}{\partial x_j} = 0 \tag{1}$$

$$\frac{\partial \overline{\rho}\tilde{u}_i}{\partial t} + \frac{\partial \overline{\rho}\tilde{u}_i\tilde{u}_j}{\partial x_j} = -\frac{\partial \overline{p}}{\partial x_i} + \frac{\partial \overline{\sigma}_{ij}}{\partial x_j} - \frac{\partial \tau_{ij}}{\partial x_j} \tag{2}$$

$$\frac{\partial}{\partial t}(\overline{\rho}\tilde{T}) + \frac{\partial}{\partial x_j}(\overline{\rho}\tilde{u}_j\tilde{T}) = -\frac{\partial \overline{q_j}}{\partial x_j} - \frac{\partial Q_j}{\partial x_j} \tag{3}$$

$$\overline{p} = \overline{\rho}R\tilde{T} \tag{4}$$

where the viscous stress tensor and heat conduction vector are given as,

$$\overline{\sigma}_{ij} = \overline{\frac{\mu}{Re}\left(\frac{\partial u_i}{\partial x_j} + \frac{\partial u_j}{\partial x_i} - \frac{2}{3}\frac{\partial u_k}{\partial x_k}\delta_{ij}\right)} \quad ; \quad \overline{q}_j = -\overline{\frac{k}{Pr\,Re}\left(\frac{\partial T}{\partial x_j}\right)} \tag{5}$$

and the subgrid scale stress tensor and heat conduction vector are given as,

$$\tau_{ij} = \overline{\rho}(\widetilde{u_iu_j} - \tilde{u}_i\tilde{u}_j) \quad ; \quad Q_j = \overline{\rho}(\widetilde{u_jT} - \tilde{u}_j\tilde{T}) \tag{6}$$

The turbulent stress τ_{ij} and the turbulent heat flux Q_j have to be modeled in order to close the system of equations. The compressible extension [3] to the dynamic subgrid scale model [4] employing the Smagorinsky model as the base model has been used in this study. The compressible flow version of the Smagorinsky model is given as

$$\tau_{ij} = \frac{1}{3}\tau_{kk}\delta_{ij} - 2\mu_T(\tilde{S}_{ij} - \frac{1}{3}\tilde{S}_{kk}\delta_{ij}) \; ; \quad \left\{\tilde{S}_{ij} = \frac{1}{2}\left(\frac{\partial \tilde{u}_i}{\partial x_j} + \frac{\partial \tilde{u}_j}{\partial x_i}\right)\right\} \tag{7}$$

where μ_T is the eddy-viscosity, and $\tilde{S}_{ij}$ is the Favre-filtered strain rate tensor. $\tau_{kk} = 2C_I\bar{\rho}\Delta^2|\tilde{S}|^2$ is used to model the sub-grid scale turbulent kinetic energy, τ_{kk}, as proposed by [5]. For closure, μ_T is parameterized by equating the sub-grid scale energy production and dissipation, and the subgrid scale heat flux vector Q_j is modeled using a gradient-diffusion hypothesis, to obtain

$$\mu_T = C_s\bar{\rho}\Delta^2\sqrt{2\tilde{S}_{ij}\tilde{S}_{ij}} \quad ; \quad Q_j = -\frac{\bar{\rho}C_s\Delta^2|\tilde{S}|}{Pr_T}\frac{\partial \tilde{T}}{\partial x_j} \tag{8}$$

where C_s is a model parameter and Pr_T is the turbulent Prandtl number defined as the ratio of eddy-viscosity ν_T to eddy-diffusivity α_T. Both C_s and Pr_T are computed "dynamically". Δ is the filter width which is typically assumed to be a function of the grid resolution, and calculated as $\Delta_{av} = (\Delta x \Delta y \Delta z)^{1/3}$.

3. Numerical Procedure

A coupled finite volume procedure, in primitive variables $[p, u, v, w, T]$ was used to solve the filtered NS equations. The method was fully implicit, second order accurate in time, with advective terms disretized using second order central differences and viscous terms with fourth order central differences. Time derivative preconditioning [6] was incorporated to alleviate the stiffness and convergence problems associated with the computation of low Mach number flows using traditional compressible formulations. An all-speed strategy has thus evolved that enables the application of the same methodology to incompressible flows and compressible flows at low Mach numbers where effects of property variations need to be accounted for. Sixth order compact filtering [7] was used to eliminate the pressure-velocity decoupling peculiar to collocated-grid methods. The system of algebraic equations was solved using the strongly implicit procedure (SIP) [8, 9]. A code well optimized for performance on the CRAY T-90 was used to perform the large eddy simulations.

4. Simulation Details and Results

The computational domain for the large eddy simulations was designed to match the backward-facing step geometry from the particle tracking velocimetry (PTV) experiments [10] and is shown in Fig.1. The Reynolds number, based on the step height and upstream centerline velocity (which was also the reference velocity) was 5,540. Reference values of thermal conductivity, density and dynamic viscosity were obtained at the reference temperature, T_{ref}, of 293 K. The grid resolution used for the simulations was: (1) Upstream of step: $17 \times 31 \times 48$, (2) Downstream of step: $72 \times 46 \times 48$ in the streamwise, wall-normal and spanwise directions respectively. Non-uniform grids were employed in the wall-normal (y), and streamwise (x) directions as opposed to a uniform grid in the spanwise (z) direction. No-slip boundary conditions were enforced at the top and bottom solid walls. Periodicity of flow was assumed in the spanwise direction. The Navier-Stokes characteristic boundary condition strategy [11] was employed at the inflow and outflow boundaries. Turbulent inflow conditions for each time step of the simulation were provided by planes of data stored from an independent LES of a channel flow with the same Reynolds number and time step. For the simulations with heat transfer, the bottom wall downstream of the step was the only one supplied with a constant heat flux. The remaining walls were insulated (adiabatic conditions).

4.1. ISOTHERMAL FLOW CASE

The streamwise (Fig. 3), wall-normal (Fig. 4) and spanwise mean velocity distributions, and the respective root mean square fluctuations (Figs. 5, 6) from the simulation showed excellent agreement with experimental results. Third order moments also showed good qualitative agreement with the experiment. The mean reattachment length from the simulation was predicted to be 6.0 x/h, as compared with 6.51 x/h reported in the experiment. The simulations captured the presence of a smaller corner eddy in addition to the large recirculation bubble (Fig. 2). Details of the isothermal simulation and results have been presented in [12].

4.2. CONSTANT WALL HEAT FLUX CASES

Heat flux (q_w) levels of 1.0, 2.0, and 3.0 kW/m^2 corresponding to normalized heat flux, Q^+ ($= q_w/\rho_{ref}U_{ref}C_pT_{ref}$) levels of 0.0014, 0.0028, 0.0042 were supplied to the surface downstream of the step, yielding maximum T_{wall}/T_{bulk} ratios of about 1.7, 2.3, and 2.9, respectively. The bulk temperature profiles (Fig. 7) were in good agreement with analytical estimates based on an overall energy balance for the uniform heat flux condition. The

wall temperatures (Fig. 8) showed a dramatic increase downstream of the step, and reached their peak values in the neighborhood of the streamwise distance of $x/h \sim 2$. This increase in temperature is accompanied by a decrease in convective heat transfer (as evidenced by the Stanton number profiles in Fig. 9) and suggests that the air in this zone is almost in a "stagnant" state. The Stanton number, St $(= h/\rho_{ref}U_{ref}C_p)$ is a modified Nusselt number $(St = Nu/Re\,Pr)$, where $Nu = hL_y/k_b$, L_y is the step height, h is the convective heat transfer coefficient, and k_b is the bulk thermal conductivity. The Stanton number attains a maximum slightly upstream of reattachment, which is in agreement with [13], as opposed to results from several other studies that have indicated the location of the peak Stanton (or Nusselt number) to coincide with the mean reattachment point. In the region of reattachment, the impinging shear layer is responsible for the depression in the wall temperature around reattachment. Downstream of reattachment, linear increase of the wall temperature and the monotonic decrease in the mean Stanton number profiles is consistent with the growth of the thermal boundary layer following reattachment.

The Reynolds analogy does not hold in the mean sense, *i.e.*, the mean Stanton number profiles (Fig. 9) do not correlate with the mean skin friction profiles (Fig. 10). However, it is interesting to note that the mean Stanton number profiles show a more striking similarity with the fluctuating skin-friction profiles (Fig. 11) than they do with the profiles of the average absolute skin-friction (Fig. 12), or the mean skin friction. The high degree of correlation between the fluctuating skin-friction coefficient and Stanton number suggests that the correct velocity scale governing the strength of convective effects in the reattachment zone must be related to the velocity fluctuations rather than the mean velocity [13].

The bottom wall skin-friction coefficient (Fig. 10), in terms of normalized quantities can be written as $C_f = (2/Re)\,[(\mu/\rho)\,\partial u/\partial y]_w$. The influence of the wall temperatures for the three heat flux cases on the skin-friction coefficient is through the density and viscosity evaluated at the wall.

It is indicated in [13] that the streamwise turbulent heat flux is negligible as compared to the wall-normal turbulent heat flux. However, we show that the streamwise turbulent heat flux (Fig. 13), and the wall-normal turbulent heat flux (Fig. 14) are of the same order of magnitude. Probable reasons for their observation of negligible streamwise heat flux are that the heat flux levels in their work are an order of magnitude smaller and the Reynolds numbers are three to five times greater than the ones in this study.

Root mean square density fluctuations of up to 20 % were observed. At the peak wall temperatures for the three heat flux cases, the viscosity and thermal conductivity are roughly about 20%, 40% and 60% greater than

the values at the inlet, which are at the reference temperature of 293 K, thus demonstrating the need for property variations to be considered in calculations involving high heat fluxes.

5. Concluding Remarks

Large eddy simulations to study the heat transfer and fluid dynamics of the turbulent reattaching flow past a backward-facing step have been successfully conducted. The choice of the formulation enabled the inclusion of property variations, and facilitated the study at low Mach numbers. An increase in heat flux supplied to the bottom wall downstream of the step results in the heat transfer rate starting to be dominated by conduction as opposed to convection. Large variation in the wall temperature is observed, and the wall temperature attains a maximum close to the step face. The peak heat transfer rate occurs slightly upstream of reattachment. Streamwise and wall-normal turbulent heat fluxes are of the same order of magnitude. The Stanton number profiles correlate strongly with the fluctuating skin-friction profiles, and this observation underscores the importance of the near-wall region in determining the heat transfer rate.

6. Acknowledgments

The current research was partially supported by the Air Force Office of Scientific Research under Grant F49620-94-1-0168 and by the National Science Foundation under grants CTS-9414052 and CTS-9806989. The use of computer resources provided by the National Partnership for Advanced Computational Infrastructure at the San Diego Supercomputing Center is gratefully acknowledged.

References

1. Abrous, A., and Emery, A. F., 1996, Benchmark computational results for turbulent backward-facing step flow with heat transfer, HTD-Vol. 331, National Heat Transfer Conference, Vol. 9, ASME.
2. Mori, Y., Uchida, Y. and Sakai, K., 1986, A study of the time and spatial structure of heat transfer performances near the reattaching point of separated flows, *Procs. 8th Int. Heat Transfer Conference*, pp. 1083-1088.
3. Moin, P., Squires, K., Cabot, W., and Lee, S., 1991, A dynamic subgrid scale model for large eddy simulations of compressible turbulent flows, *Phys. Fluids A-Fluid*, Vol. 3, pp. 2746-2757.
4. Germano, M., Piomelli, U., Moin, P., and Cabot, W. H., 1991, A dynamic subgrid scale eddy viscosity model, *Phys. Fluids A-Fluid*, **3**, 1760-1765.
5. Yoshizawa, A., 1986, Statistical theory for compressible turbulent shear flows, with the application to subgrid modeling. *Phys. Fluids A-Fluid*, Vol. 5, pp. 3186-3196.
6. Pletcher, R. H. and Chen, K.-H., 1993, On solving the compressible Navier-Stokes equations for unsteady flows at very low Mach numbers, AIAA Paper 93-3368.

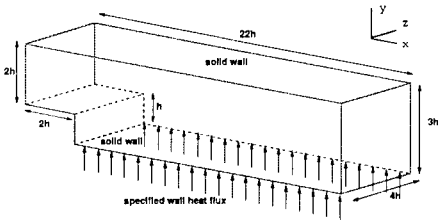


Figure 1. Backward-facing step geometry

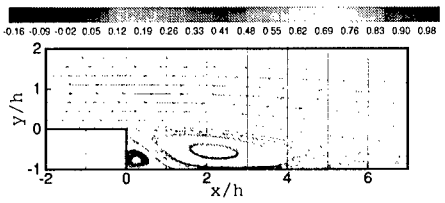


Figure 2. Mean streamlines

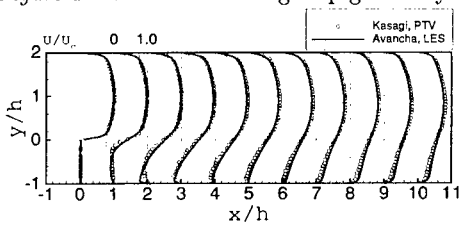


Figure 3. Mean streamwise velocity

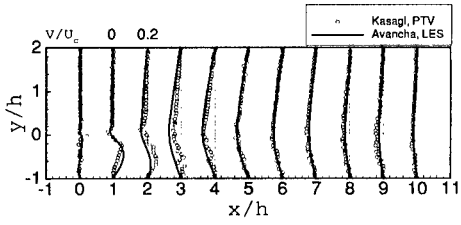


Figure 4. Mean wall-normal velocity

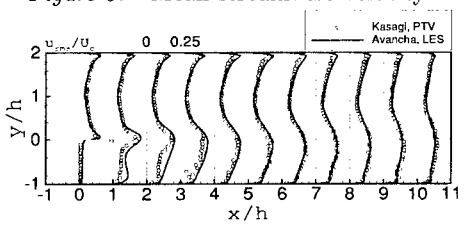


Figure 5. RMS streamwise velocity fluctuations

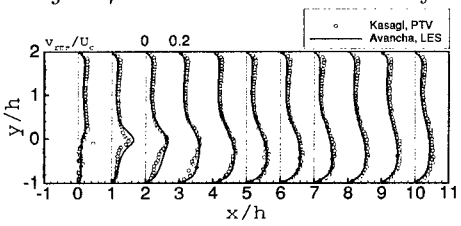


Figure 6. RMS wall-normal velocity fluctuations

7. Lele, S., 1992, Compact finite difference schemes with spectral-like resolution, *J. Comp. Phys.*, Vol. 103, pp. 16-42.
8. Stone, H. L., 1968, Iterative solution of implicit approximations of multidimensional partial differential equations. *SIAM J. Numer. Anal.*, Vol. 5, pp. 531-558.
9. Weinstein, H. G., Stone, H. L., and Kwan, T. V., 1969, Iterative procedure for solution of systems of parabolic and elliptic equations in three dimensions. *I & E C Fundamentals*, Vol. 8, pp. 281-287.
10. Kasagi, N., and Matsunaga, A., 1995, Three-dimensional particle-tracking velocimetry measurement of turbulence statistics and energy budget in a backward facing step flow, *Int. J. Heat and Fluid Fl.*, Vol. 16, pp. 477-485.
11. Poinsot, T. J., and Lele, S. K., 1992, Boundary conditions for direct simulations of compressible viscous flows, *J. Comp. Phys.*, Vol. 101, pp. 104-129.
12. Avancha, R., and Pletcher, R. H., 2000, Large eddy simulation of the turbulent flow past a backward facing step, AIAA 2000-0542, 38th Aerospace Sciences Meeting and Exhibit, 10-13 January 2000, Reno, NV.
13. Vogel, J. C., and Eaton, J. K., 1984, Heat transfer and fluid mechanics measurements in the turbulent reattaching flow behind a backward facing step, Report MD-44, Thermosciences Division, Department of Mechanical Engineering, Stanford University.

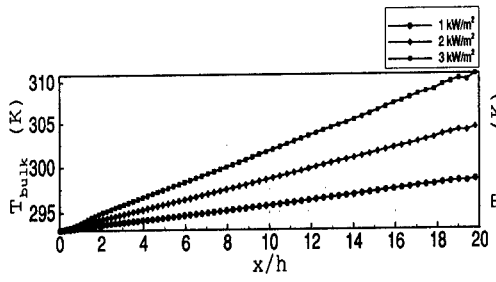


Figure 7. Bulk temperature

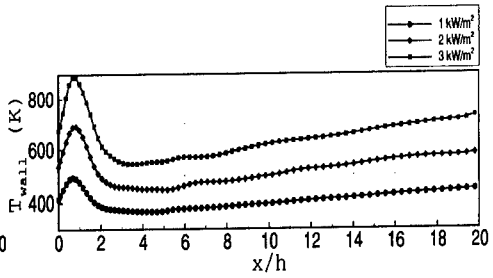


Figure 8. Wall temperature

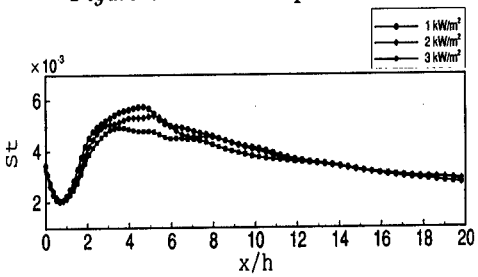


Figure 9. Stanton number

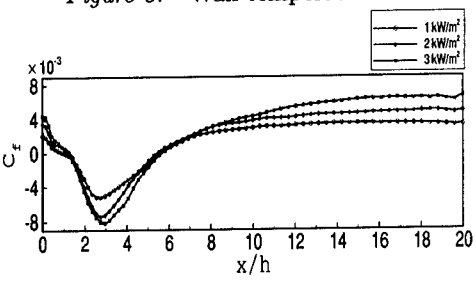


Figure 10. Skin-friction coefficient

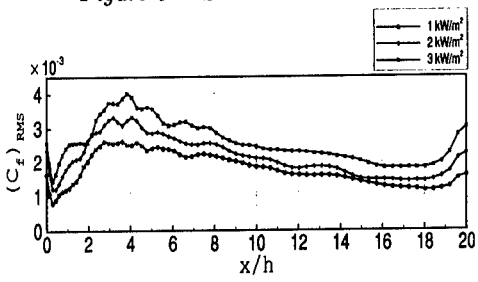


Figure 11. Fluctuating skin-friction

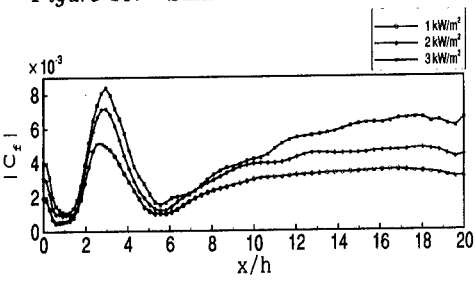


Figure 12. Average of absolute skin-friction

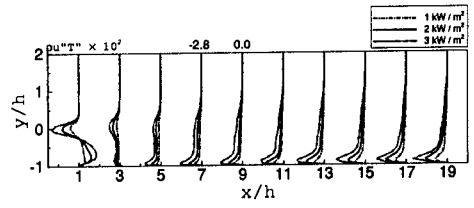


Figure 13. Streamwise turbulent heat flux

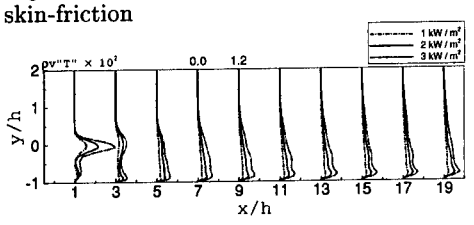


Figure 14. Vertical turbulent heat flux

LES STUDIES OF SCALAR FLUCTUATIONS AT HIGH CONVECTIVE MACH NUMBERS

WILLIAM H. CALHOON, JR., CHANDRASEKHAR KANNEPALLI AND SANFORD M. DASH
Combustion Research and Flow Technology, Inc. (CRAFT Tech)
Dublin, PA 18917

Abstract

A need has arisen for the development of RANS models for the prediction of scalar fluctuations and turbulent transport in the high speed flow regime. These models will have application, for example, in scramjet combustors and missile exhaust plume signature analyses and other important areas. However, in the high speed flow regime, experimentally derived scalar fluctuation validation data is not readily available due to the inability of relevant experimental measurement techniques (e.g. hot wires) to cope with this flowfield environment. Consequently, model development in this flow regime is difficult. To address this issue, a two part program has been initiated to fill the data gap and thus facilitate model development. Part I of this program involves the collection of LES data over a wide range of conditions. Part II involves the use of these data to evaluate and develop RANS tools to improve predictive capabilities. This paper presents results and preliminary finding of Part I of this program; the collection of LES data regarding scalar transport in planar shear layers. The findings of this study elucidate the effects of compressibility on the character of mean scalar profiles, variations in turbulent Prandtl number, and on scalar rms fluctuations.

1. Introduction

The ability of LES methodology to predict scalar variance properties for both hot and variable composition jets and free shear layers at subsonic conditions has been amply demonstrated, as exemplified by a number of comparisons with the Brown and Roshko Nitrogen/Helium shear layer density variance data of Konrad (see, e.g. Ref. 1). The time-averaged statistics from these type of simulations, in combination with available subsonic hot jet and helium jet data, have served as the basis for RANS (Reynolds Average Navier-Stokes) scalar variance model equation calibration [2], which are in turn utilized for both variable turbulent Prandtl (Pr_t) and Schmidt (Sc_t) number modeling [3] and for PDF-based turbulent combustion modeling [4].

For supersonic flows with high convective Mach numbers, compressibility effects reduce the rate of mixing and turbulent fluctuation levels. However, while significant data is available for Favre averaged velocity fluctuations at high convective numbers, there is a lack of comparable data for scalar correlations. The lack of data in this flow regime makes the calibration and application of RANS scalar fluctuation models difficult. Recently, Calhoon [4] found that a RANS scalar fluctuation model, which had been calibrated using available low speed data, overpredicted fluctuation levels leading to substantive errors in missile exhaust plume flows. This failure of RANS modeling resulted from a lack of adequate data which could provide an understanding of the effects of compressibility on scalar fluctuations. Available experimental data for scalar fluctuations in this high speed flow regime are not readily available.

LES provides the opportunity to investigate compressibility effects on scalar fluctuations in the high speed flow regime where experimental data are difficult to obtain. Data from LES in this regime could also be used to develop and calibrate RANS models to be applied to large scale problems such as scramjet combustors, rocket plume signatures and missile sensor window aero-optics. Proper understanding of scalar fluctuations in the high speed regime is a prerequisite to the development of reliable turbulent-combustion models for scramjet and rocket propulsive applications.

With these points in mind, the objective of this overall study is to investigate compressibility effects on scalar fluctuations and evaluate RANS modeling for the prediction of these fluctuations. This will be accomplished by conducting LES simulations of hot shear layers at varying degrees of compressibility. The primary scalar fluctuations of interest will be those of temperature. Analysis of the simulation results will enable the assessment of compressibility effects on fluctuation levels and the effect of variable turbulent Prandtl number in these flows. Time-averaged statistics will also be used to evaluate and calibrate RANS models for temperature fluctuations and variable Pr_t.

This study has been broken into two parts. Part I deals with the collection of LES data for shear layers at varying degrees of compressibility. Part II deals with the analysis and use of these data for the development of RANS models for the prediction of scalar fluctuations, and turbulent Prandtl and Schmidt numbers, which accurately characterize compressibility effects. This paper concerns Part I of this study and presents a summary of the LES data that has been collected thus far. Though not complete, the data collected so far does reveal some interesting aspects of compressibility effects on free shear layer development and scalar fluctuations.

The following section briefly describes the computational methodology used for the LES simulations. Next, a description of the simulations carried out for Part I is presented, followed by the presentation and discussion of the results and analysis. Concluding remarks follow.

2. Computational Methodology

The simulations for this study were carried out using the CRAFT NS code [5,6]. CRAFT is a structured, finite-volume code applicable to compressible, reacting, multi-phase flows. For LES applications, the code is implemented with an upwind-biased, Roe-flux-extrapolation procedure extended to fifth order [7] and fourth order central differencing for the inviscid and viscous spatial schemes, respectively. Temporally, the code includes both a fourth order Runga-Kutta scheme and second order three-factor Approximate Factorization (AF) implicit scheme. For this study, the AF scheme was used and applied with sub-iterations to remove the splitting error. Regarding subgrid modeling, the code includes a compressible version of the algebraic Smagorinsky model as well as the compressible, one equation model of Menon [8]. The one equation model solves a transport equation for subgrid turbulent kinetic energy, k^{sgs}. The subgrid-scale stresses are then modeled using an eddy viscosity approach based on k^{sgs}.

For high speed applications where shock waves are present, the higher order numerical scheme requires modification for stability. Shock capturing options for higher order schemes range from standard limiting approaches to WENO schemes (e.g., Ref. [10]). An alternative approach was used in this study. In order to stabilize the code in the vicinity of strong gradients, such as shock waves, a modification of the classic Jameson, *et al.* [11] 2-4 dissipation scheme was used. In the original scheme, a fourth order dissipation term was employed to stabilize the central difference scheme in smooth, high cell Reynolds number regions of the flow. In the vicinity of shocks, a pressure based switch was used to deactivate the fourth order dissipation and turn on a second order dissipation term. In the present context, the fourth order dissipation term is not required and is discarded. The second order dissipation term is retained to provide sufficient stability for the fifth order code in the vicinity of shock waves. The original Jameson second order dissipation term, including the calibration constant, was used with only the following modification. The pressure based switch was modified to also include temperature to prevent instabilities along slip lines. Also, both the pressure and temperature switches were threshold to allow the dissipation to be tuned for shock waves, to ensure no dissipation is added elsewhere. The following form of the second order dissipation switch, ν, was used,

$$\nu = \max(\nu_p, \nu_T) \qquad (1)$$

where,

$\nu_p = \frac{|p_{i+1} - 2p_i + p_{i-1}|}{|p_{i+1}| + |2p_i| + |p_{i-1}|}$ and $\nu_T = \frac{|T_{i+1} - 2T_i + T_{i-1}|}{|T_{i+1}| + |2T_i| + |T_{i-1}|}$ with p and T being the pressure and temperature, respectively. These values were then threshold as $\nu_p = 0$ if $\nu_p < \nu_{p,0}$ and $\nu_T = 0$ if $\nu_T < \nu_{T,0}$. Values of the threshold cuts-offs in numerical tests were $\nu_{p,0} = 0.2$ and $\nu_{T,0} = 0.3$. Tests of the scheme were carried out for vortex convection, a shock-vortex interaction, wave propagation, and a supersonic flat plate boundary layer. These tests demonstrated the second order dissipation to be isolated around shock waves and to have no impact on the development of unsteady flow features elsewhere.

3.0 LES Shear Layer Simulation

Sandham and Reynolds [9] found three distinct flow regimes for compressible mixing layers using linear stability analysis and DNS. These flow regimes are characterized by the convective Mach number, M_c, which may be defined as,

$$M_c = \frac{M_1\sqrt{\rho_2/\rho_1}(1-u_2/u_1)}{(\gamma_2/\gamma_1)^{1/4}(1+\sqrt{\rho_2/\rho_1})} \tag{2}$$

where u, M, ρ and γ are the velocity, Mach number, density and ratio of specific heats, respectively, for the high speed (subscript 1) and low speed (subscript 2) sides. For $0 < M_c < 0.6$, two-dimensional instabilities are amplified most rapidly so that the shear layer is dominated by large scale 2-D spanwise structures. For $0.6 < M_c < 1.0$, oblique (three-dimensional) instability modes become dominant while 2-D instabilities are still significantly amplified resulting in a shear layer which is composed of both strong 2-D and 3-D structures. For $M_c > 1.0$, 2-D instabilities are amplified by a factor of five less than 3-D modes resulting in a flow dominated by 3-D large scale structures with little or no organized 2-D structures.

To characterize compressibility effects on the evolution of shear layer scalar fluctuations, simulations for Part I of this study must be carried out in each of these flow regimes. Convective Mach numbers chosen for the study were $M_c = 0.27$, 0.8 and 1.3. Additionally, all the simulations were for spatially evolving shear layers, as opposed to temporally evolving layers. Other numerical studies of spatially evolving compressible shear layers have been undertaken (e.g., Lou et al. [12], Ameur and Chollet [13], and Nelson [14]). However, this study considers a wider range of convective Mach numbers for a fixed set of velocity and density ratios, so as to isolate compressibility effects. The velocity and density ratios for each case was specified as $u_2/u_1 = .164$ and

$\rho_2/\rho_1 = 3.33$. This density ratio corresponds to temperatures of $T_1 = 1000\ K$ and $T_2 = 300\ K$ at atmospheric conditions. For the high convective Mach number case, $M_1 = 2.41$ and $M_2 = .72$. The Mach numbers and temperature for this case roughly approximate the conditions of a nearfield missile exhaust plume shear layer for a low altitude trajectory condition. This high M_c case has been specifically chosen to approximate a missile plume to facilitate the development of RANS models for scalar fluctuations. These RANS models may then be used, for example, to make more reliable missile exhaust plumes predictions, as previously mentioned.

Progress toward the completion of the LES simulations for Part I of this study is currently limited to only the $M_c = 0.27$ and 1.3 cases. The $M_c = 0.8$ case has not yet been undertaken. For the $M_c = 1.3$ case, a full 3-D simulation has been completed. However, for the $M_c = 0.27$ case, only a 2-D simulation has been completed thus far. The lack of a full, 3-D simulation for the low speed case should not significantly degrade a preliminary assessment of compressibility effects because this case should be dominated by strong 2-D spanwise structures, with little contribution from 3-D effects to the mean scalar fluctuations. For example, several researchers have accurately reproduced the density fluctuations measured by Konrad for the Brown and Roshko [16] N_2/He shear layer using 2-D LES methodology.

The computational set-up for the $M_c = 0.27$ and 1.3 cases were different due to the Mach numbers involved. The low speed case used a rectangular domain .6 m in length along the streamwise coordinate. The computational domain was discretized using a $551x241$ grid. At the inflow boundary, hyperbolic tangent mean velocity and temperature profiles were specified using a characteristic subsonic boundary condition given the total temperature and mass flow rate. These profiles had a vorticity thickness of 7.3×10^{-3} m. The mean inflow profiles were also perturbed with sinusoidal streamwise velocity fluctuations at a 0.5 kHz frequency. For the high speed case, an additional upstream domain was added on the subsonic side to which total temperature and mass flow rate boundary conditions were applied. The multi-block grid for this case was ($551x100x65$, $28x47x65$). On the supersonic side, the mean velocity and temperature profiles were specified using a hyperbolic tangent profile with the same vorticity thickness. Sinusoidal forcing was applied to the transverse and spanwise velocity components at frequencies of 50, 100 and 200 kHz with phase angles that varied in the transverse direction and in time. A random component was also added to these velocity fluctuations.

4.0 Results and Discussion

Figure 1 presents contours of spanwise vorticity for both the low and high speed shear layer simulations. For the low speed case (Figure 1(a)), strong coherent structures are evident which pair and result in rapid shear layer growth.

These distinct structures are what may be expected for low speed shear layers as observed in the Brown and Roshko [16] N_2/He shear layer experiment. Also evident from this figure is the generation of vorticity due to baroclinic torque effects, which results from nonaligned density and pressure gradients. This may be seen by the large positive vorticity values primarily around the outer edges of the organized structures. For the high speed case (Figure 1(b)) the contours are quite different. As discussed by Sandham and Reynolds [9], at this high convective Mach number little or no coherent spanwise structures are readily apparent. This case shows a large amount of fine scale structure, which grows linearly in the downstream direction, as expected. From Figure 1(b), no well defined braid structures are apparent as seen in Figure 1(a). However, toward the end of the domain, there does appear to be the beginnings of large scale spanwise rotation of the fine scale structures, possibly resulting from the long delayed growth of the 2-D, spanwise modes.

For the high convective Mach number case, the flow is highly 3-D as seen in Figure 2, which presents a contour plot of the spanwise vorticity along several streamwise planes. This figure displays a flow rich in both small and large scale 3-D structure. The streamwise vorticity (Figure 3) also shows similar complexity. The 3-D structures seen in these figures were found to grow rapidly starting just shortly downstream of the shear layer origin. This is in agreement with the findings of linear stability analysis [9] for high convective Mach numbers that predicts 3-D modes to be amplified by a factor of five greater than 2-D modes.

The strong vortical features seen in Figures 1–3 result in complex scalar mixing patterns as seen in Figure 4. This figure presents temperature contours for both the low (Figure 4(a)) and high speed (Figure 4(b)) cases. For the low speed case, strong coherent structures with well defined braid regions (seen in Figure 1(a)) result in the penetration of hot fluid from the high speed side deep into the layer. The high speed case, with the lack of these well defined 2-D structures, exhibits a very different character. Large amounts of hot unmixed fluid are unable to traverse the layer before being mixed with surrounding fluid by the action of the fine scale structures. The highly complex mixing pattern associated with these fine scale 3-D structures may also be seen in Figure 5, which is a plot of temperature contours in several streamwise planes. Here again the highly complex mixing pattern is clearly evident. From both Figures 4 and 5, temperature overshoots above 1000 K on the high speed side are evident. These excess temperature regions result from compression waves, which move downstream with the vortical structures seen in Figure 1(b). These compression waves, and resulting temperature overshoots, are seen to persist the entire length of the layer, starting just downstream of the weak shock emanating from the inflow boundary. To facilitate direct comparison with Favre average RANS models, the LES data for these simulations are Favre time averaged assuming the

contribution from the subgrid is small. With these averaged data, relevant fluid dynamic quantities may be calculated, such as the streamwise evolution of the vorticity thickness (δ_ω).

Figure 6 presents a comparison of the vorticity thickness evolution for both cases. From this figure, both cases exhibit a linear growth regime downstream of ~ $x = 0.1$ m. The asymptotic growth rate for the high speed case is substantially lower than for the low speed case. This strong growth rate reduction is expected from the well known reduction of turbulent transport phenomenon with increasing compressibility. Within this linear region, the mean flow variable profiles are self-similar. For example, Figure 7 presents the Favre-averaged mean streamwise velocity profiles for both cases. The profiles in this figure are plotted against the transverse distance divided by the vorticity thickness. This is done to remove the growth rate difference seen in Figure 6. From Figure 7, there is clearly a shape change in the mean velocity with M_c. The high speed profiles have an anti-symmetric, hyperbolic tangent like profile. The low speed case, however, is not anti-symmetric and has a higher curvature on the high speed side. The source of this feature is unclear, but may be related to the baroclinic torque features seen in Figure 1(a).

Regarding the scalar property profiles, Figure 8 presents the Favre mean temperature in the linear growth regime. From this plot, first notice the 'hump' in the mean profile for the low speed case. This feature is characteristic of low speed, planar shear layers as observed by Friedler [15]. He suggested this feature was a result of the entrainment process associated with coherent, large scale spanwise structure characteristic of the low speed flow regime. As compressibility is increased and these spanwise structures disappear (Figure 1), this hump feature also disappears as seen for the high speed case. Figure 8 supports the suggestion that this hump feature is a result of the spanwise structures. Currently available RANS scalar transport models cannot capture this feature. Neither can the transition regarding compressibility be captured by current models. Time averaged transport data from these calculations will be used in Part II of this study to evaluate and improve RANS models for scalar transport to capture these features.

A further examination of Figure 8 suggest a dependence of turbulent Prandtl number on compressibility. Notice the low speed profile is considerably broader than for the high speed case. This difference is not a result of the growth rate difference between the two cases because this variation has been removed by normalization using the vorticity thickness. This difference suggests an increase in $\mathrm{Pr_t}$ with increasing compressibility. To make a preliminary assessment of this hypothesis, an estimate for $\mathrm{Pr_t}$ was made using the gradient hypothesis assumption, analogous to the eddy-viscosity, i.e.,

$$\nu_T = -\langle u'v' \rangle / (\partial \langle u \rangle / \partial y) \tag{3}$$

$$\alpha_T = \nu_T / \mathrm{Pr}_t = -\langle T'v' \rangle / (\partial \langle T \rangle / \partial y) \tag{4}$$

where the brackets (< >) represent Favre averaged quantities. Using Equations (3) and (4), Pr_t was constructed from the Favre average LES data. Figure 9 presents a plot of Pr_t across the layer of both cases. For the low speed case, Pr_t shows large variations and significantly lower values than for the high speed case over most of the layer. This drop in Pr_t implies a higher transport of temperature and hence a thicker temperature layer as seen in Figure 8. A similar observation was inferred by Sinha, et al. [6] for low speed jets. The high speed case, however, is more or less uniform across the layer with a value approaching the classic value of .9. This analysis supports the assertion that Pr_t increases with increased compressibility. This seems to be a significant finding regarding RANS modeling. However, this represents only a preliminary analysis and that will need to be borne out with further investigation.

Finally, Figure 10 presents the variation of rms temperature fluctuation intensity across the layer for the low and high speed cases. For the low speed case, the self-similar profile exhibits a double peak structure, while at high speeds the profile does not. This double peak structure for scalar fluctuations has been observed in the plane shear layer experiments of Friedler [15] and Brown and Roshko [16]. This feature is a common characteristic of low speed flows and results from the entrainment process involved with the large scale spanwise structures. Since the high speed case does not contain these structures, the profile only exhibits a single peak. This high speed profile is also thinner owing to the turbulent Prandtl number variation seen in Figure 9. Also observe the drop in peak intensity value as M_c is increased. The peak intensity drops by a factor of ~ .6 for the high speed case.

This reduction in peak intensity with increased compressibility is an interesting point in the context of the missile exhaust plume study of Calhoon and Kenzakowski [4]. In that study, a turbulent combustion model for RANS application was evaluated for the prediction of missile exhaust plume signatures. The combustion model used was strongly dependent on the prediction of temperature fluctuations from a modeled RANS transport equation. Due to the lack of available high speed data, this transport equation was calibrated based on available low speed data. Calhoon and Kenzakowski found this calibration to produce unrealistic results in the context of high speed missile exhaust plumes. To address this issue, the production coefficient in the temperature fluctuation transport equation was reduced to produce signatures consistent with flight data. This ad-hoc modification resulted in a reduction of the peak predicted temperature intensity values by a factor of ~ .75 below the low speed calibrated values. *It seems remarkable that this required reduction in predicted temperature intensity is in reasonable agreement with the reduction seen in Figure 10 resulting from compressibility effects.* The modeled fluctuation equation used by Calhoon and Kenzakowski did not include any validated model for compressibility, suggesting that the lack a compressibility correction was responsible for the observed error. This illustrates how LES may be used for the development of models to improve the prediction of production level codes. As

discussed earlier, Part II of this study will focus on the evaluation and development of RANS methodologies through the use of this LES data.

5.0 Conclusions

LES of hot planar shear layers have been carried out over a wide range of convective Mach numbers in order to assess the impact of compressibility effects on scalar fluctuations and turbulent transport. Simulations were completed for both low speed (M_c = .27) and high speed cases (M_c = 1.3). Analysis of the results leads to the following conclusions. In agreement with previous linear stability analysis, shear layer development from low compressibility to high compressibility is characterized by a transition from a flow dominated by coherent 2-D structures to one in which 3-D features dominate. This transition, or loss of 2-D structure, results in an evolution of mean scalar profiles that eliminates the 'hump' feature observed in low speed shear layer experiments. This transition also was found to modify the distribution of turbulent Prandtl number from a nonuniform profile at low speeds to an approximately uniform profile at high speed. This resulted in a smaller ratio of mean temperature profile width to vorticity thickness for the high speed case than for the low speed case. Also, the compressibility increase was found to modify the shape of the scalar fluctuation variation across the shear layer from a low speed two peak structure to a high speed single peak structure. This again is due to the reduction of 2-D structures in high speed shear layers. Finally, the identified reduction in peak temperature fluctuation values as compressibility was increased was found to be a credible explanation for the deficiencies of a RANS temperature fluctuation model applied to missile exhaust plume signature predictions in the study of Calhoon and Kenzakowski [4].

References

[1] Chien, K.Y., Ferguson, R.E., Kuhl, A.L., Glaz, H.M., and Collela, P., "Inviscid Dynamics of Two-Dimensional Shear Layers," 22nd AIAA Fluid Dynamics, Plasma Dynamics and Lasers Conference, Honolulu, HI, AIAA 91-1678, Jun. 24-26, 1991.

[2] Chidambaram N., Dash, S.M., and Kenzakowski, D.C., "Scalar Variance Transport in the Turbulence Modeling of Propulsive Jets," *Journal of Propulsion & Power*, Vol. 17, No. 1, Jan., Feb., 2001.

[3] Kenzakowski, D.C., Papp, J., and Dash, S.M., "Evaluation of Advanced Turbulence Models and Variable Prandtl/Schmidt Number Methodology for Propulsive Flows," AIAA Paper No. 2000-0885, 38th AIAA Aerospace Sciences Meeting at Reno, NV, Jan. 10–13, 2000.

[4] Calhoon, W.H. and Kenzakowski, D.C., "Flowfield and Radiation Analysis of Missile Exhaust Plumes Using a Turbulent-Chemistry Interaction Model," Paper No. AIAA-2000-3388, 36th AIAA/ASME/SAE/ASEE JPC and Exhibit, Von Braun Civic Center, Huntsville, AL, July 17–19, 2000.

[5] Sinha, N., Hosangadi, A., and Dash, S.M., "The CRAFT NS Code and Preliminary Applications to Steady/Unsteady Reacting, Multi-Phase Jet/Plume Flowfield Problems," CPIA Pub. 568, May 1991.

[6] Sinha, N., Lee, R., Dash, S.M., and Pelz, R.B., "Advances in 3D Unsteady Jet Simulation Using LES Methodology in a Parallel Environment," AIAA paper 96-1779, May 1996.
[7] Rai, M.M., "Navier-Stokes Simulations of Blade-Vortex Interaction Using High-Order Accurate Upwind Schemes," 25th AIAA Aerospace Sciences Meeting, Reno, NV, AIAA Paper 87-0543, Jan 12–15, 1987.
[8] Menon, S., "Active Control of Combustion Instability in a Ramjet Using Large-Eddy Simulations," 29th AIAA Aerospace Sciences Meeting, Reno, NV, AIAA Paper 91-0411, 1991.
[9] Sandham, N.D. and Reynolds, W.C., "Three-Dimensional Simulations of Large Eddies in the Compressible Mixing Layer," *J. Fluid Mech*, Vol. 224, pp. 133–158, 1991.
[10] Liu, X.-D., Osher, S., and Chan, T., "Weighted Essentially Non-oscillatory Schemes," *J. Comp. Phys.*, Vol. 115, pp. 220–212, 1994.
[11] Jameson, A., Schmidt, W., and Turkel, E., "Numerical Solutions of the Euler Equations by Finite Volume Methods Using Runge-Kutta Time-Stepping Schemes," presented at the AIAA 14th Fluid and Plasma Dynamics Conference, June 23–25, Palo Alto, CA, AIAA 81-1259, 1981.
[12] Liou, T.-M., Lien, W.-Y., and Hwang, P.-W., "Compressibility Effects and Mixing Enhancement in Turbulent Free Shear Flows," AIAA J, Vol. 33, No. 12, pp. 2332–2338, 1995.
[13] Ameur Si, M. and Chollet, J. P., "Large Eddy Simulations of Shear Flows: Mixing Layers," in *Advances in Turbulence*, V. Kluwer Acedemic Publishers, 1995.
[14] Nelson, C. C., "Simulations of Spatially Evolving Compressible Turbulence Using a Local Dynamic Subgrid Model," PhD thesis, Georgia Institute of Technology, 1997.
[15] Fiedler, H. E., "Transport of Heat Across a Plane Turbulent Mixing Layer," Advances in Geophysics, Vol. 18A, pp. 93–109, 1974.
[16] Brown, G. L. and Roshko, A., "On Density Effects and Large Structures in Turbulent Mixing Layers," *J. Fluid Mech*, Vol. 63, No. 2, pp. 775–816, 1972.

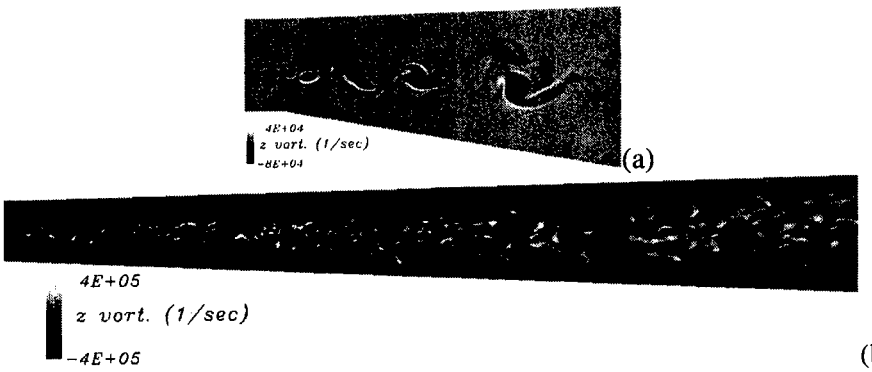


Fig. 1. Spanwise vorticity contours for (a) $M_c = .27$ and (b) $M_c = 1.3$. Flow is from left to right.

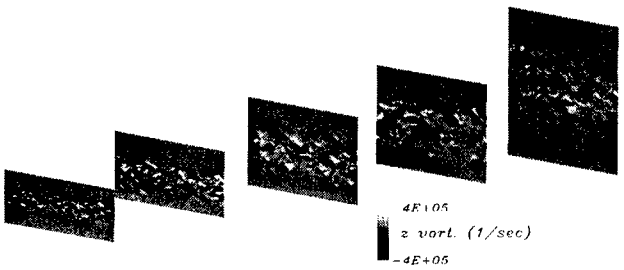


Fig. 2. Spanwise vorticity contours in streamwise planes for the $M_c = 1.3$ case.

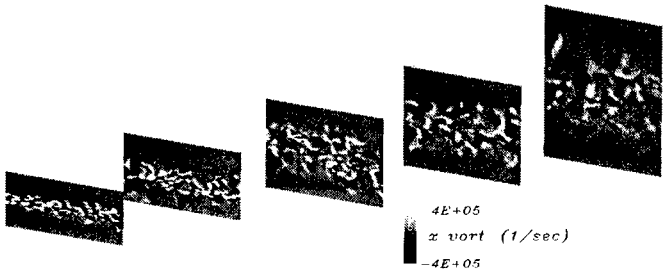


Fig. 3. Streamwise vorticity contours in streamwise planes for the $M_c = 1.3$ case.



Fig. 4. Temperature contours in a spanwise plane for (a) $M_c = .27$ and (b) $M_c = 1.3$.

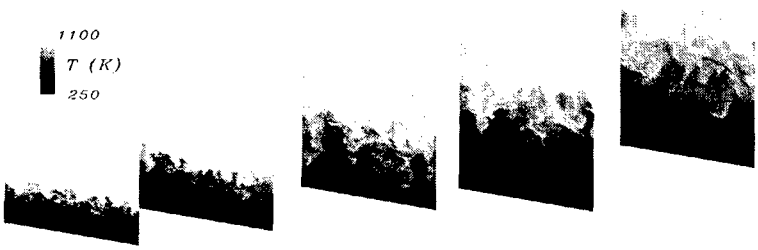


Fig. 5. Temperature contours for $M_c = 1.3$ at several streamwise planes.

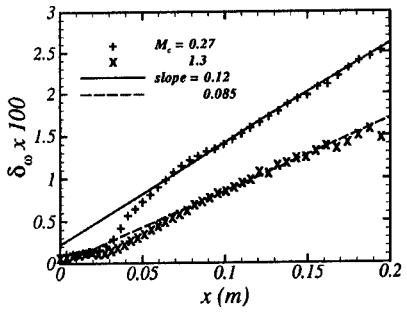


Fig. 6. Vorticity thickness evolution as function of downstream distance.

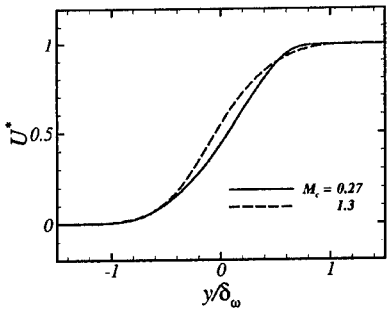


Fig. 7. Favre mean normalized streamwise velocity in the linear growth rate regime for the low and high speed cases.

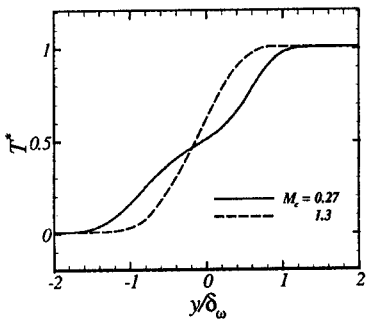


Fig. 8. Favre mean normalized temperature profiles in the linear growth rate regime.

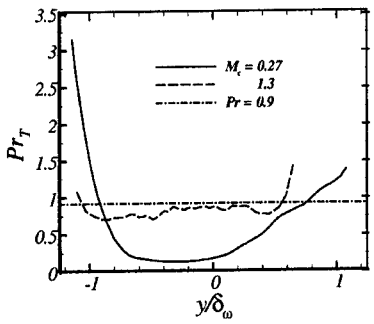


Fig. 9. Estimated turbulent Prandtl number variation across the shear layer for the low and high speed cases.

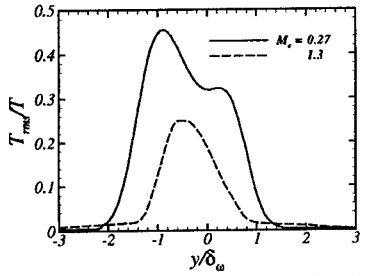


Fig. 10. Shear layer temperature intensity variation for the low and high speed cases.

INSTABILITY OF THE SHEAR LAYER SEPARATING FROM A CIRCULAR CYLINDER

JINSUNG KIM AND HAECHEON CHOI
School of Mechanical and Aerospace Engineering
Seoul National University, Seoul 151-742, Korea

Abstract. The instability of the shear layer separating from a circular cylinder has been investigated using large eddy simulation at two different Reynolds numbers of 1600 and 3900 based on the free-stream velocity and cylinder diameter. Two distinct types of the shear layer instability are found in this study: one is a completely three-dimensional type and the other is a quasi-two-dimensional type. The instability of three-dimensional type is generated by a strong counter-rotating streamwise vortex pair underneath the separating shear layer and thus occurs locally in the spanwise direction. On the other hand, the instability of quasi-two-dimensional type is associated with the breakdown of the Karman vortex shedding process and thus occurs globally across the cross-stream direction as well as the spanwise direction, resulting in the in-phase shear layer instability. It is also conjectured that at high Reynolds number, the instability of quasi-two-dimensional type should be more frequent than the instability of three-dimensional type.

1. Introduction

The separated shear layer is one of the important flow characteristics in the flow around a circular cylinder. Bloor (1964) is the one who first performed the systematic measurement of the shear layer separating from a circular cylinder. She used a hot-wire probe to measure the frequency of transition wave in the shear layer. She concluded that the transition wave exists for $Re > Re_{crit} = 1300$ and suggested that the shear-layer frequency normalized by the primary vortex-shedding frequency (f_{SL}/f_K) scales with $Re^{1/2}$, where $Re = u_\infty d/\nu$, u_∞ is the free-stream velocity, d is the cylinder diameter, and ν is the kinematic viscosity. After Bloor's (1964) experiment, several other researchers have investigated the shear-layer instability. Wei

& Smith (1986) found that the transition wave of Bloor (1964) is an identical phenomenon to the roll-up of small-scale secondary vortices in the shear layer. They also reported that the normalized shear-layer frequency varies as $Re^{0.77}$ from hot-wire measurements and as $Re^{0.87}$ from flow visualization, which are contrary to the 0.5 power law of Bloor (1964). Unal & Rockwell (1988a) reported that the instability could not be perceived for $Re < 1900$ from both the hot-film measurement and flow visualization and pointed out the influence of background disturbances to Re_{crit}. Recently, Prasad & Williamson (1996, 1997) showed that a power law of the form $Re^{0.67}$ accurately represents the Re-variation of f_{SL}/f_K. The effect of the spanwise end condition on Re_{crit} is also examined by Prasad & Williamson (1996, 1997). They reported that $Re_{crit} \approx 1200$ for parallel shedding and $Re_{crit} \approx 2600$ for oblique shedding.

In this study, we investigate the shear-layer instability around a circular cylinder at two different Reynolds numbers of $Re = 1600$ and 3900, which are higher than Re_{crit} suggested by Prasad & Williamson (1996, 1997), using large eddy simulation.

2. Numerical method

Large eddy simulations are performed with the dynamic subgrid-scale model (Germano *et al.* 1991; Lilly 1992) in generalized coordinates. The time integration method is based on a fully implicit, fractional step method (Choi *et al.* 1992; Choi & Moin 1994). All terms including cross-derivative diffusion terms are advanced with the Crank-Nicolson method in time and are resolved with the second-order central-difference scheme in space. The computational domain is $-19d \leq x \leq 17d$, $-25d \leq y \leq 25d$, where $(x = 0, y = 0)$ corresponds to the center location of the cylinder. The spanwise length of the cylinder is chosen to be πd. This spanwise domain length was used by other investigators (Mittal & Moin 1997; Kravchenko & Moin 1998). A C-type mesh with $673 \times 160 \times 64$ grid points is used and the computational time step used is $\Delta t u_\infty / d = 0.0095$. With this mesh and computational time step, the maximum CFL number is about 3.0 for Re=1600 and about 3.4 for Re=3900. The computations are performed using 42 processor elements in CRAY T3E. The computational cost is about 8 hours per vortex shedding period per processor element.

3. Result

We observe the instability of the shear layer from both vortical structures and velocity time traces. Figure 1 shows the time traces of the streamwise velocity at $x/d = 1.0$ and $y/d = 0.8$ at a few different spanwise locations at Re=1600. The same (x, y) location was also selected by Prasad &

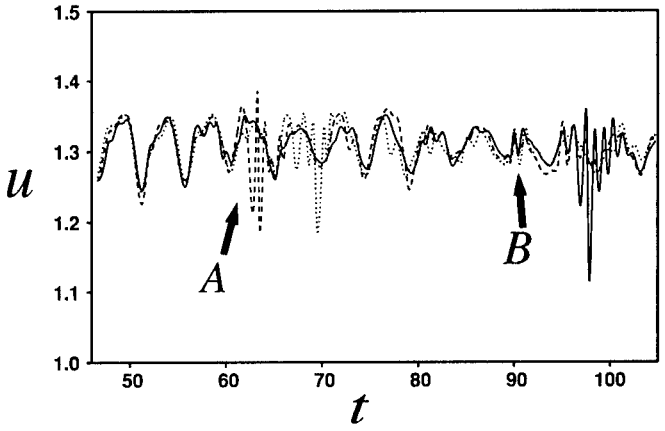


Figure 1. Time traces of the streamwise velocity at $x/d = 1.0$ and $y/d = 0.8$ (Re=1600).

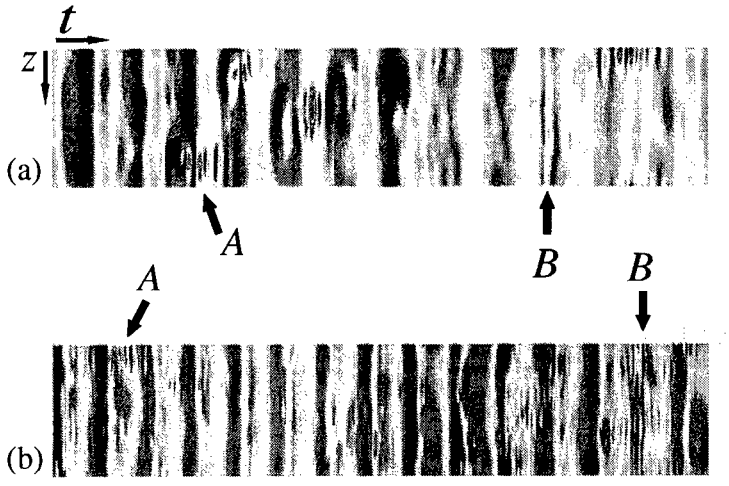


Figure 2. Contours of the streamwise velocity fluctuations at $x/d = 1.0$ and $y/d = 0.8$ in the $t - z$ plane: (a) Re=1600; (b) Re=3900.

Williamson (1996, 1997) to observe the shear-layer instability. It is clearly seen from figure 1 that the shear-layer instability (packet of intermittent high frequency velocity fluctuations) occurs. The time traces at Re=3900 are similar to those shown in figure 1 (not shown here). It is interesting to note that there exist two distinct types of the shear-layer instability: one is denoted by 'A', whereas the other is denoted by 'B' (figure 1). In the case of type 'A' instability, the intermittent velocity fluctuations exist locally in the spanwise direction. That is, the shear-layer instability of this type is a completely three-dimensional phenomenon. So we call this type

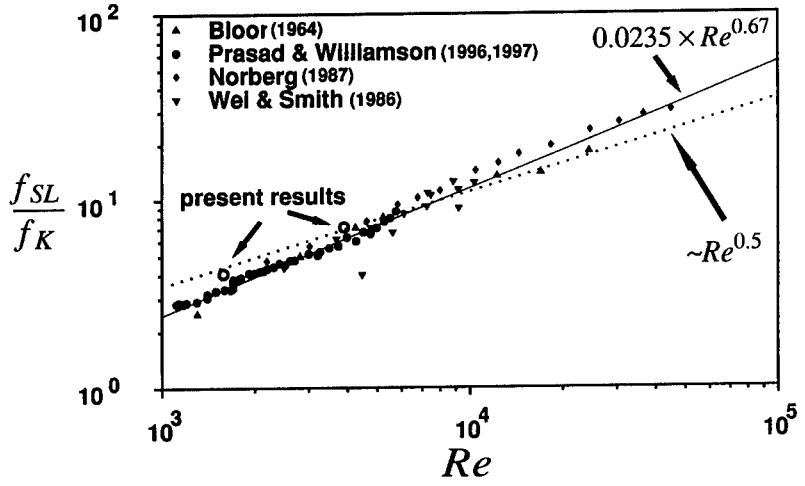


Figure 3. Variation of the normalized shear-layer frequency with respect to the Reynolds number (f_{SL}: shear-layer frequency, f_K: natural-shedding frequency).

'A' instability as a 3-D instability. For the type 'B' instability, the intermittent velocity fluctuations occur simultaneously at all spanwise positions and thus we call this type as a quasi-2-D instability.

The difference between the 3-D and quasi-2-D instabilities can be seen more clearly from figures 2(a) and 2(b). All the data from every other grid points in the spanwise direction are included in figures 2(a) and 2(b) where the horizontal direction is the time axis and the vertical direction is the spanwise direction. One can see that the 3-D instability signals form an 'island' in the $t - z$ plane, whereas the quasi-2-D instability appears as vertical lines. Figure 2 also shows that the packets of shear-layer velocity fluctuations occur more frequently at $Re = 3900$ than at $Re = 1600$, which agrees with the finding of Prasad & Williamson (1997) about the Reynolds-number dependence.

The frequency of the shear-layer instability is calculated from the streamwise velocity time trace. The normalized shear-layer frequencies are shown in figure 3, together with the results of other experiments (from Prasad & Williamson 1996, 1997). Two lines in figure 3 are $Re^{0.5}$ and $Re^{0.67}$ variations suggested by Bloor (1964) and Prasad & Williamson (1996, 1997), respectively. The shear-layer frequencies of the present study are a little higher than other results, but the difference is acceptable considering the discrepancy between the experiments.

Figure 4 shows the vortical structures near the cylinder at $Re = 1600$. The vortex-identification method by Jeong & Hussain (1995) is used to visualize the three-dimensional vortical structures, where λ_2 is the second

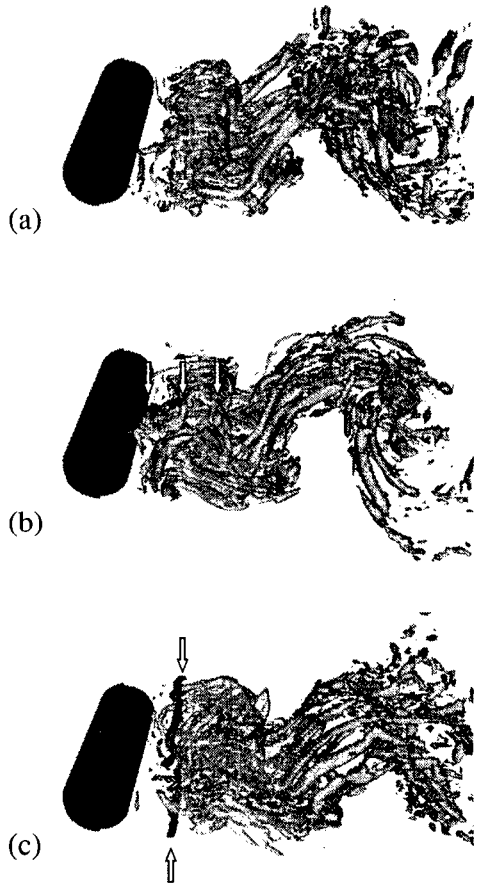


Figure 4. Vortical structures at $Re = 1600$ (iso-surfaces of $\lambda_2 = -10$): (a) no shear layer vortex; (b) 3-D type shear-layer vortices; (c) quasi-2-D type shear-layer vortices.

largest eigenvalue of $S^2 + \Omega^2$ (S and Ω are the strain rate and rotation rate tensors, respectively). Figure 4(a) is instantaneous vortical structures when there is no shear-layer vortex. On the other hand, figures 4(b) and 4(c) show the spanwise roll-up vortices for the cases of 3-D and quasi-2-D instabilities, respectively, from which one can easily figure out the difference between two instabilities. In the case of quasi-2-D type, roll-up of shear-layer vortex occurs throughout the span, whereas the roll-up vortices exist locally in the spanwise direction in the case of 3-D type. Another important difference between the 3-D and quasi-2-D type roll-up vortices is the correlation between the upper and lower shear-layer vortices. The

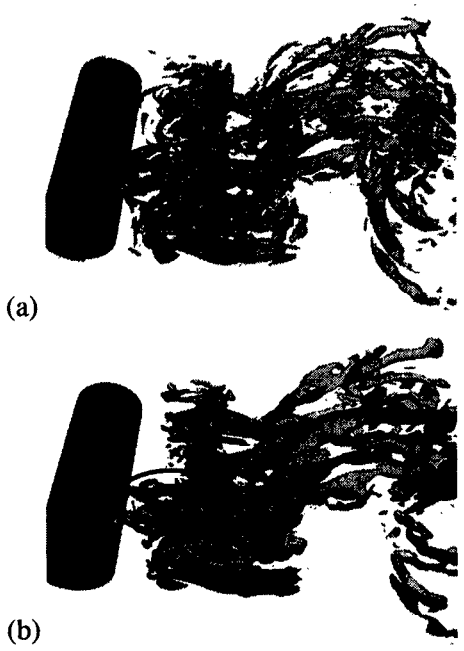


Figure 5. 3-D type shear-layer vortices and streamwise vortices: (a) iso-surface of λ_2 = -10; (b) iso-surfaces of $\omega_x = +10$ (light color) and $\omega_x = -10$ (dark color).

quasi-2-D vortices appear in-phase in the upper and lower shear layers of the cylinder, but for the 3-D type there is no correlation between the upper and lower shear layers. Flow visualization of Prasad & Williamson (1997) shows the in-phase behavior of the shear-layer instability that is analogous to the quasi-2-D instability of the present study. Wei & Smith (1986) used the hydrogen-bubble flow-visualization method and showed several side and top views. Some of the top views are similar to our 3-D instability, although their side views show the configuration similar to the in-phase roll-up. At $Re = 3900$, the shear-layer characteristics are similar to those at $Re = 1600$, although the length scale of vortical structures is smaller at $Re = 3900$.

Figure 5 shows an instantaneous flow structure together with the iso-surfaces of the streamwise vorticity, when the 3-D type vortex roll-up occurs. It is clearly seen that a strong streamwise vortex pair exists underneath the shear layer roll-up vortices of 3-D type. That is, the 3-D instability is locally stimulated by strong streamwise vortices underneath the separated shear layer.

The quasi-2-D instability is closely related to the natural vortex-shedding process. When the natural vortex-shedding process is weakened or disor-

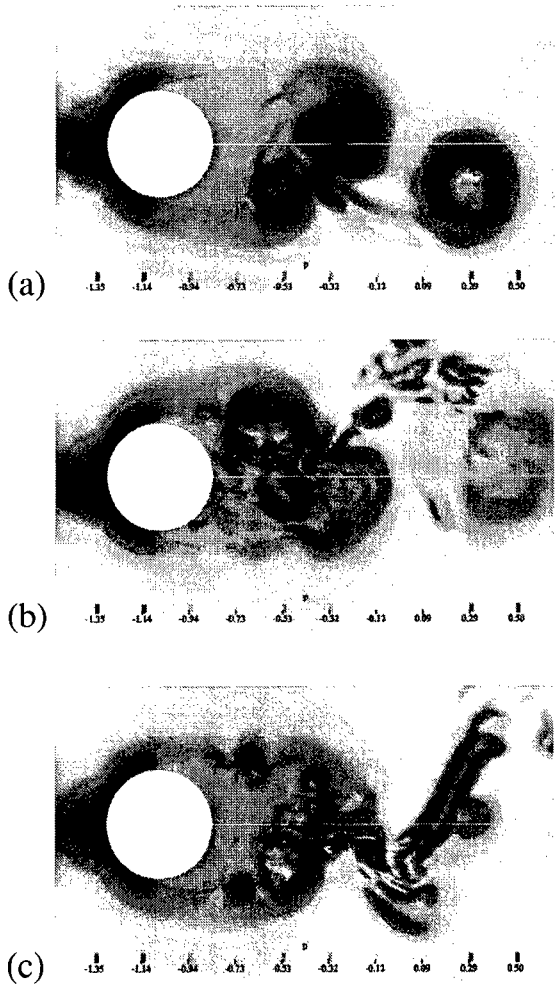


Figure 6. Contours of the instantaneous pressure in an $(x-y)$ plane: (a) regular shedding; (b) corrupted vortex core; (c) quasi-2-D vortex roll-up.

dered due to turbulence, the shear layers both in the upper and lower sides of the cylinder evolve further downstream and thus both the shear layers become thinner and nearly symmetric with respect to each other. When this happens, the quasi-2-D vortex appears in the shear layer and the shear-layer instability occurs at the upper and lower sides simultaneously (in-phase). This process is shown in figure 6. Figure 6(a) shows the instantaneous pressure contours in the case of regular vortex shedding, whereas figure 6(b) shows those in the case of breakdown of the Karman vortex shedding process, resulting in the in-phase roll-up of quasi-2-D shear-layer vortices as shown in figure 6(c).

4. Summary

In summary, two distinct types of the shear-layer instability are found using large eddy simulation for flow over a circular cylinder at $Re = 1600$ and $Re = 3900$. One is the 3-D type instability that is generated locally by a strong counter-rotating streamwise vortex pair. The other instability is the quasi-2-D type instability, characterized by vortex roll-up occurred simultaneously along the spanwise direction as well as at upper and lower sides of the cylinder. This instability is initiated from disorder of the Karman vortex shedding process. It is conjectured that when the Reynolds number is higher than the present ones, the shear-layer thickness should become smaller and the quasi-2-D vortex roll-up is more likely to occur than the 3-D vortex roll-up.

This work is supported by the Creative Research Initiatives of the Korean Ministry of Science and Technology.

References

BLOOR, M. S. 1964 The transition to turbulence in the wake of a circular cylinder. *J. Fluid Mech.* **19**, 290–304.

CHOI, H., MOIN, P & KIM, J. 1992 Turbulent drag reduction: Studies of feedback control and flow over riblets. *Report No.* **TF-55.** Department of Mechanical Engineering, Stanford University

CHOI, H. & MOIN, P. 1994 Effects of the computational time step on numerical solutions of turbulent flow. *J. Comput. Phys.* **113**, 1–4.

GERMANO, M., PIOMELLI, U., MOIN, P. & CABOT, W. 1991 A dynamic subgrid-scale eddy viscosity model. *Phys. Fluids.* **3**, 1760–1765.

JEONG, J. & HUSSAIN, F. 1995 On the identification of a vortex. *J. Fluid Mech.* **285**, 69–94

KRAVCHENKO, A. G. & MOIN, P. 1998 B-spline methods and zonal grids for numerical simulations of turbulent flows. *Report No.* **TF-73.** Department of Mechanical Engineering, Stanford University

LILLY, D. K. 1992 A proposed modification of the Germano subgrid scale closure method. *Phys. Fluids.* **4**, 633–635.

MITTAL, R. & MOIN, P. 1997 Suitability of upwind-based finite difference schemes for large-eddy simulation of turbulent flows. *AIAA J.* **35**, 1415–1417.

NORBERG, C. 1987 Effect of Reynolds number and a low-intensity freestream turbulence on the flow around a circular cylinder. *Publ.* **87/2** Dept. Applied Thermodynamics and Fluid Mechanics, Chalmers University of Technology

PRASAD, A. & WILLIAMSON, C. H. K. 1996 The instability of the separated shear layer from a bluff body. *Phys. Fluids.* **8**, 1347–1349.

PRASAD, A. & WILLIAMSON, C. H. K. 1997 The instability of the shear layer separating from a bluff body. *J. Fluid Mech.* **333**, 375–402.

UNAL, M. F. & ROCKWELL, D. 1988a On vortex shedding from a cylinder: Part 1. The initial instability. *J. Fluid Mech.* **174**, 491–512.

WEI, T. & SMITH, C. R. 1986 Secondary vortices in the wake of a circular cylinder. *J. Fluid Mech.* **169**, 513–533.

LARGE EDDY SIMULATION OF TURBULENT FLOW OVER A SPHERE USING AN IMMERSED BOUNDARY METHOD

DONGJOO KIM AND HAECHEON CHOI
School of Mechanical and Aerospace Engineering
Seoul National University, Seoul 151-742, Korea

Abstract. Large eddy simulation of turbulent flow over a sphere is conducted at two different Reynolds numbers (Re = 3700 and 10^4) based on the free-stream velocity and the sphere diameter, in order to investigate the flow characteristics over the sphere. The present numerical method is based on a newly developed immersed boundary method in a cylindrical coordinate (Kim *et al.* 2001). Also, a hybrid numerical method of eliminating 2-Δ waves in laminar accelerating flow region and also avoiding numerical dissipation in turbulent flow region is newly proposed for large eddy simulation of turbulent flow over a bluff body. At Re = 3700, the shear layer is elongated in the streamwise direction to form a cylindrical vortex sheet and its instability begins to appear at $x \approx 2d$. Also, the flow behind the sphere is nearly laminar at $x < d$ and contains few vortices. On the other hand, at Re = 10^4, the shear layer instability occurs right behind the sphere in the form of vortex tube and the flow becomes turbulent in the near wake. Therefore, at Re = 10^4, the size of the recirculation region is smaller and the wake recovers more quickly than at Re = 3700.

1. Introduction

Flow behind a sphere shows completely unsteady three-dimensional phenomena even at low Reynolds numbers (Sakamoto & Haniu 1990; Johnson & Patel 1999; Mittal 1999). Therefore, flow over a sphere has not been well understood as compared to that over a circular cylinder, even though the sphere geometry is simple. Previous studies on flow over a sphere have been mostly based on experimental methods, where vortical structures behind the sphere were presented using flow visualization and the high and low frequency characteristics in the shear layer, respectively, associated with the shear layer instability and the wake instability were investigated (Sakamoto

& Haniu 1990). When the Reynolds number exceeds about 800, the wake flow behind a sphere changes from laminar to turbulent flow. In recent years, a few numerical studies have been made on turbulent flow over a sphere (Tomboulides 1993; Constantinescu & Squires 2000). However, the detailed quantitative information on the turbulence statistics behind the sphere is still limited in the literature.

The objective of the present study is to investigate the characteristics of turbulent flow over a sphere using large eddy simulation at two different Reynolds numbers of 3700 and 10^4 based on the free-stream velocity u_∞ and the sphere diameter d.

2. Numerical Method

The present numerical method is based on a newly developed immersed boundary method in a cylindrical coordinate (Kim *et al.* 2001), where the sphere in the flow is treated as momentum forcing in the Navier-Stokes equations. Therefore, flow over the sphere can be easily handled with orthogonal (cylindrical) grids that do not coincide with the body surface. Numerical simulations are performed at two different Reynolds numbers of $\mathrm{Re} = u_\infty d/\nu = 3700$ and 10^4. The computational domain used is $-15d \le x \le 15d$, $0 \le r \le 15d$, $0 \le \theta \le 2\pi$, and the number of grid points is $577(x) \times 141(r) \times 40(\theta)$. Here, x, r and θ, respectively, denote the streamwise, radial and azimuthal directions. A Cartesian coordinate system (x, y, z) is also defined in order to present the drag and lift forces, where the y and z coordinates coincide with $\theta = 0^o$ and $\theta = 90^o$, respectively.

One of the important issues for large eddy simulation of turbulent flow over a bluff body at high Reynolds number is that the second-order central difference scheme produces serious dispersion errors for convection-dominated flow, and thus 2-Δ waves appear in the region of velocity acceleration (for example, at front surface of a sphere). To resolve this problem, two different approaches have been taken: One is to apply a filtering procedure which corresponds to adding numerical dissipation in an *ad hoc* manner, and the other is to use upwind or upwind-biased schemes. In these approaches, however, the numerical dissipation becomes larger than the dissipation from the subgrid-scale viscosity (Beaudan & Moin 1994).

In this study, we propose a hybrid approach for the spatial discretization of the convection terms for flow over a bluff body, where a high-order upwind scheme is used in the region of laminar accelerating flow and the second-order central difference scheme is used elsewhere. The diffusion terms are discretized with the second-order central difference scheme. With this approach, we can avoid possible contamination of solutions resulting from the application of the dissipative schemes to the whole flow field.

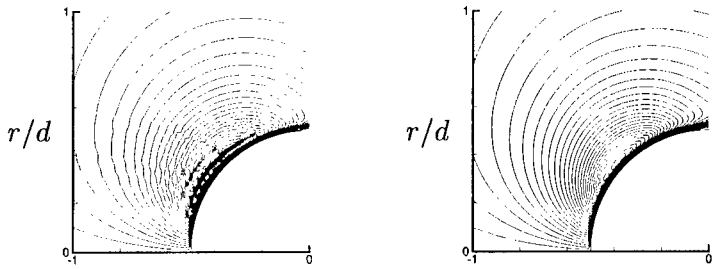


Figure 1. Contours of the instantaneous radial velocity in front of the sphere at Re = 3700: (a) second-order central difference scheme (CD); (b) hybrid scheme (CUDZ3+CD).

For the high-order upwind scheme, we use the third-order compact upwind scheme (CUDZ3) by Zhong (1998), which is stable and less dissipative than the straightforward compact upwind scheme using an upwind-biased grid stencil (Tolstykh 1994). For the flow over a sphere, we apply CUDZ3 to the laminar accelerating flow region ($x < 0$ and $r < d$).

Figure 1 shows the contours of the instantaneous radial velocity in front of the sphere at Re = 3700 using two different numerical schemes. Figure 1 (a) is obtained from the second-order central difference scheme (CD) applied to the whole flow field, whereas figure 1 (b) is from the hybrid scheme proposed in the present study. It is clear that the present hybrid scheme effectively removes the wiggles appeared in figure 1 (a). Therefore, all the following results presented in this paper are obtained using the hybrid scheme.

3. Results

The simulation results are summarized in table 1, where time-averaged drag coefficient ($\bar{C}_d$), base pressure coefficient ($\bar{C}_{p_b}$), separation angle ($\bar{\alpha}_s$), recirculation bubble size ($\bar{L}$), and Strouhal number (St) associated with the wake instability are presented together with experimental and computational data available. Here, LES and DES denote large eddy simulation and detached eddy simulation, respectively, and DES is a hybrid approach reducing to Reynolds-averaged Navier-Stokes (RANS) near the wall and LES away from the wall. The recirculation bubble size ($\bar{L}$) is the distance from the base of the sphere to the point where the time-averaged streamwise velocity is zero. The drag coefficient, base pressure coefficient, Strouhal number and separation angle are in reasonably good agreement with the

	Re	$\bar{C}_d$	$\bar{C}_{p_b}$	St	$\bar{\alpha}_s$	$\bar{L}/d$
Present	3700	0.36	-0.20	0.22	90^o	2.60
	10^4	0.40	-0.28	0.18	90^o	1.34
Exp^1	3700			0.22		
	4200		-0.23			
	10^4			0.16		
Exp^2	3700			0.21		
	10^4			0.18		
$Comp^1$ (LES)	10^4	0.393		0.195	$84^o - 86^o$	
(DES)	10^4	0.397		0.200	$84^o - 87^o$	

TABLE 1. Flow parameters of turbulent flows over a sphere. Exp^1, Kim & Durbin (1988); Exp^2, Sakamoto & Haniu (1990); $Comp^1$, Constantinescu & Squires (2000). Here, *Exp* and *Comp* denote experimental and computational studies, respectively.

previous results. $\bar{C}_d$ at Re = 3700 is smaller than that at Re = 10^4 in this study, which is closely related to the fact that the base pressure coefficient is larger at Re = 3700. It is interesting to note that even though the separation angle is the same for both Reynolds numbers, the recirculation bubble size at Re = 3700 is about twice that at Re = 10^4. This is closely associated with the characteristics of the separating shear layer, which is explained in the following.

Figure 2 shows the contours of the instantaneous azimuthal vorticity at Re = 3700 and 10^4 on the (x, y)-plane. At Re = 3700, the separating shear layer is elongated in the streamwise direction to form a cylindrical vortex sheet and its instability begins to appear at $x \approx 2d$. On the other hand, at Re = 10^4, the shear layer instability appears right behind the sphere. Note that the flow behind the sphere ($x < d$) at Re = 3700 contains few vortices, whereas at Re = 10^4 many small-scale vortices exist right behind the sphere. Therefore, at Re = 3700, the base pressure is higher and the drag coefficient is smaller than at Re = 10^4. Because strong vortical motion exists at $x \approx 2d$ for Re = 3700, the lift fluctuations are much smaller than those at Re = 10^4. Due to early onset of the shear layer instability and strong vortical motions in the near wake at Re = 10^4, the size of the recirculation region at Re = 10^4 is much smaller than that at Re = 3700.

For clear understanding of the three-dimensional structures in the near wake, vortical structures are drawn in two different ways in figure 3, where vortical surfaces are identified using the method of Jeong & Hussain (1995).

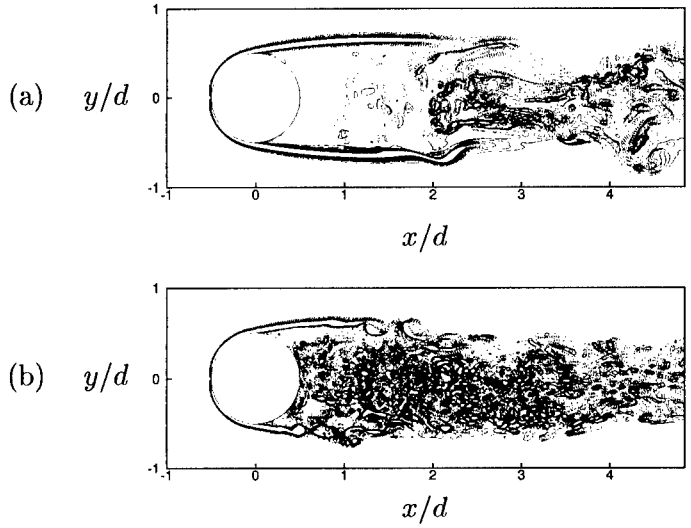


Figure 2. Contours of the instantaneous azimuthal vorticity: (a) Re = 3700; (b) Re = 10^4.

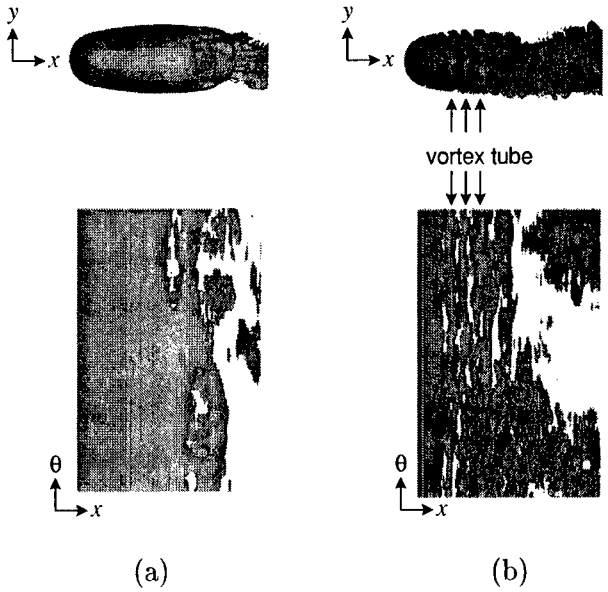


Figure 3. Vortical structure in the near wake: (a) Re = 3700; (b) Re = 10^4. In bottom figures, vortical surfaces are unfolded in the azimuthal direction.

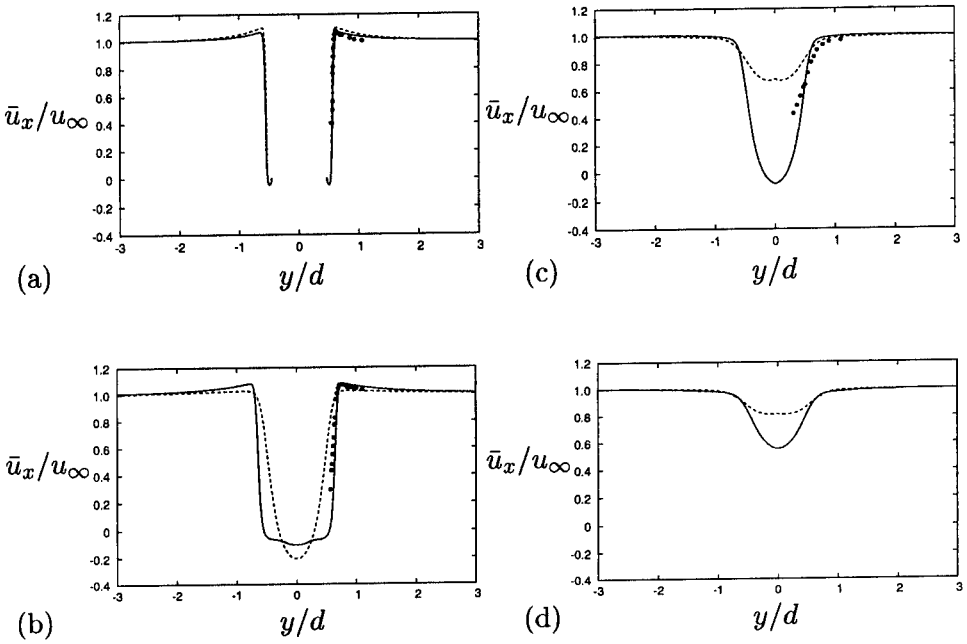


Figure 4. Streamwise velocity averaged in time and azimuthal direction: (a) $x/d = 0.2$; (b) $x/d = 1.6$; (c) $x/d = 3.0$; (d) $x/d = 4.0$. ———, Re = 3700 (present study); – – –, Re = 10^4 (present study); •, Re = 3700 (Kim & Durbin 1988).

That is, top figures are the projection of vortical surfaces on the (x, y)-plane, whereas in bottom figures the vortical surfaces are unfolded in the azimuthal direction. At Re = 3700, the vortex sheet of the shear layer is broken away locally in the azimuthal direction. However, at Re = 10^4, the vortex sheet is broken away along the azimuthal direction to form vortex tubes. The term of vortex tube was defined by Sakamoto & Haniu (1990) as the cylindrical vortex shed from the vortex sheet separated from the sphere surface.

Figure 4 shows the streamwise velocities averaged in time and azimuthal direction at Re = 3700 and 10^4. The present results at Re = 3700 are in good agreement with those of single-wire measurements by Kim & Durbin (1988) at $x/d = 0.2$, 1.6 and 3.0. A difference is observed at $x = 3.0d$ because the measurement error of a single-wire probe becomes large near the end of the recirculation region, where the magnitude of the radial velocity is comparable to that of the streamwise velocity and thus the flow angle approaching the wire is not small. It is clear that the wake at Re = 10^4 recovers more quickly than that at Re = 3700.

Figures 5 shows the contours of the Reynolds shear stresses $(-\overline{u'_x u'_r}/u_\infty^2)$

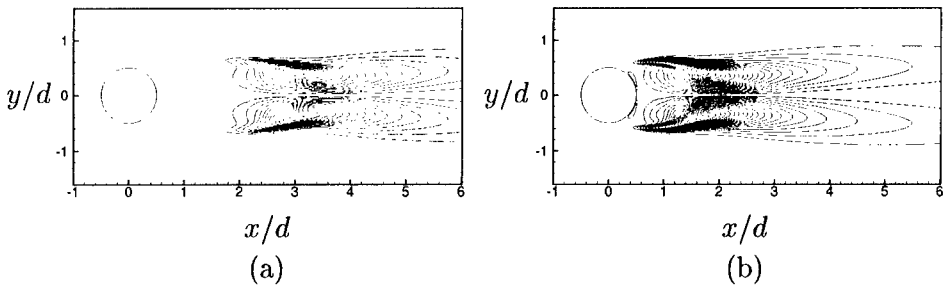


Figure 5. Contours of the Reynolds shear stress ($-\overline{u_x' u_r'}/u_\infty^2$) in the near wake: (a) Re = 3700; (b) Re = 10^4.

in the near wake at Re = 3700 and 10^4, where the shear stress is averaged in time and azimuthal direction. The Reynolds shear stress as well as the normal stresses (not shown here) are zero up to the separation point ($\alpha_s = 90^o$) for both Reynolds numbers, showing that the boundary layer flow before separation is laminar. It is clear that the transition of the wake to turbulence occurs right behind the sphere at Re = 10^4, whereas at Re = 3700 the transition occurs far downstream ($x \approx 2d$). This phenomenon is closely related to different onset of the shear layer instability between two Reynolds numbers.

4. Summary

In summary, the flow characteristics between two Reynolds numbers of Re = 3700 and 10^4 are quite different. At Re = 3700, the shear layer is elongated in the streamwise direction to form a cylindrical vortex sheet and its instability begins to appear at $x \approx 2d$. On the other hand, at Re = 10^4, the shear layer instability occurs right behind the sphere in the form of vortex tube and the flow becomes turbulent in the near wake. Note that the flow behind the sphere ($x < d$) at Re = 3700 is nearly laminar and contains few vortices. Therefore, at Re = 3700, the base pressure is higher and the drag coefficient is smaller than at Re = 10^4. Because the vortices exist at $x \simeq 2d$ for Re = 3700, the lift fluctuations are much smaller than those at Re = 10^4. At Re = 10^4, mixing in the near wake is much stronger than that at Re = 3700, and thus the wake recovers more quickly.

This work is supported by the Creative Research Initiatives of the Korean Ministry of Science and Technology.

References

BEAUDAN, P. & MOIN, P. 1994 Numerical experiments on the flow past a circular cylinder at sub-critical Reynolds number. *Report No. TF-62*, Department of Mechanical Engineering, Stanford University.

CONSTANTINESCU, G. S. & SQUIRES, K. D. 2000 LES and DES investigations of turbulent flow over a sphere. *AIAA paper 2000-0540.*

JEONG, J. & HUSSAIN, F. 1995 On the identification of a vortex. *J. Fluid Mech.* **285**, 69–94.

JOHNSON, T. A. & PATEL, V. C. 1999 Flow past a sphere up to a Reynolds number of 300. *J. Fluid Mech.* **378**, 19–70.

KIM, H. J. & DURBIN, P. A. 1988 Observations of the frequencies in a sphere wake and of drag increase by acoustic excitation. *Phys. Fluids* **31**, 3260–3265.

KIM, J., KIM, D. & CHOI, H. 2001 An immersed-boundary finite volume method for simulations of flow in complex geometries. *J. Comput. Phys.* **171**, 132–150.

MITTAL, R. 1999 Planar symmetry in the unsteady wake of a sphere. *AIAA J.* **37**, 388–390.

SAKAMOTO, H. & HANIU, H. 1990 A study on vortex shedding from spheres in a uniform flow. *J. Fluid Eng.* **112**, 386–392.

TOLSTYKH, A. I. 1994 High accuracy non-centered compact difference schemes for fluid dynamics applications. World Scientific, Singapore.

TOMBOULIDES, A. 1993 Direct and large-eddy simulation of wake flows: flow past a sphere. Ph.D. dissertation, Princeton University

ZHONG, X. 1998 High-order finite-difference schemes for numerical simulation of hypersonic boundary-layer transition. *J. Comput. Phys.* **144**, 662–709.

LARGE EDDY SIMULATION OF TRANSONIC TURBULENT FLOW OVER AN AIRFOIL USING A SHOCK CAPTURING SCHEME WITH ZONAL EMBEDDED MESH

ICHIRO NAKAMORI AND TOSHIAKI IKOHAGI
Institute of Fluid Science
Tohoku University, Sendai, Japan

Abstract

In this study, large eddy simulation(LES) of transonic flow around the NACA 0012 airfoil is performed accounting for the Leonard stress terms, the cross–stress terms and the subgrid–scale(SGS) Reynolds stress terms as the scale–similarity model at a free stream Mach number of 0.8, a Reynolds number of 9×10^6 and an angle of attack of 2.26°. An upwind finite volume formulation is used for the discretization of compressible spatial–filtered Navier–Stokes equations. To exclude excessive numerical damping due to the shock–capturing scheme, a hybrid method which uses linear combination of the third–order upwind scheme and the TVD scheme is employed. To reduce the total number of grid points, zonal embedded mesh is employed in the present LES analysis, in which a computational domain is decomposed near the wall–boundary. In the case represented here, it is shown that the statistical values in the turbulent boundary layer with shock/turbulence interaction is able to be estimated, and characteristics are clarified on the statistic of the turbulence.

1. Introduction

The analyses of unsteady flow on aircraft and fluid machinery in the transonic speed region will be required in future. With the recent development of the super–computer, LES will be used for such complicated flow field in future. Since the present LES analysis needs a shock-capturing scheme in the transonic region, it is required to investigate the effect of the inherent numerical dissipation on LES. Referring to third–order accurate shock–capturing scheme, the third order numerical viscosity is dominant in the smooth region, whereas the first–order viscosity is dominant in the region where the discontinuity appears. The numerical dissipation due to the third–order numerical viscosity is investigated by applying the fourth-order central scheme with the third-order numerical viscosity to the turbulent channel flow. As the results, the third-order viscosity with appropriate coefficient is found to be substituted in the Smagorinsky model on its SGS dissipation rate. Then, in this study, eddy viscosity SGS model is not used explicitly, and the third–order accurate scheme is used to substitute the SGS dissipation with the appropriate artificial viscosity coefficient. The analysis is carried out taking the sum of the Leonard stress terms, the cross–stress terms, and the SGS Reynolds stress terms as the scale–similarity model into account on the curvilinear coordinates. Still, the inviscid numerical flux is estimated by combining

the third–order scheme with the TVD scheme in order to stabilize the solution near the discontinuities.

A single structured grid is not suitable for LES at flight Reynolds numbers, since the viscous sublayer needs the very fine resolution in all directions(Chapman, 1979). As the result, the structured grid has numerous grid points throughout the domain. On the other hand, the unstructured grid is efficient to avoid the unnecessarily grid resolution for much of the computational domain(Jansen, 1999). The reduction of total number of grid points can be realized by the embedded mesh system. In this study, we have chosen the embedded mesh system to solve, because of the following points: 1) the number of grid points can be reduced in the spanwise and streamwise direction, 2) the computational efficiency is almost the same per unit cell in comparison with the efficiency in a single structured mesh system, and 3) it is comparatively effortless to improve the spatial accuracy.

2. LES Methodology

In this section, we summarize the LES methodology, including governing equations, SGS model, descritizing formula and numerical implementation.

2.1. GOVERNING EQUATIONS

The governing equations are the spatially filtered compressible Navier-Stokes equations. The spatial filtering removes the small–scale components of the fluid motion, retaining the unsteadiness associated with the large–scale turbulent motion. For an arbitrary function f, $\bar{f}$ represents space–filtered variable. For compressible flows, it is expedient to define the Favre filtered variable $\tilde{f}$. Applying these definitions to the compressible Navier–Stokes equations, we obtain the filtered governing equations

$$\frac{\partial \bar{\rho}}{\partial t} + \frac{\partial \bar{\rho}\tilde{u}_i}{\partial x_i} = 0, \tag{1}$$

$$\frac{\partial \bar{\rho}\tilde{u}_i}{\partial t} + \frac{\partial(\bar{\rho}\tilde{u}_i\tilde{u}_j + \delta_{ij}\bar{p} - \bar{\sigma}_{ij})}{\partial x_j} = -\frac{\partial \tau_{ij}}{x_j}, \tag{2}$$

$$\frac{\partial \bar{e}}{\partial t} + \frac{\partial(\bar{e}+\bar{p})\tilde{u}_j - \bar{\sigma}_{lj}\tilde{u}_l - \kappa\frac{\partial \tilde{T}}{\partial x_j}}{\partial x_j} = -\frac{\partial(q_j + d_j)}{x_j}, \tag{3}$$

$$\bar{p} = \bar{e} - \frac{\bar{\rho}}{2}\tilde{u}^2 - \frac{\bar{\rho}}{2}\tau_{ii}, \tag{4}$$

where x_i represents the Cartesian coordinates(i=1, 2, 3), $\bar{\rho}$ is the mean density, $\tilde{u}_i$ are the Cartesian components of the filtered velocity, $\bar{p}$ is the mean pressure, τ_{ij} is the subgrid scale stress tensor, σ_{ij} is the molecular stress tensor, $\bar{e}$ is the filtered total energy per unit volume, q_j is the subgrid heat flux, and d_j is the energy diffusion by the subgrid stresses. We neglect the summation term τ_{ii} in the equation of state, which would be very small compared to the thermodynamic pressure $\bar{p}$.

2.2. DESCRITIZATION

The governing equations can be descritized in finite volume method for a control volume V with surface ∂V:

$$\frac{\partial}{\partial t}\int_V Q dV + \int_{\partial V}(E_1 n_{11} + E_2 n_{12} + E_3 n_{13})dA = 0, \tag{5}$$

where

$$Q = \begin{bmatrix} \bar{\rho} \\ \bar{\rho}\tilde{u}_i \\ \bar{e} \end{bmatrix}, \; E_i = \begin{bmatrix} \bar{\rho}\tilde{u}_i \\ \bar{\rho}\tilde{u}_i\tilde{u}_j + \delta_{ij}\bar{p} - \bar{\sigma}_{ij} + \tau_{ij} \\ \bar{\rho}\tilde{u}_i\tilde{h}_t - \kappa\frac{\partial\tilde{T}}{\partial x_i} - \bar{\sigma}_{ij}\tilde{u}_i + q_i + d_i \end{bmatrix}. \tag{6}$$

$(n_{11}, n_{12}, n_{13})^t$ denotes the normal vector to each cell-interface. The explicit Runge-Kutta method is employed for the time integration. The third-order numerical inviscid flux $f^{(3rd)}_{i+1/2}$ is estimated by using the fourth-order central scheme and the additional third-order dissipation.

$$f^{(3rd)}_{i+1/2} = f^{(4th)}_{i+1/2} + \varepsilon_4(R|\Lambda|)_{i+1/2}(\alpha_{i+3/2} - 2\alpha_{i+1/2} + \alpha_{i-1/2}), \tag{7}$$

$$f^{(4th)}_{i+1/2} = f^{(4th)}_{i+1/2}(Q^L_{i+1/2}, Q^R_{i+1/2}), \tag{8}$$

$$\alpha_{i+1/2} = R^{-1}_{i+1/2}\Delta_{i+1/2}Q, \tag{9}$$

where R and Λ represent the diagonalization matrix of the right eigenvectors and the diagonal matrix of the eigenvalues, respectively. The values of each variables on either side of cell interfaces are

$$Q^L_{i+1/2} = Q_i + \frac{1}{12}(\Delta_{i-1/2}Q + 6\Delta_{i+1/2}Q - \Delta_{i+3/2}Q),$$

$$Q^R_{i-1/2} = Q_i - \frac{1}{12}(\Delta_{i+1/2}Q + 6\Delta_{i-1/2}Q - \Delta_{i-3/2}Q). \tag{10}$$

The values of artificial viscosity coefficient ε_4 is calibrated at $1/256$ in the airfoil simulation.

The method mentioned above cannot treat the transonic flow, since the shock wave appears. Then, the numerical flux $f^{TVD}_{i+1/2}$ is differently prepared by using a finite difference splitting(Roe, 1981) and extrapolated variables $\bar{Q}^{R/L}_{i\pm1/2}$ with a slope-limiter(Daiguji *et al.*, 1997). To exclude excessive numerical damping due to the limiter, we employ self-adjusting hybrid, that uses linear conbination of the third-order upwind scheme and the TVD scheme. the numerical flux $f_{i+1/2}$ is blended as follows:

$$f_{i+1/2} = (1-\theta)f_{i+1/2}{}^{(3rd)} + \theta f^{TVD}_{i+1/2}, \tag{11}$$

$$\theta = \begin{cases} 0, & \text{for } \frac{|\bar{\rho}_{i+1} - 2\bar{\rho}_i + \bar{\rho}_{i-1}|}{\bar{\rho}_{i+1} + 2\bar{\rho}_i + \bar{\rho}_{i-1}} \le 0.01 \\ 1, & \text{for } \frac{|\bar{\rho}_{i+1} - 2\bar{\rho}_i + \bar{\rho}_{i-1}|}{\bar{\rho}_{i+1} + 2\bar{\rho}_i + \bar{\rho}_{i-1}} > 0.01 \end{cases}. \tag{12}$$

2.3. SGS MODEL

SGS stresses can be decomposed into the following terms(Leonard, 1974):

$$\tau_{ij} = L_{ij} + C_{ij} + R_{ij}, \tag{13}$$

the Leonard stress terms, $L_{ij} = \bar{\rho}(\widetilde{\tilde{u}_i\tilde{u}_j} - \tilde{u}_i\tilde{u}_j)$; the cross-stress terms, $C_{ij} = \bar{\rho}(\widetilde{\tilde{u}_i u'_j} + \widetilde{u'_i\tilde{u}_j})$; and the SGS Reynolds stress terms, $R_{ij} = \bar{\rho}\widetilde{u'_i u'_j}$. Present study follows the hypothesis that

the SGS energy dissipation would be substituted in the numerical dissipation due to the inherent artificial viscosity of the shock-capturing scheme. Consequently, the eddy viscosity model was not employed in the present LES analyses. However, a scale–similarity model is taken into account. They can be estimated using Taylor expansion. To eliminate the terms which violate the Galilean invariance(Speziale, 1985), these terms are summated with the Bardina model(Bardina *et al.*, 1980) being applied to the cross–stress terms and the SGS Reynolds stress terms.

$$\begin{aligned} L_{ij} + C_{ij} + R_{ij} &\approx \bar{\rho}(\widetilde{\tilde{u}_i\tilde{u}_j} - \tilde{\tilde{u}}_i\tilde{\tilde{u}}_j) \\ &= \frac{\bar{\rho}}{12}\Delta_k^2 \frac{\partial \tilde{u}_i}{\partial x_k}\frac{\partial \tilde{u}_j}{\partial x_k} + O(\Delta_k^4) \end{aligned} \tag{14}$$

For the SGS terms q_j and d_j in energy equation, the following models are employed by approximating $u_j \cong \tilde{u}_j$ and $T \cong \tilde{T}$.

$$\begin{aligned} q_j &= C_p\bar{\rho}(\widetilde{u_jT} - \tilde{u}_j\tilde{T}) \cong C_p\bar{\rho}(\widetilde{\tilde{u}_j\tilde{T}} - \tilde{\tilde{u}}_j\tilde{\tilde{T}}) \\ &= \frac{C_p}{12}\Delta_k^2 \frac{\partial \tilde{T}}{\partial x_k}\frac{\partial \tilde{u}_j}{\partial x_k} + O(\Delta_k^4), \end{aligned} \tag{15}$$

$$\begin{aligned} d_j &= \frac{1}{2}\bar{\rho}(\widetilde{u^2u_j} - \widetilde{u^2}\tilde{u}_j) \\ &\cong \frac{\bar{\rho}}{24}\Delta_k^2 \frac{\partial \tilde{u}_i}{\partial x_k}\frac{\partial \tilde{u}_i}{\partial x_k}\tilde{u}_j + \frac{\bar{\rho}}{24}\Delta_k^2 \frac{\partial \tilde{u}^2}{\partial x_k}\frac{\partial \tilde{u}_j}{\partial x_k} + O(\Delta_k^4), \end{aligned} \tag{16}$$

where a perfect gas with a constant specific heat capacity C_p is assumed.

3. Results and Discussion

3.1. CODE VALIDATION

A validation test for the shock–capturing is performed for the shock tube problem(Shu *et al.*, 1989), which has several extrema in the smooth region. Figure 1 shows the solution via the present method with 400 cells. For the comparison, we have included the line of solution via the 8th-order ENO scheme(Harten, 1989) with 1600 cells. Note that there is no serious overshooting or undershooting neat the discontinuity. This fact shows that the present method is suitable for LES with strong discontinuities.

A validation test for large eddy simulation is carried out by applying the present method to the channel flow. The analyses are performed for the turbulent plane Couette flow of $8.0h\times2.0h\times4.0h$ at $Re(\frac{\rho_w U_w h}{\mu_w}) = 1300$ and thc Mach number $M(\frac{U_w}{c_w}) = 0.3$. Thc number of cells is (64,64,32) with the size of cells in the wall coordinate varying from 1 to 1.4 wall units. Figure 2 shows the mean velocity profiles via the TVD scheme and the present method. The ensemble data are obtained from the averaged flow over 100000 time steps. We have included incompressible DNS results(Bech *et al.*, 1995) for the comparison. The artificial coefficient ε_4 is calibrated at 1/256, that is also used in the present airfoil simulation. In this case, the hybridization of the scheme is absolutely necessary since the inherent numerical dissipation due to the flux-limiter of the TVD–scheme becomes dominant.

In Fig. 3 we show the mean velocity profiles with and without the SGS models for the same channel flow. We have included the root mean square (*rms*) of the velocity

components in Fig. 4. The predictions in all *rms* quantities, especially the streamwise component, are of great improvement by using the present SGS models, although a little bit greater artificial coefficient ε_4 of 1/128 is taken to produce more dissipative solution compared to the DNS results.

3.2. AIRFOIL SIMULATION

The flow configuration is that of experiments(Harris, 1981) at a Reynolds number based on chord $Re = 9 \times 10^6$, a free-stream Mach number $M = 0.8$, and an angle of attack $\alpha = 2.26°$. A single structured grid system makes it difficult to perform LES for the flow of the present Reynolds number. The use of embedded mesh reduces the computational memory and the CPU to some extent. The mesh size is refined near the wall and the mesh system is replaced 6 times toward the wall surface regarding the streamwise direction and the spanwise direction so that the large eddy can be resolved, as shown in Fig. 5. The extent of spanwise direction is chosen as $L_z = 0.04c$. Current simulation employs approximately 11 million cells.

Figure 6 shows the instantaneous Mach number distribution in the mid-span plane. On the suction side, the shock wave appears at about 60% of the chord length from the leading edge. It is found that there is no serious numerical oscillation near the shock wave. Figure 7 shows the isosurfaces of instantaneous spanwise velocity $\tilde{w}$ on the suction side. Weak three-dimensionalization occurs, and secondary flow is formed(Fig. 8). It is also shown that the three-dimensionalized structure becomes larger, as it goes to the trailing edge, as shown in Fig. 9. The increase of the friction coefficient can be also confirmed with the relation to the three-dimensionalization. In Fig. 10, we show the friction coeficient, which increases at about 5% of the chord length from the leading edge on the suction side where the transition takes place naturally.

Figure 11 shows mean wall pressure distribution, which almost agrees with the experimental result, however there is a little discrepancy of the shock position between the simulation and the experimental data. The aspect of the pressure distribution under the influence of adverse pressure gradient by the shock wave is predicted so as to produce the B. L. separation more extensively.

Figures 12 and Fig. 13 show the turbulence energy profiles on the pressure side and the suction side, respectively. The distance from the wall is represented by η. On the suction side, the turbulence energy rises ($x/c = 0.7$) behind the shock wave, while it contrastively decreases downstream the position of ($x/c = 0.4$) on the pressure side.

The spanwise one-dimensional energy spectrum distribution is examined in order to understand whether it reproduces the energy cascade process in the turbulent boundary layer. The energy spectrum is defined as,

$$E_{i,i}(k) = \frac{2}{\pi} \int_0^\infty R_{i,i}(r) e^{-ikr} dr, \tag{17}$$

where $R_{i,i}$ represents the correlation tensor given by

$$R_{i,i}(r) = < u_i'(x) u_i'(x+r) > . \tag{18}$$

u_i' is approximated by using the grid-scale differences $\tilde{u_i} - < \tilde{u_i} >$. r is in spanwise direction in this case. Figure 14 shows the spanwise one-dimensional energy spectra of the velocity at $y^+ \cong 10$. It is confirmed that the energy cascade with the close gradient of the 5/3 law in the sampling point ($x/c = 0.4, 0.7$) is obtained.

4. Conclusions

The scale–similarity models are taken into account in the generalized curvilinear coordinate system in order to represent the SGS effect which includes the backscatter in the energy cascade in turbulent boundary layer. To keep the resolution of the near wall turbulence, the embedded mesh system is employed in this study. Also, an highly accurate scheme is obtained in order to capture generation of the turbulent boundary layer from the leading edge and its developing process. Concurrently, the present hybridization of the scheme produces no serious oscillation near the shock wave in the present simulation. As a result of applying the present method to transonic turbulent flow around the airfoil, it is possible to reproduce the flow field with large–scale structure of the turbulent boundary layer. It is found that the qualitative analysis is possible on the turbulent characteristics, that includes the interaction with shock wave by the present LES method.

5. Acknowledgement

The simulations were performed using the super–computer, SX–5 in the Institute of Fluid Science, Tohoku University.

References

Bardina, J., Ferziger, J. H. and Reynolds, W. C. (1980) Improved subgrid scale models for large eddy simulation. AIAA Paper 80–1357

Bech, K., Tillmark, H., Alfredsson, N. and Andersson, H. I. (1995) Investigation of turbulent plane Couette flow at low Reynolds number. *J. Fluid Mech.* **286**, pp. 291–325

Boris, J. P., Grinstein, F. F., Oran, E. S. and Kolbe, R. L. (1992) New insights into large eddy simulation. *Fluid Dynam. Res.* **10**, pp. 199–228

Chapman, D. R. (1979) Computational aerodynamics development and outlook. *AIAA J.* **17**, pp. 1293–1313

Clark, R. A., Ferziger, J. H. and Reynolds, W. C. (1979) Evaluation of subgrid–scale models using an accurately simulated turbulent flow. *J. Fluid Mech.* **91**, pp. 1–16

Daiguji, H., Yuan, X. and Yamamoto, S. (1997) Stabilization of higher–order high resolution schemes for the compressible Navier–Stokes equations. *Numer. Meth. Heat. !u Fluid Flow* **7**, pp. 250–274

Garnier, E., Mossi, M., Sagaut, P., Comte, P. and Deville, M. (1999) On the use of shock–capturing schemes for large–eddy simulation. *J. Comp. Phys.* **153**, pp. 273–311

Harris, C. D. (1981) Two-dimensional aerodynamic characteristics of the NACA 0012 airfoil in the Langley 8–foot transonic pressure tunnel. NASA TM 81927

Harten, A. (1989) ENO schemes with subcell resolution. *J. Comp. Phys.* **83**, pp. 148–184

Jansen, K. E. (1999) A stabilized finite element method for computing turbulence. *Comp. Meth. in Appl. Mech. and Eng.* **174**, pp. 299–317

Leonard, A. (1974) On the energy cascade in large eddy simulations of turbulent fluid flows. *Adv. Geophys.* **18A**, pp. 237–248

Moin, P. and Jimenez, J. (1993) Large eddy simulations of complex turbulent flows. *AIAA Paper–03–3099*

Roe, P. L. (1981) Approximate Riemann solvers, parameter vectors and difference schemes. *J. Comp. Phys.* **43**, pp. 357–372

Shu, C–W. and Osher, S. (1989) Efficient implementation of essentially non-oscillatory shock–capturing schemes. *J. Comp. Phys.* **83**, pp. 32–78

Speziale, C. G. (1985) Galilean invariance of subgrid-scale stress models in the large eddy simulation of turbulence. *J. Fluid Mech.* **156**, pp. 55–62

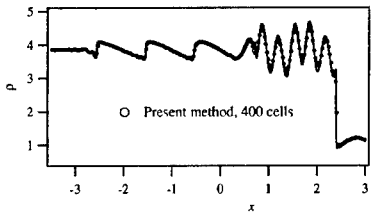


Figure 1. Code verification for the shock– capturing

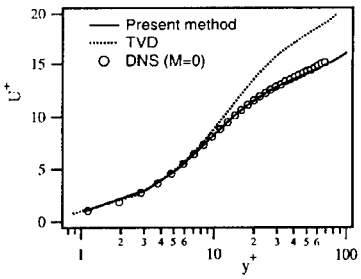


Figure 2. Code verification for the channel turbulent flow

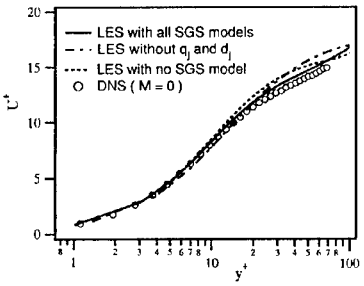


Figure 3. Model verification for the channel turbulent flow

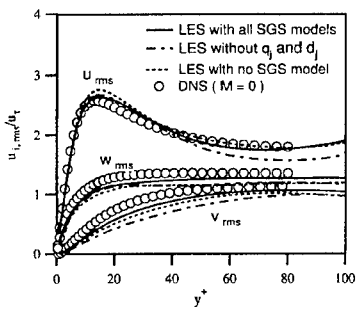


Figure 4. Model verification for the channel turbulent flow

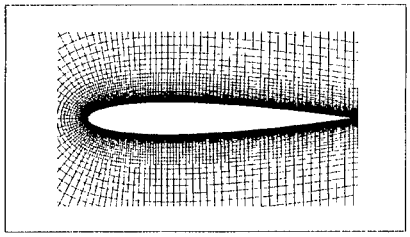


Figure 5. Side view of embedded mesh around the NACA0012 airfoil

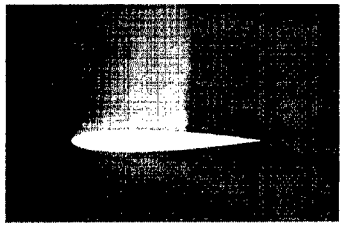


Figure 6. Side view of instantaneous Mach number contours

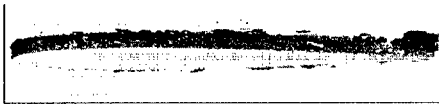


Figure 7. Isosurfaces of spanwise velocity

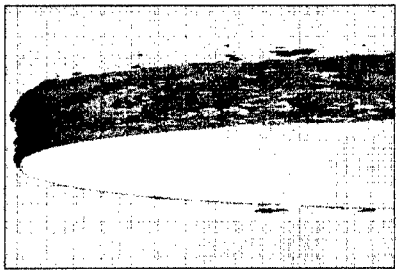


Figure 8. Isosurfaces of spanwise velocity near the leading edge

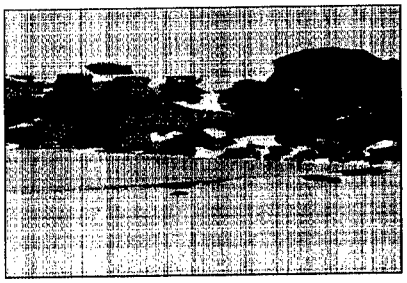


Figure 9. Isosurfaces of spanwise velocity near the trailing edge

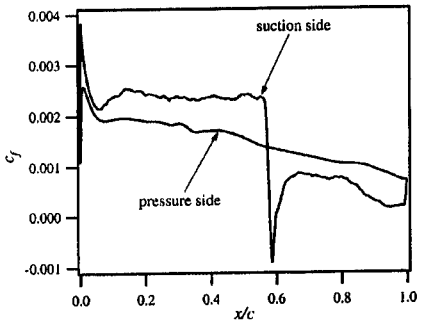


Figure 10. Skin friction distribution

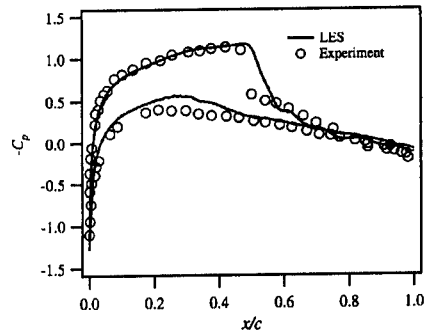


Figure 11. Wall pressure distribution

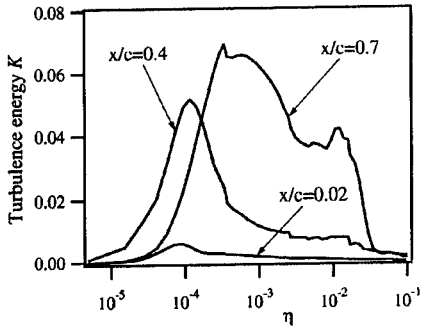


Figure 12. Turbulence energy profiles on the suction side

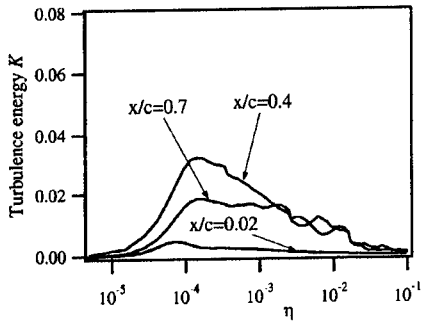


Figure 13. Turbulence energy profiles on the pressure side

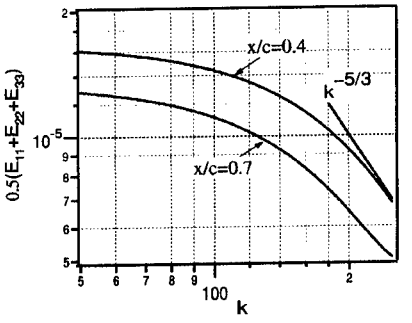


Figure 14. Spanwise one dimensional energy spectra on the pressure side at $y^+ \simeq 10$

NUMERICAL STUDY ON POLLUTANT DISPERSION IN URBAN STREET CANYON

GUIXIANG CUI, YI LIU, XUELING CHENG, ZHAOSHUN ZHANG
Department of Engineering Mechanics
Tsinghua University, Beijing, China

Abstract

The dispersion of car exhaustion in street canyon is studied by LES and unsteady RANS. Both velocity field and distribution of pollutant concentration are computed. The influence of the geometry of building blocks on the pollution is investigated.

1. Introduction

The prediction of the pollutant dispersion is of great significance for the air quality in urban area [1, 2]. The source of the pollution comes from the emission released by the motor vehicles at the street floor. The large eddy simulation is used to predict the unsteady flow as well as the dispersion of pollutants in the street canyon. Unsteady RANS, so-called VLES is also applied to this flow and the results show that LES and VLES give similar results in 2D cases and they are acceptable for the environmental problem.

2. The governing equation

The governing equations for LES can be written as

$$\frac{\partial \overline{u}_i}{\partial x_i} = 0 \tag{1}$$

$$\frac{\partial \overline{u}_i}{\partial t} + \frac{\partial \left(\overline{u}_i \overline{u}_j\right)}{\partial x_j} = -\frac{1}{\rho}\frac{\partial \overline{p}}{\partial x_i} + \nu \frac{\partial^2 \overline{u}_i}{\partial x_i \partial x_i} - \frac{\partial \tau_{ij}}{\partial x_j} \tag{2}$$

$$\frac{\partial \overline{c}}{\partial t} + \overline{u}_j \frac{\partial \overline{c}}{\partial x_j} = D \frac{\partial^2 \overline{c}}{\partial x_i \partial x_i} - \frac{\partial M_j}{\partial x_j} \tag{3}$$

in which τ_{ij} and M_i are the subgrid stress and mass flux respectively.

The total shear stress, i.e. the subgrid stress plus molecular viscous stress, is closed by the RNG-based Smargorinsky model [3] as follows

$$\tau_{ij} + \tau_{ij}^{m} = -\left(\nu_{eff}\bar{S}_{ij} + \delta_{ij}\tau_{kk}/3\right) \tag{4}$$

in which $\nu_{eff} = \nu + \nu_t$. The effective viscosity is defined as

$$\nu_{eff} = \nu\left[1 + H\left(\nu_s^2\nu_{eff}/\nu^3 - C\right)\right]^{1/3} \tag{5}$$

with $\bar{S}_{ij} = \left(\partial\bar{u}_i/\partial x_j + \partial\bar{u}_j/\partial x_i\right)/2$, $\nu_s = \left(C_{rng}V^{1/3}\right)^2\sqrt{2\bar{S}_{ij}\bar{S}_{ij}}$ and $H(x) = x$ when x>0, $H(x) = 0$ otherwise. The V is the grid volume and C_{rng}=0.157, C=1.00.

The subgrid mass flux, including the molecular diffusion, is closed by a gradient model such that

$$M_i = D_t\frac{\partial\bar{c}}{\partial x_i} \tag{6}$$

where the turbulent diffusion coefficient is defined as $D_t = \nu_{eff}/Sc_t$, in which Sc_t is the turbulent Schmidt number and assumed to be 1.0.

When we use k-ε model to close the subgrid Reynolds stress and mass flux, it is so-called VLES. The k- and ε-equations with standard coefficients are ignored and can be found elsewhere [4]. Same formulae as eq. (6) is used for average mass flux.

The finite volume method is applied for the numerical solution with QUICK scheme and the time advance is second order Runge-Kutta integration.

3. The testing cases

3.1 Two dimensional street canyon

The geometry of the street canyon is illustrated in Figure 1.The upstream wind speed which is assumed to be varied with time period of 8 minutes, i.e. $U_\infty(y,t) = U_0(y)\sin(2\pi t/480)$. The pollutant is located at the street floor and assumed as a constant, presumably the pollutant concentration equals to 1.0 at a local spot and zero outside of the spot.

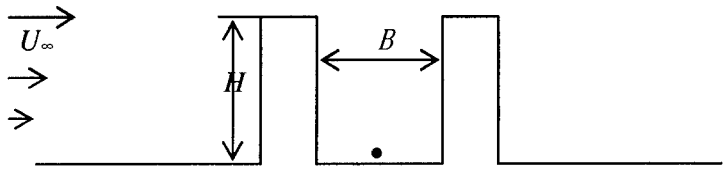


Figure 1 The illustration of the street canyon, ● is the spot of the pollution

The computational domain and grid meshes are sketched in Figure 2 for B/H=1. The mean velocity and Reynolds stress profiles are given at the inlet and the fully developed flow condition is posed at the outlet. The wall function is used at the solid walls and free stream condition is given on the upper boundary.

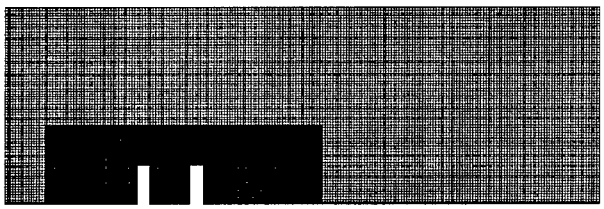


Figure 2 The computational domain and the grid meshes

3.2 Street canyon on the cross road

The cross road is illustrated in Figure 3. A symmetrical condition is added in respect to the plane at y=0. The car exhaustion is simplified as a line source in the middle of the street and it located at y axis at the floor of street canyon, i.e. z=0. The geometry and flow parameters of the testing cases are listed in Table 1.

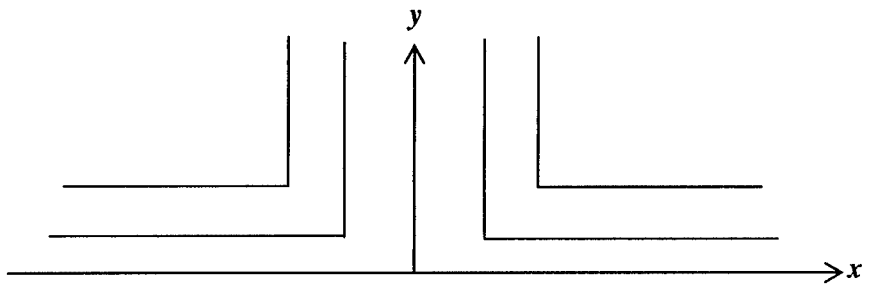


Figure 3 The plane layout of street canyon on cross road

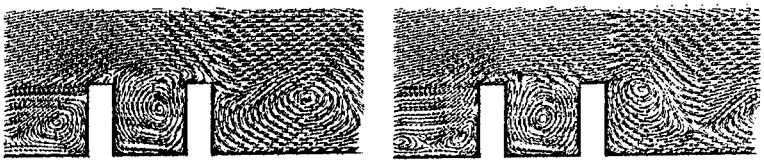
Table 1 The geometry and flow parameters

	Case A1	Case A2	Case B1	Case B2
B/H	1	3	1	3
Reynolds number	10^6	10^6	10^6	10^6
Turbulent model	LES	LES	k-ε	k-ε
3D cross road	yes	no	no	no
H (meter)	30	30	30	30

4. The results

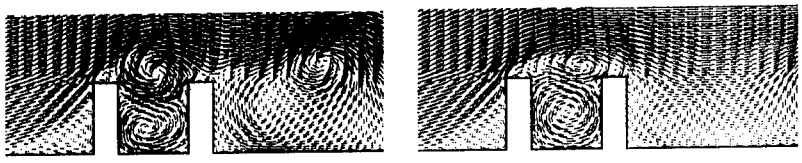
4.1 Case A1 and B1

The flow fields at two typical time-steps are presented in Figure 4 and 5. It clearly shows a vortex in the street canyon that transports the pollutant outside of the canyon. The iso-contours of concentration are shown in Figure 6 and 7.



(a) t=240s **(b) t=480s**

Figure 4 The flow field for B/H=1 by k-ε model

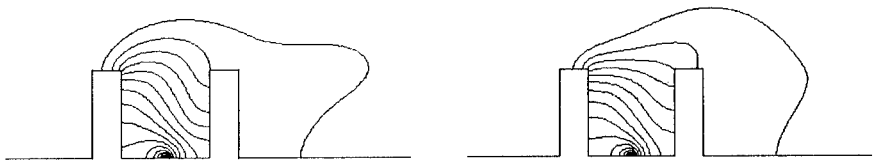


(a) 240s **(b) 480s**

Figure 5 The flow field for B/H=1 by LES

Note that the velocity and concentration fields are phase averaged on six periods in LES. The flow patterns inside the street canyon are nearly same in both LES and VLES, however more vortices outside of the canyon in LES, particularly at the corns of the building.

Results of the concentration distributions are in good agreement between LES and VLES inside the street canyon and the concentration is greater on the lee side of the front building and smaller at the front of the back building. The concentration distributions are different greatly outside the street canyon between LES and VLES, this is due to the different flow fields.



(a) 240s **(b) 480s**

Figure 6 The iso-contours of concentration for B/H=1 by k-ε model



(a) 240s **(b) 480s**

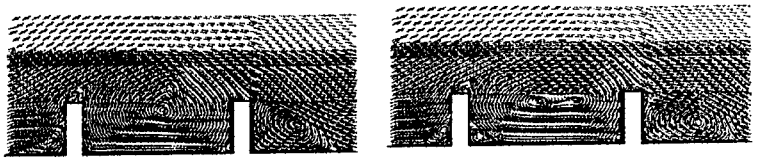
Figure 7 The iso-contours of concentration for B/H=1 by LES

4.2 Case A2 and B2

The results for B/H=3 are presented in Figure 8 and Figure 9. It is clearly shown that the pollutants are transported more quickly out of the street canyon for the wider spacing of the building block.

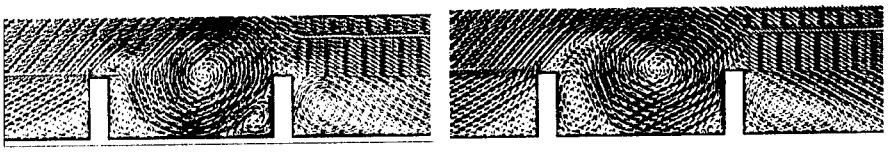
Compared with Figure 4 and 5, Figure 8 and 9 clearly show that the bigger vortices are formed in the wider street canyon. It is useful for transporting the pollutants outside of the canyon and reduced the concentration of pollution on both front and back buildings, as shown in Figure 10 and 11.

Compared between LES and VLES results it is found that the main large vortices are nearly same inside the canyon but flow patterns are different in the outside.



(a) 240s (b) 480s

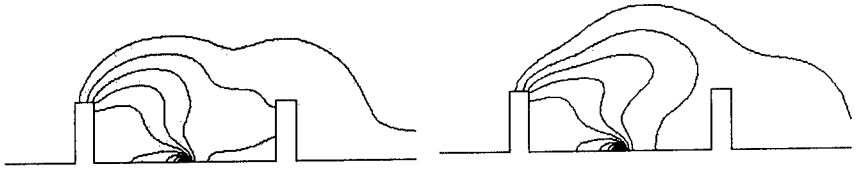
Figure 8 The flow field with B/H=3 by k-ε model



(a) 240s (b) 480s

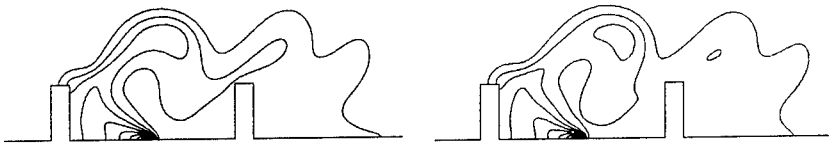
Figure 9 The flow field with B/H=3 by LES

Larger differences between LES and VLES prediction of concentration occur due to the wider spacing between front and back buildings. We believe that the LES has better resolution and it may be approximate to practical situation.



(a) 240s (b) 480s

Figure 10 The iso-contours of concentration for B/H=3 by k-ε model

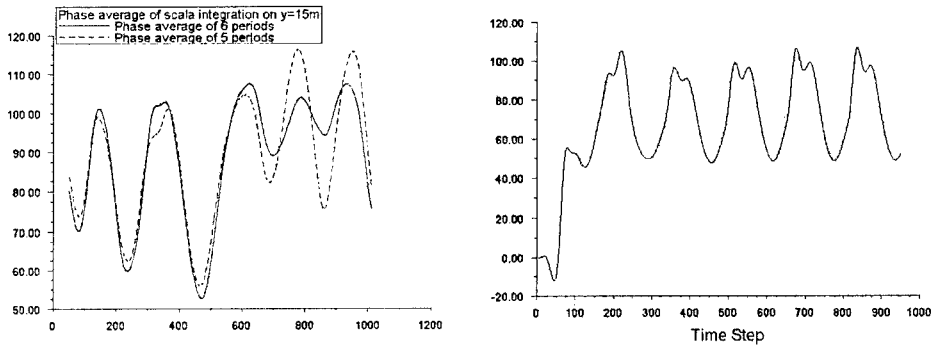


(a) 240s (b) 480s

Figure 11 The iso-contours of concentration for B/H=3 by LES

4.3 Integral flux

Integral flux, shown in Figure 12, is a useful design parameter in building engineering and defined as the integration of the vertical mass flux.



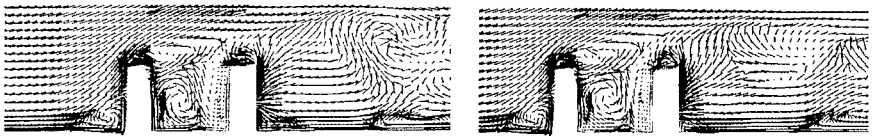
(a) LES **(b) k-ε**

Figure 12 The integration flux $\int_0^B \overline{w'c'}dx$

Both LES and k-ε model show the same periodicity as the free stream velocity. On average the agreement between LES and k-ε model is good but the peak values are different. It is due to the different flow and concentration fields.

4.3 Three dimensional dispersion at cross road

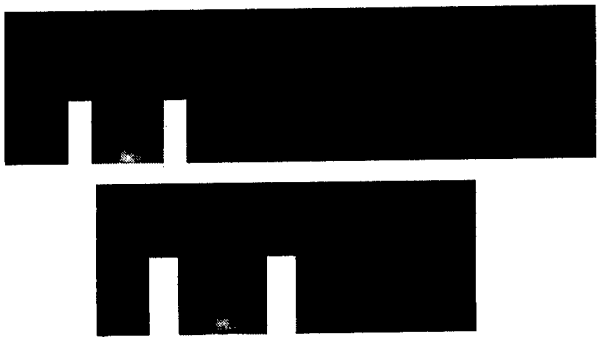
The typical velocity and concentration fields are presented in Figure 13 and 14. The velocity fields are in fairly agreement between LES and k-ε models, however the difference is obvious outside of the street canyon.



(a) LES on cross section at y=100 **(b) k-ε on cross section at y=100**

Figure 13 Velocity field by LES and k-ε

The similar situation appears in the concentration field as shown in Figure 14. Inside the street canyon the concentration distributions are quite similar but big difference occurs outside of the canyon.



(a) LES at y=100 **(b) k-ε at y=100**

Figure 14 Iso-contours of concentration in 3D street canyon by LES and k-ε

5. Concluding remarks

Both LES and VES give similar results for flow and concentration fields inside the street canyon in both 2D and 3D cases. However LES has better resolution in flow field than VLES and is expected to have better prediction for more complicated street canyon. On the other hand LES spend more computation time than VLES, 5-8 times more. Therefore the computational efficiency of LES must be improved and the models for unsteady RANS should be also consider in order to satisfy the complex 3D flows.

Acknowledgement

This work is supported by the University Foundation of Tsinghua University.

6. Reference

1. Tate J.E. and Bell M.C. (2000) Evaluation of a traffic demand management strategy to improve air quality in urban areas **10th International on Road Transportation Information and Control** p158-162
2. Chabni A. et al (1998) Modelling of pollutant dispersion in Urban street canyon by means of large-eddy simulation. **Int. J. Vehicle Design 20**:1-4
3. Yakhot A. et al (1989) Renormalization group formulation of Large Eddy Simulation **Journal of Scientific Computing 4**:139
4. Pope S. B. (2000) Turbulent Flows **Cambridge University Press**

LARGE-EDDY SIMULATION OF A SUBSONIC FLOW OVER A DEEP, OPEN CAVITY

L. LARCHEVÊQUE, O. LABBÉ, I. MARY AND P. SAGAUT
ONERA
29 av. de la division Leclerc, 92322 Châtillon cedex, France
Tel : 33 (0)1 46 73 42 07
email : lionel.larcheveque@onera.fr

Abstract. MILES and traditional LES computations of a high subsonic flow over a deep and open cavity using wall function and 2D-3D domain coupling strategy have been carried out ($Re_L = 6.7 \times 10^5$). Both Reynolds and phase averages have been computed. Results show especially good agreement with experimental data.

1. Introduction

High-speed flow over a cavity generates a complex flowfield whose dynamics are governed by various physical mechanisms such as shear layer instabilities, acoustic forcing, etc. This class of flows is not only of fundamental interest, but also occurs in many aerodynamic configurations, such as weapon bay or wheel wells, where large pressure fluctuations induced by this flow are known to result in possible structural damages. The capability of numerically predicting these flows in a time-accurate fashion is consequently an important issue. In the past twenty years, numerous RANS computations, mostly supersonic, have been carried out. The increase of available computational resources yet allows LES computations of such configurations.

The studied cavity has a length L to depth D ratio of 0.42, and therefore belongs to the deep cavity category. There is no reattachment of the flow on the floor (open cavity). The Reynolds number (based on the inflow velocity U_∞ and the length L of the cavity) and the Mach number are 6.7×10^5 and 0.8 respectively. This configuration has been chosen because of the availability of an experimental data base compiled by Forestier et

al.[1], which was specially designed for the accurate evaluation of DNS and LES computations. These data include averaged and phase averaged (20 phases) velocity measurements in various locations along the channel and inside the cavity. According to this experience, the flow is characterized by a fundamental frequency of 1975 Hz. Spectrum exhibits multiple harmonics of decaying SPL levels (see left part of the figure 4). The length of a period is not constant (jitter), the standard deviation being approximatively equal to 1% of the mean value. During one period, shadowgraphs and phase averaged velocity reveal the existence of three coherent vortices (see left part of the figure 8). Shadowgraphs also show the presence of strong pressure waves.

2. Numerical methods

Spatial discretization is accomplished using a finite volume scheme. Two categories of computations have been carried out. The preliminary results were obtained without the use of any subgrid model, an approach known as MILES, introduced by Boris et al.[2], and which is based on the idea that an upwind scheme is able to mimic the dissipative behaviour of the small structures. According to this technique, the convective fluxes are evaluated by means of an upwinding formulation derived from the AUSM+(P) scheme originally proposed by Edwards and Liou[3]. With the intention of getting to the root of this study, a more traditional LES approach was also tested, using the mixed-scale model of Sagaut coupled with a selective function (Sagaut and Troff[4]). In that case, the second order spatial scheme is centered in order to ensure minimal numerical dissipation. To prevent the apparition of oscillations, a detector proposed by Mary[5] locally switches if necessary to the former scheme. Explicit temporal integration is achieved using a third order Runge-Kutta scheme. In order to greatly reduce the computational cost, an instantaneous log law is used at the wall. Periodic boundary conditions are set in the spanwise direction. Velocity profile is imposed at the entrance of the channel, with additional white noise velocity fluctuations. Both mean and fluctuating velocities are adjusted in concordance with experimental measurements. Non-reflective outflow boundary conditions are used on the left extremity of the channel.

The computational domain extends from -1L to 5L in the streamwise direction and from -2.4L to 2L in the vertical direction, the origin being set in the leading edge of the cavity (see figure 2 for a glimpse of the complete domain). The computation is done on a multibloc structured mesh, with 2D-3D coupling strategy. The upper side of the channel, in which the flow is almost two-dimensional, is discretized in the spanwise direction with less cells than the lower part of the channel. The remaining part of the computational domain (including the cavity) is fully 3D. Two meshes

have been employed, a coarse one with 800,000 cells and a fine one with approximatively twice this number, obtained by multiplying the number of cells in both the streamwise and normal directions by 1.5, the number of cells in the spanwise direction remaining constant. The MILES approach was tested only on the coarse mesh. The following table summarizes the typical size of the cells in wall unit for the LES computations.

Mesh	**streamwise**	**spanwise**	**$\perp$ to wall**
Coarse	150 - 400	50 - 200	20 - 30
Fine	100 - 300	50 - 200	15 - 20

Due to the restrictive CFL conditions, dimensionless time-steps of 9.1×10^{-4} on the coarse mesh and 7.28×10^{-4} on the fine one have been adopted.

As seen in figure 1, the procedure used to compute phase averages consists in splitting the interval between five consecutive peaks of filtered pressure into 80 sub-intervals. The goal of such an approach is to provide against dephasing due to the jitter. For all the computations the standard deviations of the length of the period were found of the same magnitude as the experimental one. Tests with experimental data have proved than with up to four by four periods splitting, the effect of the jitter is negligible. Therefore this upper value has been adopted. The averaging time for both Reynolds and phase averages corresponds to $13 \times 4 = 52$ cavity cycles.

3. Numerical results and comparison with experimental data

Figures 2 and 3, based on instantaneous data issued from the fine mesh, show coherent structures highlighted using Q criterion ($\underline{\underline{\nabla}}\,\underline{u}$ tensor 2^{nd} invariant) combined with a pseudo-Schlieren view. The main characteristics of the flow are recovered, with the existence of three major structures (the two vortical tubes on the left of the figure 3 are about to pair) and pressure waves with similar shapes compared to the experimental shadowgraphs.

The experimental and computed spectra are shown in figure 4. The concordance is really good, with an accurate prediction of both the mean value and peaks levels up to 26000 Hz (12^{th} harmonic). The frequencies of the peaks are slightly over-evaluated (2.5%), but it has to be noticed that the spectral resolution is about 2.2% of the fundamental frequency. This spectrum is obtained from fine mesh data. On the coarse mesh, the levels are decaying faster, especially with the MILES computation, and only the first four peaks are present, with the same levels as for the fine mesh.

The evolution of the incompressible momentum thickness θ along the shear layer is plotted in figure 5. All the three computed graphs are close

of the experimental data, with the exception of an earlier effect of the trailing edge. MILES and LES computations on the coarse mesh give similar results, with a slightly underestimated growth rate in the initial region ($5 \leq x/\theta_r \leq 20$). Using the fine mesh, we obtain initially a higher growth rate, but the layer grows weakly in the region $40 \leq x/\theta_r \leq 60$, where the flow is supposed to be near to the equilibrium. In the first region, Forestier et al.[6] suppose that the fast growth may be explain by an early pairing of small vortical tubes, a mechanism similar to the "collective interaction" introduced by Ho and Huang[7]. Therefore a plausible explanation for the higher growth rate may be that because of the reffinement of the mesh, small structures in the vicinity of the leading edge and their dynamics are more accurately described.

Figures 6 shows the evolution of the vorticity thickness δ, defined by:

$$\delta(x) = (U^+ - U^-) \,/\, \left[\max_z \left(\frac{\partial u}{\partial z}\right)\right]$$

where U^+ is the velocity in the center of the channel and U^- is the velocity inside the cavity, here considered equal to 0. Beyond $x/\theta_r = 25$, computations and experience are well correlated, especially when using a subgrid model. Here again, there is an earlier influence of the trailing wall. Before $x/\theta_r = 25$, the evaluation of the experimental values of δ is of a poor accuracy because of the sharp vertical velocity gradient resulting from the small thickness of the shear layer and the coarse size of the measure mesh.

Figure 7 presents Reynolds and phase averaged streamwise velocity and 2D turbulent kinetic energy profiles at a location corresponding to $x/\theta_r = 50$, in the middle of the self-similarity growth region. Focusing on the streamwise velocity, we see that the LES profiles associated with the coarse and the fine meshes are almost indistinguishable. MILES profiles differ mainly inside the cavity, with smaller speed. However for each case the agreement with experimental data is good. If we consider the turbulent kinetic energy profiles, the two types of LES calculations are still closely connected. On Reynolds average, MILES computation generates more turbulent kinetic energy. On the contrary, LES leads to slightly underestimated turbulent kinetic energy peaks, but the shapes are correct. The two phases selected show deficit in energy for each case, when the locations of the peaks are well predicted.

Figure 8 shows a comparison of the loci of the coherent structures between experimental data and numerical results on the fine mesh, for four different phases. The structures are highlighted using the Weiss criterion (equivalent to 2D Q criterion). If we consider that the experimental measurement mesh is really coarse compared with the computing mesh and that this difference between the two meshes has an important effect on the computation of $\underline{\nabla}\,\underline{u}$, it stands to reason that the overall agreement is excellent.

Each experimental structure can be linked to a numerical structure with quite correct location and size, except perhaps for the less energetic ones (see structure 3 in phase 11). The results of the computation on the coarse mesh (MILES and LES), which are not shown here, are closely similar to the results on the fine mesh. As a remark, we can notice that the figures 2 and 3 correspond to a time which takes place into the first phase.

4. Conclusion

All the computations presented here show good agreement with the experimental data. This similarity despite various numerical methods and meshes may be explain by the energetic predominance of the low frequencies (and therefore the large structures). These simulations have then proved the (MI)LES techniques capability of studying this category of cavity problems, and therefore the possibility to use them to improve our understanding of the flow dynamics inside and above the cavity.

References

1. N. Forestier, P. Geffroy, and L. Jacquin. Flow over cavities in transonic regime: a test case for numerical simulations. In *Proceedings of the First International Symposium on Turbulence Shear Flow Phenomena*, pages 933–938, September 11-15, 1999.
2. J. P. Boris, F. F. Grinstein, E. S. Oran, and R. L. Kolbe. New insights into large-eddy simulation. *Fluid Dyn. Res.*, 10:199–228, 1992.
3. J.R. Edwards and M.S. Liou. Low-diffusion flux-splitting methods for flows at all speed. *AIAA Journal*, 36:1610–1617, 1998.
4. P. Sagaut and B. Troff. Subgrid-scale improvement for non-homogeneous flows. In *First AFOSR International Conference on DNS and LES*, Ruston, USA, August 4-8, 1997.
5. I. Mary and P. Sagaut. LES of a flow around an airfoil near stall. *AIAA paper*, 2001-2559, 2001.
6. N.Forestier, L. Jacquin, and P. Geffroy. The flow-field over a deep cavity at high-subsonic speed. Submitted to J. Fluid Mech.
7. C.-M. Ho and L.-S. Huang. Subharmonics and vortex merging in mixing layers. *J. Fluid Mech.*, 119:443–473, 1982.

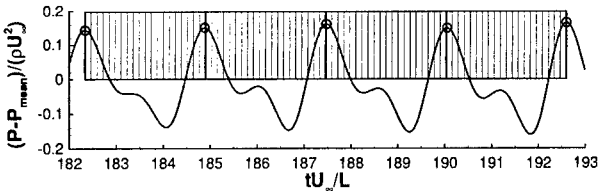


Figure 1. Procedure to compute phase averages : localization of maxima P_{max} for filtered pressure fluctuations and splitting of the interval between P^i_{max} and P^{i+4}_{max} into 80 sub-intervals with equal duration.

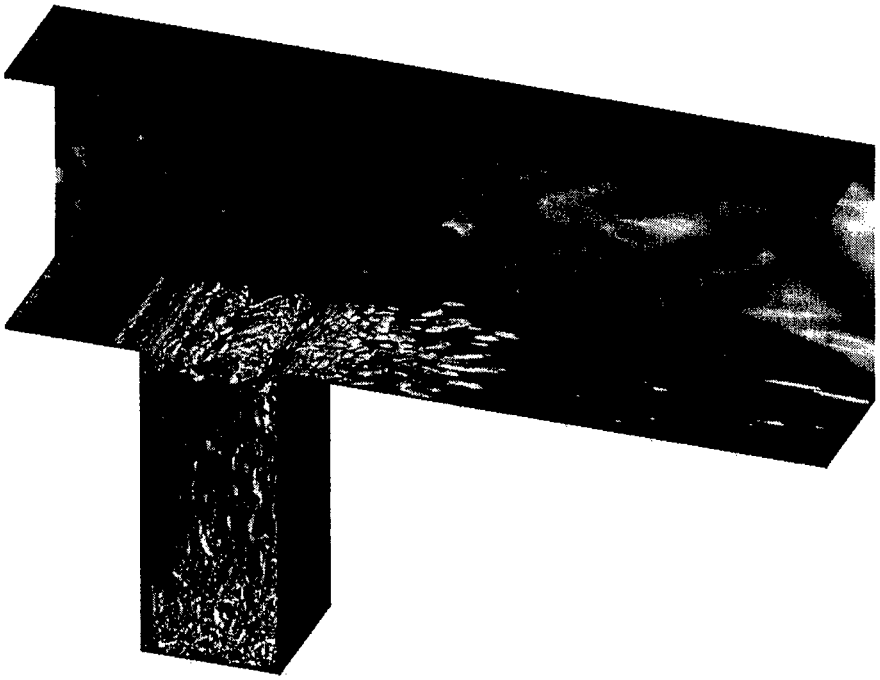


Figure 2. View of the computational domain. Structures are visualized using iso-surface of Q equal to $10\left(\frac{U_\infty}{L}\right)^2$ combined with a Schlieren-like picture in the background.



Figure 3. Closeup view of the mixing layer above the cavity: Q value equal to $20\left(\frac{U_\infty}{L}\right)^2$.

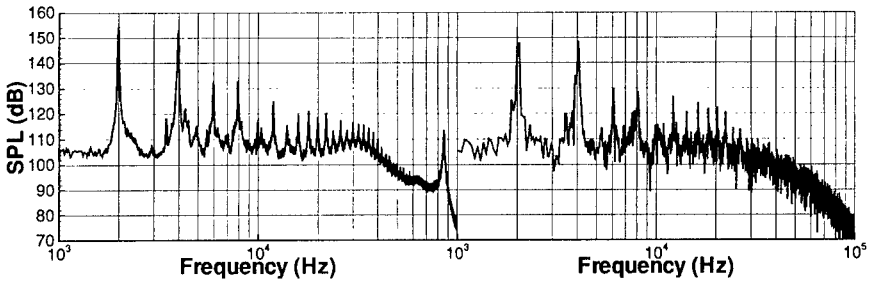


Figure 4. Experimental (left) and computed (right) spectra. The computation is done on the fine mesh with subgrid model (LES).

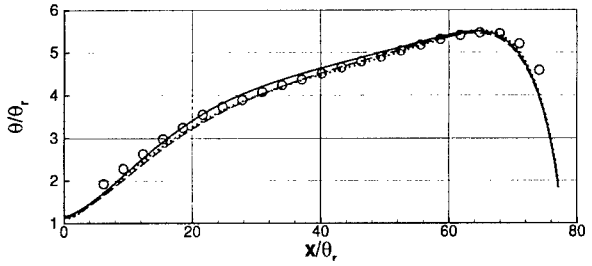


Figure 5. Momentum thickness θ of the mixing layer normalized with initial experimental momentum thickness θ_r. ·····: MILES with coarse mesh; – – –: LES with coarse mesh; ———: LES with fine mesh; o: experimental data.

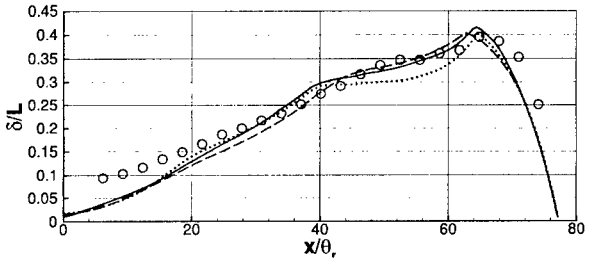


Figure 6. Vorticity thickness δ of the mixing layer normalized with L. ·····: MILES with coarse mesh; – – –: LES with coarse mesh; ———: LES with fine mesh; o: experimental data.

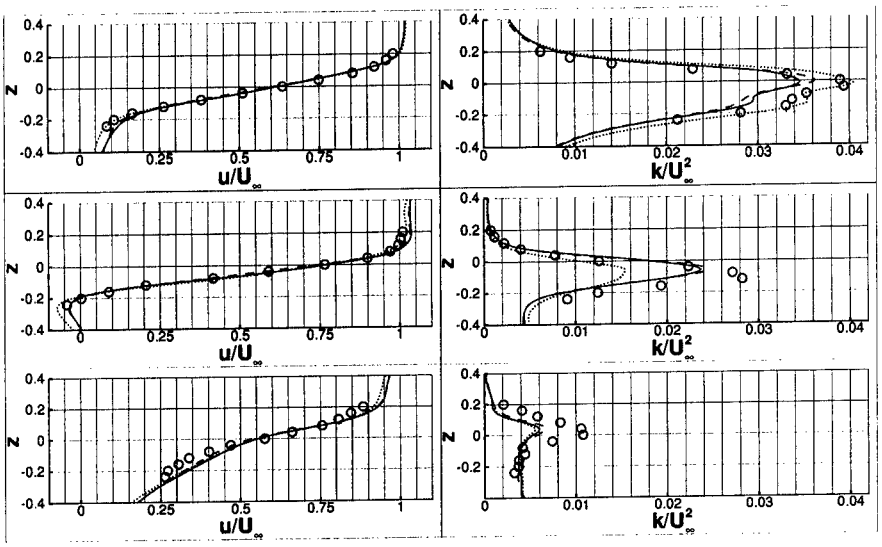


Figure 7. Mean streamwise velocity (left) and 2D turbulent kinetic energy (right) profiles at $x = 0.6L$: Reynolds average (top), phase average for phase 1 (middle) and phase average for phase 11 (bottom).· · · · · · · : MILES on coarse mesh; – – –: LES on coarse mesh; ———: LES on fine mesh; ○: experimental data.

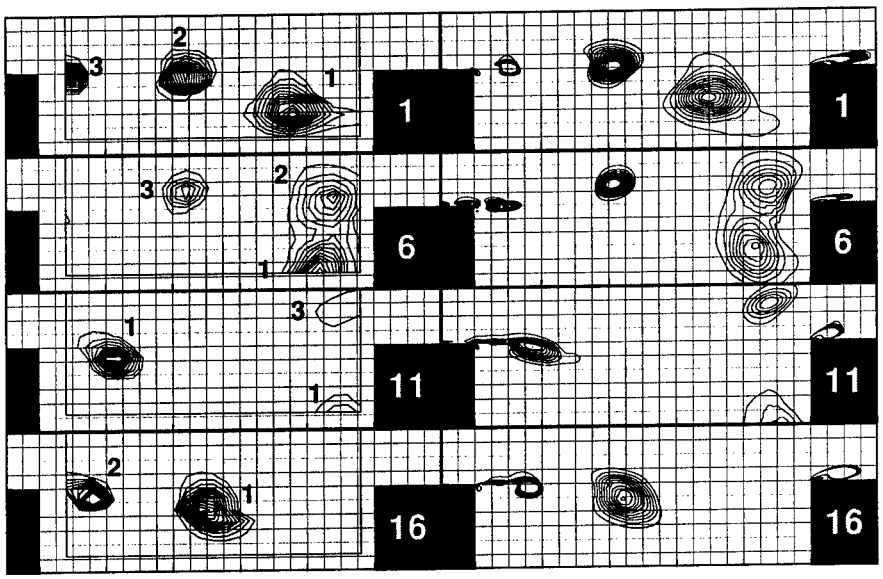


Figure 8. Phase averaged coherent structures isolated using Weiss criterion (levels from 1 to 25 by increment steps of 2, normalized using $\left(\frac{U_\infty}{L}\right)^2$): experimental data (left) and LES on fine mesh (right) for phases 1, 6, 11 and 16.

LARGE EDDY SIMULATION OF SHOCK/BOUNDARY LAYER INTERACTION

E. GARNIER AND P. SAGAUT
ONERA
29, Av. de la Division Leclerc, BP72, 92322 Châtillon Cedex, FRANCE

AND

M. DEVILLE
Laboratoire de Mécanique des Fluides
Ecole Polytechnique Fédérale de Lausanne, CH-1015 Lausanne SWITZERLAND

1. Introduction

Shock/Boundary layer interaction is still an important problem for supersonic aircraft designers. Such phenomena play an important role both for internal and external aerodynamic. These interactions can lead to an increase of drag, separation, loss of performances. Moreover, unsteadiness of the shock produces strong constrains on the structure, noise and modifies local heat transfer.

Since, for such interactions, results obtained with the RANS approach are not satisfactory [12], it appears natural to assess the capacity of LES to simulate such interaction. From a numerical point of view, it necessitates the use of schemes designed to minimize the numerical dissipation in shock-free region of the flow since it was demonstrated in [1] that the numerical dissipation of high-order shock-capturing scheme can exceed the subgrid-scale dissipation. To satisfy this requirement, we use a strategy [2] built on the mixing of the characteristic based filters [3] and a sensor [4] able to distinguish a turbulent fluctuation from a shock. To validate this approach, the case of the interaction of an oblique shock with a boundary layer developing on a plane plate was chosen since it has been extensively studied experimentally at IRPHE [6] [7].

2. Mathematical model

In this study, we have used the system of filtered Navier-Stokes equations proposed by Vreman [8]. Some terms are neglected as in [5]. The subgrid-scale model is the selective mixed scale model proposed by Sagaut [9]. This model was proven to behave particularly well for wall-bounded flow.

The numerical scheme is based on non-linear WENO filters defined in Ref. [2]. Let U^n denote the vector of the conservative variables evaluated at the time $n\Delta t$ and Δt be the time step, $\widehat{U}^{(n+1)}$ the vector of the conservative variables after the application of any explicit time integration scheme. This vector is spatially filtered to give the final state U^{n+1} ($U^{n+1} = \mathcal{F}(\widehat{U}^{(n+1)})$). The main point is that the time advancement is performed with a non-dissipative spatial operator (noted L). The filtering pass is decomposed as follows:

$$U^{(n+1)} = \mathcal{F}(\widehat{U}^{(n+1)}) = (I_d + \beta \Delta t L_f)(\widehat{U}^{(n+1)}) \tag{1}$$

where L_f is any dissipative operator, I_d is the identity and the switch β is defined as:

$$\begin{cases} \beta = 0 & \text{if } \Psi < \epsilon \\ \beta = 1 & \text{if } \Psi \geq \epsilon \end{cases} \tag{2}$$

where Ψ is the sensor of Ducros *et al.*[4] defined as:

$$\Psi = \frac{(div(\mathbf{u}))^2}{(div(\mathbf{u}))^2 + (rot(\mathbf{u}))^2} \tag{3}$$

where $\mathbf{u}$ denotes the velocity vector. This sensor was demonstrated to be able to distinguish a turbulent fluctuation from a shock in Refs. [4] and [2].

In this study, the time integration is performed by means of a third-order accurate TVD Runge-Kutta method proposed by Shu and Osher [10]: Note that L is referred to as "base scheme" and can be any qth order accurate finite volume or finite difference non-dissipative scheme.

As mentioned by Yee *et al.* [3], L_f can be the dissipative part of any shock-capturing scheme. Here, such operator is derived of ENO schemes. The dissipative part of ENO scheme is extracted easily by subtracting a centered scheme to the ENO one.

In this study, we have used a combination of a fourth-order centered base scheme with a fifth-order accurate WENO filter. The threshold ϵ is fixed to 0.04. In practice, this method limits the computation of the filter to about 20 percents of the total number of grid points.

Viscous fluxes are discretized by means of a second order accurate centered scheme. The CFL number is fixed to 0.5.

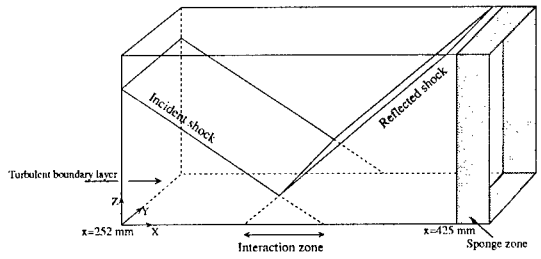


Figure 1. Computational domain

3. Description of the configuration

The shock is generated by a corner fixed to the upper plate of the wind tunnel and interacts with the turbulent boundary layer which develops on the lower plate (which is assumed to be adiabatic).

The length of the computational domain was restricted to the measurement zone (it begins at $x = 252\ mm$ and ends at $x = 440\ mm$). The height of the domain is $70,7\ mm$ whereas the height of the wind tunnel is $120\ mm$. The computational domain is presented in Fig. 1 (note that the axe x denotes the longitudinal direction, y the spanwise direction and z the wall-normal direction). The width of the computational domain is about $15\ mm$ in the spanwise direction (for the test cases A, C and D) whereas the wind tunnel is 10 times larger.

At the inflow (at $x = 252\ mm$), the temperature T_e outside of the boundary layer is $144.6\ K$, the density is equal to $9.66\ 10^{-2}\ kg/m^3$ and the Mach number is fixed to 2.3. The Reynolds number Re based on the displacement length $\delta_1 = 3.535\ mm$ is equal to 19132. Periodic boundary conditions are applied in the spanwise direction y. Non reflective conditions are applied on the upper frontier. At the outflow, a $13\ mm$ long sponge zone ensures the damping of turbulent fluctuations which are evacuated by means of non-reflective conditions. No-slip and adiabaticity conditions are applied on the wall.

In this study, four simulations have been carried out in order to check the sensitivity of the results to computational details. The characteristics of these simulations are reported in Table 1. The number of grid points (N_x, N_y, N_z) in each direction are mentioned and the size of the computational meshes (Δ_x^+, Δ_y^+, Δ_z^+) are given in wall units. We precise that these wall units are based on a experimentally measured friction velocity of $24.75m/s$ at $x = 260\ mm$. Test case A is the base case. In test case B, the influence of a doubling of the domain size in the spanwise direction is investigated. The effect of a refined grid in the longitudinal direction is studied using case C and case D is devoted to the investigation of the importance of a

	N_x	N_y	N_z	Δ_x^+	Δ_y^+	$\Delta_z^+(min)$	SGS Model
Case A	255	55	151	50	18	1	*yes*
Case B	255	110	151	50	18	1	*yes*
Case C	510	55	151	25	18	1	*yes*
Case D	255	55	151	50	18	1	*no*

SGS model.

The generation of realistic inflow conditions is a very important issue in LES. In this study, we follow the methodology introduced by Lund *et al.* [11] and extended to compressible flow by Urbin *et al.*[13]. This strategy prevents the thickening of the boundary layer using an *ad hoc* re-scaling. The loss of self-similarity induced by the shock requires the Lund procedure to be applied on a second simulation of time-developing canonical turbulent boundary layer. A $x = cste$ plane of this second simulation is extracted and introduced in the shock/turbulence LES inflow plane at each time step.

4. Analysis of the results

First, iso-values of the mean pressure are presented in Fig. 2. The incident shock (which would impact near $x = 336\ mm$ in absence of boundary layer) curves penetrating the boundary layer (thick of 11 mm at the inflow) and reflects on the sonic line (also represented on the picture) as an expansion fan. The compression related to the rising of pressure waves in the subsonic part of the boundary layer focuses to form a reflected shock (whom the trace begins in the vicinity of the position $x = 290\ mm$ at the wall). The continuation of this shock would impact on the wall near $x = 275\ mm$ and marks the beginning of the interaction zone.

Iso-values of longitudinal velocity fluctuations are shown in Fig. 3. Upstream the interaction, these fluctuations are strong in the near wall region. One can observe that the fluctuations are amplified by a factor two under the reflected shock (near $x = 290\ mm$). The explanation given by Laurent [7] to explain this amplification of the fluctuations is a linear effect by rapid distorsion. The zone concerned by a high level of fluctuation spreads above the separated zone (near $x = 320\ mm$). In agreement with experimental observations, one can notice an alignment of the isovalue lines of the fluctuations with the reflected shock just downstream of this one. Downstream of the interaction zone, longitudinal and vertical (not shown) fluctuations are maximum in the middle of the boundary layer ($z/\delta \sim 0,6$). However, one can observe a second extremum of longitudinal fluctuations in the near wall region close to the outflow, this an evidence of a (slow) return toward an equilibrium state. A particular attention must be paid to the interpre-

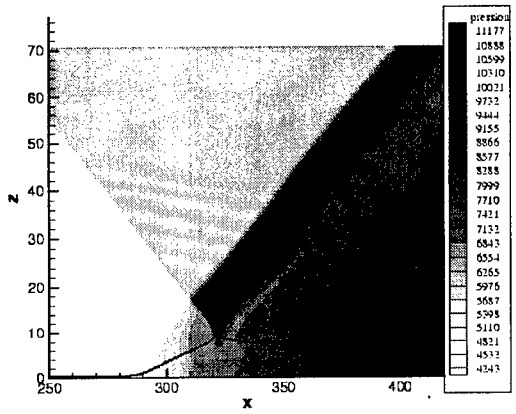


Figure 2. Iso-values of the mean pressure and sonic line (in black)

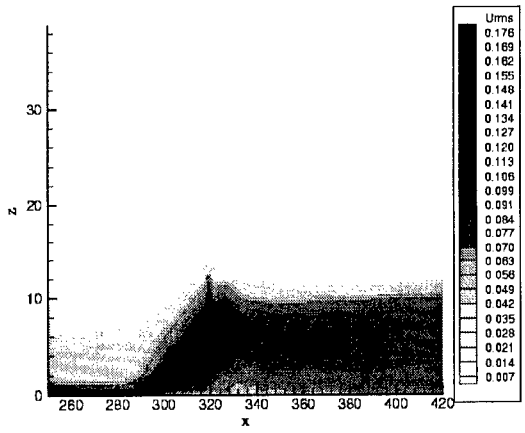


Figure 3. Iso-values of the mean longitudinal velocity fluctuations

tation of data concerning the fluctuations in the interaction zone since the unsteadiness of the shocks and of the recirculation bubble can be at the origin of a part of the fluctuations (it is then not possible to consider turbulent fluctuations).

Longitudinal evolution of the displacement thickness is displayed in Fig. 4. The computation of this integral quantity is not trivial since the external velocity $U_e(x)$ varies in the longitudinal direction. The potential flow is supposed to be reached when the Ducros sensor value exceeds 0.1.

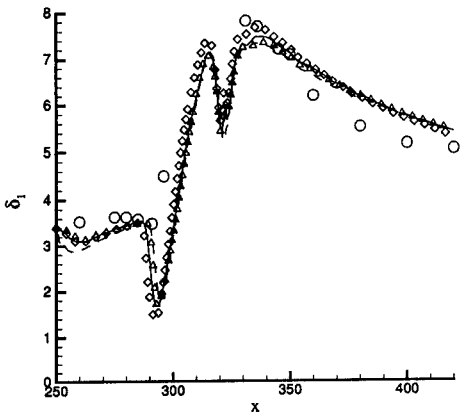


Figure 4. Longitudinal evolution of the displacement thickness
Case A ———, Case B △, Case C - - - - -, Case D ◇, HWA ○

This method gives results coherent with measurement since the value of δ_1 at the inflow of the computational domain is correctly predicted (at $x = 260\ mm$) after a short transient. The evolution of δ_1 in the interaction zone ($290\ mm < x < 340\ mm$) will not be commented in absence of corresponding experimental data. Looking at figure 4, one can observe that the displacement thickness is multiplied by a ratio larger than two during the interaction. This amplification rate is well predicted by computations and during the relaxation phase where δ_1 decreases, the discrepancies do not exceed 10 %.

The longitudinal evolution of the friction coefficient C_f is presented in Fig. 5 for the four cases and compared with Hot Wire Anemometry (HWA) data [7]. At the inflow, the discrepancies on the C_f between computations and experience is lower than 10 % for cases A and B. (such kind of underestimation is classical with LES [14]). Cases C (with the best resolution) and D give levels of C_f very close to the experiment. The flow is seen to be separated for cases A, B and C between $x = 290\ mm$ and $x = 340\ mm$. The quasi totality of the interaction zone is concerned by the separation. For the case D (without SGS model), the velocity fluctuations in the near wall zone are stronger and the flow separates latter (near $x = 305\ mm$). Just after the interaction zone ($x = 340\ mm$), experimental evaluations based on hypothesis of the existence of a logarithmic zone lead to a friction coefficient clearly positive at the opposite of the computations. In the relaxation zone, the increase of C_f between computations and experiment is very similar and, at the outflow, the discrepancies are comparable to those

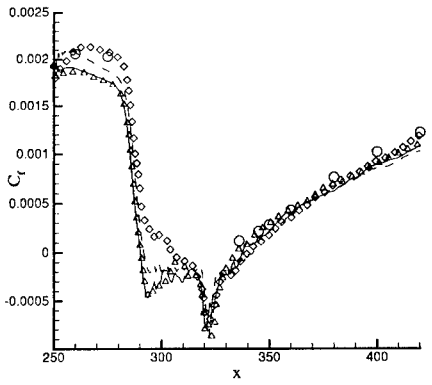


Figure 5. Longitudinal evolution of friction coefficient
Case A ———, Case B △, Case C - - - - -, Case D ◇, HWA ○

observed at the inflow (about 10 %). The results quality is clearly superior to the one obtained with RANS computations (see [12]) in the same configuration (but at $Ma = 2.9$).

Independently of the analysis of the results concerning physical variables, we verify in Fig. 6 that the Ducros sensor applies nearly exclusively in the zone where we have noticed in Fig. 2 the presence of shock or expansion. Consequently, the SGS model is effective (his effect is not masked by numerical dissipation) in the most part of the boundary layer. Nevertheless, one can observe low values of the sensor on the upper limit of the boundary layer where the adaptation of the inflow conditions may not be perfect. Even if this strategy of minimization of the numerical dissipation would merit other validation (see also [2]) on different test cases, results presented here allows to be confident with this concept.

5. Conclusion

Bidimensional interaction an oblique shock with a plane plate has been studied numerically using LES and compared with experimental data. Numerical results are in quantitative agreement with experimental results and LES can now be considered as a predictive tool for such physically complex flow. The separated zone is correctly described. The effects of the size of the domain in the spanwise direction, of the resolution in the longitudinal direction and the presence of a SGS model do not appear to be deciding.

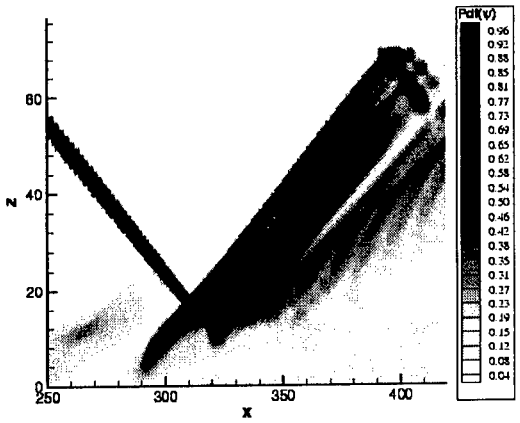


Figure 6. Iso-values of the mean PDF of Ducros sensor

References

1. E. Garnier, M. Mossi, P. Sagaut, P. Comte and M. Deville. On the use of shock-capturing scheme for Large-Eddy Simulation, *J. Comput. Phys.*, **153**, 273-311, 1999
2. E. Garnier, P. Sagaut and M. Deville. A class of explicit ENO filters with applications to unsteady flows, *J. Comput. Phys.*, **170**, 184-204, 2001
3. Yee, H. C., Sandham, N. D., and Djomehri, M. J., "Low-dissipative High-Order Shock-Capturing Methods Using Characteristic-Based Filters," *J. Comput. Phys.*, **150**, 199-238, 1999
4. F. Ducros, V. Ferrand, F. Nicoud, C. Weber, D. Darracq, C. Gacherieu and T. Poinsot. Large-Eddy Simulation of shock/turbulence interaction, *J. Comput. Phys.*, **152**, 517-549, 1999
5. Garnier, E., Sagaut, P., and Deville, M., "Large-Eddy Simulation of shock / homogeneous turbulence interaction," to be published in *Computers & Fluids*
6. J. Deleuze. Structure d'une couche limite turbulente soumise à une onde de choc incidente, *Thèse de doctorat, Université Aix-Marseille II*, 1995
7. H. Laurent. Turbulence d'une interaction onde de choc / couche limite sur une paroi adiabatique ou chauffée, *Thèse de Doctorat, Université Aix-Marseille II*, 1996
8. Vreman, B., Geurts, B., and Kuerten, H., "A priori tests of large eddy simulation of the compressible plane mixing layer," *Journal of Engineering Mathematics*, **29**, 299-327, 1995
9. Sagaut, P., "Large Eddy Simulation for incompressible flows," *Springer*, 2001
10. Shu, C. W., and Osher, S., "Efficient implementation of Essentially Non-Oscillatory shock-capturing schemes II," *J. Comput. Phys.*, **83**, 32-78, 1989
11. T. S. Lund, X. Wu and K. D. Squires. Generation of Turbulent Inflow Data for Spatially-Developing Boundary Layer Simulations. *J. Comput. Phys*, **140**, 233-258, 1998
12. D. P. Rizzetta. Evaluation of explicit Algebraic Reynolds-Stress Models for Separated Supersonic Flows, *AIAA J.*, **36**, 24-30, 1998
13. G. Urbin and D. Knight, Large Eddy Simulation of a Supersonic Boundary Layer Using an Unstructured Grid, *AIAA J.*, **39**, 1288-1295, 2001
14. E. T. Spyropoulos and G. A. Blaisdell. Large-Eddy Simulation of a spatially Evolving Supersonic Turbulent Boundary-Layer Flow, *AIAA J.*, **32**, 1983-1990, 1998

LARGE-EDDY SIMULATION OF THE FLOW AROUND A SIMPLIFIED BUS

SINISA KRAJNOVIC AND LARS DAVIDSON
Department of Thermo and Fluid Dynamics
Chalmers University of Technology
SE-412 96 Göteborg, Sweden
sinisa@tfd.chalmers.se

Abstract. Two large eddy simulations of the flow past a bus-like vehicle body were made and the results are compared with experimental data [3]. The effect of the near wall resolution and the modeling of the unresolved coherent structures in the near wall flow were studied. It was determined that, although the wall functions are inadequate to represent the thin vortices close to the wall, their use leads to results in a near wake region that are similar to those in the simulation with a sufficient wall normal resolution. This study indicates that the wall normal resolution has little influence on the pressure coefficient at the rear face.

1. Introduction

The drag forces of importance to the vehicle designer are dominated primary by the wake forces. Thus the prediction of the pressure coefficient at the rear of the vehicle is of great importance. Although the RANS simulations have been successful in predicting many parts of the flow around vehicles, they have failed to predict the effects of the unsteady wake on the body. It is believed than an unsteady simulation such as large eddy simulation (LES) will have greater success than RANS in predicting the pressure at the rear of the vehicles and give better insight into the flow around these bodies. Large eddy simulation has already been applied to various bluff body flows. Early bluff body LES were made of the flow around a surface-mounted cube and a rectangular cylinder. These flows are characterized by the separations defined by the sharp edges of the obstacle. Breuer [2] made LES of the flow around a circular cylinder at Reynolds number 140000

based on the free stream velocity and cylinder diameter. This flow involves transition and a very thin separation shear layer, which makes LES very challenging. While the drag generation on the two-dimensional cylinders is dominated by the regular shedding of intense vortices, the flow around highly three-dimensional vehicles is highly irregular [1]. The cylinders studied in these LES were isolated (i.e. not in the vicinity of the ground plane) and the cube was mounted on the ground, whereas the vehicle body is in the vicinity of the ground. The vicinity of the ground forces the stagnation point away from the center of the front face towards the bottom of the body, which produces different flows on the top and bottom surfaces and thus generates a lift force [1]. All these factors make these LES of limited relevance to flow past a vehicle. Krajnović and Davidson [5] recently presented LES of the flow around a bus-like body where they modeled the coherent structures near the wall with wall functions. The shape and the ground clearance of this body are similar to the shape and clearance of the buses. This makes it an excellent test case for investigation of the applicability of LES in vehicle aerodynamics.

The long term goal of this study is to develop a LES that is able to simulate the flow around a vehicle. The main obstacle of a LES of this kind is the near wall resolution required to represent the vortex structures in the shear layer. The purpose of this paper is to present LES of the flow around a bus-like bluff body at $Re = 210000$. We compare two LES in which the near wall region was treated in different ways.

2. Subgrid-scale modeling and numerical method

The effect of the small scales, which appears in the subgrid-scale stress tensor in the filtered Navier-Stokes equations, is modeled using the Smagorinsky model. The Smagorinsky constant, C_s, equal to 0.1 is used in this work and the Van Driest damping function was used only in the $LES2$ simulation. The formation of a turbulent boundary layer in the experiment was ensured with boundary layer trip wires mounted at the front of the model. Because of this there is no laminar boundary layer on the body and the assumption of non zero SGS stresses used in our LES is thus correct. In the case of transition from laminar to turbulent flow on the body, some correction is needed to force SGS stresses to zero in the laminar region. An alternative is to use a different SGS model, e.g. the dynamic eddy viscosity model, in which the eddy viscosity vanishes in laminar flows.

Calculations are made with the CALC-BFC code. This is based on a 3-D finite volume method for solving the incompressible Navier-Stokes equations using a collocated grid arrangement. Both convective and viscous fluxes are approximated by central differences of second order accuracy. A

Crank-Nicolson second order scheme was used for time integration. The SIMPLEC algorithm was used for the pressure-velocity coupling. The code is parallelized with block decomposition and the PVM and MPI message passing systems [6].

3. Description of the geometry and numerical details

The geometry of the computational domain is given in Fig.1. A domain with an upstream length of $x_1/H = 8$, a downstream length of $x_2/H = 16$ and a span-wise width of $B = 5.92H$ was used for the simulation. The values of other geometrical quantities are $L = 0.46$ m, $H = 0.125$ m, $W = 0.125$ m, $S = 0.3075$ m, $R = 0.019$ m, $r = 0.0127$ m, $c = 0.01$ m and $C = 0.5$ m. The ground clearance of $c/H = 0.08$ is similar to the clearance ratio of buses. The Reynolds number $Re = U_\infty H/\nu$ was 210000 on the basis of the incoming mean velocity, U_∞, and the vehicle height, H. In the experimental set-up, the location of the front side relative to the inlet was 0.564 m and the distance from the test section exit to the back wall perpendicular to the flow was 1.854 m. A moving ground belt and boundary layer scoop were used to simulate the floor boundary condition and to minimize boundary layer effects. The cross-section of the tunnel test section, the ground clearance and the position of the model's cross-section with respect to the tunnel were identical in LES and the experimental set-up.

In the experiments of Duell and George [3], the inlet mean velocity was uniform within 1% and the average turbulent intensity was 0.3%. A uniform velocity profile constant in time was thus used as the inlet boundary condition in this work. The convective boundary condition $\frac{\partial u_i}{\partial t} + U_c \frac{\partial u_i}{\partial x} = 0$ was used at the downstream boundary. Here, U_c was set equal to the incoming mean velocity, U_∞. To simulate the moving ground, the velocity of the lower wall was set equal to U_∞. The lateral surfaces were treated as slip surfaces using symmetry conditions $\frac{\partial u}{\partial z} = \frac{\partial v}{\partial z} = w = 0$. The wall functions based on the 'instantaneous logarithmic law' are used at all walls in simulation $LES1$. We refer to Ref. [5] for the details of the implementation of the wall functions. In the $LES2$ simulation, no-slip boundary conditions were used on the wall. The homogeneous Neumann condition was used for the pressure at all boundaries.

The topology of the mesh consists of 24 blocks where one block forms an O grid. An additional larger bus surface was made for the outer surface of the O grid. The O grid with a thickness of 0.005 m was made between this surface and the surface of the vehicle body. The number of cells in the wall normal direction in the O grid was 10 in simulation $LES1$ and 30 in simulation $LES2$. The rest of the mesh was the same in both simulations. Meshes of 1.8 million and 2.1 million nodes were used in simulations $LES1$

and $LES2$, respectively. The time step was 2×10^{-4} in $LES1$ and 1×10^{-4} in $LES2$, giving a maximal CFL number of approximately 4.5. The CFL number was smaller than one in 98% of the cells. The averaging time in the simulation was $tU_\infty/H = 48$ (30000 time steps in $LES1$ and 60000 time steps in $LES2$). The computational cost using 24 SGI R10000 CPUs was $\simeq$ 600 hours (elapsed time) for $LES1$ and 1200 hours for $LES2$.

4. Results

4.1. THE MEAN FLOW

Time-averaged velocities $\overline{V}_{eff} = \left(\langle\bar{u}\rangle_t{}^2 + \langle\bar{v}\rangle_t{}^2\right)^{1/2}$ are compared with hot wire anemometry experimental data in Fig. 2. Here, $\langle\bar{u}\rangle_t$ and $\langle\bar{v}\rangle_t$ are time-averaged resolved velocity components in the x and y directions obtained from LES. The agreement of LES results with experimental data is relatively good, and all the peaks and trends of the experimental profile are represented in the LES results. Although the two LES gave very similar velocity profiles, there are some differences, especially at position $x/H = 0.32$. The velocity profile in simulation $LES1$ is in better agreement at this location with the experimental data than is the one in $LES2$. In the experiments of Duell and George [3], the free stagnation point was assumed to be at $y = 0$. They plotted $\overline{V}_{eff}/U_\infty$ along the x-axis and used the local minimum as the indication of the free stagnation point. The distribution of the mean velocity components, $\langle\bar{u}\rangle_t/U_\infty$ and $\overline{V}_{eff}/U_\infty$, at $y = 0$ observed in our LES are plotted in Fig 3a. The recirculation length was found to be $X_r = 1.36H$ in $LES1$ and $X_r = 1.39H$ in $LES2$ using the local minimum of $\overline{V}_{eff}/U_\infty$. Using the intersection of $\langle\bar{u}\rangle_t/U_\infty$ with the x-axis, we found $X_r = 1.44H$ in $LES1$ and $X_r = 1.41H$ in $LES2$. This is larger than the $X_r = 1.1H$ measured in Duell and George's experiment [3]. The local minimum of $\overline{V}_{eff}/U_\infty$ in Fig. 3a is larger than zero, which indicates that the free stagnation point is not fixed. This finding agrees with experimental result [3]

The pressure coefficient at the rear face, $C_{p_{base}} = (p - p_\infty)/(0.5\rho U_\infty^2)$, in LES is computed and compared with the experimental data in Fig. 3b. It can be seen that the shape of the profile is the same as in the experiment, while the level of $C_{p_{base}}$ is over-predicted in both simulations. The integrated value of $C_{p_{base}}$ over the rear surface, $\overline{C}_{p_{base}}$, was -0.216 in the $LES1$ simulation and -0.224 in the $LES2$ simulation as compared to the experimental value of -0.286.

4.2. THE INSTANTANEOUS FLOW

The $C_{p_{base}}$ signal was Fourier transformed and a peak is found in the spectrum. The Strouhal number, $St = fH/U_\infty$, of this periodic component signal was 0.069 in simulation $LES1$, whereas two peaks were found in simulation $LES2$ corresponding to the non-dimensional frequencies of $St = 0.055$ and $St = 0.195$. This can be compared to the experimental value of 0.073.

The velocity signals for two points in the near wake were sampled and turbulent energy spectra computed. The selected points are located in the upper shear layer of the recirculation region and in the wake region close to the free stagnation point. The same points were chosen for the velocity signal sampling in the experiments of Duell and George [3]. The energy spectra of these signals exposed several dominant frequencies. Distinct peaks corresponding to the non dimensional frequencies of $St = 0.032$, $St = 0.21$ and $St = 0.29$ in simulation $LES1$ and 0.517, 1.079 and 1.323 in simulation $LES2$ were measured near the separation point. In the experiment, Duell and George [3] measured $St = 1.155$ at this position. The power density spectrum at the second point close to the free stagnation point has a peak at $St = 0.11$ in $LES1$ and $St = 0.472$ in $LES2$ as compared to the experimental value of $St = 0.155$.

4.3. THE FLOW STRUCTURES

The coherent structures were visualized and compared with the experimental observations. Simulation $LES2$ was found to be superior to $LES1$ in resolving the flow structures around the bus. The reason is that the near wall resolution of one wall unit in $LES2$ makes it possible to resolve these structures, whereas the wall functions used in $LES1$ are not able to reproduce the re-attachments and separations. The flow separates at the rounded leading edge in simulation $LES2$, similar to experimental observations, and forms the vortex on the roof (R) and two vortices on the lateral sides of the bus (L). These vortices can be seen in Figs. 4 and 5a. We calculated vortex cores using EnSight post-processing software and according to algorithms based on techniques outlined by Sujudi and Haimes [7]. Core segments are then used as emitters for the streamlines shown in Fig. 5a. This figure shows that the roof vortex (R) and the lateral vortices (L) end at the surface of the body and that they are connected with smaller vortices in between, over the rounded edges. This satisfies Helmholtz's second vortex theorem, which states that the vortices must end at a solid boundary, extend to infinity or be connected to each other. The trailing vortices (T) were predicted in both simulations (see Fig. 5 and Ref.[5]). The vortex shedding from the sharp rear edges of the model forms four straight vortices shown in Figs. 5b, 6b and 7b. Similar vortices were found in a study of the shedding from the

separation lines of discs and square plates [4]. Figures 6a and 7a show that the $LES1$ simulation failed to predict these vortices, again showing that wall functions are unable to deal with these coherent structures.

The experimental observation [3] of the strong ring-type vortex (W) was confirmed in LES1[5] and is shown in Fig. 5b in LES2. Although both simulations show two wake vortices, in agreement with experimental observations, there are evident differences in their size and the position of the foci (F1 and F2) and saddle point (SP). In agreement with experiments, the lower vortex is smaller than the upper one. Figure 6 shows that the position of the stagnation point on the rear face of the model is different between the two simulations. Similar differences between the two simulations were observed in plane $y = 0$ in Fig. 7. Asymmetry in the flow behind the body in Fig. 7 indicates strong vortex interaction in the spanwise direction, which increases the requirement of longer time averaging.

4.4. ACKNOWLEDGMENTS

This work was supported by NUTEK and the Volvo Car Corporation. Computer time on the SGI ORIGIN 2000 machines, provided by UNICC at Chalmers, is gratefully acknowledged.

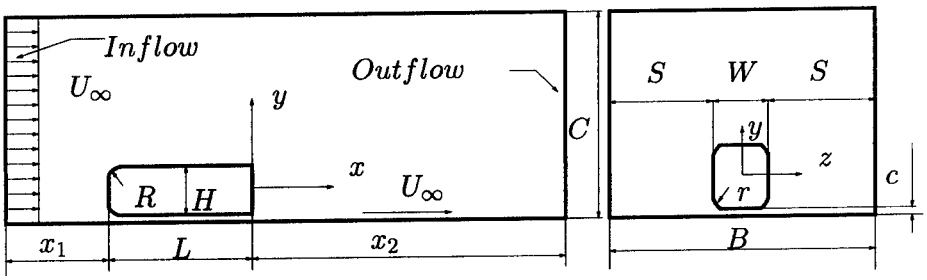


Figure 1. Geometry of the vehicle body and computational domain.

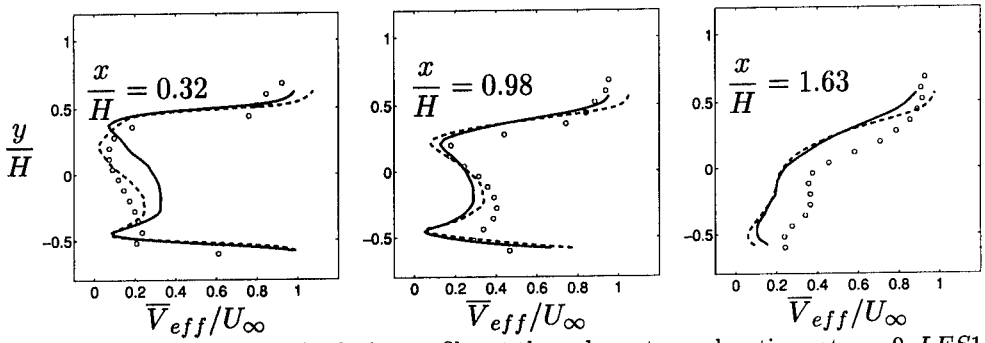


Figure 2. Time-averaged velocity profiles at three downstream locations at $z = 0$. $LES1$ (dashed line); $LES2$ (solid line); experiment (symbols).

References

1. P. W. Bearman. Review - bluff body flows applicable to vehicle aerodynamics. *ASME: Journal of Fluids Engineering*, 102:265–274, 1980.
2. M. Breuer. A challenging test case for the large eddy simulation: high Reynolds number circuler cylinder flow. *Int. J. Heat and Fluid Flow*, 21:648–654, 2000.
3. E. G. Duell and A. R. George. Experimental study of a ground vehicle body unsteady near wake. SAE Paper 1999-01-0812, 1999.
4. Y. I. Frucht. *High Reynolds number incompressible flow simulation about parachute canopies and similar bluff bodies.* PhD thesis, University of Leicester, 1987.
5. S. Krajnović and L. Davidson. Large eddy simulation of the flow around a ground vehicle body. In *SAE 2001 World Congress*, SAE Paper 2001-01-0702, Detroit, Michigan, USA, 2001.
6. H. Nilsson and L. Davidson. CALC-PVM: A parallel SIMPLEC multiblock solver for turbulent flow in complex domains. Int.rep. 98/12, Dept. of Thermo and Fluid Dynamics, Chalmers University of Technology, Gothenburg, 1998.
7. D. Sujudi and R. Haimes. Identification of swirling flow in 3-D vector fields. AIAA Paper AIAA 95-1715, 1995.

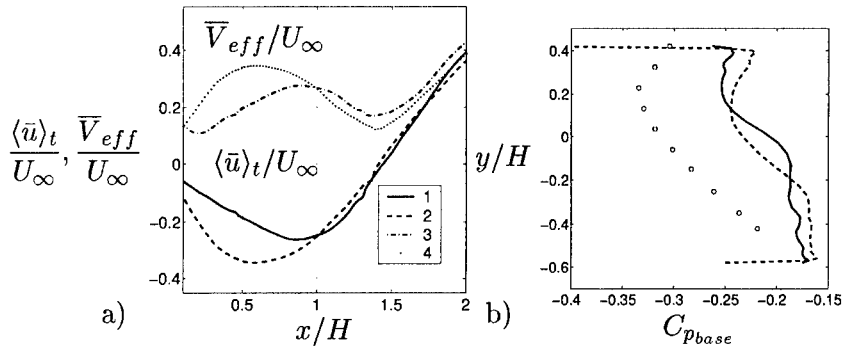


Figure 3. a) Distribution of the mean velocity component, $\langle\bar{u}\rangle_t/U_\infty$, $LES1$ (1); $LES2$ (2) and the mean velocity, $\overline{V}_{eff}/U_\infty$, $LES1$ (3); $LES2$ (4) along the x-axis at $y = 0$, $z = 0$. b) Distribution of the $C_{p_{base}}$ along the y-axis. Experimental data (symbols); $LES2$ (solid line); $LES1$ (dashed line).

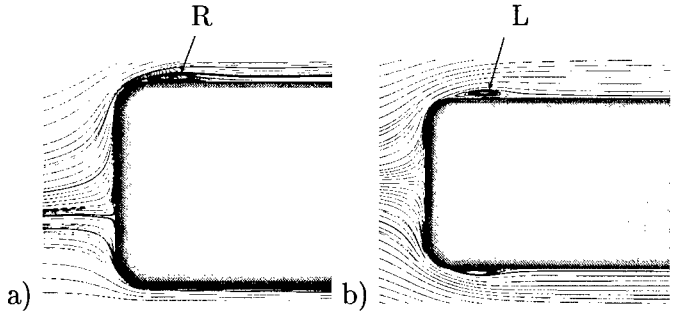


Figure 4. Simulation $LES2$. a) Time-averaged streamlines projected onto the symmetry plane, $z = 0$, of the bus. b) Time-averaged streamlines projected onto the symmetry plane, $y = 0$, of the bus.

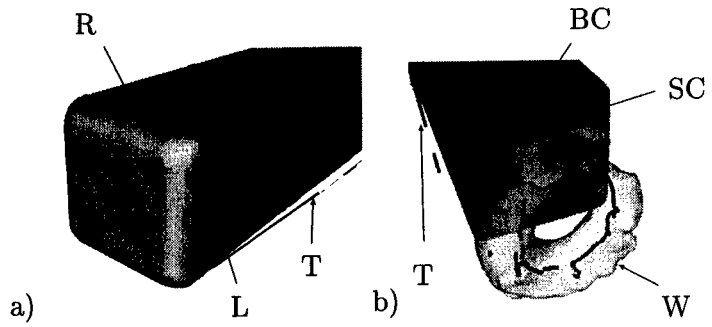


Figure 5. Simulation *LES2*. a) Streamlines emitted from the vortex cores on the roof (R), lateral sides (L) of the bus and trailing vortices (T). b) View of the rear face of the bus. The ring-type vortex (W) visualized with isosurface of pressure $p = -0.21$ and its vortex core. BC and SC are thin corner vortices behind the rear face of the model.

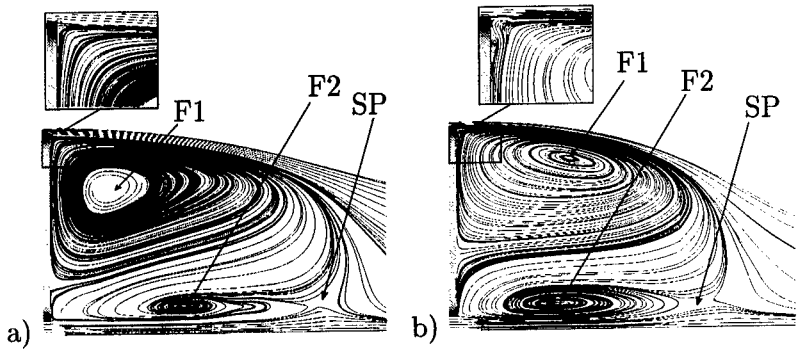


Figure 6. Time-averaged streamlines projected onto the symmetry plane, $z = 0$, of the bus. F1 and F2 are foci of vortices and SP is saddle point. a) *LES1*; b) *LES2*.

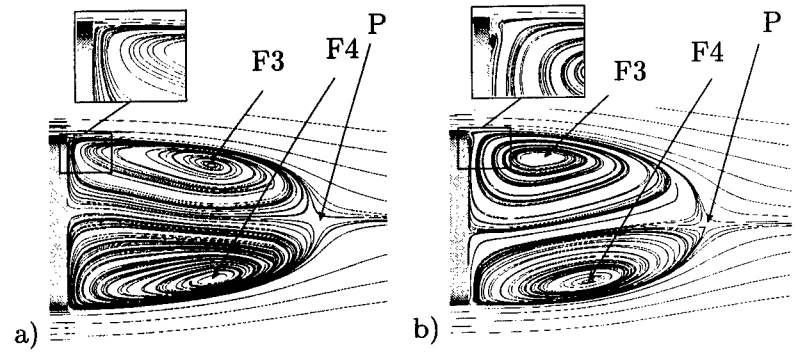


Figure 7. Time-averaged streamlines projected onto the symmetry plane, $y = 0$, of the bus. F3 and F4 are foci of vortices and P is free stagnation point. a) *LES1*; b) *LES2*.

LARGE EDDY SIMULATION OF A SUPERSONIC CAVITY FLOW WITH AN UNSTRUCTURED GRID FLOW SOLVER

BRIAN R. SMITH
Lockheed Martin Aeronautics Company
Fort Worth, Texas 76101

Abstract

Large Eddy Simulation methods were implemented in a hexahedral based unstructured grid flow solver and tested for the analysis of transonic flow over an open cavity. This approach was developed for efficient application of Computational Fluid Dynamics methods to the highly unsteady flows in a geometrically complex weapons bay. A compressible sub grid scale model was implemented. The compressible flow solver uses an upwind flux difference splitting scheme. A Mach 1.2 flow over an open cavity was simulated. Comparisons of computed and experimental spectra of the sound pressure level at several locations in the cavity are presented. Good agreements between the simulations and test were obtained.

1. Introduction

Weapons bay flowfields present significant design challenges for tactical aircraft. Unsteady resonant phenomena in an open bay can result in unsteady pressure levels above 170 dB. The aircraft structure, weapons bay doors and internally carried stores can be damaged by loads of this magnitude. Accurate prediction of these loads is important for the structural design of the aircraft, determination of suitability of stores for the weapons bay environment, and assessment of devices used for control and suppression of acoustic loads. Computational methods for predicting these loads will be useful in reducing the significant testing cost and design cycle time required for bay design and weapons integration.

A typical weapons bay geometry is highly complex and includes bulkheads, irregularly shaped doors, loaded stores with fins, and launchers. Generation of a structured mesh for this type of complex geometry is impractical because of the large number of man hours required. For simulation, unsteady Reynolds averaged Navier-Stokes methods have proven to be excessively diffusive for cavity simulation. Several studies have demonstrated the use of structured grid methods with Large Eddy Simulation (LES) for simple cavity flows.[1] In this work, LES methods implemented in the Lockheed Martin Aeronautics Splitflow unstructured grid solver are applied to a simple cavity flow to assess the accuracy of the methodology.

2. Numerical Methods

The Splitflow code includes two grid generation approaches, both of which are used in this work. The LES method implemented in Splitflow includes filter length smoothing required by the unique nature of Splitflow grids. The strong, moving shockwaves generated in a cavity flow are the motivation for the use of an upwind flow solver for the cavity simulations. Background information on Splitflow is available in the paper by Domel and Karman.[2]

2.1 Grid Generation Two grid generation options are available in Splitflow. The first, "cut grid" method, is a tree based splitting method for Cartesian cells. Cells aligned with the Cartesian axes are refined by splitting into two, four or eight cells. A triangulated surface mesh is used to define solid boundaries. Where Cartesian cells are cut by the triangulated surfaces, irregularly shaped cells result. Cells can be refined to flowfield gradients and structures in the course of a run by subdividing and recombining cells. The refinement process does not require regeneration of the entire mesh, and is therefore highly efficient. In the second, "body conforming" method, cells cut by boundary surfaces are deleted, and new body conforming cells are created by extrapolating from the inner cell faces to the surface. The resulting grid is then smoothed to improve grid quality. In this approach, the resulting grid is not aligned with the coordinate axes, and grid generation requires more computer time to complete than in the "cut grid" approach.

Both approaches are highly automated and require very few man hours to develop computational grids for complex configurations. The "cut grid" method is best suited to applications where high fidelity boundary layer resolution is not required, or where walls are aligned with Cartesian axes. The "boundary conforming" approach is best suited to problems requiring high fidelity simulation of turbulent boundary layers.

Because of the cell splitting approach, both types of Splitflow grids are extremely well suited to LES. Near no slip walls, the computational mesh can be refined in normal, lateral and streamwise directions, while coarser grids can be used in all three directions away from the wall.

2.2 LES Methods A compressible form of the Smagorinsky model was used.[3] The sub grid scale stresses are represented by a Favre mass averaged Bousinesq approximation using the mean velocities. The eddy viscosity is

$$\mu_t = \rho\ l^2|S|, \text{ where } |S| = \sqrt{2S_{ij}S_{ij}}$$

and $S_{ij} = \frac{1}{2}(\partial U_i/\partial x_j + \partial U_j/\partial x_i)$ is the strain tensor. The mixing length, l, is the product of the Smagorinsky constant, C_s, and the filter length, Δ. The constant C_s

is set to 0.1 for this study. Initially the filter length is set $\Delta = (\text{cell volume})^{1/3}$. However, unlike a structured grid, neighboring Splitflow cells can vary in volume by a factor of 8, resulting in a doubling of the filter length across a cell face. This is inconsistent with sub grid scale filtering assumptions. To alleviate this problem, the filter length at each cell is smoothed in multiple passes through a smoothing routine that sets the filter length equal to the average of the maximum of the filter length for the current cell and all of its immediate neighbors,

$$\Delta_c^{p+1} = \frac{1}{N}\sum_{n=1}^{N} \max(\Delta_c^p, \Delta_n^p)$$

where N is the number of neighboring cells, and p is the sweep index. This approach provides a smoother variation in the filter length through the flowfield. Regions of locally fine mesh effectively have a larger value of eddy viscosity. As a result, the numerical accuracy of the flow solver is improved by reduction in truncation error, but the level of the sub grid scale stresses in regions of locally fine mesh is higher than it would be if the mesh were more uniformly fine.

2.3 Flow Solver Methods The flow domain is segmented into multiple subdomains and solved in parallel using PVM. The convective terms are evaluated using a third order accurate, finite volume upwind scheme. The primitive variables, (ρ, *u, v, w, T*) are extrapolated to the left and right sides of each cell face using the cell center gradients of the primitive variables on each side of the cell face. The resulting left and right states are the basis for the upwind diffusion term. This approach is formally third order accurate where cells are evenly spaced, and second order accurate where cell division creates local variations is cell size. In regions of the flow field with strong shock waves, a flux limiter is employed.

Because the cavity application has strong shocks, a compressible solution algorithm including the Roe upwind flux difference split scheme is employed.[4] This scheme is considerably less diffusive in low speed and wall boundary layer regions than flux vector split algorithms. Nevertheless, the scheme tends to damp unsteady flow structures in wall boundary layers, particularly when the local flow velocity is not aligned with the grid direction. The diffusion term was reduced by multiplying it by a function of the ratio of the contravarient velocity to the local velocity magnitude. This approach significantly reduces the damping of unsteady structures while providing sufficient upwind influence for numerical stability.

The solution is advanced in time using a pointwise block implicit algorithm. In order to obtain second order accuracy in time, multiple sub-iterations are employed to converge the solution at each time step. This approach allows local CFL numbers significantly larger than one to be used. For compressible flow

simulations with fine grid spacing normal to the wall, the acoustic wave speed can severely limit the allowable time step.

3. Cavity Flow Application

A cavity flow from the Weapons Internal Carriage and Stores test was used to evaluate the code's accuracy.[5] The geometry tested was a simple rectangular cavity in a model with a sharp leading edge. The model has a 15 inch long, 16.5 inch wide flat plate in front of the cavity. The LxWxD of the cavity is 18"x4"x4". The Mach number for the demonstration case is 1.2, the Reynolds number per foot of the flow is 1.0×10^6. The diagram of the cavity in Figure 1 includes relevant sensor locations.

3.1 Simulation Approach To reduce the computational requirements, a turbulent channel flow was used to generate a turbulent boundary layer for the inflow boundary condition for the cavity flow simulation. The channel flow domain is two inches long, one inch wide and its height is 0.56 inches, twice the incoming boundary layer thickness of the cavity flow. The Reynolds number for the channel based on half the channel height is 19,000. Periodic boundary conditions are applied in the lateral and streamwise directions. Flow pressure, momentum and total enthalpy are adjusted between the inflow and outflow periodic boundaries to account for compressibility effects. A cut grid mesh containing 138,000 cells was generated. Figure 2 shows a cross section view of the channel grid. The near wall spacing was $\Delta z^+ = 1.7$, $\Delta y^+ = 29$, $\Delta x^+ = 58$. The channel outflow solution was repeated across the lateral "y" direction to span the cavity inflow. The channel and cavity solutions were run simultaneously, and information was passed at each iteration from the channel to the cavity flow solution.

The cavity grid was generated using the body conforming approach. The grid contains 614,000 cells. The grid is most highly resolved in the shear layer near the leading edge of the cavity. Figure 3 shows a centerline view of the cavity grid.

The solutions were performed using a time step of 5×10^{-7} second. Over 60,000 iterations were completed. Figure 4 shows instantaneous velocity contours along the centerline of the cavity. Figure 5 shows instantaneous velocity contours 2, 10 and 16 inches downstream of the leading edge of the cavity. Vortical structures at the edge of the cavity near the trailing edge are clearly visible. The shear layer disturbances are much smaller near the cavity leading edge.

Sound pressure level spectra from test and simulation at four locations in the cavity are shown in Figure 6. The simulation clearly captures most of the resonant tones in the cavity. In addition, the levels are predicted with reasonable accuracy.

The significant variations in the SPL between the front and back wall of the cavity are also predicted well.

Acknowledgements This work was funded by AFOSR under the "Large Eddy Simulation for the Analysis of Weapons Bay Flows" program, Contract No. F49620-99-C-0020. The author would like to thank Dr. Leonidas Sakell and Dr. Robert Herklotz for their support.

References

1. Smith, B. R., Jordan, J. K., Bender, E. E., Rizk, S. N. and Shaw, L. L., "Computational Simulation of Active Control of Cavity Acoustics," AIAA Paper 2000-1927, Lahaina, HI, June, 2000.

2. Domel, N. D. and Karman, S. L. "Splitflow: Progress in 3D CFD with Cartesian Omni-tree Grids for Complex Geometries,", AIAA Paper 2000-1006, Reno, NV, January, 2000.

3. Smagorinsky, J., "General Circulation Experiments with the Primitive Equations," Mon. Weather Rev., (1963), Vol. 91. pp. 99-164.

4. Roe, P. L., "Characteristic-Based Schemes for the Euler Equations," *Annual Review of Fluid Mechanics*, Vol. 18, 1986, pp. 337-365.

5. Dix, R. E. and Dobson, T. W. Jr., "Database for Internal Store Carriage and Jettison," Final Report, AEDC-TR-90-23.

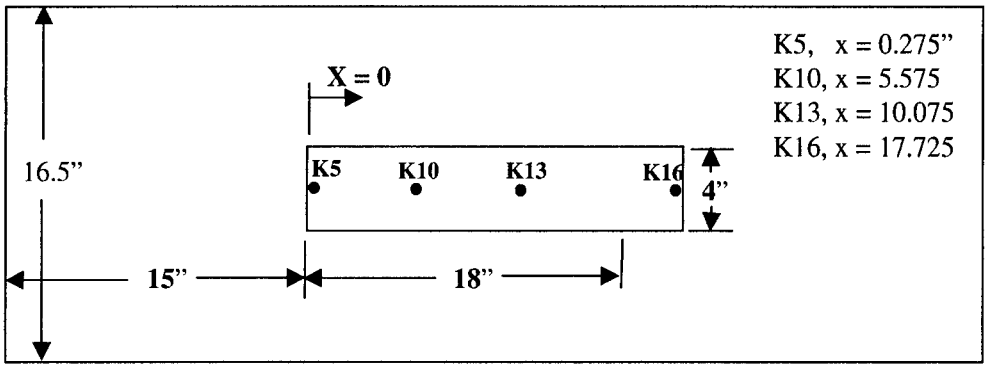


Figure 1 Diagram of cavity geometry including pressure sensor locations

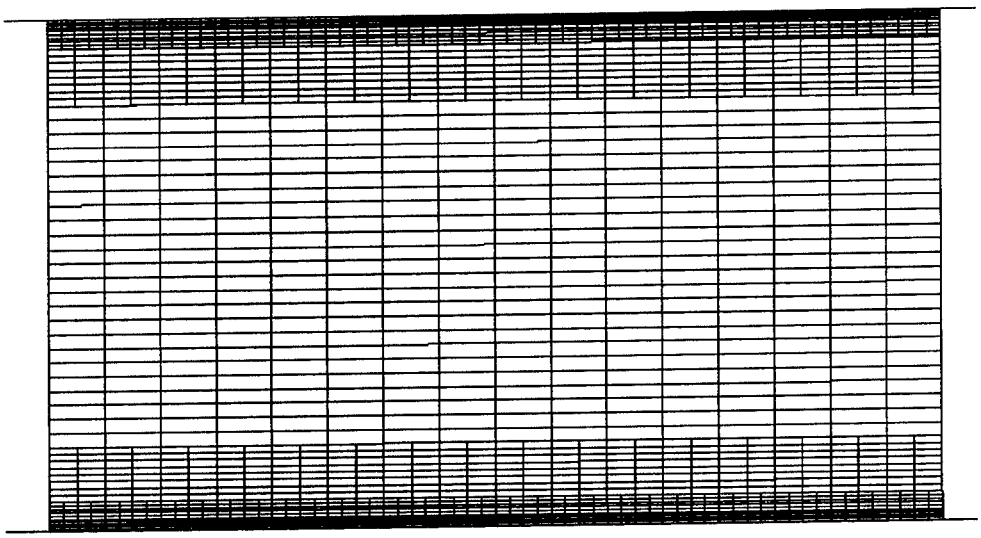


Figure 2 Cross section view of channel grid

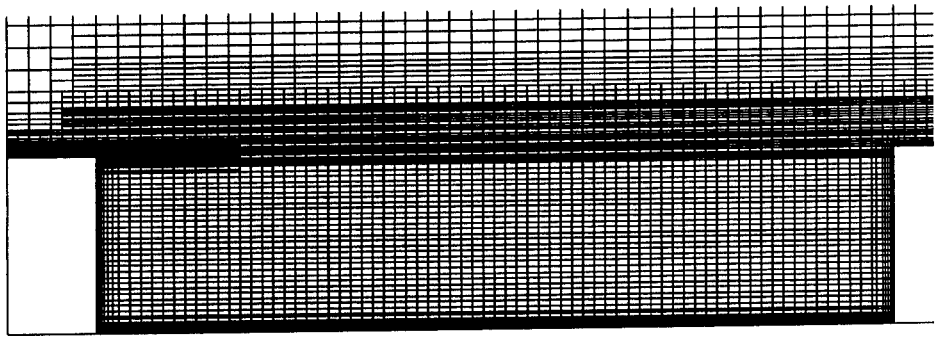


Figure 3 Centerline view of cavity grid

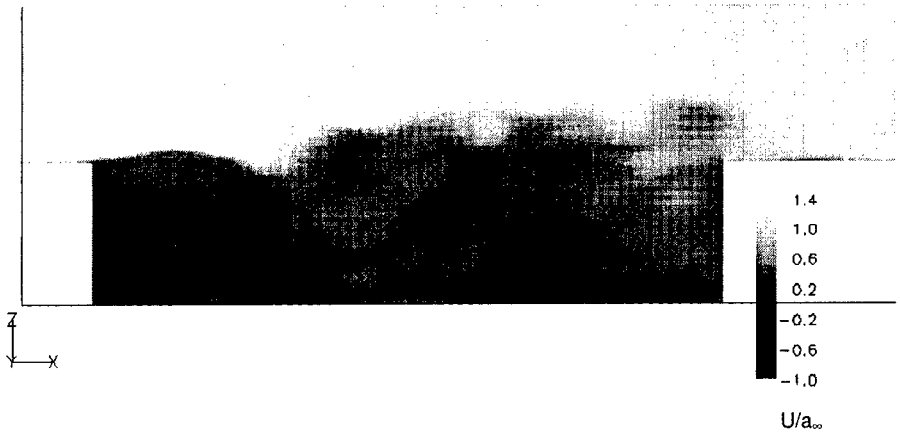


Figure 4 Contours of instantaneous stream wise velocity on cavity center-line.

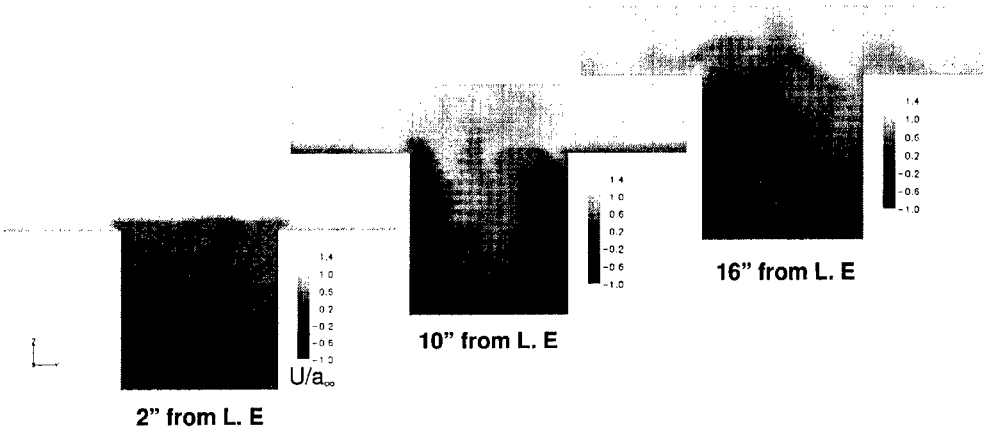


Figure 5 Contours of instantaneous stream wise velocity 2", 10" and 16" from cavity leading edge.

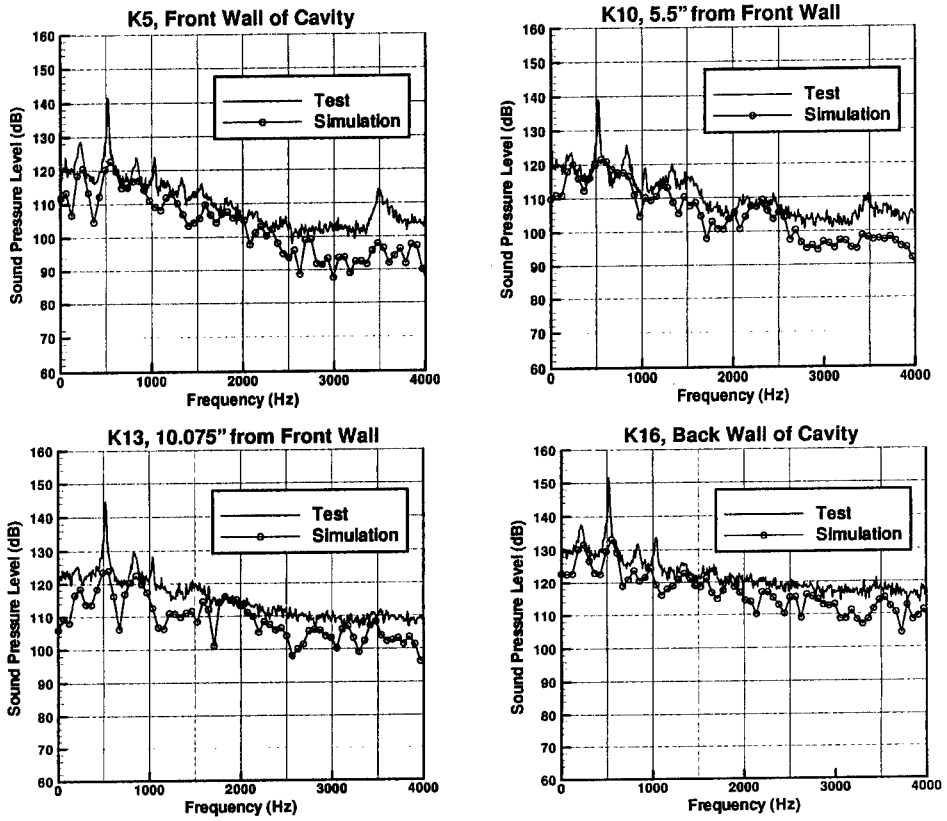


Figure 6 Test and simulation spectra of sound pressure level at pressure sensor locations.

PRELIMINARY LES OVER A HYPERSONIC ELLIPTICAL CROSS-SECTION CONE

M.P. MARTIN
Mechanical and Aerospace Engineering, Princeton University, Princeton, NJ 08544

M. WRIGHT
Eloret Corporation, NASA Ames Research Center, Moffett Field, CA 94035

G.V. CANDLER
Aerospace Engineering and Mechanics, University of Minnesota, Minneapolis, MN 55455

U. PIOMELLI
Mechanical Engineering, University of Maryland, College Park, MD 20742

G. WEIRS
ASCI Flash Center, University of Chicago, Chicago, IL 60637

AND

H. JOHNSON
Aerospace Engineering and Mechanics, University of Minnesota, Minneapolis, MN 55455

Abstract. The characteristics of the hypersonic flow around an elliptical-cross section cone and the computational code to perform large-eddy simulations of this flow are described. Preliminary results of the Lagrangian implementation used to compute the subgrid-scale terms are presented.

1. Introduction

Many aspects of transitional and turbulent flows are not fully understood. This is especially true in the hypersonic regime, where examples of unresolved issues include the effect of freestream disturbances and three-

dimensionality. In the absence of detailed experimental or computational databases to better understand these physical phenomena, we are left with excessive design conservatism and unrefined conceptual designs.

When investigating these phenomena via CFD, direct numerical simulations (DNS) are not affordable. Turbulence models provide a wide range of accuracy in predicting turbulent flows of engineering interest. Depending on the level of detail required, one may choose the Reynolds-averaged Navier-Stokes (RANS) models or the state of the art subgrid scale (SGS) models in a large-eddy simulation (LES) to obtain a more refined prediction. The study of fundamental physical phenomena must be done using the finest possible prediction, namely LES. However, one must keep in mind that a key feature of the prediction is the validation with experiments.

Using the most recent laser and camera technologies, Huntley[1] and Huntley *et al.*[2] present the first detailed flow visualization of natural transition on an elliptical cross-section cone at Mach 8. Mean flow features and details about the unstable modes in the boundary layer for the same configuration are given by Kimmel *et al.*[3,4] and Poggie *et al.*,[5] respectively. Because this flow is being extensively documented experimentally and because the geometric configuration resembles that of the forebody of a hypersonic vehicle, this database is ideal to test the state of the art SGS models and LES methodology for hypersonic flows.

The present work is an ongoing effort to provide detailed flow simulations of unsteady, hypersonic, transitional or turbulent flows. In Martin *et al.* (2000a) we develop and test SGS models for compressible LES using the apriori test in compressible, isotropic turbulent flow. In Martin *et al.* (2001) we validate the LES methodology against the DNS of supersonic boundary layers, and in Martin *et al.* (2000b) we extend the LES code to generalized curvilinear coordinates and validate the implementation in supersonic turbulent boundary layer flow. In this paper, we present preliminary LES results of the flow around a section of an elliptical cross-section cone away from the tip of the cone. The flow conditions, simulation procedure, preliminary flow assessments, and future work are given in the following sections.

2. Geometry and flow conditions

Following the experimental configuration of Huntley *et al.*,[2] the lifting body geometry is a sharp-nosed, elliptical cross-section cone. The nominal radius of the experimental model is less than 200 μm. In our simulations, we use an ellipsoidal nose with an 80 μm diameter of nose ellipsoid measured on the major axis. The afterbody is an elliptical cross-section cone of 4:1 aspect ratio, 17.5 degrees half-angle in the major axis, and 0.242 m in length, resulting in base dimensions of 0.152 m across the major axis and 0.038 m

across the minor axis.

The freestream flow conditions are $Re_\infty = 14 \times 10^6$ /m, $M_\infty = 8$, $\rho_\infty = 0.5$, and $T_\infty = 58$ K. For these conditions, the boundary layer is fully turbulent at position x=17.5 cm from the nose.[1] The wall-temperature condition is prescribed to 450 K, which is nearly adiabatic. As in the experiments, air is the working fluid.

The Mach 8 flow around the 4:1 elliptical cross-section cone at zero angle of attack is highly compressed behind the shock. The difference in shock strength between the major and minor axis causes a higher compression at the leading edge producing a cross flow from the leading edge to the centerline of the cone. This is illustrated in Fig. 1a. At the centerline the cross-flow velocities are zero and mass conservation induces a bulge, see Fig. 1b, where the boundary layer is twice as thick as the boundary layer in the off-center region.[1] Experiments show that transition occurs first on the centerline.[1]

3. Grid resolution

We estimate the resolution requirements by considering the dimensions of the turbulence structure and the data provided by the experiments. From the experimental data[1], the estimated wall unit is 7.5×10^{-5} m and the boundary layer along the centerline is laminar at $x = 9$ cm, late-transitional at 11.4 cm, and fully turbulent at 17.5 cm from the nose. See Figure 2. The turbulent boundary layer at the center line is 5 to 6 mm thick. Note that the shock-standoff distance is $\theta_s = 1.2\theta_c$, where θ_s and θ_c are the shock and cone angles, respectively. The turbulence structures on a flat plate boundary layer extend about 100 wall units in the spanwise direction and a few boundary layer thicknesses in the streamwise direction.

In the spanwise direction we use a uniform grid spacing of 22 wall units. This estimate is based on the grid resolution used in previous LES of a supersonic boundary layer.[7] For the conditions chosen, the boundary layer at the leadingedge is laminar.[1] Since the flow is supersonic and the cone is at zero angle of attack, the flow around the top of the cone is not affected by the flow on the bottom. Thus only the top of the cone is simulated. In the streamwise direction, the flow is laminar at $x = 9$ cm from the nose. Thus, the resolution requirements up to 9 cm from the nose are given by the grid convergence studies of the laminar flow at the nose. From $x = 9$ cm to the base of the cone we require that the maximum grid spacing on the surface is 33 wall units. In the wall-normal direction the grid is exponentially stretched, we require 0.3 and δ^+ wall units for the minimum and maximum grid spacings within the boundary layer,[7] where $\delta^+ = \delta/z_\tau$ is about 70 for the turbulence case. The computational domain is large

enough to include the standoff shock wave.

4. Simulation procedure

For the LES, we use a third-order accurate WENO[9] to compute the convective fluxes. This scheme has low dissipation properties, and was designed to perform DNS and LES of compressible flows. The time advancement technique is based on the DPLU relaxation method of Candler *et. al*[10] and was extended to second-order accuracy by Olejniczak and Candler.[11] The viscous fluxes are evaluated using fourth-order central differences. Finally, the transformation metrics are evaluated using fourth-order central differences so that the inaccuracy of the numerical evaluation of the metrics coefficients is less than the inaccuracy of the convected fluxes.

The initial condition will be a superposition of laminar flow and a prescribed freestream energy disturbance spectrum. To generate the laminar solution we use a finite volume code,[12] where we only compute 90 degrees of the cone geometry and use bilateral symmetry to reflect the resulting solution across the centerline and generate the full 180 degrees. We then interpolate the laminar solution from the finite-volume cell centers to the finite-difference grid points using tri-linear interpolation.

The required SGS terms and the model representations are given in Martin *et al.* (2000a, 2000b). To evaluate the model coefficients we use the Lagrangian-averaging operation, where the averaging is performed along a fluid particle pathline. A full description of the Lagrangian-average procedure can be found in Meneveau *et al.* (1996).

5. Preliminary flow assessments and future work

In this section we present a brief progress report in performing the LES. A portion of the cone has been initialized using the interpolated laminar solution to test the Lagrangian implementation of the SGS models. To minimize the complexity of this test, the disturbances introduced by the tri-linear interpolation are used as initial disturbances. Figures 3 through 5 show contours of the SGS terms at the exit plane of the cone on spanwise wall-normal planes. These figures include a quarter of the computational domain (centered about the centerline) in the spanwise direction, and about ten boundary layer thickness in the wall normal direction, the boundary layer thickness along the centerline is about 2 mm, three times smaller than the turbulent boundary layer. Figures 3 through 5 show that the SGS terms are dominant in the bulge region. This would not be the case if the model coefficients were calculated using the ensemble average procedure.

The magnitude of the initial disturbances is very small and do not grow significantly in time. Future work includes imposing a prescribed distur-

bance energy spectrum and running the LES to gather sufficient statistical data to assess the effect of freestream disturbance and study the transition and turbulence phenomena.

Computer time was provided by NASA Ames Research Center. This work was supported in part by the Air Force Office of Scientific Research under grant AF/F49620-01-1-0060.

6. References

[1] Huntley, M., "Transition on elliptic cones at Mach 8," PhD thesis, Princeton University, November 2000.

[2] Huntley, M., Wu, P., Miles, R.B., Smits, A.J., "MHZ Rate Imaging of Boundary Layer Transition on Elliptic Cones at Mach 8," *AIAA Paper No. 2000-0379*, January 2000.

[3] Kimmel, R.L., and Poggie, J., "Laminar-Turbulent Transition in a Mach 8 Elliptic Cone Flow," *AIAA Journal,* **37**, 1080, 1999.

[4] Kimmel, R.L., Klein, M.A., and Schwoerke, S.N., "Three-Dimensional Hypersonic Laminar Boundary-Layer Computations for Transition Experiment Design," *Journal of Spacecraft and Rockets,* **34**, 409, 1997.

[5] Poggie, J., Kimmel, R.L., and Schwoerke, S.N., "Traveling Instability Waves in a Mach 8 Flow over an Elliptic Cone," *AIAA Journal,* **2**, 2000.

[6] Martín, M.P., U. Piomelli and G.V. Candler, "Subgrid-Scale Models for Compressible Large-Eddy Simulations," *Theoretical and Computational Fluid Dynamics*, **13**, 361, 2000a.

[7] Martín, M.P., U. Piomelli and G.V. Candler, "Direct and large-eddy simulations of turbulent supersonic boundary layers," *Submitted to Journal of Fluid Mechanics,* 2001.

[8] Martín, M.P., G. Weirs, G.V. Candler, U. Piomelli, H. Johnson, I. Nompelis, "Toward the large-eddy simulation over a hypersonic elliptical cross-section cone," *AIAA Paper No. 00-2311*, June 2000b.

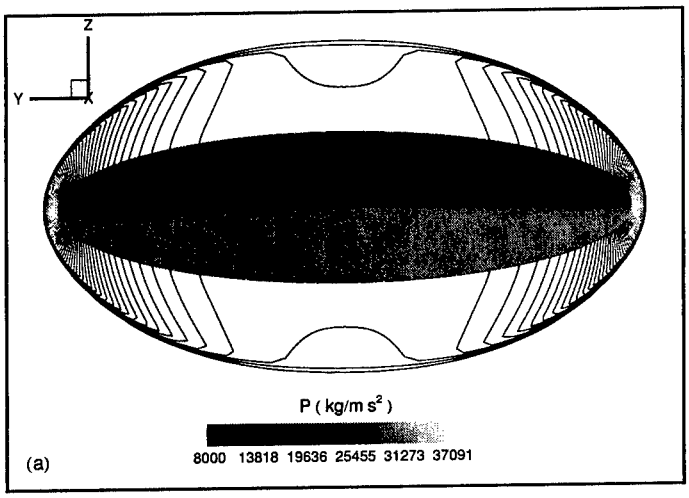
[9] Weirs, V.G., and G.V. Candler, "Optimization of weighted ENO schemes for DNS of compressible turbulence," *AIAA Paper No. 97-1940*, June 1997.

[10] Candler, G.V., Wright, W.J. & McDonald, J.D. *AIAA Journal,* 32, 2380-2386, 1994.

[11] Olejniczak, D.J. , and G.V. Candler, "A Data-Parallel LU relaxation method for DNS of compressible flows," *1st International Conference in DNS and LES*, Louisiana, August 1997.

[12] Wright, M.J., G.V. Candler, and D. Bose, "Data-Parallel Line Relaxation Method for the Navier-Stokes Equations," *AIAA Journal,* **36**, 9, 1998.

[13] Meneveau, C., T.S. Lund and H.Cabot, "A Lagrangian Dynamic Subgrid-scale Model of Turbulence," *Journal of Fluid Mechanics,* **319,** 353-385, 1996.



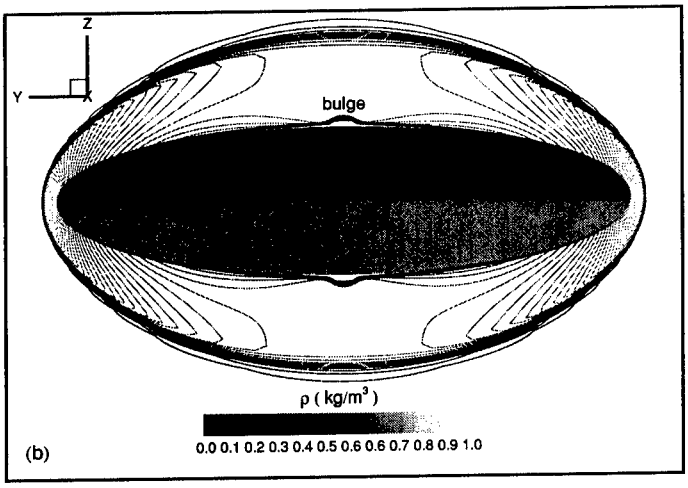


Figure 1. (a) Pressure and (b) density contours in the exit plane of the cone geometry for the laminar solution.

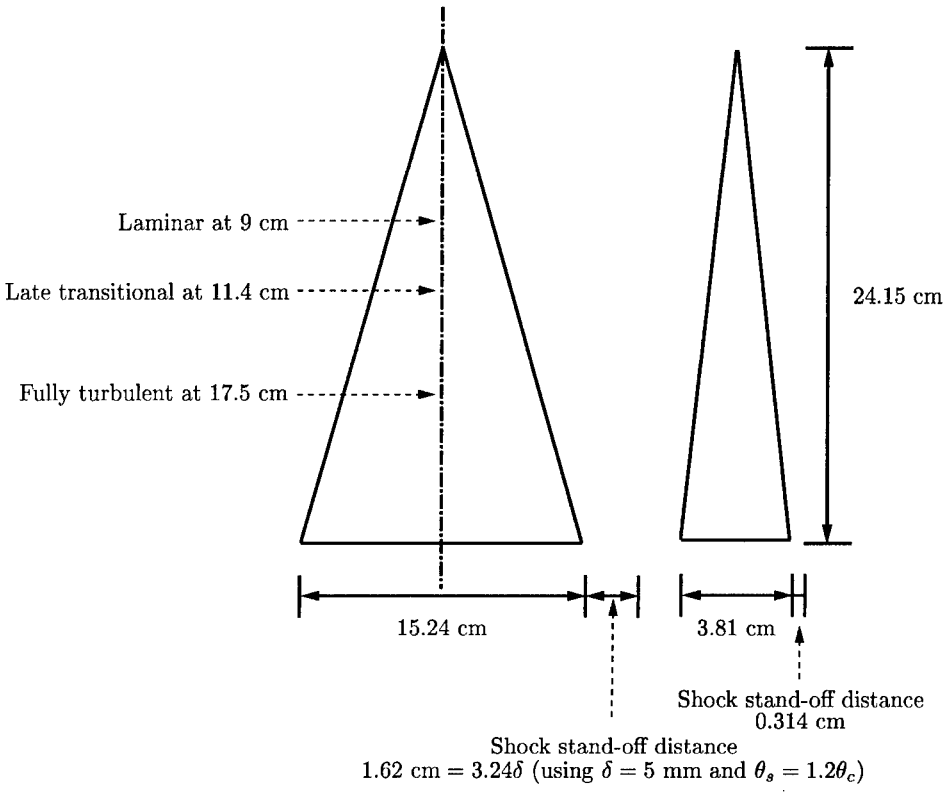


Figure 2. Model dimensions and key flow features required to determine the grid resolution and computational domain size.

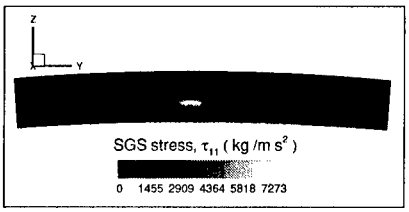


Figure 3. SGS stress contours on the exit plane, the flow is into the page.

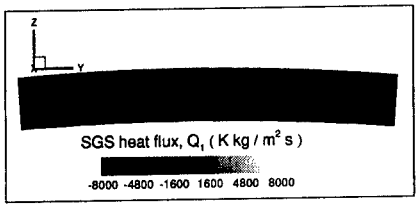


Figure 4. SGS heat flux contours on the exit plane, the flow is into the page.

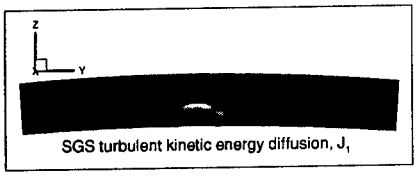


Figure 5. Contours of SGS turbulent kinetic energy on the exit plane, the flow is into the page.

FLOW AND HEAT TRANSFER PREDICTIONS FOR FILM-COOLING FLOWS USING LARGE EDDY SIMULATIONS

MAYANK TYAGI, SUMANTA ACHARYA
Mechanical Engineering Department
Louisiana State University, Baton Rouge, LA

Abstract

Large eddy simulations are performed to study the flow physics and heat transfer for the film-cooling of gas turbine blade surface. The coolant jet issues out from a cylindrical delivery tube into the mainflow at an inclination angle of 35°. The Reynolds number based on the jet velocity and the diameter of the delivery tube is approximately 11100. The jet to mainflow velocity ratio is 0.5. Heat transfer calculations are also performed simultaneously to study the mixing of the passive scalar with the mainflow, evaluate film-cooling effectiveness and heat transfer predictions on the blade surface. The parameters in the simulation correspond to the experiments performed at UTRC (Lavrich and Chiappetta, 1990)

1. Introduction

Advanced gas turbines are designed to operate at high turbine inlet temperatures. Increased temperatures improve the second law efficiency as well as the specific thrust obtained by the turbines. This poses a challenge to design better and efficient cooling methodology for gas turbine blades in the stages after the combustor. Film-cooling is used to maintain the turbine blade temperature below their melting point for the increased blade life. In film-cooling, coolant jets are injected at an angle into the hot mainflow that deflects these coolant jets over the blade surface to provide a coolant film coverage. However, the increased amount of coolant injection can deteriorate the aerodynamic performance and the gas path temperature drastically. Therefore, the amount of coolant should be optimal.

There is enormous amount of literature on the numerical studies done for a jet-in-crossflow configuration (Acharya et al, 2001). Most of the studies employed two-equation turbulence models with varied degree of success in predicting the flow field and heat transfer. Earlier LES studies of jet-in-crossflow flow situations (Jones and Wille, 1996, Yuan et al., 1999, Tyagi and Acharya, 1999) were performed for normal injections and high blowing ratios. In this study, a computational domain was chosen that represented the experiments conducted at UTRC. In general, the RANS calculations under-predict the lateral spread and mixing of the jet while they over-predict the vertical penetration of the coolant jet. In figure 1, predictions of the transverse shear stress component $u'w'$ that is responsible for the lateral spread are shown for Reynolds Averaged Navier Stokes (RANS) calculations using two-equation turbulence model, second moment closure model and previous LES studies for a square jet injected normally into the crossflow (Walters and Leylek, 1997, Tyagi and Acharya,

1999). Clearly, RANS modeling either at two-equation level or at the second moment level is inaccurate for this stress component while LES can capture the flow physics well.

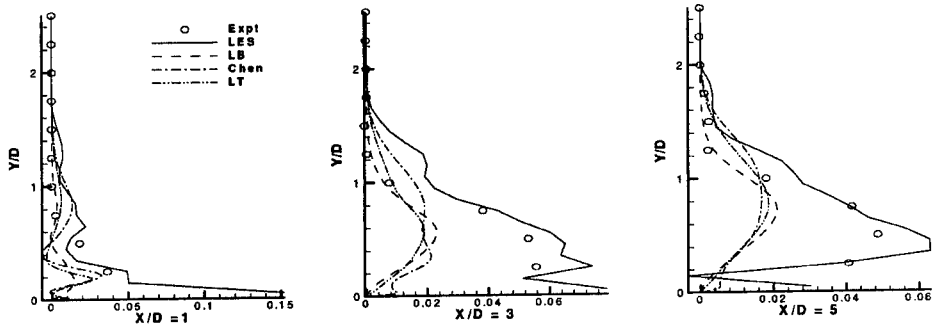


Figure 1 Transverse shear stress ($u'w'$) along Z/D = -0.5. RANS vs LES predictions. The experimental data is from Ajersch et al (1995).

2. Governing Equations and Computational Method

The non-dimensional governing equations for conservation of mass, momentum and energy for an incompressible Newtonian fluid in LES methodology are as follows

$$\frac{\partial U_j}{\partial x_j} = 0$$

$$\frac{\partial U_i}{\partial t} + \frac{\partial U_i U_j}{\partial x_j} = -\frac{\partial p}{\partial x_i} + \frac{1}{\mathrm{Re}} \frac{\partial^2 U_i}{\partial x_j^2} + \frac{\partial \tau_{ij}}{\partial x_j} + f_i$$

$$\frac{\partial \Theta}{\partial t} = [1-\Phi]\left(-U_j \frac{\partial \Theta}{\partial x_j} + \frac{1}{\mathrm{Re}\cdot \mathrm{Pr}} \frac{\partial^2 \Theta}{\partial x_j^2} + \frac{\partial q_j}{\partial x_j} \right) + \Phi \frac{\Lambda}{\mathrm{Re}\cdot \mathrm{Pr}} \frac{\partial^2 \Theta}{\partial x_j^2}$$

where U_i is the filtered velocity field, f_i is the body force terms arising due to immersed solid surfaces, $\Theta = \dfrac{T - T_\infty}{T_j - T_\infty}$ where T_j is the coolant jet temperature and T_∞ is the mainflow temperature, Λ is the ratio of thermal diffusivity of the immersed solid to thermal diffusivity of the fluid and Φ is the indicator function for solving the solving the unsteady diffusion problem in the immersed solid. The indicator function is 1 inside the solid and zero everywhere else. The SubGrid Scale (SGS) stress tensor and SGS scalar flux vector are given by τ_{ij} and q_j respectively. In this study, Dynamic Mixed Model (DMM) is used to model these SGS stress tensor and scalar flux vector (Moin et al., 1991, Vreman et al., 1994). The box filters are used in the Germano identity for the calculation of

dynamic coefficient and for the calculation of Leonard stresses. The dynamic coefficient is test filtered to avoid numerical instabilities.

The momentum equations are solved using projection method. The temporal scheme is explicit second order accurate Adams-Bashforth scheme. The spatial descretization is done using fourth order central finite-difference schemes for all the terms except the convective term $\left(\frac{\partial U_\alpha U_\alpha}{\partial x_\alpha}\right)$ that is upwind-differenced with a third accurate scheme. The pressure-Poisson equation is solved using a direct solver based on matrix diagonalization. The Laplacian operator is approximated using 4-2 formaulation i.e. the gradient operator is fourth order central difference operator and the divergence operator is second order accurate central difference operator. All the terms in energy equation are fourth order centrally differenced.

3. Problem Description

A uniform grid of 172×102×42 is used to model the computational domain of size 17D×5D×4D, where D is the diameter of the coolant jet delivery tube. The film-cooled surface is placed at 1.5D from the bottom of the computational domain. The center of the jet injection hole at the film-cooled surface is 5D downstream from the inlet plane. The jet delivery tube is simulated as a cylindrical surface inclined at 35° in the streamwise direction (X) using Immersed Boundary Method. A crossflow-stagnation type plenum is simulated in this study for the coolant supply. The top wall for the plenum is placed at 0.5D from the bottom of the computational domain. The bottom plane of the computational domain is treated using symmetry boundary conditions. Top boundary of the computational domain is treated as freestream boundary. At the inlet, fully developed turbulent profile is specified. At the outflow, a convective boundary condition is used where the convection speed is obtained from the mass flux balance. The spanwise direction (Z) is assumed to be periodic.

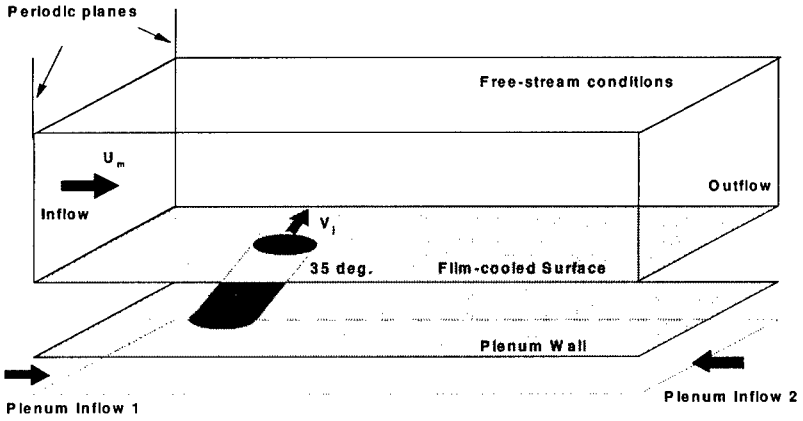


Figure 2 Schematic of the computational domain

4. Results and Discussion

The experiments were conducted with a large tube-length (approx. 5.5D) and a can-type plenum. However, in this study, the plenum is simulated as a stagnation flow field below the jet-delivery tube. The mass flow rate into the plenum is such that the velocity ratio of 0.5 is achieved at the coolant hole exit. The jet-delivery tube is short (approx. 1.74D). These changes are made to simulate a reasonable computational domain that retains all the essential physics. Such discrepancies are not expected to change the flow field dynamics and heat transfer in this flow situation drastically.

FLOW FIELD DESCRIPTION

There is a recirculation region inside the tube at the leeward surface (Figure 3a). This effect has been reported in earlier RANS studied (Walters and Leylek, 1997). The stagnation flow field below the jet delivery tube as well as the recirculation regions in the tube are observed in figure 3b. The development of the vorticity field inside the delivery tube leads to complex internal structure to the counter-rotating vortex pair (CVP) or the kidney vortex in this flow situation (Fric and Roshko, 1994, Andreopoulos and Rodi, 1984). The recirculation region behind the jet on the wall is also noted.

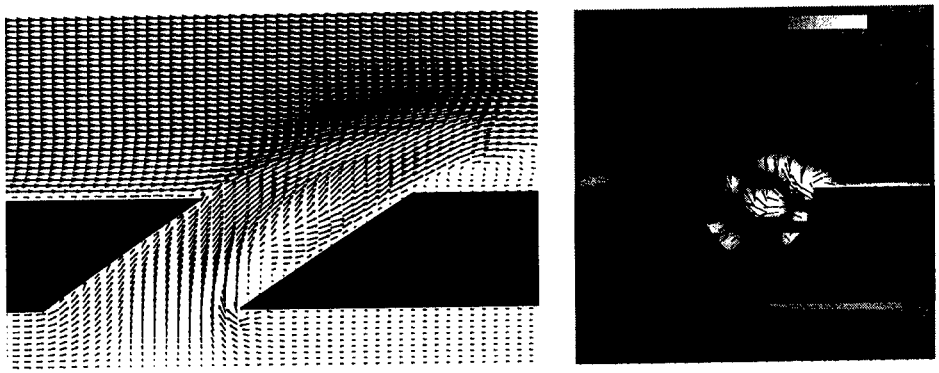
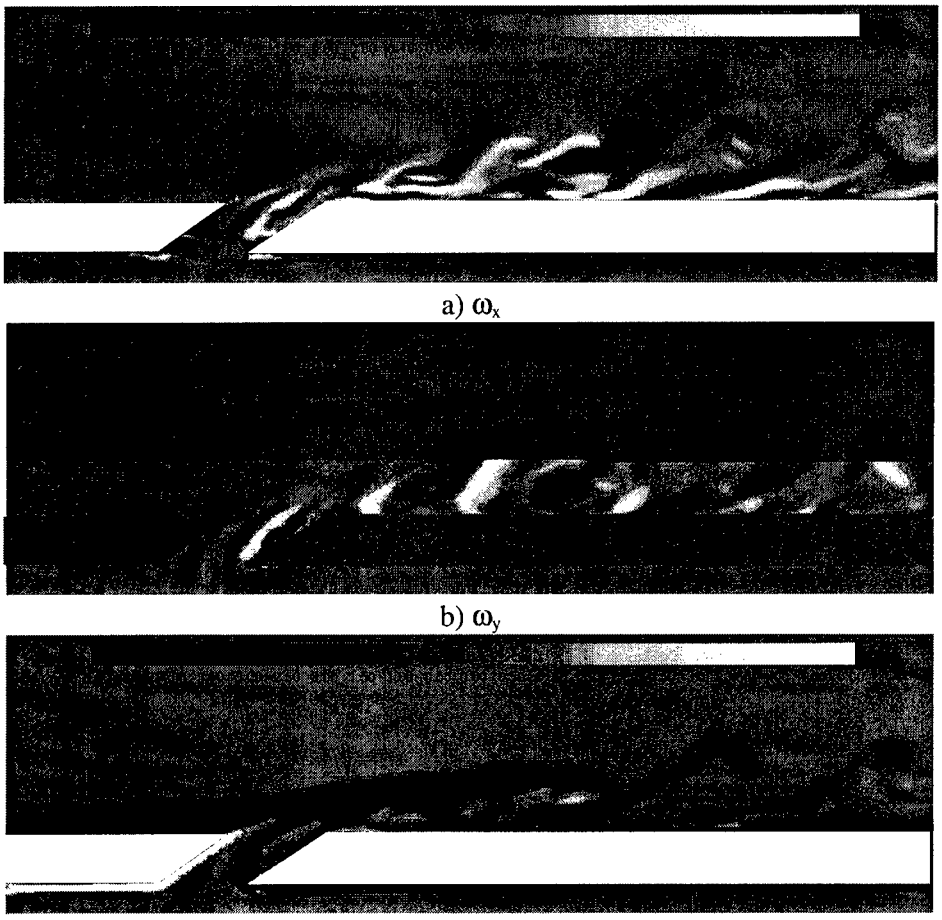


Figure 3 Details of the velocity field inside the coolant jet delivery tube

In figure 4a-c, the instantaneous vorticity field components are presented on the jet-centerplane (Z/D = 0.0). The streamwise component of vorticity, ω_x indicates the location of the lobes of CVP and the intertwining of this vorticity component is an indicator of crossplane mixing. The contours of ω_y correspond to the upright wake vortices that are shed into the wake of the deflected jet. The contours of ω_z show the vorticity generated inside the tube around the recirculation region near the plenum, is shed along with the vorticity generated at the leeward edge of the coolant jet. The interaction of the vorticity generated at windward edge of the coolant jet inside the delivery tube and the oncoming boundary layer vorticity is also observed. The delivery tube vorticity dynamics gives rise to complex and unsteady CVP.



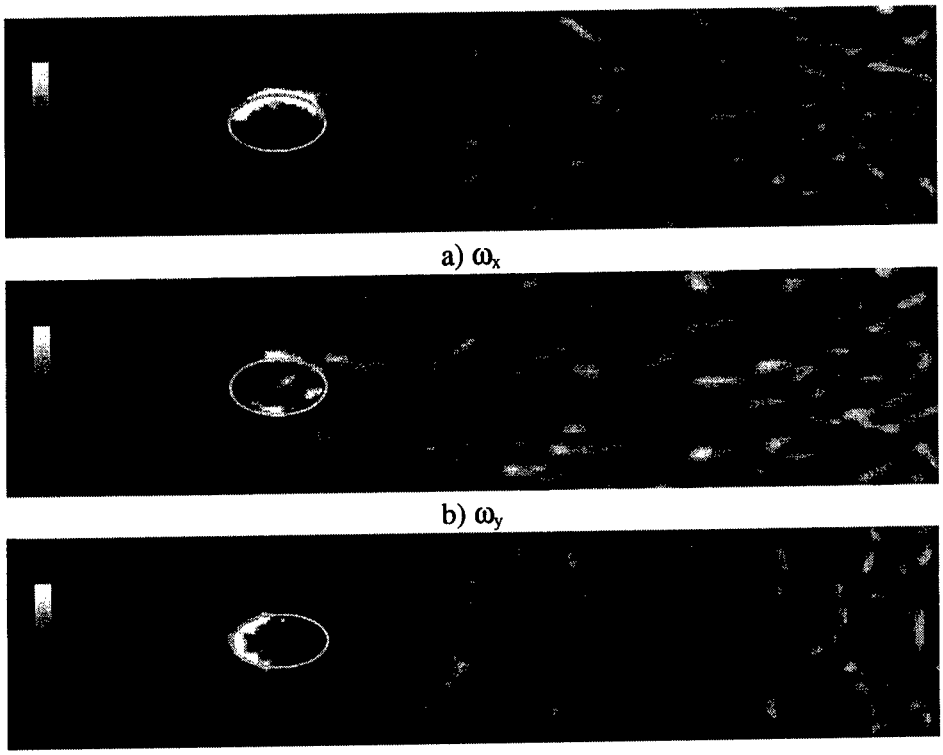
a) ω_x

b) ω_y

c) ω_z

Figure 4 Instantaneous vorticity field components (a-c) on the jet-centerplane.

In figure 5a-c, the instantaneous vorticity field components are presented over the film-cooled surface (Y/D = 1.5). The streamwise component of vorticity, ω_x around the periphery of the injection-hole shows the origin of the CVP. The contours of ω_x are aligned with the streaks formed due to the entrainment of the crossflow into the wake region. The contours of ω_y show a complicated structure of the coolant jet inside the injection hole. The upright wake vortices are shed from the edges of the coolant jet due to the interaction with the crossflow, entrained into the wake region and convected downstream. The contours of spanwise vorticity component, ω_z show the vorticity generated along the delivery tube walls. This component plays an important role in changing the structure of CVP in the near field of the jet.



a) ω_x

b) ω_y

c) ω_z

Figure 4 Instantaneous vorticity field components (a-c) on the film-cooled wall surface.

PASSIVE SCALAR (TEMPERATURE) FIELD DESCRIPTION

The details of instantaneous temperature field are given at several section of the computational domain (figure 6). The centerplane corresponds to Z/D = 0.0 and shows the mixing of the mainflow and the coolant jet. The coolant jet temperature drops in the downstream direction, however the coherent structures in the wake region retain their scalar value further (Fig. 6a). The temperature distribution corresponding to adiabatic wall boundary conditions corresponds to film-cooling effectiveness too (fig. 6b). The coolant jet provides good coverage immediately downstream of the injection hole, however the film-cooling effectiveness decreases monotonically in the wake region along the centerplane. The development of the coolant jet along the streamwise direction is shown at three different X/D locations (fig 6c-e). The coolant jet is observed to have a well defined kidney shaped structure (Andreopoulos and Rodi, 1984, Fric and Roshko, 1994). The crossplane mixing of scalar leads to the decrease in scalar value in the core of coolant jet at downstream stations. Moreover, the jet is attached to the surface near the centerplane but is lifted off below the lobes of the kidney vortex.

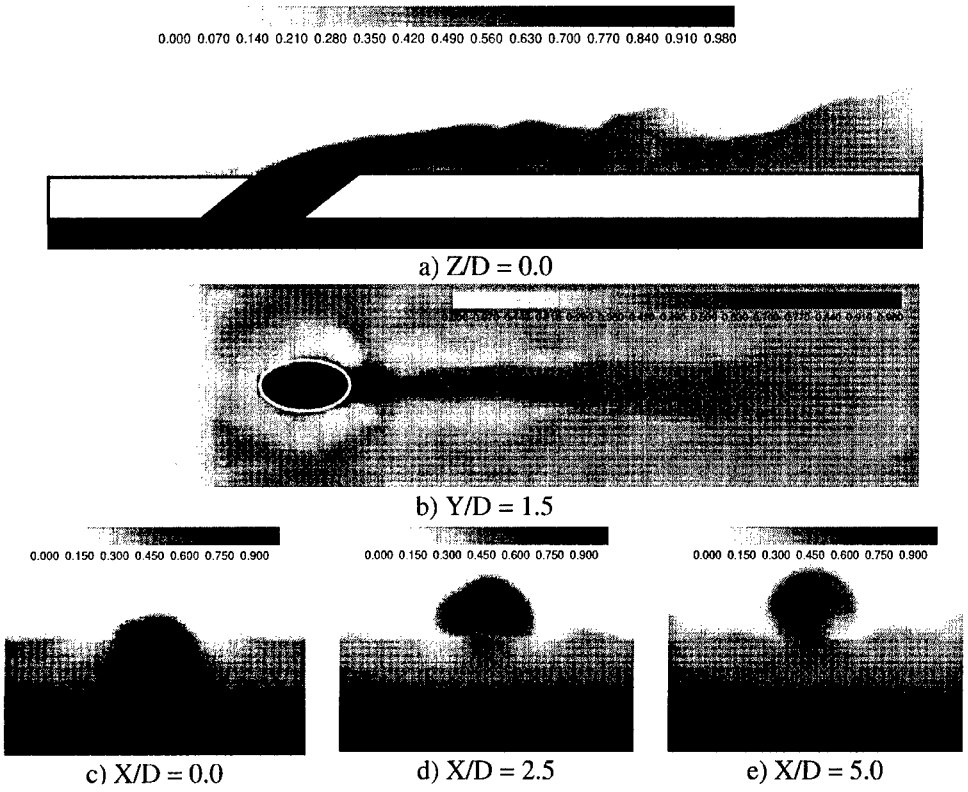


Figure 6 Instantaneous temperature field at different computational domain sections.

5. Conclusion

Large eddy simulations were performed for a simplified geometry representing film-cooling of a gas turbine blade surface. The heat transfer calculations were performed in a conjugate heat transfer mode to study the heat transfer on the film-cooled wall. The plenum was simulated by a stagnation flow field. The unsteady dynamics inside the coolant jet delivery tube showed complex internal structure of the CVP. The coherent vortices observed were in agreement with the experiments conducted by various researchers (Kelso et al., 1996, Haven and Kurosaka, 1997, Fric and Roshko, 1994). The heat transfer results showed the unsteady mixing of the coolant with crossflow and the instantaneous film-cooling effectiveness. The detailed comparison of film-cooling effectiveness, mean flow field and the turbulence statistics will be presented in the future.

References

Acharya, S., Tyagi, M., and Hoda, A. (2001) Flow and heat transfer predictions for film cooling, *Heat transfer in gas turbine systems*, Annals of the New York Academy of Sciences, Vol. 934, pp. 110-125.

Ajersch, P., Zhou, J.M., Ketler, S., Salcudean, M. and Gartshore, I. (1995), Multiple jets in a crossflow: detailed measurements and numerical simulations, *ASME-95-GT-9.*

Andreopoulos, J. and Rodi, W. (1984), Experimental investigation of jets in a crossflow, *J. Fluid Mech.*, Vol. 138, pp.93-127.

Fric, T.F. and Roshko, A. (1994), Vortical structure in the wake of a transverse jet, *J. Fluid Mech.*, Vol. 279, pp. 1-47.

Haven, B.A. and Kurosaka, M. (1997), Kidney and anti-kidney vortices in crossflow jets, *J. Fluid Mech.*, Vol. 352, pp. 27-64.

Jones, W.P. and Wille, M. (1996), Large eddy simulations of a round jet in crossflow, *Engineering turbulence modeling and experiments* 3, pp. 199-209.

Kelso, R.M., Lim, T.T. and Perry, A.E. (1996), An experimental study of round jets in crossflow, *J. Fluid Mech.*, Vol. 306, pp. 111-144.

Lavrich, P.L., and Chiappetta, L.M. (1990) An investigation of jet in a cross flow for turbine film cooling applications, *UTRC Report* No. 90-04.

Moin, P., Squires, K., Cabot, W. and Lee, S. (1991), A dynamic subgrid-scale model for compressible turbulence and scalar transport, *Phys. Fluids* A 3, Vol. 11, pp. 2746-2757.

Tyagi, M. and Acharya, S. (1999), Large eddy simulations of rectangular jets in crossflow: Effect of hole aspect ratio, *Recent advances in DNS and LES*, Ed. Knight and Sakell, pp. 431-442.

Vreman, B., Guerts, B. and Kuerten, H. (1994), On the formulation of the dynamic mixed subgrid scale model, *Phys. Fluids*, Vol. 6, pp. 4057-4059.

Walters, D.K. and Leylek, J.H. (1997), A detailed analysis of film-cooling physics part 1: streamwise injection with cylindrical holes, *97-GT-269.*

Yuan, L.L., Street, R.L. and Ferziger, J.H. (1999), Large eddy simulations of a round jet in crossflow, *J. Fluid Mech.*, Vol. 379, pp. 71-104.

LARGE EDDY SIMULATIONS OF ROTATING SQUARE DUCT WITH NORMAL RIB TURBULATORS

MAYANK TYAGI, ARUN K. SAHA, SUMANTA ACHARYA
Mechanical Engineering Department
Louisiana State University, Baton Rouge, LA

Abstract

Large Eddy Simulations (LES) were performed to study the flow physics and heat transfer in a rotating ribbed duct. This numerical study is simulating the experiments conducted to investigate the effects of buoyancy and Coriolis forces on heat transfer in a turbine blade internal coolant passages (Wagner et al., 1992). The computations were performed at a Reynolds number (*Re*) of 12,500 based on average velocity in the duct and the hydraulic diameter of the square duct. The rotation number (*Ro*) is 0.12 and the inlet coolant-to-wall density ratio ($\Delta\rho/\rho$) is 0.13. The rib height-to-hydraulic diameter ratio (*e/D*) is 0.1 and the rib pitch-to-height ratio (*P/e*) is 10. The ribs are square in cross-section and are placed transverse to the flow in the duct. A direct method of computing a source term due to unsteady calculation of uniform wall temperature case in periodic geometries is presented. The details of flow field and the temperature field are presented and analyzed.

1. Introduction

Modern gas turbines operate at very high turbine inlet temperatures for better second law efficiency and specific thrust. However, such increased thermal loads can deteriorate the blade life in a rotating environment. These blades are internally cooled by using the serpentine channels with turbulators inside the blade to enhance the heat transfer (Morris, 1981). The increment in heat transfer due to rib turbulators as compared to the increased pressure drop in the channel is a crucial design parameter. The problem is complicated further due to the interplay of Coriolis forces and buoyancy forces. Several experimental investigations to study the effect of centrifugal buoyancy, rotation number and Reynolds number have been performed (Wagner et al., 1992). However, a numerical study can provide much more detailed information on flow physics as well as heat transfer in such situations. The secondary flow in non-circular duct without rotation is generated due to the anisotropy in turbulent stresses. In rotating ducts, the Coriolis forces give rise to secondary flow as well. Again, buoyancy forces can generate secondary flow field to enhance the crossplane mixing. Low-level turbulence modeling using two-equation models is incapable of capturing essential physics due to isotropic nature of modeled turbulent stresses (Hermanson et al., 2001). Second moment closure has some promise in that direction (Jang et al., 2001). To understand the unsteady dynamics of various flow structures on the heat transfer, it is inevitable to use LES (Murata et al., 2000 and 2001).

2. Governing Equations

The non-dimensional governing equations for conservation of mass, momentum and energy for an incompressible Newtonian fluid in LES methodology are as follows

$$\frac{\partial U_j}{\partial x_j}=0$$

$$\frac{\partial U_i}{\partial t}+\frac{\partial U_i U_j}{\partial x_j}=-\frac{\partial p}{\partial x_i}-\frac{dP}{dz}\delta_{i3}+\frac{1}{\mathrm{Re}}\frac{\partial^2 U_i}{\partial x_j^2}+\frac{\partial \tau_{ij}}{\partial x_j}-2Ro\varepsilon_{ijk}\Omega_j U_k+Bo\left(1-\frac{\Theta}{\Theta_b^0}\right)\varepsilon_{ijk}\varepsilon_{klm}\Omega_j\Omega_l r_m$$

$$\frac{\partial \Theta}{\partial t}+\lambda\Theta+U_j\frac{\partial \Theta}{\partial x_j}=\frac{1}{\mathrm{Re}\,\mathrm{Pr}}\frac{\partial^2\Theta}{\partial x_j^2}+\frac{\partial q_j}{\partial x_j}$$

where U_i is the filtered velocity field, $\Theta=\dfrac{T-T_1}{T_w-T_2}$ where T_w is the wall temperature and T_1 , T_2 are yet undefined reference temperatures. The mean pressure gradient in flow direction is dP/dz. Therefore, p is the periodic component of the pressure field. δ_{ij} is the Kronecker delta tensor. ε_{ijk} is the alternating tensor. The distance vector can be written as $r_i = R_m\delta_{i3} + x_i$, where R_m is the mean radius of the periodic module from the rotation axis. The important parameters for such flows are Reynolds number ($Re = U_m D_h/\nu$), rotation number ($Ro = \dfrac{\Omega}{\alpha}\left(\dfrac{D_h/U_m}{\nu/U_m}\right)^2 = \dfrac{Ra_\Omega}{\mathrm{Pr}\,\mathrm{Re}^2}$) and centrifugal buoyancy number ($Bo = \dfrac{\beta(T-T_{in})\Omega^2 R_m D_h^3}{\nu\alpha}$). The SubGrid Scale (SGS) stress tensor and SGS scalar flux vector are given by τ_{ij} and q_j respectively. In this study, Dynamic Mixed Model (DMM) is used to model these SGS stress tensor and scalar flux vector (Moin et al., 1991, Vreman et al., 1994). The box filters are used in the Germano identity for the calculation of dynamic coefficient and for the calculation of Leonard stresses. The dynamic coefficient is test filtered to avoid numerical instabilities. Treatment of the non-dimensional temperature in the periodic direction needs special attention. Patankar et al. (1977) described a method to solve the uniform heat flux (UHF) and uniform wall temperature (UHT) problems in the ducts with periodic cross-sections for steady situations. Wang and Vanka (1989) presented an iterative procedure to calculate λ. However, this parameter can be calculated directly for explicit schemes. Most of the simulations were performed using non-dimensionalization with respect to friction velocity and uniform heat flux case. As it will be explained later, that renders the sink terms in momentum and energy equations, i.e. dP/dz and λ, constant. In experiments, usually the mass flow rate and wall temperatures are control parameters, therefore reference velocity should be the average velocity and λ is no more constant.

Boundary conditions for non-dimensional temperature in the periodic direction is written as

$$\frac{\Theta^0}{\Theta_b^0}=\frac{\Theta^L}{\Theta_b^L}$$

where superscript indicates the z-location and subscript b denotes the bulk non-dimensional temperature. Differentiating the periodic boundary condition in the wall-normal direction we get

$$\frac{1}{\Theta_b^0}\left(\frac{\partial\Theta^0}{\partial X}\right)=\frac{1}{\Theta_b^L}\left(\frac{\partial\Theta^L}{\partial X}\right)$$

This is equivalent to enforcing periodicity on the Nusselt number in a periodic geometry.

Uniform Heat Flux (UHF) case:

$$\left(\frac{\partial\Theta^0}{\partial\eta}\right)=\left(\frac{\partial\Theta^L}{\partial\eta}\right)=q_w$$

$$\therefore \Theta_b^0=\Theta_b^L$$

Clearly, setting T_2 to T_b will render the denominator as a constant. Moreover, the independence of non-dimensional bulk temperature from periodic direction implies that T_1 is equal to T_b. Therefore, the scaling at the inlet plane and periodicity of Nusselt number can uniquely determine the non-dimensionalization and the sink term in the energy equation.

Uniform Wall Temperature (UWT) case:

From the energy balance, one can write

$$\rho C_p U_{avg}\left(T_b^L-T_b^0\right)A_c=\iint_S q_w dS$$

$$\iint_S q_w dS\approx\sum_{in} q_w dS+\sum\left(q_w^0+q_w^L\right)\frac{dS}{2}$$

$$\rho C_p U_{avg}\left(T_w-T_2\right)\left(\Theta_b^L-\Theta_b^0\right)A_c\approx k\left(T_w-T_2\right)H\left[\sum_{in}\left(\frac{\partial\Theta}{\partial\eta}\right)_w dS+\sum\left(\left(\frac{\partial\Theta}{\partial\eta}\right)_w^0+\left(\frac{\partial\Theta}{\partial\eta}\right)_w^L\right)\frac{dS}{2}\right]$$

Here η is the wall normal direction and dS is the differential area element on the wall.

For the square channel, we use Nusselt number periodicity to define the flux at the inlet in terms of the flux at the exit as

$$\left(\frac{\partial\Theta}{\partial\eta}\right)_w^0=\frac{\Theta_b^0}{\Theta_b^L}\left(\frac{\partial\Theta}{\partial\eta}\right)_w^L$$

$$\lambda\equiv\frac{\Theta_b^0}{\Theta_b^L}$$

Using these relations in the energy balance, we get

$$\left(\Theta_b^L - \lambda\Theta_b^L\right)A_c \approx \left(\frac{1}{\mathrm{Re}\cdot\mathrm{Pr}}\right)\left[\sum_{in}\left(\frac{\partial\Theta}{\partial\eta}\right)_w dS + \sum\left(\lambda\left(\frac{\partial\Theta}{\partial\eta}\right)_w^L + \left(\frac{\partial\Theta}{\partial\eta}\right)_w^L\right)\frac{dS}{2}\right]$$

$$\therefore \lambda \approx \frac{\left\{\Theta_b^L - \left(\frac{1}{\mathrm{Re}\cdot\mathrm{Pr}}\right)\left[\sum_{in}\left(\frac{\partial\Theta}{\partial\eta}\right)_w dS + \sum\left(\frac{\partial\Theta}{\partial\eta}\right)_w^L \frac{dS}{2}\right]\right\}}{\left\{\Theta_b^L + \left(\frac{1}{\mathrm{Re}\cdot\mathrm{Pr}}\right)\left[\sum\left(\frac{\partial\Theta}{\partial\eta}\right)_w^L \frac{dS}{2}\right]\right\}}$$

To enforce the validity of scaling relation up to the wall, we choose T_1 equal to T_w. Therefore, the non-dimensional temperature is zero at the wall and the scaling ensures the periodicity of the Nusselt number in the periodic geometries.

3. Problem Description and Computational Method

The computations were performed at a Reynolds number (*Re*) of 12,500 based on average velocity in the duct and the hydraulic diameter of the square duct. The rotation number (*Ro*) is 0.12 and the inlet coolant-to-wall density ratio ($\Delta\rho/\rho$) is 0.13. The rib height-to-hydraulic diameter ratio (*e/D*) is 0.1 and the rib pitch-to-height ratio (*P/e*) is 10. The ribs are square in cross-section and are placed transverse to the flow in the duct. This numerical study is simulating the experiments conducted to study the effects of buoyancy and Coriolis forces on heat transfer in turbine blade internal coolant passages (Wagner et al., 1992).

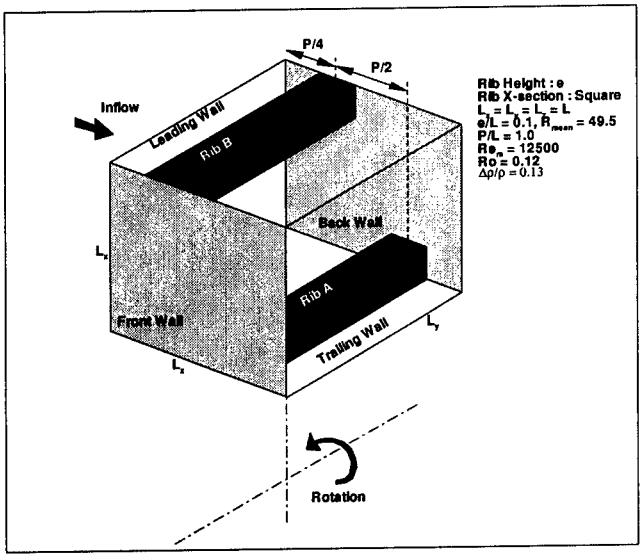
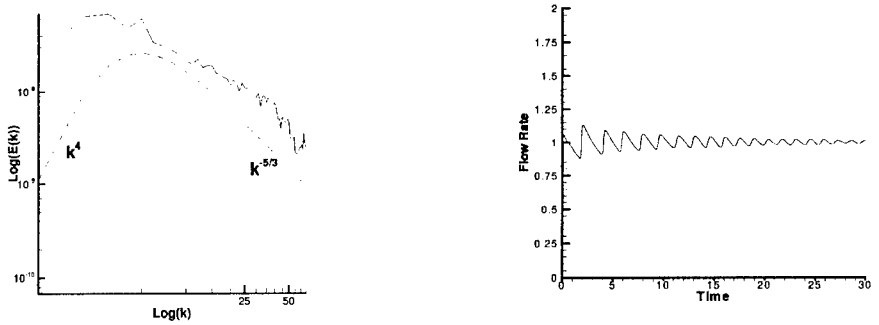


Figure 1 Schematic of the computational domain

4. Results and Discussion

The three-dimensional spectrum of the instantaneous flow field is shown in figure 2a. The grid resolution is sufficient to capture the energy producing

events as well as the portion of the inertial subrange. A peak in energy spectrum is also observed around the wave number corresponding to a length scale l/D = 0.16. Clearly, this can be attributed to the energy production by vortex shedding behind the ribs (e/D = 0.1). To maintain the flow rate, the mean pressure gradient is applied. However, this pressure gradient is subjected to temporal variations corresponding to the Strouhal frequency of vortex shedding due to ribs. This pulsation causes the flow rate to vary with the same frequency (figure 2b). The average flow rate is maintained at 1.0 as desired.



(a) (b)

Figure 2 (a) Three dimensional energy spectrum of the flow field (b) Flow rate vs time.

FLOW FIELD DESCRIPTION

The instantaneous snapshots of the streamwise component of vorticity field at three different streamwise stations (z/D = 0.25, 0.50 and 0.75) depict the complex flow field in the duct (figure 3). At z/D = 0.25, the rib is placed on the leading wall and sheds vortices into the mainflow with significant streamwise vorticity. The boundary layer on the trailing wall is highly turbulent and intensified. The local increase in velocity magnitude near the trailing wall is due to decrease in cross-sectional area as well as body forces. At the streamwise centerplane z/D = 0.50, the recirculation region behind the rib on the leading wall contains intense vortices along the flow. The trailing wall vortices are gathered towards the center of the duct due to secondary flow in the crossplane of the duct. At z/D = 0.75, the rib is placed on the trailing wall and interacts with the oncoming turbulent boundary layer vortices. In this snapshot, the vortices are pushed towards the center of duct by the rib as well as the secondary flow. The leading wall boundary layer shows a lot of activity too. The vortices at the front and the back wall do not penetrate into the core flow to the similar extent as the leading and trailing wall vortices.

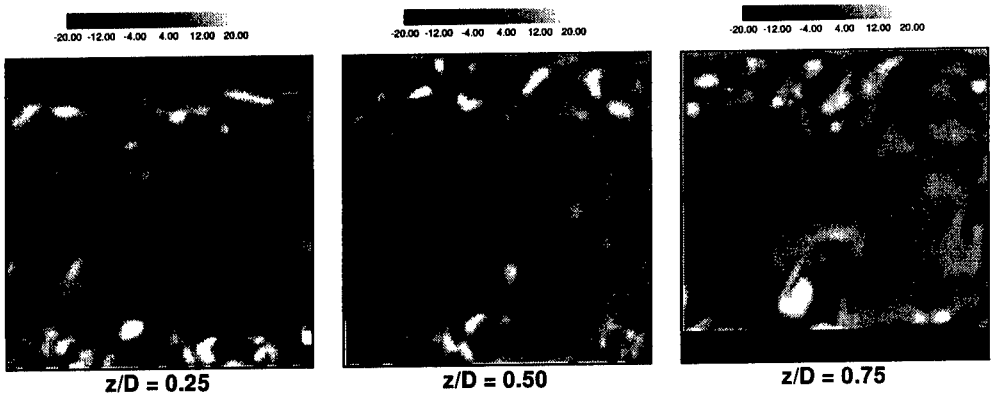


Figure 3 Streamwise component of instantaneous vorticity ω_z at three XY planes

Time-averaged velocity field shows the skewed profile (Figure 4). The boundary layer on the trailing wall (unstable) is much steeper than on the leading wall (stable). The details near the ribs show the difference in the size of recirculation regions in front and behind the ribs. The flow attaches over the top of the rib B (on the trailing wall) while it remains detached on the top face of rib A (on the leading edge). The impingement of the oncoming flow on the front of the ribs results in high heat transfer rates. The recirculation behind the ribs accompanied with enhanced crossplane mixing will result in the increased heat transfer rates.

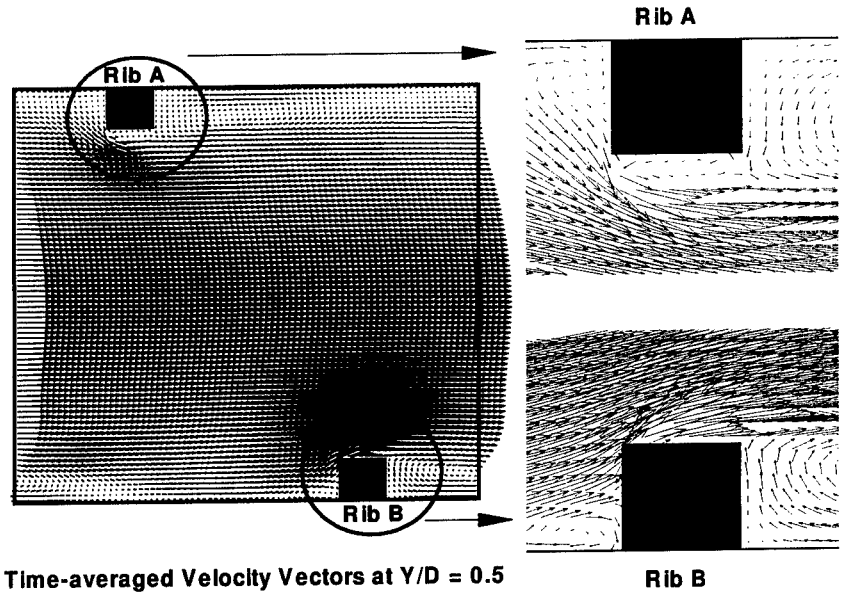


Figure 4 Time-averaged velocity vectors and details of flow field near the ribs at the Y/D = 0.5

HEAT TRANSFER RESULTS

Instantaneous non-dimensional temperature field is shown at the first cell node over the corresponding walls. There is more coolant accumulation on the trailing wall as compared to the leading wall (note the difference in the range). The heat transfer is enhanced on the trailing wall by a factor of two approximately. The temperature field show streaks correlated with the streamwise component of vorticity on these walls. The coolant fluid in front of the ribs increases heat transfer in the stagnation (front recirculation) region. In the leeward recirculation regions, the non-dimensional temperature is close to wall temperature. The temperature distribution on the front and back wall is similar. However, there is more coolant near the back wall as compared to front wall (and it is observed through out the computational duration). This might be caused by a low frequency mode in the coreflow. Again, the temperature field correlates with the streamwise streaks of coolant fluid on these walls.

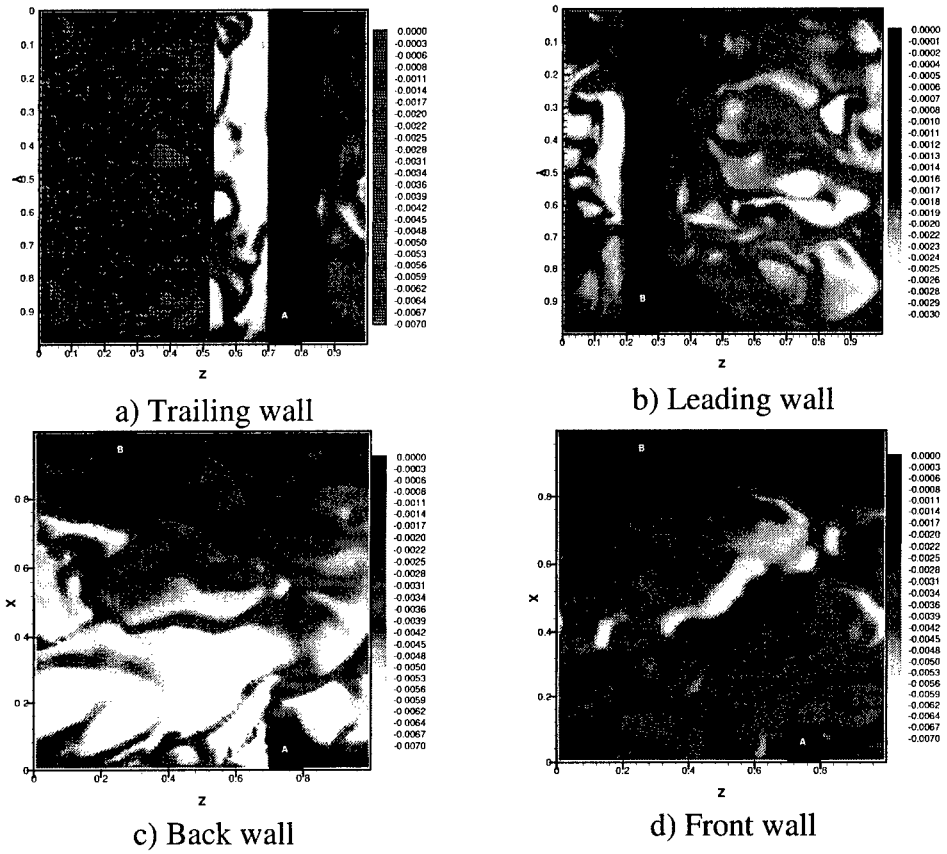


Figure 5 Instantaneous temperature field on the walls of the duct a) Trailing wall, b) Leading wall, c) Back wall and d) Front wall.

5. Conclusion

Large eddy simulations were performed for a rotating square duct with normal rib turbulators to enhance the heat transfer. The Coriolis force as well as

centrifugal buoyancy parameter has been included in this study. A direct approach is presented for the unsteady calculation of non-dimensional temperature field in periodic domains. The complex flow field shows dominant secondary flow vortices that enhance the mixing of the thermal boundary layers on the duct walls with the coolant fluid in the core. The temperature field is highly unsteady and may contain low frequency mode that allows the coolant to adhere to either front or the back wall of the duct. In the future, the assessment of heat transfer enhancement with respect to increased pressure loss will be presented.

References

Chen, Y., Nikitopoulos, D.E., Hibbs, R., Acharya, S. and Myrum, T.A. (2000) Detailed mass transfer distribution in a ribbed coolant passage with a 180° bend, *Int. J. Heat Mass Transfer*, Vol. 43, pp. 1479-1492.

Hermanson, K., Parneix, S. and Von Wolfersdorf, J. (2001), Prediction of pressure loss and heat transfer in internal cooling passages with rotation (*Preprint*).

Jang, Y.-J., Chen, H.-C. and Han, J.-C. (2001) Flow and heat transfer in a rotating square channel with 45° angled ribs by Reynolds stress turbulence model, *J. Turbomachinery*, Vol. 123, pp.124-132.

Moin, P., Squires, K., Cabot, W. and Lee, S. (1991), A dynamic subgrid-scale model for compressible turbulence and scalar transport, *Phys. Fluids* A 3, Vol. 11, pp. 2746-2757.

Morris, W.D. (1981) *Heat transfer and fluid flow in rotating coolant channels*, Research Studies Press.

Murata, A. and Mochizuki, S. (2000) Large eddy simulation with a dynamic subgrid-scale model of turbulent heat transfer in an orthogonally rotating rectangular duct with transverse rib turbulators, *Int. J. Heat Mass Transfer*, Vol. 43, pp. 1243-1259.

Murata, A. and Mochizuki, S. (2001) Effect of centrifugal buoyancy on turbulent heat transfer in an orthogonally rotating square duct with transverse or angled rib turbulators, *Int. J. Heat Mass Transfer*, Vol. 44, pp. 2739-2750.

Patankar, S.V., Liu, C.H. and Sparrow, E.M. (1977) Fully developed flow and heat transfer in ducts having streamwise-periodic variations of cross-sectional area, *J. Heat Transfer*, Vol. 99, pp. 180-186.

Vreman, B., Guerts, B. and Kuerten, H. (1994), On the formulation of the dynamic mixed subgrid scale model, *Phys. Fluids*, Vol. 6, pp. 4057-4059.

Wagner, J.H., Johnson, B.V., Graziani, R.A. and Yeh, F.C. (1992) Heat transfer in rotating serpentine passages with trips normal to the flow, *J. Turbomachinery*, Vol. 114, pp. 847-857.

Wang, G. and Vanka, S.P. (1995) Convective heat transfer in periodic wavy passages, *Int. J. Heat Mass Transfer*, Vol. 38, pp. 3219-3230.

LARGE-EDDY SIMULATION OF A SHEAR-FREE MAGNETOHYDRODYNAMIC MIXING LAYER

O. DEBLIQUY, B. KNAEPEN AND D. CARATI
Univeristé Libre de Bruxelles, Statistical and Plasmas Physics,
Bld du Triomphe, Campus Plaine - CP 231,
B-1050 Brussels, Belgium

Abstract. We present LES results of the evolution of a decaying magnetohydrodynamic (MHD) mixing layer using dynamic eddy-viscosity subgrid scale models. The LES results are obtained using a spectral code with a 32^3 resolution and are compared to a direct numerical simulation (DNS) with 128^3 Fourier modes. The evolution of the kinetic and magnetic energies is presented and their profiles along the inhomogeneous direction is also discussed.

1. Introduction

MHD is recognized as a valid approximation in various problems of plasma physics such as nuclear fusion, astrophysics, geophysics, ... In many cases, highly turbulent processes are encountered and the magnetic Reynolds number R_m characterizing the magnetic turbulence can reach values ranging from 10^8 to 10^{12}. For such values, the use of DNS for investigating the MHD turbulence is inappropriate. In this context, developing the LES technique, which has been already widely used in fluid mechanics, appears to be an elegant solution for solving the incompressible MHD equations:

$$\partial_t u_i = -\partial_j(u_j u_i - b_j b_i) + \nu\nabla^2 u_i - \partial_i p \quad (1)$$

$$\partial_t b_i = -\partial_j(u_j b_i - b_j u_i) + \eta\nabla^2 b_i \quad (2)$$

where $b_i = B_i/\sqrt{\rho\mu_0}$ denotes the components of the reduced magnetic field, ρ is the constant density and p represents the sum of the hydrodynamic and magnetic pressure $b_l b_l/2$ usually evaluated by enforcing the incompressibility condition ($\partial_i u_i = 0$). The parameters ν and η are the kinematic

viscosity and the magnetic diffusivity, respectively. Although LES has already been adapted to MHD (Theobald et al., 1994; Agullo et al., 2001; Müller and Carati, 2001), its use has been limited to homogeneous turbulence. In this work, we explore the capabilities of this technique for inhomogeneous flows. The particular case treated here is the mixing layer. Our choice is motivated by the fact that interactions between regions of different turbulent activities are very commonly observed in many geophysical and astrophysical problems. Our choice is however also motivated by practical computational arguments. Indeed, the mixing layer can be computed with a spectral code (fully de-aliased) for which the modelling issues do not interfere too strongly with the numerics. The mixing-layer we have considered is the interface between two regions of almost homogeneous turbulence with different mean energy and different energy spectra. In our case, the direction of inhomogeneity will be oriented along the y-axis. The u_i and b_i fields are initialized to resemble a magnetohydrodynamic mixing layer by adapting the well-documented hydrodynamic case of Veeravalli and Warhaft (1989) (see also, Briggs et al., 1996).

2. LES equations

Within the framework of LES, a filter kernel is applied to the MHD equations in order to obtain a set of equations for the resolved quantities. Here, because our code is spectral, we adopt the sharp fourier cut-off for the filtering operator and the filter width is noted by $\overline{\Delta}$. The filtered MHD equations thus read:

$$\partial_t \overline{u}_i = -\partial_j(\overline{\overline{u}_j\overline{u}_i} - \overline{\overline{b}_j\overline{b}_i}) + \nu\nabla^2\overline{u}_i - \partial_i\overline{p} - \partial_j\overline{\tau}^u_{ji} \quad (3)$$

$$\partial_t \overline{b}_i = -\partial_j(\overline{\overline{u}_j\overline{b}_i} - \overline{\overline{b}_j\overline{u}_i}) + \eta\nabla^2\overline{b}_i - \partial_j\overline{\tau}^b_{ij} \quad (4)$$

In contrast with traditional notations, we have explicitly expressed that the non-linear term is filtered since our code is fully de-aliased. Also, we have explicitly written the filtering operator on the subgrid-scale stress tensors $\overline{\tau}^u_{ij} = (\overline{u_iu_j} - \overline{\overline{u}_i\overline{u}_j}) - (\overline{b_ib_j} - \overline{\overline{b}_i\overline{b}_j})$ and $\overline{\tau}^b_{ij} = (\overline{u_ib_j} - \overline{\overline{u}_i\overline{b}_j}) - (\overline{u_jb_i} - \overline{\overline{u}_j\overline{b}_i})$ for two reasons. First, this might avoid some confusion because the notation τ_{ij} usually refers in the Navier-Stokes case to the term $\overline{u_iu_j} - \overline{u}_i\overline{u}_j$. Second, since $\overline{\tau}_{ij}$ has to be computed on the LES grid, it is unavoidably a filtered quantity. Those terms account for the effects of the small scales on the large scales and cannot be computed directly from the resolved quantities. Therefore, in order to close the equation (3) and (4) , we need to model them.

The model proposed here is based on the eddy-viscosity assumption and is referred to as the Kolmogorov model (Agullo et al., 2001). One

uses therefore a MHD-generalization of the Smagorinsky model with Kolmogorov scaling for the eddy-diffusivities:

$$\overline{\tau}^u_{ij} \approx -2C_1\overline{\Delta}^{4/3}\overline{S}_{ij} \quad (5)$$

$$\overline{\tau}^b_{ij} \approx -2C_2\overline{\Delta}^{4/3}\overline{W}_{ij} \quad (6)$$

where $\overline{S}_{ij}$ is the symmetric part of the filtered velocity gradients and $\overline{W}_{ij}$ is the anti-symmetric part of the filtered magnetic field gradients. We have adopted the MHD-extension of the *dynamic procedure* (Germano et al., 1991; Lilly, 1992) for computing the parameters C_1 and C_2. To that end, we introduce a second filter referred to as the test-filter and whose action is noted by $\widehat{\ }$. The test filter is also a Fourier cut-off with $\widehat{\Delta} = 2\overline{\Delta}$. Because of the properties of the Fourier cut-off filters, the following relation $\widehat{\overline{\cdots}} \equiv \widehat{\cdots}$ can be used to simplify the notation. The application of the filter $\widehat{\cdots}$ to the MHD equations introduces two additional unknown stress tensors, $\widehat{T}^u_{ij}$ and $\widehat{T}^b_{ij}$. They will be referred to as the subtest-stress tensors and their definitions are similar to $\overline{\tau}^u_{ij}$ and $\overline{\tau}^b_{ij}$ for test-level quantities. They are assumed to be modeled as follows:

$$\widehat{T}^u_{ij} \approx -2C_1\widehat{\Delta}^{4/3}\widehat{S}_{ij} \quad (7)$$

$$\widehat{T}^b_{ij} \approx -2C_2\widehat{\Delta}^{4/3}\widehat{W}_{ij}\,. \quad (8)$$

The Germano identities obtained for the stresses $\overline{\tau}$ and $\widehat{T}$ thus read:

$$\widehat{T}^u_{ij} - \widehat{\overline{\tau}}^u_{ij} = \widehat{L}^u_{ij} \quad (9)$$

$$\widehat{T}^b_{ij} - \widehat{\overline{\tau}}^b_{ij} = \widehat{L}^b_{ij} \quad (10)$$

where $\widehat{L}^u_{ij} = (\widehat{\overline{u}_i\overline{u}_j} - \widehat{\overline{u}}_i\widehat{\overline{u}}_j) - (\widehat{\overline{b}_i\overline{b}_j} - \widehat{\overline{b}}_i\widehat{\overline{b}}_j)$ and $\widehat{L}^b_{ij} = (\widehat{\overline{u}_i\overline{b}_j} - \widehat{\overline{u}}_i\widehat{\overline{b}}_j) - (\widehat{\overline{b}_i\overline{u}_j} - \widehat{\overline{b}}_i\widehat{\overline{u}}_j)$. These expressions can be used to evaluate C_1 and C_2 if we assume that C_1 and C_2 are independent of the filter width. Here, C_1 and C_2 are also assumed to be function of the inhomogeneous direction, i.e. the y-direction, and are chosen to minimize the errors defined as

$$Q_1(y) = \langle(\widehat{T}^u_{ij} - \widehat{\overline{\tau}}^u_{ij} - \widehat{L}^u_{ij})^2\rangle_{xz} \quad (11)$$

$$Q_2(y) = \langle(\widehat{T}^b_{ij} - \widehat{\overline{\tau}}^b_{ij}\widehat{L}^b_{ij})^2\rangle_{xz}\,, \quad (12)$$

where $\langle\,\rangle_{xz}$ represents the average over the xz-plan.

3. Initial Conditions

The velocity and magnetic fields are initialized using the same procedure. We will thus discuss this procedure for a generic field denoted c. In the

following, both the three-dimensional $c(k_x, k_y, k_z)$ and the two-dimensional $\tilde{c}(k_x, y, k_z)$ Fourier transforms of this field are used. For isotropic turbulence, the averaged amplitude of $c(k_x, k_y, k_z)$ only depends on the norm of the wave vector $k = \sqrt{k_x^2+k_y^2+k_z^2}$: $\langle |c(k_x, k_y, k_z)|^2 \rangle = A^2(k)$. Also, the averaged amplitude of $\tilde{c}(k_x, y, k_z)$ only depends on the norm of the wave vector perpendicular to the y-axis $k_\perp = \sqrt{k_x^2+k_z^2}$: $\langle |c(k_x, y, k_z)|^2 \rangle = B^2(k_\perp)$. The relation between these two amplitudes is readily derived from the Parseval theorem:

$$B^2(k_\perp) = \int_{-\infty}^{+\infty} dk_y A^2(\sqrt{k_\perp^2 + k_y^2}), \tag{13}$$

We also know that for isotropic turbulence, the field amplitude $A^2(k)$ is related to the energy spectrum $E(k) = 2\pi k^2 A^2(k)$. Hence, if the statistical properties of the field slowly vary along the axis y, we can assume, in a first approximation, that:

$$B^2(k_\perp, y) = \frac{1}{2\pi} \int_{-\infty}^{+\infty} dk_y \frac{E(\sqrt{k_\perp^2 + k_y^2}, y)}{k_\perp^2 + k_y^2} \tag{14}$$

In our case, the energy spectrum will be given by

$$E(k, y) = A \frac{k^4 e^{-k^2/\alpha^2}}{(q^4 + k^4)^{17/12}} \cdot \tag{15}$$

The y-dependence is controlled through the parameters: $A = A(y)$, $\alpha = \alpha(y)$ and $q = q(y)$. The values of these parameters have been chosen so that the initial conditions mimick the experimental fields produced by Veeravalli and Warhaft (1989) using the 3:1 grid. They are constant in the two regions corresponding to the quasi-homogeneous layers and vary continuously in the mixing layer in order to connect smoothly the two quasi-homogeneous layers. They are chosen so that the ratio of turbulence intensities is about 6 while the ratio of typical lengths (corresponding to the spectral energy peak) is about 3.

The velocity and magnetic field are initially uncorrelated. However, turbulent phases are build using hundred time steps for which both u_i and b_i are advanced in time and then rescaled to the desired amplitudes $B^2(k_\perp, y)$.

4. Results

In order to assess the LES results, we have performed a 128^3 DNS in which the u_i and b_i fields are initialized with the procedure described in the previous section. The same spectra and the same set of parameters as in (15) have been chosen for the velocity and magnetic fields. The kinematic viscosity and the magnetic diffusivity are identical ($\nu = \eta = 4.10^{-3}$) so that

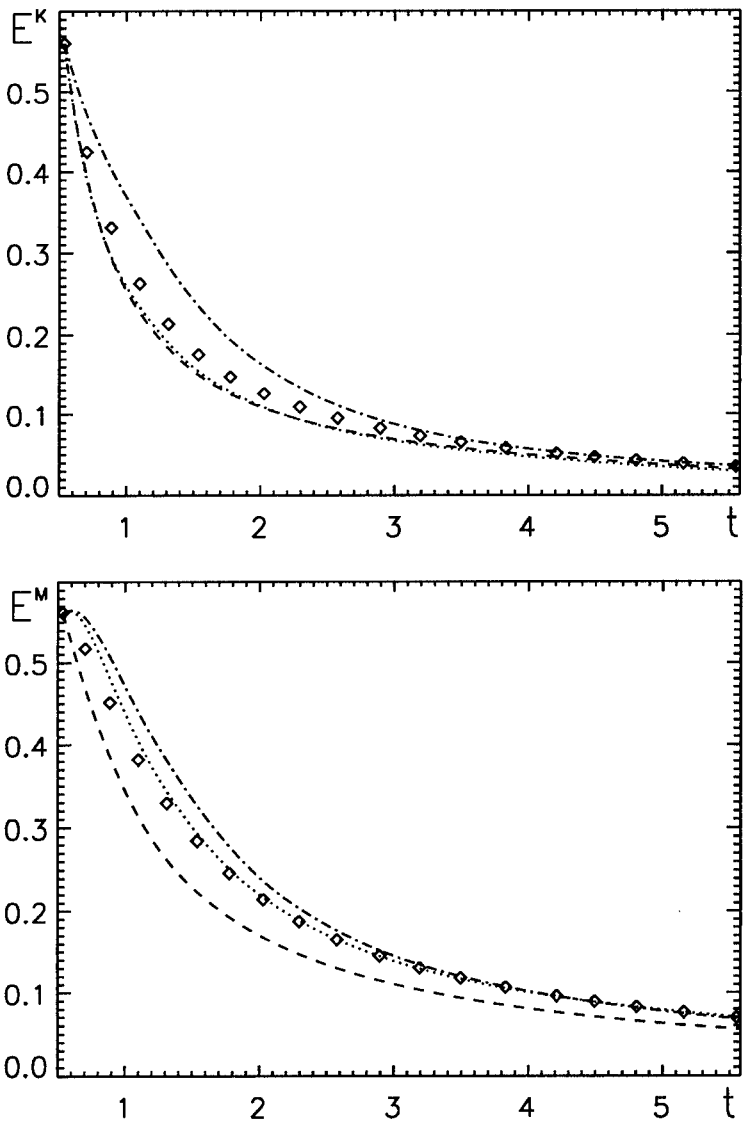


Figure 1. Evolution of the kinetic (top) and magnetic (bottom) energies as a function of time using the K-K model (dashed line), the K-NO model (dotted line) and the NO-NO model (dot-dashed line). The DNS filtered to 32^3 modes is represented by the symbol $\diamond$.

the Prandtl number=1. We present results for three types of LES. The first one, hereafter referred to as the K-K model, uses the Kolmogorov scaling (5) in both the equations for $\overline{u}_i$ and $\overline{b}_i$. It was however realized that this model is too strongly dissipative as long as the magnetic energy is concerned. This has motivated the used of the Kolmogorov model for the

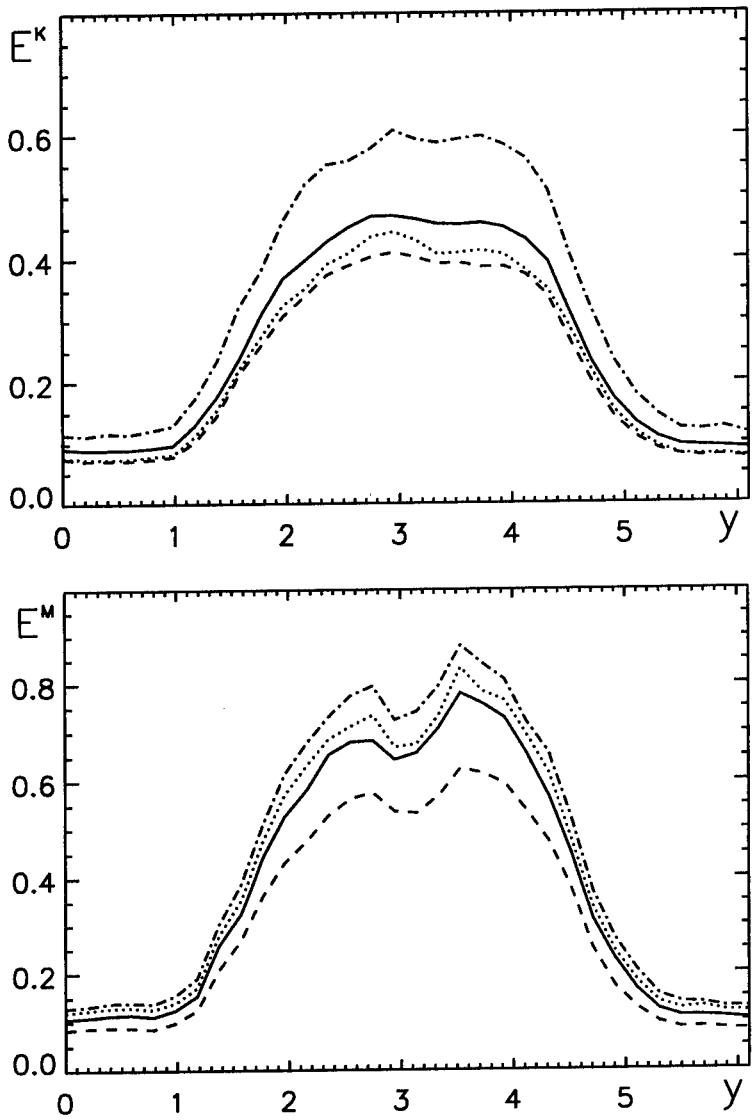


Figure 2. Profile of the kinetic (top) and magnetic (bottom) energies along the inhomogeneous y-direction at $t = 1.1$. The DNS filtered to 32^3 modes is represented by the solid line.

velocity equation only, while neglecting the effect of the subgrid-scale in the equation for $\overline{b}_i$. This model is referred to as the K-NO model. Finally, in order to emphasize the importance of the model, results obtained without any model (referred to as the NO-NO model) are also presented. Figure 1 shows the decay of the volume averaged kinetic and magnetic energies as a function of time.

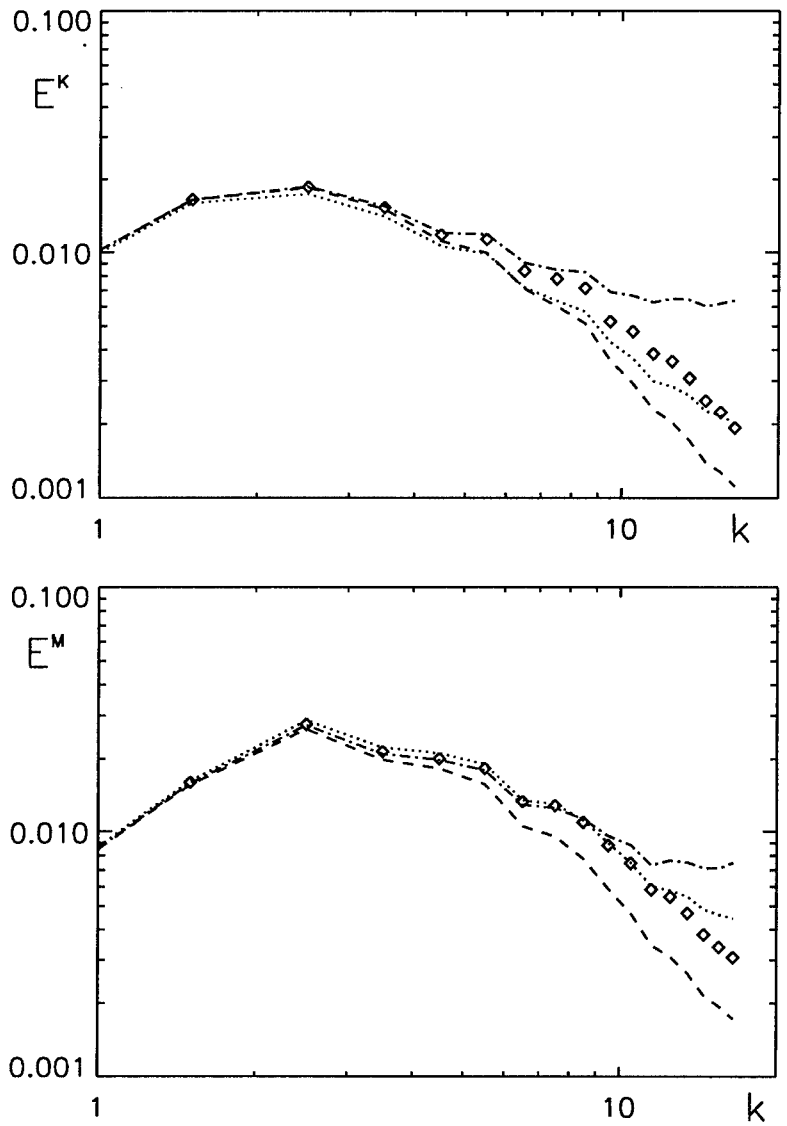


Figure 3. Kinetic (top) and magnetic (bottom) energy spectra at $t = 1.1$. Symbols are the same as in Fig. 1.

We can see that the K-K model predictions agree reasonably well with the filtered DNS as long as the kinetic energy is concerned. However, this model appears to dissipate too much magnetic energy. The K-NO model has a much reasonable behavior for the magnetic energy and it even improves slightly the prediction of the kinetic energy.

Figure 2 shows the profile of the energies along the anisotropic direction

at time $t = 1.1$ for which about 50% of the initial energy has been dissipated. We observe the same trends as in Figure 1, i.e. the kinetic energy profile predicted by the K-K model is quite close from the filtered DNS results, while the magnetic energy profile is significantly below the DNS filtered results. Again, using the K-NO model significantly improves the agreement with DNS data for both the energy profiles.

We also present the energy spectra at the same time which are quantities rather sensitive to the modeling (Figure 3). Indeed, for the NO-NO model, the expected piling up of the energy in the high wave vector modes is observed for both the kinetic and magnetic energies. Here also the best performances are obtained when using the K-NO model.

5. conclusion

We have performed a preliminary study of a magnetohydrodynamic mixing-layer LES. We have proposed the use of the Kolmogorov model for which the parameters were computed by the MHD-extended dynamic procedure with an explicit dependence of the parameters on the inhomogeneity direction.

The results clearly show that the K-NO model outperforms significantly the other models. This seems to indicate that the modelling of the subgrid-scales in much more important for the velocity than for the magnetic field. Our preliminary results seem also to demonstrate that the effects of the subgrid-scales in the magnetic field equation cannot be appropriately modelled in terms of a simple eddy magnetic diffusivity.

References

Agullo, O., Müller, W.-C., Knaepen, B., and Carati, D. (2001). Large eddy simulation of decaying magnetohydrodynamic turbulence with dynamic subgrid-modeling. *Phys. Plasmas*, 8(7):3502–3505.

Briggs, D., Ferziger, J., Koseff, J., and Monismith, S. (2000). Entrainment in a shear-free turbulent mixing-layer. *J. Fluid Mech.*, 310:215–241.

Germano, M., Piomelli, U., Moin, P., and Cabot, W. H. (1991). A dynamic subgrid-scale eddy viscosity model. *Phys. Fluids A*, 3(7):1760–1765.

Lilly, D. K. (1992). A proposed modification of the germano subgrid-scale closure method. *Phys. Fluids A*, 4(3):633–635.

Müller, W.-C. and Carati, D. (2001). Dynamic gradient diffusion models for les of magnetohydrodynamic turbulence. In Geurts, B. J., Friedrich, R., and Metais, O., editors, *Direct and Large-Eddy Simulation Workshop 4*, pages 129–132.

Theobald, M., Fox, P. A., and Sofia, S. (1994). A subgrid-scale resistivity for magnetohydrodynamics. *Phys. Plasmas*, 1(9):3016–3032.

Veeravalli, S. and Warhaft, Z. (1989). The shearless turbulence mixing layer. *J. Fluid Mech.*, 207:191–229.

ENERGY-CONTAINING-RANGE MODELING OF FULLY-DEVELOPED CHANNEL FLOW USING A HYBRID RANS/LES TECHNIQUE

FRANK J. ZAJACZKOWSKI, LEONARD J. PELTIER
The Applied Research Laboratory
The Pennsylvania State University, State College, Pennsylvania

Abstract

Turbulent channel flow is used to study energy-containing-range modeling using a hybrid RANS/LES approach. The hybrid model relates the mean component of an LES-type subgrid diffusivity to the turbulence diffusivity from RANS via a transfer function. Details of this transfer function in the energy-containing-range of the turbulence are shown to be very important when modeling coarsely resolved flows. Three transfer function models are compared. One interpolates the turbulence diffusivity between the LES and RANS limits using an algebraic blending. The second uses von Karman's empirical fit to the turbulent kinetic energy spectrum to diagnose energy-containing-range structure. The third uses a modified Smagorinsky subgrid model corrected to have the proper mean time scale as diagnosed from RANS. Our Reynolds number is 640, based on the channel half height and on the friction velocity. Comparison of mean-field and root-mean-square statistics to other studies clearly identify the mean time-scale model as the best performer.

1. Introduction

Reynolds-Averaged Navier-Stokes (RANS) modeling is the contemporary workhorse for CFD. The demands on a RANS model can be severe, since it must accommodate the geometric scales of a flow under complicated conditions. Most RANS models perform well for flows similar to the ones for which they are tuned but fail, often severely, for other flows. Large-eddy simulation (LES), as an alternate technology, resolves the geometric scale of a flow modeling only the effects of the inertial range scales. The cost of a LES can be quite high because of high grid density and the need to collect statistics from instantaneous solutions.

Recent work proposes a middle ground between RANS and LES. Spalart, et al. (1997) and Speziale (1998) have shown that a RANS code can be used to give LES-like solutions if the RANS eddy diffusivity is decremented appropriately using a grid-resolution-dependent transfer function. It is constructed so that in the coarse-grid limit, when no turbulence fluctuations are resolved, the model becomes RANS. Similarly when the energy-containing-range scales are resolved, the model becomes a Smagorinsky-type LES. Peltier, Zajaczkowski, and Wyngaard (2000) implemented a hybrid RANS/LES model based on that idea.

We evaluate three candidate transfer functions and select from them a "best" choice. Fully-developed channel flow at Reynolds number 640, based on channel half height and on friction velocity, is used as the test case, since the expected results are well known from the literature.

2. Mathematical formulation

2.1 The Transport Budgets

The filtered, incompressible Navier-Stokes equations are solved for the resolvable scales of fully-developed turbulent channel flow. The flow is divergence free to enforce continuity. The equations are

$$\tilde{u}^r_{i,t} + (\tilde{u}^r_i \tilde{u}^r_j)_{,j} = -\tilde{p}^r_{,i} + \frac{1}{\mathrm{Re}_\tau}\tilde{u}^r_{i,jj} - \tilde{\tau}^{SGS}_{ij,j} - 1 \quad \text{and} \quad \tilde{u}^r_{i,i} = 0. \qquad (1)$$

The superscript "r" refers to "resolvable scale". The capping tilde is used to denote a variable with both mean and fluctuating parts. The "-1" on the right side is the mean pressure gradient nondimensionalized on the channel half-height and on the friction velocity. The pressure gradient term on the right side of (1) is the deviation from the mean gradient. Re_τ is the appropriate Reynolds number. Noslip conditions are enforced at the lower and upper walls of the channel. Wall functions are not used. The streamwise and cross-stream directions are periodic.

2.2 The Subgrid Model

We use an eddy diffusion model for the subgrid stress in (1): $\tilde{\tau}_{ij} = -2\tilde{\nu}^{SGS}_T \tilde{S}^r_{ij}$, where $\tilde{S}^r_{ij} = (\tilde{u}^r_{i,j} + \tilde{u}^r_{j,i})/2$ is the resolvable-scale strain-rate tensor. Contributions to the eddy diffusivity are from direct interactions with the mean flow and interactions within the fluctuating field, $\bar{\nu}^{SGS}_T = \bar{\nu}^{MS}_T + \bar{\nu}^{FL}_T$. Peltier and Zajaczkowski (Reg. Paper #81 of this conference) show that $\bar{\nu}^{FL}_T >> \bar{\nu}^{MS}_T$ in the fine-grid limit (LES). Traditional LES subgrid models (like the Smagorinsky model) already perform well for filter scales in the inertial range, so no additional work must be done to identify a suitable model for $\bar{\nu}^{FL}_T$. In the coarse grid limit, $\bar{\nu}^{FL}_T << \bar{\nu}^{MS}_T$ (Peltier and Zajaczkowski, Reg. Paper # 81), so direct interactions with the mean straining field are of primary importance. $\bar{\nu}^{MS}_T$ can be inferred from RANS:

$$\bar{\nu}^{MS}_T = T(\ell, \Delta, \eta)\bar{\nu}^{RANS}_T. \qquad (2)$$

$T(\ell, \Delta, \eta)$ is an appropriate grid-resolution-dependent transfer.

A diffusivity is the product of the characteristic length and velocity scales for the subgrid turbulence. For RANS, $\bar{\nu}^{RANS}_T = q\ell$, where ℓ is the dissipation length and

q is the square root of the turbulence kinetic energy. Note: the familiar coefficient, $C_\mu = 0.09$, and any viscous damping function are absorbed in our definition of ℓ. Similarly, for a partially resolved flow field with characteristic length and velocity scales, Δ and v, the mean diffusivity is $\overline{\nu}_T^{MS} = \mathrm{v}\Delta$ giving

$$T(\ell,\Delta,\eta) = \frac{\mathrm{v}}{q}\frac{\Delta}{\ell} \tag{3}$$

for the transfer function. Again, coefficients like the Smagorinsky constant, $C_s = 0.065$, and damping functions are absorbed in Δ, a filter scale proportional to the characteristic length of a local grid-cell volume. The velocity scale, v, is the square root of the subgrid turbulence kinetic energy. Dependence of (3) on the Kolmogorov scale, η, arises because of the viscous cutoff scale for turbulence near η.

We use the traditional Smagorinsky eddy-diffusivity closure of LES whose velocity scale is inferred from the strain-rate invariant, $\mathrm{v} = \Delta \cdot S$. The Smagorinsky model breaks down under coarse resolution, apparently because this velocity scale is inappropriate in the energy containing range. Our modeling effort seeks to correct the Smagorinsky closure by defining a more appropriate energy-containing-range velocity scale:

$$\widetilde{\nu}_T^{SGS} = \widetilde{\nu}_T^{SMAG} + T(\ell,\Delta,\eta)\left(\overline{\nu}_T^{RANS} - \overline{\nu}_T^{S}\right) \tag{4}$$

where $\overline{\nu}_T^{MS} \equiv \Delta\left(\Delta\overline{S}\right)$, the Smagorinsky model applied to the mean flow. $\overline{S} = (U_{i,j} + U_{j,i})/2$ is the mean-field strain-rate invariant (from RANS). Three models for $T(\ell,\Delta,\eta)$ are evaluated in this study.

Model 1

Following Peltier et al. (2000), we diagnose v by integrating the inertial-range form for the turbulence kinetic energy spectrum, $E(\kappa) = \frac{8}{3}\varepsilon^{2/3}\kappa^{-5/3}$ between the filter-scale wavenumber, $\kappa_\Delta = 2\pi/\Delta$, and a dissipation-range cutoff wavenumber, $\kappa_\eta = 2\pi/\Delta_\eta$, where $\Delta_\eta \approx 0.1\eta$ (see Hinze, 1975, p. 224). Denoting the inertial-range form of the transfer function $I(\ell,\Delta,\eta)$, we blend between the inertial range and RANS via:

$$T(\ell,\Delta,\eta) = \left[\frac{I(\ell,\Delta,\eta)^2}{1+I(\ell,\Delta,\eta)^2}\right]^{1/2}. \tag{5}$$

The power of 2 used in the blending function comes from Peltier et al.'s (2000) preliminary optimization of the model.

Model 2

By integrating von Karman's empirical fit to the turbulence kinetic energy spectrum from κ_Δ to κ_η, we can compute $T(\ell,\Delta,\eta)$ directly. Von Karman's spectrum is given by (Hinze, 1975, p. 244):

$$E(\kappa) = C_{vK} \frac{(\kappa/\kappa_e)^4}{\left[1+(\kappa/\kappa_e)^2\right]^{17/6}} . \tag{6}$$

The coefficient C_{vK} and the wavenumber κ_e are set by requiring (6) to have the proper inertial range amplitude, $\frac{8}{3}\varepsilon^{2/3}$, in the limit of very large wavenumbers and by requiring the spectrum to integrate to the turbulent kinetic energy, q^2; the dissipation rate, ε, and the turbulent velocity scale, q, are provided by RANS. One drawback to using (6) is that an inertial range will be imposed for all Reynolds numbers, even very low Reynolds numbers for which an inertial range does not exist.

Model 3

Our final model adopts the Smagorinsky length scale for Δ but replaces the incorrect time scale in (4), $\overline{S}^{-1}$, with the turbulence time scale from RANS, ℓ/q:

$$\overline{\nu}_T^{MS} \approx \Delta\left(\Delta\frac{q}{\ell}\right) \rightarrow T(\ell,\Delta,\eta) = \left(\frac{\Delta}{\ell}\right)^2 . \tag{7}$$

3. Numerical Method

A finite difference discretization of Eq. (1) with discretized boundary conditions and turbulence modeling is solved. The solution procedure follows the fractional step approach outlined by Rai and Moin (1991); however, a linear blending of second-order accurate weighted-average central differencing with first-order accurate upwind differencing is used for the nonlinear advection terms for values of the transfer function greater than 0.9. This range was chosen by numerical experiment emphasizing the need to support turbulence scales of motion while retaining stability for very coarse grids. Explicit dependence of the blending on cell Peclet number was not used. The code was validated based on the previous study by Peltier et al. (2000) and based on comparisons to other experimental and numerical data.

4. Numerical Results

We use fully developed channel flow at Re=640 based on the friction velocity and on the channel half height as our test problem because this case is common in the literature and is a simple flow field that emphasizes all of the difficulties inherent in modeling wall bounded flows. The domain size is $2\pi\times\pi\times2$, similar to cases

studied by Moin & Kim (1982), and our grid resolution is $42\times23\times65$. The wall-normal direction is aligned with our z coordinate, which uses hyperbolic tangent stretching toward the solid boundaries. The near-wall spacing is prescribed to give $y^+=1$ for the second grid point. Four cases are compared: our three transfer functions and a baseline case using a traditional Smagorinsky subgrid model. Since the RANS statistics are stationary, the RANS input data is computed *apriori*.

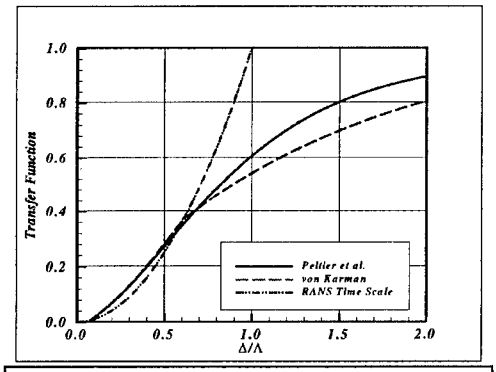


Figure 1 $T(\ell,\Delta,\eta)$ **vs** Δ/ℓ

Figure 1 presents the three candidates for $T(\ell,\Delta,\eta)$ plotted as a function of Δ/ℓ. The Peltier et al. (2000) and von Karman formulations transition to RANS much slower than the mean time scale model (Model 3). For grid resolutions giving $\Delta/\ell=1$, the mean time-scale model becomes RANS, whereas, the Peltier et al. (2000) and von Karman models use only 40% and 60% of the RANS diffusivity.

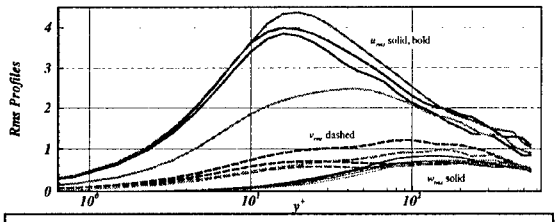


Figure 3 Profiles of root-mean-square velocity

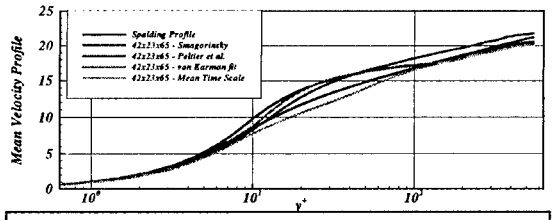


Figure 2 Mean velocity profiles plotted against

Mean-field statistics are presented in Figs. 2 and 3. The Spalding profile is included in Fig. 2 for reference. The Smagorinsky baseline case overshoots the Spalding profile in the buffer layer but recovers a log-law slope in the logarithmic layer. The Peltier et al. (2000) and von Karman models also overshoot the Spalding Profile in the buffer layer, then recover toward the channel core. The mean time scale model tracks the Spalding Profile well across the domain though a mild undershoot is apparent in the buffer layer.

The peak values of our root-mean-square (rms) statistics (Fig. 3) agree well with observations from Moin & Kim (1982): 2.4, 1.3, and 0.9 for the longitudinal, cross-stream, and wall-normal rms velocities. Moin & Kim (1982) show that the horizontal velocity rms values peaks near $y^+ \approx 30$ in agreement with our mean time-scale model. The peak location for the transfer functions based on Peltier et al. (2000) and the von Karman spectrum occurs near $y^+ \approx 20$. Moin & Kim show that the cross-stream and wall-normal velocity rms peak locations occur near $y^+ \approx 120$, similar to our results. Only the mean time-scale model yields an rms value for the horizontal velocity at the peak near the 2.4 presented by Moin & Kim (1982). Each of the other models at our grid resolution overshoot the target value by between 58% to 83%. It is difficult to distinguish significant quantitative differences for the other rms components.

5. Conclusions

Three transfer functions relating the mean turbulence diffusion from direct interactions with the mean straining field to the eddy diffusivity from RANS were evaluated. They represent 1) a simple blending to interpolate between the RANS and LES limits, 2) use of von Karman's spectrum to diagnosis the proper velocity scale, and 3) a correction of the mean time scale from the Smagorinsky model using the turbulence time scale from RANS. Our results showed clearly that *Model 3* agreed best with accepted physics. We recommend that Model 3 be used for future work using this hybrid RANS/LES approach.

Acknowledgments

This work was funded through internal support from The Applied Research Laboratory at Penn State University.

References

1. Hinze, "Turbulence", Second Edition, McGraw-Hill.1975, New York.
2. Moin, P., and Kim, J., 1982, "Numerical Investigation of Turbulent Channel Flow," J. Fluid Mech,. Vol. 118, pp. 341-377
3. Peltier, L.J., Zajaczkowski, F.J., and Wyngaard, J.C., "A Hybrid RANS/LES Approach to Large-Eddy simulation of High-Reynolds-Number Wall-Bounded Turbulence," FEDSM2000-11177, ASME 2000 Fluids Eng. Div. Summer Meeting, June 11-15, 2000, Boston, MA.
4. Spalart, P.R., Jou, W.H., Strelets, M., and Allmaras, S.R., 1997, "Comments on the Feasibility of LES for Wings, and on a Hybrid RANS/LES Approach," Proceedings 1st AFSOR Int'l Conf. On DNS/LES. Ruston, Louisiana, Aug. 1997.
5. Speziale, C.G., 1998, "Turbulence Modeling for Time-Dependent RANS and VLES: A Review," AIAA J., Vol. 36(2), pp.173-184.

MAINTENANCE OF THE NEAR-WALL CYCLE OF TURBULENCE FOR HYBRID RANS/LES OF FULLY-DEVELOPED CHANNEL FLOW

LEONARD J. PELTIER, FRANK J. ZAJACZKOWSKI
The Applied Research Laboratory
The Pennsylvania State University, State College, Pennsylvania

Abstract

Hybrid RANS/LES modeling of near-wall turbulence is investigated for fully-developed turbulent channel flow under very coarse resolution, a resolution not resolving the longitudinal eddies of the buffer layer in near-wall flow but not coarse enough to encompass an "effective" ensemble of eddies to give RANS. Without bursting from the buffer layer, the partially-resolved turbulence is suppressed. We model the effects of the buffer-layer eddies using a field of white noise and show that the core flow is able to extract energy from these artificial fluctuations to organize turbulence eddies that maintain a physical turbulence mixing. Results for $Re_\tau = 640$, based on the channel half-height and on the friction velocity, are presented. Mean-velocity and root-mean-square statistics are compared to results from higher resolution simulations.

1. Introduction

Reynolds-Averaged Navier-Stokes modeling (RANS) and large-eddy simulation (LES) are the contemporary tools for modeling/simulating high-Reynolds-number flows. RANS, as a statistical approach, is particularly efficient for predicting mean velocity statistic and basic turbulence information. RANS models perform especially well near solid boundaries, since the underlying parameterizations are tuned for that class of flows. Unfortunately, RANS models do not generalize well for modeling the geometry-dependent scales. Large-eddy simulation, as a quasi-exact technique, is capable of simulating with fidelity the geometry-dependent scales of motion, so long as the LES filter scale lies in the inertial-range of the turbulence. For high-Reynolds-number flows, maintaining an inertial-range filter scale becomes difficult, particularly near walls where kinematic constraints restrict the energy-containing-range of the turbulence to progressively higher wavenumbers.

The apparent synergy between strengths of RANS and LES has been recognized by a number of authors. Speziale (1998) motivated their connection by recognizing that the RANS equations belong to a superclass of filtered Navier-Stokes equations. He proposed relating the subgrid turbulence diffusivity to the RANS eddy diffusivity using an appropriate transfer function. The RANS solution then becomes part of the subgrid model. Spalart, Jou, Strelets, and Allmaras (1997) outlined such a model which they called detached-eddy

simulation (DES). Their work and follow-on work by Nikitin et al. (2000) and Strelets (2001) shows that DES is able to yield good mean-field statistics and higher-order turbulence statistics as well.

Peltier, Zajaczkowski, and Wyngaard (2000) noted that the formal connection between RANS and LES is the convergence of an ensemble average (filtered over a characteristic volume) and a volume average of a flow field for averaging volumes that are large relative to the energy-containing-range length scale of the turbulence. They proposed a related hybrid RANS/LES technique that populates a stationary RANS field with turbulence scales.

Baggett (1998) concluded hybrid RANS/LES models are unlikely to work in near-wall regions of a flow because they cannot maintain a physical near-wall cycle for the turbulence. Similarly, Nikitin et al. (2000) describe "a danger zone" in which hybrid RANS/LES modeling of the near-wall flow cannot support turbulence. This work is a preliminary investigation of these observations using a modified version of the hybrid RANS/LES model proposed by Peltier et al. (2000).

2. Governing Equations

2.1 The Transport Budgets

The filtered, incompressible Navier-Stokes equations are solved for the resolvable scales of fully-developed turbulent channel flow. The flow is divergence free to enforce continuity. The equations are

$$\tilde{u}^r_{i,t} + (\tilde{u}^r_i \tilde{u}^r_j)_{,j} = -\tilde{p}^r_{,i} + \frac{1}{\mathrm{Re}_\tau}\tilde{u}^r_{i,jj} - \tilde{\tau}^{SGS}_{ij,j} - 1 \quad \text{and} \quad \tilde{u}^r_{i,i} = 0. \quad (1)$$

The superscript "r" refers to "resolvable scale". The capping tilde is used to denote a variable with both mean and fluctuating parts. The "-1" on the right side is the mean pressure gradient nondimensionalized on the channel half-height and on the friction velocity. The pressure gradient term on the right side of (1) is the deviation from the mean gradient. Re_τ is the appropriate Reynolds number. Noslip conditions are enforced at the lower and upper walls of the channel. Wall functions are not used. The streamwise and cross-stream directions are periodic.

2.2 Turbulence modeling

The deviatoric part of the subgrid stress is modeled using eddy-diffusion,

$$\tilde{\tau}^{SGS}_{ij} - \frac{1}{3}\tilde{\tau}^{SGS}_{kk}\delta_{ij} = -\tilde{\nu}_T 2\tilde{s}^r_{ij} \ . \quad (2)$$

A modified Smagorinsky formulation is used to define the eddy diffusivity, $\tilde{\nu}_T$. The eddy diffusivity is the product of the characteristic velocity scale and the characteristic length scale of the turbulent flow. When the filter scale of a

computational model is suitably coarse, RANS modeling provides the appropriate diffusivity. Using ℓ and $q = \sqrt{\overline{u_i u_i}}$ to denote the RANS length and velocity scales, one writes

$$\overline{\nu}_T^{RANS} = \ell q \,. \tag{3}$$

The overbar denotes an ensemble-mean value and u_i is the fluctuating part of $\tilde{u}_i$. Note, we have absorbed the familiar coefficient $c_\mu = 0.09$ in our definition of ℓ and have embedded the standard damping coefficient in ℓ as well. For filter widths in the inertial range of the turbulence, one can define the characteristic scales Δ and v to write

$$\tilde{\nu}_T = \Delta \mathrm{v} \,. \tag{4}$$

The Smagorinsky subgrid model has been used extensively for inertial-range modeling. It relates v to the strain-rate invariant of the resolved flow, $\mathrm{v} = \Delta \tilde{S}$ where $\tilde{S} = 2\sqrt{\tilde{s}_{ij}^{\,r} \tilde{s}_{ij}^{\,r}}$, and uses the characteristic linear dimension of the local grid-cell volume to define Δ. Again, our notation absorbs the Smagorinsky coefficient, $c_s = 0.065$, and near-wall damping terms in Δ. Equations (3) and (4) define the limits of our hybrid RANS/LES model. We propose a simple blending between them to accommodate energy-containing-range modeling.

2.3 Energy-Containing-Range Modeling

The contraction defining the resolvable-scale strain-rate invariant has two components,

$$\overline{\tilde{s}_{ij}^{\,r} \tilde{s}_{ij}^{\,r}} = S_{ij} S_{ij} + \overline{s_{ij} s_{ij}} \,, \tag{5}$$

a mean strain-rate contribution, S_{ij}, and a contribution from the fluctuating strain-rate, s_{ij}. The mean-strain-rate part scales with the RANS length and velocity scales, so

$$S^2 \equiv S_{ij} S_{ij} \sim \left(\frac{q}{\ell} \right)^2 . \tag{6}$$

Inertial-range arguments for $\Delta << \ell$ show

$$s^2 \equiv \overline{s_{ij} s_{ij}} \sim \left(\frac{\Delta}{\ell} \right)^{-4/3} \left(\frac{q}{\ell} \right)^2 , \text{ so } S_{ij} S_{ij} << \overline{s_{ij} s_{ij}} \text{ for } \Delta << \ell \,. \tag{7}$$

Equation (7) says that when a flow field is resolved well, the mean strain-rate contributes minimally to the mean eddy diffusivity. Direct interactions with the mean flow are weak and the fluctuating field maintains the turbulence diffusion. Similar scaling, considering $\tilde{\nu}_T$ to be a property of a turbulent fluid, shows that

turbulence diffusion by the largest scales is dominated by direct interactions with the mean-strain-rate field,

$$\overline{s_{ij}s_{ij}} \sim \left(\frac{\Delta}{\ell}\right)^{-4}\left(\frac{q}{\ell}\right)^{2}, \text{ so } S_{ij}S_{ij} >> \overline{s_{ij}s_{ij}} \text{ for } \Delta >> \ell \ . \qquad (8)$$

Results (7) and (8) have important implications to modeling. The fine-grid limit is insensitive to the mean flow but requires reasonable modeling of turbulence fluctuations. No additional modeling is needed for this range, since traditional LES subgrid models are already adequate. The coarse mesh limit is sensitive to mean-flow parameterizations though insensitive to details of the evolving fluctuations. We infer that the well known failure of the Smagorinsky model in the coarse mesh limit comes from its interaction with the mean flow. Zajaczkowski and Peltier (Reg. Paper #68 of these proceedings) propose a correction to the Smagorinsky model based on accommodating the RANS prediction of the mean time scale. We use their corrected Smagorinsky model:

$$\tilde{\nu}_T = \tilde{\nu}_T^{SMAG} + T(\ell,\Delta,\eta)(\bar{\nu}_T^{RANS} - \bar{\nu}_T^{S}) \text{ where } \bar{\nu}_T^{S} = (c_s\Delta)^2\left(2\sqrt{S_{ij}S_{ij}}\right). \qquad (9)$$

$\bar{\nu}_T^{S}$ represents the incorrect part of the Smagorinsky model, it's application to the mean flow, that is replaced by a correction from RANS. The correction imposes the proper time scale. The transfer function is $T(\ell,\Delta,\eta) = (\Delta/\ell)^2$.

3. Numerical Method

A finite difference discretization of Eq. (1) with discretized boundary conditions and turbulence modeling is solved. The solution procedure follows the fractional step approach outlined by Rai and Moin (1991); however, a linear blending of second-order accurate weighted-average central differencing with first-order accurate upwind differencing is used for the nonlinear advection terms for values of the transfer function greater than 0.9. This range was chosen by numerical experiment emphasizing the need to support turbulence scales of motion while retaining stability for very coarse grids. Explicit dependence of the blending on cell Peclet number was not used. The code was validated based on the previous study by Peltier et al. (2000) and based on comparisons to other experimental and numerical data.

4. Numerical Results

Our test problem is fully-developed channel flow at $\mathrm{Re} = 640$, based on the friction velocity and on the channel half height. This configuration is a common test case because of its geometric and flow condition simplicity; however, it imposes all of the difficulties associated with modeling near-wall flows. Our domain size is $2\pi \times \pi \times 2$, similar to cases studied by Moin & Kim (1982). Our grid resolution is varied from fine, $42\times23\times65$, to coarse, $14\times7\times17$. Intermediate resolutions are $14\times23\times33$, $14\times23\times17$, $14\times15\times17$, and

$14\times7\times33$. Hyperbolic tangent stretching is used in the wall-normal direction, our z coordinate. The near-wall spacing is prescribed to give $y^+=1$ at the second grid point. Equal spacing is used in the streamwise (x) and cross-stream directions (y). The mean statistics for this case are stationary, so the RANS input to (9) is sampled *apriori* to increase code efficiency.

Our parametric variations of grid resolution in the streamwise and wall-normal directions show that the accuracy of our predictions is affected by resolution, however, turbulence fluctuations are supported for cross-stream resolutions greater than 7. Considering the cross-stream resolutions, one sees that the dimensionless grid spacing in the cross-stream direction of the fine resolution case is 0.14, a value that can support turbulence based on observations by Nikitin et al. (2000), while the cross-stream spacing of coarse resolution case is 0.45, well within the "danger zone" outlined by Nikitin et al. (2000) for which turbulence cannot be supported.

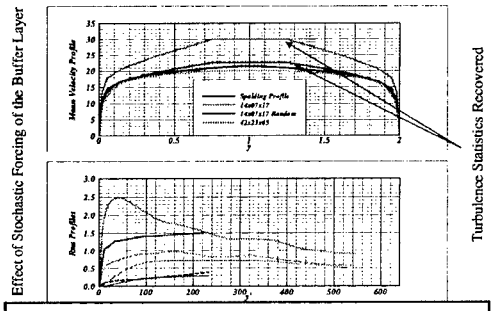


Figure 1 Mean velocity and rms profiles

Figure 1 shows that without special intervention, turbulence in our coarse resolution case is suppressed, as expected, leading to a nonphysical bulge in the mean velocity profile and zero turbulence fluctuations.

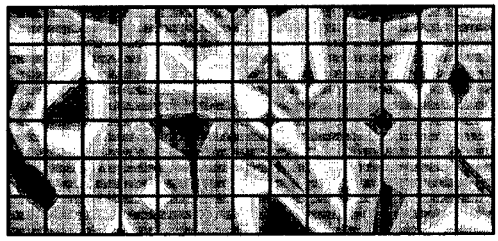


Figure 2 White noise applied to buffer layer, 10% turbulence intensity.

Since the buffer layer is predominantly decoupled from the core flow with the exception of isolated bursting events, we postulate that the effects of an under-resolved buffer-layer can be modeled using white noise of sufficient intensity. Figure 2 presents a white noise field used in this study. Ten percent turbulence intensity is arbitrarily chosen. The core flow responded with organized large-scale structures correcting the lost turbulence diffusion. Figure 1 shows that the mean-velocity profile computed from the coarse resolution case forced by buffer-layer noise recovers the Spalding profile as hoped.

5. Conclusions

The results of this work independently confirm the observations of Nikitin et al. (2000) that a "danger zone" exists in hybrid RANS/LES modelin g. Our hybrid model is markedly different than the DES they used showing that this "danger zone" is general. We show that a simple model bursting events from the underresolved buffer layer is able to sustain turbulence in the core flow. This result provides one route for constructing an hybrid RANS/LES modeling capability that is truly insensitive to grid resolution.

Future work will involve estimating bounds for the required turbulence intensity needed to model under-resolved buffer layer events.

Acknowledgments

This work was funded through internal support from The Applied Research Laboratory at Penn State University.

References

1. Baggett, J.S, 1998: "On the Feasibility of Merging LES with RANS for the Near-Wall Region of Attached Turbulent Flows", *CTR Ann. Research Briefs.*
2. Nikitin, N.V., Nicoud, F., Wasistho, B., Squires, K.D., and Spalart, P.R., 2000: "An Approach to Wall Modeling in Large-Eddy Simulations," *Phys. Fluids*, 12(7), 1629-1632.
3. Peltier, L.J., Zajaczkowski, F.J., and Wyngaard, J.C., 2000, "A Hybrid RANS/LES Approach to Large-Eddy Simulation of High-Reynolds-Number Wall-Bounded Turbulence," *FEDSM2000-11177*, ASME 2000 Fluids Eng. Div. Summer Meeting, Boston, MA.
4. Rai, M.M., and Moin, P., 1991: "Direct Simulations of Turbulent Flow Using Finite-Difference Schemes," *J. Comp. Phys.*, 96(1), 15-53.
5. Spalart, P.R., Jou, W.-H., Strelets, M., and Allmaras, S.R., 1997: "Comments on the Feasibility of LES for Wings, and on A Hybrid RANS/LES Approach," *Proceedings 1st AFOSR Int'l Conf. on DNS/LES*, Ruston, Louisiana, Aug. 1997.
6. Speziale, C.G., 1998: "Turbulence Modeling for Time-Dependent RANS and VLES: A Review," *AIAA J.*, 36(2), 173-184.
7. Strelets, M., 2001: "Detached Eddy Simulation of Massively Separated Flows," *AIAA 2001-0879*, 39th AIAA Aerospace Seiences Meeting, Reno, NV.
8. Zajaczkowski, F.J. and Peltier, L.J., 2001: "Energy-Containing-Range Modeling of Fully-Developed Channel Flow using a Hybrid RANS/LES Technique," *Proceedings 3rd AFOSR Int'l Conf. on DNS/LES.* Arlington, Texas, Aug. 2001.

APPENDICES

Third AFOSR International Conference on DNS/LES

University of Texas at Arlington, Arlington, Texas, USA
August 5-9, 2001

A. PANEL DISCUSSION

Chairman:
Dr. Chaoqun Liu, UTA

Panel Members:
Dr. Shuhyi Chern (Lockheed-Martin)
Dr. Massimo Germano (Politecnico di Torino, Italy)
Dr. Ronald Joslin (Penn State)
Dr. Foluso Ladeinde (Aerospace Research Corp., LI)
Dr. Ugo Piomelli (U. of Maryland)
Dr. David Pruett (James Madison University)
Dr. Pierre Sagaut (ONERA, France)
Dr. Brian Smith (Lockheed-Martin)

Discussion Topics:
1) The needs for DNS/LES from science research and engineering applications
2) The capability of current DNS/LES methods
3) The critical problems with current DNS/LES methods
4) The critical experimental data required to advance or validate LES simulations
5) The perspective of future development of DNS/LES

Time: 4:40-5:40, pm, August 8th, 2001
Place: Engineering Auditorium, UTA

Chaoqun Liu (UTA): Good evening, ladies and gentlemen. I hope you do not feel too tired with this busy day today. This is the last session for today before the banquet. I know the time is too short for this discussion. We have five questions, but only have one hour of time. It is very difficult to cover all topics and let people give more complete answers, but we will try to do our best. I would like to run the session in the following way. I will first raise the questions one by one and invite some panel members to give answers first and then let the audience to ask the questions or give the answers. I have to limit each speaker to have 2-3 minutes and limit to have 2-3 speakers from the audience for each question. I want to take recording for the discussion. I will edit the recording and send to all speakers for the final approval before the publication. You can make corrections or ask me to remove your talk if you want. I also request each speaker can give your name, organization, and your country at the beginning of your talk. Let me first introduce the panel members one by one, ... My name is Chaoqun Liu from University of Texas at Arlington. I am a local person. Let me

raise the first question why we need DNS/LES? I want to get some opinion from industry. We have three people from industry join the panel today. Who wants to be the first speaker?

Foluso Ladeinde (Aerospace Research Corp., LI): It is obvious that we need to calculate realistic engineering systems. Existing procedures are not general. One of the problems with RANS is that the model is not robust enough. When you change the problem, you almost have to change the model. LES promises to avoid such a problem on the assumption that the small-scale problem (and its model) is universal, from application to application. The large-scale features are problem-dependent but are presumed understood and are easier and cheaper to calculate. Therefore, there is some hope that LES will represent a universal procedure for acceptably-accurate calculations, even for realistic systems. That is why I think we should look up to it for realistic calculations. For DNS, I don't think the industry has any plans to use it for calculations intended to generate design data for either components or systems. It is simply too expensive for the parameter range of interest in engineering.

Brian Smith (Lockheed-Martin): I think in this conference people come from two different places when they make their presentations. One group comes from a very theoretical viewpoint. They are looking at theory, numerical methods, and models. The other group is trying to use and apply LES to real problems. Among people applying LES some users do not use an LES model at all and just use second order accurate methods for their calculations with complex geometry and use numerical diffusion as a sub grid scale model. I think what we need to do is to move to an area between these two groups and focus the theoretical work on what improvements we can do. We need to address real problems. I have another thought here about where we are and where we need to go. I have been working at Lockheed and General Dynamics for 15 years. When I started 15 years ago we were in about the same place with RANS, e.g. steady state 3-D calculations that we are now with LES for unsteady flow. We can make a lot of nice pictures and animations, but we really need to be cautious about the simulation accuracy. I know the channel flow is the beginning point, but we need to get beyond the channel flow. Looking at the development history for 3-D RANS may provide some guidance for development needs for LES. The goal should be to accelerate the development cycle required to obtain useful engineering methods based on LES.

Shuhyi Chern (Lockheed-Martin): I got some examples in the transparences, so I do not have to talk (showing several transparencies). There are some examples we need more accurate calculations. Here is a launch of vehicles. Upon ignition of a large solid rocket motor exhausting into a launch duct deflector, combustion gases enter the launch duct at high velocity. This piston-like action causes the blast-like overpressure and acoustic wave propagation. The ignition

induced overpressure and acoustic waves have the potential of causing damage to the vehicle. If we have many pressure spikes, they will affect the structure of vehicle. This is very sensitive for the vehicle structure responding to the impulse forces caused by over-pressured and acoustic waves. It will have 10% to 20% pressure difference. Then the structure need to redesign. The calculation has to be very accurate. I give another example. We have problems to calculate the basic flow accurately. Why is it so important? Because the pressure distribution in the nozzle surfaces of base region are affected by the re-circulation flow, the freestream and nozzle plume interaction causes the re-circulation. The pressure distribution is so strong that can causes different temperature distribution. If the temperature is too high, we need to put more insulation material, which will increase the weight of the launch vehicle. We really need to predict more precious pressure distribution, but RANS may not get accurate prediction. That is why we look for more accurate calculations. Besides, we also have the acoustic propagation problem created by plume of the motor nozzles. Also the re-circulation flow between the vehicle and rocket boosters causes acoustic spread in this region. We need accurate prediction for the acoustics, but it is very difficult to predict the acoustics. That is why industry needs more accurate way for flow prediction.

Chisachi Kato (University of Tokyo, Japan): As far as engineering applications of LES are concerned, I think that there are two major areas of applications of LES as I presented in my talk. One is the simulation of unsteady flow fields, which possibly lead to generation of aerodynamic noise and/or vibrations of the machines. The other is the simulation of flow fields with large-scale separations. For both types of simulations, I think that LES can do better job than RANS model does in general.

Chaoqun Liu (UTA): Let us switch to the second question. What is the capability of the current DNS/LES methods. I would like to invite Dr. Germano to give his opinion first.

Massimo Germano (Italy): If we look at the presentations in this conference, the capability of LES is really high. We saw the wake-boundary layer interaction, wall boundary flows, cavity flows, acoustics, roughness, flow around complex body, so on. It is clear to me that the capability is increased so much from one year to another. But the problem, in my opinion, is with the role of modeling which is not so clear. That is a big problem. In many cases it is not easy to evaluate it more precisely. This is my opinion. The capability is really increased, but it is not easy to understand which one is the real merit.

Pierre Sagaut (ONERA, France): We can make some comments on the capability of current DNS/LES methods to see what we can use, where we do use, and what we truly use. First, we can think about different research activities. If

we are looking for fundamental research and fundamental results, we already use DNS/LES. People are dealing with acoustics, stability, etc, you can see DNS/LES are already used and are matured. Now we want to deal with general engineering applications. We are all appealing to get funding to do some engineering applications. We know it works for fundamental problems, but we also know it will not work for engineering in a few days. From what presented in this workshop around the room, we can see a lot of impressive work on complex flow. Professor Kato gave very nice demonstration that LES is an efficient method which can really be used for complex flow. I can take an example from our latest computation that the second order method with wall model has very little dissipation. My computation can predict the vortex breakdown location and the mean velocity profile well. From these kinds of simulation, we may not need to improve much. The fundamental results are there already. I want to go back to Professor Kato's conclusion for the attached boundary layer flow. If we want to go to very high Reynolds number, we meet a very big problem, because many applications with boundary layer get transition, separation, etc. I know many people use wall model but are unable to recover transition as well as separation and reattachment. Many times we can see people focus on a simple geometry on a basic problem, forgetting the complex geometry, but we insist things are coupled. For example, for the A-profile wing, if you do not get the transition, you lose the separation. You have to deal with coupled geometry with realistic Reynolds number. For this kind of computation, we have to make more progress. That is a comment made by Professor Germano. I do agree with him. I think most improvements for results come from coupling LES with multiple domains with mesh refinement. Yesterday, we saw a good example. For the future improvement, we need this kind of coupling including moving grids with time dependent feature.

Ronald Joslin (Penn State): Most of my background is in spatial DNS, so pretty much every time I hear a talk, I try to relate the information to the spatial problem. It appears that a lot of tools are available for channel flows, which is pretty obvious from the talks over the past few days. I spent a lot of time trying to understand inflow and outflow boundary conditions. That is a very important issue for spatial DNS and external flow problems. If I couple my comment with question No. 5, that is one area we need to pay attention to, for example for the external flow in particular, perhaps some kind of meeting between the stability theory and random noise based on what we know from the mean flow properties may be a logically correct approach. That is what I am going to try; this meeting of instability theory with randomness may produce a more logical inflow boundary condition. I think that a shortcoming of DNS in the near term is how do we generate inflow boundary conditions. I spent a lot of time over the past few months on outflow boundary conditions. There is always a reflection at the outflow boundary, albeit small. That is unless you add some artificial dissipation, there is always some kind of reflection. I don't have good feelings yet about how

important it is for subsonic flow or incompressible flow, but it is an important issue.

Foluso Ladeinde (Aerospace Research Corp., LI): I believe the majority of the people in the audience might want to hear the answer to a question I want to ask. If I were a company executive or a program manager trying to make a funding decision, I will particularly want an answer to the following question. Since the 1999 Rutgers' meeting, besides the impressive "Power Point" presentations we have seen in this meeting, how much progress have we made on LES, especially from the standpoint of application to realistic systems? I would like to have one of my colleagues here answer this question.

David Pruett (James Madison University): Recently, several researchers, myself included, have raised a number of mathematical issues about LES. I am frankly quite impressed with this conference that many of the mathematical issues are being addressed and that there is convergence toward a common understanding. Understanding about things such as model-filter consistency, I think, will help LES in many ways. I am actually encouraged that there has been much progress.

Chaoqun Liu (UTA): Foluso, does he answer your question?

Foluso Ladeinde (Aerospace Research Corp., LI): I agree with Dave, although he addressed only one half of the issue. He talked from mathematical viewpoint, but I am also looking for something for the industry. Are we ready to forgo the Spalart-Allmaras or the Baldwin-Lomax models and switch to LES? What he said is correct. I agree with him one hundred percent. But from defense application standpoint, are we now more capable of solving more complicated problems since 1999, based on the funding that we have received in this field?

Chaoqun Liu (UTA): Anyone wants to answer his question?

Pierre Sagaut (ONERA, France): I have good answers, but have not enough research funds.

Chaoqun Liu (UTA): You need more money (the audience were laughing)?

Pierre Sagaut (ONERA, France): Two years ago in 1999, everybody in Europe was asking what kind of engineering application we can do using LES? There is a big chance for the European industry during the past two years, e.g. Airbus, NATO Aircraft. We definitely need something like RANS for applications, but our job now is to promote LES to deal with these applications, e.g. aero-acoustics, instability, especially for flow separation and active flow controls. You will need high order accuracy and more accurate solutions for these problems. You can use

LES and coarse grid DNS which we need. We also know these are very useful even for people who are designing. We know we may not be able to get favorable coefficients. These could be a design tool for active flow control which RANS cannot be. These are what we are looking for now.

Shuhyi Chern (Lockheed-Martin): We know DNS/LES are accurate. My question is how complicated geometry we can use them to do calculations. Does anyone have ideas?

Dimitri Mavriplis (ICASE): I don't think it is necessarily the geometric complexity, but more the issue with disparate scales. For example, external aerodynamics has such a wide range of scales, particularly the very small scales in the boundary layer regions, that it will be pretty hard to treat with LES in the near future. However, something like flow in a combustor, or some internal flow with low Reynolds number is going to benefit much earlier from LES in spite of the added geometric complexity.

Brian Smith (Lockheed-Martin): Geometric complexity pushes you towards unstructured grid formulation. There is a lot of work to do in this area in terms of making LES methods accurate This is not nearly mature. I agree with you with that exception.

Shuhyi Chern (Lockheed-Martin): Which method is more accurate comparing structured grid with unstructured grid?

Brian Smith (Lockheed-Martin): It is much easier to achieve high-order accuracy for LES using structured grids, especially for Cartesian grids.

Chgaoqun Liu (UTA): That is much easier for structured grid, especially for rectangular grids, to achieve high-order accuracy that DNS/LES require.

Shuhyi Chern (Lockheed-Martin): Do you mean the unstructured grid code is not as accurate as the structured grid code?

Brian Smith (Lockheed-Martin): Correct – unstructured grids are not as accurate.

Chaoqun Liu (UTA): Especially for high-order scheme. Because of the time limit, we have to switch to the third question. What is the critical problem with the DNS/LES methods? Can we directly use DNS/LES methods for engineering application now? If that was the case, we would not need to sit here. That means we still have serious problems with the current DNS/LES methods. What is the most critical problem with the current DNS/LES methods?

David Pruett (James Madison): I'm now at James Madison University, a teaching institution. I'm not doing DNS as much as I used to, but I was heavily involved in DNS from about 1984-1996. I then saw CFD as divided into two very different camps. One camp was interested in applied aerodynamics, for example, in the flow over a Boeing 747. They had to contend with shocks, and, of course, had to use dissipative numerical methods. In another camp were those like myself doing more basic work (e.g., laminar-turbulent transition) with the numerical tool of DNS. Simulating wave propagation requires non-dissipative numerical methods. For me, the Holy Grail of CFD has always been the search for a single scheme that could capture shocks *and* accurately predict instability waves. Quite frankly, I was not certain that was possible. I am actually pleasantly surprised by some of the talks I've heard here to realize that there now exist several schemes that apparently can do both. We saw Dr. Nikolaus Adams' presentation today of shock boundary-layer interaction. Certainly, we saw shocks co-existing with very small-scale instability waves. We have heard a talk by Prof. Shu of Brown U. on the weighted ENO (WENO) method. From UTA, we have seen a beautiful presentation of a weighted compact scheme that appeared to capture shocks quite well. And HC Yee of NASA Ames has proposed high-order schemes in which wavelets are used to detect shocks and to impose dissipation locally, just where needed. Frankly, I am quite amazed that we have made so much progress. This does not mean that DNS is now applicable to all types of problems. No, because the computational cost of fully resolved DNS scales as the cube of Reynolds number. We need 3 or 4 decades before DNS can do realistic engineering simulations, but I think DNS can move gradually toward more complex geometries. I would like to suggest that the most appropriate use of DNS is still for prototypical flows--what Tom Gatski calls unit problems--for example, compression ramps or wake flows. To my mind, the best use of DNS is for understanding basic phenomena and for validating LES (or other methodologies), which can now be used as either a research tool or an engineering tool.

Ugo Piomelli (U. of Maryland): David and I decided to split the subject. I think there are several critical areas for LES that need to be advanced. Some of them have been addressed in this conference, some of them not. There are several issues. First, numerics, e.g. the shock capturing schemes for LES, that David mentioned also. Some of the numerical issues were mentioned by Dave Pruett in his presentation; other people also talked about consistency between modeling and filtering. Very important, in my opinion, are the conservation properties of the scheme, something that was discussed by Felton and Lund as well as by Verstappen. A lot of progress has been made in LES application in curvilinear coordinates, and people start to worry about filtering for unstructured meshes, an issue that has not been fully transferred from the mathematical formulation step to the implementation in a code. Another critical problem is the definition of the inflow condition. Typically, when we perform a large eddy simulation, we want

to compare it with some experiments. If the inflow condition is not trivial (periodic boundary condition for channel flow, for instance), it can affect the comparison very significantly, to first order typically. In an experiment, the inflow conditions are usually not fully documented. In real problems, the inflow condition may be not fully documented, but also uncertain. One cannot expect to be able to compare the large eddy simulation or direct numerical simulation with experimental data unless the boundary conditions are matched very precisely. From the point of view of validation that is a problem. Second, from the point of view of prediction that also presents a problem. The presentation by George Karniadakis today was addressing this very important issue. I think the last main issue for LES is to apply it to the high Reynolds number wall-bounded flow, which is known as the wall modeling. I am not very happy with any of the approximation for the wall boundary conditions or wall functions used right now, even though I have developed several ones by myself. Right now, the approach is accurate only if we are not interested in what happens near the wall, for instance in separated flows with large scale structures affecting the physics. If we are interested in what is happening at the wall, we are still limited. I did not mention the subgrid modeling because we have several models that are satisfactory. It is always good to have better models, but I think the priority now should be on the other issues I mentioned. Of course, that is just my personal opinion.

Chaoqun Liu (UTA): Any questions?

Liqiu Wang (U. of Hong Kong): Turbulence is a typical multi-scale problem. It seems very important in understanding and controlling turbulence to understand the interaction among transport phenomena at different scales including mass, momentum, energy and entropy transfer. My question is: what is the way and the best way for us to understand such the interaction?

Chaoqun Liu (UTA): Who can answer this question? No one? I think people may not understand your question fully. Can you repeat your question?

Liqiu Wang (U. of Hong Kong): My question is not only for DNS or LES, but also for the turbulence in whole. The question is regarding the interaction among transport phenomena including the mass, momentum, energy and entropy transport at different spatial and temporal scales. To understand the nonlinear interaction among transport processes at different scales is quite critical for us to understand turbulence. What is the way to understand such the interaction?

Chaoqun Liu (UTA): You mean the transport phenomena among different length scales are very important? Who can answer that question?

Pierre Sagaut (ONERA, France): Physical or mathematical models are really getting deeper. Putting new problems into your computation for modeling, you always find new questions. Then you have do DNS to understand. However, it will be limited if you look at the Reynolds number. You may trust for what you see in DNS just for numerics.

Liqiu Wang (U. of Hong Kong): How about the future, next ten years or so, of turbulence study? Should we focus on analytical, numerical or experimental work to understand turbulence?

Chaoqun Liu (UTA): That is the question No. 5 when we talk about the future for next ten years.

Chisachi Kato (Japan): Professor Piomelli, I just want to know how much time do you think we'll need or you'll need to develop an appropriate wall model for LES. I am pretty sure that industry needs that for practical applications of LES. Also, in which direction should we go in developing wall models for use in LES?

Ugo Piomelli (U. of Maryland): That is two questions. First is how much time we need to develop wall model. I don't know. The other question is which way we should go? I think, first of all, we should forget wall modeling if we deal with the problems in which the inner layer drives the outer layer. We have some hope if the outer layer drives the inner layer. In these cases, most approaches have been averaged methods, either the Schumann-type boundary conditions or the two layer model or Spalart's DES. All of these models perform RANS in the inner layer and LES in the outer layer. There are two problems with these approaches. First of all, even if the RANS model is accurate for particular inner layer physics, there is no assurance that the inner layer predicted by RANS is going to match the outer layer predicted by LES. Typically, it is shown in the channel flow that mismatching in the log law. Therefore, the physics of the transition between RANS and LES are quite critical to the wall modeling. Another tool that has been successful are based on Linear Stochastic Estimation and require the two-point correlation tensor to be known, so that it is not predictive unless one can use some sort of scaling on two-point correlations taken from known flows. For a more extended discussion (begin commercial) you have to wait until my article in the next issue of the Annual Review (end commercial).

Nobuyuki Taniguchi (Japan): I agree with Prof. Piomelli that the inflow condition is important. I have another question how to apply initial condition for the time-marching problem? How to make appropriate initial conditions?

Ugo Piomelli (U. of Maryland): Let us go to your first question. How do you apply or how do you develop?

Nobuyuki Taniguchi (Japan): How to make the initial condition?

Ugo Piomelli (U. of Maryland): There have been several methods. We saw the recycling method proposed by Lund with the modification by Kaltenbach. That is a possible way. However, it is another tough problem and most successful simulation so far have assumed a detailed knowledge of the flow state for the inflow (which was, for example a boundary layer). If you have much more complicated flow, inflow to compressor for example, it is going to be very difficult. One probably needs combination of experiment and RANS and some smart way to generate fluctuation. It could take, for example, the experimental distribution of turbulence kinetic energy to manufacture the spectrum and some phases as much as possible. For complex flows, it is going to be very significant issue.

Chaoqun Liu (UTA): Because of the time limit, I have to move to the question No. 4. What is the critical experimental data to advance and validate the LES simulation. This question is raised by Dr. Tom Beutner, the AFOSR Program Manager. I think it is very important.

Pierre Sagaut (ONERA, France): Once again, you want to get the European point of view. I cannot talk if French government should fund it, but we really think about it because it appears as a critical issue if you really want to go further to develop new model and codes. We usually compare LES with the data base which have been developed for RANS during the past ten years. It appears that most times we cannot get conclusion with the simulation because there is always something unknown in the experimental data. It may be inflow data, wind tunnel boundary conditions, so on. Also the data was got through post-processing during the experiment. It was run for validation, but did not treat the unsteady data or something linking with unsteady flow. We need LES to know something about the coherent structure, spectrum, and two point correlation. We need this kind of information to develop models or validate LES. It is now our obligation to develop next generation of data to validate all of these things. We know it is expensive. Tomorrow, Larcheveque will give an example of many applications with the cavity flow, e.g. acoustic, etc. We have been thinking about that we need to develop a unique data base. It was a one million dollar experiment. With that we can do comparison of LES with that data base. That is the only data base we can do some comparison. If we cannot validate the simulation and compare it with experimental data, how for the design people to use these simulations. There would be a real problem.

Chaoqun Liu (UTA): I have a question. If you are the program manager, what kind of data base you would like to set up?

Pierre Sagaut (ORNEA, France): I have a list of things to consider.

Ugo Piomelli (U. of Maryland): I agree with these comments regarding the documentation of the experimental data. I would like to distinguish between the large eddy simulation validation and model development. For validation of LES, the inflow condition, the boundary condition, and the way data were obtained need to be documented much better than they have been so far. There have been several cases in which discrepancies between numerical results and experimental were observed, and new experiments that matched the conditions of the calculation were performed resulting in a better agreement. The other thing we can do with experiments is to help develop models, playing the role that DNS has filled, with PIV measurement and multiple point measurement, especially at higher Reynolds numbers than DNS.

Chaoqun Liu (UTA): Do you have any idea what kind of examples which we should set for validating the LES results.

Ugo Piomelli (U. of Maryland): I think the experiment needs to have a geometry that should be easy for gridding. A very simple geometry with some complex physics is appropriate. I think in more complex geometry it is hard to separate the numerical errors, truncation errors, local commutation errors. The ideal example should use Cartesian meshes.

Chaoqun Liu (UTA): Any other ideas about what kind of data base we should set for validation?

Pierre Sagaut (ONERA, France): You have to do validation for homogeneous turbulent flow, channel flow, etc.

Ugo Piomelli (U. of Maryland): You have to do additional computation to match the inflow condition with the data base.

Chaoqun Liu (UTA): Any other problems?

Foluso Ladeinde (Aerospace Research Corp., LI): I think we should deal with realistic engineering problems. Otherwise, we are out of business. One problem I would like to hear us discuss is the speed of DNS/LES calculation. How can we make the calculations go faster? Validation data is crucial. However, even if we have all the validation data that we need, I think we will still not be able to calculate realistic systems with LES. Also, how do we post-process the data, with the number of data points in the billions?

Chaoqun Liu (UTA): This is the problem with DNS/LES, but our topic now is what kind of experimental data we should set to check the LES results.

Foluso Ladeinde (Aerospace Research Corp., LI): Yes, but it seems as if we are going to have to address this issue if we have any plans to use our procedures to benefit engineering analysis and design calculations.

Chaoqun Liu (UTA): That is all right. Any other proposal or we just accept the examples proposed by the above two people to check the LES results? No? We may need to move to the last question, what is the future of DNS/LES? Any ideas on the perspective of DNS/LES?

Foluso Ladeinde (Aerospace Research Corp., LI): Speed, speed.

Chaoqun Liu (UTA): Is it the only one? Let me invite Dr. Germano to give his opinion.

Massimo Germano (Italy): Sorry. I am supposed to speak about the perspective of LES future development, but I can just speak about perspective of modeling. Well, you may say we have good models and that this point is not so critical. Probably, you are right. However, also in this meeting we continue to see a big number of models that continue to go like airplanes in the first years of aviation, monoplanes, biplanes, triplanes, etc. We have not a mature situation with the models. This is very bad. Today, we still need for modeling more physics, and first of all good ideas, and cooperation, because without cooperation good ideas may not work, and we have not good results if we do not have a big cooperation between people. We saw dynamic models, dynamic modeling variants, and very interesting new ideas about probability distribution models. I think that is a good work to look at no models. We have seen a lot of calculations and results without models. These are very interesting and we should understand why they work. This is very important. I have only one suggestion, that it is very important to continue seeing to the physics. By doing LES, we are also understanding turbulence. We are writing equations, and we have to separate the equations from the numerics. They are different things. This is very important, in my opinion, for future development.

David Pruett (James Madison University): My comments are just on theoretical developments for the future. I hope someone else will jump in to address applications. Two of the early speakers in this conference, Prof. Germano and Tom Gatski, suggested that we look at RANS, LES, and DNS as a spectrum of numerical technologies. I agree. I like to think that perhaps 10 years down the road, maybe 15, a single computational code will exist with a "knob," that is, a parameter—the filter width--that can be varied from zero to infinity. With the filter width set to zero, the code performs DNS; with it set to something finite, it does LES. With the knob set to infinity, the code accomplishes RANS. Such a code would be a valuable tool in its own right, but I think more valuable

is the theoretical connection between RANS, LES, and DNS, that would have to be firmly established to develop such a code. Personally, I am a lot more comfortable with DNS than I am with either LES or RANS, because it seems to me that both LES and RANS have implemented many ad hoc methodologies that are not necessarily theoretically sound. As we try to bridge the gap between RANS, LES, and DNS, the theoretical weaknesses of LES and RANS methods will be exposed, which is a good thing. Both technologies will shed light on one another. Finally, as we try to bridge the DNS, LES, RANS gap, I suggest that, if possible, the supporting analysis should be done in Fourier space, where the essence of the connections resides.

Ronald Joslin (Penn State): I am pretty impressed by some of the talks that focus on the numerics in turbulent flows. Some numerical work advocated second order, fourth order, or high order, depending on who was speaking. One of speakers talked about an unconditional stable approach; the results were pretty impressive even with very coarse grids. That is a good thing. David Pruett said the shock-boundary layer interaction is pretty impressive work as well with ENO schemes. I do not know where we will end up in the 2004 conference. Let me make a motion that nothing is going to happen unless we drink and eat; therefore let us adjourn to the food and drink (audience were laughing).

Nobuyuki Taniguchi (Japan): I think we need a solver which is at least an order faster than current solvers to solve the complex flow such as the boundary flow, spray, combustion, and other applications, which is even not clear with the governing system yet.

Chaoqun Liu (UTA): Anyone else? Audience? No. Ok, let us just stop here. I am sorry to keep you staying for so long time and keep you being hungry. So, I hope you will enjoy the dinner. Thank you! (Long time applause)

-----The End-----

B. SCIENTIFIC ORGNIZING COMMITTEE

Liu, Chaoqun, Chair	University of Texas at Arlington
Sakell, Len, Co-Chair	AFOSR
Herklotz, Robert, Co-Chair	AFOSR

Adams, Nikolaus	Swiss Federal Institute of Technology (Switzerland)
Blaisdell, Gregory A.	Purdue University
Carati, Daniele	Universit Libre de Bruxelles (Belgium)
Chelyshkov, Vladimir	University of New Orleans
Chern, Shuhyi	Lockheed Martin
Dalton, Charles	University of Houston
Friedrich, Rainer	Technische University Muenchen (Germany)
Germano, Massimo	Politecnico di Torino (Italy)
Hadid, Ali	Boeing/Rocketdyne Propulsion & Power
Jimenez, Javier	U. Politecnica (Spain)
Johansson, Arnea	Royal Institute of Technology (Sweden)
Joslin, Ronald D.	Penn State University
Karniadakis, George	Brown University
Knight, Doyle	Rutgers – The State University of New Jersey
Kwak, Dochan	NASA Ames Research Center
Ladeinde, Foluso	Aerospace Research Corp., LI
Lee, Moon Joo	Pohang Univ. of Science and Technology (South Korea)
Lele, Sanjiva K.	Stanford University
Miyake, Yutaka	Graduate School of Osaka University (Japan)
Nieuwstadt, F.T.M.	Delft University of Technology (the Netherlands)
Pantelis, Garry	University of Sydney (Australia)
Piomelli, Ugo	University of Maryland
Sagaut, Pierre	ONERA (France)
Tam, Christopher	Florida State University
Visbal, Miguel R.	WPAFB, AFRL/VAAC
Voke, Peter	The University of Surrey (UK)
Zhang, Zhaoshun	Tsinghua University (China)

C. INVITED SPEAKERS

Adams, Nikolaus	Swiss Federal Institute of Technology (Switzerland)
Beutner, Thomas	Air Force Office of Scientific Research
Gatski, Thomas B.	NASA Langley Research Center
Germano, Massimo	Politecnico di Torino (Italy)
Givi, Peyman	State University of New York at Buffalo
Jiang, Li	University of Texas at Arlington
Joslin, Ronald D.	Penn State University
Liu, Chaoqun	University of Texas at Arlington
Karniadakis, George	Brown University
Kato, Chisachi	University of Tokyo (Japan)
Knight, Doyle	Rutgers – The State University of New Jersey
Piomelli, Ugo	University of Maryland
Sagaut, Pierre	ONERA (France)
Satofuka, Nobuyuki	Kyoto Institute of Technology (Japan)
Shan, Hua	University of Texas at Arlington
Shu, Chi-Wang	Brown University
Vasilyev, Oleg V.	University of Missouri-Columbia
Verstappen, Roel	University of Groningen (the Netherlands)
Visbal, Miguel R.	WPAFB, AFRL/VAAC
Zhong, Xiaoling	University of California, Los Angeles

D. LOCAL ORGANIZING COMMITTEE

Deng, Shutian, PhD Student, Math, UTA
Higbee, Beverly, Coordinator, Administrative Assistant II, Math, UTA
Hoang, Ngocle, MS Student, Math, UTA
Jiang, Li, Research Associate, Math, UTA
Liu, Chaoqun, Professor, Math, UTA
Kadjo, Hilaire, PhD Student, Math, UTA
Luo, Sheng, PhD Student, Math, UTA
Shan, Hua, Research Associate, Math, UTA
Xia, Jian, Research Associate, Math, UTA

E. CONFERENCE PARTICIPANTS

Adams, Nikolaus
Swiss Federal Institute of Technology
Institute of Fluid Dynamics
ETH Zentrum, CH-8092 Zurich
Switzerland
Tel: +4116325271
Fax: +4116321147
Email: Nikolaus.Adams@ethz.ch

Amati, Giorgio
CASPUR
P.le Aldo Moro 5
Roma 1-00-185
Italy
Tel: 0039-06-4991-13095
Fax: 0039-06-4957083
Email: g.amati@caspur.it

Arunajatesan, Srinivasan
Combustion Research and
Flow Technology, Inc
174 N. Main St, P O Box 1150
Dublin, PA 18917, USA
Tel: 215-249-9780
Fax: 215-249-9796
Email: ajs@craft-tech.com

Avancha, Ravikanth
2025 H.M. Black Eng. Building
Iowa State University
Ames, IA 50011
USA
Tel: 515-292-6954
Fax: 515-294-3261
Email: ark@iastate.edu

Bernfeld, Stephen R.
Department of Mathematics
Box 19408
University of Texas at Arlington
Arlington, TX 76019, USA
Tel: 817-272-5682
Fax: 817-272-5802
Email: bernfeld@uta.edu

Beutner, Thomas
AFOSR/NA
801 N. Randolph St
Arlington, VA 22203-1977
USA
Tel: 703-696-6961
Fax: 703-696-8451
Email: tom.beutner@afosr.af.mil

Boersma, Bendiks Jan
Delft University of Technology
Mekelweg 2, 2628 CD Delft
The Netherlands
Tel: +31 15 2787979
Fax: +31 15 2782947
Email: b.j.boersma@wbmt.tudelft.nl

Blaisdell, Gregory A.
Purdue University
West Lafayette, IN 47907-1282
USA
Tel: 765- 494-1490
Fax: 765- 494-0307
Email: blaisdel@ecn.purdue.edu

Braun, Carsten
Mechanics Department
RWTH Aachen, Templegraben 64
Aachen 52062, Germany
Tel: 49 (0)241 80-4637
Fax: 49 (0)241 8888126
Email: carsten@lufmech.rwth-aachen.de

Broglia, Riccardp
INSEAN
Via di Vallerano 139
Rome 00128
Italy
Tel: +39-06-50299297
Fax: +39-06-5070619
Email: r.broglia@insean.it

Calhoon, Jr., William
Combustion Research and Flow Technology, Inc.
174 N. Main St., P O Box 1150
Dublin, PA 18917, USA
Tel: 215-249-9780
Fax: 215-249-9796, Email: calhoon@cfd.rdec.redstone.army.mil

Chelyshkov, Vladimir S.
Deparment of Mathematics
University of New Orleans
New Orleans, LA 40148
USA
Tel: 504-280-7498
Fax: 504-280-5516
Email: vchelysh@uno.edu

Chern, Shuhyi
Lockheed Martin
P O Box 179
Mail Stop TSB5009
Denver, CO. 80201
USA
Tel: 303-971-4279
Email: shuhyi.y.chern@lmco.com

Choi, Haecheon
School of Mechanical and Aerospace Engineering
Seoul National University
Seoul 151-742, Korea
Tel: 82-2-880-8361
Fax: 82-2-878-3662
Email: choi@socrates.snu.ac.kr

Chyczewski, Thomas
Applied Research Laboratory
Penn State Univ.
P O Box 30
State College, PA 16804
USA
Tel: 814-865-2251
Fax: 814-865-8896
Email: tsc@wt.arl.psu.edu

Das, A.
Department of Theoretical and Applied Mechanics
Univ. of Illinois
at Urbana-Champaign
104 S. Wright St.
Urbana, IL 61081, USA
Tel: 217-333-3578
Email: arupdas@uiuc.edu

De Lange, H.C.
Section Engergy Technology
Dept. of Mechanical Engineering
Eindhoven University of Technology
P O Box 513 (wh 3.128)
Eindhoven, The Netherlands
Tel: +31-247-2129
Fax: +31-2433445
Email: h.c.d.lange@tue.nl

Debliquy, Olivier
Universite Libre de Bruxelles
Physique Statistique et Plasmas
Boulevard du Triomphe
Campus Plaine-CP.231
B-1050 Bruxelles, Belgium
Tel: 32-2-650.59.08
Fax: 32-2-650.58.24
Email: odebliqu@ulb.ac.be

Deng, Shutian
Department of Mathematics
Box 19408
University of Texas at Arlington
Arlington, TX 76019
USA
Tel: 817-272-3261
Fax: 817-272-5802
Email: deng_shutian@yahoo.com

De Stefano, Giuliano
Dipartimento di Ingegneria
Aerospaziale
Seconda Universita' di Napoli
via Roma 29, 81031 Aversa
Italy
Tel: 0039 081 5010265
Fax: 0039 081 5010264
Email: giuliano.destefano@unina2.it

Dyer, Danny
Mathematics Department
University of Texas at Arlington
Box 19408
Arlington, TX 76019
USA
Tel: 817-272-3246
Fax: 817-272-5802
Email: dyer@uta.edu

Ertem-Müller, Senem
Darmstadt University of Technology,
Department of Numerical Methods in
Mechanical Engineering,
Petersenstr. 30, 64287 Darmstadt
Germany
Tel: 0049-6151-162879
Fax: 0049-6151-164479
Email: ertem@fnb.tu-darmstadt.de

Eshpuniyani, Brijesh
School of Aeronautics
and Astronautics
Purdue University
West Lafayette, IN 47907-1282
USA
Tel: (765) 494-7864
Fax: : 765-494-0307
Email: eshpuniy@ecn.purdue.edu

Felten, Frederic N.
Department of Mechanical
Engineering
Box 19019
University of Texas at Arlington
Arlington, TX 76010-0019
USA
Tel: 817-272-2860
Email: felten@surya.uta.edu

Garnier, Eric
ONERA D.A.A.P/M.H.L.
29, Avenue de la Division Leclerc
BP72
92322 Chatillon cedex
France
Tel: 01.46.73.42.65
Email: Eric.Garnier@onera.fr

Garrick, Sean C.
Dept. of Mechanical Engineering
111 Church Street S. E.
University of Minnesota-Twin Cities
Minneapolis, MN 55455-0111, USA
Tel: 612-624-5741
Fax: 612-624-5230
Email: garrick@me.umn.edu

Gatski, Thomas B.
M/S 128, Computational Modeling & Simulation Branch
NASA Langley Research Center
Hampton, VA 23681-2199
USA
Tel: 757-864-5552
Fax: 757-864-8816
Email: t.b.gatski@larc.nasa.gov

Germano, Massimo
Politecnico di Torino
Dip. Ing. Aeronautica e Spaziale – DIASP -
C.so Duca degli Abruzzi, 24
10129 Torino, Italy
Tel: +39 011 564.6814
Fax: +39 011 564.6899
Email: germano@polito.it

Givi, Peyman
Mech. and Aero. Engineering
State University of New York at Buffalo, Buffalo, NY 14260-4400
USA
Tel: 716-645-2593 ex2320
Fax: 716-645-3875
Email: givi@eng.buffalo.edu

Goldstein, David
Dept. of Aerospace Engineering and Engineering Mechanics
The University of Texas at Austin
Austin, TX 78712
USA
Tel: 512-471-4187
Email: david@cfdlab.ae.utexas.edu

Hamed, Awatef
Dept. of Aerospace Engineering and Engineering Mechanics
University of Cincinnati
Cincinnati, OH 45221-0070
USA
Tel: 513-556-3553
Fax: 513-556-5038
Email: a.hamed@uc.edu

Haselbacher, Andreas
Center for Simulation of Advanced Rockets
Univ. of Illinois at Urbana-Champaign
Urbana, IL 61801, USA
Tel: 217-333-8683
Fax: 217-333-8497
Email: haselbac@uiuc.edu

Higbee, Beverly
Mathematics Department
University of Texas at Arlington
Box 19408
Arlington, TX 76019
USA
Tel: 817-272-5259
Fax: 817-272-5802
Email: bjhigbee@uta.edu

Hoang, Ngocle
Math Department
Box 19408
University of Texas at Arlington
Arlington, TX 76019
USA
Tel: 817-272-7526
Fax: 817-272-5802
Email: hoangle@uta.edu

Huckaby, E. David
U.S. Department of Energy
National Energy Technology
Laboratory, PO Box 880
Morgantown, WV 26507-0880
USA
Tel: 304-285-5457
Fax: 304-285-4403
Email: huckaby@netl.doe.gov

Iannelli, Pierluigi
Dipartimento di Ingegneria
Aerospaziale
Seconda Universita di Napoli
81031 Aversa
Italy
Tel: +39 081 5010265
Fax: +39 081 5010264
Email: pierluigi.iannelli@unina2.it

Iliescu, Traian
Argonne National Laboratory
Bldg. 221, C-219, 9700 S. Cass Ave
Argonne, IL 60439
USA
Tel: 630-252-0926
Fax: 630-252-5986
Email: iliescu@mcs.anl.gov

Jenkins, Karl. W.
Cambridge University
Trumpington Street
Cambridge CB2 1PZ
UK
Tel: +44-0-1223-332748
Fax: +44-0-1223-332662
Email: kwj20@eng.cam.ac.uk

Jiang, Li
Department of Mathematics
Box 19408
University of Texas at Arlington
Arlington, TX 76019
USA
Tel: 817-272-7119
Fax: 817-272-5802
Email: ljiang@omega.uta.edu

Joslin, Ronald D.
Applied Research Laboratory
Penn State University
P.O. Box 30
State College, PA 16804
USA
Tel: 814-863-6128
Fax: 814-865-889
Email: RDJoslin@psu.edu

Kadjo, Hilaire
Department of Mathematics
Box 19408
University of Texas at Arlington
Arlington, TX 76019
USA
Tel: 817-801-7172
Fax: 817-272-5802
Email: hilaire@uta.edu

Kaltenbach, Hans-J.
Hermann-F"ottinger-Institut
Technische Universit"at Berlin
Sekretariat HF-1
Strasse des 17. Juni 135
D-10623 Berlin, Germany
Tel: +49-30-314 23463
Fax: +49-30-314-21101
Email: kaltenbach@pi.tu-berlin.de

Kannepalli, Chandrasekhar
Craft-Tech
1 Coliseum Dr
Room 1150
University, MS 38655
USA
Tel: 662-915-6748
Fax: 662-915-6745
Email: kchandra@olemiss.edu

Karniadakis, George
Division of Applied Mathematics
Box F
Brown University
Providence, RI 02912
USA
Tel: 401-863-1217
Fax: 401-863-3369
Email: gk@cfm.brown.edu

Kato, Chisachi
Institute of Industrial Science
University of Tokyo
4-6-1 Komaba Meguro-ku
Tokyo, 153-8505
Japan
Tel: +81-3-5452-6190
Fax: +81-3-5452-6191
Email: ckato@iis.u-tokyo.ac.jp

Kimmel, Shari J.
Department of Mechanical
Engineering and Mechanics
Lehigh University
Bethlehem, PA 18015-3085
USA
Tel: 610-758-4017
Fax: 610-758-6224
Email: sjk4@lehigh.edu

Klioutchnikov, Igor
Mechanics Department
RWTH Aachen
University of Technology
Templegraben 64, Aachen 52062
Germany
Tel: +49-0-241-80-4637
Email: klutchnikov@lufmech.rwth-aachen.de

Knaepen, Bernard
Université Libre de Bruxelles
Service de Physique Théorique
et Mathématique
Campus Plaine - CP 231
Boulevard du Triomphe
B-1050 Bruxelles, Belgium
Tel: 32-2-650.59.18
Email: bknaepen@ulb.ac.be

Knight, Doyle
Dept of Mech. and Aero. Engineering
Rutgers-The State University of New
Jersey, 98 Brett Road
Piscataway, N.J. 08854-0858
USA
Tel: 732-445-4464
Fax: 732-445-3124
Email: ddknight@rci.rutgers.edu

Krajnovic, Sinisa
Department of Thermo and Fluid
Dynamics
Chalmers University of Technology
SE-412 96 Goteborg
Sweden
Tel: +46-31-772-1400
Fax: +46-31-180-976
Email: sinisa@tfd.chalmers.se

Lacor, Chris
Department of Fluid Mechanics
Vrije Universiteit Brussel
Pleinlaan 2
1050 Brussel
Belgium
Tel: ++ 32.(0)2.629.23.79
Fax: ++ 32.(0)2.629.28.80
Email: chris.lacor@vub.ac.be

Ladeinde, Foluso
Director of Research
Aerospace Research Corp., LI
25 East Loop Road, Suite 202
P. O. Box 1527
Stony Brook, NY 11790
USA
Tel: 631-632-9293
Email: ladeinde@thaerocomp.com

Larcheveque, Lionel
ONERA-DSNA/ETRI
BP72-29 Avenue
de la division Leclerc
92322 Chatillon cedex
France
Tel: 33 (0)1 46 73 42 07
Email: lionel.larcheveque@onera.fr

Layton, William
Department of Mathematics
University of Pittsburgh
Pittsburgh, PA 15260
USA
Tel: 412-624-8312
Fax: 412-624-8397
Email: wjl@pitt.edu

Lei, Kangbin
Computer and Information Division
Advanced Computing Center, (RIKEN)
The Institute of Physical and Chemical
Research, 2-1 Hirosawa
Wako-shi, Saitama 351-0198, Japan
Tel: +81-(0)48-462-1111 Ext. 3848
Fax: +81-(0)48-462-4634
Email: lei@riken.go.jp

Lessani, Bamdad
Department of Fluid Mechanics
Vrije Universiteit Brussel
Pleinlaan 2
1050 Brussel
Belgium
Tel: ++ 32.(0)2.629.29.94
Fax: ++ 32.(0)2.629.28.80
Email: bamdad@stro.vub.ac.be

Liao, Guojun
Department of Mathematics
Box 19408
University of Texas at Arlington
Arlington, TX 76019
USA
Tel: 817-272-2647
Fax: 817-272-5802
Email: liao@uta.edu

Liu, Yue
Department of Mathematics
Box 19408
University of Texas at Arlington
Arlington, TX 76019
USA
Tel: 817-272-5680
Fax: 817-272-5802
Email: yliu@uta.edu

Liu, Chaoqun
Department of Mathematics
Box 19408
University of Texas at Arlington
Arlington, TX 76019
USA
Tel: 817-272-7527
Fax: 817-272-5802
Email: cliu@uta.edu

Lund, Thomas S.
Dept of Mech. and Aero. Engineering
Box 19018
University of Texas at Arlington
Arlington, TX 76019-0018
USA
Tel: 817-272-7053
Fax: 817-272-5010
Email: lund@uta.edu

Luo, Sheng
Department of Mathematics
University of Texas at Arlington
Box 19408
Arlington, TX 76019
USA
Tel: 817-272-7527
Fax: 817-272-5802
Email: sluo@uta.edu

Madnia, Cyrus K.
Dept of Mech. and Aero. Engineering
State University of New York at
Buffalo
Buffalo, NY 14260
USA
Tel: 716-645-2593 ext. 2315
Fax: 716-645-3875
Email: madnia@eng.buffalo.edu

Mallier, Roland
Department of Applied Mathematics
University of Western Ontario
London, ON N6A 5B7
Canada
Tel: 519-473-6133
Fax: 519-661-3523
Email: mallier@uwo.ca

Martin, M. Pino
Princeton University
Mech. and Aero. Engineering
D_307 Engineering Quadrangle
Olden Street, Princeton, NJ 08544
Tel: 609 258-7318
Fax: 609 258-6109
Email: pmartin@princeton.edu

Mavriplis, Dimitri
ICASE MS 132C
NASA Langley Research Center
Hampton, VA 23681
USA
Tel: 757-864-2213
Fax: 757-864-6134
Email: dimitri@icase.edu

Meinke, Matthias
Aerodynaisches Institut
RWTH Aachen, 52062 Aachen
Wullnerstr.zw 5 u. 7
Germany
Tel: +49-241-805417
Fax: +49-241-8888257
Email: matthias@aia.rwth-aachen.de

Meng, Ning
2200 Waterview Pkwy. #1826
Richardson, TX 75080
USA
Email: nmeng@iastate.edu

Mitchell, Brian
GE Corporate Research
and Development
P O Box 8, Bldg. K1-ES203
Schenectady, NY 12301
USA
Tel: 518-387-7845
Fax: 518-387-7104
Email: mitchellb@crd.ge.com

Mitran, Sorin M.
Department of Applied Mathematics
University of Washington
Box 352420
Office 408C
Seattle, WA 98195-2420
USA
Tel: 206-685-9298
Fax: 206-685-1440
Email:
mitran@amath.washington.edu

Miyake, Yutaka
Department of Mechano-physics
Graduate School of Osaka University
2-1 Yamada-oka
Suita 565-0871
Japan
Tel: +81-6-6879-7248
Fax: +81-6-6879-7250
Email: miyake@mech.eng.osaka-u.ac.jp

Nakamori, Ichiro
Complex Flow Systems Laboratory
Complex Flow Division
Institute of Fluid Science
Tohoku University, Sendai
Japan
Tel: +81-22-217-5229
Fax: +81-22-217-5311
Email:
nakamori@cfs.ifs.tohoku.ac.jp

Nakayama, Akihiko
Graduate School of Science and
Technology
Kobe University
1-1 Rokkodai, Nada-ku
Kobe 657-8501
Japan
Fax: +81-78-803-6011
Email: nakayama@kobe-u.ac.jp

Pantelis, Garry
School of Aerospace
Mechanical and Mechatronic Eng.
University of Sydney
Sydney NSW 2006
Australia
Tel: +61-2-9351-2591
Fax: +61-2-9351-7060
Email: gpa@mech.eng.usyd.edu.au

Peltier, Leonard Joel
The Applied Research Laboratory
The Pennsylvania State University
P O Box 30
State College, PA 16804
USA
Tel: 814-863-3014
Fax: 814-865-8896
Email: ljp@wt.arl.psu.edu

Piller, Marzio
Dipartimento di Ingegneria Navale
del Mare e per l'Ambiente-Sezione
di Fisica Tecnica
University of Trieste, 34127 Trieste
Italy
Tel: +38-040-676-3502
Fax: +39-040-572033
Email: piller@univ.trieste.it

Piomelli, Ugo
Department Of Mechanical
Engineering
University of Maryland
College Park, MD 20742
USA
Tel: 301-405-5254
Fax: 301-314-9477
Email: ugo@eng.umd.edu

Pletcher, Richard
Department of Mechanical Engineering
Iowa State University
Ames, IA 50011
USA
Tel: 515-294-2656
Fax: 515-294-3261
Email: pletcher@iastate.edu

Pruett, C. David
Dept. of Mathematics & Statistics
MSC 7803,
James Madison University
Harrisonburg, VA 22807, USA
Tel: 540-568-6227
Fax: 540-568-6857
Email: dpruett@math.jmu.edu

Rizzetta, Donald P.
AFRL/VAAC
Bldg. 146 Room 225
2210 Eight Street
WPAFB, OH 45433-7521
USA
Tel: 937-904-4077
Fax: 937-656-7867
Email: rizzetta@vaa.wpafb.af.mil

Sagaut, Pierre
ONERA
DSNA/ETRI
29, Avenue de la Division Leclerc
92320 Chatillon
France
Tel: (33) 01 46 73 42 71
Fax: (33) 01 46 73 41 66
Email: sagaut@onera.fr

Satofuka, Nobuyuki
Department of Mechanical Engineering
Kyoto Institute of Technology
Matsuzaki Gosho Kaidou-cho
Sakyou-ku,Kyoto 606-0962
Japan
Tel: +81-75-724-7312
Fax: +81-75-724-7390
Email: satofuka@ipc.kit.ac.jp

Shan, Hua
Department of Mathematics
Box 19408
University of Texas at Arlington
Arlington, TX 76019
USA
Tel: 817-272-7119
Fax: 817-272-5802
Email: hshan@omega.uta.edu

Shu, Chi-Wang
Division of Applied Mathematics
Brown University
Providence, RI 02912
USA
Tel: 401-863-2549
Fax: 401-863-1355
Email: shu@cfm.brown.edu

Smith, Brian R.
Lockheed Martin Aeronautics
P. O. Box 748, MZ 9333
Fort Worth, TX 76101
USA
Tel: 817-935-1127
Fax: 817-935-1212
Email:
Brian.R.Smith@lmco.com

Sudduth, R.D.
Chemical Engineering
University of Louisiana at Lafayette
Lafayette, LA 70504
USA
Tel: 337-482-6837
Email: richsudduth@earthlink.net

Taniguchi, Nobuyuki
Institute of Industrial Science
University of Tokyo
4-6-1, Komaba, Meguro-Ku
Tokyo,153-8505, Japan
Tel: 81-3-5841-2741
Fax: 81-3-5452-6196
Email: ntani@iis.u-tokyo.ac.jp

Tokunaga, Hiroshi
Department of Mechanical & System Engineering
Kyoto Institute of Technology
Matsugasaki
Sakyo-ku, Kyoto 606-8585
Japan
Tel: 81+75-724-7314
Fax: 81+75-724-7300
Email: tokunaga@ipc.kit.ac.jp

Tsujimoto, Koichi
Department of Mechanical Engineering
Osaka University
2-1 Yamada-oka, Suita 565-0871
Japan
Fax: +81-6-6879-7250
Tel : +81-6-6879-7250
Email:
tujimoto@mech.eng.osaka-u.ac.jp

Tyagi, Mayank
Mechanical Engineering Department
Louisiana State University
Baton Rouge, LA 70803
USA
Tel: 225-578-5217
Fax: 225-578-9195
Email: tyagi_mayank@hotmail.com

Uittenbogaard, Rob
Delft Hydraulics
P O Box 177
2600 M H Delft
The Netherlands
Tel: +31 15 285 87 81
Fax: +31 15 285 85 82
Email: rob.uittenbogaard@wldelft.nl

Vasilyev, Oleg V.
E2411 Engr. Bldg. East
Mechanical & Aerospace Engineering
University of Missouri-Columbia
Columbia, MO 65211, USA
Tel: 573-882-3755
Fax: 573-884-5090
Email: VasilyevO@missouri.edu

Veenman, M. P. B.
Section of Process Technology
Dept. of Mechanical Engineering
Eindhoven University of Technology
P.O. Box 513, 5600 MB Eindhoven
The Netherlands
Tel: +31-0-40-2472135
Email: M.P.B.Veenman@tue.nl

Verstappen, Roel
Dept. of Math
University of Groningen
P O Box800
Groningen NL-9700AV
The Netherlands
Tel: +31-503633958
Fax: +31-503633800
Email: verstappen@math.rug.nl

Visbal, Miguel R
AFRL/VAAC
Bldg. 146 Room 225
2210 Eight Street
WPAFB, OH 45433-7521
USA
Tel: 937-255-2551
Fax: 937-656-7867
Email: visbal@vaa.wpafb.af.mil

Wang, Liqiu
Department of Mechanical Engineering
The University of Hong Kong
Pokfulam Road
Hong Kong
Tel: 852-2859-7908
Email: lqwang@hku.hk

Xia, Jian
Department of Mathematics
University of Texas at Arlington
Arlington, TX 76019, USA
Tel: 817-272-7527
Fax: 817-272-5802
Email: jxia@uta.edu

DNS/LES - Progress and Challenges

Proceedings of the Third AFOSR International Conference on DNS/LES
University of Texas at Arlington, Arlington, Texas, USA
August 5-9, 2001

Chaoqun Liu, Leonidas Sakell, Thomas Beutner (Eds.)

This book is a collection of papers presented in the Third AFOSR International conference on Direct Numerical Simulation and Large Eddy Simulation (TAICDL), University of Texas at Arlington, Arlington, Texas, USA, August 5-9, 2001. The conference attracted 104 participants from 15 countries and regions. The book includes 18 invited papers and 71 contributed papers which cover a broad range of topics related to DNS and LES including the LES methodology and mathematical foundation, advanced numerical methods, high-order schemes for shock capturing in particular, DNS and LES applications toward understanding fundamental flow physics, flow instability and transition, aeroacoustics, flow control, combustion, complex flow and some real engineering applications, etc. A panel discussion on the DNS/LES demands, capability, critical problems, validation, and future development is also documented.

ISBN 1-57074-488-2

Chaoqun Liu
Leonidas Sake
Thomas Beutn

DNS/LES Progress and Challenges